

Junbo Jia

Soil Dynamics and Foundation Modeling

Offshore and Earthquake Engineering

 Springer

Soil Dynamics and Foundation Modeling

Junbo Jia

Soil Dynamics and Foundation Modeling

Offshore and Earthquake Engineering

 Springer

Junbo Jia
Aker Solutions
Bergen
Norway

ISBN 978-3-319-40357-1 ISBN 978-3-319-40358-8 (eBook)
<https://doi.org/10.1007/978-3-319-40358-8>

Library of Congress Control Number: 2017956333

© Springer International Publishing AG 2018

This work is subject to copyright. All rights are reserved by the Publisher, whether the whole or part of the material is concerned, specifically the rights of translation, reprinting, reuse of illustrations, recitation, broadcasting, reproduction on microfilms or in any other physical way, and transmission or information storage and retrieval, electronic adaptation, computer software, or by similar or dissimilar methodology now known or hereafter developed.

The use of general descriptive names, registered names, trademarks, service marks, etc. in this publication does not imply, even in the absence of a specific statement, that such names are exempt from the relevant protective laws and regulations and therefore free for general use.

The publisher, the authors and the editors are safe to assume that the advice and information in this book are believed to be true and accurate at the date of publication. Neither the publisher nor the authors or the editors give a warranty, express or implied, with respect to the material contained herein or for any errors or omissions that may have been made. The publisher remains neutral with regard to jurisdictional claims in published maps and institutional affiliations.

Printed on acid-free paper

This Springer imprint is published by Springer Nature
The registered company is Springer International Publishing AG
The registered company address is: Gewerbestrasse 11, 6330 Cham, Switzerland

*To my beloved Danning and Jing, who make
life a gift.*

Preface

Offshore and land-based structures represent large capital investments. They are designed to withstand various types of environmental loads such as earthquakes, winds, ocean waves, tidal currents, and ice, and other loads due to explosions, machinery vibrations, dropped objects, and other factors. Many of them essentially induce dynamic and cyclic loading transferred into foundations. Therefore, understanding soil dynamics and foundation modeling is essential to ensure foundation and structural integrity and operational functionality. However, in spite of increased engineering knowledge, practical problems regarding foundation modeling and soil dynamics are in many cases handled unsuccessfully despite large expenditures. Moreover, even if engineers can perform sophisticated computer-based analysis tasks, many of them lack an actual understanding of the essential principles of soil dynamics and foundation modeling, and hence of the links between theory and applications. This leads to an insurmountable barrier when they are asked to validate/verify and provide insightful explanations of analysis results, or to further improve designs, which poses a significant safety hazard and can also result in significant economic loss.

With the objective of providing practical knowledge of foundation modeling and dynamic analysis, which is essential for both offshore and earthquake engineering, the book covers a wide range topics in this area, such as soil behavior, soil dynamics, seismic site-response analysis, soil–structure interactions, liquefactions, and modeling and assessment of shallow and deep foundations, considering various levels of detail and associated engineering challenges. Differences in soil and foundation modeling and response due to earthquake and ocean wave loading are also discussed. To facilitate the understanding and utilization of knowledge for each topic, general theory and principles are linked to their engineering applications. Moreover, recent developments in offshore foundation engineering such as anchor piles, suction piles, large-diameter piles, soil aging effects, and scours are also discussed. Special focus is placed on their engineering applications utilizing state-of-the-art knowledge.

Although offshore geotechnical principles are very similar to those of land-based structures, for offshore geotechnical engineering applications, soil conditions are often more difficult to measure and have larger uncertainties, site investigations are more expensive, and structural loads are usually more significant. Further, the focus of offshore geotechnical design is often placed on capacity control, while foundation stiffness remains important for the dynamic response of soil–foundation–structure systems.

Chapter 1 presents the basics of soil mechanics and behaviors, methods for testing soil strength, and their implications in geotechnical designs. Chapter 2 introduces the characteristics and modeling of soil properties under cyclic and dynamic loading, focused on treating soil nonlinearities. Chapters 3 and 4 present details of site-response analysis with a focus on how the response amplification and de-amplification of soil media are accounted for, and how to apply seismic excitations in a site-response analysis. Chapter 5 describes soil–structure interactions and analysis, which estimate the collective response of the entire soil–foundation–structure system to specified ground motions by accounting for effects of kinematic interaction (normally by site-response analysis), soil–foundation flexibility (foundation impedance), and inertia interaction (seismic structural analysis) and which can be performed by either direct or substructure approaches. Chapter 6 introduces various seismic testing methods including field testing, laboratory element testing, and model testing. Chapter 7 presents the causes and evaluation of soil liquefactions, followed by presentations of slope stability due to seismic loading presented in Chap. 8. Chapter 9 provides a general overview of offshore structures and their common and distinguishing features compared to those of land-based structures and also presents the hydrodynamic modeling to determine the ocean environmental loading in a seismic analysis. Chapters 10 and 11 present the theoretical background of seismic response spectrum and power spectrum and how earthquake loading is determined from a seismic hazard point of view. Chapters 12 and 13 present the bearing capacity assessment and modeling for shallow foundations. Chapters 14–26 discuss various aspects of pile foundations, such as pile capacity assessment, pile–soil interactions, large-diameter piles, pile group, grout connections, torsional behaviors of piles, scour, seismic assessment of piles, anchor piles, and suction piles. In Chap. 27, design issues for shallow and deep foundations, relevant international design codes, and hierarchy of codes and standards are briefly discussed.

The book is intended to serve as an introduction to the subject and also as a reference book with advanced topics. A balance between the theoretical and practical aspects is sought. All the chapters are addressed to practitioners who are looking for answers to their daily engineering problems, and to students and researchers who are looking for links between theoretical and practical aspects, and between phenomena and analytical explanations. It should also be of use to other science and engineering professionals and students with an interest in this subject.

The book is written in such a way that it can be followed by anyone with a basic knowledge of engineering dynamics and soil mechanics.

While the book does not seek to promote any specific “school of thought,” it inevitably reflects this author’s “best practice” and “working habits.” This is particularly apparent in the topics selected and the level of detail devoted to each of them, their sequences, the choices of mathematical treatments and symbolic notations, etc. The author hopes that this does not deter readers from seeking to find their own “best practice.”

Most of the chapters in this book can be covered in a two-day industry course in a brief manner, a one-week intensive course for either industry or academia, or a one-semester course in an elaborated form for graduate students.

In preparing such a text, it is rather difficult to acknowledge all the help given to the author. First, I am indebted to geotechnical, earthquake, and offshore engineering communities who have undertaken the extensive research and development that has led to accumulated knowledge, methods, and engineering applications in this field, on which this book is based. I would also like to thank individuals for assistance of various kinds, such as participation in book reviews, technical discussions, and research cooperation. These include (in alphabetical order) the following: Atilla Ansal (European Association for Earthquake Engineering), Kuvvet Atakan (University of Bergen), Gunnar Bremer (Aker Solutions), Ove Tobias Gudmestad (University of Stavanger), Yingcai Han (Fluor Canada), Nils-Christian Hellevig (Aker Solutions), Viggo Karlsen (Statoil), Amir M. Kaynia (Norwegian Geotechnical Institute), Steven L. Kramer (University of Washington), BM Lehane (The University of Western Australia), Conrad Lindholm (NORSAR), Lance Manuel (University of Texas at Austin), Peter Middendorp (Allnamics Geotechnical & Pile Testing Experts), George Mylonakis (University of Bristol), Laurens de Neef (CAPE Holland), Giuliano F. Panza (University of Trieste and China Earthquake Administration), John Michael Rotter (University of Edinburgh and Imperial College), Richard Snell (Oxford University), Douglas Stock (Digital Structures, Inc. Berkeley), Gary Torosian (GeoTesting Express, Inc.), and RJS Whitehouse (HR Wallingford). Furthermore, I would like to thank Norwegian Geotechnical Institute, Statoil, DongEnergy, BP, and DNV-GL for their cooperation on relevant engineering projects. Moreover, there are numerous others not named to whom I extend my sincere thanks.

This book has an extensive list of references reflecting both the historical and recent developments of the subject. I would like to thank all the authors in the references for their contribution to the area.

Most importantly, I dedicate this book to my parents Shufeng and Wangeng, my wife Jing, and daughter Danning; I conclude this preface with an expression of deep gratitude to them.

About this Book

This book presents a comprehensive topical overview of soil dynamics and foundation modeling in offshore and earthquake engineering. The spectrum of topics covered includes, but is not limited to, soil behavior, offshore and land-based structures, soil dynamics, seismic testing, site-response analysis, representation and determination of seismic ground motions, seismic hazard assessment, soil liquefactions, slope stability, offshore environmental loads, earthquake loads, modeling and assessment of shallow and deep foundations, soil–foundation interactions, and relevant design codes and recommended practices, design methods. The author provides the reader with both theory and practical applications and links the methodological approaches with engineering applications. The book also contains recent developments in offshore foundation engineering such as large-diameter piles, anchor piles, suction piles, soil aging effects, and scour estimation. The target audience primarily comprises research experts and practitioners in the field of offshore, geotechnical, and earthquake engineering, but the book is also beneficial for graduate students.

Contents

Part I Soil Behavior and Dynamics

1	Soil Behavior	3
1.1	Introduction	3
1.2	Soil Classification	3
1.3	Saturation, Water Table, Drainage, and Capillary Effect	5
	1.3.1 Saturation	5
	1.3.2 Drainage	6
	1.3.3 Water Table	7
	1.3.4 Capillary Effect	8
1.4	Effective Stress	8
1.5	Mohr's Circle for Describing Stress Condition	13
1.6	Soil Failure	17
	1.6.1 Shear Failure for Cohesionless Soils	18
	1.6.2 Shear Failure for Cohesive Soils	18
1.7	Total Stress Analysis Versus Effective Stress Analysis	21
1.8	Clay Soil Consistency	22
1.9	Testing Methods to Measure Shear Strength	24
	1.9.1 Laboratory and Field Test Methods	24
	1.9.2 Direct Shear Test	24
	1.9.3 Triaxial Shear Test	25
	1.9.4 Vane Shear Test	29
	1.9.5 Standard Penetration Test (SPT)	31
	1.9.6 Cone Penetration Test (CPT)	36
	1.9.7 Other in Situ Testing Methods	42
1.10	Soil Stiffness and Poisson's Ratio	42
1.11	Consolidation	46
	1.11.1 Introduction to Consolidation	46
	1.11.2 Effects of Consolidation on Soil Stiffness	47
	1.11.3 Effects of Consolidation for Shallow Foundations	48

1.11.4	Effects of Consolidation and Aging for Deep Foundations	50
1.12	Obtaining Soil Parameters for Engineering Design	53
1.13	Allowable Stress Design and Load Resistance Factor Design	56
1.13.1	Allowable Stress Design	56
1.13.2	Load Resistance Factor Design	56
1.13.3	Levels of Reliability Method	69
1.13.4	Essential Differences Between LRFD and ASD	70
1.13.5	Applying Partial Safety Factors in Geotechnical Analysis	71
1.14	Incorporating Uncertainties of Soil Parameters	71
1.15	General Soil Conditions at Offshore Sites Worldwide	73
2	Dynamic and Cyclic Properties of Soils	75
2.1	Introduction	75
2.2	Equivalent Linear Soil Models	78
2.2.1	Equivalent Shear Modulus Modeling	78
2.2.2	Determination of G_{\max}	82
2.2.3	Equivalent Damping Modeling	86
2.3	Soil Stiffness and Damping Modeling in an Equivalent Linear Model	89
2.3.1	Trends in Dynamic Soil Properties and Strain Thresholds	89
2.3.2	Stiffness Modeling	93
2.3.3	Damping Modeling	95
2.4	Nonlinear Soil Models	97
2.4.1	General	97
2.4.2	Cyclic Nonlinear Soil Models	98
2.4.3	Small Strain Damping Modeling in Time-Domain Analysis	100
2.4.4	Nonlinear Constitutive Soil Models	103
2.5	Strain Rate Effects Due to Seismic Loading	106
2.6	Differences Between Soil Properties Subjected to Earthquake Loadings and Ocean Wave Loadings	107
3	Site-Response Analysis in Geotechnical Earthquake Engineering	109
3.1	General	109
3.2	Site Period	115
3.2.1	General	115
3.2.2	Influence of Soil Depth on the Site Period	119
3.3	Non-stationary and Peak Ground Motions	121
3.3.1	Peak Ground Motions and Their Relationship with Magnitude and Intensity	121

3.3.2	Contribution of Body and Surface Wave to Ground Motions	124
3.3.3	Moving Resonance	125
3.4	Measuring Soil Amplification or De-amplification	126
3.5	One-Dimensional Site-Response Analysis	126
3.5.1	One-Dimensional Seismic Wave Propagation Analysis	126
3.5.2	One-Dimensional Frequency-Domain Site-Response Analysis Using Equivalent Linear Soil Model	133
3.5.3	One-Dimensional Site-Response Analysis Using Nonlinear Soil Models	143
3.6	Surface (Topographic) and Subsurface Irregularities	146
3.6.1	General	146
3.6.2	Effects of Irregular Surface Topology	147
3.6.3	Effects of Subsurface Irregularity	149
3.7	Two- and Three-Dimensional Site-Response Analyses	151
3.7.1	Applicability of One-, Two-, and Three-Dimensional Site-Response Analyses	151
3.7.2	Seismic Wave Propagation Effects	152
3.7.3	Site Geometric Effects	155
3.8	Using Site-Response Analysis Results for Seismic Analysis	159
3.9	Characteristics of Site Responses	159
3.9.1	Horizontal Ground Motions	159
3.9.2	Vertical Ground Motions	161
3.10	Vertical Ground Motion Calculations	162
3.10.1	Site-Response Analysis for Calculating Vertical Ground Motions	162
3.10.2	V/H Spectrum	163
3.11	Water Column Effects on Seismic Ground Motions	165
4	Record Selection for Performing Site-Specific Response Analysis	167
4.1	General	167
4.2	Selections of Motion Recordings	168
4.3	Modification of the Recordings to Fit into the Design Rock Spectrum	169
4.3.1	Direct Scaling	169
4.3.2	Spectrum/Spectral Matching	169
4.3.3	Pros and Cons of Direct Scaling and Spectrum Matching	173
4.4	Performing the Site-Response Analysis Using Modified/Matched Recordings	174
4.5	Sources of Ground Motion Recording Data	175

5	Soil–Structure Interaction	177
5.1	Introduction	177
5.2	Direct and Substructure Approach	178
	5.2.1 Direct Analysis Approach	178
	5.2.2 Substructure Approach	178
5.3	Kinematic Interaction	180
	5.3.1 Objective	180
	5.3.2 Applications	181
5.4	Subgrade Impedances and Damping	181
	5.4.1 Objective	181
	5.4.2 Applications for Pile Foundations	181
	5.4.3 Applications for Shallow Foundations	182
5.5	Inertial Interaction	184
	5.5.1 Objective	184
	5.5.2 Applications	186
5.6	Effects of Soil–Structure Interaction	186
5.7	Boundary Modeling in Geotechnical Analysis	187
5.8	Remarks on Substructure Approach	189
6	Seismic Testing	191
6.1	Introduction	191
6.2	Field Testing	192
	6.2.1 General	192
	6.2.2 Low-Strain Field Test	192
	6.2.3 High-Strain Field Test	210
6.3	Laboratory Element Testing	211
	6.3.1 Low-Strain Element Test	211
	6.3.2 High-Strain Element Test	217
6.4	Model Testing	218
	6.4.1 Shaking Table Test	218
	6.4.2 Centrifuge Test	224
7	Liquefaction	227
7.1	Introduction to Liquefaction	227
	7.1.1 Causes of Liquefactions	227
	7.1.2 Liquefaction Damages	231
7.2	Evaluation of Liquefaction Initiation	236
	7.2.1 Introduction	236
	7.2.2 Cyclic Stress Approach	237
	7.2.3 Cyclic Strain Approach	248
7.3	Liquefaction Mitigations	249
8	Slope Stability Due to Seismic Loading	251
8.1	General	251
8.2	Pseudo-Static Analysis Approach	252

- 8.3 Dynamic Stress-Deformation Analysis Approach 255
- 8.4 Newmark Sliding-Block Approach 256
 - 8.4.1 Rigid-Block Analysis 257
 - 8.4.2 Decoupled Analysis 259
 - 8.4.3 Coupled Analysis 260
 - 8.4.4 Selection of Analysis Methods 260
 - 8.4.5 Potential of Landslides Based on the Predicted Displacement 261
- 8.5 Testing Method 262
- 8.6 Post-Earthquake Slope Instability Assessment 262
- 8.7 Landslides 263
 - 8.7.1 General 263
 - 8.7.2 Assessment of Regional Landslide Potential by Arias Intensity 264

Part II Offshore Structures and Earthquake Engineering

- 9 Offshore Structures and Hydrodynamic Modeling 269**
 - 9.1 Introduction to Offshore Structures 269
 - 9.1.1 Offshore Platforms 269
 - 9.1.2 Offshore Wind Turbine Substructures and Foundations 277
 - 9.2 Dynamic Design of Structures 283
 - 9.2.1 Dynamics Versus Statics 283
 - 9.2.2 Characteristics of Dynamic Responses 288
 - 9.2.3 Frequency Range of Dynamic Loading 294
 - 9.3 Difference Between Offshore and Land-Based Structures 299
 - 9.4 Hydrodynamic Modeling of Offshore Structures 302
 - 9.4.1 Introduction to Hydrodynamic Force Calculation 302
 - 9.4.2 Effects of Drag Forces 308
 - 9.4.3 Effects and Determination of Added Mass 308
 - 9.4.4 Effects of Buoyancy 310
 - 9.4.5 Effects and Modeling of Marine Growth 311
- 10 Representation of Seismic Ground Motions 315**
 - 10.1 General 315
 - 10.2 Earthquake Excitations Versus Dynamic Ocean Wave, Wind, and Ice Loading 316
 - 10.3 Power Spectrum of Seismic Ground Motions 319
 - 10.3.1 Introduction to Fourier and Power Spectrum 319
 - 10.3.2 Power Spectrum of Seismic Ground Motions 328
 - 10.4 Response Spectrum 330
 - 10.4.1 Background 330
 - 10.4.2 Elastic Response and Design Spectrum 332

- 10.4.3 Ductility-Modified (Inelastic) Design Spectrum Method 351
- 10.5 Time History Method 357
 - 10.5.1 General Method 357
 - 10.5.2 Drift Phenomenon and Its Correction 358
- 11 Seismic Hazard Assessment 363**
 - 11.1 Seismic Hazard Analysis 363
 - 11.1.1 Introduction 363
 - 11.1.2 Deterministic Seismic Hazard Analysis (DSHA) 365
 - 11.1.3 Probabilistic Seismic Hazard Analysis (PSHA) 367
 - 11.1.4 Deaggregation (Disaggregation) in PSHA for Multiple Sources 385
 - 11.1.5 Logic Tree Method 390
 - 11.2 Seismic Hazard Map 392
 - 11.3 Apply PSHA for Engineering Design 395
 - 11.4 Conditional Mean Spectrum 399
 - 11.5 The Neo-deterministic Approach 405
 - 11.6 Forecasting “Unpredictable” Extremes 409

Part III Shallow Foundations

- 12 Bearing Capacity of Shallow Foundations 413**
 - 12.1 Introduction 413
 - 12.2 Failure of Shallow Foundations 415
 - 12.3 Bearing Capacity of Drained Soil 421
 - 12.3.1 Bearing Capacity Due to General Shear Failure 421
 - 12.3.2 Bearing Capacity Due to Local and Punching Shear Failure 425
 - 12.3.3 Bearing Capacity for Layered Soil 426
 - 12.4 Bearing Capacity for Undrained Clay 426
 - 12.5 Bearing Capacity of Unliquefiable Soil Subjected to Seismic Loading 427
 - 12.6 Bearing Capacity Control of Soils with Liquefaction Potential Subjected to Seismic Loading 428
 - 12.7 Sliding Stability of Shallow Foundations 430
 - 12.8 Effects of Cyclic Loading on Shallow Foundations 430
 - 12.9 Piping Actions and Scour for Shallow Foundations 432
- 13 Modeling of Shallow Foundation Dynamics 435**
 - 13.1 Foundation Impedance 435
 - 13.2 Combination of Damping for Foundations and Superstructures 450

Part IV Pile Foundations

14 Introduction to Deep Foundations 455

15 Capacity Control, Modeling of Pile Head Stiffness, and Mitigation Measures to Increase Pile Capacity 465

15.1 Capacity Control of Pile Foundations 465

15.2 Representation of Piles, Surrounding Soils, and Soil–Pile Interactions 467

15.3 Winkler Foundation Modeling 472

15.4 Simplified Calculation of Pile Stiffness and Natural Frequency for Pile–Structure System 475

15.4.1 Stiffness of Pile–Structure System 475

15.4.2 Pile Head Stiffness 477

15.4.3 Natural Frequency of Non-uniform Beams 477

15.5 Increasing Existing Pile Foundation Capacity for Offshore Structures 480

16 Lateral Force–Displacement of Piles— p - y Curve 481

16.1 Introduction to p - y Curve 481

16.2 Calculation of p_u for Clays 486

16.3 Calculation of p_u for Sands 490

16.4 Constructing p - y Curves for Clays 491

16.5 Constructing p - y Curves for Sands 495

16.6 Effects of Cyclic Loading on p - y Curves and Structural Dynamic Response 498

16.7 Effects of Dynamic Loading on p - y Curves 503

16.8 Effects of Pile Diameter on Lateral Load–Displacement Behavior 505

16.8.1 Introduction 505

16.8.2 Effects of Pile Diameter Under Sand Soil Conditions 508

16.8.3 Effects of Pile Diameter Under Clay Soil Conditions 512

16.9 Hybrid Spring Model for Modeling Piles’ Lateral Force–Displacement Relationship 518

17 Axial Force–Displacement of Piles: t - z and Q - z Curve 521

17.1 Pile–Soil Modeling Under Axial Pile Loading 521

17.2 Axial Compression Capacity 522

17.3 Axial Tension Capacity 529

17.4 Determining Unit Friction Capacity for Cohesive Soils 531

17.4.1 Friction Capacity for Highly Plastic Clays by API 531

17.4.2 Friction Capacity for Other Types of Clays by API 532

17.4.3	Friction Capacity by Revised API Method (α -Method)	533
17.4.4	Friction Capacity for Long Piles in Clay	533
17.4.5	β -Method	534
17.4.6	λ -Method	535
17.5	Determining Unit Friction Capacity for Cohesionless Soils . . .	535
17.5.1	Unit Friction Capacity by API 1993 Method	536
17.5.2	Unit Friction Capacity by API 2000 Method	537
17.6	Modeling of Pile–Soil Friction Behavior by FEM	538
17.7	Modeling of t - z Curves	539
17.8	Determining Unit End-Bearing Capacity for Cohesive Soils . . .	540
17.9	Determining Unit End-Bearing Capacity for Cohesionless Soils	541
17.10	Modeling of Q - z Curves	541
17.11	Effects of Soil Layer Boundaries on End-Bearing Capacity . . .	542
17.12	Soil Plugging	543
17.13	Recently Developed CPT-Based Methods to Assess the Axial Pile–Soil Interaction Capacity	545
17.13.1	Skin Friction Calculation for CPT-Based Method . . .	546
17.13.2	End-Bearing Capacity Calculation for CPT-Based Method	548
17.13.3	Comments on the CPT-Based Methods	552
17.14	Ultimate End-Bearing Capacity from Tests	554
17.15	Effects of Cyclic Loading on Axial Capacity of Piles	554
18	Torsional Moment–Rotation Relationship	559
18.1	General	559
18.2	Behavior of Single Piles Under Torsion	560
18.3	Behavior of Pile Groups Under Torsion	564
19	Modeling, Response Calculation, and Design of Piles Under Seismic Loading	565
19.1	Loading of Piles During Earthquakes	565
19.2	Pseudo-static Approach	568
19.2.1	Inertia Loading on Piles	568
19.2.2	Kinematic Loading and Pile Response	569
19.3	The Location for Transferring the Earthquake Input Energy from Soils to Piles or Shallow Foundations	576
19.4	Simple Modeling of Pile Impedance	577
19.5	Determination of Pile Impedance	579
19.6	Kinematic and Inertia Loading Modeling in the Direct Analysis Approach	584

- 20 Scour for Pile Foundations 589**
 - 20.1 Introduction to Scour 589
 - 20.2 Influence of Scours 592
 - 20.3 Scour Modeling 595
 - 20.4 Determination of Scour Depth for Single Piles
and Bridge Piers 595
 - 20.5 Scour Depth Influenced by Pile Groups 597
 - 20.6 Influence of Scour on Pile’s Capacity 599
 - 20.6.1 Influence of Scour on Axial Pile Capacity 599
 - 20.6.2 Influence of Scour on Lateral Pile Capacity 600
 - 20.6.3 The Consideration of Scour in Pile Designs
by DNV-OS-J101 600
- 21 Effects of Pile Group, Adjacent Structures, and Construction
Activities 601**
 - 21.1 Introduction to Pile Group 601
 - 21.2 Pile Group Effects Under Axial Loading 605
 - 21.2.1 General 605
 - 21.2.2 Modifying Friction Resistance 608
 - 21.2.3 Modifying Tip Resistance 609
 - 21.3 Pile Group Effects Under Lateral Loading 609
 - 21.3.1 General 609
 - 21.3.2 Modifying Soil Resistance 612
 - 21.4 Effects of Cyclic Loading on Pile Group Behavior 615
 - 21.5 Effects of Dynamic Loading on Pile Group Behavior 615
 - 21.5.1 General 615
 - 21.5.2 Modifying Pile Resistance Due to Dynamic
Loading 615
 - 21.6 Modifying Pile Displacement to Account for Both Pile Group
and Dynamic Loading Effects 616
 - 21.7 Pile Cap 618
 - 21.8 Influence of Adjacent Structures and Construction Activities
on the Existing Piled Foundations 619
 - 21.8.1 Problem Description 619
 - 21.8.2 Pile–Soil Interaction Influenced by the Presence
of Spudcan 620
 - 21.8.3 Influence of Pile–Soil Interaction Due to
Construction Activities 622
- 22 Grout Connections 625**
 - 22.1 Introduction 625
 - 22.2 Grout Connection Capacity Control 627
 - 22.3 Typical Mechanical Properties of Grout 627

23	Vertical Piles Versus Inclined/Battered/Raked Piles	629
23.1	Introduction to Inclined/Battered Piles	629
23.2	Seismic Performance of Pile Groups with Battered Piles	629
23.3	Wave- and Wind-Induced Response of Pile Group with Battered Piles	632
24	Negative (Downward) Friction and Upward Movement	637
24.1	Negative Friction	637
24.2	Upward Movement	640
25	Anchor Piles	641
25.1	Introduction	641
25.2	Behavior of Anchor Lines	643
25.2.1	Behavior of Anchor Lines on Seabed	643
25.2.2	Behavior of Buried Anchor Lines	644
25.3	Anchor Pile Padeye(s)	646
25.4	Seismic Response of Anchor Pile	648
25.5	Required Safety Factors for Offshore Anchor Pile Design	648
25.6	Fatigue Capacity Control of Anchor Line–Pile Connection	649
25.6.1	Method	649
25.6.2	Derivation of Hot-Spot Stress	652
26	Suction Piles/Caissons	655
26.1	Introduction	655
26.2	Suction Pile Installations	656
26.3	Modeling and In-place Capacity Control for Suction Piles	658
26.4	Modeling of Suction Piles Subjected to Seismic Loading	661
26.5	Advantages of Suction Piles/Caissons	664
26.6	Engineering Applications	665
26.6.1	Application for Offshore Structures	665
26.6.2	Application as Deep-Water Anchors	667
26.6.3	Application for Subsea Production Facility Foundations	668
27	General Design Issues for Offshore Foundations and Relevant International Codes and Guidelines	669
	Appendix	673
	References	675
	Index	727

About the Author

Dr. Junbo Jia is an engineering expert at Aker Solutions, Norway. He is currently a committee member of ISO TC67/SC7 Fixed Steel Structures and an invited member of Eurocode 3. He has been invited as speakers and lecturers for industry training and university graduate courses, and permanent members of Ph.D. examination committees by various organizations and research institutes. Dr. Jia has published two other Springer engineering monographs on Applied Dynamic Analysis and Seismic Engineering. He is currently editing a handbook volume entitled “Structural Engineering in Vibrations, Dynamics and Impacts”, to be published by CRC press.

Part I

Soil Behavior and Dynamics

All land-based or fixed offshore structures transfer their loads to the earth through foundations, either directly or indirectly. For floating offshore structures, it is also important to have a reliable anchor solution to “fix” the structures, which needs sufficiently strong anchor(s) fixed to the earth. Therefore, foundations are critical components for ensuring global stability, transferring loads from the upper structures down to base soils or rocks.

Figure 1.1 shows the Leaning Tower of Pisa. Designed to be vertical, it started leaning during its construction, which began in 1173. By 1990, it was leaning 5.5° . Its tilt is mainly caused by an inadequate foundation on ground that on one side is too soft to support the structure’s weight. The tower was closed from 1990 to 2001 due to fears of an imminent collapse. By siphoning earth from beneath and adding counterweights to the tower’s north end, the tilt of the tower was reduced to 4.0° . The straightening continued after the tower reopened in 2001, and in 2008, sensors showed the subsiding motion had stopped. Engineers now believe that the Leaning Tower of Pisa will remain stable for some 200 years and can sustain a design earthquake.

The capacity of the earth to support various types of loadings depends on the strength and stability of the supporting soil and/or rock materials. In geotechnical earthquake engineering, not only is the behavior and responses of soils and foundations of importance, but how soils and foundations affect seismic wave propagations and the subsequent loading transferred to main structures are also of great interest.

Part I presents basic knowledge of behavior and properties of soils (Chap. 1) and its characteristics and modeling under cyclic and dynamic loading (Chap. 2), followed by a discussion on methods used to evaluate: (1) seismic ground motions through local dynamic site-response analysis (Chaps. 3 and 4); (2) soil—structure



Fig. 1.1 Leaning Tower of Pisa, with a height of 55.86 m

interactions (Chap. 5); (3) liquefactions (Chap. 7); and (4) slope stability subject to seismic loading (Chap. 8). Moreover, seismic testing methods for characterizing soil behavior and examining seismic performances of foundations are also presented in Chap. 6.

In geotechnical earthquake engineering, it is important to implement proper mitigation measures to increase the foundation resistance. These include, for example, soil improvement using measures such as densification, reinforcement, grouting, drainage; selecting ground topology and site conditions. However, as such measures do not fall within the scope of the current book, readers may refer to relevant sources on geotechnical earthquake engineering for information on them. The source by Kramer [1] gives essential coverage on this topic.

Chapter 1

Soil Behavior

1.1 Introduction

This chapter briefly presents the background information on soil mechanics.

The earth's crust comprises both rock and soil, of which the former is a natural aggregate of minerals connected by a strong and permanent cohesive force, and the later is a natural aggregate of mineral grains that can be separated by such gentle mechanical means as agitation in water [2]. In soil dynamics/mechanics, rock is often treated as an elastic or rigid medium, while the modeling of soils usually requires more detailed consideration, as will be discussed in this book.

As shown in Fig. 1.1, soil can be regarded as a gathering of particles/grains. Most of these particles originate from the degradation of rocks and are referred to as mineral particles. Some, meanwhile, originate from residues of plants or animals (rotting leaves, pieces of bone, etc.), and these are called organic particles or organic matter. There are also spaces/voids between particles, and they contain water and/or air, making the soil a three-phase material.

If one digs tens of meters down into soil, one will observe various layers (also called horizons or strata) of soil with different colors and compositions. This succession of soil layers is called the soil profile, as illustrated in Fig. 1.2.

1.2 Soil Classification

Soil can generally be categorized as granular or cohesive. Granular soil consists of gravel, sand, and cohesionless silt. Cohesive soil is normally referred to as clay. These soils can be clearly distinguished by their sizes, as shown in Table 1.1. Granular classification (i.e., cohesive, granular, or mixed) enables engineers to predict the soil's behavior, which has important implications for the mechanical and erosion properties of sediment [3, 4].

Fig. 1.1 Soil can be realized as a skeleton of solid particles enclosing spaces/voids

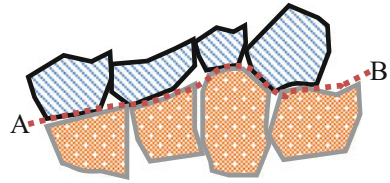


Fig. 1.2 Illustration of soil profile



Table 1.1 Classification of soil type based on particle sizes and shapes

Soil type		Particle size (mm)	Particle shape	Distinguishable with naked eye
Granular soil	Gravel	2–60	Granular	Obviously
	Sand	0.06–2	Granular	Easily
	Silt	0.002–0.06	Granular	Barely
Cohesive soil	Clay	<0.002	Flat plate	Impossible

Regarding mechanical properties, for granular soil, grain-to-grain contact and friction are the governing aspects. Therefore, the magnitude of contact force and the geometrical nature of grain packing play a major role.

For clay, chemical and electrical interactions among clay particles are important. Therefore, the shear strength of clay is activated even at zero effective stress when the past stress–strain history allows it. The degree of cohesion increases with the fraction of clay minerals within the sediment and starts to become significant when the sediment contains more than 5–10% of clay by weight. The most important types of clay minerals are kaolinite, chlorite, montmorillonite, and illite [26].

Sometimes, the terms “clay” and “mud” are incorrectly used as synonymous. Mud is a mixture of water, clay, and silt and also includes organic material and sometimes gas (e.g., hydrogen sulfide resulting from organic decomposition). Mud is generically classified as having particle sizes of less than 63 μm (which includes silt). Conversely, clays have a plate-like structure and generally have a diameter of less than 2 μm .

From the perspective of foundation design, the best sites are obviously those with direct bedrock as the soil surface. Sand and gravel are normally also desirable site conditions, but liquefaction needs to be carefully addressed, as discussed in Chap. 7. Medium-to-hard clay (kept dry) sites are still regarded as good. On the other hand, poor sites are comprised predominately of silts and soft clay, or even organic silts and organic clay.

Soil classification in offshore geotechnical engineering normally follows the Unified Soil Classification System (USCS), which is given in ASTM D2487, ASTM D2488 [5], and BS 5930 [6]. The offshore soil classification for different countries may differ slightly from the one given in USCS.

In the context of soil dynamics, the MIL Handbook for soil dynamics and special design aspects [7] lists four additional items for engineers to categorize soils:

1. Is the material saturated (Sect. 1.3.1)? If it is saturated, a transient dynamic loading (e.g., seismic loading) will usually last for such a short time that the soil's response will be essentially undrained. If it is not saturated, the response to dynamic loadings will probably include some volumetric component.
2. Are there fines present in the soil? The presence of fines, especially clays, not only inhibits the dissipation of excess pore pressure, but also decreases the tendency for liquefaction (Chap. 7).
3. How dense is the soil? Dense soils are not likely to collapse under dynamic loads, but loose soils may. Loose soils may densify under vibratory loading and cause permanent settlements.
4. How are the grain sizes distributed? Well-graded materials are less susceptible than uniform soils to losing strength under dynamic loading. Loose, uniform soils are especially prone to collapse and failure.

1.3 Saturation, Water Table, Drainage, and Capillary Effect

1.3.1 Saturation

During rainfall or irrigation, voids in soils will be filled with water. When all voids are filled with water (i.e., no air is left in the soil and no more water can be absorbed by the soil), the soil is said to be saturated. Saturated soil can be easily identified:

For example, if one squeezes soils by hand, some water (often muddy) will come out from the saturated soil.

It is worth mentioning that conventional soil mechanics treat soil as either fully saturated (pores filled with water) or dry (pores filled with air). However, a large number of geotechnical problems involve the presence of partially saturated soil zones where voids between soil particles are filled with a mixture of air and water. These zones are usually ignored in practice, and soils are assumed to be either fully saturated or completely dry. It has long been established, however, that the behavior of partially saturated soils can be very different from that of fully saturated or completely dry soils [8].

To analyze the response of saturated or partially saturated soils using numerical methods such as finite element method, both soil deformations and groundwater flows have to be taken into account. Moreover, constitutive models of saturated soils have also been implemented in various geotechnical analyses and coupled flow-deformation analyses, such as the Barcelona Basic Model (BBM) [9] or a similar model by Gonzalez and Gens [10].

For more details on saturated soil, readers may refer to Briaud [11]. For numerical analysis of saturated and partially saturated soils, source [12] is recommended.

1.3.2 Drainage

After rainfall or irrigation action, the water in large voids of soil will move downward, and the process of this movement is called drainage or percolation. Figure 1.3 illustrates the mechanism of drainage. The left figure shows the drained condition in which water is easily drained out of the hole in the left side. It is normally assumed that the pressure is constant under drained condition. On the other hand, undrained condition occurs when the water cannot leave via the left hole, as shown in the figure on the right. Under undrained condition, the water pressure increases with the increase in force.

If materials of a site are very permeable, such as gravel, drained behavior can normally be assumed even during an earthquake. However, for sand, the process of drainage may last for a few hours, and for clays a few days, while seismic loading

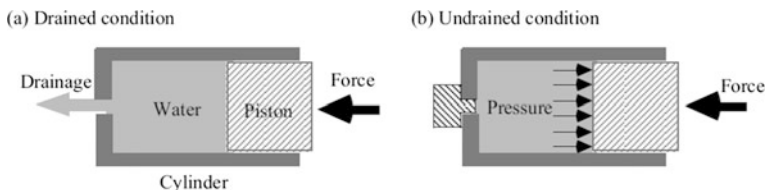


Fig. 1.3 Illustrations of drained and undrained conditions [194]

normally lasts for less than a minute, and the period of ocean wave loading is also less than 20 s. Therefore, for fine-grained materials, due to the short duration of earthquakes and the low permeability of the material, the undrained condition may be assumed. For fine-grained soils beneath offshore shallow foundations, due to the variation of pressure load induced by ocean wave loading, undrained and partially drained condition may also be assumed.

If no drainage occurs during loading due to earthquake shakings or ocean wave loading, the corresponding loading is called undrained loading. If soil is fully saturated with water, the volume of the soil does not change during the undrained loading.

Drained analysis may be carried out by using a constitutive model in which the material model is specified in terms of drained parameters. The analysis can be carried out based on either the effective stress concept or the total stress concept, as will be presented in Sect. 1.4. In the effective stress analysis, water and soils are addressed separately, while in the total stress analysis, water and soils are treated as a single material. These two concepts can be implemented with various soil models.

In engineering practice, the total stress soil model to analyze undrained problems is more widely used because the modeled soil parameters are more familiar and more easily obtained with conventional soil tests. In this model, the development of pore-water pressure and the influence of stress history are normally accounted for by different soil parameters. For example, the effective stress is implicitly implemented in the soil parameters. Otherwise, the parameters are often determined with empirical correlations. The Coulomb model is one that is widely used, while there are also a number of recently developed soil models such as the undrained soft clay model (USC model) [13].

Effective stress soil models are preferred by researchers because this type of soil model has a stronger theoretical formulation [14]. Several effective stress soil models have been used in geotechnical analyses, such as the modified Cam-Clay model (MCC model) [15], hardening soil model (HS model) [16], and the hardening soil small strain model (HS small model) [17]. Due to their simplicity compared to other advanced effective stress soil models, these models have been widely used and implemented by various commercial software programs, such as PLAXIS, FLAC.

In summary, drained analysis is necessary when soils' permeability is high, while the loading rate is low, and the short-term soil behavior is not of interest for the problem considered. Undrained analysis is appropriate under the opposite conditions. A widely accepted criterion on how to decide which type of analysis is appropriate is proposed by Vermeer and Meier [18].

1.3.3 Water Table

After saturation has stopped, the water will be drained downward at some depth from the soil surface as shown in Fig. 1.2, but the soil layers below a given depth

will be saturated permanently (or for long durations). The top of this saturated soil layer is called the water table. After a heavy rainfall or irrigation, the water table normally rises.

1.3.4 Capillary Effect

Contrary to drainage, in which the water in the large voids moves downward, the water in very small voids can also move upward due to the capillary effect. This process is referred to as capillary rise. In sand, this process is quick, but the water in voids moves upward by only 0.2–0.5 m. In clay, this capillary rise process takes longer, but the water in voids can move upward by more than 0.8 m, sometimes even reaching a few meters.

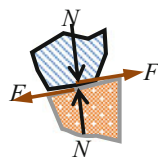
1.4 Effective Stress

As mentioned above, physically, soil can be considered a skeleton of solid particles (grains) enclosing continuous voids that contain water and/or air as shown in Fig. 1.1. Let us take two adjacent particles from Fig. 1.1, resulting in the configuration shown in Fig. 1.4.

For sand, the soil's shear resistance is mainly provided by the slipping contact friction force F at the contact surface between two adjacent particles. Obviously, shear modulus of soils increases as the effective stress increases. Therefore, soil at a greater depth has higher shear rigidity and shear strength than the same soil close to the ground due to the resulting higher overburden pressure at a larger depth, although this difference may also be influenced by density and geological history. The maximum friction force F is determined by the contact normal force N .

An important concept in soil mechanics, effective stress, proposed by Terzaghi [19] in 1923, is defined as the magnitude of contact pressure per unit area of soil, which represents the stress transmitted through the soil skeleton only. Many types of soil behaviors, such as strain-and-stress state, volume variation, and strength, are essentially governed by effective stress rather than total stress. Bishop [20] summarized the historical development of the concept of effective stresses in soil masses and has considered the theoretical aspects of the principle in detail.

Fig. 1.4 Inter-particle contact forces containing normal (N) and friction force (F)



Practically, the effective stress σ' for saturated soil is equal to the total (conventional) normal stress σ minus the water and/or air pressure u :

$$\sigma' = \sigma - u \tag{1.1}$$

The equation above has been validated by various testing results, which enables the solution of numerous geotechnical engineering problems, such as consolidation of porous permeable soils, sand liquefaction due to earthquakes or ocean waves.

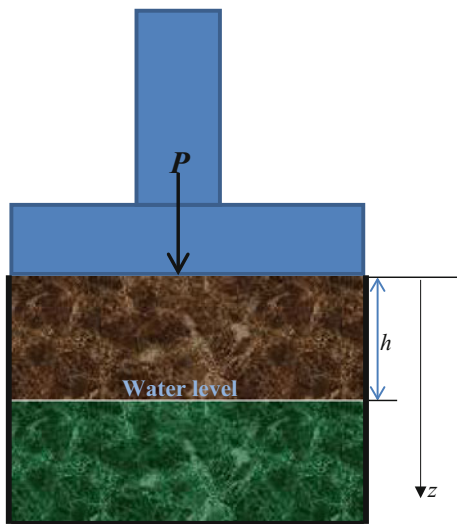
The total stress σ in the equation above is the sum of all forces divided by the total area (the sum of area of solid and void), including those transmitted through inter-particle contact and those transmitted through pore-water and/or air pressure [24], which is the pressure of water and/or air filling the void space between solid particles.

Practically, the total normal stress σ is calculated as the overburden pressure of soils per unit area transmitted in the normal direction. It is equal to the weight of the soil and the water and/or air enclosed in the continuum.

Note that the pore air pressure is normally negligible: u in the equation above is equal to pore-water pressure. Figure 1.5 shows a gravity-based foundation resting on the ground surface. The load P induced by the weight of the upper structure and the foundation is transferred to the soil surface with an area of A in the horizontal plane, and the underground water level is h meters below the soil surface. The soil particles transfer this load through inter-particle contact. From the equation above, the effective stress at a given depth z can be calculated as:

$$\sigma' = \begin{cases} \frac{P}{A} + \gamma_{\text{sat}}gz & \text{for } z < h \\ \frac{P}{A} + \gamma_{\text{sat}}gz - \rho_w g(z - h) & \text{for } z \geq h \end{cases} \tag{1.2}$$

Fig. 1.5 A gravity-based foundation resting on ground surface



where γ_{sat} and ρ_w are the density (in kg/m^3) of saturated soil including both soil and water, if applicable (typically around 1.5–2.1 times that of water), and water, respectively; γ_{sat} is referred to as total unit weight of soil, where the range of γ_{sat} is around 15–20 kN/m^3 when the soil is dry, and 18–21 kN/m^3 more under the ground water table; g is the acceleration of gravity; ρ_w is normally taken as 9.8 kN/m^3 .

Readers need to bear in mind that the area A in the equation above is generally 30–100 times the real contact (intergranular) area between soil particles. Therefore, the effective stress is an engineering means of measuring the soil stress state rather than a true representation of the contact stress between adjacent particles.

If the void between solid grains/particles of soil is fully filled with water without air or gas bubbles, the soil is regarded as saturated as described in Sect. 1.3.1. Generally, the soil submerged below the water table is saturated. Usually, the soil is also saturated at the adjacent area above the water table due to capillary action (Sect. 1.3.4). At soil layers further upward, the soil voids are occupied by both water and air. This type of soil is referred to as unsaturated. Continuing upward and coming close to the ground's surface, finally, the soil usually reaches a dry condition. The degree of water saturation S_r is defined as the ratio of the volume of water between the voids to the volume of the voids. Therefore, it is 100% when the soil is fully saturated, which is typically assumed for soil below the ground water table, and S_r is equal to 0% when the soil is in a fully dry condition. Therefore, the total unit weight of the water-saturated soil can be calculated as:

$$\gamma_{\text{sat}} = \frac{\gamma_{\text{sd}} + eS_r\rho_w}{1 + e} \quad (1.3)$$

where γ_{sd} is the density of dry soil (at $S_r = 0\%$); e is the void ratio, defined as the ratio of open void volume among solid grains/particles to the volume of the soil solid, with its typical values given in Table 1.2.

In geotechnical analyses, the effective unit weight (density) of soil is often used:

$$\gamma' = \gamma_{\text{sat}} - \rho_w \quad (1.4)$$

Table 1.2 Typical values of void ratio [25]

Soil type	e
Loose uniform sand	0.8
Dense uniform sand	0.45
Loose angular-grained silty sand	0.65
Dense angular-grained silty sand	0.4
Stiff clay	0.6
Soft clay	0.9–1.4
Loess	0.9
Soft organic clay	2.5–3.2
Glacial till	0.3

The pore-water pressure that acts equally in every direction will act on the entire surface of all submerged particles, but is assumed not to change the volume of the particles. It is obvious that the pore-water pressure does not contribute positively to the shear rigidity and shear strength, because it does not cause particles to be pressed together. For example, the sand on the seabed 200 m beneath the sea surface does not have a higher shear rigidity and strength due to the increased pore-water pressure than the same sand at the ground surface onland, even if the former has a pore-water pressure of 2 MPa and the latter has zero pore-water pressure. Moreover, the presence of water in the inter-particle voids also causes buoyancy effects, making each particle lighter, leading to a decrease in inter-particle friction.

It is obvious that if a certain amount of time is allowed for the pore-water pressure to be relieved, the effective stress is identical to the total stress. Therefore, the drainage prevents excessive water pressure building up, which is particularly apparent for sand.

For cohesive soil such as clay, both friction (stress and friction) and cohesive resistance contribute to the soil strength, as will be discussed in Sect. 1.6.2.

Example A layer of saturated clay of 6 m thick is overlain by a sand layer of 4 m thick. The water is 3 m below the ground surface, as shown in Fig. 1.6. The densities of the dry sand (above the water level), the saturated sand, and clay are 16, 18, and 17 kN/m³, respectively. Calculate the total vertical stress and effective stress at depths of 3, 4, and 10 m below the ground surface.

Solution: The total vertical stress (σ), the pore-water pressure (u), and the effective stress (σ') can be calculated as:

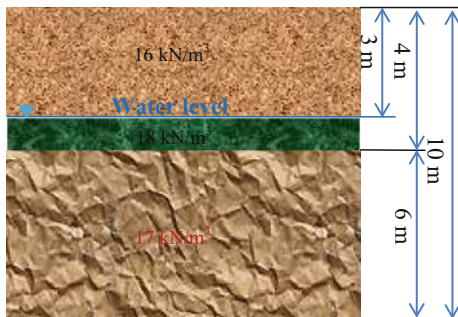
$$\sigma' = \sigma - u$$

At the depths of 3, 4, and 10 m below the ground surface, they are calculated as shown in the following table:

Depth (m)	σ (kN/m ²)	u (kN/m ²)	σ' (kN/m ²)
3	$3 \times 16 = 48$	0	$48 - 0 = 48$
4	$48 + [(4 - 3) \times 18] = 66$	$(4 - 3) \times 9.8 = 9.8$	$66 - 9.8 = 56.2$
10	$66 + (6 \times 17) = 168$	$9.8 + (6 \times 9.8) = 68.6$	$168 - 68.6 = 99.4$

It should be noted that Terzaghi theory [19] cannot be adequately applied to low-permeable fine-grained soils (clay) with closed porosity, as it leads to a discrepancy between calculated and experimental data. The main areas of concerns are [21]:

Fig. 1.6 Soil profile



1. As the total average stresses (σ) caused by external forces are adopted in Terzaghi theory [19], it does not consider internal forces creating additional stresses in the soil skeleton, which can be significantly more important in the case of the finer-grained soil.
2. At the same height of the water column, the pore pressure measured in a clay system may differ from the pore (hydrostatic) pressure in a permeable porous body.
3. Effective stresses are transmitted to the skeleton through the contacts between structural units. Although the total effective stress is constant, the effective contact stresses may differ due to the disjoining effect of hydrate films, changing amount of contacts, orientation of contact sites, and area of contacts. All these factors influence the strength and deformational properties of soils.

The limitations above have been partially addressed by Skempton [22], who proposed an equation of effective stress as the average intergranular force per unit area of horizontal projection of the plane, by using a correction for the area of contact:

$$\sigma' = \sigma - (1 - a_c)u \quad (1.5)$$

where a_c is the ratio between the contact area of soil particles and the total loaded area.

However, the equation above is only valid for some soils, cements, and hard rocks, because it does not account for the effects of physicochemical forces on the effective stress. To cope with this limitation, Mitchell and Soga [23] have proposed an equation of forces acting in soil involving the influence of physicochemical forces. Interested readers may read the source cited above.

Nevertheless, $\sigma-u$ controls the volume changes of a granular soil independently of the contact area, as demonstrated by Bishop [20], who also pointed out that the proposition that shear strength depends on $\sigma-u$ alone and not on a_c is still a matter of conjecture. Therefore, the definition of effective stress given by Terzaghi theory [19] remains valid for most relevant geotechnical engineering problems.

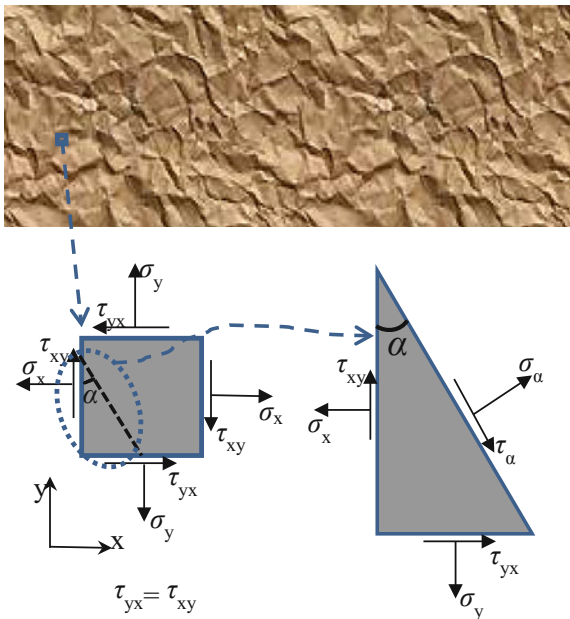
1.5 Mohr's Circle for Describing Stress Condition

To assess soil failure particularly related to shear failure (Sect. 1.6) and sand liquefaction (Chap. 7), which can occur normally under a complex stress field, engineers first need to assess the stress condition in the soil. In addition, soil properties under cyclic loading also depend on the stress condition in the soil prior to and during the loading.

The stress state in any element in a solid can be described by normal and shear stress acting on a particular plane passing through that element. The lower left figure in Fig. 1.7 shows a stress state in a two-dimensional solid (plane stress condition), which is characterized by normal and shear stress components σ and τ . The subscript xy on the shear stress components refers to the shear stress on the x side acting in the y -direction.

Typically, in solid mechanics, tensile stress is defined as positive and compressive stress is defined as negative. Consequently, positive shear stresses are those that tend to cause clockwise rotation of the body they act upon, and negative compressive stresses are those that tend to cause counterclockwise rotation. However, in geotechnical engineering, compressive normal stress is often defined as positive since the soils are regarded as having no resistance under tensile stress conditions. Consequently, in geotechnical engineering, positive shear stresses are those that tend to cause anticlockwise rotation of the body they act upon.

Fig. 1.7 Representation of a stress state in two-dimensional solids (lower left) and stress components on an inclined plane (lower right)



On a plane with an inclination angle of α shown in Fig. 1.7, with the force equilibrium at the inclined plane, the normal and shear stresses on the inclined plane are:

$$\sigma_\alpha = \frac{\sigma_x + \sigma_y}{2} + \frac{\sigma_x - \sigma_y}{2} \cos 2\alpha - \tau_{xy} \sin 2\alpha \tag{1.6}$$

$$\tau_\alpha = \frac{\sigma_x - \sigma_y}{2} \sin 2\alpha - \tau_{xy} \cos 2\alpha \tag{1.7}$$

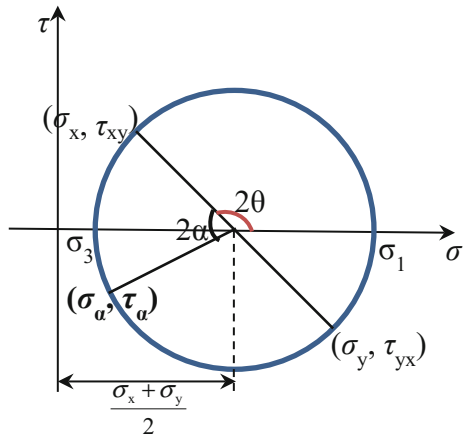
It can be seen from the two equations above that, when the stress state in a plane is known, any stress component in any plane can be calculated. Therefore, by combining the two equations above, one obtains:

$$\left(\sigma_\alpha - \frac{\sigma_x + \sigma_y}{2}\right)^2 + \tau_\alpha^2 = \left(\frac{\sigma_x - \sigma_y}{2}\right)^2 + \tau_{xy}^2 \tag{1.8}$$

The equation above can be conveniently represented by a graphical circle with the normal stress plotted along the horizontal axis and shear stress along the vertical axis, known as Mohr's circle, which was developed by the German civil engineer Otto Christian Mohr (1835–1918) in 1882. As illustrated in Fig. 1.8, the center of the circle is located at $[\sigma = \frac{\sigma_x + \sigma_y}{2}, \tau = 0]$ and the radius of the circle is $\sqrt{\left(\frac{\sigma_x - \sigma_y}{2}\right)^2 + \tau_{xy}^2}$.

Obviously, to calculate the normal and shear stresses on a plane inclined at a counterclockwise angle of α relative to the x -axis (Fig. 1.7), one needs to first measure a counterclockwise angle equal to 2α from the line determined by the known normal and shear stresses on the plane associated with the original x - and y -axis (Fig. 1.7), as shown in Fig. 1.8. The normal stress σ_α and the shear stress τ_α can then be calculated as a stress state at that particular inclined plane.

Fig. 1.8 Mohr's circle in two-dimensional solid



From Fig. 1.8, it is shown that at the plane with zero shear stress, normal stresses reach their maximum (σ_1) and minimum (σ_3) value, which are termed principal stresses:

$$\sigma_1 = \frac{\sigma_x + \sigma_y}{2} + \sqrt{\left(\frac{\sigma_x - \sigma_y}{2}\right)^2 + \tau_{xy}^2} \quad (1.9)$$

$$\sigma_3 = \frac{\sigma_x + \sigma_y}{2} - \sqrt{\left(\frac{\sigma_x - \sigma_y}{2}\right)^2 + \tau_{xy}^2} \quad (1.10)$$

The rotation angle θ_p between the original x plane and the principal plane on which the principal stresses occur can be determined by:

$$\tan 2\theta_p = \frac{-2\tau_{xy}}{\sigma_x - \sigma_y} \quad (1.11)$$

From Fig. 1.8, it is also shown that, even though principal stresses occur at the plane with zero shear stress, the maximum shear stresses occur when the normal stress is $\sigma = \frac{\sigma_x + \sigma_y}{2}$ (corresponding to the horizontal axis at the center of Mohr's circle) and the corresponding maximum shear stress plane is at an angle θ of 45° to the principal plane. The maximum (τ_{\max}) and minimum (τ_{\min}) shear stress can be calculated as:

$$\tau_{\max} = \sqrt{\left(\frac{\sigma_x - \sigma_y}{2}\right)^2 + \tau_{xy}^2} = \frac{\sigma_1 - \sigma_3}{2} \quad (1.12)$$

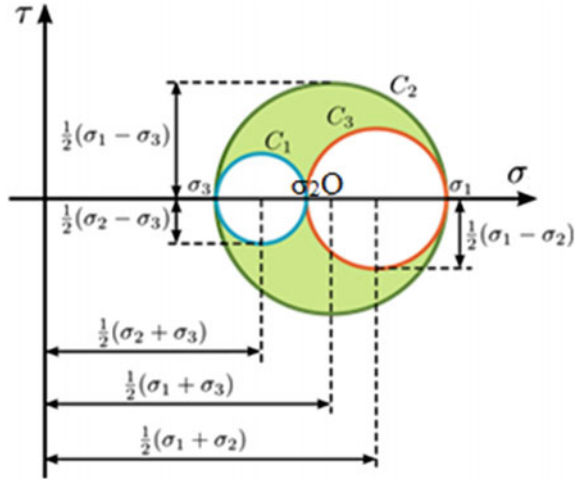
$$\tau_{\min} = -\sqrt{\left(\frac{\sigma_x - \sigma_y}{2}\right)^2 + \tau_{xy}^2} = -\frac{\sigma_1 - \sigma_3}{2} \quad (1.13)$$

The rotation angle θ_s between the original x plane and the plane on which the maximum shear stresses occur can be determined by:

$$\tan 2\theta_s = \frac{\sigma_x - \sigma_y}{2\tau_{xy}} \quad (1.14)$$

Figure 1.9 shows Mohr's circle extended from a two-dimensional solid to a three-dimensional solid. In addition to the maximum (σ_1) and minimum (σ_3) principal stress, intermediate principal stress σ_2 appears. Note that the mechanical behavior is normally much more sensitive to the relationship between the maximum and minimum principal stress than to the intermediate principal stress, and in many cases, the intermediate principal stress is often close to the minimum principal stress. Therefore, the value of σ_2 is often neglected. Obviously, the three principal stress planes are perpendicular to each other.

Fig. 1.9 Mohr's circle for a three-dimensional stress state, with three principal stresses for characterizing the state of stress notated as σ_1 , σ_2 , and σ_3 (figure by Sanpaz)



Example An element in plane stress condition is subjected to stress $\sigma_x = -1.0$ MPa, $\sigma_y = -0.4$ MPa, $\tau_x = -0.2$ MPa, and $\tau_y = 0.2$ MPa. Use Mohr's circle to determine the stress state on an element oriented at an angle of 30° counterclockwise to the x -axis and an angle of 40° clockwise to the x -axis.

Solution: The center (point O in Fig. 1.10) of the Mohr's circle on the x -axis is:

$$\sigma = \frac{\sigma_x + \sigma_y}{2} = \frac{-1.0 - 0.4}{2} = -0.7 \text{ MPa}$$

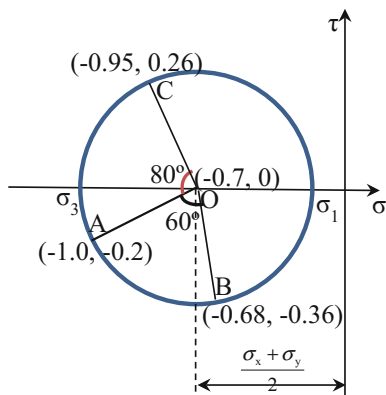
At point A , draw the stress state point with the coordinate $(-1.0, -0.2)$ MPa.

Draw the Mohr's circle with center O and radius of OA .

Rotating line OA counterclockwise through an angle of 60° ($2^\circ \times 30^\circ$), one obtains the stress state oriented at an angle 30° counterclockwise to the x -axis, i.e., point B at coordinate $(-0.68, -0.36)$ MPa.

Rotating line OA clockwise through an angle of 80° ($2^\circ \times 40^\circ$), one obtains the stress state oriented at an angle 40° clockwise to the x -axis, i.e., point C at coordinate $(-0.95, 0.26)$ MPa. The results are shown in Fig. 1.10.

Fig. 1.10 Mohr's circle



1.6 Soil Failure

Soil failure needs to be treated differently from failure of a typical structural member. For the latter, in most cases, failure is due to excessive normal stress. In the stability analysis of soil masses, in contrast, if the shear stress at a location on any plane within a soil mass reaches the shear strength of the soil, i.e., the resistance of soil to shear failure is not sufficient, shear failure will occur.

As presented in Sect. 1.4, for cohesionless soil such as sand, the soil's shear resistance is mainly provided by the slipping contact friction. Cohesionless soil can be held together only by a confining pressure, and it will fall apart if the confining pressure is released. This will be further presented in Sect. 1.6.1.

On the other hand, cohesive soils, such as clay and silts, have the ability to be rolled and molded (and hence they have a plasticity index, as will be presented in Sect. 1.8). The shear failure occurs when both cohesive resistance and friction (stress and friction) together are insufficient, which will be discussed in Sect. 1.6.2. Nevertheless, the normal effective stress rather than total (conventional) normal stress is preferred to calculate the shear resistance.

The determination of soils' shear strength is essential for the design of many geotechnical structures, such as shallow and deep foundations, natural and human-made slopes, retaining walls. The shear strength parameters can often be measured in the field using the vane shear test presented in Sect. 1.9.4. They can also be obtained from correlations with the standard number N obtained from the standard penetration test (SPT) presented in Sect. 1.9.5, or from correlations with the cone resistance obtained from the cone penetration test (CPT) presented in Sect. 1.9.6. The shear strength parameters can also be measured in the laboratory using direct shear (Sect. 1.9.2) and/or triaxial compression testing (1.9.3) methods on undisturbed or reconstituted soil samples.

1.6.1 Shear Failure for Cohesionless Soils

Cohesionless soils such as sands subject to static loading have high permeabilities and are usually fully drained in the field. Since they are cohesionless, the particles do not adhere to one another, and shear failure occurs when the resistance (τ_{sand}) due to friction is lower than the shear stress on sand:

$$\tau_{\text{sand}} = \sigma'_n \tan(\phi') \quad (1.15)$$

where σ'_n is normal effective stress normal to the slip plane (Fig. 1.12); ϕ' is the angle of shear resistance measured with normal effective stress, often named effective friction angle or angle of internal friction. Table 1.3 gives typical values of effective friction angles ϕ' for different types of cohesionless soils.

The shear strength for sands can be obtained from the results of either direct shear tests or drained (no stress-induced pressure in the pore water) triaxial tests [26]. In practice, the drained strength of sands is more frequently used. For test methods, see Sects. 1.9.2 and 1.9.3, and reference [26].

1.6.2 Shear Failure for Cohesive Soils

For cohesive soil, the shear failure occurs when both cohesive resistance and friction together (τ'_{clay}) are insufficient to resist the shear loading (effective stress of clay). τ'_{clay} is often expressed by Mohr–Coulomb failure criterion in terms of effective stress parameters, as shown in Fig. 1.11 and expressed as:

$$\tau'_{\text{clay}} = c' + \sigma'_n \tan(\phi') \quad (1.16)$$

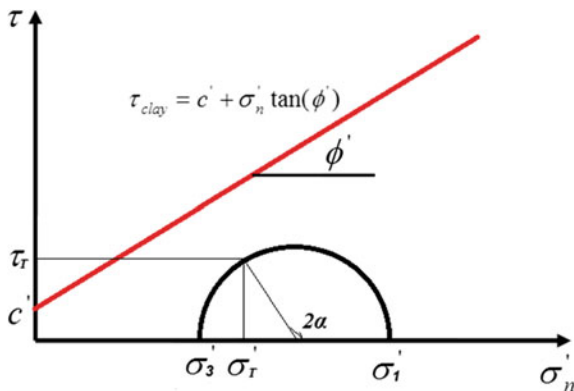
where c' is the cohesion intercept or cohesion strength, which is associated with the attractive forces between clay particles, attributed to the chemical and electrical

Table 1.3 Typical effective friction angles ϕ' for different types of cohesionless soils

Type of soil	Effective friction angles ϕ' at peak strength ^a		Effective friction angles ϕ' at ultimate strength ^a
	Medium	Dense	
Silt (non-plastic)	28°–32°	30°–34°	26°–30°
Uniform fine to medium sand	30°–34°	32°–36°	26°–30°
Well-graded sand	34°–40°	38°–46°	30°–34°
Sand and gravel mixtures	36°–42°	40°–48°	32°–36°

^aThe effective friction angle ϕ' at the ultimate shear strength state could be considered to be the same as the friction angle ϕ' for the same soil in a loose state

Fig. 1.11 Mohr–Coulomb failure criterion (shear stress varied with effective normal stress)



interactions among clay particles as presented in Sect. 1.2. Table 1.4 shows its typical values for soils with different consistencies. Therefore, shear strength of clay is activated even at zero normal effective stress when the past stress–strain history allows it. This also explains why sands do not have noticeable shear strength without confining pressure. That is why it is difficult to make shapes out of dry sand, although one can make shapes out of clay. For this reason, sands and gravels are called cohesionless, whereas clays are called cohesive.

Both σ'_n and c' are mathematical constants defining a linear relationship between shear strength and effective normal stress; for cohesive soils, the angle of internal friction ϕ' can often be assumed to be zero.

Both c' and ϕ' are referred to as the strength parameters of soils and can be obtained from laboratory or field tests, as will be presented in Sect. 1.9.

The Mohr–Coulomb failure criterion describes the boundary between soil’s linear-elastic and plastic behavior. As shown in Fig. 1.11, as the difference between the major principal stress σ_1 and the minimum principal stress σ_3 is increased, the radius of the circle will increase until the circle touches the line, or the failure envelope. This stress combination will result in shear failure. In special cases, σ_3 is negative, indicating that the soil is in tension, even though soil generally has a very low strength in tension.

Table 1.4 Cohesion strength (c') for clays from unconfined compressive strength [25]

Consistency	c' (kN/m ²)
Very soft	0–48
Soft	48–96
Medium	96–192
Stiff	192–384
Very stiff	384–766
Hard	>766

The shear failure criterion in terms of total stress parameters can be expressed as:

$$\tau_{\text{clay}} = c + \sigma_n \tan(\phi) \quad (1.17)$$

where c is the total stress cohesion intercept or cohesion strength; ϕ is the total stress friction angle.

For saturated clays, $\phi = 0$, the undrained strength is then:

$$\tau_{\text{clay}} = c \quad (1.18)$$

For normally consolidated clays that have not been subject to greater compression than that at the existing site, the cohesive part is small. However, for over-consolidated clay that has been subject to increased compression in the past (caused by, for instance, the erosion of higher soil layers), the cohesion may be significant [27].

In practice, rather than measuring the σ'_n and c' individually, τ_{clay} is directly obtained by unconsolidated–undrained triaxial laboratory test (Sect. 1.9.3), which is more often called undrained shear strength s_u (some literatures use c_u). Different test methods can be used for determining the shear strength. For example, as shown in Fig. 1.16, unconsolidated–undrained (UU) triaxial tests can be carried out on cylindrical soil samples or field vane tests in situ, as will be discussed in Sect. 1.9.

The shear strength of silts in terms of effective stress can also be expressed by the Mohr–Coulomb strength criterion as used for clay. However, the range of their behavior is wide, and sufficient data are not available to anticipate or estimate silts' properties with the same degree of reliability as is possible in the case of granular soils or clays [24].

Example A building with a gravity-based foundation is built on a site (Fig. 1.12) with soils having $c' = 11$ kPa and $\phi' = 32^\circ$. The applied normal effective stress and shear stress at location O are 170 and 98 kPa, respectively. Evaluate if the soil's shear strength is sufficient at location O.

Solution: using $\tau = c' + \sigma'_n \tan(\phi')$ to calculate the shear strength:

$$\tau = c' + \sigma'_n \tan(\phi') = 11 \text{ kPa} + 170 \text{ kPa} \cdot \tan(32^\circ) = 117 \text{ kPa}$$

This is above the applied shear stress of 98 kPa. Therefore, the shear strength of the soil is sufficient.

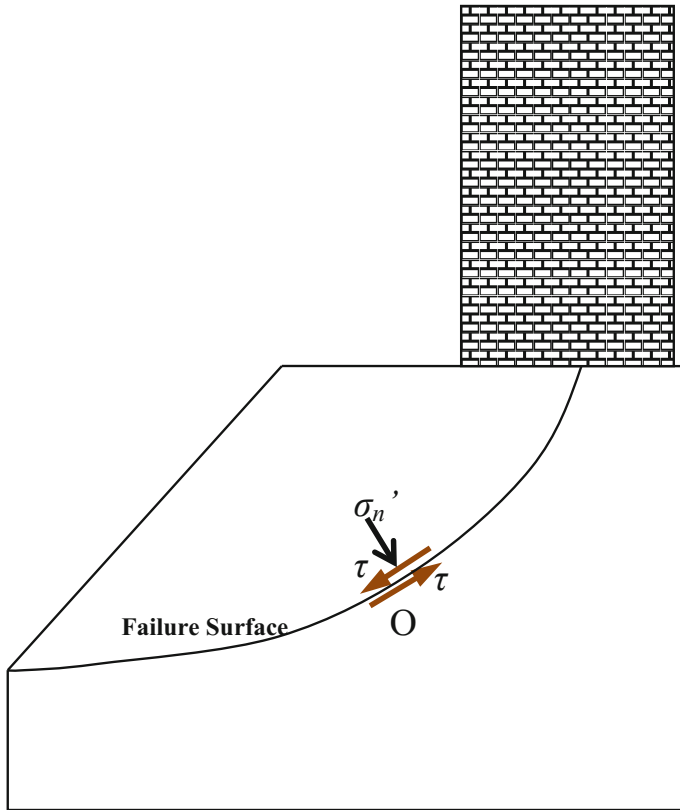


Fig. 1.12 Illustration of shear strength of soils

1.7 Total Stress Analysis Versus Effective Stress Analysis

Many types of geotechnical engineering problems require a determination and evaluation of soils' shear strength. There are two basic types of analyses that utilize the shear strength of the soil: (1) total stress analysis; (2) effective stress analysis. It is not generally allowed to combine the two types of analysis to solve a single geotechnical engineering problem.

The total stress analysis uses the total stress shear strength parameters s_u (untrained shear strength) for cohesionless soil or c and ϕ for cohesive soils, as presented in Sect. 1.6. The total stress analysis is typically only performed for cohesive soil. The actual analysis is performed for rapid loading or unloading conditions that usually develop during earthquakes. This analysis is ideally suited for response analysis of cohesive soil subject to seismic loading, because there is a change in shear stress that occurs so rapidly that soft cohesive soil does not have time to consolidate, or in the case of heavily over-consolidated cohesive soils, in

which negative pore-water pressures do not have time to dissipate. The total stress analysis uses the total unit weight γ_{sat} of the soil, and the location of the water table is not considered in the analysis. An important advantage of the total stress analysis is that the undrained shear strength can be obtained from tests (such as vane shear test, as will be presented in Sect. 1.9.4) that are easy to perform [28]. A significant limitation of this approach is that the accuracy of the undrained shear strength is not ensured because it depends on the shear-induced pore-water pressure that is not measured, which in turn depends on other details such as sample disturbance, strain rate effects, and anisotropy of the test procedures [29].

On the other hand, effective stress analysis uses the drained shear strength parameters (c' and ϕ'). In soil dynamics, they are widely used for soil analysis of cohesionless soils such as sands and gravels. Because shear strength is directly related to effective stress, effective stress analysis models the shear strength of the soil more fundamentally. A major drawback of using effective stress analysis is that the pore-water pressure must be included in the earthquake site-response analysis (Chap. 3). The accuracy of the pore-water pressure is often in doubt because many factors can affect the magnitude of pore-water pressure changes, such as the determination of changes in pore-water pressure resulting from changes in seismic loads. For effective stress analysis, assumptions are often made to calculate the pore-water pressure generated due to earthquake loading [28].

Sarma and Tsatsanifos [30] performed nonlinear dynamic response analysis of horizontally layered soils when subjected to seismic excitations. The soil is modeled with a hyperbolic stress–strain constitutive relationship and dynamic pore-water pressure development equation (to predict the pore pressure rise under cyclic loadings). They found that, compared to calculations using a total stress analysis, the predicted results based on the effective stress analysis can significantly reduce the calculated liquefaction potential (as will be presented in Sect. 7.2) of the deposit as well as the induced ground acceleration, while increasing the calculated induced ground displacements.

1.8 Clay Soil Consistency

The surface of clay mineral has a net negative charge, while water has a net positive charge. This makes clay prone to bonding with surrounding water. Moreover, clay has a large specific surface (total surface of clay particles per unit mass). For example, the specific surfaces for the three types of clays, namely kaolinite, illite, and montmorillonite, are 15, 80, and 800 m²/g, respectively. Therefore, the large specific surface means that clay generally can absorb a significant amount of water. And the larger the specific surface area per unit mass is, the more significantly the volume will increase as a result. On the other hand, clay will shrink when it dries.

Obviously, the water content has a significant influence on clay's behavior. Here, we define four important states of consistency for clays [26], which are often

referred to as Atterberg limits shown in Fig. 1.13: When clay is significantly wet (high water content) and does not have any strength, the clay reaches a liquid state. When clay has a moderate amount of moisture, it can deform easily to be made into different shapes without springing back like a normal elastic material does; the clay is then in a plastic state. When plastic state clay begins to dry out, cracks first appear, indicating a loss of the clay’s plasticity, and the clay then reaches a semisolid state. If the clay dries out further, it achieves a solid state, exhibiting strongly brittle behavior.

As shown in Fig. 1.13, in soil mechanics, the liquid limit (LL) is defined as the boundary between the liquid and plastic states. The plastic limit (PL) is the boundary between the plastic and the semisolid state; and the shrinkage limit (SL) is the boundary between the semisolid and the solid state.

A useful measure of the ability of soils to retain water is the plasticity index, which provides an indication of how much soil can shrink or swell:

$$I_p = 100\% \times (w_L - w_p) \tag{1.19}$$

where w_L is called liquid limit, which represents water content corresponding to the behavior change between the liquid and plastic state of soils; w_p is the plastic limit, which represents water content corresponding to the behavior change between the plastic and semisolid state of soils.

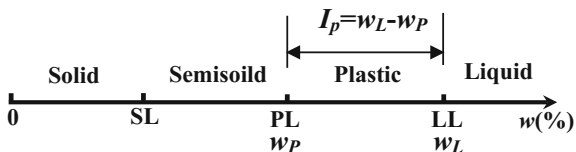
From the equation above, it is seen that I_p essentially represents the range within which clay behaves as a plastic material. The higher the I_p , the greater is the shrink-swell potential. A low plasticity index ($I_p < 15\%$) means that the addition of only a small amount of water can change a strong soil, when close to the plasticity index, into a weak soil. In contrast, a high plasticity index ($I_p > 15\%$) indicates that the soil is highly compressible; clays generally have higher I_p than sand.

However, there is another parameter to determine the state of soils at a water content level w , called liquid index (I_1):

$$I_1 = 100\% \times (w - w_p)/(w_L - w_p) \tag{1.20}$$

For strongly over-consolidated clays, $w < w_p$ so I_1 is negative, and the corresponding clay is non-plastic (brittle); if $w_p < w < w_L$ (i.e., $0 \leq I_1 \leq 1$), the clay is in a plastic state; and if $w > w_L$ (i.e., $I_1 > 1$), the soil is in a liquid state [26].

Fig. 1.13 Atterberg limits
(w is the water content)



1.9 Testing Methods to Measure Shear Strength

1.9.1 Laboratory and Field Test Methods

The shear strength of soils is an essential parameter for geotechnical engineering design because the capacity of any foundations and slope stability are dependent on the soil's shearing resistance. Therefore, it must be determined with acceptable reliability. Various testing methods have been proposed and applied in geotechnical engineering projects, either in the laboratory or at sites. The most widely used laboratory test methods in engineering practice are direct shear test (Sect. 1.9.2) and triaxial compressional test (1.9.3) on undisturbed or reconstituted soil samples, respectively. The most widely applied field tests include vane shear test (Sect. 1.9.4), standard penetration test (SPT) (Sect. 1.9.5), and cone penetration test (CPT) (Sect. 1.9.6).

Other laboratory shear tests are also available primarily for research purposes, including simple shear tests [31]. For details of the test methods, readers may refer to the source cited above.

1.9.2 Direct Shear Test

Direct shear test is one of the oldest soil strength tests. It uses the most straightforward method to measure the friction at the interface between two bodies. As shown in Fig. 1.14, a soil specimen is placed in a shear box that is split horizontally to allow the upper and lower halves of the sample to be displaced relative to one another. The shape of the shear box may be square or circular in plane. The contact between the two halves is at approximately the mid-height of the sample. The soil may be consolidated prior to shearing if the soil being tested is clay. A confining stress is applied vertically to the specimen, and the upper half is gradually pulled laterally at a constant rate, via the horizontal actuator, to generate shear stresses within the soil, until the sample fails or a maximum displacement is reached. The shear force, T , is measured using a load cell attached to the piston of the horizontal actuator. The applied load and the induced strain/displacement are recorded at frequent intervals to determine a stress–strain curve for each confining stress. Moreover, the vertical displacement of the loading plate is measured during shearing using a vertical displacement transducer.

By plotting the shear stress versus the displacement along the shearing direction, the maximum shear stress τ is obtained for a specific vertical confining stress σ_n . Several specimens are tested at varying confining stresses, resulting in a plot of the maximum shear stresses versus the vertical (normal) confining stresses for each of the tests as shown in Fig. 1.11. From the plot, a straight-line approximation of the Mohr–Coulomb failure envelope curve can be drawn. The cohesion c and the friction angle ϕ can be computed from the shear strength equation (Sect. 1.6.2):

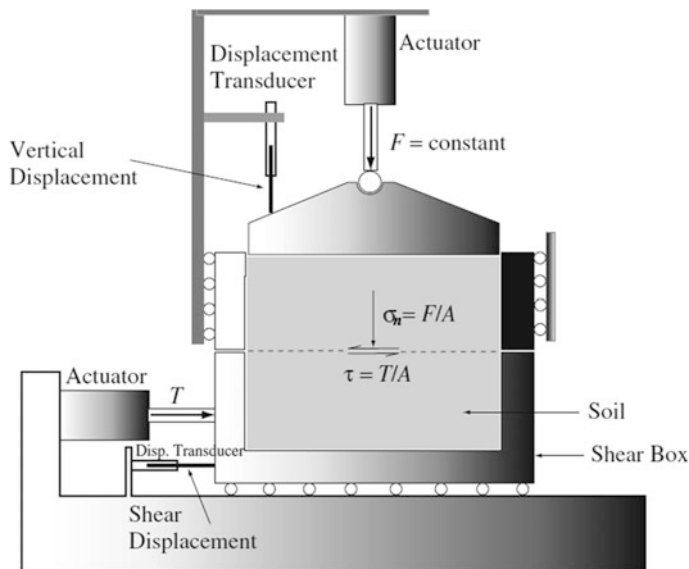


Fig. 1.14 Direct shear test [31]

$$\tau = c + \sigma_n \tan(\phi) \tag{1.21}$$

It is noted that since the test results on each specimen are plotted on a graph with the peak (or residual) stress on the y -axis and the confining stress on the x -axis, the y -intercept of the curve that fits the test results is the cohesion c , and the slope of the line or curve is the friction angle ϕ .

A major disadvantage of the direct shear test is that pore-water pressure cannot be measured, as drainage conditions cannot be controlled. Moreover, only an approximation of the state of pure shear is produced in the specimen, and the shear stress on the failure plane is not uniform, i.e., failure occurs progressively from the edges toward the center of the specimen. The area under shear and vertical loads does not remain constant throughout the test [26].

1.9.3 Triaxial Shear Test

1.9.3.1 Method

To control the drainage condition, triaxial shear test can be adopted, which allows a measurement of pore-water pressure. As illustrated in Fig. 1.15, in a triaxial shear test, a cylindrical specimen, typically having a length/diameter ratio of 2 (the diameter varies from about 33 to 100 mm), is stressed in a way that results in

stresses along one axis being different from the stresses in perpendicular directions. This is typically achieved by placing the sample between two parallel loading plates (base pedestal and top cap) that apply stress in one (usually vertical) direction and apply fluid pressure (through the confining pressure tube shown in Fig. 1.15) to the specimen in the perpendicular directions (the soil sample is laterally confined by a thin, impervious rubber membrane). Different compressive stresses in the test apparatus cause shear stress to develop in the soil sample. The membrane is sealed to the top cap and base pedestal using silicone grease and rubber O-rings. It is not possible to develop a shear stress on the rubber membrane covering the sides of the specimen because it is flexible. The vertical load is applied through the loading plate on the sample until the soil fails and sliding regions within the soil form, known as shear bands. When a compressive load is applied through the loading piston, the vertical stress acting on horizontal planes is the maximum principal stress (σ_1), the horizontal stress acting on vertical planes is the minimum principal stress (σ_3), and the intermediate principal stress (σ_2) is equal to the minor principal stress. The axial stress applied to the soil specimen by the loading piston is ($\sigma_1 - \sigma_3$), which is often referred to as the principal stress difference (also known as deviator stress). In addition to the tube to pressurize the confining fluid, the two drainage tubes (with valves) are used to connect the top and bottom of the soil specimen to control the drainage into the soil specimen.

It is especially important to make sure that drainage conditions of the test correspond to the field conditions. The undrained strength can be expressed in terms of total stress concept, while the drained strength can be expressed in terms of effective stress concept. By obtaining the test data, it is possible to determine the tested sample's fundamental material parameters such as angle of shearing resistance, cohesion, and dilatancy angle, which (along with other tests) can be further used to assess the soil and foundation capacity related to various geotechnical issues. Here, the dilatancy angle ψ controls the amount of plastic volumetric strain developed during plastic shearing and is assumed to be constant during plastic yielding. In most cases, $\psi = 0$ can be assumed to correspond to the volume preserving deformation while in shear. Clays (regardless of over-consolidated layers) are characterized by a very low amount of dilation ($\psi \approx 0$). For sands, the value of ψ depends on the angle of internal friction. For non-cohesive soils (sand, gravel) with the angle of internal friction $\phi > 30^\circ$, ψ can be approximated as $\psi = \phi - 30^\circ$. A negative value of dilation angle is acceptable only for rather loose sands.

1.9.3.2 Types of Triaxial Shear Test

Triaxial shear test is the most widely used shear strength test and is suitable for all types of soils.

A triaxial shear test is normally carried out in two (or more) stages: The first stage is the conditioning stage, during which the initial stress condition of the soil specimen is established, which may be hydrostatic (isotropic) or may be made to simulate the in situ state of stress by using different values for the vertical and radial

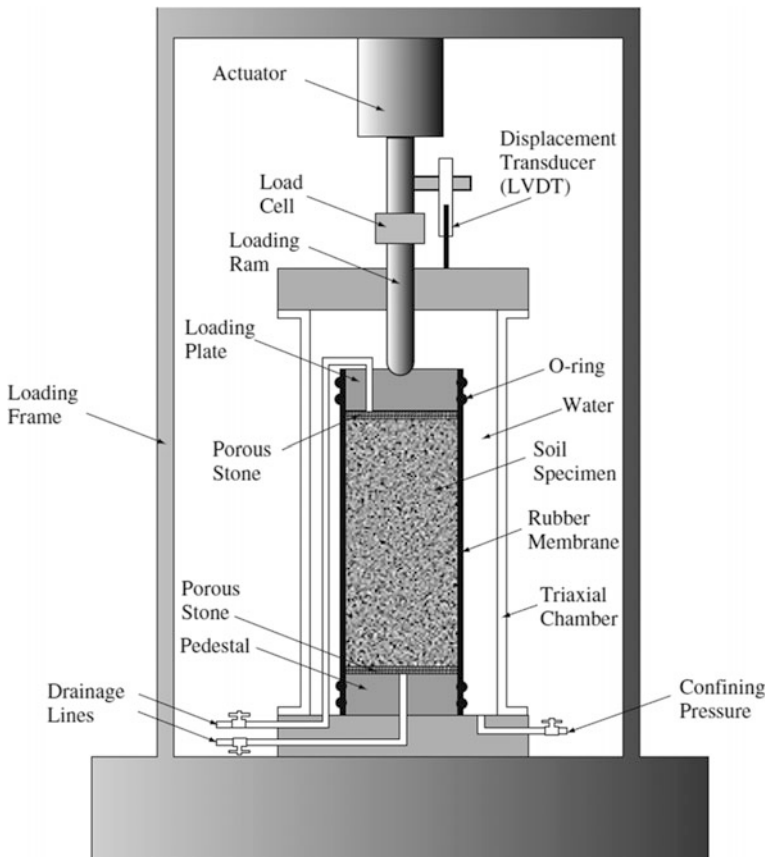


Fig. 1.15 Illustration of triaxial shear test [31]

stresses (anisotropic). The triaxial test specimen may be allowed to consolidate after the confining stress is applied. If consolidation is permitted, multiple stages of consolidation pressures may be used. The second (final) stage is the shearing stage, during which the principal stress difference is applied until soil failure occurs. In this stage, the soil may or may not be allowed to drain.

During a typical triaxial compression test, drainage may be allowed or prevented at both stages: (1) In the initial stress condition, if drainage is allowed, then the soil will consolidate under the confining pressure. If drainage is prevented, the soil will not consolidate and the shearing stage of the test will commence with an initial pore pressure in the soil. (2) During application of the deviator stress in the shearing stage to induce soil sample failure: If drainage is allowed, i.e., the test is performed sufficiently slowly that any developed pore pressures are allowed to dissipate, then a slow or drained test is performed. If drainage is prevented, i.e., any developed pore pressures are not allowed to dissipate, then a quick or undrained test is performed.

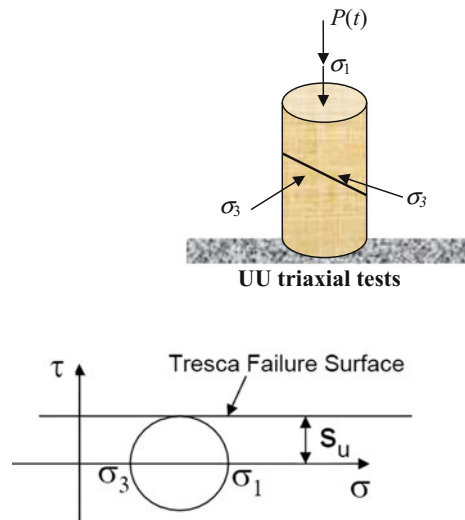
Therefore, depending on the consolidation condition in the first stage and the drainage condition in the second (final) stage, the triaxial shear test can be categorized into three types [26]:

1. Consolidated–Drained (CD) test: The soil sample is drained under a specified all-round pressure until consolidation is complete, and it is then slowly sheared so that the principal stress difference ($\sigma_1 - \sigma_3$) is applied at a rate slow enough to ensure that the excess pore-water pressure is maintained at zero. The test may take a long time to allow the sample to adjust, and low permeability samples need a long time to drain and adjust strain to stress levels.
2. Consolidated–Undrained (CU) test: Drainage of the specimen is permitted under a specified all-round pressure until consolidation is complete; the principal stress difference is then applied under undrained conditions and the sample is normally assumed to be fully saturated. Pore-water pressure measurements may be made during the undrained part of the test, and this allows for an approximation of the consolidated–drained strength.
3. Unconsolidated–Undrained (UU) test: The soil specimen is subjected to a specified all-round pressure and is not allowed to consolidate during the test. The principal stress difference is then applied quickly, with no drainage being permitted at any stage of the test. The sample is compressed at a constant rate (strain-controlled).

Figure 1.16 illustrates a determination of undrained shear strength s_u by unconsolidated–undrained (UU) triaxial shear tests on a cylindrical soil sample.

In addition, triaxial testing systems have been developed to allow independent control of the stress in three perpendicular directions, which is not attainable using conventional axisymmetric triaxial apparatus. This allows an investigation of stress

Fig. 1.16 Illustration of using UU test data to determine undrained shear strength s_u



paths not capable of being generated in axisymmetric triaxial test machines, which can be useful for studying cemented sands and anisotropic soils [32]. For details of three-axis triaxial testing, see the source cited above.

It should be noted that it is not possible to perform unconsolidated–drained tests because consolidation would occur whenever the drained specimens are opened during the shearing stage [33].

1.9.3.3 Standards Describing Triaxial Shear Test

A few widely adopted international and national standards elaborating the procedure and requirement of triaxial shear test are listed below:

ISO/TS 17892-8:2004 Geotechnical Investigation and Testing—Laboratory Testing of Soil—Part 8: Unconsolidated–Undrained Triaxial Test.

ISO/TS 17892-9:2004 Geotechnical Investigation and Testing—Laboratory Testing of Soil—Part 9: Consolidated Triaxial Compression Tests on Water-saturated Soils.

ASTM D4767-11 (2011): Standard Test Method for Consolidated–Undrained Triaxial Compression Test for Cohesive Soils.

ASTM D2850-03a (2007): Standard Test Method for Unconsolidated–Undrained Triaxial Compression Test on Cohesive Soils.

BS 1377-9:1990 Part 8: Shear Strength Tests (effective stress) Triaxial Compression Test.

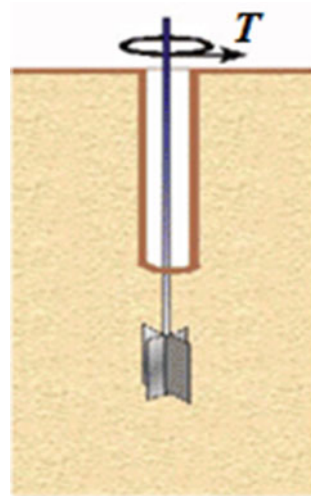
1.9.4 Vane Shear Test

The undrained strength of intact soft and firm clays can also be measured in situ by vane shear test. As shown in Fig. 1.17, the vane shear test typically involves pushing a four-bladed vane and rod into the undisturbed cohesive soil (fine-grained clays and silts or other fine geomaterials soil such as mine tailings, organic muck; if the soil is not soft, a borehole is required to perform this test), and gradually rotating it from the surface (the rate of rotation of the vane should be within the range of 6°–12° per minute); sufficient torque is required to rotate the embedded vane and shear a cylindrical surface, causing a cylindrical soil failure with the vane. The measured torque at failure is converted into a correlated undrained shear strength s_u by limit-equilibrium analysis:

$$s_u = \frac{T_f}{\pi \left(\frac{d^2 h}{2} + \frac{d^3}{2} \right)} \quad (1.22)$$

where T_f is the torque at failure; d is the overall vane width; and h is the vane length.

Fig. 1.17 Illustration of field vane test

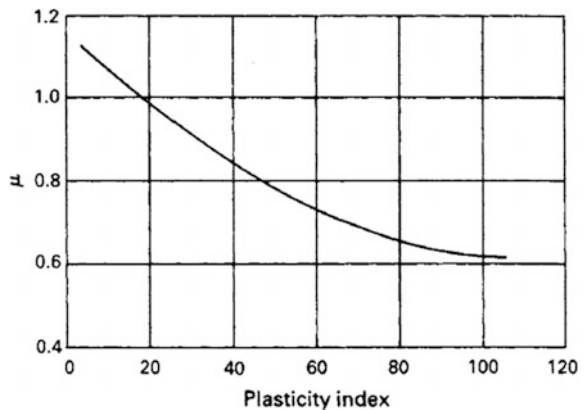


The shear strength is normally determined at intervals over the depth of interest. Friction of the vane rod and instrument is either minimized during readings by special casings or housing, or else accounted for and subtracted from the total torque to determine the torque applied to the vane.

As a simple alternative, by inserting a smaller hand-operated shear vane into the soil sample recovered from a test boring, and twisting it until soil failure, the undrained shear strength of samples can also be measured.

Vane test provides a direct and reliable measurement of the in situ undrained shear strength. However, Bjerrum [34] stated that undrained strength as measured by field vane test is generally greater than the average strength mobilized along a failure surface in a field situation. The discrepancy was found to be greater for clays with higher plasticity index, which is attributed primarily to the rate effect. He further presented a correction factor μ to the undrained strength measured by the vane test as shown in Fig. 1.18.

Fig. 1.18 Correction factor μ to the undrained strength measured by the vane test [34]



1.9.5 Standard Penetration Test (SPT)

The standard penetration test (SPT) is an in situ dynamic penetration test designed to provide information on the geotechnical engineering properties of soils. It is one of the oldest and most popular in situ tests used for soil exploration in soil mechanics and geotechnical engineering and is widely used due to the simplicity of both its equipment and procedure.

In geotechnical earthquake engineering, SPT is used to investigate seismic site characterization, site-response, and liquefaction studies toward seismic microzonation due to large data availability. Because it is relatively easy to use, cheaper than other types of field test methods, and SPT equipment can be quickly adapted and included as part of almost any type of drilling rig, SPT remains the most widely used field test method—despite its limitations and the numerous corrections that have to be applied, as will be discussed in this section.

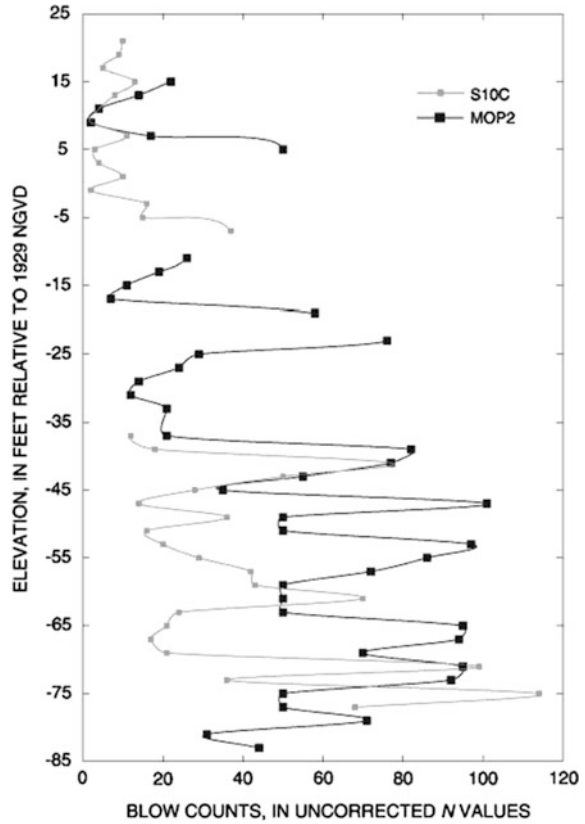
Generally, correlations between N -values and soil properties should only be used for cohesionless soils. Note that gravel particles can plug the sampler, resulting in higher blow-counts and higher estimates of friction angles than reality. Care should therefore be taken when using N -values obtained in gravelly soil. Caution should also be taken when using N -values to determine silt or clay parameters, due to the dynamic nature of the test and resulting rapid changes in pore pressures and disturbance within the deposit. Correlations of N -values with cohesive soil properties should generally be considered preliminary [41]. N -values can also be used for liquefaction assessment (see Sect. 7.2.2 for details). As mentioned above, other parameters such as the angle of internal friction and relative density also influence the $(N_1)_{60}$.

For gravelly soils, the Becker hammer penetration test (BPT) [56] can be deployed. It is similar to SPT applied for sands.

1.9.5.1 Performing SPT

A typical SPT is carried out in a borehole, by driving a standard “split spoon” sampler (a thick-walled sample tube, with an outside diameter of 50.8 mm and an inside diameter of 35 mm, and a length of around 650 mm) using repeated blows (30–40 blows per minute) of a 63.5 kg hammer falling through 762 mm. The hammer is operated at the top of the borehole and is connected to the split spoon sampler by rods. The split spoon sampler is lowered to the bottom of the hole and is then driven a distance of 450 mm in three 150-mm intervals, with the blows required for each 150 mm penetration being counted. Note that, as the soil is considered to have been disturbed during the first 150 mm of penetration, the penetration resistance for the first 150 mm of penetration should therefore be neglected. The sum of the number of blows required to drive the split spoon for the last 300 mm of penetration (the second and third 150 mm of penetration) is termed the standard penetration resistance, “ N -value” or “SPT- N value .”

Fig. 1.19 Illustration of SPT “ N -value”



The standard penetration resistance is influenced by soil type, confining pressure, and soil density. Moreover, types of test equipment and procedure also influence the “ N -value.” For example, the energy delivered to the soil by each blow of the hammer of different equipment can differ significantly.

Many correlations developed to determine soil properties are based on “ N -value.” The blow-count provides an indication of the density of the ground, and it is used in many empirical geotechnical engineering formulas. The required test procedure is described by various codes and standards, such as the test procedure described in ISO 22476-3 [35] and ASTM D1586 [36]. Figure 1.19 illustrates an example of SPT- N value obtained from an SPT.

1.9.5.2 Determine $(N_1)_{60}$

SPT blow-counts (SPT- N values) do not represent a simple physical property of the soil and therefore must be correlated to soil properties of interest, such as strength or density. Even though multiple correlations exist, none of them are of very high quality.

The “ N -values” (N_{field}) obtained in the field test depend on the equipment used and the skill of the operator and should normally be corrected before they are used in geotechnical design so that they are consistent with a particular design method and correlations being used.

A widely accepted method is to correct SPT- N values to allow for hammers of varying efficiency to be accounted for [37]. This corrected blow-count is normally referred to as N_{60} , because the original SPT hammer has about 60% efficiency with regard to the free-fall energy delivered to the soil sample:

$$N_{60} = E_m \cdot C_B \cdot C_R \cdot C_S \cdot N_{\text{field}}/ER \quad (1.23)$$

where E_m is the hammer efficiency [38]; C_B is the borehole diameter correction factor and it can be set according to the selected diameter from the dropdown list and can be taken as follows: $C_B = 1.0$ for boreholes with diameters between 65 mm and 115 mm, $C_B = 1.05$ for a borehole diameter of 150 mm, $C_B = 1.15$ for a borehole diameter of 200 mm; C_R is the rod length correction factor and this is mainly due to the fact that when the hammer strikes the rods, a compression wave travels down the rods and is reflected as a tension wave after it reaches the bottom of the split spoon, but when the tension wave travels back to the hammer, the hammer is lifted and the energy transmission essentially terminates, and incomplete hammer energy is then transferred when rod lengths are less than 10 m. Therefore, C_R may be taken as follows: $C_R = 0.75$ for a rod length between 3 and 4 m, $C_R = 0.85$ for a rod length between 4 and 6 m, $C_R = 0.95$ for a rod length between 6 and 10 m, and $C_R = 1.00$ for a rod length above 10 m; C_S is the liner correction factor and its value depends on the sampler used to perform the test, the split spoon sampler may contain liner or not, and the C_S value for samplers with liners is 1.00, while for samplers without liners, the C_S value ranges from 1.10 to 1.30; N_{field} is the “ N -value” obtained in the field test; ER is the hammer efficiency expressed as a percentage of theoretical free-fall energy delivered by the hammer system and it may be taken as 60% for conventional drop hammer using rope and cathead and 80% for automatic trip hammer.

In general, corrections for rod length, hole size, and use of a liner are only significant in unusual cases or where there is significant variation from standard procedures. These corrections may be significant for liquefaction evaluation. For more details on this topic, sources [37, 39] are recommended.

The overburden pressure also influences the N -values [40]. Therefore, N -values corrected for both overburden pressure (σ'_v) and the hammer efficiency can be used for design, which is designated as $(N_1)_{60}$, as determined by:

$$(N_1)_{60} = E_m \cdot C_N \cdot C_E \cdot C_B \cdot C_R \cdot C_S \cdot N_{\text{field}}/ER \quad (1.24)$$

where $C_N = (p_a/\sigma'_{v0}(z))^{0.5}$ is the overburden correction factor; $\sigma'_{v0}(z)$ is the effective vertical overburden stress at depth z ; p_a is the reference stress of 100 kPa or about atmospheric pressure; C_E is the energy correction factor for the SPT hammer and it may be taken as follows: for donut hammers, $C_E = 0.5$ – 1.0 ; for safety hammers,

$C_E = 0.7\text{--}1.2$; for trip-type donut hammers, $C_E = 0.8\text{--}1.3$, and it is recommended to consult the manufacturer to obtain a reliable value of C_E .

The significant advantage of using $(N_1)_{60}$ values is that they have less variability or scatter due to the test method, and the relevant cost can be reduced from the consistent data reporting by adopting the $(N_1)_{60}$.

1.9.5.3 Assess Soil Class Using SPT Test

Seismic ground response characteristics, roughly defined as “site effects,” are incorporated into modern seismic code provisions in many countries. SPT can be used to estimate the velocity for soils that have certain resistance (e.g., ground types B-D in Eurocode 8 [198], see Table 1.5). Due to SPT’s working principle, it cannot be used for rock materials.

Table 1.5 Category of soil classes A–E in Eurocode 8 [198]

Ground type	Description of stratigraphic profile	Parameters		
		$v_{s,30}$ (m/s)	N_{SPT} (blows/30 cm)	s_u (kPa)
A	Rock or other rock-like geological formation, including at most 5 m of weaker material at the surface	>800	–	–
B	Deposits of very dense sand, gravel, or very stiff clay, at least several tens of meters in thickness, characterized by a gradual increase in mechanical properties with depth	360–800	>50	>250
C	Deep deposits of dense or medium dense sand, gravel or stiff clay with thickness from several tens to many hundreds of meters	180–360	15–50	70–250
D	Deposits of loose to medium cohesionless soil (with or without some soft cohesive layers), or of predominantly soft to firm cohesive soil	<180	<15	<70
E	A soil profile consisting of a surface alluvium layer with v_s values of type C or D and thickness varying between about 5 m and 20 m, underlain by stiffer material with $v_s > 800$ m/s			
S ₁	Deposits consisting of, or containing, a layer at least 10 m thick, of soft clays/silts with a high plasticity index ($I_p > 40$) and high water content	<100 (indicative)	–	10–20
S ₂	Deposits of liquefiable soils, of sensitive clays, or any other soil profile not included in types A–E or S ₁			

Although different researchers have tried to correlate shear wave velocity v_s (an important item for characterizing seismic site effects and soil stiffness modeling) in terms of various soil and site parameters such as depth and geological age, soil type and SPT- N value are the most favorable parameters [668]. Numerous formulations have been proposed to estimate the correlation between SPT- N value and shear wave velocity v_s . For example, Ohba and Toriumi [43] proposed that:

$$v_s = 69N_{\text{SPT}}^{0.17}z^{0.2}F \quad (1.25)$$

where N_{SPT} is the penetration resistance in an SPT, determined as the number of blows required to drive the split spoon for the last 300 mm of penetration as described previously; z is the depth of the soil material in meters; F is a factor depending on the soil type, ranging from 1.0 to 1.45, and can be taken as 1.1 for sand and 1.2 for gravel.

Marto and his co-workers [44], and Thaker and Rao [45] presented summaries of relationship between v_s and SPT- N value.

In many seismic design codes, it is specified that in case the shear wave velocities are not available, the classification of the site shall be estimated based on SPT- N value (N_{SPT}), such as the one defined in Eurocode 8 [198] as shown in Table 1.5, which defines five different soil types from A to E.

A typical relationship to correlate the SPT results and average shear wave velocity can be expressed as follows:

$$N_{30} \text{ or } v_{s,30} = \frac{\sum_{i=1}^N h_i}{\sum_{i=1}^N \frac{h_i}{N_i \text{ or } v_{si}}} \quad (1.26)$$

where $\frac{h_i}{N_i \text{ or } v_{si}} \sum_{i=1}^N h_i$ is summation of total depth, for the uppermost 30 m average $\sum_{i=1}^N h_i = 30$ m; h_i and v_{si} or N_i denote the thickness (in meter) and corresponding shear wave velocity or standard penetration resistance not to exceed 100 blows per 0.3 m (directly measured in field without corrections) of the i th soil layer, respectively, in a total of N layers, existing in the uppermost 30 m or lower at sites with shallow sedimentary soil (see Sect. 3.2 for more details).

In geotechnical earthquake engineering design, note that SPT- N values may vary even for identical soil conditions due to the high sensitivity to operator techniques, equipment, malfunctions, and poor boring practice [46]. Therefore, while SPT- N values may be used for projects in preliminary design stage or where there is a financial limitation, for important projects, it is preferable to measure dynamic soil properties directly [47].

1.9.6 Cone Penetration Test (CPT)

Originally developed in the 1950s at the Dutch Laboratory for Soil Mechanics in Delft to investigate soft soils, cone penetration test (CPT) has recently gained importance in geotechnical engineering. Due to both the reduction of the cost of such investigations and the need for more precise and accurate estimations of the bearing capacity of piles, it is especially useful for pile design.

As shown in Fig. 1.20, a typical CPT is similar to SPT, but instead of a thick-walled sampler, a steel cone is pushed into the soil. CPT involves steadily pushing an instrumented cone penetrometer, with the tip facing down, into the ground at a controlled rate of 1.5–2.5 cm/s. The resolution of the CPT in delineating stratigraphic layers is related to the size of the cone tip, with typical cone tips having a cross-sectional area of either 10 or 15 cm², corresponding to diameters of 3.6 and 4.4 cm. The apex angle of the conical tip is typically 60° immediately below a cylindrical friction sleeve. The cone and friction sleeve are each connected to load cells that measure the cone/tip resistance (q_c) and sleeve resistance (f_s or R_f) during penetration. The penetrometer can be mounted in various ways, such as on a truck for CPT onshore (Fig. 1.21) or an offshore vessel.

In a CPT, the cone is typically first pushed into the soil to the desired depth (initial position) and then a force is applied to the inner rod that moves the cone downward into the extended position. By continually repeating the two operations above, the measured soil data is obtained at increments of depth. The results from CPT include the distribution of cone resistance (q_c , which is the force required to move the cone into the extended position divided by the horizontally projected area of the cone), sleeve friction (f_s or R_f), pore pressure, and relative density along the depth of the soil layers. In addition, the friction ratio, $FR = f_s/q_c$, is also an

Fig. 1.20 Illustration of a penetrometer in a CPT (picture by Lusilier)

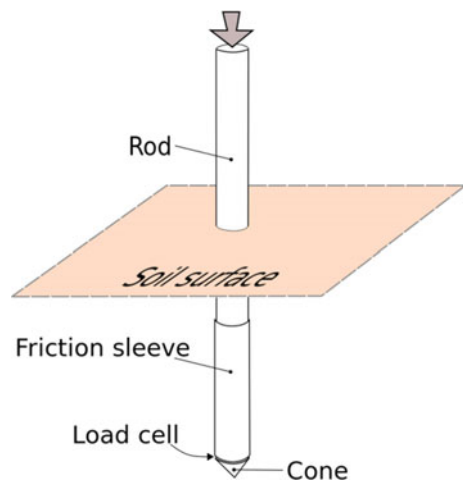


Fig. 1.21 A truck operating CPT (courtesy of USGS)



important parameter, which is generally low in cohesionless soils and high in cohesive soils.

Figure 1.22 shows an example of the CPT results from an offshore windfarm site just off the UK coast. Figure 1.23 shows the distribution of cone resistance at different depths obtained by CPT for seven boreholes (B1, B1A, ..., B5).

In many geotechnical engineering evaluations, the cone resistance q_c is corrected for the overburden pressure, with the corrected cone penetration tip resistance notated as q_{c1} and calculated as:

$$q_{c1} = \frac{1.8q_c}{0.8 + (\sigma'_{v0}(z)/100)} \quad (1.27)$$

where $\sigma'_{v0}(z)$ is the effective vertical overburden stress at depth z .

For offshore applications, there are basically two methods to push a cone penetrometer into the sea bottom [49, 50]:

1. By pushing it from the sea floor until refusal, or a predetermined penetration, which is typically the most economical solution and gives the highest quality results. It is traditionally referred to as seabed mode, as shown in Fig. 1.24.
2. By drilling a borehole and pushing the penetrometer into the soil at the bottom of the borehole, which is usually called the down-hole mode or drilling mode, as shown in Fig. 1.25. It has the advantage of allowing much deeper penetrations and drilling through hard soil layers.

The growing interest in constructing onshore and offshore pile installations has prompted several design codes to adopt new and more refined CPT-based design methods. A recent version of API RP2A 2007 [53] has accepted four CPT-based methods (ICP-05, UWA-05, NGI-05, and Fugro-05) to assess the axial pile–soil interaction capacity, as will be discussed in Sect. 17.13.

Compared to SPT, which obtains soil data at intervals in soil deposits, CPT can obtain a continuous subsurface record of the cone resistance. However, unlike SPT, in a CPT, soil samples cannot be recovered and special equipment is required to produce a steady and slow penetration of the cone. Therefore, the ability to obtain a

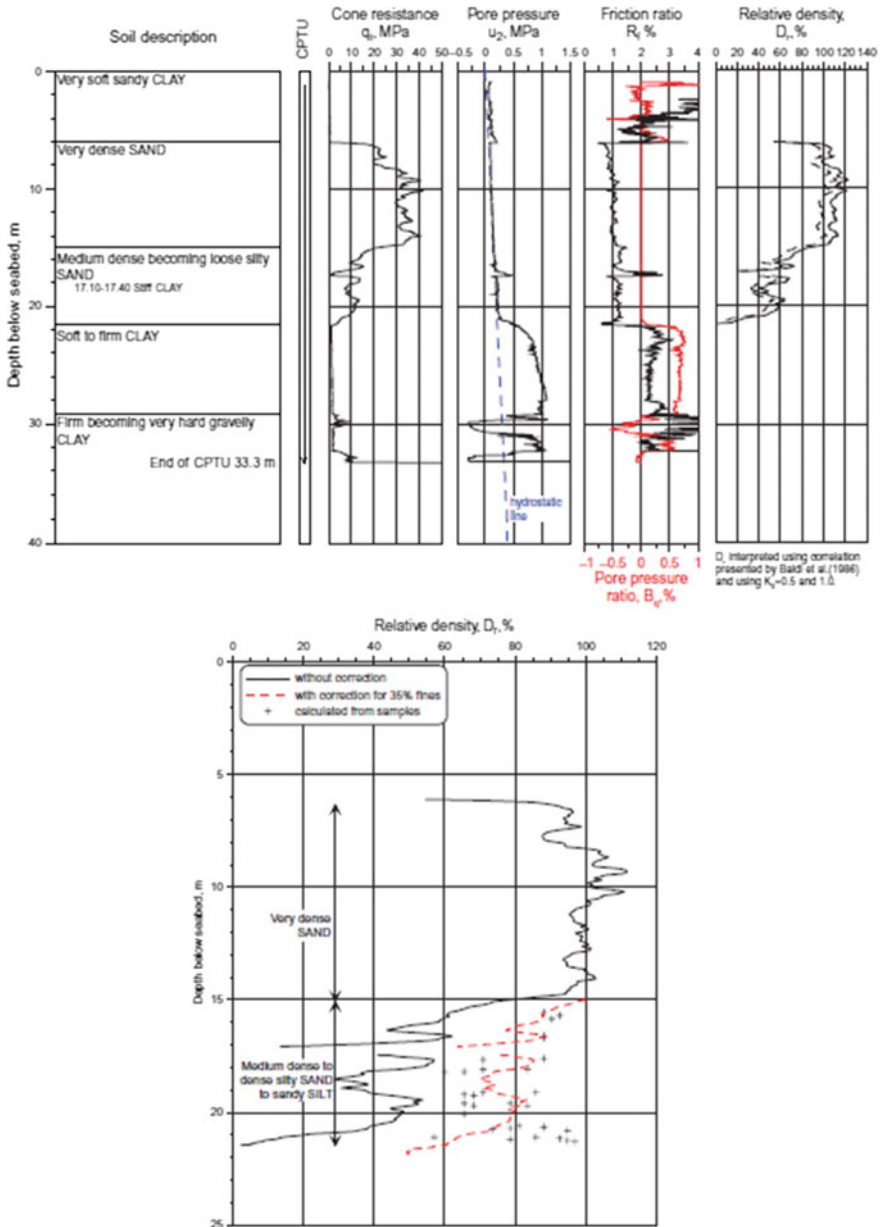
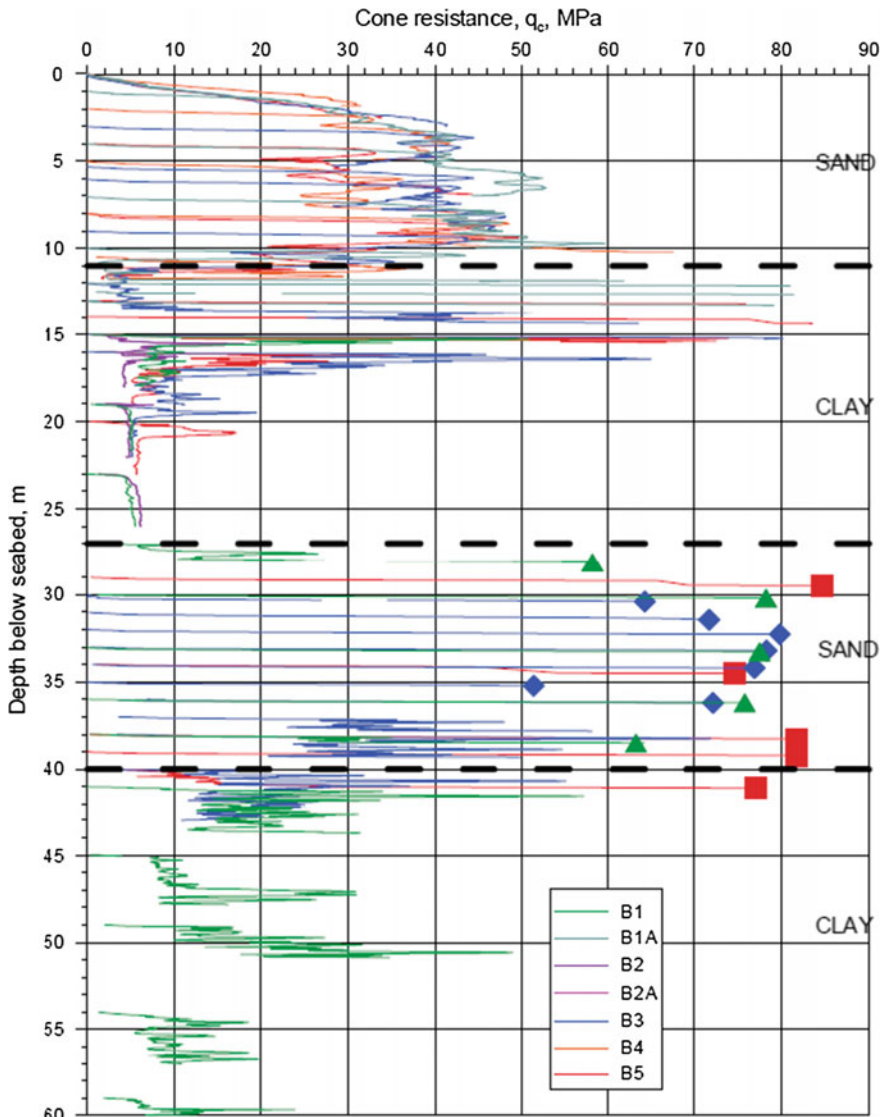


Fig. 1.22 CPT measurements from an offshore windfarm site [48]

steady and slow penetration of the cone is not included as part of conventional drilling rigs [28]. Mainly due to this drawback, CPT is less used than SPT in geotechnical engineering practice. Moreover, CPT is not suitable for deployment at



Note. Symbols indicate the value of q_c when maximum thrust of the CPT equipment was reached in the CPTs below 27 m depth

Fig. 1.23 CPT measurements at a North Sea offshore site (courtesy of Aker Solutions and NGI)

sites with very stiff and dense soil conditions, because the penetration process may damage the probe and rods. The presence of gravel-size particles may also limit the application of CPT.

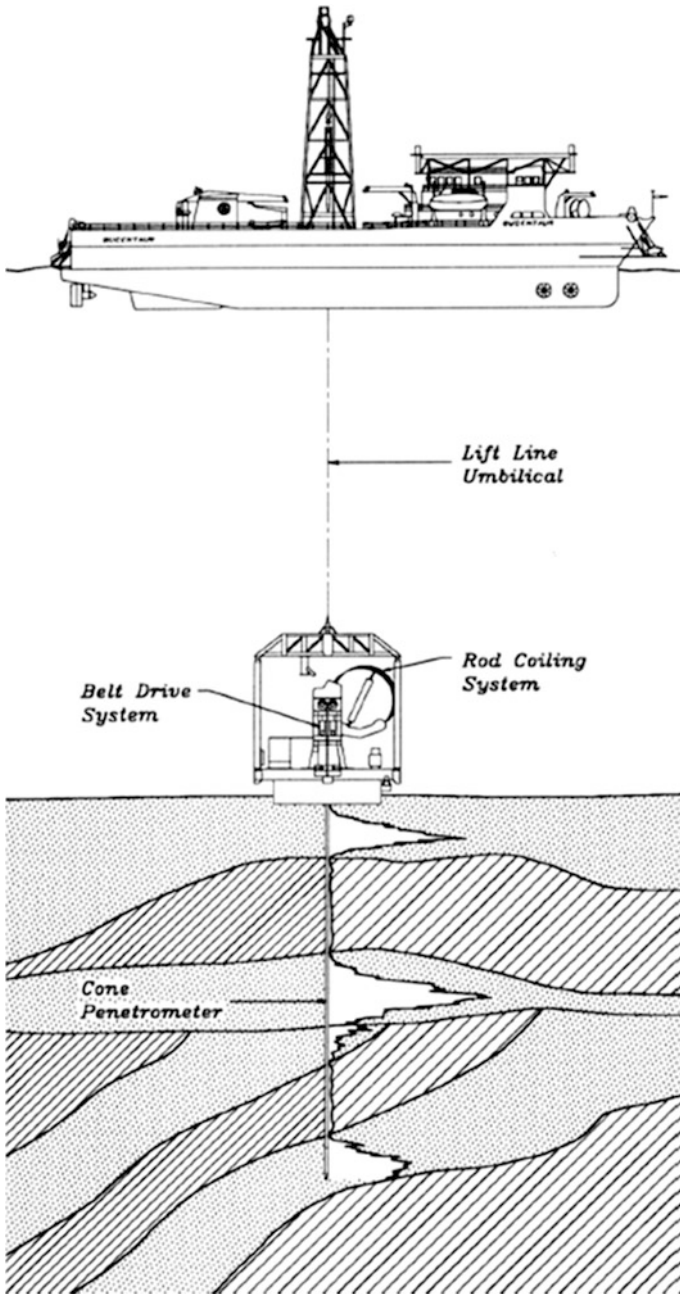


Fig. 1.24 Illustration of a CPT test with a seabed mode [51] Source [48] gives an overview of CPT operations for offshore applications

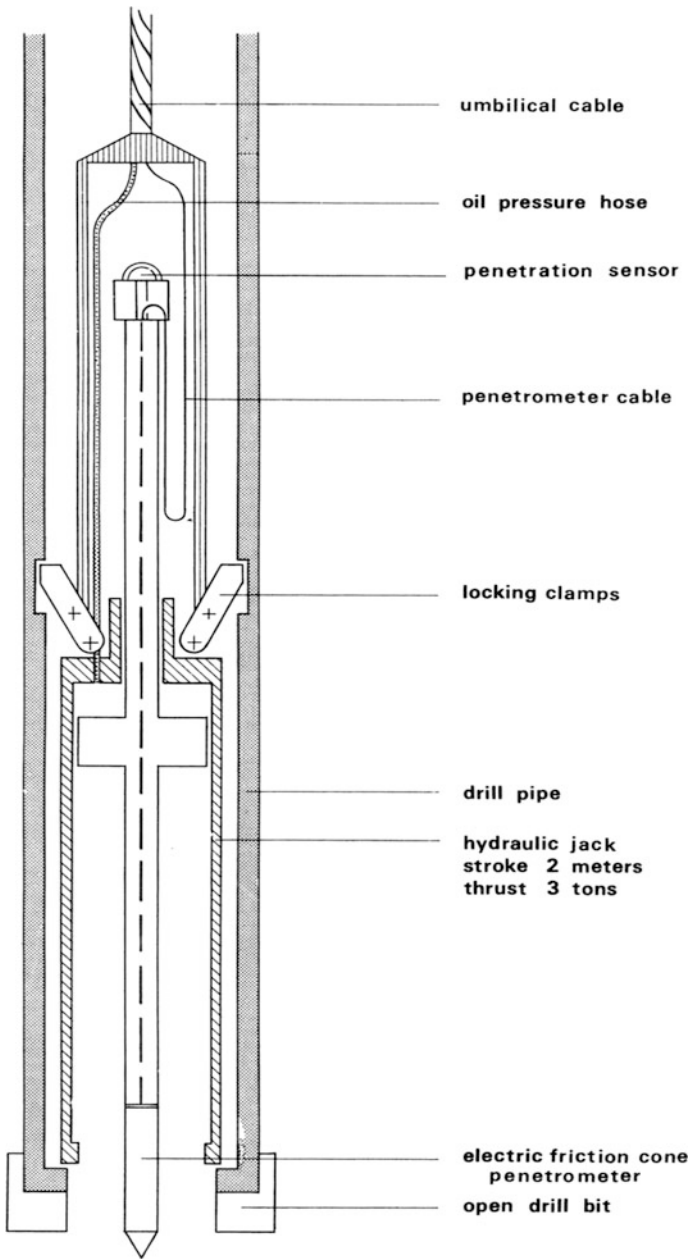


Fig. 1.25 Illustration of a CPT test with a drilling mode [52]

1.9.7 Other in Situ Testing Methods

Along with the SPT, CPT, and seismic wave velocity measurement (Sect. 6.2.2) methods, other in situ testing methods are also used for the exploration of sub-surface soils, which have been utilized in the evaluation of liquefaction potential. For example, for sites with gravel deposits, especially if sites contain mainly coarse to very coarse-grained soils, Becker penetration test (BPT) [56] can be employed. Because the diameter of the BPT penetrometer tip is much larger than that of the SPT sampler or the cone penetrometer, gravel-sized particles have much less effect on the BPT, whereas results obtained from SPT for sites with gravel contents greater than as low as 15–20% can be erroneous. BPT is similar to a small pile-driving test: It consists of driving a plugged steel casing into the ground typically using a diesel pile-driving hammer. The number of blows per unit length (usually foot) of penetration is recorded and adjusted for driving conditions and has been designed to be correlated with the SPT- N values so that the procedure for evaluating liquefaction potential using SPT can also be used by BPT. Two methods [54, 55] are widely adopted for this correlation, with the one proposed by Harder and Seed [54] as shown in Table 1.6. However, another BPT method, called iBPT [56], emerged in 2014 and is currently regarded as state of the art for BPT interpretation. Although there is insufficient empirical data available on the application of the iBPT method at the time of writing (2015), its use is strongly encouraged for any future BPT applications for high-hazard dams. For more details, readers may refer to the sources cited above.

1.10 Soil Stiffness and Poisson's Ratio

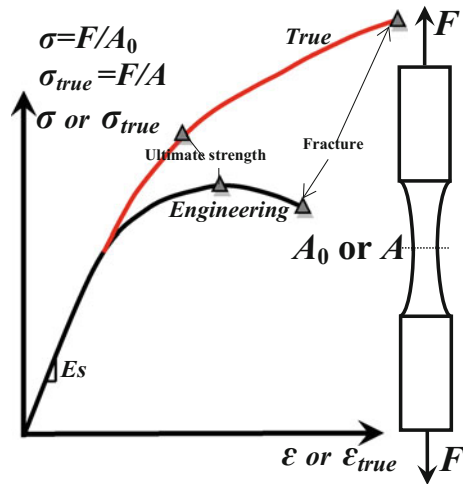
In solid mechanics, the stiffness of isotropic solid material can usually be simply modeled with a Young's modulus E_s (Fig. 1.26):

$$E_s = \frac{\sigma}{\varepsilon} \quad (1.28)$$

Table 1.6 Equivalence of corrected BPT and SPT resistance [54]

Corrected BPT blow-count N_{BC}	Corrected SPT blow-count N_{60}
0	0
20	~20
40	~34
60	~46
80	~58
100	~70

Fig. 1.26 Uniaxial tension test measured with both the engineering (σ and ϵ) and true stress-strain (σ_{true} and ϵ_{true}) curve (not to scale)



where σ is the normal stress and ϵ is the corresponding strain.

Table 1.7 lists representative values of Young's modulus for soils.

In a similar manner, the shear modulus G_s is defined as the ratio between the shear stress τ_{xy} and shear strain γ_{xy} , which are more often used as an important parameter to define the soil stiffness:

$$G_s = \frac{\tau_{xy}}{\gamma_{xy}} \tag{1.29}$$

E_s and G_s may be obtained from laboratory tests by measuring the vibration frequency of the soil specimen and correlating these frequencies to the stiffness and density properties of the specimen (Sect. 6.3.1); from field tests by measuring seismic wave velocity or velocity differences between different types of waves and

Table 1.7 Typical values of Young's modulus for soils

Type of soils	Soil details	Young's modulus (MPa)
Clay	Very soft	2–15
	Soft	5–25
	Medium	15–50
	Hard	50–100
	Sandy	25–250
Sand	Silty	7–21
	Loose	10–24
	Dense	48–81
Sand and gravel	Loose	48–148
	Dense	96–192
Silt		2–20
Shale		144–14,400

correlating these results to soil properties (Sect. 6.2.2); or based on SPT- N values (Sect. 1.9.5) and undrained shear strength.

When the strain level is sufficiently high, changes in soils' cross section are not negligible and are related to the Poisson's ratio of the material as shown in Fig. 1.27. Poisson's ratio for soils typically ranges from 0.2 to 0.5, while sometimes, it may be as low as 0.1 for loose deposits. Table 1.8 shows the typical values of Poisson's ratio for different types of soils. Moreover, regardless of whether soil is sand or clay, when it is saturated and kept in perfect undrained condition, its Poisson's ratio is 0.5. The ratio of sand in satisfactory drained condition shows a Poisson's ratio around 0.3, and it depends on the confining pressure, principal stress ratio, and shear strain. By assuming that the soil is isotropic, at low strain level, the Poisson's ratio can be calculated as:

$$v = \frac{E_S - 2G_S}{2G_S} \quad (1.30)$$

When soil exhibits noticeable plasticity, it can be modeled as elasto-plastic material as shown in Fig. 1.26.

Although initially controversial among seismologists and engineers [57], it is now widely recognized that soils exhibit linear-elastic behavior only at very small shear strain value γ . For example, $\gamma < 10^{-6}$ (more precisely $\gamma < 0.0005\%$, see Sect. 2.3.1) is commonly regarded as the range in which soil can be assumed to behave linear-elastically, for all types of soils including clays, silts, sands, gravels, and rocks, under static and dynamic loading [58], and for drained and undrained loading conditions [59]. The shear modulus of soils below this shear strain level is often referred to as initial shear modulus G_0 . With an increase in shear strain, soil stiffness decays nonlinearly, as shown in Fig. 2.5.

To illustrate the effects of soil nonlinearity, Fig. 1.28 shows power spectral density obtained from measurements of acceleration of a deck above a concrete shaft for a gravity-based structure (GBS) in the North Sea. The values shown in the figure include the data measured before, during and after a storm. The time interval between each two subsequent measurements is around 10 days. It is clearly shown that the natural frequency (frequency corresponding to the peak value of power spectrum density) of the GBS during the storm is lower than that before and after the storm, and higher ocean wave heights (indicating large wave-induced force on foundations) lead to lower documented natural frequencies of the structural

Fig. 1.27 Deformed shape (solid line) of a solid bar under uniaxial tension F

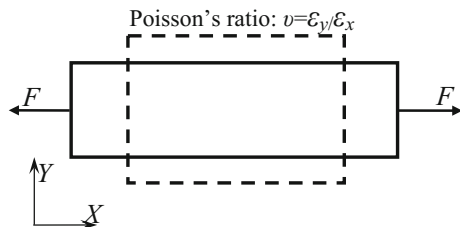


Table 1.8 Typical values of Poisson’s ratio ν for soils

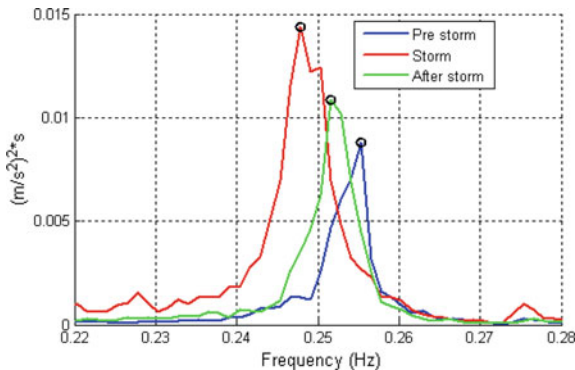
Type of soil	ν
Clay (saturated)	0.4–0.5
Clay (unsaturated)	0.1–0.3
Sandy clay	0.2–0.3
Silt	0.3–0.35
Sand (dense)	0.2–0.4
Sand (coarse, with void ratio = 0.4–0.7)	0.15
Sand (fine-grained with void ratio* = 0.4–0.7)	0.25
Rock	0.1–0.4 (depends on type of rock)
Ice	0.36
Concrete	0.15

vibrations. The difference in the system response spectral peak period between the measured storm sea states and calm sea is approximately 0.1 s. As the concrete shafts and topside steel structures remain linear-elastic during the storm event, this variation in stiffness is attributed to a degradation of soil stiffness during the storm. This soil nonlinearity can be approximated by a nonlinear backbone curve shown in Fig. 2.5.

The soil’s constitutive relationship can also be assumed to be stress-dependent. Soils can exhibit nonlinearity at a stress level as low as 10% of the yield stress of the soil. To account for the nonlinearity, one can use the elasto-plastic material law with Mohr–Coulomb failure criterion (Sect. 1.6.2), widely adopted by various commercial FE codes such as ABAQUS [344]. This material law was extended in the elastic range by a stress dependency of the oedometric stiffness modulus using the following equation:

$$E_S = \kappa \sigma_{ref} \left(\frac{\sigma}{\sigma_{ref}} \right)^\lambda \tag{1.31}$$

Fig. 1.28 Power spectral density from measurements of a deck above a concrete shaft for a GBS structure in the North Sea, for before, during, and after storm (courtesy of NGI, Statoil and Aker Solutions)



where $\sigma_{\text{ref}} = p_a = 100 \text{ kN/m}^2$ is called the reference (atmospheric) stress; σ is the current mean principal stress in the considered soil element; κ determines the soil stiffness at the reference stress state; and the parameter λ determines the stress dependency of the soil stiffness.

Even though the equation above is often used in geotechnical engineering, there is no direct empirical data on how to determine the magnitude of the two parameters κ and λ in the calculation of soil behavior. This is more obvious when the application is associated with pile foundations. In order to calibrate these parameters in connection with the numerical model, Achmus et al. [60] compared the numerical results and the results of the API p–y curve method (Chap. 16) with pile diameters of 1.0 and 2.0 m. As for such diameters, the p–y curve method is known to give a suitable estimation of pile deflection. They presented that, for dense sand, $\kappa = 800$ and $\lambda = 0.55$ were found to give the best matching results with respect to the p–y curve method.

1.11 Consolidation

1.11.1 Introduction to Consolidation

For both clay and sand at saturated condition, the volume of voids among soil particles decreases when the effective stress increases, leading to a decrease in the soil volume. This phenomenon is called consolidation (primary consolidation). Consolidation is more significant in clay than in sand. Primary consolidation has always been a geotechnical concern related to the foundation settlement (a vertical displacement of soil), especially for structures built at sites with soft clay layers or if the water table is lowered permanently in a stratum overlying a clay layer, when the soil is subjected to surcharge or pumping of water. In reality, significant settlement due to consolidation may take a few years.

At low stress level, based on the assumption that soil behaves linearly, one can calculate the volumetric strain of an element in the soil under three principal stresses ($\sigma_1, \sigma_2, \sigma_3$) as:

$$\Delta\varepsilon_{\text{vol}} = \frac{\Delta V}{V} = \frac{1 - 2\nu}{E} (\Delta\sigma_1 + \Delta\sigma_2 + \Delta\sigma_3) \quad (1.32)$$

Under a small increment of effective stress $\Delta\sigma'$, the volumetric strain $\Delta\varepsilon_{\text{vol}}$ of the clay can be calculated as:

$$\Delta\varepsilon_{\text{vol}} = m_v \Delta\sigma' \quad (1.33)$$

where m_v is called volume compressibility of soil.

Here, we define the over-consolidation ratio (*OCR*) as the maximum value of effective stress in the past divided by the present value. When the *OCR* equals to

unity, the clay is considered normally consolidated, meaning that the soil has never been subjected to a load greater than the existing overburden pressure.

When the over-consolidation ratio is larger than unity, the clay is called over-consolidated, indicating that the soil has been subjected to a load exceeding the overburden pressure. Soils with an *OCR* of between 1 and 3 are lightly over-consolidated, while soils with an *OCR* above 8 are heavily over-consolidated. Over-consolidated soil is usually the result of geological mechanical factors, such as the erosion of overburden, the melting of ice sheets after glaciation, and the permanent rise of the water table. Sometimes, it may also be due to higher stresses previously applied to a specimen in the triaxial apparatus [26]. Other processes, including drained creep (aging) and physicochemical processes such as cementation, ion-exchange, and thixotropy, can also cause soils to become over-consolidated.

On the other hand, in some cases, soils can be subjected to a vertical stress that is less than the overburden pressure, which is called under-consolidated soil. This condition occurs when a soil stratum is subjected to an excess hydrostatic pressure that prevents the soils from consolidating [27]. Under-consolidated soil can often be found in near-shore areas, particularly near river mouths, because the sea level over the past thousands of years has varied by more than 100 meters, causing relatively rapid deposition, and soils in those areas can accumulate faster than the escape of pore water. Under-consolidated soils have also been found at offshore sites in the Gulf of Mexico. However, in deep water or away from sediment sources, the accumulation rate can be extremely slow (millimeters per thousand years), such that the pore-water pressures remain at hydrostatic pressure values during the deposition process. This gives rise to normally consolidated clays. The clay shear strength in these soils will increase more or less linearly with depth. Moreover, if soils are eroded from an area subsequent to deposition, they are over-consolidated, as they will be stronger than normally consolidated soils.

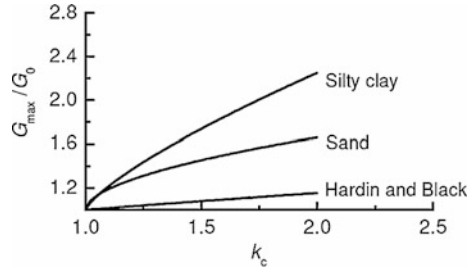
Besides consolidation due to the grain compression load, heating due to thermal excitation of H_2O molecules, which are electrically absorbed on the clay mineral surface, can also accelerate the consolidation. This type of consolidation is often referred to as secondary consolidation.

Under negative excess pore-water pressure, the reverse process of consolidation, called swelling, occurs with a form of gradual volume increase in soils. An example of this is that, in the excavation in a saturated clay, whereby heaving (soil moving upward) may occur at the bottom of the excavation due to clay swelling.

1.11.2 Effects of Consolidation on Soil Stiffness

The consolidation of soils may only slightly influence dynamic shear modulus of undisturbed soil, while the degree of the consolidation can significantly influence the ground motion accelerations in the case of a strong earthquake [61]. When soils are subjected to the condition of confining stress, with the three principal ones being

Fig. 1.29 Comparison of $\frac{G_{\max}}{G_0}$ varied with k_c for formulas proposed by Harding and Black's and Sun and Yuan (silty clay and sand) [63]



$\sigma_1 = k_c \sigma_3$, $\sigma_2 = \sigma_3$ (k_c is often called consolidation ratio and it typically varies in the range of 1.4–3.0 in actual soils), the relative increment ($\frac{G_{\max}}{G_0}$) of the maximum dynamic shear modulus due to the consolidation may be calculated by Hardin and Black's formula [62]:

$$\frac{G_{\max}}{G_0} = \sqrt{\frac{2 + k_c}{3}} \quad (1.34)$$

where G_0 is the dynamic shear modulus of undisturbed soils; G_{\max} is the dynamic shear modulus of the undisturbed soil due to consolidation with a consolidation ratio of k_c .

Note that Hardin and Black's formula does not distinguish different types of soils. By performing the resonant column tests for three types of undisturbed cohesive soils (silty clay, silt, and sludgy soil) under different consolidation ratios of k_c , Sun and Yuan [63] presented an estimation of the relative increment of maximum dynamic shear modulus:

$$\frac{G_{\max}}{G_0} = 1 + C(k_c - 1)^m \quad (1.35)$$

where coefficients C and m are 1.25 and 0.76 for silty clay, 1.20 and 1.05 for silt, 1.85 and 0.47 for sludgy soil, and 0.66 and 0.54 for sand.

By comparing the two formulas above, which are also shown in Fig. 1.29, it is noticed that the one proposed by Sun and Yuan [63] gives a significantly higher $\frac{G_{\max}}{G_0}$ than that from Hardin and Black's formula, and this is more obvious for silty clay than the sand. Similar results can also be found in another research by He [64].

1.11.3 Effects of Consolidation for Shallow Foundations

For shallow foundations, consolidation mainly induces foundation settlement and causes an increase in the bearing capacity. Regarding settlement, Fig. 1.30 illustrates the vertical settlement records of five gravity-based platforms in the North

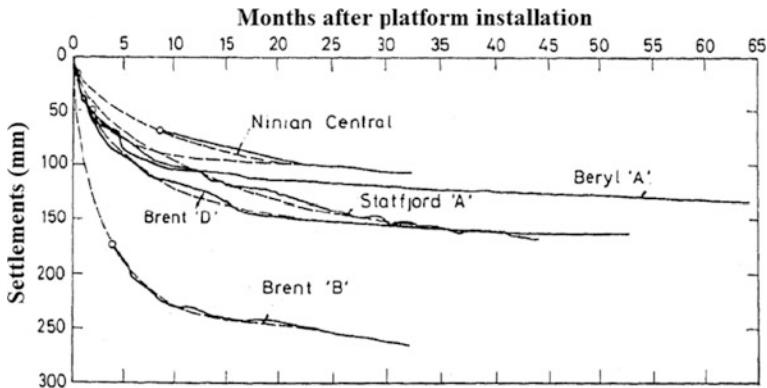


Fig. 1.30 Settlements due to consolidation for five North Sea GBS platforms (excluding initial settlements) [66]

Sea. All five platforms are installed on stiff to hard over-consolidated clays and dense sands. The measurements were carried out a few months after the platforms had been installed. The initial settlements are not included in the records. The long-term settlement of foundation may cause storm waves to impact the topside of a platform (the so-called wave-in-deck) due to a possible significantly decrease in air gap between the bottom of the topside and the water surface.

On the other hand, it may be justified to include the positive effects of consolidation on increasing the bearing capacity. It is a normal practice to design a gravity-based structure (GBS) based on the assumption that the design storm would not arrive until the autumn after its installation. For example, the foundation design of Gullfaks C platform shown in Fig. 1.31 is based on the assumption that the first design storm will arrive 4 months after its installation. Moreover, if the soil condition of a GBS foundation is dominated by sand, drainage will occur relatively rapidly, and it is reasonable to assume that the associated soil will consolidate under the weight of the platform before the design storm arrives. For example, pore pressure measurements in the sand beneath the Ekofisk tank during ballasting indicate that the vertical pressure increased by 60 kPa in the duration of approximate 55 days. However, this did not cause an excess of pore pressure in the sand [65].

To accelerate the consolidation and improve the stability shortly after the installation of platforms, different types of filter systems (depending on structure and top soil conditions), known as soil drain systems, are often installed on the concrete wall and skirt of platforms and are connected to a hydrostatic head lower than that in the still water level. The drainage system has been operated by a suction pressure 10–20 m below the lowest astronomical tide level [67]. Moreover, the system also helps to reduce the generation of excess pore pressure caused by earthquakes or ocean storms. The excess pore pressure is relevant to potential soil liquefaction under cyclic loading, as will be discussed in Chap. 7. In addition, the



Fig. 1.31 Gullfaks C platform with a topside weight of 74,000 tons

drainage system can facilitate the removal of platforms as the water pressure in the skirt compartments can be increased in order to pull the skirts out of the ground after the platform has been deballasted.

1.11.4 Effects of Consolidation and Aging for Deep Foundations

Under consolidation, deep foundations such as piles will experience settlement as shallow foundations do. Various methods exist to estimate the settlement of piles and pile groups, ranging from simple empirical approaches to more complicated nonlinear finite element analysis. The simplest approach may be the one proposed by Terzaghi and Peck [68], who stated that the settlement of a piled raft could be calculated as the settlement for an equivalent raft placed at the lower third points of the average pile length and loaded by a raft stress equal to the total load on the piles divided by the footprint, and the stress is distributed into the soil at a slope of 2:1 (vertical/horizontal). An elastic modulus, E_s , was applied to determine the strain due to the applied stress, and the settlement can then be determined as the sum of the accumulated strain. Combined with a depth factor F_D , which accounts for the influence of depth proposed by Fox [69] and is defined as the ratio between the mean vertical displacement of the embedded foundation and that of a similar foundation placed on the ground surface, the settlement of a pile raft using Terzaghi–Peck equivalent depth approach can then be calculated as:

$$S_{\text{raft}} = F_D \sum_{i=1}^n \left(\frac{\Delta q_i}{E_{si}} h_i \right) \quad (1.36)$$

where Δq_i is the effective stress increase in i th layer using the stress distributed into the soil at a slope of 2:1 (vertical/horizontal); h_i is the thickness of the i th layer; E_{si} is the elastic modulus of the i th layer.

It should be noted that, in the equation above, the axial compression of the piles for the length above the equivalent raft was not included in the Terzaghi–Peack equivalent depth approach.

Other simplified methods have been proposed by various researchers: Meyerhof [70], Schmertmann [71], Poulos [72], and Fellenius [73]. Interested readers may refer to the sources cited above.

On the other hand, pile loading tests indicate that the skin friction between piles and surrounding soils increases with time after pile driving, which is often referred to as soil/pile setup. This increase applies for piles in both clays and sands [74, 75]. Although complete mechanisms contributing to pile/soil setup are not well understood, the increase in skin friction with time is likely to be caused mainly by a combination of the two effects:

1. Consolidation: the excess pore-water pressures due to pile driving will dissipate with time, followed by subsequent remodeling and reconsolidation of soil, which are displaced and disturbed during pile driving. The horizontal effective stress between piles and surrounding soil therefore increases, causing an increase in skin friction. For piles driven in clean sands, excess pore pressures will dissipate within a few hours. For piles in clay, many months may be spent for a full consolidation. Depending on soil permeability and amount of disturbance, dissipation of excess pore-water pressures is non-uniform (nonlinear) with respect to the log of time for some time after pile driving. Subsequently, excess pore-water pressure dissipation becomes uniform (linear) with respect to the log of time.
2. Aging: after full dissipation of excess pore-water pressures, the skin friction increases with time. The physical phenomena involved are only partially understood. Soil grain bonding and loss of arching are likely to be the contributors.

Pile/soil setup occurs in most parts of the world, for virtually all driven pile types, in organic and inorganic saturated clay, and loose to medium dense silt, sandy silt, silty sand, and fine sand, and is influenced by both soil and pile properties. In cohesive soils, the shear strength of the disturbed and reconsolidated soil has been found to be higher than the soil's undisturbed shear strength. In fine-grained granular soils, the majority of setup is related to both creep-induced breakdown of driving-induced arching mechanisms and aging. Setup develops faster for more permeable soils. Setup rate decreases as pile size increases [76].

In addition, pile capacity may increase as a result of the previous test loading of the pile [75, 77].

Figure 1.32 shows a typical development of the skin friction with time for a pile in clay.

The increase in skin friction after dissipation of the excess pore-water pressures can be expressed as:

$$Q(t) = Q(t_0) \cdot [1.0 + \Delta_{10} \cdot \log_{10}(t/t_0)] \tag{1.37}$$

where $Q(t)$ is the pile skin friction in a given layer; t is the time since pile driving; t_0 is the reference time, often taken as 100 days for piles in clay [78, 79]; Δ_{10} is a dimensionless soil parameter.

The value of Δ_{10} can be determined from pile tests carried out on identical piles at different times. A few pile load tests exist with measurements of the increase in capacity with time. For piles in clays, Δ_{10} may be calculated as:

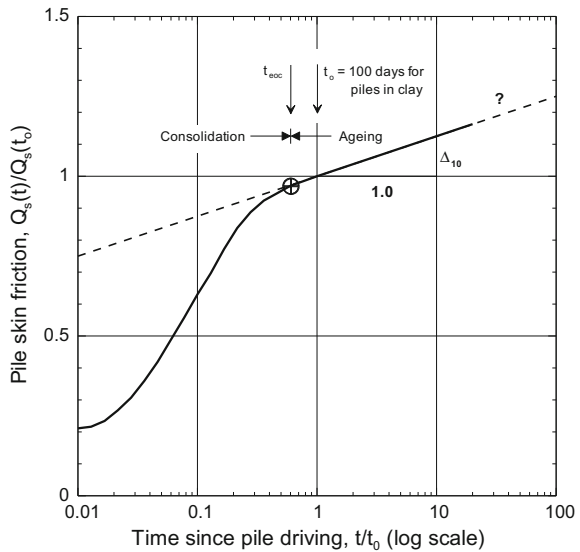
$$\Delta_{10} = 0.1 + 0.4(1 - I_p/50) \cdot OCR^{-0.8} \tag{1.38}$$

$$OCR \approx (4 \cdot s_u/\sigma'_v)^{1.25} \tag{1.39}$$

where $I_p = 100\% \times (w_L - w_p)$ is the clay plasticity index as defined in Sect. 1.8. It is determined by using the average value along the pile; OCR is also determined by the average value along the pile; s_u is the undrained shear strength, see Sect. 1.6.2 and Fig. 1.16 for its determination; σ'_v is the vertical effective stress; Δ_{10} normally ranges from 0.1 to 0.5, with a typical value lower than 0.25.

It is noted that the benefits of even a modest increase in pile skin friction due to consolidation and aging may eliminate the problems of insufficient pile foundation capacity that some offshore platforms suffer. However, this type of increase in skin

Fig. 1.32 Typical development of skin friction in time for a pile in clay (courtesy of Aker Solutions and NGI)



friction is not properly documented for offshore piles subjected to cyclic loading induced by ocean wave and wind and is therefore not widely accepted by regulatory authorities and even offshore industry yet.

Example Based on the soil parameter given in Table 1.9, estimate the increase in soil friction resistance due to the time effects for the clay layers at 11.0–27.0 m below the ground surface.

Solution: Based on the data given in Table 1.9, the weighted average *OCR* is about 8 for the clay layer between 11.0 and 27.0 m below the ground surface. And $I_p = 23.7\%$. Using these values yields $\Delta_{10} = 0.15$.

$$Q(t) = Q(100) \cdot [1 + 0.15 \cdot \log_{10}(3650/100)] = Q(100) \cdot 1.23. \quad (1.23)$$

This implies that there is an increase of around 23% in the pile wall friction due to time effect compared to the skin friction capacity when piles had just been installed. A similar time effect factor is expected for the pile's end-bearing capacity.

In addition, the initial consolidation can also significantly increase the vertical effective stress in the vicinity of pile [89].

1.12 Obtaining Soil Parameters for Engineering Design

Field testing and laboratory testing are required to obtain the required soil properties, including drilling and logging, sampling, in situ testing, and laboratory testing. The level and extent of a soil investigation should be a function of several factors including, but not limited to, geology of the area, local soil conditions, project requirements, availability of previous investigations, accessibility, environmental conditions, and any limitations related to budget and time available. The detailed plans and specifications for the investigation should be based on a consideration of the following factors [90]:

1. Type of investigation, regional, or site specific;
2. Expected soil conditions, bathymetry, and seabed features;
3. Active geological processes and possible geohazards;
4. Type of problems, soil–structure interaction, slope stability, etc.;
5. Required soil parameters;
6. Previous knowledge from the area, geological, geophysical, and geotechnical;

Table 1.9 Soil parameters for a site in the North Sea

Unit	Depth (m)	Soil description	γ_{tot} (kN/m ³)	I_p (%)	OCR	q_c (CPT tip resistance or cone resistance) (MPa)	ϕ' (°)	s_u (kPa)
A	0.0–11.0	Sand, coarse to fine, medium dense to dense	20.0	–	–	0–35 (0–2 m) 35 (2–11 m)	42	–
B	11.0–27.0	Clay, sandy, silty, very stiff to very hard	20.5	12.5 22.7 27.8	5 13 4.2	–	–	180 (11–13 m) 400 (13–20 m) 290–350 (20–27 m)
C	27.0–40.0	Sand, fine, silty, dense	20.5	–	–	80 (27–35 m) 80–25 (35–40 m)	42	–

7. Equipment that can be used;
8. Budget restraints;
9. Time schedules.

Internationally, there are several guidance regarding soil investigations for offshore structures, such as ISO 19902 [91], ISO 19901-4 [92], and DNVGL-RP-C212 [93]. There are also many national guidance and codes to regulate soil investigation, such as Norsok G-001 [90], which often makes reference to the international guidelines cited above.

After field and laboratory tests are completed, a review of the quality and consistency of the data will be carried out, and it is important for geotechnical engineers to determine whether the results are consistent with expectations. Once the laboratory and field data have been collected, the process of soil parameter selection can be carried out.

The design requirements must be studied carefully to determine the type and quantity of soil information to be developed during the geotechnical investigation. During this phase, it is necessary to perform the following tasks [41]:

1. Identify design and constructability requirements (e.g., provide grade separation, transfer loads from superstructure, provide for dry excavation) and their effects on the geotechnical information needed
2. Identify performance criteria (e.g., limiting settlements, right of way restrictions, proximity of adjacent structures) and schedule constraints.
3. Identify areas of concern on site and potential variability of local geology.
4. Develop likely sequence and phases of construction and their effects on the geotechnical information needed.
5. Identify engineering analyses to be performed (e.g., bearing capacity, settlement, global stability).
6. Identify engineering properties and parameters required for these analyses.
7. Determine methods to obtain parameters and assess the validity of such methods for the material type and construction methods.
8. Determine the number of tests/samples needed and appropriate locations for them.

Tables 12.1, 14.2 and 14.3 summarize the soil data required and testing considerations for the design of shallow foundations, driving pile foundations, and drilling pile foundations, respectively.

For offshore structural and foundation design, ISO 19901-4 [92] provides a systematic guidance for the soil investigation and characterization of soil properties.

1.13 Allowable Stress Design and Load Resistance Factor Design

1.13.1 Allowable Stress Design

In traditional geotechnical design until 1979, allowable/working stress design (ASD or WSD) was the norm. This requires that the working/service loads (loads at their actual levels) do not exceed the resistance. All uncertainty is lumped into the factor of safety (resistance factor) FS , which is determined on the basis of experience and observed performance. The margin of safety is introduced by considering soil, foundation, or structural behavior under working/service load conditions and comparing the responses under these conditions with allowable strength:

$$S_n \leq R_n/FS \quad (1.40)$$

where S_n is applied load effects, which can be the load effects due to a single load or a combination of different types of loads by considering the probability of their simultaneous occurrence; R_n is the nominal strength/capacity.

One of the greatest problems with the use of ASD is that it does not lend itself to the estimation of probability of failure. Additionally, it commonly misleads engineers into believing that the factor of safety used in the design is a true measure of the safety of foundations and structures [94], and the variability in both loads and resistance is therefore not fully realized.

1.13.2 Load Resistance Factor Design

1.13.2.1 Method

Due to the limitations of ASD, in recent decades, structural and geotechnical design codes have been moving toward load resistance factor design (LRFD) embedded in limit state designs (serviceability limit state (deflection), ultimate limit state (yielding, fracture and buckling), fatigue limit state, and accidental limit state (progressive collapse limit state)), in which load factors are applied to various types of loads and resistance factor(s) are applied to several resistance parameters (such as strength, friction angle). Therefore, LRFD is essentially meant to consider the uncertainties in both loading and resistance and to ensure a prescribed safety margin by using procedures from probability theory.

As shown in Fig. 1.33, LRFD design can be described as:

$$\gamma_{F1}S_{k1} + \gamma_{F2}S_{k2} + \cdots + \gamma_{FN}S_{kN} \leq R_{ki}/\gamma_{Mi} \quad (1.41)$$

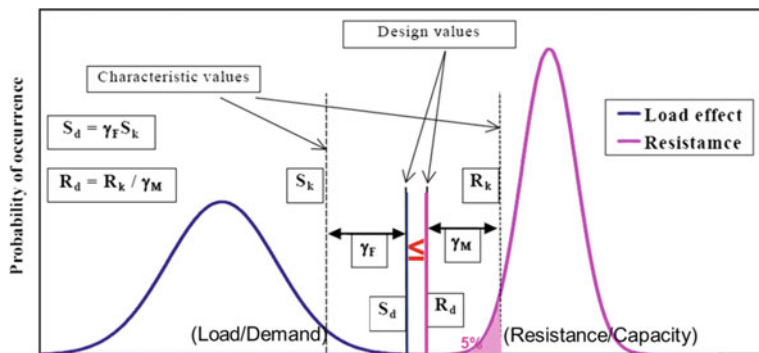


Fig. 1.33 An illustration of LRFD design (courtesy of John Michael Rotter, University of Edinburgh and Imperial College)

where S_{k1}, \dots, S_{kN} are the characteristic values of N types of load effects acting on a structure. They typically represent load effects corresponding to a specific annual probability of occurrence (or return period). However, the characteristic load effects at fatigue limit condition normally correspond to a load with expected load history, and the characteristic load effects at serviceability limit condition correspond to a load effect with a specified value depending on operational requirements; $\gamma_{F1}, \dots, \gamma_{FN}$ are the load factors (partial safety factors) for N types of loads. They are used to account for the possibility of unfavorable deviations of the action values from the representative values (fundamental variability in environmental loads), the uncertainties in the modeling of load effects (such as the computational model and statistical uncertainty due to a lack of knowledge), and the uncertainties in the assessment of the limit states being considered; it is noted that in foundation designs, the separation of load categories to which different partial safety factors could be applied is sometimes not straightforward, and this also applies to load applications to risers, TLP tendons, mooring lines. R_{ki} is the characteristic value of a particular (i) resistance of soils or foundations, which typically corresponds to characteristic or nominal ($=R_{ni}$) values for the material properties and dimensions. For example, it can be determined by a 5%-fractile material strength (a lower bound or 95% exceedence value) from tests; γ_{Mi} is the partial factor (resistance factor or partial safety factor) for that particular (i) resistance, which accounts for the uncertainties due to each component of soil strength such as friction angle of sand, cohesion strength of clay. The result of $R_d = R_{ki}/\gamma_{Mi}$ is often called factored strength or design resistance, which is based on past experience, but is in principle meant to provide an acceptable level of safety or performance. For structures, its value also depends on the limit states and the material (indicating different degrees of control in the manufacturing process of structural materials, e.g., steel, concrete, composites, timber, mortar, and bricks) applied.

The equation above can be simply expressed as:

$$S \leq R \quad (1.42)$$

where S and R represent the factored loads and factored resistance (strength), respectively.

Readers should notice that, in LRFD, both the applied loads (left-hand side of the equation above) and the strength/resistance (right-hand side in the equation above) are fictitious due to the factors applied. Moreover, as the partial safety factors for both load and resistance represent the uncertainties in the characteristic values, while due to a lack of detailed statistical data on all the parameters considered in design and also the complexity of the statistical analysis, there is a compromise to use a more subjective assessment of the partial safety factors than is mathematically consistent with the design philosophy.

Furthermore, readers must bear in mind that even though uncertainties due to design errors and construction errors are important, they are normally not accounted for by design codes, but are instead addressed through proper quality assurance (QA) such as third-party verification and/or QA by engineers who are not involved in the same design project before the QA.

In cases where a high resistance is unfavorable for design, the characteristic resistance may be determined as an upper characteristic resistance. The corresponding probability may be of the same level as the probability of a lower value, e.g., 5% versus 95% fractile. For geotechnical analyses, “low probability” will in most cases mean a conservatively estimated mean value. As will be discussed in Sect. 3.5, for performing site-response analysis, it is recommended that a sensitivity analysis be performed by accounting for the variation of soil properties from lower-bound, average (best estimate) to upper-bound value. If the ground motions are not sensitive to the variation in soil properties, typically, the best-estimate value of soil properties can be used to compute the ground motion time histories. It is consequently expected that the designers involved should consider the relevant cases. When the action effect is increased with the material resistance, the design may also be based on an upper characteristic resistance, e.g., based on 95% fractile. An example of this is an analysis of pile driving or lifting, in which the upper-bound soil resistance is normally used. Design against fatigue failure in steel, aluminum, and concrete may adopt S-N curves with characteristic resistance based on 2.3% fractile. Fracture mechanics analyses of crack propagation can be used in special cases. Design actions and resistances may be calculated by using deterministic computational models.

It is noted that both the load and resistance factors vary significantly depending on the applications. For example, in structural engineering problems, the determination of loads is usually less certain than that of resistances/materials. Therefore, S typically has a larger variability than R , implying that S has a higher coefficient of variation, hence a wider probability density distribution. On the other hand, unlike typical structural materials such as steel or concrete, which are quality controlled during their manufacture process, soils and rocks are natural material and site

specific and are therefore highly variable. This poses a significant challenge during the development of LRFD in geotechnical engineering.

1.13.2.2 Probability of Failure

It is important to build the equation of LRFD design in connection with probabilistic measures. Therefore, the probability of failure, which is the probability that the factored loads exceed the factored resistance, can be expressed as:

$$P_f = P(R \geq S) \quad (1.43)$$

Given that the load effects s and resistance r are varying randomly in a statistically known manner, a safety margin can then be established as:

$$m = r - s \quad (1.44)$$

For all combinations of r and s that satisfy the condition $m > 0$, the design is on the safe side, and for those combinations giving a safety margin $m \leq 0$, the soil, the foundation, or the structure is suspected to fail. Therefore, the equation above can be utilized as a measure of failure probability. By observing Fig. 1.33, it is noticed that failure probability depends on both the difference between the load and resistance, as well as their variability.

With the construction of the equation above, one has moved from deterministic design to probabilistic design, in which the soil and structural material properties, structural member dimensions, and loads are interpreted as random variables x . Uncertainties can be described if the probability density function of the random variables are known. Therefore, if their probability density functions $f_R(x)$ and $f_S(x)$, with the corresponding probability distribution functions or cumulative distribution functions (CDFs), $F_R(x)$ and $F_S(x)$, are known, the safety margin m can be defined as a random variable M , with a probability density function $f_M(x)$ and a probability distribution function $F_M(x)$. The equation to determine the probability of failure can then be rewritten as:

$$P_f = P[M \leq 0] = F_M(0) = \int_{-\infty}^0 f_M(x) dx \quad (1.45)$$

Since it is not possible to define $f_M(x)$ and $F_M(x)$ analytically except for a few special cases, the equation above can be written in terms of load and resistance effects:

$$P_f = P[R - S \leq 0] = \int_{-\infty}^{+\infty} F_R(x) f_S(x) dx = F_M(0) \quad (1.46)$$

The equation above indicates that when the load effects lie in the interval $(x, x + dx)$ and the resistance is smaller than x , the probability of failure is $F_R(x) f_S(x) dx$. The total probability of failure is equal to the integral above when the load effect is in the interval $(-\infty, +\infty)$.

Alternatively, the probability of failure expressed in the equation above can also be written as:

$$P_f = \int_{-\infty}^{+\infty} (1 - F_S(x)) f_R(x) dx = F_M(0) \quad (1.47)$$

Since the resistance cannot be negative, the lower boundary for the integrals in the two equations above may be changed into 0. Moreover, the integral of the three equations above usually does not have a closed-form solution. It can be solved numerically by either numerical integration or Monte Carlo methods [95].

The reliability can then be calculated as:

$$P_R = P[R - S > 0] = 1 - P_f = 1 - \int_{-\infty}^{+\infty} F_R(x) f_S(x) dx = 1 - F_M(0) \quad (1.48)$$

Due to a lack of statistical data that defines probability density functions of load and resistance variables, as well as the fact that the expression of probability density functions is complicated, the load and resistance variables can normally be defined by their mean values and variance. It is then convenient to present a less complicated probabilistic measure for the reliability, namely safety index or reliability index β , originally proposed by CA Cornell [96] in 1969, which is the number of standard deviations of the derived probability density function m , separating the mean safety margin from the nominal failure value of m being zero:

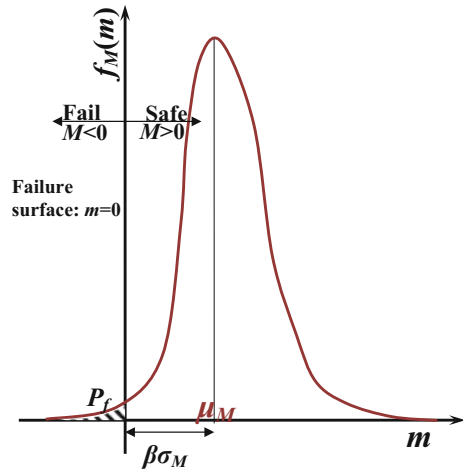
$$\beta = \mu_M / \sigma_M \quad (1.49)$$

where μ_M and σ_M are the mean value and standard deviation (square root of the variance) of safety margin M .

Provided the safety margin can be described by only one normally distributed random variable, where the failure surface is a point $m = 0$, the exact safety index β can be defined as the distance between the expected value μ_M of the safety margin and the boundary for failure $m = 0$, as shown in Fig. 1.34. And the distance is usually measured in terms of σ_M .

When both R and S are independent and normally or lognormally distributed variables, the exact safety index is directly related to the failure probability through the standard normal distribution function:

Fig. 1.34 Illustration of safety index β



$$P_f = P[M \leq 0] = \Phi[(0 - \mu_M)/\sigma_M] = \Phi(-\beta) = 1 - \Phi(\beta) \leftrightarrow \beta = -\Phi^{-1}(P_f) \tag{1.50}$$

where $\Phi()$ is the standard normal distribution function, defined as:

$$\Phi(x) = \int_{-\infty}^x \frac{1}{\sqrt{2\pi}} e^{-t^2/2} dt \tag{1.51}$$

The values of the standard normal distribution function can also be obtained by a spreadsheet (e.g., NORMSDIST in Excel) or from various mathematical handbooks. Table 1.10 shows a few correspondences between β and P_f .

For a quick estimation, the failure probability can also be approximated as:

$$P_f \approx 0.475 \exp(-\beta^{1.6}) \tag{1.52}$$

or be more roughly estimated as:

$$P_f \approx 10^{-\beta} \tag{1.53}$$

Table 1.10 Correspondences between β and P_f

β	1.0	1.2	1.28	1.4	1.6	1.8	2.0	2.2
P_f (%)	16	12	10	8.1	5.5	3.6	2.3	1.4
β	2.33	2.7	3.09	3.3	3.7	4.0	4.4	4.9
P_f (%)	1.0	0.35	0.1	0.048	0.011	0.0032	0.00054	0.000048

By assuming that both R and S are independent and normally distributed variables (as shown in Fig. 1.33), the safety margin m , which is a linear combination of R and S , also follows a normal distribution. Their mean value μ_M and variance σ_M^2 can be calculated as:

$$\mu_M = E_M = \mu_R - \mu_S \quad (1.54)$$

$$\sigma_M^2 = V_M = \sigma_R^2 + \sigma_S^2 \quad (1.55)$$

where $E[\]$ and $V[\]$ are the expected value and variance, respectively.

Therefore, the safety index can be calculated as:

$$\beta_N = \frac{\mu_R - \mu_S}{\sqrt{\sigma_R^2 + \sigma_S^2}} = \frac{\mu_R/\mu_S - 1}{\sqrt{(\mu_R/\mu_S)^2 V_R^2 + V_S^2}} \quad (1.56)$$

As the performance of the physical behavior of engineering systems usually cannot obtain negative values (load and resistance), it is better described by a lognormal distribution [97]. The safety margin can then be expressed as:

$$m = \ln R - \ln S = \ln(R/S) \quad (1.57)$$

In case both R and S are independent and lognormally distributed variables, even though R/S is not lognormally distributed, $\ln R$ and $\ln S$ follow normal distributions, and thus, the safety margin, $m = \ln R - \ln S$, still follows a normal distribution. As such, the relationship obtained in Eq. (1.50) is still valid to calculate the probability of failure. One can show that the safety index can be calculated as [98]:

$$\beta_{LN} = \frac{\ln\left[(\mu_R/\mu_S)\sqrt{(1+V_S^2)/(1+V_R^2)}\right]}{\sqrt{\ln[(1+V_R^2)(1+V_S^2)]}} \approx \frac{\ln(\mu_R/\mu_S)}{(V_R^2 + V_S^2)} \quad (1.58)$$

Upon the presentation above, it is known that in LRFD, it is important to perform a calibration process to determine the load factor and the resistance factor so that the distributions of R and S can answer the requirements of a specified safety index. In other words, the γ_F and γ_M described in Fig. 1.33 need to answer to the prescribed target reliability (i.e., a predetermined probability of failure) in the two equations above. Several solutions are available for this calibration purpose, such as first-order reliability method (FORM) and Monte Carlo simulation. Sources [95] and [99] also give elaborations of this topic.

The definition of safety index in Eq. (1.49) and one-to-one relation between the failure probability and the safety index calculated in Eq. (1.50) are also valid when R and S are correlated, but the variance σ_M^2 must be calculated to account for the correlation between R and S :

$$\sigma_M^2 = \sigma_R^2 + \sigma_S^2 - 2\rho_{R,S} \cdot \sigma_R \cdot \sigma_S \quad (1.59)$$

where $\rho_{R,S}$ is the correlation coefficient between R and S , ranging from -1.0 to 1.0 , as defined by:

$$\rho_{R,S} = \text{Cov}[R, S]/(\sigma_R \cdot \sigma_S) \quad (1.60)$$

where $\text{Cov}[R, S]$ is the covariance of R and S , defined by:

$$\text{Cov}[R, S] = \sigma_{R,S} = E[(R - \mu_R)(S - \mu_S)] = \int_{-\infty}^{+\infty} \int_{-\infty}^{+\infty} (r - \mu_R)(s - \mu_S)p(r, s)drds \quad (1.61)$$

where $p(r, s)$ is the probability density function, which can be represented as a surface above a horizontal plane, and the cumulative probability ($P(r, s)$) of r lying in the range between r and $r + dr$ as well as s lying between s and $s + ds$ is $p(r, s)drds$.

If the safety margin $m = f(x)$ is a linear combination of n basic variable x_i , and the random variation of all basic variables can be described by normally distributed independent random variables X_i , the resulting safety margin can then be described by a normally distributed random variable M :

$$M = f(X) = a_0 + a_1X_1 + a_2X_2 + \cdots + a_nX_n \quad (1.62)$$

where $i = 1, \dots, n$.

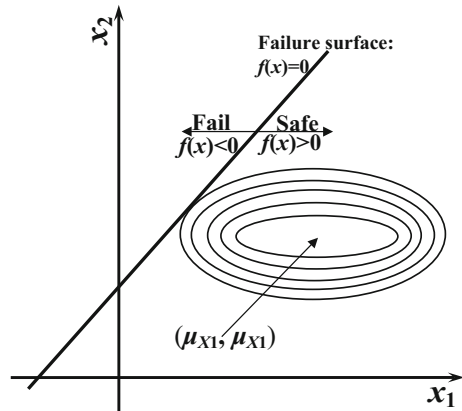
And the mean value and variance of the safety margin function above are:

$$\mu_M = a_0 + a_1\mu_{X_1} + a_2\mu_{X_2} + \cdots + a_n\mu_{X_n} \quad (1.63)$$

$$\sigma_M^2 = a_1^2\sigma_{X_1}^2 + a_2^2\sigma_{X_2}^2 + \cdots + a_n^2\sigma_{X_n}^2 \quad (1.64)$$

As a special case of the three equations above, if the safety margin is defined by two independent random variables that give $M = f(X) = a_0 + a_1X_1 + a_2X_2$, the failure surface is a curve $f(x) = 0$. If X_1 and X_2 are normally distributed random variables, their probability density functions are then symmetrical with respect to their mean values, and the curves for each constant level of the probability density function are in a form of ellipses, which is shown in Fig. 1.35. Since the variance $\sigma_{X_1}^2$ and $\sigma_{X_2}^2$ are different in x_1 and x_2 axes, it is difficult to find a simple measurement of the distance between point (μ_{X_1}, μ_{X_1}) and the failure surface $f(x) = 0$. Therefore, a linear variable transformation must be made to replace the two independent normally distributed random variables X_1 and X_2 by two standardized normally distributed random variables Z_1 and Z_2 with $\mu_{Z_1} = \mu_{Z_2} = 0$ and

Fig. 1.35 Contours of the joint probability density function for normally distributed X_1 and X_2



$\sigma_{z1} = \sigma_{z2} = 1$, which is essentially to transform the linear failure surface $f(x) = 0$ in x -space to linear failure surface $f_z(z)$ in z -space:

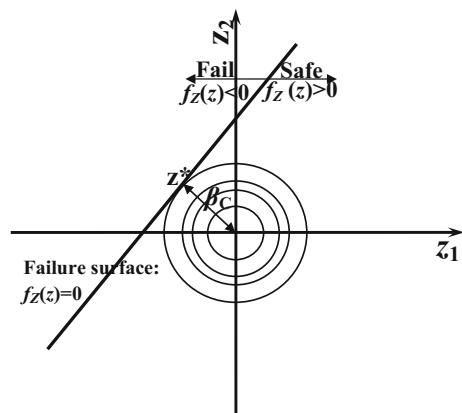
$$z_1 = (x_1 - \mu_{x1})/\sigma_{x1} \tag{1.65}$$

$$z_2 = (x_2 - \mu_{x2})/\sigma_{x2} \tag{1.66}$$

Therefore, the contours with elliptical shape shown in Fig. 1.35 in x -space can now be transformed into concentric circles with their center at the origin in z -space as shown in Fig. 1.36. Cornell's reliability β_C can then be defined as the shortest distance from the origin to the failure surface as shown in Fig. 1.36. The point z^* shown in Fig. 1.36 is called the design point.

Obviously, a high value of safety index indicates a lower possibility of failure, but normally a more expensive design. A rational assessment on the basis of both failure probability and consequence of failure will allow for a more pragmatic allocation of construction budget. Therefore, the design must account for the cost

Fig. 1.36 Contours of the probability density function for the standardized normally distributed Z_1 and Z_2 and an explanation of Cornell's reliability index β_C



and consequence, so that a target safety index acceptable to various parties can be reached. In reality, consequences and risk acceptability are also implicitly considered in geotechnical and structural design codes, leading to required levels of reliability in various situations and consequences. Examples of possible classes of consequences include [100]:

1. Minor consequences: Risk to life, given a failure, is small to negligible, and economic consequences are small or negligible (e.g., agricultural structures, silos, masts).
2. Moderate consequences: Risk to life, given a failure, is medium, or economic consequences are considerable (e.g., office buildings, industrial buildings, apartment buildings).
3. Large consequences: Risk to life, given a failure, is high, or economic consequences are significant (e.g., major bridges, theaters, hospitals, high-rise buildings, offshore platforms).

1.13.2.3 Probability of Failure for Nonlinear Safety Margin Functions

As presented in Sect. 1.13.2.2, the safety margin function $m = f(x)$ is a linear function of basic variables, and the resultant safety index is Cornell's reliability index. However, many safety margin functions are nonlinear, which can be expressed by Taylor series expansion. In case a safety margin function is only approximated by its first-order (linear) Taylor series terms, the resultant safety index is called first-order-reliability index. In case both the first and second-order terms are retained, the resultant safety index is called second-order-reliability index. The corresponding methods are first-order reliability method (FORM) and second-order reliability method (SORM), respectively. Below a brief introduction of the two methods is given.

By generating Taylor series of the safety margin $m = f(x)$ around point $q(q_1, q_2, q_3, \dots, q_n)$, and retaining only the first-order terms, one obtains a linearized safety margin:

$$m = f(x) \approx f(q) + \sum_{i=1}^n \frac{\partial f}{\partial x_i}(q)(x_i - q_i) \quad (1.67)$$

If x_i can be described by normally distributed random variables X_i , the safety margin m can then be approximately described by a normally distributed random variable:

$$M \approx M_{FO} = f(q) + \sum_{i=1}^n \frac{\partial f}{\partial x_i}(q)(X_i - q_i) \quad (1.68)$$

Based on the equation above, a first-order-reliability index β_{FO} can be calculated as:

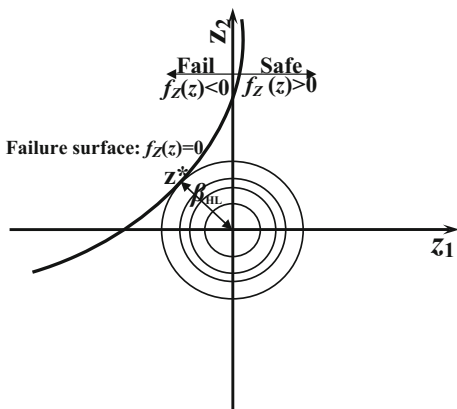
$$\beta_{FO} = \frac{f(q) + \sum_{i=1}^n \frac{\partial f}{\partial x_i}(q)(E[X_i] - q_i)}{\sqrt{\sum_{i=1}^n \left(\frac{\partial f}{\partial x_i}(q)\sigma_{X_i}\right)^2}} \tag{1.69}$$

If the linearized point q is chosen such that $q = (\mu_1, \mu_2, \mu_3, \dots, \mu_n)$, the first-order-reliability index can be determined by:

$$\beta_{FO} = \frac{f(q)}{\sqrt{\sum_{i=1}^n \left(\frac{\partial f}{\partial x_i}(q)\sigma_{X_i}\right)^2}} \tag{1.70}$$

It should be noticed that the first-order-reliability index β_{FO} is not a unique measure of the reliability since the determination of its value depends on the choice of the linearization point and the approximation made for the safety margin (which is not unique either), and a structure can have more than one reliability index. However, the failure surface for a structure is always unique because regardless how the safety margin function is calculated, it is always the same combination of $x_1, x_2, x_3, \dots, x_n$ that gives failure. Therefore, it is desirable to have a safety index defined based on the failure surface rather than safety margin, so that the resulting safety index is unique (i.e., a failure function invariant) since all equivalent failure functions result in the same failure surface in the x -space and therefore also in z -space. This is exactly what Hasofer and Lind proposed [101], which results in Hasofer–Lind safety index β_{HL} to determine the reliability of a structure. Similar to what Cornell’s reliability is defined in z -space, β_{HL} is defined as the shortest distance from the origin to the point z^* on the failure surface ($f_Z(z) = 0$) as shown in Fig. 1.37, such that:

Fig. 1.37 Illustrations of contours of the probability density function for nonlinear failure surface, normalized coordinates, an explanation of Hasofer–Lind safety index β_{HL} and design point z^*



$$\beta_{\text{HL}} = |z^*| = \min |z^*| = \min \sqrt{\sum_{i=1}^n z_i^2} \quad (1.71)$$

From the definition above, the reliability index for a nonlinear failure surface is equal to the reliability index for the linear tangent hyperplane in the design point z^* . In order to calculate β_{HL} , various types of optimization method can be used to determine point z^* on the failure surface.

A second-order-reliability index can be solved with an exact analytical expression. For a detailed solution, readers may refer to [102].

Note that the transformed probability density function $f_Z(z)$ in z -space decreases rather quickly with an increasing $|Z|$. The largest contribution to the probability of failure comes from the area around the design point z^* shown in Fig. 1.37. Therefore, to calculate reliability of many structures, β_{HL} is a close approximation of the exact value of safety index β defined in Eq. (1.50).

Moreover, it is obvious that for linear failure surface and normally distributed basic variables X_i , the definition in Eq. (1.49) and the Hasofer–Lind safety index result in the same β -value. Therefore, Hasofer–Lind safety index β_{HL} and Cornell's reliability index β_C equal the exact safety index β :

$$\beta_{\text{HL}} = \beta_C = \beta \quad (1.72)$$

On the other hand, if the safety margin function is nonlinear, it cannot be described by a normally distributed random variable. Even though Eq. (1.50) is still valid to calculate the exact failure probability β , it is approximate:

$$\beta_{\text{HL}} \approx \beta = -\Phi^{-1}(P_f) \quad (1.73)$$

In summary, the probability of failure with FORM/SORM can be determined in four steps [95]:

1. Transform the random vector X in x -space to a standardized normal random vector Z in z -space.
2. Determine the design point z^* .
3. Approximate the failure surface in z -space with respect to z^* .
4. Determine the β_{FO} , β_{HL} , or β_{FO} as an approximation of the reliability index β .

For more details about FORM and SORM, references [99, 103, 104, 105] are recommended.

1.13.2.4 Monte Carlo Method for Calculating Probability of Failure

Instead of calculating the reliability index, the reliability can also be directly calculated using the Monte Carlo method, which essentially involves performing a simulation (virtual experiments) based on repeated random sampling to obtain

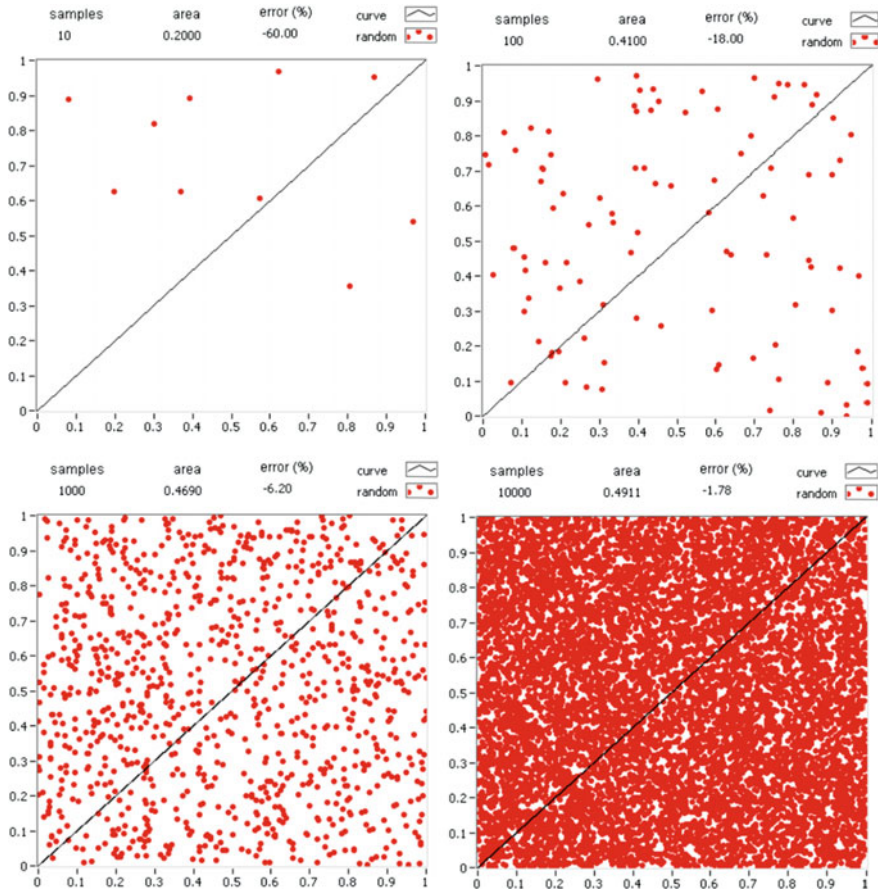


Fig. 1.38 Random value generation in a Monte Carlo simulation and a comparison of random value points with the value of the variable function (line) for different number of samplings; the coordinates of random values in horizontal and vertical axis are randomly varied and compared to the value of the variable function for each coordinate; it is obvious that with an increase in the number of samples, the percentage of error decreases

numerical results. In this method, for each variable, the random values are generated using, for example, a Gaussian random number generator and are scaled with the specified standard deviation. If a two standard deviation is assumed, it means a 95% confidence estimate. Figure 1.38 shows an example of random number generator in a Monte Carlo simulation. The individual error values are then summed and added to the true value of a variable to obtain a calculated value (“measured” from a “sampling”) of that variable with errors from the specified error populations. After obtaining the measured values of the variables, result(s) of an objective test are calculated. The 95% confidence uncertainty of each result is obtained by multiplying the calculated standard deviation by a factor of 2. The procedure above

corresponds to running the test once, and it should be repeated many times (thousands or even more depending on the problem considered), and the means and standard deviations of the distribution of the results can then be determined. The Monte Carlo method is a relatively convenient way to incorporate assumed non-Gaussian error distributions for the variables or to specify any degree of confidence level. Moreover, this method is straightforward for investigating complex cases, especially when the number of variables is large [106]. Obviously, the major drawback of this method is its relatively high computation cost as mentioned above.

Both FORM and SORM are analytical and approximate methods that can be conveniently used in numerical solution. They generally apply when the probability of failure is small, e.g., 10^{-3} to 10^{-8} . When such low probability of failure is concerned, the computation time by using FORM or SORM is much less than other numerical methods such as Monte Carlo method. Further, the difference between FORM and SORM is small for cases with large safety index (small probability of failure). However, for higher probability of failure, the error in the FORM approximation can be significant. Moreover, the CPU time for FORM increases linearly with the number of the basic variables, where the CPU time for SORM increases approximately with the square of the number of basic variables.

1.13.3 Levels of Reliability Method

In case only mean values, variance, and correlation of load and resistance variables are used to calculate a nominal probability of failure, usually expressed in terms of a reliability or safety index, as presented in Sect. 1.13.2, the evaluation method is referred to as semi-probabilistic method (level 2), which is sometimes also called the second-moment reliability method.

In contrast, a direct calculation of failure probability is referred to as a full-probabilistic method (level 3). This method makes use of a full-probabilistic description of joint occurrence of various quantities that affect the response of structures and take the true nature of the failure domain into account, which can determine the “exact” probability of failure and be used to calibrate the semi-probabilistic approach. In some design codes, they are also recommended for particular situations. It is noted that the results based on a full-probabilistic method strongly depend on the modeling of the tails in the probability distribution involved. This makes the use of full-probabilistic method rather difficult or not attainable in practice, as for instance the tail in the load (and response, e.g., seismic loading and response) and/or resistance (e.g., soil strength) is rather uncertain (i.e., “fat tail” in the probability distribution).

On the other hand, in ASD (level 1), the failure probability cannot be defined (an essential reason why LFRD is preferred over the ASD). Instead, factors for resistance and/or load are used separately, and engineers work with random resistance and/or load variables that are represented only by their mean value (lowest

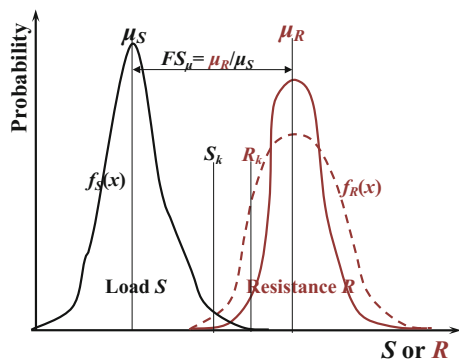
statistical moments of load and resistance), or any other characteristic value, while the variation in both load and resistance cannot be reflected, which will be further explained in Sect. 1.13.4.

In addition to the three levels of methods introduced above, in some literatures, there is further a level 4 method, which is essentially an extension of the level 3 (full-probabilistic) method by introducing consequences of a failure with respect to economical and environmental terms. This can be regarded as a decision support tool, as it can be used to compare the overall (life-cycle) cost of various alternative designs [107].

1.13.4 Essential Differences Between LRFD and ASD

In ASD, it is almost impossible to incorporate the uncertainties associated with either load or resistance. This is because in ASD, engineers work with random load and resistance variables that are represented only by their mean value, or any other characteristic value, but the variation in both load and resistance cannot be accounted for. This can be explained by observing Fig. 1.39, which shows probability distribution for load effects and resistance. Here, we define two safety factors: One is the central safety factor $FS_\mu = \mu_R/\mu_S$, and the other is the nominal factor of safety $FS_k = \mu_k/\mu_k$. If uncertainties in the resistance R are increased, the probability density function curve changes from a solid line into a dashed line, which is broader, indicating an increase in the variation (uncertainties), as shown in Fig. 1.39. On the other hand, it is likely that the mean resistance μ_R of the curve does not change. Therefore, even though the central safety factor FS_μ (associated with ASD) remains unchanged, utilizing the distribution with the higher variation in resistance will require applying a higher partial safety factor (resistance factor) γ_M (associated with LRFD), so that the same prescribed probability of failure can be achieved.

Fig. 1.39 A schematic illustration of probability density distribution for both loads (S) and resistance (R) with smaller uncertainties (solid curve) and larger uncertainties (dashed curve) for the resistance



Following from the explanation above, it is seen that LRFD and ASD loads are not directly comparable because they are used differently by design codes and do not normally admit of combination in the same design project. For example, the service load in ASD is unfactored, while the load defined in LRFD is factored.

By splitting the factor of safety into the independent load and resistance factors, one can apply a higher safety margin in the form of a higher partial safety factor to a design parameter that is considered less predictable or that could have a negative impact on the design. This allows for a more explicit way of accounting for uncertainties. LRFD can result in safer (i.e., more reliable) and probably less expensive structures, depending on the predictability of the load types being used. For example, by using LRFD in design for certain geotechnical engineering projects, it may be more economical and safer to reduce uncertainties by devoting more effort to site investigation, geotechnical analysis, and/or foundation load estimation, rather than allocating more budget to foundation construction. Moreover, LRFD-based geotechnical design is also compatible with structural design codes, in which LRFD rather than ASD is a norm. In addition, through a rational and consistent estimation of uncertainties and quantification of the probability of failure, geotechnical and structural designs can be harmonized with societally acceptable levels of risks (risk = failure probability \times failure consequence).

The reliability-based geotechnical design codes and standards using LRFD are largely developed through calibrations with traditional ASD method and sometimes also by using reliability analysis when a target reliability level is known.

1.13.5 Applying Partial Safety Factors in Geotechnical Analysis

Partial safety factors for loads and materials proposed in current design codes are essentially devoted to designs based on linear analysis and in many cases not suitable for nonlinear geotechnical analysis. Because other foundation modeling parameters (such as the pile stiffness, as will be discussed in Chaps. 16 and 17) are also influenced by the soil's strength, it is often practical to apply the material factor on the loading side together with the load factor rather than on the soil's material strength (resistance) side.

1.14 Incorporating Uncertainties of Soil Parameters

In geotechnical design, the predominant sources of uncertainties are the soil properties and the calculation model uncertainty [111]. Soil parameters are usually given in one or more of the following expressions: characteristic value of the soil property (which is intrinsically linked to semi-probabilistic formats as presented in

Sect. 1.13.3), best estimate of the soil property, and upper and lower bounds of the soil property. Engineers can sometimes encounter confusion regarding the definition and applicability of those expressions. A brief description of these concepts and their applicabilities is given in the following, based mainly on the guidance given by DNV-RP-C207 [108].

Characteristic values are used to specify soil properties, such as soil shear strength, and always used together with a partial safety factor. The exact definition of the characteristic value usually depends on the design code used and on the actual application. In cases where local fluctuations of the soil property can be assumed to average out over large soil volumes, the mean value of the soil property is normally used, such as in the case of the axial capacity of long friction piles, i.e., the characteristic undrained shear strength for the shaft friction of a pile is the spatial average along the length of the pile. In cases in which the soil strength at a single point has a critical bearing on failure, such as in the case of the tip resistance of an end-bearing pile, the characteristic value defined as a lower-tail quantile (typically the 5% quantile) in the distribution of the property (within a bulb of soil below the pile tip) typically applies. Eurocode 7 [109] suggests that characteristic soil strengths should instead be taken as the mean value with a confidence level of 95% within the volume of soil involved in failure. Sometimes, the mean value minus or plus two standard deviations, which corresponds to the 2.3% quantile, is also used, such as S-N curves for fatigue designs. Occasionally, the most probable value, for which the probability density function reaches the peak, is also used. The definition of design profiles of characteristic values for soil properties is established with reference to a specific application, i.e., with reference to a specific type and size of foundation, and will not necessarily be valid for other applications. The design profiles or design values referred to in a design code are often the factored characteristic value—but not always. Therefore, the user must be sure to clarify this at the beginning of a relevant design or analysis project.

Geotechnical design should account for spatial variability of the soil by an explicit introduction of a random field. However, most engineering projects rely on deterministic design, in which partial safety factors are applied to convert characteristic values of the soil properties into design values. It is then important to note that the reliability of the final design is highly dependent on the manner in which the characteristic value has been chosen and assessed, not only on the partial safety factors used [110].

Best estimates of soil properties are introduced as central unbiased estimates with lowest possible standard errors, and they are normally used for assessment of serviceability limit states. An example of this is the prediction of the expected consolidation settlements for which best-estimate values of governing soil deformation parameters are required. Also, in a site-response analysis as will be presented in Chap. 3, it is recommended that one perform a sensitivity analysis by accounting for the variation of soil properties from lower-bound, average (best estimate) to upper-bound value, as this may detect some significant impacts of soil properties on the ground motions. If the ground motions are not sensitive to the

variation of soil properties, typically, the best-estimate value of soil properties can be used to compute the ground motion time histories.

Lower- and upper-bound values are often used as characteristic values in design. Lower bounds are usually adopted in the design against the ultimate limit state in which lower soil strengths are normally unfavorable. On the other hand, upper bounds are usually used where larger strengths are unfavorable. For example, the seismic response of structures may be higher with a foundation resting on soils with higher strength and stiffness, due to the fact that the higher foundation stiffness results in a decreased natural period of the structure, which typically induces higher seismic responses [188]. As another example, upper-bound values may be more relevant than lower-bound ones to assess the pile-driving resistance rather than pile in-place performance.

For designing structures subjected to cyclic loading or influenced by dynamic behavior, it may also be necessary to perform sensitivity studies based on both lower-bound and upper-bound values of relevant soil properties for foundation soils.

In contrast to structural materials that are manufactured with quality control, geomaterials are naturally occurring and in situ variability cannot be well controlled or efficiently decreased. Therefore, the coefficients of variation of geotechnical design parameters can be potentially large (a wider probability density distribution). Designers should thus evaluate whether or not the commonly used material factor (e.g., 1.3) is sufficient, as it is not likely to cover the uncertainties in the soil properties. This requires a dedicated probabilistic analysis of a large number of variations in soil conditions, which is sometimes too demanding for a typical geotechnical design project. Spatial variability of geotechnical design parameters cannot be dismissed either, because the volume of geomaterials interacting with structures is related to characteristic lengths (e.g., diameter of tunnel, height of slope, depth of excavation) of structures and these characteristic lengths are typically larger than the scale of fluctuation of the design parameter, particularly in the vertical direction [111]. There are three primary sources of geotechnical uncertainties: (1) inherent variability, which results primarily from the natural geologic processes that produced and continually modify the soil mass in situ; (2) measurement error, which is caused by equipment, procedure/operator, and random testing effects; and (3) transformation uncertainty, which is introduced when field or laboratory measurements are transformed into design parameters using empirical or other correlation models. For a detailed discussion on this topic, see ISO 2394 [111] Appendix D (Reliability of geotechnical structures).

1.15 General Soil Conditions at Offshore Sites Worldwide

In a very rough manner, one may select a preliminary foundation design strategy based on the general soil conditions in each offshore region of the world. For example, soils beneath the North Sea seabed generally consist of medium dense to

Fig. 1.40 Illustration of turbidite sequence at Carboniferous Ross Sandstone Formation (Namurian), Western Ireland (courtesy of USGS)



very dense sands and very soft to hard clays. The dense sand condition is very beneficial from a foundation point of view, and thus, the gravity-based foundation concept (as will be introduced later) has its unique advantages. However, since significant overturning load in the foundation occurs mainly due to storm wave loading, and many structures and foundations are not heavy enough to resist this significant overturning moment, pile foundations are also frequently used for fixed offshore structures in the North Sea. In the Gulf of Mexico, offshore Brazil, and West Africa, normally consolidated clays are more usual. At offshore sites in the Far East and Middle East, engineers found that loose to medium dense sand as well as soft clays are common. In addition, soils at deepwater sites often consist of homogenous soft clay. However, a particular offshore site may have soil conditions totally different from the general ones presented above.

Soils at deep and ultra-deep water normally comprise of turbidite (Fig. 1.40) and/or pelagic deposits. The former of these are deposited by turbidity currents or debris flows, which are responsible for distributing vast amounts of clastic sediment into the deep ocean, and are short-lived deposition episodes typically associated with a distant submarine landslide or other short duration sources. Pelagic sediments consist primarily of the fine-grained carbonate remains of the skeletons of microorganisms. Alternating turbidite and pelagic layers can be found in many deepwater sites. Normally, consolidated clay is typical at deepwater sites in the Gulf of Mexico, while at deepwater sites in many other regions, under-consolidated clays are found extensively, indicating that the rate of deposition has been faster than the rate of consolidation and that the resulting excess pore pressures have not yet been dissipated. The shear strength of under-consolidated clays at such sites increases much more slowly with depth than the normally consolidated clays in the Gulf of Mexico [112].

Chapter 2

Dynamic and Cyclic Properties of Soils

2.1 Introduction

Response of soil depends on both the mechanical properties of soil itself and the nature of loading. Many geotechnical engineering problems are associated with dynamic and cyclic loadings, such as ocean wave or ice loading applied on foundations of offshore structures or bridges, dynamic loading applied on foundations of offshore wind power structures, ocean wave loading on harbor structures, seismic wave propagation through soils, machine vibration-induced loading on foundations, seismic loading, liquefaction and cyclic transient loading, and dynamic working loads [113].

Soils' responses subject to dynamic and cyclic loadings are strongly controlled by the mechanical properties of the soil, which basically include shear modulus (shear wave velocity), damping, Poisson's ratio, and density (mass). Of these, shear modulus and damping are the most important material properties with which to characterize the dynamic behavior of soils. Both these properties are affected by effective stress and over-consolidation ratio. While the determination of shear modulus is normally well established, the damping modeling is less clearly understood. Furthermore, both shear modulus and damping depend on the strain level, while the strain response level also depends on the modulus and damping. Moreover, at high strain levels, in addition to the strain level, other parameters such as rate and number of cycles of cyclic loading are also important influences on the shear modulus. The strain rate of soils due to dynamic loading also influences soils' strength (mainly for clay soils) and shear modulus, as will be presented in Sect. 2.5. Volume change characteristics are also important at high strain levels. In addition, the location of the water table, degree of saturation, and grain size distribution may be important, especially when liquefaction is a potential problem. All the issues above complicate the geotechnical analysis and challenge analysis accuracy requirements.

The constitutive relationship of soils can normally be categorized into two classes: At extremely small strain levels of soils, perfectly elastic (fully recoverable) behavior can be assumed; as the strain amplitude increases, the soil stiffness decreases and the plastic soil behavior has to be accounted for. This information will be presented in Sect. 2.3.

Experimental observations also show that the stiffness observed for a subsequent stress path depends on the immediate past history of soils. Stress paths that represent a continuation of the immediate past stress path result in the lowest stiffness, while those involving a complete reversal of direction result in the highest stiffness. Intermediate values are observed for stress paths that represent a sudden change of direction from the immediate past history [117].

Various types of constitutive equations are proposed to describe the stress–strain–strength behavior of materials. However, in most of the conventional design methods, simpler representations of material behavior are typically assumed. An example of such conventional design methods is a bearing capacity analysis (Chap. 12), which assumes a rigid perfectly plastic behavior of soils. On the other hand, separate deformation calculations often assume linear-elastic behavior.

Under static loads, such as gravity loads, the material behavior of soil for both clay and sand can normally be considered as linear-elastic. Under cyclic loadings, meanwhile, such as earthquake loading or ocean storm wave-induced loading, the cyclic soil behavior is more complex than for its static counterpart. The cyclic behavior of soils is responsible for many geotechnical failures, such as slope instability due to degradations in soils' properties subject to earthquake loading. The stress–strain response is then considered elastic-plastic, and even the strength is nonlinear and depends on the strain, stress, and possibly strain rate.

For clay, plasticity may be formulated based on the multi-surface (nested surfaces) concept, with an associated flow rule. The yield surfaces are normally of von-Mises type as shown in the left figure of Fig. 2.1. For sand, plasticity can also be formulated based on the multi-surface concept, but with a non-associative flow rule [123] to reproduce dilatancy effect, and the yield surfaces can be modeled as Drucker-Prager type shown in the right figure of Fig. 2.1.

Hardin and Drnevich [115] discussed the relative importance of parameters affecting shear modulus and damping. Shear strain amplitude, effective stress level, and void ratio were listed as affecting shear modulus mostly in clean sands. Damping was considered to be affected by these too, with the number of loading cycles also being a major influencing factor. For clays, the increase in the number of loading cycles has been correlated to a decrease in shear modulus with associated pore pressure increase, as summarized by Idriss and his co-workers [116]. Over-consolidation ratio (*OCR*) and plasticity index (*I_p*) also influence the clay behavior.

As discussed in Sect. 1.10, to perform a site-response analysis, if the shear strain under seismic or other types of cyclic loading is less than 10^{-6} , a linear soil model by modeling the soil with an initial shear modulus is preferred due to both its wide availability and computational convenience. In case the shear strain γ is in the range

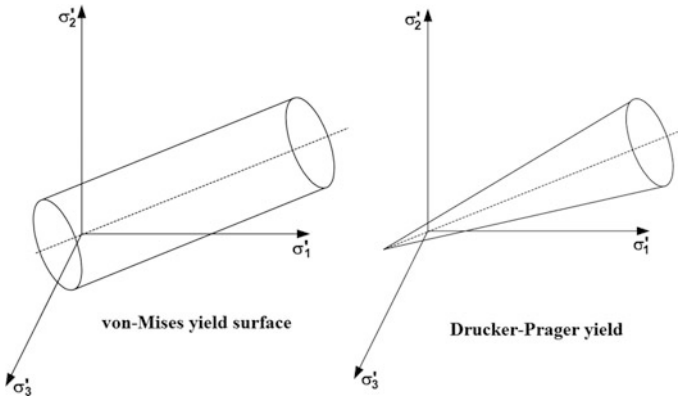


Fig. 2.1 von-Mises (left) and Drucker-Prager (right) yield criteria in principal stress space (σ_1' , σ_2' , and σ_3' are the maximum, intermediate, and minimum principal stresses)

$10^{-6} \leq \gamma \leq 10^{-2}$, in most cases the site response due to seismic loading is evaluated using the equivalent linear method (as will be presented in Sect. 2.2), in which compatible values of shear modulus and damping ratio are chosen according to the shear strain level in soil deposit. However, in this simplified method, the developed pore-water pressure and the residual soil displacements cannot be calculated, even though the ground motion response can be related to the liquefaction potential through approximation (Chap. 7). If shear strain responses are very large (above 10^{-2}) and/or there is permanent strain (the shear strain is not zero when the shear stress is zero), the soil actually exhibits elasto-plastic behavior, and it is recommended to use cyclic nonlinear modeling of soils (Sect. 2.4), which can model the actual stress–strain path and soil’s stiffness degradation. In this more complicated soil modeling, the developed pore-water pressure and the residual soil displacements can be calculated by cyclic nonlinear soil models.

In the determination of soil properties, engineers should always bear in mind that the selected soil properties must produce safe design results. If a design is sensitive to variations in the soil properties being considered, a sensitivity analysis should be performed (Sect. 1.14).

Chen [114] provided three criteria for evaluating soil modeling. The first is a theoretical evaluation of the models with respect to the basic principles of continuum mechanics to ascertain their consistency with the theoretical requirements of continuity, stability, and uniqueness. The second criterion is to perform evaluation of the models with respect to their suitability to fit the laboratory test data from available test results and the ease of the determination of the material parameters from standard test data. The third one is to perform numerical evaluation of the models with respect to the implementation convenience of the modeling into computer calculations.

In summary, mainly depending on the amplitude of dynamic loading, the soil characteristics, and the resultant soil response, soils can generally be modeled by

three classes of models: equivalent linear models (Sects. 2.2 and 2.3), cyclic nonlinear models (Sect. 2.4.2), and more dedicated advanced constitutive nonlinear models (Sect. 2.4.4). Of these, the equivalent linear models require the description of the degradation of soil's secant shear modulus and damping with the change of shear strain, whereas the cyclic nonlinear models use backbone curves together with a number of rules that govern the unloading and reloading behavior and other effects, and the advanced constitutive soil models describe the soil's mechanical properties using constitutive laws, which is capable of reproducing a more realistic nonlinear response. Due to the simplicity of equivalent linear models, they are most widely used in site-response analysis, as will be presented in Chap. 3. They work fairly well at low strain levels, which are normally associated with mild seismic motions. At high shear levels, nonlinear models (Sect. 2.4) are usually adopted.

2.2 Equivalent Linear Soil Models

2.2.1 Equivalent Shear Modulus Modeling

For soils a certain level below the ground surface and far from adjacent structures, under symmetric cyclic loadings, the shear stress–strain relationship exhibits a hysteresis loop, as shown in Figs. 2.2 and 2.15. The hysteresis loop of a typical soil can be described by the path of the loop itself or by parameters that describe its shape. These parameters are the inclination and the breadth of the hysteresis loop, shear modulus, and damping.

Figure 2.3 shows a hysteresis loop describing variations of secant stiffness with the number increase in cyclic loading, which is used to describe the secant stiffness degradation of soils in an equivalent linear model shown in Fig. 2.5. In Fig. 2.3, it can be seen that the openness of the hysteresis loop increases with strain amplitude, which is actually an effect of the immediate past history of the soil.

Fig. 2.2 Secant shear modulus G_{sec} and tangent shear modulus G_{tan} in a hysteresis loop (τ' and γ' are shear stress and shear strain, respectively)

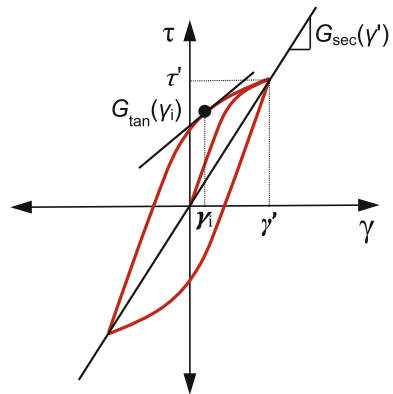
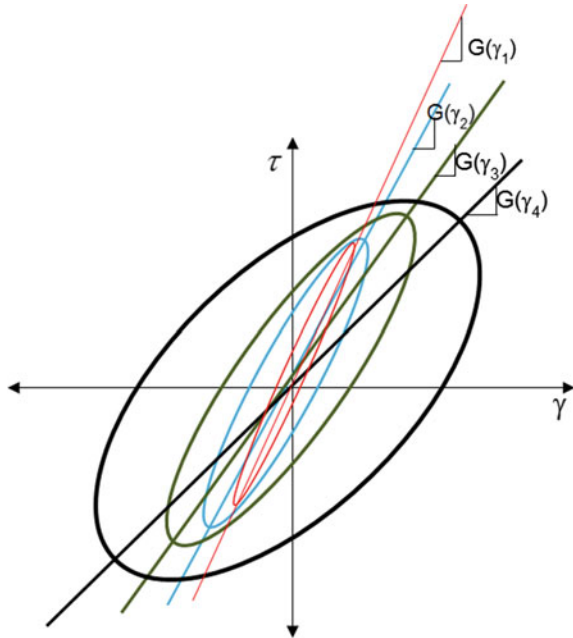


Fig. 2.3 Variation of the secant shear modulus with the number increase (1, 2, 3 ...) of cyclic loading in an equivalent linear model



Furthermore, the tangent shear modulus G_{tan} (Fig. 2.2) changes along the path of the hysteresis loop under cyclic loadings. At low shear strain amplitudes, the tangent shear modulus is high and vice versa. However, one may approximate the average value of the tangent shear modulus over the entire loop as the secant shear modulus G_{sec} :

$$G_{sec} = \frac{\tau'}{\gamma'} \tag{2.1}$$

Note that the secant shear stiffness is strongly influenced by the shear strain amplitude, i.e., it decreases with an increase in shear strain. The locus of points corresponding to the tips of hysteresis loops of cyclic strain amplitudes forms a backbone shape shown in Fig. 2.4. From this figure, it is obvious that at zero strain, the shear modulus reaches its maximum value G_{max} . In an equivalent linear model, the modulus ratio G_{sec}/G_{max} (often written as G/G_{max}) is usually adopted to describe the secant shear stiffness degradation of soils, resulting in a modulus reduction (also called normalized shear modulus) curve as shown in Fig. 2.5, which describes the same information as the backbone curve (Fig. 2.4). Furthermore, they can be determined from each other. The shear modulus reduction curves for coarse- and fine-grained soils are commonly modeled separately. However, the backbone curve cannot reflect a gradual transition of the modulus reduction curve between non-plastic coarse-grained soil and plastic fine-grained soils [1].

Fig. 2.4 Modulus reduction curve represented by a backbone curve showing the secant shear modulus, G_{sec} , and maximum shear modulus G_{max}

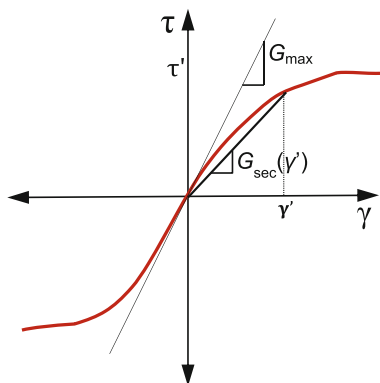


Fig. 2.5 Normalized shear modulus reduction curve

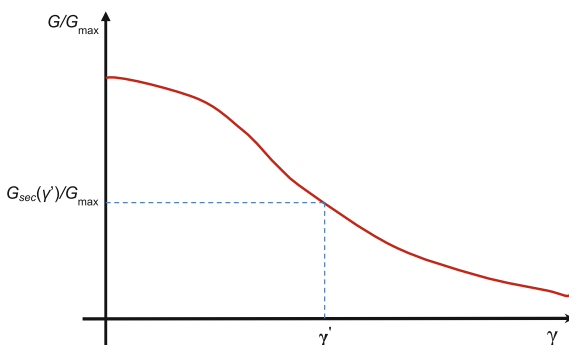


Figure 2.6 shows widely used modulus reduction curves proposed by Vucetic [118]. The charts are recommended only for preliminary studies due to large data scatters [231].

It is important to point out that the nonlinear curves shown in Figs. 2.4, 2.5, and 2.6 are essentially hypoelastic models because unloading occurs along the loading path. Under cyclic loading, these models do not account for hysteretic behavior as shown in Fig. 2.2 and possible residual displacements as observed for real soils, which can be implemented by nonlinear soil modeling (Sect. 2.4).

The soil stiffness is affected by many parameters such as the soil type, cyclic shear strain level, plasticity index, mean effective confining stress (more significant for soils with low plasticity), loading history, frequency of loading, number of loading cycles, over-consolidation ratio, void ratio, degree of saturation, grain characteristics. For example, the soil stiffness is significantly influenced by soil plasticity, i.e., the stiffness of soils with high plasticity decreases more slowly with the increase in shear strain than that of the low-plasticity soils.

Tests are needed to characterize dynamic soil properties, mainly including soils' shear wave velocity and damping. Generally, the test methods can be categorized as direct field measurement (such as seismic reflection test, seismic refraction test,

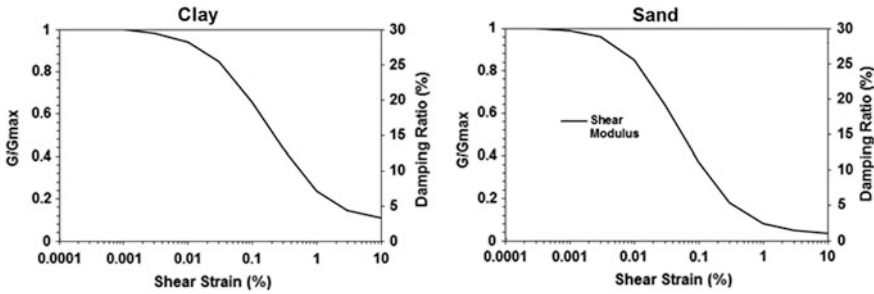


Fig. 2.6 Typical normalized shear modulus reduction curves for clay (left) and sand (right)

seismic cross-hole test, seismic down-hole test, up-hole test, suspension logger test), indirect field measurement (such as a correlation with standard penetration blow-count as discussed in Sect. 1.9.5), and laboratory measurement (such as resonant column test or bender elements test). The test can also be categorized as either measuring the local strain in triaxial testing using linear variable differential transformer (LVDT) [121] and submersible proximity sensor [122], or laboratory testing under quasi-static loading, including the use of dynamic testing, such as resonant column, bender elements, and cyclic triaxial testing. They are valid at different levels of shear strain, as shown in Fig. 2.13.

All tests that characterize soil behavior need to apply the initial stress conditions and anticipate cyclic loading as best as possible. The geophysical field tests have the advantage of testing undisturbed soil in actual field conditions, with the effective stress and drainage conditions that pertain in practice, while the laboratory tests need to confine and consolidate the soil sample back to the state of stress to replicate field conditions. Therefore, G_{\max} obtained from the laboratory test is normally lower than that in the field due to the sample disturbance or limited reconsolidation time in the laboratory. For more details about those methods, readers may read Chap. 6 and sources [1] and [194].

In summary, through extensive research on dynamic soil properties, it may be generally concluded that, for sands, shear strain amplitude, effective stress level, and void ratio are the most dominant parameters affecting shear modulus and soil damping [115]. For clays, an increase in the number of loading cycles has also been correlated to a decrease in shear modulus with associated pore pressure increase, as summarized by Idriss et al. [116]. In addition, the over-consolidation ratio (OCR) and plasticity index (I_p) are also rather influential parameters to affect clay behavior. For various proposed shear modulus reduction curves used for equivalent linear soil models, see Sect. 2.3.2.

Moreover, as discussed in Sect. 2.5, it is widely recognized that shear modulus can also be significantly influenced by a variation in strain rate. G_{\max} increases with the increase of strain rate. The effects of strain rate on shear modulus will increase with an increase in soil plasticity. Nevertheless, when using equivalent linear soil

models, it is generally acceptable to neglect the dependency of soil properties due to strain rate.

Readers may be reminded that, if it is necessary to calculate motion time histories among various depths of the soil, nonlinear time domain analysis is preferred to the equivalent linear analysis in frequency domain, because the nonlinearity of the springs, and more importantly the phase of motions at different soil depths, can be explicitly accounted for. As an example, at different depths, kinematic loading on pile foundations can vary to a certain extent, as will be discussed in Sects. 19.2.2 and 3.5.2.

For more details on the calculation of the shear stiffness, source [1] is recommended.

2.2.2 Determination of G_{\max}

Given that the shear strain is smaller than $3 \times 10^{-4}\%$, the maximum shear modulus G_{\max} can be calculated directly by measuring soils' shear wave velocity v_s :

$$G_{\max} = \rho v_s^2 \quad (2.2)$$

Most soils such as loose gravel and sand have a shear wave velocity ranging from 330 to 1200 m/s. If soils are firm gravel or soft rock, the shear wave velocity increases to within the range 1200–2300 m/s. For stiff gravel and hard rock, this value further increases to the range 2300–6600 m/s. To give a feeling for the rate of shear velocity, the velocity of sound is 330 m/s in air and around 1500 m/s in water. Table 2.1 shows typical ranges of shear wave velocities for various types of soils.

In many cases, as the measured shear wave velocity is not available, the G_{\max} can be assessed by correlating it with other soil properties such as the void ratio (e), over-consolidation ratio (OCR).

Table 2.1 Typical ranges of shear wave velocities for various types of soils [119]

Soil type	Shear wave velocity (m/s)
Dry silt, sand, loose gravel, loam, loose rock, moist fine-grained top soil	180–750
Compact till, gravel below water table, compact clayed gravel, cemented sand, sandy clay	750–2250
Weathered rock, partly decomposed rock, fractured rock	600–3000
Sound shale	750–3300
Sound sandstone	1500–4200
Sound limestone and chalk	1800–6000
Sound igneous rock (granite, diabase)	3600–6000
Sound metamorphic	3000–4800

Section 1.11.2 presents the relative increment $\left(\frac{G_{\max}}{G_0}\right)$ of the maximum dynamic shear modulus due to soil consolidation.

The shear wave velocity v_s is a linear function of void ratio (e) and depends on the mean effective normal stress p' with a power of $n/2$, as proposed by Hardin and Richart [120]:

$$v_s = C(B - e)p'^{m/2} \quad (2.3)$$

where B , C , and n are constants depending on the type of soils.

The total mass density of soil ρ is a function of soil particle density ρ_s and the void ratio e :

$$\rho = \rho_s / (1 + e) \quad (2.4)$$

By combining the three equations above, one obtains:

$$G_{\max} = \rho_s C^2 (B - e)^2 p'^m / (1 + e) \quad (2.5)$$

From laboratory tests, it is suggested that the maximum shear modulus may be calculated as:

$$G_{\max} = 625 \cdot F(e) \cdot (\text{OCR})^k \cdot p_a^{1-n} \cdot (\sigma'_m)^n \quad (2.6)$$

where $F(e)$ is a function of void ratio e , and it may be taken as $1/(0.3 + 0.7e^2)$ [147] or $1/e^{1/3}$ [148]; σ'_m is the mean principal effective stress; k is an over-consolidation ratio exponent related to plasticity index (I_p) as shown in Table 2.2; $p_a = 100$ kPa is the atmosphere pressure with the same unit as σ'_m and G_{\max} ; n is the stress component and is usually taken as 0.5, but can be computed for individual soils at different effective confining pressures [1].

By adopting $F(e) = 1/(0.3 + 0.7e^2)$ proposed by Hardin in 1978 [147] and assuming that the soil is normally consolidated ($\text{OCR} = 1$), the equation above can be rewritten as:

$$G_{\max} = 625 \cdot (p_a \cdot \sigma'_m)^{0.5} / (0.3 + 0.7e^2) \quad (2.7)$$

Based on the effective octahedral stress σ'_{oct} and the void ratio e , Harding and Drnevich [141] also proposed another maximum shear modulus calculation in 1972:

$$G_{\max} = 3230 \cdot (\sigma'_{\text{oct}})^{0.5} (2.793 - e)^2 / (1 + e) \quad (2.8)$$

Earlier, in 1970, Seed and Idriss [149] proposed a calculation of maximum shear modulus:

Table 2.2 Over-consolidation ratio exponent k varied with I_p [141]

I_p (%)	k
0	0.00
20	0.18
40	0.30
60	0.41
80	0.48
≥ 100	0.50

$$G_{\max} = 22 \cdot K_{2,\max} \cdot (p_a \cdot \sigma'_m)^{0.5} \quad (2.9)$$

where $K_{2,\max}$ is determined by the relative density to water D_r and void ratio e , as shown in Table 2.3.

In 1992, Rix and Stokoe [150] proposed a calculation of maximum shear modulus:

$$G_{\max} = 1634 \cdot (q_c)^{0.250} \cdot (\sigma'_v)^{0.375} \quad (2.10)$$

where q_c is cone resistance obtained from the cone penetration test (Sect. 1.9.6), defined as the force acting on the cone divided by the projected area of the cone; σ'_v is the vertical effective stress.

Figure 2.7 shows an example of the resulting estimates of G_{\max} in an upper sand layer at a North Sea site. It is obvious that the estimates based on different methods differ to some extent. Practically, the final design G_{\max} can sometimes be taken as the average of the resulting estimates by all methods.

For clay, G_{\max} can roughly be estimated from its correlation with penetration parameters obtained in an in situ test, which is shown in Table 2.4.

For clay, Mayne and Rix [152] presented a calculation of G_{\max} based on the cone penetration correlation with a constant tip resistance of 2 MPa:

$$G_{\max} = 406 \cdot (q_c)^{0.695} \cdot e^{-1.130} \quad (2.11)$$

Table 2.3 $K_{2,\max}$ as a function of relative density to water D_r and void ratio e [149]

e	$K_{2,\max}$	D_r (%)	$K_{2,\max}$
0.4	70	30	34
0.5	60	40	40
0.6	51	45	43
0.7	44	60	52
0.8	39	75	59
0.9	34	90	70

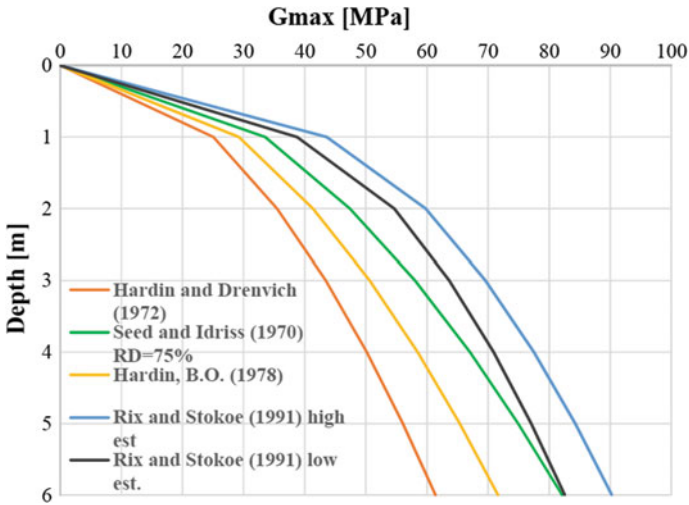


Fig. 2.7 An example of G_{max} estimated by different formulations. The upper and lower estimates based on the method proposed by Rix and Stokoe [150] correspond to upper and lower cone resistance (courtesy of Aker Solutions and NGI)

Table 2.4 G_{max}/s_u (s_u is the undrained strength measured in a consolidated–undrained triaxial shear test, see Sect. 1.9.3) [151]

I_p	OCR		
	1	2	5
15–20	1100	900	600
20–25	700	600	500
35–45	450	380	300

Based on various laboratory results available for different types of soils, Santos [155] proposed two unified curves representing the lower- and upper-bound values of G_{max} :

$$G_{max} = 4000e^{-1.3} p_a^{0.5} \text{ for the lower-bound} \tag{2.12}$$

$$G_{max} = 8000e^{-1.1} p_a^{0.5} \text{ for the upper-bound} \tag{2.13}$$

where e and p' are void ratio and the mean effective normal stress, respectively.

The two equations above for a given value $p_a = 100$ kPa (atmospheric pressure) are given in Fig. 2.8.

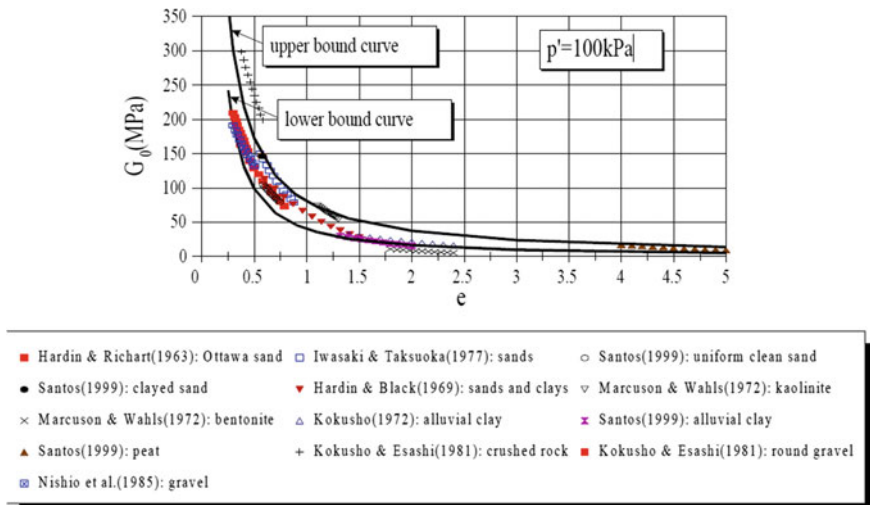


Fig. 2.8 Lower and upper bounds of G_{max} [156] ($p' = p_a = 100 \text{ kPa}$)

2.2.3 Equivalent Damping Modeling

Responses of soil are mainly influenced by both mechanical properties of soil and the characteristics of loading. Static loading is the simplest one and often well described. Long-duration cyclic loading may generally result in a noticeable degradation in soils' mechanical properties. Furthermore, strictly speaking, dynamic loading impedance (Sect. 5.4) is also partially determined by damping related to loading rate, even though seismic loading, being a form of short-duration, cyclic, high-rate loading, is somewhat different in this sense. Therefore, predicting actual soil responses is complicated and often poorly presented in overly simple models. Reliable simple models with which to represent soil damping are essential for performing efficient calculations of dynamic soil responses, and the equivalent damping model is widely adopted for this sake.

To describe the equivalent damping model in soil dynamics, we first go through the concept of equivalent damping in engineering dynamics [123]. Even though viscous damping modeling has obvious advantages, the energy dissipation for actual soil is both displacement proportional and velocity proportional. This leads to the concept of equivalent viscous damping, which is used to define the damping of a system using viscous damping based on the equivalent energy dissipation between the viscous damping and that of the actual system. In case of relatively low damping (less than 15%), viscous, friction, and hysteretic damping can be conveniently expressed by a unified model called equivalent viscous damping.

Consider an SDOF system with viscous or hysteretic damper (Fig. 2.9) subjected to harmonic loading $F(t) = F_0 \sin(\Omega t)$, where F_0 is the maximum amplitude of $F(t)$. It is noted that the work done by conservative forces such as elastic, inertia,

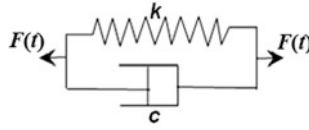


Fig. 2.9 Physical representation of frequency-dependent hysteretic damping mechanism

and gravitational forces in a complete loading cycle will be zero. Therefore, the network is dissipated by damping only. The left figure of Fig. 2.10 illustrates the energy dissipation (E_d) during a complete cycle by viscous damping when the motions reach a steady state, which can be expressed as:

$$E_d = \int F_d d\delta = \int_0^{2\pi/\omega} (c\dot{\delta})\dot{\delta} dt = c \int_0^{2\pi/\omega} [\Omega X_{0d} \cos(\Omega t - \phi)]^2 dt = \pi\Omega c X_{0d}^2 \quad (2.14)$$

From the equation above, it is found that, rather than being a constant value, the energy dissipation is proportional to the excitation frequency Ω or the square of the motion amplitude X_{0d} .

Furthermore, the equation above is only valid with the presence of spring stiffness k , as shown in the middle figure of Fig. 2.10, which gives:

$$E_d = \pi\Omega c X_{0d}^2 = 2\pi\zeta \frac{\Omega}{\omega_n} k X_{0d}^2 \quad (2.15)$$

With total energy expressed as either the maximum potential/strain energy ($\frac{1}{2} k X_{0d}^2$) or the maximum kinetic energy ($\frac{1}{2} m \Omega^2 X_{0d}^2$), one can measure the dissipation as a fraction of the total energy, called specific damping capacity:

$$\frac{E_d}{E_{total}} = \frac{2\pi\zeta \frac{\Omega}{\omega_n} k X_{0d}^2}{\frac{1}{2} k X_{0d}^2} = 4\pi\zeta \frac{\Omega}{\omega_n} \quad (2.16)$$

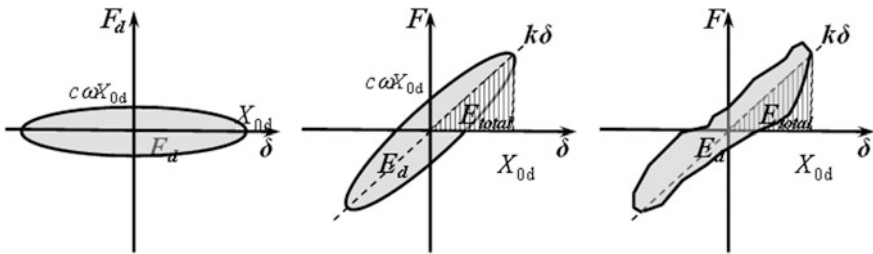


Fig. 2.10 Energy dissipation and strain energy by a viscous damper (left, strain energy is zero), hysteretic damper (middle), and real measurement (right)

If the loss of energy due to damping is only supplied by the excitations, the steady-state responses can only be reached if the excitation frequency Ω is equal to the soil system's nature frequency ω_n . Therefore, the specific damping expressed by the equation above can be rewritten as:

$$\frac{E_d}{E_{total}} = 4\pi\zeta \quad (2.17)$$

Realistic measurement of force-response diagram (right figure of Fig. 2.10) does not show a perfectly ellipse shape. However, damping level can be conveniently calculated by measuring the total energy (E_{total}) and energy dissipation (E_d) as shown in the right figure of Fig. 2.10.

The most convenient determination of equivalent damping ζ_{eq} is by measuring the harmonic force and harmonic responses at $\Omega = \omega_n$:

$$E_d = E_{total} 4\pi\zeta_{eq} \frac{\Omega}{\omega_n} = E_{total} 4\pi\zeta_{eq} \quad (2.18)$$

This gives:

$$\zeta_{eq} = \frac{E_d}{4\pi E_{total}} \quad (2.19)$$

If one replaces the force F and displacement δ by the shear stress τ and strain γ in Fig. 2.2 and replaces the stiffness k by the secant shear modulus $G_{sec}(\gamma')$ at the maximum shear strain γ' , resulting in Fig. 2.11, the equation above can be reformulated as:

$$\zeta_{eq} = \frac{E_d}{4\pi E_{total}} = \frac{1}{2\pi} \frac{A_{loop}}{G_{sec}(\gamma')\gamma'^2} \quad (2.20)$$

where A_{loop} is the area of the hysteresis loop shown in Fig. 2.11.

Fig. 2.11 Energy dissipated in one cycle E_d and the total energy (maximum strain energy) stored in one cycle E_{total} in a hysteresis loop

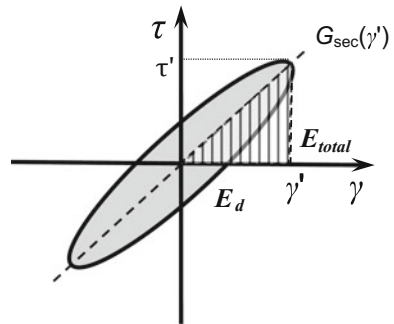
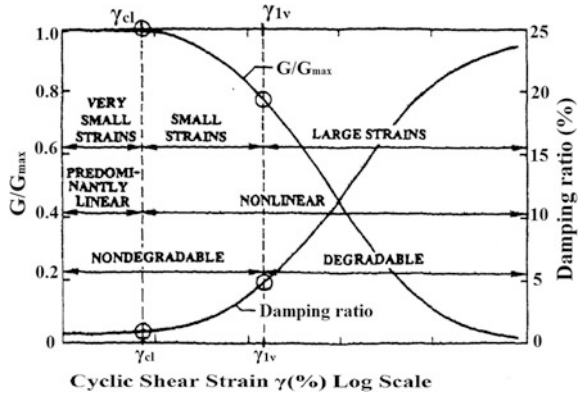


Fig. 2.12 Curves of secant modulus reduction (expressed in normalized terms) and damping (expressed in absolute terms) varied with the cyclic shear strain [118], γ_{cl} and γ_{lv} are the linear threshold shear strain and the volumetric cyclic threshold shear strain, respectively



The soil damping is mainly influenced by the cyclic strain amplitude, soil type, mean effective confining stress, plasticity index, frequency of loading, and the number of loading cycles. Soil damping generally decreases with an increase in mean effective confining stress for all strain amplitudes. Even though soil damping generally increases with an increase in plasticity index, at high strain levels, it even decreases with an increase in plasticity index [124, 125]. Moreover, as soil damping is strongly influenced by the frequency of loading and the number of cycles, it is suggested that one measure the damping value at frequencies and number of loading cycles similar to those of the anticipated cyclic and dynamic loadings.

The secant shear modulus $G_{sec}(\gamma')$ and equivalent damping ζ_{eq} are often referred to as equivalent linear material parameters as shown in Fig. 2.12, which will be further discussed in Sect. 2.3.

2.3 Soil Stiffness and Damping Modeling in an Equivalent Linear Model

2.3.1 Trends in Dynamic Soil Properties and Strain Thresholds

Based on the conceptual framework of soil behavior varied with strain [126, 127] and stress–strain response [128], several strain levels can be defined, as presented by Atkinson and Salfors [129] and Vucetic [118] (shown in Fig. 2.12): the very small strain regime, where the stiffness modulus is constant and soils show elastic behavior; the small strain regime, where the stiffness modulus varies nonlinearly with the strain; and the large strain regime, where the soil is close to failure and the soil stiffness is relatively small. The large strain regime is sometimes further divided into medium strain regime and large strain regime.

For all types of soils, there is a strain γ_{c1} (some literatures use γ_{tl}), called linear threshold shear strain as shown in Fig. 2.12, or also called nonlinearity threshold by Vucetic and Dobry [231]. Below γ_{c1} , the shear modulus measured from tests under either drained or undrained conditions is similar because no notable excess pore pressure can be generated at such a small strain level. Above γ_{c1} , the nonlinear behavior of soil stiffness appears.

The region below γ_{c1} is called the very small strain elastic regime (some literatures also call it the small strain regime [144]) since the soil with strains at this regime essentially exhibits linear-elastic material behavior, i.e., the soil stiffness is approximately constant, bonds at molecular level remain unchanged, very minor energy is dissipated, and no pore-water pressure is generated. γ_{c1} is normally at a shear strain level of 0.0005–0.003%, corresponding to a modulus reduction G/G_{max} of around 0.98–0.99. The main source of energy dissipation is friction between soil particles and/or viscosity, and the material damping ratio is constant at a minimum value, also called the small-strain damping ratio ξ_{min} .

Just above linear threshold shear strain γ_{c1} , soils behave nonlinearly but still elastically with minor fabric change, i.e., the stress–strain relationship is curved, but the deformation is recoverable upon unloading. There is no accumulation of pore-water pressure during undrained cyclic loading and no volume change for drained conditions. The upper-bound value of this nonlinear-elastic region is called elastic threshold strain, which is typically at a shear strain level of around 0.005%. Due to the increased cyclic strain level compared to the very small elastic strain regime, the material damping is slightly increased. Obviously, elastic threshold strain establishes the difference, among strain regimes, between fully recoverable behavior and strength degradation.

Volumetric cyclic threshold shear strain or degradation threshold [231] occurs when the strain further increases to a level below which the structure of soils does not change, and beyond which the soil skeleton (microstructure) starts to change irreversibly, indicating the onset of volume change (drained condition) and possible pore-water pressure generation (undrained condition). This strain level is commonly notated as γ_{1v} or γ_{tv} , as shown in Fig. 2.12.

The region below γ_{1v} but above the linear threshold shear strain (γ_{c1}) is defined as the small strain regime, as shown in Fig. 2.12. At γ_{1v} , soil deformations become irrecoverable. γ_{1v} has been derived from strain-controlled conditions [126] and stress-controlled conditions [130, 131]. For sands, γ_{1v} is in the order of 0.01%; while for clay, this value can be one order of magnitude larger. For example, Hsu and Vucetic [132, 133] presented that, for silts and clays having plastic index from 14 to 30, γ_{1v} ranges from 0.024 to 0.06%. Such difference indicates that γ_{1v} depends on the microstructure of soils and is likely to be influenced by the soils' plasticity index. Its value relates to both G/G_{max} ratio ranging from 0.6 to 0.85 and a material damping ranging from 2 to 4% (in absolute terms) which is higher than the small-strain damping ratio ξ_{min} (Sect. 2.3.3).

There is also yet another strain value, called large strain threshold γ_{td} . γ_{td} represents the higher strain value that induces the decisive de-structuring of soil specimen. γ_{td} has been derived from stress-controlled conditions [134] and used as a

type of strain threshold by Diaz-Rodriguez [135]. The large strain threshold has been represented as a critical level of cyclic loading below which soil failure will never occur. Below this loading, soil exhibits a hysteretic equilibrium behavior and a nearly elastic pore pressure response. In some tests for clays, high residual pore pressure under the critical stress ratio can be observed, which potentially accelerates soil creep and eventual failure under undrained condition. The effects of cyclic loading associated with the strain level around γ_{td} have been investigated through experiments, in which 30,000 [136] to 300,000 cycles [137] of loading have been applied during tests. This amount of cycles is regarded as far greater than any realistically possible real-world scenario, because even for offshore structures subject to continuous ocean wave loading, undrained shearing is unlikely to persist for more than 1000 loading cycles [138]. Under such critical cyclic stress, the first cycle of loading predominantly causes deformations and the accumulation of pore-water pressure [81, 136], and a gradual stabilization or strain-hardening can be reached [139].

As shown in Fig. 2.13, the majority of geotechnical engineering issues are associated with the small strain and large strain regimes.

Reference [139] presents a review of various types of strain thresholds used in soil dynamics.

Along with strain level, effective confining pressure, plasticity characteristics, etc., also significantly influence both the modulus reduction curve and the damping. For example, at the same strain level, the shear modulus reduction is more significant for low-plasticity than for high-plasticity soils. The damping ratio is higher

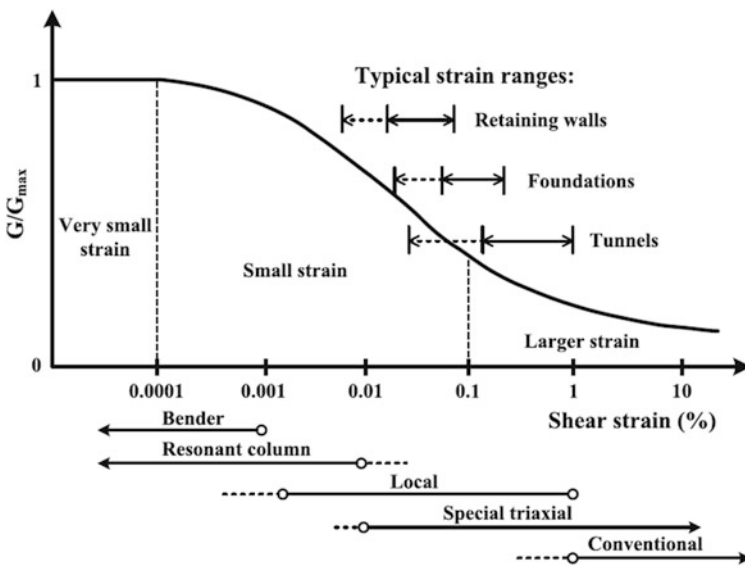


Fig. 2.13 Normalized stiffness degradation curve with corresponding geotechnical applications [140]

Table 2.5 Parameters that control nonlinear soil behavior and their relative importance in terms of affecting shear modulus and material damping presented by Hardin and Drnevich [141]

Parameters	Impact on shear modulus		Impact on material damping	
	Clean sands	Cohesive soils	Clean sands	Cohesive soils
Strain amplitude	***	***	***	***
Mean effective confining pressure	***	***	***	***
Void ratio	***	***	***	***
Number of loading cycles	+	*	***	***
Degree of saturation	*	***	**	—
<i>OCR</i>	*	**	*	**
Effective strength envelope	**	**	**	**
Octahedral shear stress	**	**	**	**
Frequency of loading (above 0.1 Hz)	*	*	*	**
Other time effects (thixotropy)	*	**	*	**
Grain characteristics, size, shape, gradation, mineralogy	*	*	*	*
Soil structure	*	*	*	*
Volume change due to shearing strain below 0.5%	—	*	—	*

***: Very important

** : Less important

*: Relatively unimportant

+: Relatively unimportant except for saturated sand

—: Unknown

for low-plasticity than for high-plasticity soils. Tables 2.5 and 2.6 rank the relative importance of various soil parameters on the shear modulus and material damping, as presented by Hardin and Drnevich [141] and Darendeli [144], respectively.

The current state of the practice to determine soil stiffness and damping comprises measuring and estimating (1) shear wave velocity, (2) soil stiffness varied with shear strain, (3) soil damping varied with shear strain. Furthermore, more recent proposed methods to estimate the soil stiffness and damping account for influences of a range of soil parameters in addition to just the shear strain, even though some of those methods involve excessively complex procedures and are essentially not suitable—or even feasible—for engineering practice.

Table 2.6 Parameters that control nonlinear soil behavior and their relative importance in terms of affecting normalized modulus reduction and material damping curves presented by Darendeli [144]

Parameters	Impact on normalized shear modulus reduction curve	Impact on material damping curve (Sect. 2.3.3)
Strain amplitude	***	***
Mean effective confining pressure	***	***
Soil type and plasticity	***	***
Number of loading cycles	*+	***++
Frequency of loading (above 1 Hz)	*	**
OCR	*	*
Void ratio	*	*
Degree of saturation	*	*
Grain characteristics, size, shape, gradation, mineralogy	*	*

***: Very important

**: Important

*: Less important

+: On competent soils included in the study by Darendeli [144]

++: Soil type dependent

2.3.2 Stiffness Modeling

2.3.2.1 General

Stiffness modeling in an equivalent linear model that requires two types of information can be obtained from either established equations or testings. The strain level and the testing apparatus used to obtain the two types of information are different. The first type is related to very small strain properties, tested with, for example, the resonant column apparatus (Chap. 6), where the major focus is on the determination of G_{\max} . The second type is to model the changes in shear modulus and damping ratio varied with shear strain, which are measured with various types of cyclic loading test apparatus and cover a larger strain level [139]. Sections 2.3.2 and 2.3.3 will present the modeling of soil stiffness and damping, respectively. The relevant testing methods will be presented in Chap. 6.

2.3.2.2 Modulus Reduction Curve

Extensive experimental data for modulus reduction (also called normalized shear modulus) curves G/G_{\max} are accessible through various published researches. In

those studies, typically “average” normalized modulus reduction and material damping curves (Sect. 2.3.3) have been presented. There are typically two elements to establish such curves: (1) Determine the target shape of the modulus reduction curve; (2) Select model parameters that describe the target relationships with reasonable simplification/approximation. Several well-recognized hyperbolic soil models [118, 141–143] have been proposed, making the analysis possible even without running relevant laboratory tests.

Hardin and Drnevich [141] assumed that the stress–strain curve of soils can be represented by a hyperbola asymptotic to the maximum shear stress, and the normalized modulus reduction curve may be expressed as:

$$\frac{G}{G_{\max}} = \frac{1}{1 + (\gamma/\gamma_r)} \quad (2.21)$$

where G is the shear modulus at shear strain γ (%); the reference strain $\gamma_r = \frac{\xi_{\max}}{G_{\max}}$.

Hardin and Drnevich [141] also observed that soil type has an impact on the stress–strain relationship and found through measurement that stress–strain curves deviate from the simple mathematical model depending on the soil type. Therefore, they proposed to approximate the observed soil behavior by distorting the strain scale so that the measured stress–strain curve can have a hyperbolic shape. For this purpose, they defined a hyperbolic strain γ_h , which replaces the γ/γ_r term in the equation above:

$$\gamma_h = \frac{\gamma}{\gamma_r} \left[1 + a \cdot \exp\left(-b \cdot \left(\frac{\gamma}{\gamma_r}\right)\right) \right] \quad (2.22)$$

where a and b are coefficients that adjust the shape of the stress–strain curve for different soil types, number of cycles, and loading frequencies.

The empirical equations proposed by Hardin and Drnevich [141] account for the effects of plasticity index, over-consolidation ratio, and confining pressure mainly through adjusting reference strain γ_r . Effects of soil type, number of loading cycles, loading frequency, and saturation are taken into consideration by adjusting ξ_{\max} (the maximum damping ratio of the soil presented in Sect. 2.3.3) and the a and b coefficients in the equation above. Although complexities of the procedure in the equation proposed by Hardin and Drnevich [141] militate against their extensive application, their work represented an important step forward in characterizing dynamic soil behavior [144].

It is noticed that in the proposed equation by Hardin and Drnevich [141] above, only one curve fitting variable (reference strain γ_r) is involved, making it difficult to fit to experimental data. To solve this problem, Stokoe et al. [143] and Darendeli [144] proposed that modulus reduction curves can be established by fitting the experimental data into the equation as follows:

$$\frac{G}{G_{\max}} = \frac{1}{1 + (\gamma/\gamma_t)^\alpha} \quad (2.23)$$

where α is a curvature parameter ($\alpha = 1.0$ corresponds to a standard hyperbolic backbone curve) and can normally be taken as 0.92; γ_t is called the pseudo-reference strain, corresponding to the shear strain when $G/G_{\max} = 0.5$; empirical relationships exist to predict γ_t as a function of basic parameters such as plasticity index I_p , overburden (effective confining) stress σ'_m , and over-consolidation ratio (OCR):

$$\gamma_t = (\varphi_1 + \varphi_2 \cdot I_p \cdot OCR^{\varphi_3}) \times \sigma'_m{}^{\varphi_4} \quad (2.24)$$

where $\varphi_1 = 0.0352$; $\varphi_2 = 0.0010$; $\varphi_3 = 0.3246$; $\varphi_4 = 0.3483$.

It is noticed that, in the equation describing modulus reduction curves, pseudo-reference strain γ_t is used to avoid confusion with the reference strain as defined by Hardin and Drnevich [141]. The advantages of using the pseudo-reference strain are: (1) γ_t can be conveniently evaluated from the material-specific modulus reduction curves obtained from laboratory tests; (2) even if in many cases, material-specific testing is not available, empirical relationships do exist to predict γ_t [144, 145]. However, because pseudo-reference strains are determined from modulus reduction curves that are typically defined for strains less than 1%, a backbone curve described by a hyperbolic curve fit using γ_t may not accurately represent soil behavior at large strain level [146].

To develop the two equations above, Darendeli [144] used an extensive database from various research projects. The database consisted of combined resonant column (Chap. 6) and cyclic torsional shear (Sect. 6.3.2.2) tests, sequentially performed on intact samples from soils described as having low void ratio and not liquefiable during earthquakes. The tested soil samples ranged from natural clean sands to clays, characterized by broad intervals of sampling depth (3–263 m), confining pressure (0.3–27.2 atmosphere pressure), I_p (0–132%) and OCR (1–8). A statistical analysis of the database was undertaken to calibrate all of the required parameters.

2.3.3 Damping Modeling

Energy dissipation occurs even if the level of soil's shear strain is rather small [144]. This is still not fully understood, as theoretically, the damping exists only when soil strain is above a threshold value.

In geotechnical engineering, a typical way to specify the soil damping is to relate it to the strain level or G/G_{\max} . Borden et al. [157] and Ishibashi and Zhang [158] established the relationship between soil damping and G/G_{\max} using a polynomial

expression. Hardin and Drnevich [141] proposed an approximate shape for the material damping curve as:

$$\frac{\xi}{\xi_{\max}} = \frac{\gamma/\gamma_r}{1 + (\gamma/\gamma_r)} = 1 - \frac{G}{G_{\max}} \quad (2.25)$$

where ξ_{\max} is the maximum damping ratio of the soil, which depends on soil type, confining pressure, number and frequency of cyclic loadings.

Note that, among those models, the influence from plasticity index (I_p) is not included, even if it is a rather important parameter to affect the soil damping. At the reference soil confining pressure $p_a = 100$ kPa, the small-strain damping ratio (ξ_{\min}) increases proportionally to the increase in I_p :

$$\xi_{\min(\text{ss})} = a(I_p) + b \quad (2.26)$$

where a and b are fitting parameters and may be taken as 0.008 and 0.82, respectively.

Darendeli [144] and Stokoe et al. [159] proposed a rather simple damping equation by assuming Masing damping (Sect. 2.4.2) behavior [160, 161] and an adjusting function ($f(G/G_{\max})$) to fit the Masing damping to the experimental data, and by further adding the ξ_{\min} to calculate the total damping:

$$\xi = f(G/G_{\max}) + \xi_{\min} \quad (2.27)$$

ξ_{\min} in the equation above can be calculated by converting $\xi_{\min(\text{ss})}$ at a confining pressure σ'_m rather than the reference soil confining pressure p_a :

$$\xi_{\min} = \xi_{\min(\text{ss})} (\sigma'_m/p_a)^{-0.5k} \quad (2.28)$$

where $p_a = 100$ kPa (reference atmospheric pressure); k is a stress correction exponent depending on I_p and geologic age [145].

Since the value of $f(G/G_{\max}) = \xi - \xi_{\min}$ is also frequency-dependent, the best-fit curve based on torsional shear test results is more preferred, as proposed by Zhang and his co-workers [145]:

$$f(G/G_{\max}) = 10.6(G/G_{\max})^2 - 31.6(G/G_{\max}) + 21.0 \quad (2.29)$$

From the equation above, it is noticed that when $G/G_{\max} = 1$, i.e., at zero or small strain condition, the total damping ξ is equal to ξ_{\min} . And when $G/G_{\max} = 0$, i.e., at very large strain condition, the $\xi - \xi_{\min}$ is 21%.

Sugito et al. [153] and Assimaki et al. [154] recommended that the frequency dependence of soil damping be included in a frequency domain analysis.

2.4 Nonlinear Soil Models

2.4.1 *General*

Soil is a complicated material that behaves nonlinearly and often shows time-dependent behavior when subjected to time-varying stresses, and under cyclic loading, it can exhibit complex behavior associated with irregular loading, densification, pore pressure generation, etc. Therefore, to better represent the behaviors, there is a need for more dedicated constitutive laws that can incorporate both the hysteretic nature of the damping and the strain dependence of shear modulus and damping ratio.

In engineering applications, a broad range of simplified and advanced soil models have been employed to perform nonlinear soil response analysis. Those nonlinear inelastic soil properties can be modeled in two ways. The first is through cyclic soil models (Sect. 2.4.2) including backbone curves together with a number of rules that govern the unloading and reloading behavior and other effects. The second is by dedicated nonlinear constitutive soil models (Sect. 2.4.4) with a yield criterion/surface to determine the onset of the yielding and plasticity, a hardening rule to describe how the yield surface changes with the progression of plastic deformation, and a flow rule to describe the progression of yielding in the plastic domain, i.e., to define plastic strain rate outside the yield surface [123]. Such nonlinear models are normally used in time-domain response analyses.

It is noted that, theoretically, soil damping should be included in the hysteretic response modeled by nonlinear soil models. In reality, however, most soil models give nearly zero damping at small strains compared with that obtained from field measurements. Therefore, viscous damping is often used to supplement hysteretic damping from nonlinear soil models in soil response analyses. At small levels of strain, linear viscous Rayleigh damping can be used to represent the damping effects, as will be presented in Sect. 2.4.3. On the other hand, an over-estimation of damping at large strain can result when the hysteretic damping is calculated using unload–reload stress–strain loops in traditional cyclic nonlinear soil models adhering to Masing’s rule (Sect. 2.4.2). A modification to reduce the damping can then be performed, as will be presented in Sect. 2.4.2.

As a general rule, for sites with soft soil or subject to strong seismic motions or high amplitude of cyclic loading, especially when the soils’ shear stresses approach their shear strength, the use of stiffness and damping modeling applied to equivalent linear soil models is not appropriate. The nonlinear soil models have then to be used to calculate the nonlinear responses of soils, which are suitable to model soils with large strain amplitude.

2.4.2 Cyclic Nonlinear Soil Models

To represent the variation in shear stiffness under cyclic loading, cyclic nonlinear models are used, which can follow the actual stress–strain path (without reversal loading). A very simple way to describe this is to use a backbone curve (also called skeleton curve or initial loading curve) as shown in Fig. 2.14, which is essential to describe the soil behavior subject to initial loading. The path of the curve can easily be modeled with two parameters, the initial shear modulus G_{\max} at low strain condition and the shear strength τ_{\max} at high strain level:

$$\tau(\gamma) = \frac{G_{\max}\gamma}{1 + (G_{\max}/\tau_{\max})|\gamma|} \tag{2.30}$$

To be able to represent the effects of reversal loading (the load changes its direction), besides the backbone curve, a number of rules that govern the unloading and reloading behavior and other effects must be included.

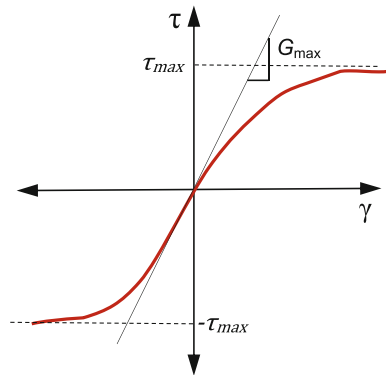
Matasovic [162] proposed a modified Kondner-Zelasko (MKZ) model to describe the hyperbolic stress–strain model with two equations, corresponding to the stress–strain relationship in the loading (backbone curve) and unloading phases, respectively:

$$\tau(\gamma) = \frac{G_{\max}\gamma}{1 + \beta(\gamma/\gamma_r)^s} \tag{2.31}$$

$$\tau(\gamma) = \frac{2G_{\max}\left(\frac{\gamma - \gamma_{\text{rev}}}{2}\right)}{1 + \beta\left(\frac{\gamma - \gamma_{\text{rev}}}{2\gamma_r}\right)^s} + \tau_{\text{rev}} \tag{2.32}$$

where γ is the given shear strain; γ_r is the reference shear strain; β is a dimensionless factor; G_{\max} is the maximum shear modulus; and s is a dimensionless exponent; γ_{rev} and τ_{rev} are the reversal strain and stress at the hyperbolic stress–strain curve.

Fig. 2.14 Backbone curve showing a simple nonlinear soil model

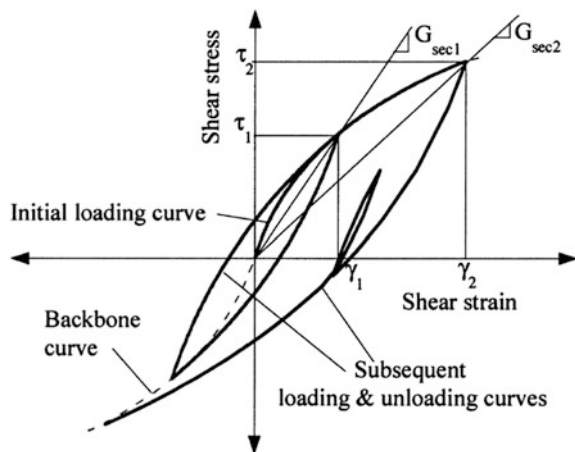


Many nonlinear soil models to describe the hysteretic behavior for unloading and reloading follow Masing's rule [160] and extended Masing's rules [161, 163, 164], which are adopted in conjunction with the backbone curve to describe unloading, reloading, and cyclic degradation behavior of soils, as shown in Fig. 2.15. In this figure, at the initial loading stage, the stress–strain relationship follows a backbone curve as illustrated in Fig. 2.14. The shape of the stress–strain curve remains unchanged during the unloading and reloading stage, but with the origin shifted to the loading reversal point and a scaling of values of curves, which is often referred to as Masing behavior [160]. Moreover, in order to uniquely determine the stress–strain curve in irregular cycles, Kramer [1] stated that two additional rules are needed: (1) If the unloading and reloading curves cross the previous unloading and reloading cycles, the curve will follow the previous one; (2) If the unloading and reloading curves exceed the past maximum strain and intersect the backbone curve, the curve will still follow the backbone curve until the next stress reversal.

Originally developed to describe the plasticity of metal, Masing's rule assumes that both the backbone curve and cyclic response are stable. However, this may not be the case. In practice, it may be feasible to incorporate a gradual change to the backbone curve as cyclic loading effects accumulate [112]. Furthermore, the damping at large strain that results from the use of Masing's rule or the extended Masing's rule tends to be over-estimated relative to laboratory measurements [146].

On the other hand, when adopting Masing's rule and the extended Masing's rule, zero damping is implemented at small strain level, where the modulus reduction curve is linear. Even if this is theoretically true, it contradicts laboratory test observations, as at small soil strain conditions, energy dissipation does occur, as aforementioned in Sect. 2.4.1. To solve this problem, one may add a viscous damping in the form of dashpots embedded within the material elements (implemented in many codes such as DMOD_2, DEEPSOIL, OpenSees, and SUMDES) or introduce a numerical scheme that can produce nonzero damping at small strains

Fig. 2.15 Hyperbolic nonlinear soil model with extended Masing model to define loading and unloading behavior [165]



[164], even though the soil damping is actually neither perfectly viscous nor hysteretic [166, 167].

By introducing a reduction factor $F(\gamma_{\max})$, Phillips and Hashash [168] presented a formulation that modifies the loading–unloading criteria resulting from the Masing’s rules, which provides a better agreement with the damping curves for large shear strains:

$$F(\gamma_{\max}) = p_1 - p_2 \left(1 - \frac{G(\gamma_{\max})}{G_{\max}} \right)^{p_3} \quad (2.33)$$

where p_1 , p_2 , and p_3 are non-dimensional parameters selected to obtain the best possible fit with the target damping curve through curve fitting; $G(\gamma_{\max})$ is the shear modulus at the maximum shear strain γ_{\max} ; G_{\max} is the maximum shear modulus.

The reduction factor above can then be implemented into the backbone curve and stress–strain relationship for unloading or reloading conditions:

$$\begin{aligned} \tau(\gamma) &= \frac{G_{\max} \gamma}{1 + \beta(\gamma/\gamma_r)^s} \quad (2.34) \\ \tau(\gamma) &= F(\gamma_{\max}) \cdot \left[\frac{2G_{\max} \left(\frac{\gamma - \gamma_{\text{rev}}}{2} \right)}{1 + \beta \left(\frac{\gamma - \gamma_{\text{rev}}}{2\gamma_r} \right)^s} - \frac{G_{\max} (\gamma - \gamma_{\text{rev}})}{1 + \beta \left(\frac{\gamma_{\max}}{\gamma_r} \right)^s} \right] + \frac{G_{\max} (\gamma - \gamma_{\text{rev}})}{1 + \beta \left(\frac{\gamma_{\max}}{\gamma_r} \right)^s} + \tau_{\text{rev}} \quad (2.35) \end{aligned}$$

Cyclic nonlinear soil models enable the determination of shear strength and effective stress during cyclic loading, of which the latter is essential to calculate the pore-water pressure and subsequently to evaluate the potential of soil liquefaction (Sect. 7.2), given that the effective stress and the subsequent G_{\max} and τ_{\max} change when the pore-water pressure changes. Moreover, they are especially necessary when the shear strain level is high (above 10^{-2}) or there is permanent strain (the shear strain is not zero when the shear stress/loading is zero). All these capabilities make nonlinear soil models significantly advantageous compared to the equivalent linear soil models discussed in Sect. 2.3.

More complex cyclic nonlinear soil models are proposed by various researchers by incorporating a large number of rules to account for the effects of irregular loading, densification, pore pressure generation, etc. Due to their complexity, they are seldom used in engineering practice.

2.4.3 Small Strain Damping Modeling in Time-Domain Analysis

For a convenient modeling in nonlinear time-domain wave propagation analysis, rather than modeling damping by a complex hyperbolic nonlinear Masing model

(Sect. 2.4.2) or an even more complicated nonlinear constitutive soil model (Sect. 2.4.4), many time-domain site-response analysis codes include small strain damping by implementing linear viscous Rayleigh damping. This is essentially an extension of the equivalent damping model presented in Sect. 2.2.3, but with a variation of damping at different frequencies. Rayleigh damping is expressed as a linear combination of the system’s mass and stiffness, as shown in Fig. 2.16, and the damping at frequency ω_i is:

$$c_i = \alpha m_i + \beta k_i \tag{2.36}$$

where α with the unit of s^{-1} and β with the unit of s are two coefficients to be determined from two given damping ratios at two specific frequencies of vibrations.

αm_i and βk_i , namely mass proportional and stiffness proportional damping, respectively, are the simplest way to formulate a proportional damping matrix, because the undamped mode shapes are orthogonal with respect to each of these [169].

α and β can be evaluated by the solution of a pair of simultaneous equations at two separate frequencies as follows:

With the orthogonality properties of mass and stiffness matrix [123], the equation above can be rewritten as:

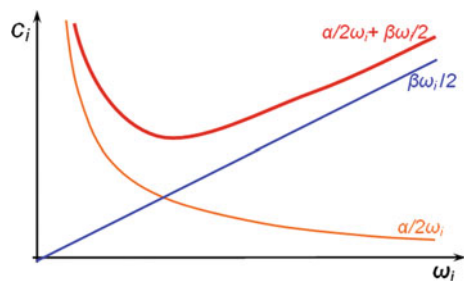
$$2\omega_i \zeta_i = \alpha + \beta \omega_i^2 \tag{2.37}$$

Rearranging the equation above, the relationship between modal damping (ζ_i) and Rayleigh damping is finally expressed as (Fig. 2.16):

$$\zeta_i = \frac{\alpha}{2\omega_i} + \frac{\beta \omega_i}{2} \tag{2.38}$$

For soil profiles with a constant damping ratio, coefficients α and β can be computed using two significant eigenmodes i and j :

Fig. 2.16 Rayleigh damping as a function of frequency



$$\begin{Bmatrix} \zeta_i \\ \zeta_j \end{Bmatrix} = \frac{1}{4\pi} \begin{bmatrix} 1/f_i & f \\ 1/f_j & f_j \end{bmatrix} \quad (2.39)$$

And the eigenfrequency of the n th mode is calculated as:

$$f_n = (2n - 1)/T_{\text{site}} \quad (2.40)$$

where T_{site} is the site period as will be presented in Sect. 3.2.

The use of a two-frequency scheme allows the model to respond to the predominant frequencies of the input motion without experiencing significant over-damping. It is normally recommended that the two specific frequencies for determining Rayleigh damping should ensure reasonable damping values in all the modes significantly contributing to the soil's dynamic response. At frequencies outside the range of these two, the damping will dramatically increase (Fig. 2.16) and the modal responses at the corresponding frequency range will almost be eliminated. Practically, this can be used to damp out the high- and low-frequency vibrations/noises that are outside the range of frequencies of interest.

The frequencies corresponding to the first-order mode of the soil column and a higher order mode that corresponds to the predominant frequency of the input motion are normally chosen to determine Rayleigh damping. Kwok et al. [170] recommended using the natural frequency and five times the natural frequency of soil columns as the two frequencies to determine Rayleigh damping. Park and Hashash [171] presented a series of recommendations for determining these two frequencies. Equal values of modal damping ratios are specified at each of the two modes. Hudson, Idriss, and Beirkae [172] suggested setting the first frequency equal to the fundamental frequency of the entire soil profile, and the second one as the closest odd number given by the ratio of the fundamental frequency of the input signal at the bedrock and the fundamental frequency of the entire soil profile. It is also suggested to keep the same value of damping, typically ranging from 0.5 to 2%, at both frequencies.

If one needs to specify damping ratios at more than two eigenmodes, instead of Rayleigh damping, an extended or more generalized form of Rayleigh damping called Caughey damping (also called the extended Rayleigh formulation) can be used:

$$c = m_n \sum_{i=0}^{N-1} \gamma_n (m_n^{-1} k_n)^n \quad (2.41)$$

where γ_n is a constant, and n is the number of modes one wants to specify damping; m_n and k_n are the modal mass and stiffness corresponding to mode n ; N is the number of modes incorporated.

The modal damping ratio ζ_n at modes n can then be expressed as:

$$\zeta_n = \frac{1}{2} \sum_{n=0}^{N-1} \gamma_n \omega_n^{2n-1} \quad (2.42)$$

Note that the equation above implies that the damping can be extended to include any number of frequencies/modes. The resultant Caughey damping is then numerically ill-conditioned since $\omega_n^{-1}, \omega_n, \omega_n^3, \omega_n^5, \dots, \omega_n^{2n-1}$ differ by orders of magnitude.

The mass and stiffness matrices adopted in formulating Caughey damping satisfy the mode shape orthogonality condition. However, Caughey damping normally results in a full matrix, which is computationally demanding for solving equations of motions.

When utilizing Caughey damping, it must be observed that using more than four frequencies/modes can result in a singular matrix depending on ω_n such that γ_n cannot be calculated. An increase in the frequencies/modes used in the calculation of the damping matrix also leads to an increase in the number of diagonal bands of the viscous damping matrix and therefore a significant time increase for solving the wave propagation problem. In addition, one must be careful in selecting the number of frequencies/modes to be employed so as not to obtain negative damping [87]. Incorporating an odd number of modes will result in negative damping at certain frequencies [169].

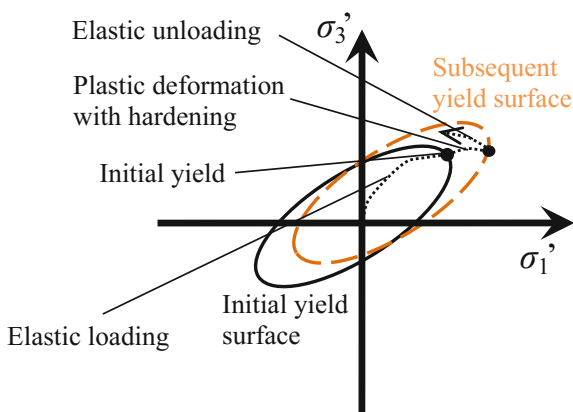
2.4.4 *Nonlinear Constitutive Soil Models*

Similar to the representation of a nonlinear material stress–strain constitutive relationship [173], a more fundamental, universal, and accurate way to describe nonlinear soil behavior is to adopt a constitutive model of soil materials using principles of material mechanics. This involves the modeling of initial stress conditions on the basis of a wide variety of stress paths, rotating principal stress axes, cyclic or monotonic loading, high or low strain rates, and drained or undrained conditions [1].

Under reversal loading, yielding due to unloading normally occurs prior to the stress reaching the yield strength, i.e., a hardening in one direction will lead to a softening in subsequent loading in the opposite direction. To account for this early yielding effect, the kinematic hardening rule with multiple yield surfaces/lines is often used as a convenient way to describe the pre-failure of soils. The rule states that the shape and size of yield surface do not change, while the center of the yield surface changes in the stress space. This is illustrated in Fig. 2.17 for a two-dimensional soil stress state.

The convenience of this approach lies in the fact that it gives a gradual change in soil stiffness, as more surfaces/lines can be used to increase the smoothness of this change. Furthermore, it can also describe the influences from the intermediate past load history. Moreover, kinematic hardening also allows a possible implementation

Fig. 2.17 Kinematic hardening rule in a two-dimensional principal stress space (σ_1' and σ_3' are the maximum and minimum principal stresses)



of anisotropic behavior of soils. In kinematic hardening, when the stress point touches the yield surface as shown in Fig. 2.17, plastic strain will then occur and can be evaluated by the flow rule. The surface is dragged by the stress point, following a kinematic hardening rule until the surface contacts the state boundary surface (SBS). Various formulations of SBS have been proposed, such as those by Dafalias and Herrmann [174], the Hashiguchi model (two- and three-surface models) proposed by Hashiguchi [175], and the MIT-E3 model proposed by Whittle [176]. The two-surface model is adopted due to its simplicity and can capture three types of soil behavior: (1) fully elastic: when the stress state is within the initial elastic yield surface; (2) transitional zone: with stress state point on the initial yield surface but inside the subsequent yield surface; (3) fully plastic: when the initial yield and subsequent yield surface come into contact, which is the normally consolidated state condition.

For engineering and research purposes, a large number of constitutive soil models have been proposed, including the Mohr-Coulomb, Drucker-Prager, Cam-Clay [177], modified Cam-Clay, modified Duncan-Chang or hyperbolic, PLAXIS soft soil (creep), PLAXIS hardening, hyperelastic, hypoelastic, viscoelastic, and viscoplastic soil models. Source [178] presents a review of soil constitutive models above. Some of those models are briefly discussed below.

The simplest soil model is to represent the soil behavior with an elastic-perfectly plastic model, which is referred to as the Mohr-Coulomb model. It is essentially a combination of Hooke's and Coulomb's laws formulated in a plasticity framework. In general stress state, the model has a linear stress-strain relationship in the elastic range, with two defining parameters from Hooke's law (Young's modulus and Poisson's ratio). There are two parameters that define the failure criteria (the friction angle and cohesion) and yet another parameter to describe the flow rule: Dilatancy angle ψ , which controls an amount of plastic volumetric strain developed during plastic shearing, is assumed to be constant during plastic yielding and comes from the use of the non-associated flow rule (the plastic potential function is the same as the yield function that is used to model a realistic irreversible change in volume due

to shearing) [178]. Note that the Mohr-Coulomb model does not account for any strain-hardening or softening effects, and it can then deviate from laboratory test results significantly because of this.

The Drucker-Prager model [179] is essentially a simplification of the Mohr-Coulomb model, where the hexagonal shape of the failure cone is replaced by a simple cone. It has similar pros and cons as the Mohr-Coulomb model, even though the Mohr-Coulomb model is the most widely accepted model in the geotechnical engineering community.

The Duncan-Chang model [180], also known as the hyperbolic model, is a stress-dependent model and widely applied because its soil parameters can be easily obtained directly from standard triaxial test (Sect. 1.9.3) for both clay and sand. The stress-strain curve is a hyperbola with a high degree of accuracy. It describes three important characteristics of soils including nonlinearity, stress dependence (using a power law), and inelastic behavior for both cohesive and cohesionless soils. Even though its failure criterion is defined based on Mohr-Coulomb's two strength parameters, it is a simple yet obvious enhancement to the Mohr-Coulomb model. This model can capture soil behavior in a very tractable manner on the basis of only two stiffness parameters and has been widely used by geotechnical engineers. However, in contrast to an elasto-plastic type of model, this model cannot consistently distinguish between loading and unloading, and the model is not fit for collapse load computations in the fully plastic range. The Duncan-Chang model is therefore not popular among geotechnical researchers [181].

The modified Cam-Clay [15, 182] is an elastic-plastic strain-hardening model, where the nonlinear behavior is modeled by means of hardening plasticity. The model is based on critical-state theory [183] by combining the effective soil stress and specific volume of soil in any state, and the resulting basic assumption is a logarithmic relationship between the mean effective stress and the void ratio. This model is more suitable for describing deformation than failure, especially for normally consolidated soft soils. The model also performs very well in applications involving loading conditions associated with embankments or foundations. However, the critical state had generally been limited to saturated clays and silts. It is not applicable for modeling over-consolidated clays and granular materials due to its inability to predict observed softening and dilatancy of dense sands and the undrained response of very loose sands [184].

In the hyperelastic model, the stress is a function of the current strain rather than of the previous strain history, i.e., soil is assumed to be Cauchy elastic material. This type of formulation can be quite accurate for concrete and rock in proportional loading, but the model cannot capture inelastic behaviors of concrete and rock deformation, a shortcoming that becomes apparent when the material experiences unloading. Moreover, the hyperelastic model often requires too many material parameter inputs, thus limiting its wide application [114].

Based on a discussion of pros and cons of basic and practical soil constitutive models among Hooke's law, the Mohr-Coulomb, Drucker-Prager, modified Duncan-Chang or hyperbolic, Cam-Clay, PLAXIS soft soil (creep), and PLAXIS hardening soil model, Brinkgreve [185] discussed the applicability of each model

and selection of soil parameters from correlation with laboratory testings, which can be implemented into finite element models.

When adopting constitutive soil models, it must be observed that a good constitutive model should not only be useful to its designers, but also be user-invariant [186], i.e., different users should be able to obtain same solutions.

Compared to equivalent linear soil models and cyclic nonlinear soil models, the nonlinear constitutive soil models require inputs of more material parameters. Some of them are difficult to evaluate or exhibit large scatters in their values. For example, an advanced constitutive soil model proposed by Manzari and Dafalias [187] needs to input 16 parameters including elastic parameters, critical-state parameters, and model parameters. Even though all 16 of these parameters have physical meanings, some of them cannot be determined by conventional soil tests. Therefore, the application of advanced constitutive soil models in geotechnical engineering is still rather limited, even though it has attracted an increasing effort in research and geotechnical engineering practice.

Note the fact that high-quality input data for stress–strain relationships of soil is very limited due to the high expenses of soil testing. Therefore, there is no real engineering sense in adopting complex soil models unless the required data can be obtained conveniently or the foundation under investigation is of significant importance. Furthermore, readers should also bear in mind that no single soil constitutive model can provide a completely valid description of the complex behavior of real soils under all conditions.

2.5 Strain Rate Effects Due to Seismic Loading

For sand, strain rate has little effect on soil strength, but strength may decrease due to pore-water pressure build-up. However, similar to metal materials subject to impact loading, clay soil strength depends on strain rate. It has long been recognized that the shear strength of clay soils under seismic loading is higher than that found in static loading tests [80, 81].

It has been observed in the laboratory triaxial compression test that, for low-to-medium applied strain rates of 10^{-7} – 10^{-4} /s, clay soils typically show a rough increase in undrained shear strength (Δs_u) of 5–20% per log-cycle increase in the strain rate [82, 83]:

$$\Delta s_u = \log_{10}(T_{\text{static}}/T_{\text{dyn.}}) \times \Delta s_{u,10} \quad (2.43)$$

where T_{static} is the duration of the static testing to obtain soil shear strength; $T_{\text{dyn.}}$ is the time duration for increasing variable loading from zero to the peak; $\Delta s_{u,10}$ is the increase in undrained shear strength (Δs_u) (in percent) per tenfold increase in strain rate, ranging from 5 to 20%.

By applying the relationship between Δs_u and strain rate variation above for clay soil subject to seismic loading, and by assuming $T_{\text{static}} = 500\text{s}$, $T_{\text{dyn.}} = 0.3\text{s}$ (in case

of seismic loading), and the shear strength increases 8% per tenfold increase in strain rate, the equation above gives a 26% increase in undrained shear strength.

Therefore, most clay soils subjected to typical undrained seismic loading may exhibit an increase in shear strength by 20–50% compared with the shear strength obtained from static loading tests. The critical-state strength of clays, however, remains largely unaffected by the rate of induced strains under low-to-medium strain rates. Here, the critical-state concept states that soils and other granular materials, if continuously distorted (sheared) until they flow as a frictional fluid, will come into a well-defined critical state. At the onset of the critical state, shear distortions occur without any further changes in mean effective stress or deviatoric stress or void ratio. Readers may read [183] for further details.

OCR (Sect. 1.11.4) plays an important role in the rate-dependent mechanical response of clay. For a constant *OCR*, the deviatoric stress attains its peak at approximately the same strain level for different strain rates. However, the strain at which the peak occurs increases with increasing *OCR*. Significant post-peak softening is observed for low *OCR* of 1 and 2 due to the generation of positive excess pore pressure, while for *OCR* of 4 or greater, the post-peak softening is relatively small [84].

Moreover, it is worth mentioning that soil's shear modulus generally degrades with a decrease in strain rate, as has been presented by several researchers [85, 86] through laboratory tests. Matesic and Vucetic [86] presented that the initial shear modulus increases at a rate of about 10% per log-cycle increase in the applied strain rate. However, soil damping does not have a clear correlation with a variation in strain rate [87].

By calculating the site response by developing a series of modified equivalent linear analyses (Sect. 3.5.2) to characterize the effects of the rate-dependent soil behavior, Park and Hashash [88] concluded that, compared with the response excluding strain rate dependence, the inclusion of strain rate dependence results in up to 20% difference in the computed response for very mild ground motions, and within 10% for higher amplitude motions.

2.6 Differences Between Soil Properties Subjected to Earthquake Loadings and Ocean Wave Loadings

Even if soil properties under earthquake loading and ocean wave loading can be obtained from the same laboratory test, they can be significantly different from each other. These differences are mainly caused by the difference in cyclic loadings' type, duration, and frequency, as well as the level of cyclic shear strain.

During an earthquake event, the seismic wave travels from the earthquake source to the ground surface. Not only the zone close to the foundation but the entire soil–foundation system is influenced by the seismic wave propagation. In addition, the soil zone near the foundation is also influenced by inertia loading due to vibrations

of the structure and the foundation. On the other hand, under ocean wave loading, essentially only the soil zones close to the foundation will be influenced by the ocean wave loading and inertia loading transmitted from the structure. Therefore, under seismic loading, the shear modulus for soils far from the foundation is generally lower than that under ocean wave loading, as the shear modulus decreases with an increase in cyclic shear strain level.

As aforementioned, the level of cyclic shear strain caused by seismic loading and ocean wave loading can be significantly different. The shear modulus of the surrounding soil may be quite different as it is shear strain dependent, leading to a difference in foundation stiffness. For example, it has been reported that the calculated soil spring stiffness for a typical GBS structure in the North Sea under seismic loading is, in terms of lateral stiffness, 1.2–3.2 times that under the influence of storm wave loading, and this ratio increases to 1.3–4.0 times in terms of rocking stiffness [67]. Obviously, this is because the seismic loading is less significant than the storm loading in terms of inducing the soil's cyclic shear strain in a typical North Sea site. The opposite trend can also be found at sites with high seismicity but mild design sea state condition.

Typical ocean wave loadings have much longer durations than seismic loadings. The number of significant cycles may be 100 times higher in a storm than in an earthquake, which also contributes to the difference in soil stiffness with regard to cyclic loading.

While the dominant frequency of seismic loading is between 0.2 and 0.5 s (Fig. 9.31), the period of ocean wave loading rises to 20 s for an extreme storm and 4–7 s for a mild sea state condition. This also indicates the importance of inertia loading under seismic loading. Furthermore, the strain rate induced by seismic wave transmission is significantly higher than that induced by ocean wave loading or wave-induced foundation loading, in which the higher strain rate may affect both the strength and shear modulus of soils, as has been presented in Sect. 2.5.

Chapter 3

Site-Response Analysis in Geotechnical Earthquake Engineering

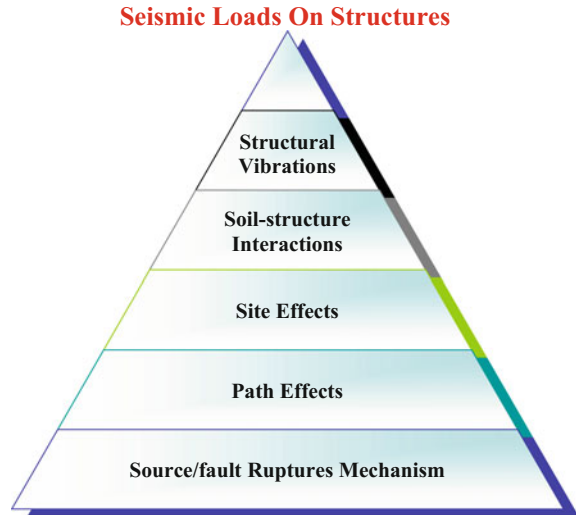
3.1 General

Unlike the loads generated by the wind, waves, current, and ice, which are due to the external forces applied on structures, earthquake loads are purely induced by the ground accelerations transferred to the foundation of the structures. Therefore, the determination of earthquake ground motion is an essential part of earthquake engineering.

The rupture of faults generates seismic wave, which is the cause (or source effect) of earthquakes. The wave is then transmitted and modified by wave scattering, anelastic attenuation, and geometric spreading, known as path effects, and is further transmitted through soil layers before it reaches the ground surface. These effects are known as site effects. However, as the rate and duration of energy released from the earthquake source (the source effects) are relatively random, and the path effects are complex, it is not possible to obtain the exact excitation to which the foundation of the structure will be subjected. Therefore, extrapolating the effects of the energy released from sites of potential seismic activity to the location of the structure under investigation is a rather complex process.

As shown in Fig. 3.1, four major characterizations enable the determination of earthquake ground excitation (seismic input): the seismic source, i.e., the rupture mechanism at the source; the transmission of the excitation from the sources to the sites, i.e., wave propagations; local geotechnical effects on the motions of the soil; and soil–structure interactions (SSI) during the earthquake events. Therefore, the level of ground shaking is mainly influenced by the fault-rupture mechanism (characteristics), source-to-site distance, and local soil effects. Moreover, seismic loading applied on structures is strongly influenced by dynamic/vibration characteristics of the structures, primarily due to the interaction between the stiffness and the inertia of the structures affected by the seismic wave transmission. This effect can typically be characterized by the eigenpairs (eigenfrequencies and the

Fig. 3.1 “Journey” of seismic wave transmission from fault rupture to seismic loading applied on structures [188]



corresponding mode shapes) of the most important eigenmodes with high modal mass participations.

The fault-rupture mechanism is rather complicated to predict and is still a topic under further development. It generates waves in a wideband frequency range with both high- and low-frequency contents. The high-frequency seismic waves have high intensity but dampen out rather quickly during seismic wave propagation. The low-frequency seismic waves possess low acceleration but large displacement properties, and they damp out much more slowly.

When seismic waves travel away from the fault rupture, they spread out (radiation damping) and are also partially absorbed by the media they travel through (material damping). Therefore, the seismic energy will be reduced with an increase in source-to-site distance. With the assumption of isotropically elastic characteristics of the transmission media, the effects of the nature and length of the intermediate path from the fault to a site at bedrock or rock outcrop can be estimated by the attenuation relationship or ground motion prediction equations/models (GMPEs) [188]. This is normally established using statistical regression analysis based on observations from a large amount of ground motion observation data collected from past earthquakes.

After arriving at bedrock or rock outcrop, the seismic wave will continue to transmit through soil media before arriving at ground surface or structural foundations, as illustrated in Fig. 3.2. The soil media work as a filter to tune both the energy and frequency of the seismic wave. This tuning process usually eliminates the high-frequency motion and filters the motion into a narrow frequency motion at seabed, with an amplification at and around the resonance period of the soil column at the site, known as the site period (Sect. 3.2). This is illustrated in Fig. 3.3. Here, the bedrock is defined as consolidated rocks underlying the surface of a terrestrial

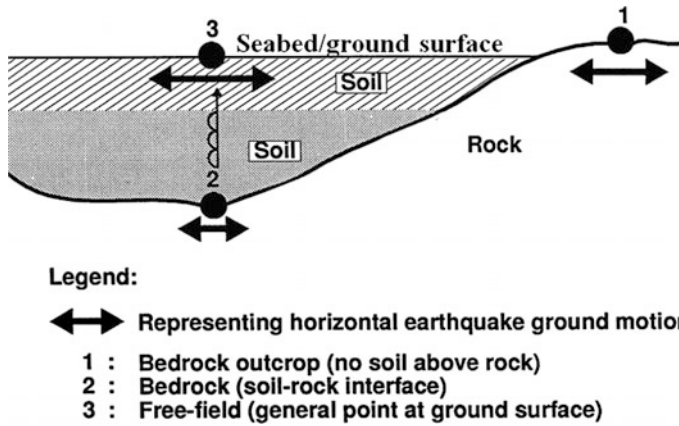
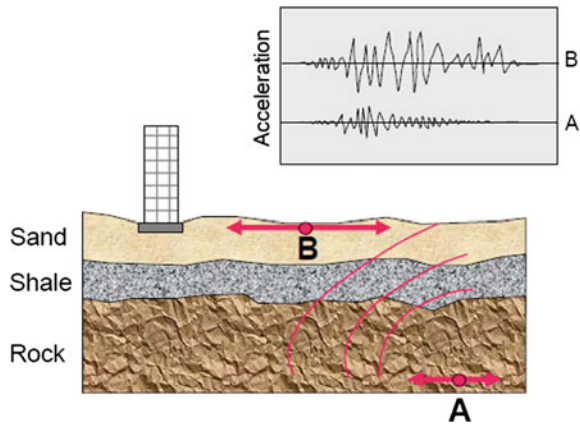


Fig. 3.2 Illustrations of seismic wave transmission from the bedrock (2) to the ground surface/seabed (3). Courtesy of NORSAR

Fig. 3.3 Transmission of seismic wave through soil layers with a tunation of seismic wave in both energy (represented by motion amplitude) and frequency content. Courtesy of FEMA



planet, usually the earth, as shown in Fig. 3.4, and there is often an area of broken and weathered unconsolidated rock lying above the bedrock in the basal subsoil. The rock outcrop is a visible exposure of bedrock or ancient superficial deposits on the surface of the earth, which can be viewed as a continuation of bedrock at the ground surface, as shown in Fig. 3.5. Readers need to distinguish the rock outcrop from the cliffs: Outcrops have a continuous line around each area of bare rock, while cliffs have a continuous line along the top edge with lines protruding down.

In engineering practice, due to the complexity of fault rupture and seismic wave transmission from fault rupture to the bedrocks, their influence can normally be assessed through a seismic hazard analysis by also accounting for various types of uncertainties, as will be presented in Chap. 11. After the seismic motion at bedrocks

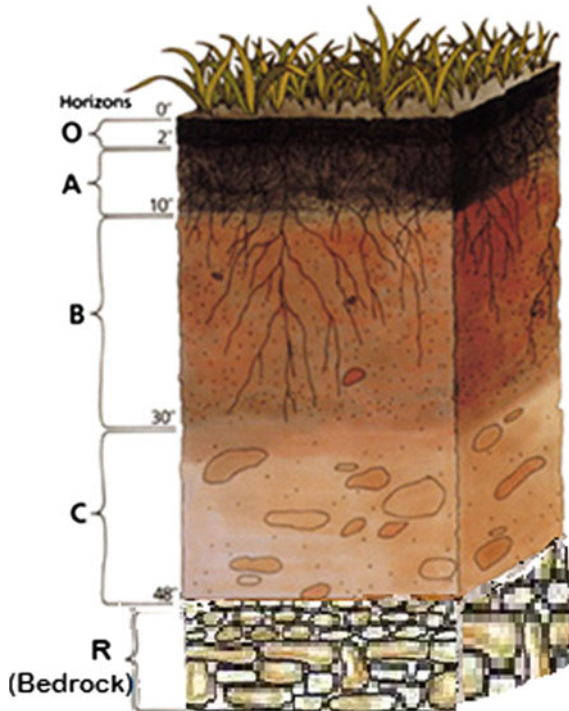


Fig. 3.4 Bedrock underneath broken and weathered unconsolidated rocks in the basal subsoil



Fig. 3.5 Appearance of rock outcrop

is obtained, the site effects can be assessed by using either the simple relationship between the ground motion and the site characteristics such as soil type or site topology (typically given in either design codes or relevant handbooks), or performing a site-response analysis.

In order to perform a site-response analysis (also called ground response analysis), it is necessary to establish information regarding the soil types, properties, layering, and the depth to rock or rocklike material. This can normally be obtained from site-specific geotechnical investigation field tests, boring for soil samples, and laboratory soil testing as presented in Sect. 1.9 and Chap. 6.

The amplitude, frequency content, and duration of bedrock/rock outcrop motions are important factors influencing the soil response and the subsequent seismic motions at ground surface. High amplitude of bedrock motion tends to cause inelasticity in the soil; i.e., the soil will absorb a certain amount of seismic wave energy, and the ground motions are not amplified proportionally to the bedrock motions. Compared to cases in which the soil is elastic, this will in general decrease the ground acceleration while increasing the displacement, placing higher demand on structures with medium and long natural periods of vibration. The process of transmission of seismic wave from bedrock/rock outcrop through soil media to the ground surface is typically referred to as kinematic interaction, which is an important task in a site-response analysis. The results of a site-specific response are design ground motions, provided that the seismic motion input in the analysis is consistent with the bedrock or rock outcrop motion predicted from a seismic hazard analysis (Chap. 11). Alternatively, design ground motions can also be obtained based on the relevant seismic design code provisions, in which sites are roughly grouped into a few classes, each representing similar soil profiles rather than the exact soil profile as a site-response analysis does. Therefore, the design ground motion determined from codes and standards is usually more conservative than that developed from a site-response analysis. This difference between the site-specific response analysis and the code-based design ground motions provides an economic incentive for the development of site-specific design ground motions.

Moreover, soil properties for the soil surrounding the foundation may change due to seismic excitations, which also influence the stiffness and damping of the foundation, thus affecting structural responses. The foundation stiffness and damping are typically referred to as subgrade impedances.

By obtaining the seismic ground motion and the foundation stiffness and damping, a seismic structural analysis can then be performed, which is usually referred to as inertial interaction, as will be introduced in Sect. 5.5.

In many cases, by establishing a modeling (typically using finite element method) comprising soil media (for seismic wave transmissions), foundations, and structures as an integrated system, it is possible to include the kinematic interaction, subgrade impedance, and inertial interaction in one analysis. The solution is typically obtained in the time domain by direct numerical integration. This is referred to as the direct analysis approach.

On the other hand, for improving computational efficiency, various types of frequency-domain methods are adopted to address the influence from the soil, even though it cannot explicitly account for the nonlinear effects of soil–structure interactions. This method is often referred to as the substructure approach, in which the soil–foundation–structure system is partitioned into distinct parts as soil, foundation, and superstructure: Their responses are first obtained independently and

then combined to satisfy compatibility of forces and displacements to formulate the complete solution.

One-dimensional site-response analysis to model and solve the vertical propagation of horizontal shear waves (SH-waves) through a horizontally layered soil deposit is first presented in Sect. 3.5.1. Horizontal soil layer behavior can be approximated as a Kelvin–Voigt solid, whereby elastic shear moduli and viscous damping characterize soil properties. A solution of wave propagation equations is performed in either the frequency (Sect. 3.5.2) or time domain (Sect. 3.5.3) depending on how significant are the seismic motions and soil nonlinearities exhibited.

However, there are many exceptions in engineering practice. During the transmission of seismic waves, the geometric properties of sites due to topographic irregularity (such as sloping or irregular ground surface) and subsurface irregularity (such as sloping layer boundaries, irregular boundaries, or basins) may significantly affect the seismic wave propagation. When their effects are significant, special considerations of modeling, such as two-dimensional or even three-dimensional modeling, may be required in relevant analysis. Two-dimensional or three-dimensional modeling can also capture different types of seismic wave (body and surface wave) propagation. As will be discussed in Sect. 3.7, the two-dimensional or three-dimensional site-response analysis is usually performed using finite element analysis.

It is noticed that local soil effects are one of the most significant causes of local spatially varied ground motion, which is a variation of seismic ground motion in magnitude, phase, and frequency at different locations, with a scale of a few hundred meters apart. This effect can be accounted for by performing local site-response analysis at each support location of a structure, even though other effects such as the seismic wave passage effect are also responsible for spatially varied ground motions.

Chapters 2–4 provide a general overview of the essential information required to perform a practical site-response analysis. For readers who are interested in a relatively complete coverage on this topic, Kramer [1] is recommended.

It should be noted that a future earthquake at given site can never be predicted with great confidence [209, 210], even though the strong motion accelerograms that are available and properly interpreted may be the closest thing to the scientific truth in earthquake engineering [211]. Therefore, it is essential to determine a set of ground motions. These do not need to be an accurate representation of real ground motions at a target site in future earthquakes, but they must induce responses, damages, and other impacts on the target infrastructure with sufficient accuracy and levels of severity to allow for a sound assessment of risk and necessary conservatism. This also requires an explicit requirement of significance of ground shaking associated with a certain level of probability of exceedance. Because a structure required to sustain little or no damage during any possible earthquakes may result in a prohibitively high cost, there must be trade-offs between short-term cost of providing an earthquake-resistant design and long-term cost of earthquake-induced damage. The latter of these, for the majority of structures, will never be realized.

Once the ground excitations of the structure have been determined, depending on the seismic analysis demand with respect to characteristics of excitation and structures, and also in line with the purpose and accuracy requirements of the analysis, the ground motions will be represented in certain formats, i.e., in time domain, expressed as a response spectrum (different from a frequency spectrum), or converted into frequency domain, with either deterministic or stochastic implication. They can then be applied to a structure model representing the superstructure together with the foundation and the effects of the surrounding environment (water and/or ice). Depending on the level of excitations accounted for, many of the properties during structural modeling may be nonlinear in nature, such as a degradation of foundation stiffness, yielding and large deformations of the structural members, and fluid–structure interactions. These can lead to considerable demand in terms of modeling and calculation. By fulfilling these requirements, the structural response can be calculated with sufficient accuracy for a reliable demand modeling to be established.

After the demand modeling is established, the capacity control can then be performed. If the structural responses are still in the elastic range, demand can be expressed as force and the capacity control in terms of strength. If the structural members reach yielding, demand can normally be expressed with displacement, and the capacity control is then strain based. As the strain-based control may need to reflect cyclic degradation and strain rate effects, dynamic testing may therefore be required to set appropriate limits. In addition to the strength and strain capacity, the stability check should also be included in the capacity control.

The criteria of capacity control are typically provided by prescriptive design codes based on a limit state concept (Sect. 1.13.2). However, since the prescriptive codes include a great number of provisions, which are designed to ensure life safety and damage control (safety check) required by regulatory authorities, they cannot explicitly provide acceptable levels of life-cycle performance, which is an important concern for infrastructure owners and operators as well as other relevant parties such as insurance companies. To solve this limitation, performance-based design can be used. Performance-based design introduces design checks at more limit states than the ones specified by prescriptive design codes, to the probability that the seismic action can reach the intensity required to induce the corresponding failure modes. See Jia [188] for further details on this.

3.2 Site Period

3.2.1 General

Besides the characteristics of structures and ground motions, the characteristics of soil between the bedrock and the structural foundations further complicate the task of carrying out seismic assessment. The soil media act as a filter to bedrock/rock

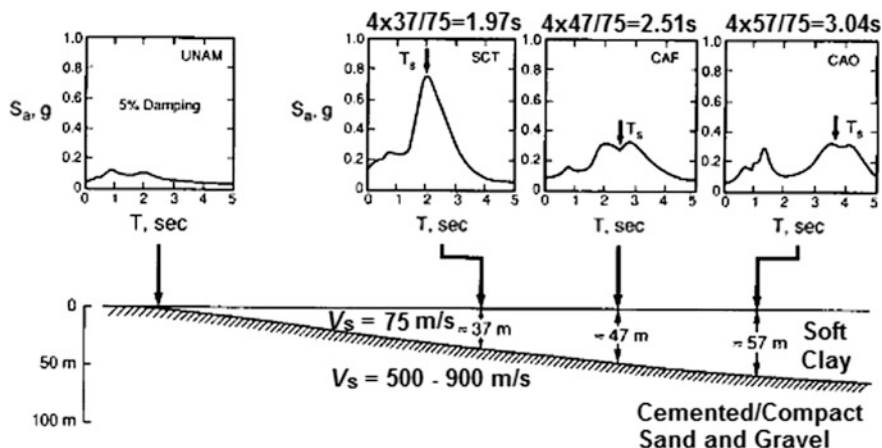


Fig. 3.6 Acceleration spectra from recorded time histories at several stations in Mexico City during the magnitude 8.1 Mexico City earthquake of 1985 [196, 197]

outcrop motions and influence both the frequency and magnitude of the ground motions.

If the soil is stiff, e.g., the foundation rests on rock, the ground motions will generally be short period, and if the soil is loose, the ground motions will generally be long period. If the natural period of soil is close to the predominant period of bedrock motions, the ground motions will be amplified compared with the bedrock motions. Furthermore, such amplification may be further enhanced on structural response if the natural period of the structures at the site is close to the dominant period of ground motions. To avoid double resonances (resonance of seismic wave in soil with bedrock motions and then resonance of ground motions with the natural period of structures), in a preliminary design stage of a structure, engineers should design a structure with the natural period far from (normally above) the natural period of ground motions, which is also called the site period. A number of analytical studies confirm that the amplification of soil is more or less independent of soil thickness [189]. Based on wave propagation energy models, the site amplification is a function of the wave velocity (or the impedance) of the shallow soil rather than of the thickness of the soil deposit [190, 191]. Moreover, the stiffness of the soil layers deeper than 30 m is often well correlated with the wave velocity in the top 30 m [192], even if there are some exceptions as will be discussed in Sect. 3.2.2. Therefore, by assuming the soil is elastic and the bedrock displacement is dominated by shear motions, the eigenperiod of soil layers can be calculated based on the average shear wave velocity down to certain depths along the soil profile (taken as 30 m by the majority of seismic design codes):

$$T_{\text{site}} = 4H/v_s(1 + n/2) \quad n = 0, 1, 2, \dots \tag{3.1}$$

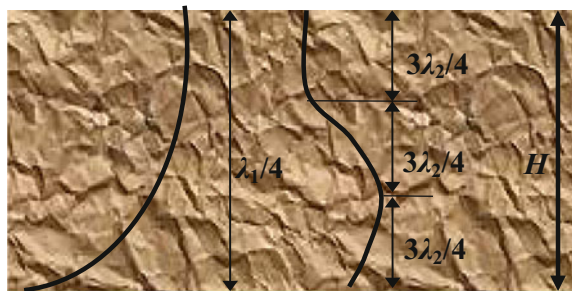
where H (in meters) is the depth of soil layers.

Normally, the most important eigenperiod of soil deposits is the first one, corresponding to $n = 0$ in the equation above, which is used as an estimation of site period. Physically, this period is the longest time that a seismic wave can travel within one wavelength, as shown in Fig. 3.7. As an example, for a rough estimation, the shear wave velocity in soil media may be approximated as 300 m/s. Therefore, for a soil with thickness of 30 m, the site period is 0.4 s ($= (4 \times 30) \text{ m} / 300 \text{ m/s}$). At this period, the ground surface will vibrate at an amplitude much higher than the bedrock motions. This can be clearly shown by reading the response spectrum as presented in Chap. 10. However, for rather loose and soft soil, the shear wave velocity can be as low as 60–80 m/s, in which case the above example gives a site period of only 1.5–2.0 s, which is within the possible range of the natural vibration period for an offshore platform.

By modeling a soft soil site consisting of 27 soil layers and performing a site-response analysis, Fig. 3.17 shows a comparison of the peak ground acceleration at the bedrock and ground surface (seabed) with a site period of 2.4 s. By observing the response spectrum shown in this figure, it is noticed that the soil layers de-amplify the acceleration response at lower period range (related to the peak ground acceleration) while amplifying the response at medium and high period range. It is shown that the motions at ground surface are slightly lower than those at bedrock. On the other hand, Fig. 3.15 shows the significant magnification of site response of the ground surface compared with the seismic excitations at the bedrock at a relatively stiff soil site. The site is modeled with 17 soil layers with a calculated site period of 0.48 s. Furthermore, even at the same site, the amplitude of seismic motions at the bottom of the soil layers can influence the amplification or de-amplification of the site-response characteristics, primarily due to the presence of soil nonlinearity.

Site amplification can be the cause of abundant structural damages during large earthquake events. An example of this was the massive damage in downtown Mexico City during the 8.1 magnitude Mexico City earthquake of 1985. Although

Fig. 3.7 Relationship between the first and second eigenmodes due to horizontal shaking



1st eigenmode 2nd eigenmode

the downtown of Mexico City is located 390 km away from the fault-rupture area, it is built on the soil from an ancient 37- to 60-m-thick soft layer of lake deposits under the Mexico City Basin, which used to be a big lake and was buried naturally and artificially over a long period of time. The soil has an average shear wave velocity of around 75 m/s, as shown in Fig. 3.6. This gives a site period of 2.0–3.0 s [193, 194]. A total of 412 buildings collapsed, and another 324 were seriously damaged in Mexico City. A large percentage of the buildings that were damaged were between 8 and 18 stories high, indicating possible resonance effects of around 2–3 s. The site amplifications during the 1994 Northridge earthquake also caused several structural collapses [195].

Several methods are available to perform a manual calculation of site period:

Based on the weighted average of shear wave velocity:

$$v_s = \left(\sum_{i=1}^{i=n} v_{si} H_i \right) / H \quad (3.2)$$

where v_{si} and H_i are shear wave velocity and depth of the soil layer i , n is the total layer of the soil, $H = \sum H_i$.

Then, the site period can be calculated as:

$$T_{\text{site}} = 4H / v_s \quad (3.3)$$

Based on the weighted average of the soil's shear modulus and density:

$$T_{\text{site}} = 4H / \left[\left(\sum_{i=1}^{i=n} \mu_i H_i \right) / \left(\sum_{i=1}^{i=n} \rho_i H_i \right) \right] \quad (3.4)$$

where μ_i , ρ_i , and H_i are shear modulus, density, and depth of the soil layer i , n is the total layer of the soil, $H = \sum H_i$.

Based on the sum of site period for each layer:

$$T_{\text{site}} = \sum_{i=1}^n (4H_i / v_{si}) \quad (3.5)$$

Based on a linear approximation of fundamental mode shape

$$T_{\text{site}} = 2\pi / \sqrt{3 \sum_{i=1}^{i=n} (v_i^2 H_i) / H^3} \quad (3.6)$$

For seismic design of offshore and land-based structures, based on the soil properties in the uppermost 30 m of the soil, various seismic design codes, such as ISO 19901-2 [289] and Eurocode 8 [198], provide the estimation value of v_s .

3.2.2 Influence of Soil Depth on the Site Period

The consideration of the top 30 m of soil layers (as in the majority of seismic design codes) or 20 m (as in the China building code [199]) to calculate the average shear velocity is most appropriate for rather short period content of bedrock motions. For seismic waves with longer periods, the wavelengths are much longer than 30 or 20 m, and the site response is likely to be affected by soil characteristics at much greater depths. Moreover, the consideration of the top 30 or 20 m depth often assumes that the soil layers extend to a few hundred meters depth before reaching the bedrock. The calculation may not be suitable for regions where a soil–bedrock interface is found at even a few meters below the soil surface. Even for sites having deep soil but a stiffness of the deeper soils well correlated with the shear wave velocity at the top 30 m, Boore et al. [192] found that the depth over which average shear wave velocity should be averaged is one-quarter of the wavelength associated with the period of interest, which can be greater than 30 m. Significant soil amplifications can be produced due to high-impedance contrasts and associated seismic wave reflections at depths much greater than 30 m, which have almost no correlation with the soil properties of the top 30 m. Therefore, averaging the soil deposit characteristics over depth may result in inaccurate predictions of actual site amplification. A better estimate can generally be obtained by performing a site-response analysis including a more dedicated soil layering modeling of the deposit.

Example Calculate the first and second eigenperiods of a homogeneous soil layer due to the horizontal shaking. The soil layer has a height $H = 26$ m and a shear wave velocity $v_s = 250$ m/s.

Solution: The wavelengths corresponding to the first eigenperiod (T_1) and second eigenperiod (T_2) are λ_1 and λ_2 , respectively. Their relationship with the soil layer height H is shown in Fig. 3.7 and can be expressed as:

$$\lambda_1 = 4H = v_s T_1 \quad (3.7)$$

$$\lambda_2 = 4H/3 = v_s T_2 \quad (3.8)$$

Therefore:

$$T_1 = 4H/v_s = 4 \times 26/250 = 0.416 \text{ s}$$

$$T_2 = 4H/(3v_s) = 4 \times 26/(3 \times 250) = 0.139 \text{ s}$$

Example The shear wave velocity distribution for a site with shallow soil layers is shown in Table 3.1. Calculate the site period and the average shear wave velocity.

Table 3.1 Soil's shear wave velocity distribution along the soil depth

Layer number i	Thickness H_i	Shear wave velocity v_{si}
1	4	360
2	5	575
3	11	1050
4	26	2060
5	>60.0	2400

Solution: The site period based on the average shear wave velocity of the uppermost 30 m soil is often used to classify the type of site and estimate the site period. Therefore, the site period for the uppermost 30 m soil can be calculated as:

$$T_{\text{site}} = \sum_{i=1}^n (4H_i/v_{si}) = \frac{4 \times 4 \text{ m}}{360 \text{ m/s}} + \frac{4 \times 5 \text{ m}}{575 \text{ m/s}} + \frac{4 \times 11 \text{ m}}{1050 \text{ m/s}} + \frac{4 \times 10 \text{ m}}{2060 \text{ m/s}} = 0.14 \text{ s}$$

The shear wave velocity for the uppermost 30 m soil is calculated as:

$$v_{si,30} = \sum_{i=1}^n H_i / \sum_{i=1}^n (H_i/v_{si}) = \frac{30}{\frac{4}{360} + \frac{5}{575} + \frac{11}{1050} + \frac{10}{2060}} = 854 \text{ m/s}$$

However, it is noticed from Table 3.1 that the site consists of a shallow sedimentary soil, and the soil stiffness dramatically increases below soil layer 2, indicating that the impedance contrast between soil layer 2 and soil layer 3 is rather high. Therefore, in reality, soil dynamic response will be dominated by the response of soil on the upper two layers (uppermost 9 m) rather than the uppermost 30 m. The realistic site period for the uppermost 9 m soil can be calculated as:

$$T_{\text{site}} = \sum_{i=1}^n (4H_i/v_{si}) = \frac{4 \times 4 \text{ m}}{360} + \frac{4 \times 5 \text{ m}}{575} = 0.08 \text{ s}$$

The realistic shear wave velocity for the uppermost 9 m soil is calculated as:

$$v_{si,9} = \sum_{i=1}^n H_i / \sum_{i=1}^n (H_i/v_{si}) = \frac{9}{\frac{4}{360} + \frac{5}{575}} = 454 \text{ m/s}$$

A significant difference can be observed between the realistic estimations based on the uppermost 9 m (below soil layer 2, the soil stiffness increases significantly) and the estimation based on the uppermost 30 m soil.

3.3 Non-stationary and Peak Ground Motions

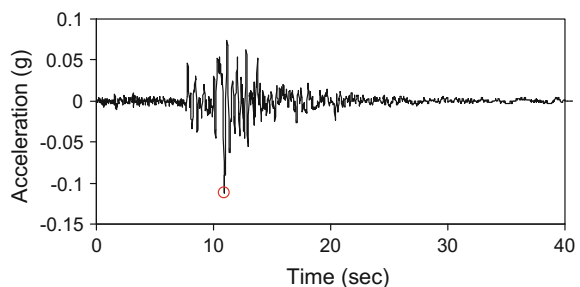
3.3.1 Peak Ground Motions and Their Relationship with Magnitude and Intensity

Compared to magnitude and intensity, peak ground acceleration (PGA) does provide more direct information for geotechnical and structural engineers and is especially useful for constructing the design spectrum for structural analysis. It is defined as the peak of the ground motion acceleration, as shown in Fig. 3.8. The PGA is normally below $0.5g$ (g is the acceleration of gravity) for even a destructive earthquake. However, PGA of more than $1.0g$ has also been reported in many earthquakes, such as the 1994 Northridge earthquake.

Generally, the horizontal PGA motions are higher than their vertical counterparts. However, at sites near the epicenter, the vertical PGA motions can be close to the horizontal ones, as will be discussed in Sect. 3.10. For example, the accelerogram readings at the Pacoima Dam during the 1971 Richter magnitude 6.6 San Fernando earthquake reached $1g$ in both horizontal and vertical directions, and the one recorded at Cedar Hills Nursery (near the epicenter) in Tarzana, California, during the Richter magnitude 6.9 Northridge earthquake of 1994 also reported a similar phenomenon: Both the horizontal and vertical ground acceleration components approached $2g$, being the strongest ground movement recorded in the Northridge earthquake, and most of the sites with high ratios of vertical to horizontal PGA were deep soil sites, often in alluvial basins. In particular, of the nine sites with the ratios of vertical to horizontal PGA greater than unity, only one was located on a rock site [200], which is believed to have been caused by S- to-P-wave conversion and wave scattering at the basin–bedrock interface, supplying energy to vertical components of strong ground motions. In addition, this fact is also responsible for the observed frequency content differences of the vertical and horizontal components of the ground motions.

The conversion between the intensity level MMI and the horizontal peak ground acceleration (PGA) a in cm/s^2 may be expressed as follows [201]:

Fig. 3.8 Recorded horizontal ground motions at a site (the cycle shows that the PGA is $-0.11g$)



$$\log_{10} a = \frac{\text{MMI}}{3} - 0.5 \quad (3.9)$$

The equation above indicates that, if other conditions are the same, the PGA at a magnitude 8 earthquake is around 100 times of that of a magnitude 6 earthquake.

It should be noted that, although PGA can provide a reliable measure for the relative intensity of ground motions, it does not give any information regarding the frequency content that influences the amplification of a structure's dynamic response subject to ground motions. On the other hand, the frequency content of ground motions can be illustrated by using earthquake time histories, power spectrum or design spectrum, etc.

Furthermore, by observing Fig. 3.9, which shows the recorded horizontal ground motion at a site expressed in acceleration, velocity, and displacement, it can be concluded that the PGA is associated with high-frequency motions, the peak ground velocity (PGV) with intermediate-frequency motions, and the peak ground displacement (PGD) with low-frequency motions. This can be explained by the relationship among time histories measured by acceleration, velocity, and displacement: A time derivate of the displacement history gives velocity history, and a time derivate of velocity history is the acceleration history. In the opposite way, the acceleration history integrated with time is the velocity history, and the velocity history integrated with time is the displacement history. This means that, if one

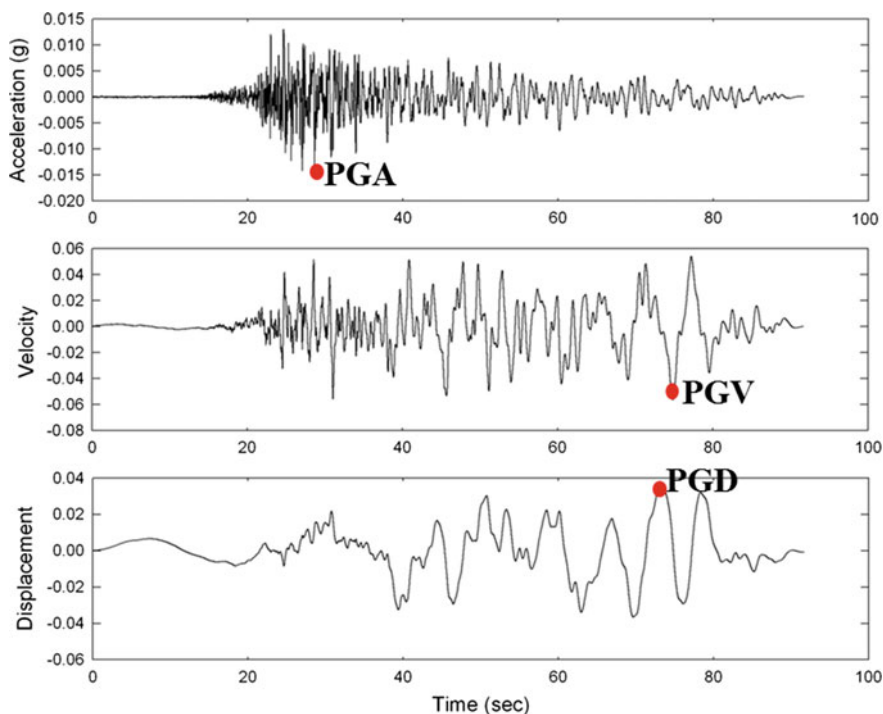


Fig. 3.9 Recorded horizontal ground motion at a site in acceleration, velocity, and displacement

defines the angular frequency of the motion as ω , the amplitude of the acceleration record is ω^2 times that of the displacement. As this ω^2 ratio increases with an increase in frequency, an acceleration record intensifies high-frequency components, while low-frequency components of motion are more visible in a derived or recorded displacement time history.

Furthermore, from Fig. 3.9, it is also seen that the PGA is related to motions due to the shear wave at high-frequency range and it occurs much earlier than the PGV and PGD. In this case, the PGV and PGD are mainly associated with the surface wave propagation in the intermediate- and low-frequency range. Even if the PGV and PGD sometimes occur at around the same time as the PGA, the three measures still reflect the peak responses at different frequency ranges, as mentioned above.

In case the ground movement and deformation are of interest, the PGV is a better measure for the ground motion intensity. For example, for the assessment of capacity of buried structures such as pipe networks subjected to substantial ground motions, design codes often employ PGV rather than PGA when correlating ground motion intensity and damage to pipe networks. PGV is also much less sensitive to the high-frequency content variability in ground motions, which is highly variable even on small length scales due to wave scattering, and hence, it has a smaller spatial variability than the PGA. PGD is often quite difficult to determine in an accurate manner due to signal-processing errors and long-period noise and is less used than PGA and PGV.

Table 3.2 shows peak values of near-source ground motion recordings for five significant earthquakes that occurred from 1978 to 1989. It is worth mentioning that some of the peak ground motions shown in this table are higher than what is required in relevant seismic design codes.

The discussion above clarifies that the peak velocities and peak accelerations are typically associated with motions at different frequencies as mentioned above. In order to determine the significance of seismic responses and the potential damage, the seismic excitations can be categorized based on the ratio between the peak ground accelerations and peak ground velocities, namely a/v ratio [203]. This ratio is interpreted as the angular frequency of the equivalent harmonic motions. It provides a rough indication of which frequency contents of ground motions are most significant and reflects the characteristics of sources, travel path, site conditions, duration of seismic motions, and structural responses. A low a/v ratio smaller than 0.8 g/m s^{-1} indicates that significant responses are contained in a few long duration ground motion acceleration pulses, which are likely to occur at a soft soil site. Such ground motions can amplify responses of flexible structures with high natural period. A high a/v ratio greater than 1.2 g/m s^{-1} indicates that the ground motions contain many high-frequency oscillations with large amplitude, which are likely to occur at a rock and rather stiff soil site. A stiff structure is sensitive to oscillations within this frequency range. Ground motions with an a/v ratio between 0.8 and 1.2 g/m s^{-1} have significant energy content for a wide range of frequencies [204], and a/v ratio also has a significant effect on maximum inelastic response and hysteretic energy dissipation of structures.

Table 3.2 Peak near-source ground motions from five significant earthquakes [202]

Earthquake		Distance (km)	Acceleration (g)	Velocity (cm/s)	Displacement (cm)
Tabas (1978 Tabas, Iran, M_w 7.4)		3	0.92	125	106
El Centro (1979 Imperial Valley, USA, M_w 6.5)	Array 6	1	1.74	110	55
	Array 7	1	0.65	110	41
1987 Superstition, USA, M_w 6.6	Parachute test site	0	0.53	138	60
	Superstition mountain	0	0.91	44	16
1989 Loma Prieta, USA, M_w 6.9	Los Gutos presentation center	0	0.62	102	40
	Lexington dam	5	0.44	120	40
1988, Langcang, Yunnan, China, $M_s = 6.7$	Zhutang	1	0.44	46.1	13.1

3.3.2 Contribution of Body and Surface Wave to Ground Motions

By further observing Fig. 3.9, we see that, in general, the records are non-stationary in both amplitude and frequency content. The non-stationary amplitude is characterized by the initial buildup of the ground acceleration after the arrival of the first seismic waves, a period of strong motion at a roughly constant amplitude (stationary stage), and a gradual decay. The non-stationarity of frequency content is reflected by a change in time of the frequency content of the ground motions—that is, the relative amplitudes of the various frequency components of the ground acceleration change with time, and the frequency contents depend on the source mechanism, source-to-site distance, and site conditions.

Typically, the high-frequency content arrives sooner, leading to a tendency for the ground motion frequency content to shift toward lower frequencies as time elapses. This is partially due to seismic wave dispersion: The P-wave, S-wave, and surface wave travel at different speeds, arriving at a given site at different time instants, and most of the surface wave energy (dispersive energy) with low frequency arrives after the body wave (non-dispersive energy wave) has subsided (since high-frequency energy is more rapidly attenuated). In other cases, the effect

of decreasing dominant frequencies in ground motions has been attributed to site resonance.

The relative significance of body and surface wave forms depends on various factors such as source mechanism, source-to-site distance, direction to the source, topography, and sediment geometry.

3.3.3 *Moving Resonance*

The frequency non-stationarity is sometimes responsible for collapses of structures with natural period lower than the dominant period of ground motions. Under the excitations due to initial buildup of ground motions, those structures only exhibit partial damages due to the development of plasticity of structural members or damage to secondary structures (such as windows or doors), while the partial damages will lead to degradation in the global stiffness of the structures, causing an increase in natural period of the structures. The increased natural period may track the decreasing predominant frequency of the ground motion (most likely due to the arrival of surface wave with lower dominant frequency than the initial body wave, and sometimes also due to soil liquefaction, which decreases the natural frequency of soil columns), leading the structures to respond in resonance. This phenomenon is called moving resonance and is discussed by Conte [205]. Broadly, moving resonance is defined as a type of resonance of structures subject to excitations, due to changes in their natural period and/or in the dominant period/frequency of non-stationary ground excitations with time. From a case study, Conte [205] stated that, for initially stiff structures, moving resonance can lead to a significant increase of maximum ductile response of structures, by up to 60%. Paradimitriou and Beck [206] found that the variation in both frequency content and amplitude with time may significantly affect the response of both linear and softening nonlinear structural systems. By studying the influence of nonlinear structural response under two non-stationary seismic excitations, Wang and Zhou [207] found that the structural responses under two excitations are essentially similar during the buildup of ground motion stage (initial 25 s), while significant differences appear during the decay stage, and structural collapse and significant damages, if they happened, often occurred during this decay stage. By carrying out a systematic study of seismic response using wavelet transform, Naga [208] concluded that a significant effect of moving resonance is observed for ground motions with energy that was concentrated in a narrow period band, but the motions spread out in time, such as the seismic motions recorded during the 1994 Northridge earthquake at Canyon County and 1995 Kobe earthquake at Nishi-Asaki, and the 1940 Imperial Valley earthquake. Even pulse-like ground motions such as the ones that occurred during the 1999 Chi-Chi earthquake have a propensity to moving resonance.

3.4 Measuring Soil Amplification or De-amplification

In a site-response analysis, the amplification or de-amplification of soil media under particular seismic excitations can be measured in various ways, such as the ratio of Fourier amplitude or response spectrum acceleration between the seismic excitation and the response at each frequency/period.

The excitation can be applied at either the bedrock or rock outcrop. The responses can be taken either at the free surface (seabed or ground surface) or at a designated soil layer(s).

In many cases, the peak ground acceleration/velocity/displacement ratio between soil responses at designated location(s) and seismic excitations is also used as an indication of amplification or de-amplification. As PGA, PGV, and PGD are associated with motions at very low, intermediate, and high period range discussed in Sect. 3.3, the frequency-dependent characteristics of amplification or de-amplification cannot be fully captured by only studying the peak ground motions with one of those unit measures.

3.5 One-Dimensional Site-Response Analysis

3.5.1 *One-Dimensional Seismic Wave Propagation Analysis*

When the seismic wave reaches the boundary between various soil materials, both reflection and refraction occur. Generally, the shear wave velocity in soil decreases gradually with a decrease of depth due to overburden pressure change, sediment age, cementation, etc., causing the oblique seismic waves to be bent by successive refractions to a more vertical direction toward the ground surface [212], as illustrated in Fig. 3.27. Therefore, it is normally assumed that the seismic stress wave is propagated vertically at the ground surface due to the multiple refractions at the boundaries of two adjacent soil layers, bending the seismic wave to propagate in an almost vertical direction.

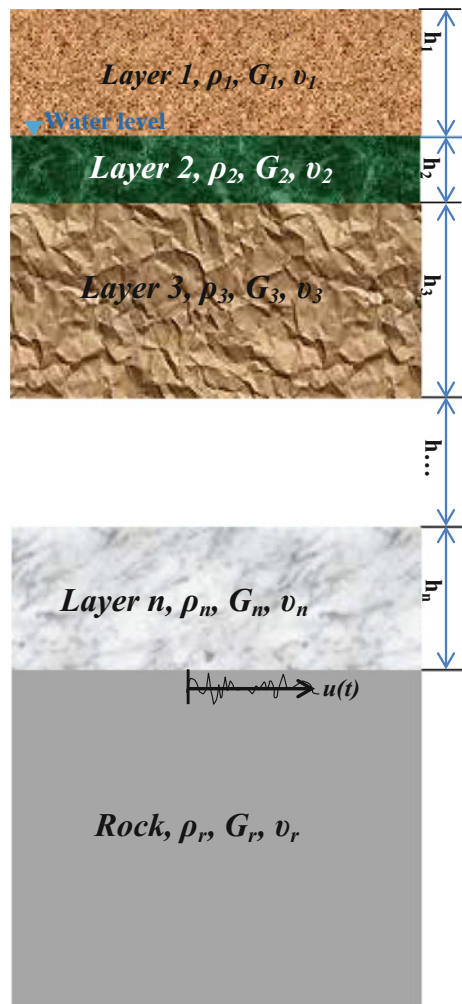
One may argue that, in reality, the soil along the horizontal direction varies. For example, the soil properties at the same depth between two boreholes even a few meters apart are normally not identical, i.e., the soil properties change not only in depth, but also along the horizontal directions, lending justifiability to a two-dimensional or even three-dimensional analysis (Sect. 3.7). However, it is practically difficult or even impossible to carry out many field tests by drilling many boreholes to obtain the variation of soil in horizontal directions. Also, because soil properties normally vary more rapidly in the vertical direction than in the horizontal direction, the assumption that soils only vary with depth is often accepted in engineering practice.

The assumption above promotes the use of one-dimensional site-response analysis (Sects. 3.5.2 and 3.5.3), based on either the solution to the wave equation

[213, 214, 215, 216] or a lumped mass simulation [217]. In a one-dimensional site-response analysis, the soil and bedrock are assumed to extend infinitely in the horizontal direction, and only the horizontal shear wave transmits vertically toward the ground surface. In the majority of applications for seismic site-response analysis, the layered soil can be represented as a number of horizontal layers rested on either elastic or rigid bedrock, as shown in Fig. 3.10. As aforementioned, by assuming that the horizontal soil layers extend infinitely in the horizontal direction, the site-response analysis can be assumed to be one-dimensional.

As will be discussed later on, if one knows the thickness, density, shear modulus, and Poisson’s ratio for each soil layer and rock, and the input of prescribed

Fig. 3.10 Layered soil is idealized as a number of horizontal layers (represented by the thickness, density, shear modulus, and Poisson’s ratio) rested on either an elastic or rigid bedrock subjected to seismic motion $u(t)$



seismic motions at bedrock, rock outcrop, or any soil layers, one is in a position to perform the site-response analysis.

One-dimensional site-response analysis generally results in a conservative evaluation of site response. Even though this analysis has a few important limitations (Sect. 3.7), many structures designed based on this method sustained the loading during major earthquake events.

Shear waves are normally the most important waves contributing to horizontal ground accelerations, inducing forces on foundations and structures. In most cases, ground motions caused by the horizontal shear wave dominate seismic designs of structures and foundations, though there are exceptions, as will be discussed in Sects. 3.6 and 3.7. The vertically propagating horizontal shear wave (SH) propagation at each soil layer may then be modeled by the Kelvin–Voigt solid with a stack of infinitesimal element as shown in Fig. 3.11. Under vertically propagating SH-waves, a one-dimensional equation of motions is written as:

$$\rho \frac{\partial^2 u}{\partial t^2} = \frac{\partial \tau}{\partial z} \quad (3.10)$$

where u is the horizontal displacement; ρ stands for the mass density of soils; t is the time; τ is the shear stress in a horizontal plane at the top and the bottom of the soil element under study; z is the vertical depth.

Note that as we assume that a homogeneous level ground is subjected to horizontal shaking, this leads to the normal stresses on the left and right sides of the soil element equaling and canceling each other out. Therefore, in the equation above and in Fig. 3.11, the lateral normal stresses on the two sides of the soil element are not included in the equation.

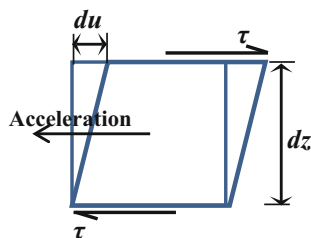
And the shear stress is determined as:

$$\tau = G\gamma + \eta \frac{\partial \gamma}{\partial t} = G \frac{\partial u}{\partial z} + \eta \frac{\partial^2 u}{\partial z \partial t} \quad (3.11)$$

where γ is the shear strain; $\eta = 2G\xi/\omega$ is the equivalent viscosity of the soil material that the shear wave is propagating through; ξ is the damping of the soil material at a given level of shear strain.

Combining the two equations above, one obtains the wave equation as:

Fig. 3.11 Shear stress τ and shear deformation du in the horizontal plane of a soil element due to the transmission of SH-wave



$$\rho \frac{\partial^2 u}{\partial t^2} = G \frac{\partial^2 u}{\partial z^2} + \eta \frac{\partial^3 u}{\partial z^2 \partial t} \quad (3.12)$$

Note that the velocity of shear wave is $v_s = \sqrt{\frac{G}{\rho}}$. By dividing both sides of the equation above with ρ , one obtains:

$$\frac{\partial^2 u}{\partial t^2} = v_s^2 \frac{\partial^2 u}{\partial z^2} + \frac{\eta}{\rho} \frac{\partial^3 u}{\partial z^2 \partial t} \quad (3.13)$$

Assume that the displacement responses are harmonic at any frequency ω :

$$u(z, t) = U(z)e^{i\omega t} \quad (3.14)$$

where $U(z)$ is the maximum amplitude of the displacement at z .

By combining the two equations above, the ordinary differential equation of wave motions is:

$$(G + i\omega\eta) \frac{d^2 U}{dz^2} = -\rho\omega^2 U \quad (3.15)$$

where $G + i\omega\eta$ is referred to as complex shear modulus.

Under the shaking at the base, the seismic wave propagates through multiple soil layers, and each soil layer exhibits the shearing characteristics of a Kelvin–Voigt solid. By solving the wave equation presented above, the response at any soil layer and soil surface can be calculated. This can be performed in either time or frequency domain.

In time domain, the nonlinearity of the springs and the phase of motions among each layer can be explicitly accounted for, but this implies a high computational effort.

On the other hand, the solution in frequency domain requires significantly less computational efforts but with only equivalent soil damping and stiffness of the true nonlinear system. By using the soil properties of equivalent linear soil models (Sect. 2.2), one may efficiently establish the motion transfer function relating the displacement amplitude at one soil layer to that at another soil layer or bedrock/rock outcrop. The motion in any layer can then be calculated from the motion in any other layers where the motion is known. This is known as de-convolution, which is not only useful for calculating site responses under predefined motions, but also helpful in the interpretation of actual ground motions recorded on the surface of soil deposits.

It is worth mentioning that, in history, many seismic motion records were measured on the surface of soil deposits. More recently, more accelerometers have been installed on rock outcrops or very stiff soils. In various computation codes to calculate site responses, the response can be computed for a design motion given any depth in the system. Therefore, accelerograms obtained from instruments on

soil deposits can be used to generate new rock motions first, which, in turn, can be used as design motions for other soil deposits. For details of solutions of the ground motions under base excitations, source [1] is recommended.

If the rock is assumed to be elastic, the downward traveling stress wave will partially be reflected at the soil–rock boundary and partially be further transmitted downward to the rock. If the rock has a large thickness, seismic wave energy will be removed from the soil layers, causing the ground motions to be smaller than that with a rigid bedrock modeling. In this way, the elastic rock modeling introduces a form of radiation damping when the shear wave is transmitted through it [1]. Generally, similar to the effect of soil damping, bedrock elasticity also decreases the amplification of ground motions. By modeling a single soil layer, a transfer function can be expressed as the ratio between the ground surface amplitude to the rock outcrop, known as Roesset’s site-response amplification [219]:

$$A(f) = \frac{2}{|(1 + \alpha_z)e^{ikH} + (1 - \alpha_z)e^{-ikH}|} \quad (3.16)$$

where H is the thickness of the soil layer; α_z is the soil–rock impedance ratio as a function of soil and rock density (ρ_s and ρ_r), shear wave velocity (v_s and v_r), and damping ratio (ξ_s and ξ_r):

$$\alpha_z = \frac{\rho_s v_s (1 + \xi_s)}{\rho_r v_r (1 + \xi_r)} \quad (3.17)$$

k is the wavenumber, which is a function of frequency ω :

$$k = \frac{\omega}{v_s (1 + \xi_s)} \quad (3.18)$$

If the bedrock is modeled as rigid, its motion will not be affected by motions in or the presence of overlying soil. Any downward traveling stress wave that goes through the soil will be completely reflected back to the ground surface due to the rigid bedrock assumption, and thereby, all the elastic wave energy within the soil layer will only be transmitted within the soil layers without going further downward to the rock. The amplification can then be simplified as:

$$A(f) = \frac{1}{\sqrt{\cos^2\left(\frac{\omega H}{v_s}\right) + \left(\frac{\omega H \xi_s}{v_s}\right)^2}} \quad (3.19)$$

If a soil profile is homogeneous or close to homogeneous, and ground motion levels are not very high, Roesset’s approximation can be regarded as a reasonable estimate of site-response amplification. However, in practice, for a site with multiple soil layers and which is subject to significant seismic excitations, the Roesset’s

site-response approximation needs to be extended to consider the soil nonlinearity and the influence from all soil layers. See source [1] for an elaboration of this topic.

By modeling an elastic half-space with the rock formation underlying soil deposits, Fig. 3.12 shows the ratio of transfer function among soil surface, bedrock (“Base-rock” notated in Fig. 3.12), and rock outcrop. Slight differences between the motions in the outcrop and bedrock can be identified, with a minimum of their motion ratio at the resonance frequency (inverse of site period) of the soil deposits.

As presented in Sect. 1.14, in a site-response analysis, the carrying out of a sensitivity analysis is recommended by accounting for the variation in soil properties from lower-bound, average (best estimate) to upper-bound values. This may detect some significant sensitivity impacts of soil properties on ground motions. If ground motions are not sensitive to the variation in soil properties, typically, the best-estimate value of soil properties can be used to compute the ground motion time histories.

As a general recommendation, if available input motions are recorded from rock outcrop, one may use these input motions together with an elastic base-rock modeling. If the input motions are recorded within the bedrock, meanwhile, one should use input motions with a rigid base modeling. However, the recordings are more often assigned at a hypothetical bedrock outcrop (point 1 in Fig. 3.2) rather than the base of the soil profile (point 2 in Fig. 3.2). This is because, as the rock is generally not perfectly rigid, motions at the base of the soil profile (rock) are not identical to those of the rock outcrop, while the stations for measuring recordings are generally located at the rock outcrop rather than the bedrock [220].

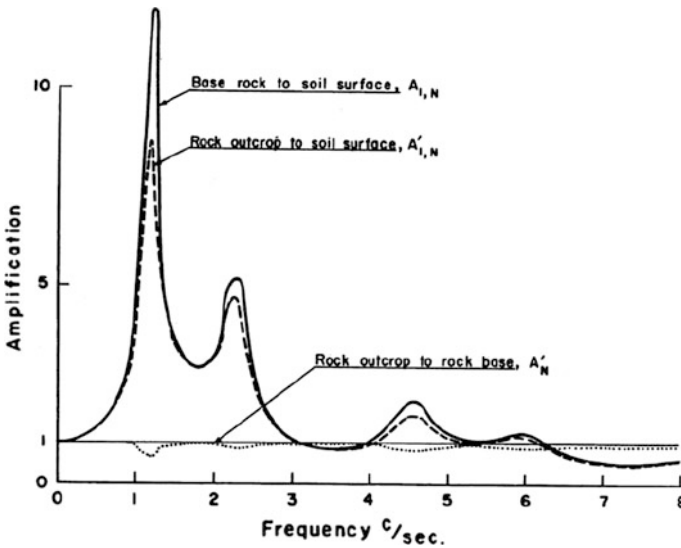


Fig. 3.12 Ratios of transfer function among soil surface, bedrock (base-rock), and rock outcrop [223]

The seismic motion records to be used in a site-response analysis for a site should generally be compatible with the geologic conditions at the bottom of the site profile being simulated. If bedrock is reasonably shallow and its depth is known, the profile should extend into rock. If the site consists of deep soils that cannot reasonably be simulated in their entirety, the soil profile may then be extended to a firm soil horizon with a strong impedance contrast with the soil layers above. In this case, one may adopt input motions at the rock outcrop or the firm soil [218]. In practice, to avoid too significant a response amplification of soils at high frequencies, the rock may be modeled with a shear wave velocity of around 1000 m/s, which is lower than in reality. Figure 3.13 shows that generated design response spectral accelerations are reduced when using the deep soil profile modeling compared to when using the shallow soil profile modeling. This is achieved by performing one-dimensional site-response analyses using the equivalent linear soil model, applying the same time series of seismic excitations, and modeling two clay-dominated soil profiles at the same site, one with a shallow depth (100 m) and another extended much deeper from the shallow one for a better match of bedrock properties at an even greater depth. This reduction is more significant in the lower period range below 1 s, as this deep soil profile can more effectively filter out high-frequency response of soils.

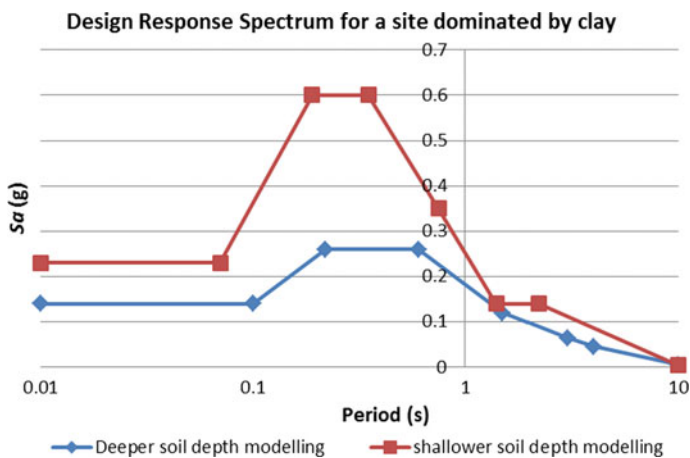


Fig. 3.13 Design response spectra based on a shallow and a much deeper soil profile modeling

3.5.2 *One-Dimensional Frequency-Domain Site-Response Analysis Using Equivalent Linear Soil Model*

3.5.2.1 Method

In a typical soil dynamic analysis using equivalent linear model, shear modulus and damping at each soil layer are assumed to be constant within each individual site-response time history. The equivalent linear model is combined with a harmonic base motion to calculate the dynamic response of soils. The seismic excitation time histories at a location/depth of soil profile are divided (de-convoluted) into harmonic components through Fourier series expansion. This is followed by a computation of each individual response to each divided harmonic component, and these individual responses are finally combined to obtain the responses at various depths in the soil column.

When using the equivalent linear soil models, the computational cost to solve the dynamic equation of motions is normally reduced dramatically compared to the use of a site-response analysis using nonlinear soil models based on the step-by-step time integration method tracing the nonlinear soil behavior. Its merits are also reflected in the aspects of convenience and robustness. As linear analyses give exact solutions of the governing wave propagation equation(s), incident and reflected waves can be separated, input wave can be specified at any point for any types of wave (incident, composite, or reflected), and any wave type can be retrieved at any location, which are not attainable in analyses using nonlinear soil models.

Even though shear modulus and damping level vary with the variation of strain during a seismic event, for mild earthquakes, this variation of strain is limited, and it would thus be convenient to assume a constant soil strain level at each soil layer, so that a constant shear modulus and damping value will be used to compute the dynamic response throughout the entire time history of the seismic excitations. This is often performed by assuming an initial strain to estimate the shear modulus and damping level, which are used to compute the dynamic soil response, from which the effective shear strain $\gamma_{\text{eff},i}$ at soil layer i can be obtained by reducing the maximum shear strain response $\gamma_{\text{max},i}$ (peak shear strain) in the computed soil response with a reduction factor R_γ :

$$\gamma_{\text{eff},i} = R_\gamma \cdot \gamma_{\text{max},i} \quad (3.20)$$

Seed and Idriss [221] suggested that soil properties should be calculated for a strain equal to 2/3 of the maximum strain level in a given soil layer. Idriss and Sun [222] suggested that the reduction factor R_γ could be calculated based on the magnitude of an earthquake M , and this is widely used nowadays:

$$R_\gamma = 0.1(M - 1) \quad (3.21)$$

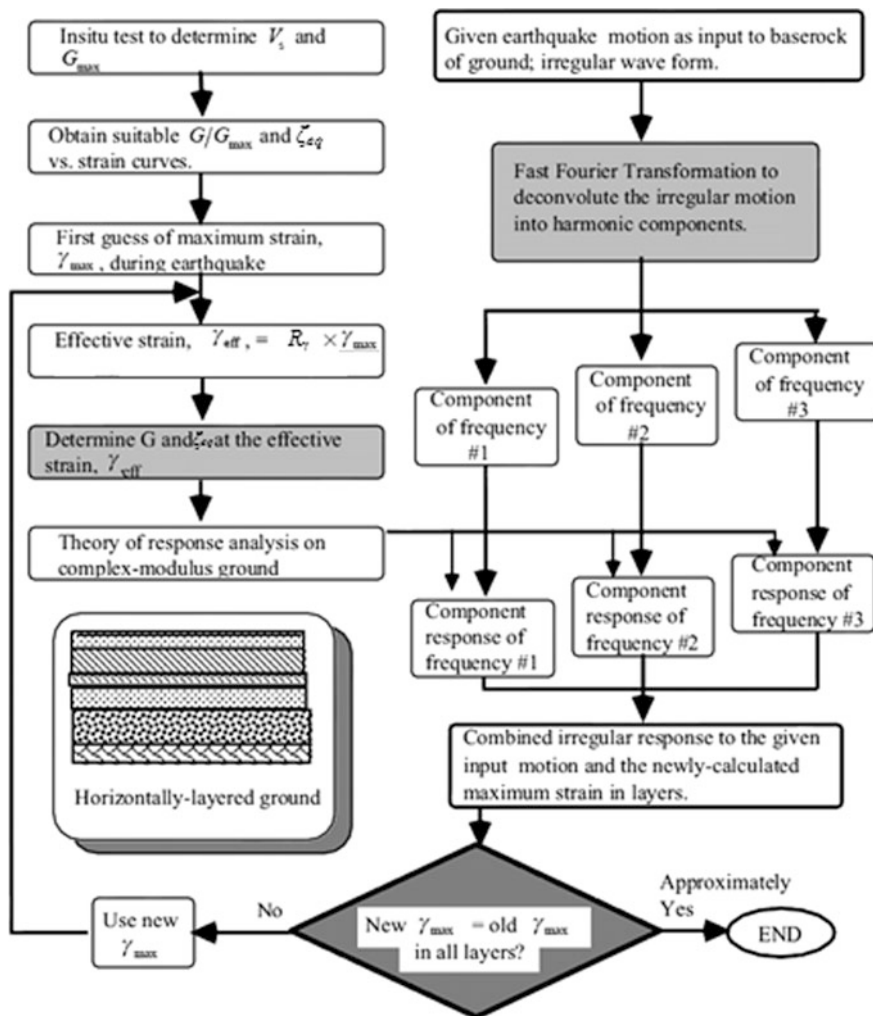


Fig. 3.14 Procedure of dynamic soil analysis using equivalent linear soil modeling [194]

When soils are subjected to transient motions during an earthquake, the factor R_γ is usually taken as 0.65, an approximation based on comparing measured transient shear strain time histories during previous earthquake events with the harmonic ones (obtained from typical laboratory tests, which normally represent more significant loading conditions than transient ones) that have the same peak cyclic shear strain. However, there is as yet no solid theoretical means with which to determine the factor R_γ .

Using the equivalent linear soil model, an iterative procedure has to be implemented as it is not possible to determine the maximum level of strain in each layer

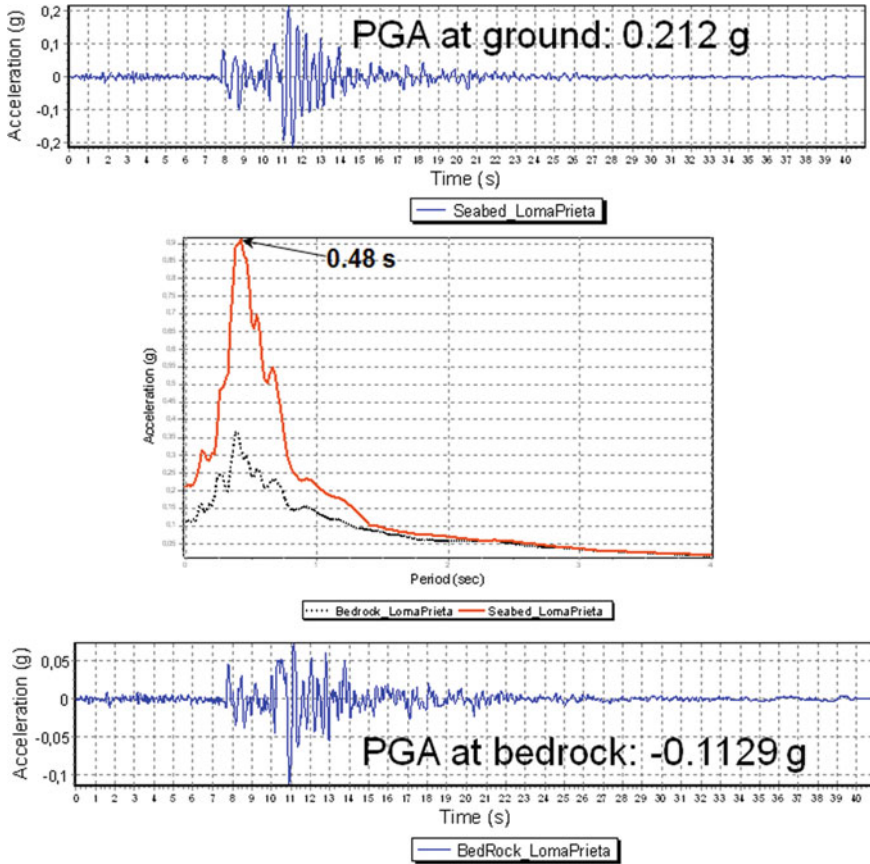


Fig. 3.15 Time history of seismic excitations at bedrock (lower) and site responses at soil surface (upper) and their acceleration response spectra with a site modeled by 17 soil layers with a site period of 0.48 s (relatively stiff soil). The site-response analysis is performed based on the equivalent linear soil model to model both shear modulus and damping (Sect. 2.2)

of the soil profile before the analysis is completed. Firstly, one needs to predefine initial values of shear modulus and damping properties for each layer and then perform a shear wave propagation analysis. From the calculated maximum shear strain response $\gamma_{max,i}$, the effective strain $\gamma_{eff,i}$ can be determined by the two equations above. Thereafter, the shear modulus and damping for layer i will be recalculated and used to compute the dynamic responses again in the next iteration, which is used to estimate the effective strain further. This iteration will be repeated until the differences between the effective strain in two successive iterations is smaller than a specified tolerance. Although a convergence of iterations is not guaranteed, Schnabel et al. [223] stated that 3–5 iterations are normally sufficient to achieve a tolerance level of less than 5–10%. The procedure of equivalent linear analysis is illustrated in the flowchart shown in Fig. 3.14.

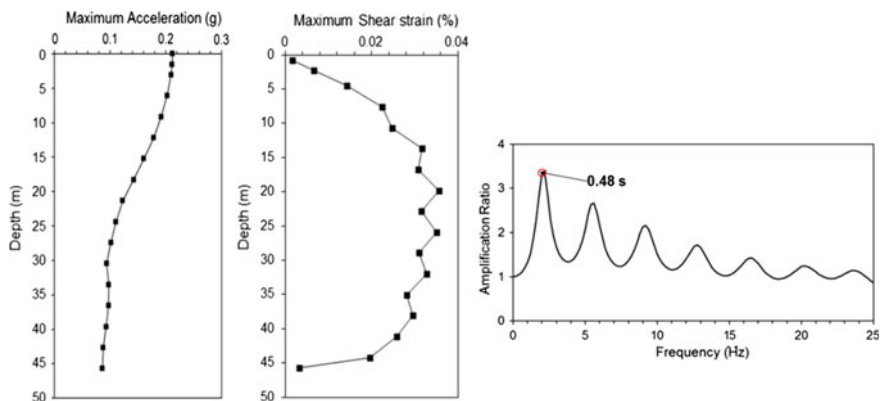


Fig. 3.16 Distribution of maximum acceleration (left) and maximum shear strain (middle) with depth and the amplification ratio of the time histories in frequency domain (right)

SHAKE [223] is thus far the most widely used code for performing one-dimensional site-response analysis.

Based on a site-response analysis using the equivalent linear soil model for both shear modulus and damping, Fig. 3.15 shows a significant magnification of site response at the ground surface (seabed) compared with the seismic excitations at the bedrock and their acceleration response spectrum. The soil is modeled with 17 soil layers, with a calculated site period of 0.48 s. It is noticed that accelerations increase with a decrease in depth, and they show a dramatic increase at depth close to the ground surface as shown in Fig. 3.16. A similar trend is observed for another site as shown in Fig. 3.17. This increase in accelerations close to the ground surface is mainly attributed to the decrease of shear wave velocity with the decrease of depth, the impedance contrast in surface soil, and the zero shear stress (free surface) at the ground surface. However, the maximum shear strain reaches its peak at a range of depth, and from there, it decreases toward both the upper and lower soil layers, as shown in Fig. 3.16.

Readers need to bear in mind that the magnification of site-response depends on various factors, such as the characteristics of seismic excitations at the bedrock or rock outcrop, and soil layers' characteristics. Figure 3.17 shows that the peak ground acceleration at the ground surface is even less than that at bedrock at a site with a soft soil condition and a high site period of 2.4 s, and the soil profile consists of 27 soil layers. By observing the response spectrum in Fig. 3.17, it is noticed that the soil layers de-amplify the acceleration response at lower period range (related to the peak ground acceleration) while amplifying the response at medium and higher period range.

Furthermore, even at the same site, the amplitude of seismic excitations can influence the amplification or de-amplification of the site-response characteristics, primarily due to the presence of soil nonlinearity. Normally, when a site is subjected to significant seismic excitations with higher peak accelerations at bedrock

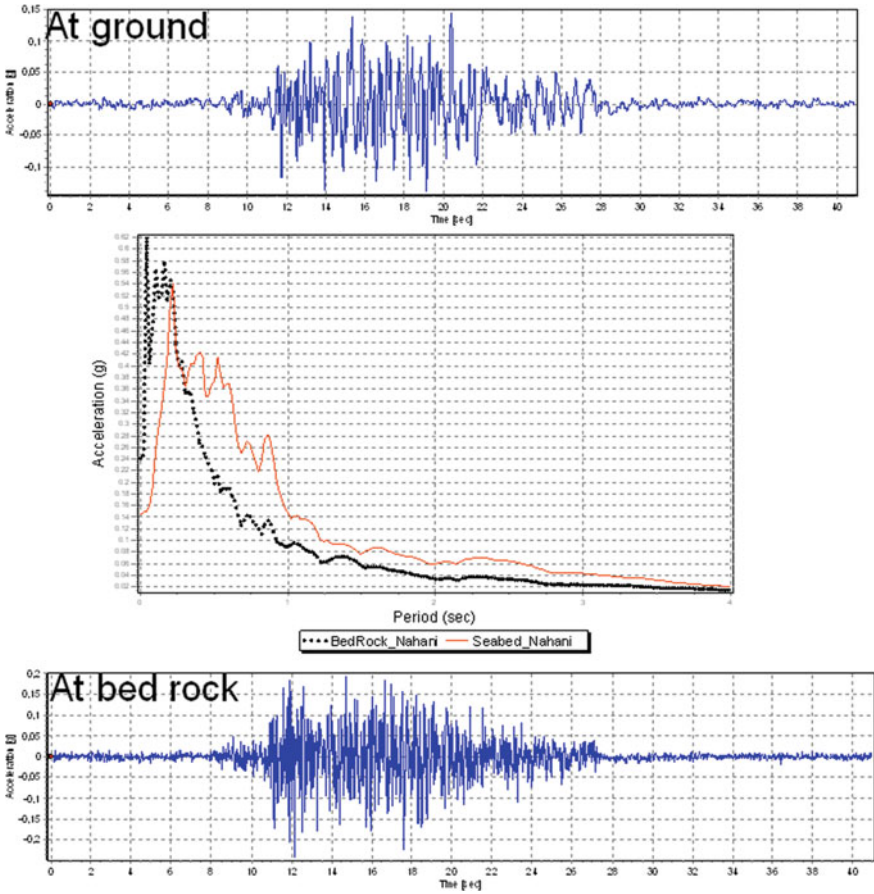


Fig. 3.17 Acceleration time-histories of seismic excitations at bedrock (lower) and site responses at ground surface (upper) and their acceleration response spectra at a site modeled with 27 soil layers with a site period of 2.4 s. The site-response analysis is performed based on the equivalent linear soil model

during a strong earthquake event than during a mild earthquake event, significant nonlinearity and plasticity of soil can mitigate the amplification of the site response at the ground surface [224]. This is illustrated in Fig. 3.18, with lower amplification ratio of maximum accelerations at each soil layer for the site subjected to stronger excitations at the bedrock than that for the same soil column subjected to smaller excitations.

Under the seismic excitations at the bedrock and site conditions presented above, by comparing the response between a relatively stiff soil site (Fig. 3.15) with a site period of 0.48 s and a relatively soft soil site (Fig. 3.17) with a site period of 2.4 s, it is found that the PGA is higher at rock or stiff soil site than that at the soft soil site. Moreover, at the soft soil site, the ground response at low period is low, while

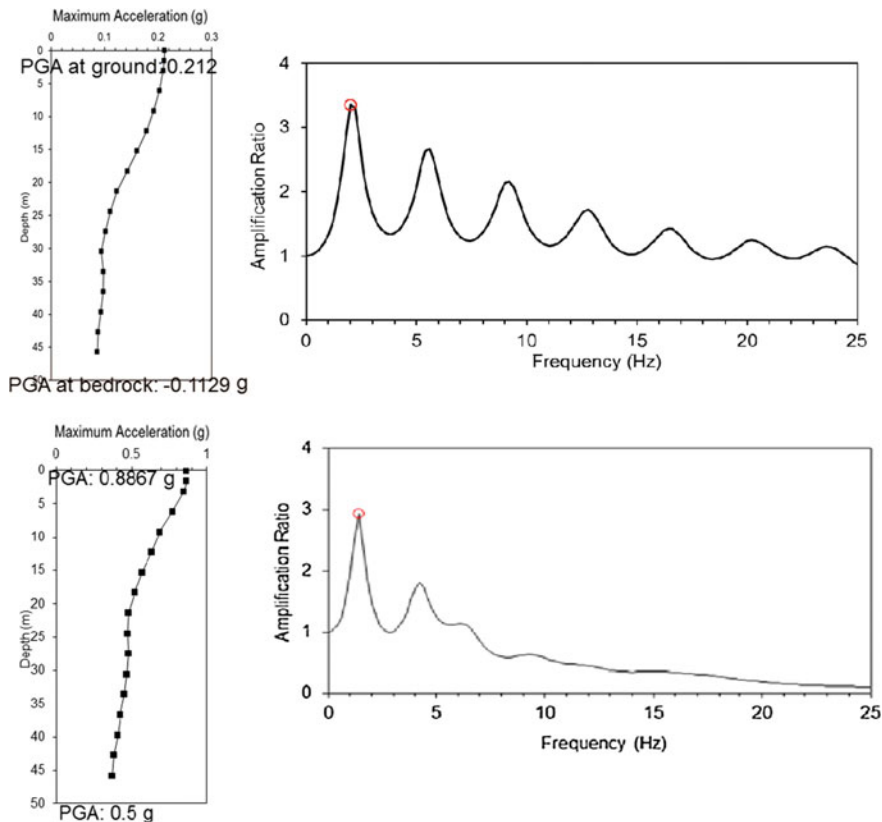


Fig. 3.18 Maximum accelerations (left) and amplification ratio between the ground surface acceleration and bedrock acceleration in frequency domain (right) for the same site with higher (lower) and smaller (upper) peak acceleration excitations at the bedrock

it is high at high period. On the other hand, at the stiff soil site, the response at lower period is high, at intermediate period it is normally higher than the rock, while at high period range it is low, indicating a strong frequency dependence of the soil response. It should be emphasized that different conclusions can be drawn with different site conditions and seismic excitations.

Figure 3.19 shows the variation of amplification ratio with frequency at various soil strata subject to the excitations of the 1995 Kobe and 2011 Sikkim earthquakes. It is observed that for the 2011 Sikkim motion the amplification ratio between the ground surface acceleration and bedrock acceleration is 9.63 at 1.5 Hz (site period: 0.67 s) for layered soil, while for a dry dense sand site with a lower site period, this ratio becomes 4.38 at 2.12 Hz (site period: 0.47 s).

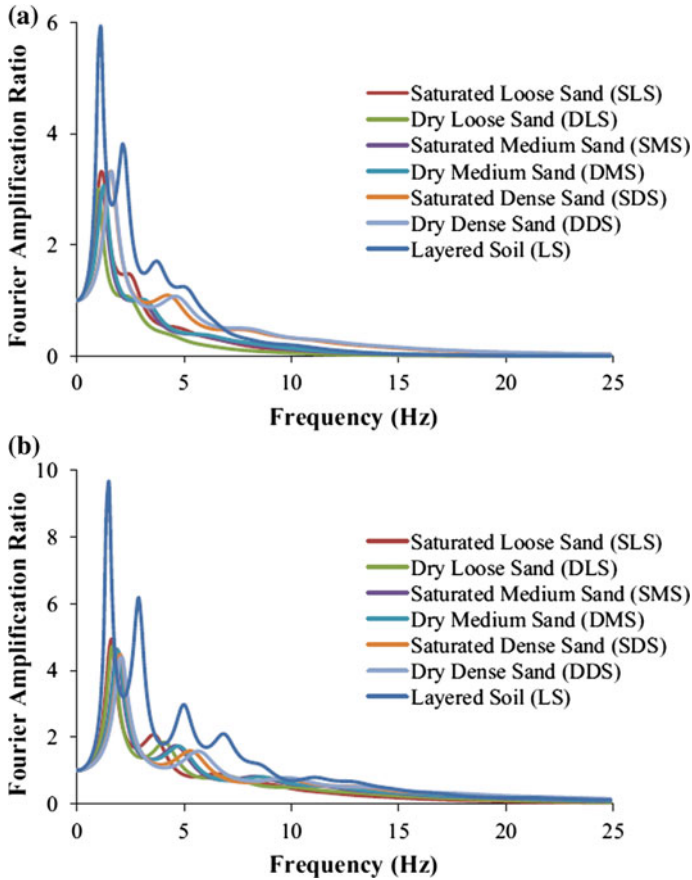


Fig. 3.19 Amplification ratio between the ground surface acceleration and bedrock acceleration, subject to **a** 1995 Kobe and **b** 2011 Sikkim earthquake motions. The soil column (homogenous soil or layers soil) has a thickness varying between 20 and 25 m and was underlain by soft base-rock having a shear wave velocity lying between 360 and 760 m/s subject to earthquake record excitations [225]

3.5.2.2 Applicabilities of Equivalent Linear Models

The equivalent linear model can be applied to many types of seismic site-response analysis with various categories of soils. Because this method works in frequency domain, compared to a time-domain analysis that computes soil responses at each time step, it only computes the transfer function at a number of frequency points, thus requiring significantly less computation efforts, as previously mentioned. This merit is more significant for a two-dimensional or three-dimensional soil modeling, which requires significantly higher computation effort than a one-dimensional soil modeling does. Furthermore, the equation of wave propagation is rigorously solved

mathematically, i.e., a large thickness of soil layer modeling does not cause a serious error in the computation. This is in contrast to the finite element method in which significant errors can be generated due to the modeling of soil layers of large size [194]. This method has been implemented into various site-response computation codes such as SHAKE [223].

In spite of the robustness, simplicity, flexibility, and low computational cost associated with the site-response analysis using equivalent linear soil models, there are several important disadvantages associated with this method. Because the shear modulus and damping are kept constant during entire seismic motion time history regardless of how significantly the strain will vary at different time instants, the variation in shear stiffness and effective stress during the cyclic loading cannot be calculated, and it is not possible to determine the maximum level of strain in each soil layer before the analysis is completed. If the peak shear strain is significantly higher than the rest of the shear strain history, the use of the effective strain in the equivalent linear method causes the soil layers to be modeled with unrealistically high damping or low stiffness. Therefore, a site-response analysis using equivalent linear soil models is still a linear method and has its essential limitations. Also, under cyclic loading of constant stress amplitude, with an increase in the number of cycles, the shear modulus of dry sand will increase and the damping will decrease. Furthermore, for loose saturated sand under seismic excitations, the pore-water pressure is likely to increase with the number of applied loading cycles, leading to a decrease in effective stress. However, as the excess of pore-water pressure is normally limited, in many engineering analyses, the equivalent linear model can still be utilized. This justification also renders the equivalent linear model valid in a site-response analysis to estimate the liquefaction initiation, as will be discussed in 7.2, with approximate equivalent linear modulus and damping values able to be assigned to liquefied soil layers based on an analysis of ground motions at vertical array sites that liquefy [227, 228]. On the other hand, when the total stress is completely taken by pore-water pressure under cyclic loading, the effective stress and the shear resistance of sands are reduced to zero (or close to zero), leading to liquefaction, which results in a significant decrease in shear modulus and shear strain, and this cannot be analyzed using the equivalent linear model.

The equivalent linear model combined with the theory of harmonic shaking should not be applied for loose sand under strong seismic shaking. Moreover, due to the inherent linearity of equivalent linear analysis, the spurious resonance condition may occur as a consequence of the coincidence of a strong component of the input motion with either the site period or a higher order eigenperiod of the soil layers. Errors indicated by the exhibition of violating responses can also be attributed to relatively short transients with low-frequency content followed by the short period of rest included at the end of the input signal [554]. The previous response period may then not be sufficiently damped out at the start of the considered response. If introduced errors are too significant, the input signal may be elongated, or an improved Fourier method with corrective solution may need to be applied.

To solve the problems described above, a more computationally demanding method using nonlinear soil models solved in time domain can be adopted, which will be presented in Sect. 3.5.3.

3.5.2.3 Procedure for Performing One-Dimensional Analysis

The following steps illustrate typical procedures to perform one-dimensional site-response analyses (kinematic interaction analysis) using for example computational code SHAKE [229, 230]:

1. A one-dimensional soil profile with implementations of soil layer with thickness, G_{\max} , and the unit weight. In order to approximate the nonlinearity of soils in an equivalent linear manner, the shear modulus reduction curve G/G_{\max} (Fig. 3.20) and damping ratio (Fig. 3.21) varied with shear strain have to be inputted, which may be based on, for example, recommendations by Darendeli [144] for sand layers and Vucetic and Dobry [231] for clay layers
2. Ground motion histories such as acceleration time-histories representing the bedrock or rock outcrop motions are inputted. The time histories should at least approximately match or reasonably envelop the target design spectrum (normally given by various seismic design codes) at the bedrock/rock outcrop. Artificial time histories can be generated by modifying the recorded ground motion histories, see Chap. 4 for detail. The time history recordings are available from various open sources (Sect. 4.5)
3. Solve the equation of seismic wave propagation in the soil from the bedrock or rock outcrop to ground surface/seabed by using one-dimensional site-response computation codes such as SHAKE [229, 230]

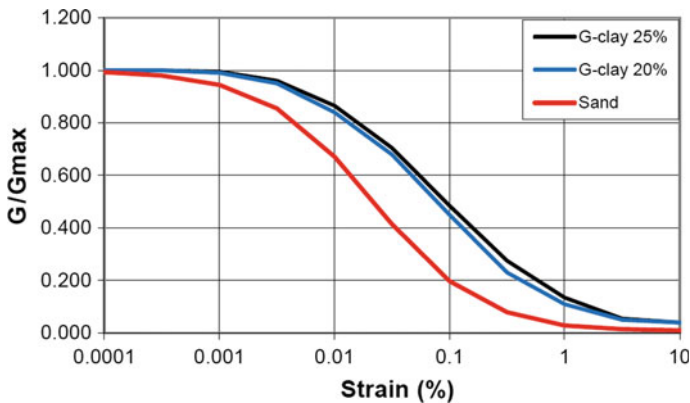


Fig. 3.20 An example of shear stiffness of soil varied with strain, the plasticity index for clay is 25 and 20%. Courtesy of Aker Solutions and NGI

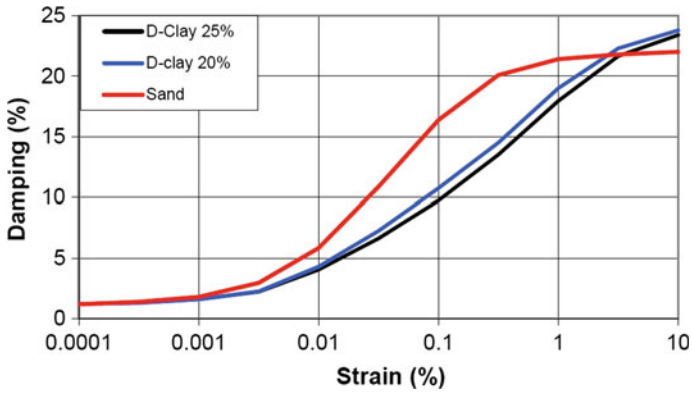


Fig. 3.21 An example of damping ratio of soil varied with strain, the plasticity index for clay is 25 and 20%. Courtesy of Aker Solutions and NGI

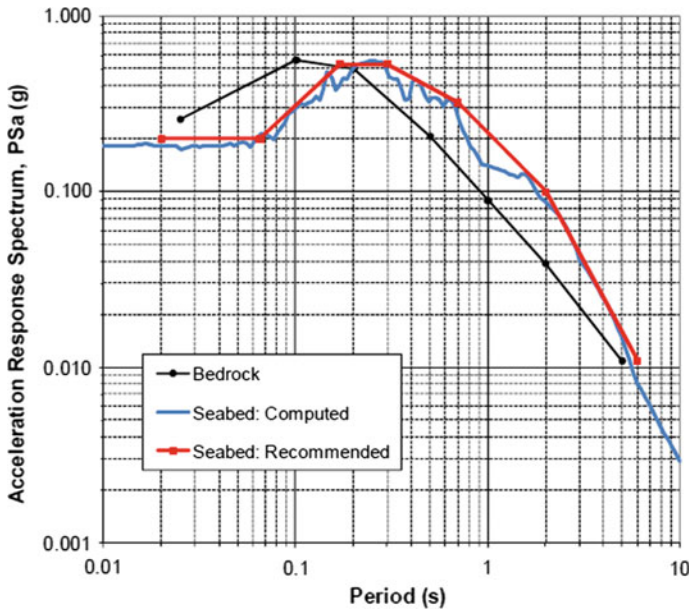


Fig. 3.22 An example of a comparison between the response spectrum at bedrock and seabed. Courtesy of Aker Solutions and NGI

4. Post-process results such as time histories of motions, shear stress or strain in a specified soil layer/depth, and the response spectrum at ground surface/seabed or certain soil layers. Figure 3.22 shows response spectra at bedrock and seabed for a site in the North Sea. Comparison of the spectra shows that, for the target site, the soil media filter out a certain amount of response at low period range, while magnifying the response at medium to high period range.

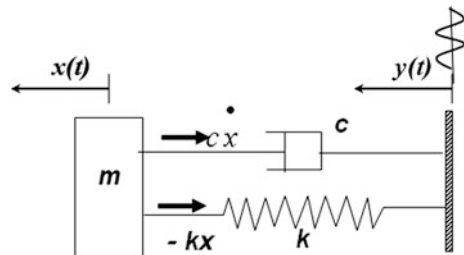
3.5.3 One-Dimensional Site-Response Analysis Using Nonlinear Soil Models

The essential difference between the site-response analysis using an equivalent linear soil model (total stress analysis, see Sects. 2.2 and 3.5.2) and a nonlinear soil model (effective stress method, see Sect. 2.4 and the current section) arises from consideration of dilatancy for sands (Sect. 1.9.3). Actually, in both methods, the material properties of soils are evaluated on the basis of the effective stress. If dilatancy does not occur or is insignificant, even though effective mean normal stress will fluctuate during an earthquake event, the average value will be kept nearly constant. Under this assumption, the use of material properties evaluated from an initial selection of strain/stress state can normally be justified. The equivalent linear soil model can then be used. However, if significant dilatancy occurs, average effective mean normal stress changes monotonically. The material properties must then be evaluated at each time instant following the change in the effective stress [232]. The nonlinear soil model must then be adopted.

In a nonlinear analysis, a nonlinear constitutive relation is used to represent the hysteretic behavior of soil during cyclic loading. The simplest of all nonlinear constitutive relations is to model the relationship between shear stress and shear strain, using a backbone curve (Fig. 2.4) represented by a hyperbolic function. The dynamic equation of motions is then solved by integrating the equation of motions in time domain.

To solve the equation, one needs to first set up the dynamic equations of motions. Consider the system shown in Fig. 3.23 excited by prescribed motions (absolute motions) $y(t)$ at its base. The force on the spring is proportional to the

Fig. 3.23 An SDOF spring-mass-damper system under base excitations located at the bedrock or rock outcrop



relative displacement $z(t) = x(t) - y(t)$ between the base and the mass. For simplicity, we assume that the bedrock or rock outcrop motion is $y(t)$, and the soil has only one layer that can be represented with the spring and dashpot. With the absolute motion at the ground surface $x(t)$, the equation of motions can then be written as:

$$m\ddot{z}(t) + c\dot{z}(t) + kz(t) = -m\ddot{y}(t) \tag{3.22}$$

It is worth mentioning that the equation of motions above represents a large number of practical engineering problems, such as a structure subjected to earthquake loading or running vehicles subjected to ground excitations due to road roughness.

The horizontally layered soil shown in Fig. 3.10 can be discretized into soil layers modeled by multi-degrees-of-freedom lumped parameter model or finite elements subjected to base excitations, which is shown in Fig. 3.24. As proposed by Seed and Idriss [221], each layer is represented by a spring (nonlinear)-mass-damping (dashpot) component in shear, with the spring and dashpot in parallel, known as the Kelvin–Voigt solid model. The mass matrix is formed by

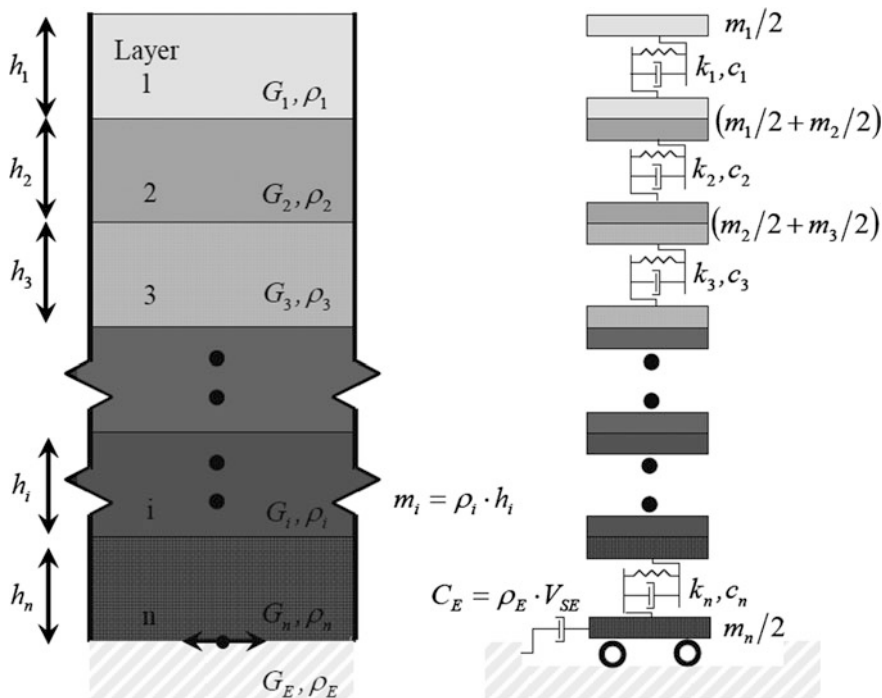


Fig. 3.24 Horizontally layered soil can be discretized into soil layers modeled by multi-degrees-of-freedom lumped parameter model (Kelvin–Voigt solid) subjected to base excitations (a vertically propagating horizontal shear wave) at the base of the soil column [87]

lumping half the mass of each two consecutive layers at their common boundary. The stiffness and damping matrix are updated at each time increment to incorporate the nonlinear soil behavior. The equation for the single-degree-of-freedom system can be extended to a multi-degrees-of-freedom system as:

$$[M]\{\ddot{u}(t)\} + [C]\{\dot{u}(t)\} + [K]\{u(t)\} = -[M]\{I\}\{\ddot{u}_g\} \quad (3.23)$$

where $[M]$ is the mass matrix; $[C]$ is the viscous damping matrix; $[K]$ is the stiffness matrix; $\{\ddot{u}(t)\}$ is the vector of nodal relative acceleration; $\{\dot{u}(t)\}$ is the vector of nodal relative velocity; $\{u(t)\}$ is the vector of nodal relative displacement; $\{\ddot{u}_g\}$ is the acceleration at the base of the soil column; and $\{I\}$ is a unit vector; the mass, damping, and stiffness matrix are normally assembled based on the response of the soils at each time instant.

In time-domain analysis, the thickness h_i of the modeled soil layer i controls the maximum frequency f_{\max} that a seismic wave can propagate:

$$f_{\max} = (v_s)_i / 4h_i \quad (3.24)$$

where $(v_s)_i$ is the shear wave velocity for modeled soil layer i .

As the nonlinear soil properties are modeled, the equation(s) of motions can be solved by using a numerical step-by-step procedure for the integration of the equation(s) of motions. The method used is called the direct integration method.

Without loss of generality, for solving the equation(s) of motions for the single-degree-of-freedom, the Newmark time-stepping scheme is normally used for integrating the equation(s) of motions in small time steps. It is based on the following assumptions:

$$x_{t+\Delta t} = x_t + \Delta t \dot{x}_t + \frac{\Delta t^2}{2} (1 - 2\beta) \ddot{x}_t + \Delta t^2 \beta \ddot{x}_{t+\Delta t} \quad (3.25)$$

$$\dot{x}_{t+\Delta t} = \dot{x}_t + \Delta t (1 - \delta) \ddot{x}_t + \Delta t \delta \ddot{x}_{t+\Delta t} \quad (3.26)$$

where Δt is the time increment; β and δ are the coefficients that define the variation of acceleration over a time step and are related to the integration accuracy and stability. The coefficient β denotes the variation in the acceleration during the time-incremental step from t to $t + \Delta t$. Different values of β indicate different schemes of interpolation of the acceleration over each time step.

Note that the number of operations in the direct integration method is directly proportional to the number of time steps in the analysis. Hence, the direct integration scheme is effective when the duration of an event to be analyzed is short (i.e., for a few time steps).

The direct integration may be performed by either explicit (conditionally stable) or implicit (unconditionally stable) schemes. The latter requires an updating of soil property matrix at each time step to account for the nonlinearity of the soil behavior. Readers may read source [123] for more details on this topic.

Different solutions in time-domain site-response analysis have been implemented into various computation codes. For example, MASH developed by Martin and Seed [233] uses an implicit time integration scheme based on the cubic inertia method and Martin–Davidenkov constitutive model. The response analysis code CHARSOIL developed by Streeter et al. [234] implements a finite difference scheme (method of characteristics) and a Ramberg–Osgood constitutive model [235]. Lee and Finn [236] developed DESRA-2C with a hyperbolic stress–strain relationship [180] for modeling the soil constitutive relationship, which can calculate both the total and effective stress site-response analysis, allowing the modeling of generation, redistribution, and eventual dissipation of pore-water pressure in soils. Gerlymos and Gazetas [237] implemented a phenomenological constitutive soil model and an explicit finite difference algorithm into the computation code NL-DYAS to perform nonlinear one-dimensional site-response analyses.

It is noted that nonlinear stress–strain soil models are not as established as those of equivalent linear models. Therefore, field or laboratory tests may be requested to evaluate the nonlinear soil model parameters [1]. Moreover, because there are many potential pitfalls in nonlinear analyses that users can readily identify by comparing the results with those of equivalent linear analysis, it is expected that equivalent linear and nonlinear analyses will provide different results. Nevertheless, a comparison of the two will help users quickly identify obvious errors in the analysis methodology [87].

3.6 Surface (Topographic) and Subsurface Irregularities

3.6.1 *General*

Ground motions are not only influenced by the properties and thickness of soil layers due to the filter effects of soil profile on the seismic wave propagations, but also affected by the surface topology of the site and the subsurface's irregular interfaces of soil materials and rock(s). The irregular shape of surface and subsurface topography is often responsible for the focusing and defocusing of seismic energy as seismic waves propagate within the irregularity, and for the generation of surface waves due to diffraction phenomena at the lateral discontinuities, which interfere with body waves and lead to complex compositions of seismic wave field and consequently irregular distribution of damages [238, 239, 240, 241].

Typical examples of surface irregularities are sloping or irregular ground surface, while typical examples of subsurface irregularities are sloping layer boundaries and irregular boundaries or basins. Some relevant examples are illustrated in Figs. 3.34 and 3.35. The effects from both types of irregularities can be significant. Evidence of amplification effects is available from both weak and strong motion events worldwide.

The relevant site-response analysis to account for the surface and subsurface effects requires two- or even three-dimensional analyses as will be presented in Sect. 3.7, usually through finite element analysis, which may require significant analysis efforts. On the other hand, a preliminary evaluation of those effects is sometimes possible based on simple hand calculation.

3.6.2 *Effects of Irregular Surface Topology*

It has long been recognized that infrastructures constructed at the top of hills, ridges, and canyons suffer more intensive damage than those situated at the bases of hills (Fig. 3.25) or on level surfaces, as have been reported in past earthquakes such as the 1909 Lambesc earthquake in France [242], the 1976 Friuli earthquake in Italy [243], the 1980 Irpinia earthquake in Italy [244], the 1985 Chile earthquake [245], the 1989 Loma Prieta earthquake [246], the 1999 Chi-Chi earthquake [247], and the 1999 Athens earthquake [248]. As an example, apparent topographic effects were observed on the abutment of Pacoima Dam in San Fernando during an earthquake in 1971[249], and an unexpectedly high acceleration of 1.25g was recorded at the crest of a narrow rocky ridge adjacent to the dam in Tarzana station during the Northridge 1994 earthquake [1]. In Europe, seismic motion measurements reported similar observations of large amplifications, almost with a ratio of 10, in a narrow frequency band around 5 Hz [250, 251].

These effects are mainly related to three physical phenomena: (1) the sensitivity of surface motion to the incidence angle around the critical, especially for



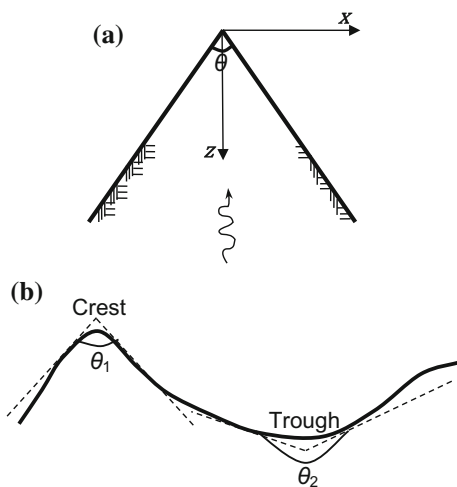
Fig. 3.25 U-shaped valley (by BorisFromStockdale, under license BY-SA 3.0)

SV-waves; (2) the focusing and de-focusing of seismic waves along the topographic relief; (3) the diffraction of body and surface waves that propagate downward and outward from the topographic features and lead to interference patterns between direct and diffracted waves [241].

Aki [252] has examined effects of elementary irregular surface topology with simple exact solutions. For an idealized wedge topology subject to vertical propagating SH-wave excitation, the frequency-independent amplification ratio of $2\pi/\theta$ can be applied at the vertex of a wedge with angle θ , as illustrated in the upper figure in Fig. 3.26. By using this relationship, the amplification of a real topographic profile such as a ridge-valley terrain, shown in the lower figure of Fig. 3.26, can be calculated. Provided that the crest and the trough are sufficiently far apart, as they are in this figure, the ratio of amplification between the crest and trough can be approximated as θ_2/θ_1 . He also stated that the amplification in simple irregularities due to incident P-SV waves, although somewhat larger on average than that for SH-waves, is roughly of the same magnitude. Castellani et al. [253] and Bard [254] also presented that amplifications for incoming SV-waves are slightly larger than those of the SH-wave.

The surface topographic effects have been considered in various seismic design codes. For example, in Eurocode 8 [198], a correction factor for both ridge and cliff-type topographies as a function of the height and the slope angle is used. The so-called aggravation factor gives an extra amplification of 20% to 40% compared with the one determined based on the one-dimensional site-response estimation. The Italian Building Code [255] introduces an amplification factor to modify the ordinates of the acceleration response spectra referred to soil category A and horizontal topographic surface for dynamic design. Such factor depends on the contributions of both soil layer and irregular surface topology. However, neither code

Fig. 3.26 Simple ground surface topology irregularities (solid line) for: **a** an infinite wedge subject to plane seismic waves in the direction of its axis; **b** approximation of actual ground surface at crest and trough of wedges [252]



explicitly specifies the contribution of seismic motion amplification due to subsurface geometric irregularities of bedrock and contacts between soil strata.

3.6.3 Effects of Subsurface Irregularity

Many urban areas are located on or near alluvial valleys. It is important to evaluate the seismic motions influenced by the curvature of basins in which alluvial soils have been deposited, as the lateral variation along the horizontal direction can trap body waves and cause some incident body waves to propagate through the alluvium and generate local surface waves [256]. This can eventually lead to increased amplifications and longer duration of ground motions compared with those obtained from conventional one-dimensional site-response analysis, which only considers vertically propagating shear wave [1].

The importance of subsurface irregularity for earthquake ground motions has been discussed by several researchers [257, 258, 259, 260]. For example, studies have shown that lateral discontinuities in a shallow sedimentary valley at a site located in northern Greece generate locally diffracted surface waves that affect the frequency content and the amplification of seismic motion as well as the duration of observed ground motions [261, 262].

In the case of deep valleys, the amplification functions from one-dimensional and two-dimensional numerical simulations are different both at the center and at the edges. Bard and Bouchon [263] proposed an empirical criterion that can be applied to sine-shaped valleys in order to identify the significance of two-dimensional effects:

$$\frac{h}{l} \begin{cases} \geq \frac{0.65}{\sqrt{C_v-1}}, & \text{two-dimensional resonance} \\ < \frac{0.65}{\sqrt{C_v-1}}, & \text{one-dimensional resonance + lateral propagation} \end{cases} \quad (3.27)$$

where h is the thickness of the soil deposit; l is the half width of the valley; C_v is the soil–bedrock velocity contrast.

The equation above can be interpreted as an empirical boundary between truly two-dimensional valley effects (when $\frac{h}{l} \geq \frac{0.65}{\sqrt{C_v-1}}$) and side effects that are focused at the valley edges that are coupled to one-dimensional behavior (when $\frac{h}{l} < \frac{0.65}{\sqrt{C_v-1}}$). However, it is noticed that the equation has been derived from numerical simulations of propagation of P-waves and S-waves under simplified hypotheses on soil behavior and valley geometry. Since the reality is much more complex, the border between the two effects shall be considered with respect to each case studied [264].

Silva et al. [265] summarized the effects of surface and subsurface irregularities with comments on their quantitative predictability, as presented in Table 3.3.

Even though many studies have been performed to present the importance of the effects of subsurface topology on the ground motions, they have not been fully

Table 3.3 Effects of surface and subsurface irregularities on seismic ground motions [265, 1]

Structure	Conditions	Effects	Significance	Most suitable quantitative predictions
Surface irregularity	Sensitive to shape ratio, very significant for frequencies corresponding to wavelengths equal to the mountain width	Amplification at the crest, de-amplification or amplification at base, rapid changes in amplitude phase along slopes	Amplification up to a factor of 30, with a typical value ranging from 2 to 10	Poor, generally under-predict the amplification, may be due to ridge–ridge interaction and three-dimensional effects
Sediment-filled valleys	Local changes in shallow sediment thickness	Increased duration	Duration of significant motion can be doubled	Fair
	Generation of long-period surface waves from body waves at shallow incidence angle	Increased amplification and duration due to trapped surface waves	Duration and amplification of significant motions may be increased over one-dimensional projections	Good at periods above 1 s
Shallow and wide soil-filled valley (depth/width < 0.25)	Effects are most pronounced near edges; largely vertically propagating shear waves away from edges	Wide range frequency amplification near edges due to generation of surface waves	One-dimensional models may under-predict at higher frequencies by about 2 near edges	Away from edge, one-dimensional site-response analysis is good; near edges, higher dimensional site-response analysis is recommended
	Effects throughout valley width	Broad range frequency amplification across the valley due to whole valley modes	One-dimensional model may under-predict for a wide range frequency range by about 2–4; resonant frequencies shifted from one dimension	Fair: given detailed description of vertical and lateral changes in soil properties
Deep and narrow soil filled valley (depth/width > 0.25)				

recognized by engineering communities, mainly due to a lack of measurement data that can provide a better understanding of the effects in a simplified manner and also due to associated complexities in the two- or three-dimensional site-response analysis (Sect. 3.7).

3.7 Two- and Three-Dimensional Site-Response Analyses

3.7.1 *Applicability of One-, Two-, and Three-Dimensional Site-Response Analyses*

For simplicity, it is normally reasonable to assume that typical soil layers are horizontally extended to infinity with a flat ground surface, and the incident earthquake motions are spatially uniform, horizontally polarized shear waves that only propagate vertically. These assumptions can be justified by the fact that soil properties normally vary more rapidly in the vertical direction than in the horizontal direction, as previously discussed in Sect. 3.5. The stress waves from the source propagate almost vertically when they arrive at the ground surface, and waves' velocity normally decreases from the source toward the ground.

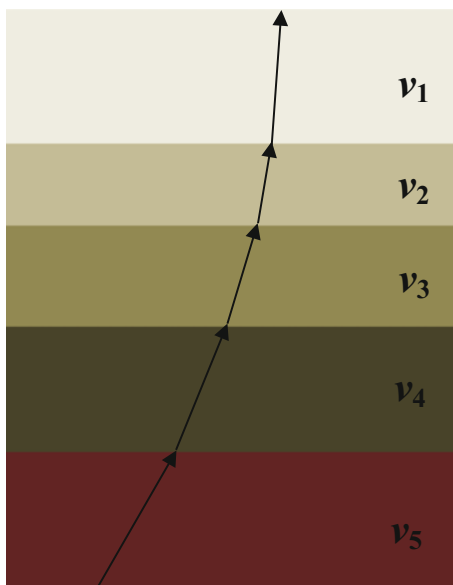
The wave bending phenomena above can be quantitatively explained by Snell's law of wave refraction: For a seismic wave traveling through media comprising isotropic materials, the ratio of sines of wave angles ($\theta_1, \theta_2, \dots, \theta_n$) relative to the normal of the soil layer (1, 2, ..., n) boundaries and the wave propagation velocities (v_1, v_2, \dots, v_n) is constant:

$$\sin \theta_1 / v_1 = \sin \theta_2 / v_2 = \dots = \sin \theta_n / v_n = \text{constant} \quad (3.28)$$

Near the earth surface, upper soil layers are generally softer than the lower ones, and seismic waves travel upward from the bedrock and through soil layers with a trend of decreasing velocities. Therefore, if soil layers can be assumed to be horizontal, according to the equation above, seismic waves traveling upward from higher-velocity (hard soil) layers to the low-velocity (soft soil) layers will be bent/refracted toward a vertical path, as shown in Fig. 3.27. Therefore, even though the waves within firm ground propagate in a shallow inclined direction, they propagate and are bent nearly vertical between the shallow soil and the ground surface by successive refractions [212]. With this assumption, the one-dimensional wave propagation analysis (Sects. 3.5.2 and 3.5.3) can be performed, based on either the solution to the wave equation or a lumped mass simulation. It generally results in a conservative evaluation for site responses, and many structures designed based on one-dimensional analysis have sustained the loading during major earthquake events.

However, more recent research has characterized two-dimensional site effects on ground motions [238, 239, 266, 267]. Compared to one-dimensional effects, the differences of two-dimensional effects are related to the propagation of locally

Fig. 3.27 Refraction of SH-wave traveling upward through consecutive decreasing velocity ($v_5 > v_4 > v_3 > v_2 > v_1$) soil layers



generated surface waves and possible two-dimensional resonance [257, 268, 269, 270].

Theoretically, three-dimensional site-response analysis is only quantitatively different from its two-dimensional counterpart. The third dimension can increase ground motion amplification, and the additional lateral restriction shifts peak frequencies to higher values.

Therefore, for more irregular soil deposits, two-dimensional or three-dimensional effects may need to be accounted for. As a general rule, to capture different types of seismic wave propagation (Sect. 3.7.2), and/or to account for site geometric properties (Sect. 3.7.3) that may affect the seismic wave propagation, two-dimensional and three-dimensional site-response analyses may be required. These are usually performed by finite element analysis.

3.7.2 Seismic Wave Propagation Effects

The relative importance of body and surface wave depends on various factors such as source mechanism, source-to-site distance, direction to the source, topography, and sediment geometry. From point of view of wave propagation, one-dimensional site-response analysis can only model one of the following waves at any one time: SH-wave, SV-wave, or P-wave, as shown in Figs. 3.28, 3.29, and 3.30, respectively. In engineering practice, one-dimensional site-response analysis is usually

Fig. 3.28 Refraction and reflection of SH-wave in one dimension

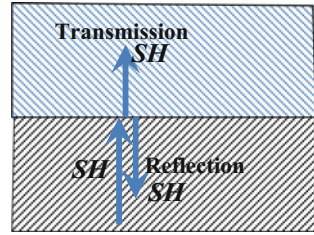


Fig. 3.29 Refraction and reflection of SV-wave in one dimension

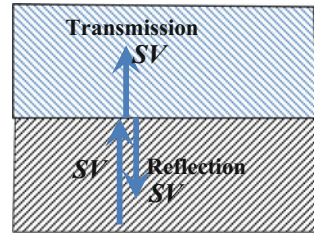


Fig. 3.30 Refraction and reflection of P-wave in one dimension

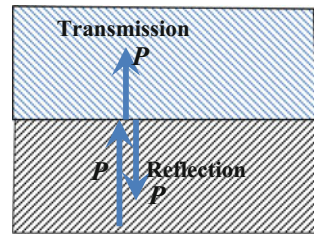
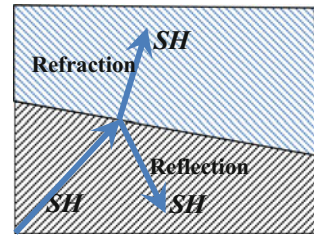


Fig. 3.31 Refraction and reflection of SH-wave in two dimensions



used for calculating SH-wave propagation, due to its importance compared to SV-wave and P-wave.

During the propagation of SH-wave, the particle motion is perpendicular to the wave propagation direction and dominated by uncoupled SH (out of plane) wave after it arrives at the boundary of two adjacent soil layers, although the direction of wave propagation may change due to refraction and reflection. This is illustrated in Fig. 3.31.

Fig. 3.32 Refraction and reflection of SV-wave in two dimensions

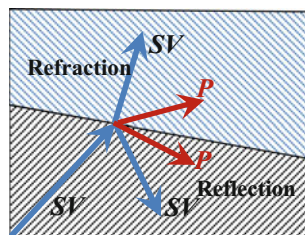
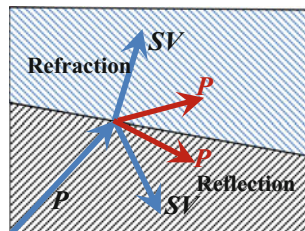


Fig. 3.33 Refraction and reflection of P-wave in two dimensions



SV-wave (in plane) and P-wave interact with each other during their propagation as shown in Figs. 3.32 and 3.33. Because the particle motion associated with SV-wave and P-wave is perpendicular to the plane of the interface between two adjacent soil layers, when they arrive at the boundary/interface between the two soil layers, they will each produce both P-wave and SV-wave in refracted and reflected phases. On the other hand, the particle motion associated with SH-wave is not perpendicular to the interface; therefore, when SH-wave arrives at the boundary, only the SH-wave is reflected and refracted.

Because ground accelerations are usually dominated by SH-wave, and most site-response analyses assume that each soil layer is horizontally extended, one-dimensional site-response analysis is often valid for the calculation of ground responses. However, for many geotechnical structures and site conditions, the second dimension is also of significant importance, and two-dimensional analysis must be carried out to account for SV-wave propagation as well.

Moreover, the long-period components of motions are mainly contributed by the Rayleigh (surface) waves [188], which are the result of interaction between P-wave and SV-wave, and therefore cannot be predicted by a normal one-dimensional analysis. Significant amounts of surface wave energy (dispersive energy) concentrated in a high period range (compared to that of the body wave energy) have been identified in ground motion records on many sedimentary basins and bowl-shaped structures during earthquakes around the world. In addition, the spatial variation of seismic ground motions due to the wave passage effects may also need to be simulated using two-dimensional or three-dimensional analysis.

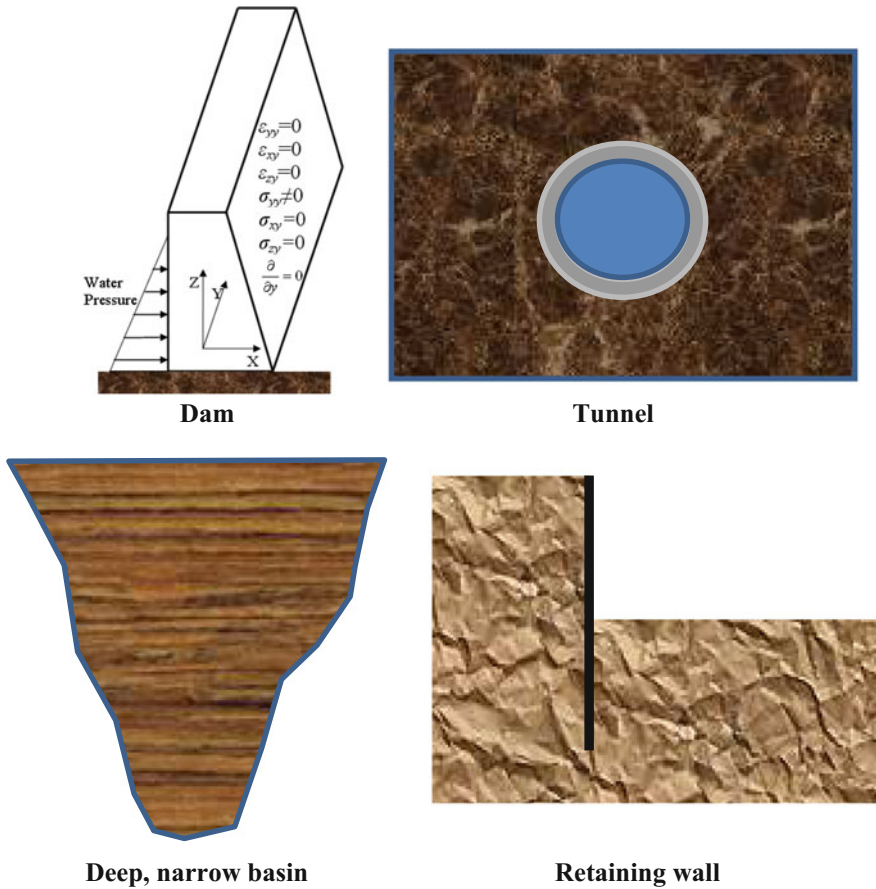


Fig. 3.34 Typical examples of geometric properties of sites that require two-dimensional plane-strain site-response analysis

3.7.3 Site Geometric Effects

Two-dimensional and three-dimensional analyses not only capture different types of seismic wave propagations, but also account for the geometric properties of sites due to surface topographic irregularity (such as sloping or irregular ground surface) and/or subsurface irregularity (such as sloping layer boundaries, irregular boundaries or basins). As shown in Fig. 3.34, both topographic and subsurface irregularity may significantly affect the seismic wave propagation. As presented in Sect. 3.6, one-dimensional analysis can normally be applied for level or gently sloping sites with soil layers in parallel. However, for geometry in which one dimension is significantly higher than others, such as sloping or irregular ground surface, deep and narrow basin, the presence of heavy structure or stiff, embedded



Fig. 3.35 A wide, shallow basin may allow for one-dimensional site-response analysis in the basin center but requires two-dimensional analysis for areas near edges

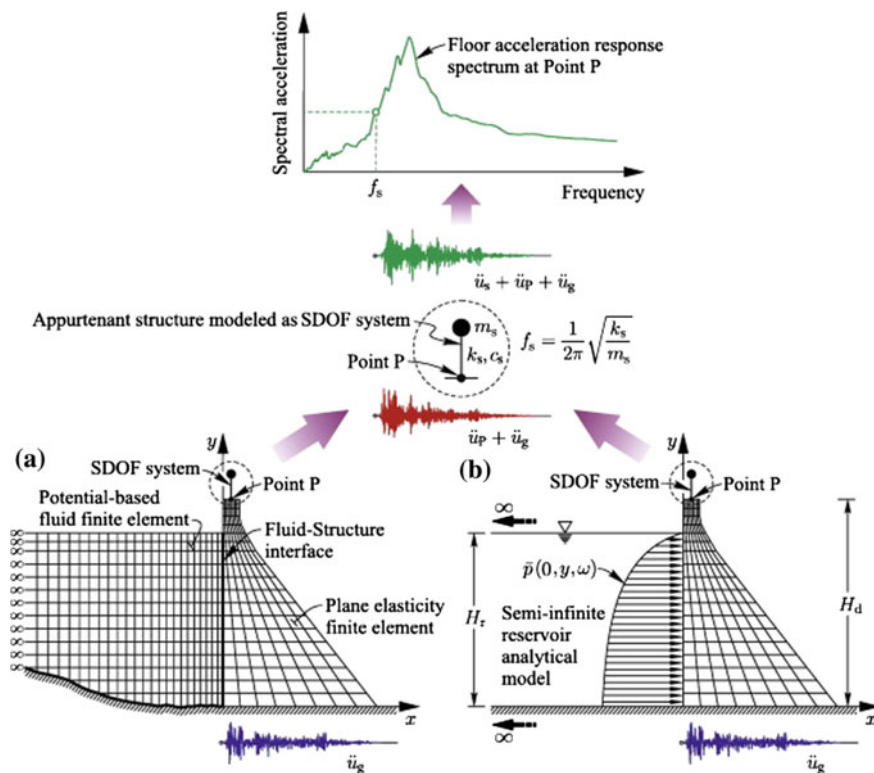


Fig. 3.36 Illustration of a computation of acceleration spectra at a given point P for a gravity dam using **a** a coupled dam–reservoir finite element model and **b** a semi-infinite reservoir analytical model [271]

structures, or walls and tunnels [1], one-dimensional analysis may not be applied. Instead, these can often be treated as two-dimensional plane-strain problems. As mentioned before, an exception is the analysis for shallow and wide basins as shown in Fig. 3.35. At areas near the center of the basin, one-dimensional analysis is normally valid as the geometric effects are not significant. However, near the edges, the geometric effects become significant, and two-dimensional site-response analysis is then required. Figure 3.36 shows an example of the use of the 2D plane

element to model a gravity dam in order to calculate the response spectral acceleration at the dam top.

By considering the sedimentary basin effects and neglecting the topographic site effects, Chávez-García and Faccioli [257] investigated the possibility of including provisions for the two-dimensional complex effects in a seismic design code. Their study indicates that, compared to one-dimensional effects, two-dimensional site effects significantly increase (with a factor of larger than 2 on the response spectra) the ground motion amplitude in a wide period range. Owing to the additional lateral restriction to motions of sediments, two-dimensional amplification becomes significant for lower periods than does one-dimensional amplification. They also showed that the most significant parameter controlling the two-dimensional basin amplification factor is the velocity contrast between sediments and bedrock. Therefore, not only top soil layers (used for one-dimensional site effects), but also bedrock properties may need to be accounted for to perform a two-dimensional site effects analysis. By using the equivalent linear method, Hudson et al. [226] presented a two-dimensional finite element solution in frequency domain, which also accounts for the effects of topographic features.

When soil conditions or problem boundaries vary in three dimensions, or when the response of a three-dimensional structure is important (sites where the response of soils is influenced by structures and vice versa, or when the response of one structure influences the response of another structure) [1], three-dimensional rather than two-dimensional site-response analysis is required. Figure 3.37 shows a three-dimensional finite element model of a pile–soil system with a modeling of nonlinear properties of the surrounding soil. Figure 26.6 shows the three-dimensional finite element model utilized to analyze the manifold and suction pile using the FE code OpenSees [272].

As mentioned earlier, theoretically, three-dimensional site-response analysis is only quantitatively different from two-dimensional site-response analysis. The third dimension can increase somewhat ground motion amplification, and the additional lateral restriction shifts peak frequencies to higher values.

In practice, 2D or 3D analysis is commonly performed using finite element analysis. The site-response analysis using finite element analysis can be categorized as finite element free-field site-response analysis and coupled finite element analysis of sites and structures. Moreover, free-field site-response analysis using finite element analysis is often performed to validate the finite element models with respect to disturbances by model boundaries and sensitivity to mesh coarseness. The term “free-field” refers to motions that are not affected by structural vibrations or the scattering of waves at, and around, the foundation. It is often a preliminary step toward coupled dynamic analysis including a modeling of both sites and structures. When a proper dynamic free-field model is obtained, the structure can be included in the system and the response of the coupled soil–structure system can be calculated [274].

In addition to the dynamic finite element method, other more simplified approaches are also available, such as the shear beam approach [275, 276], layered inelastic shear beam method [277], which allow the 2D or 3D problems to be

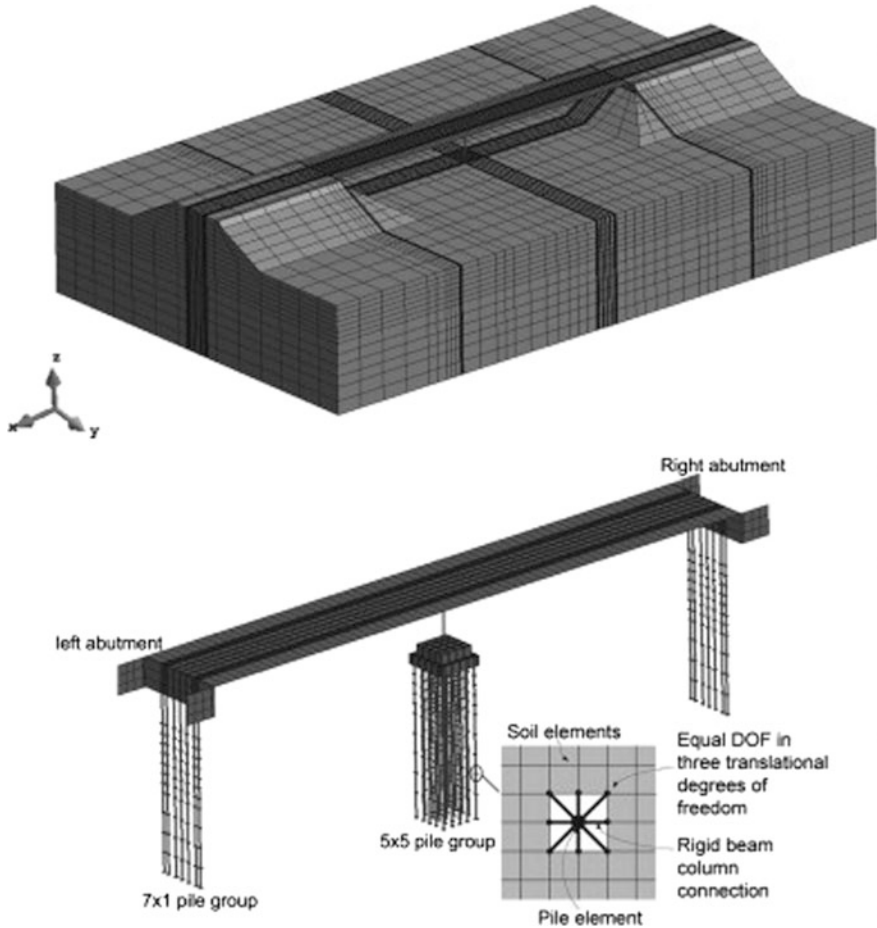


Fig. 3.37 Three-dimensional finite element meshes to model the bridge piles and the surrounding soils [273]

solved by 1D analysis. The shear beam approach is very efficient for calculating responses of dams under an earthquake, even though it makes quite restrictive assumptions regarding the mode of dam responses. For more details, readers may refer to the sources cited above.

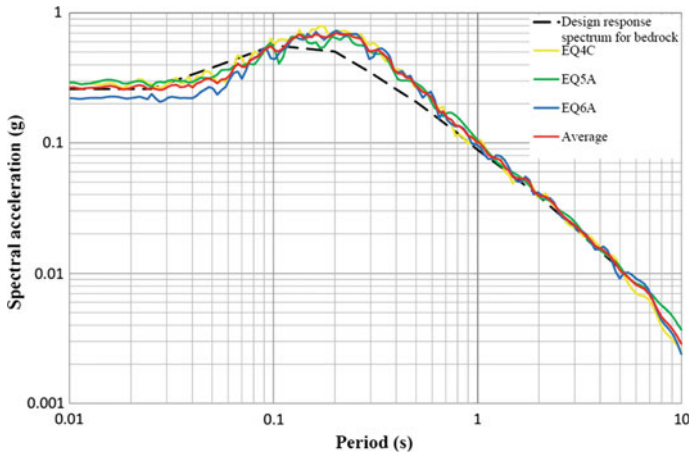


Fig. 3.38 Calculated seabed/ground surface acceleration response spectra (EQ4C, EQ5A, and EQ6A and the “average” of the three) based on site-response analyses using three bedrock horizontal ground motions matched to a target bedrock design response spectrum. Courtesy of Aker Solutions and NGI

3.8 Using Site-Response Analysis Results for Seismic Analysis

A set of time histories of ground motions computed through a site-response analysis can be used for calculating structural responses. As an alternative, the set of response spectra obtained from the time histories of ground motions can also be interpreted in some manners (e.g., taking the mean value of the all response spectra) and be smoothed to develop one design response spectrum at seabed/ground surface, which can be used for calculating structural responses using response spectrum analysis [188]. Figure 3.38 shows response spectra of three computed horizontal acceleration time-histories on a seabed/ground surface for earthquake events with a return period of 10,000 years. By smoothing the average values of the three computed spectra, a design response spectrum can be obtained as shown in Fig. 3.39.

3.9 Characteristics of Site Responses

3.9.1 Horizontal Ground Motions

The horizontal amplification factor F_a (ratio between peak horizontal ground acceleration at seabed/ground surface and that at bedrock or rock outcrop) is mainly influenced by local soil conditions, ground topology, and intensity and frequency

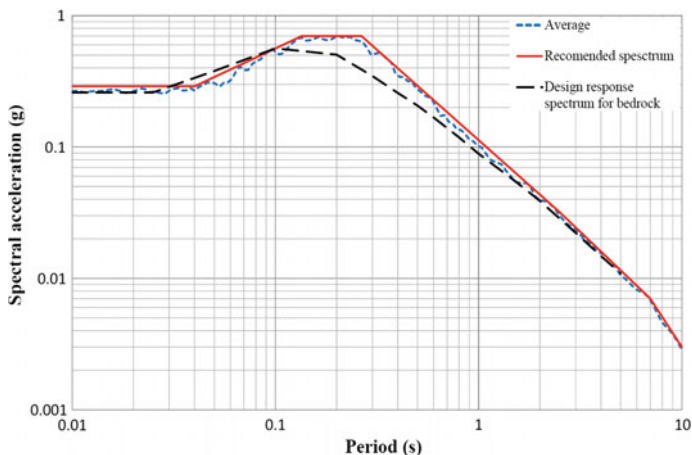


Fig. 3.39 Recommended horizontal design spectrum (solid line) at seabed/ground surface. Courtesy of Aker Solutions and NGI

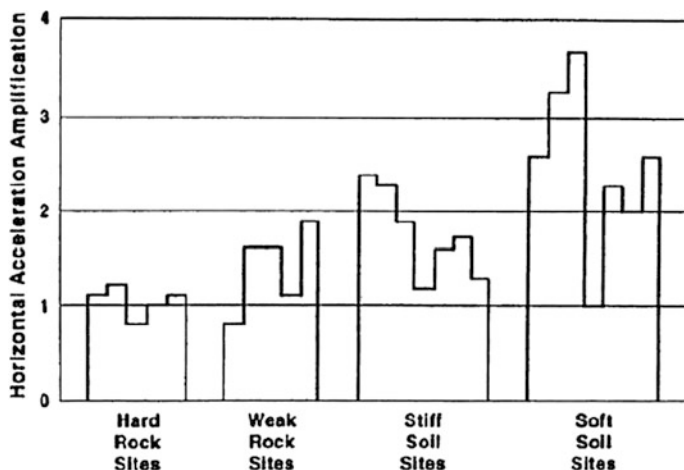


Fig. 3.40 An example of horizontal acceleration amplification at various soil sites. Courtesy of FEMA

content of earthquake motions [278, 279]. Figure 3.40 illustrates an example of horizontal acceleration amplification for different soil conditions. Even though the variation trend of amplification depends on various factors such as site conditions and characteristics of seismic ground motions at bedrock or rock outcrop, the figure nevertheless still provides an indication that soils can amplify or de-amplify the ground motions. The variation in amplification for different soil conditions is large. Within a certain frequency range, by accounting for the soil stiffness degradations

due to increased strain, the soil can amplify rock outcrop motions by a factor up to 6 at relatively low seismic intensity levels (e.g., corresponding to probability of exceedances of 10^{-2}) and a factor up to 5 for high intensity levels (e.g., corresponding to probability of exceedances of 10^{-4}).

In addition, the increase in sediment depth (depth of control motions) may also lead to significant changes in response, which is the case for several offshore regions such as the Norwegian continental shelf, where very deep unconsolidated sediments underlain by a few kilometers of sedimentary rock are typical.

Based on a parametric study of site-response analysis at three offshore sites on the Norwegian continental shelf [280], it has been found that the local soil conditions may have rather pronounced effects on both the level and the distribution of energy of ground motions and may be an important factor in hazard studies.

3.9.2 Vertical Ground Motions

Since a typical fixed offshore structure has a natural period (corresponding to the first global flexural vibration) above 1.0 s, the short period range of seismic ground motions does not have significant influence on the amplification of its lateral structural response. However, the influence of the vertical ground motion at the short period range would be potentially important for responses of various types of structures with rather high vertical stiffness, such as heavily loaded deck structure with large cantilevers, horizontal cantilever structures (e.g., cantilever beams at module support frame or a stiff flare boom), or topside module structures installed on offshore platforms.

The vertical ground motions are mainly contributed by P-waves and partially contributed by S-waves. Because the P-wave velocities of the soil and the underlying rock differ little, i.e., high vertical stiffness, the ground motions at seabed/ground surface are essentially quite similar and can in many cases be assumed to be identical to the seismic motions at bedrock. Therefore, different from that of the horizontal response, the amplification of vertical ground motions due to local soil conditions is often insignificant [188].

The vertical peak ground acceleration is generally 10–50% lower than the horizontal peak ground acceleration. The relationship between vertical and horizontal components of the seismic action mainly depends on the period, the distance between sites to relevant faults, the local site conditions, and earthquake magnitude, while the ratio is relatively insensitive to earthquake mechanism and sediment depth [281].

The derivation of the vertical ground motion spectrum by scaling the horizontal motion spectrum using either a factor or different factors at different frequency ranges, as will be presented in Sect. 3.10.2, is widely accepted. For designs of important structures such as nuclear power plants, dedicated vertical ground motion spectra may be directly provided. The vertical to horizontal spectral ratio is generally less than 2/3 at mid- to long periods but significantly higher at short periods,

and at short periods, the V/H spectral ratio is sensitive to the site-to-source distance. It is higher on soil sites than on rock sites and is higher on soft soil sites than on stiff soil sites. Recent research by Bozorgnia and Campbell [282] presents that V/H spectral ratio for soil sites is relatively less sensitive to magnitude than the site-to-source distance.

In addition, water column also has effects to decrease the vertical accelerations, as will be presented in Sect. 3.11.

3.10 Vertical Ground Motion Calculations

3.10.1 *Site-Response Analysis for Calculating Vertical Ground Motions*

Compared to site-response analysis to estimate the horizontal ground motions, the calculation of vertical ground motion has attracted much less engineering and research effort.

However, recent field observations and studies have concluded that vertical ground motions can be significant and cause structural and foundation failures as well as geotechnical hazard [283, 284, 282]. In the vicinity of the epicenter, the vertical component of motion is even larger than the horizontal components [285]. Moreover, alluvial basins enable the S- to P-wave conversion and wave scattering at the basin–bedrock interface, supplying energy to vertical components of strong ground motions, and this also increases the ratios of vertical to horizontal PGA. The available data shows that the peak vertical acceleration (PVA) amplification mainly occurs within the top 20 m of soil. At the ground surface, PVA can be amplified by a factor of 2–3 [284].

As a universal method, the vertical ground motion can be calculated using finite element analysis to simulate the seismic wave propagation through soil media and on the surface, even though this requires considerable efforts in the aspects of meshing, material modeling, and computation.

As a simpler alternative, similar to a site-response analysis to obtain horizontal ground motions, Mok et al. [286] performed the site-response analysis by controlling compressive P-wave propagation velocity instead of the shear wave velocity in a traditional site-response analysis. Regarding the damping modeling for vertical ground motion calculations, they recommended using average values estimated from site-response analyses for horizontal components without exceeding 10% of the critical damping ratio in any soil layer. By following these recommendations, they obtained a good agreement between the results of the site-response analysis and measured the vertical component of ground motions at Lotung and Port Island sites.

By using vertical seismic motion records of the Lotung down-hole vertical array, Elgamal and He [284] examined a vertical wave propagation model based on the

equivalent linear model employed in SHAKE91 [222], in which an optimization procedure earlier proposed by Elgamal et al. [287] was utilized to obtain the properties of the soil model. It is noticed that, in order to match the measured time histories at different depths of the vertical array, high level of damping (even for mild seismic motions) in the range of 15% and wave velocity equal to around 3/4 of P-wave velocity must be used in their site-response analysis for calculating vertical seismic motions.

In engineering practice, as there is usually relatively little difference in P-wave (in most cases, the major contributor of vertical soil and ground motions) velocities among different soil layers and underlying rock, the vertical ground motion time histories (and response spectra) are practically very similar/identical in all soil layers and may simply be assumed to be equal to that in the bedrock, even though a dedicated site-response analysis described above is still regarded as more reliable.

3.10.2 *V/H Spectrum*

In engineering practice, a site-response analysis to calculate vertical ground motion is rarely performed due to the complexity in the modeling, the limited research efforts, and lack of concrete theoretical background. Furthermore, given the distinct characteristics of frequency contents in vertical and horizontal ground motions, a simple scaling of horizontal motions to represent vertical seismic motions should be avoided. Therefore, the estimation of vertical ground motions makes use of the magnitude and distance data from the deaggregation of the seismic hazard and an appropriate ground motion prediction equation (GMPE) to develop a period-dependent *V/H* (vertical to horizontal) ground motion spectrum ratio, which can then be applied to the horizontal design spectrum to generate a target vertical spectrum for design with an associated return period. Special attention should be paid to characteristics of short period range of *V/H* spectra [188]. This method is implemented by the majority of seismic codes for both offshore and land-based structures, such as ISO 19901-2 [288], Eurocode 8 [198], BSSC[290], JTG/T B02 [291], GB 50011-2010 [199].

In traditional seismic design codes, the vertical component of seismic motion is smaller than its horizontal counterpart. Based on the recent study by Bozorgnia and Campbell [282], an updated *V/H* model is recommended that supersedes the previous *V/H* model [281] proposed by the same authors. This updated model is applicable for shallow crustal earthquakes occurring worldwide in active tectonic domains for magnitudes ranging from 3.3 to as large as 8.5, depending on the style of faulting, and distances as far as 300 km from the source.

The significance of vertical ground motions has been realized by several recently updated seismic codes. For example, the second edition of ISO offshore standard for seismic design ISO 19901-2 [288] recommends a modification of *V/H* ratio (Fig. 3.41) compared with its previous version released in 2004 [289], which uses a unified 0.5 ratio for all period range. This update can pose a higher demand for

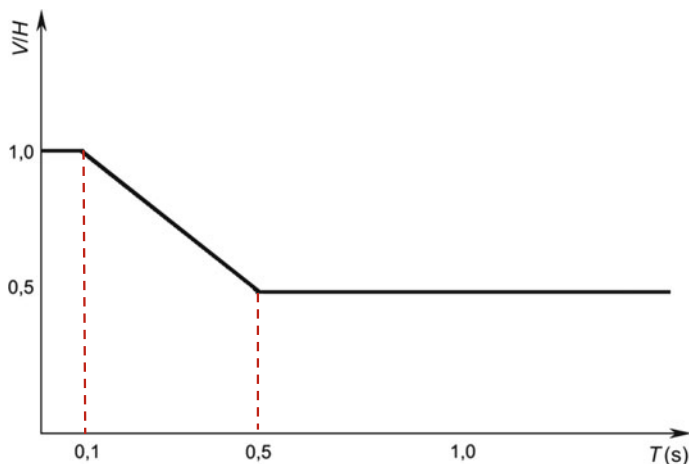


Fig. 3.41 V/H spectral ratio varied with period T recommended by the second edition of ISO in 2015 [288]

topside structures, subsea structures, and equipment on the topside as the increase in vertical spectral acceleration in the low period range of design spectrum can cause a noticeable increase of vertical seabed motions. Note that supporting structures of most fixed offshore platforms are generally stiff in the vertical direction, and the increased vertical accelerations in the lower period range are likely to be transferred to the topside through the supporting structures without significant modification in either amplitude or frequency content (the opposite trend can be found for the horizontal accelerations). Therefore, since topside structures rather than substructures generally have low natural periods, the low period part of acceleration components transferred to the topside structures may then cause a response amplification of the topside structures.

The guidelines for Seismic Design of High Bridges in China [291] also specify that the V/H spectrum can be established depending on the site conditions:

$V/H = 0.65$ for rock site (3.29)

$$V/H = \begin{cases} 1.0 & \text{for } T < 0.1 \text{ s} \\ 1.0 - 2.5(T - 0.1) & \text{for } 0.1 \text{ s} \leq T \leq 0.3 \text{ s} \text{ for sites with other soil conditions} \\ 0.5 & \text{for } T \geq 0.3 \text{ s} \end{cases} \quad (3.29)$$

where T is the vibration period of target structures.

For more details regarding V/H spectrum, see the sources cited above.

3.11 Water Column Effects on Seismic Ground Motions

The presence of water suppresses vertical seabed motions in the frequency ranges close to the eigenfrequency of the seawater column f_n :

$$f_n = (2n - 1) \cdot C_w / (4d) \quad (3.30)$$

where n is the order of the eigenfrequency; C_w is the speed of sound in water (around 1500 m/s); and d is the depth of the water.

Smith [292] and Sleafte [293] studied the ground motion measurements for the earthquake at Santa Barbara Island during September 1981 and compared them with the record for an onshore location nearby that was a comparable distance from the epicenter (85 and 98 km). They showed that, due to the presence of the water column (which is defined as a column of water extending from the surface of a sea, river, or lake to the bottom sediments), the vertical seismic ground motions at seafloors are much less than those measurements onshore. This is especially important for mat-supported structures, because they receive most of the motions from the soils near the seabed. This statement is also confirmed by other researchers [294, 295], who developed analyses that include the effects from the finite water column. They indicated that, depending on the water depth, some frequencies can be reinforced and amplified by the water column effects, while others can be canceled. The peak vertical accelerations at the seabed can be reduced by as much as 50%.

By studying eight offshore seismic records with magnitudes ranging from 4.7 to 6.1 during a 20-year period, and comparing them with onshore records with comparable epicentral distance (ranging from 49.4 to 309 km) and site characteristics, Boore and Smith [296] concluded that offshore earthquake ground motion is in general the same as its onshore counterpart. However, similar to the prior findings by Smith [292] and Sleafte [293], Boore and Smith also presented that the sediment layer and the water volume over the site dampened the vertical component of the ground motions. As a result, the V/H ratios (vertical to horizontal component of motion) for offshore locations are smaller than those with comparable site characteristics at onshore locations. In addition, as the amount of damping is proportional to the period of the ground motions, the difference between the vertical component of the onshore motions and the offshore motions decreases as the periods become longer and increases as the periods become shorter [297].

Chapter 4

Record Selection for Performing Site-Specific Response Analysis

4.1 General

Compare to simplified methods using design codes, site-specific response analysis is a more refined method to determine ground motions. Even though the P-waves arrive first and cause the vertical shaking of the ground, it is normally the shear waves that cause strong horizontal ground motions and possible subsequent structural damage. Therefore, apart from the shear waves transmitted vertically through soil (from bedrock to ground), which normally show little amplification or de-amplification, a site-response analysis places special focus on the estimation of the horizontal ground and soil motions due to the transmission of horizontal shear (SH) waves propagated vertically. In addition, to capture different types of seismic waves (body and surface waves) propagations, and also to account for the irregular geometric properties of the sites (Sect. 3.6) that may affect the seismic wave propagation, a two-dimensional or three-dimensional site-response analysis, usually with the aid of finite element analysis, may need to be performed.

In a site-response analysis, it is normally required to use a minimum of three to seven accelerogram sets for response history analysis. Each accelerogram set selected must consist of at least two horizontal components, and in many cases, the vertical component may also be included. It is important to select records that are generally compatible with the earthquake magnitude and source-to-site distance found from deaggregation (Sect. 11.1.4). If multiple magnitude–distance combinations contribute significantly to the hazard, then one should select records from each contributing earthquake as part of the total number of records. When the hazard is controlled by faults producing moderate to large magnitude earthquakes at locations near to the site, an appropriate number of ground motion records should be selected to include near-fault and directivity effects, such as velocity pulses producing relatively large spectral ordinates at long periods [218].

Obviously, the selection of time history records is essential in a site-response analysis to calculate the design ground motions. Ideally, recorded accelerograms

with response spectra equal to the design spectra should be used in site-response analyses. However, this is almost impossible because the design spectra are based on the medians of numerous response spectra, each with varying frequency content. The resulting design spectra are therefore smoother or more uniform than any individual spectrum derived from recorded time histories of earthquake motions. Moreover, the equal probability of exceedance design spectra (also called uniform hazard spectrum, as will be discussed in Chap. 11) can result from contributions from various earthquakes with different sources and magnitudes at different spectra periods, with the larger magnitude seismic events contributing more to the higher period.

Therefore, artificial accelerograms must be generated to best approximate the design response spectrum at bedrock. This requires selection of motion recordings and a modification of the recordings to fit into the design spectrum at bedrock. The obtained artificial accelerograms at the bedrock are used to perform site-response analyses in order to calculate the ground motion time histories at the selected locations (depth), which are used to best estimate the ground motion response spectra at the selected locations to reach a design response spectrum. The entire procedure above is presented in Sects. 4.2, 4.3, and 4.4.

It is noted that selecting, scaling, and matching ground motions to obtain a compatible set of records play a key role in seismic assessment with an acceptable level of confidence. No unanimous consensus has yet been achieved on this subject. The current book briefly introduces a few popular and general methods for selecting and modifying ground motions recordings in order to perform a site-response analysis. For more elaborated information on this topic, source [299], which was developed as part of the PEER Transportation Research Program, is recommended.

Readers should bear in mind that the general rules for selecting, scaling, and matching ground motions discussed in this chapter can also be applied for obtaining artificial ground motion histories that are compatible with the design spectra at ground surface of a site, which may also be used for seismic time history analyses, even if the site effects are roughly accounted for when using a code-based design spectrum.

4.2 Selections of Motion Recordings

The ground motion suite must include a wide range of intensity measures representative of seismic hazard at the area of interest. Ideally, the response spectra of the selected recordings (obtained from measured recordings at different stations) should approximately fit or reasonably envelop the ground motion design spectra (typically given by seismic design codes) at the bedrock or rock outcrop. However, if this is not attainable, a modification of selected recordings or generation of artificial bedrock seismic motions has to be performed to fulfill the requirements above, as will be discussed in Sect. 4.3.

4.3 Modification of the Recordings to Fit into the Design Rock Spectrum

As mentioned in Sect. 4.2, in order to generate time histories to best approximate the design response spectrum at bedrock, it is important to match the motion recordings to the target design spectrum. This process to obtain the matched time histories is typically carried out by trial and error. Note that there is no general consensus on the best practice for the scaling/modification of the ground motion records; it is still a subject of significant study, and the results vary with the degree of inelastic response of structure for the chosen level of seismic hazard [300]. Generally, two methods are available for performing the matching, namely direct scaling and spectrum matching, as will be discussed in Sects. 4.3.1 and 4.3.2.

4.3.1 Direct Scaling

Direct scaling involves applying one constant factor to individual pairs of ground motions to make their response more closely match the target design spectrum over a certain range of periods [301]. Because elastic response spectra correspond to linear response of SDOF systems, the same scale factor applies to spectral accelerations at all periods.

4.3.2 Spectrum/Spectral Matching

Spectrum/spectral matching, also called response spectrum compatibilization, is intended to manipulate each individual ground motion record in the time domain by the addition of wave packets, i.e., the recordings are scaled with different factors in different frequency ranges, using, for example, wavelets algorithm [302, 303], such that the response spectra would approximate target design spectra at the bedrock or rock outcrop.

A slightly different method is to scale each ground motion record so that the average response spectrum over the periods of interests is equal to the average of the target spectrum over the same periods.

By modifying the spectral shape of each individual ground motion record, spectral matching essentially adjusts the frequency content of accelerograms until the response spectrum is within user-specified limits of a target response spectrum over a defined period range [304, 305]. One way to determine the scaling factor β is, for example, to minimize the errors with respect to a target acceleration spectrum at a number (N_r) of eigenperiods typically below 4 s:

$$\text{error} = \min \left(\sum_{i=1}^{N_r} \left(1 - \frac{\beta \cdot S_a(T_i)^{\text{record}}}{S_a(T_i)^{\text{target}}} \right) \right) \quad (4.1)$$

where $S_a(T_i)^{\text{target}}$ and $S_a(T_i)^{\text{record}}$ are the spectral accelerations for the i th eigenperiod from the target spectrum and the response spectrum of the original selected record, respectively.

Figure 4.1 shows that three original selected recordings (Kobe earthquake, January 17, 1995; Imperial Valley of El Centro Site earthquake, May 18, 1940; Trinidad earthquake, March 1988) are matched to the target design spectrum with respect to both amplitude and frequency content, and the three matched spectra are transferred back to the time histories as shown in Fig. 4.2.

Therefore, spectral matching generally reduces spectral variability among a suite of records and increases the pool of available ground motions with a certain shape. It is the former point that has made this process especially appealing to practicing engineers [306]. Moreover, the reduction in spectral variability due to spectrum matching generally leads to a reduction in nonlinear structural response variability [307], which essentially implies that fewer ground motions are required to obtain an estimate of a particular response quantity [308].

Another widely adopted spectrum scaling method is based on the 5% damped first mode spectral acceleration, which can minimize the bias of damage estimation statistically [309]. This is because the response spectra for time histories matched with the first mode spectral acceleration are generally less “broadband” than those matched with uniform hazard spectra at entire periods or over a large range of periods, even though uniform hazard spectra usually envelope the first mode spectral acceleration. However, for many structures, the higher order of vibration modes also makes an important contribution to seismic responses. For example, shear forces at the upper stories of a building or floor accelerations can be more sensitive to higher order mode excitation than that of the first eigenmode vibrations, even if the displacement response is more dependent on the fundamental global vibration mode response. Therefore, a scale factor that covers a larger period range should then be adopted.

The seismic records can be obtained from several public ground motion record databases, which are often accompanied by a number of earthquake and site parameters, such as earthquake magnitude, source-to-site distance, and ground type at the corresponding recording stations. Section 4.5 provides links to some such databases.

The target spectra can be obtained using one of the following two options: (1) the design response spectra calculated from the relevant seismic design code procedures, which correspond roughly to uniform hazard spectra (Chap. 11) for the site; or (2) site-specific scenario spectra that preserve realistic spectral shapes for controlling earthquakes and match the design spectral ordinate at different periods of interest, also known as conditional mean spectra (CMS), as will be presented in Sect. 11.4.

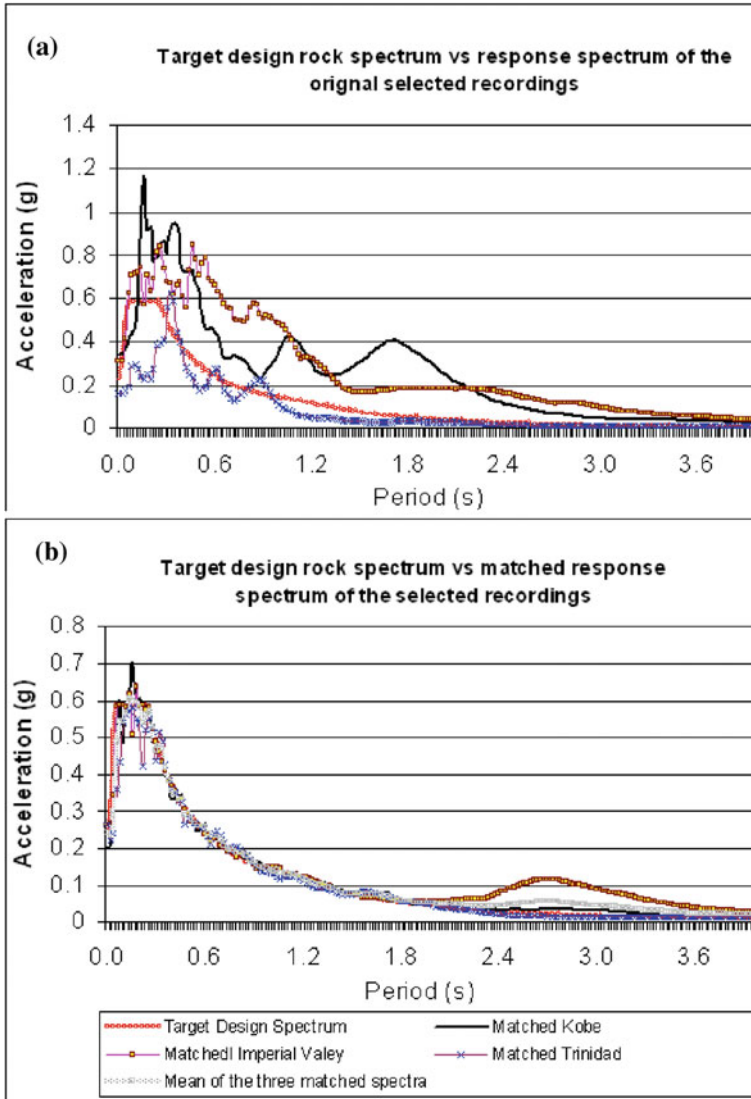
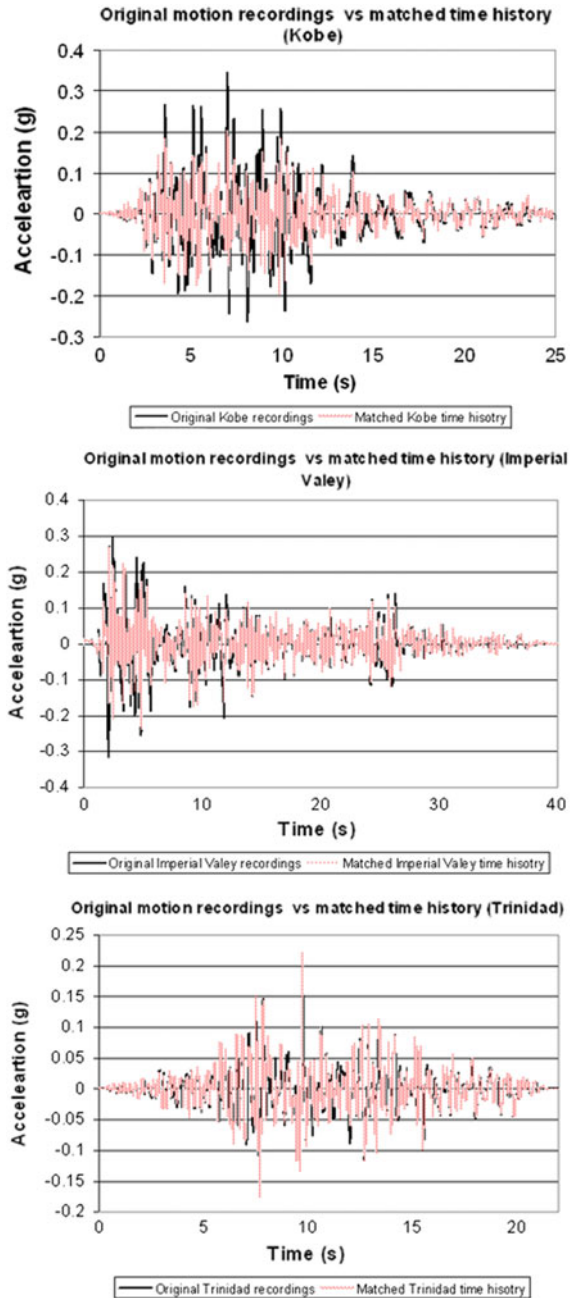


Fig. 4.1 Comparison between the target design rock spectrum and the response spectrum for 5% damping of **a** the three selected recordings (upper) and **b** the matched spectra and their average (lower)

The process of spectrum matching can be carried out by several commercial codes, such as SeismoMatch [567] or RspMatchEDT [230], through which the response spectrum of an individual motion record can be modified to match the target design spectrum.

Fig. 4.2 Comparison between the original motion recordings and the time history calculated from the matched spectra (Fig. 4.1) with 5% damping



4.3.3 *Pros and Cons of Direct Scaling and Spectrum Matching*

Both direct scaling and spectrum matching have merits and drawbacks.

Both methods are inconsistent with the physical conditions and can result in characteristics that differ from the ground motion recordings [310, 311], except for cases in which time histories are matched to a conditional mean spectrum (Sect. 11.4).

Direct scaling in certain senses retains the original ground motion characteristics, including peaks and valleys in the response spectrum. However, it is questionable, since scaling a ground motion does not account for variations in ground motion characteristics (e.g., frequency content), which change with intensity [312], i.e., extreme intensity ground motions have different frequency contents than low-intensity ground motions. This is more obvious for long-period ground motions. Moreover, natural periods for many structures are high, while ground motion records may not have such a long period; this hence requires a large scaling factor, which may result in unrealistic structural responses.

The drawbacks of simple scaling can be overcome by the spectrum matching method, which usually presents a larger number of cycles than the recorded ground motions, indicating a stronger ground motion for a wider range of structural periods, which implies a more conservative loading scenario [313]. However, since the spectrum matching method changes the frequency content of the original records, it may eliminate the inherent record-to-record spectral shape variability and the variability of the structural response. This drawback of spectrum matching has been realized by many researchers, and recent research [310, 314–318] shows a non-conservative bias in the median nonlinear displacement of structural models analyzed by a suite of matched ground motions compared to a suite of unmatched ground motions representing an equivalent scenario. Note that a time-domain analysis requires only a few ground motions to be analyzed. This may eliminate the variability of a structure's dynamic response if those ground motions are obtained from spectrum matching [319]. This bias appears to result partially from the scaled ground motions having inappropriate values of spectral shape or the parameter ε (Sect. 11.4), which is an indirect measure of spectral shape [555]. This bias is more apparent for uniform hazard spectra, which often represent unrealistic seismic motions, as they combine the statistical variability of several earthquakes rather than a single one. Therefore, a number of seismic design codes discourage the use of this method, or only permit its use with great care by fulfilling a list of strict criteria, or if several site-response analyses are performed, with the majority of the seismic motion time histories obtained from the real records and the rest (the minority) from calculation by the spectrum matching method, as recommended by the code for seismic design of buildings in China [199]. A recently proposed method to eliminate the bias due to the inappropriate values of spectral shape, or the parameter ε is to adopt a few conditional mean spectra conditioned at a number of periods of interests, which will be presented in Sect. 11.4.

Moreover, the duration of strong ground motion is dependent on magnitude and is not explicitly represented in a spectral shape [320], though peak displacement amplitude does tend to increase with time based on random vibration theory. Therefore, demand parameter depending on degradation (e.g., collapse capacity) may be biased if the duration is not included in the ground motion selection criteria.

4.4 Performing the Site-Response Analysis Using Modified/Matched Recordings

After selecting the ground motion recordings, a modification or matching of those recordings may be performed to fit them into the design response spectrum at bedrock/rock outcrop as has been presented in Sects. 4.2 and 4.3. By inputting the modified/matched motion histories at the bedrock/rock outcrop and carrying out site-response analysis, response time histories and response spectra at seabed can then be calculated. As mentioned before, most of the codes and standards, such as Eurocode 8 [198], Norsok N-003 [628], and China's building code [199], require using at least three bedrock motion histories to compute the ground motion time histories and the response spectra. ISO 19901-2 [289] requires a minimum of four and recommends that seven-time history analyses be used to capture the randomness in a seismic event.

As discussed in Sect. 3.5.1, as rock is generally not perfectly rigid, the motions at the base of the soil profile (rock) are not identical to that of the rock outcrop, while stations for measuring recordings are generally located on rock outcrop (or even soil layers) rather than the bedrock [220]. Therefore, the recordings are preferably assigned at a hypothetical bedrock outcrop (point 1 in Fig. 3.2) rather than the base of the soil profile (point 2 in Fig. 3.2). Moreover, it is noticed that, historically, seismic records have been measured on a variety of soil conditions, ranging from rock outcrop to very soft soil, but rarely at bedrock due to technical challenges. More recently, researchers have become more careful in selecting the locations for installing the accelerometers and tried their best to place the accelerometers on rock outcrops or very stiff soil.

It is recommended that one performs a sensitivity analysis. Accounting for the variation of soil properties from lower bound, average (best estimate) to upper-bound value may detect some significant impact of soil properties on the ground motions. If the ground motions are not sensitive to the variation of soil properties, typically, the best-estimate value of soil properties can be used to compute the ground motion time histories. Thereafter, a site-response analysis can be carried out typically by either equivalent linear analysis (Sect. 2.2) or by non-linear analysis. Various computation codes are available to perform this task, such as SHAKE 2000 or D-MOD2000.

The set of time histories of ground motions computed through a site-response analysis can then be directly used for calculating structural responses in time

domain. Alternatively, the set of response spectra obtained from the time histories of ground motions may be interpreted in some means (e.g., by taking the mean value of the all response spectra) and smoothed to develop one design response spectrum at seabed/ground surface, which can account for the contribution from all individual ground motion histories of the set of time histories, and be applied for calculating structural responses using response spectrum analysis, as will be presented in Chap. 11. Figure 3.38 shows an example of response spectra of three computed horizontal acceleration time-histories on the seabed/ground surface for earthquake events with a return period (Sect. 11.1.3) of 10,000 years. Using the average values of the three computed spectra, a design response spectrum can be obtained as shown in Fig. 3.39.

4.5 Sources of Ground Motion Recording Data

Records of seismic ground motions are essential for the development of earthquake engineering, for purposes such as to study the attenuation relationship, to calculate the site-specific ground motions, to develop the seismic hazard map. Fortunately, several databases of ground motion records have been made publicly available, accompanied by a number of earthquake and site parameters, such as earthquake magnitude, source-to-site distance, and ground type at the recording station. The best-known ones are listed below:

- The Pacific Earthquake Engineering Research Center, PEER (<http://peer.berkeley.edu/smcat/>)
- US Geological Survey (USGS) (<http://nsmg.wr.usgs.gov> for time histories of ground motion and <http://earthquake.usgs.gov/eqcenter/> for earthquake data)
- SeismicPortal (<http://www.seismicportal.eu/>)
- The National Geophysical Data Center, NGDC (<http://www.ngdc.noaa.gov/nndc/struts/form?t=101650&s=1&d=1>)
- The China Earthquake Data Centre (www.smsd-iem.net.cn)
- The Broadband Seismograph Network of Japan (www.fnet.bosai.go.jp)
- Kyoshin Network K-NET (at <http://www.k-net.bosai.go.jp/>)

The time history records in the databases above are normally corrected by the standard processing techniques that remove low- and high-frequency noise from them. This is because raw records may contain also nonstandard errors, and therefore, uncorrected records should not be used for the analyses [321]. The nonstandard errors include insufficient digitizer resolution, transversal wave trigger, insufficient sampling rate, multiple baselines, spikes, multiple shocks, early termination during recording and clipping [322].

Chapter 5

Soil–Structure Interaction

5.1 Introduction

The response of a structure under seismic excitations is affected by interactions between three connected structural parts: the structure, the foundation, and the soil underlying and surrounding the foundation [290]. A soil–structure interaction (SSI) analysis estimates the collective response of the entire system to specified ground motions by accounting for the effects of kinematic interaction (normally by site-response analysis), soil–foundation flexibility (foundation impedance), and inertia interaction (seismic structural analysis).

The motion of soil is different from what it would have been in the presence of the structure. Therefore, two obvious facts emphasize the importance of SSI. Firstly, the structural response due to ground motions for a structure on deformable soils can be significantly different from that of a structure supported on a rigid foundation. Secondly, the ground motion at the base of a structure and its vicinity can also be different from what it would be were there no structure standing above. Even for a relatively rigid structure supported on hard soils, SSI can still be important in that the relative stiffness between the structure and the foundation can significantly influence the energy and force transferring from the foundation to the structure. The effects of SSI generally increase the natural period of the structure and modify the damping ratio and seabed/ground motion with respect to amplitude, frequency content, and duration, thus affecting the structure's response.

Originally motivated by the design of infrastructures for which failure implies serious consequences, such as nuclear power plants, and which therefore require high safety measures for infrastructure and equipment, and SSI analysis is now widely used for various types of infrastructures both onland and offshore.

In a SSI analysis, two different mechanical problems need to be treated: those of the structures and of the surrounding soil media. In general, it is challenging or even impossible to obtain an analytical or even semi-analytical solution. Therefore, computational models are normally used for solving the problem. Practically, two

types of analysis approaches are available: direct analysis approach (Sect. 5.2.1) and substructure approach (Sect. 5.2.2). A successful implementation of SSI analysis often involves/requires collaborations between structural and geotechnical engineers.

5.2 Direct and Substructure Approach

5.2.1 Direct Analysis Approach

The direct analysis approach involves the direct modeling of a structure, foundations, and surrounding soils (represented as a continuum or a simplified soil–foundation interaction system) as an entire system and to compute the response at various parts. For a complex foundation–soil system, the direct analysis is often performed through finite element analysis. The solution is typically obtained in time domain by direct numerical integration. The approach can consider nonlinear behavior of soils and superstructures but requires a special consideration of the external fictitious boundary of the soil model to eliminate wave reflections (Sect. 5.7) and to apply seismic excitations. It is obvious that the required computational cost associated with the direct analysis approach is high, especially when the system is geometrically complex or contains significant nonlinearity in soils or structures.

5.2.2 Substructure Approach

For improving the computational efficiency, various types of frequency domain methods using the substructure approach can be adopted to address the influence from soils, even though this cannot explicitly account for the nonlinear effects of soil–structure interactions. In the substructure approach, the SSI problem is partitioned into distinct parts as soil, foundation, and superstructure. Their responses are first obtained independently and then combined to satisfy compatibility of forces and displacements and to formulate the complete solution.

Soil motions at free-field are calculated. Due to the soil nonlinearity, the corresponding soil material properties are then determined based on the strain level calculated for the free-field. This is followed by an evaluation of and converting free-field motions into foundation input motions, after which the foundation impedance, dealing with the coupling of soil to the lumped mass model to represent the stiffness and damping at the soil–foundation interface, can then be implemented to calculate responses under combined structure-impedance subjected to the foundation input motions. It is obvious that the substructure approach is normally limited to linear behavior and results in frequency-dependent equations that are

solved by using Fourier synthesis. In this approach, the interaction effects are typically accounted for by modeling a number of frequency-dependent springs and dashpots representing the flexibility of the soil and the radiation of energy away from the foundation, and they are attached to the fixed-base structural model.

From the discussion above, it is seen that obvious advantages of the substructure approach are the convenience for both modeling and computation: The approach requires few modifications to the fixed-base structural model and offers the possibility of using well-established techniques to derive the solution. However, a certain number of approximations (perhaps inaccuracies) appear in the aspects of foundation modeling (geometry, stiffness) and the soil behavior (elastic, linear), etc. [323].

Compared to bedrock/rock outcrop motion, seabed/ground surface motion due to SH-wave propagation is in many cases high, while the interaction usually eliminates the high-frequency motion and filters the motion to a narrow frequency motion. Furthermore, soil properties surrounding the foundation will also influence the stiffness of the foundation, which directly affect the structural response. Moreover, the overall stability of the offshore installations may be dominated by the strength of the local soil.

As discussed in Sect. 3.5.2, one-dimensional site-response analysis is normally performed due to its computation efficiency, and strictly speaking, it is only valid if soil layers are horizontal and extend infinitely in the horizontal direction. Even if this assumption is not strictly satisfied, in most cases, it is sufficiently valid for engineering purposes. Two-dimensional or three-dimensional ground response analysis (Sect. 3.7) can take more effects associated with wave propagation and site geometry into account, and it is normally performed by finite element analysis.

By partitioning the soil–structure system into a simpler set of soil and upper structure, Fig. 5.1 illustrates a standard 3-step method in a substructure approach [325] for soil–structure interaction analysis. It includes both geotechnical analysis (kinematic interaction and subgrade impedances) and structural analysis (inertia interaction), which will be presented in Sects. 5.3–5.5.

For linear and equivalent linear analyses, the effects of kinematic interaction and inertia interaction can be separated. This means that one can first obtain the kinematic interaction and use it as input for structural analysis. By combining the results from both analyses, the overall response can be obtained.

It should be noted that SSI analysis is not only applied in earthquake engineering, but also in problems involving vibrations or impulses transmitted to soils and wave propagating through soils that can result in vibrations of structures nearby. An example is transmissions of soil vibrations (due to, for example, construction activities) to the upper structure, which influence the inhabitant comfort and even the safety of structures.

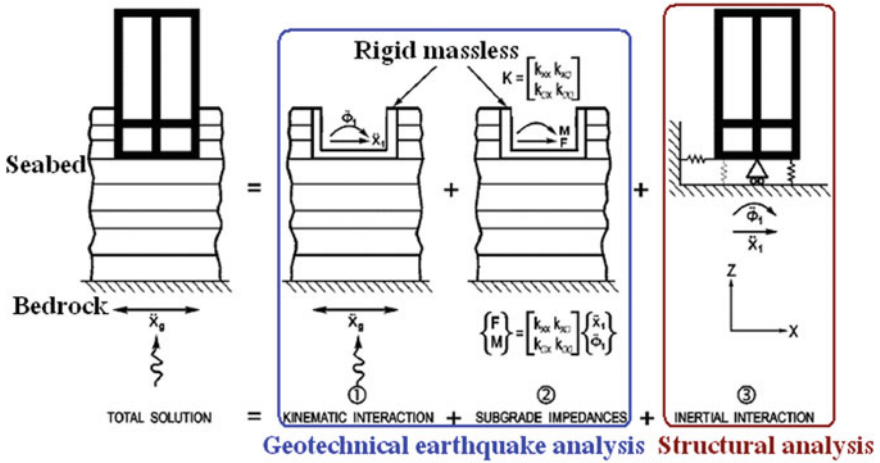


Fig. 5.1 Schematic illustration of 3-step method in engineering practice to represent the actual soil–foundation–structure interactions [324]

5.3 Kinematic Interaction

5.3.1 Objective

The purpose of the kinematic interaction is to compute the motions (\ddot{x}_1 and $\ddot{\phi}_1$) at soil surface or a designated location in soils for given bedrock motions \ddot{x}_g . This is often referred to as site-response analysis or ground response analysis, as presented in Chap. 3.

Ground motion induces the soil deformation known as free-field motion. However, the foundation embedded in the soil will not follow the free-field motion. This inability of the foundation to match the free-field motion leads to the kinematic interaction. Practically, it calculates the motion of a rigid massless foundation at seabed/ground surface subject to the same bedrock seismic excitation \ddot{x}_g as the original structure and soil, and the modeled foundation has the identical shape as the actual foundation. As a starting point, the conventional method based on one-dimensional SH-wave propagation model and linear or equivalent linear soil modeling (Sect. 2.3) may be used. However, if significant soil nonlinearities associated with stiffness and damping are relevant, as typically is the case at high strain levels, nonlinear soil models (Sect. 2.4) have to be implemented. Sometimes, in a kinematic interaction analysis, the influence of foundation on soil properties (especially shear modulus) is neglected, making the calculated motions identical to that of the free-field motions.

The earthquake input motion should be known, either at a specific point (e.g., ground surface, bedrock, rock outcrop, or a soil layer) or in the form of incident waves (e.g., oblique shear waves) propagating up from a reference depth.

For validating analysis, one may use a comparison of calculated and frequency contents and those measured by Fourier amplitude spectrum or response spectrum. This is because a single comparison of peak ground responses between the calculated and measured one may not sufficiently reflect all aspects of differences.

5.3.2 Applications

See site-response analysis in Chap. 3.

5.4 Subgrade Impedances and Damping

5.4.1 Objective

The purpose of this step is to calculate the frequency-dependent impedance representing the foundation stiffness and dashpots of soil media surrounding the foundation, taking the embedment and soil layers into account.

5.4.2 Applications for Pile Foundations

For pile foundations, if the mode shape and the period range of interest for a structure are significantly different from that of the foundation–soil system, the frequency dependence can be neglected, and a static nonlinear pile–soil interaction analysis (Sect. 15.2) can then be performed to determine the foundation impedance. In this task, soil modulus compatible with strain as calculated from kinematic interaction analysis (Sect. 5.3) can be used. Various numerical pile–soil interaction analysis codes such as *splice* [326] can be used for this task.

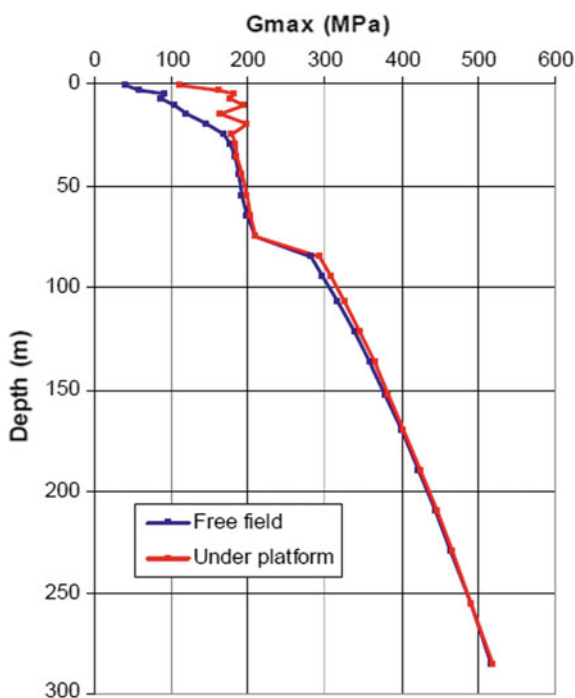
However, if the frequency dependence cannot be neglected, in order to calculate the dynamic stiffness matrix of a foundation, one should first compute the corresponding flexibility matrix by applying unit harmonic forces and moments (at a frequency range that is of interests) to the foundation. The inverse of the flexibility matrix gives the stiffness matrix. In practice, dynamic analyses by modeling the soil and piles subjected to the harmonic loadings have to be performed either by analytical methods or by finite element analyses, using numerical codes such as *SASSI* [327] or *PLAXIS Dynamics* [328], or by *DYNAN* [329]. The first two of these are FEM-based codes, while *DYNAN* is based on the improved Novak's method [330], where a non-reflective boundary is formed between the near-field and far-field to account for the mass of soil in the boundary. Note that the codes above are suitable to calculate the impedance for both pile and shallow foundations.

5.4.3 Applications for Shallow Foundations

For shallow foundations, the presence of the platform will influence the maximum shear stiffness G_{\max} as shown in Fig. 5.2, which can be obtained from laboratory or in situ test results (see Chap. 6 for details of relevant seismic testing methods). It is also shown that the effects are more significant at ground surface than at deep soils. This influence may be significant for soils under a heavy gravity-based structure (GBS) foundation. However, for soils around pile foundations, the effects are minor and can normally be neglected in engineering practice.

Similar to that of the pile foundation, both analytical and FE analyses can be utilized to calculate the subgrade impedances. Figure 5.3 illustrates an example of modeling for calculating the foundation impedance of a GBS structure. The foundation was replaced by a plate. The core area (corresponding to the outer boundary of the GBS shafts) is assumed to be rigid, and the rest (representing the caissons outside the shafts) is modeled as a flexible plate. The soil is assumed to consist of two regions (Figs. 5.3 and 13.7): the interior region, corresponding to the soil mass under the foundation with increased stiffness due to the overburden pressure influenced by the platform weight, and the exterior region consisting of the free-field surrounding the interior region. For the exterior region, the strain-compatible shear moduli computed by the site-response analyses can often be used. The shear modulus of each soil layer in the interior region is often reduced by

Fig. 5.2 Illustration of the maximum shear stiffness varied with soil depth due to the presence of a GBS platform and its free-field counterpart (without the presence of the platform) (courtesy of Aker Solutions and NGI)



the same factor as the reduction of shear modulus of that layer based on the free-field site-response analyses. For more details on the calculation of impedance and damping, see Sect. 12.9.

Similar to that of the pile foundation, the computation of foundation impedances and damping for shallow foundations can also be performed by commercial codes such as the geotechnical finite element code SASSI [327], which is a 3D nonlinear SSI analysis code based on the so-called flexible volume method. The most powerful feature of this code is its transmitting boundary that makes it possible to accurately represent infinite systems, such as soil media. In a SASSI model, the ground is modeled by viscoelastic properties of soil layers, and the main input for each layer is thickness, Poisson’s ratio, soil density, and shear wave velocity. The structure can be represented by beam, plate, and solid elements or a combination of them.

The complexity of the SSI problem can be significantly simplified if the foundation of the structure can be assumed as rigid, which reduces the number of additional degrees of freedom to account for the interaction, making it possible to present general results that can be used for different structures (the substructure approach for linear models).

By modeling the structure as an elastic circular wedge supported by a flexible circular foundation embedded into a half-space and excited by incident plane SH-wave (Fig. 5.4), Todorovska and his co-workers [331] studied the transfer function between the displacement of the wedge and the incident wave. They concluded that a foundation with the same mass density as the soil but 50 times larger shear modulus can essentially be regarded as a “rigid” foundation. If the ratio of shear moduli between the foundation and the soil is less than 16, the rigid foundation assumption cannot be justified.

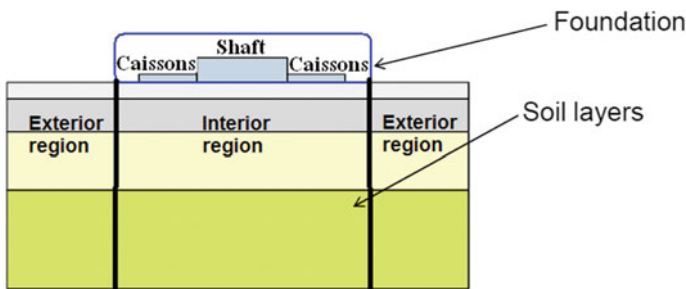


Fig. 5.3 Illustration of a simplified physical modeling for calculating the foundation impedances for a GBS foundation

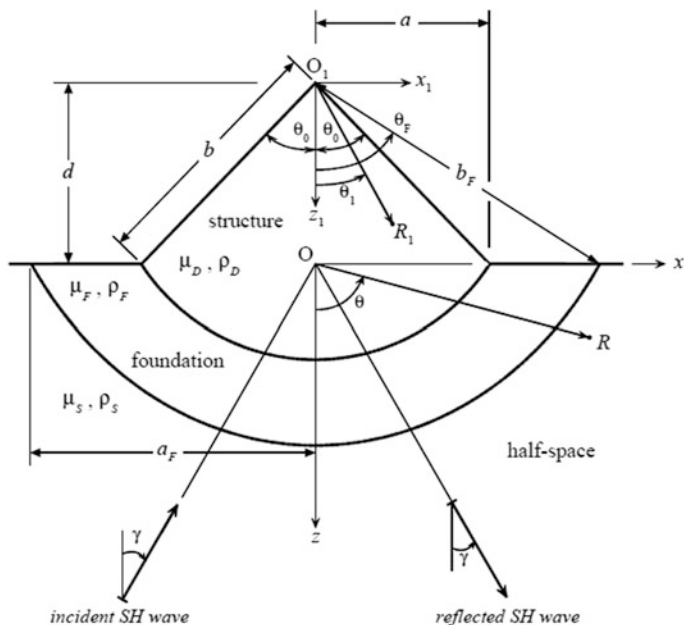


Fig. 5.4 Analytical model of a circular wedge (structure) supported by a flexible circular foundation embedded into a half-space and excited by incident plane SH-waves [331]

5.5 Inertial Interaction

5.5.1 Objective

Inertial interaction is used to calculate the dynamic response of a structure supported on a foundation modeled by foundation impedance (Sect. 5.4) and subjected at the base to the excitation time histories (\ddot{x}_1 and $\ddot{\phi}_1$) obtained in kinematic interaction analysis (Sect. 5.3).

While kinematic interaction and subgrade impedance are related to geotechnical earthquake analysis, inertia interaction analysis is essentially a structural analysis as illustrated in Fig. 5.1.

The major objective of seismic structural analysis is to develop a quantitative measure or a transfer function that can convert the strong ground motions at a structure's foundation into loading and displacement demands of the structure, which provides essential input for a reliable assessment of structural capacity.

Traditional methods work by accounting for various aspects of structural effects due to nonlinearity and dynamics. With respect to ground motion characteristics, several methods can also account for effects due to spatial variation, non-Gaussian, and non-stationary properties. The five traditional seismic analysis methods are as follows [188]:

- Simplified static coefficient method
- Response spectrum analysis
- Nonlinear static pushover analysis
- Random vibration analysis
- Nonlinear dynamic time-domain analysis

It should be emphasized that the engineering intention behind earthquake-resistant design is not to make earthquake-proof structures that will not get damaged during even the rare extremely strong earthquake as such structures will be too robust and expensive to build. Instead, engineers should design structures to resist the effects of strong ground motions in such a way that damages to structures can be significant in case ground motions are significant (associated with an extremely high return period), but the system integrity of the structures shall be maintained and structural collapse will not occur; while under minor earthquakes, infrastructures should remain intact. Subject to ground motions at the intermediate level (between strong and minor), local damage to infrastructures is allowable but should be repairable. However, this latter requirement is in many senses difficult for engineers to manage because the definition of “repairable” is not explicit.

With the advent of performance-based design (PBD) [332] for land-based structures, which is a design philosophy for engineers to manage the cost of construction as well as maintaining the safety and functionality performance of structures in an efficient manner, various seismic analysis methods are emerging. Note that while traditional seismic analysis methods aim for accuracy of the calculated responses, the recently developed methods place more focus on the compatibility between the structural response calculation and the evaluation of detailed performance demand, on revealing a structure’s intrinsic seismic response and essential performance characteristics, and on improving the robustness of seismic load estimation and analysis results. This is because the random nature of seismic loading makes the satisfactory prediction of seismic response an extremely difficult task. Therefore, it would be unwise to place too strong a focus on the accuracy of calculated seismic response. To cope with the requirements above, the most widely presented or researched methods are [188]:

- Incremental dynamic analysis (IDA), also named dynamic pushover analysis
- Endurance time analysis (ETA)
- Hybrid method
- Probability-based seismic design (PBSD)
- Critical excitation analysis
- Wavelet analysis

However, it is noticed that structural engineering, and especially that for designs related to offshore structures, appears not to have kept pace with the newly developed methods. This is mainly due to the difficulties of implementing PBD in structural design.

Furthermore, readers need to bear in mind that regardless of the sophistication of the numerical methods, it is not exact. Many uncertainties still exist. Therefore, in

the development of new methods for future seismic analysis, even more attention should be paid to the robustness of their performance.

For more details about the various types of seismic analysis methods and their theoretical background, sources [123, 188, 169] are recommended.

5.5.2 Applications

See Chapter 15 in source [188] for the applications of seismic analysis method.

5.6 Effects of Soil–Structure Interaction

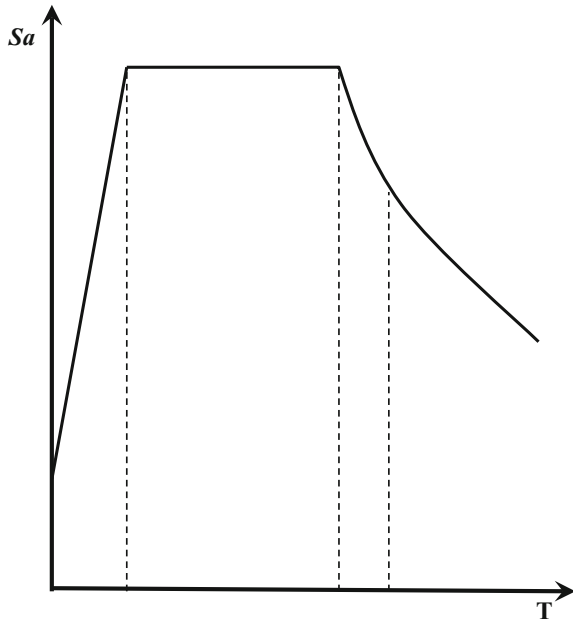
In general, the soil–structure interaction can be rather significant for stiff structures resting on soft soil sites, while it may not be that significant for soft (flexible) structures founded on stiff soil deposits. The natural period of the soil–structure system is longer than that of a fixed-base structure. The ground motions due to SSI may be amplified or de-amplified, and their estimation is important for attaining dedicated seismic designs of structures.

The main effects of SSI on structural response are softening a structure's foundation, thus lengthening the natural period of the structure and increasing damping of the foundation–structure system.

The SSI has traditionally been considered to have dominating beneficial effects because it was believed to cause a reduction of dynamic forces (e.g., bending moments and shear forces) applied on structures. This is mainly due to an increase in the structures' natural period and increased damping associated with soil deformability. By observing a smooth design acceleration spectrum as shown in Fig. 5.5, which has an essentially constant acceleration branch and a declining acceleration branch, it is noticed that an increase in natural periods of structures may lead to a decrease of accelerations in structures and foundations. The damping involved in the SSI is generally beneficial to reduce dynamic responses of the upper structure. Furthermore, soft soil foundations increase the flexibility of superstructures and generally reduce the responses at the superstructures.

Those beneficial effects above have been realized by various design codes by suggesting that SSI effects in a seismic analysis can be neglected. However, this conservative simplification is only valid for certain types of structures and soil conditions, such as light structures in relatively stiff soils. Neglecting SSI may lead to an unsafe design for both superstructures and foundations. From a geotechnical earthquake engineering point of view, soft soil sediments can significantly increase the period of seismic waves, and this is reflected in the design acceleration spectrum with a higher period range of constant acceleration plateau up to 1 s for soft soil than a lower period range for stiff soil. This effect can be seen in the spectra of ground motion records of the earthquakes in Brancea 1977, Michoacan 1985, and

Fig. 5.5 A schematic illustration of a seismic design acceleration spectrum (linear scale)



Kobe 1995 [333]. From the seismological rather than geotechnical nature point of view, the fault-rupture propagation toward a site, referred to as forward fault-rupture directivity causes most of the seismic rupture energy to arrive in the form of a long-period pulse of motion, which increases the spectral values of the horizontal component normal to the fault strike at periods longer than about 0.5 s [334]. From a structural engineering point of view, with the presence of SSI, the natural period of a structure is increased, which may induce the resonance of the structure when it is subjected to longer period ground motions due to SSI. Therefore, the effects of SSI are not beneficial if the lower order eigenfrequencies of superstructures are close to the dominant frequency of ground shaking. It is particularly important to make a dedicated accounting for the effects of SSI if the superstructure is heavy and the soil is soft [345]. Therefore, as a result of geotechnical, seismological, and structural factors, the effects of SSI increase the fundamental period for both soils and structures and may even increase the structural response under certain circumstances.

5.7 Boundary Modeling in Geotechnical Analysis

In a two- and three-dimensional site-response analysis or soil–structure analysis, one has to model the soil strata with infinite extent in the horizontal direction, and the extent in the vertical direction needs also to be adequately represented, i.e., both

concerns have to be carefully considered by a model with finite size. The far-field soil medium is often modeled by restricting the theoretically infinite computational domain to a finite one by using artificial boundaries so that the reduction of the solution domain makes the analysis feasible and economical. However, the performance of the artificial boundaries can influence the accuracy of the results significantly.

There are mainly three types of artificial boundary modelings:

1. Elementary boundaries, which are commonly used for static analyses (i.e., zero stress or zero displacement boundary conditions), and they, therefore, cannot model the geometrical spreading of energy toward infinity. However, they are efficient in cases where the radiation damping is not important, such as soft soil–stiff rock interfaces
2. Consistent boundaries [335, 336], which satisfy exactly the radiation condition at the artificial boundary using mathematically complex formulations. However, in practice, both elementary and consistent boundaries are seldom adopted as they are computationally expensive, frequency-dependent, and their implementation in finite element codes is often problematic
3. To solve these challenges of both boundary modelings above, local absorbing boundary, also called energy absorbing boundary, energy transmitting boundary, silent boundary, transparent boundary, or infinite boundary is used, in which the radiation condition is satisfied approximately at the artificial boundary, as the solution is local in space and time. Local boundary modeling is widely used in engineering practice as in most cases it provides results with acceptable accuracy while requiring much less computational effort than more rigorous consistent boundaries

Lysmer and Kuhlemeyer [337] proposed a simple viscous local boundary modeling, which comprises two series of dashpots oriented normal and tangential to the boundary of FE mesh. As characteristics of viscous local boundary are independent of frequency, the viscous boundary modeling is suitable for both harmonic and non-harmonic waves. However, it gives exact solution only for one-dimensional propagation of body waves, while for two- and three-dimensional cases perfect absorption is achieved only for angles of incidence greater than 30° . As seismic waves with large angle of incidence are less likely to develop, the performance of the viscous local boundary improves significantly if it is placed farther away from the source of excitation or the area of interest (i.e., foundations or structures) of the model. Furthermore, for low-frequency excitations, this type of boundary modeling gives permanent displacement even in an elastic system [338]. Therefore, modifications of the standard viscous boundary were proposed, such as the boundaries using Kelvin elements [339, 340], the doubly asymptotic multi-directional boundary [341], and the cone boundary [342]. Interested readers may read the sources cited above.

The realization of the boundary modeling in finite element analyses is to introduce a fictitious “box”: If the boundary of the “box” is modeled very close to

the foundation, the seismic energy that should realistically be dissipated will numerically reflect back into the “box,” thus distorting its dynamic characteristics and changing responses of foundations and supported structures [343]. However, locating the boundaries very far from the foundation requires more modeling and computational efforts. Therefore, a local absorbing boundary to absorb the seismic wave energy has to be introduced to account for the radiation of the energy into the regions outside the “box,” thus reducing the infinite system into one with finite size, as previously discussed. In finite element modeling, the boundary is often modeled with energy absorbing meshes adopting large element size or energy absorbing boundaries. For example, nodal damping coefficient can be modeled at lateral exterior nodes to prevent reflections of energy back to the “box” from the lateral surfaces. Calculations of the damping coefficient may be based on the theory of equilibrium between the soil wave force and the damping force. The damping coefficient is specified as force per velocity (N/(m/s)) where the velocity is the relative motion between two nodes [344]:

$$D_c = A_n \rho v_s \quad (5.1)$$

where A_n is the area of a node face (m²); ρ is the density of the soil; v_s is the seismic wave velocity of the soil.

In finite element analyses of foundation dynamics, the element size must be carefully selected because larger elements induce a filtering effect on stress waves in the higher frequency range. This is particularly obvious in geotechnical earthquake engineering as seismic waves are normally dominated by high-frequency components. The maximum mesh size l can be selected as a function of the shear wave propagation velocity v_s and maximum frequency component of seismic motions f_{\max} :

$$l = b v_s / f_{\max} \quad (5.2)$$

b is a factor depending on the type of element (linear or quadratic) used, and it normally ranges from 0.1 to 0.25.

5.8 Remarks on Substructure Approach

The 3-step method in the substructure approach is practically exact from a mathematical point of view, i.e., the response of an upper structure is not significantly influenced by the simplification in the substructure approach (partitioning the soil–structure system into soil and the upper structure). On the other hand, due to the fact that the kinematic interaction is estimated based on a massless foundation modeling, the method gives unreliable results for conditions in which nonlinear soil behavior is significant.

Since the method to implement impedance functions is essentially a frequency domain approach, when performing seismic analyses in time domain, the frequency

domain solutions for soil must be converted into an equivalent soil model in time domain.

For structures supported on soft soils or sites under strong ground shaking, a dedicated site-response analysis rather than a simplification is preferred.

For important structural elements, such as the base of a shear wall, massless elastic springs can often be used to estimate the foundation stiffness. For massive structures, such as large and heavy offshore GBS structures or gravity dams, a part of the foundation may be modeled by three-dimensional solid elements.

Chapter 6

Seismic Testing

6.1 Introduction

To model important dynamic properties of soils for designing of geotechnical structures, various field and laboratory testing techniques are developed.

Even though the strength parameters are essential for assessing geotechnical problems, deformation characteristics are also important in the performance evaluation of geotechnical engineering practice. Therefore, soil's shear modulus and damping at both small and large strain levels are important to perform site-response analyses and seismic assessments of foundations. As discussed in Sect. 2.3.1, at very small strain level, the soil stiffness and damping do not change or can be assumed to be constant in the elastic range; when the strain further increases into the small strain regime, the stiffness and the damping vary nonlinearly with the strain, as indicated in Fig. 2.12. At both very small strain and small strain regimes, soil properties that influence the seismic wave propagation and other low-strain behavior should be measured, which basically comprise the shear modulus, damping, Poisson's ratio, and density. Among them, the shear modulus and damping are the most important ones to influence the soil's dynamic response. When soil strain is further increased to high strain level, the soil is close to failure, the soil stiffness is relatively small, and strength parameters are essential to assess the soil behavior and foundation integrity. The measurement of strength parameters under monotonic loading has been discussed in Sect. 1.9.

Since in many cases, soil properties due to applied monotonic loading and cyclic loading are quite different, the measurement of soil properties due to applied cyclic loading will be further discussed in this chapter. Relevant testing tools may therefore be different, or at least a modified version of monotonic loading tests has to be adopted to measure soil properties under cyclic loading.

Tests or test procedures that characterize soil behaviors may need to apply initial stress conditions and anticipate cyclic loading as best as possible. Field or in situ tests have the advantage that the state of stress is inherently included in the

procedure. However, laboratory tests need to confine and consolidate the soil sample back to the state of stress to replicate field conditions [113]. Larsson and Mulabdic [346] stated that laboratory values of shear modulus are typically lower than those measured in the field due to the disturbance caused by the sampling process. For example, they proposed using a strain-based correction factor of about 10% at a shear strain level of 10^{-5} .

6.2 Field Testing

6.2.1 General

As the soil specimen used in laboratory tests is often disturbed or subjected to errors due to sample disturbance, field tests are a more reliable way to measure dynamic soil properties. In field tests at low soil strain levels, seismic waves are generated artificially at sources. Sensors/receivers (geophone or accelerometers) are used to detect the seismic wave and to measure wave travel time. Based on the distance corresponding to the wave traveling, seismic wave velocity, or the velocity difference between different types of waves, soil properties can be determined.

The source generating the seismic wave usually has a limited power, and the strain amplitude in the traveling wave is very small (in an order of 10^{-6} as discussed in Sect. 2.3.1); thus, the seismic wave velocity measured in tests also shows values corresponding to this low strain level, and soil behaves almost linear-elastically. The stiffness modulus can be assumed to be constant in the elastic range. The relevant methods will be discussed in Sect. 6.2.2.

However, at high strain, field tests are also needed to obtain the soil strength, normally without generating seismic waves, as presented in Sects. 6.2.3 and 1.9.

6.2.2 Low-Strain Field Test

Active low-strain field tests, sometimes called geophysical tests, are nondestructive tests that work by applying an active source of energy to excite soil mass, thus inducing measureable seismic waves. This type of test has the advantage of reducing time and cost of drilling, and also avoiding the potential environmental consequences of drilling.

Figure 6.1 shows different methods to generate P-wave, S-wave, and Rayleigh wave. Using either (a) vertical impact or (b) shallow explosive can effectively generate P-wave. SH-wave (c) can be generated by horizontally striking with a sledge-hammer a horizontal wood member pressed tightly to the ground surface. Rayleigh wave is the major component of ground vibration caused by (d) traffics

and construction works such as pile driving. The relative amplitudes of each wave depend on how the impulse is generated.

In case ground water is present in the soil that is of interest, it is customary to measure S-wave rather than P-wave in order to determine the shear modulus. This is because P-wave still propagates in water and travels at a speed of around 1500 m/s in soft saturated soil deposits even though the velocity of P-wave is not indicative of the soil skeleton stiffness of soft and saturated soil. Moreover, during the geophysical test, one should consider anisotropic stress conditions that may cause the measured shear wave velocities to vary with directions of wave propagation and particle movement [347, 348].

As the shear strain during the test is quite small and below 0.001%, which is difficult or impossible to measure, elastic theory of wave propagation can be used to relate the measured seismic wave propagation velocity with the shear modulus of soil media.

Field measurements of seismic wave velocity include surface reflection test (Sect. 6.2.2.1), surface refraction test (Sect. 6.2.2.2), spectral analysis of surface waves (SASW) (Sect. 6.2.2.3), cross-hole test (CHT) (Sect. 6.2.2.4), down-hole test (DHT) (Sect. 6.2.2.5), seismic cone penetrometer test (Sect. 6.2.2.6), and suspension logging test (Sect. 6.2.2.7). The first three methods are nondestructive because they require no borehole.

Each method has its limitations in terms of the testing applicability and the type of results it can provide. Therefore, it may be preferred to combine several seismic testing methods to enhance strengths and minimize the effects of the drawbacks of each method. As an example, sometimes it can be necessary to obtain the distribution of both strength at high strain and stiffness at low strain of soil columns. Therefore, tests applied to each strain category must be employed, such as using SPT and cross-hole test to measure the strength (at high strain) and stiffness (at low strain) parameters, respectively. The data obtained from a combination of these two tests are shown in Fig. 6.2. Another example is the operation of the seismic cone penetrometer test, as will be presented in Sect. 6.2.2.6.

In addition to using an active source to generate the seismic wave for measurement, background noise and microseismicity due to frequent minor earthquakes

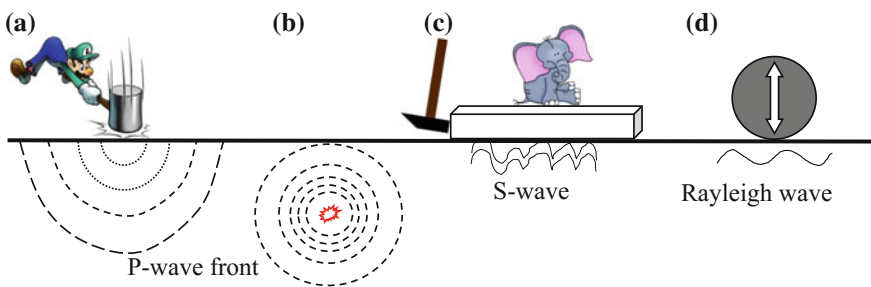


Fig. 6.1 Methods to create impulse waves: **a** vertical impact; **b** shallow explosive; **c** horizontal impact; and **d** frequency-controlled surface waves

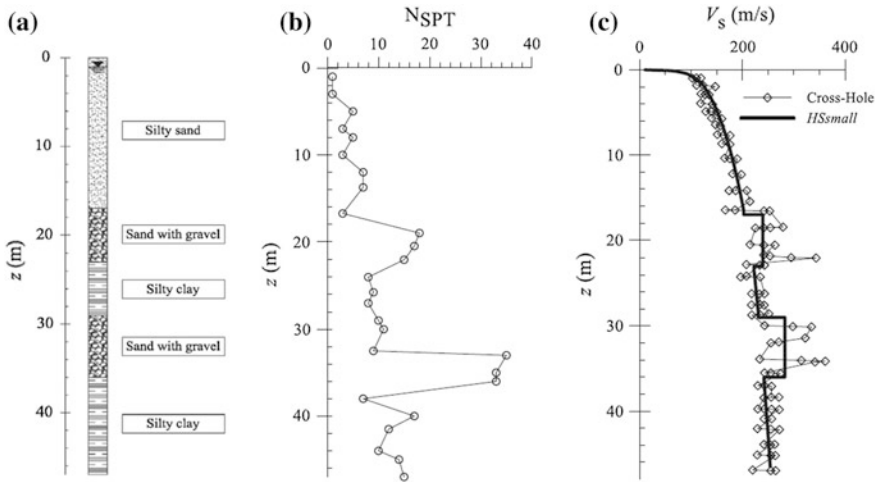


Fig. 6.2 Local soil profile at a site: **a** soil stratigraphy; **b** SPT-N values versus depth; **c** shear wave velocity profile from cross-hole test [349]

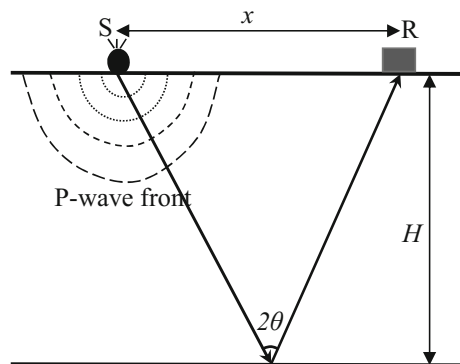
or construction activities can be taken as a passive system to generate acoustic and seismic emissions, which can also be measured to characterize soil properties.

It is noted that advanced signal-processing capabilities, mostly developed by the petroleum industry, are increasingly adopted in geotechnical field testing.

6.2.2.1 Surface Reflection Test

As shown in Fig. 6.3, the surface reflection method basically places both the active source (S) and receiver(s) (R) on the ground surface. The source can be mechanical sources that are vertically oriented, or explosive sources that generate impulses

Fig. 6.3 Illustration of surface reflection method (adapted from [1])



usually rich in P-wave. It is then reflected from interfaces at depth and monitored with vertically sensitive geophones [350].

Part of the wave energy will be transmitted directly from S to R, and by measuring the transmission time t_d and distance of the direct path x (S to R), the P-wave velocity v_{p1} of the upper soil layer can be calculated as:

$$v_{p1} = x/t_d \quad (6.1)$$

Another part of wave energy travels downward, strikes the horizontal layer boundary at an angle of incidence θ (Fig. 6.3), and is then reflected back to the receiver(s) at the ground surface. The traveling time (t_r) of the reflected wave is:

$$t_r = \frac{2\sqrt{H^2 + \left(\frac{x}{2}\right)^2}}{v_{p1}} \quad (6.2)$$

By knowing the v_{p1} (from the direct wave calculation), x , and measured t_r , the thickness of the upper layer can be calculated as:

$$H = \frac{1}{2}\sqrt{t_r^2 v_{p1}^2 - x^2} \quad (6.3)$$

In case the site's soil layering is not horizontal, multiple measurements at different locations have to be performed in order to determine the profile of soil layering.

The surface reflection test is often used for investigations of large-scale and/or very deep stratigraphy. For example, it is an important tool in identifying and characterizing seismogenic sources and capable (neotectonic) faults. It is rarely used for delineation of shallow soil layers [1].

Different patterns of the source-receiver layout can be used in the surface reflection method to optimize the measurements, which depend on the specific application. For example, the normal moveout NMO pattern shown in Fig. 6.4 is used to estimate the average velocity of the formation. Detection of reflectors is usually obtained using the common offset pattern as shown in Fig. 6.5. The common depth point pattern is used to enhance the signal-to-noise ratio at a specific location as shown in Fig. 6.6 [350].

Advanced signal-processing capabilities, mostly developed by the petroleum industry, are available and becoming more widely used in geotechnical engineering.

Figure 6.7 shows an example of the layout of seismic reflection cross section of 24 geophone recording with 2.5 m spacing. Note that the vertical axis (times) essentially indicates the wave traveling velocity (soil stiffness), and significant impedance (black line) between 280 and 320-m s time can be identified, which actually corresponds to limestone interface contrasts for this particular site.

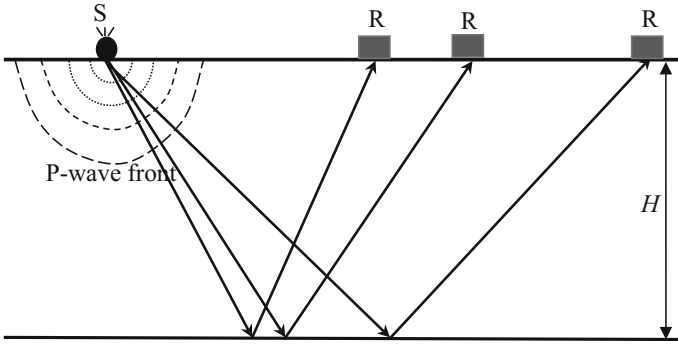


Fig. 6.4 Normal moveout (NMO) used in surface reflection tests

Fig. 6.5 Common offset used in surface reflection tests

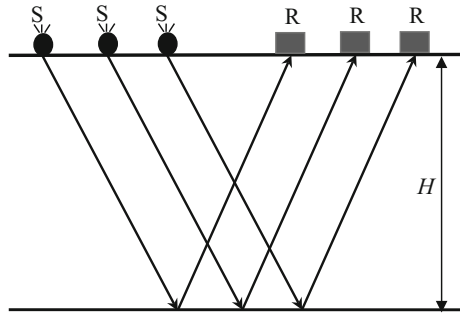
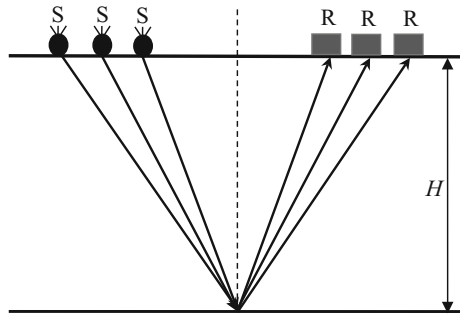


Fig. 6.6 Common depth point (CDP) used in surface reflection tests



6.2.2.2 Surface Refraction Test

Based on the ability to detect the arrival of seismic wave energy that is critically refracted from a higher velocity layer underlying lower velocity sediment, surface refraction test measures the travel time of P-wave and/or S-wave (practically, P-wave is more often investigated than S-wave) from an impulse source to a linear

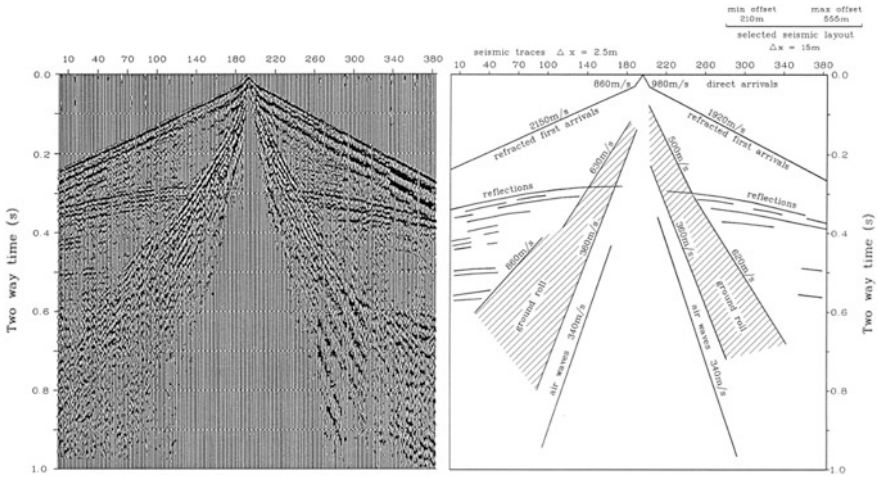


Fig. 6.7 Example of seismic reflection cross section for investigating the underground geology profile [351]

array of ground surface locations at various distances from the source. It is more widely used than the surface reflection test.

As illustrated in Fig. 6.8, during the test, the active impulsive source (vertical mechanical sources or explosives) located at or close to ground surface generates seismic waves. The waves then propagate into the ground and along the ground surface. The refracted waves on the ground surface are monitored by a series of linear array of receivers (usually vertically sensitive geophones).

As shown in Fig. 6.8, close to source with a horizontal distance x from the source, the first arrival of ground vibration is associated with the surface

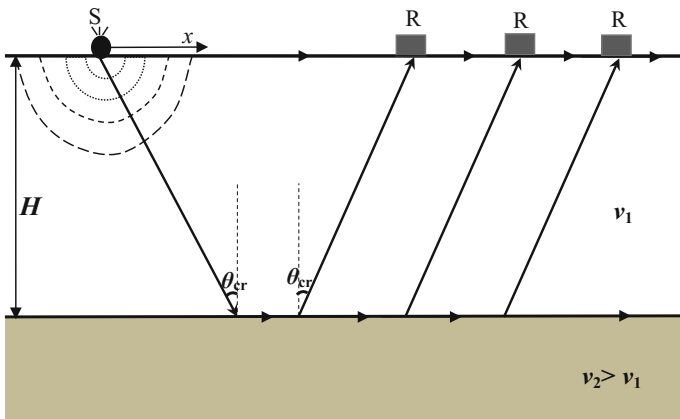


Fig. 6.8 Illustration of surface refraction test for a two-layered elastic half-plane

propagation in the form of a direct wave, which travels away from the source in all directions with a hemispherical wave front. The travel time is given by:

$$T = x/v_1 \quad (6.4)$$

where v_1 is the wave propagation velocity in the soil layer 1.

In addition to the direct wave, other waves travel toward the bottom of layer 1, and at the boundary between layer 1 and the underlying layer 2 (normally harder than layer 1), they are reflected and refracted. As shown in Fig. 6.9, according to Snell's law as presented in Sect. 3.7.1, for refracted waves traveling through media comprising isotropic materials, the ratio of the sines between the angles of incidence θ_1 and refraction θ_2 is equivalent to the ratio of phase velocities in the two media:

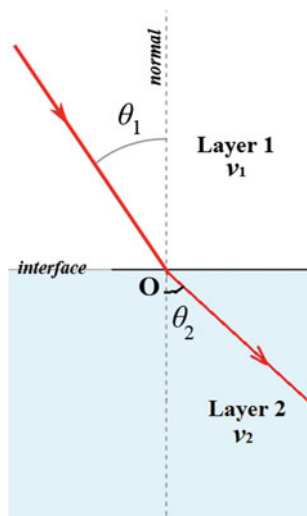
$$\sin \theta_1 / \sin \theta_2 = v_1 / v_2 \quad (6.5)$$

Therefore, when the angle of refraction $\theta_2 = 90^\circ$, i.e., the refracted wave travels parallel to the boundary/interface and produces a head wave in its adjacent layer, the corresponding angle of incidence wave θ_1 reaches a critical angle of incidence θ_{cr} :

$$\theta_{cr} = \arcsin(v_1 / v_2) \quad (6.6)$$

At a short distance, the direct wave generates the first arriving wave. At a distance greater than the critical distance x_{cr} from the source, the head wave arrives before the direct wave, the wave propagation downward at layer 1 is critically refracted along the harder underlying deposit (layer 2) and then critically refracted back up to layer 1. Its travel time can be calculated as:

Fig. 6.9 Refraction of waves between layer 1 and layer 2; layer 2 is of a harder medium than layer 1



$$T = 2H/(v_1 \cos \theta_{cr}) + (x - 2H \tan \theta_{cr}) / v_2 \tag{6.7}$$

It is noted that in the four equations above, H , v_1 , and v_2 are unknowns, and θ_{cr} is a function of v_1 and v_2 .

Figure 6.10 schematically illustrates the relationship between x and T based on measured data from surface refraction test. The data points are approximated by piece-wise linear curves. The slope of each individual curve in the travel time-distance diagram gives the value of wave velocity for each layer and the corresponding θ_{cr} . This travel time-distance diagram can also be transformed into wave velocity-depth curves.

For two-layer soil deposits, at a location the critical distance x_{cr1} from the source, the direct wave and refracted wave reach the receiver simultaneously, which gives:

$$\frac{x_{cr1}}{v_1} = \frac{x_{cr1}}{v_2} + 2H_1 \sqrt{\frac{1}{v_1^2} - \frac{1}{v_2^2}} \tag{6.8}$$

where H_1 is the thickness of the upper soil layer 1.

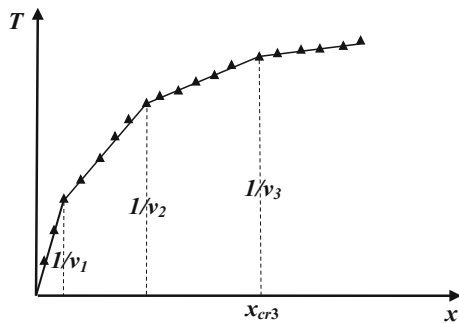
Therefore, the thickness of soil layer 1 can be calculated as:

$$H_1 = \frac{x_{cr1}}{2} + 2H_1 \sqrt{\frac{v_2 - v_1}{v_2 + v_1}} \tag{6.9}$$

For sites with multiple layers of soil, several intersection points can be found on the piece-wise linear curves shown in Fig. 6.10. The thickness of the m th layer can be calculated as [352]:

$$H_m = \frac{x_{crm}}{2} \sqrt{\frac{v_{m+1} - v_m}{v_{m+1} + v_m}} + \sum_{j=1}^{m-1} \left(\frac{H_j v_{m+1} \sqrt{v_m^2 - v_j^2} - v_m \sqrt{v_{m+1}^2 - v_j^2}}{v_j \sqrt{v_{m+1}^2 - v_m^2}} \right) \tag{6.10}$$

Fig. 6.10 Schematic illustration of a travel time-distance diagram



Surface refraction test is appropriate to detect boundaries and dipping layers at shallow depths with the wave velocity increasing with depth. Even though this is the case for the majority of site conditions, exceptions do exist. A lower velocity deposit underlying a higher velocity soil layer (velocity reversal) will not introduce an intersection point between two continuous piece-wise linear curves as shown in Fig. 6.10 [1]. Instead, the calculated depth of this layer boundary will be larger than that in reality [353]. Moreover, the refraction test cannot detect very thin layers or layers having insufficient wave velocity contrast with adjacent layers [354], which are referred to as blind zones. The presence of blind zones can cause the calculated depth of a deeper soil layer to be less than the actual depth [353].

Table 6.1 compares the pros and cons of the surface reflection test and surface refraction test methods.

At sites with inclined soil layers, the refraction test can be repeated in both positive and negative *X*-directions.

6.2.2.3 Surface Wave Method

The displacement at ground surface due to excitations from a vertical excitation source nearby is mainly caused by the Rayleigh wave energy transmission. Note that Rayleigh wave transmission produces both horizontal and vertical

Table 6.1 Pros and cons of surface reflection and surface refraction test method [355]

Reflection test method		Refraction test method	
Merits	Drawbacks	Merits	Drawbacks
Observations are collected at small source-receiver offsets	Many source and receiver locations must be used to produce meaningful images; expensive to acquire	Observation generally uses fewer source and receiver locations: relatively cheap to acquire	Observation requires relatively large source-receiver offset
Method can work no matter how the propagation speed varies with depth	Processing can be expensive as it is very computer intensive, needing sophisticated hardware and a high level of expertise	Little processing is needed except for trace scaling or filtering to help pick arrival times of the initial ground motion	Only works if the wave velocity increases with depth
Reflection observations can be more readily interpreted in terms of complex geology; subsurface directly imaged from observations	Interpretations require more sophistication and knowledge of the reflection process	Modeling and interpretation fairly straightforward	Observation generally interpreted in layers that can be dip and topography; produces simplified models

displacements; at a constant loading frequency ω , the ground surface will be distorted as shown in Fig. 6.11. During the vertical excitation of the source S, if one moves the receiver at various distances from the source to measure the vertical vibrations of the ground surface, locations where vibrations are in-phase with the source excitation can be found. Horizontal distances between the source and the adjacent locations where the vibrations are in-phase with those of the source are equal to the wave length of the Rayleigh wave λ_R . The Rayleigh wave phase velocity v_R can then be determined as:

$$v_R = \omega \lambda_R / 2\pi \tag{6.11}$$

Based on the value of v_R and the Poisson’s ratio, the shear wave velocity can be estimated according to relative velocity among shear wave, P-wave, and Rayleigh wave as shown in Fig. 6.12.

Based on the dispersion of Rayleigh waves in layered systems, i.e., the velocity of the wave is frequency-dependent, spectral analysis of surface waves (SASW) method has been proposed by plotting a Rayleigh wave dispersion curve, i.e., v_R

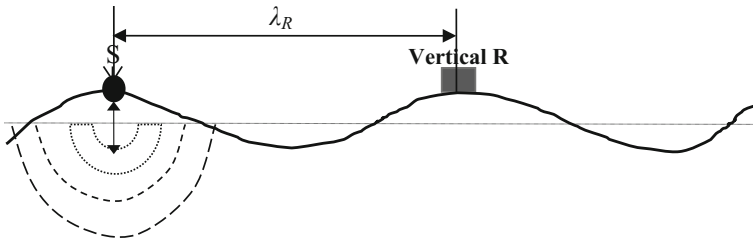
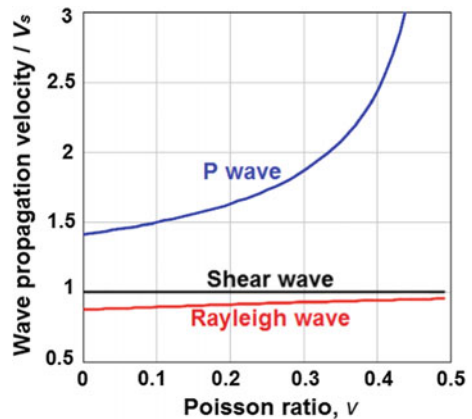


Fig. 6.11 Schematic illustrations of ground deformation induced by Rayleigh wave due to a vertically vibrating source (S)

Fig. 6.12 Variation of wave propagation velocity with different Poisson’s ratios



varies with frequency (wave length). Through the process of inversion of the dispersion curve, the shear wave velocity profile can then be determined.

As shown in Fig. 6.13, in a SASW, two vertical receivers were placed on the ground at an equal distance $\Delta d/2$ (Δd is typically taken to be equal to d_1) from a fixed centerline (CL). Note that producing a dispersion curve by conducting tests at different source excitation frequencies would be time consuming, and therefore the source excitation is typically in the form of impulse or random loading, which produces surface waves with a broadband frequency. With digital data acquisition and signal-processing devices, surface motion time history is then measured by a pair of transducers and transformed to the frequency domain using, for example, fast Fourier transform. The phase difference $\phi(f)$ for each frequency $f (= \omega/2\pi)$, which represents the phase difference between two receiver signals, was obtained. The Rayleigh wave length and phase velocity can then be calculated as:

$$\lambda_R(f) = v_R(f) / f = 2\pi\Delta d / \phi(f) \tag{6.12}$$

$$v_R(f) = \lambda_R(f) f \tag{6.13}$$

The two equations above give an experimental dispersion curve (v_R vs. λ_R) for the receiver spacing. Once all experimental dispersion curves for a set of receiver spacings are constructed, they are combined together and a composite experimental dispersion curve of the site can then be developed.

As a result of the varying shear stiffnesses along the depth of soil column, waves with different wave lengths travel at different phase velocities. A surface wave dispersion curve is the variation of v_R with λ_R or f , with an example shown in Fig. 6.14. This characteristic of the site is sometimes called the “signature” of the site.

As previously mentioned, the obvious advantages of SASW are that it does not require drilling, and compared to body waves, the attenuation of Rayleigh waves is low [188]. However, SASW has several drawbacks [350]. First, the accuracy of

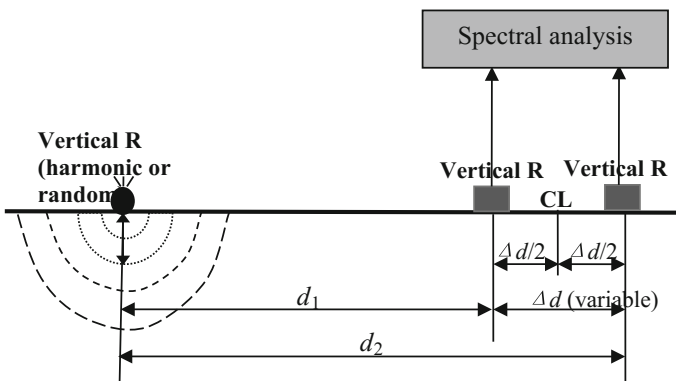
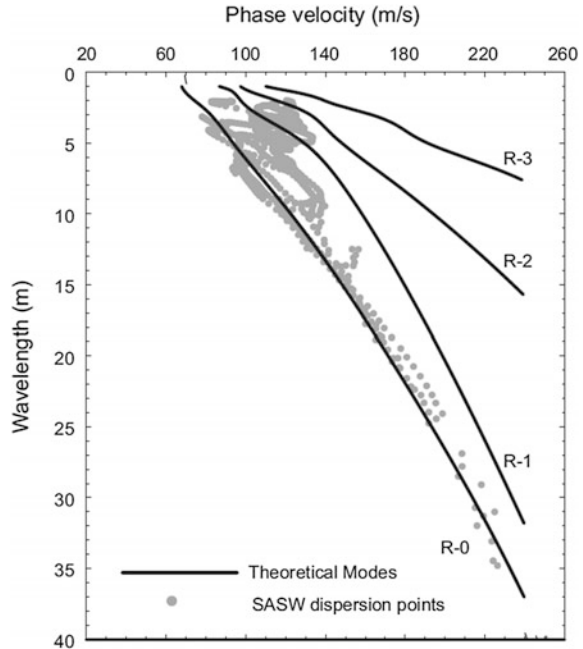


Fig. 6.13 Schematic illustrations of SASW

Fig. 6.14 SASW dispersion points and dispersion curves of fundamental (R-0) and higher orders of Rayleigh modes (R-1, R-2, and R-3) [360]



SASW decreases with an increase in depth below the ground surface (SASW can normally be used to considerable depth of more than 100 meters [1]). Secondly, thin layers those are either much stiffer or much softer than the surrounding material can be missed in an SASW. Moreover, a portion of each soil layer adjacent to a large velocity contrast is difficult to resolve.

Surface wave tests have been conducted both inland and offshore [356–359].

6.2.2.4 Cross-Hole Test

As shown in Fig. 6.15, the cross-hole test (CHT) involves generating seismic waves (P-wave, SV-wave, and SH-wave) in one borehole and measuring the wave propagation velocity along horizontal paths by geophones in two or more adjacent boreholes at the same depth. In order to investigate a complete profile of shear and compression wave velocities versus depth, the test is normally repeated at multiple depths. This method is only applied at sites on land, but is used extensively in such contexts.

The source can be either mechanical or explosive, with the mechanical being used more frequently. This is because, when the source is located in the borehole, it is more difficult to induce a variation of P-wave/S-wave content than is the case in a surface test method, and an explosive source generally produces more P-waves than does a mechanical source. In addition, a mechanical source also enables a reversible

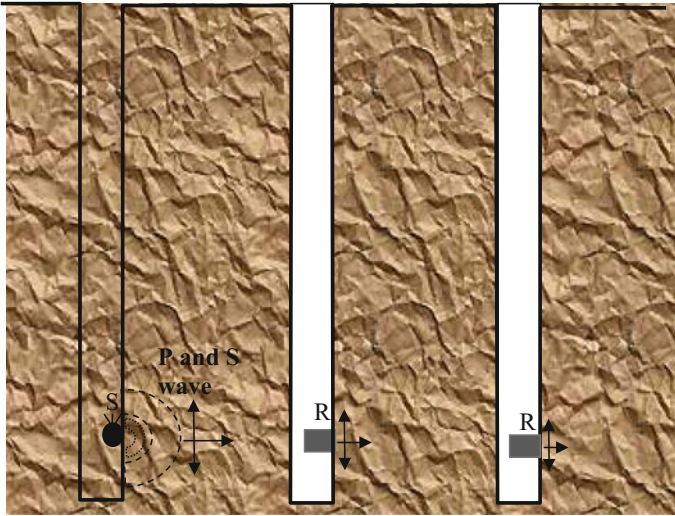


Fig. 6.15 Illustrations of cross-hole test

polarity of the impulse, which provides better measured results than do explosive sources. Mechanical sources include the driving of a SPT test sampler, vertical impact loading of rods connected to borehole packers or jacks, torsional impact loading of a torque foot at the bottom of borehole, etc. [1].

During a cross-hole test, by post-processing the measured time series of the source and the receiver(s), the times of travel from the source to the receiver(s) can be calculated, which is called direct travel times (upper figure in Fig. 6.16). The times of travel between receivers, called interval travel times (lower figure in Fig. 6.16), are measured. Figure 6.16 shows that P-wave motion first appears in the receiver's signal measurement. However, this was not influenced by the polarity of the impact, and it is a later time instant at which the SV-wave arrives and the polarity is reversed due to the reversal of impact polarity. Based on the time-of-travel measurements between source and one or more receivers, the shear wave velocity can be determined by dividing the borehole spacings at the testing depth by the respective travel times.

Compare to surface test methods, cross-hole test can increase the resolution of the results for various depths of soil and it generally yields reliable results to depths of 30–60 m. However, it requires drilling in order to place the source and the receiver(s). Therefore, more efforts are required to carry out this test than for surface test methods, making it more expensive to perform than a down-hole test (Sect. 6.2.2.5). On the other hand, if three or more holes can be drilled, shear wave propagation can be measured at various distances from the source, and the decrease/decay in shear wave amplitude can be measured and used to directly calculate the damping of the soils.

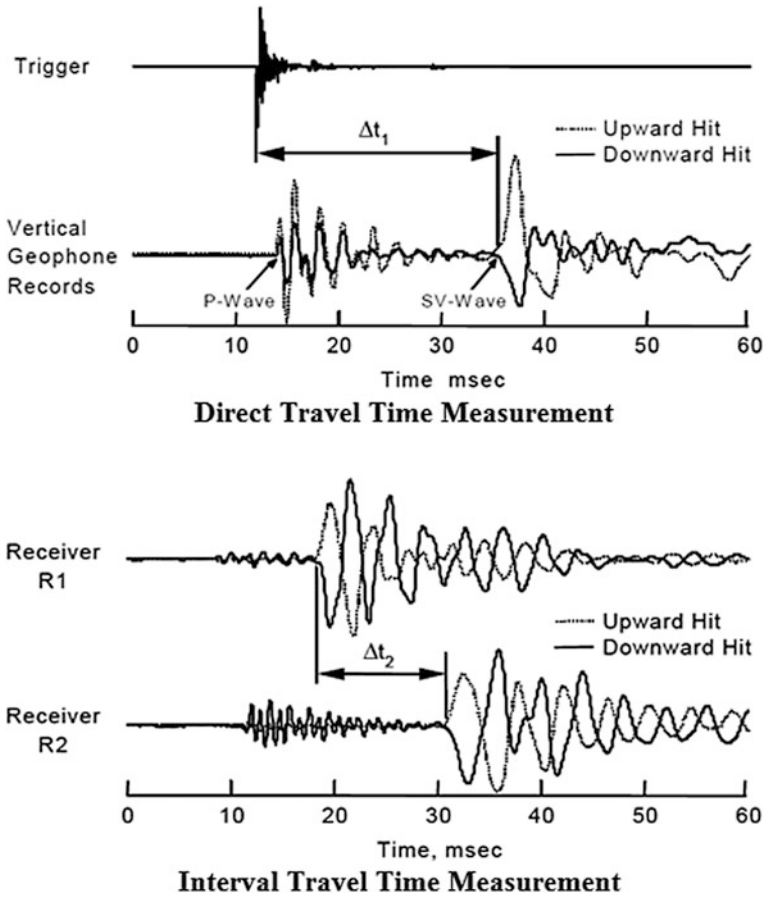


Fig. 6.16 Example of shear wave records measured in a cross-hole test using upward and downward mechanical impacts to identify the initial SV-wave arrival [361] (courtesy of the University of Texas at Austin)

6.2.2.5 Down-Hole (Up-Hole) Test

As shown in Fig. 6.17, in a down-hole test, an impulsive source placed at ground surface generates both P-wave and S-wave, and a triggering receiver located close to the source is required to measure the motions of the source. At a borehole adjacent to the source, a single receiver moves along various depths within the borehole to measure the wave time series. Alternatively, one may place a string of several receivers at predetermined depths. The time for the P-wave and S-wave to travel between the source on ground surface and receivers placed in the borehole can then be measured. Wave velocities are therefore calculated from the corresponding travel time after travel distances have been determined. Travel distances are typically based on assumed straight ray paths (Fig. 6.17) between the source

and the receivers, although the analysis may sometimes account for refracted travel paths. Based on the measurement above, travel-time curves (Fig. 6.18) depicting wave traveling versus depth can be plotted. And at each depth, the steepness of the curves' slopes indicates the wave propagation velocity at that depth.

An up-hole test does the opposite in terms of the placement of receivers and source. In an up-hole test, a source is placed in and moves along the borehole, while a receiver is placed on the ground surface adjacent to the borehole, as illustrated in Fig. 6.19. However, as S-wave is more easily generated by down-hole test than up-hole test, the up-hole test is less commonly used.

Compared to the cross-hole test, down-hole or up-hole tests require only one borehole, thus reducing the cost. Moreover, as the seismic wave travels through all soil media between a source and receiver(s), the down-hole test is capable of detecting soil layers that are not identified in a surface refraction test.

However, as the wave has to travel increasingly larger distances as the depth of testing increases, the identification of seismic wave can be difficult with a large traveling distance primarily due to the material and radiation damping. Therefore, depending on the energy developed by the source (various high-energy, mechanical sources have been constructed [363]), the optimum testing depths typically range from about 10–50 m [350]. Moreover, the disturbance of soil during borehole

Fig. 6.17 Illustrations of down-hole test

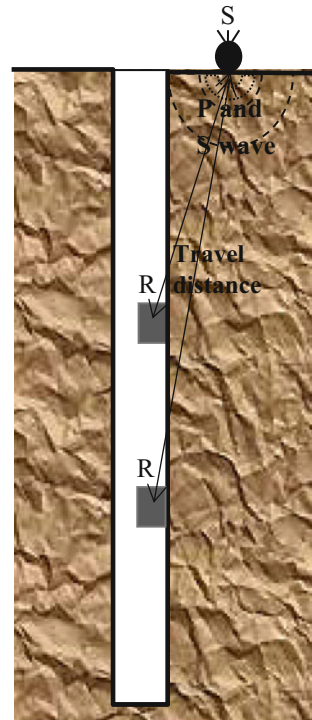
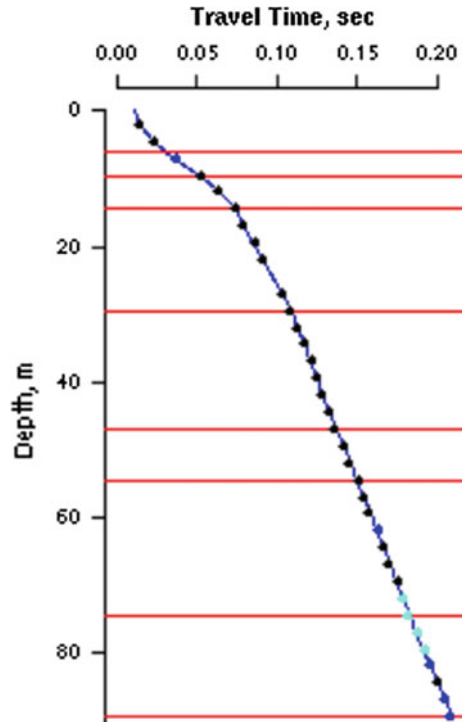


Fig. 6.18 Travel-time curve obtained from down-hole test [362]



drilling and casing, and borehole fluid effects, insufficient or excessively large impulse source, background noise effects, and water table effects, may pose further difficulties for performing a successful down-hole (up-hole) test.

6.2.2.6 Seismic Cone Penetrometer Test

As a combination of CPT (Sect. 1.9.6) and down-hole test, seismic cone penetrometer test measures shear wave velocities using a conventional cone penetration test setup by mounting geophone or accelerometers immediately above the friction sleeve, as illustrated in Fig. 6.20. The operation of penetration will be stopped during different penetration stages. During this pause, a horizontal striking on each end of a pressed beam against the ground (by outriggers of cone penetration rig or on an embedded anvil) generates impulse, which mainly contains SH-waves at the ground surface location near the insertion point of the cone. Travel time of the shear wave energy, either direct or interval, is measured by the geophone or accelerometers. After testing at a depth, the cone is penetrated further into the soil, and the test is performed again. A curve depicting the travel time-depth can then be plotted, which can be explained in the same way as that of the down-hole test.

Fig. 6.19 Illustration of up-hole test

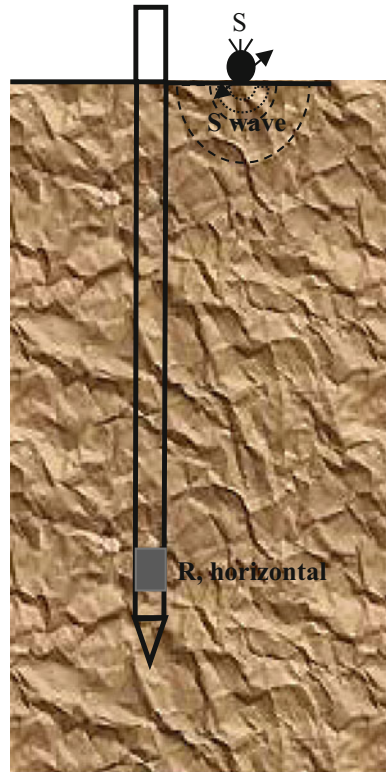


An obvious benefit of seismic cone penetrometer test is that it is combined with CPT. Therefore, no additional borehole is required. Furthermore, the test provides data of both the strength and stiffness of the soil column.

6.2.2.7 Suspension Logging Test

As shown in Fig. 6.21, suspension logging test is performed using a 5–6-m probe to place logging tools into an uncased borehole filled with water or drilling fluid (such as mud), and generating sharp, impulsive compression wave in the fluid using a horizontal reversible-polarity solenoid installed on the bottom part of the probe. When this compression wave reaches the borehole wall, it produces both P-wave and S-wave. The test measures arriving time of the P-wave and S-wave, which travel through soil media and transmit energy back through the fluid to two biaxial geophones (typically around 1 m apart) near the top of the probe. Differences in arrival times are used to compute the average P-wave and S-wave velocities of the

Fig. 6.20 Illustration of the seismic cone penetrometer test



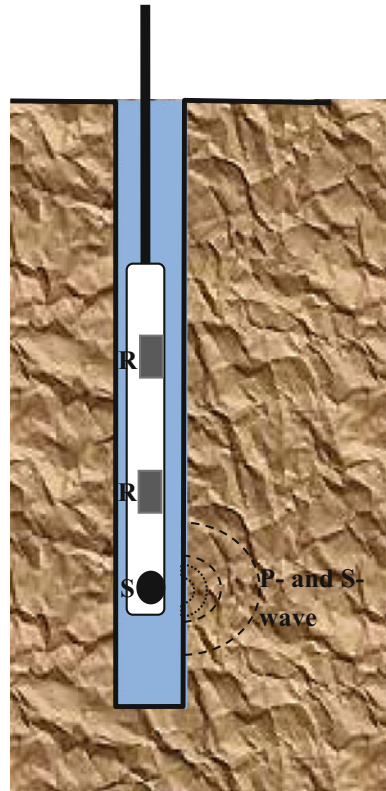
soil between the geophones. To enhance the capability of identifying P-wave and S-wave arrivals, the procedure is repeated with an impulse of opposite polarity.

Different parameters can be estimated using borehole logging, including: density, conductivity, acoustic velocity, clay content, degree of fracturing, etc. [364–366].

Prior to application in geotechnical engineering, the suspension logging test method had already been extensively used in petroleum exploration. The test is effective at a large depth, of up to 2 km [367]. To detect the thick layers of soft and weak soil, by overlapping the measurement depths, suspension logging test can attain a resolution of less than 1 m [1].

The main limitation of the test is associated with the effects of casing and drilling fluids on the measured response. Moreover, the suspension logging test generally cannot be performed in a steel or thick plastic casing at sites dominated by soft soils, and this potentially limits its application in soft sediments.

Fig. 6.21 Illustrations of suspension logging test



6.2.3 High-Strain Field Test

The high-strain field test primarily aims to obtain the soil strength. It mainly comprises the SPT (Sect. 1.9.5), CPT (Sect. 1.9.6), vane shear test (Sect. 1.9.4), dilatometer test (DMT), and pressuremeter test (PMT).

In a DMT [368], a stainless steel blade with a thin flat circular expandable steel membrane is installed on the side of the dilatometer. When at rest, the external surface of the membrane flushes with the surrounding flat surface of the blade. The blade is then jacked into the soil using a penetrometer rig or a ballasted drilling rig. The blade is connected to a control unit on the surface by a tube (running through the penetrometer rod) containing an electrical wire. At a penetration interval of 10–20 cm, the penetration is paused to allow the inflation of the membrane with pressure gas. The pressure at which the membrane moves by 0.05 mm and the pressure at which its center moves by 1.1 mm are recorded. When these values are then combined with the corresponding effective overburden pressure, soil properties can be determined by correlating these three measured data with the soil properties.

To measure both stress–strain relationship and soil strength, a PMT [369] uses a cylindrical device comprising a flexible membrane to apply a uniform pressure to the borehole wall. By measuring the pressure and the deformation/volume change, and correcting them for system compliance, elevation differences, and membrane effects, a pressure-corrected volume curve is plotted, which can be used to determine the stress–strain relationship of the soil.

6.3 Laboratory Element Testing

The soil properties can also be determined through laboratory tests using a specimen of a small size or with a decreased scale. Both intact and reconstituted specimens can be used in laboratory tests, with the choice often controlled by the capability to obtain intact specimens. Since dynamic soil properties are influenced by various factors, it is essential to prepare undisturbed soil specimen (by carefully taking samples from fields) or specimens that represent the soil behavior at sites as closely as possible. However, the prepared specimen for testing can in most cases only represent the initial stress and void ratio of the original soil from the site, and other factors such as the age, loading history, and actual soil fabric or structure are difficult or even impossible to reflect in the prepared specimen. Therefore, it is important to have a clear picture of how these factors can influence the testing results compared to the actual soil behavior at sites.

Laboratory test allows a parametric study that enhances the reliability of the soil property data. Generally, to account for the influence from the effective stress on seismic wave propagation parameters, the specimen has to be placed within pressure cells.

Similar to the field testing, laboratory test can also be categorized as low-strain and high-strain test, which will be presented in Sects. 6.3.1 and 6.3.2, respectively.

6.3.1 *Low-Strain Element Test*

6.3.1.1 Resonant Column Test

To measure important dynamic soil properties, including shear or elastic modulus (or shear wave velocity), modulus reduction curve, and damping ratio at low shear strain levels (typically in the range of 0.0001–0.1%), based on the theory of wave propagation in prismatic rods, resonant column tests are widely used.

Conventionally, after resonant column specimen has been prepared and consolidated, by using an electromagnetic loading system to apply cyclic torque (typically harmonic, but random noise loading and impulse loading have also been used) on cylindrical specimen, for which the amplitude and frequency of loading are controlled, the frequency of loading is initially set at a low value and is

increased step-by-step until the dynamic response (strain amplitude) of the soil specimen reaches a maximum, and the response to this loading is then measured typically in terms of velocity and/or acceleration. While a precise measurement of small displacement (deformation) is difficult, velocity and acceleration at a high frequency are large enough to be measured. By varying the loading frequency, the variation of amplification in amplitude of response is plotted against the frequency, as shown in Fig. 6.22. The resonant frequency is then measured, from which the velocity of the propagating wave is derived. Based on the derived velocity and the density of the soil sample, the low strain shear modulus of the material can be computed from the basic equation of torsional vibration. Figures 6.23 and 6.24 illustrate the test setup and typical test apparatus for performing the resonant column test.

Fig. 6.22 Schematic illustrations of measured soil response varied with frequency

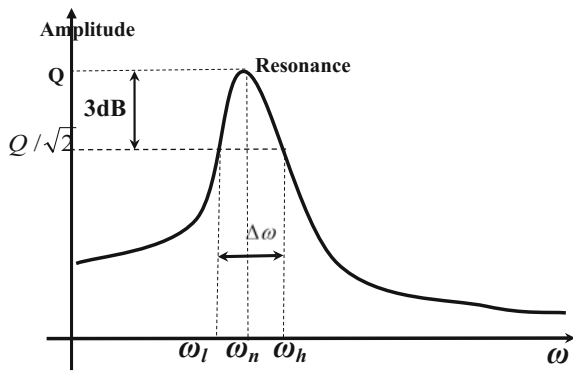


Fig. 6.23 Illustrations of typical resonant column test

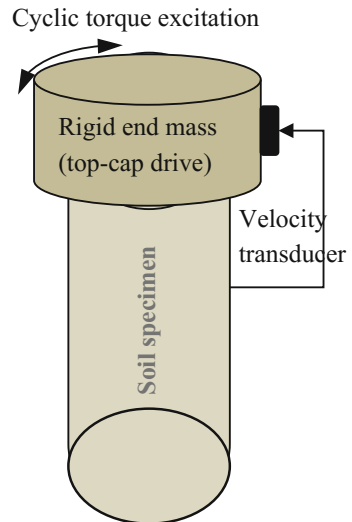




Fig. 6.24 Test apparatus for resonant column test (courtesy of Geocomp/GeoTesting Express)

The soil specimen shown in Fig. 6.23 is normally fixed at the bottom (occasionally tests can also be performed with a free–free boundary conditions) and subjected to torsion at the top. By applying the idea of wave propagation to the torsion of a solid cylinder with a rigid mass at the top, a theoretical value of resonant (natural) frequency can be calculated. As the natural frequency of the soil specimen is a function of shear modulus, the geometry of the soil specimen, and some characteristics of the resonant column apparatus, by equating the theoretical and experimental resonant frequencies (frequency corresponding to the peak response shown in Fig. 6.22), the shear modulus can then be obtained. The diameter of soil specimen to be tested in a resonant column test is normally less than 100 mm.

If there is no rigid mass at the top, the natural frequency ω_n of the soil column specimen in torsion shear is given by:

$$\omega_n = 2\pi v_s / (4l) \quad (6.14)$$

where v_s is the shear wave velocity of the soil specimen and l is the height of the soil column specimen.

If there is no rigid mass at the top of the specimen, the shear modulus G is calculated by:

$$G = \rho v_s^2 = \rho(4l \omega_n / 2\pi)^2 \quad (6.15)$$

where ρ is the density of the specimen.

If there is rigid mass at the top, the shear modulus of the testing specimen is calculated by the equation derived using elastic theory:

$$I/I_0 = (\omega_n l / v_s) \tan(\omega_n l / v_s) \quad (6.16)$$

where I is the mass polar moment of inertia of the specimen and I_0 is the mass polar moment of inertia of the system attached at the top of the specimen.

While I can be easily calculated, I_0 is usually evaluated by experimental method, which is more difficult than the determination of I . For example, by performing two tests with different circular flanges at the top of the specimen, I_0 can be calculated by solving simultaneous equations:

$$I + I_0 = K/\omega_n^2 \quad (6.17)$$

where K is the torsional stiffness of the specimen.

Compared to the case without top rigid mass, the effect of the top rigid mass generally results in a more linear variation of rotation and, consequently, more uniform strain conditions over the height of the specimen [1].

The shear strain in a specimen (equal to ratio between the top displacement and specimen height) varies in the radial direction: It is zero at the center and reaches its maximum at the outer edge. Hence, the average value is normally used for interpretation.

For details on the resonant column test, reader may refer to sources [370–372].

The damping can be determined from the frequency response curve (Fig. 6.22) using, for example, the half-power/bandwidth method, from the logarithmic decrement by placing the specimen in free vibration, or by measuring phase shift between the input force and the output displacement. See source [123] for the details of test methods to estimate damping.

Here, we briefly present the method of half-power/bandwidth method to calculate the equivalent damping at the natural frequency ω_n , which is given by:

$$\zeta_i = \frac{\omega_h - \omega_l}{2\omega_n} = \frac{\Delta\omega}{2\omega} \quad (6.18)$$

where ω_h and ω_l are frequencies on either side of the natural frequency ω_n ; and the amplitudes of frequency response curve at ω_l and ω_h are defined as having $1/\sqrt{2}$ (corresponding to 3 dB) times the amplitude at the natural frequency ω_n .

Therefore, the sharpness of each peak on the frequency curve indicates the value of the loss factor (η_i) at each resonance frequency.

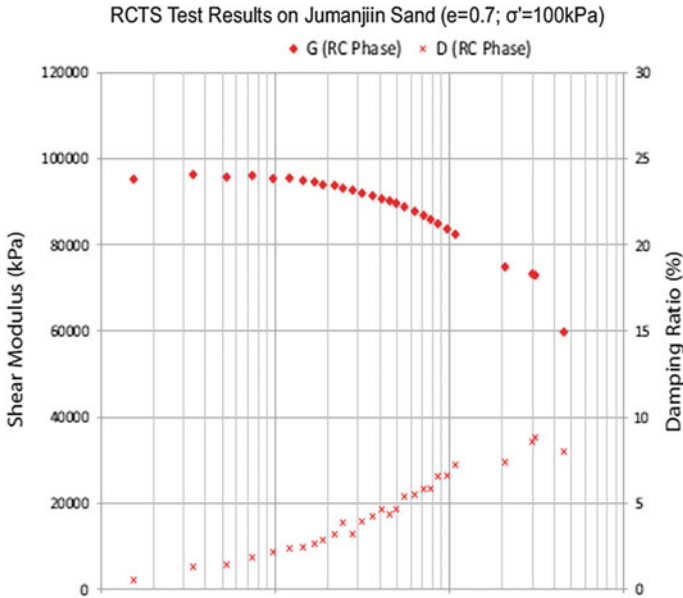


Fig. 6.25 Schematic illustration of shear modulus and damping varied with shear strain measured from a resonant column test (courtesy of Geocomp/GeoTesting Express)

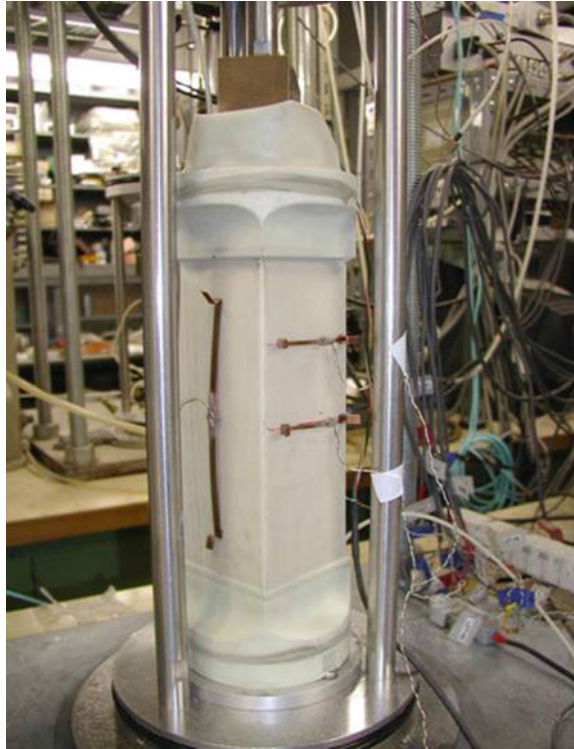
Figure 6.25 illustrates an example of shear modulus and damping varied with shear strain measured from a resonant column test.

While the excitation frequency of loading has unimportant effects on the low strain shear modulus [115], it can have significant influence on damping. Therefore, a noticeable variation of damping with loading frequency is likely to be observed during the resonant column test [350].

There is significant engineering demand to evaluate dynamic properties of fill materials and ballast material for foundations of nuclear power plants, dams, and railway constructions, etc. However, these materials usually contain relatively large gravel particles or even crushed rubbles. Even if alternative methods to estimate the strength parameters of original coarse materials using small samples by adjusting grain size distributions have been presented [373], the effect of this adjustment on stiffness parameters is not clear. To measure stiffness and damping of those materials such as gravel soils [374] and rocks [375] at low strain level, large-diameter resonant column test apparatus is desired. A few systems designed by various researchers [376–378] are capable of using specimens larger than 150 mm in diameter.

It is noticed that even if the effective confining pressure and strain amplitude varying with time can be readily measured in a resonant column test, the pore-water

Fig. 6.26 Local displacement transducer attached on triaxial shear specimen [194]



pressure is difficult to measure, and the material properties are usually measured at frequencies above dominant frequency of most seismic ground motions [1]. Moreover, note that number of torsional loading cycles in a resonance sample test is much higher than that in a real earthquake, which may influence the closeness of measured soil shear modulus and damping to the reality.

In recent decades, other testing devices have been developed to measure stress-strain data at small strain amplitude with sufficient accuracy, such as a local displacement transducer (shown in Fig. 6.26) which is able to record a very small displacement of 0.25 mm [379]. This sensitivity is equivalent to a strain of 1.25×10^{-6} for a sample size of 20 cm. This development has, however, made the resonant column test less important than before [194].

6.3.1.2 Other Low-Strain Element Tests

Other low-strain soil specimen tests are also available, such as ultrasonic pulse test [380, 381] and piezoelectric bender element test [382]. Interested readers may refer to the sources cited above.

6.3.2 High-Strain Element Test

At higher strain levels due to extreme loads such as earthquakes and ocean wave loading, the measurement of soil properties cannot be achieved by low-strain element test, and high-strain laboratory tests have to be performed. These mainly include cyclic direct shear test, cyclic triaxial test, and cyclic torsional shear test, etc. The current section gives a brief introduction to these three types of high-strain test. For more details, readers may read sources [1, 194].

6.3.2.1 Cyclic Direct Shear Test and Cyclic Triaxial Test

Cyclic direct shear test and cyclic triaxial test are very similar to their static counterpart presented in Sects. 1.9.2 and 1.9.3, but with the loading applied cyclically. The cyclic direct shear test is widely used for assessing liquefaction potential (Chap. 7), and it can more accurately represent the seismic stress condition than the cyclic triaxial test can.

6.3.2.2 Cyclic Torsional Shear Test

The cyclic torsional shear test applies torque on the cylindrical soil specimen, which can overcome various difficulties imposed by the cyclic triaxial test and cyclic direct shear test. A typical torsional shear device utilizes a ring-shaped soil sample that is supported laterally by inner and outer rings as indicated. The soil is subjected to a normal stress, and then the upper half of the box is subjected to a torque that causes the upper surface of the sample to rotate relative to the lower surface, so that a shearing stress is generated. The same apparatus as that used for low-strain resonant column tests can also be used for performing cyclic torsional shear tests.

To obtain shear modulus and damping at both small and large strain levels, as well as the shear strength, the resonant column and torsional shear tests can also be combined together. They typically involve the following steps [383]:

1. Consolidate the soil specimen to an first stress condition.
2. Measure shear modulus and damping versus shear strain at end of primary consolidation and at a few times during secondary consolidation.
3. Run torsional shear or triaxial compression test to measure shear strength of the specimen.
4. Consolidate to the second stress condition.
5. Repeat the steps above to final stress condition.
6. Run torsional shear test to much larger strain levels to measure shear modulus and damping at these higher shear strain levels.

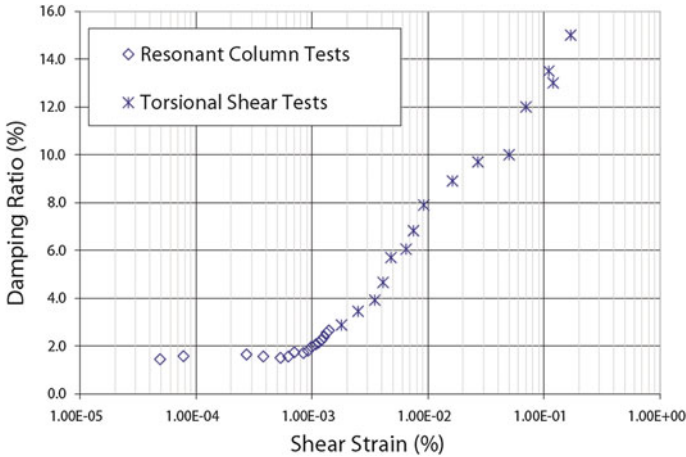


Fig. 6.27 Example of damping ratio versus shear strain at both low and high strain levels (courtesy of Geocomp/GeoTesting Express)

Figure 6.27 shows a typical example of measured damping obtained from both resonant column tests at small strain levels and torsional shear tests at large strain levels.

6.4 Model Testing

Model testing aims to investigate the seismic response of a small-scale physical model of a realistic structure subject to seismic ground motions. It mainly includes the shaking table test and centrifuge testing, which will be presented in Sects. 6.4.1 and 6.4.2, respectively. The former places the test model (typically soils held by a designed box and sometimes also with the associated foundations and structures) on the shaking table that is subject to designated ground motion excitations. The latter places the test model under increased gravitational fields using a centrifuge, so that the stress dependency matches that of the full-scale prototype.

Similitude and boundary effects are important aspects to consider for performing both types of model testing.

6.4.1 Shaking Table Test

In a shaking table test, a scale testing model or full-scale model is mounted on a shaking table (a flat plate), which is subject to table excitations driven by actuators

(typically of a servohydraulic type for which the capacity is determined by the capacity of hydraulic pumps that serve the actuators).

Figure 6.28 shows a 3×3 m shaking table with motion frequencies ranging from 0.4 to 50 Hz. The shaking table has a horizontal displacement, velocity, and acceleration limit of ± 127 mm, 600 mm/s, and 1.0 g, respectively. The maximum weight of the test models applied to this particular shaking table is 60 tons.

In addition to model testing to obtain seismic responses of structures and to validate the structural modeling, seismic model testing is also sometimes required to validate numerical analyses of seismic site-response and foundation response. Similar to the site-response analysis using finite element method, in such a shaking table test, a series of scale-model shaking table tests in free-field (without foundation and structure) are often first carried out to measure the responses at different locations in the soil. This is mainly to validate that the soil in the soil container/box is not influenced by the artificial boundary constraints at the container walls. The free-field test is often followed by a soil–foundation (shallow or deep foundation)–superstructure interaction testing. The response of soils, foundations, and/or structures can be measured using, for example, strain gauges or accelerometers and be transmitted through amplifier, which converts the response into electric signal for post-processing.

Shaking tables were originally designed to simulate ground motions in a uniaxial horizontal direction. In recent decades, various shaking tables capable of simulating multiple axial directions (2D or 3D) of motions have also been constructed. Moreover, to simulate multiple points of excitations for extended structures (e.g., tunnels, bridges, and pipelines), systems with multiple subarrays, in which each array is essentially a single shaking table, have also been developed. Figure 6.29



Fig. 6.28 Shaking table test for a cable-stayed bridge model on a 3×3 m shaking table

shows a nine-subarray shaking table system; each array has a dimension of 1×1 m.

In both free-field and interaction testings, when the soil is only under the gravity field in a static state, the effective vertical stress σ_{vo}' and horizontal stress σ_{ho}' at a depth z are given by:

$$\sigma_{vo}' = \gamma'z \quad (6.19)$$

$$\sigma_{ho}' = K\sigma_{vo}' \quad (6.20)$$

where γ' is the effective unit weight of the soil; $K = \sigma_{ho}'/\sigma_{vo}'$ is the lateral (at rest) earth pressure coefficient, which may be taken with the following values: For coarse-grained soils, $K = 1 - [\sin \phi' \cdot (\text{OCR})^{\sin \phi'}]$, where ϕ' and OCR are the angle of internal friction and over-consolidation ratio; for fine-grained soils, $K = [0.44 + (0.42I_p (\%)/100)] \cdot \text{OCR}^{0.5}$.

Under horizontal seismic excitations, the normal stresses almost remain constant while seismic shear stresses $\tau(z)$ in both vertical and horizontal planes increase due to the cyclic seismic loading. For a soil element at a depth of z , $\tau(z)$ can be approximated as:

$$\tau(z) = a(t)\gamma'z \quad (6.21)$$



Fig. 6.29 Nine subarray shaking table system for scale-model test of large-scale prototype infrastructures (courtesy of Beijing Laboratory of Earthquake Engineering and Structural Retrofit, Beijing University of Technology)

where $a(t)$ is the horizontal acceleration of the soil element at time t .

Different from a realistic site condition, the artificial boundary conditions of soil containers may reflect and generate P-waves, resulting in a distortion of free-field conditions. If the container end-walls are frictionless, vertical stresses cannot develop and the stress field near the boundaries will be different from reality. However, if the test model is placed in the center of the container and at a considerably large distance from the end-walls, such effects may be assumed to be negligible. Therefore, in the setup of a shaking table test under horizontal shaking (vertical shaking is not considered), it is of great importance to make sure that the horizontal shear deformation is realistically developed in the soil under horizontal earthquake action and the effects of soil container (finite dimensions) boundary constraints are not significant, i.e., to allow the replication of semi-infinite extent of the ground in a finite dimension soil container.

To fulfill the objective above, three strategies can be employed to reduce the reflection of waves from the container wall:

The first one (rigid wall container) is to place soft material such as conventional foam on the internal sides of the rigid walls of a container, while the test results are strongly dependent on the mechanical properties and thickness of the soft materials, i.e., the soil will deform in bending rather than in shear if the soft material glued on the container wall is too soft or too thick.



Fig. 6.30 Full-scale cylinder soil container mounted on a shaking table, with support struts, and soil mixer/pump in background (courtesy of Pacific Earthquake Engineering Research Center and PJ Meymand, University of California, Berkeley, and California Department of Transportation)

The second method (flexible wall barrel) is to use rubber membrane as the material for the soil container, to form a flexible cylinder with an integral bottom, as was originally designed by Meymand [384]. As shown in Fig. 6.30, the cylinder is reinforced by circular bands at a certain vertical distance interval and is attached at the top to a ring, which is in turn supported by steel rods with universal joints at top and bottom. A steel plate over the rubber base is bolted directly to the shaking table. This method allows the shear deformation to develop in multiple directions in the horizontal plane. However, if the distance between each two adjacent bands to reinforce the container is too small, the horizontal shear deformation in the soil will be over-constrained. On the other hand, if the distance is too large, the soil volume will be expanded, causing an unrealistic release of the confined soil pressure, and may also induce soil's bending deformation [385].

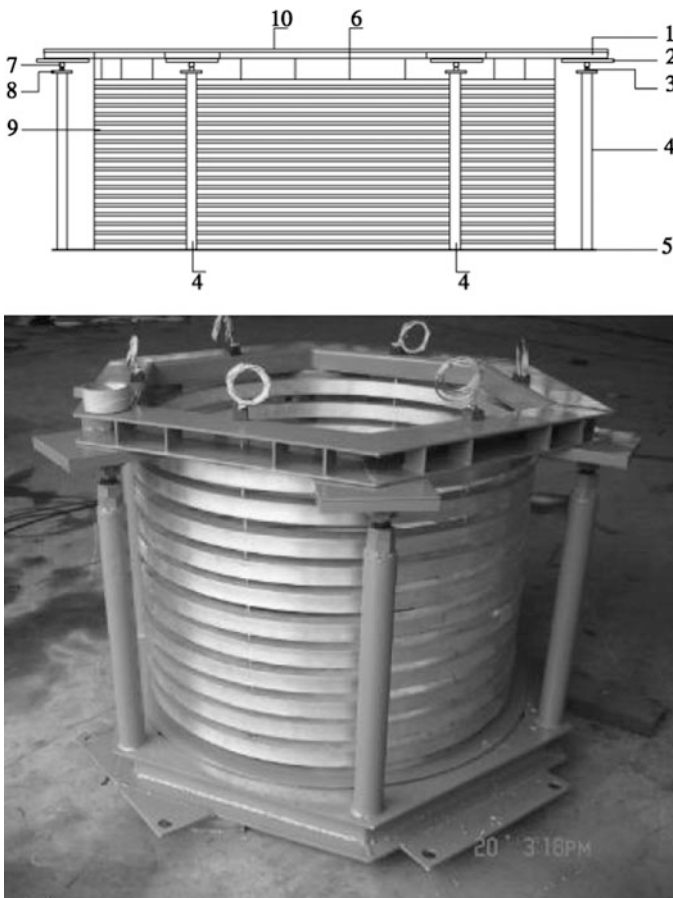


Fig. 6.31 Laminar container to allow soils' shear deformation in horizontal directions [386]

The third method is to use laminar container, comprising multiple slices (rings) of container wall, as shown in Fig. 6.31. The laminar container must fulfill the requirement that the composite shear stiffness of the laminar box should be significantly less than that of the soil deposit so that the response of the soil and specimen (foundation) is driven by the soil and not by the laminar box itself. These rings were used to provide flexibility and to approximate a continuous shear strain field in the soil during shaking. Between each two adjacent rings, flexible bearings are placed to allow horizontal slidings of the rings, so that the horizontal deformation of the soil is not restricted. In recent years, this method has received an increasing number of utilizations.

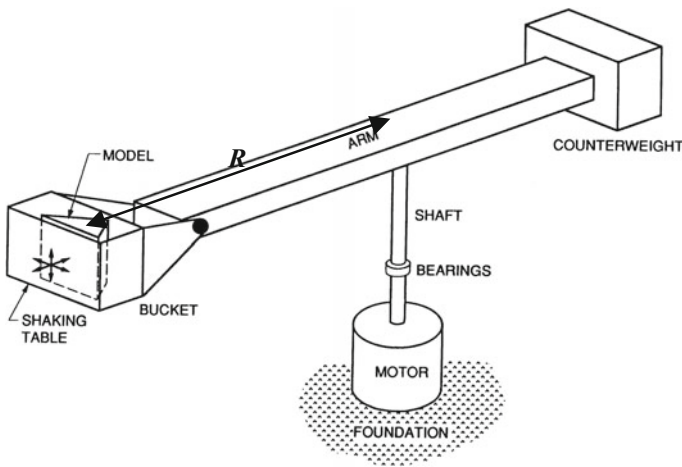


Fig. 6.32 Illustration of a typical centrifuge test [387]

6.4.2 Centrifuge Test

Another important issue in a seismic model test is to properly represent soils' overburden pressure. This is sometimes addressed by performing a centrifuge of scale-model testing, in which a centrifuge apparatus consisting of a rotating arm with an experiment package (such as a moderate-sized shaking table) is fixed to a swivel at one end. The centrifugal acceleration of the rotating arm induces an elevated gravitational field onto the model, which swivels to a position normal to the arm as shown in Fig. 6.32.

The overburden pressure is important for sands whose stress–strain behavior is a function of confining pressure. In clay soils, where overburden stresses are not so significant, centrifuge tests also enable the consolidating process of the deposit during spin-up, thereby achieving a more realistic soil strength profile [384].

Similitude is an essential factor to consider in a centrifuge testing. However, because different aspects of response of a $1/N$ -scale test model are governed by different scale factors, it is not possible to fulfill the similitude requirement for all parameters simultaneously. Table 6.2 shows scaling factors for different types of parameters. It is known from this table that the stresses and strains in a full-scale prototype soil can be modeled by a $1/N$ -scale test model with an acceleration of N -g. Therefore, for an $1/N$ -scale test model with a distance of R from the shaft (center) of the centrifuge, a rotation speed of $(N/R)^{1/2}$ would be sufficient to induce an acceleration field that is N times the acceleration of gravity. Generally, the overburden pressure at any point in the test model should then represent the stress

Table 6.2 Scaling factors of different types of parameters for centrifuge modeling [389]

Type of event	Quantity	Model dimension/prototype dimension
All events	Stress	1
	Strain	1
	Length	$1/N$
	Mass	$1/N^3$
	Density	1
	Force	$1/N^2$
	Gravity	N
Dynamic events	Time	$1/N$
	Frequency	N
	Acceleration	N
	Strain rate	N
Diffusion events	Time	$1/N^2$
	Strain rate	N^2

Values are based on the assumption that the same soils and fluid are used in the model and the prototype and that the soil properties are not rate-dependent

condition at the corresponding point in the full-scale prototype [1]. It should be noticed that the dissipation time of the pore-water pressure in a $1/N$ -scale model would only be $1/N^2$ of the prototype model. This requires a use of higher viscosity fluid in the test model such as silicon oil. To enhance the reliability of the centrifuge test, results of models of different sizes at the same prototype scale can be compared [388].

Chapter 7

Liquefaction

7.1 Introduction to Liquefaction

7.1.1 Causes of Liquefactions

Liquefaction means the transformation of any substance into a liquid state. When soils around structures' foundations are subject to cyclic loading due to earthquakes or adverse ocean storms, they may lose their shear strength, causing a catastrophe such as local or global failures of foundations and even the collapse of entire structures. Nowadays, liquefaction is an important soil failure mode relevant for the geotechnical design and integrity of both offshore and land-based structures.

Under static monotonic loading, drainage helps soils to prevent excess water pressure building up. However, under cyclic loading, especially for loose saturated sand, it tends to densify and settle, break down the soil structure and cause a tendency toward volumetric compression. Because the duration of the shaking is too brief, the water does not have time to dissipate. A higher pressure load may then be taken by the water pressure, leading to a reduction in effective stress and a decrease in shear resistance and stiffness. This is mainly because, under repeated loading, the loose particles in sand tend to compact more tightly, resulting in a decrease in volume and an increase in pore-water pressure that cannot be dissipated under undrained or partly drained conditions.

Figure 7.1 shows the development of pore-water pressure and shear stress–strain behavior as functions of time under undrained cyclic loading with a constant cyclic shear stress. The cyclic loading generates a pore pressure characterized by a permanent pore pressure component, u_p , and a cyclic pore pressure component, u_{cy} . Each load cycle gives an additional incremental pore pressure, which reduces the effective stresses in the soil, resulting in increased average, γ_a , permanent, γ_p , and cyclic, γ_{cy} , shear strains with time [390]. And after a number of load cycles, the stress path reaches the failure envelope as shown in Fig. 7.2. Figure 7.3 shows the excess pore-water pressures under different consolidation ratios ($k_c = \sigma_1/\sigma_3$, where

σ_1 and σ_3 are the maximum principal stress and confining pressure), measured by the stress-controlled torsional shear test method. By observing this figure, it is also found that, under anisotropic consolidation condition ($k_c = 1.5$ and 2.0), the excess pore-water pressure cannot reach the confining pressure σ_3 , and the liquefaction cannot occur. Furthermore, the peak value of the pore-water pressure decreases with an increase in initial consolidation ratio. It should be mentioned that, for the cases without liquefaction occurrence, the number of load cycles to induce liquefaction N_f is defined as the load cycles corresponding to a deformation (i.e., strain) of 5%. In addition, it is important to consider the simultaneous occurrence of both dynamic shear stress and applied axial dynamic bidirectional loading. For saturated sand, the number of loading cycles leading to liquefaction failure is highly influenced by the ratios and phase between the axial dynamic stress and horizontal dynamic stress [391].

Obviously, the liquefaction requires considerable “excess pore pressure.” Here, the pore pressure is defined as the difference between the actual pore pressure and the hydrostatic pressure for still water level. A possible scenario causing liquefaction is a gravity-based offshore platform resting on sands as shown in Fig. 7.4: when it is subjected to significant ocean wave loading, a large part of dynamic loading can be taken by the water pressure change [27].

If almost all overburden pressure is taken by pore-water pressure in sandy soils (i.e., the pore pressure is close to the maximum total stress and the effective stress approaches zero), the sand then behaves like a liquid without noticeable shear resistance. This failure is called partial liquefaction, indicating that the sand almost loses both its shear modulus and shear strength, and causes a significant subsidence

Fig. 7.1 Pore pressure and shear strain as functions of time under undrained cyclic loading [390]

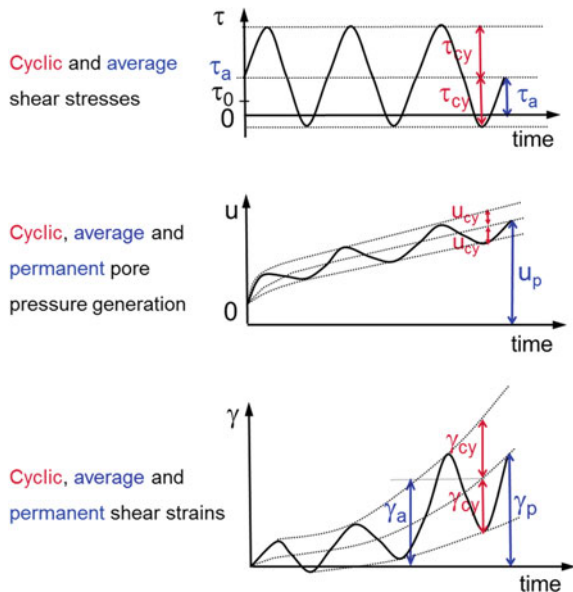


Fig. 7.2 Development of effective stress for undrained tests in a contactant soil from monotonic to cyclic loading. In each load cycle, a single amplitude shear stress τ_{cy} around a constant shear stress τ_a can be defined [390]

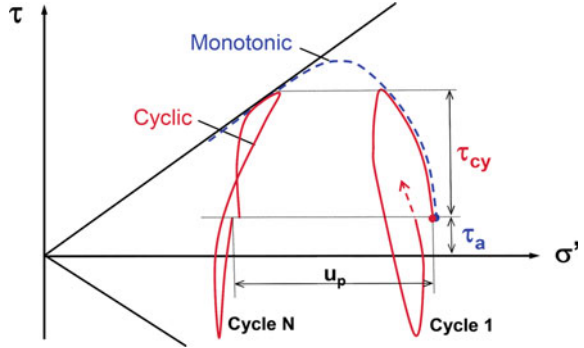
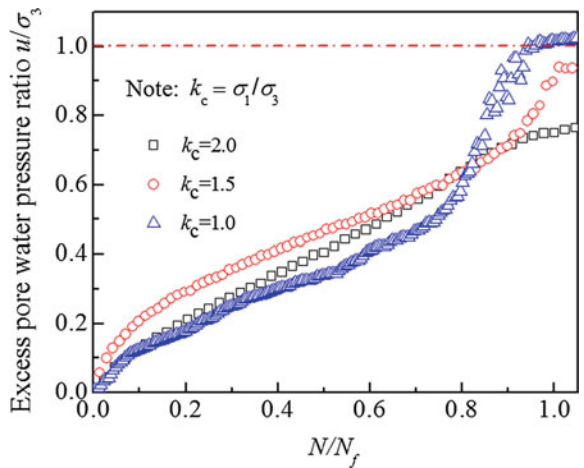


Fig. 7.3 Excess pore-water pressure under different consolidation ratios (k_c), measured by the stress-controlled torsional shear test method. u is the pore-water pressure, N_f is number of load cycles to induce soil liquefaction (courtesy of Key Laboratory of Urban Security and Disaster Engineering of Ministry of Education, Beijing University of Technology)

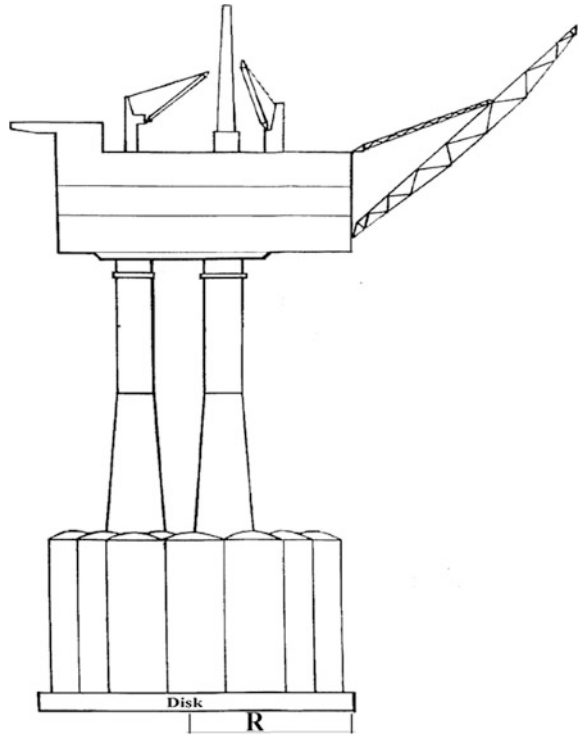


under even a minor load disturbance in shear. If the sand completely loses its shear modulus and shear strength and behaves like a Newtonian fluid, the failure is called full/complete liquefaction.

Liquefaction can cause ground surface settlement, loss of foundation bearing capacities, and lateral movement of slopes. It is responsible for damage during many earthquakes. For example, during the Loma Prieta earthquake on 17 October 1989, 18,306 houses were damaged, and the most severe damage occurred in areas where infrastructures were built on loosely consolidated and saturated soils, which are susceptible to liquefaction. During the Kobe earthquake in 1995, in the artificial islands off Kobe, significant ground shaking caused the liquefaction of reclaimed lands, and the quay wall built by the caisson method suffered serious damage.

Under seismic excitations, the seismic accelerations go along with horizontal shear stresses due to vertically propagating shear waves. The shear stress in the upper sand layers is roughly proportional to the depth below the ground surface, just like the vertical stress, causing a relative shear stress that does not vary

Fig. 7.4 A GBS structure with a shallow foundation directly resting on soils (courtesy of Aker Solutions)



significantly with depth [392]. As the cyclic excitations induce cyclic shear stress in the soil, this causes the soil to undergo cyclic shear deformation, leading to a pressure buildup, and eventually a possible liquefaction if the soil is undrained and comprises silt, fine sand, and even medium sand [393].

Sites with soils having low plasticity index, such as sand and occasionally silt soils, are most susceptible to liquefaction. On the other hand, for soils with high plasticity index such as clay, even if high pore-water pressure can build up in those soils, liquefaction is not likely to occur. However, evidence has also shown that liquefaction can occur in cohesive soils, such as the ejection of some cohesive soil observed at Port Island after the 1995 Kobe earthquake [394]. In certain cases, liquefaction can even take place in gravels [395], even though the observational data are insufficient for establishing a reliable liquefaction chart.

Because liquefaction occurs only in saturated soil, it mainly influences the low-lying areas near water, such as oceans, rivers, lakes, and bays. It also often occurs at sites with young alluvial planes, and human reclamations, on which infrastructures were normally not built until the rapid urbanization that began in the twentieth century. In this sense, liquefaction as a natural hazard is a consequence of the spreading of urbanization into areas of unsuitable ground conditions [194].

When soils liquefy, as their stiffness generally decreases, the corresponding site period increases. Therefore, the acceleration amplitude becomes lower while the

displacement amplitude increases. Even though the decreased ground accelerations can reduce the response of superstructures, as the liquefaction is not controllable and can cause a sudden collapse of foundations. Therefore, the reduction in seismic response of structures due to liquefaction of foundation soils is not acceptable.

With regard to foundation and superstructure stability, it is worth pointing out that the highest excess pore pressure normally lags the highest acceleration loading. Therefore, the time instant when foundation strength with regard to liquefaction reaches its minimum usually does not coincide with the highest loading occurrence.

Liquefaction can be readily predicted at sites comprising sediments of either sands or silts that are loose and saturated. Therefore, numerous hazard maps for identifying liquefaction hazard have been established by national or international regulatory bodies and governmental agencies.

In addition to earthquakes and ocean wave loadings, the sorts of repeated loading that can potentially induce liquefaction are, for example, wind or even vibrations transmitted from vibrating machinery or ground vehicles to soils.

The investigations regarding earthquake-induced liquefaction have been focused on two aspects: liquefaction mechanism, and evaluation of liquefaction potential. Generally, four methods are adopted to perform these studies: laboratory [407], experience or statistical methods [408, 409], simplified analysis methods [410, 411, 412], and numerical methods [413, 414].

7.1.2 Liquefaction Damages

Lateral spreading is the downslope lateral movement occurring when cyclic inertial loads exceed the reduced effective soil strength, as shown in Fig. 7.5. It is generally associated with shallow surface ground slopes with a slope of less than 1%. Lateral spreading has caused more damage than almost any other form of liquefaction-induced ground failure [396]. It has been observed in almost all significant earthquakes, from the 1923 Kanto earthquake in Japan [397] to the recent 2008 Wenchuan earthquake in China [398] and 2016 Christchurch earthquake in New Zealand [399]. During historical earthquakes, lateral spreading displacement has pulled apart or sheared shallow and deep foundations of buildings, pipelines and other structures and utilities, buckled bridges or other structures, and toppled retaining walls, etc., that lie in the path of the spreading ground. Port facilities have been particularly vulnerable to ground displacement because they are normally located on poorly consolidated natural deposits or fills that are particularly susceptible to liquefaction and lateral spreading, as mentioned earlier [400]. For example, lateral spreading due to liquefaction damaged over 250 bridges and numerous embankments along the Alaskan Railroad and Highway during the 1964 Alaska earthquake.

Even if liquefaction itself does not kill people, it is responsible for many accidents associated with the tilting or the collapse of structures and failure of slopes. For example, during the Tangshan earthquake in 1976, 15 out of 18 bridge



Fig. 7.5 Lateral spreading due to soil liquefaction (courtesy of USGS)

collapses were caused by liquefaction, leading to the failure of foundations and bridge piers.

Niigata in Japan lies on the banks of the Shinano River where it enters the sea. The city is underlain by about 30 m of fine alluvial sand. The M_w 7.6 Niigata earthquake in 1964 caused damage of more than US\$1 billion, and most of those damages were related to soil liquefaction of loose sand deposits in low-lying areas [401]. Figure 7.6 shows collapsed buildings due to bearing capacity failure in the liquefied ground during the Niigata earthquake, in which the building in the middle tilted about 80° . All buildings shown in this figure tilted to some extent, some more extremely than others. Interestingly, almost all buildings tilted in the direction of the eccentricity of gravity caused by the eccentricity of the roof, indicating an effect due to a resultant rotational moment generated by gravity and buoyancy on these buildings [194]. Since liquefied sand has a density 1.7–2. One times that of water, when the weight of a supported structure is not larger than the buoyancy force provided by the liquefied sand, the structure will float.

The building on the upper right of Fig. 7.6 did not collapse, as it was the only structure built on pile foundations instead of gravity-based foundations. However, almost 20 years after the earthquake, in order to increase the building height, an excavation beneath the building was performed to upgrade the foundations. It was then discovered that the piles had been severely damaged during the Niigata earthquake. Furthermore, even for the buildings that fell down completely, the entire collapse process took a few minutes, thus providing sufficient time for the people inside the buildings to escape. This is also the reason why none of the buildings exhibited significant structural damages [194]. After the Niigata earthquake, several apartment buildings were jacked back to a vertical position and underpinned with new foundations.



Fig. 7.6 Inclined apartment buildings at Kawagishi-cho in Niigata due to soil liquefaction, after the M_w 7.6 magnitude Niigata earthquake, Japan, 16 June 1964

During the Niigata earthquake, underground structures such as storage tanks, septic tanks, sewage conduits and manholes floated upwards out of the ground. Sand flows and mud volcanoes ejected water shortly after the earthquake and were reported to continue for up to 20 min after shaking had stopped. Sand deposits 20–30 cm in thickness covered much of the city [401].

Figure 7.7 shows the collapse of the Showa Bridge during the Niigata earthquake. From eyewitness reports, it appears that failure began 70 s following the main (initial) shock of the earthquake but before the lateral spreading of the ground started 83 s after the start of the initial shock [402, 403]. This observation suggests that neither the ground motion nor the lateral spreading (caused by liquefaction) was responsible for the bridge collapse. Nevertheless, the increased natural period of the bridge (due to the elongation of unsupported length of the piles caused by soil liquefaction) tuned with the period of the liquefied ground, both of which were close to 6 s at about 70 s after the onset of the ground shaking, as shown in Fig. 7.8. This tuning effect caused resonance between the bridge and the ground motions with excessive deflection at the pile head, resulting in the unseating of the bridge deck from the supporting pier and thereby initiating the collapse of the bridge [404].

During the 1964 Anchorage Alaska earthquake, serious liquefaction and damages were also found in many sites.

The liquefaction accidents that occurred in both the Niigata and Anchorage earthquakes challenged the previous knowledge that sand soils have high bearing capacities and low consolidation settlements, and piles are not required for sites with sand soils. Moreover, for infrastructures supported by pile foundations, liquefaction can still be a potential threat for structural and foundation integrity,



Fig. 7.7 Collapse of Showa Bridge during Niigata earthquake

mainly related to pile buckling due to the reduction in lateral supporting stiffness or pile friction (in case the end-bearing capacity is not sufficient).

Liquefaction has in past earthquakes also been an important contributor to pipeline distress. Figure 7.9 shows the breakage of a buried water pipe due to liquefaction. Large ground movements and deformations (in extension, compression, shear, and combined modes), including ground distortion, cracks, fissures, and venting sinkholes, resulted from severe liquefaction and subsequent lateral spreading, causing damage to underground pipe networks. For example, the 2010 and 2011 earthquakes in Christchurch left a 1700-km pipe network severely damaged.

As noticed through both observation and numerical analysis of the damage during past earthquakes, the damaging effects of liquefaction generally decrease as the depth of the liquefiable soil layer increases. This reduction in damage is largely attributed to decreased levels of relative displacement and the need for potential failure surfaces to extend down to the liquefying layer. These effects are relevant to the most damaging effects of liquefaction, such as lateral deformation and instability. Deeper liquefaction can, however, increase the magnitude and impact of vertical movement (settlement) and loading (down-drag) on foundations [41].

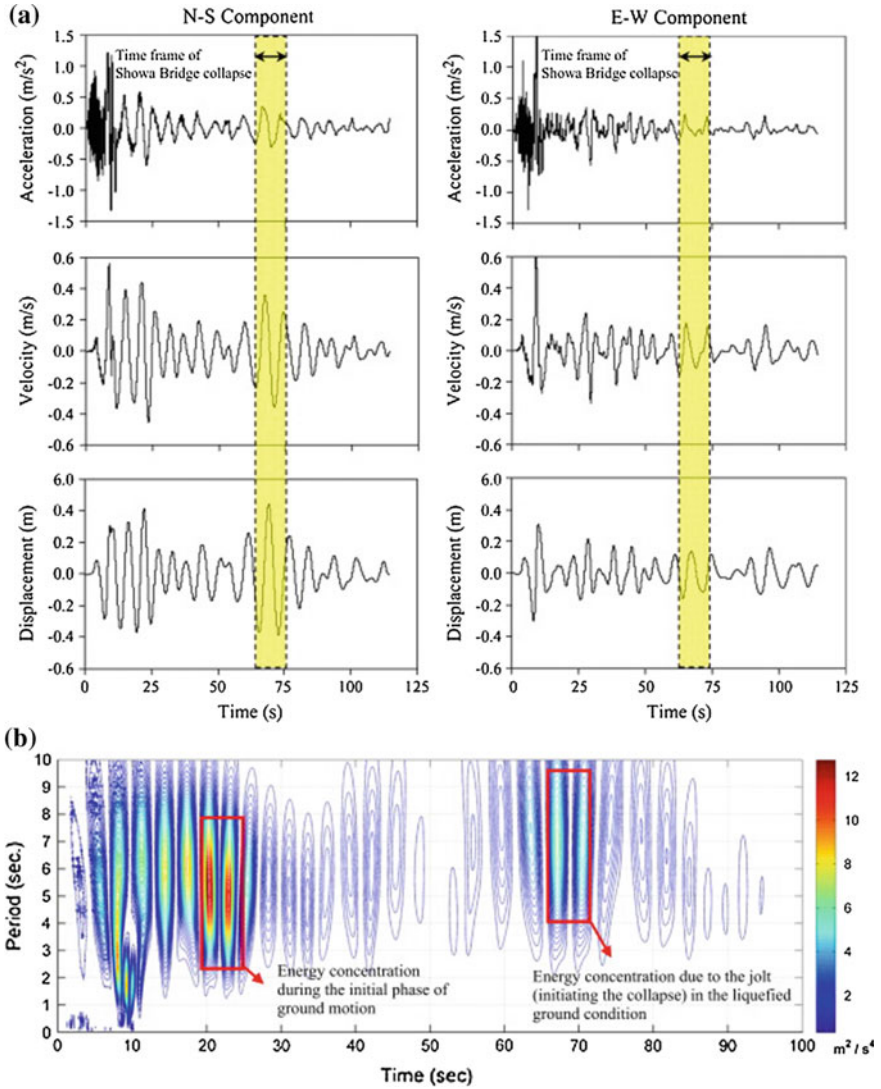


Fig. 7.8 a Recorded acceleration record and its corresponding velocity and displacement time histories [405, 406]; b Wavelet energy spectrum of NS component of the ground motions [402]



Fig. 7.9 A water pipe broken due to liquefaction

7.2 Evaluation of Liquefaction Initiation

7.2.1 Introduction

Convenient assessment of liquefaction potential requires a screening of liquefaction potential and detailed site-response analysis.

1. Screening the liquefaction potential:

The screening of liquefaction is normally carried out by studying the site geology, soil types and density, depth to water table, ground surface slope and proximity to free-face conditions as well as potential for lateral and vertical differential displacement [415].

FEMA gives a quantified evaluation for liquefaction potential. Soils with the following conditions are not vulnerable to liquefaction: granular sandy soils with $(N_1)_{60} > 30$ blows/ft ($(N_1)_{60}$ is described in Sect. 1.9.5), stiff clay or clayey silt with plasticity index over 20 and a ground water table 10 m below foundation level or 15 m below ground surface.

2. Site-response analysis:

For sites found to be susceptible to liquefaction potential in the screening stage above, a detailed site-response analysis may be performed. Various approaches have been used to evaluate the potential for liquefaction, and the majority of them are focused on the evaluation of initiation of liquefaction. It is desirable to incorporate the buildup of soils' pore-water pressures and the consequent reduction in

soil stiffness and strength in a nonlinear soil model (Sect. 2.4), even if this is in many cases too complicated to be adopted in engineering design.

In practice, the most commonly used ones are the cyclic stress approach and cyclic strain approach, which will be presented in Sects. 7.2.2 and 7.2.3.

In the cyclic stress approach, by comparing induced cyclic shear stresses obtained from a site-response analysis with cyclic soil resistances, the likelihood of the liquefaction can be identified.

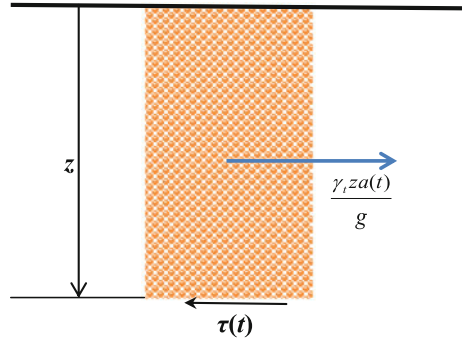
Cyclic soil resistance can be determined based upon SPT “ N -values” from soil borings, tip resistance (q_c) from CPT test, and shear wave velocity (v_s) from for example seismic down-hole test. As presented in Sect. 1.9.5, to obtain the normalized, standardized (N_1)₆₀, field SPT blow-counts (“ N -values”) should be adjusted to account for various correction factors, such as overburden, delivered energy, rod length, borehole diameter, and liners corrections. Similarly, q_c and v_s should be corrected against overburden pressure to obtain the normalized q_{c1} and v_{s1} values. Using charts found from relevant handbooks, cyclic soil resistance of granular soil deposits can be determined based on values of normalized (N_1)₆₀, q_{c1} , and v_{s1} . For more details, readers may read the NCEER chart [416].

The induced cyclic shear stresses can be calculated from either a simplified Seed–Idriss equation [416] or a more detailed dynamic site-response analysis. The later analysis method is recommended because a site-response analysis has more dedicated considerations for the frequency content of ground motions, the variation of soil layer and shear wave velocity with depth, and the depth to bedrock. Therefore, it gives more reliable results than the simplified See-Idriss equation.

7.2.2 *Cyclic Stress Approach*

The cyclic stress approach is perhaps the method most widely used in the civil engineering field to assess the liquefaction potential. It is based on converting the irregular shear stress time history with various amplitudes into an equivalent number of cycles of a regular time history with constant amplitude, so that this equivalent uniform cyclic shear stress amplitude due to earthquake loading can easily be compared with the liquefaction initiation criteria from tests (mainly by SPT or CPT). Therefore, the evaluation is divided into three steps: (1) estimate an equivalence of earthquake loading to calculate the cyclic stress ratio (*CSR*); (2) determine cyclic resistance ratio (*CRR*) from charts based on tests; (3) calculate safety factor against liquefaction based on the two steps above.

Fig. 7.10 Equilibrium of a soil column under seismic excitation accelerations $a(t)$ acting at the center of the soil column



7.2.2.1 Calculation of Cyclic Stress Ratio (CSR) Caused by Earthquake Loading

By first adopting a rigid-block analogy to model the soil columns under horizontal excitations as shown in Fig. 7.10, the horizontal cyclic shear stress τ varied with time t can be calculated as:

$$\tau(t) = \frac{\sigma_{v0}(z)a(t)}{g} = \frac{\gamma_t z a(t)}{g} \quad (7.1)$$

where $\sigma_{v0}(z)$ is the total vertical stress before the earthquake shaking; $a(t)$ is the horizontal acceleration of the soil element under study at time t ; γ_t is the total weight of the associated soil; z is the depth of the soil column; τ is the shear stress at the bottom face of the soil column as shown in Fig. 7.10.

Since in reality the soil column is deformable and does not act as a rigid body, to account for the flexibility of the soil profile, a stress reduction factor $r_d(z)$ as a function depth can be further applied, with $r_d = 1.0$ at the ground surface and $r_d < 1.0$ below the ground surface. This factor can be obtained by checking standard charts such as the one proposed by Seed and Idriss [417] or by directly using formulas as a function of the depth and sometimes a function of moment magnitude M_w . Several formulas are presented as follows.

The NCEER [39] and Liao and Whitman [418] presented a stress reduction factor $r_d(z)$ as:

$$r_d(z) = 1.0 - 0.0765z \quad \text{for } z \leq 9.15 \text{ m} \quad (7.2)$$

$$r_d(z) = 1.174 - 0.0267z \quad \text{for } 9.15 \text{ m} < z \leq 23 \text{ m} \quad (7.3)$$

$$r_d(z) = 0.744 - 0.08z \quad \text{for } 23 \text{ m} < z \leq 30 \text{ m} \quad (7.4)$$

$$r_d(z) = 0.5 \quad \text{for } z > 30 \text{ m} \quad (7.5)$$

Idriss [419] proposed $r_d(z)$ as:

$$\ln[r_d(z)] = \alpha(z) + \beta(z)M_w \quad (7.6)$$

where:

$$\alpha(z) = -1.012 - 1.126 \cdot \sin [5.133 + (z / 11.73)] \quad (7.7)$$

$$\beta(z) = 0.106 + 0.118 \cdot \sin [5.142 + (z / 11.28)] \quad (7.8)$$

Kayen [420] presented that:

$$r_d(z) = 1.0 - 0.012z \quad (7.9)$$

After obtaining the stress reduction factor $r_d(z)$, the maximum stress $\tau_{\max}(z)$ at a depth z is calculated as:

$$\tau_{\max}(z) = r_d(z) \frac{\sigma_{v0}(z)a_{\max}}{g} \quad (7.10)$$

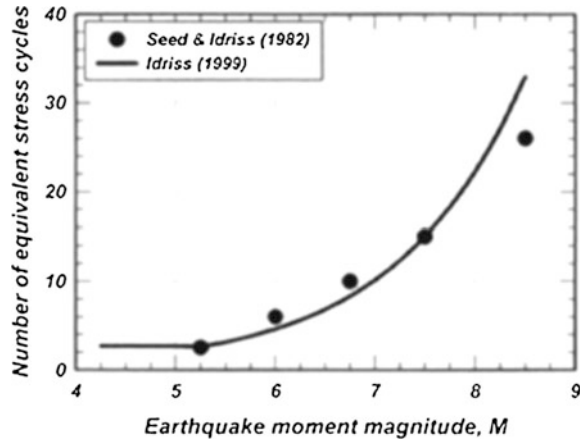
where a_{\max} is the maximum absolute value of the horizontal acceleration histories $a(t)$ at the ground surface that would occur in the absence of liquefaction, which can be obtained from available strong motion recordings nearby, or from site-response analyses calculated by computer codes such as SHAKE, DESRA, etc., or attenuation relations [188, 416, 421]; $\sigma_{v0}(z)$ is the total stress at depth z .

Because the acceleration in each soil layer during an actual earthquake is transient with unequal cyclic amplitude, leading to an irregular shear stress time history consisting of widely different cycles of acceleration and stress, laboratory tests to obtain the liquefaction resistance are usually performed with a constant and harmonic amplitude of excitations. To correlate the number of uniform stress cycles that cause the liquefaction initiation obtained from laboratory tests with the irregular shear stress time history during real earthquakes, an equivalent uniform cyclic shear stress, with a corresponding number of equivalent cycles N_{eq} is introduced by multiplying the maximum shear stress in the irregular time history with a reduction factor ψ [422], which would result in the same amount of increase in pore-water pressure as the irregular stress history does. The factor ψ is normally taken as 65%, and the equivalent number of cycles is related to the time duration, which is strongly influenced by the moment magnitude of earthquake as shown in Fig. 7.11.

The equivalent uniform cyclic shear stress amplitude is then written as:

$$\tau_{\text{cyc}}(z) = \Psi r_d(z) \frac{\sigma_{v0} a_{\max}}{g} \quad (7.11)$$

Fig. 7.11 Number of equivalent cycles N_{eq} dependent on earthquake magnitude [423] (courtesy of Earthquake Engineering Research Institute, California)



Readers need to bear in mind that the equivalent uniform cyclic shear stress amplitude is typically not used in the development of liquefaction resistance chart shown in Fig. 7.12, while it is still useful to relate the chart to laboratory tests involving uniform loading cycles.

A cyclic stress ratio (CSR) can be defined as:

$$CSR = \Psi r_d(z) \frac{\tau_{\max}(z)}{\sigma'_{v0}(z)} \quad (7.12)$$

where $\sigma'_{v0}(z)$ is the initial vertical effective stress at depth z , which is normally equal to the effective vertical overburden stress before an earthquake shaking.

From the two equations above, it is obvious that, based on the cyclic stress approach, two alternative methods can be used to obtain CSR for a site: (1) from the value of a_{\max} estimated at the ground surface; or (2) directly from τ_{\max} calculated by a site-response analysis.

It should be noticed that the establishment of the equation above implies that $\tau_{\max}(z)$ and a_{\max} are not affected by pore-water pressure buildup and liquefaction in softening the soil during an earthquake. $\tau_{\max}(z)$, a_{\max} , and CSR are more properly engineering means of defining parameters related to liquefaction than realistic physical measures to quantify the soil liquefaction. This makes the entire liquefaction evaluation procedure rather simple. In the calculation of site response to obtain $\tau_{\max}(z)$ and a_{\max} , G/G_{\max} versus γ can be kept constant throughout the entire seismic motion histories. This allows the use of equivalent linear soil modeling (Sect. 2.2). The calculation of $\tau_{\max}(z)$ and a_{\max} is only useful when CSR is not larger than cyclic resistance ratio (CRR), i.e., no liquefaction occurs. Moreover, $\tau_{\max}(z)$ and CSR should not be compared with results obtained from nonlinear site-response analyses (Sect. 2.4) that use an effective stress approach and allow G/G_{\max} to degrade with time (as the pore pressure increases).

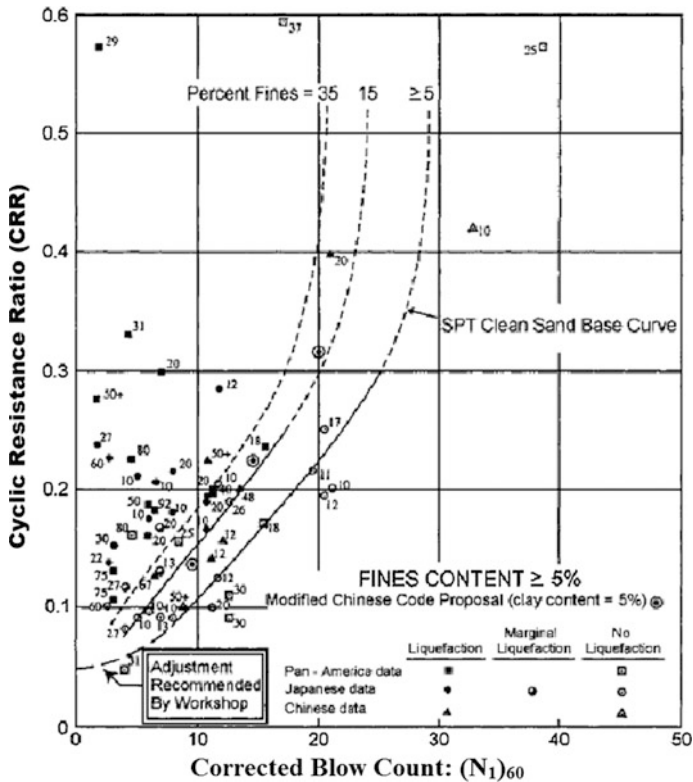


Fig. 7.12 CRR versus $(N_1)_{60}$ for earthquakes with a magnitude of 7.5, based on standard penetration tests (courtesy of National Center for Earthquake Engineering Research)

7.2.2.2 Determine Cyclic Resistance Ratio (CRR) from Recommended Charts

SPT is the most widely used tool to determine the liquefaction resistance, which is characterized by the standard penetration resistance of soils normalized to a vertical effective overburden pressure of one atmospheric pressure, known as the corrected standard penetration resistance $(N_1)_{60}$. $(N_1)_{60}$ is normally defined as a corrected number of blows to a reference overburden pressure of 100 kPa, and to a 60% ratio between the actual energy delivered by the hammer to the theoretical free-fall energy in the last 30 cm of penetration, obtained from field SPT measurements. See Sect. 1.9.5 for more details.

The method was successfully calibrated with recorded time histories during earthquakes. By performing SPTs, boring is excavated and the ground water table location can be measured in boreholes. It is well understood that well-graded dense

sands are more resistant to liquefaction and have high standard penetration value. However, uniformly graded soil with loose or segregated soil is more susceptible to liquefaction and has a lower N -value. For example, sand with a standard penetration value of between 0 and 20 is highly susceptible to liquefaction.

Even if the adoption of $(N_1)_{60}$ has obvious advantages, the method is still not widely adopted in practice. Empirical charts are normally used for simplified liquefaction analyses, which represent field correlations between in situ measurements and cyclic shear stresses known to have caused liquefaction during past earthquakes. Those charts give the relationship between the CRR and $(N_1)_{60}$ [416], with an example shown in Fig. 7.12. Each curve in the chart separates sites where liquefaction has been observed from those where liquefaction did not occur, and these curves have been calibrated by case histories of liquefaction or no liquefaction during actual earthquakes for which a CSR is calculated and used to plot the data points [424]. In principle, data to the left of the line indicates liquefaction during earthquakes, while data to the right indicates no liquefaction during earthquakes. Sometimes, more than one curve is given, which corresponds to soils with different fines contents or to different earthquake magnitudes.

Recently, it has been argued that the empirical graphs with the forms shown in Fig. 7.12 are fundamentally wrong, as they ignore the initial stress level on one axis but use a pressure normalized penetration resistance on the other axis. The implied relationship for post-liquefaction strength is dimensionally inconsistent, and the chart cannot possibly be useful in a predictive sense [401].

In order to be able to continue to use the chart above, the percentage of fines in the soil sample should be determined by performing field and laboratory analysis. It is obvious that soils with a higher percentage of fines have higher liquefaction resistance. By knowing $(N_1)_{60}$ and estimated percentage of fines, CRR of soils can be estimated by checking the chart.

The equivalent number of uniform stress cycles changes with the earthquake magnitude due to the fact that the duration of an earthquake is strongly influenced by its magnitude [188], with examples shown in Table 7.1 and Fig. 7.11. The majority of the similar CRR charts available nowadays are applicable for earthquakes with a moment magnitude of 7.5 and corresponding uniform stress cycles of around 20. With an increase in earthquake magnitudes, the duration of ground shaking and hence the equivalent number of uniform stress cycles also increase [188]. Consequently, cyclic shear strain will increase. On the other hand, if the earthquake magnitude decreases, the number of uniform stress cycles decreases by increasing the soil resistance. On the other hand, in the case of a smaller earthquake including only a few stress cycles, the soil can resist a much greater stress ratio. Practically, this change is accounted for by adjusting the CRR of soils. Therefore, for earthquakes with a moment magnitude different from 7.5, the CRR obtained

Table 7.1 Equivalent number of uniform stress cycles presented by Seed and Idriss [425]

Anticipated earthquake magnitude in Richter scale	Approximate equivalent number of stress cycles
5.25	2–3
6	5–6
6.75	10
7.5	15
8.5	26

Table 7.2 *MSF* based on moment magnitude [425]

Anticipated moment magnitude	Magnitude scaling factor
5.25	1.5
6	1.32
6.75	1.13
7.5	1.00
8.5	0.89

Table 7.3 *MSF* based on surface wave magnitude [426]

Anticipated surface wave magnitude	Magnitude scaling factor
5.5	2.86
6	2.20
6.5	1.69
7.0	1.30
8.0	0.67

from Fig. 7.12 (also denoted as $CRR_{7.5}$) should be multiplied by a magnitude scaling factor (*MSF*), which is originally introduced by Seed and Idriss [425] as given in Table 7.2. This table shows a typical set of *MSFs* based on moment magnitude. The *MSF* can also be calibrated based on surface wave magnitude, such as the one used by Eurocode 8 [198], as shown in Table 7.3.

In addition, Idriss and Boulanger [427, 428, 423] proposed that *MSF* can be calculated as follows:

$$MSF = 6.9e^{-(M_w/4)} - 0.058 \leq 1.8 \tag{7.13}$$

Andrus and Stokoe [429] proposed that:

$$MSF = (M_w/7.5)^{-2.56} \tag{7.14}$$

The calculation above is adopted in Eurocode 8 [198].

Youd and Noble [430] used a probabilistic and logistic analysis to study case history data and defined three sets of *MSFs* with different moment magnitude (M_w) ranges and probability of liquefaction occurrence (P_L):

$$P_L < 20\% : MSF = 10^{3.81} / M^{4.53} \text{ for and } M_w < 7.0 \quad (7.15)$$

$$P_L < 32\% : MSF = 10^{3.74} / M^{4.33} \text{ for and } M_w < 7.0 \quad (7.16)$$

$$P_L < 50\% : MSF = 10^{4.21} / M^{4.81} \text{ for and } M_w < 7.0 \quad (7.17)$$

The NCEER workshop report [416] provides a practical recommendation for the choice from various methods above to determine $MSFs$.

It is noted that at sites supporting heavy structures or with sloping ground, the resultant high effective confining stress will increase the cyclic shear stress that potentially leads to liquefaction. On the other hand, if the initial static shear stress is larger than the steady-state strength, the liquefaction resistance will be reduced. Special expertise is then required for an evaluation of liquefaction resistance with a sloping of more than 6% [416]. Therefore, in addition to MSF , the CRR must also be corrected for overburden pressure with an overburden correction factor K_σ , and be corrected for the initial shear stress, with a static shear stress correction factor K_x .

As the laboratory cyclic triaxial compression tests show that liquefaction resistance increases with the increase in confining stress, the resistance, measured by the stress ratio, is a nonlinear function that decreases with the increased normal stress. Various methods to determine the overburden correction factor K_σ are available to account for this nonlinearity for overburden pressure higher than 100 kPa. Hynes and Olsen [431] proposed that:

$$K_\sigma = \left[\frac{\sigma'_{v0}(z)}{p_a} \right]^{f-1} \quad (7.18)$$

where $\sigma'_{v0}(z)$ is the effective overburden stress at depth z ; p_a is the atmospheric pressure; the parameter f is a function of site conditions, for clean and silty sands and gravels, it can be conservatively estimated as: $f = 0.7-0.8$ for relative density to water D_r ranging from 40 to 60% and $f = 0.6-0.7$ for D_r ranging from 60 to 80%.

Idriss and Boulanger [423] in 2008 proposed that:

$$K_\sigma = 1 - C_\sigma \ln \left[\frac{\sigma'_{v0}(z)}{P_a} \right] \leq 1.1 \quad (7.19)$$

where $C_\sigma = \frac{1}{(18.9 - 2.55\sqrt{(N_1)_{60}})} \leq 0.3$.

At sloping ground condition, initial shear stress exists. It is accounted for using the static shear stress correction factor K_x as originally introduced by Seed [432] to account for the effects of static shear stresses on CRR. In the 1996 NCEER workshop [433], it was concluded that the wide ranges in K_x values developed in past investigations indicated a lack of consensus and a need for continued research and field verifications, and general recommendations for use of K_x by the engineering professionals were not advisable at this time. Since then a few methods

have been proposed, with the most widely accepted one being proposed by Idriss and Boulanger [434]:

$$K_\alpha = CRR_\alpha / CRR_{\alpha=0} = a + b \cdot e^{(\zeta/c)} \tag{7.20}$$

where $a = 1267 + 636\alpha^2 - 634e^\alpha - 632e^{-\alpha}$; $b = \exp[-1.11 + 12.23\alpha^2 + 1.31 \ln(\alpha + 0.0001)]$; $\alpha = \tau_{h,static} / \sigma'_{v0}(z) \leq 0.35$; $\tau_{h,static}$ is the static shear stress; $c = 0.138 + 0.126\alpha + 2.56\alpha^3$; $\zeta = [Q - \ln(100p'/p_a)]^{-1} - D_r$; Q is an approximate function of grain-type-related empirical constant, it equals to 10 for quartz and feldspar, 8 for limestone, 7 for anthracite, and 5.5 for chalk; p' is the mean effective normal stress; $-0.6 \leq \zeta \leq 0$;

Finally, CRR can be calculated as:

$$CRR_f = CRR_{7.5} \cdot MSF \cdot K_\sigma \cdot K_\alpha \tag{7.21}$$

Liquefaction can then be evaluated by comparing the loading and resistance at various depths of interests, which is normally performed by calculating the factor of safety (F_s) against liquefaction:

$$F_s = CRR_f / CSR \tag{7.22}$$

Once the factors of safety throughout soil deposits of interest are obtained, the potential liquefaction area can be conveniently identified graphically as shown in Fig. 7.13. From this figure, it also shows that at certain depth and below, the safety factor is sufficient. This fact is reflected in various codes. For example, Eurocode 8 [426] specifies that, for buildings on shallow foundations, evaluation of the liquefaction potential may be omitted when the saturated sandy soils are found at depths more than 15 m below the surface.

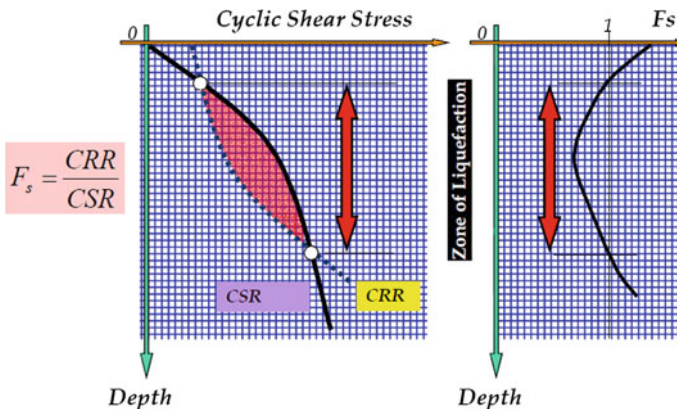


Fig. 7.13 Potential liquefaction area at the depth with $F_s < 1.0$ [435]

Theoretically, a minimum F_S of at least 1.0 is required. However, soils having a factor of safety slightly greater than unity can also liquefy. A possible relevant scenario is that if a deeper soil layer liquefies, the upward water flow could induce liquefaction of upper layer as well. In Eurocode 8 [426], based on the simplified method, a F_S of at least 1.25 is required.

In addition SPT, CPT can also be used to determine the liquefaction resistance. Compared to SPT, CPT can detect thick seams of loose soils. This is why SPT-based liquefaction criteria are normally valid only when potentially liquefiable soils occur in layers or seams no more than a few tens of a centimeter thick. Similarly, the resulting chart contains the relationship between CRR and a liquefaction resistance parameter, which is the normalized static cone penetration resistance $q_{c1,N}$, with typical ones shown in Fig. 7.14 for clean sands given by Idriss and Boulanger [428, 423]. Figure 7.15 shows a similar chart using probabilistic approach to identify the liquefaction occurrence.

Originally motivated by the strain approach (Sect. 7.2.3) to identify liquefaction [437, 438], and subsequently compared with liquefaction performance at sites subjected to the Imperial Valley earthquake [439], the normalized shear wave velocity v_{s1} has also been introduced as a liquefaction resistance parameter in the horizontal axis of the chart, as shown in Fig. 7.16. This is obtained by correlating the penetration resistance with shear wave velocity at potentially liquefiable sand sites. A widely known method is proposed by Andrus and Stokoe [440] as shown in Fig. 7.16 and expressed as:

$$CRR = 0.22 \left[\frac{(v_{s1})_{cs}}{100} \right] + 2.8 \left[\frac{(v_{s1})_{cs}}{215 - (v_{s1})_{cs}} - \frac{1}{215} \right] \tag{7.23}$$

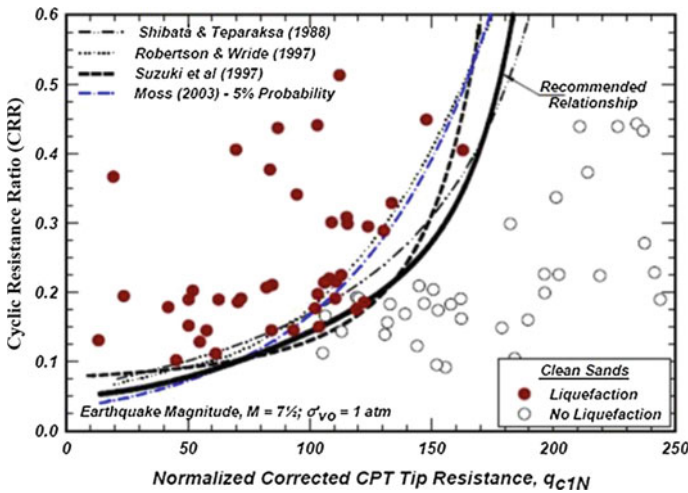


Fig. 7.14 Liquefaction chart for clean and silty sands based on point resistance measured during static CPTs by Idriss and Boulanger [428, 423]

Fig. 7.15 Probabilistic contours for liquefaction of sands during earthquakes with a magnitude of 7.5 using static CPTs [436]

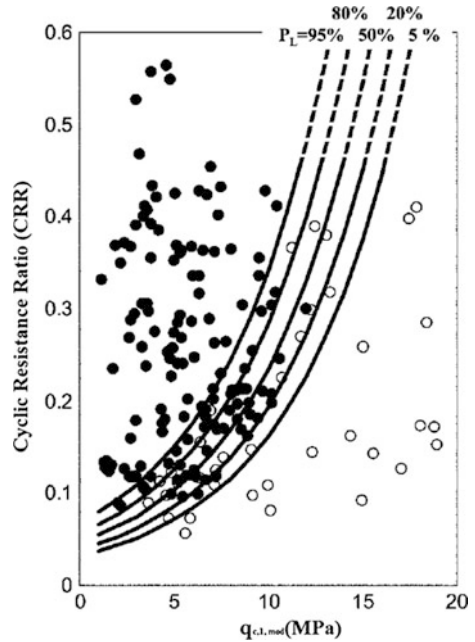
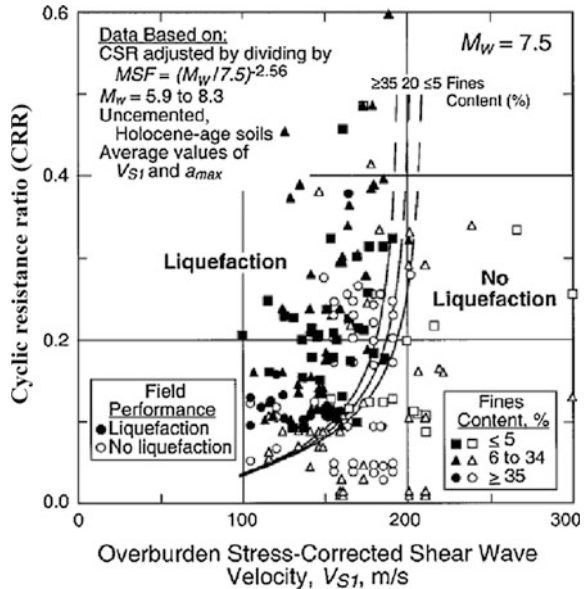


Fig. 7.16 Liquefaction chart based on measured shear wave velocity [440]



where the subscript *cs* is the abbreviation for clean sand (soils with 5% or less fines); $(v_{s1})_{cs}$ is the overburden stress-corrected shear wave velocity to account for the influence of the state of stress in soils, defined as:

$$(v_{s1})_{cs} = K_{cs} v_{s1} = K_{cs} v_s (p_a / \sigma'_{v0}(z))^{0.25} \quad (7.24)$$

where v_{s1} is the overburden stress-corrected shear wave velocity of sandy soils; p_a is the reference stress of 100 kPa or about atmospheric pressure; K_{cs} is the correction factor associated with fines content, which is normally measured from SPT samples, in case no measured data is available, estimation based on CPT data may also be used, see [441]; v_s is the measured shear wave velocity without considering overburden stress.

K_{cs} may be calculated based on Juang et al. [442]:

$$K_{cs} = 1.0 \text{ for } FC \leq 5\% \quad (7.25)$$

$$K_{cs} = 1.0 + (FC - 5)T \text{ for } 5\% < FC < 35\% \quad (7.26)$$

$$K_{cs} = 1.0 + 30T \text{ for } FC \geq 35\% \quad (7.27)$$

where FC is the fines content; $T = 0.009 - 0.0109 (v_{s1}/100) + 0.0038 (v_{s1}/100)^2$.

However, correlations between shear wave velocity and the soil resistance to liquefaction are still under development with limited research efforts and should normally be used with assistance from relevant specialists.

Readers must bear in mind that the current simplified procedure is based on the criteria for the initiation of liquefaction, which is well understood. However, the behavior after initial liquefaction is understood with much less clarity due to its complexity and lower accessibility of associated data.

7.2.3 Cyclic Strain Approach

As pore-water pressure is physically more associated with cyclic strains than stresses, and also because a large number of factors influence the cyclic stresses that lead to the soil liquefaction, a more reliable approach is to use cyclic strain rather than stress to characterize the earthquake-induced loading and liquefaction resistance [1], as originally proposed by Dorby and his co-workers [443, 444].

Similar to the cyclic stress approach, in the cyclic strain approach, the evaluation is based on a comparison between uniform cyclic strain and the liquefaction resistance.

Dorby and his co-workers [444] proposed a simplified method to calculate the uniform cyclic strain:

$$\gamma_{cyc}(z) = 0.65 \cdot r_d(z) \frac{\sigma_{vo}(z) a_{max}}{gG(\gamma_{cyc}(z))} \quad (7.28)$$

where $G(\gamma_{cyc}(z))$ is soils' shear modulus when the shear strain is at the level of $\gamma_{cyc}(z)$, obviously, it must be calculated using iteration from measured G/G_{max} .

After the uniform cyclic strain is obtained, it can be compared with the threshold shear strain γ_t . It is obvious that no water pressure can be generated if $\gamma_{\text{cyc}}(z) < \gamma_t$, i.e., liquefaction initiation is not possible. However, if $\gamma_{\text{cyc}}(z) > \gamma_t$, liquefaction initiation may occur, and further evaluation must then be performed to identify the liquefaction resistance.

For an elaboration of liquefaction assessment, readers may read the reference by Idriss and Boulanger [423].

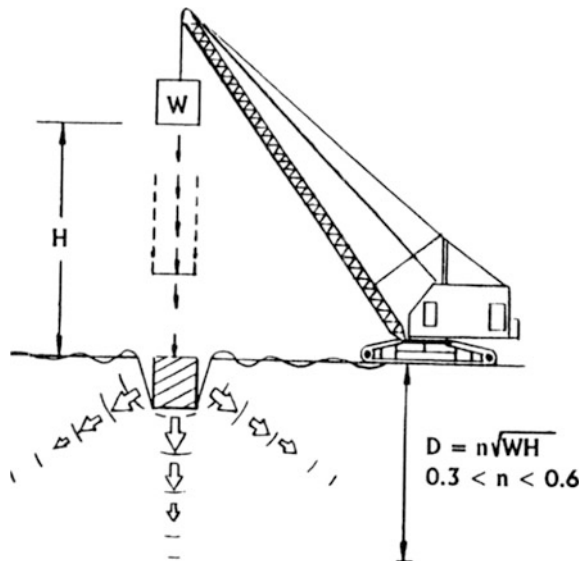
7.3 Liquefaction Mitigations

The general strategy to mitigate the liquefaction hazard can be realized through the following measures:

1. Improve the strength, density, and/or drainage characteristics of relevant soils.
This can be fulfilled by using a variety of soil improvement techniques.
2. Design foundation elements to resist liquefaction.
3. Avoid liquefaction susceptible soils.

More often, the liquefaction damage can be mitigated through a few practical approaches, such as soil densification (such as vibro-compaction, deep soil mixing, dynamic compaction (Fig. 7.17), or explosive compaction); increasing the overburden pressure so that the vertical effective stress also increases; stone columns (dense columns of gravel) to reinforce the soil deposit and drain the water (dewater) in soils so that the pore pressure buildup can be avoided; removal of liquefiable soils; using piles as additional supporting foundations, etc.

Fig. 7.17 Illustration of dynamic compaction [449]



It is noted that soil densification has generally proven to be effective in clean sands, but not for sands with higher fines contents. In such cases, drainage to reduce excessive pore-water pressures during the cyclic loading can be applied. The concept of using vertical gravel drains for liquefaction mitigation was proposed by Seed and Booker [445], who also presented design charts to determine drain diameter and spacing. Improved curves that account for head losses were developed by Onoue [446]. Although the introduction of a stone column (gravel drains) of freely draining gravel into a liquefiable soil deposit has been utilized at many sites for liquefaction mitigations, most designers have relied on the densification provided by the stone column installation rather than the drainage. One concern has been that the drainage may cause significant settlement [447]. In addition, investigators indicate that sand infiltration can reduce hydraulic conductivity and flow capacity of gravel drains in practice relative to laboratory values [448]. More recently, vertical, slotted drain pipes (often referred to as “earthquake drains”) with diameters from 75 to 150 mm have been installed using vibrating steel mandrel. The drains are typically placed in a triangular grid pattern at center-to-center spacings of 1–2 m depending on the permeability of the treated soil. A 100 mm diameter of such drain pipe can carry sufficient flow volumes ($0.093 \text{ m}^3/\text{s}$) to relieve water pressure in sands. This flow volume is more than 10 times that provided by a 1 m diameter stone column ($6.51 \times 10^{-3} \text{ m}^3/\text{s}$). Filter fabric tubes are placed around the drains to prevent infiltration of silt and sand. These vertical drains can be installed faster than and at a fraction of the cost of stone columns and can reduce the settlement by 20–60% compare with that in untreated sites [447].

It is obvious that, by draining the excess water in soils, potential risk associated with the liquefaction can be greatly minimized. In many offshore gravity-based structures, anti-liquefaction systems have been installed to minimize the excess pore-water pressure in the skirt compartments, preventing the buildup of excessive water pressure during storms or earthquakes. Moreover, since heavy gravity-based structures normally induce high effective stress on soils, it is difficult for pressure buildup to significantly decrease the effective stress to a rather low level, and this also helps for mitigating liquefaction. However, liquefaction can also be triggered by water flowing to the gravity-based foundation, which can dramatically increase the pore pressure.

Chapter 8

Slope Stability Due to Seismic Loading

8.1 General

Slope instability due to earthquakes is one of the most damaging collateral hazards. Earthquakes are the greatest threat to the long-term stability of slopes in earthquake-active regions. Damage from triggered landslides and other ground failures has sometimes exceeded damage directly related to strong shaking and fault rupture. Seismically triggered landslides damage and destroy homes and other structures, block roads, sever pipelines and other utility lifelines, and block stream drainages [450].

Subject to earthquake loading, the acceleration produced by the ground motions will induce cyclically varying forces on slopes, embankments, and dams. Moreover, the soil's shear strength degrades to a certain extent (Sect. 2.1). Both effects are relevant to slopes' instability. On the other hand, due to strain rate effects (Sect. 2.5), instant shear strength for clay soils will increase by 20–50% subject to undrained seismic loading. This increase can offset the reduction in shear strength due to an increase in soil strain. Therefore, in many cases, it is reasonable to neglect the degradation in soils' shear strength.

Four methods have been widely used to assess the slope stability subject to earthquake loading: pseudo-static analysis approach, dynamic stress-deformation analysis approach, Newmark sliding-block approach, and testing method.

Pseudo-static analysis approach (Sect. 8.2) was the earliest developed method and involves simply adding a permanent body force representing the earthquake shaking to a static limit-equilibrium analysis. It is suitable for preliminary analyses and screening procedures that precede more sophisticated analyses [451].

Stress-deformation analysis (Sect. 8.3) involves a much more complex modeling of slopes by using numerical methods such as finite element method (most often), finite difference method, boundary element method, and discrete element method. In this method, the internal stresses and strains within elements are computed based on the applied gravity and seismic loads. With a dedicated modeling for

stress–strain behavior of soils, this type of analysis provides a reliable prediction of mode of failure, even though this method is much more demanding with respect to soil data input and computation efforts required. This analysis method is applicable for critical infrastructures such as dams and embankments or slopes adjacent to critical lifelines or structures.

The Newmark sliding-block approach (Sect. 8.4) is much more convenient than the stress-deformation analysis and yields more useful information than pseudo-static analysis, even though the Newmark sliding-block approach is slightly more complex than that of pseudo-static analysis. Subsequent modifications to sliding-block analysis have made it applicable to a wider range of landslide types [452].

Depending on which method presented above is adopted, tools for analyzing stability of slopes include simple equations, charts, spreadsheet software, and slope stability analysis codes. In many cases, more than one tool is used to evaluate the stability for a particular slope [24].

Various testing methods (Sect. 8.5) can be used to identify more realistic weak geological features, damage mechanisms, and stability states of slopes.

It should be noticed that both the pseudo-static analysis approach and Newmark sliding-block approach are suitable for analyzing the inertial instability of slopes, in which the shear strength is assumed to be unchanged during an earthquake event, but slope instability takes place when a temporary exceedance of strength due to cyclic stress occurs. If a shear strength reduction occurs due to, for example, pore-water pressure generations, weakening instabilities can occur when the static and dynamic shear stress in a slope is larger than the reduced strength of the soil. Different approaches have to be adopted, and these are discussed in source [1].

Moreover, problems regarding post-earthquake slope instabilities have been reported worldwide mainly due to the reduced shear strength under cyclic loading, which should be assessed by accounting for the effects of pore-water pressure development in soils, as will be briefly discussed in Sect. 8.6.

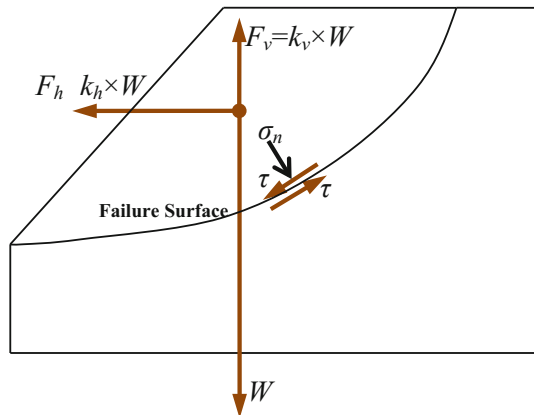
8.2 Pseudo-Static Analysis Approach

If the reduction in the strength of soils is not significant (typically less than 15%), semi-empirical pseudo-static analyses [453] using the limit-equilibrium concept can normally be adopted.

This method consists of analyzing the cross-section of the potential slide mass, called the failure surface, as either a circular or non-circular surface as shown in Fig. 8.1. The area enclosed between the slope face and the failure surface, known as the failure mass or sliding soil mass, is subdivided into a series of slices that are then analyzed for equilibrium.

The earthquake loading is simplified as static horizontal forces and in many cases also vertical forces, applied to the potential sliding soil mass, normally represented by horizontal and vertical pseudo-static (seismic) coefficients. Typical

Fig. 8.1 Illustration of pseudo-static analysis approach, k_h and k_v are horizontal and vertical pseudo-static (seismic) coefficients, respectively; W is the weight of the potential sliding soil mass



horizontal pseudo-static coefficients range from 0.05 to 0.5 as given by various seismic design codes (e.g., Eurocode 8-5 [426]). By summarizing a number of published methods for determining an appropriate seismic coefficient, Kramer [1] concluded that “there are no hard and fast rules for selection of a pseudo-static coefficient for design”: a rigorously rational basis for selecting a pseudo-static coefficient remains elusive, and engineering judgment along with standard of practice generally is invoked in the selection process [452]. To cope with this dilemma, based on calibrations measured by allowable displacements, in recent years, various researchers have attempted to find rational ways to determine pseudo-static coefficient. Stewart et al. [451] developed a screening analysis procedure based on the statistical relationship presented by Bray and Rathje [454], in which a pseudo-static coefficient is calculated as a function of maximum horizontal ground acceleration, earthquake magnitude, source-site distance, and two possible levels of allowable displacement (5 and 15 cm). Bray and Travasarou [455] proposed a direct approach to determine the pseudo-static coefficient as a function of allowable displacement, earthquake magnitude, and spectral acceleration.

Since soil slopes are not rigid and the peak acceleration generated during an earthquake lasts for only a very short duration, while the earthquake shaking in pseudo-static analysis assumes a permanent, unidirectional body force, seismic coefficients used in practice generally correspond to acceleration values within the failure mass well below the anticipated peak accelerations [1], and the effects of transient nature and duration of earthquake motion may not be captured in this method. Shear strengths measured in cyclic loading tests are appropriate for analyses of stability during earthquakes. This analysis is normally performed first to judge the significance of the deformation due to seismic loading, and the selection of an appropriate seismic coefficient is essential for the reliability of this type of analysis. Unfortunately, there are no widely accepted specific rules for selecting an appropriate seismic coefficient for design [456].

The center of gravity (CoG) of the potential sliding soil mass is normally taken as the acting point of the equivalent forces [457]. However, strictly speaking, this

assumption is only valid if the accelerations are constant over the entire soil mass, which is in the majority cases not true. For example, peak accelerations increase due to soil amplification from the bottom to the top of a dam. The location of the resultant seismic force is then expected to be above the CoG of the slice. By studying the sensitivity of the locations of the action point for Sheffield Dam, Seed [453] showed that the location assumed for the seismic force can have a small but noticeable effect on the computed factor of safety, a change in the location of the pseudo-static force from the CoG to the bottom of the slice reduces the factor of safety from 1.32 to 1.21 for a seismic coefficient of 0.1. However, the assumption that the force is acting on the CoG is normally slightly conservative for most dams [24].

The factor of safety in terms of total stress can be calculated as a ratio of capacity (shear strength of soil: $c + \sigma_n \tan \phi$) to demand (shear stress induced on the potential failure surface: τ):

$$SF = \frac{c + \sigma_n \tan \phi}{\tau} \quad (8.1)$$

See Sect. 1.6.2 for the definition of the items in Eq. (8.1).

Similar definitions of factor of safety can be derived based on effective stress concept.

The required factor of safety typically ranges from 1.3 to 1.6 and should always be above unity to account for the uncertainties in assumed mechanism of failure, soil properties, ground water conditions, slope geometry, likelihood and duration of exposure to various types of external loading, and potential consequence of slope failure, etc. [1].

It is noted that, to render the inherently indeterminate analysis determinate, conventional limit-equilibrium methods generally make use of assumptions regarding the relationship between the inter-slice forces, and it is commonly accepted that factors of safety are identical at all points along the failure surface because the sliding soil mass is assumed to be rigid. These assumptions may appear to be unreasonable since the actual stresses acting along the slip surface are quite approximate and the location of the critical slip surface depends on the shape assumed by analysts [458], and the soil along the failure surface in actual slopes does not fail simultaneously. As many soils exhibit a strain-softening stress-strain behavior, in which a dramatic decrease in shear strength will occur after the soil reaches its peak strength, stress redistribution will then take place to transfer the difference between the peak and residual strength of the soil to the surrounding soil, potentially causing the exceedance in the peak strength for the surrounding soil, leading to a reduction in shear resistances to residual values for the surrounding soil. As this process continues, a zone of failure may grow until the entire slope becomes unstable. Therefore, even when the limit-equilibrium factor of safety based on the peak strength is well above 1.0, progressive failure of soil may still occur. Moreover, it is important to compare the analysis results with field measurements.

It should be noticed that the presence of a hard cohesive layer at the top of the slope or the presence of a very dense granular layer at the bottom of the slope can produce slip surfaces that are almost vertical [459]. In such cases, it is recommended to adopt the modeling of tension cracks at the top of the slope to flatten the exit angle at the lower end of the slip surface [460]. Such cases are mostly ignored by most engineers due to a lack of engineering understanding of slope stability analysis limitations, which may result in misleading factors of safety.

Even though in most cases, pseudo-static analysis is too conservative, Kramer [1] stated that this approach can be unconservative for slopes composed of materials that build up significant dynamic pore pressures during ground shaking or that lose more than about 15% of their peak shear strength. This statement is enhanced by a few case studies for dams that have a sufficient factor of safety through pseudo-static analysis but exhibit instability problems during previous earthquakes [453].

For more details of the pseudo-static analyses, readers may refer to source [24].

Readers may notice that even if pseudo-static analysis method has been termed “pseudo-static” for many years, it is essentially a static approach and therefore may correctly be termed “pseudo-dynamic.”

8.3 Dynamic Stress-Deformation Analysis Approach

If the reduction in the soil strength is greater than 15%, dynamic stress-deformation analysis [461] is often employed to assess the deformation, performed using numerical methods such as finite element method, finite difference method, boundary element method, and discrete element method. Dedicated nonlinear soil behaviors, with relatively simple hyperbolic soil models [462, 463], can be implemented. Various boundary conditions, irregular slope geometries, and a variety of construction operations can all be accounted for [1].

This method can determine much more parameters (such as magnitudes and patterns of stresses, movements, and pore-water pressures in slopes during and after construction/deposition) than factors of safety do in a pseudo-static analysis.

This method has been developed and implemented in 2D and 3D models (e.g., Ref. [464–466]). It is noted that 3D slope stability analysis is still not routinely used by geotechnical engineers even though most slope stability problems are 3D. This may be due to the facts that (1) it is commonly believed that 2D slope stability analysis provides a more conservative estimate of the 3D slope stability problem [467–469], even though the factors of safety obtained from 2D slope stability analyses are not necessarily more conservative than 3D slope stability analyses [459]; (2) a 3D slope stability analysis is much more demanding with regard to computational efforts than a 2D analysis. On the hand, with the development of computer technology, 3D slope stability analysis is more accessible to geotechnical engineers nowadays [470].

For real engineering applications, dynamic stress-deformation analyses are often carried out with the aid of commercial codes such as FLAC, which uses the explicit finite difference method to solve the full dynamic equations of motions using lumped grid point masses derived from the surrounding finite elements. Other programs, such as PLAXIS, QUAD-4, and FLUSH, are also available for dynamic analysis to assess the slope stability. However, readers may observe that the finite element analysis may not capture some important failure phenomena such as liquefaction at large deformations, slipping and rolling, which do exist during the process of realistic ground motions.

Because the stress-deformation analysis is demanding with respect to complexity of soil data input and computational efforts (as very fine mesh is required to capture local deformation for landslides), it is normally used only for critical projects such as earth dams and slopes affecting critical lifelines or structures. Moreover, stress-deformation analysis is rather site specific and cannot be applied to regional problems, as pseudo-static analysis or Newmark sliding-block approach can.

8.4 Newmark Sliding-Block Approach

Like all approaches using the limit-equilibrium method, the pseudo-static approach can only check whether or not slope instability will occur by judging the factor of safety. However, the deformation associated with slope instability failure cannot be obtained.

Therefore, based on the pseudo-static method and by utilizing Newmark's direct integration method, Newmark [471] considered the situation when the factor of safety decreases to less than 1.0 and proposed a simple method to assess permanent displacements in a slope due to seismic ground motions. As shown in Fig. 8.3, this is referred to as the Newmark sliding-block approach, rigid-block method, or permanent displacement analysis method. In this method, the sliding soil mass is taken as a rigid sliding-block, which slides on a plane surface as shown in Fig. 8.2. Analysis using the Newmark sliding-block approach has been found to agree with both laboratory model tests [472–474] and dynamic analysis of earthquake-induced landslides in natural slopes [475]. Permanent displacement analysis begins at exactly the point where pseudo-static analysis ends: at the time when the critical or yield acceleration is exceeded.

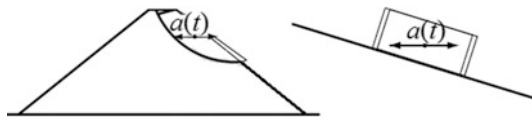


Fig. 8.2 Sliding soil mass in an actual slope (left) is taken as a rigid sliding-block (right) to compute permanent soil displacements in a slope subjected to seismic acceleration $a(t)$ [24]

The Newmark sliding-block analysis can be categorized into three types of analysis: rigid-block, decoupled, and coupled, among which the rigid-block analysis is that originally proposed by Newmark [471].

8.4.1 Rigid-Block Analysis

When the acceleration of the block exceeds a_{yield} , the block begins to slip along the plane, i.e., the factor of safety is below 1.0. The a_{yield} for a soil block sliding in the downslope direction (Fig. 8.2) can be calculated as:

$$a_{\text{yield}} = g \tan(\phi - \alpha) \quad (8.2)$$

where α is the angle of the slope; g is the acceleration of gravity.

When α is small, the soil block can also slide in the uphill direction, the a_{yield} can then be calculated as:

$$a_{\text{yield}} = g (\tan\phi + \tan\alpha) / (1 + \tan\phi \tan\alpha) \quad (8.3)$$

Based on the limit-equilibrium method, the mass experiences no permanent displacement until the acceleration of the block exceeds the critical acceleration ($a(t)$ in Fig. 8.2) at a_{yield} ; velocity time history is determined by integrating the parts of an acceleration time-history that lies above a_{yield} , which is further integrated to yield the cumulative displacement. The block continues to move after the acceleration falls below the yield acceleration. Sliding continues until the relative velocity between the block and base reaches zero. The block will slip again if the acceleration again exceeds the a_{yield} . The process above continues until the accelerations fall below the yield acceleration, and the relative velocity drops to zero for the last time.

In practice, an acceleration time-history (upper figure in Fig. 8.3) is selected first, and before accelerations reaches a_{yield} for the first time, the acceleration causes no permanent displacement of the block. When the acceleration first exceeds a_{yield} , it is integrated once to obtain the velocity profile of the block (middle figure in Fig. 8.3). A second integration is performed to obtain the cumulative displacement history of the block (lower figure in Fig. 8.3).

By using a relatively simple limit-equilibrium model of an infinite slope in material having both frictional and cohesive strength, the factor of safety SF can be estimated as:

$$SF = \frac{c'}{\gamma h \sin \alpha} + \frac{\tan \phi'}{\tan \alpha} - \frac{m\gamma_w \tan \phi'}{\gamma \tan \alpha} \quad (8.4)$$

where ϕ' is the friction angle in terms of effective stress measures; c' is the effective cohesion; γ is the unit weight of soil; γ_w is the unit weight of water; h is the

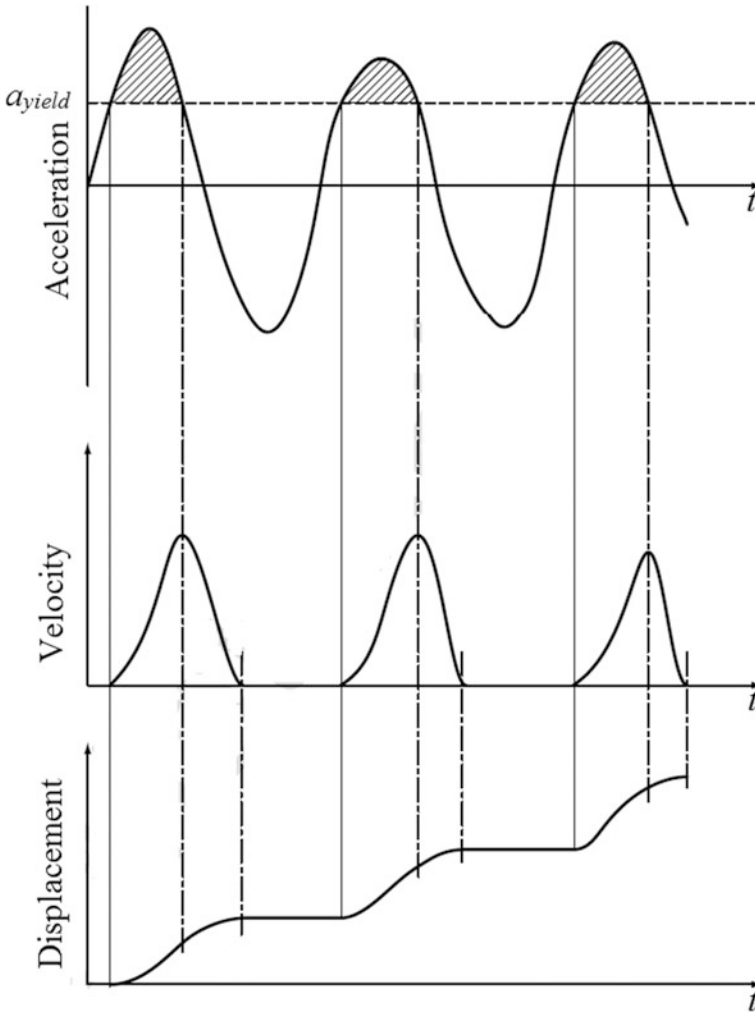


Fig. 8.3 Permanent displacement (lower) is calculated by a double integration of relative seismic acceleration time-history (upper) [24]

slope-normal thickness of the sliding soil block; m is the proportion of the slab thickness that is saturated, with $m = 0$ meaning that no pore-water pressure is accounted for.

In the equation above, the first term on the right hand side accounts for the cohesive strength component; the second term accounts for the frictional component, and the third term accounts for the reduction in frictional strength due to pore pressure.

Different from the pseudo-static method, this method depends on the limited sliding displacement of sliding blocks rather than the minimum factor of safety.

Therefore, to carry out the analysis using the Newmark sliding-block approach in a conservative manner, rather than searching for the slip surface that gives the minimum factor of safety (as the pseudo-static analysis does), slip surface that gives the minimum value of acceleration should be searched for, which is normally different from the slip surface that gives the minimum factor of safety.

Similar to the pseudo-static analysis approach, conventional Newmark's sliding-block assumes rigidity–perfect plasticity of the soil block, implying a yield acceleration that does not change with displacement, which is not realistic. Moreover, it cannot capture the process of dynamic pore-water pressure buildup subject to cyclic loading that can lead to initiations of liquefaction and failures other than simple distinct slip surfaces (the method can account for the influence due to pore-water pressure with a constant value), even though the pore pressure buildup process can normally be neglected for compacted or over-consolidated clays and very dense or dry sands [471, 476]. As a result, more rigorous methods, such as finite element analysis or finite difference analysis utilizing more dedicated soil constitutive modeling, have been utilized to overcome these shortcomings.

8.4.2 *Decoupled Analysis*

Subject to seismic loading, the sliding soil mass in reality deforms internally. This effect is in many cases important for assessing slope instability. However, the rigid-block analysis assumes a rigid sliding soil mass. To solve this, by performing the dynamic site-response analysis and the permanent displacement calculation independently, Makdisi and Seed [476] proposed a two-step procedure to estimate the effect of dynamic soil response on permanent sliding, in which a dynamic site-response analysis (Chap. 3), by neglecting the modeling of failure surface, is first performed to calculate the seismic acceleration time-histories at several points within the slope. The average acceleration time-history at the several points within the slope is taken as an equivalent acceleration and used as input into a rigid-block analysis, and the permanent displacement is finally estimated. The average acceleration has been referred to variously as k or horizontal equivalent acceleration (HEA); peak values are generally referred to as k_{\max} or maximum horizontal equivalent acceleration (MHEA). To facilitate the decoupled analysis, design charts are presented to estimate displacement as a function of critical acceleration, ground motion, and earthquake magnitude [476].

Even though the decoupled analysis has been shown to accurately predict field behavior [477], it does not account for the interaction between the sliding displacement on the seismic ground motion. Lin and Whitman [478] compared the calculated results between coupled (Sect. 8.4.3) and decoupled analyses and stated that the assumptions of the decoupled analysis introduces errors in the estimation of total slip.

8.4.3 Coupled Analysis

As its name suggests, in a coupled analysis, the effect of sliding displacement on the ground motions is accounted for by modeling the interaction between dynamic response of the sliding mass and the permanent displacement.

By using a nonlinear, fully coupled sliding-block model to produce a semi-empirical relationship, Bray and Travararou [479] have developed a simplified approach to calculate the sliding-block displacement. The model typically requires a specification of a_{yield} , the fundamental period of the sliding mass, and the spectral acceleration of the ground motion at a period of 1.5 times of the fundamental period of the sliding mass.

8.4.4 Selection of Analysis Methods

Numerical instability problem associated with coupled analysis may occur when the period ratio ($T_{\text{site}}/T_{\text{m}}$) between the site period (Sect. 3.2) and the period of the seismic motion (as will be defined below) is less than 0.1, where landslide masses behave rigidly.

Therefore, a general recommendation for selecting a sliding-block analysis is to use rigid-block analysis for period ratios less than 0.1 (analysis of data from previous earthquakes in the world has indicated that the majority of earthquake-triggered landslides have $T_{\text{site}}/T_{\text{m}}$ ratios less than 0.1) and coupled analysis for period ratios greater than 0.1 [452].

Here, T_{m} is defined as the average period of seismic motions weighted by the Fourier amplitude coefficients over a frequency range of 0.25–20 Hz [480]. It is strongly dependent on the moment magnitude (M_{w}) and source distance (r). For shallow crustal earthquakes, based on the seismic motion data obtained from western North America, at rock sites, with no forward directivity, T_{m} can be calculated as [481]:

$$\ln(T_{\text{m}}) = -1.00 + 0.18(M_{\text{w}} - 6) + 0.0038r \quad \text{for } M_{\text{w}} \leq 7.25 \quad (8.5)$$

$$\ln(T_{\text{m}}) = -0.775 + 0.0038r \quad \text{for } M_{\text{w}} > 7.25 \quad (8.6)$$

In the equation above, r has a unit of kilometers.

Even though the coupled analysis presents the most reliable results of all three methods, due to its complexity, engineers may also select decoupled or rigid-block analysis, but with careful judgment. By comparing these two methods with the more reliable coupled analysis as shown in Table 8.1, Jibson [452] presented that for $T_{\text{site}}/T_{\text{m}}$ greater than about 2, coupled analysis should be used.

Seed [453], Marcuson et al. [482], and Duncan and Wright [24] presented detailed and comprehensive analysis procedures based on a synergy of the

Table 8.1 Comparison of rigid-block analysis and decoupled analysis with the coupled analysis [452]

Slide type	T_{site}/T_m	Rigid-block analysis	Decoupled analysis
Stiffer, thinner slides	0–0.1	Best results	Good results
↓	0.1–1.0	Unconservative	Conservative to very conservative
Softer, thicker slides	1.0–2.0	Conservative	Conservative
	>2.0	Very conservative	Conservative to unconservative

pseudo-static analysis approach, dynamic stress-deformation analysis approach, and Newmark sliding-block approach. In this comprehensive analysis procedure, both undrained and drained shear strengths may be tested to determine which strengths are most critical to induce slope instability.

8.4.5 Potential of Landslides Based on the Predicted Displacement

An essential task is to identify the likelihood of landslide based on the predicted displacement. There is no consensus on exact criteria about this issue globally, but a rule of thumb is that the potential of landslide is high if the predicted displacement is greater than 5–10 cm. This is because, for the majority of the cases, this range of displacement causes ground cracking, and previously undeformed soils can end up in a weakened or residual strength condition [452]. In such a case, static stability analysis in residual strength conditions can be performed to determine the stability after the earthquake shaking ceases [483].

Blake et al. [484] proposed a guideline for the application of Newmark sliding-block analysis in Southern California:

1. For slip surfaces intersecting stiff improvements (buildings, pools, etc.), median Newmark displacements should be less than 5 cm.
2. For slip surfaces occurring in ductile (non-strain-softening) soil that do not intersect engineered improvements (landscaped areas, patios, etc.), median Newmark displacements should be less than 15 cm.
3. In soils having significant strain softening, if the critical acceleration was calculated from peak shear strengths, displacements as large as 15 cm could trigger strength reductions, which could in turn destabilize the slope. For such cases, the design should be performed using either residual strengths and allowing median displacements of less than 15 cm, or using peak strengths and allowing median displacements of less than 5 cm.

By studying the landslide data during the Northridge earthquake with the Newmark sliding-block method and fitting the data into a Weibull distribution model, Jibson et al. [485, 486] proposed that the probability of failure $p(f)$ can be expressed as a function of predicted Newmark displacement D_{newmark} for any ground shaking conditions:

$$p(f) = 0.335 \left[1 - \exp(-0.048 D_{\text{newmark}}^{1.565}) \right] \quad (8.7)$$

It is noted that the model above was calibrated at regional scale using data from Southern California, which include primarily shallow falls and slides in brittle rock and debris. Therefore, it is only rigorously applicable to these types of landslides. Jibson [452] stated that assigning geotechnical properties on a regional scale introduces significant uncertainty to such a model, which accounts for the upper-bound probability of only 33.5%; calibration at a site-specific scale with more accurate geotechnical characterization would likely yield larger probability estimates.

8.5 Testing Method

Various testing methods are also available to assess the slope stability, and these can identify more realistic weak geological features, damage mechanisms, and stability states of slopes. The most typical testing method is the shaking table test (Sect. 6.4.1), normally limited to simple surface and small scale. For large-scale shaking table and centrifuge tests of large-scale slopes with complex sliding surfaces, this method is rarely considered by using real ground motions [487].

8.6 Post-Earthquake Slope Instability Assessment

The post-earthquake slope instability may also occur even if the slope does not collapse during the earthquake. One possible reason for this may be that the soil's shear strength increases with the increase in strain rate (Sect. 2.5). Therefore, the soil has an initial gain in strength due to the seismic loading.

The post-earthquake slope stability can be analyzed using a 3-step method [24], in which the reduction in shear strength is normally treated differently depending on whether or not liquefaction occurs:

1. Estimate the potential occurrence of liquefaction, see Sect. 7.2 for details.
2. Assess the reduction in undrained shear strength of relevant soils. If liquefaction is expected to occur, a reduction of undrained (short-term) residual shear strength is estimated. Even if soil is not expected to liquefy, the pore-water pressure may increase in the soil and consequently a reduction in shear strength

can be expected. This evaluation can be based on the published results as summarized by Duncan and Wright [24]. It can also be assessed by performing laboratory tests in which specimens are consolidated to a stress level comparable to those expected in the field before the earthquake, subjected to loads simulating the earthquake, and finally, sheared to failure in a static load test.

3. Compute the slope stability using a conventional static approach. In cases where some combinations of undrained and drained (or partially drained) shear strengths control the stability, use the lower value of the two strengths.

8.7 Landslides

8.7.1 General

Damages from triggered landslides and other ground failures have sometimes exceeded damages directly related to strong ground shaking and fault rupture such as structural collapses.

As shown in Fig. 8.4, landslides can occur with five types of geology appearances:

Fall: also shown in Fig. 8.5, is a detachment of soil or rock from steep slopes along surface, with little or no shear displacement

Topple: a forward rotation of soil or rock about a point

Slides, also shown in Fig. 8.6, are a downslope displacement of soil or rock masses. They include: rotational, translational, and debris slide

Flow: a continuous movement of soil masses where shear surfaces are short lived

Spread: is a sudden movement of water-bearing rock masses

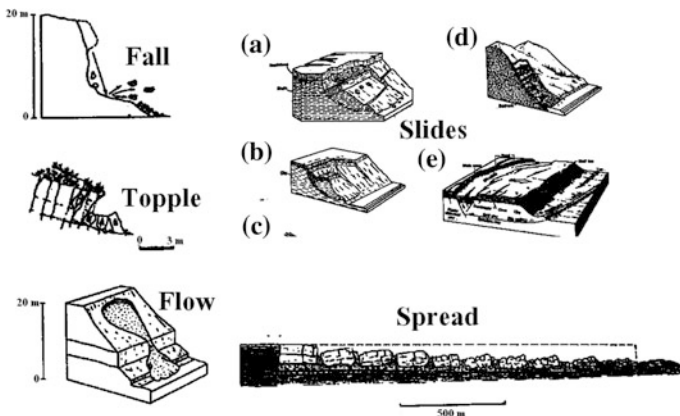


Fig. 8.4 Landslides appearances [488]



Fig. 8.5 Fall of a stone from the steep slope after the Wenchuan earthquake, May 12, 2008, China [489]

Several sources can trigger landslides: earthquake ground shaking, volcanic eruption, intense rainfall, change of water level, ground water flow, rapid snowmelt, and human activities.

8.7.2 Assessment of Regional Landslide Potential by Arias Intensity

Landslides triggered by earthquakes can roughly be classified into three types [490]: (1) Type I is rock falls and disrupted soil slides, which are mainly found in closely jointed or weakly cemented rocks (rock falls) or on steep slopes in loose, residual, or colluvial materials with low cohesion (disrupted soil slides); (2) type II is coherent deep-seated slumps, which are often found in relatively flat zones in deposits with significant cohesion; (3) type III is lateral spreads, which are sometimes formed as a consequence of liquefaction.

To characterize landslide potential on a regional scale with landslide hazard zonation, the Arias Intensity (I_A), which is a measure of the strength of a ground motion, can be used to identify possible occurrence of landslide and the associated type. It has been found to be a fairly reliable parameter to describe earthquake



Fig. 8.6 Appearance of slides after the Wenchuan earthquake, May 12, 2008, China [489]

shaking necessary to trigger landslides [493]. As mentioned before, it is typically defined as the sum of all the squared acceleration values from seismic ground motion records. Wilson and Keefer [491] presented a calculation of the spatial distribution of Arias Intensity as a function of earthquake moment magnitude M_w , distance to the closest point on the surface projection of the fault rupture R_{JB} (Fig. 11.3), focal depth h , and probability of exceedance P_e :

$$\log_{10} I_A = -4.1 + M_w - 2 \log_{10} \sqrt{R_{JB}^2 + h^2} - 0.5P_e \text{ (m/s)} \quad (8.8)$$

Based on this definition of Arias Intensity, Harp and Wilson [492] found a minimum Arias Intensity of 0.11 m/s to initiate landslides of type I. The same authors reported a minimum Arias Intensity of 0.32 m/s to be required for the initiation of landslides of type II. Larger Arias intensities indicate that stronger and longer duration shaking is required to trigger type II landslides. The knowledge above can lead to a creation of seismic landslide hazard zonation map.

For more details on evaluating landslide potential and seismic landslide hazard zonation, readers may read the sources cited above and [493].

For assessing slope stability locally due to the cyclic seismic loading, Sects. 8.2–8.5 present relevant analysis and testing methods.

Part II
Offshore Structures and Earthquake
Engineering

Chapter 9

Offshore Structures and Hydrodynamic Modeling

9.1 Introduction to Offshore Structures

9.1.1 Offshore Platforms

Offshore structures (Fig. 9.1) with their facilities are used to drill wells, to extract and process oil and natural gas, or to temporarily store product until it can be brought to shore for refining and marketing. In many cases, an offshore platform also contains facilities (e.g., living quarters) to house the workforce as well. They are defined by either their functions or their circumstances and configurations [494]. A brief review of the different types of platforms with their structural forms and uses, and the developments, is presented in a few literatures [495–497].

The functions of an offshore structure may be one of the following (even though multiple functions may be possible for a structure):

1. Exploratory Drilling Structures: a Mobile Offshore Drilling Unit (MODU) configuration is largely determined by the variable deck payload and transit speed requirements.
2. Production Structures: a production unit can have several functions, e.g., processing, drilling, workover, accommodation, oil storage, and riser support.
3. Storage Structures: used for storing the crude oil temporarily at the offshore site before its transportation to the shore for processing.

Depending on the circumstances and configuration, offshore platforms may be fixed to the ocean floor, which is typically referred to as fixed offshore platforms, including the conventional fixed jacket platforms (shown in Fig. 9.1) for a water depth of less than 400 m, jack-ups (shown in Fig. 9.34) being placed in relatively shallow waters (less than 150 m), compliant piled tower (shown in Fig. 9.1) that can be used for water depths up to 900 m, and an artificial island (Fig. 9.2). Offshore platforms may also be floating structures, including buoyant (e.g., semi-submersibles shown in Fig. 9.3, FPSO, and spars shown in Fig. 9.1) and

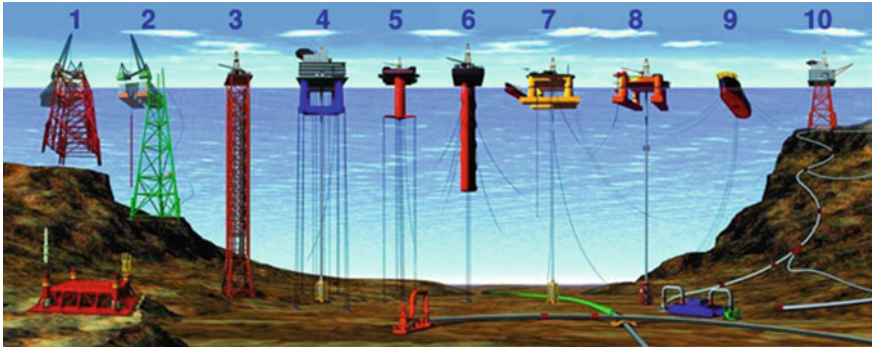


Fig. 9.1 Various types of offshore structures. 1 and 2 Conventional fixed jacket platforms; 3 Compliant piled tower; 4 and 5 Vertically moored tension leg and mini-tension leg platform (TLP); 6 Single point anchor reservoir platform (SPAR); 7 and 8 Semi-submersibles; 9 Floating production, storage, and offloading facility (FPSO); 10 Subsea completion and tie-back to host facility (courtesy of US National Oceanic and Atmospheric Administration)

Fig. 9.2 An artificial island (Northstar Island) for oil drilling in the Beaufort Sea



positively buoyant (e.g., tension leg platforms shown in Fig. 9.1). In addition, remote subsea wells, as shown in Fig. 9.4, may also be connected to a platform by flow lines and by umbilical connections. These subsea solutions may consist of one or more subsea wells or of one or more manifold centers for multiple wells. It is noted that the function, water depth, and environmental loading are essential factors to influence the structural design concepts for offshore platforms.

For fixed offshore structures, they can be piled (Fig. 9.8) or gravity-based (GBS, as shown in Fig. 9.9), or a compliant (number 3 in Fig. 9.1) or articulated structure. A significant advantage of fixed platforms is that they use conventional well systems that developed along with platforms, leading to an economical design until water depths increase to the point where the cost of the structure outweighs the savings from the well system. These platforms use the minimum possible amount of

Fig. 9.3 A floating drilling platform Aker H6e (courtesy of Aker Solutions)

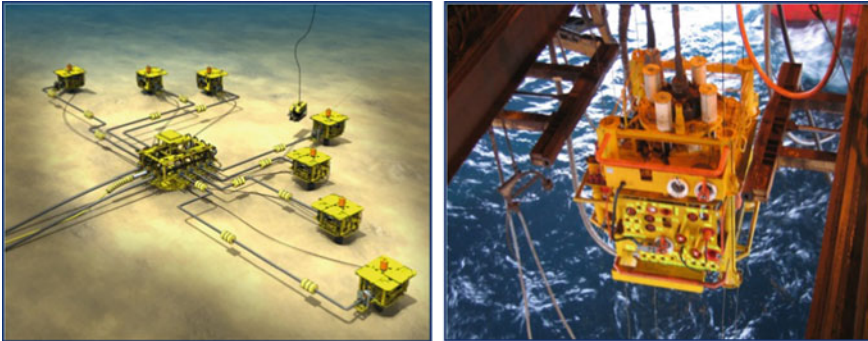


Fig. 9.4 Subsea wells (courtesy of Aker Solutions)

material and expose the least possible area to environmental loads. The most widely used fixed offshore structures are jacket structures as shown in Fig. 9.8. They are especially advantageous when operated at offshore sites with soft soil condition. The pile foundations supporting the jacket structures are put in place and connected to each leg to support the jacket. This leads to a transformation of the moment loading at mudline caused by lateral loading due to earthquake, or ocean wave and wind loading applied at superstructure, into axial forces in the jacket piles, as illustrated in Fig. 9.5. Therefore, jacket piles are usually insensitive to the lateral loads. Jacket piles can support a significant amount of load from substructure. Moreover, jacket structures can be constructed in sections and transported, making it more efficient for construction. Gravity-based structures, which rely on the weight of the structure itself to resist the environmental loading, are also adopted, particularly in the North Sea. They are frequently installed at sites where driving piles

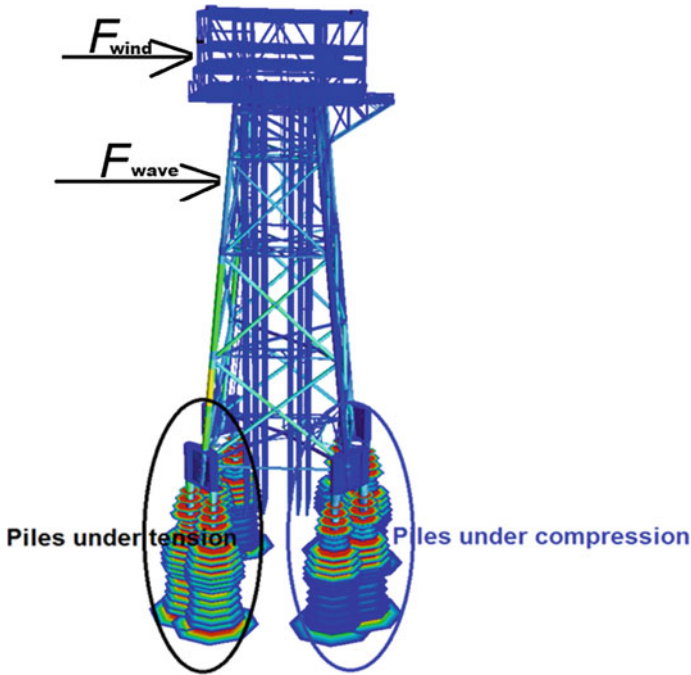


Fig. 9.5 Piles subjected to tensile and compressive axial loading due to the lateral wind and wave loading transferred from the upper part of the structure

becomes difficult. These structures have foundation elements that contribute significantly to the required weight and spread over a large area of the sea floor to prevent failure due to overturning moments caused by lateral loads. They are capable of supporting large topside loads during towing out, thus minimizing the hookup work during installation. Moreover, their merits also include (1) construction onshore for transport; (2) towing to the site of installation; (3) quick installation by flooding; and (4) use of traditional methods and labor for installation [500]. GBS is typically constructed with reinforced concrete and consists of a large cellular base surrounding several unbraced columns that extend upward from the base to support the deck and equipment above the water surface. Gravity-based platforms consist of production risers as well as oil supply and discharge lines contained in one of the columns; the corresponding piping system for exchange of water is installed in another column, and drilling takes place through the third column [500]. This particular type is referred to as a CONDEEP (concrete deep water) structure. Gravity-based structures are particularly suitable to resist enormous horizontal loading such as ice loading, in which a jacket or a jack-up structure would not offer the required global capacity to resist ice or ice ridge loading or is forced to limit operations (in case of a mobile jack-up structure) to a short summer season, which may damage legs and/or unprotected conductors/risers (conductors/risers are

Fig. 9.6 Troll A platform

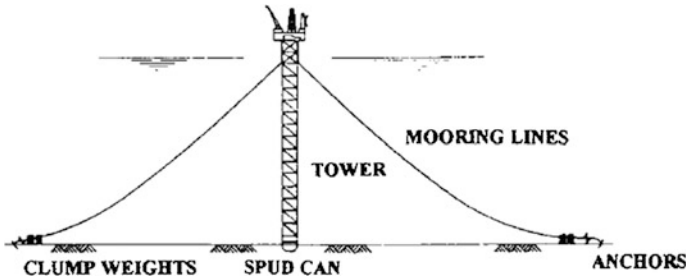


Fig. 9.7 Illustration of a guyed tower

typically installed inside the concrete shaft in a GBS). It should also be noted that the gravity-based platform can also be constructed with steel instead of concrete, such as the Maureen Alpha steel gravity platform in the UK. Table 9.1 lists the water depths of typical GBS platforms operated in the North Sea, with the highest one being Troll A platform (Fig. 9.6) with a total height of 481 m. It is operated at a water depth of 330 m and has a bottom dimension of 160 m × 60 m and a natural period of 4 s. Troll A is also the tallest structure that has ever been moved on earth.

As the water depth increases, bottom supported compliant structures are more economical. As this type of structure is rather flexible, they move with the dynamic environmental loads such as winds, waves, and currents to a limited extent, rather than resisting them as a GBS or a jacket structure does. Therefore, the compliant platforms resist lateral environmental loading by their relative movements instead

Table 9.1 Water depths of representative gravity-based platforms installed in the North Sea

Platform	Water depth (m)
Troll A	330
Gulfaks A	133
Gulfaks B	133
Gulfaks C	214
Oseberg North	100
Oseberg A	100
Ekofisk 1	70
Draugen	251
Heidrun	350
Statfjord A	145
Statfjord B	145
Statfjord C	145
Frigg TP 1	104
Frigg TP 2	103
Frigg MCP01	94
Frigg CDP1	98
Frigg TCP2	104
Brent B	140
Brent C	141
Brent D	142
Cormorant A	149
Dunlin A	153
Beryl A	118

of their weight as a GBS structure does. These types of structures are attached to the seabed by means of tension legs, guy lines, flexible members, or articulated joints. The buoyancy force or the force of elasticity of the axially stressed legs generates the restoring forces. As the system is not soft, the fundamental natural frequency remains low. The designs are technically and economically feasible as they increase the natural periods of the structure to such an extent that typical storm wave periods are far below the natural periods of the structures. Examples of bottom supported compliant platforms are compliant towers (3 in Fig. 9.1), guyed towers (Fig. 9.7), buoyant towers, flexible towers, articulated towers, and hybrid compliant platforms. Given the discussion above, it would be assumed that the load distribution and transfer mechanism is quite different between the fixed and the compliant structures [501]: in a fixed structure, the static and dynamic forces are almost all transmitted to the seafloor; while for the compliant structures, the horizontal dynamic loads are counteracted by the inertia forces. This reduces the internal forces in the structure as well as the support reactions. The vertical dynamic loads are transferred to the seafloor, much as with a fixed offshore structure.

As the water depth further increases and the sites are sometimes located far off the continental shelf, floating structures are more used because they are

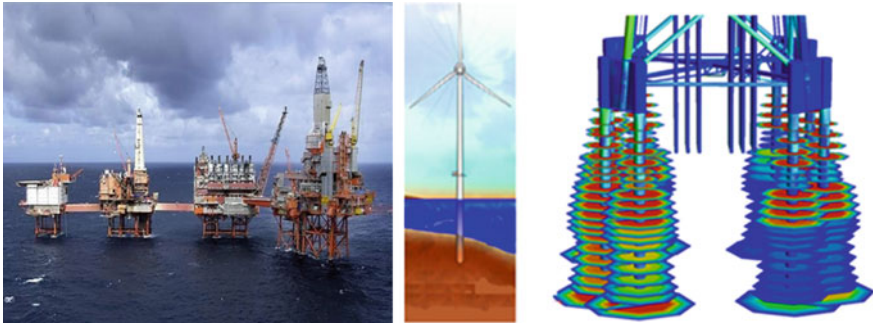


Fig. 9.8 Fixed jacket structures (left), pile foundations of a fixed monopile (middle) and of a jacket structure (right)

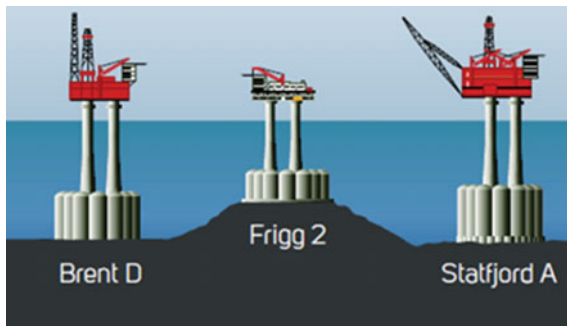
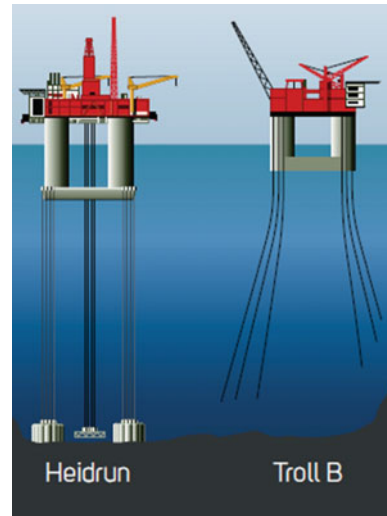


Fig. 9.9 Fixed GBS offshore structures with gravity-based foundation design (courtesy of Aker Solutions)

economically attractive for deep water sites with a reduced structural weight compared to conventional fixed and bottom supported platforms. Floating structures resist loads by undergoing large excursions when subjected to environmental loads and thereby reducing the forces on the structures. However, as large motions are expected, geometric nonlinearity is an important consideration in the analysis of floating structures. Floating structures are required to be moored in place. Subject to the environment loading, the floater remains within a specified circle of operation from a desired mean location, which is generally achieved by mooring lines or a dynamic positioning system [499]. Typical floating offshore structures include the semi-submersibles shown in Fig. 9.3, FPSO, and spars shown in Fig. 9.1, tension leg platforms (which are vertically restrained while horizontally compliant, permitting surge, sway and yaw motions) shown in Fig. 9.10, and tension buoyant towers. As floating structures have low stiffness, their natural periods of motions are higher than that of the wave loading, thus avoiding the resonance with wave loading. For example, typical natural periods of motions for a TLP are more than 100 s for surge and sway, more than 80 s for yaw, and 3–5 s for heave, pitch, and roll.

Fig. 9.10 A tension leg drilling platform (left) and a semi-submersible platform (right) (courtesy of Aker Solutions)



For platforms operating in deep waters, since the distance between platforms and ports increases, deck spaces of the topside need to be designed with variable load capacities. For example, for drilling platforms, deck space is very important because more space is required for third-party equipment for well completion and well testing activities, in addition to the space for drilling equipment. This typically requires that the topside be designed with variable load capacities between 10,000 and 20,000 tons [500].

In addition to functionality, environmental loading, and water depth, dynamic behavior and performance of each type of offshore structures also strongly influence the selection of structural form and design concept. As shown in Fig. 9.11, the natural periods corresponding to the global bending and global torsional vibrations for fixed offshore structures and the period of axial leg tension vibrations of TLPs should be below the period of ocean wave and wind loading, thus avoiding resonance conditions, which would otherwise cause excessive dynamic responses. On the other hand, to avoid resonance motion responses of floating structures due to wave loading (normally the dominating loads for offshore structural designs), they generally have natural periods of motions higher than the period of ocean wave loadings, even though they may potentially reach a resonance condition due to dynamic loading caused by wind turbulence.

Typically, the design of fixed offshore structures has to consider the impact from earthquakes. The design of TLP also needs to consider the influence from the seismic loading transferred to tension leg(s) and the response of connected floating structures.

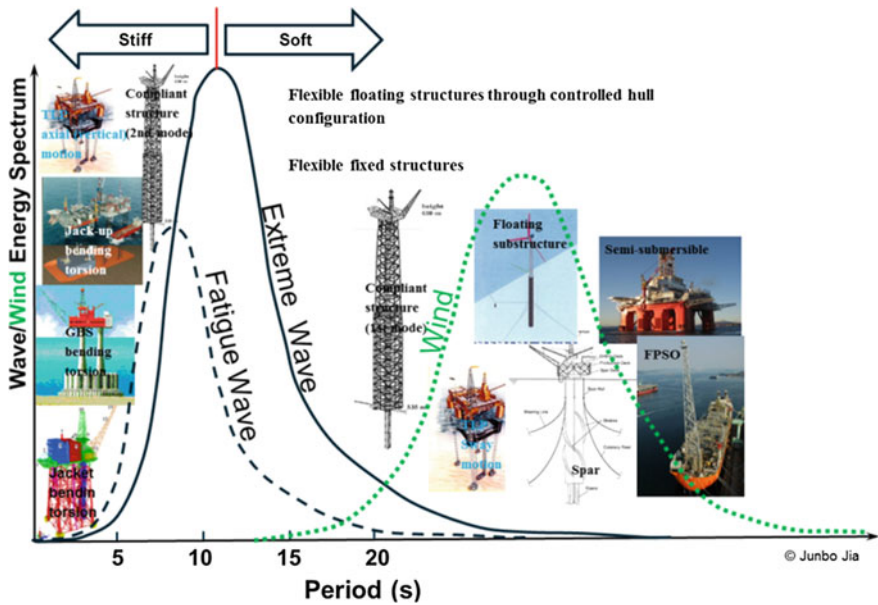


Fig. 9.11 Accounting of dynamics in the design of offshore structures (from a short course presentation “Dynamic Analysis and Design of Offshore Structures” by Junbo Jia and Lance Manuel at OMAE 2016, Pusan)

9.1.2 Offshore Wind Turbine Substructures and Foundations

Offshore sites provide a reliable source of strong winds due to the cooling and heating effect of water and land. Moreover, wind turbulence offshore is generally lower than that of inland sites. Therefore, due to the higher wind speed and lower wind turbulence offshore than over adjoining land, in recent years, offshore wind farms have rapidly developed across the world, dominated by developers in Europe and East Asia. In the meantime, the USA is also catching up by completing its first offshore wind farm with five steel jacket substructures (each carry a 6 MW wind turbine), installed at the Block Island Wind Farm site in December 2015. So far, more than 80% of the operated and currently planned offshore wind farms are located in Europe.

A wind turbine-supporting structure system includes both rotor-nacelle assembly and support structure. The former includes rotor (blades and hub) and nacelle assembly (all components above tower except the rotor, including driven train, bed plate, yaw system, and nacelle enclosure). The latter include a tower (connecting the substructure to rotor-nacelle assembly), substructure (for fixed substructure, it extends upwards from the seabed and connects the foundation to the tower; for

Fig. 9.12 Wind turbines with their substructures and electrical substation located in the North Sea (license under CC BY-SA 3.0, by StekrueBe)



floating substructure, it is the part below the tower), and foundation (transferring various types of load acting on the structure into the seabed soil).

The substructures and foundations for offshore wind turbines (OWTs), as shown in Fig. 9.12, can be either fixed to the seabed, bottom supported compliant structures, or floating structures.

The types of fixed offshore structures can be gravity foundation, monopile, tripod pile, tripile, jacket (braced frame) pile, and suction bucket, as shown in Fig. 9.13. The basic types of floating structure concepts used for offshore wind turbines are TLP (Fig. 9.14), spar (Fig. 9.15), and semi-submersibles (Fig. 9.16). The world’s first floating wind farm Hywind Scotland is planned to be completed by 2017. It lies 25 km off the northeast coast of Scotland near Peterhead and

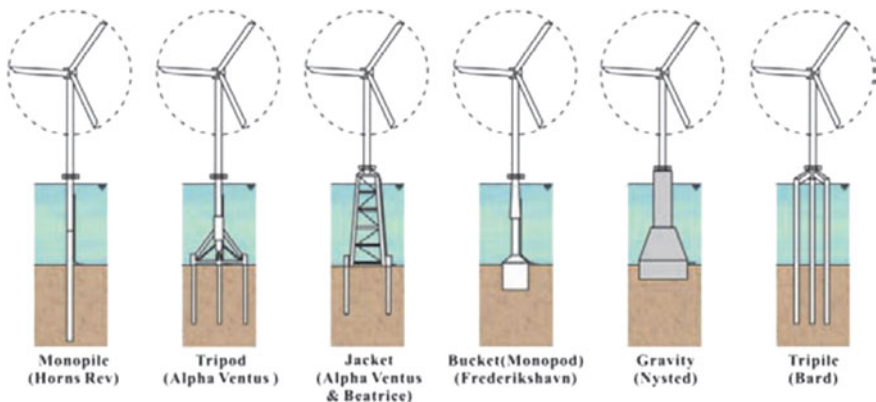


Fig. 9.13 Types of existing substructures and foundations for fixed offshore wind turbines [503]

Fig. 9.14 Schematic illustration of a TLP used for an OWT substructure

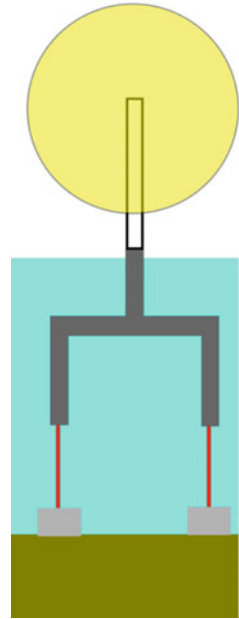
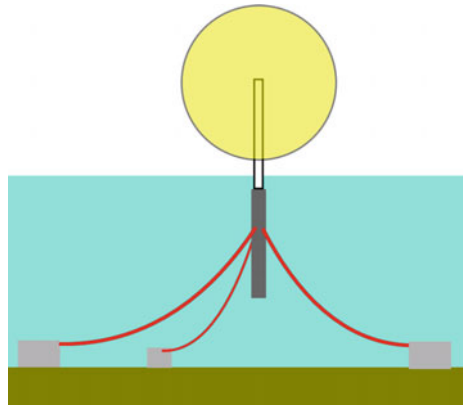


Fig. 9.15 Schematic illustration of a single floating cylindrical spar buoy moored by catenary cables



consists of five 6 MW spar-type floating turbines operating in water depths of between 95 and 120 m. The concept designs using bottom supported compliant structures for OWTs have not received much popularity, because the low frequency wind turbulence may interfere with the natural frequency of the compliant structure, potentially causing resonance. Moreover, the interaction between a compliant structure and the wind turbine can exert significant forces on the top of the relatively flexible structure, leading to significant deflections of the compliant structure.

Fig. 9.16 WindFloat, which is a semi-submersible structure for an OWT operating at a rated capacity of 2 MW approximately 5 km offshore of Aguçadoura, Portugal (under license CC BY-SA 3.0 by untraktrover)



Monopile currently represents the most common substructure application for OWT in shallow waters. It is a relatively simple design in which the tower to supporting turbines, made up of steel pipe, is supported by the monopile, either directly or through a transition piece. The vertical loads are transferred to the seabed by shaft friction and tip resistance. The vertical bearing capacity is therefore largely determined by the diameter of the monopile (typically between 2 and 6 m), which attracts the lateral hydrodynamic loads due to wind, waves, and current. These horizontal loads dominated by bending moments will be further transferred to the soil. Monopile is so far a cost competitive solution and suitable for shallow waters up to 30 m. One critical issue for the design of monopiles is the consideration of cyclic behavior of piles with large diameter. Investigations have shown that the horizontal deflections of large diameter monopiles are underestimated for extreme loads. On the other hand, experiences from operating offshore wind farms supported by monopiles indicate that the foundation stiffness for small operational loads is significantly underestimated. The installation method involves lifting or floating the structure into position using equipment such as floating crane vessels, drilling jack-up units, and specially constructed installation vessels before driving the piles into the seabed.

Jacket designs are more and more utilized in the applications of OWT. As an example, jacket structures were chosen as substructures by the Moray Offshore Wind Farm project (1500 MW total) in the UK, with up to 8 MW for each offshore wind turbine. The obvious benefits (compare to a monopile) are the reduction in hydrodynamic loading and weight, and suitability for increased water depth (30 m +). Jacket structures are less dependent on soil conditions compared to monopile and tripod, and are more suitable for sites with soft soil conditions. They are easily capable of supporting OWT with 6 MW or more. The smaller diameter of the piles (typically less than 2.5 m) also means a reduction in required driving power and less noise during piling. In addition, better precision for pile orientation and

Fig. 9.17 A close look at a tripod used as a substructure for OWT (courtesy of Aker Solutions)



positioning can be ensured. By considering the financial limits, OWT using jacket works well for water depths up to 60 m.

The main part of the tripod, shown in Fig. 9.17, consists of a tubular pole, but the lower part consists of braces and legs. The tubular steel foundation piles are driven through the sleeves in the three legs. As a tripod has a large base surface, it performs well in resistance to overturning moments. Moreover, it also has more redundancy due to three installed piles rather than one (monopile) [502].

Gravity-based foundations consist of a slender steel or concrete substructure mounted onto a single large reinforced concrete or a ballast-filled steel shell. To maintain stability, tensile loads between the bottom of the support structure and the seabed are resisted by self-weight of the foundation. The gravity-based foundations require a flat base and scour protection. A significant advantage of gravity-based foundations is associated with their transportation, as they can be fabricated and partially assembled in local yards, transported and completely installed at sea, depending on the fabrication yard capacity, the available draft during their transportation, and the availability of ballast materials.

Bucket foundations consist of a substructure column connected to an inverted steel bucket through flange-reinforced shear panels. The length of the skirt is normally in the same order as the bucket diameter, where the volume of soil inside the foundation may act as a permanent gravity-based foundation. Bucket foundation is therefore similar to gravity-based foundations in shape and size but differ in the method of installation and primary mode of stability. The installation of a bucket foundation is typically through pushing due to the weight of the foundation and its associated mass and/or creating a negative pressure inside the foundation to generate a downward pressure. These operations enable the foundation to penetrate into the seabed and to finally reach a desirable penetration depth. To create the negative pressure, water and air inside the foundation are pumped out through top of bucket when the rim of bucket seals with the seabed.

The dynamic characteristics of offshore wind turbine structures are slightly different from those of traditional offshore platform structures. An offshore wind turbine system comprises five physical components: rotor, transmission, generator, support structure, and control system. Each of these influences the dynamic behavior of the complete turbine system. It is noticed that the two most significant excitations are due to the rotation of blades and wave induced forces. In order to avoid resonance due to the excitations from wind turbine blade rotation and wave loadings, the support structure should be designed with a natural period as far as possible from the periods of both blade and wave excitations. This gives three possible natural period ranges for designing the support structure as shown in Fig. 9.18: a natural period larger than the first blade excitation period T_{1p} (soft-soft design), the one between the first (T_{1p}) and the second blade excitation period T_{3p} (soft-stiff design), and the one below the second blade excitation period T_{3p} (stiff-stiff design).

Traditionally, the soft-soft design is preferred because this usually leads to an economical design due to the need for less material and construction cost. In the offshore wind energy industry, the general trend is that the scale of turbines is becoming larger and larger. This would result in an increase of the blade's diameter, e.g., a 170 m diameter for a 7 MW wind turbine. The first and second excitation periods are also significantly increased for those large OWTs. This motivates the engineer to shift from a soft-soft to a soft-stiff or even to a stiff-stiff design. Moreover, the variable tip speed of the turbine also becomes a design alternative, which adds additional restrictions on the natural period range of the structures. In

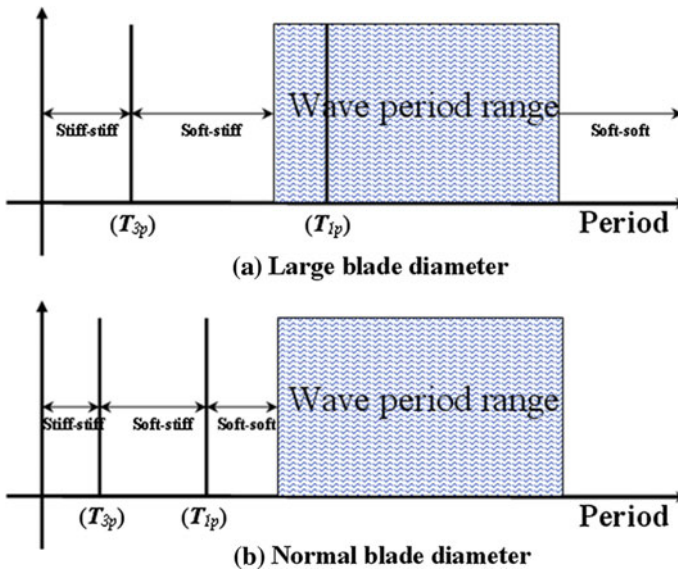


Fig. 9.18 Period interval for stiff-stiff, soft-stiff and soft-soft design of OWT substructures

addition, it is also possible to convert the existing/abandoned offshore rigs into substructures for OWT systems, which can avoid/delay enormous decommissioning costs for energy companies as well as avoid cost and pollution for constructing new substructures for OWTs. Most of the existing fixed offshore platform structures have natural periods below 3.5 s; after removing part of the heavy topside modules at the top of the platforms, the natural periods will further decrease. This period range is then relevant to the soft-stiff or even soft-soft design. For developing this concept, one also needs to account for the cost with respect to maintenance and power grid integration.

In addition to artificial damping devices such as tuned mass dampers (TMDs) [188], an optimized control system and the associated control algorithm for both generator torque and pitch angle of wind turbine blades can also mitigate dynamic loadings applied on an OWT tower. Such a control supplies additional damping to a generally lightly damped tower, and it normally involves a modeling of an extra pitch demand responsible for counter-balancing the vibrations and motions of the tower. This load reduction will allow for a more cost-effective structural design. Experiences and measurements from offshore wind farm operations have also indicated that an optimized control system can significantly reduce dynamic loadings on blade root, shafts, yaw bearing, tower base, etc. And fatigue damage accumulation on an OWT tower may even be lower if the turbine operating full load hours per year is higher.

9.2 Dynamic Design of Structures

9.2.1 Dynamics Versus Statics

Over history, the safety and serviceability of structures have basically been measured on the basis of their static behavior, which required adequate stiffness and strength. This was perhaps because the necessary knowledge of dynamics was less accessible to engineers than their static counterpart. Nowadays, it is common knowledge that all bodies possessing stiffness and mass are capable of exhibiting dynamic behavior.

The major difference between dynamic and static responses is that dynamics involves the inertia forces associated with the accelerations at different parts of a structure throughout its motion. If one ignores the inertia force, the predicted responses can be erroneous. As an example, let us consider a bottom-fixed cantilevered tower subjected to sea wave loadings as shown in Fig. 9.19 [504]. In addition to the static bending moment due to wave loadings applied on the structure, as shown in Fig. 9.19b, the stiffness and mass of the structure will react to the wave loadings and generate internal forces on both the top mass block (Q_i) and the tower (q_i), shown in Fig. 9.19c. Rather than a single function of mass, the amplitudes of the inertia forces are related to a ratio between stiffness and mass

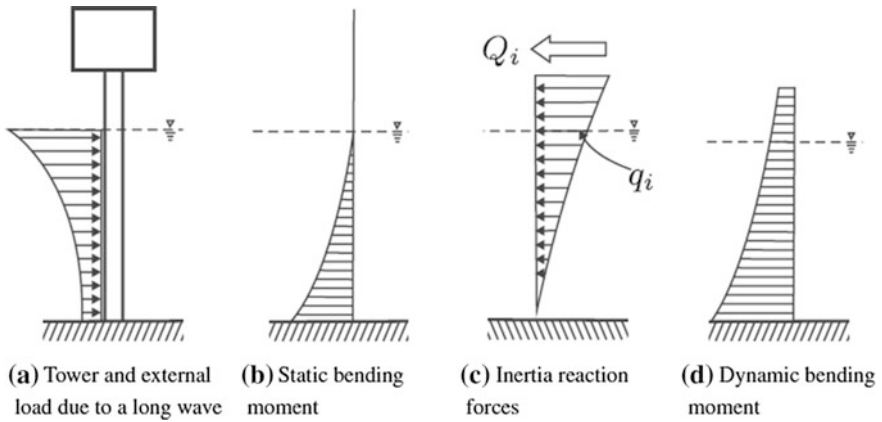


Fig. 9.19 Wave-induced static versus instantaneous dynamic forces and moments in a bottom-fixed cantilevered tower [504]

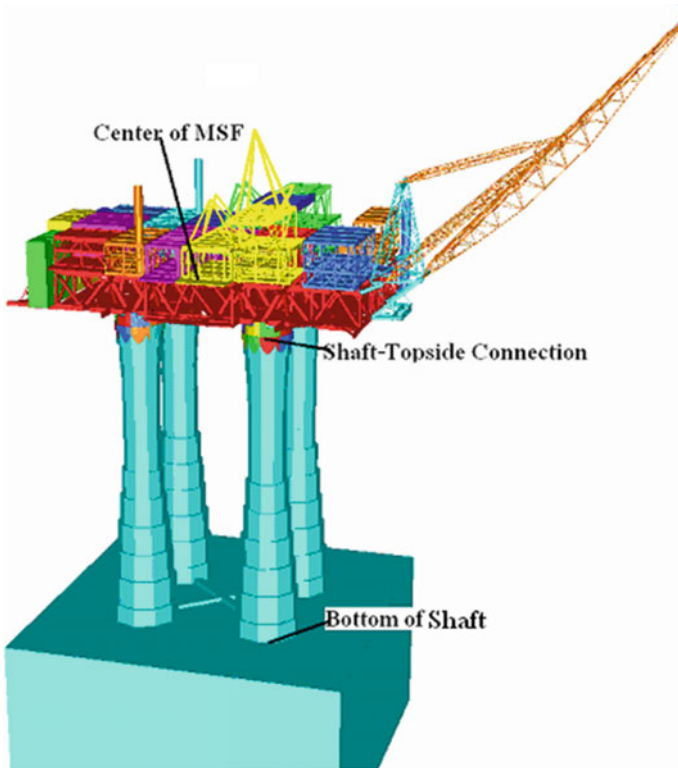


Fig. 9.20 A GBS with a heavy topside supported by four concrete shafts (legs)

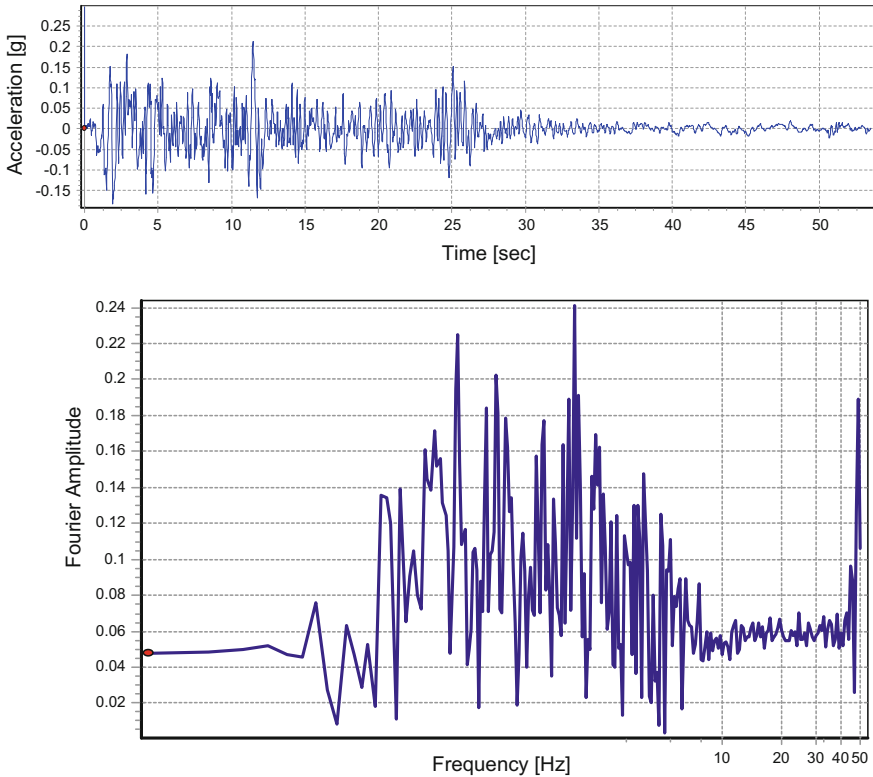


Fig. 9.21 Ground motions EW component (upper) recorded during El Centro earthquake and its Fourier amplitude (lower)

(eigenfrequency), mass, as well as damping, thus resulting in additional dynamic bending action (Fig. 9.19d).

As another example, consider a gravity-based structure (GBS), shown in Fig. 9.20, that is subjected to the ground motions recorded during El Centro earthquake, which have a high energy content at the vibration period above 0.2 s (below 5 Hz in Fourier amplitude shown in Fig. 9.21). The dynamic responses of the platform are investigated by varying the thickness of four shafts from half of the reference thickness, to the reference thickness, to twice the reference thickness. It is obvious that the GBS becomes stiff by increasing the shafts' thickness. If a static analysis is performed, under the same seismic excitations the stiffer structure would have lower responses. However, the seismic responses involving dynamic effects may not obey this rule. Figure 9.22 shows the acceleration at the shaft-topside connection. It is clearly shown that the peak acceleration for the reference shaft thickness case is higher than that of the half-thickness case. However, the trend of peak acceleration response variation with the change of stiffness cannot be identified, as the peak acceleration for the double shaft thickness (the stiffest one) is

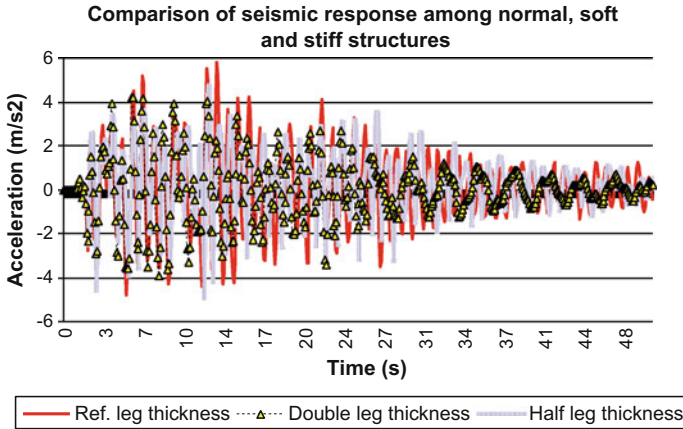


Fig. 9.22 Acceleration at the shaft-topside connection with various leg/shaft stiffness (peak acceleration: 4.7 m/s^2 for double leg thickness, 5.8 m/s^2 for reference leg thickness, 4.2 m/s^2 for double leg thickness)

lower than that for other cases with lower stiffness. This indicates the effects of inertia, which are more complex than their static counterpart. The response variation trend can be identified by relating the seismic responses to the dynamic characteristics of both structures and excitations.

Even for dynamic insensitive structures with low periods of resonance compared to that of the dynamic loading, dynamics does include the inertia effects due to loading that varies with time, even if this load variation may be quite slow. The inertia effects could lead to the fatigue failure of the materials at stress conditions well below the breaking strength of the materials. They may also be responsible for the discomfort of human beings. Figure 9.23 shows an offshore jacket structure subjected to two consequent sea waves; the jacket has a resonance period of 2.5 s. Figure 9.24 compares the calculated axial force time history at a leg C1 with and without accounting for the dynamic inertia effects. When the dynamic effects are ignored (right figure), the axial forces history entirely follows the variation of the wave and has a period of wave loading (15.6 s) well above the structure's resonance period (2.5 s). However, when the dynamic effects are accounted for, fluctuations (left figure) of the axial force can be clearly observed as a background noise with the resonance period of the structure (2.5 s). Depending on the magnitude of this background noise, it may influence the integrity of the structure with regard to fatigue damage.

From another angle, the dynamic loading often has a different orientation than the static one. For example, the static loading of a structure under the gravity of the earth is strictly toward the earth. However, when the structure is subjected to dynamic loading due to, for example, wind, earthquake, or sea waves, the direction of resultant loadings change from downward to the one that is more toward a horizontal orientation, this can result in an entirely different pattern regarding the

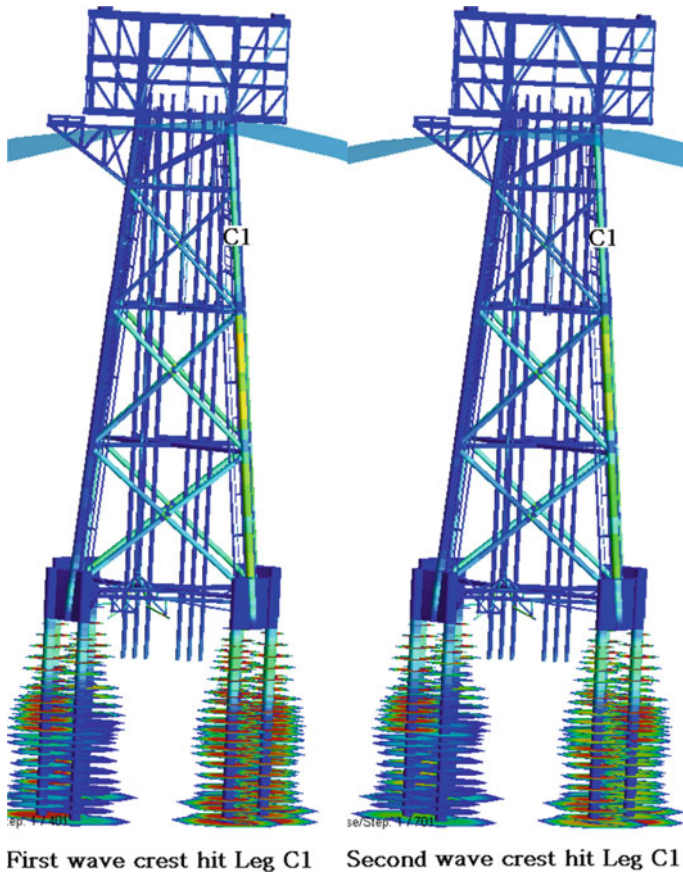


Fig. 9.23 An offshore jacket structure subjected to a wave with a wave height of 31.5 m and a wave peak period 15.6 s (courtesy of Aker Solutions)

load level and load path, and this obviously influences the structural design. Therefore, structural engineers are required to have a complete picture of load path and level, and structures designed must have corresponding load resisting systems that form a continuous load path between different parts of the structures and the foundation. The structure shown in Fig. 9.23 represents a typical configuration of the jacket structure and a clear path for load transferring, i.e., the gravity and acceleration loads from topside, the wave load applied on the upper part of the jacket, and the jacket gravity and acceleration loads are all transferred through legs and braces down to the pile foundation at the bottom.

Before concluding this section, it is of great importance to emphasize that dynamics is a rather more complex process than its static counterpart. The natural frequency of a structure can change when a change in its stiffness, mass, or damping occurs. What makes dynamics even more complicated is that, strictly speaking,

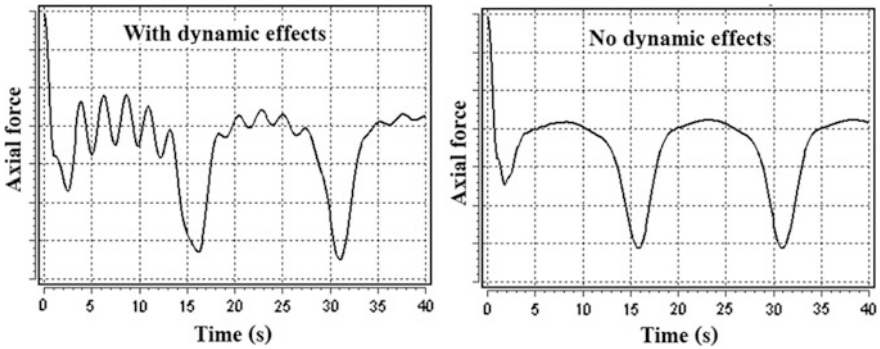


Fig. 9.24 Axial force time history on the lower part of leg C1 of the offshore jacket with and without dynamic inertia effects. (The exact magnitude of axial forces are omitted to protect the interests of the relevant parties)

regular harmonic loadings and responses, with a sine or cosine form at a single frequency, do not represent environmental loadings (such as earthquake loadings) and the associated responses in the real world, even if they can be a good simplification when the dynamics at a single frequency is dominating. This implies that one should always assess whether the vibrations in various frequencies need to be accounted for or not.

9.2.2 Characteristics of Dynamic Responses

If we take an SDOF spring-mass-damper system under forced excitation as an example, which is illustrated in Fig. 9.25, the equation of motions for the system is expressed as:

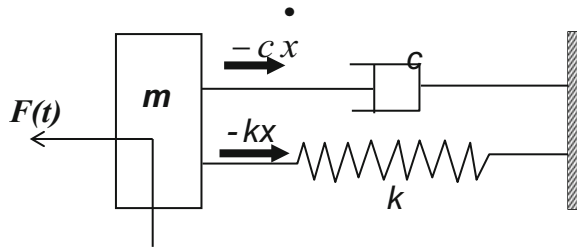
$$m\ddot{x}(t) + c\dot{x}(t) + kx(t) = F(t) \quad (9.1)$$

By exerting an external harmonic force ($F(t) = F_0 \sin(\Omega t)$) with an amplitude of F_0 and an angular frequency of Ω as shown in Fig. 9.25, or displacement excitations in a harmonic form on the spring-mass-damper system, an SDOF spring-mass-damper system under forced harmonic excitation is constructed. The governing linear differential equation of motions for this system in case of harmonic force excitations can then be written as:

$$m\ddot{x}(t) + c\dot{x}(t) + kx(t) = F_0 \sin(\Omega t) \quad (9.2)$$

Dividing both sides of the equation above by m , this equation is rewritten as:

Fig. 9.25 An SDOF spring-mass-damper system under an external force $F(t)$



$$x''(t) + \frac{c}{m}x'(t) + \omega_n^2x(t) = (F_0/m) \sin(\Omega t) \tag{9.3}$$

It is noted that the viscous damping is very important in an oscillating system because it helps to efficiently limit the excursion of the system in a resonance situation. As a reference, we first define the critical damping C_C , which is the lowest damping value that gives no oscillation responses, i.e., the system does not vibrate at all and decays to the equilibrium position within the shortest time. This represents the dividing line between oscillatory and non-oscillatory motions:

$$c_c = 2\sqrt{km} = 2m\omega_n \tag{9.4}$$

The actual damping ratio can be specified as a percentage of critical damping:

$$\zeta = \frac{c}{c_c} \tag{9.5}$$

By realizing that $c = 2\omega_n m \zeta$, the equation of motions for the system finally gives:

$$x''(t) + 2\omega_n \zeta x'(t) + \omega_n^2 x(t) = (F_0/m) \sin(\Omega t) \tag{9.6}$$

As the equation above is a second-order non-homogeneous equation, the general solution for it is the sum of the two parts: the complementary solution $x_c(t)$ to the homogeneous (free vibrations) equation and the particular solution $x_p(t)$ to the non-homogeneous equation:

$$x(t) = x_c(t) + x_p(t) \tag{9.7}$$

The complementary solution exhibits transient vibrations at the system's natural frequency and only depends on the initial condition and the system's natural frequency, i.e., it represents free vibrations and does not contain any enforced responses:

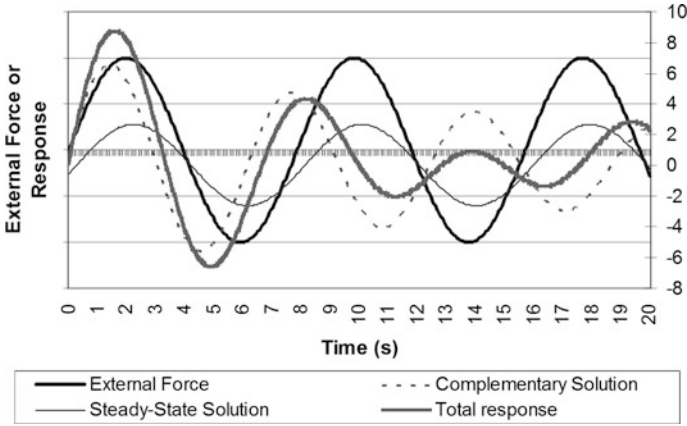


Fig. 9.26 Transient and steady-state responses due to external harmonic force excitations applied on a system with $\omega_n = 1.0$, $\Omega = 0.8$, $\zeta = 0.05$, and $\varphi = 0.1$

$$x_c(t) = X e^{-\zeta \omega_n t} \sin\left(\sqrt{1 - \zeta^2} \omega_n t + \varphi\right) \quad (9.8)$$

It is noticed that this aspect of the vibration dies out due to the presence of damping, leaving only the particular solution exhibiting steady-state harmonic oscillation at excitation frequency Ω . This particular solution is also called the steady-state solution that depends on the excitation amplitude F_0 , the excitation frequency Ω as well as the natural frequency of the system, and it persists motions for ever:

$$x_p(t) = E \sin(\Omega t) + F \cos(\Omega t) \quad (9.9)$$

By substituting the equation above and its first and second derivatives into Eq. (9.6), one obtains the coefficients E and F as:

$$E = \frac{F_0}{k} \frac{1 - (\Omega/\omega_n)^2}{\left[1 - (\Omega/\omega_n)^2\right]^2 + [2\zeta(\Omega/\omega_n)]^2} \quad (9.10)$$

$$F = \frac{F_0}{k} \frac{-2\zeta\Omega/\omega_n}{\left[1 - (\Omega/\omega_n)^2\right]^2 + [2\zeta(\Omega/\omega_n)]^2} \quad (9.11)$$

By inserting the expression for coefficient E and F into Eq. (9.9) and rearranging it, one can rewrite the steady-state solution as:

$$x_p(t) = \frac{F_0}{km} \frac{\sin(\Omega t - \phi)}{\sqrt{[1 - (\Omega/\omega_n)^2]^2 + [2\zeta(\Omega/\omega_n)]^2}} \quad (9.12)$$

where ϕ is the phase between the external input force and the response output, with the most noticeable feature being a shift (particularly for underdamped systems) at resonance. It can be calculated as:

$$\phi = \tan^{-1} \left(\frac{2\zeta(\Omega/\omega_n)}{1 - (\Omega/\omega_n)^2} \right) \quad (9.13)$$

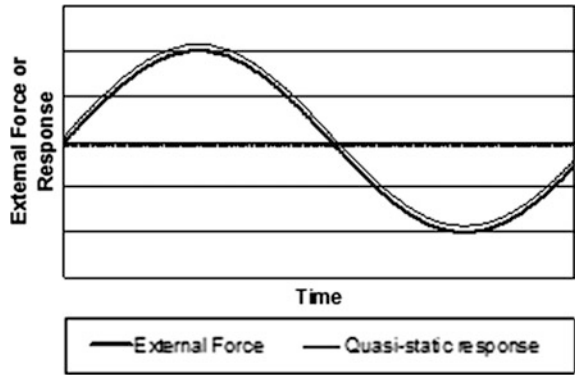
It is clearly shown that the steady-state solutions are mainly associated with the excitation force and the natural frequency. Figure 9.26 shows an example of the dynamic responses due to the contribution from both transient and steady-state responses, with a Ω/ω_n ratio of 0.8, a damping value of 0.05 ($\phi = 0.21$), and $\varphi = 0.1$. Phases between the two types of response can be clearly observed.

When mass m in Fig. 9.25 is subjected to harmonic excitations, the magnitude and phase of the displacement responses strongly depend on the frequency of the excitations, resulting in three types of steady-state responses, namely quasi-static, resonance, and inertia dominant responses, which are illustrated in Fig. 9.27.

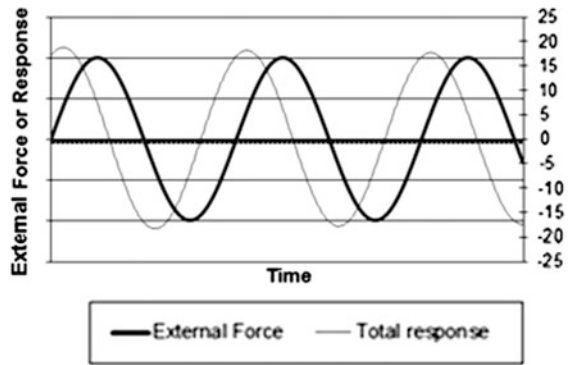
When the frequencies of excitations Ω are well below the natural frequencies of the structure ω_n , both the inertia and damping term are small and the responses are controlled by the stiffness. The displacement of the mass follows the time-varying force almost instantaneously. Subject to environmental loading such as wind or ocean wave loading, the majority of land-based structures and fixed offshore structures are designed to reach this condition, as shown in Fig. 9.28. However, earthquake loading is likely to have a dominant frequency higher than the natural frequency of structures.

When the excitation frequencies are close to the natural frequency of the system, the inertia term becomes larger. More importantly, the external forces are almost overcome (controlled) by the viscous damping forces. Resonance then occurs by producing responses that are much larger than those from quasi-static responses, as shown in the circle in the upper figure of Fig. 9.28, and there is a dramatic change of phase angle, i.e., by neglecting the damping, the displacement is 90° out of phase with the force, while the velocity is in phase with the excitation force. In a typical situation in which the damping is well below 1.0, the responses are much larger than their quasi-static counterparts. From an energy point of view, when the frequency of excitations is equal to the natural frequency, the maximum kinetic energy is equal to the maximum potential energy. Almost all engineering structures are designed to avoid this resonance condition. Possible scenarios of resonance conditions are as follows: When the resonance period (site period) of soil layers at sites due to shear wave transmission is close to the natural period of the structure; when the resonance period of the surface wave is close to the natural period of the structure; or when significant plasticity develops on structural members during a

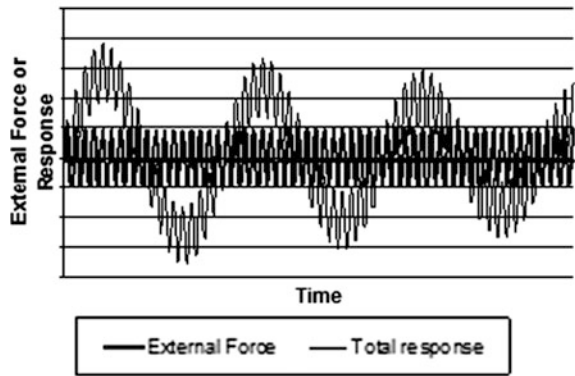
Fig. 9.27 Damped responses due to harmonic excitations with the characteristics of **a** quasi-static ($\Omega/\omega_n \ll 1$); **b** resonance (Ω/ω_n close to 1); and **c** inertia dominant responses ($\Omega/\omega_n \gg 1$), for a system with $\omega_n = 1.0$ and viscous damping ratio $\zeta = 0.03$ [123]



(a) Quasi-static $\Omega/\omega_n \ll 1$



(b) Resonance Ω/ω_n close to 1



(c) Inertia dominant response $\Omega/\omega_n \gg 1$

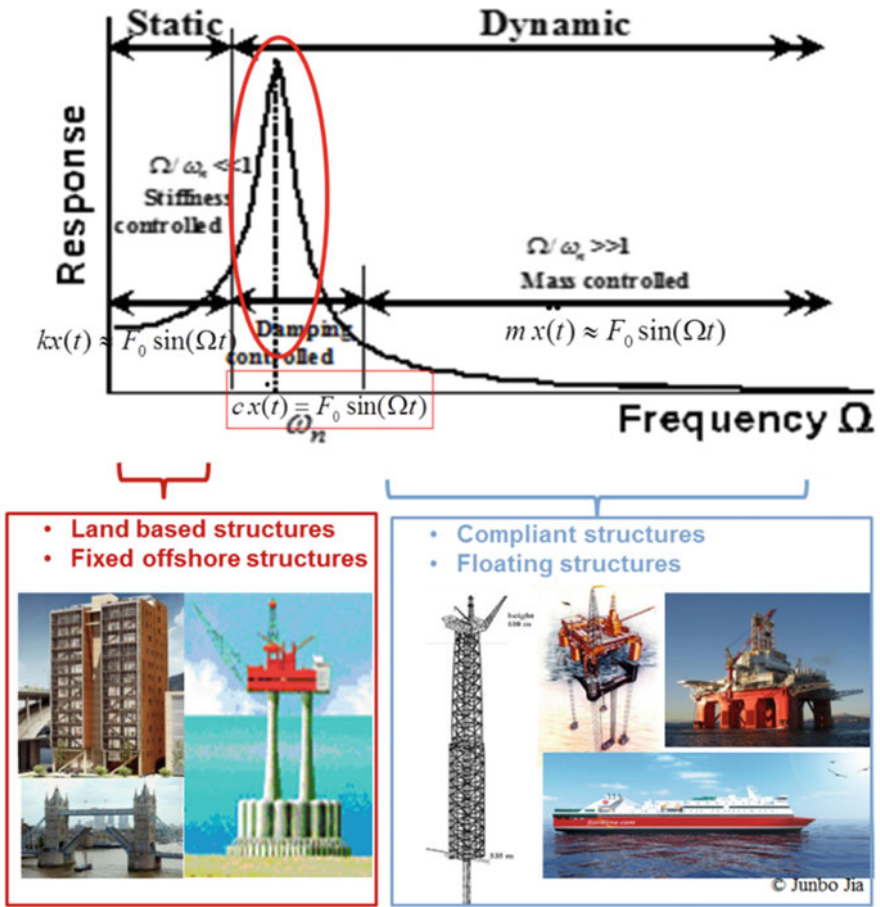


Fig. 9.28 Response of various types of offshore and land-based structures in three frequency ranges subjected to external environmental loading with a frequency of Ω , the natural frequency of the structure is denoted as ω_n (from an oral presentation by the author at the 11th International Conference on Recent Advances in Structural Dynamics, Pisa, 2013)

strong earthquake, leading to a decreased natural frequency of the structure, which may track the decreasing predominant frequency of the ground motions, causing resonance with ground motions (moving resonance), etc.

When the excitation frequencies are well above the natural frequency of the system, the external forces are expected to be almost entirely overcome by the inertia force, the excitations are so frequent that the mass cannot immediately follow the excitations. The transient vibrations are normally more significant than steady-state oscillations. The responses of the mass are therefore small and almost out of phase (phase angle approaches 180°) with the excitation forces, as illustrated in Fig. 9.28. From an energy point of view, this reflects the condition in which the

maximum kinetic energy is larger than the maximum potential energy [123]. Offshore compliant structures and floating structures are normally designed to behave “softly” in their motion responses and therefore have natural frequencies of motion ω_n well below the external wave loading frequency. This condition is also a most usual scenario encountered during an earthquake event. It is noted that for most of the engineering structures and typical site conditions, the long period of seismic ground excitations are usually small, except for the ground motions caused by the seismic surface (Rayleigh) waves, which can have dominating long period components of ground motions. Therefore, subject to seismic ground excitations, a large amount of offshore and land-based structures are likely to reach this condition.

As a structure typically has—or more precisely, has to be represented modeled by—a large number of degrees of freedom, in addition to the natural frequency, which is typically the first eigenfrequency of the structure, it has more numbers/orders of eigenfrequencies, and the total number of eigenfrequencies is equal to the number of degrees of freedom of the structure. However, the first few eigenfrequencies, especially the natural frequency, normally dominate the majority of the total modal mass participating in structural vibrations and are therefore the most important ones contributing to the dynamic response of the structure [123]. From a modal response point of view, the lower order eigenfrequencies of the structure are normally separated well apart. In this frequency range, with small damping, the modal response will generally be dominated by a single mode with frequency close to the loading frequency and a single mode with natural frequency of the structure. And if the loading frequency is lower than the first eigenfrequency of the structure, then the structural response will show two peaks at the loading frequency corresponding to quasi-static response and the natural frequency of the structure contributing to dynamic response of the structure. As an example, Fig. 9.29 shows ocean wave-induced frequency responses of a welded joint on an offshore jacket structure (Fig. 9.30) in the North Sea. Generally, two peaks in this frequency response graph can be identified: one corresponds to the wave modal frequency (0.08 Hz); the other corresponds to the structure’s natural frequency (0.24 Hz). On the other hand, the higher order eigenfrequencies are more closely spaced and modal mass participation of each mode vibration is much less than that of the first few eigenmodes. This is more obvious for highly redundant structures. With a dynamic loading in this frequency region, multiple eigenmodes contribute in a similar extent to the modal response, and vibration modes above the loading frequency will be out of phase with those below the loading frequency, the net vibration is likely to be less than any of the single mode vibrations in this frequency range (dynamic cancelation).

9.2.3 Frequency Range of Dynamic Loading

If relevant, subjected to environmental loading, such as wind, earthquakes, ocean waves, current, and ice, all engineering structures should be designed by accounting

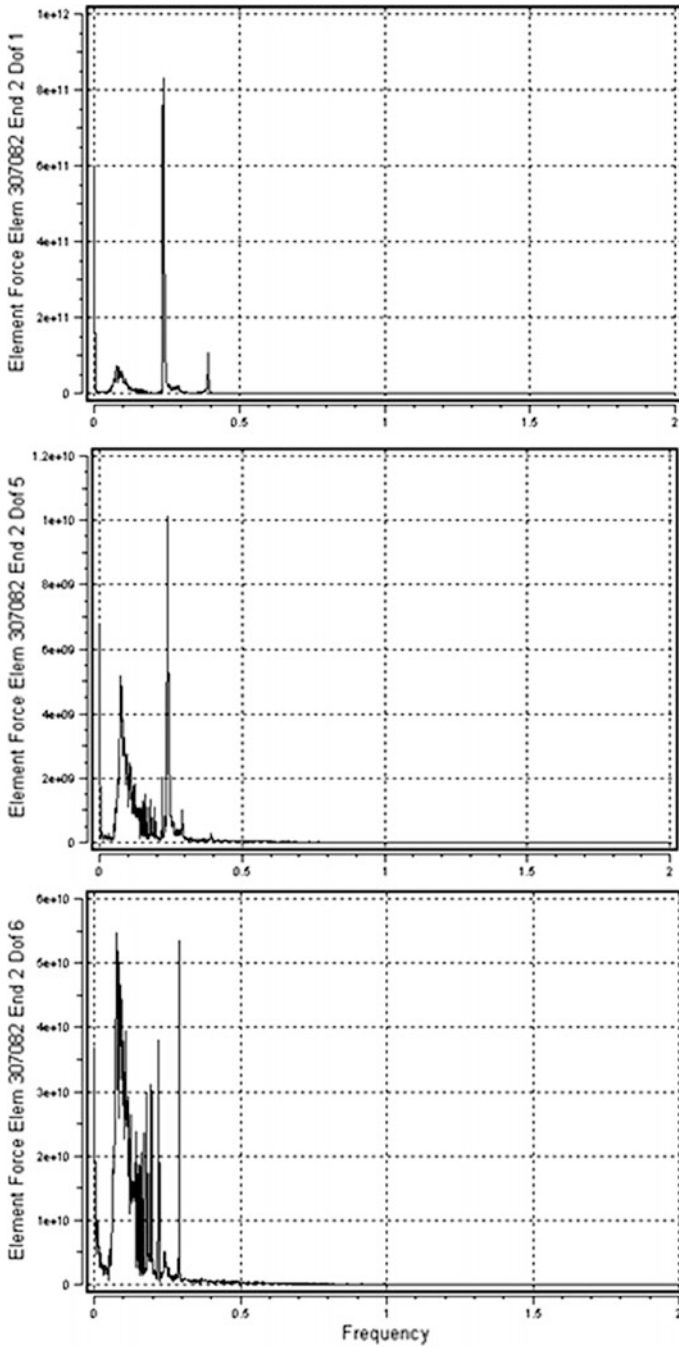
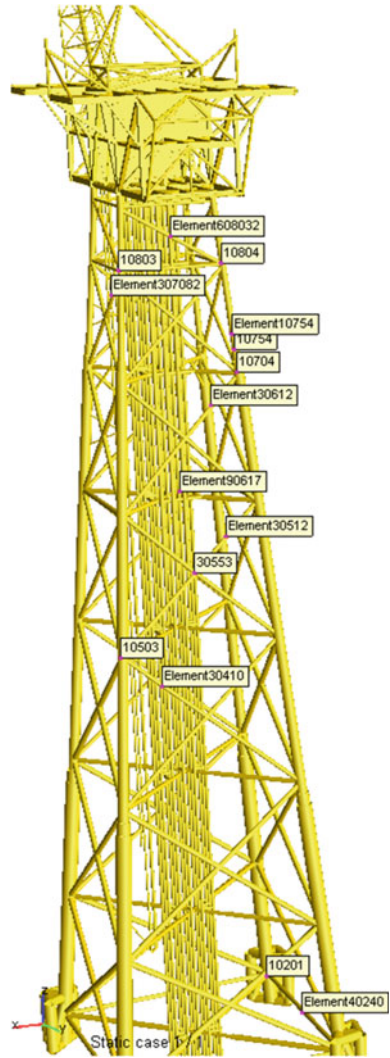


Fig. 9.29 Frequency responses of the axial force (Dof 1) [N], in-plane bending moments (Dof 5) [Nm] and out-of-plane bending moments (Dof 6) [Nm] for a weld joint 10,803 (Fig. 9.30) at the top of a jacket, and the jacket is subject to wave loading corresponding to a sea state with a significant wave height $H_s = 8.8$ m, and a modal wave period $T_p = 13.2$ s (0.08 Hz) [505]

Fig. 9.30 Location of the welded joint 10,803 on the jacket



for their dynamics with a special consideration on resonance, which can be relevant to structural performances associated with ultimate strength, fatigue strength, and serviceability limits. Each type of loading has different dominant ranges of loading frequency as shown in Fig. 9.31. In addition, other types of dynamic loading induced by explosion, machinery vibrations, vehicle- or human-induced excitations

may also require a dedicated consideration on solving relevant dynamic problems in the design.

It is noted that the dominant frequency of seismic ground motions is not only dependent on the frequency of seismic waves generated at the source due to fault fractures, but also even more influenced by site conditions associated with soil layers and ground topology. Therefore, their peak period has a large range of up to 4 s.

Furthermore, Fig. 9.31 also indicates that the difference of dominant frequency range for different types of environmental loading is significant. This can pose a challenge in designing an optimized structure to resist the different types of dynamic loading. For example, for fixed offshore structure or land-based structures, to avoid significant dynamic amplification and/or excessive vibrations, it is usually desirable to design a stiff structure to resist wind and ocean wave loading, so that the natural period of the structure is far below the dominant period range of wind and wave loading, thus avoiding resonance and limiting excessive vibrations. On the other hand, the low-dominant period of seismic loading requires a “softer” structure design that cherishes a higher natural period. This contradiction has been encountered in various structural design projects. Sometimes a “balance” between

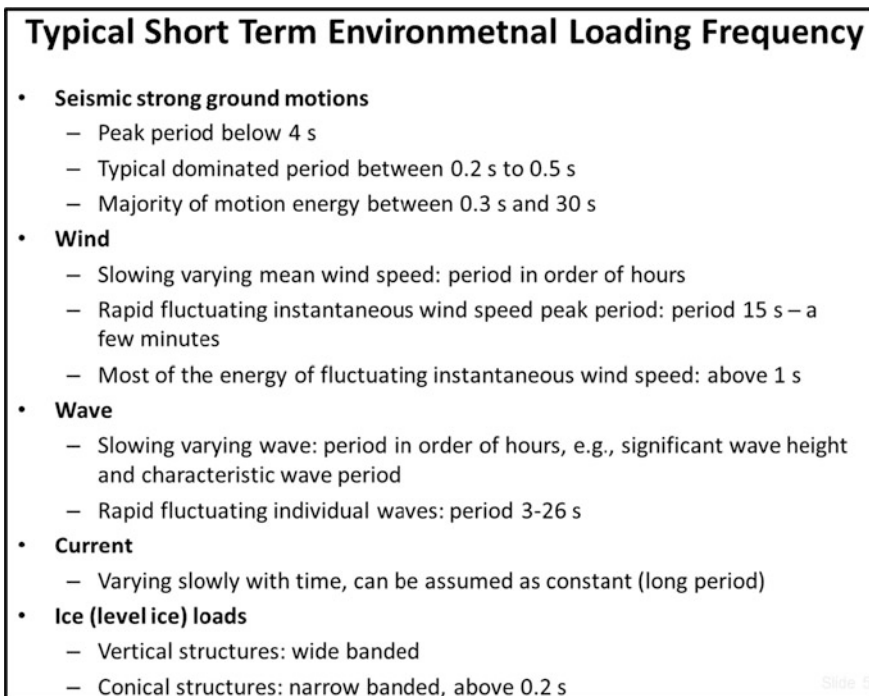


Fig. 9.31 Typical short-term environmental loading frequency/period (from an oral presentation by the author at the 11th International Conference on Recent Advances in Structural Dynamics, Pisa, 2013)

the two needs to be sought, such as the design of Taipei 101. It has a natural period of around 7 s, which is obviously above the dominant period of earthquake loading. Even though this natural period of 7 s is also far below the period of loading due to wind turbulence (fluctuating part of wind), it can induce significant peak acceleration at the top of Taipei 101, causing both human discomfort and structural metal fatigue. To solve this problem, a large tuned mass damper (TMD) weighing 660 tons (Fig. 9.32) was introduced to mitigate sway motion of the building, particularly in major typhoons or earthquakes where movement of the top floor can exceed 1.5 m. The TMD will reduce peak acceleration of the top occupied floor from 7.9 to 5.0 mg due to wind storm with a return period of half year. For a 1000–2500 year return period of strong earthquake, the TMD will be rather effective to mitigate the dynamic response of the structure, and to remain in place and intact after strong seismic ground motions cease and the vibration of the structure terminates. In addition, another two small TMDs are designed to mitigate vibration at two tip vibration modes at periods of around 1 s.

Slender light weight structures such as guyed steel stacks, chimneys, slender tips of flare booms or other elevated structures, with two examples shown in Figs. 9.32

Fig. 9.32 A tuned mass damper (upper) suspended from the 92nd to the 87th floor at Taipei 101 (lower) (under licenses of CC BY-SA 3.0 by Guillom and Peellden)



Fig. 9.33 A flare boom with a slender tip (courtesy of Aker Solutions)



and 9.33, the structural design is governed by the wind loading rather than the seismic loading because the structure has a high natural period (compared with the dominant period of earthquake loading) and the wind loading increases with the height from the ground surface. However, due to the tips of those slender structures normally being much softer (with much lower stiffness) than the structural parts below the tips, during earthquakes, they can exhibit significant vibrations, which are referred to as a whipping effect. Therefore, the design of the slender tips of structures may be governed by seismic loading and therefore requires a dedicated consideration of their seismic resistance.

9.3 Difference Between Offshore and Land-Based Structures

The major difference between offshore structures and their land-based counterparts is reflected in the aspects regarding cost and consequence, possibility of evacuation, the availability of seismic ground motion records, structural dynamic behavior and geometry characteristics, structural and hydrodynamic damping, other accompanied environmental and operational loads, as well as special geotechnical issues such as site conditions and sudden subsidence. Therefore, the assessment and design experience adopted for land-based structures must be borrowed with care before applying them for offshore structures.

Compared to that of an infrastructure on land, evacuation during a strong earthquake at a site offshore is almost impossible and can have very serious consequences. This also leads to a higher safety requirement for structural and non-structural elements for offshore structures than structures onshore.

The cost and consequence of structural failure or collapse of offshore structures are normally much more significant than a typical land-based structure such as a building. Therefore, seismic performance assessment for offshore structures is generally associated with a higher required reliability and assessment accuracy.

This may limit the applicability of some simplified analysis methods and simplification in the structural modeling that are typically adopted for structural analysis for typical land-based structures.

Offshore structures generally have a much wider range of natural period (1–120 s, depending on the types) than typical onshore building structures (below 9 s). This may sometimes significantly alter the dynamic response subject to earthquake loading and other types of environmental loading.

Due to the significant environmental loading mainly induced by ocean waves, offshore structures are generally much larger in plan than most buildings but do not have a common foundation form to resist the overturning moment generated by the wave and other environmental loads. Hence, subjected to seismic or ocean wave loading, offshore structures are more likely to exhibit a combined torsion and bending (translation) response [506].

An offshore platform generally has a heavy topside at the top of the supporting structure. For example, for a typical jacket (Fig. 9.8) or a jack-up (Fig. 9.34) platform, the weight of the topside is normally up to a few times higher than the weight of the supporting structure. Elevation control is applied for onshore buildings or tower (Fig. 9.35) structures to avoid a global resonance associated with one or two vibration modes due to earthquake and other dynamic loadings. This requires that a structure should generally be designed with a pyramid shape (with a gradually decreased stiffness and mass per unit height with the increase in its height) to prevent the resonance amplification. This is difficult to achieve in offshore structural design, because a significant mass (in many cases the major mass) is located at the top of the supporting structure. This makes the modal mass participation corresponding to the most important global bending or torsional vibration mode rather high, so that when the resonance occurs due to the vibration participation of the topside, a significant inertia force will be generated and applied on the supporting structure, leading to a large vibration response.

Fig. 9.34 Two jack-ups with supporting structures made of tubular legs (left) or trusses (right). The jack-ups are towed to the site and legs are jacked down, engaging the seafloor raising the platforms (courtesy of Dong Energy)



Fig. 9.35 320-m-high Eiffel tower with an elevation control design, comprising more than 15,000 wrought-iron structural members joined by 2.5 million rivets. The structural weight is 7300 tons (photo courtesy of Jing Dong)



The presence of heavy offshore foundations together with the weight of the platform may change the soil properties, which influences both the foundation impedance (stiffness and damping) and the foundation capacity control.

Compared to that of onshore structures, the space in an offshore platform is generally limited, making it more difficult to place dampers and other mitigation equipment to attain an effective reduction in dynamic response.

The presence of sea water induces additional loads due to added mass, hard marine growth, and hydrodynamic damping. Marine growth also adds weight on supporting structures. Therefore, in addition to inertia forces due to ground accelerations transferred to structures, for offshore structures, the relative motions between the submerged structural members and their surrounding fluids also create hydrodynamic damping forces. Furthermore, the surrounding fluids will also enhance the inertia effects of the submerged structural members, which are referred to as the effects of added mass. Both the added mass and the hard marine growth can introduce significant inertia effect to the structure, leading to an increase in natural periods.

The hydrodynamic damping induced by fluid–structure interaction will generally slightly decrease the dynamic response, even though this effect is rather limited and can normally be neglected in mild sea states. When a strong earthquake occurs together with a significant storm (i.e., large wave height), the hydrodynamic damping forces applied on offshore structures can be dramatically increased. Note that the joint probability of occurrence of both events (significant earthquakes and extreme storm waves) is practically extremely low and is therefore not considered by typical offshore structural design codes.

Due to the abrasion of soil surface by the passing of current, wave, and flood, the shear stress generated from the flowing water may exceed the threshold value of the

soil erosion resistance, removing the sediment such as sand and rocks from around the foundation (such as piles, bridge abutments, or piers). A hole is then formed at the upper soil surface, which is called scour as shown in Fig. 20.4. Scour leads to a reduction in capacity for both the upper structure and the foundation. It particularly reduces the stability of the foundation and increases the maximum design moments in the pile, which requires a larger pile penetration depth and pile cross-sectional area. For a small diameter subjected to monotonic horizontal load, the maximum pile bending stress increases almost linearly with the scour depth [507]. Due to the degrading of the foundation stiffness, the presence of scour hole also decreases natural frequency of the structure system. In case the change in natural frequency is significant, it can dramatically alter (decrease or increase) the seismic spectral acceleration value corresponding to the natural frequency, thus significantly changing the seismic force and responses in the foundation and superstructure. In addition, geometrical variation of the mudline leads to more complicated design requirements for the pipeline and cables at seabed.

In addition, due to the effects of water column, depending on the water depth, vertical ground motion acceleration at seabed will be decreased by the effects of finite water column at some frequency ranges while being amplified at other frequency ranges. However, in general, the peak vertical acceleration at seafloor can be reduced by as much as 50% [508, 509]

The variation of fluid tank levels on offshore structures also changes the mass of the structure. This alternates the dynamic response and presents potential challenges to perform vibration-based structural health monitoring [123], which is to detect structural damages through the observation of changes in measured eigenfrequencies and corresponding vibration mode shapes.

Compared to land-based structures, offshore structures are generally designed to resist more significant lateral environmental loads due to the presence of wave, current, and/or ice crushing loading. Therefore, even though the action points of those loadings on structures may be far from that of the earthquake-induced ground excitations, the seismic performance of offshore structures is normally better than their land-based counterparts.

Finally, but not the least consideration, as a consequence of a special type of earthquake, the sudden subsidence of offshore platforms, has been realized to be a serious risk by more and more energy companies as well as authority bodies, which needs consideration during the design.

9.4 Hydrodynamic Modeling of Offshore Structures

9.4.1 Introduction to Hydrodynamic Force Calculation

Under strong seismic ground motion, the structure may undergo large motions. Compared to land-based structures, offshore structures are subject to unique fluid–

structure interaction effects: the hydrodynamic forces due to the relative velocity and acceleration between structural members and their surrounding waters. This induces drag and inertia forces applied on offshore structures. In addition, the hydrodynamic interaction with the offshore environment, such as waves, current, and wind, also gives rise to additional environmental loading applied on structures.

For slender tubular members, the accelerated flow separates from the surface of the submerged structural member, forming a wake (low-pressure region) “behind” the member. Subject to ocean wave and current loading, the hydrodynamic forces due to this effect include both drag and inertia forces as shown in Fig. 9.36. The hydrodynamic forces per unit length on members along the relative motion direction between members and water are calculated by Morison’s equation [510], which is only applicable when the diameter of the structural member d is less than $1/5$ of the ocean wave length, as is the case for typical jacket/jack-up structures:

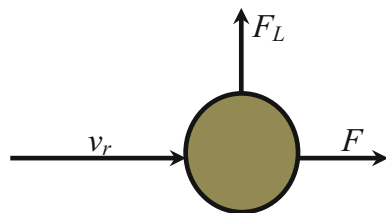
$$F = \rho \cdot A \cdot a_w + \rho \cdot C_m \cdot A_r \cdot a_r + \frac{1}{2} \rho \cdot C_D \cdot v_r \cdot |v_r| \cdot d \tag{9.14}$$

where ρ is the density of the fluid; A is the cross-sectional area of the body; a_w is the component of the water particle acceleration normal to the member axis; C_m is the added mass coefficient, which is defined as the ratio between added mass of fluid and the associated displaced fluid mass, which will be discussed in Sect. 9.4.3; A_r is the reference area normal to the structural member axis; a_r is the relative acceleration between water particle and member normal to member axis; C_D is the drag coefficient; v_r is the water particle velocity relative to the member normal to the member axis; and d is diameter of the member exposed to the water.

The first item $\rho \cdot A \cdot a_w$ on the right-hand side of the equation above is the wave potential-related Froude Krylov excitation force, which is the sum of the hydrodynamic pressures acting on the surface of the body, and which would exist even in the absence of a structure ($\rho \cdot C_m \cdot A_r \cdot a_r$)

The pressure disturbance due to the presence of the structure modifies the flow, which is taken into account in the second item $\rho \cdot C_m \cdot A_r \cdot a_r$, which is the added mass ($\rho \cdot C_m \cdot A_r$) related force due to the relative acceleration (a_r) between the structure and the fluid. In general, this depends on the flow condition as well as the location of the body. Even if, when a structure is subject to ocean wave loading, the added mass in the vicinity of a free surface is strongly wave frequency-dependent (it is sometimes misunderstood by people that the added mass

Fig. 9.36 Direction of hydrodynamic drag and inertia force F and lift force F_L relative to motion between structure member and fluid v_r .



is a finite amount of water that oscillates rigidly connected to structural members), this dependence characteristic may be disregarded for deeply submerged bodies provided that the dimension of the body is smaller than the wave length. For seismic analysis of offshore structures, the added mass may in most cases be simply approximated with a constant value, which will be discussed in Sect. 9.4.3.

Note that both the Froude Krylov force and added mass force are due to the inertia of the structures and the surrounding fluid. The viscous effects are then accounted for in the third item (drag force) $\frac{1}{2}\rho \cdot C_D \cdot v_r |v_r| \cdot d$. This item also indicates a nonlinear relationship between the resultant forces on structural members and the wave particle velocity. The effect of drag force is usually to introduce hydrodynamic damping, which can normally be conveniently estimated using Borgman's linearization, in which the expanded series of $v_r |v_r|$ can be approximated as the first term of the series by replacing $|v_r|$ with $(8/\pi)^{0.5} v_{r(\text{rms})}$ for sinusoidal velocity of wave, where $v_{r(\text{rms})}$ is the root-mean-square of v_r [511]. For the case of a sinusoidal velocity superimposed on a current flow, the drag force-induced damping can be approximated based on a minimum average error between $v_r |v_r|$ and the linear approximation [512].

For conditions with a fixed body or in which the acceleration and velocity of structural components are small, one has $a_r = a_w$ and $v_r = v$. By assuming $A_r = A$, the equation above can be rewritten as:

$$F = \rho \cdot C_M \cdot A \cdot a_w + \frac{1}{2}\rho \cdot C_D \cdot v \cdot |v| \cdot d \quad (9.15)$$

in which the inertia coefficient is defined as $C_M = 1 + C_m$, which may be determined based on a root-mean-square measured average value of inertia coefficients.

For moving structures in still water, the hydrodynamic drag and inertia force can be calculated as:

$$F = -\rho \cdot C_m \cdot A \cdot a_s - \frac{1}{2}\rho \cdot C_D \cdot v_s \cdot |v_s| \cdot d \quad (9.16)$$

where a_s and v_s are acceleration and velocity of structures/members normal to its axis.

Both C_D and C_M can be determined experimentally. They can also be obtained by checking relevant handbooks and diagrams.

For circular members, the drag and inertia coefficients are a function of the following non-dimensional parameters:

$$\text{Reynolds (Re) number : } Re = v_{\text{max}}d/\nu \quad (9.17)$$

$$\text{Keulegan-Carpenter (K_C) number : } K_C = v_{\text{max}}T/d \quad (9.18)$$

$$\text{Surface roughness : } \delta = k/d \tag{9.19}$$

where v_{\max} is the maximum velocity between water particle and members; ν is the kinematic viscosity of water, typically taken as $1.1 \times 10^{-6} \text{ m}^2/\text{s}$; T is the period of ocean wave loading; and k is the surface roughness height, typically ranging between 0.004 and 0.06.

Figure 9.37 shows drag coefficients for smooth cylinders and cylinders of various roughnesses varied with Reynolds number (Re) in steady uniform flow. Note that there is a distinct drop in the drag coefficient in a certain Reynolds number range. This is referred to as the critical flow regime and is very pronounced for a smooth circular cylinder. The surface roughness height can be selected based on the material and surface condition, with one recommended by DNV [513] as listed in Table 9.2.

Figure 9.38 shows variations of inertia coefficient with K_C number for smooth and rough cylinders. For intermediate roughness, the values can be determined by a linear interpolation between the curves for smooth and rough cylinders. For large K_C number, the drag force is the dominating force compared with the inertia force; asymptotic values of inertia coefficient for smooth and rough cylinders can be taken as 1.6 and 1.2, respectively [513].

As mentioned before, Morison’s equation is only applicable when the diameter of structural members is less than 1/5 of the wave length, which is the case for many offshore structures such as jacket or jack-up structures. However, for large volume bodies with $\pi d/\lambda > 0.5$ (where D is the dimension of structure body and λ is the

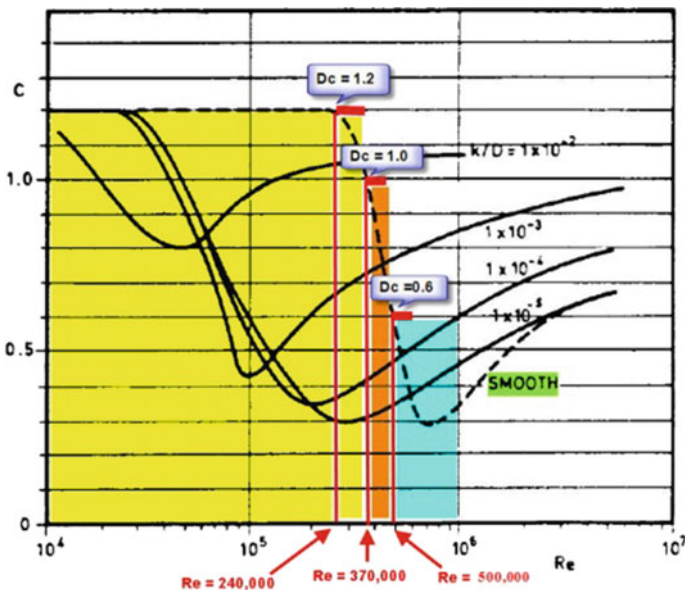
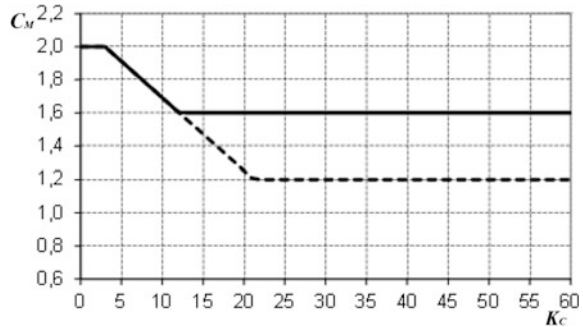


Fig. 9.37 Variation of drag coefficient with Reynolds (Re) number and surface roughness

Table 9.2 Surface roughness recommended by DNV [513]

Structural surface exposed to fluid	k (m)
Steel, new uncoated	5×10^{-5}
Steel, painted	5×10^{-6}
Steel, highly corroded	3×10^{-3}
Concrete	3×10^{-3}
Marine growth (see Sect. 9.4.5)	5×10^{-3} to 5×10^{-2}

Fig. 9.38 Variations of inertia coefficient with K_c number for smooth (solid line) and rough (dashed line) cylinder



ocean wave length), the incident waves undergo significant scattering or diffraction surrounding the structure, the drag effects are small while the diffraction of the waves from the surface of the structure plays a dominant role in the calculation of hydrodynamic forces, and the structure is large enough to fall into the diffraction wave force regimes II and IV shown in Fig. 9.40. In engineering practice, the hydrodynamic force due to wave diffraction can be calculated by modeling the structure as a panel model and integrating the panel pressure on each part of the structure, together with the Morison model, the hydrodynamic forces applied on the structure can be determined as shown in Fig. 9.39. For more details, readers may refer to [514, 515].

On the basis of the discussion above, it can be summarized that the calculation of hydrodynamic forces can be handled as two types of problems [514]:

1. Forces on a body when the structure is restrained from oscillating and there are incident ocean waves. The forces are referred to as wave excitation loads, comprising Froude-Kriloff and diffraction forces.
2. Forces on the body when the structure is forced to oscillate with the excitation frequency in any rigid-body motion mode without interference from incident waves, which include added mass, damping, and restoring terms.

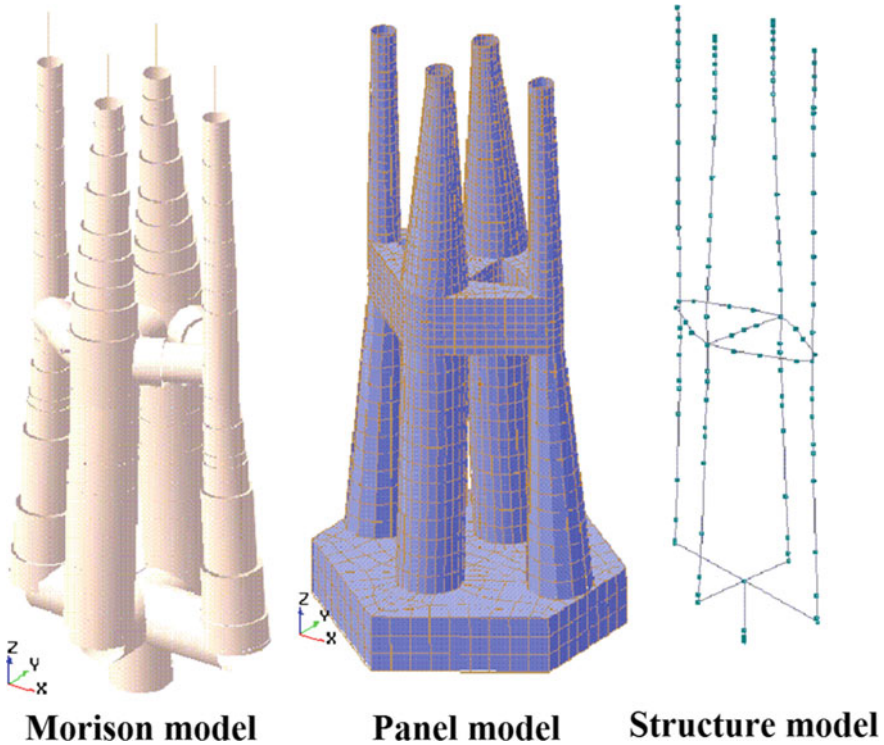


Fig. 9.39 Combining the Morison and panel model to calculate the hydrodynamic loads transferred to the structural model (courtesy of Aker Solutions)

In addition to the hydrodynamic force applied along the direction of relative motion between a structure member and surrounding fluid, the structural member can also receive lift force (Fig. 9.36) perpendicular to direction of the relative motion:

$$F_L = \frac{1}{2} \rho \cdot C_L \cdot v_r \cdot |v_r| \cdot d \tag{9.20}$$

where C_L is the lift coefficient, which is a function of Reynolds number.

In the following sections, the effects of drag and added mass coefficients, buoyance, and marine growth on seismic responses of offshore structures will be discussed briefly.

9.4.2 Effects of Drag Forces

The drag forces applied on structures are caused by the relative velocity between the member and the water flow. Under storm wave condition, they can cause a significant wave loading, which is a dominant environmental load for designing the majority of offshore structures constructed with slender members. On the other hand, drag loading also introduces a hydrodynamic damping to mitigate the seismic response of offshore structures [517]. This hydrodynamic damping is higher in choppy seas than in still water and is more significant under sea states with large wave height than under small wave height, even though this effect is generally small [518].

However, under certain circumstances, the combination of seismic and wave loading on offshore structures can even increase the dynamic response. By studying the seismic responses of jacket structures under both earthquake and wave loading, Jin et al. [519], Etemad et al. [520], and Bargi et al. [521] showed that when the ocean waves propagate in different directions from that of seismic loading, the structural response can even be increased.

9.4.3 Effects and Determination of Added Mass

As mentioned before, added mass accounts for the inertia of the fluid entrained by the accelerating structure, i.e., since the structure accelerates, the fluid surrounding the structure must also accelerate. Added mass increases the effective mass and effective mass moment of inertia of the structure. Since the water has a comparable density to that of the body of the marine structures, added mass plays a significant role in the dynamic analysis of marine structures [522]. Table 9.5 shows an example of mass distribution of a jacket among the jacket, added mass, marine growth, and the topside. It is found that the value of added mass is in the same order of significance as the jacket's structural mass.

In practical analysis, the added mass can normally be accounted for by a simplified modeling of an additional mass distributed on each submerged structural member or along all surfaces of the structure that interact with surrounding water and be effective only along direction(s) of fluid–structure relative motion direction. For tubular members with circular cross sections, the contribution to the added mass per unit length can be calculated as:

$$m_a = \left[\rho \frac{\pi d^2}{4} (C_M - 1) \right] + \left[\rho \left(\frac{\pi}{4} (d - 2t_g)^2 - \sigma \right) (1 - I) \right] + \left[\rho_g \pi (dt_g - t_g^2) \right] \quad (9.21)$$

where ρ is the density of the fluid; ρ_g and t_g are the density and thickness of marine growth (Sect. 9.4.5); d is the member diameter including marine growth; C_M is the

inertia coefficient; σ is the solid area of member's cross section; $I = 0$ for fully flooded member (internal water is to be included), and $I = 1$ for non-flooded member (internal water is not to be included).

The first, second, and third item on the right-hand side of the equation above indicate, respectively, the added mass contributed from parts outside the members, inside the members, and marine growth.

Even though the inertia coefficient C_M in the equation above is frequency-dependent (a function K_c or Re), indicating that the finite volume of fluid connected to the member does not oscillate rigidly, for calculating the seismic responses of offshore structures with high-frequency vibrations (typically much higher than wave loading frequency), it may roughly be taken as 2.0. As a further simplification, the added mass of non-flooded (buoyant) members can be modeled as the mass of water (along the direction of structure-fluid relative motion direction) with the enclosed volume of the structure members. For flooded members, the added mass is modeled as twice the mass of the water with the enclosed volume of the structural members.

For the added mass for various cross sections or body shapes, readers may check the relevant handbooks or guidelines, such as Appendix D in DNV-RP-C205 [513]. For example, depending on the relative direction between structural members and the water particle motions, Table 9.3 shows the added mass coefficient for structural members with square prismatic shape, which can be used to calculate added mass:

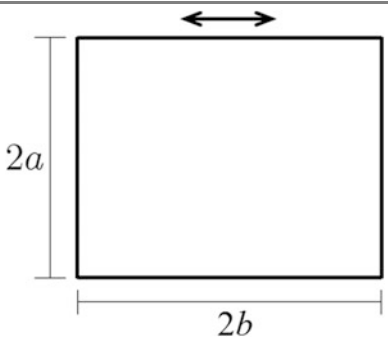
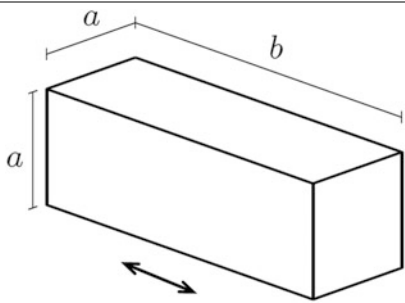
$$m_a = \rho C_m V = \rho C_m A l \quad (9.22)$$

where V is reference volume of the structural object in m^3 ; A is reference area of the object in m^2 ; both V and A are given in Table 9.3; and l is the length of the object affected by added mass effects, which is applicable when two-dimensional geometry is assumed.

Added mass generally gives an increase in natural period of the structure due to its contribution to the inertia of the structure. This normally results in a decrease in spectral acceleration, but may sometimes increase local forces on the submerged part of the structure due to a possible increase in inertia force on that part.

It is noted that in many engineering practices, for simplicity, the effects of added mass are represented modeled as point masses attached to the submerged part of the offshore structures that are equivalently effective in all three translational degrees of freedom in a dynamic analysis. This is likely to give an incorrect representation of the added mass as it is in reality only active along the direction(s) of relative oscillatory motion between the structural object and the water particle. This inappropriate modeling can be non-conservative. For example, when the added masses are modeled as real structural masses that are effective in all three translational degrees of freedom, it can cause additional gravity loads applied throughout the structure, which artificially reduces the tensile stresses or increases/induces compressive stresses on concrete shafts' cross sections for a GBS structure, or artificially decreases the uplifting forces on pile foundations for a jacket structure. In addition, the inappropriate modeling of added mass can also induce artificial inertia forces in the vertical direction of the structure, which can be either conservative or non-conservative.

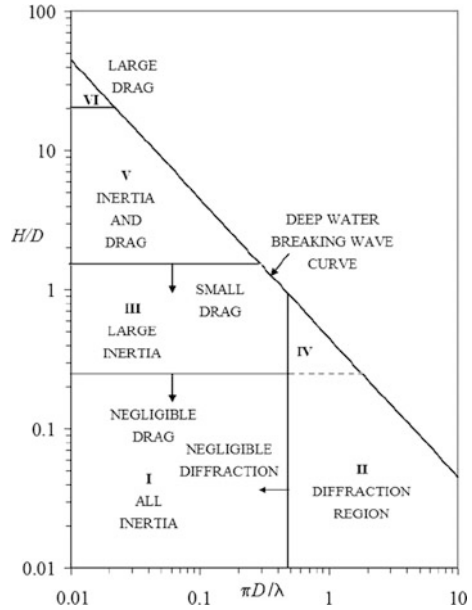
Table 9.3 Analytical added mass coefficient C_m for structural objects with square prismic shape in two and three dimensions [513]; the direction of motion for structural objects is indicated by double-end arrow line

Section through body or body shape	a/b	C_m	V or A
	∞	1.0	$A = \pi a^2$
	10	1.14	
	5	1.21	
	2	1.36	
	1	1.51	
	0.5	1.70	
	0.2	1.98	
	0.1	2.23	
	1	0.68	$V = a^2 b$
	1/2	0.36	
	1/3	0.24	
	1/4	0.19	
	1/5	0.15	
	1/6	0.13	
	1/7	0.11	
	1/10	0.08	

9.4.4 Effects of Buoyancy

The buoyance force applied to non-flooded members or large volume submerged structures can be rather significant. Its effects on structural and foundation capacity can be both positive and negative. For example, for an offshore structure with submerged concrete shafts, the buoyance force along the shafts generally decreases the compressive stress along the longitudinal axis of the shafts. However, when combined with horizontal earthquake or ocean wave loading, it can result in an increase of tensile stress in the tensile side of each concrete shaft. Similarly, for an offshore structure’s foundation constructed in the form of a pile group, when combined with seismic or ocean wave loading, the buoyance force on the offshore structure can decrease the compressive forces on some piles, but at the same time also increases the tensile forces on some other piles.

Fig. 9.40 Dominant types of wave forces at different regimes (D is the characteristic dimension of structures/members, H is the wave height, and λ is the wave length) [516]



9.4.5 Effects and Modeling of Marine Growth

After a certain period of installation for an offshore structure, various types of marine fouling organism may be found on the structure’s submerged member. They are referred to as marine growth as shown in Fig. 9.41. Their distributions on structural members vary depending on many factors, such as geographical location, water depth, water temperature and season, ocean current, platform design, and operation.

Marine growth can be classified into three main categories, namely hard growth, soft growth, and long and flapping weed. Hard growth includes mussels, oysters, barnacles, and tubeworms. Soft growth includes seaweeds, soft corals, sponges, anemones, hydroids, sea-squirts, and algae. Long flapping weed is kelp, which could also come under soft growth but is singled out because of its much larger size.

The major effects of marine growth can be summarized as [523]: (1) increase in structural diameter and displaced volume; (2) increase in structural weight (normally insignificant); (3) change in hydrodynamic drag coefficient (Fig. 9.37), and decrease in added mass coefficient due to the surface roughness (Fig. 9.38); (4) possible increase in hydrodynamic forces; (5) increase in natural period due to contributions from the increased added mass and structural weight; (6) coverage of the member’s outer surface, causing difficulties for subsea inspection; (7) physical obstruction that restricts functionality.

From the seismic response point of view, as marine growth will cause an increase of a structure’s eigenperiod by adding more mass, it may slightly modify

Fig. 9.41 Marine growth at water depths of 14 m (upper) and 41 m (lower) on an offshore jacket structure in the North Sea



frequency content of the seismic response. It may also increase the hydrodynamic forces and modify the static stability of the structure.

It is also worth mentioning that, among different types of marine growth, it is mainly the hard marine growth that contributes to the hydrodynamic forces. Soft marine growth hardly contributes accountable hydrodynamic forces and can therefore normally be omitted in the hydrodynamic load calculation.

In structural design and analysis, the marine growth is typically assumed to be a function of location. It would be preferable to measure the marine growth on structural members. In the absence of site-specific information on the types and thickness of marine growth, various design codes provide recommended values, such as the one recommended by Norsok [627] as listed in Table 9.4. The density of marine growth can typically be taken as 1325 kg/m^3 .

Table 9.4 Marine growth varied with altitude applied for offshore design in Norway [627]

	Latitude 56–59°N	Latitude 59–72°N
Water depth (m)	Thickness (mm)	Thickness (mm)
+2 to -40	100	60
below -40	50	30

Table 9.5 An example of mass and added mass distribution of a jacket structure with a water depth of 110 m located in the North Sea

Item	Mass (tons)
Structural weight of jacket	8600
Marine growth	700
Added mass	4600
Total jacket mass	13,900
Topside modules	13,000

Table 9.5 shows an example of mass distribution of a jacket platform among the jacket steel, added mass, marine growth, and the topside modules. It is found that even though the value of added mass is in the same order of significance as the jacket’s structural mass, the mass of marine growth is much less significant.

Instead of using the marine growth thickness provided by codes and standards, such as the one given by Norsok [627] as listed in Table 9.4, it is preferred to perform in-site measurement to reduce the uncertainties. The measured thickness is normally less than that given by Table 9.4, thus reducing the hydrodynamic forces and slightly increasing the natural frequency of the structure. Moreover, to reduce the hydrodynamic forces, a cleaning of marine growth can be performed at certain intervals. It is also a practice in some offshore jacket structures to install metal bands around the legs and conductors that are moving up and down with the ocean wave, which can clean the marine growth in the wave zone.

Chapter 10

Representation of Seismic Ground Motions

10.1 General

It is noted that the most important parameters of an earthquake ground motions are its maximum motion, predominant period, and effective durations [524]. However, different from other loadings, earthquake-induced loading and ground motion have high uncertainties in these aspects, as well as, more broadly, in respect of occurrence, magnitude, frequency content, and duration. The uncertainties come from many sources: The energy suddenly released during an earthquake is built up rather slowly through tectonic movements; historical records over a time span of a couple of hundred years do not provide a complete picture of the seismic hazard. Moreover, the rupture and faulting process during an earthquake is extremely complex and affected by many parameters that are difficult to predict [525].

In the frequency domain, three types of spectra can be applied to describe the ground motion, namely Fourier spectrum (Sect. 10.3.1) and its closely related power spectrum (Sect. 10.3.2), and response spectrum (Sect. 10.4). The two former ones are stochastic methods, while the latter is categorized as a deterministic one due to the response spectra being generated from deterministic time history responses. As will be elaborated in Sect. 10.4, the Fourier spectrum or power spectrum combined with the phase information (through phase spectrum) can completely describe a ground motion (provided that the ground motion is stationary) while the response spectrum cannot. On the other hand, the use of Fourier spectrum and power spectrum normally requires that the seismic excitation is close to a stationary process, which is likely to be the case for only the central (strong motion) part of an earthquake record. The response spectrum method does not have this restriction. Moreover, from an engineering point of view, the response spectrum is a more convenient and valuable tool to represent the ground motions, and it is especially suitable for a direct assessment of the effects of ground motions on structural response. Section 10.3 will present the power spectrum to represent the

ground motions and how non-stationary characteristics of seismic motions can be approximated in this method.

Time history method (Sect. 10.5) enables the application of nonlinear dynamic structural analysis, which has the unique advantage of reducing the computational and modeling uncertainties, accompanied by an increase in computational efforts (compared to power spectrum and response spectrum methods).

Before the advent of computer techniques in daily engineering work, to avoid intensive computation cost, the response spectrum was the most widely adopted approach for defining the earthquake ground motion input regardless of types of structural analysis (i.e., equivalent static analysis or response spectrum analysis), as will be discussed in Sect. 10.4. From the late twentieth century, with the rapid development of computer techniques and subsequent dramatic reduction in computation cost, time history analysis became more and more popular since it can reduce more uncertainties in the seismic loading and response calculations. However, spectrum method is still the most widely used not only in seismic structural analysis, but also within the context of (spectrum compatible) accelerogram generation (Chap. 4) and time history analysis, even though this method has been questioned by many researchers, including one of its original promoters [526].

Since earthquake ground motion is in general non-stationary, as mentioned above, analysis in the frequency domain loses the time-located information. To solve this problem and also to more efficiently represent the ground motions in the time–frequency domain, wavelet transform method [527] is also promoted as a way to represent the time-located information [188].

10.2 Earthquake Excitations Versus Dynamic Ocean Wave, Wind, and Ice Loading

Compared to other random environmental loadings such as ocean wave, wind, and ice loadings, seismic loading has both similar and unique characteristics with respect to frequency, duration, action locations, linearity of loading and response, as well as stationarity, which is illustrated in Table 10.1.

The characteristics above are essential to determine the relevant design philosophy, analysis and design methods, load representation, as well as required engineering skills. For example, ocean wave, wind, and ice loadings can sometimes be approximated as a stationary process and, being linear, the loading can be represented by power spectra. If the structures subject to those loading are also linear or nearly linear (response is proportional to the magnitude of loading), the response can be obtained based on stochastic dynamics and be calculated in frequency domain rather than in time domain. This will significantly reduce the computational efforts. However, seismic loading is non-stationary in both amplitude and frequency content, as discussed in Sect. 3.3. Therefore, it may be challenging to directly



Fig. 10.1 A monopod structure with vertical leg structure (left) during the first winter, later modified with an ice-breaking cone (right) installed during the second winter [528]

represent the entire process of seismic loading with power spectra. On the other hand, power spectra can be used to represent the strong/central motion part of the seismic loading, and by scaling the seismic loading with different factors at different time range, the non-stationary properties can also be approximated. As another example, the applied loading due to seismic and ocean wave loading can normally be defined at a single location/point or a few locations/points, while the load data for the dynamic gust wind loading has to be defined on many points/locations in a structure, and their correlations become stronger for closer locations [123]. Similar issues have to be addressed for extended structures subject to earthquake loading, in which the relative motion between structural supports or various locations cannot be ignored.

Table 10.1 Essential characteristics of various types of environmental loading

Item	Earthquake	Ocean wave	Wind	Ice
Loading period	Narrow- or wide-banded, 0.3–30 s	Approximately narrow-banded, 3 s (small wave)–26 s (storm wave)	Approximately narrow-banded, 15 s–a few minutes	Wide-banded for vertical structures; narrow-banded and above 0.2 s for conical structures, see Fig. 10.1
Durations (s)	A few second to 3 min	Hours	Hours	Varies significantly depending on the ice condition
Single point load data	Single point for shallow foundation; various points for pile foundations; multiple excitations for extended structures	Single point	Multiple points over the entire structure exposed to wind	Single point or a small area during ice–structure interaction
Linearity regarding loading	Yes	Theoretically nonlinear mainly due to the fluid–structure interaction and wave nonlinearity; can be linearized for small amplitude of waves	Theoretically nonlinear mainly due to the fluid–structure interaction; can normally be linearized	Yes
Linearity regarding response	Linear for small amplitude of loading while nonlinear for significantly high amplitude of loading or loading causing structural resonance	The same as to the left	The same as to the left	The same as to the left
Stationary or not	Non-stationary, but with a period of strong motion being stationary	Approximately stationary	Approximately stationary	Stationary for homogenous level ice sheet continuously crushing at a sufficiently high drift speed; non-stationary for non-homogeneous ice sheets, pressure ridges, open leads, and low drift speeds

10.3 Power Spectrum of Seismic Ground Motions

The concept of spectrum can be attributed to Isaac Newton, who, with the aid of a prism, discovered that sunlight can be decomposed into a spectrum of colors from red to violet in about 1700. This indicates that any light comprises numerous components of light of various colors (wave lengths). The earliest function most closely resembling the spectral density function was developed by Arthur Schuster, who investigated the presence of periodicities in meteorological [529], magnetic [530], and optical [531] phenomena. The spectrum provides a measure of the light’s intensity varied with respect to its wavelength. This concept has been generalized to represent many physical phenomena by decomposing them into their individual components.

10.3.1 Introduction to Fourier and Power Spectrum

10.3.1.1 Fourier Spectrum

Invented by Baron Jean Baptiste-Joseph Fourier in 1807, but the subject of great skepticism from his contemporaries at that time, the Fourier transform has now become a major analysis method in the frequency domain across a wide range of engineering applications. It states that any periodical function $\delta(t)$ in the time domain, not necessarily harmonic, has an equivalent counterpart in the frequency domain, which can be represented by a convergent series of independent harmonic functions as a Fourier series:

$$\delta(t) = c_0 + \sum_{i=1}^N c_i \sin(\omega_i t + \gamma_i) \tag{10.1}$$

where

- c_0 is the average value of $\delta(t)$, $c_0 = \frac{1}{T_0} \int_0^{T_0} \delta(t) dt$
- T_0 is the duration of the motions
- c_i is the amplitude of the n th harmonic of Fourier series,
 $c_i = \sqrt{a_i^2 + b_i^2}$
- $a_i = \frac{2}{T_0} \int_0^{T_0} \delta(t) \cos(\omega_i t) dt$ is the amplitude of cosinusoidal excitations,
- $b_i = \frac{2}{T_0} \int_0^{T_0} \delta(t) \sin(\omega_i t) dt$ is the amplitude of sinusoidal excitations,
- ω_i is the n th frequency of component, with the lowest one being $\omega_0 = \frac{2\pi}{T_0}$
- γ_i is the phase angle, $\gamma_i = \tan^{-1} \left(\frac{a_i}{b_i} \right)$, which defines the stagger related to time origin, controls the times at which the peaks of harmonic motions/loadings/responses occur, and influences the variation of $\delta(t)$ with time.

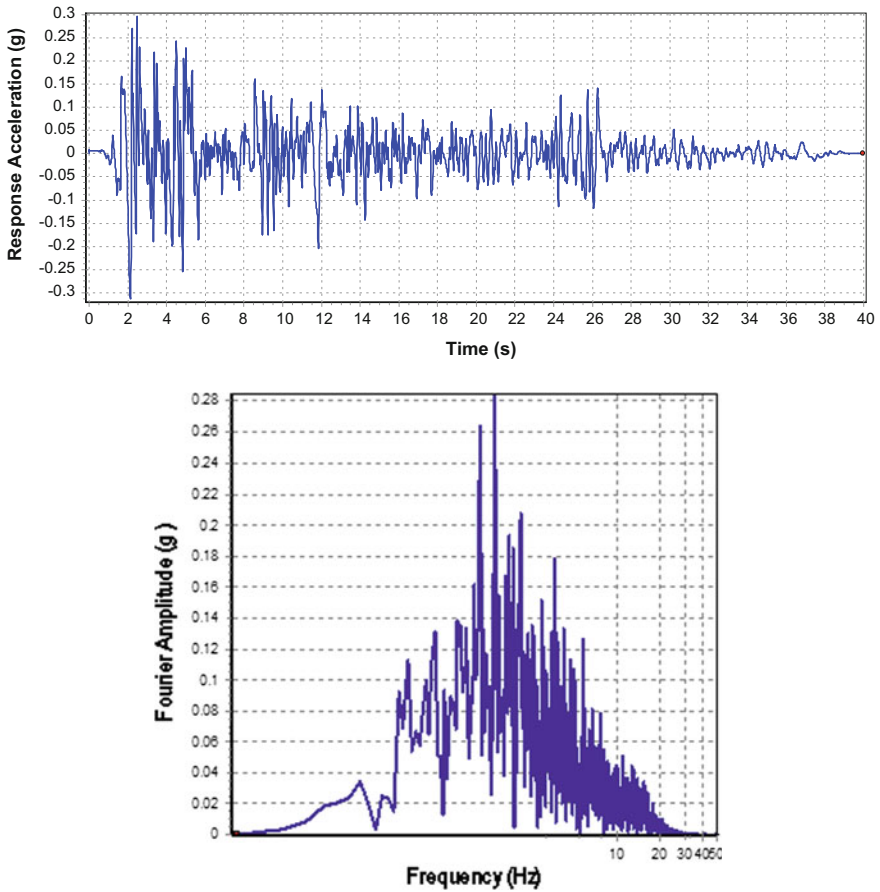


Fig. 10.2 Fourier amplitude spectrum (lower) of the strong ground motions (upper) recorded at Imperial Valley, California

Physically, the equation above is a representation of irregular records by the sum of an N sine waves of amplitudes c_i and frequency ω_i .

The Fourier series gives a complete description of motions since the motions can be recovered by the inverse Fourier transform.

For most motion records, such as sea wave elevations, by judicious choice of the datum level of the measurements, its average value (c_0) can be assumed to be zero. Equation (10.1) can then be reduced to:

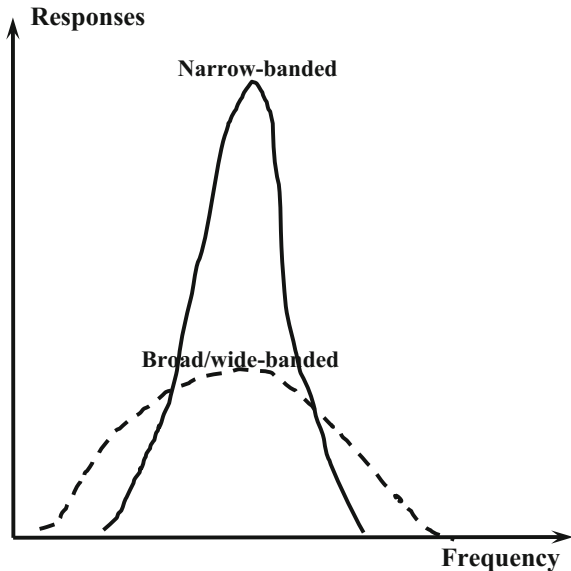
$$\delta(t) = \sum_{i=1}^N c_i \sin(\omega_i t + \gamma_i) \tag{10.2}$$

Total energy is proportional to the average of the squares $\delta(t)$, which is the sum of the energy contents for each individual component at each frequency ω_i (Parseval’s theorem).

A plot of c_i versus ω_i from Eq. (10.2) is called a Fourier amplitude spectrum (normally referred to as a Fourier spectrum) (Fig. 10.2). To further explain the application of this concept, let’s take the analysis of earthquake ground motions as an example. For a given earthquake and site, in order to obtain a complete picture of the strength of seismic ground motions (upper figure in Fig. 10.2) in each individual frequency or period, the Fourier spectrum is introduced as the Fourier amplitude (c_i) that varies with frequency or period, as shown in the lower figure in Fig. 10.2. From Fourier analysis of abundant strong ground motion time histories, it is found that the periods (inverse of frequency) of major motion contents range from 0.3 to 30 s.

Readers may bear in mind that narrow-banded time series have a dominant frequency, and it is typically the result of resonance or near-resonance responses, while broad-/wide-banded motions or excitations have a noticeable variety of frequencies. Since the mean values of the time series are constant and do not contribute to the Fourier amplitude in the frequency domain, the narrow- and broad-banded time series can be illustrated in the frequency domain using the Fourier amplitude spectrum as shown in Fig. 10.3.

Fig. 10.3 Fourier amplitude spectrum for a narrow-banded and a broad-banded random process with both of their origins of ordinate at the mean value of each time series



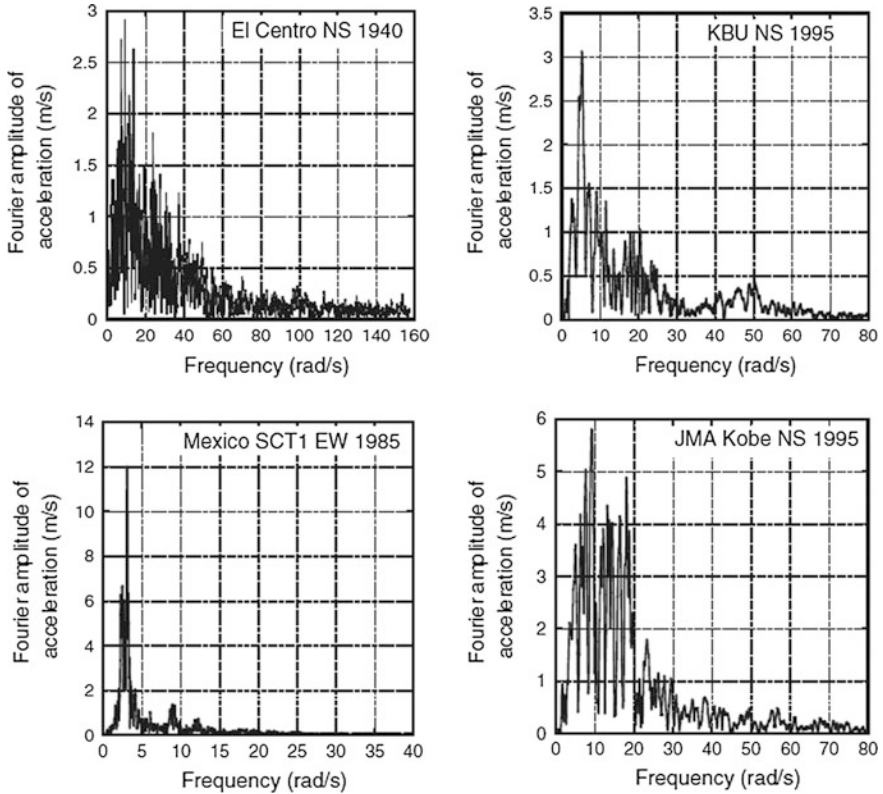


Fig. 10.4 Fourier amplitude spectrum of strong ground motions recorded at four different earthquake events [556]

Figure 10.4 shows the Fourier amplitude spectrum of the ground acceleration histories (Fig. 10.5) for four earthquake events: El Centro NS (Imperial Valley 1940), Kobe University NS (Hyogoken-Nanbu 1995), SCT1 EW (Mexico Michoacan 1985), and JMA Kobe NS (Hyogoken-Nanbu 1995). It is clearly shown that, within the period range longer than 0.25 s, where the majority of seismic motion energy is concentrated, spectrum peaks appear at different frequencies. The Fourier amplitude spectrum for Mexico SCT1 EW record is comparatively narrow-banded, with the majority of energy concentrated at a period of around 2.4 s. For the JMA Kobe NS record, the energy content is spread over a wide range of frequencies.

The ups and downs in a Fourier spectrum can be smoothed and plotted in a logarithmic scale. The smoothed spectrum shown in Fig. 10.6 has a standard shape with the largest acceleration over an immediate range of frequency. This immediate range of frequency is defined by its upper boundary frequency (cutoff frequency) f_{cutoff} and the lower boundary frequency (corner frequency) f_{corner} as shown in Fig. 10.6.

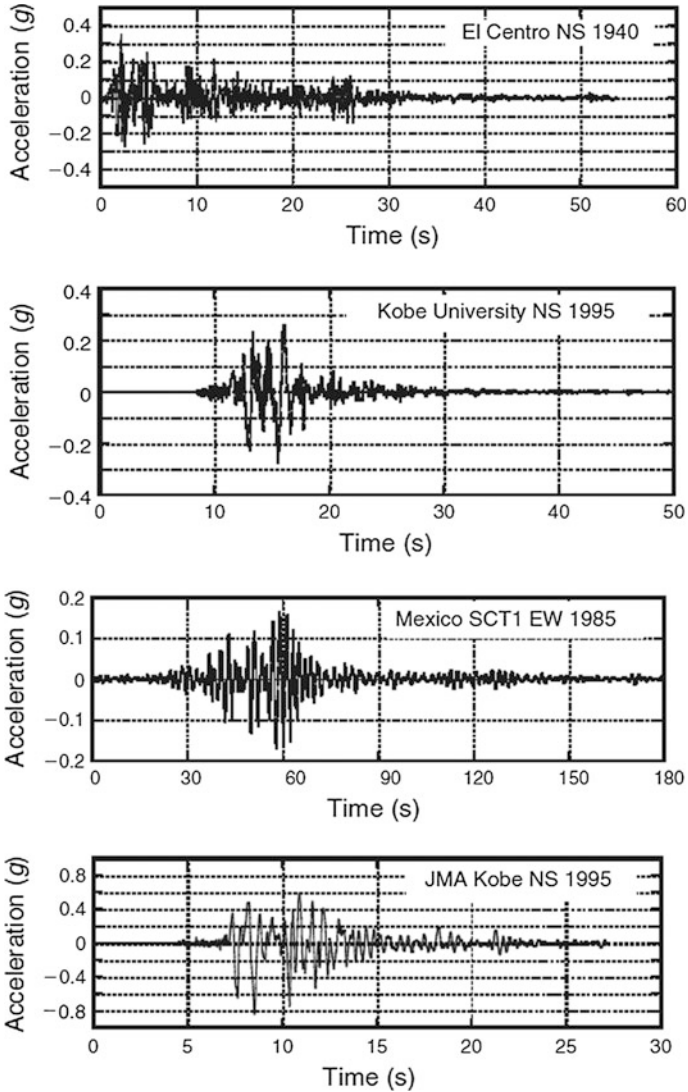
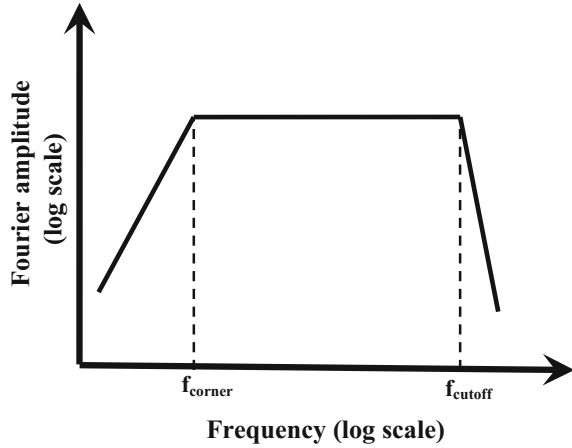


Fig. 10.5 Time history of strong ground accelerations recorded during the four different earthquake events [556]

In earthquake engineering, if a Fourier amplitude spectrum is used to represent ground motions, f_{corner} is the one above, in which earthquake radiation spectra are inversely proportional to the cube root of the seismic moment [557, 558]. The ground motions at corner frequency are higher for large earthquakes than for small ones. Below f_{corner} , the spectra are proportional to the seismic moment. However, the characteristics of cutoff frequency are unfortunately much less clearly

Fig. 10.6 Smoothed Fourier amplitude spectrum with corner and cutoff frequency logarithmic space



understood. Hanks [559] and Papageorgiou and Aki [560] indicated that the cutoff frequency relates to the near-site effects and source effects and can be regarded as constant for a given geographic region.

A plot of γ_i versus ω_i from Eq. (10.2) is called a Fourier phase spectrum. Different from the Fourier amplitude spectrum, the Fourier phase spectra from actual earthquake records do not have any standard shape [1].

10.3.1.2 Power Spectrum Density

In most cases, engineers are only interested in the absolute value of the Fourier amplitude, rather than whether it is part of the sine or cosine series. This is because the absolute value provides the total amount of information contained at a given frequency. Since the square of the absolute value is considered to be the power of the signal, instead of the Fourier spectrum, the motions can then be expressed in terms of power $P(\omega_i)$, defined as:

$$P(\omega_i) = \frac{1}{2} c_i^2 \quad (10.3)$$

where c_i is the amplitude of the i th harmonic of the Fourier series.

Imagining that $\zeta(t)$ is voltage, the power dissipated across a 1Ω resistor is then $[\zeta(t)]^2$, and the total power dissipated across the resistor is $\int_0^{T_0} [\zeta(t)]^2 dt$. By assuming that the total power of motions calculated from the sum of each individual frequency component (Parseval's theorem) equals that of the time domain, one reaches:

$$\sum_{n=1}^{+\infty} P(\omega_i) = \int_0^{T_0} [\zeta(t)]^2 dt = \frac{1}{\pi} \int_0^{\omega_N} c_i^2 d\omega = \frac{1}{\pi} \sum_{i=1}^N c_i^2 \Delta\omega_i \quad (10.4)$$

where $\omega_N = \frac{\pi}{\text{sample time interval } \Delta t \text{ over the time history}}$ is the highest frequency in the Fourier series, or Nyquist frequency, i.e., the frequency range beyond which the motion content cannot be accurately represented. In such a condition, a distorted Fourier spectrum called aliasing will be introduced. $\Delta\omega_i$ is half of the spacing between two adjacent harmonics ω_{i+1} and ω_{i-1} .

For an efficient (optimal) signal sampling, in order to extract valid frequency information, one must bear in mind that the sampling of the motion/loading/response signals must occur at a certain rate: (1) For a time record with the duration of T seconds, the lowest frequency component measurable is $\Delta\omega_{\min} = \frac{2\pi}{T}$ or $\Delta f_{\min} = \frac{1}{T}$. (2) The maximum observable frequency is inversely proportional to the time step, i.e., $\omega_{\text{obs}} = \frac{2\pi}{\text{sample time interval } \Delta t \text{ over the time history}}$, and the sampling rate must be at least twice the desired frequency (ω_{max} or f_{max}) to be measured, i.e., $\omega_{\text{obs}} > 2\omega_{\text{max}} = 2\omega_N$, where ω_N is the Nyquist frequency. With the two properties (1) and (2) above, the sampling parameters can be expressed as:

$$\omega_{\text{max}} = \omega_N = \frac{\pi}{\Delta t} \quad \text{or} \quad f_{\text{max}} = \frac{1}{2\Delta t} \quad (10.5)$$

$$\Delta t = \frac{\pi}{\omega_{\text{max}}} = \frac{\pi}{\omega_N} \quad \text{or} \quad \Delta t = \frac{1}{2f_{\text{max}}} \quad (10.6)$$

The description above is often referred to as the Shannon or Nyquist sampling theorem.

By dividing the total power in Eq. (10.4) by the duration T_0 , one gets the average power intensity λ_0 :

$$\lambda_0 = \frac{1}{T_0} \int_0^{T_0} [\zeta(t)]^2 dt = \frac{1}{\pi T_0} \int_0^{\omega_N} c_i^2 d\omega = \frac{1}{\pi T_0} \sum_{i=1}^N c_i^2 \Delta\omega_i \quad (10.7)$$

By observing this equation, it is also noticed that the average power intensity λ_0 is equal to the mean squared motion record (σ_ζ^2).

Numerically, time history $\zeta(t)$ contains no energy at frequencies between adjacent sample frequencies ω_i . If the time duration T_0 is doubled, $\Delta\omega$ is reduced by half, but λ_0 remains constant.

The power spectral density $S(\omega)$ is therefore defined such that the following equation can be fulfilled:

$$\lambda_0 = \int_0^{\omega_N} S(\omega) d\omega \quad (10.8)$$

It is obvious that:

$$S(\omega_i) = \frac{1}{\pi T_0} c_i^2 \quad (10.9)$$

The expression above also shows the relationship between the power spectral density $S(\omega)$ and the Fourier amplitude c_i .

The benefits of using power spectral density lie in the fact that it can characterize many different motion records and identify their similarities, and can be used for further computation to obtain the responses. This is especially the case for characterizing stationary Gaussian-type motions. For example, for sea wave elevation or wind velocity, even though a one-to-one wave elevation or wind velocity does not generally exist, all records that result in identical spectral density do have the same statistical properties, i.e., the details of records that vary greatly may have identical spectral density.

The calculation of power spectrum can be used to estimate the statistical properties of many records, such as wave elevations, wind velocities, ground surface roughness, seismic ground motions, and these can then be further used to compute stochastic responses using random vibration techniques. It also has the merit of executing the computation much faster than the fast Fourier transformation (FFT), because the computation is performed in place without allocating memory to accommodate complex results. However, since phase information is lost and cannot be reconstructed from the power spectrum's output sequence, power spectrum cannot be utilized if phase information is desired.

When using the power spectrum, various terminologies that are slightly different from each other exist in different fields or different purposes of applications. For example, the ordinate of the wave spectral density can be based on an amplitude spectrum $((\frac{\zeta}{2})^2)$, an amplitude half-spectrum $((\frac{\zeta}{2})^2/2)$, a height spectrum (ζ^2) , or a height double spectrum $(2\zeta^2)$, etc. [532]. The abscissa can be chosen as angular frequency, cyclic frequency, or period.

Figure 10.7 shows an example of the power spectrum density of strong ground motions (Fig. 10.2) recorded at Imperial Valley.

In some applications, the power spectral density $S(\omega)$ is normalized by its area (λ_0), which gives:

$$S_\zeta(\omega) = \frac{1}{\lambda_0} S(\omega) \quad (10.10)$$

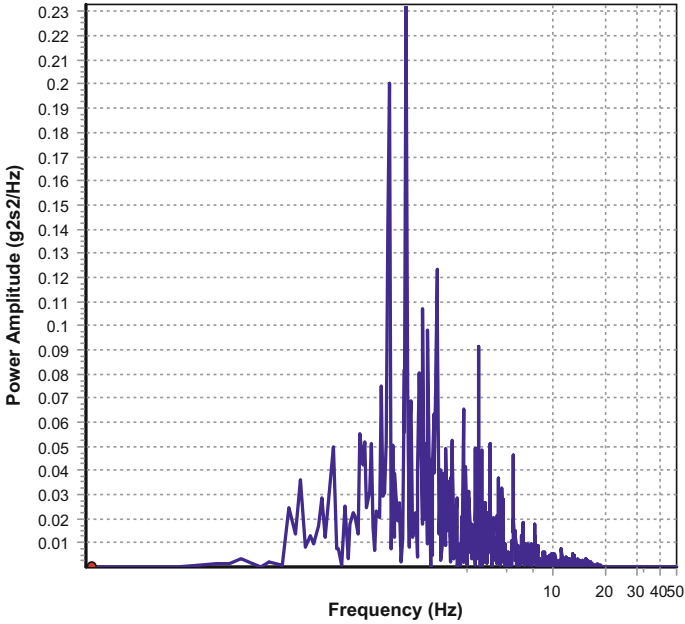
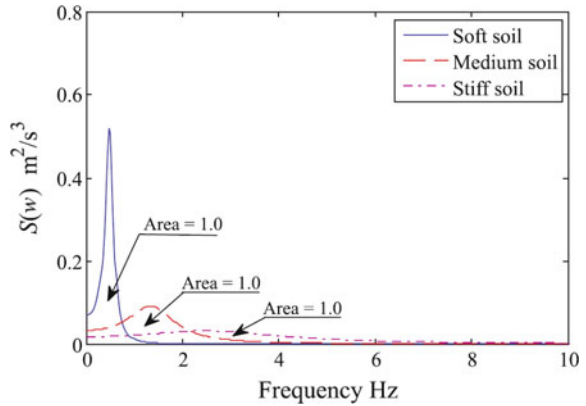


Fig. 10.7 Power of the strong ground motion (Fig. 10.2) recorded at Imperial Valley; g represents the acceleration of earth’s gravity

Fig. 10.8 The Kanai–Tajimi power spectral density functions for different types of soil (ξ_g is assumed to be 0.2 for soft soil, 0.4 for medium soil, and 0.6 for stiff soil) [537]



Readers should bear in mind that only processes with finite variance can be represented by spectra. Fortunately, even if theoretically the variance of a process can be infinite, almost every process considered in engineering has a finite variance.

Although using the Fourier transformation is the most common way of generating a power spectrum, other techniques such as the maximum entropy method [533] can also be employed.

10.3.2 Power Spectrum of Seismic Ground Motions

Even though many excitations are nearly periodical and stationary, such as wave and wind loadings on structures and ships' propeller excitation forces, [553] earthquakes' ground motions are neither periodical (e.g., strong ground motions have not repeated themselves during any earthquake event), nor stationary, i.e., the intensity builds up to a maximum value in the early part of the motions, then remains constant for a period of time, and finally decreases near the end of the motions [1].

However, as a modification of the traditional power spectrum density function, Kanai [534] and Tajimi [535] presented that, for both engineering and research purposes, one may still assume that strong ground accelerations are a stationary stochastic process by passing a white noise process through a filter, i.e., the actual excitations are regarded as a function of output from a series of filters (usually a linear second-order system) subjected to white noise input S_0 . In terms of acceleration amplitude, the Kanai–Tajimi model can be expressed as:

$$S_g(\omega) = \frac{\omega_g^4 + 4\xi_g^2\omega_g^2\omega^2}{\left(\omega_g^2 - \omega^2\right)^2 + 4\xi_g^2\omega_g^2\omega^2} S_0 \quad (10.11)$$

where ω_g and ξ_g are characteristic ground frequency and damping ratio, respectively, they are filter parameters representing the natural frequency and damping of the soil layer, respectively; S_0 is a scaling factor to define the white noise intensity level depicting earthquake amplitude; the power spectral density is often filtered twice in order to remove the singularities at $\omega = 0$, i.e., the nonzero power spectrum density occurs for zero frequency.

The spectral density has its maximum value when $\omega = \omega_g$. By a proper selection of ω_g and ξ_g , the equation above can be used to represent different spectral density shapes. Kanai [534] and Tajimi [535] reported that ξ_g varies from 0.2 (relatively narrow-banded) for soft soil to 0.6 (relatively wide-banded) for hard rock sites. While many researchers and engineers tend to use $\xi_g = 0.6$, from a geotechnical engineering point of view, it is reasonable to assume that the power spectra of the horizontal ground motions have a similar shape, while the vertical motion component is more wide-banded. Based on this assumption, Kubo and Penzien [536] simulated the 1971 San Fernando earthquake ($M_w = 6.5$) with $\xi_g = 0.2$ and $\xi_g = 0.3$ for two horizontal ground motion components and $\xi_g = 0.6$ for the vertical component. Figure 10.8 illustrates the Kanai–Tajimi power spectral density

functions for soft, medium, and stiff soil conditions. It is obvious that the spectrum under soft soil conditions is more narrow-banded than that of the stiff soil conditions. Therefore, resonance of structures is more likely to occur under soft soil conditions than under stiff.

Compared to the selection of ζ_g , the determination of ω_g is more important. This is because even if the wideband power spectral density tends to over-estimate the contribution from high frequencies, this normally does not result in a significant change of ground motions. However, the ω_g determines the dominant frequency of ground motion input. When the dominant frequency is close to the natural frequency of a structure subjected to ground motions, resonance of structural responses would occur. A typical value of $\omega_g = 5\pi$ can be assigned for rock sites.

A few previously adopted values of ζ_g and ω_g are listed as follows [538]: for EI Centro 1940 N–S component, $\omega_g = 12$ and $\zeta_g = 0.6$; for Kobe 1995 N–S component, $\omega_g = 12$ and $\zeta_g = 0.3$; for Uemachi, the simulated ground motion using the fault-rupture model gives $\omega_g = 3$ and $\zeta_g = 0.3$. Those selections of values are widely used in the research of tuned mass dampers [539, 540].

Clough and Penzien [541] modified the Kanai–Tajimi model by introducing a second filter to ensure a finite power for the ground displacement:

$$S_g(\omega) = \left[\frac{\omega_g^4 + 4\zeta_g^2\omega_g^2\omega^2}{(\omega_g^2 - \omega^2)^2 + 4\zeta_g^2\omega_g^2\omega^2} \right] \left[\frac{\omega^2}{(\omega_f^2 - \omega^2)^2 + 4\zeta_f^2\omega_f^2\omega^2} \right] S_0 \quad (10.12)$$

where ω_f and ζ_f are the parameters of a second filter, for medium stiffness soil, $\omega_g = 10.0$ rad/s, $\zeta_g = 0.4$, $\omega_f = 1.0$ rad/s, and $\zeta_f = 0.6$ [542].

In order to represent the non-stationary characteristics of ground motions, based on the power spectra, the time series of ground motion can be generated first, and then further modified by a shape function $\delta(t)$ varying with time to reflect the non-stationary characteristics of ground motions (Sect. 3.3).

It should be noted that models expressed with the power spectral density presented above can only provide the excitation information phenomenally. They give no information on how spectra amplitudes are scaled with earthquake source and distance (attenuation effects). This drawback may be eliminated by calibrating the model to the measured ground motions or target response spectra. In cases when no such data is available, an alternative is to fit them into physical power spectra density models based on seismological description of source and wave propagation [543]. Interested readers may read Hanks and McGuire [544], Boore [545], and Herman [546].

Before leaving this section, readers need to make a clear distinction between the power spectrum and response spectrum (Sect. 10.4) in earthquake engineering applications. Even if both of them are expressed in terms of frequency and indicate the amplification of seismic response varying with frequency, the former is of a stochastic nature while the latter is based on a calculation of maximum responses

under ground motion history, i.e., the response spectrum is essentially of a deterministic type.

10.4 Response Spectrum

10.4.1 Background

Since earthquake ground motion is by nature of short duration, non-stationary, transient and non-periodic, and is also broad-banded in frequency content, it can never reach steady-state vibrations. This means that even if the structure has a zero damping, the motion amplitude is limited to a finite value. Therefore, the stochastic-based root of mean square response utilized by the power spectrum method is in many cases not appropriate to represent the earthquake ground motions, and a deterministic time history analysis is therefore desired to estimate the response. However, a dynamic time history analysis is computationally demanding. Moreover, to reach a design in a conservative manner, often only the maximum amplitude of the response time history is needed for carrying out the seismic analysis, which needs a special consideration when combining each individual component of the response.

To solve the dilemma above, a response spectrum [547, 548], originally calculated from accelerograms [549, 550], is now widely used to represent the earthquake loading for seismic analysis. A typical response spectrum is defined as a plot of maximum responses in terms of displacement, velocity, or acceleration of an ensemble of linear, single-degree-of-freedom oscillators having various natural periods, but the same value of internal damping ratio (typically 5%) to a specified input time history of seismic motions, as is illustrated in Fig. 10.9.

The elastic response spectrum method for calculating seismic response was first proposed in the 1940s [548], and it provides a convenient means for representing the elastic behavior of simple structures, as will be discussed in Sect. 10.4.2.

However, it was followed by a reorganization of the fact that the forces predicted by such spectra far exceed normal design requirements [551] if rare and significant seismic loading associated with a high return period (Sect. 11.1.3) is applied. Because structures having much less strength than prescribed by the elastic spectral values were observed to have performed well in rather severe earthquakes, it became apparent that the elastic response spectrum is not a direct and realistic measure of behaviors of many structures during significant earthquake events, and even moderate earthquakes may be expected to produce inelastic deformations in typical building structures. Therefore, response spectrum was later extended to evaluate the inelastic forces and deformation [552], leading to a ductility-modified spectrum, as will be discussed in Sect. 10.4.3.

Before going into technical details on response spectrum, it should be emphasized that the response analysis using seismic response spectrum only calculates the

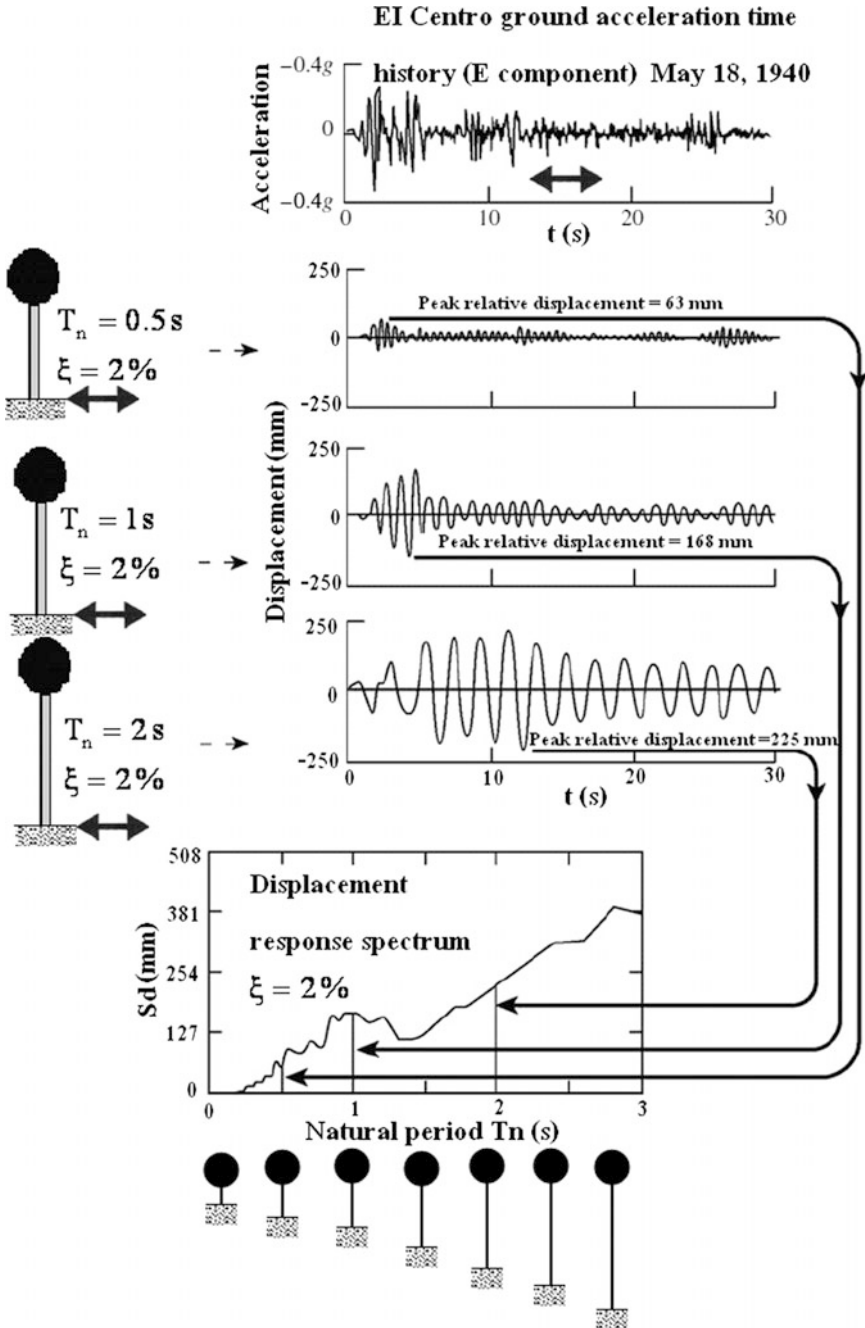


Fig. 10.9 Schematic illustration of construction of ground motion response spectrum ($S_d - T_n$) for EI Centro earthquake ($M_w = 6.9$) [600]

maximum responses (typically measured by displacement) and member forces in each vibration mode of structures without sign and phase information. However, in reality, the members will not necessarily be designed for this maximum peak value. Therefore, the response spectrum analysis may lead to an over-conservative design.

10.4.2 Elastic Response and Design Spectrum

10.4.2.1 Elastic Response Spectrum

In practice, a single-degree-of-freedom (SDOF) system with a constant damping ratio of a few percent, representing target structures, is subjected to a prescribed ground excitation time history as shown in Fig. 10.9. As the ground motion typically excites a large number of vibration modes of the structures, by varying the natural period of the SDOF in a range of engineering interest for the structure's eigenperiod (e.g., 0.02–10 s), and using numerical time integration methods such as Newmark's method [123], the maximum calculated relative displacement magnitude of the SDOF at each natural period is then plotted on a response spectrum graph. This spectrum is often referred to as the deformation/displacement response spectrum. Figure 10.9 illustrates a schematic flowchart for constructing a ground motion displacement response spectrum S_d varied with natural period T_n , which can be expressed as:

$$S_d = \max(u(t|T_n)) \quad (10.13)$$

From the equation above, it is obvious that the most important task to establish the displacement response spectrum is to calculate the responses of the SDOF with varied natural periods. To perform this task, let us consider an SDOF system excited by suddenly applied excitations $F(t)$ (shown in Fig. 10.10) that are neither harmonic nor periodical. The general form of the governing equation of motions is:

$$m\ddot{x}(t) + c\dot{x}(t) + kx(t) = F(t) \quad (10.14)$$

By dividing the equation above by m and rearranging it, one obtains:

Fig. 10.10 An SDOF spring-mass-damper system under an external force $F(t)$

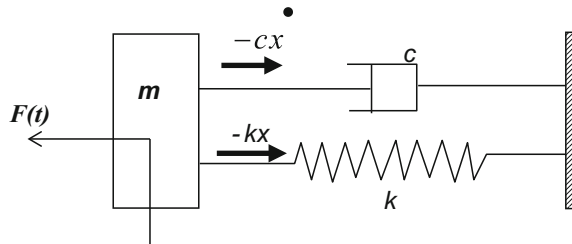
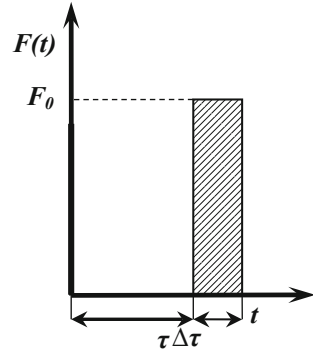


Fig. 10.11 Impulsive force excitations



$$x(\ddot{t}) + 2\zeta\omega_n x(\dot{t}) + \omega_n^2 x(t) = \frac{1}{m} F(t) \tag{10.15}$$

where ω_n and ζ are the natural angular frequency and ratio of critical damping for the system, respectively.

For developing a formula for evaluating response to a general dynamic loading, the unit impulse response procedure [123] for approximating the response of a structure to arbitrary excitations may be used as the basis. We then consider a system subjected to a force with a short duration as shown in Fig. 10.11. For a general closed-form solution of the equation above, the convolution integral method can be used to obtain the responses. This method is derived using the equilibrium of momentum:

$$\int_{t_1}^{t_2} F(t)dt = m [x(\dot{t}_2) - x(\dot{t}_1)] \tag{10.16}$$

The time integral of force is designated by the symbol $\hat{\hat{F}}$:

$$\hat{\hat{F}} = \int_{\tau}^{\tau + \Delta\tau} F_0 dt \tag{10.17}$$

We hereby define an impulsive force with the amplitude of $\hat{\hat{F}} / \Delta\tau$ and the time duration of $\Delta\tau$. When $\hat{\hat{F}}$ is equal to unity, the force in the limiting case $\Delta\tau \rightarrow 0$ is called the unit impulse or Dirac delta function ($\delta(t - \tau)$), which has the following properties:

$$\int_0^{+\infty} \delta(t - \tau) d\tau = 1 \quad (10.18)$$

$$\delta(t - \tau) = 0 \quad \text{for } t \neq \tau \quad (10.19)$$

Therefore, the impulsive force applied at time τ is:

$$F(t) = F_0 \delta(t - \tau) \quad (10.20)$$

The responses to a unit impulse applied at $t = 0$ with initial conditions equal to zero are called impulsive responses and are denoted by $h(t)$. For any time later than τ , the impulsive responses $h(t - \tau)$ can be obtained by shifting $h(t)$ to the right along the scale by $t = \tau$.

Thereafter, at $t = 0$, a radical change in the system motions takes place when the short duration and high amplitude forces excite an initial motion of the system, followed by free vibrations. For a unit impulse at $t = 0$, i.e., $F_0 = 1$, the velocity and displacement of the mass immediately after the initial impulse at $t = 0^+$ are therefore:

$$\dot{h}(0^+) = \frac{1}{m} \quad (10.21)$$

$$h(0^+) = 0 \quad (10.22)$$

The velocity and displacement due to an applied step force $F(0)$ are:

$$\dot{x}(0^+) = \frac{1}{m} \quad (10.23)$$

$$x(0^+) = 0 \quad (10.24)$$

By realizing the initial condition $h(0) = 0$, one can derive the impulse of the undamped system:

$$h(t) = \begin{cases} \frac{1}{m\omega_n} \sin(\omega_n t) & \text{for } t > 0 \\ 0 & \text{for } t < 0 \end{cases} \quad (10.25)$$

or:

$$x(t) = \begin{cases} \frac{F_0}{m\omega_n} \sin(\omega_n t) = \frac{F_0}{k} [1 - \cos(\omega_n t)] & \text{for } t > 0 \\ 0 & \text{for } t < 0 \end{cases} \quad (10.26)$$

From the equation above, it is noticed that the maximum displacement of the system due to the step excitations is twice the quasi-static displacement ($\frac{F_0}{k}$).

The responses of the damped system are:

$$h(t) = \begin{cases} \frac{1}{m\omega_d} e^{-\zeta\omega_n t} \sin(\omega_d t) & \text{for } t > 0 \\ 0 & \text{for } t < 0 \end{cases} \quad (10.27)$$

or

$$x(t) = \begin{cases} \frac{F_0}{m\omega_d} e^{-\zeta\omega_n t} \sin(\omega_d t) & \text{for } t > 0 \\ 0 & \text{for } t < 0 \end{cases} \quad (10.28)$$

Note that the entire excitation history may be considered to consist of a succession of short impulses. The derivation above can then be extended to calculate the responses under arbitrary excitation histories as shown in Fig. 10.12. The excitations $F(t)$ can be regarded as a series of impulses with different amplitudes. We here examine one impulse starting at time τ . Again, in the limiting case $\Delta\tau \rightarrow 0$, its contribution to the total responses at time t is:

$$\Delta x(t, \tau) = F(\tau)\Delta\tau h(t - \tau) \quad (10.29)$$

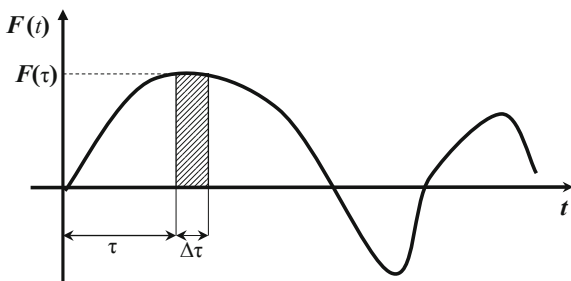
For a linear system, the principle of superposition is applicable. Therefore, the response at time t is the sum of responses due to a sequence of individual impulses; this is known as convolution integral:

$$x(t) = \int_0^t F(\tau)h(t - \tau)d\tau \quad (10.30)$$

or

$$x(t) = \sum F(\tau)h(t - \tau)\Delta\tau \quad (10.31)$$

Fig. 10.12 Arbitrary force histories applied on a system



$h(t - \tau)$ is obtained from Eq. (10.27) by replacing t by $t - \tau$. Therefore, the damped responses in Eq. (10.27) can be rewritten as:

$$\begin{aligned} x(t) &= \frac{1}{m\omega_d} \int_0^t F(\tau) e^{-\zeta\omega_n(t-\tau)} \sin[\omega_d(t-\tau)] d\tau \\ &= \frac{1}{\omega_n \sqrt{1-\zeta^2}} \int_0^t a(\tau) e^{-\zeta\omega_n(t-\tau)} \sin\left[\omega_n \sqrt{1-\zeta^2}(t-\tau)\right] d\tau \end{aligned} \quad (10.32)$$

The equation above is referred to as Duhamel's integral, which is often adopted to calculate the responses of SDOF with varied natural periods in order to calculate the spectral displacement responses.

The earthquake displacement response in terms of velocity response function $V(t)$ can be expressed as:

$$x(t) = \frac{V(t)}{\omega} \quad (10.33)$$

The effective earthquake force, or base shear, applied on a target structure can then be approximated as:

$$Q(t) = m\omega V(t) \quad (10.34)$$

The two equations above actually describe the earthquake response at any time t for an SDOF structure, with solutions depending upon how Eq. (10.27) is evaluated.

As mentioned before, for design purposes, it is usually sufficient to evaluate only the maximum responses, instead of the entire history of forces and displacements. For each SDOF system with a designated natural period $T_n (=2\pi/\omega_n)$, the maximum value of response velocity function $V(t)$ is called the spectral velocity:

$$S_V = \{V(t)\}_{\max} \quad (10.35)$$

It is noted that the three equations above are based on the assumption that the displacement vibrations are harmonic (in reality the seismic ground motion displacement cannot be harmonic) at each undamped natural period T_n , and the corresponding maximum velocity response is also called pseudo-velocity values since it is not exactly the maximum velocity of a damped system. By following this assumption, the pseudo-relative-velocity spectrum (or pseudo-velocity spectrum), denoted as PSV, and the pseudo-acceleration spectrum, denoted as PSA, can be defined by the two equations below:

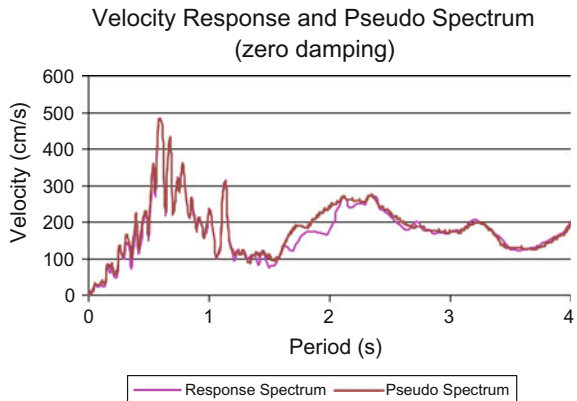
$$PSV = \omega S_d = \left(\frac{2\pi}{T_n}\right) S_d \tag{10.36}$$

$$PSA = \omega^2 S_d = \left(\frac{2\pi}{T_n}\right)^2 S_d = \omega \cdot PSV \tag{10.37}$$

From the three equations above, it is obvious that, if the relative spectral displacement is known, the pseudo-velocity and the pseudo-acceleration can be calculated. In addition, readers may bear in mind that spectrum measured by acceleration intensifies high-frequency (higher than the natural frequency of the SDOF system) components, and the spectrum measured by velocity intensifies vibration components around the natural frequency of the SDOF system, while low-frequency components are more clearly identified by a response spectrum measured with displacement.

Special attention should be paid to the construction of the velocity and acceleration spectrum: As discussed above, they are derived from the “true” displacement response spectrum instead of the maximum value of velocity and acceleration time-history directly calculated from a dynamic analysis of an SDOF system. In general, the maximum value of velocity and acceleration time-history at each natural period T_n are not equal to the value of velocity and acceleration spectrum derived from the displacement response spectrum. This is illustrated in Fig. 10.13 with a comparison between the “true” response spectrum and pseudo-spectrum under the same ground motions. Generally, for a short period system, the pseudo-velocity is higher than the “true” velocity response. This trend is more significant when the natural period of the system becomes shorter. On the other hand, for a long-period system, the pseudo-velocity is less than the “true” velocity response. The differences between the two types of velocity spectra are smallest for undamped systems and increase with an increase in damping. Similarly, the pseudo-acceleration spectra and “true” response spectra are identical when the damping of the system is zero. Even with damping, the difference between the two

Fig. 10.13 Velocity response and pseudo-velocity spectrum subject to the ground motion documented from Chi-chi earthquake, September 21, 1999



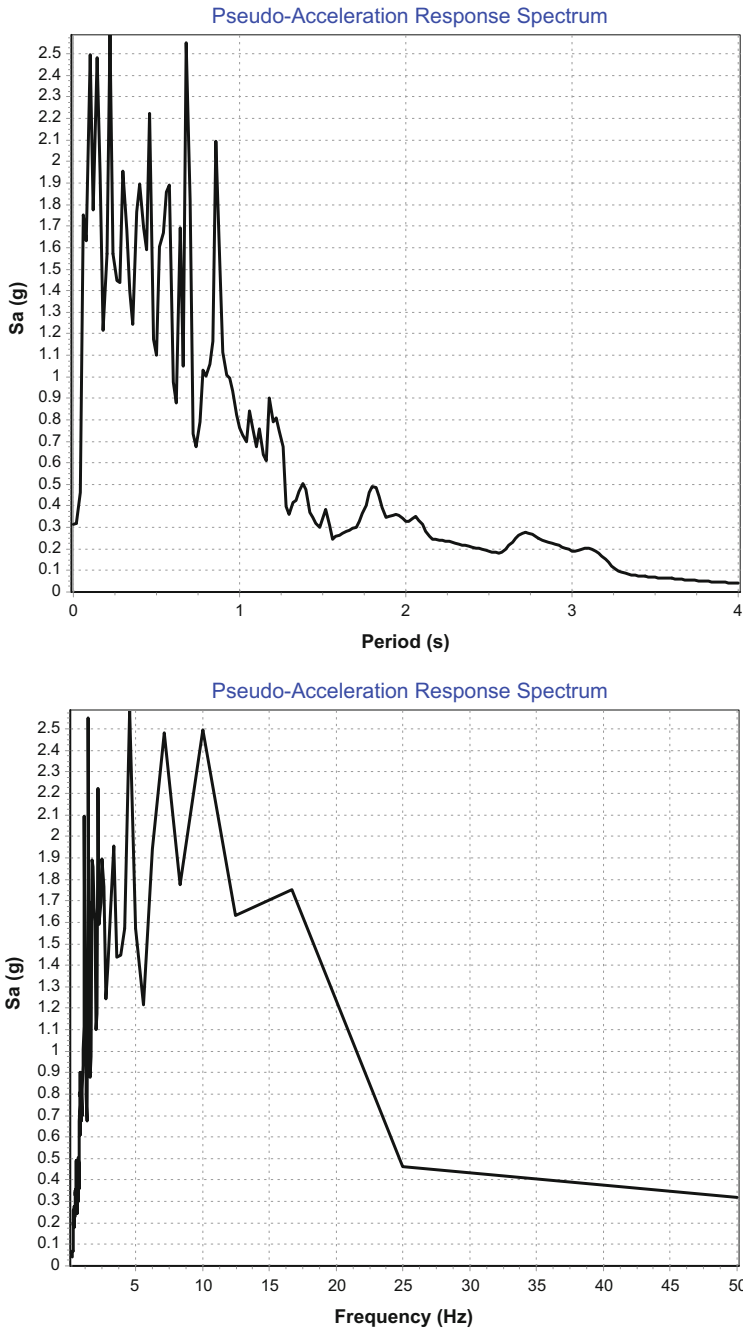


Fig. 10.14 Pseudo-acceleration response spectrum (zero damping) with either a period or frequency horizontal axis. The ground motion was documented from the Imperial Valley earthquake

acceleration spectra is rather small for short period systems and is of some significance only for long-period systems with large values of damping [553]. Therefore, under earthquake excitations, within the frequency and damping ranges that are of engineering interest, the maximum value of velocity and accelerations can be assumed to be equal to their pseudo-counterparts, with the acceleration equivalence being closer to the “true” one than the velocity equivalence. Moreover, since only the displacement response is needed to calculate exact values of seismic forces applied on a structure, displacement spectra (the basis for deriving the pseudo-velocity and pseudo-acceleration spectra) provide sufficient information, and there is therefore little motivation to study the “true” response spectra because they are not required to determine the peak deformations and forces in a system. For a clear mathematical explanation of this difference, source [553] is recommended.

It should also be noted that the acceleration spectrum indicates accelerations due to ground motions, without accounting for a constant acceleration of gravity g . Moreover, by reviewing the concept of acceleration, velocity, and displacement, it should be further emphasized that the spectral acceleration is an absolute acceleration of a structure in space, since the force causing the acceleration itself is determined by the relative compression/extension of the spring with respect to the ground motion, while the spectral velocity and spectral displacement are relative values with respect to the moving ground.

As mentioned above, different from the power spectrum or Fourier spectrum (Sect. 10.3), which are stochastic representations of motions in frequency domain, the response spectrum is a deterministic method in frequency domain, i.e., a time-domain quantity. This is because, for each frequency, it represents the response of a structure from the passing of an entire seismic excitation time history. The unit of the ordinate for response spectrum should therefore possess the same unit as that which the spectrum stands for, i.e., the same unit of acceleration for acceleration spectrum, velocity for velocity spectrum. The horizontal axis may be expressed either in period or frequency (Fig. 10.14). In the pseudo-acceleration response spectrum measured with frequency shown in Fig. 10.14, it is noticed that the curve covers a large range of frequency, but the frequency content below 5 Hz has many ups and downs. In order to reduce a wide range to a more manageable size, one can use a logarithmic scale plot as shown in Fig. 10.15.

Not only the value of the spectrum but also the spectral shape strongly influences the structural responses. If scaled ground motions have the same or very similar spectral shapes as the target ground motions, the resulting structural responses from scaled ground motions are statistically similar to responses from unscaled ground motions. Earthquake magnitude, source-to-site distance, and local site condition can affect the spectral shape of records. The normalized residual ε (a constant number of standard deviations ($\sigma_{\ln Y}$) measured as the difference relative to the mean predicted ground motion $f(M, R, \theta)$ and representing the observed variability in $\ln Y$, where Y is the ground motion intensity) is also an important parameter to influence the spectral shape [554, 667]. Large positive ε values at a given period are typically associated with a peak in the response spectrum at that period, because the ε value

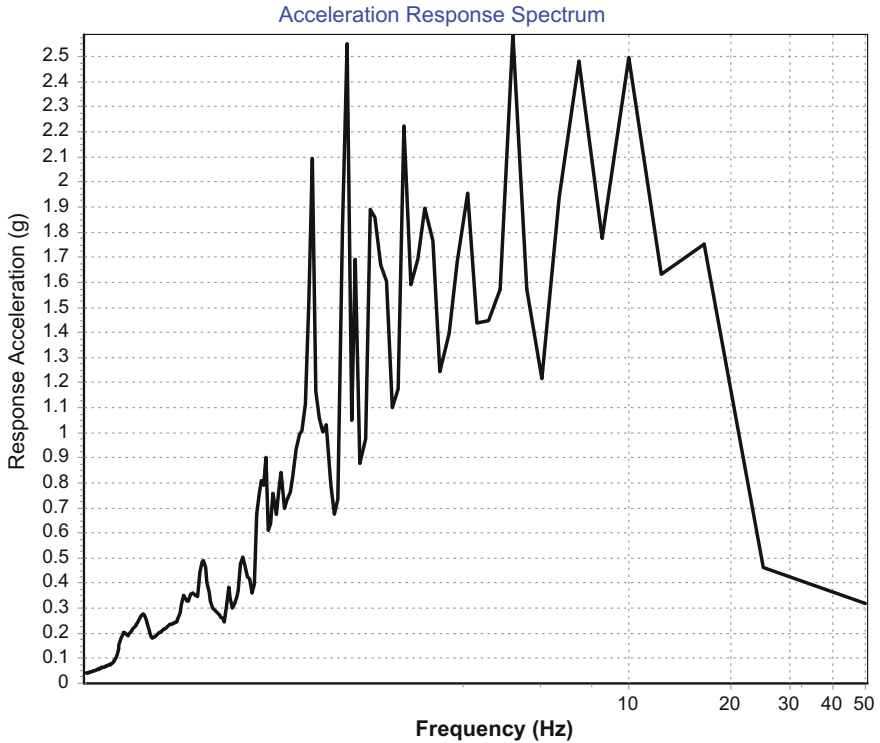
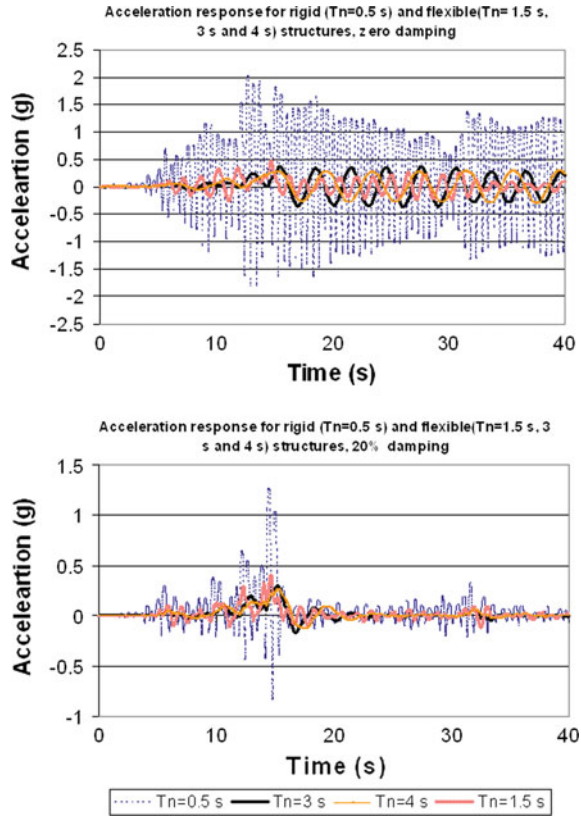


Fig. 10.15 Response spectrum (zero damping) of ground motion at Imperial Valley measured with logarithmic scale

indicates an extreme/rare spectral value at that period while other spectral values at other periods are not necessarily so extreme.

Because all structures have some degrees of damping, the peaks in the response spectra are of limited significance and are therefore smoothed out by introducing damping for structures (in the current example shown in Fig. 10.9, the damping ratio is 2%). This also indicates that the damping is already included and is assumed in a design response spectrum. It is therefore important not to remodel this damping in a structural modeling when performing the seismic response spectrum analysis. Moreover, since the design response spectrum is usually generated based on a constant damping ratio of 5%, for many structures, a transformation between a spectrum with the target damping level and the one with 5% damping is needed. This is usually performed by applying a damping correction factor relative to a reference value of 1.0 (for 5% damping ratio), such as the one presented in ISO 19901-2 [289] and Eurocode 8 [198], as will be presented in Sect. 10.4.2.3. Moreover, the generation of a response spectrum with zero damping is not only physically unrealistic, but also numerically problematic because a significant amplification of response will appear when no damping is presented.

Fig. 10.16 Acceleration response time history with a variation in undamped structural natural periods ($T_n = 0.5$ s and $T_n = 3.0$ s) and damping (zero damping and 20% of critical damping), subject to the ground motion documented from Chi-chi earthquake on September 21, 1999



For stiff structures, PGA is preferably used since the acceleration has a large portion of frequency content in high-frequency range. For less stiff structures, PGV, which cherishes a significant portion of frequency content in the intermediate frequency range, is preferred for calculating structural response. It is not usual to use PGD for seismic design.

Readers also need to bear in mind that, in a probabilistic seismic hazard analysis as will be presented in Sect. 11.1.3, the spectra acceleration at different periods is associated with different earthquake events. At the longer period, it normally represents the peak response accelerations of high magnitude of earthquake(s), whereas the spectral accelerations at lower period range typically correspond to peak response accelerations of relatively small magnitude earthquakes.

Figure 10.16 shows the ground acceleration time-history for both rigid and flexible structures with zero and 20% critical damping values. It shows that flexible structures can work as a filter to dramatically reduce the acceleration and therefore forces. With zero damping, the rigid structure follows the acceleration of the ground motion. However, the flexible structure shows a sort of harmonic vibration without

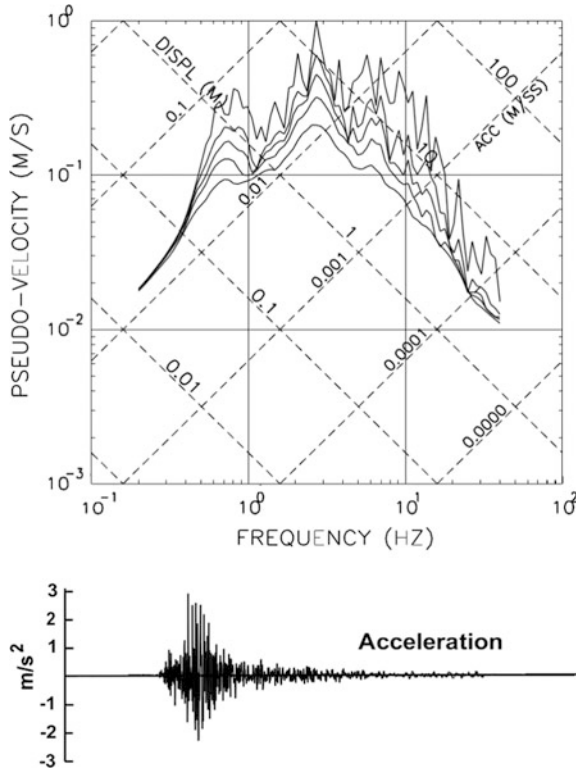


Fig. 10.17 Single-degree-of-freedom response spectra (upper figure) plotted in a “tripartite” fashion for levels of damping 0, 2, 5, 10, 20% of critical (top to bottom) subject to the seismic acceleration recordings of the surface wave magnitude 6.0 Whittier Narrows Dam earthquake in Los Angeles, October 1, 1987 [629]

significant influences from the ground motions. The more flexible a structure is, the closer the structure’s response is to the harmonic vibrations.

The unique relationships among the spectral displacement, pseudo-velocity, and pseudo-acceleration make it possible to present response spectral values in a tripartite plot as shown in Fig. 10.17, where displacement, velocity, and acceleration can be read on separate axes from the same curve.

Attention should also be paid to the response spectrum recorded on soft soil. As response spectra of motions recorded on soft soil attain their maxima at different, well-separated periods, averaging them can eliminate their peaks, resulting in a flat shape of spectrum (analogous to that used in current seismic design codes) as shown in Fig. 10.18. It is therefore more rational to use response spectra plotted against the normalized periods, T/T_g (T_g is the period of spectral velocity) [631]:

$$S_a = S_a(T/T_g) \tag{10.38}$$

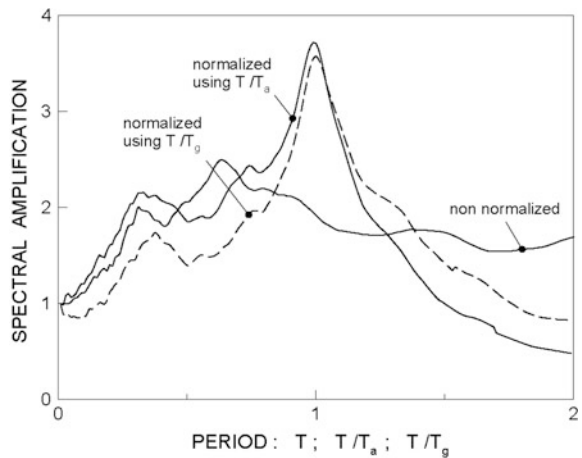
10.4.2.2 Elastic Design Spectrum

The actual response spectrum curve shown in Fig. 10.9 only represents one single excitation and exhibits many fluctuations with peaks and valleys. For the design and safety assessment of infrastructures, the spectrum needs to account for every possible future earthquake likely to occur in a given zone (with a certain probability of occurrence, as will be discussed in Sect. 11.1.3). This can be fulfilled by including information to represent ground motion characteristics of various past earthquakes at the same site, or if this is not possible, from other sites under similar conditions. Here, similar conditions mean similar magnitude of the earthquake, local soil conditions, distance of site from the causative fault, fault mechanism, and geology of the travel path of seismic waves from the source to the sites [553]. However, Iervolino and Cornell [633] argue that magnitude and fault are not important criteria in the selection of seismic motions.

Even though the jaggedness (peaks and valleys) indicates the sensitivity of the response of structures to a slight variation of structures’ natural period, in engineering practice, design specification should not be too sensitive to a slight variation of structures’ natural period. Therefore, the fluctuations in the actual response spectrum must be smoothed using curve fitting techniques to reach a design spectrum with an idealized spectrum shape, which is called design response spectrum or design spectrum.

Based on the calculation of response spectrum for each individual ground motion, statistical analysis shall be carried out to obtain the mean standard deviation of the ordinate at each period of the response spectrum. By averaging several spectra from past earthquakes, the mean or median response spectrum can be

Fig. 10.18 Average acceleration spectra based on 24 actual motions recorded on soft soil; the periods are normalized before averaging with: **a** period of peak spectral acceleration (T_a); **b** period of peak spectral velocity (T_g); the assumed damping is 5% [632]



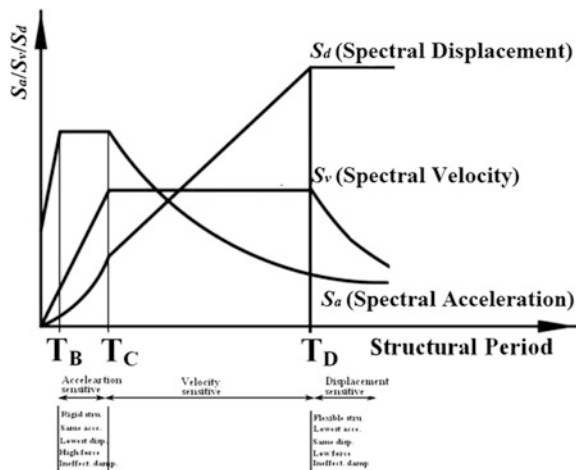
obtained. In addition, the mean (or median) plus one or two standard deviations (sigma) is also of interest for engineering applications with a reliability-based design. Both spectra are much smoother than the response spectrum of an individual ground motion. Below, the general method to obtain design spectrum for practical seismic design will be presented. For a more detailed presentation of background knowledge and procedure to obtain seismic design spectrum by seismic hazard analysis, see Chap. 11.

A design acceleration response spectrum generally has a trapezoidal shape as shown in Fig. 10.19. Even though the idealized trapezoidal shape spectrum is not a close approximation to the actual spectrum, it is helpful in constructing a design spectrum representing many ground motions [553].

As an example, we hereby characterize the design spectrum by defining three regions with the assumed boundary periods of $T_A = 0.03$ s, $T_B = 0.125$ s, $T_C \approx 0.5$ s, and $T_D \approx 3.0$ s as shown in Fig. 10.19. Note that for a specific ground motion, the control periods for constructing the design spectrum, i.e., T_B , T_C , and T_D , vary with damping. Their values depend on the soil type and earthquake magnitude. Various design codes such as Eurocode 8 [198] specify the values for these periods.

1. At short period range between T_B and T_C as shown in Fig. 10.19, the spectrum generally has a constant acceleration. Stiff structures' natural periods may be within this region. Their responses are governed by the ground acceleration motions, and the structure moves like a rigid body with significant inertia forces due to the large acceleration. Even though the structural accelerations are rather close to the ground accelerations, the displacements are relatively small. In addition, the viscous damping has little effect on the response behavior of a stiff/rigid structure. Actually, in the right portion of this period range toward T_C , the structures' accelerations are larger than ground accelerations, with the amplification depending on the structures' natural periods and viscous damping values.

Fig. 10.19 Earthquake design spectrum measured by acceleration, velocity, and displacement



For simplicity, the structures' accelerations can still be assumed to be constant with amplification depending on damping value.

2. At rather higher periods than T_D , the spectrum has a constant displacement. In a sense its maximum deformation is controlled by the characteristics of ground motion displacement and is insensitive to the characteristics of associated ground velocity and acceleration. Soft structures' natural periods are likely to be in this regime. Their responses are governed by the ground displacement motions, and the structure moves like a flexible body with rather small inertia forces due to small or zero acceleration. The structural displacement rather than acceleration is close to the ground motions, i.e., the absolute displacement is close to zero. In addition, viscous damping has little influence on the response behavior of a flexible structure. This phenomenon is actually the basis for the utilization of base isolated structures [188]. Actually, in the left portion of this period range toward T_D , the structures' displacements are larger than ground motions, with the amplification depending on the structures' natural periods and viscous damping values. However, for simplicity, the structures' displacements can still be assumed to be constant, with amplification depending on damping value.
3. In the intermediate period between T_C and T_D , strictly speaking, the structures' velocity should be higher than ground motion velocities, while for simplicity, the spectrum can be idealized as having a constant velocity. The responses of structures with natural periods lying within this period range will be governed by the ground motion velocities. In addition, viscous damping has a strong influence to mitigate dynamic structural responses for structures with natural periods lying within this period range.

The procedure of constructing a design spectrum, based on the amplification of peak ground motions in different period range, can be summarized as follows:

1. Calculate the peak ground acceleration, peak ground velocity, and peak ground displacement. The relationship between these three items can normally be based on a statistical study of previous earthquake ground motion records, such as the one recommended by Newmark et al. [634] as illustrated in Table 10.2. For example, a horizontal peak ground acceleration of 0.4 g in alluvium gives a horizontal peak ground velocity of 0.48 m/s (0.4×1.2 m/s) and gives a horizontal peak ground displacement of 0.364 m (0.4×0.91 m).
2. Define the boundary of each period range of the spectrum; the following values are recommended by Chopra [553]: $T_A = 0.03$ s, $T_B = 0.125$ s, $T_C \approx 0.5$ s, $T_D \approx 3.0$ s, $T_E = 10.0$ s, and $T_F = 33$ s as shown in Figs. 10.20, 10.21, and 10.22. The spectrum can be defined completely by peak ground motions (PGA, PGV but rarely PGA) and the amplification factor at T_A , T_B , T_C , T_D , T_E , and T_F , among which T_A , T_B , T_E , and T_F are fixed values, while T_C and T_D vary with damping. Without further details, they can be determined by the intersection points of the constant acceleration, constant velocity, and constant displacement

Table 10.2 Spectral bounds for alluvium and crystalline rock

	Horizontal ground motion		Vertical ground motion	
	Crystalline rock	Alluvium	Crystalline rock	Alluvium
Peak ground acceleration (g)	1		2/3	
Peak ground velocity (m/s)	0.71	1.2	0.43	0.74
Peak ground displacement (m)	0.3	0.91	0.28	0.84

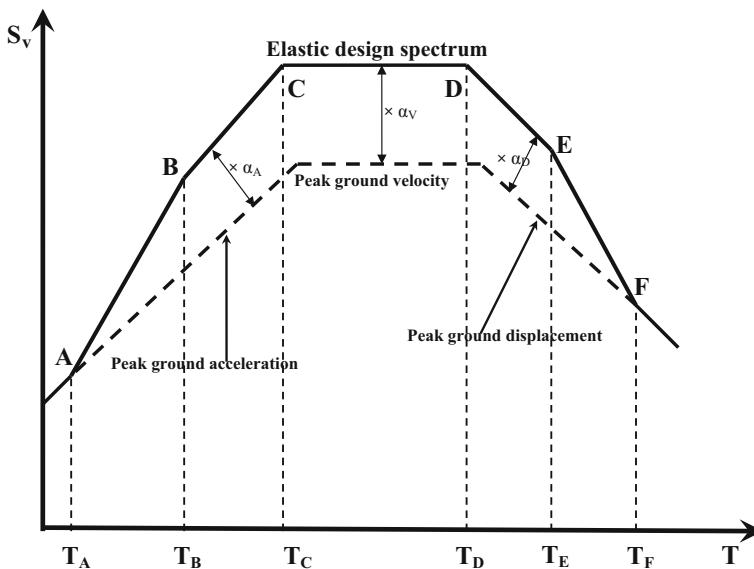


Fig. 10.20 Construction of elastic pseudo-velocity design spectrum

branches of the spectrum. In various design codes, the value of T_B is also specified depending on the soil type and earthquake amplitude.

- Plot three dashed lines corresponding to the peak ground acceleration (between T_B and T_C), peak ground velocity (between T_C and T_D), and peak ground displacement (between T_D and T_E) as shown in Fig. 10.20 (for elastic pseudo-velocity design spectrum), Fig. 10.21 (for elastic pseudo-acceleration design spectrum), and Fig. 10.22 (for elastic displacement design spectrum).
- Estimate the spectral amplification factors for three period regions of the spectrum: α_A for peak/constant acceleration region, α_v for peak/constant velocity region, and α_D for peak/constant displacement region. The amplification factors depend on both the cumulative probability level considered, e.g., mean (50%) or mean plus one sigma (84.1%), and the damping. Table 10.3

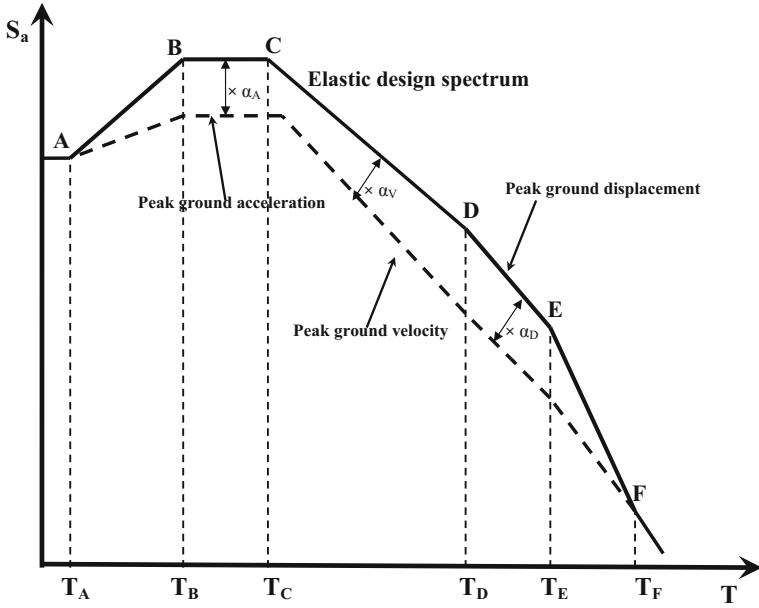


Fig. 10.21 Construction of elastic pseudo-acceleration design spectrum

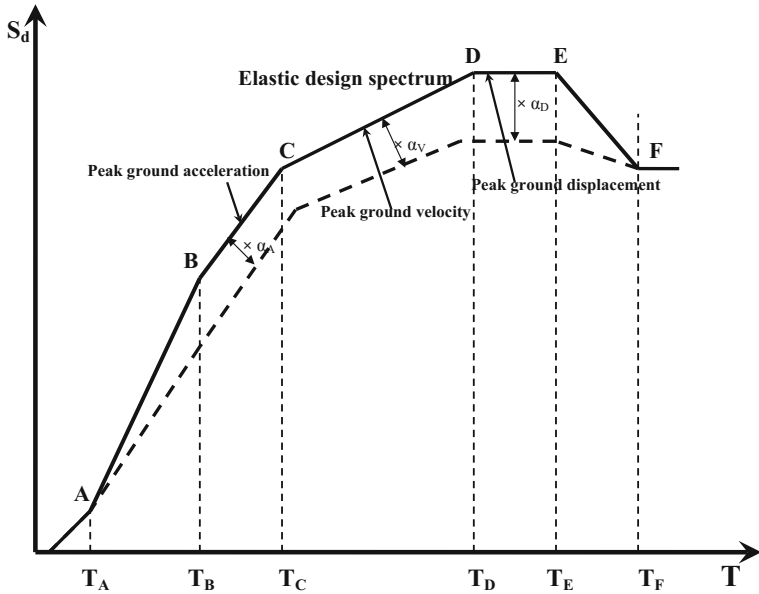


Fig. 10.22 Construction of elastic displacement design spectrum

Table 10.3 Amplification factors for elastic design spectra with different damping ratio and non-exceedance probabilities of 84.1 and 50%, respectively

Damping ζ (%)	Mean plus one sigma (84.1%)			Median (50%)		
	α_A	α_V	α_D	α_A	α_V	α_D
0.5	5.10	3.84	3.04	3.65	2.59	2.01
1	4.38	3.38	2.73	3.21	2.31	1.82
2	3.66	2.92	2.42	2.74	2.03	1.63
3	3.24	2.64	2.24	2.46	1.86	1.52
5	2.71	2.30	2.01	2.12	1.65	1.39
7	2.36	2.08	1.85	1.89	1.51	1.29
10	1.99	1.84	1.69	1.64	1.37	1.20
20	1.26	1.37	1.38	1.17	1.08	1.01

shows an example of recommended amplification factors by Newmark and his co-workers [634] for elastic design spectra. It is based on the statistical studies of a large number of ground motion records on firm ground (rock and competent sediments) with different damping levels from 0.5 to 20%. The damping value is defined as the total structural (system) and soil damping in the form of some percentages of critical damping. It should be noted that the amplification factor listed in Table 10.3 only applies to firm ground. In engineering practice, various types of soil need to be considered. Therefore, most seismic design codes give the soil-type-dependent amplification factor in the form of soil factor together with a correction factor. In addition, various damping values are accounted for in the design codes by a damping correction factor. See Sect. 10.4.2.3 for details.

5. Multiply the ordinate for peak ground acceleration at the BC branch with the factor of α_A . Multiply the ordinate for peak ground velocity at the CD branch with the factor of α_V . Multiply the ordinate for peak displacement at the DE branch with the factor of α_D .
6. Draw a line $S_v = \frac{S_a}{\omega} = \left(\frac{T_d}{2\pi}\right)S_a$ for periods shorter than T_A . Draw a line $S_v = \omega S_d = \left(\frac{2\pi}{T_n}\right)S_d$ at periods longer than T_F .
7. Use a straight line to connect A and B as well as E and F.
8. Based on the elastic pseudo-velocity design spectrum shown in Fig. 10.20, the construction of elastic pseudo-acceleration (Fig. 10.21) and elastic displacement (Fig. 10.22) design spectrum can be performed using the relationships among the pseudo-acceleration, pseudo-velocity, and displacement.

At this stage, readers should have a general picture of how to construct a response and design spectrum and understand the differences between them.

10.4.2.3 Effects of Damping

When a structure is stiff with a low natural period below 0.5 s, it is more sensitive to acceleration than displacement, and the structure tends to move in the same acceleration amplitude as the ground. Viscous damping has little influence on the structural response. When a structure is flexible with a rather high period, the structural masses tend to remain motionless and do not generate any significant loading. The viscous damping also has little influence on the structural responses. However, when a structure is in between the very high and the very low period above, i.e., at velocity sensitive region, the damping has the greatest effects. Furthermore, if a structure's natural period is close to the period of earthquake ground motions, the energy is effectively fed into the structure and the structural responses are amplified, leading to a resonance or a close-to-resonance condition. However, in this condition, the viscous damping in the structure will efficiently absorb the energy from the structural response and dissipate it, thus mitigating the buildup of the resonant responses and reducing the response amplitudes. It is also noted that the damping effects are greater for small than for high damping values, i.e., when the damping ratio is increased from 0 to 5%, the reduction in response is much more significant than that due to a damping increase from 15 to 30%. Because the inherent damping for the majority of structures is low, it can be realized that in order to reduce the dynamic response, one can either increase damping by adding, for example, dampers or increase the structures' natural period by using for example a base isolation system, which is discussed in Jia [188].

Design response spectra in design codes are normally given based on an inherent system damping of 5%. If spectral values for other damping ratios are required, then the spectral accelerations can be adjusted using a scaling factor (correction coefficient). For example, in Norsok [635] and ISO 19901-2 [289], with a damping of $\zeta\%$ ($\zeta\%$ should be between 2 and 10%), η can be calculated as:

$$\eta = -\ln(\zeta/100)/\ln(20) \quad (10.39)$$

NORSAR [629] recommends:

$$\eta = 1.48 - 0.30\ln(\zeta) \quad (10.40)$$

Eurocode 8 [198] recommends:

$$\eta = \sqrt{\frac{10}{5 + \zeta}} \geq 0.55 \quad (10.41)$$

10.4.2.4 Shear Wave Velocity Estimation with Shallow Soil Depth or Soils and Rock Below 30 M

In the classification of soils, the average shear wave velocity ($v_{s,30}$) is determined based on the characteristics of the top 30 m [636] (or 20 m [199]) thickness of soil layers, which is the travel time of seismic shear wave from soil surface to 30 or 20 m depth divided by 30 or 20 m. However, this is based on the assumption that the sites have very deep soil layers, of depth much greater than 30 m thickness, such as the recommendations made by ICC [637] and NEHRP [638], in which regression analyses of recorded seismic ground motions in the USA are available for sites with soil layers extended up to a few hundred meters downward before reaching the bedrock, and the stiffness of the soil layers deeper than 30 m is often well correlated with the wave velocity in the top 30 m.

However, as shallow bedrocks are very common in high-seismicity regions, this classification method is under significant research scrutiny [639–643] and may not be suitable for regions where a soil–bedrock interface is found at even a few meters below the soil surface. Studies [644] of a large number of records at sites with soil layers at depths from a few meters to 180 m in China, Australia, and India have shown that when engineering rock (with shear wave velocities larger than 700 ± 60 m/s) depths are shallow, the site classification approaches adopted in the design codes give a higher shear wave velocity (stiffer soil column) than reality. Site response [641] also indicates that a simplified site amplification analysis by seismic codes may be on the unconservative side.

Therefore, for sites having depths of less than 30 m, a detailed site-specific response analysis is recommended to estimate the shear wave velocity and amplification characteristics.

In case the shear wave velocity or site class for any particular site is not important, statistical data from many earthquake records in various stations can be used to estimate the average shear wave velocity for sites with shallow soil depths. Based on this assumption, Boore [645] and Atkinso and Boore [646] proposed methods for extrapolating the velocities between site depth and 30 m of depth.

As discussed in Sect. 3.2.2, the estimation of site period and shear wave velocity based on the top 30 or 20 meters of soil layers is most appropriate for rather short period content of the bedrock motions. For longer periods, seismic wave lengths are much longer, and the site response is then likely to be affected by soil characteristics at much greater depths. Furthermore, even for deep soil for which the stiffness of the deeper soils is well correlated with the shear wave velocity at the top 30 m, Boore et al. [647] found that the depth over which average shear wave velocity should be averaged is one-quarter of the wave length associated with the period of interest, which can be greater than 30 m. Moreover, significant soil amplifications can be produced due to high impedance contrasts and associated seismic wave reflections at depths much greater than 30 m, which have almost no correlation with the soil properties at the top 30 m. The soil amplification estimation based on the top 30 or 20 m of soil layers may then be on the non-conservative side, especially for long site period soil columns having deep and low damping deposits of soil on

very hard rock [648]. This is suspected to have been the cause of destructive site amplification in the magnitude 6.5 Caracas, Venezuela earthquake of 1967 [649, 650], the Loma Prieta earthquake of 1989 [651], and the Kobe earthquake of 1995 [652].

10.4.3 Ductility-Modified (Inelastic) Design Spectrum Method

10.4.3.1 Ductility for Elastic-Perfect-Plastic Structures

Subject to extremely strong ground motions, for an economical design, most structures are expected to deform into their inelastic range through structures' plasticity development. Note that the elastic design spectrum assumes that structures exhibit linear-elastic behavior under ground motion. This can be justified if ground motion is mild and the structures do not exhibit plastic deformation. However, under strong earthquake motions, due to the fact that ductile materials such as steel or aluminum have a significant amount of ductility to develop above their yield strength, structural ductility promotes the following effects:

1. After yielding, accelerations are limited and therefore the forces on structures are also limited.
2. Damping due to ductility/plasticity can dissipate a certain amount of energy.
3. Yielding increases the natural period, i.e., reduced acceleration in the response spectrum.
4. Plastic hinges form in one direction but close in the other.

To avoid explicit inelastic structural analysis in design, the capacity of the structure to dissipate energy, through mainly ductile behavior of its elements and/or other mechanisms, is taken into account by performing an elastic analysis based on a modified response spectrum reduced with respect to the elastic one [198]. This modified spectrum is called the ductility-modified (inelastic) design spectrum. It should be noted that the modified spectrum does not account for the change of natural period, while this can be addressed using a dynamic time history analysis.

For a local structural member such as a steel beam or column subject to bending, one may define the ductile characteristics as the ratio of maximum displacement (δ_u) over the displacement (δ_y) at the initial yielding of the member:

$$\mu = \frac{\delta_u}{\delta_y} \quad (10.42)$$

For a global ductile structure such as an offshore steel structure or a steel frame building, this is indicated by a significant amount of plastic deformation over elastic range. However, after the plasticity has been developed in each individual member of a structural system, unlike that in the elastic range, the relationship between the global load level and the deformation of each individual member may be different among each member, i.e., the member deformation is not proportional to global loads. In addition, due to the formation of plastic hinge, an increase in global load may even decrease the member forces in certain members. This raises difficulties in determining a unified ductility coefficient for a structural system that can be applied to every member in the system. On the other hand, investigations show that the maximum structural displacement amplitudes produced by a given ground motion tend to be reasonably independent of the yield strength of the structure, i.e., the maximum displacement in a typical engineering structure was found to be about the same whether it remains elastic or yields [653–655]. For engineering purposes, by assuming that all inelastic deformation is caused by the formation of plastic hinges and the plastic hinges in a structure occur simultaneously [656–657], one can express the ductile characteristics of a structure system with ductility coefficient or ductility factor [658] as:

$$\mu = \frac{\Delta_p}{\Delta_y} \quad (10.43)$$

where Δ_p is maximum horizontal displacement of a structure with inelastic behavior; Δ_y is maximum horizontal displacement of the structure when it just reaches yielding.

Based on the relationship between elastic and inelastic response as shown in Figs. 10.23 and 10.24, unit shape factor analysis can be used to determine the ductility of a structure.

For structures with relatively high natural period corresponding to Fig. 10.23, the velocity ($T_C < T < T_D$) or displacement ($T > T_D$) in the linear-elastic spectrum (Fig. 10.19) is constant, and the difference between the elastic (Δ_e) and inelastic displacement (Δ_p) is rather small. Therefore, the “equal maximum displacement” assumption is valid as an approximation:

$$\Delta_e = \Delta_p \quad (10.44)$$

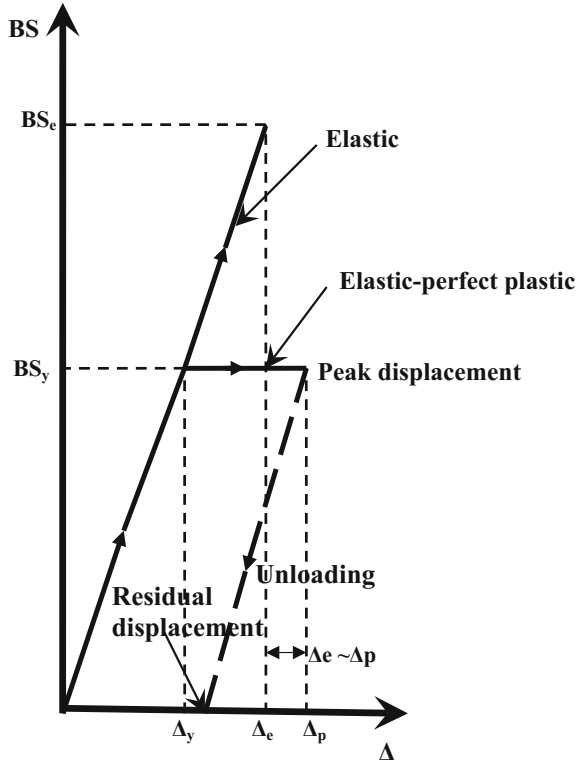
By adopting the rule of similarity of triangles, one has:

$$\frac{(BS_e - BS_y)}{(\Delta_e - \Delta_y)} = \frac{BS_e}{\Delta_p} \quad (10.45)$$

where BS_e is the horizontal elastic inertia force; BS_y is the horizontal yield force.

By rearranging the equation above, one obtains:

Fig. 10.23 Global base shear (BS_e is the horizontal elastic inertia force, and BS_y is the horizontal yield force) and displacement (Δ) relationship for elastic and inelastic response of a structural system at relatively *high* natural period of the structure (i.e., velocity is constant in the linear-elastic spectrum)



$$\frac{BS_e}{BS_y} = \frac{\Delta_p}{\Delta_y} = \mu \tag{10.46}$$

At low natural period of a structure corresponding to Fig. 10.24, the acceleration in the linear-elastic spectrum (Fig. 10.19) is constant, and the difference between the elastic (Δ_e) and inelastic displacement (Δ_p) is rather significant. Therefore, the “equal maximum energy” can be assumed to be:

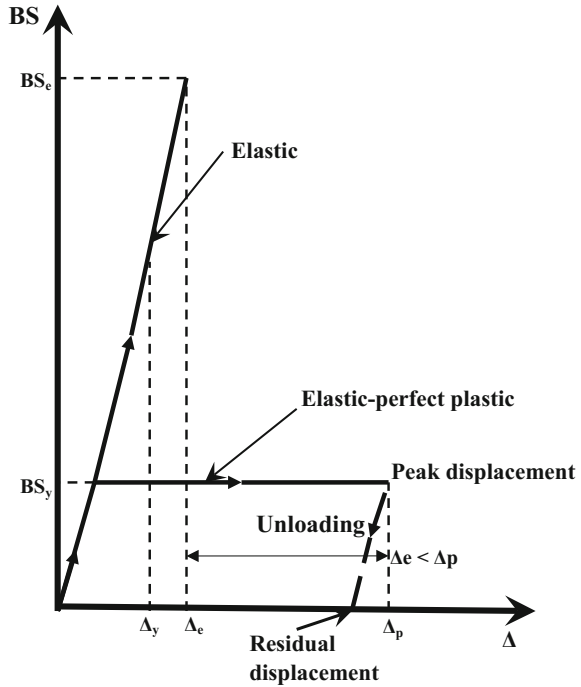
$$E_e = E_p \tag{10.47}$$

The absorbed energy due to the elastic response E_e and the absorbed energy due to the inelastic response E_p can be expressed by two equations as follows:

$$E_e = \frac{1}{2} BS_e \cdot \Delta_e \tag{10.48}$$

$$E_p = \frac{1}{2} BS_y \cdot \Delta_y + BS_y(\Delta_p - \Delta_y) \tag{10.49}$$

Fig. 10.24 Global base shear (BS_e is the horizontal elastic inertia force, and BS_y is the horizontal yield force) and displacement (Δ) relationship for elastic and inelastic response of structural system at relatively *low* natural period of the structure (i.e., acceleration is constant in the linear-elastic spectrum)



By inputting the two equations above into Eq. (10.47), one obtains:

$$\frac{BS_e}{BS_y} = \sqrt{\frac{2\Delta_p}{\Delta_y} - 1} = \sqrt{2\mu - 1} \quad (10.50)$$

The ratio of base shear $\frac{BS_e}{BS_y}$ above is known as behavior factor (R) in structural design codes for both offshore and land-based structures.

For structures with relatively high natural period, it is obvious that $R = \mu$. For structures with low natural period, $R = \sqrt{2\mu - 1}$.

From a comparison between Eqs. (10.46) and (10.50), it is noted that structures with high natural period can more effectively resist the earthquake excitations than structures with low natural period, provided the structure has sufficient ductility.

Readers should note that an important assumption in using ductility-modified spectrum is that, whether a structure responds elastically or yields significantly, the deformations of a structure produced by a given ground motion are essentially the same, which is often referred to as the equal displacement rule. However, currently, there is not enough research to examine the validity of the equal displacement rule.

The introduction of the ductility factor makes it possible to account for inelastic effects of structures in a linear analysis by means of specific response modification coefficients and deflection amplification factors that are dependent on the structural

and ductility class/level, which are related to both the force reduction factor (FRF) and the deflection amplification factor (DAF). Note that US recommendations [290, 659] propose two different dedicated factors for force and deflections; Eurocode 8 [198] uses the equal displacement rule in most cases, implicitly assuming that DAF and FRF are equal to the behavior factor. This Eurocode 8 procedure was used to obtain a set of ductility-modified (inelastic) design spectra, as will be presented in Sect. 10.4.3.2. In addition, it is also noted that the deflection amplification factors proposed in US provisions are in general either equal to or lower than the corresponding force reduction factor, depending on the structural system and its level of inelasticity [660, 661]. As a result, the US provisions are less conservative than Eurocode 8, since the latter approach considers the DAF-to-FRF ratio as unity [662].

Despite the benefits of using a ductility-modified spectrum, it has many limitations, which deter its applications. For example, the plastic deformations may not be distributed similarly to the elastic deformation. Furthermore, for more complex (redundant) structures, in which several modes of vibration may be excited significantly due to a ground excitation history, even elastic behavior cannot be predicted precisely by elastic response spectrum method [665]. Moreover, yielding pattern may appear as a general or an extremely localized phenomenon and may then eliminate the vibration mode characteristics based on the elastic assumption, which is the basis for the validation of superposition techniques used for modal response combination in a response spectrum analysis, and the relationship between the total inelastic energy absorption and the maximum local yield amplitudes can be extremely complex [552].

10.4.3.2 Construction Ductility-Modified (Inelastic) Design Spectrum Method

In Sect. 10.4.2, the construction of elastic design spectrum has been elaborated. By recognizing boundary periods (T_B , T_C , and T_D) of the displacement-, velocity-, and acceleration-constant regions in Fig. 10.19, the ductility-modified design spectrum can be obtained by dividing the elastic design spectrum with the behavior factor R varying with period/frequency, as described in Sect. 10.4.3.1:

$$R = \begin{cases} 1 & \text{for } T < T_B \\ \sqrt{2\mu - 1} & \text{for } T_B < T < T_C \\ \mu & \text{for } T_C < T < T_D \end{cases} \quad (10.51)$$

It should be emphasized that the operation of dividing spectrum applies to different ordinates of the spectrum: At acceleration-constant region ($T_B < T < T_C$), the acceleration design spectrum is divided by a factor of $\sqrt{2\mu - 1}$; at velocity-constant region ($T_C < T < T_D$), the velocity design spectrum is divided by a factor of μ ; at displacement-constant region ($T_D < T < 10$ s), the displacement design spectrum is divided by a factor of μ . Furthermore, at the lower bound of the

spectrum (e.g., $T = 0.03$ s), one may set the ordinate of either displacement-, velocity-, or acceleration design spectrum for inelastic spectrum as the same value as that of the elastic one and then join this value with the ordinate of inelastic design spectrum at T_B with a straight line. At the upper bound of the spectrum (e.g., $T = 33$ s), divide the ordinate of elastic displacement design spectrum by the value of μ , then join this value with the ordinate of inelastic displacement design spectrum at $T = 10$ s with a straight line. During this construction process, attention should always be paid to the transformation between displacement-, velocity-, or acceleration design spectrum using the equations in Sect. 10.4.2. Figure 10.25 shows an example of inelastic design spectra. It should be noted that the value of T_c is not fixed and depends on the damping [553].

Figure 10.26 shows a comparison of inelastic spectrum according to Eurocode 8 [198] with various ductility factors. The peak ground acceleration is 0.6 g, with soil type 1 and subsoil class B. It should be noted that the ductility factors for a structure may be different along different horizontal directions, although the ductility classification is the same for all directions.

For the construction of vertical ground motion, readers may read Sect. 3.10.

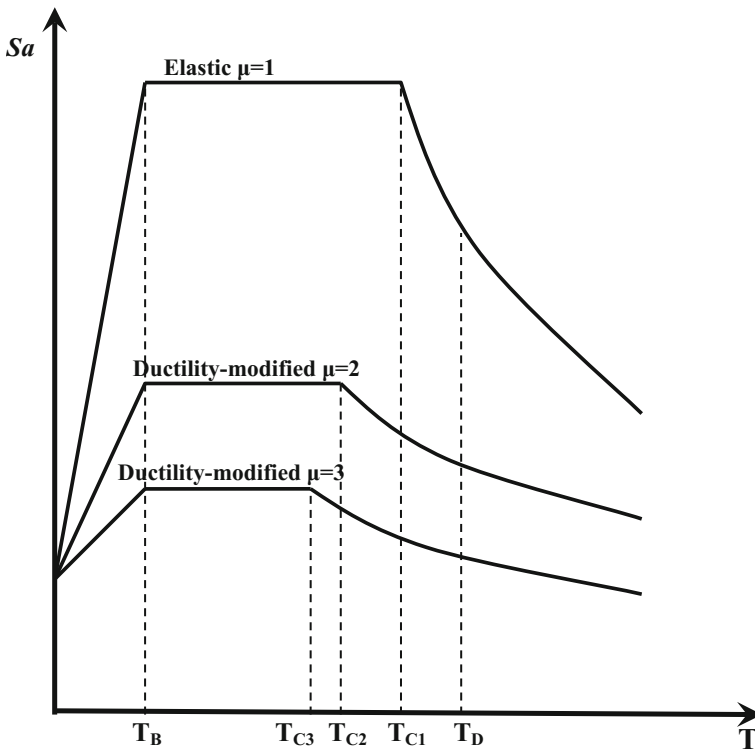
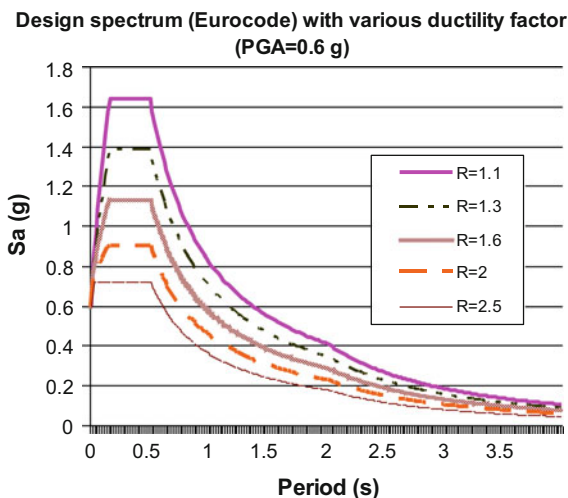


Fig. 10.25 Inelastic pseudo-acceleration design spectrum (linear scale)

Fig. 10.26 Inelastic (pseudo-acceleration) design spectrum with various values of ductility factor R



10.5 Time History Method

10.5.1 General Method

The time history method requires a set of deterministic excitation time histories to be used as input, which account for the uncertainties and differences in frequency characteristics, duration, and severity. Each time history takes the non-stationary characteristics of ground motions into account. The information regarding the phase lag of the ground motion among three translational directions and signs (compression or tension) of the structural member forces is also explicitly included in the analysis. Moreover, the duration of the time history should be sufficiently long to capture the load sequence and hysteretic effects on the responses for structures, foundations, and soil.

The required number of time histories varies among various seismic design codes, with a minimum of three. For example, ISO 19901-2 [289] requires at least four time histories, while Eurocode 8 [198] requires at least three.

Note that, as a set of recorded accelerograms in detail is only available for very few sites in the world, simulated (usually by performing site-specific response analyses) and artificial accelerograms are often used for dynamic analysis. These accelerograms should be consistent with a design spectrum, i.e., their corresponding response spectrum will be approximately equal to a prescribed or target spectrum.

In the application of the time history method for assessing structural response, there is debate as to whether the characteristic strength or the mean strength of structural materials should be used to assess the structural response: Modeling the structural system using characteristic material strength could lead to unrealistic behavior, but on the other hand, modeling the mean values may not always be representative of reality—for example, the contractor may over-specify material strength.

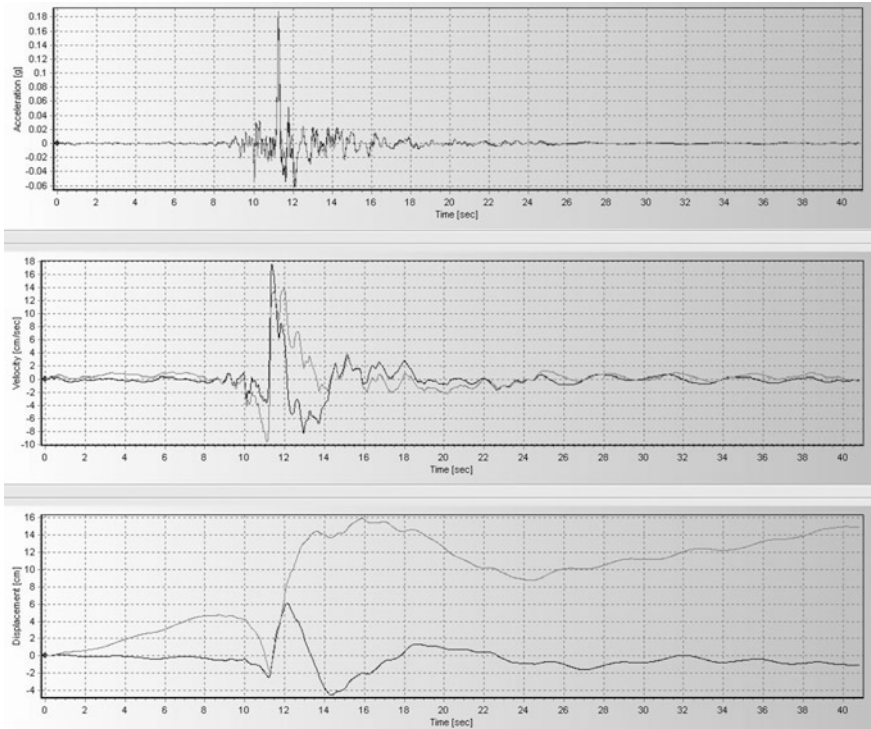


Fig. 10.27 Horizontal acceleration (upper) recorded during the Friuli earthquake in Italy, and its corresponding velocity (middle) and displacement (lower) time series derived from single and double integrations of the acceleration record using SeismoSignal; the black and gray line indicates the time series with and without baseline-correction, respectively

10.5.2 Drift Phenomenon and Its Correction

Velocity and displacement time series are derived from corresponding accelerograms by single and double integrations of the acceleration record as shown in Figs. 10.27 and 10.28. However, by observing these two figures, noticeable drifts (gray lines) can be identified especially for displacement time series: While the velocities oscillate around zero near and after the end of the strong ground motions, the displacement time series reach essentially constant residual values.

This phenomenon is obviously unphysical and can lead to erroneous estimates of peak ground displacement and structural response at long-period spectral range. A correctly derived long-period ground motion can be used in understanding the source- and path-related specific features of far- and near-fault ground motions [561]. Long-period motions are also important for a reliable estimation of deformation demand for structures, particularly with an increasing interest in displacement-based design and nonlinear seismic response. Furthermore, the drift

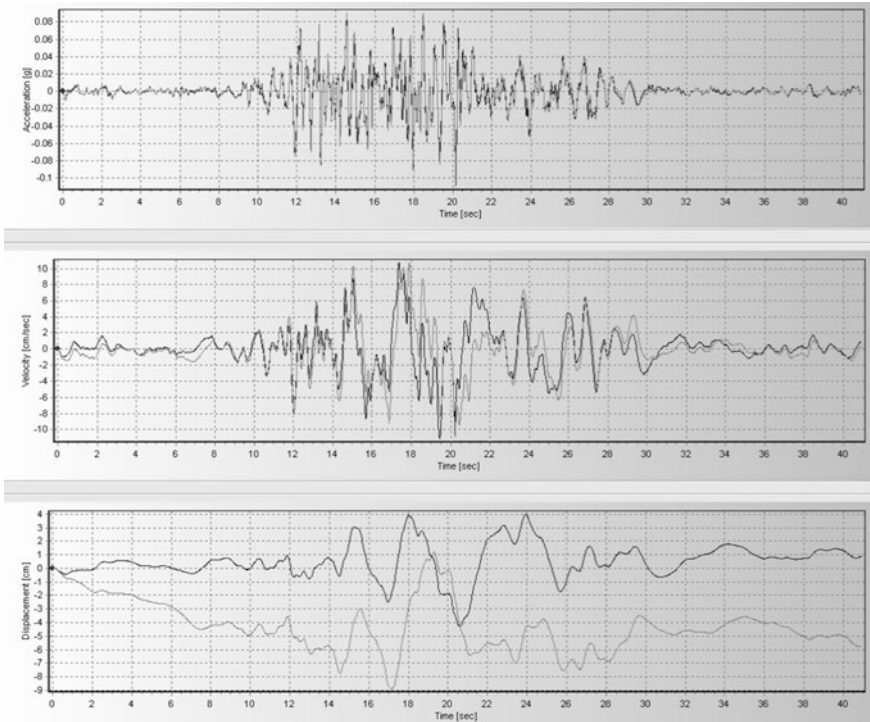


Fig. 10.28 Horizontal acceleration (upper) recorded during the Nahanni earthquake in Canada, and its corresponding velocity (middle) and displacement (lower) time series derived from integrations of the acceleration record using SeismoSignal; the black and gray line indicates the time series with and without baseline-correction, respectively

also often affects a robust estimate of large-scale soil–structure interaction response, especially for structures having large horizontal dimensions where the traveling wave effects become significant [562].

The drift-related noise is embedded in records from both analog and digital accelerographs, although the characteristics of the noise are usually different for the two types of records. It is not necessarily distributed in a stationary manner throughout the record, but can be confined to a certain short portion of time series [563].

The source of the long-period noise seems to be variations in the acceleration baseline. These variations could be due to true ground motion (tilting and rotation produced by wave propagation, as well as local permanent ground failures), instrument effects (amplitude-dependent mechanical or electrical hysteresis in the sensor), analog-to-digital conversion [564], and the accumulation of random noise in time series also result from the single integration and double integration.

Various methods are proposed to solve the problems of baseline-offsets, even though there is no universal correction method for any kind of ground motion records [565].

As mentioned before, since the unrealistic drift to be removed can be different at different portions of time series, one popular baseline-correction method, as implemented in SeismoSignal [566], consists of (1) determining, through regression analysis (e.g., least-squares-fit method), the polynomial curve (typically is of a type among linear, quadratic or cubic) that best fits the acceleration time-series; (2) subtracting from the actual acceleration values by their corresponding counterparts obtained with the regression-derived equation. By performing the two steps above, spurious baseline trends, usually well noticeable in the displacement time history obtained from double time integration of uncorrected acceleration records, can normally be removed from the input motion.

In step (1) above, the polynomial curve $\ddot{x}(t)$ to fit the acceleration can normally be assumed to be linear, quadratic, and cubic:

$$\ddot{x}(t) = a_0 + a_1 t \quad \text{for linear curve} \quad (10.52)$$

$$\ddot{x}(t) = a_0 + a_1 t + a_2 t^2 \quad \text{for quadratic order curve} \quad (10.53)$$

$$\ddot{x}(t) = a_0 + a_1 t + a_2 t^2 + a_3 t^3 \quad \text{for cubic order curve} \quad (10.54)$$

where a_1 , a_2 , a_3 , and a_4 are four constants to be determined during the curve fitting; t is time.

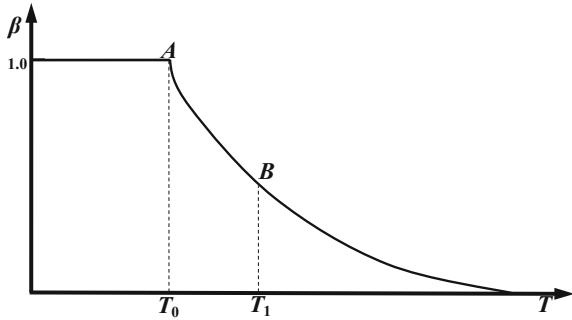
The curve fitting to acceleration time-series can be obtained by, for example, minimizing the mean square acceleration:

$$\min \left\{ \sum_{t=0}^{N\Delta t} \left[\ddot{x}(t) - \ddot{\bar{x}}(t) \right]^2 \right\} \quad (10.55)$$

where N is the total number of time steps for the baseline-correction of time series, with each time step being Δt .

Based on the fact that the baseline of the acceleration record has random shifts during the interval of strong shaking and the shifts could be represented by an average baseline-correction over this interval, Iwan et al. [567] proposed that two baselines should be removed at two portions of time series: a_m between times t_1 and t_2 , and a_f from time t_2 to the end of the record. The value a_m is an average shift in baseline that could occur during strong shaking. Strictly speaking, t_2 can be any time instant between t_1 and the end of the acceleration record, which satisfies the constraint that the average of the corrected velocity is zero near the end of the record. Note that the degree of drift strongly depends on the value of t_2 [565]. Iwan et al. [567] proposed two specific options for determining t_2 : (1) t_2 is the time after which the acceleration never exceeds 0.5 m/s^2 ; (2) t_2 is chosen to minimize the final

Fig. 10.29 An example of a windowed filter



displacement. As a third alternative, t_2 can also be chosen as a time instant at which the line fitting to velocity series becomes zero [565]. The black lines in Figs. 10.27 and 10.28 show the baseline-corrected time series. It is clearly shown that the drift in derived displacement time series is essentially eliminated.

In cases where undesirable long-period fluctuations still appear in the baseline-corrected time series, a windowed filter process in frequency domain can be carried out by applying a high-pass filter to the baseline-corrected acceleration data, with an example equation expressed as below and shown in Fig. 10.29 [568]:

$$\beta(T) = \begin{cases} 1 & 0 \leq T \leq T_0 \\ e^{-(T-T_0)/\alpha} & T \geq T_0 \end{cases} \quad (10.56)$$

where T is period in seconds, and a and T_0 are two parameters that can be determined by using two key points A and B shown in Fig. 10.29.

Based on the data from laboratory tests, Zhou and his co-workers [569] suggested that after the baseline-corrected acceleration series have been obtained, the velocity series calculated by integrating the baseline-corrected acceleration series may be further put through a similar baseline-correction process. By integrating the updated baseline-corrected velocity time series, the displacement time histories can be obtained. These obtained displacement time histories can go through a high-pass filter to further remove the long-period oscillations.

In case a response spectrum analysis using design spectra is performed, the drift of time history for generating the design spectra can normally be omitted as the influence of baseline-correction on the variation of design spectrum is normally very marginal. Similarly, the baseline-correction has minor effects on the frequency content in case a power spectrum or a Fourier spectrum is used in the calculation of seismic responses.

However, it should be noted that the process of drift correction also eliminates the permanent ground deformation, which can degrade the reliability of the assessment results in case permanent ground displacement is of engineering concern.

Chapter 11

Seismic Hazard Assessment

11.1 Seismic Hazard Analysis

11.1.1 Introduction

Hazard is defined as inherent physical characteristics that pose potential threats to people, property, or the environment. The main purpose of hazard analysis is to quantitatively assess ground shaking level at a site, through either deterministic analysis (as when a specific earthquake scenario is assumed, as will be introduced in Sect. 11.1.2), or probabilistic analysis, in which various earthquake scenarios and uncertainties are explicitly accounted for [1], as will be presented in Sect. 11.1.3. The effects of local soil on the seismic wave transmission are often assessed separately by a site-specific response analysis, as discussed in Chap. 3.

A seismic hazard analysis normally comprises the following two tasks:

1. Identify earthquake sources: This is to identify all the possible earthquake sources and the fault geometry associated with a specific region or site. It is normally performed by studying the geologic evidence, tectonic evidence, historical seismicity, and recent instrumental seismicity records. Based on this information, the potential for future earthquakes can be evaluated. In this task, it is important to determine the occurrence rate of earthquake activities and the associated range of magnitude. For more detailed information on identification and characterization of earthquake sources, readers may refer to source [1].
2. Determine the ground motions or ground motion parameters: Typically based on selected attenuation relations, this is normally performed by carrying out either deterministic (DSHA) or probabilistic (PSHA) seismic hazard analysis, of which the former is based on a single earthquake scenario (a predefined earthquake source) with a selected magnitude and single source-to-site distance, and the latter is based on various scenarios (earthquakes on different sources); it also accounts for the uncertainties associated with earthquake size, location, time of earthquake occurrence, etc. For the PSHA, the median of the ground motion

parameter or the mean of natural-log of ground motion parameter value and standard deviation of earthquake spectral ordinates for different levels of given magnitudes, source-to-site distance, site conditions, etc., should be established. The resulted ground motion selection provides a necessary link between seismic hazard and structural response [570]. Moreover, the ground motion can also be calculated by directly modeling physical processes of earthquake source generation, seismic wave propagation, and site effects, forming an essential part of the neo-deterministic approach, as will be presented in Sect. 11.5.

A dedicated seismic hazard analysis may help not only to increase the reliability of structural design, but also greatly reduce the uncertainties without degrading a required safety level, leading to a more economical design. For example, Diablo Canyon nuclear power plant (Fig. 11.1) at the edge of the Pacific Ocean in San Luis Obispo, California, was constructed in 1968. The original design was based on a deterministic seismic hazard analysis to determine the ground motion from an earthquake associated with a particular fault in the region, based on historical records and geological evidence, then by using this information to perform the capacity control of structures, systems, and components at the facility to ensure they could withstand seismic ground shaking [571]. Since then, different new faults have been identified that almost circle the plant, with the closest one, the Shoreline Fault found in 2008, coming within only 600 m of the reactors, and Hosgri fault, found in 1971, lying 5 km away. However, with a dedicated PSHA, seismologists have recently been able to show an even lower ground motion intensity demand than



Fig. 11.1 The Diablo Canyon Power Plant, north of Avila Beach, in San Luis Obispo County, California (courtesy of ML Baird)

what was required in the original design using DSHA [572, 573]. However, even if the US Nuclear Regulatory Commission was motivated to move toward more probabilistic approaches, the US Geological Survey recommended to follow a deterministic one by postulating that a magnitude 7.5 earthquake may occur anywhere along the Hosgri fault zone, including the point closest to the plant.

Most of the seismic design codes rely on both DSHA and PSHA for seismic hazard analyses. Especially for assessing seismic hazard with a high return period but in a low seismicity area, the calculated ground motion intensity may be unreasonably high. To solve this, seismic maps obtained from PSHA have been complemented by the use of DSHA, as specified in FEMA P-750 [290] and ASCE 7-10 (ASCE 2010), which defines the “risk-targeted Maximum Considered Earthquake” (MCER) as the minimum between probabilistic and deterministic ground motions.

Note that both DSHA and PSHA rely on an excessively simplified attenuation relationship to derive the bedrock motions. Therefore, neo-deterministic seismic hazard assessment (NDSHA) has recently been proposed [575] to calculate the ground motion by using the most updated seismological, geological, geophysical, and geotechnical databases for the site of interest, as well as advanced physical modeling to account for physical processes of earthquake source generation, wave propagation, and site effects, which may provide a more reliable and robust assessment as a deterministic design basis (Sect. 11.5).

Sometimes, analysis with real-time recorded ground motion amplitude time histories at the locations of seismic (strong motion) stations can also be performed to assess the seismic hazard. While a major problem involved in this method is that the locations for which ground motion data is available are not likely to comply with the sites of interests, this problem can be partially solved by seeking the available records at stations nearby (typically less than 30 km) the sites of interest. As most of the ground motion data available are realistic ground motion data recorded at the ground surface, the soil amplification effects are already included in the analysis with real-time data.

11.1.2 Deterministic Seismic Hazard Analysis (DSHA)

Prior to PSHA, DSHA was prevalent. In DSHA, by identifying the potential earthquake sources (faults), individual earthquake scenarios in terms of magnitude and location are developed for each relevant seismic source and a predefined ground motion probability level.

After identifying the earthquake source location(s), the source-to-site distance can be computed (see Sect. 11.1.3.1 for details). Given the magnitude, the distance, and the number of standard deviations for the ground motion, the ground motion is then computed for each earthquake scenario using a ground motion model (attenuation relation) that is based on either an empirical ground motion model or numerical simulations. The largest ground motion from any of the considered

scenarios is used for the design ground motion. The approach is “deterministic” in that single values of parameters (magnitude, source-to-site distance, and number of standard deviations for the ground motion) are selected for each scenario [576].

It should be noted that even if deterministic estimates of ground motion extremes at a site are basically obtained by considering a single event of a specified magnitude and source-to-site distance, if a site has several known active faults in its proximity, a maximum magnitude is normally defined for each fault.

Practically, a DSHA can be performed by the following four steps [1]:

1. Identify all earthquake sources (e.g., known faults) capable of producing non-negligible ground motions at a site, determine their locations relative to the site, and specify the source models by defining source zones and the largest amplitude (earthquake potential) that each source is capable of producing.

The source models at the target region are basically derived from the earthquake catalogs of historical and instrumental seismicity. This data is inevitably obtained from what are, from a geological perspective, relatively short periods. Therefore, it may be supplemented by additional data, such as the results from seismic monitoring, geodetic monitoring, deep geologic investigation.

The maximum magnitude is normally a function of the fault length and historical knowledge of past earthquakes on that particular source and is therefore not strictly associated with a defined return period (Sect. 11.1.3). In this step, the probability of occurrence for potential source rupture is implicitly assumed to be unity. As will be discussed in Sect. 11.1.3.1, this probability can be taken into account in a PSHA.

Determining the earthquake potential (magnitude) is a rather subjective choice. The results may be very sensitive to the background and objectives of the decision maker. An event chosen in this manner was historically described as a maximum credible earthquake (MCE), which is the largest earthquake that is capable of occurring under the known tectonic framework for a specific fault or seismic source, as based on geologic and seismologic data. There may be several MCEs for one site, each from a different fault or seismic source.

2. For each source zone, select source-to-site distance. Typically, the shortest distance is selected. This actually implicitly assumes that, in each source zone, the probability of occurrence is 100% at the points closest to the site and zero elsewhere.
3. Specify the controlling earthquake that produces the largest ground shaking among all ground shakings and relationship that describes the attenuation of ground motion with distance identified, i.e., it is based on the source potential determined in step 1 and source-to-site distance obtained in step 2.
4. Determine the ground motion by the controlling earthquake.

Again, readers need to bear in mind that, by its nature, a DSHA does not explicitly account for the likelihood of a particular earthquake scenario occurrence, and it is not associated with a specific return period, although the particular earthquake event used can have a return period associated with it. The return period

for the maximum event on a given fault can vary from several hundred to several thousand years, depending on the activity rate of the fault. Therefore, deterministic results cannot be used for a quantitative assessment of the overall risk of an infrastructure.

Although DSHA has the merit of being simple, the relevant conceptual problems arise quickly and are difficult to solve. It is commonly misunderstood by engineers that the hazard determined from the four steps above is the “worst case,” because the largest amplitude and shortest source-to-site distance are usually used to calculate the design ground motions [577]. However, this may not be the case, because of the limitations due to the deterministic method itself, i.e., the variability/scatter of the design event and ground motion intensity. It provides no information on the likelihood of occurrence of the controlling earthquake and the effects of uncertainties in the various steps required to calculate the ground motion characteristics. Therefore, nowadays, DSHA should only be used to complement PSHA, as will be discussed in Sect. 11.1.3. For example, a deterministic seismic hazard analysis sometimes specifies a mean plus one standard deviation response spectrum (the mean value of $\text{Ln}Y \pm \sigma_{\text{Ln}Y}$), but even this response spectrum will be exceeded 16% of the time. Because the scatter is normally distributed, there is no theoretical upper bound on the amplitude of ground motion that might be produced at a given magnitude and distance. Obviously, there is a true physical upper bound on ground motion intensity caused by an inability of the earth to carry more intense seismic waves without shattering or otherwise failing. Even though this limit can provide information to determine extremely high ground motions used for design of rather important structures such as nuclear waste repositories, it has almost no engineering sense for the majority of structures such as buildings or bridges, which are analyzed for ground motion intensities that are exceeded once every few thousand years. Thus, the theoretical upper bound of ground motions has no practical sense for most seismic designs [578].

As mentioned before, historically, the result obtained from a DSHA is often referred to as maximum credible (or capable) Earthquake (MCE). More recently, however, the acronym has been retained but taken to indicate Maximum Considered Earthquake, as the most severe earthquake effects considered, in recognition of the fact that larger earthquakes (and larger ground motion intensities) than those shown by MCE can happen. The Maximum Considered Earthquake is often quantified by MCE maps based on a combination of the results of deterministic and probabilistic estimates of ground motions.

11.1.3 Probabilistic Seismic Hazard Analysis (PSHA)

Different from DSHA, which only calculates so-called “worst-case” ground motion parameters, PSHA seeks to consider all possible earthquake scenarios to calculate the ground motion parameters with their associated probabilities of occurrence. This is also the primary advantage of PSHA over DSHA.

It is obvious that a great number of uncertainties pose challenges to the quantification of future earthquakes. Those uncertainties mainly relate to the earthquake location, the magnitude, source-to-site distance, resulting shaking intensity for the given magnitude, site condition, time of occurrence of future earthquakes, etc. All or most of these parameters can only be characterized by probability distributions with randomness. Moreover, the source-to-site distance is a computed parameter that depends on the earthquake location and rupture dimension, which in turn have randomness [576].

To quantify these uncertainties and combine them to produce a description of the distribution of future seismic motions that may occur at a site, Cornell [579] first explicitly described the procedure to perform a PSHA. This essentially involves considering many scenarios (earthquakes on various sources) and accounting for the uncertainties mentioned above, and calculating the annual rate of exceedance of different levels of selected ground motion parameters. The uncertainties typically include: (1) aleatory uncertainties associated with random variability and characterized by probability distributions, which can be integrated in a PSHA procedure described in the current section; (2) epistemic uncertainties due to lack of knowledge with respect to earthquake source processes and wave propagation, which can be reduced by additional data characterized by a probability distribution; the identification, quantification, and incorporation of epistemic uncertainty require a dedicated judgment from a number of experts and can be accounted for using logic trees, as will be introduced in Sect. 11.1.5.

In a PSHA, when a site is selected, all the zones within a certain radius from the site are being taken into account. For the probabilistic analysis, all scenarios from deterministic analysis are therefore included, forming a full set of scenarios and with all possible magnitude and location combinations for the site. For each earthquake scenario, all possible ground motions are computed for each possible value of standard deviations above or below the median (or mean) ground motion [576].

Practically, a PSHA also involves four steps that are similar to that of DSHA. The major difference between the two methods is that, in each step of a PSHA, the uncertainties mentioned above are taken into account through probability descriptions (typically using probability distribution functions), as shown in Fig. 11.2.

PSHA has been developed since the late 1960s and prevailed over DSHA in the 1990s. As many of the major potential pitfalls in executing a successful PSHA are procedural rather than technical, a significant amount of research efforts during the past decades have been directed at procedural guidance.

11.1.3.1 Define Earthquake Source and Geometry

The first step in a PSHA is to define source seismicity, geometry, and probability distribution of magnitude and source-to-site distance, including: (1) Identify all earthquake sources; (2) Characterize the probability distribution of earthquake

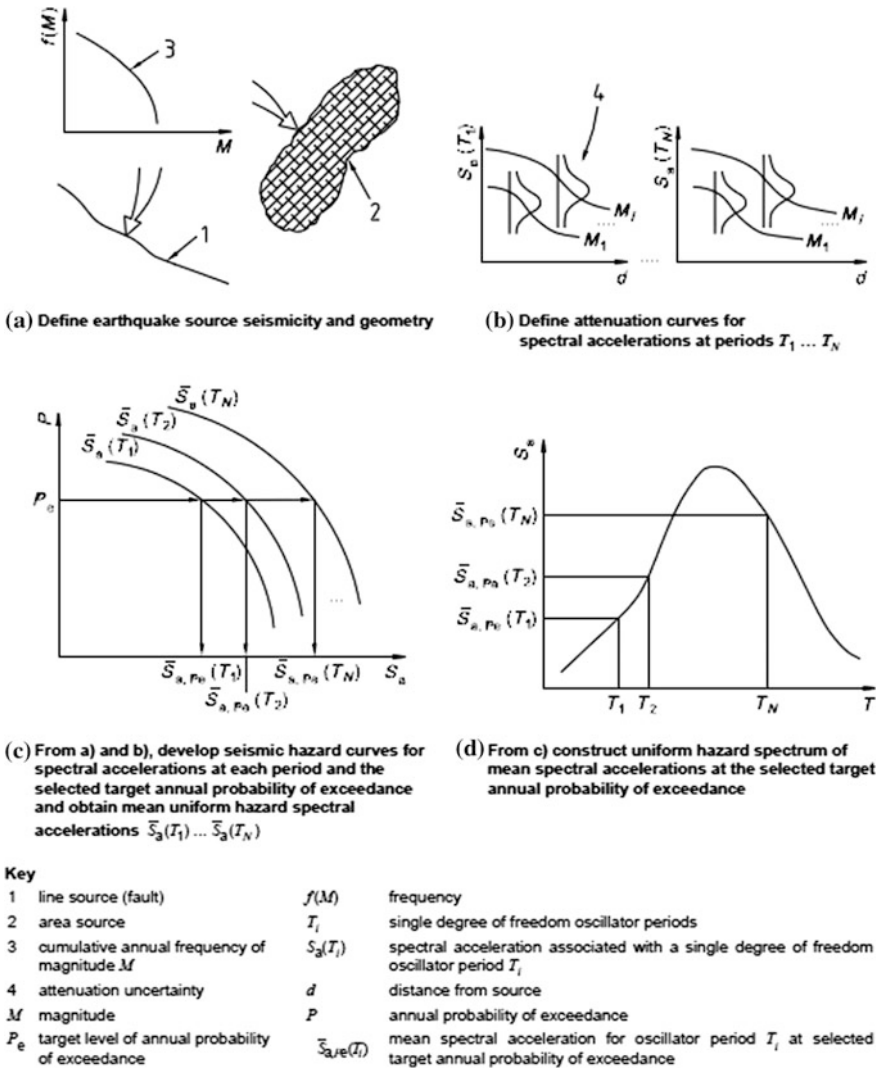


Fig. 11.2 Four steps for performing a PSHA [289]

magnitudes; and (3) Characterize the probability of source-to-site distances associated with potential earthquakes.

This is similar to that of DSHA, the only difference being that the probability of various magnitudes on all potential sources affecting the site should be considered. Here, the potential earthquake sources can be either faults or area sources of diffused seismicity not directly attributable to a known fault. Also, a maximum magnitude is assigned to each source [289]. In many cases, the probability

distribution of source-to-site distance also needs to be characterized, as will be presented in step (3).

(1) Identify all earthquake sources:

The source zones can be categorized as point, linear, or three-dimensional sources. Earthquakes induced by volcanic activities or short fault ruptures can generally be assumed to be point sources, as the zones are small. For shallow fault zones that have well-defined planes in which the changes in hypocentral depth distance have insignificant influence on hypocentral distance, the linear (areal) source is the most suitable one to adopt. However, for areas where the fault mechanism (especially the fault geometry) is poorly understood or defined, which typically corresponds to dispersed seismic activity and that not directly associated with known faults, one has to use three-dimensional volumetric sources. In the calculation of source-to-site distances and the associated uncertainties, the linear source and volumetric source are sometimes simplified as a line source and area source, respectively, as will be discussed in step (3).

(2) Characterize the probability distribution of earthquake magnitudes:

The probability of source rupture is generally assumed to be uniformly/homogeneously distributed within each seismogenic/source zone, implying that earthquakes are equally likely to occur at any location within each seismogenic zone. This assumption may be revised if detailed seismological studies on the local area deviate from the homogenous zone model. By combining with source geometry, the probability distribution of the corresponding source-to-site distance can be calculated. It should be noted that a uniform fault-rupture distribution in space may not result in a uniform distribution of source-to-site distance.

It is necessary to establish an annual frequency of earthquake occurrence for each source as a function of earthquake magnitude, by specifying the average rate at which an earthquake with a certain magnitude will be exceeded. Globally, the earthquake occurrence varying with magnitude is usually expressed in terms of the Gutenberg-Richter relationship (also called the Gutenberg-Richter recurrence law) [580], which defines that the magnitude M is exponentially distributed:

$$\log_{10} N_c = a - bm \quad (11.1)$$

where N_c is the cumulative number of earthquakes of a magnitude larger than m occurring on a seismic source per unit time, and it is also referred to as the rate of occurrence of earthquakes of magnitudes greater than m ; a and b are region constant, which is estimated through curve fitting using statistical analysis of historical earthquake observations, with additional constraining data provided by other types of geological evidence; a is the activity rate parameter indicating the overall rate of earthquakes in a region, it is a function of sample size and is therefore liable to vary substantially from one seismic source to another, and the total number of earthquakes with magnitude larger than or equal to zero is $10a$; b describes the relative number of small and large earthquakes in the region, worldwide it is around 1.0

with a deviation of ± 0.3 . For the North Sea, by using curve fitted linear regression with a correlation coefficient of 0.99 complied with the instrumentally determined earthquakes 1980 through 1989 [581], it is obtained that $a = 4.42$ and $b = 0.84$. This indicates that the number of earthquakes above magnitude 4.0 that occurred annually in the North Sea is around 2.

Note that earthquakes with smaller magnitude are not of interest for structural designs. The Gutenberg-Richter relationship described above is normally used to calculate the cumulative distribution function (CDF) for earthquakes within a range of magnitude larger than m_{\min} (m_{\min} must be smaller than m):

$$\begin{aligned} F_M(m) &= P(M \leq m | M > m_{\min}) \\ &= \frac{10^{1-bm_{\min}} - 10^{a-bm}}{10^{a-bm_{\min}}} = 1 - 10^{-b(m-m_{\min})} \end{aligned} \quad (11.2)$$

By taking the derivative of the CDF above, one obtains the probability density function (PDF) for M :

$$f_M(m) = \frac{d}{dm} F_M(m) = b \ln(10) 10^{-b(m-m_{\min})} \quad (11.3)$$

However, since the energy that can be released by relevant fault ruptures is limited based on the fault size, the maximum magnitude of earthquake that can occur over that particular region is limited as well. Physically, there is an upper limit m_{\max} of earthquake magnitude that each source can produce. In such a case, the linear Gutenberg-Richter relationship can still be applied but with an upper limit of earthquake magnitude, which is normally modeled by a truncated (bounded) Gutenberg-Richter relationship, with the corresponding CDF rewritten as:

$$F_M(m) = \frac{1 - 10^{-b(m-m_{\min})}}{1 - 10^{-b(m_{\max}-m_{\min})}} \quad (11.4)$$

And the corresponding PDF is then rewritten as:

$$f_M(m) = \frac{b \ln(10) 10^{-b(m-m_{\min})}}{1 - 10^{-b(m_{\max}-m_{\min})}} \quad (11.5)$$

For numerical or hand calculations, the continuous distribution of the magnitude has to be rewritten as a discrete set of magnitudes, and the probability of occurrence between magnitude m_i and m_{i+1} ($m_{i+1} > m_i$) is:

$$P(M \in (m_i, m_{i+1})) = F_M(m_{i+1}) - F_M(m_i) \quad (11.6)$$

The Gutenberg-Richter relationship is essentially a power law typical for fractal sets that implies scale invariance and self-similarity. It may not be capable of predicting earthquakes with very large magnitudes.

More realistic than what the Gutenberg-Richter relationship can predict, statistics and geological evidence show that annual probability of occurrence of ruptures for specific faults has repeated occurrences with a reasonably consistent magnitude [581]. The relationship based on this observation is normally referred to as the characteristic earthquake model and requires a minor modification of the probability density function [583].

- (3) Characterize the probability distribution of source-to-site distances associated with potential earthquakes:

It is normally assumed that the probability distribution of earthquakes within a source zone is uniformly distributed, i.e., earthquakes will occur with equal probability of occurrence at any location on the relevant fault. However, sometimes, non-uniform distribution is also possible. As the definition of source point can vary significantly as shown in Fig. 11.3, a uniform distribution of the source zone does not often result in a uniform distribution of source-to-site distances, as mentioned before. The uncertainty in source-to-site distance can be characterized by a PDF or CDF.

For a point source, the PDF is equal to 1 when the distance is equal to the site-to-point source distance, and otherwise, it is equal to 0.

To model the faults on the boundary of two tectonic plates, a line fault source model with a total length of $2l$ km is normally adopted, as shown in Fig. 11.4. By assuming that earthquake epicenters are equally likely at all locations, the

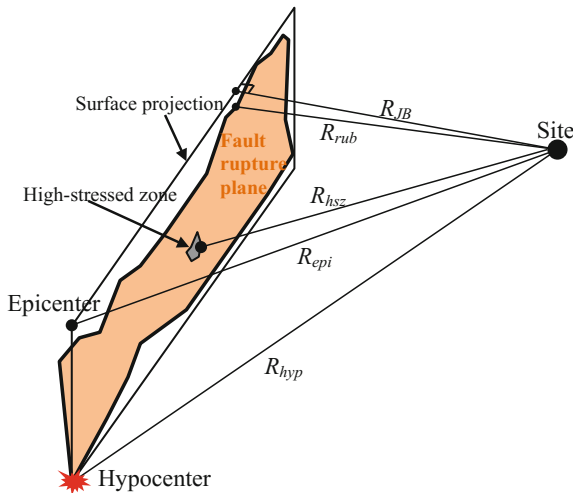
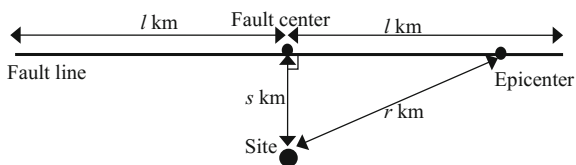


Fig. 11.3 Schematic definition of source-to-site distance: The distance can be site-to-epicenter (R_{epi}), site-to-hypocenter (R_{hyp}), site to the high-stressed zone (R_{hsz}), site to the closest point on the rupture surface (R_{rub} , not including sediments overlying basement rock) or to the closest point on the surface projection of the fault rupture (R_{JB} , also called Joyner-Boore distance)

Fig. 11.4 An illustration of line source



probability of observing a distance R less than r km is equal to the fraction of the fault located within a radius of r , and the corresponding CDF is then calculated as:

$$F_R(r) = \begin{cases} 0 & \text{for } r < s \\ P(R \leq r) = \frac{2\sqrt{r^2 - s^2}}{2l} & \text{for } s \leq r < l + 1 \\ 1 & \text{for } r \geq l + 1 \end{cases} \quad (11.7)$$

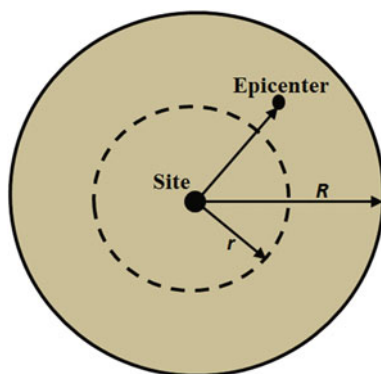
The corresponding PDF is expressed as:

$$f_R(r) = \frac{d}{dr} F_R(r) = \begin{cases} \frac{r}{l\sqrt{r^2 - s^2}} & \text{for } s \leq r < l + 1 \\ 0 & \text{for } r \geq l + 1 \text{ or } r < s \end{cases} \quad (11.8)$$

Note that the two equations above are based on the assumption that the fault can be represented as a line source. By following a similar procedure, the CDF and PDF corresponding to a plane source can be developed, which is more typical in a seismic hazard analysis.

For earthquakes that are not produced by specific faults, a circular shape area source (Fig. 11.5) with a radius of R (say 100 km) can be adopted. By assuming a uniform probability distribution of earthquake epicenter within the area, the corresponding CDF of an epicenter that is located within a distance of less than r from the site is equal to the ratio of the area of a circle with the radius r and the area of the circle with the radius of R :

Fig. 11.5 An illustration of a circular shape area source with a radius of R



$$F_R(r) = \begin{cases} 0 & \text{if } r = 0 \\ P(R \leq r) = \frac{\pi r^2}{\pi R^2} = \frac{r^2}{R^2} & \text{for } 0 \leq r < R \\ 1 & \text{for } r \geq R \end{cases} \quad (11.9)$$

The corresponding PDF is:

$$f_R(r) = \frac{d}{dr} F_R(r) = \begin{cases} \frac{2r}{R^2} & \text{for } 0 \leq r < R \\ 0 & \text{otherwise} \end{cases} \quad (11.10)$$

Note that within the seismogenic zones delimited for seismic hazard analysis, the number of strong earthquakes (whose source size becomes comparable with the region size) generally exceeds the estimation based on the extrapolation of the Gutenberg-Richter relationship (i.e., self-organized criticality only up to a certain magnitude, while for the larger events, it usually exhibits an upward bend), and hence, they can be considered abnormally strong within the given region. By modifying the Gutenberg-Richter relationship, Kossobokov and Mazhkenov [584] proposed that the dependence of the linearity of the Gutenberg-Richter relationship on the dimensions of the investigated area can be illustrated considering different regions of the world, which is often referred to as the Unified Scaling Law [585]:

$$\log_{10} N_c = a + b(5 - m) + c \log_{10} l \quad (11.11)$$

where l is the linear dimension of an area (size $l \times l$) considered; c estimates the fractal dimension of the earthquake-prone faults.

The equation above indicates that the distribution of rates or waiting times between earthquakes depends only on the local value of the control parameter $10^{-bm} \cdot l^c$, which represents the average number of earthquakes per unit time, with magnitude greater than m occurring in the area of size $l \times l$. With increasing magnitude, the linearity truncates with decreasing dimension of the area, as soon as the recurrence of such earthquakes in it compares to the time span of the catalog used [586].

11.1.3.2 Establish Attenuation Relationship

The second step in a PSHA is to calculate the ground motion intensity by specifying the ground motion attenuation relationships as a function of earthquake magnitude, source-to-site distance etc., with a consideration of its randomness. This requires a probability distribution of magnitude and source-to-site distance, as mentioned above in the previous step, to represent the uncertainty of the predicted ground motion at a site. The attenuation relationships are normally developed based on statistical analyses of ground motion records from past earthquakes occurring in similar geological and tectonic conditions.

In this step, it is assumed that the fault-rupture energy is released at the hypocenter. However, for major earthquakes, as the area of fault rupture is so large that parts may be much closer to the site than the hypocenter, the effects may potentially lead to a situation in which the resultant location measured by released energy can be closer to the site than the hypocentral distance. This is especially the case for large earthquakes with a distant hypocenter [587].

In the modeling of ground motion attenuation relationship, the ground motion parameter Y (i.e., PGA, PGV, modified Mercalli intensity (MMI), or peak spectral acceleration at different periods) is normally modeled as a function of earthquake magnitude M , source-to-site distance R (sometimes also includes θ to account for rupture mechanism, local soil conditions, as well as directivity parameters), and uncertainty E , which can be expressed as follows:

$$\ln Y = f(M, R) + E \quad (11.12)$$

11.1.3.3 Develop Seismic Hazard Curve

The third step in PSHA is to perform probabilistic calculation to obtain the exceedance probability for a given ground motion (y), $P[Y \geq y]$ from the ground motion attenuation relationship selected in the previous step, i.e., to calculate the probability that a ground motion will be exceeded during a specified time period/duration. This is carried out by accounting for the various uncertainties in earthquake size, location, and ground motion intensity as mentioned above, and a summation over individual probabilities from all sources. This finally provides the total annual probability of exceedance for a given level of ground motions.

Note that the uncertainty E can normally be assumed to follow a normal distribution with a zero mean and a standard deviation $\sigma_{\ln Y}$, i.e., $E = \varepsilon\sigma_{\ln Y}$, where ε is a constant number of standard deviations ($\sigma_{\ln Y}$) measured as the difference relative to the median or mean ground motion $f(M, R)$. One can then compute the probability of exceeding any y level of ground motion intensity level:

$$P(Y > y|m, r) = 1 - \Phi\left(\frac{\ln y - \overline{\ln Y}}{\sigma_{\ln Y}}\right) \quad (11.13)$$

where $\Phi()$ is the standard normal cumulative distribution function, which can be checked from various mathematical handbooks; $\ln Y$ and $\sigma_{\ln Y}$ can be calculated from the statistical calculation of data observed from historical earthquakes (with an example shown in Fig. 11.6).

The equation above can be expressed by incorporating the probability density function $f_Y(u)$ of the ground motion parameter Y (given m and r) without checking the $\Phi()$ value, i.e., $f_Y(u)$ can be written out analytically [578]. An integral form of expression can then be used, calculated either analytically or numerically:

Fig. 11.6 An illustration of observed PGA at various sites during an earthquake event with a measured magnitude; the solid line indicates the mean value of $\text{Ln}Y$ (Y is the observed PGA), and the two dashed lines indicate $\text{Ln}Y \pm \sigma_{\text{Ln}Y}$. Each round dot indicates the PGA obtained from a recorded ground motion

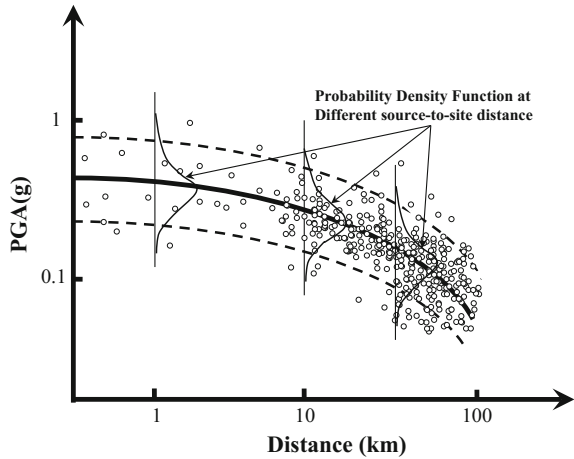
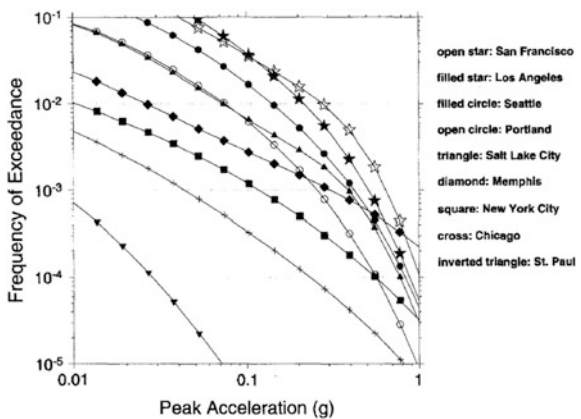


Fig. 11.7 Seismic hazard curve showing the peak ground acceleration versus annual probability of exceedance for various sites in the USA (courtesy of USGS)

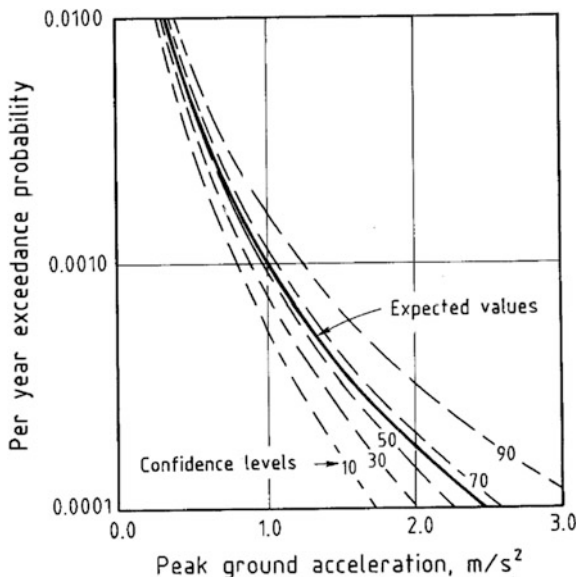


$$P(Y > y|m, r) = \int_y^\infty \frac{1}{\sqrt{2\pi}\sigma_{\text{Ln}Y}} e^{-\frac{1}{2}\left(\frac{\ln u - \ln Y}{\sigma_{\text{Ln}Y}}\right)^2} du \quad (11.14)$$

Based on the equation above, which can be evaluated numerically using a PSHA software, Fig. 11.7 shows the peak ground acceleration versus annual probability of exceedance for various sites in the USA. This type of curve is often referred to as a seismic hazard curve.

The majority of design codes use design spectrum to characterize the ground motion intensity. For each spectral period (dominant period) T_i and the selected target probability of exceedance P_e , one can plot a site-specific hazard curve with a \log_{10} - \log_{10} basis. This shows the probability distribution of the spectral parameters (such as spectral acceleration $\overline{S_{a,P_e}(T_i)}$). Figure 11.8 shows the peak ground

Fig. 11.8 Seismic hazard curve showing the peak ground acceleration for different levels of confidence versus annual probability of exceedance for a site on the Norwegian continental shelf [588]



acceleration ($T_i = 0$ s) versus annual probability of exceedance for an offshore site on the Norwegian continental shelf. It is noticed that the slope of the curve is steep, and the peak ground acceleration with a return period of 10,000 years (with an annual probability of exceedance of 0.0001) is around 2.5 times of that for a return period of 1000 years (with an annual probability of exceedance of 0.001).

It is worth mentioning that, as an alternative to PSHA, one may directly utilize the ground motion attenuation and earthquake occurrence frequency relationships to derive a hazard curve that can be used for seismic risk assessment. In this method, M is expressed as a function of R , $\ln Y$, and E . This approach is referred to as seismic hazard assessment (SHA). For more details, readers may read Wang [589, 590].

For each target annual probability of exceedance P_e , it is required to construct a uniform hazard spectrum (UHS) such that at each period, the spectral acceleration at that period corresponds to the target annual probability of exceedance. UHS is not only the PSHA-based design spectrum [591], but also the state of the practice and the basis for the definition of design seismic actions on structures in the most advanced seismic codes.

Since in PSHA the probabilities associated with ground motion values are calculated by combining the probabilities of ground motion from various sources, the ground motion probabilities are not associated with a specific fault or event. In fact, while it seems conservative to use the expected ground motion from the largest possible earthquake occurring at the closest location on the nearest fault, those values can be significantly smaller than ground motions calculated from a probabilistic method. This outcome becomes increasingly likely if the largest earthquake on the nearest fault is associated with a shorter return period than that being

considered in a probabilistic method, or if the site is affected by several faults, each contributing to the overall probability of exceedance. The opposite outcome is also possible when the return period of the largest earthquake on the nearest fault is much greater than the desired return period of the ground motion [289]. This can be studied through deaggregation analyses, as will be presented in Sect. 11.1.4.

To find a probability of exceedance, one needs to know the distribution of earthquakes in time. By assuming that the earthquake occurrence in time has a constant rate, and time to the next earthquake is independent of time to the last earthquake, the relationship between the average return period (or inverse of the average recurrence rate) and the target annual probability of exceedance can be described by the Poisson model, which defines the probability of at least one exceedance ($N \geq 1$) of an earthquake with a specific ground motion level in a period of t years:

$$P_e[N \geq 1] = 1 - e^{-\lambda t} \quad (11.15)$$

where λ is the average recurrence rate (also called the average rate of annual occurrence, annual rate of exceedance, or annual frequency of exceedance) of the event with considered earthquake magnitude. This model is adopted by the majority of current seismic design codes.

If the average recurrence rate is small, say less than 0.05, there is a convenient approximation of the exceedance probability for small probability:

$$1 - e^{-\lambda t} \approx \lambda t \quad (11.16)$$

If one sets time period of interest $t = 1$ year, the annual probability of exceedance can be calculated as:

$$q = 1 - e^{-\lambda \cdot 1} = 1 - e^{-\frac{1}{R}} \quad (11.17)$$

where R is called return period, or recurrence interval, which is defined as the average time between the design conditions being exceeded.

It should be emphasized that return period is the average time span between shaking intensity that is equal to or greater than a specified value. It does not mean that a certain event associated with a return period must necessarily occur in the return period time, and it is simply used as an estimate of the likelihood of an event. For example, a 100-year earthquake may not regularly happen every 100 years. Therefore, PSHA presents earthquake occurrence only implicitly.

Readers need to bear in mind that the Poisson process is a memoryless model, in that it is independent of elapsed time. In addition, it is also independent of size or location of any previous events. Therefore, this model is only applicable for a large area with many tectonic faults [592].

Example: Based on Poisson process, calculate the average rate of annual occurrence λ and return period of at least one event that has 10% probability of being exceeded in the next 50 years (time span).

Solution: With $P_e[N \geq 1] = 10\%$, $t = 50$, one then has: $10\% = 1 - e^{-\lambda \cdot 50}$, and the average rate of annual occurrence λ is 0.0021; and the return period $R = 1/\lambda = 475$ years.

Obviously, a structure and/or its foundation shall be designed and constructed to withstand a seismic action having a lower probability of occurrence than the design seismic action. However, if it is required to sustain unrealistically/impossibly high seismic loading within its service life without damage and the associated limitations of use, the costs would be extraordinarily high. Therefore, the seismic action to be considered for a “damage limitation requirement” at component level and a “non-collapse limitation level” at the system level should have reasonable probability of exceedances. Therefore, for the design of critical structures, such as nuclear power plants, offshore platforms, dams, bridges, smaller values of the reference probability of exceedance, or longer reference return periods would be selected. Table 11.1 shows the interrelation of these two parameters.

Sometimes, it is more desirable to use a certain ground motion having a P_f probability of exceedance in T_f years, to determine the probability P_Q , which is the same ground motion that is exceeded at least once in Q years. Since the level of ground motion (defined by its annual exceedance rate or return period) remains constant, working with the above equations, it can easily be derived that the sought probability is:

Table 11.1 Typical values and relationships of reference probabilities of exceedance and corresponding return periods

Probability of exceedance (%)	Time span (years)	Return period (years)
50	50	72
50	100	144
20	10	45
10	10	95
20	50	224
10	50	475
5	50	975
10	100	949
5	100	1950
2	50	2475
1	50	4975

$$P_Q = 1 - (1 - P_f)^{Q/T_f} \tag{11.18}$$

Based on the equation above, Table 11.2 shows relationships among typical exceedance probabilities and associated time spans for a certain level of ground motion. If we take the peak ground acceleration (event) that has 10% probability of being exceeded in the next 50 years as a reference, it is noticed that the probability of exceeding this reference peak ground acceleration is reduced to 1/5 for a 10-year span, while the probability for a 1000-year span becomes almost 9 times that of the reference.

By combining the Gutenberg-Richter occurrence model with Poisson distribution, Ritsema [593] applied the theory of extremes from the Gumbel model [594] to calculate the extreme value of earthquake magnitude for the whole North Sea region, which is presented in Table 11.3. One fact that needs to be mentioned is that the largest North Sea earthquake during the last century was the Oslofjord earthquake of 1904, with a magnitude M_s of around 5.4. Further, it is also noticed that the seismicity in the Norwegian part of the North Sea is in general greater than that in the UK part [595]. Figure 11.9 shows that the probability for at least one earthquake of more than magnitude 6.7 to occur in the USA between 2003 and 2032 is 62%.

It should be mentioned that more complicated models for calculating earthquake occurrence have been developed over recent decades, including time-dependent models [596], renewal models [597, 598], and time-predictable models [599]. For example, with sufficient data available, more time-dependent models were used for the estimation of seismic hazard for San Francisco Bay Area by the US Geological Survey [600].

So far, we have learned how to calculate the probability distribution of earthquake magnitude (Gutenberg-Richter relationship) and source-to-site distance,

Table 11.2 Relationships among typical exceedance probabilities and associated time spans for a certain level of ground motion

If a ground motion has a probability of exceedance in 50 years (%)	In 10 years, this ground motion will have a probability of exceedance (%)	In 100 years, this ground motion will have a probability of exceedance (%)	In 1000 years, this ground motion will have a probability of exceedance (%)	In 3000 years, this ground motion will have a probability of exceedance (%)	In 10,000 years, this ground motion will have a probability of exceedance (%)
20	4	36	99	100	100
10 (corresponding to a return period of 475 years)	2	19	88	100	100
5	1	10	64	95	100
2	0.4	4	33	70	98

Table 11.3 Extreme value of earthquake magnitudes with various levels of return period in the whole of the North Sea

Return period (years)	Magnitude	Uncertainty in magnitude
5	4.6	±0.4
10	5.1	±0.2
15	5.4	±0.2
25	5.6	±0.2
50	5.9	±0.2
75	6.0	±0.3
100	6.1	±0.4
200	6.3	±0.6
500	6.5	±0.9
1000	6.6	±1.1
5000	6.7	±1.6
7000	6.7	±1.7
10,000	6.8	±1.8

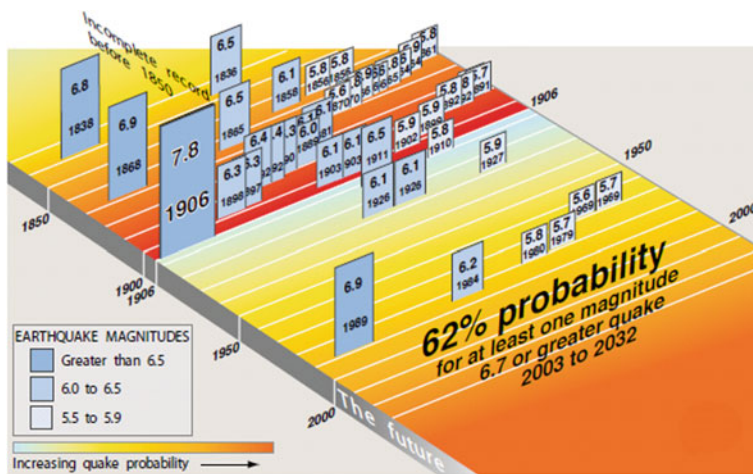


Fig. 11.9 History and probability of earthquakes in the USA (courtesy of USGS)

denoted as $f_M(m)$ and $f_R(r)$, respectively. We have also learned how to compute the probability of exceeding any y level of ground motion intensity level $P(Y > y | m, r)$. Each of the parameters above can be determined through scientific studies of historical earthquakes and processing of observed data. In addition, by understanding how to correlate the average rate of annual occurrence λ with the annual probability of exceedance P , one can then assess the annual occurrence rate $\lambda(Y > y)$ for ground intensity level $Y > y$. By assuming that for each source the probability of occurrence for magnitude and source-to-site distance is independent, the annual

occurrence rate for all n sources is equal to the sum of annual occurrence rate $\lambda(M_i > m_{\min})$ for each individual source i :

$$\lambda(Y > y) = \sum_{i=1}^n \lambda(M_i > m_{\min}) \int_{m_{\min}}^{m_{\max}} \int_0^{r_{\max}} P(Y > y | m, r) f_{M_i}(m) f_{R_i}(r) dr dm \quad (11.19)$$

where $\lambda(M > m_{\min})$ is the rate of occurrence of earthquakes greater than m_{\min} from the source.

Strictly speaking, magnitude and source-to-site distance are dependent on each other with a joint distribution. One may thus use a joint distribution for magnitude and source-to-site distance $f_{M,R}(m, r)$, but the independence assumption above allows a significant simplification of the expression.

For numerical calculation, the integral in the equation above has to be converted into discrete summation of occurrence rate with n_M and n_R intervals (for a range of possible M_i and R_i combinations):

$$\lambda(Y > y) = \sum_{i=1}^n \lambda(M_i > m_{\min}) \sum_{j=1}^{n_M} \sum_{k=1}^{n_R} P(Y > y | m_j, r_k) P(M_i = m_j) P(R_i = r_k) \quad (11.20)$$

The above results can easily be converted into a seismic hazard curve as illustrated in Figs. 11.7, 11.8, and 11.10, which show the annual occurrence rate ($P_e[N \geq 1] = 1 - e^{-\lambda t}$) versus the ground motion intensities.

For uncertainties that are not reflected in the seismic hazard curve, a correction factor C_c above unity may then be adopted to account for those uncertainties, as implemented in ISO 19901-2 [288]. The value of C_c is strongly dependent on the slope of the seismic hazard curve. For regions with low seismic ground motion levels, correction factors are normally close to unity.

11.1.3.4 Construction of Spectra Acceleration at Discrete Periods

As mentioned above, several ground motion parameters can be accounted for, such as PGA, PGV, PGD, spectral accelerations at various periods, with the methodology of PSHA remaining essentially the same for all cases [602]. For example, a typical objective of a PSHA is to generate design response spectra for structural design. Therefore, one has to first perform the PSHA for spectral accelerations at various periods of interests, and then, based on the target probability of exceedance P_e , one can find the spectral value at each individual period (T_1, T_2, \dots, T_N). The uniform hazard spectrum (UHS) used for design can finally be generated, as shown in Fig. 11.11.

Obviously, every ordinate in a UHS has an equal rate of being exceeded (the reason why it is called “uniform hazard”). However, a UHS is an envelope of

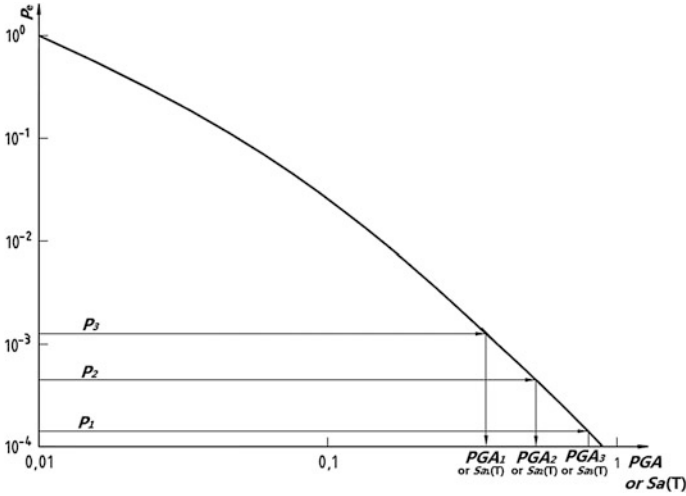


Fig. 11.10 Seismic hazard curve showing the relationship between various levels of ground motion intensity [peak ground acceleration (PGA) or spectrum acceleration at a period $T: S_a(T)$] and the corresponding annual probability of exceedances (P_e)

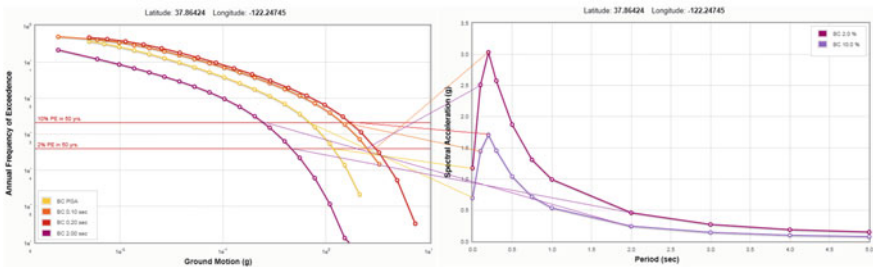
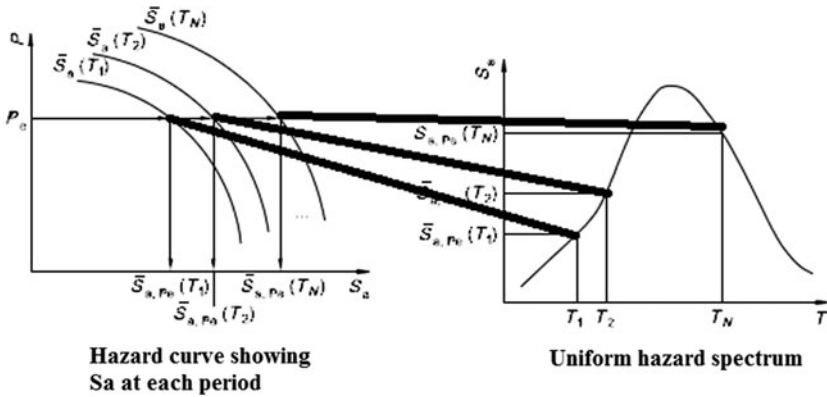


Fig. 11.11 Illustrations of generation of spectra acceleration at each individual period from the seismic hazard curve (left) to generate the UHS (right)

separate spectral acceleration values at different periods, each of which may have come from a different earthquake event. This mixing of events to create a spectrum has sometimes been used to criticize the entire PSHA procedure: UHS conservatively implies that large amplitude spectral values will occur at all periods within a single ground motion time history. Therefore, it is important to recognize that a UHS is only one way to use the output of PSHA [578], as the concept of a design earthquake is lost, i.e., there is no single event (specified in simplest terms, by a magnitude and source-to-site distance) that represents a realistic earthquake threat at, for example, a 3000-year return period of ground motion level (so-called “target ground motion”). This disadvantage results directly from the integrative nature of PSHA, and it means that other characteristics of the ground motion (e.g., the duration or non-stationarity characteristics of motion) must be estimated in an ad hoc fashion if these characteristics are important for analysis or design [603]. It also creates a barrier to the use of UHS, identified by the AKI committee in 1988 PSHA [604], who recommended that a “recursive” PSHA be performed to determine the dominant earthquake at any particular hazard level. The earthquake and attenuation models can then be revised to reasonably reflect the realistic characteristics of this dominant earthquake, and the hazard analysis can be repeated using these more reasonable models. Another method to solve the problem associated with the utilization of the UHS is to replace the UHS with conditional mean spectrum (CMS) for the design, which will be discussed in Sect. 11.4.

Various software are available to perform seismic hazard analysis such as EZ-FRISK [605], Deqas-R [606], or SELENA [607]. With an implementation of various attenuation equations for various regions, those codes can calculate the probability of earthquake ground shaking in the bedrock/rock outcrop based on the location of surrounding faults. Some of these software may even calculate the response spectra at ground surface if a site-response analysis package accounting for the local site condition is also implemented, or if site correction factors dependent on site condition are given (which is used to scale the spectral ordinates at the bedrock to the appropriate values corresponding to the spectral values at ground surface).

In seismic design of infrastructures, the risk involved strongly depends on the ground shaking level of the earthquake. Figure 11.12 shows a typical relationship between the expected damage to building and ground shaking levels. It is obvious that under an earthquake that has only a 50% chance of being exceeded in a 50-year period, no damage is expected. On the other hand, in an extremely large earthquake, with a chance of only 2% of being exceeded in a 50-year period, serious damages without structural collapse can be expected.

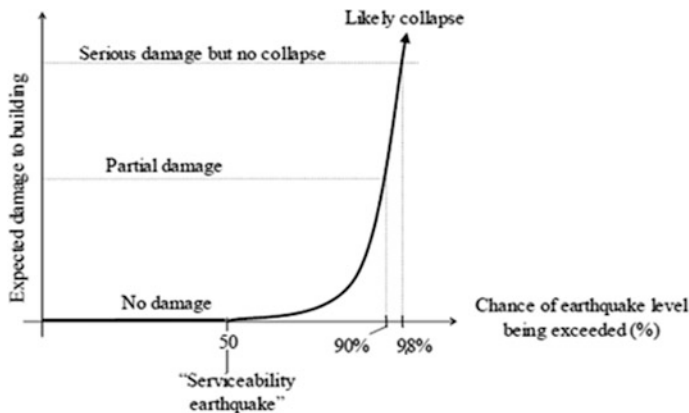


Fig. 11.12 Expected damage of a building versus probability of exceedance [608]

11.1.4 Deaggregation (Disaggregation) in PSHA for Multiple Sources

During the process of a PSHA, for a site with multiple earthquake sources, it is necessary to assess the probability of occurrence for $Y > y$ from all earthquake sources. As discussed previously, since the annual occurrence rate for all n sources is equal to the sum of annual occurrence rate $\lambda(M_i > m_{\min})$ from each individual source i , the relative contribution from each source can be identified. The process for this identification is called deaggregation [603] or disaggregation [609], which is essentially a part of the results obtained from PSHA.

Seismic hazard can be deaggregated to show the contribution by magnitude M , distance R , and ϵ . Any uncertainties in seismicity parameters can be incorporated and represented in this deaggregation. As an example, we examine the method to characterize the contribution of the earthquake magnitude. Given that a ground motion $Y > y$ has occurred, the probability that an earthquake’s magnitude will equal to m can be expressed as:

$$P(M = m | Y > y) = \frac{\lambda(Y > y, M = m)}{\lambda(Y > y)} \tag{11.21}$$

In Sect. 11.1.3.3, we learned that the annual occurrence rate for all n sources is equal to the sum of annual occurrence rate $\lambda(M_i > m_{\min})$ for each source i . This is exactly the solution for the denominator of the equation above. The numerator can also be calculated in a similar manner:

$$\lambda(Y > y, M = m) = \sum_{i=1}^n \lambda(M_i > m_{\min}) \sum_{k=1}^{nR_i} P(Y > y | m, r_k) P(M_i = m) P(R_i = r_k) \quad (11.22)$$

Figures 11.13, 11.14, and 11.15 show an example of deaggregation for PGA, spectral acceleration at 1.0 and 5.0 s, during a process of PSHA, for a site at the University of California, Berkeley (Fig. 11.16), with return periods of 2475 years (an exceedance probability of 2% in 50 years) and 475 years (an exceedance probability of 10% in 50 years). It is clearly shown that for the longer return period of 2475 years with higher acceleration levels, sources nearby (1.5–3.5 km from the site) and magnitudes ranging from 5.5 to 7.5 contribute most to the seismic hazard. For the lower return period of 475 years with lower acceleration levels, there is an additional contribution from sources around 28 km away from the site with magnitudes of more than 8.0. This is more obvious for longer periods of spectral acceleration than for shorter periods. In addition, even with the same return period, the contribution from various magnitudes and source-to-site distances also depends on which spectral period of the spectral acceleration is under study.

Note that compared to UHS, the disaggregation of seismic hazard identifies values of some earthquake characteristics providing the largest contributions to the hazard in terms of exceeding a specified spectral ordinate threshold. These events are essentially the earthquakes dominating the seismic hazard in a probabilistic sense and may be used as design earthquakes (DEs) as originally introduced by McGuire [610]. If the contribution from a single seismic source dominates the hazard at all period ranges that are of interest, one may use a single design earthquake to represent the entire response spectrum. However, if the contribution from several seismic sources dominates the hazard at different period ranges, the single design earthquake is not appropriate. Then, values of M , R , and ε derived at different periods, for example, at $T = 0.1$ and 1 s, by weighting earthquakes for each GMPE, can be used to represent design earthquakes for short and long periods, respectively [603].

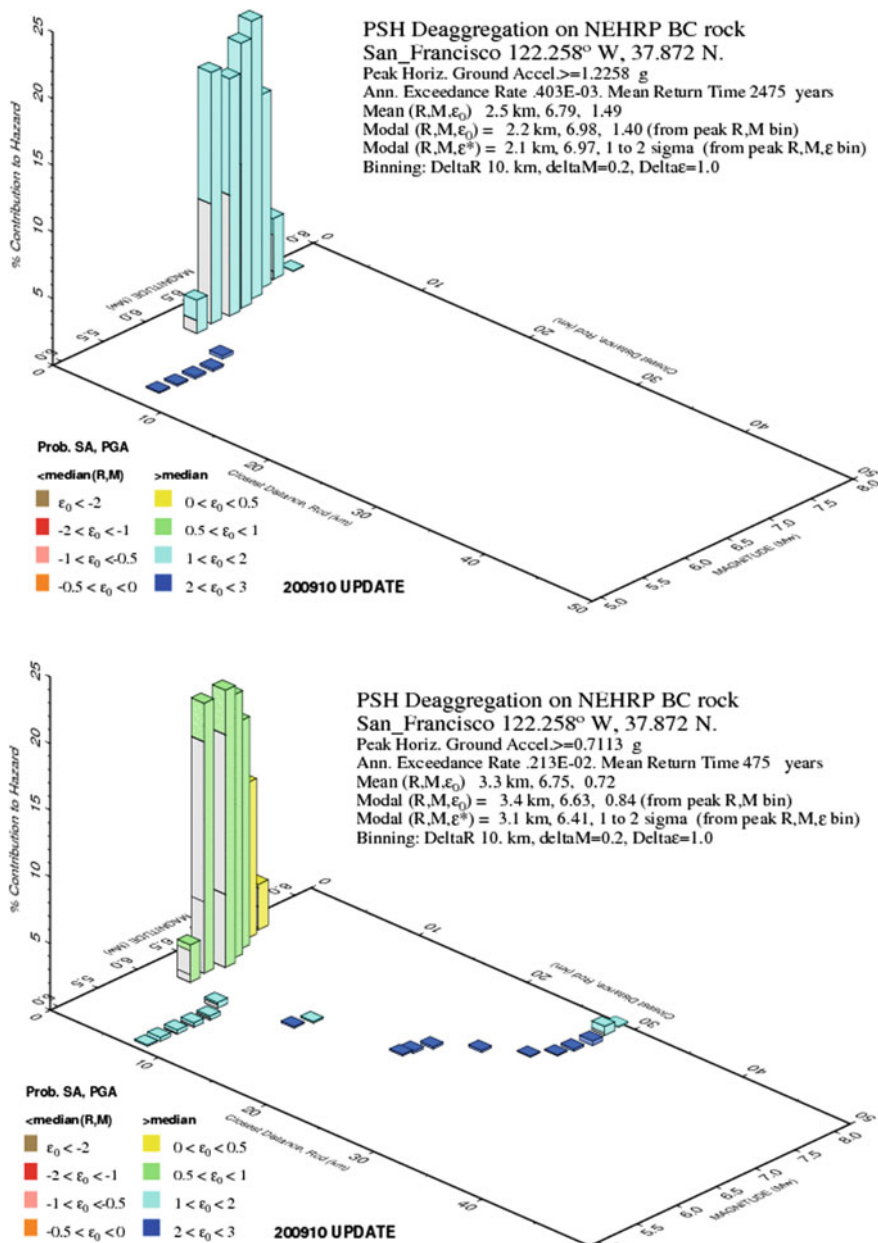


Fig. 11.13 PSHA deaggregation for the PGA at the University of California, Berkeley (courtesy of US Geological Survey 2008 Interactive Deaggregation), with return periods of 2475 years (upper) and 475 years (lower)

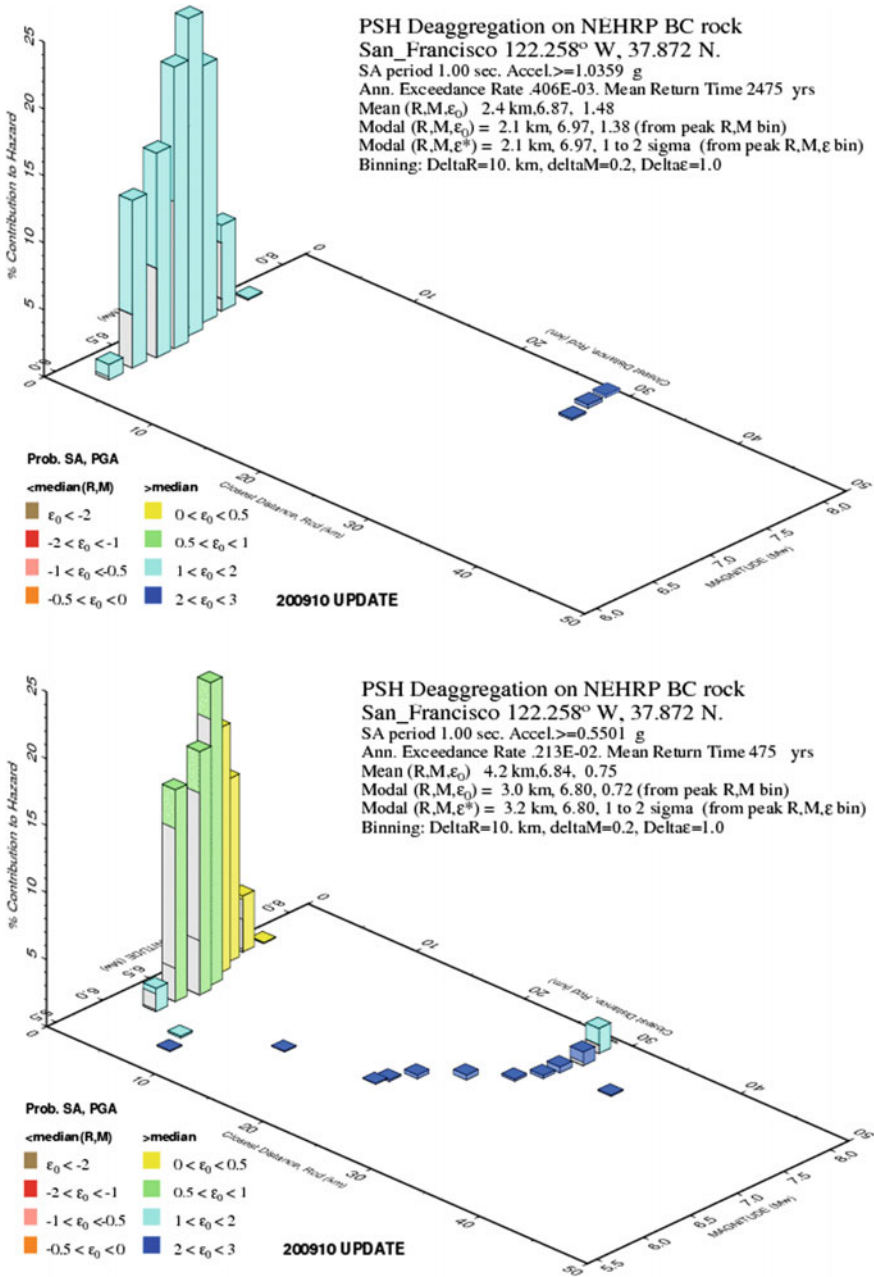


Fig. 11.14 PSHA deaggregation for the spectral acceleration at 1.0 s at the University of California, Berkeley (courtesy of Geological Survey 2008 Interactive Deaggregation), with return periods of 2475 years (upper) and 475 years (lower)

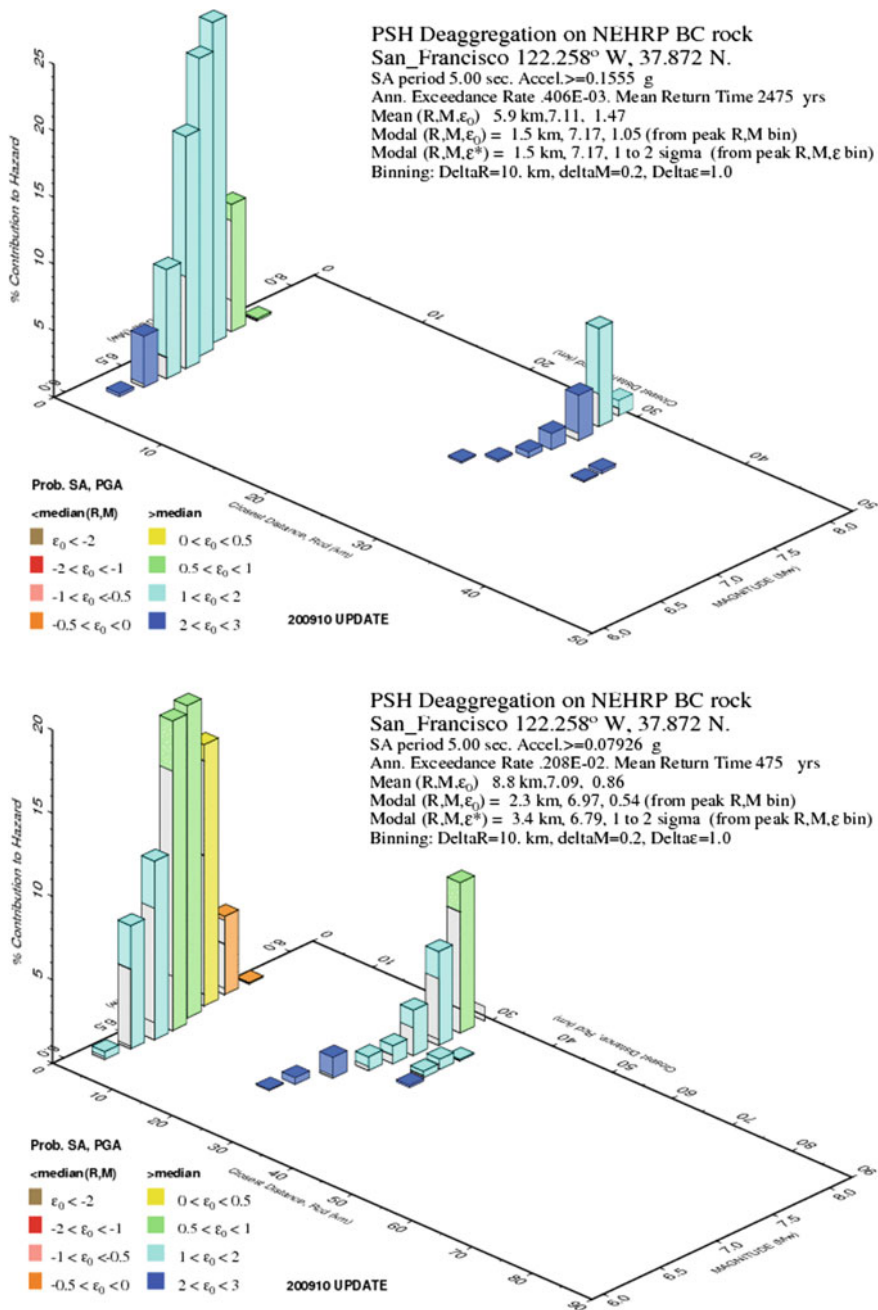


Fig. 11.15 PSHA deaggregation for the spectral acceleration at 5.0 s at the University of California, Berkeley (courtesy of US Geological Survey 2008 Interactive Deaggregation), with return periods of 2475 years (upper) and 475 years (lower)

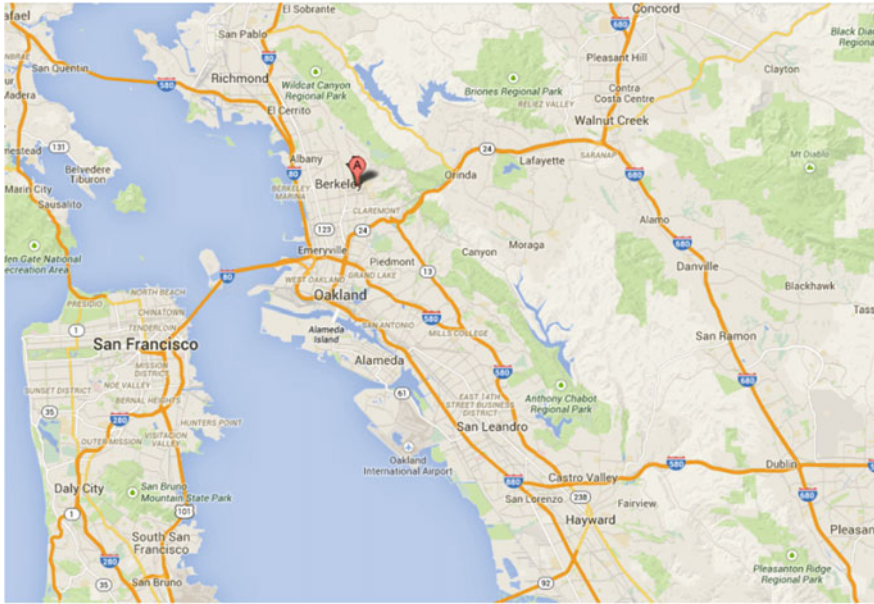


Fig. 11.16 Location of University of California, Berkeley (generated from Google Maps)

11.1.5 Logic Tree Method

The PSHA requires, either fully or partially probabilistically, extensive treatments of uncertainties in many aspects in a systematic and rational way. To perform this task, a logic tree [611, 612] is often employed to address the statistical uncertainties in the major elements of seismicity. This is because the best choices for elements of the seismic hazard model itself may not be clear, where various alternatives for the input parameters can be used, and each is assigned different weights that are interpreted as the relative likelihood of that particular model being correct and based on expert judgment, etc. [600]. There is still an ongoing debate on how logic tree should be interpreted [601]. This is more important for earthquakes that occur off known faults and with magnitudes smaller than a certain magnitude limit, say 6.5, so that they do not need to be modeled on faults. The seismicity may then be assumed as a random seismicity-derived source accounting for earthquakes that occur off known faults, and for moderate-size earthquakes that are not modeled on faults; the seismicity can also be modeled by gridded seismicity models based on historical earthquakes to account for the observation that larger earthquakes occur at or near clusters of previous smaller earthquakes [613, 614]; or modeled as uniform background zones to account for the future random seismicity in areas without historical seismicity documentation; or as special zones allowing for local variability in seismicity characteristics within a zone (e.g., changes in b -value in Gutenberg-Richter relationship as presented in Sect. 11.1.3, changes in maximum magnitude, and variations of uniform seismicity characteristics) [615]. The complexity

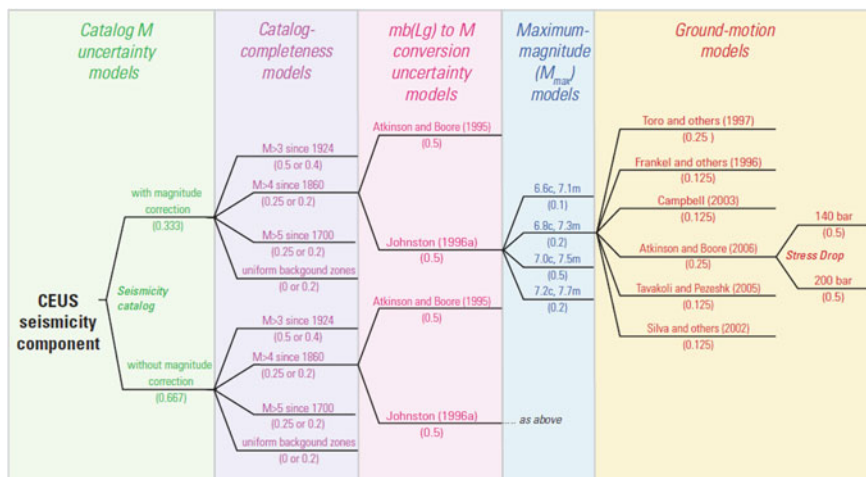


Fig. 11.17 An example of a logic tree for seismicity-derived hazard component in the Central and Eastern USA (courtesy of USGS)

of the logic tree is a function of several factors such as the scientific knowledge of the causes of earthquakes, the association of seismicity with geologic structure, the understanding of the geological behavior of individual seismic sources, the adequacy of the historical seismicity database [611].

An example of a logic tree is shown in Fig. 11.17. The nodes in the logic trees are sequenced to provide for the conditional aspect or dependencies of the seismic parameters and a logical development to determine the ground motions statistically. A series of branches represent various models. Each of those branches (models or values) is assigned a weighting factor, reflecting relative degree of belief in each model or value. And the weights are in practice treated as (subjective) probabilities. The branches follow a hierarchy from the left to the right, comprising five columns for this particular example, each of which represents various model categories to model the uncertainties in the aspects of source, magnitude, maximum magnitude, and attenuation model (ground motion models in Fig. 11.17). The relative likelihood of a combination of models along a complete hierarchy (from left to the right) is the product of the relative likelihood of each model (branch) in this combination, and the sum of the probability of all branches under each column is equal to 100%. Compared to a convenient PSHA procedure, the logic tree method requires a significantly higher computation effort, and this effort is dramatically increased with an increase in the number of branches.

It should be noted that PSHA is simple in principle, but complex in practice. During the process of performing a PSHA, even experts tend to adopt what is familiar to them, to prefer certain models for unclear reasons, and to have pre-conceived opinions on which results to expect. The results, such as seismic hazard curves, calculated from PSHA by different experts can be significantly different. This creates a significant problem on the reliability of the entire PSHA and greatly diminishes the advantages of PSHA over

DSHA. Therefore, in performing a PSHA, people need to be wary of dismissing any data, models, or methods [601].

11.2 Seismic Hazard Map

Seismic hazard studies are a common task for an engineering project relevant to seismic design. As discussed previously, based on a reduction (attenuation relationship) in ground motion mainly due to the distance from the fault rupture, and dividing the territory into regions of approximately equal peak ground motion, it uses contour lines to illustrate the ground motion parameters such as PGA or spectral values at specific period(s). Site ground motions are estimated for specific probability of ground motion exceedance within a design time period or for selected values of annual frequency or return period for ground motion exceedance.

A typical hazard map for designing building structures commonly specifies PGA that a site can expect during, for example, the next 50 years with 10% probability (of exceedance), corresponding to a return period of 475 years, and this return period is selected rather arbitrarily. Figure 11.18 shows the global seismic hazard map for sites onshore measured with PGA for a return period of 475 years. This map is especially useful for constructing the design spectra for structural analysis. Figure 11.19 shows an example of a rather rough seismic hazard map for offshore areas worldwide with a return period of 475 years. The PGA for return periods other than the one specified in the hazard map can be calculated based on the relationship between the ground motion intensities at two different return periods. This is typically reflected in a seismic hazard curve, as presented in Fig. 11.10.



Fig. 11.18 Global seismic hazard map for sites onshore with a return period of 475 years (courtesy of GSHAP)

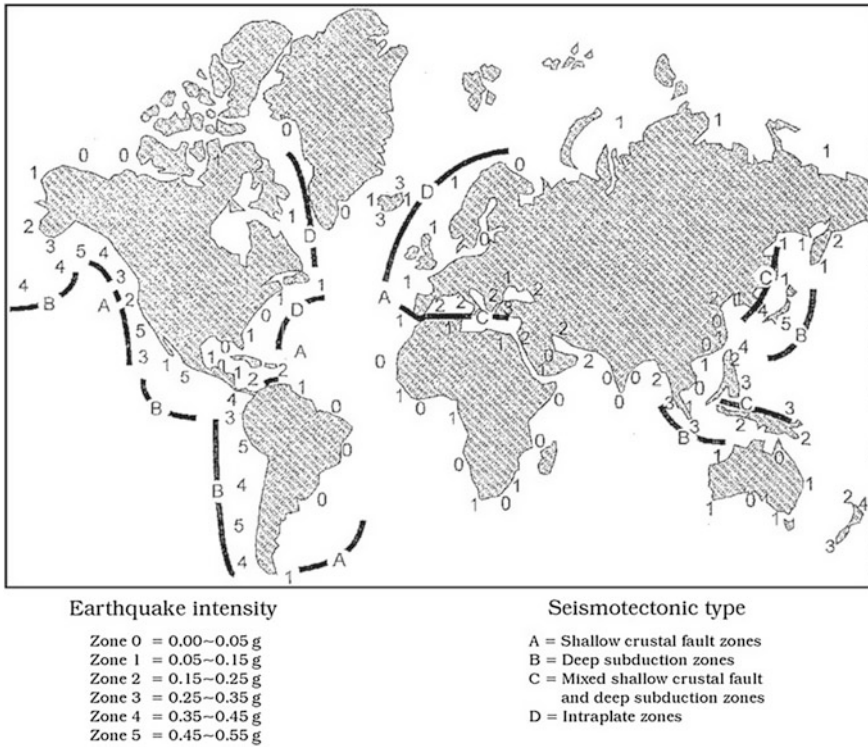


Fig. 11.19 Seismic hazard map for offshore areas worldwide with return period of 475 years [618]

In many seismic hazard maps, only the PGA at a single period is defined. By using this PGA to scale a normalized response spectral shape for each portion of the spectrum, a design response spectrum can be obtained. However, note that the response spectrum is period/frequency-dependent: It is a combination of contributions of various earthquake magnitudes at varying site-to-source distances, the ground motions of which attenuate differently at different period, and this is likely to result in a response spectrum having inconsistent or even unknown probabilities of exceedance at different periods [600]. As mentioned above, to have a constant probability of exceedance with various periods, PSHA at a number of periods/frequencies needs to be performed. Through ground motion attenuation functions, the spectral acceleration varied with period can be obtained. This results in a uniform hazard spectrum (UHS) [616]. For example, for seismic design of offshore structures, ISO 19901-2 [289] presents a coarse seismic hazard map for bedrock outcrop with a return period of 1000 years for each region, at spectral periods of both 0.2 and 1.0 s.

In the uniform hazard map, the short period end typically represents the rock motions attributed to moderate nearby earthquakes, while the long-period end

reflects the hazard from larger and more distant events. Again, readers need to bear in mind that the map typically does not resemble the response spectrum from any specific earthquake magnitude and distance. This method is already implemented in many seismic design codes. The ground attenuation functions are normally valid only within the period range below 4 s and occasionally below 10 s. Therefore, for periods larger than 4 s, the spectral acceleration is assumed to be inversely proportional to period and anchoring spectral demand at a period of 3 or 4 s. However, this assumption can be erroneous for near-fault sites as the effects of near-fault can significantly alter the spectral demand in longer period range.

Typically, it is assumed by the mappers that the structure at a site is on solid rock and the ground shaking is relatively fast (e.g., at 0.2 s period). The influence from different soil conditions within 20–50 m below ground surface is important in determining the exact seismic risk for a particular structure, and this can be accounted for in a site-response analysis or simplified selection of site coefficient. Different parts of the world use different techniques to develop seismic hazard maps [617]. Since this subject is more related to the science of seismology, it is not elaborated in the current text.

The US Geological Survey (USGS) National Hazard Mapping Project supported by NEHRP provides the latest peer reviewed and published seismic hazard data for the USA. These data are provided in probabilistic hazard maps and interactive Web-based query for certain ground motion parameters. The hazard maps are available at the USGS Web site for downloading or viewing, which correspond to PGA values, 0.2 and 1.0 s spectral acceleration values for probabilities of exceedance of 10% in 50 years and 2% in 50 years, corresponding to approximate return periods of 500 and 2500 years, respectively. Figure 11.20 shows the probabilistic maps for the 0.2 and 1.0 s spectral accelerations corresponding to a probability of exceedance of 2% in 50 years. The Web site also provides an interactive menu, where the user can obtain the mapped values for a given location specified by latitude/longitude. Ground motion values for the 48 states have been calculated for a grid spacing of 0.05°. Interpolated values are typically calculated using the four surrounding corner points. For guidance, 0.1° latitude is about 10.9 km; the 0.1° longitude varies, but for the 48 states is in the order of 9.0 km. It should be mentioned that the development of a global seismic map is a rather challenging task, mostly due to both the inconsistencies in the state of knowledge around the world, and social and political sensitivity on the part of various nations [619].

Unlike for areas onland, the seismic hazards in many offshore areas around the world remain unmapped. For example, in California, only approximately 50% of the coastline is mapped at resolution to permit hazard evaluations, but for the other regions the situation is even worse [622]. For example, in ISO 19901-2 [289], the seismic hazard maps in offshore areas are rather coarse for each region, as mentioned before. Therefore, extensive efforts are required to develop the seismic hazard maps for offshore areas.

Based on continuously updated knowledge in many aspects, such as newly discovered faults, updated GMPs/attenuation models, seismic design codes in some countries such as USA and Canada regularly update the seismic hazard maps, often at 5-year intervals.

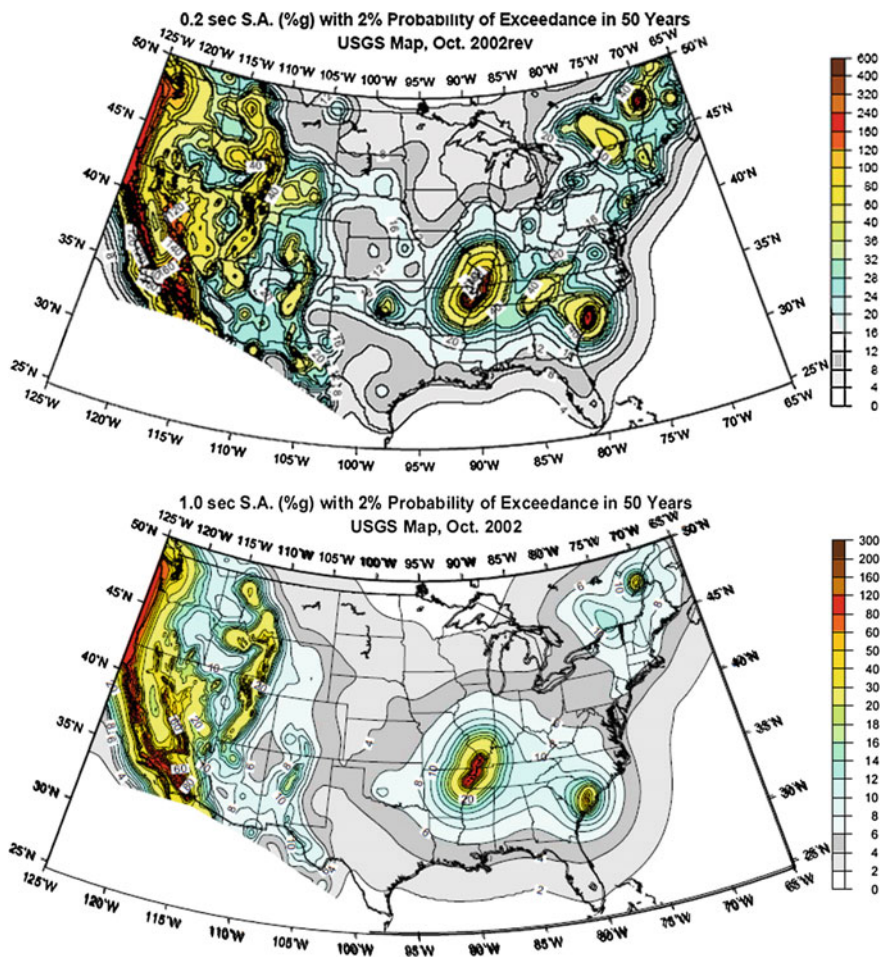


Fig. 11.20 0.2 s (upper) and 1.0 s (lower) spectral accelerations with 2% probability of exceedance in 50 years [620, 621] (courtesy of USGS)

11.3 Apply PSHA for Engineering Design

For practical structural design purposes, there are two approaches to utilizing the seismic hazard curve shown in Fig. 11.10.

In the first approach, based on the design ground motions with a specified mean annual frequency of exceedance, e.g., 0.002, a linear analysis is performed to calculate the responses of target structures, which is followed by checks with regard to an allowable stress design (Sect. 1.13.1) process to a set of forces reduced by factors that reflect the implicit member ultimate-strength/allowable-strength ratios, implicit nonlinear static over-strength ratios, and implicit nonlinear dynamic factors

that represent the system's ability to sustain nonlinear deformations without life-threatening behavior [623, 624]. Based on this method, the net effect of these conventional design criteria is to produce a frequency of collapse that is approximately half that for the design ground motions [625], i.e., a mean annual frequency of exceedance of 0.002 produces a mean annual frequency of collapse of about 0.001.

The second approach is to adopt checks in multiple levels of limit states [626]. Normally, two limit states are used. One corresponds to a lower linear design (to ensure little or no damage to a target infrastructure), which is associated with ground motion intensity having a minimum return period to ensure economic viability of a design as a function of the exposure level of a target structure, typically in the range of 50–200 years for offshore structures (e.g., 100 years for ultimate limit state required by Norsok N-003 [627] and 50–200 years for extreme level earthquake required by ISO 19901-2 [288, 289]; they mainly aim to perform checks for structures and foundations at component level). Another, more interestingly, corresponds to a system ductility level check (to ensure that no global failure modes or collapses, which can potentially lead to significant consequences such as loss of life or major environmental impact, occur) of an extreme rare event (abnormal level earthquake with a probability of exceedance P_{ALE} depending on the exposure level in ISO 19901-2 [288, 289] or an annual probability of exceedance of 0.0001 in Norsok N-003 [627], which mainly aims to perform checks for structures and foundations at a system level) associated with a target probability of exceedance P_e . The value of the target probability of exceedance depends on the structure exposure level, which is related to the life safety and consequence (which may be determined by the owner prior to the design of a new structure or the assessment of an existing structure, and must be agreed upon or given by the regulators where applicable), and the randomness and the uncertainties in seismic actions and structural resistance. The ground motion intensity in certain forms of expression (e.g., PGA or spectral acceleration etc.) at the target probability of exceedance P_e is normally given in seismic hazard curves (Fig. 11.10) or seismic hazard maps (Figs. 11.20 and 11.22). It should be noticed that, when selecting a decent exposure level, different from that of other environmental loadings such as ocean wave or wind loading that can be predicted in advance, it is not possible to predict a destructive earthquake with great certainty (earthquake prediction). Therefore, the relevant exposure level associated with evacuation (such as L2 exposure level in ISO 19900 offshore standard [288, 289]) is not feasible for a seismic event.

It is noted that the randomness and uncertainties in seismic actions and structural resistance are not captured in a seismic hazard curve and invariably increase the probability of failure, but they can affect the reliability of a structure, which is related to the uncertainty in structural resistance to earthquake actions. Therefore, in the second approach, the final annual probability of exceedance P_{ALE} should be lower than the target annual probability of failure P_f as shown in Fig. 11.21. The associated decrease of probability of occurrence (corresponding to an increase in the return period) primarily depends on two factors: the relative importance of these additional uncertainties and the local slope α_R of the seismic hazard curve at P_f

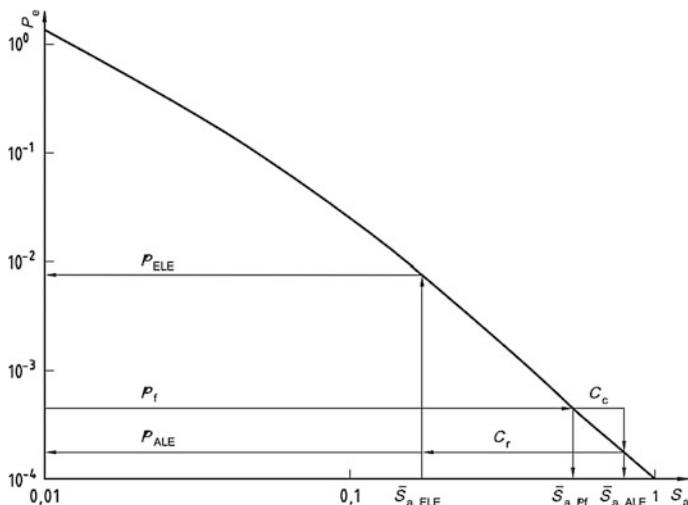


Fig. 11.21 Derivation of the ALE (abnormal level earthquake) and ELE (extreme level earthquake) spectral accelerations with associated probabilities of occurrence [289]

[626]. The local slope α_R is defined as the ratio of the spectral accelerations corresponding to two probability levels P_1 and P_3 as shown in Fig. 11.10, one either side of P_f (P_2 in Fig. 11.10), and they are typically one order of magnitude apart, while P_1 should preferably be close to P_f . The local slope (tangent) α_R of the seismic hazard curve depends on sites, structural period, and the target failure probability P_f (P_2 in Fig. 11.10). Therefore, in practice, an additional factor C_c (Fig. 11.21) can be used to determine the final annual probability of exceedance P_{ALE} , which would guarantee a failure probability P_f for the design of a structure fulfilling the abnormal level earthquake requirement. Table 11.4 lists the value of C_c given in ISO 19901-2 [288, 289], which is a function of the α_R . For example, a target P_f of 1/2500 defined for exposure L1 structures is an upper-bound value that structures will survive. In high seismic areas such as Japan and California, typical structural failures designed on this basis occur with an equivalent return period of 4000–5300 years, while in areas with less seismicity such as the Gulf of Mexico, the North Sea, and the Caspian Sea, these seismic events do not control the design and there is consequently no cost penalty for designs to meet a 10,000-year return period seismic event [628].

Table 11.4 Correction factor C_c (Fig. 11.21) in ISO 19901-2 [288, 289] to cover the randomness and uncertainties in seismic actions and structure resistance, which are not captured in the seismic hazard curve and invariably increase the probability of failure

α_R	1.75	2.0	2.5	3.0	3.5
C_c	1.20	1.15	1.12	1.10	1.10

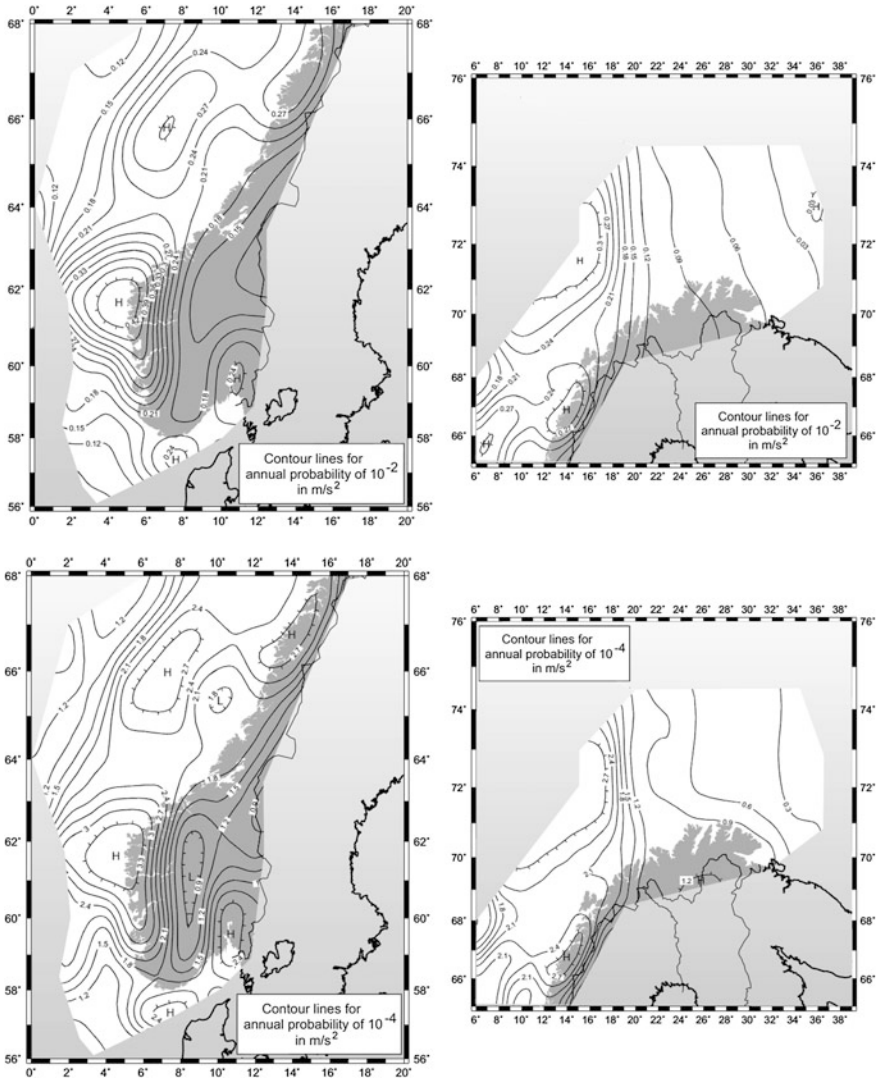


Fig. 11.22 Norwegian seismic zonation maps for 100-year (upper) and 10,000-year (lower) return periods of earthquake events in terms of PGA contour lines [629]

C_T in Fig. 11.21 is a seismic reserve capacity factor for structural systems that consider the static reserve strength and the ability to sustain large nonlinear deformations of each structure type (e.g., steel versus reinforced concrete). The C_T factor represents the ratio of spectral acceleration causing catastrophic system failure of the structure, to the extreme level earthquake (ELE) spectral acceleration. Its value can be estimated prior to the design of a structure in order to achieve an economic design that will resist damage due to an ELE and is at the same time

likely to meet the abnormal level earthquake (ALE) performance requirements. Values of C_r may be justified by prior detailed assessment of similar structures [288, 289]. In ISO offshore structural design codes, C_r ranges from 2.0 to 2.8 depending on the exposure level of the target structure, and the higher the exposure level, the higher the C_r factor will be. However, as mentioned before, it should be observed that C_r should lead to a return period for the ELE earthquake that is higher than the minimum ELE return period that is given to ensure economic viability of a design as a function of the exposure level of a target structure (e.g., 50–200 years depending on the exposure level of a target structure as required by ISO 19901-2 [288, 289]).

For infrastructures with low seismic risk, rather than performing a complicated PSHA to determine the seismic hazard curve, one may use the seismic hazard maps with one or a few given return periods (e.g., 1000 years in ISO 19901-2 [288, 289]) given by various design codes and standards. The final ground motion intensity (PGA or spectral accelerations at various periods) corresponding to the target probability of failure P_f can simply be derived from the ground motion intensity at the return period of what the given seismic hazard map implies to a return period $1/P_f$. This task can be carried out by multiplying the ground motion intensity given by the seismic hazard map with a scale factor, which is the ratio between the ground motion intensity corresponding to the target probability of failure P_f and the one implied by the seismic hazard map. This ratio is dependent on both the exposure level of the target structure and the slope of the seismic hazard curve in the target area (area dependent). If one compares the different seismic hazard curves for various locations in the USA as shown in Fig. 11.7, it is obvious that the slope of the seismic hazard curves for various locations can be quite different.

As mentioned before, with the same P_f , the seismic action in high-seismicity areas may be the dominant action for the structural and foundation design, while in low seismic regions, loads other than the seismic loads are governing loads for the structural and foundation design. This has a great influence on the structural and foundation concept selection and detailing.

11.4 Conditional Mean Spectrum

Ground motion selection is often associated with a target response spectrum. Traditionally, design target spectra for selection are often based on the uniform hazard spectrum (UHS) as discussed in Sect. 11.1.3. Readers may bear in mind that UHS is a combination of different magnitude of earthquakes with different sources and source-to-site distances. Each portion within UHS may represent a particular earthquake magnitude and a source-to-site distance. Therefore, UHS does not provide the probability of simultaneous occurrence of these parameters, i.e., UHS is significantly limited in its ability to reproduce any realistic single earthquake ground motion record. As an example, the left figure in Fig. 11.23 shows a smoothed curve being the predicted median spectral acceleration [which equals the

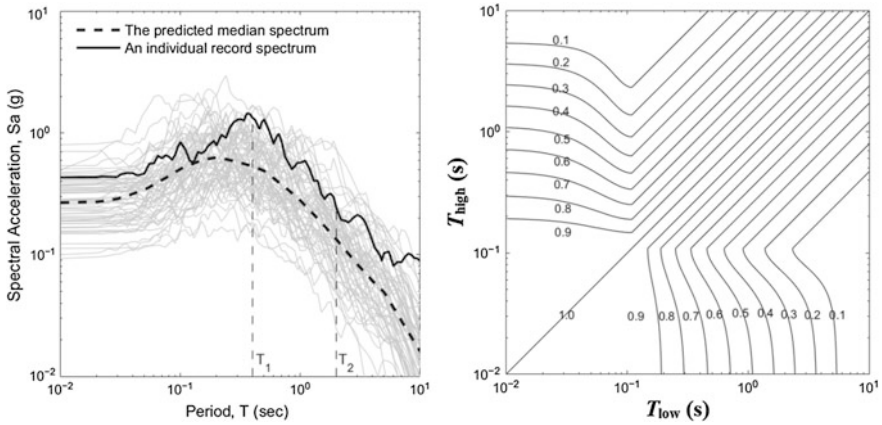


Fig. 11.23 An example of response spectrum variability and correlation with spectral acceleration variability (left) and correlation coefficient of spectral accelerations (right) [666]

exponential of the mean $\ln S_a(T)$. However, the curve does not represent the response spectrum of any actual (individual) ground motion. Instead, individual response spectrum shows variability in spectral amplitudes over different periods [666].

To solve this dilemma, the conditional mean spectrum (CMS) is proposed by Baker [591], which is essentially intended to calculate the joint distribution of ground motion intensity parameters. The resulting CMS has gradually come to be recommended by various PSHA tools and seismic design guidelines in the USA for land-based structures.

As a starting point to calculate the CMS, one may study the PSHA deaggregation for the spectral acceleration at 1.0 s with a return period of 475 years shown in the lower figure of Fig. 11.14, which indicates that the mean value of causal magnitude (M), source-to-site distance (R), and ε (ε is the number of standard deviations ($\sigma_{\ln Y}$) measured as the difference relative to the mean predicted ground motion $f(M, R, \theta)$, and it represents the observed variability in $\ln Y$) are 4.2 km, 6.84, and 0.75. Note that $\varepsilon(T)$ in this example is used to characterize the difference between the median of spectral acceleration at 1.0 s and 0.55 g amplitude associated with this deaggregation, and also by recognizing that $S_a(T)$ can be well represented by lognormal distribution. $\varepsilon(T)$ can then be expressed in terms of $\ln S_a(T)$:

$$\varepsilon(T) = \frac{\ln S_a(T) - \mu_{\ln S_a}(M, R, T)}{\sigma_{\ln S_a}(T)} \tag{11.23}$$

where $\mu_{\ln S_a}(M, R, T)$ and $\sigma_{\ln S_a}(T)$ are the mean and standard deviation of $\ln S_a(T)$, which can be determined from attenuation models; $\ln S_a(T)$ is the natural-log of the spectral acceleration at period T .

It is obvious that $\varepsilon(T)$ varies at different periods T , i.e., individual spectra are not all equally above the average of the spectral acceleration at all periods.

The predicted ground motion is typically quantified in terms of a median value if non-log of ground motion parameter is used, or mean value if natural-log of ground motion parameter $\ln Y$ is used.

Since the joint distribution follows a normal distribution, conditional distributions of one intensity measure parameter, given the other, are also normally distributed as shown in Fig. 11.24. Therefore, the conditional mean value of $\varepsilon(T)$ at a period T_i : $\varepsilon(T_i)$, given $\varepsilon(T^*)$, can be computed using only a linear correlation coefficient $\rho(T_i, T^*)$ between the two parameters:

$$\mu_{\varepsilon(T_i)|\varepsilon(T^*)} = \rho(T_i, T^*) \cdot \varepsilon(T^*) \quad (11.24)$$

where T^* is often taken to be equal to the most important eigenperiod of a target structure.

The correlation between the spectral values of different periods is found to be an intrinsic property of ground motions [667]. In Fig. 11.24, it is noticed that the slope of the solid line represents the correlation coefficient $\rho(T_i, T^*)$. The coefficient $\rho(T_i, T^*)$ can be determined in a manner similar to the way ground motion prediction models are calibrated. One may notice that $\rho(T_i, T^*)$ for different pairs of (T_i, T^*) may have different values, and practically, no $\rho(T_i, T^*)$ is equal to 1.0 (full correlation), even if $\rho(T_i, T^*)$ may be in the range of strong correlation, e.g., $\rho(T_i, T^*) > 0.7$. For a set of response spectra with N seismic ground motion records, the correlation can be calculated as:

$$\rho(T_i, T^*) = \frac{\sum_{k=1}^N \left[\ln S_a^{(k)}(T_i) - \overline{\ln S_a(T_i)} \right] \left[\ln S_a^{(k)}(T^*) - \overline{\ln S_a(T^*)} \right]}{\sqrt{\sum_{k=1}^N \left[\ln S_a^{(k)}(T_i) - \overline{\ln S_a(T_i)} \right]^2 \sum_{k=1}^N \left[\ln S_a^{(k)}(T^*) - \overline{\ln S_a(T^*)} \right]^2}} \quad (11.25)$$

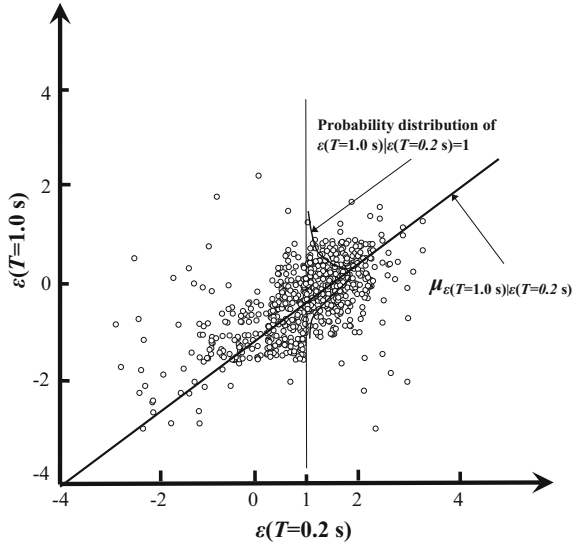
where $\ln S_a^{(k)}(T_i)$ is the $\ln S_a(T_i)$ obtained from the k th seismic ground motion record, and $\overline{\ln S_a(T_i)}$ is the mean value of $\ln S_a(T_i)$ for all N records.

For spectral period ranging from 0.05 to 5 s, Baker [591] recommended that:

$$\rho(T_{\text{low}}, T_{\text{high}}) = 1 - \cos \left[\frac{\pi}{2} - \left(0.359 + 0.163 I_{(T_{\text{low}} < 0.189)} \ln \frac{T_{\text{low}}}{0.189} \right) \ln \frac{T_{\text{high}}}{T_{\text{low}}} \right] \quad (11.26)$$

where T_{low} and T_{high} are the lower and higher of the two periods of interests, respectively [668]. The indicator function $I_{(T_{\text{low}} < 0.189)}$ is equal to 1 if $T_{\text{low}} < 0.189$ s and equal to 0 otherwise.

Fig. 11.24 A scatter plot of $\varepsilon(T)$ values from a large number of measured ground motions with $\varepsilon(T = 0.2 \text{ s})$ versus $\varepsilon(T = 1.0 \text{ s})$. Each dot represents the $\varepsilon(T = 1.0 \text{ s})$ given $\varepsilon(T = 0.2 \text{ s})$ values observed from a single ground motion measurement



For a wider spectral period ranging from 0.01 to 10 s, a more complicated expression can be adopted as proposed by Baker and Jayaram [669]:

$$\rho(T_{\text{low}}, T_{\text{high}}) = \begin{cases} \text{if } T_{\text{high}} < 0.109 \text{ s} & C_2 \\ \text{else if } T_{\text{low}} > 0.109 \text{ s} & C_1 \\ \text{else if } T_{\text{high}} < 0.2 \text{ s} & \min(C_2, C_4) \\ \text{else} & C_4 \end{cases} \quad (11.27)$$

where $C_1 = 1 - \cos\left\{\frac{\pi}{2} - 0.366 \ln \left[\frac{T_{\text{high}}}{\max(T_{\text{low}}, 0.109 \text{ s})} \right]\right\}$;

$$C_2 = \begin{cases} 1 - \left[0.105 \left(1 - \frac{1}{1 + e^{1007 T_{\text{high}}^{-5}}} \right) \left(\frac{T_{\text{high}} - T_{\text{low}}}{T_{\text{high}} - 0.0099 \text{ s}} \right) \right] & \text{if } T_{\text{high}} < 0.2 \text{ s}; \\ 0 & \text{otherwise} \end{cases}$$

$$C_3 = \begin{cases} C_2 & \text{if } T_{\text{high}} < 0.109 \text{ s} \\ C_1 & \text{otherwise} \end{cases}, \quad C_4 = C_1 - \{0.5(\sqrt{C_3} - C_3) [1 + \cos\left(\frac{\pi T_{\text{low}}}{0.109 \text{ s}}\right)]\}.$$

The right figure in Fig. 11.23 graphically represents the equations above. It is observed that the resulting covariance matrix is a symmetric positive definite matrix, allowing for a random sample generation, which is an important property for the proposed ground motion selection procedure [666].

Finally, the CMS can be computed by utilizing correlation across periods to estimate the expected spectral acceleration values at all periods T_i . Given the target spectral acceleration value at the period of interest T^* , i.e., based on the predicted mean $\mu \ln S_a(M, R, T_i)$, the predicted standard deviation $\sigma \ln S_a(T_i)$, $\varepsilon(T^*)$, as well as the correlation $\rho(T_i, T^*)$, given $\ln S_a(T^*)$, the CMS can then be calculated as:

$$\mu_{\ln S_a(T_i)|\ln S_a(T^*)} = \mu_{\ln S_a}(M, R, T_i) + \rho(T_i, T^*) \cdot \varepsilon(T^*)\sigma_{\ln S_a}(T_i) \tag{11.28}$$

where $\mu_{\ln S_a}(M, R, T_i)$ and $\sigma_{\ln S_a}(T_i)$ at period T_i can be calculated from the attenuation models, $M, R,$ and $\varepsilon(T^*)$ can be calculated by performing a PSHA deaggregation as shown in Figs. 11.13, 11.14, and 11.15. Commercial or free software (such as “Interactive Deaggregation” provided by USGS online) is available to perform such tasks.

The left figure in Fig. 11.25 shows an example of CMS given occurrence of $S_a(0.8\text{ s})$ values exceeded with 2, 10, and 50% probabilities in 50 years. The right figure shows the CMS conditioned at 0.2, 0.8, and 2 s together with their corresponding UHS. All have a 10% probability of exceedance in 50 years. By observing the figure, it is noted that the UHS has spectral accelerations higher than any conditional mean spectra. It has a peak value at the target period and decays toward the median spectrum in other periods. The decreasing process is based on a correlation model between the spectral acceleration values for all periods. This is because UHS is basically an envelope of spectral values associated with multiple earthquake scenarios rather than a single one, while the CMS acceleration values at their respective conditioning periods equal those of the UHS, and the CMS provides the information of the mean spectral shape only associated with the $S_a(T^*)$. The characteristics of CMS above remind readers that a single CMS conditional at a period T^* only reflects realistic ground motions being conditioned at this particular spectral period of T^* .

Because under strong ground motions, many structures are designed to have a degraded stiffness due to the development of plasticity, the natural period may be increased significantly. Furthermore, the natural period may not be the only period that dominates the seismic response of a structure. Therefore, to appropriately represent the response of the structure across the full period range to which it is sensitive and thoroughly assess the response, it is usually necessary to develop

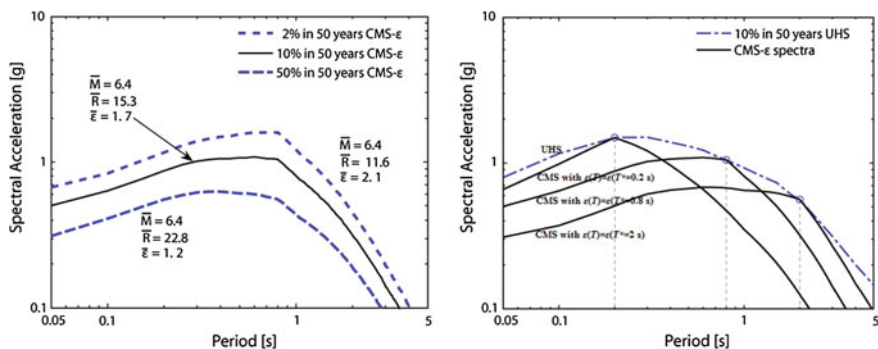


Fig. 11.25 Examples of conditional mean spectra, considering ε , for a site in Los Angeles, given occurrence of $S_a(0.8\text{ s})$ values exceeded with 2, 10, and 50% probabilities in 50 years (left) and CMS with S_a values at $T^* = 0.2, 0.8,$ and 2 s together with their corresponding UHS, all have a 10% probability of exceedance in 50 years (right) [670] (courtesy of USGS)

several CMSs at different periods. In such cases, it is not necessary that any of the selected periods represent the first mode period of the structure. Moreover, for some structures, there may not be any clearly defined first mode period, but this does not preclude the use of CMS to develop target spectra [671].

As recommended by Baker [591], four steps are necessary to compute a CMS that is likely to represent realistic earthquake records:

1. Determination of the targeted S_a at a given period, and the associated M , R , and ε . T^* is often taken as the most important eigenperiod(s) of the target structure. In practice, several T^* that are of interest should be used to generate several CMSs as mentioned above, so that the sensitivity of seismic response of the target structure can be identified.
2. Compute the mean and standard deviation of the response spectrum, given M and R .
3. Compute ε at other periods, given $\varepsilon(T^*)$.
4. Compute CMS.

Similar to the record selection to match a UHS, the ground motion matching a CMS can be performed by simply scaling the ground motion with a factor of S_c , so that the ground motion spectrum $S_{a\text{-record}}(T^*)$ at the single period T^* is matched to that of the CMS $S_a(T^*)$ [591]:

$$S_c = S_a(T^*)/S_{a\text{-record}}(T^*) \quad (11.29)$$

Alternatively, one may scale each ground motion so that the average response spectrum over the periods ($T_1 \dots T_N$) of interest is equal to the average of the target spectrum over the same periods [591]:

$$S_c = \frac{\sum_{j=1}^N S_a(T_j)}{\sum_{j=1}^N S_{a\text{-record}}(T_j)} \quad (11.30)$$

Structural responses from ground motions matching the CMS may be significantly smaller than the responses from ground motions matching the UHS having the same $S_a(T^*)$ level, even though occasionally the opposite trend may also be the case.

It is obvious that the establishment of a CMS is less demanding in terms of analysis efforts than deriving a UHS, even if the latter is much more widely adopted in earthquake engineering. However, because CMS is a newer concept than UHS—and also because, quite often, seismic criteria are defined before structures/facilities are designed, without the involvement of seismologists—most structural and geotechnical engineers are not capable of calculating a complete series of CMS with varied conditioning periods. This obstacle actually deters the application of CMS despite its obvious advantages over the UHS, and the majority of concurrent seismic design codes do not specify the requirement of using CMS.

In conclusion, it can be summarized that the advantages of using CMS is that it gives a more realistic and normally less conservative spectrum than UHS, and it utilizes deaggregation information such as magnitude, distance, and ε to predict spectral shape, and the spectrum changes in shape as one increases in amplitude. The drawbacks of CMS are that it is less widely available than UHS, and it requires a re-selection of ground motions as each case changes, the spectrum changes with increasing amplitude, requiring multiple ground motion sets.

Based on the concept of CMS, Mousavi et al. [672] proposed an E-CMS by modifying ε with a so-called Eta indicator as a control parameter to determine the spectral shape. They claimed that compared to a traditional CMS, the E-CMS is a more reliable predictor of nonlinear response of structures because the correlation of Eta and the structural response is stronger than the correlation between the conventional ε and the structural response [673]. Interested readers may read the sources cited above.

11.5 The Neo-deterministic Approach

Even though most seismic hazard analyses are based on PSHA, it is noticed that PSHA has several critical drawbacks [586]:

1. It is strongly dependent on available observations, which are too limited to constrain the probabilities associated with their occurrence and related shaking, due to long timescales involved in geological processes leading to the occurrence of a strong earthquake; therefore, the calculated seismic hazard maps resulting from extrapolations with data support may turn out to be poor approximation of reality.
2. It does not adequately consider the source and site effects, all implying some forms of physically unsound linear convolutive techniques using empirical GMPE [674], which cannot be applied when dealing with complex geological structures, because the ground motion generated by an earthquake can be formally described as the tensor product of the earthquake source tensor with the Green function of the medium [675].
3. It does not properly consider the temporal properties of seismicity, being based on the assumption of memoryless random occurrence of earthquakes [676], typically using a homogeneous Poisson distribution of earthquakes.
4. The traditional PSHA formulation involves a mathematical error that leads to equating the annual probability of exceedance (a dimensionless quantity) to the annual frequency or rate of exceedance (a dimensional quantity with the unit of 1/year). Even though the numbers are equivalent, 1% (0.01) in one year is not equal to 1% (0.01) per year because the dimensions are not equal. The reciprocal of 0.01 is 100 and means that the chance of occurrence is 1 in 100, not average recurrence time in years [677].

5. There is a lack of reliable data when treating strong earthquakes. For example, systematic comparisons of documented seismicity activities on the global scale indicate statistics contradictory to 10% of exceedance in 50 years, i.e., 50% difference for strong earthquakes about magnitude 6 and 90% for major events above magnitude 7.
6. A significant increase of mean return period often results in unrealistically high values of ground motion, especially in areas with low seismicity. This leads regulators or other authorities to promote the use of DSHA to complement the ground motion intensities obtained from PSHA.

Most of the drawbacks above have also been discussed by Geller et al. [678] and Mulargia et al. [679], who called for a new paradigm (different from PSHA) to evaluate seismic hazard.

To solve the limitations above, a scenario-based method for seismic hazard analysis, namely neo-deterministic seismic hazard assessment (NDSHA), is proposed by Panza [681]. In NDSHA, realistic and duly validated synthetic time series, accounting for physical processes of earthquake source generation, seismic wave propagation, and site effects, are used to construct earthquake scenarios in realistic three-dimensional media. In such a way, it is not necessary to resort to attenuation relations or any similar convolutive procedures, since NDSHA strongly relies on much more information than traditional PSHA studies do.

The method integrates the available information provided by the most updated seismological, geological, geophysical, and geotechnical databases for the site of interest, as well as advanced physical modeling techniques, to provide reliable and robust background for the development of a deterministic design basis. The uncertainties in earthquake scenario modeling are treated by systematically varying (within the range of related uncertainties) the modeling parameters associated with seismic sources and structural models, i.e., to perform a parametric study for assessing the effects of the parameters describing the mechanical properties of the propagation medium and of the earthquake focal mechanism (i.e., strike, dip, rake, depth). Therefore, the obtained hazard levels supplied by NDSHA are given as ranges over areas, whose values are consistent with the information content of the basic data. In regional/national studies, typical grid mesh has a density of about 25–50 km [680]; smaller uncertainties can be achieved in local studies [681, 682].

NDSHA starts from the available information on earth's structure, seismic sources, and the level of seismicity of the investigated area, thus addressing important issues that are largely omitted in the traditional PSHA or DSHA, such as how crustal properties affect attenuation. Therefore, ground motions in NDSHA are not calculated from excessively simplified GMPEs, but rather from complete synthetic seismograms, generating the related estimates PGA, PGV, and PGD or any other parameters relevant to seismic engineering (such as design ground acceleration), which can be extracted from the computed theoretical signals.

NDSHA defines the hazard from the envelope of the values of ground motion parameters determined considering a wide set of scenario earthquakes; accordingly,

the simplest product of this method is a map, where the maximum of a given seismic parameter is associated with each site [683].

The NDSHA procedure provides strong ground motion parameters based on the seismic wave propagation modeling at different scales: regional, national, and metropolitan—accounting for a wide set of possible seismic sources and for the available information about structural models. This scenario-based methodology relies on observable data being complemented by physical modeling techniques, which can be submitted to a formalized validation process.

PSHA was intended to estimate the probability that ground motion exceeds a given level from all earthquakes, whereas NDSHA estimates the ground motion from one or a set of scenario earthquakes. In other words, PSHA emphasizes the probability, which depends on the statistical models, whereas NDSHA emphasizes the ground motion, which depends on the physical models [683].

Figure 11.26 compares the PGA calculated from PSHA (return period is 475 years) and DSHA. The PSHA map, forming the basis for the Italian building code, predicts PGA to be less than 0.175 g, whereas the NDSHA map predicts values in the range 0.20–0.35 g, in good agreement with the observed motion that exceeded 0.25 g during the 6.1 magnitude of Emilia earthquake that occurred on May 20, 2012. Comparison between PSHA and NDSHA estimates in terms of macroseismic intensity [684] indicates that the epicentral area of the Emilia earthquake is in a zone, where PSHA predicted an intensity (as low as VIII on the modified Mercalli scale) at least one unit less than the NDSHA prediction, the latter

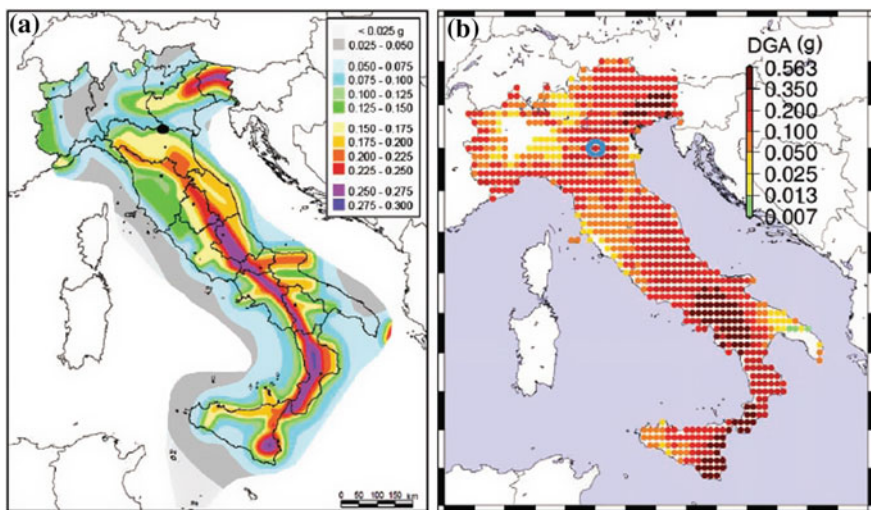


Fig. 11.26 Seismic hazard maps of Italy, developed using **a** PSHA with a return period of 475 years (figure from Gruppo di Lavoro, Redazione della mappa di pericolosità sismica, rapporto conclusivo, 2004) and **b** NDSHA, where design ground acceleration is equivalent to PGA [684] (the epicenter of the Emilia earthquake is marked with a dot in the left figure and a circle in the right figure)

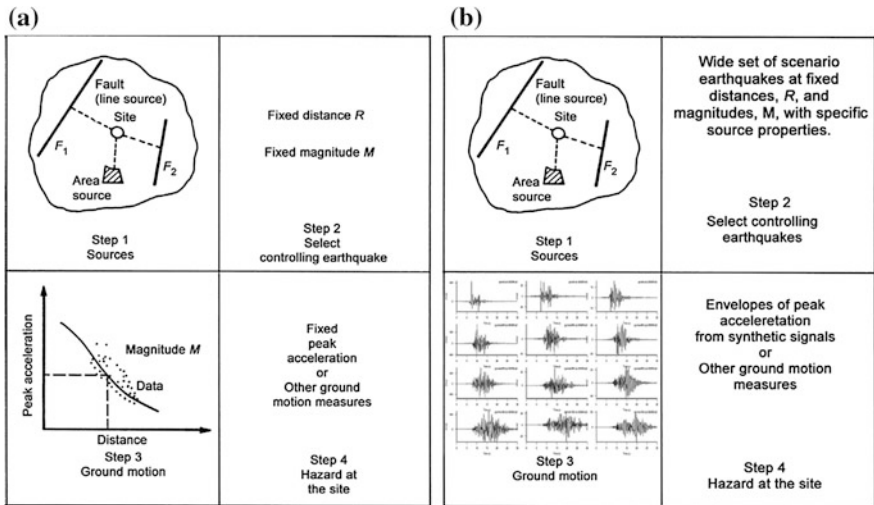


Fig. 11.27 Basic steps of **a** classical DSHA and **b** NDSHA [586]

of which is closer to the actual intensity of the earthquake. The underestimation of the PGA associated with PSHA is caused by the fact that the PSHA map in this figure gives a PGA with a return period of 475 years. If the return period is increased to 700 years, the PSHA can result in a PGA matching the observed PGA during the Emilia earthquake. This feature has made PSHA the subject of long-standing debate [685, 686], pointing to errors in the mathematics and assumptions of PSHA [687].

Figure 11.27 compares the differences of basic steps between classical DSHA and NDSHA. Obviously, NDSHA distinguishes itself from the classical DSHA by modeling seismic wave propagation rather than empirical attenuation relationship. NDSHA derives earthquake ground motions as a tensor product (of earthquake source tensor with Green function for the medium), and it avoids using an approximate scalar quantity implied in the GMPEs and/or attenuation relationships [586]:

The standard NDSHA provides the seismic hazard as the maximum ground shaking at a site, computed considering a large set of scenario earthquakes, including the maximum credible earthquake, i.e., it is not associated with the frequency of occurrence of the calculated ground motions. Recent research on NDSHA also proposes to account for the earthquake recurrence, which provides seismic hazard at specified return period(s), permitting a direct comparison with the seismic hazard generated by PSHA [683].

11.6 Forecasting “Unpredictable” Extremes

Most physical, natural, and social phenomena can be characterized by power law statistics, which is a functional relationship between two quantities, where one quantity varies as a power of another. This is usually used to model data of an event, whose frequency varies as a power of some attribute of that event, as illustrated in Fig. 11.28. This is based on the assumption that small, large, and extreme events belong to the same population, the same distribution, and reflect the same underlying mechanisms.

Figure 11.29 shows the earthquake magnitude distribution for the region of Southern California, which is measured as the number of earthquakes per year with magnitude ($M > m$). Two portions of distributions that occurred deviate from the Gutenberg-Richter rule: at low magnitudes and at very high magnitudes range, as

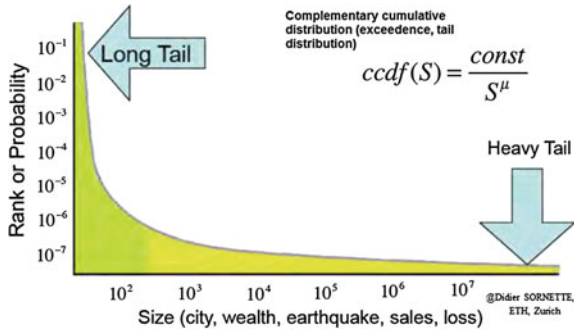


Fig. 11.28 Illustration of power law that assumes that both small and extreme value events follow the power law (courtesy of Didier Sornette, ETH Zurich)

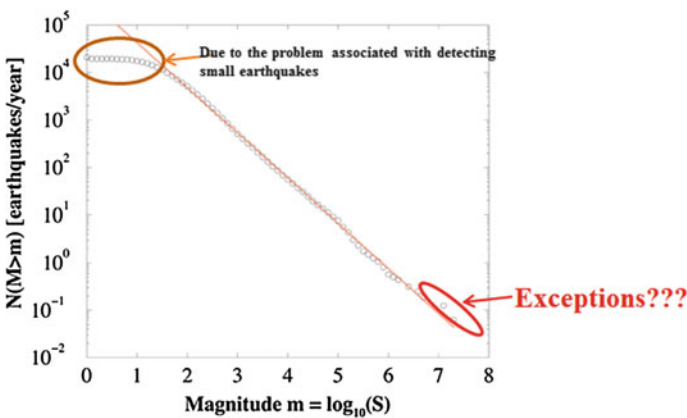


Fig. 11.29 Earthquake magnitude distribution showing a power law behavior over six decades; the solid line in the graph follows the Gutenberg-Richter model: $\text{Log}_{10}N_c(M > m) = a - bm$, where $b = 1$; the dots represent the earthquake statistics based on the actual occurrence (courtesy of Didier Sornette, ETH Zurich, Switzerland)

shown in the figure. The mismatch at the low magnitude portion is caused by the fact that many small-scale earthquakes cannot be detected. However, it is difficult to find a convincing explanation of the mismatch at large magnitude of earthquakes. The major school of thought considers this mismatch to be the result of exceptions (such as “black swans”) that are therefore not predictable, which is often called “self-organized criticality” introduced by Bak [688]. Therefore, major catastrophes are considered unpredictable as they are regarded as events that start small and do not stop growing to develop into large or extreme sizes [688, 689].

This view is particularly pessimistic, and alarming if true, as it casts a strong doubt on possibilities of precise hazard prediction, with all the societal consequences of this. As stated by Sornette and Ouillon [689], this view is dangerous as it promotes an attitude of irresponsibility: In a world where catastrophes (in human-controlled activities, for instance) are pure surprises, no one can be responsible. In response to this challenge, they proposed the concept of dragon-kings, which are defined as extreme events that do not belong to the same population as other events, in a precise quantitative and mechanistic sense that will be developed. The notion “dragon-king” stems from a combination of the supernatural powers of dragons and the anomaly of a king’s wealth relative to that of his subjects. Essentially, dragon-kings appear as a result of amplifying mechanisms that are not necessarily fully active for the rest of the population [690]. By following this thought, dragon-kings are defined with specific properties and signatures having unique characteristics close to a regime transition, where a system bifurcates through the variation of a single or a few control parameters.

The concept of dragon-kings is widely used in various fields of applications, such as financial economics, geophysics, materials science, population geography, hydrodynamics, and even brain medicine.

In parallel to the development of the concept of dragon-kings, based on the idea of “filling in” a heavy/fat tailed (scaling) distribution, Rundle et al. [691] also proposed the Natural-Time-Weibull (NTW) model to predict extreme earthquake magnitude distribution.

Part III
Shallow Foundations

Chapter 12

Bearing Capacity of Shallow Foundations

12.1 Introduction

Foundations are critical components for ensuring stability, transferring loads from structures to base soils or rocks. There are typically two types of foundations, shallow and deep foundations, as shown in Fig. 12.1.

Deep foundations include piles, piers, and drilled shafts, among which piles are the most extensively used. Piles are generally driven into the ground in situ or put in place using drilling or excavation; recently, piles have also been hydraulically jacked into the ground. Deep foundations can be made out of timber, steel, reinforced concrete and prestressed concrete. See Chap. 14 for details.

Different from deep foundations that transfer loads to a subsurface layer or a range of depths inside soils, shallow foundations transfer structural loads to soils close to the ground surface. The embedment depth for shallow foundations is less than the minimum lateral dimension of the foundation element, though recent research has suggested that foundations with a depth, measured from the ground surface, of less than 3–4 times their minimum lateral dimension may also be defined as shallow foundations [692]. Shallow foundations include spread footing foundations, mat-slab foundations, slab-on-grade foundations, pad foundations, rubble trench foundations (which uses loose stone or rubble to minimize the use of concrete and improve drainage [693]), and earth-bag foundations.

In shallow foundations, there are mainly three types of footing: strip (wall) footing, spread (pad) footing, and combined footing. As shown in Fig. 12.2, strip footing is laid along the length of the wall. Usually, they cantilever on either side of the wall. A spread footing foundation has a wider bottom portion than the load-bearing foundation walls as shown in Fig. 12.2. This wider part “spreads” the weight of the structure over larger areas for greater stability. As an extension of spread footing, a combined footing is a large continuous thick slab provided to support rows of column and walls above, as shown in Fig. 21.12. Quite often, a combined footing is designed to support columns with unequal loads, and the

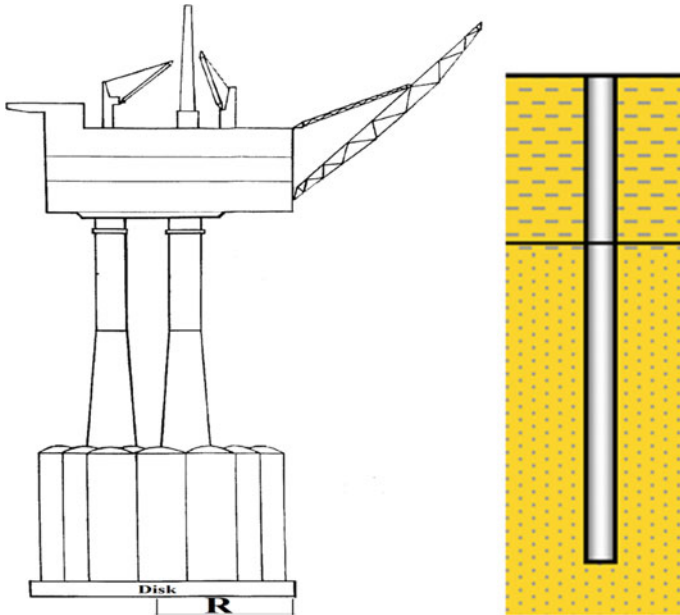


Fig. 12.1 A GBS structure with a shallow foundation directly resting on soils (left, courtesy of Aker Solutions) and a pile as a type of deep foundation penetrating into soils (right)

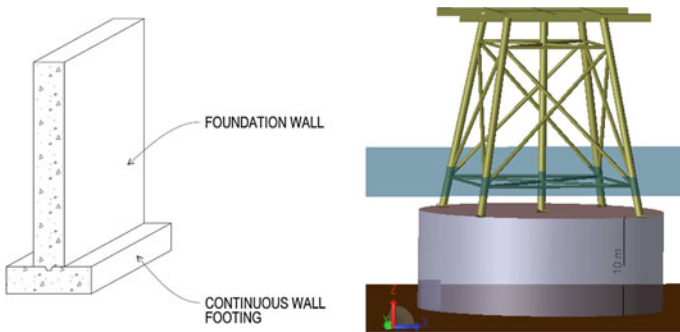


Fig. 12.2 Examples of strip footing (left) and spread footing (right)

resultant applied loads do not coincide with the centroid of the footing. The consequent soil pressure would then be non-uniform. Another situation in which a combined footing can become a rather efficient solution is when there are two columns that are close to each other and the two isolated footings' stress zones in the soil areas overlap. Combined footing can be constructed in the form of rectangular footing, trapezoidal footing, and cantilever footing. For an economical design, it is preferred to have square footing for vertical loads and rectangular

footing for columns carrying moment. When more than one line of columns is supported by a combined footing, it is called a mat or raft foundation. If the total area of the spread footing exceeds half of the building (structure horizontal) area, mat footing is economical. It is also often used for soils having low bearing capacities.

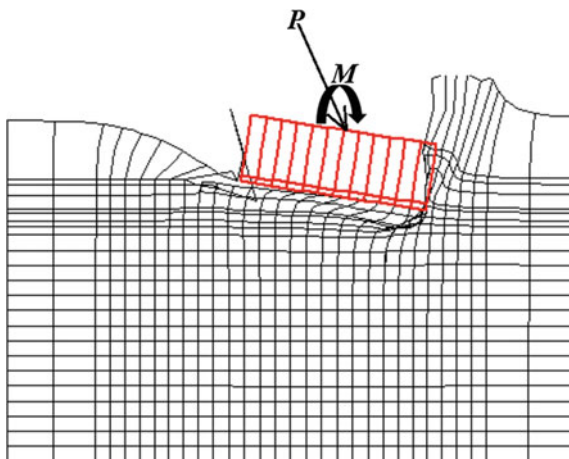
The modeling of shallow foundation accounting for its dynamics will be discussed in Chap. 13.

12.2 Failure of Shallow Foundations

Shallow foundations can fail due to (1) instability, including failure due to bearing, overturning, sliding, or a combination of these; (2) static foundation deformations, including potential damages to the foundation itself, its supported structures or attached facilities; (3) dynamic foundation characteristics, including structural responses due to the influence of foundations subjected to dynamic loading; (4) damage to foundation or its supported structure caused by scour or piping actions due to wave pressures (Sect. 12.9) [791].

Figure 12.3 shows a calculated failure mode of a GBS foundation due to the seismic loading (P and M) associated with a return period of 10,000 years. The soil below the foundation is dominated by clays. Finite element analyses are performed using two-dimensional plane-strain elements with added side shear, which is calibrated against three-dimensional finite element analysis. The GBS foundation (Fig. 12.4) is modeled with an equivalent circular area of 11,000 m². Load-displacement curves of the foundation due to two seismic load cases are plotted in Fig. 12.5, which indicate that the maximum load scaling factors when the foundation fails are 1.43 and 1.50 for the two load cases.

Fig. 12.3 Illustration of a typical failure mode for a GBS foundation subject to inclined loading P and overturning moment M determined by two-dimensional finite element analysis (courtesy of Aker Solutions and NGI)



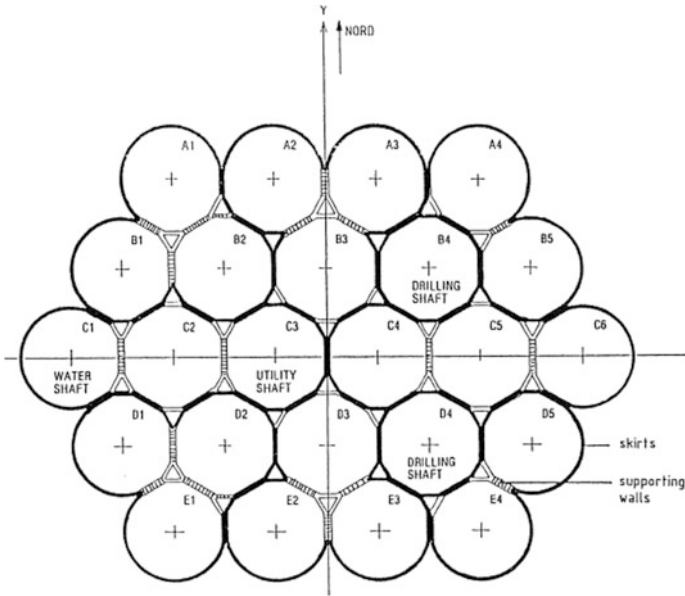


Fig. 12.4 Foundation plan of the GBS (courtesy of Aker Solutions)

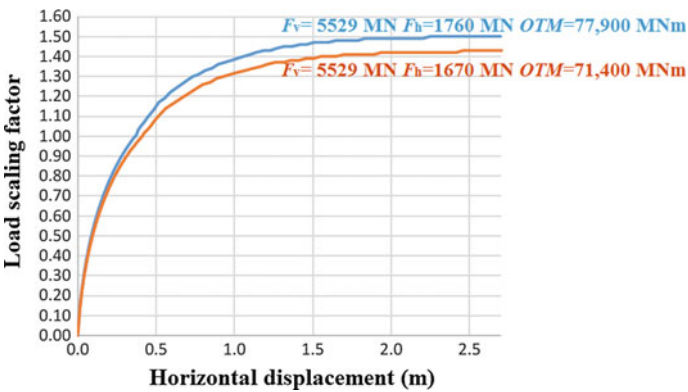


Fig. 12.5 Load-horizontal displacement for the GBS foundation due to two seismic load cases (F_v , F_h , and OTM are vertical forces, horizontal forces, and overturning moment applied on the GBS, respectively) (courtesy of Aker Solutions and NGI)

Failure modes of bearing capacity for shallow foundations can be one of the following types: general shear, local shear, or punching shear failure. In general, which failure mode occurs depends on the relative compressibility of soils, footing embedment, loading conditions, and drainage, etc.

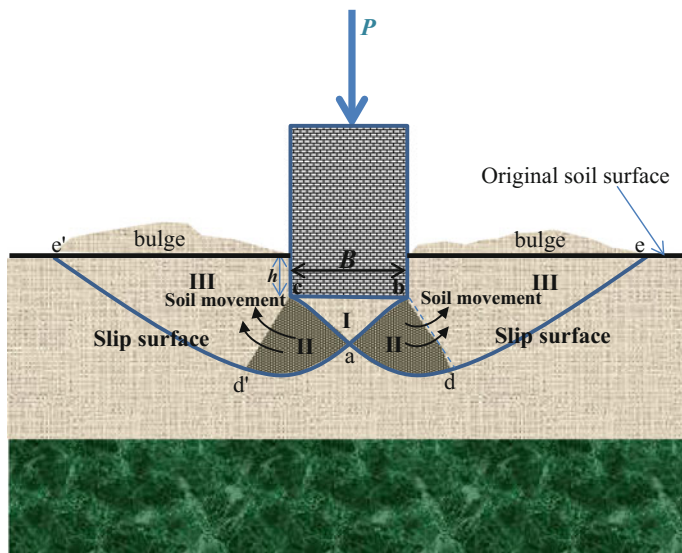


Fig. 12.6 A general shear failure scenario with slip surfaces at the boundary of a “Prandtl’s wedges” due to the vertical loading P

As shown in Figs. 12.6 and 12.7, general shear failure has a well-defined rupture pattern of total soil from below the footing to the ground surface, consisting of three zones: zone I is also called the active zone or elastic zone, and is normally located just below the foundation; zone II is also called the transition zone or radial shear zone, located between the active and passive zone, in zone II the rupture lines ad and ad' are arcs of a logarithmic spiral; and zone III is also called the passive zone, it is near the ground surface and located just beside the foundation, in zone III the lines de and $d'e'$ are straight. Both lines ca and ba form an angle ϕ with the horizontal. Lines bd , cd' , de , $d'e'$ form angles of $\pm(90^\circ + \phi)/2$ with the horizontal. Each zone has a simplified force path on its boundary, and the failure is assumed to occur when slips occur at the boundary (slip surface) of each shape; the normal and tangent (friction) forces can then be calculated. In general failure mode, under the vertical load P , the foundation settles, pushing a triangular wedge-shape soil zone (zone I) down, followed by a subsequent movement of zones II and III sideways and then upward. A clear slip surface is then formed at the ultimate distributed pressure level of q_u (also called the ultimate bearing capacity), and the soil passes into a state of plastic equilibrium and failure occurs by sliding. The soil on one or both sides of the foundation bulges, causing slip surfaces to be extended to the ground surface.

The failure pattern in local shear failure, however, consists of only clearly defined rupture surfaces beneath the footing (zones I and II) without a clearly defined failure pattern on the sides of the footing (zone III), i.e., the slip surface ends inside the soil, even if some signs of soil bulging can be observed. Actually,

Fig. 12.7 A failure scenario due to inclined loading P

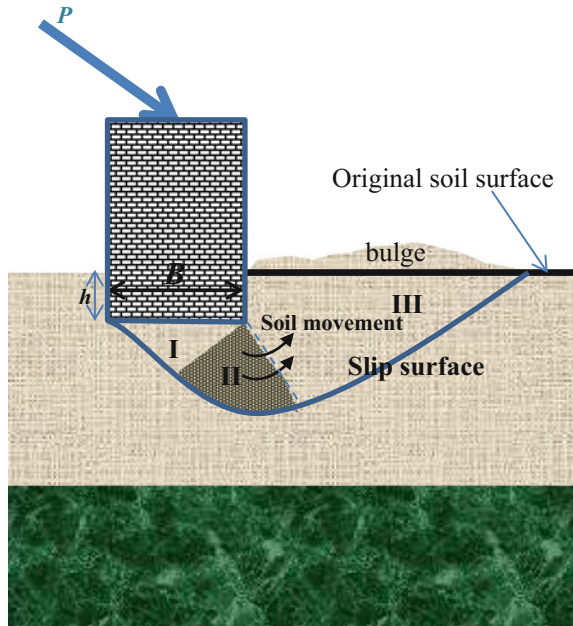
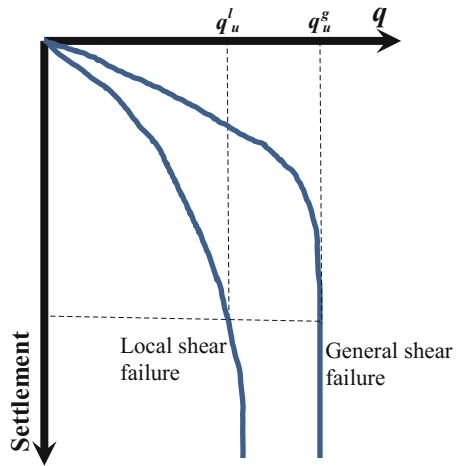


Fig. 12.8 Pressure load-settlement relationship showing general shear failure and local shear failure



local shear failure can be considered as a transitional phase between general shear and punching shear and is often associated with loose to medium dense sand.

Figure 12.8 shows a typical load-settlement relationship for a rectangular footing with a vertical distributed load pressure q applied on the soil. Initially, both the general and local shear failure curve show a dramatic increase in settlement.

However, when the general shear failure occurs corresponding to an ultimate load level q_u^g , the foundation experiences a significant settlement without any increase of loading. When the local shear failure occurs corresponding to an ultimate local shear strength load level of $q_u^l (< q_u^g)$, the settlement-load curve suddenly becomes steep, exhibiting a significant increase in settlement but still a slight increase in load q .

Punching shear failure only shows a clear rupture pattern within zone I, as shown in Fig. 12.9. It is usually associated with a large settlement and does not mobilize shear stresses in zones II and III [694]. Soils outside the loaded area remain relatively uninvolved, and there is minimal movement of soils on both sides of the footing.

As presented previously, shear failure occurs when both friction (for sand and clay) and cohesive (for clay) resistance together are insufficient to resist the shear loading.

Based on the general shear failure scenario shown in Fig. 12.6, the failure may occur with normal stresses at $\pm(90^\circ + \phi)/2$ to the maximum compressive principal stress, i.e., a slip plane at $\pm(90^\circ - \phi)/2$ to the maximum principal stress. Here, ϕ is defined as:

$$\sin \phi = \frac{\sigma_1 - \sigma_2}{\sigma_1 + \sigma_2} \quad (12.1)$$

where σ_1 and σ_2 are the maximum and minimum principal stress, respectively.

This enables a quick estimation by using the passive and active wedges as shown in Fig. 12.10.

Actually, when a shallow foundation is deeply embedded into soils, with an increase in overburden pressure, the failure mode changes from general to local or punch shear, regardless of soil compressibility [695]. This increases the complexity of the assessment of the ultimate capacity of shallow foundations. By performing a

Fig. 12.9 Punching failure

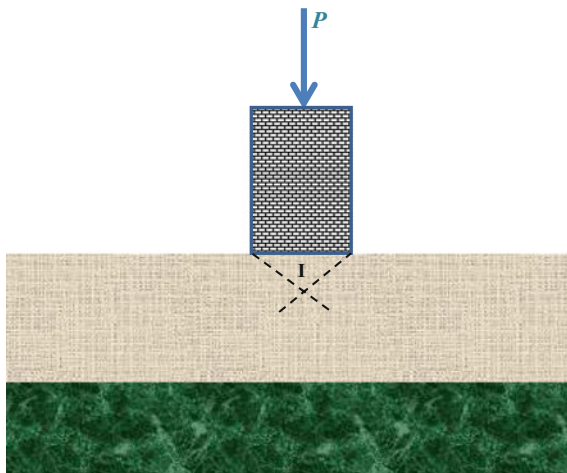


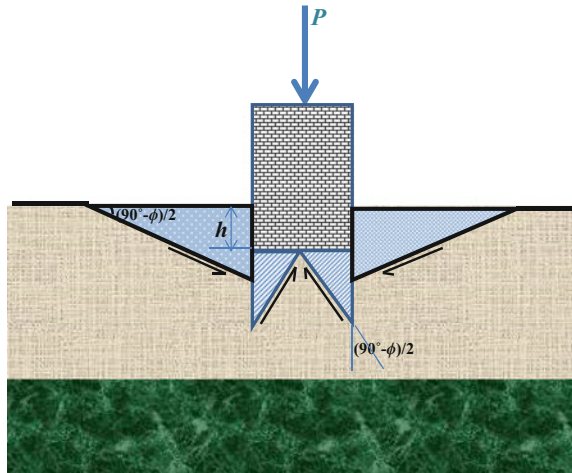


Fig. 12.10 A simplified bearing capacity failure scenario with passive and active wedges (passive wedge: ; active wedge: )



series of load tests, Vesic [697, 698] and De Beer [698] suggested that the ultimate load occurs on footings at the breakpoint of the load-settlement curve. Even though it is possible/convenient to formulate a general bearing capacity equation for a loaded footing failing in the general shear mode, it is difficult to formulate the equations for the other two failure modes because of their poorly defined rupture surfaces. Section 12.3.2 presents simple methods to approximate the bearing capacity due to local and punching shear failure. Furthermore, it is important to know the magnitude of settlements of footings required to mobilize the ultimate load.

In practice, the formulation of bearing capacity of shallow foundations can be established by setting up and solving the equilibrium of soils under foundation pressures, as will be discussed in Sects. 12.3 and 12.4, and the soil's constitutive relationship can normally be assumed to follow a rigid-plastic behavior [699, 700]. Consequently, only approximate methods are used in engineering practice, even though a more complex elastic-plastic constitutive relationship represents more realistic soil behavior.

Subject to seismic loading, shallow foundations shall be designed for both the inertia forces transferred from superstructures into the foundations in the form of axial and horizontal forces and moments (inertia loads), and soil deformations arising from the passage of seismic waves (kinematic loads). However, subjected to significant ocean storm loading, foundations are designed to resist wave loads and inertia loads transferred from superstructures.

Table 12.1 provides a list of soil data required and testing considerations for the design of shallow foundations.

To avoid uneconomical designs, the ultimate bearing capacity for a shallow foundation should not be very high compared with the net loading intensity.

It should also be mentioned that the construction of shallow foundations should neither overload the adjacent foundations and structures, nor render any instability

Table 12.1 Soil data required and testing considerations for shallow foundations [41, 701]

Engineering evaluations	Required information for analyses	Field testing	Laboratory testing
Bearing capacity Settlement (magnitude and rate) Shrink/swell of foundation soils (natural soils or embankment fill) Overall slope stability Scour Liquefaction Frost heave	Subsurface profile (soil, groundwater, rock) Shear strength parameters Compressibility parameters (including consolidation, shrink/swell potential, and elastic modulus) Frost depth Stress history (present and past vertical effective stresses) Depth of seasonal moisture change Unit weights Geologic mapping including orientation and characteristics of rock discontinuities	<ul style="list-style-type: none"> • SPT (granular soils) • CPT • PMT • Dilatometer • Rock coring (RQD) • Plate load testing • Geophysical testing 	<ul style="list-style-type: none"> • 1D Oedometer tests • Soil/rock shear tests • Grain size distribution • Atterberg limits • Specific gravity • Moisture content • Unit weight • Organic content • Collapse/swell potential tests • Intact rock modulus • Point load strength test

to any hillside or slope, nor interfere with any drain, nullah (open channel), sewer, or other services in its vicinity.

12.3 Bearing Capacity of Drained Soil

12.3.1 Bearing Capacity Due to General Shear Failure

For fully drained conditions, based on the method presented by Prandtl [702] to study the penetration of hard bodies into softer materials, Terzaghi [703] proposed that the bearing capacity of shallow foundations at a depth of h measured from the ground surface can be determined as an ultimate effective pressure q_u' , reflecting the general shear failure mode shown in Fig. 12.6:

$$q_u' = cN_c s_c d_c i_c + \gamma' h N_q s_q d_q i_q + \frac{\gamma' B'}{2} N_\gamma s_\gamma d_\gamma i_\gamma \quad (12.2)$$

where the ultimate bearing capacity q_u' is defined as the bearing stress that causes a sudden catastrophic failure of the foundation; c is the soil attraction calculated as the effective cohesion intercept of Mohr's envelope, and for cohesionless soil, $c = 0$; B' is the effective width of a rectangular foundation; γ' is the effective unit weight of the soil (in the second term in the right-hand side of the equation above, γ'

is the effective unit weight for soils located above the bottom of the footing; while for the third term, γ' is defined as the effective unit weight for soils located below the footing), see Sect. 1.4 for the definition of the effective unit weight; N_γ , N_q , and N_c are bearing capacity factors, representing the influence from unit weight, overburden pressure, and cohesion, respectively, and they are functions of friction angle of sands and can be checked from relevant geotechnical handbooks, Fig. 12.11 presents recommended values by NAVFAC DM-7.2 [705]; s_γ , s_q , and s_c are shape factors, for rectangular footings, with a width of B and length of L , $s_\gamma = 0.8$, $s_q = 1.0$, and $s_c = [1 + 0.3(B/L)]$; d_γ , d_q , and d_c are depth factors; i_γ , i_q , and i_c are load inclination factors; all the factors above can be found from relevant geotechnical handbooks; h is the depth of embedment of the foundation.

In the right-hand side of the equation above, the first term $cN_c s_c d_c i_c$ accounts for the cohesive shear strength of the soil located below the strip footing; if the soil below the footing is cohesionless (i.e., $c = 0$), this term is zero. The second term $\gamma' h N_q s_q d_q i_q$ accounts for the soil located above the bottom of the footing. The value of $\gamma' h$ indicates a beneficial surcharge pressure to increase the bearing capacity of the footing. If the footing is constructed at ground surface (i.e., $h = 0$), this term is then zero. This term indicates that the deeper the footing, the greater the ultimate bearing capacity of the footing. The third term $\frac{\gamma' B'}{2} N_\gamma s_\gamma d_\gamma i_\gamma$ accounts for the frictional shear strength of the soil located below the strip footing. The friction angle is accounted for by the bearing capacity factor N_γ .

For calculating the second and the third term, the highest anticipated ground water table should normally be used to calculate the effective unit weight. If the ground water table is at a depth D below the bottom of the foundation, the effective unit weight γ' of the soil in the third term may be replaced by a weighted average unit weight γ_{avg} :

$$\gamma_{\text{avg}} = \begin{cases} \frac{1}{B} [\gamma_{\text{sd}} D + \gamma' (B - D)] & \text{for } D \leq B \\ \gamma_{\text{sd}} & \text{for } D > B \end{cases} \quad (12.3)$$

where γ_{sd} is the unit weight of the dry soil, see Sect. 1.4 for its definition; B is the width of the foundation.

The bearing capacity according to the equation above is based on the following assumptions [704]:

1. The footing base is rough and the soil beneath the base is incompressible, implying that the wedge abc (zone I in Fig. 12.6) is no longer an active Rankine zone but is in an elastic state. Consequently, zone I must move together with the footing base.
2. Zone II (Fig. 12.6) is an immediate zone lying on a log spiral arc ad .
3. Zone III (Fig. 12.6) is a passive Rankine zone in a plastic state bounded by a straight line ed .
4. The shear resistance along bd is neglected because the equation is applied for footings where $h < B$.

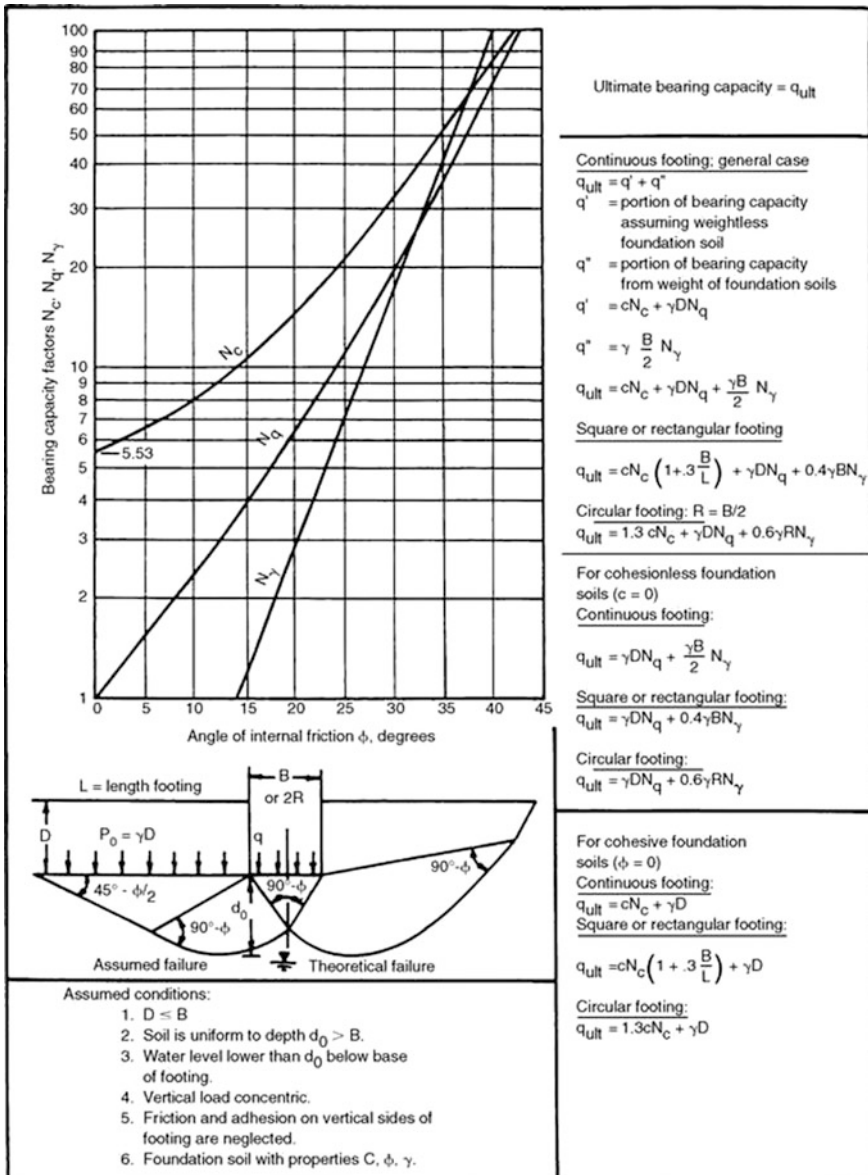


Fig. 12.11 Values of bearing capacity factors $N_\gamma, N_q,$ and N_c for shallow footings with concentric loads given by NAVFAC DM-7.2 [705] (courtesy of Naval Facilities Engineering Command)

The bearing capacity equation above can be simplified as:

$$q'_u = cN_cK_c + \gamma'hN_qK_q + \frac{\gamma'B'}{2}N_\gamma K_\gamma \quad (12.4)$$

where K_γ , K_q , and K_c are correction factors accounting for various effects associated with both loading and foundation form, such as load inclination, footing shape, depth of embedment, inclination of base, and inclination of ground surface, and they can also be checked from various geotechnical engineering handbooks. The subscripts c , q , and γ refer to the particular terms in the equation.

For a detailed elaboration to determine the parameters in the equation above, readers may refer to sources [692, 694] and API standard [791].

Load eccentricity decreases the ultimate vertical load that a footing can withstand. This effect is accounted for by a reduction in the effective area of the footing. To calculate the effective area, the effective width B' and the effective length L' of a rectangular foundation dependent on the load eccentricity can be calculated as:

$$B' = B - 2e_1 \quad (12.5)$$

$$L' = L - 2e_2 \quad (12.6)$$

where B and L is the width (minimum lateral foundation dimension as shown in Fig. 12.6) and length of a rectangular foundation, respectively; e_1 and e_2 are the eccentricity along the width and length.

In case $c = 0$ (usually for sand condition), and the foundation is subjected to a vertical, centric load applied at ground level where both foundation base and ground are horizontal, two typical cases are frequently encountered in design:

1 For square footing:

$$q'_u = 1.3cN_c + 0.4\gamma'BN_\gamma + \gamma'hN_q \quad (12.7)$$

B is the width of the foundation.

2 For circular footing:

$$q'_u = 1.3cN_c + 0.3\gamma'BN_\gamma + \gamma'hN_q \quad (12.8)$$

B is the minimum lateral dimension of the foundation.

3 For strip footing:

$$q'_u = cN_c + 0.5\gamma'BN_\gamma + \gamma'hN_q \quad (12.9)$$

B is width of the foundation.

For drained condition, the maximum net load that a footing can carry is then:

$$Q' = q'_u A' \quad (12.10)$$

where A' is the effective area (effective length \times effective width) depending on the load eccentricity.

It should be noticed that the ultimate effective pressure q'_u is the stress including both the applied load from the foundation and the overburden pressure. In case an excavation is carried out for the foundation, stresses in excess of original overburden stress at the foundation level contribute to failure. The net bearing capacity q_{netu} can then be calculated as:

$$q_{\text{netu}} = q'_u - q_{\text{ob}} \quad (12.11)$$

where q_{ob} is the total overburden stress removed at the foundation level.

The bearing capacity will be sufficient if the applied load at the foundation level is equal to that of the excavated soil, which motivates the design of floating (full-compensated) foundation.

It is worth mentioning that in a working stress design (WSD) approach (Sect. 1.13.1), all uncertainties (load and resistance) are included in a single safety factor FS , which should not be measured with respect to the ultimate effective pressure q'_u . Instead, FS should also be associated with the net bearing capacity q_{netu} , and the allowable bearing capacity should then be determined as follows:

$$q_{\text{allowable}} = (q_{\text{netu}}/FS) + q_{\text{ob}} \quad (12.12)$$

While in a load and resistance factor design (LRFD, see Sect. 1.13.2), uncertainties for load and resistance are addressed separately by using adequate factors (partial safety factors) to increase the live and permanent loads (load factors) and a reduction factor (material factor) to reduce the ultimate bearing capacity.

12.3.2 *Bearing Capacity Due to Local and Punching Shear Failure*

Terzaghi [703] presented a simple method to approximate the bearing capacity due to local and punching shear failure by reducing the soil attraction c and the angle of internal friction ϕ' to new ones:

$$c_{\text{new}} = 0.67c \text{ for soft to firm clay} \quad (12.13)$$

$$\phi_{\text{new}} = \tan^{-1}(0.67 \tan \phi') \text{ for loose sands with } \phi' < 28^\circ \quad (12.14)$$

The bearing capacity factors due to the local and punching shear failure will then be changed by using the c_{new} and φ_{new} .

Vesic [697] recommended a less conservative method to calculate the bearing capacity due to local and punching shear failure based on a reduction of φ' varied with relative density of soils D_r :

$$\varphi_{new} = \tan^{-1}[(0.67 + D_r - 0.75D_r^2) \tan \varphi'] \text{ for } 0 < D_r < 0.67 \quad (12.15)$$

12.3.3 Bearing Capacity for Layered Soil

It should be noticed that the bearing equations discussed above are based on the assumption that the ultimate shear strength of soils are reached in all plastic zones. However, the shear strength may not be fully mobilized everywhere in the plastic zones and the local or punching shear failure may occur at a level significantly lower than what is given in the bearing capacity equations.

The ultimate and allowable bearing capacities of shallow foundations on weaker (loose) sands and soft clays can be increased by placing a layer of compact (dense) sand over it. If the strong soil layer is rather thick, the failure surface will then lie entirely inside the sand layer. However, if the thickness of the strong soil layer is relatively thin, the failure in soil would occur by punching in the dense sand layer followed by a general shear failure in the weaker sand layer, or the failure surface can be extended to soft clay layer. For an elaboration of this topic, readers may read sources [33, 706].

12.4 Bearing Capacity for Undrained Clay

The bearing capacity for undrained clay (with a zero internal friction angle) can be estimated in terms of total pressure q_u rather than the effective pressure q'_u :

$$q_u = s_u N_c K_c + \gamma h \quad (12.16)$$

where s_u is undrained shear strength; N_c is the bearing capacity, which may be taken as 5.14 for soils having a zero angle of internal friction; γ is the total unit weight of soils; h is the depth of embedment of foundations; K_c is a correction factor accounting for load inclination, footing shape, depth of embedment, inclination of base, and inclination of the ground surface.

For infinitely long strip footing, the bearing capacity is:

$$Q = 5 \cdot 14s_u A_0 \quad (12.17)$$

where Q is the maximum vertical load per unit length of footing at failure; A_0 is the actual foundation area per unit length.

For circular or square footing:

$$Q = 6 \cdot 17s_u A \quad (12.18)$$

where Q is the maximum vertical load at failure; A is the actual foundation area.

12.5 Bearing Capacity of Unliquefiable Soil Subjected to Seismic Loading

Due to inertial forces applied on foundations and in the soil mass, the bearing capacity due to seismic loading is generally lower than that of static bearing capacity even if liquefaction does not occur. Rather than performing a complicated full dynamic analysis, for a simple evaluation of this reduction, a pseudo-static approach (Sect. 8.2) may be adopted.

In a pseudo-static model, a reduction in bearing capacity due to earthquake loading is examined. In this model, the loading condition consists of normal and tangential forces applied on the foundation and inertial forces transferred into soils. An upper-bound solution of the limit load of the shallow foundation is found. Reductions in bearing capacity are given in terms of ratios between seismic and static bearing capacity factors N_c^*/N_c , N_q^*/N_q , and N_γ^*/N_γ , which are dependent on seismic loading, angle of internal friction, the h/B ratio, etc.

In the pseudo-static approach, the failure mechanism of the shallow foundation subjected to seismic loading can be assumed as a circular surface from which the foundation propagates until the ground surface is reached, as shown in Fig. 12.12. The seismic forces are considered as pseudo-static forces acting on both the footing and the soil below the footing. The ultimate load can be found by the moment equilibrium with respect to the center of the circular surface, which is called the equilibrium approach [707].

Figure 12.13 shows a comparison of the reduction in bearing capacity among different proposed methods [708–710].

For an elaboration of the pseudo-static approach applied for assessing the bearing capacity, readers may read reference [708].

Fig. 12.12 Schematic illustration of failure mechanism for shallow foundations subjected to seismic loading [708]

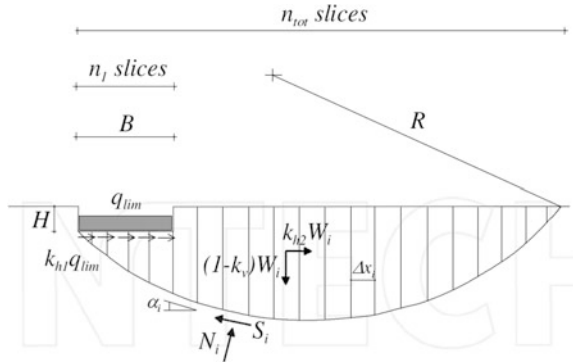
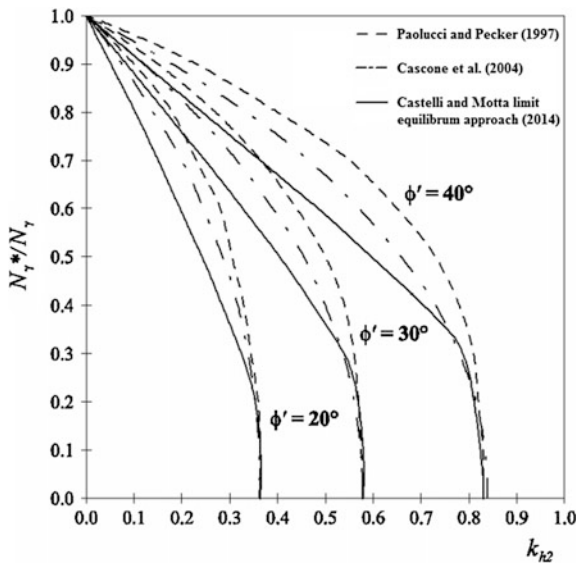


Fig. 12.13 A comparison of different methods proposed to calculate the reduction of bearing capacity as a function of soil mass inertia loading due to the kinematic seismic wave effects (k_{h2} is the horizontal seismic coefficient of the soil mass) [708]



12.6 Bearing Capacity Control of Soils with Liquefaction Potential Subjected to Seismic Loading

Subject to seismic loading, there are mainly three factors influencing soil failures: soils' shear strength (such as liquefaction), structural loads (such as excessive overturning moments transferred from an upper structures downward to foundations), and changes in site conditions (such as the rise of ground water level).

Liquefaction is more relevant to shallow foundations than deep ones, because during installation, deep foundations are often penetrated into all soil layers that are potentially liquefiable under seismic loading (even if the liquefaction has also caused failures of deep foundations during historical earthquakes as discussed in

Sect. 7.1). For liquefactions associated with shallow foundations, the depth of soil involvement could exceed the footing width. For structures supported by numerous spread footings that occupy a large portion of the footing area, the individual pressure bulbs from each footing may combine and thus the entire width of the building/structure could be involved in a bearing capacity failure [711].

Figure 12.14 schematically illustrates the earthquake-induced punching shear scenario. By assuming that load P will cause the foundation to punch through the upper unliquefiable soil layer (with shear strength τ) into the liquefied soil layer (no shear strength), the foundation (strip or spread footing illustrated in Fig. 12.2) will not punch through if the following criteria are fulfilled:

$$P \leq FS \cdot 2L \cdot H \cdot \tau \text{ for strip footings} \tag{12.19}$$

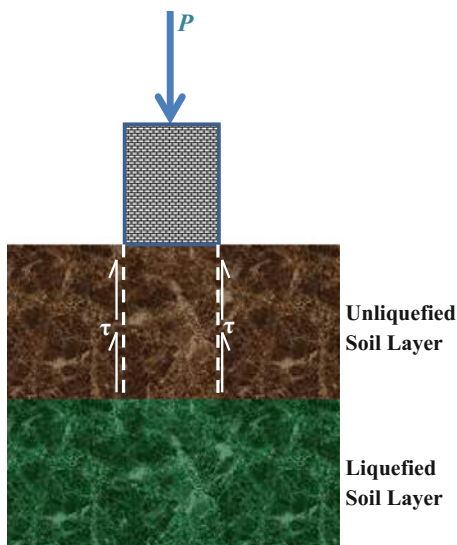
$$P \leq FS \cdot 2(B + L) H \cdot \tau \text{ for spread footings} \tag{12.20}$$

where FS is a safety factor, for seismic analysis, it is often taken as a value above 5 for earthquake-induced punching shear check, and above 3 for non-earthquake bearing capacity check; P is the footing load; L is the footing length; H is the vertical distance from the bottom of the footing to the top of the liquefied soil layer; B is the width of the footing.

For non-liquefiable clay layer, an effective stress analysis can be adopted to calculate the shear stress, the shear strength of the soil layer is:

$$\tau_{\text{clay}} = c' + \sigma'_n \tan(\phi') \text{ or } \tau_{\text{clay}} = s_u \tag{12.21}$$

Fig. 12.14 Punching shear of a footing that will punch vertically into the liquefied soil layer, the foundation is subjected to a vertically downward force P



For non-liquefiable sand layer, a total stress analysis can be adopted to calculate the shear stress, the shear strength of the soil layer is:

$$\tau_{\text{sand}} = \sigma'_n \tan(\varphi') \quad (12.22)$$

where σ'_n is the effective stress normal to the slip plane, i.e., the horizontal effective stress; φ' is the angle of shear resistance measured with normal effective stress.

12.7 Sliding Stability of Shallow Foundations

To ensure that sliding of foundations will not occur, a simple method is to assess the maximum horizontal load H at sliding failure:

$$H = s_u A \text{ for undrained condition} \quad (12.23)$$

$$H = cA + Q' \tan \varphi' \text{ for drained condition} \quad (12.24)$$

where s_u is undrained shear strength; A is the actual foundation area; c is the soil attraction calculated as the effective cohesion intercept of Mohr's envelope; Q' is the bearing capacity for drained condition, as presented in Sect. 12.3; φ' is the angle of internal friction.

12.8 Effects of Cyclic Loading on Shallow Foundations

Cyclic loadings for shallow foundations are caused by ocean wave and wind loadings (for offshore wind turbine substructures) applied on and transferred from structures above the foundations and also by seismic loading.

Cyclic loadings can induce an increase in pore pressure in soils beneath shallow foundations, leading to reduced effective stresses. For example, during a 24-hour storm with significant wave heights up to 11 m, the observed soil responses [713] of the Ekofisk oil storage tank foundation showed that the pore pressure in the sand under the center of the tank rose in the order of 20 kPa. The data also showed dissipations of pore pressures during the storm. Together with the cyclic variation of strain, the stiffness and strength of soils can change significantly. The effects of the reduced effective normal stress can be represented by a reduction in static strength, which depends on the average shear stress, the cyclic shear stress amplitude, and the number of load cycles. Furthermore, different parts of foundation soils experience cyclic loads with different magnitudes and phases, and the behavior of foundations can change gradually over time [112]. It is noticed that, even though the stress cycles in soils may be small, they occur in a large number during the

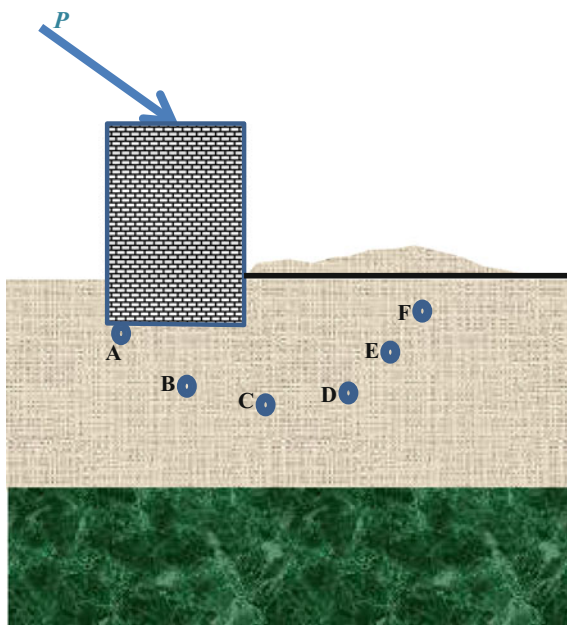
lifetime of the offshore installation. Therefore, the cumulative effect may be significant.

Contrary to the degradation of soil properties due to cyclic loading effects, strain rate effects (Sect. 2.5) can increase the soil strength. For example, for clay soils subject to seismic loadings, the increase in soils' shear strength due to rate effects can be more significant than the decrease in soils' strength due to cyclic loading.

A very efficient way to trace the foundation soil's state under cyclic loadings is to use the so-called stress path method, proposed by Bonin et al. [713] and Foss et al. [714]. In this method, based on soil analyses, the locations of trace points in foundation soils are first selected, often related to potential failure surfaces in the soil as shown in Fig. 12.15. DNV Classification Notes 30.4 [715] presents several methods for estimating the stress path.

The design process based on the stress path method is normally carried out by an iterative process. For example, to perform the capacity control of shallow foundations subject to wave loadings, analyses are performed for all sea states that can potentially affect foundation soils during the design lifetime of offshore structures, stress paths at each trace point are calculated from the analyses, and the laboratory tests are then carried out to determine the response of the soils along those stress paths. The laboratory results are used to extract engineering parameters, which are further used in a re-analysis of all relevant events. The process above is repeated until a satisfied convergence is reached between the predicted and the measured responses [112]. Under mild ocean wave condition, in which the soil nonlinearity is insignificant, the soil may be modeled using linear-elastic material with either

Fig. 12.15 Trace points (A–F) on a stress path under cyclic wave loading P transferred from the upper structure



isotropic or anisotropic properties. This requires an estimate of shear modulus and Poisson's ratio, and one or more anisotropic moduli in case anisotropic elasticity needs to be modeled.

Dynamics of GBS foundations can involve a significant soil–structure interaction. This is more obvious for foundations subjected to seismic loading. The presence of heavy GBS can influence soil motions, and in turn, it has certain influences on the soil stiffness and damping, which also influence the seismic motions transmitted to the foundations. Chapter 13 discusses the modeling of shallow foundations subject to dynamic loadings.

12.9 Piping Actions and Scour for Shallow Foundations

Piping actions are a type of hydraulic instability due to changes of water wave action, which changes the water pressure caused by the undrained cyclic loading (due to storm loading). This can lead to a significant dynamic compressive pressure and hydraulic gradients with high flow velocities in the soil around the perimeter of a gravity structure. As shown in Fig. 12.16, if this pressure gradient in the pore water (between the bottom of the foundation edge and the seabed surface) exceeds the buoyant weight of the soil, the soil will be floated up by water pressure, potentially causing foundation failure. The possibility of piping is increased dramatically if the vertical stress at foundation edges reaches zero during the cyclic loading process [735]. In practice, piping action can be minimized by increasing the depth of the foundation so that the pressure gradient can be decreased. However, the foundation capacity control due to piping action is normally not relevant to the seismic loading.

Along edges of an offshore shallow foundation, because the foundation forces water flow (due to the combined wave and current) to increase in speed as it passes

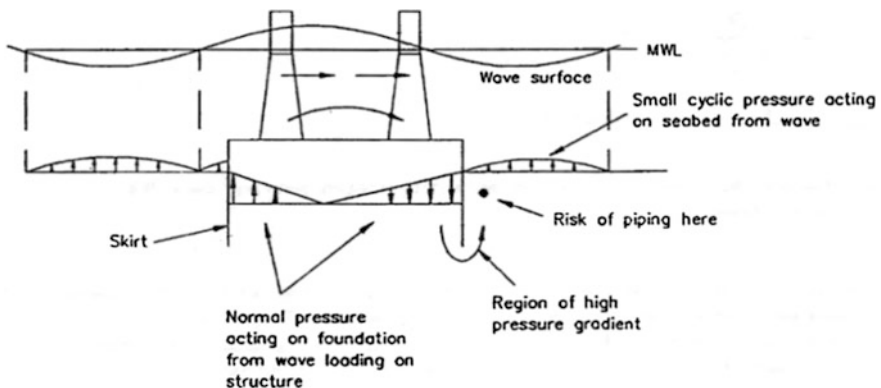


Fig. 12.16 Illustration of piping action [27]

around the foundation, some sediment such as sands and rocks from around the foundation will be removed in both depth and area, causing scour (Sect. 20.1), especially near the corners of the foundation. In the North Sea, scour holes of 5–10 m can easily develop depending on the loading conditions. Proper seabed protection to ensure the stability of the foundation is required. An efficient method is to install a thick layer of small-sized rock that extends up to a certain distance out of the side walls of the foundation. This is based on the assumption that, in principle, scouring of the rock is allowed as long as the full thickness of the layer is not eroded [736]. Other methods such as sandbags can also be installed around the foundations as scour protections. For more details of scour, see Chap. 20.

Chapter 13

Modeling of Shallow Foundation Dynamics

13.1 Foundation Impedance

Under dynamic loading, elastic waves are generated in soils and the energy is radiated away from the footing. When analyzing a gravity-based foundation structure, it should be noticed that essential differences exist between earthquake and ocean wave loading in that only a small volume of soils close to the foundation is excited under the wave loading, while under significant earthquake loading all surrounding soils are excited, possibly resulting in a softer soil response than that under wave loading. The direction of dynamic loading depends on the mechanism of sources that generate the dynamic loading. For example, during earthquakes, the dynamic loading of a foundation is mainly along horizontal directions. Under ocean wave loading, the loading transferred from the upper structure is also mainly horizontal. Some other dynamic loading may be treated as vertical loading relative to ground surface, such as blast loadings considered in designs of nuclear power plants.

To examine the influence of a shallow foundation and surrounding soils, they can normally be modeled as a rigid massless plate on an elastic half-space (characterized by shear modulus, Poisson's ratio, and density) using, for example, continuum mechanics, leading to closed-form solutions.

As shown in Fig. 13.1, the energy radiation occurs when a foundation vibrates against the soil. Stress waves originate at the contact surface and propagate outward in the form of body and surface waves, which carry away part of the energy transmitted by the foundation onto the soil, as if a viscous damper is implemented in the soil to absorb energy [343]. As the wave moves further away from the source, the volume available for dissipating the energy increases. In addition, the soil exhibits hysteretic cyclic behavior, which also contributes to the loss of energy and is practically frequency independent.

Fig. 13.1 Illustration of geometric effects generating radiation damping [717]

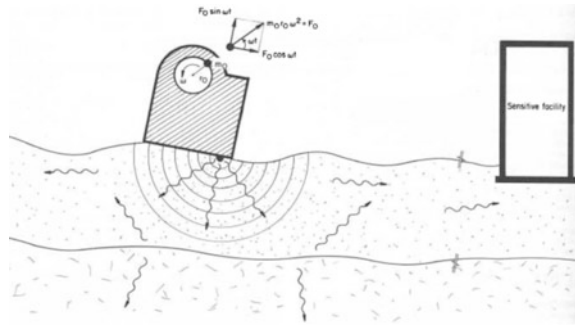
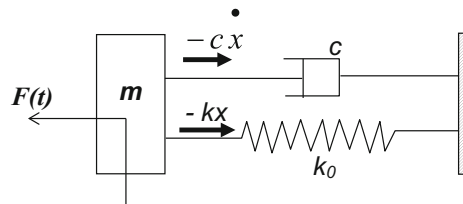


Fig. 13.2 SDOF spring-mass-damper system under an external force $F(t)$



Both the stiffness and the energy radiation (loss) can be simplified by replacing the soil mass with linear spring and dashpot elements, both of which are frequency-dependent.

A viscously damped system can be represented conveniently in a different but equivalent way for a class of techniques known as complex response analysis. If a single-degree-of-freedom (SDOF) system shown in Fig. 13.2 is excited with an external harmonic complex force ($F(t) = F_0 e^{i\omega t}$) with an amplitude of F_0 and an angular frequency of ω , the governing linear differential equation of motions for this system subjected to the harmonic force can be written as:

$$m \ddot{x}(t) + c \dot{x}(t) + k_0 x(t) = F(t) \tag{13.1}$$

Assuming that the response is harmonic, a trial solution of particular solution (steady-state response) of the mass m is:

$$x(t) = x_0 e^{i\omega t} \tag{13.2}$$

where x_0 is the initial displacement.

By combining the two equations above, one obtains:

$$(k_0 - m\omega^2) + ic\omega = \frac{F(t)}{x(t)} = \overline{k(\omega)} \tag{13.3}$$

where, at each degree of freedom among three translational and three rotational degrees of freedom, $\overline{k(\omega)}$ denotes the complex-valued impedance function, c represents the effects of damping associated with soil–foundation interaction.

The frequency (ω)-dependent spring ($k(\omega)$) and dashpot (c) elements can then be represented by a foundation impedance matrix $\overline{K(\omega)}$. Each diagonal term in the impedance matrix is a frequency-dependent complex number with a real part, representing the combined effect of stiffness and soil inertia, and an imaginary part, representing the radiation and hysteretic damping [718, 719]:

$$\overline{K(\omega)} = \text{Re}(K(\omega)) + i\text{Im}(K(\omega)) \quad (13.4)$$

where i is the imaginary unit.

Therefore, the frequency-dependent real and imaginary part of the impedance for an SDOF system can be obtained as:

$$\text{Re}(\overline{k(\omega)}) = k_0 - m\omega^2 \quad (13.5)$$

$$\text{Im}(\overline{k(\omega)}) = c\omega \quad (13.6)$$

At each degree of freedom, the modal damping of the foundation at frequency ω can then be calculated as:

$$\zeta(\omega) = \frac{\text{Im}(\overline{k(\omega)})}{2k_0} \quad (13.7)$$

where k_0 (Fig. 13.2) is the initial stiffness (often referred to as static stiffness because the initial stiffness also has other definitions in geotechnical engineering) at $\omega = 0$ at each degree of freedom.

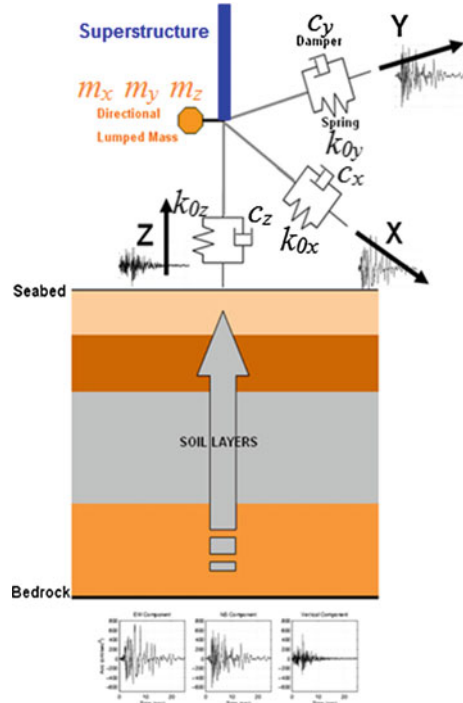
It is worth mentioning that the system damping (sum of the material and structural damping) [123] of an upper structure is normally much lower (a few percent) than the radiation damping due to soil–structure interaction.

From the three equations above, it is obvious that at zero frequency, the dynamic part becomes a real number, and the impedance coincides with the static (initial) stiffness.

Actually, the soil properties are essentially frequency independent, and the real part of the impedance reflects the influence of stiffness and frequency on the inertia. Therefore, this frequency (ω) dependency of impedance can also be modeled by a lumped parameter system, which consists of a fictitious added soil (inertia) mass m with different values in each degree of freedom so that $k_0 - m\omega^2$ fits the frequency-dependent stiffness function for each degree of freedom, typically using a second-order parabola shape equation.

Similarly, the frequency (ω) dependency of damping of the system also consists of an equivalent dashpot c with different values in each degree of freedom so that

Fig. 13.3 Under seismic loading, the frequency (ω) dependency of stiffness can be modeled by an equivalent directional added soil mass matrix m (directional lumped mass) and the static stiffness k_0 at $\omega = 0$; the frequency dependency of damping can be modeled by an equivalent dashpot c with different values in different degrees of freedom. The figure only illustrates the spring and damping modeling in three translational degrees of freedom (x, y, and z)



$c\omega$ fits the imaginary part in the same frequency range, typically using a linear equation.

Note that the location on a shallow foundation receiving seismic kinematic input energy (along all directions) can generally be assumed to be at a level close to the ground surface, the superstructure is modeled in the system, and the system is excited through the foundation by displacing the ends of the springs and dashpots in each degree of freedom, as shown in Fig. 13.3. Therefore, the effect of soil’s radiation damping due to soil–structure interactions is more significant for stiff structures with lower natural period than for soft structures with long natural period. As many soft structures such as high-rise building or high-rise offshore structures have not only a long natural period but also a high static foundation stiffness, the effects of radiation damping can even be further minimized by either neglecting the soil damping or modeling it together with the superstructure using an equivalent viscous damping ratio. This makes response spectrum analysis (widely used for seismic structural analysis) easier to perform as the dashpot cannot be directly applied in a traditional response spectrum analysis that is based on the linear modal superposition technique, where non-proportional damping cannot be modeled [123]. Note that in Fig. 13.3, the directional lumped mass is modeled using an intermediate link element rather than to connect the mass directly to soil springs and damping. This is used for extracting the foundation reaction forces for foundation capacity check, because the fictitious added soil mass is only used to simulate the

Fig. 13.4 Modeling of lumped mass parameters in case the foundation reaction forces are not of interests

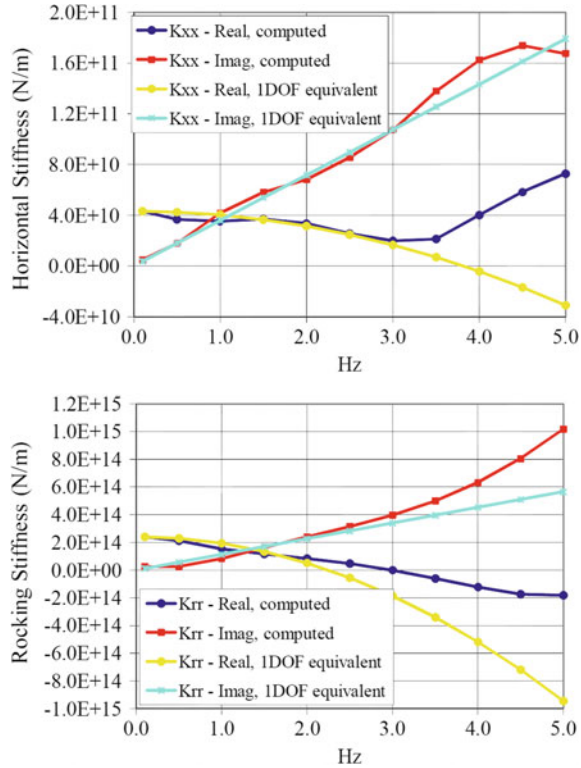


effects of frequency dependence of foundation stiffness. If the foundation reaction forces are not of interest, the fictitious added soil mass can directly connect to the springs and damping, as shown in Fig. 13.4. This frequency dependence can also be observed by analyzing Fig. 13.5, which shows that the imaginary part of the foundation impedance (related to radiation damping as discussed in the previous equation) of a high-rise offshore GBS structure increases with the increase in frequency.

Note that the inertia mass m does not represent any corresponding physical soil mass moving in-phase with the foundation but is used mainly due to the fact that the stiffness decreases with increasing frequency (hidden mass effects), instead of the stiffness remaining constant and being equal to the static stiffness. However, frequency dependence would disappear for massless soil as the soil's shear wave velocity approaches infinity. An example of frequency-dependent impedance is shown in Fig. 13.5, which illustrates the computed foundation impedance of the GBS and its equivalent impedance in horizontal and rocking directions. It is worth mentioning that, normally, the damping values are more frequency-dependent than the stiffness values.

In cases in which the dynamic responses of both foundations and structures are dominated by a specific vibration mode, only the foundation stiffness and damping corresponding to the frequency of that vibration mode may be used for modeling the foundation, without including the fictitious added soil mass. Moreover, rotational stiffness generally changes more significantly with frequency changes than translational stiffness does.

Fig. 13.5 Computed foundation impedance of a GBS foundation and its single degree of freedom equivalent impedance (by using the static stiffness $k_{0x} = 4.32 \times 10^{10}$ (N/m), $k_{0rr} = 2.4 \times 10^{14}$ (Nm/rad), mass $m_x = 7.5 \times 10^7$ (kg), $m_{rr} = 1.2 \times 10^{12}$ (kgm²/rad) and fitting them to $k_0 - m\omega^2$ to match the real part of the computed impedance, and using damping $c_x = 5.7 \times 10^9$ (Ns/m), $c_{rr} = 1.8 \times 10^{13}$ (Nms/rad) and fitting them to imaginary part of the computed impedance $c\omega$) in horizontal (upper) and rocking (lower) direction (courtesy of Aker Solutions and NGI)

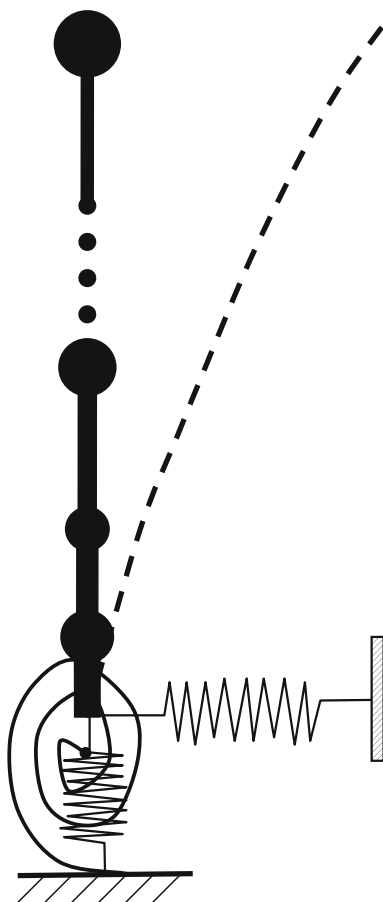


Many closed-form solutions of impedance function are available for rigid circular or rectangular foundations located on the surface of, or embedded within, a uniform, elastic, or viscoelastic half-space [720]. Based on the work by Richart and Whitman [721], Richart and his co-workers [722], and Whitman [723], a closed-form solution of the foundation impedance has been derived from the half-space theory as shown in Table 13.1 for circular foundations. These solutions are regarded as accurate, especially for low-frequency excitation on hard soils, and have been widely used among geotechnical and structural engineers. In many cases, only stiffnesses are needed for a rough estimation of foundations' dynamic behavior as shown in Fig. 13.6. From Table 13.1, it is also noticed that an increase in shear modulus of soil (e.g., a firmer soil) or the radius (more obvious for rocking and torsional degree of freedom) of circular foundation will increase the stiffness and the resonance frequency of the foundation. Here, readers should bear in mind that the soil's shear modulus is highly dependent on the magnitude of strain, for example, a tenfold variation in stiffness in the strain range between 10^{-4} and 1%. Further, an increase of the weight of the foundation will have similar effects as increasing the fictitious added soil mass, thus decreasing the resonance frequency.

Table 13.1 Equivalent lumped mass parameters for analyzing a circular foundation (regarded as a rigid plate) on an elastic half-space (G soil's shear modulus; R radius of foundation; ρ soil density; ν soil's Poisson's ratio)

Mode	Initial (static) stiffness k_0 (N/m)	Fictitious added soil mass m (kg or kgm^2/rad)	Damping coefficient c (Ns/m or Nms/rad)
Vertical	$\frac{4GR}{1-\nu}$	$\frac{1.08\rho R^3}{1-\nu}$	$\frac{3.4R^2}{1-\nu} \sqrt{\rho G}$
Horizontal	$\frac{8GR}{2-\nu}$	$\frac{0.76\rho R^3}{2-\nu}$	$\frac{4.6R^2}{2-\nu} \sqrt{\rho G}$
Rocking (rotation)	$\frac{8GR^3}{3(1-\nu)}$	$\frac{0.64\rho R^5}{1-\nu}$	$\frac{0.65R^4}{1-\nu} \sqrt{\rho G}$
Torsional	$\frac{16GR^3}{3}$	$0.24\rho R^5$	$1.32R^4 \sqrt{\rho G}$

Fig. 13.6 Modeling of a non-uniform beam to represent a superstructure with horizontal, vertical, and rocking stiffness at its bottom to resemble the foundation stiffness



Solutions for the equivalent lumped mass parameters of a rectangular foundation do exist. For simplicity, they can roughly be approximated by converting the dimensions ($L \times B$) of the rectangular foundation into an equivalent radius R_0 for a circular foundation, and then by using the simple formulation such as the one illustrated in Table 13.1. Equivalent lumped mass parameters can be conveniently calculated by using the equivalent circular area or moment of inertia solution for the rectangular footing.

For translational degree of freedom, one can use an equivalent area as:

$$R_0 = \sqrt{\frac{4BL}{\pi}} \quad (13.8)$$

For rocking degree of freedom, one can use an equivalent moment of inertia as:

$$R_0 = 4\sqrt{\frac{16BL^3}{3\pi}} \quad (13.9)$$

where the axis of the rocking is in parallel with the direction of B .

For torsional degree of freedom, an equivalent polar moment of inertia can be used as:

$$R_0 = 4\sqrt{\frac{16BL(B^2 + L^2)}{6\pi}} \quad (13.10)$$

The embedment of a shallow foundation below the ground surface generally increases the initial/static stiffness of the foundation. Based on an elastic and homogeneous half-space foundation model, and by assuming that the embedment of a foundation has a constant depth of embedment, a rigid foundation basemat, and a solid basement shape (rings and other annular shapes are excluded), Gazetas [724] presented algebraic formulas and dimensionless charts for computing the impedance (springs and dashpots) of embedded foundations, with arbitrary basement shape and any degree of contact of the vertical sidewalls with surrounding soils (from a complete contact over the whole embedment depth to no contact at all). The results of two numerical examples using the formulas are also supported by experimental evidence from model tests [724]. The study by Gazetas and his co-workers shows that the embedment can lead to substantial changes for all springs and dashpots, and increasing the embedment (in size and quality) can be a rather effective way to reduce the vibration amplitude of foundations. This effect is more pronounced in rocking and torsional degrees of freedom.

A practical question arises on how to decide a depth across which to compute an effective shear wave velocity by matching half-space static stiffness to those of non-uniform profiles. Stewart [725] studied this issue and recommended computing effective profile velocity as the ratio of depth interval (z_p) to shear wave travel time through the depth interval. The depth interval is measured from the base of the foundation footing to the depth z_p .

For horizontal translations, this depth is determined as:

$$z_p = 0.75 \sqrt{\frac{A}{\pi}} \quad (13.11)$$

where A is the foundation area; $\sqrt{\frac{A}{\pi}}$ is essentially an equivalent foundation radius that matches the foundation area.

For rocking, this depth is determined as:

$$z_p = 0.75 \sqrt{4 \frac{I}{\pi}} \quad (13.12)$$

where I is the foundation moment of inertia; $4\sqrt{\frac{I}{\pi}}$ is essentially an equivalent foundation radius that matches the moment of inertia of the foundation in the direction of excitations.

The presence of a stiff layer at depth in the soil profile can impede radiation damping. If a site consists of a relatively uniform layer of depth overlying a very stiff layer, which has a shear wave velocity more than twice that of the surface layer, damping values should be reduced; see BSSC [290] for details.

The half-space solutions based on the continuum mechanics with analytical or semi-analytical formulations provide a convenient and realistic model for foundation dynamic analysis and give closed-form solutions. As mentioned previously, these solutions are regarded as especially accurate for low-frequency excitation of hard soil. Gazetas and Roesset [726] demonstrated that small errors in modeling different soil layers are not important for heavy foundations with a high mass ratio; therefore, the solutions by half-space theory or analytical type computer programs are efficient.

However, light foundations are quite sensitive to the existence of rock at a shallow depth and of different soil layers beneath foundation footings. Moreover, the half-space theory cannot model an arbitrary foundation shape rather than circular, strip, or rectangular shapes; it cannot account for the flexibility of shallow foundations rather than a rigid plate foundation; it cannot model the inclined layering in soil deposits and has difficulty in modeling the nonlinear soil stiffness, embedment, and spatial variation of strain on soil properties.

To conquer the challenges above, a “discrete” approach, essentially finite element modeling, is recommended. Different from applications of finite element method in other engineering areas, finite element analyses applied in foundation dynamics need to model the soil strata with infinite extent in the horizontal direction and the extent in the vertical direction needs also to be adequately represented. This requires a dedicated consideration of the boundary modeling (see Sect. 5.7 for more details on this topic).

It should also be mentioned that, if correctly understood and implemented, half-space solutions and the finite element modeling yield similar results [727, 728].

Figure 13.7 illustrates an example of modeling for calculating the foundation impedance. The foundation was replaced by a rigid plate. The soil is assumed to consist of two regions: the interior region, corresponding to the soil mass under the foundation, can be modeled with increased stiffness (Fig. 13.8) due to the increased shear wave velocity by the overburden pressure caused by the platform weight, and the exterior region consisting of the free-field surrounding the interior region.

In the exterior region, the strain-compatible soil shear modulus (Fig. 13.8) and damping (Fig. 13.9) computed by site-response analyses can normally be used. The soil shear modulus and damping of each soil layer in the interior region can also be reduced by the same reduction factor as that of the shear modulus of the same soil

Fig. 13.7 Illustration of a soil–foundation model for calculating the foundation impedance for a GBS foundation (courtesy of Aker Solutions and NGI)

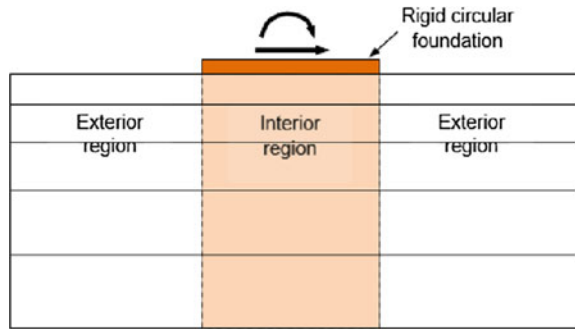


Fig. 13.8 G_{max} and strain-compatible modulus in free-field and below platform used in a computation of foundation impedance (courtesy of Aker Solutions and NGI)

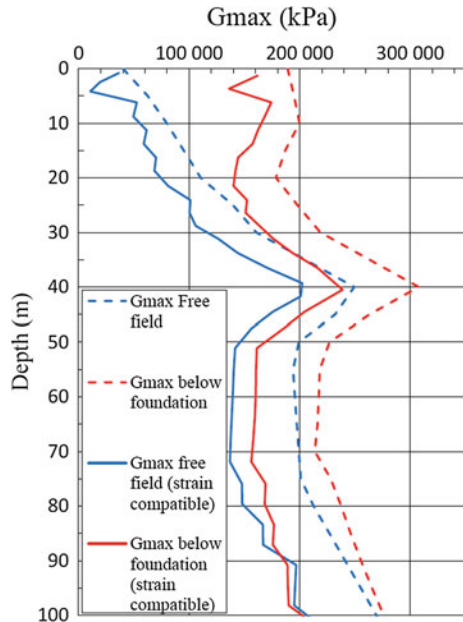
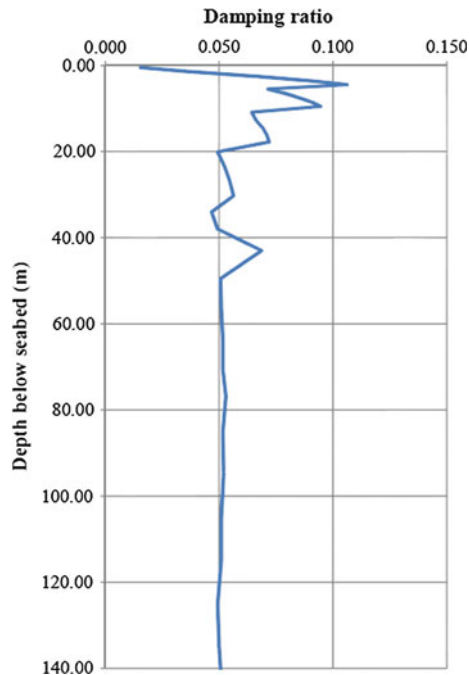


Fig. 13.9 Strain-compatible soil damping (courtesy of Aker Solutions and NGI)



layer, based on the site-response analyses (Chap. 3). For seismic applications, this reduction factor can even be less than 0.25. For machine vibration applications, this factor normally ranges from 0.25 to 0.5. In the meantime, the damping of the soil can be twice that of the original damping [329].

As shown in Fig. 13.8, the overburden pressure due to the presence of the foundation and superstructure weight will generally increase the maximum dynamic shear stiffness G_{\max} , which can be obtained from laboratory and in situ seismic cone tests. The effects are more significant at ground surface neighborhood (approximately 0.5–1 times of the foundation dimension) than at deep soils. The influence may be significant for soils under a heavy foundation. However, for soils around pile foundation, the effects are minor and can often be neglected in engineering practice.

Example A GBS foundation has an equivalent foundation radius of 74 m. From a seismic site-response analysis using equivalent linear soil models (Sect. 2.2), the equivalent shear wave velocity for the top layers is determined as 372 m/s. The soil has a mass density of 2060 kg/m^3 and a Poisson's ratio of 0.5. Calculate the equivalent lumped mass parameters according to Table 13.1.

Solution: The shear modulus can be calculated as:

$$G = \rho v_s^2 = 2060 \text{ kg/m}^3 \times (372 \text{ m/s})^2 = 285 \text{ MPa (upper-bound value)}$$

The calculated equivalent lumped mass parameters according to Table 13.1 are listed in Table 13.2.

A more dedicated foundation impedance calculation was performed based on frequency-domain solutions that use transmitting boundaries for representing the infinite lateral extent of the layered soil medium [730–732]. The foundation was replaced by a rigid circular plate with a diameter of 74 m. As mentioned previously, the soil is assumed to consist of two regions (Fig. 13.7): the interior region, corresponding to the soil mass under the foundation with increased stiffness (Fig. 13.8) due to the increased shear wave velocity, and the exterior region consisting of the free-field surrounding the interior region. For the exterior region, the strain-compatible soil shear modulus (Fig. 13.8) and damping (Fig. 13.9) computed by the site-response analyses using SHAKE [733] were used. The soil shear modulus and damping of each soil layer in the interior region are also reduced by the same reduction factor as the shear modulus of the same layer at the exterior region. The frequency-dependent foundation impedances in four degrees of freedom are shown in Fig. 13.10. By using the curve fitting so that $k_0 - m\omega^2$ fits the frequency-dependent stiffness function for each degree of freedom, the static stiffness and fictitious added soil mass can be approximated as given in Table 13.3. Similarly, the frequency (ω) dependency of damping of the system consists of an equivalent dashpot c with different values in each degree of freedom so that $c\omega$ fits the imaginary part in the same frequency range; this is also shown in Table 13.3.

By comparing the difference between the computed results and hand calculation shown in Table 13.3, it is shown that the hand calculation gives approximately similar results to the computed one for horizontal static stiffness, horizontal fictitious added soil mass, and rocking static stiffness.

In addition, at each degree of freedom, based on the equation mentioned above and the calculation shown in Table 13.4, the modal damping representing the soil radiation damping according to the computed impedance (Fig. 13.10) of the foundation at each frequency ω is also calculated by:

$$\zeta = \frac{\text{Im}(\overline{k(\omega)})}{2k_0}$$

Table 13.2 Equivalent lumped mass parameters according to Table 13.1

Mode	Initial (static) stiffness k_0 (N/m or Nm/rad)	Fictitious added soil mass m (kg or kgm ² /rad)	Damping coefficient c (Ns/m or Nms/rad)
Vertical	1.69E+11	1.80E+09	2.85E+10
Horizontal	1.12E+11	4.23E+08	1.29E+10
Rocking	6.16E+14	5.85E+12	2.99E+13
Torsional	6.16E+14	1.10E+12	3.03E+13

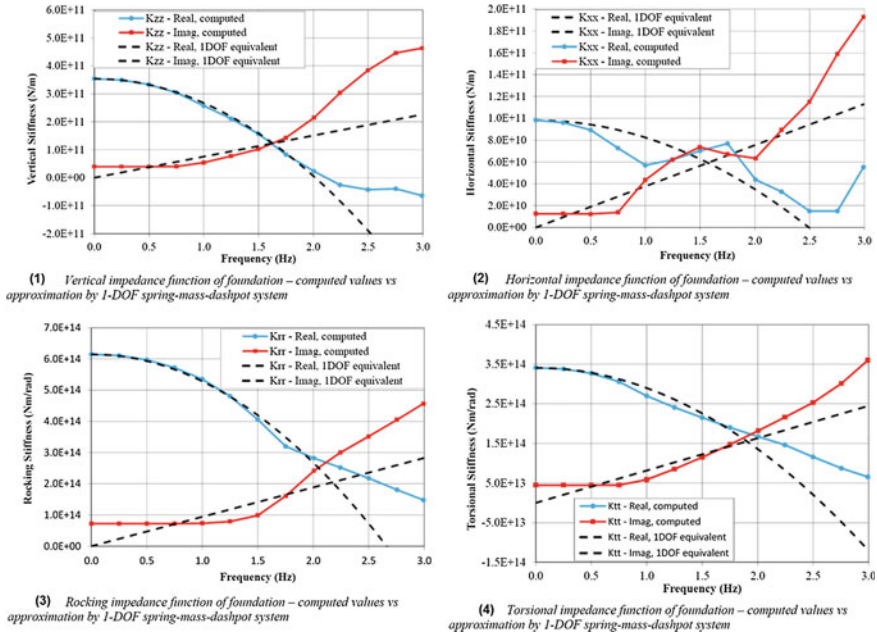


Fig. 13.10 Computed (solid dotted line) and single degree of freedom equivalent (dashed line) impedance function of a foundation (courtesy of Aker Solutions and NGI)

By observing Table 13.4, it is shown that the modal damping due to soil radiation damping is generally less than 7% at a frequency range below 0.75 Hz. If the natural frequency of a GBS structure is around 0.5 Hz, the modal damping for all degrees of freedom at 0.5 Hz is small and close to 6%.

A spring-to-ground element can be placed at the bottom of the GBS caisson (at mudline level) to model the soil stiffness. Since the platform has a very long natural period of around 4.0 s, by observing Fig. 13.10, it is noted that the damping of the soil is very marginal. The dashpot element to represent the soil damping is modeled. Because the foundation reaction forces are not of interest in the current example, the fictitious added soil mass is directly connected to the spring-to-ground element. Moreover, the mass of the caisson (made of steel and concrete) and contents inside the caisson may be modeled as a caisson mass shown in Fig. 13.11. Moreover, the hydrodynamic inertia effects of submerged structure due to the presence of surrounding water can be modeled as directional inertia mass(es) that is only active along the direction of the structure’s oscillations due to seismic ground excitations.

The merit of using impedance to represent the foundation lies in the fact that the viscously damped system to model the foundation can be simplified as an undamped system with complex stiffness. For problems in which loading is

Table 13.3 Equivalent lumped mass parameters from both the computed results (Fig. 13.10) and hand calculation (Table 13.2)

Mode	Initial (static) stiffness k_0 (N/m or Nm/rad)		Fictitious added soil mass m (kg or kgm^2/rad)		Damping coefficient c (Ns/m or Nms/rad)	
	Table 13.1	Computed	Table 13.1	Computed	Table 13.1	Computed
Vertical	1.69E+11	3.54E+11	1.80E+09	2.20E+09	2.85E+10	1.20E+10
Horizontal	1.12E+11	9.82E+10	4.23E+08	4.00E+08	1.29E+10	6.00E+09
Rocking	6.16E+14	6.15E+14	5.85E+12	2.20E+12	2.99E+13	1.50E+13
Torsional	6.16E+14	3.41E+14	1.10E+12	1.30E+12	3.03E+13	1.30E+13
					Diff. (%)	Diff. (%)
					-52	-18
					14	6
					0	166
					81	-16
						Diff. (%)
						138
						115
						99
						133

Table 13.4 Modal damping due to soil radiation damping according to the computed impedance (Fig. 13.10) of the foundation

Frequency (Hz)	Modal damping in horizontal direction (%)	Modal damping in vertical direction (%)	Modal damping in rocking direction (%)	Modal damping in torsional direction (%)
0	6.36	5.62	5.90	6.51
0.25	6.36	5.62	5.90	6.51
0.5	6.31	5.61	5.89	6.50
0.75	6.98	5.68	5.88	6.55
1	22.15	7.61	5.96	8.61
1.25	31.67	10.92	6.41	12.49
1.5	37.47	14.41	8.00	16.86
1.75	34.11	20.20	13.09	21.55
2.01	32.23	30.23	19.59	26.69
2.24	45.47	42.80	24.39	31.67
2.5	58.55	54.24	28.62	37.10
2.75	80.96	62.99	32.93	44.13
3	98.27	65.40	37.15	52.79

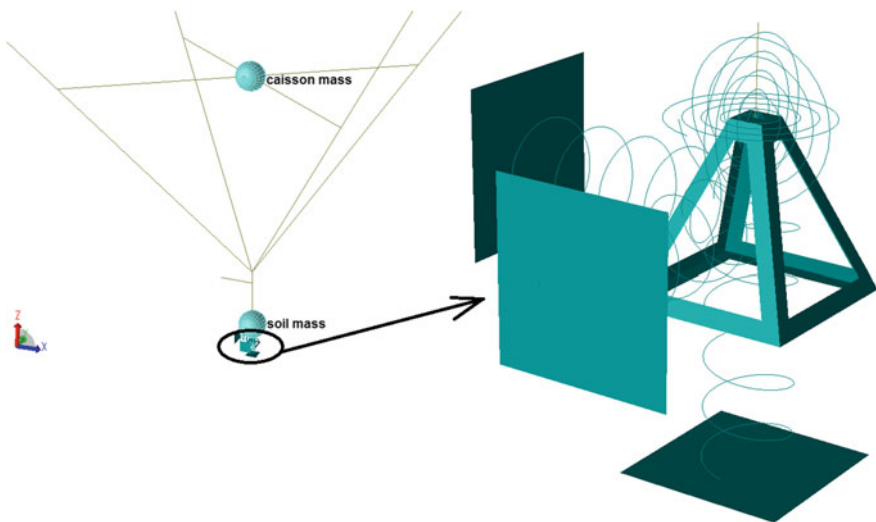


Fig. 13.11 Modeling of caisson and lumped mass (fictitious added soil mass, spring, and damping) placed at the bottom of the GBS caisson (at mudline level)

characterized as periodic (and therefore as the sum of a series of harmonic loads), the use of complex stiffness significantly simplifies the foundation modeling [1]. However, readers should bear in mind that, strictly speaking, the use of this method is restricted to cases of harmonic motions.

If the dynamic response is dominated by vibrations at a structure's eigenfrequency (typically it is the structure's natural frequency ω_n), the foundation stiffness may be simply represented by springs with constant stiffness $k_0 - m\omega_n^2$ at the structure's natural frequency. This is typically applied to cases where the inertia loading effects from superstructures are much more significant than those of the kinematic seismic loading. In certain cases, a constant foundation stiffness may also be calculated corresponding to the predominant frequency of site period or seismic wave transmissions. Of these, the former is preferred if the seismic motion has its components concentrated around the site period/frequency, and the latter is more relevant if the kinematic seismic loading on either shallow or deep foundations is wide-banded (not concentrated at the site period) and more influential than the inertia loading. However, since this predominant frequency may change for different seismic motion histories, several models need to be prepared with different foundation stiffnesses. A similar discussion applied to pile foundations is presented in Sect. 19.5.

13.2 Combination of Damping for Foundations and Superstructures

In a response spectrum analysis to obtain seismic responses, the modeling of damping can be accounted for either in the response spectrum or directly as modal damping of each modal response, which is used to compute the dynamic responses by performing modal combination. In either case, the damping is a type of proportional damping in which the corresponding damping matrices can be diagonalized in the modal matrix [734]. This provides computational convenience but only applies for lightly damped structures with uniformly distributed damping mechanism, where off-diagonal terms in the damping matrix can be neglected [123].

For many structures, the energy dissipation mechanisms in different parts vary. Under dynamic seismic excitations, the damping of a soil–foundation system is normally much higher than that of the superstructure, and the use of proportional damping such as modal damping or Rayleigh damping cannot be justified. Therefore, both analytical and FE models must account for the effect of combined damping in a more dedicated manner. A general approach to obtain the global damping matrix is to divide the entire structure into several substructures, each of which has a similar damping level; by assembling the damping matrix of all substructures together, the global damping matrix can be calculated [123].

As engineers involved in dynamic analyses are normally familiar with modal analysis and can give a proper interpretation of the calculated results, it would be very desirable to model the entire foundation–superstructure with an equivalent modal damping, even if it lacks mathematical rigor due to the reasons: (1) the foundations' damping level in different degrees of freedom is different; (2) the

damping associated with the horizontal foundation motion is essentially viscous and normally has a more dominated effect on the foundation response than that in other degrees of freedom and in the superstructure; (3) the damping associated with the foundation's rocking motions and vibrations of the superstructure is primarily hysteretic. Roesset, Whitman and Dobry [735] stated that, by assuming that the energy ratio in each vibration mode at resonance is a weighted average of energy ratios in each individual component at the same frequency, the equivalent modal damping can be calculated. They concluded that this approximation is sound even if the damping values are rather different at different parts of the foundation–superstructure system. Furthermore, since the use of a constant modal damping for all vibration modes in soil–structure interaction studies will distort the effect of the horizontal stiffness and produce unrealistic amplification of foundation motions, a weighted modal damping reproduces a more realistic dynamic behavior.

Part IV
Pile Foundations

Chapter 14

Introduction to Deep Foundations

A deep foundation is a type of foundation that transfers loads from superstructures to the earth a greater depths from the surface than a shallow foundation does to a subsurface layer or a range of depths. Compared to shallow foundations, deep foundations have the merits of being suitable for more adverse soil conditions and less site constraints.

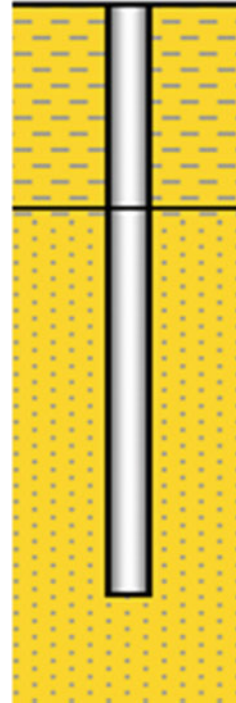
Different terms are used to describe different types of deep foundations, including the pile (which is analogous to a pole), the pier (which is analogous to a column), drilled shafts, and caissons. The use of these terms is not entirely consistent, and more than one will sometimes be used to refer to the same thing.

As shown in Fig. 14.1, the most commonly used type of deep foundation is the pile foundation, which comprises relatively long, slender, column-like members penetrating into soils and in some cases with its bottom (tip) in contact with hard rock. The pile foundation has been used for thousands of years.

The advantage of pile foundations is obvious when they are used in soft soil sites to support heavy structures, such as high-rise buildings, fixed offshore platforms, nuclear power plants, dams and bridges. Because a pile's capacity is strongly dependent on the contact area between the pile wall and the surrounding soils, and the near-surface soil is relatively soft and weak and also more erodible than the soil at a greater depth, pile foundations are often deeply embedded in soils to increase the foundation capacity and reliability.

Piles can normally be driven or cast-in-place (bored). In pile driving, piles are generally driven into the ground in situ, using a pile hammer resting on or clamped to the pile butt, and a cap block assembly is fitted between the hammer and the pile. Alignment of the pile with the hammer is provided by leads suspended by a crane. The hammer is lifted high into the air and dropped onto the pile as shown in Fig. 14.2, thus forcing the pile into the ground. Several types of hammers are available depending on the energy requirement. The lifting of the hammer may involve the use of hydraulics, steam, diesel, or manual labor. Piles can also be driven into the ground by using vibratory hammers for applications at locations both onshore (Fig. 14.3) and offshore (Fig. 14.4), in which vibratory hammers

Fig. 14.1 A vertical pile embedded in soils



drive the pile into the ground by a push and pull action of counter-rotating weights. The pile hammers are normally powered by hydraulic motors and designed in such a way that horizontal vibrations cancel out, while vertical vibrations are transmitted into the pile. Vibratory actions of the driver cause soils adjacent to the pile to act as a viscous fluid with little or no skin friction. Driven piles are efficiently manufactured at steel mill, prestressed yard, or wood yard under factory controlled condition with a consistent quality and are therefore generally less expensive than bored piles. Moreover, driven piles are normally delivered to construction sites free of defects, even though they can be damaged during or after installation. While the damage is typically easily detectable, since driven piles in the meantime serve as tested piles with driving records documented, the repair often requires adding new pile(s) for both offshore and onshore applications. A typical method of pile installation for fixed offshore structures is to float the structure into position and then to drive piles into the seabed. The noise generated during pile driving in offshore environments may cause a short-term adverse impact to aquatic life. However, generally, these adverse impacts are only short-term and relatively minor [737].

Similar to pile driving, recently, pile jacking techniques have also been utilized, in which preformed piles (e.g., prestressed spun piles, precast reinforced concrete piles, H-piles, steel pipe piles) are hydraulically jacked into the ground as

Fig. 14.2 Pile driving operations in the Port of Tampa, Florida



Fig. 14.3 A vibratory pile driver on a steel H-pile powered by a diesel engine



displacement piles, as shown in Fig. 14.5. During the operation of pile jacking, a pile is jacked into the ground with a jack-in force adjusted in steps up to between 1.8 times and 2.5 times working load. The jacking operation will continue until practical refusal where jack-in force is released and reapplied twice. Pile jacking has the advantages of generating low levels of vibrations and noise during execution [738], minimal spoils disposal, ability to achieve desirable pile verticality, small installation equipment, and good axial bearing capacity performance (has even higher bearing capacity than driving piles) [739, 740].

Bored/drilled piles are put in place using drilling/excavation as shown in Fig. 14.6, which derive their capacities mainly from end-bearing (Sect. 17.1). Compared to driven piles, drilled piles have significant advantages in terms of the

Fig. 14.4 Installation of steel piles at sea using large vibratory pile drivers, upper figure: CAPE Vibro 320 Vibro Lifting Tool—used for installing piles with a diameter of 2.1 m and a length of 45 m in the North Sea; lower figure: 8xAPE 600B for installing piles with a diameter of 22 m and a length of 50 m for Macau bridge. (Courtesy of L. de Neef, P. Middendorp and J. Bakker, Netherland, photo by L. de Neef, CAPE Holland)



Fig. 14.5 Operation of pile jacking. (Courtesy of Geotechnical Society of Singapore)



Fig. 14.6 Drilling operation in order to install a pile in-place



noise and vibration issues associated with pile driving, making them more suitable for application in urban areas. However, drilled piles can be more expensive to construct than driven piles. Defects of drilled piles may occur during construction, and there are not easily quantified. Moreover, damage after construction rarely occurs but is generally rather expensive and complex to repair.

It is worth mentioning that, in recent decades, there has been a substantial increase in the range of engineering applications of drilled shafts socketed into rock as a foundation to support significant loads. This is due to the realization of their performance benefits: the resistance to the applied loads is increased and the displacements under the applied loads are decreased. The major challenges in the use of rock-socketed drilled shafts are in characterizing the nature of rocks and determining axial and lateral load capacity. For more details on rock-socketed piles, readers may read sources [741, 742].

At offshore sites, piles can also be guided and directly dropped from the water surface into a designated location at seabed under their self-weight and penetrate into the soil at a desirable depth. This operation can be aided by hydraulic suction pump (Chap. 26) or pile hammer operated by remotely operated underwater vehicle (ROV) in case full penetration is not achieved. Drilled shafts are manufactured on-site and in-place. This requires a complex construction process during excavation, a significant quality control requirement in the field, and usually a specialty foundation subcontractor.

Driven piles with solid sections tend to displace a large volume of soil within the adjoining soil mass during the driving process, which are often referred to as full-displacement piles. Piles with hollow sections such as open-ended tubular cross-section piles displace a relatively small amount of soil during the driving process, which are called partial displacement piles. Cast-in-place/drilled/bored piles do not cause any soil displacement since no pile driving is carried out, and the excavation may or may not be supported (i.e., soils are removed). Therefore, they are called non-displacement piles or replacement piles as existing materials, usually soils, are removed as part of the process. If soil plugs (Sect. 17.12) do not form inside an open-ended pile, the pile will behave as a non-displacement pile, with heave and lateral displacement being minimized.

Different from piles, other deep foundations are typically put in place using excavation or drilling.

Piles can be made of timber, concrete, steel, or a combination of these materials. Timber piles are less common but comparatively inexpensive and most suitable for long cohesion piling and piling beneath embankment. Generally, they should not be driven into firm ground as this can easily damage timber piles by stones and boulders. To protect the timber against decay and putrefaction, it is recommended to keep the timber pile below the ground water level. Moreover, timber piles are difficult to splice and can be attacked by marine borers in salt water. Concrete piles are normally precast or prefabricated in segments with short length between 3 and 15 m, so that they can easily be connected together to form a complete pile with full length. Reinforcement steel can be used in concrete piles to sustain high driving loadings. Recently, prestressed piles have come to be preferred in engineering as they can reduce the amount of reinforcement steel used in a pile. Steel piles have higher strength than their timber or concrete counterparts, leading to a decrease in cross-section area and consequently a comparatively easy penetration into soil during pile driving. They are widely applied in offshore installations and sometimes for infrastructures onshore as well.

Piles are used to support reinforced-concrete pile caps, mat foundations, or to directly connect upper structures (such as legs of offshore structures) through pile sleeves (Fig. 21.3). In addition, piles are used as anchors (Chap. 25), which are widely utilized for stationkeeping of the floating vessels in offshore industry.

When the support capacity is predominantly provided by the resistance of soils/materials on which a pile tip rests, the pile is of an end-bearing type. On the other hand, if the support capacity is provided through the pile wall-soil friction and/or adhesion mobilized along the side of the pile, the pile is called a friction pile. In many cases, piles derive their support capacity from a combined end-bearing resistance and friction and/or adhesion resistance. The load carried by a pile's end-bearing component alone is often considered the safe load-carrying capacity of the pile, in order to avoid any settlement in the end-bearing-friction combinations.

The carrying capacity of piles mainly depends on the pile dimensions, soil conditions, and pile installation method. Two widely used methods for calculating pile capacity are available: α -method and β -method. α -method [743] is often called total stress method and used to calculate the short-term load capacity of piles in cohesive soils, as it is based on the undrained shear strength s_u of cohesive soils. β -method can be adopted to calculate both short-term and long-term load capacity of piles in both cohesive and cohesionless soils, as it is based on effective stress analysis. Yet another method called λ -method was proposed by Vijayvergiya and Focht [744]. It is based on back-calculated 47 load test results performed on pipe piles with different diameters to incorporate the skin friction resistance with both undrained strength and vertical effective stress.

Corrosion may occur on steel piles at soils with low pH value. However, a slight over-dimensioning of the cross-section area is normally sufficient to account for this corrosion. In addition, coating or cathodic protection can also be employed for mitigating corrosion; for details, see sources [745, 746, 747].

Piles can be oriented vertically (Fig. 14.1) or inclined/battered (installed at an angle to the vertical direction as shown in Fig. 14.7). Because a pile's axial stiffness is generally higher than its lateral stiffness, battered piles normally have higher stiffness along the horizontal direction than that of vertical piles. However, as the beneficial or detrimental role of battered piles on the seismic response of structures and the foundation itself is still not well identified, battered piles should be used with great caution, as will be discussed in Chap. 23.

In the design of pile foundations, it is essential to have a good estimation for the embedment of piles in order to predetermine the pile capacity. For driving piles, this can usually be fulfilled based on an anticipated level of driving resistance (the piles shall be driven to a certain blow-count) or based on an analysis of soil conditions and soil properties combined with information regarding pile bearing area and the perimeter surface area [748]. However, the former procedure may have limitations due to the fact that the required pile length cannot be predetermined with sufficient accuracy. Therefore, an adequate soil investigation and laboratory testing program are required to increase the accuracy.

Fig. 14.7 Battered piles support a precast segmented skyway of the San Francisco-Oakland Bay Bridge where upper soil layers are weak muds



Table 14.1 Comparison of construction and installation constraints between offshore GBS and pile foundation

Construction phase	Shallow (GBS) foundations	Pile foundations
Onshore construction	Local to site	No constraints
Transport offshore	More complex	Lift onto barge
Pre-placement activities	Seabed preparation	None
Placement	Lift or float-over	Lift
Fixing	Grouting	Pile driving, pile drilling, pile dropping or suction pile (Chap. 26)
Installation of topside	Potential obstacle to lift	Less obstacle to lift

When several piles are spaced far from each other (more than 8 times the pile diameter [790]), the interaction effects among piles is insignificant. However, for closely spaced piles in a pile group, the interaction effects can be significant and therefore need to be accounted for, as will be discussed in Chap. 21.

Pile foundations are widely used for offshore structures. Driven steel tubular piles provide the most common form of offshore foundation. The associated manufacture and installation technologies are relatively mature. A review by Overy [749] of Shell UK's North Sea piling operations shows a trend that, for platforms designed since 1996 employing mid-sized piles (0.660–2.134 m diameter, with penetration ranging from 26 to 87 m), the axial compressive capacities fall between 14 MN and 100 MN. However, diameters greater than 5 m have been specified for wind turbine structures in the North Sea, where piles with diameters of up to 2.5 m have also been driven for oil and gas platforms with penetrations of 100 m or greater, in a variety of geotechnical settings. Table 14.1 compares the construction and installation constraints between offshore shallow foundations (with GBS foundation as a representative example) and pile foundations, which indicate the flexibility of pile installations. Moreover, piles used offshore generally have larger diameters and higher length than those onshore, and the offshore piles are normally steel pipes, as previously mentioned.

As will be discussed in Chap. 19 and shown in Fig. 19.1, under seismic excitations, piles are subjected to both inertial forces transferred from the superstructure/substructure and kinematic forces arising from the deformation of surrounding soils due to the passage of seismic waves. Loads can also be induced due to liquefaction at the relevant soil layers.

For offshore structures, ocean environments due to wave, current and wind, as shown in Fig. 14.8, can induce significant cyclic loading on pile foundations, which has been the cause of various engineering failures of both pile foundations and substructures.

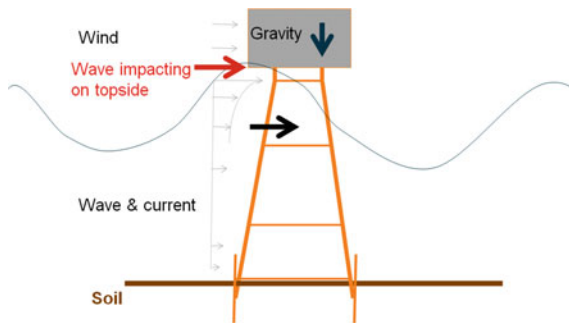


Fig. 14.8 Offshore structures subjected to ocean environmental loadings. (Courtesy of Aker Solutions)

Table 14.2 Soil data required and testing considerations for driving pile foundations [41, 701]

Engineering evaluations	Required information for analyzes	Field testing	Laboratory testing
End-bearing Skin friction Settlement Down-drag on piles Lateral earth pressures Chemical compatibility of soil and pile Drivability Presence of boulders/very hard layers Scour (for offshore structures and water crossing bridges) Vibration/heave damage to nearby structures Liquefaction Overall slope stability	Subsurface profile (soil, ground water, rock) Shear strength parameters Horizontal earth pressure coefficients Interface friction parameters (soil and pile) Compressibility parameters Chemical composition of soil/rock (e.g., potential corrosion issues) Unit weights Presence of shrink/swell soils (limits skin friction) Geologic mapping including orientation and characteristics of rock discontinuities	SPT(granular soils) Pile load test CPT Pressuremeter test (PMT) Vane shear test Dilatometer Piezometers Rock coring (RQD) Geophysical testing	Soil/rock shear tests Interface friction tests Grain size distribution 1-D oedometer tests pH, resistivity tests Atterberg limits Specific gravity Organic content Moisture content Unit weight Collapse/swell potential tests Intact rock modulus Point load strength test

Table 14.3 Soil data required and testing considerations for drilling pile foundations [41, 701]

Engineering evaluations	Required information for analyses	Field testing	Laboratory testing
Shaft end-bearing	Subsurface profile (soil, ground water, rock)	Installation technique	1-D oedometer
Shaft skin friction		test shaft	Soil/rock shear tests
Constructability	Shear strength parameters	Shaft load test	Grain size distribution
Down-drag on shaft	Interface shear strength friction parameters (soil and shaft)	Vane shear test	Interface friction tests
Quality of rock socket	Compressibility parameters	CPT	pH, resistivity tests
Lateral earth pressures	Horizontal earth pressure coefficients	SPT (granular soils)	Permeability tests
Settlement (magnitude & rate)	Chemical composition of soil/rock	PMT	Atterberg limits
Groundwater seepage/ dewatering/ potential for caving	Unit weights	Dilatometer	Specific gravity
Presence of boulders/ very hard layers	Permeability of water-bearing soils	Piezometers	Moisture content
Scour (for offshore and water crossing foundations)	Presence of shrink/swell soils (limits skin friction)	Rock coring (RQD)	Unit weight
Liquefaction	Geologic mapping including orientation and characteristics of rock discontinuities	Geophysical testing	Organic content
Overall slope stability	Degradation of soft rock in presence of water and/or air (e.g., rock sockets in shales)		Collapse/swell
			Potential tests
			Intact rock modulus
			Point load strength test
			Slake durability

Tables 14.2 and 14.3 summarize the soil data required and testing considerations for the design of driving and drilling pile foundations.

Before concluding this chapter, it is worth mentioning that the stiffness and strength of both piles and surrounding soils are normally known: extensive previous research and engineering efforts have been devoted to the study of the combined behavior at the soil–pile interface, known as soil–pile interactions, as will be elaborated from Chaps. 15 to 18.

Chapter 15

Capacity Control, Modeling of Pile Head Stiffness, and Mitigation Measures to Increase Pile Capacity

15.1 Capacity Control of Pile Foundations

The capacity of a pile foundation should be considered in all phases of its lifetime, including transportation, lifting, installation (e.g., pile driving), in-place performance, and even removal phase. The pile foundation should be checked with respect to the pile strength (yielding and buckling), axial and lateral capacity (both static and cyclic), deflections and rotations, as well as capacity of pile–structure connections (e.g., strength of pile sleeves and grout between sleeves and piles, pile grout capacity, etc.).

Obviously, the most important phase among the above is the in-place performance, i.e., the performance during the service of pile foundations carrying superstructures. In this phase, pile foundation designs should consider the following issues:

1. Piles should, in general, penetrate all soil layers that can potentially liquefy during a design earthquake event or under ocean wave loading. If soil layers having liquefaction potential are below the foundation tip (bottom), a punching shear analysis should be performed to check the possible penetration of the foundation into the liquefiable soil. In the application of end-bearing piles, it is important to know the shear strength of unliquefiable soil below the bottom of piles as well as vertical distance from pile tip to liquefiable soil layer(s).
2. The lateral resistance capacity (Chap. 16), the axial capacity (Chap. 17), and the torsional resistance capacity (Chap. 18) along piles should be sufficient with an adequate margin of safety against failure.
3. If soils at some depths around piles (relevant to pile–soil capacity control) reach their ultimate load-carrying capacity, the soil plasticity should be kept localized and not be developed into a large portion of piles.
4. The strength and stiffness of piles themselves should be sufficient.
5. The deflection of piles subject to design loads should not be larger than the tolerable deflection.

For a single pile, the consideration of bending moments and deflections often governs design, because the ultimate load-carrying capacity of the soil is reached only at very large deflections. For pile groups such as the one typically used for offshore jacket structures, axial pile–soil interaction forces are in many cases the governing forces in designs.

When sizing a pile foundation, the following items should be determined based on the basic capacity control requirements above: diameter, pile wall thickness, penetration (to provide adequate capacity due to soil–pile interaction), type of pile tips, pile spacing in a pile group, number of piles, geometry, location, mudline restraint, material strength, installation method, and other parameters as may be considered appropriate [791].

Pile diameter to wall thickness ratios (D/t) between 15 and 45 (with an average around 27) are typically used in offshore structures in the North Sea, although larger ratios have been used elsewhere. Adopting high wall thicknesses may necessitate special stress relieving treatment for the pile welds, making diameters significantly greater than 2 m potentially less attractive and economical when working with D/t ratios lower than around 40 [750]. However, thin wall piles may lead to other problems. For example, the primary piles that experienced buckling failures during installation in hard calcareous layers at the Goodwyn field (NW Australia) employed a D/t ratio of 60 [751]. Buckling took place during driving in very dense sands in other major projects, which may have been exacerbated by chamfered pile tip details and/or complex stepped pile specifications.

Furthermore, the corrosion allowance for piles made of steel must be accounted for, which is normally considered by assuming reduced wall thicknesses of piles in the assessment. In addition, piles should have a cathodic protection system to provide the required design life. All internal and external surfaces (submerged or buried) can be protected by galvanic anodes.

Moreover, effects of cyclic loading in both short-term (a few cycles) and long-term (around a million load cycles or more) should be fully recognized and accounted for in pile designs, which certainly influence the pile capacity and stability. For piles subject to frequent cyclic loading during their lifetime, the fatigue damage of piles should be considered. For example, for piles supporting offshore structures, the total fatigue damage times a safety factor (normally around 10 as recommended by several offshore design guidelines) should be less than unity for the design life of the platform. For a review of relevant fatigue calculation and analysis methodologies; see Jia [123].

Jardine [750] stated that understanding of the ground's reaction to driven pile installation, and loading has lagged behind industry's practical capabilities, and design approaches are still in an imperfect state of evolution. In addition to expensive offshore pile installation failures as demonstrated by Alm and his co-workers [752], considerable mismatches have been found in other cases where it has proved possible to check the industry-standard API/ISO recommendations in tests on large offshore piles [753–755], even though those tests are expensive to perform.

The probability of failure of pile foundations is strongly dependent on how the failure criterion is defined: it can differ significantly if the failure is defined as a full mobilization of soil plasticity surrounding piles compared to that if the failure is defined as the occurrence of local soil plasticity. For pile groups, the probability of failure can also differ significantly if the failure is defined as the single pile failure compared to that when the full capacity of the pile system is reached, which can result in a few hundred times relative differences regarding the probability of failure, and this relative difference is logically highest for the methods that predict the lowest probability of failure. It is then important to know that this effect strongly depends on the pile system and loading types. For example, the difference is higher when more piles are involved. The relative difference may also be smaller when piles are only subject to static loading. In this respect, analysis to verify the development of soil–structure failure at various stages reflecting each failure criterion and the associated probability of occurrence are desirable, which can be carried out by a conventional static pushover analysis or more advanced analysis such as incremental dynamic analysis or endurance time analysis [188].

Different from that of the in-place condition, the capacity control for pile driving often requires an adoption of upper-bound values of soil properties. Moreover, the driving fatigue to piles is an important task to perform. However, abundant offshore pile foundations installed before 1990s were only checked against fatigue due to environmental loading without a sufficient consideration of driving fatigue damage to piles.

It is worth emphasizing that piles are not only used to carry the load of superstructures but also to satisfy the serviceability limit on deformation. However, even nowadays, the common engineering practice in pile design still focuses on capacity-based design by providing sufficient capacity to carry loads, and the estimation of deflections and settlement is often regarded as a secondary design issue. This may partially be due to the common belief that it is more unreliable and difficult to estimate deflection than capacity, even if the opposite may, in fact, be the case [775, 776].

15.2 Representation of Piles, Surrounding Soils, and Soil–Pile Interactions

Soil–pile–structure interaction is an important consideration in evaluating responses of pile-supported structures, particularly in soft clays or liquefiable sands. Figure 15.1 illustrates loads applied on piles due to soil–pile–structure interactions.

Several levels of methods are available to incorporate the influence of pile foundations into the structural analyses, all of which belong to either a global approach or a substructure approach.

The global approach models soils, foundations, structures, and soil–pile interactions together. They can be either full 3D, or mixed 2D and 1D, or even 1D,

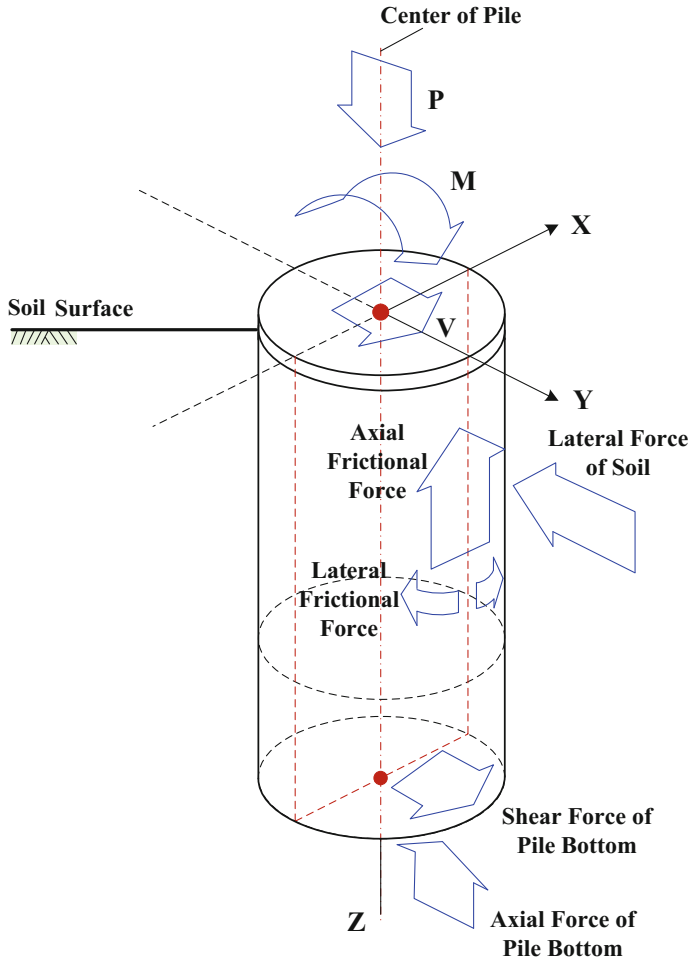


Fig. 15.1 Forces applied on the piles due to soil–pile–superstructure interactions (Courtesy of the College of Architecture and Civil Engineering, Beijing University of Technology)

whereas the substructuring approach analyzes soil foundations and structures separately. In the application of geotechnical earthquake engineering, there is a significant difference between responses of shallow foundations and responses of piles (and cap systems) due to the presence of soil–pile interactions, mainly attributed to the varied kinematic seismic motions along the length of piles.

Depending on the method of modeling and the extent of modeling details, various levels of soil–pile modeling are available:

1. Level 1 is to calculate the stiffness of a pile foundation at its interface with its superstructure under anticipated level of external loading, followed by modeling the stiffness (equivalent linear foundation model) directly at the superstructure's

interface with the pile. Therefore, there is no need to establish a dedicated model for the pile foundation. In practice, the stiffness in each degrees of freedom is normally calculated by either assuming that piles are fixed at a depth (depends on the soil and pile properties; see Sect. 15.4) and then calculating the stiffness at the pile head by hand, or by applying a small change of displacement and moment at the pile head and then calculating the pile stiffness numerically. This method normally assumes linear spring stiffness and cannot be justified when the pile is subjected to significant dynamic forces. However, under mild to medium level loadings such as frequent mild ocean wave loadings that dominate fatigue design of structures, linear stiffness foundation modeling is still most widely used for structural analysis and recommended by various design codes or recommended practices.

2. Level 2 is to use the substructure technique by cutting the pile at its top and replacing it with nonlinear springs and dashpots. The essential part of level 2 modeling is to combine a linear or nonlinear analysis of superstructure with a nonlinear analysis of the pile foundation modeling subjected to the forces obtained from the analysis of superstructure using an iterative algorithm in three phases: (1) reduction phase: the calculated load vectors and stiffness matrix at superstructures are applied to pile heads; (2) solution phase: load vectors and stiffness matrix in the reduction phase can be used to determine the responses (forces or displacements, with displacements being more typical) in piles that can be further applied on superstructures at their interface with piles; (3) re-tracking phase: the displacement applied on superstructures enables a re-tracking and calculation of the responses on superstructures based on the displacements applied from the piles. The forces obtained at the top of the pile model should be equal (with a tolerance error) but opposite to the calculated forces in the superstructure model. Substructure modeling provides exact solution for a linear system and can iterate to approximate the nonlinear effects using equivalent linearization.
3. Similar to level 2 but being a type of global approach, level 3 is to model each pile as a beam composed of a number of finite element beam elements and to represent soil–pile interaction using nonlinear springs. This model is often referred to as Beam on A Nonlinear Winkler Foundation (BNWF), which will be elaborated in Chaps. 16 and 17. Moreover, modeling of superstructures is included with the pile and pile–soil interaction modeling in the same analysis, which is a type of direct analysis, normally adopted in a time history analysis. The most distinguishing feature of the level 3 model lies in the fact that instead of modeling real soil, the soil, and soil–pile interaction are represented by mechanical components such as springs and/or dampers, thus reducing the efforts required for modeling and analysis. With its advantages of being convenience and versatility in the modeling of pile foundations, level 3 modeling is widely used in industry practice. However, it has several major drawbacks: (1) the subgrade reaction is governed only by the pile displacement at the depth where the soil reaction is considered, and the shear transfer between each two adjacent layers of soil is ignored; (2) the support ends (reference stops shown in

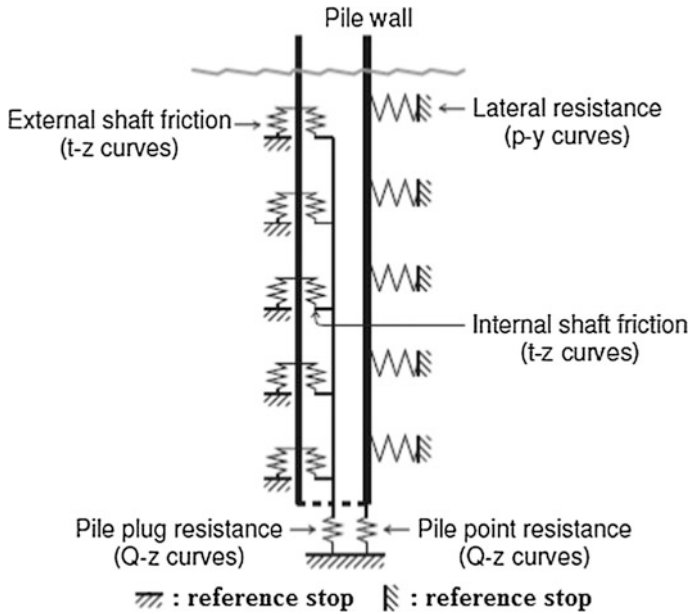


Fig. 15.2 Modeling of pile-soil interactions [757]

Fig. 15.2) of Winkler springs excited by seismic motions are based on free-field response analyses, which ignore the coupled response between piles and surrounding soils overlying bedrock subjected to bedrock excitations; (3) the three-dimensional displacement pattern of the soil as the pile pushes into the soil is ignored; (4) the spring stiffness values are foundation size dependent and difficult to determine [756]. Despite the disadvantages listed above, level 3 modeling can well represent the nonlinearity of soil media and the non-continuous contact (slippage and gap) between piles and surrounding soils. More dedicated analyses (levels 4 and 5) to calculate soil-pile-structure interactions include two-dimensional and three-dimensional modeling of piles and soil continuum using finite element or finite difference methods. They can also be categorized as a type of direct approach. Figures 3.37 and 19.9 show two examples of three-dimensional modeling of pile-soil systems. Obviously, those dedicated models are considerably more complex than that of the first three levels of analyses. In levels 4 and 5 analyses, an accurate modeling of the pile-soil interface is a key issue for many geotechnical problems. This is particularly important for axially loaded piles, where one part of the pile's total resistance is provided by frictional resistance between the pile and the soil. The interface is sometimes modeled by contact elements with friction angle and adhesion that are different from the internal friction angle and cohesion of the soils, or by interface elements with normal and tangential stiffness. For example, the interface elements can be based on elements with pairs of nodes, where one

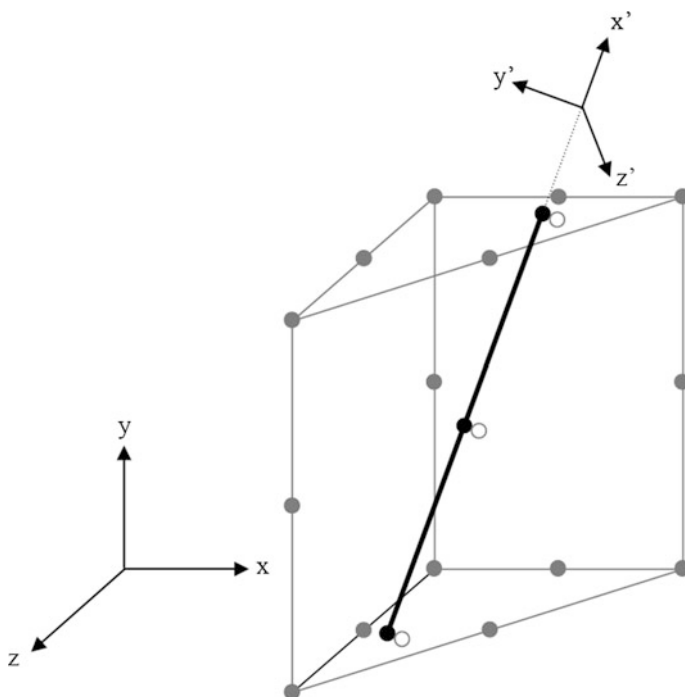
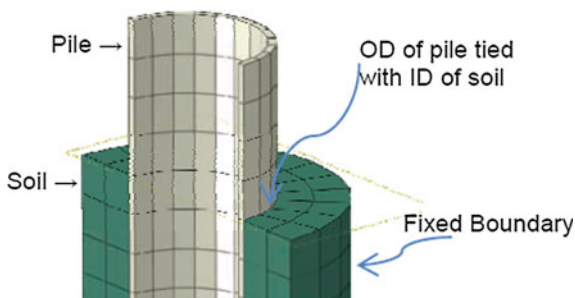


Fig. 15.3 Illustration of interface elements based on elements with pairs of nodes, where one node (black nodes in the figure) belongs to the pile element and one (blank gray circles) to the soil element [758]

node belongs to the pile element and one to the soil element, as illustrated in Fig. 15.3. In many cases, the soil is also directly tied to the pile’s outer surface at their interface by sharing the same node numbers at the same locations, with an example shown in Fig. 15.4.

4. Level 4 is to model soils surrounding piles as a homogeneous elastic continuum, and each pile is represented as an infinitely thin linearly elastic strip embedded in an elastic medium [760–762].

Fig. 15.4 Soil is directly tied to the pile’s outer surface at their interface [759]



5. Level 5 modeling often models the soil continuum surrounding piles by finite element method and piles by beam or solid finite elements. The method can account for the three-dimensional interaction, and both elastic and nonlinear soils can be modeled by giving inputs of elastic constants (e.g., Young's modulus and Poisson's ratio) or by adopting adequate nonlinear constitutive relationships. This model has the advantages of being capable of performing soil–pile–superstructure analysis in a fully coupled manner, without reverting to independent calculation of sites or superstructure responses, or applications of pile group interaction factors, as have been demonstrated by different researchers [763–765].

Levels 4 and 5 modelings reflect the state of the art in treating soil–pile–structure analysis. However, because of their complexity, in practice, levels 2 and 3, i.e., discrete models, where the soil and the soil–structure interface are idealized as beams and Winkler springs, respectively, are relatively inexpensive and can easily include inelasticity [766], and therefore reflect the state of the practice.

15.3 Winkler Foundation Modeling

In the modeling of levels 2 and 3, regardless of how complex the pile loading is, to carry out an analysis to assess the pile foundation behavior and integrity, one must reduce the soil behavior at each representative depth with simple load–deflection curves, known as Winkler foundation modeling. A rational model for the pile–soil system is shown in Fig. 15.2, in which the pile and surrounding soils are subdivided into a number of discrete layers, the pile–soil interaction system is represented by a series of nonlinear springs attached to the pile, and the springs transfer loads between piles and surrounding soils. The characteristics of those springs can be represented by the p - y , t - z , and Q - z curves, which are presented in various codes and standards such as API RP2A [791] and ISO 19902 [91]. In a typical static analysis or dynamic analysis other than the seismic analysis, the reference stops in this figure are considered to be fixed. However, in a dynamic seismic analysis in time domain, these stops are considered to follow the seismic excitations along the depths of piles, which are normally determined by a separate site-response analysis. This modeling is also adopted in finite element analysis as shown in Fig. 15.5, in which the disks represent soil layers modeled by a series of springs attached to the pile. The stiffness of springs not only vary with depth due to varied soil characteristics but also vary with a variation in relative movement between soils and the pile, i.e., the springs are nonlinear. Pile response is traced independently at nodal points of the pile segments within each layer. In addition, the soil damping can be accounted for by adding dashpots normally in parallel with the nonlinear springs.

It should be noted that the change in pile foundation stiffness due to the change in pile–soil interaction stiffness can influence deflections and dynamics of superstructures. By employing the modeling corresponding to level 2 or levels above

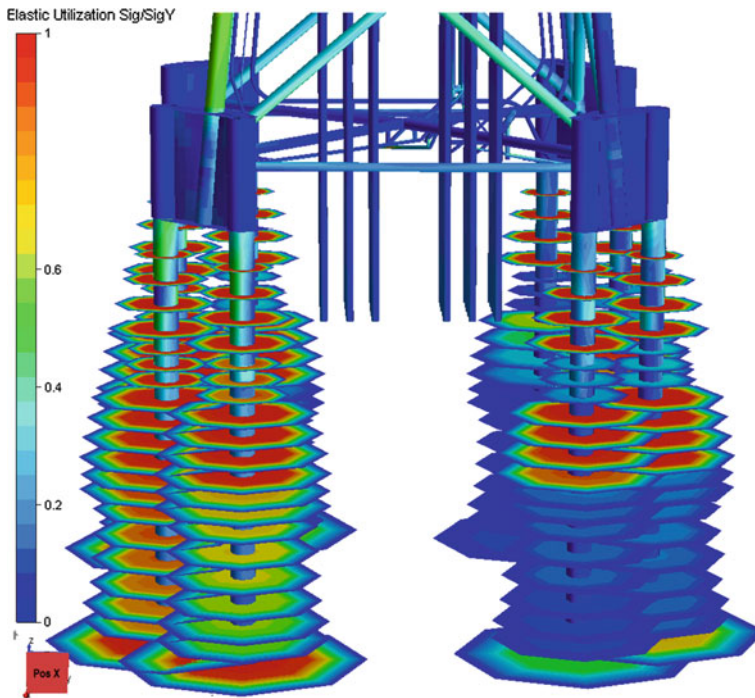


Fig. 15.5 Piles and surrounding soils visualized with disks representing soil layers modeled by a series of springs attached to the piles. The relative size of the disks reflects the relative strength of the soil weighting the soil capacity

level 2, a sensitivity study of dynamics (or even static responses) of superstructures can then be performed to conservatively determine values of pile foundation stiffness, which can be used in a structural analysis utilizing linear foundation model (level 1).

The understanding of soil–pile–structure interaction in geotechnical engineering is essential, even though it is far from matured [767, 768]. For example, many pile damages have been observed in the Kobe earthquake in 1995 [769–771], as well as in other earthquakes. The main difficulties in predicting the response of the soil–pile–structure system arise from the highly nonlinear interactions of soil–pile, pile–soil–pile, and soil–pile–structure [772]. This is mainly because dynamic behaviors of soils, piles, and structures are coupled together through the pile cap.

Figure 15.6 shows a pile group foundation supporting a jacket subjected to two subsequent ocean wave loadings, with the second wave having 93% of the amplitude of the first wave. The time instants at the two peak wave loadings are marked as points 2 and 5 in the left figure of Fig. 15.7, the points 4 and 6 indicate two time instants with close to zero wave loading after the two peak wave loadings, and point 1 is the time instant before the wave loading is applied on the jacket. The right figure in Fig. 15.7 shows the global base shear–horizontal displacement

relationship. By comparing the three subsequent instants with close to zero loading (points 1, 4, and 6), a non-reversible displacement of 0.06 m can be identified in point 6 compared with point 1. Since during the entire wave loading process, the jacket has only a slight local plastic deformation, and the pile itself remains elastic, the non-reversible displacement is mainly attributed to the nonlinear soil–pile interaction due to the occurrence of soil plasticity.

Under strong seismic excitations or other significant loadings, piles themselves can develop significant inelastic deformations. In order to consider the inelastic behavior of the piles, a modeling using plastic hinge or the fiber approach can be adopted [773].

Under cyclic loading, the stiffness of piles decreases due to the excitation intensity and contact conditions between the piles and the surrounding soils and between the cap and soil surface, so that the resonant frequency decreases and resonant displacement increases [774]. However, for piles with large diameters (> 2.5 m), the cyclic behavior of piles is different though it is not fully understood yet.

It should be noticed that in order to simulate a realistic nonlinear soil behavior, the material (resistance) factor for soil–structure interaction analysis is often applied

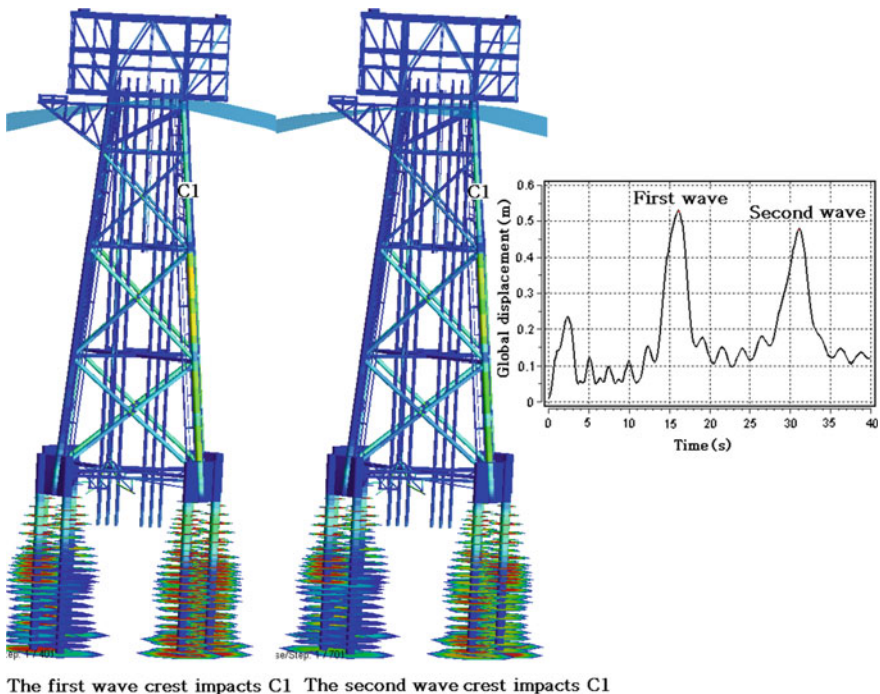


Fig. 15.6 Piles supporting a jacket are subjected to two subsequent ocean wave loadings Courtesy of Aker Solutions

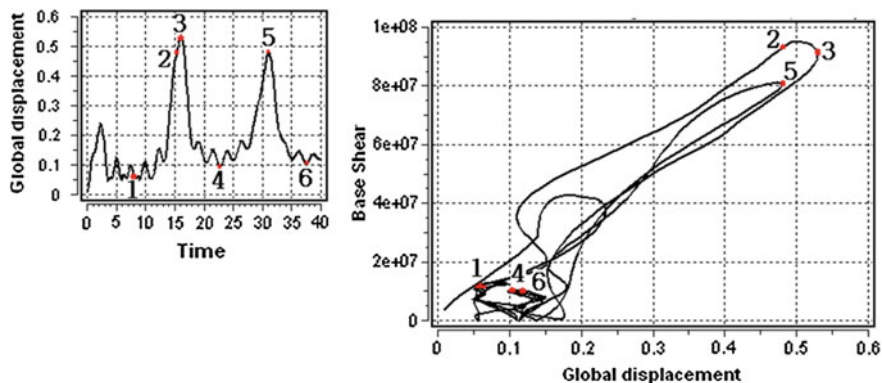


Fig. 15.7 Global base shear–horizontal jacket top displacement (right) relationship of the jacket (Fig. 15.6) at six different time instants shown in the left figure Courtesy of Aker Solutions

on the load side by defining target level(s) that accounts for both the load and resistance associated uncertainty, even though this operation contradicts with the theoretical background implied by the LRFD method (Sect. 1.13.2). Moreover, because parameters associated with a lower pile–soil resistance are usually adopted, p - y , t - z , and Q - z curves (Fig. 15.2) used for the modeling of pile–soil interaction are often design curves, implying that the curves will generally lead to a lower estimate of lateral and axial pile–soil resistance. In certain circumstances, a higher resistance is more unfavorable (e.g., pile driving design) and therefore needs to be considered in the relevant design.

It is noticed that the development of soil–pile–structure interaction analysis under dynamic loading was mainly driven by the demands of the offshore energy and nuclear power industries, and to a lesser extent by the demand from other industry sectors.

15.4 Simplified Calculation of Pile Stiffness and Natural Frequency for Pile–Structure System

15.4.1 Stiffness of Pile–Structure System

As a level 1 modeling presented in Sect. 15.2, for a preliminary estimation, the bending stiffness at the pile head can simply be calculated as:

$$k_0 = \frac{3EI}{h_c^3} \quad (15.1)$$

in which h_e is called equivalent length (height) of pile–structure system. As shown in Fig. 15.8, it is a hypothetical pile fully fixed at the base (as a cantilever, without surrounding soils), which gives the same horizontal deflection x under the same horizontal force F_x as the pile is inserted into flexible soils.

By assuming that each soil layer is homogeneous, isotropic, and linearly elastic, and the pile behaves as a linear-elastic semi-infinite beam, h_e can be approximated as [778]:

$$h_e = h_u \left[0.4 + 1.353 \left(\frac{h}{h_u} \right) + 1.875 \left(\frac{h}{h_u} \right)^2 + \left(\frac{h}{h_u} \right)^3 \right]^{\frac{1}{3}} \tag{15.2}$$

where $h_u = \left(\frac{102.9 E_p I_p}{k} \right)^{\frac{1}{3}}$; E_p and I_p are the Young’s modulus and second moment of inertia for the pile; k is horizontal subgrade reaction constant [779]; see Table 16.5 for its values.

Similar to the method presented above, for a simplified modeling of pile foundation, in order to model the pile–structure system, the pile foundation can be modeled as fixed at a distance h_a (often called effective or apparent fixity length)

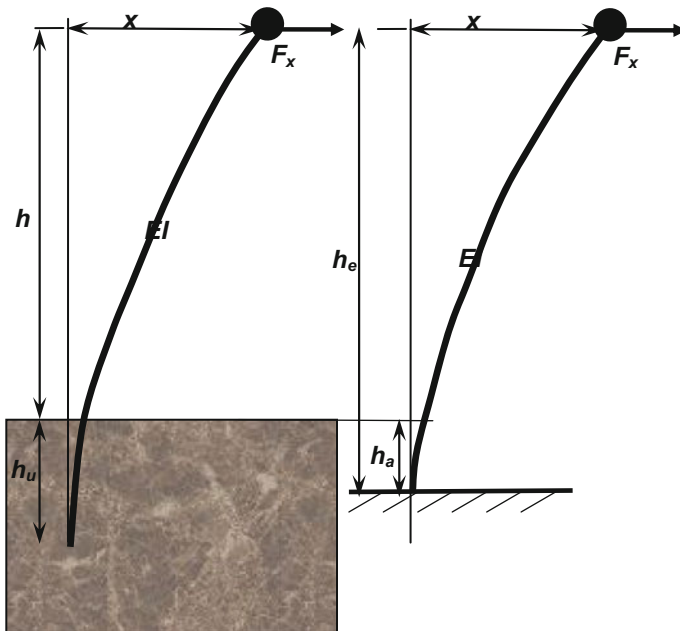


Fig. 15.8 Modeling of pile–soil stiffness from foundation–soil system (left) to its equivalent counterpart with a full fixity at the pile’s bottom (right)

below the mudline as shown in the right figure of Fig. 15.8. For stiff clays, this apparent fixity length is around $3.5\text{--}4.5d$; for very soft silts, it is $7\text{--}9d$; and for a general calculation without knowing the soil condition, an apparent fixity depth of $6d$ may be employed, where d is the diameter of the pipe pile.

More information regarding the equivalent length (height) can be found in [777].

15.4.2 Pile Head Stiffness

For long flexible piles loaded by a lateral load H and bending moment M at pile head, Hetenyi [780] derived the deflection u and rotation θ at the pile head as:

$$u = \sqrt{2} \frac{H}{k} \left(\frac{l_c}{4} \right)^{-1} + \frac{M}{k} \left(\frac{l_c}{4} \right)^{-2} \quad (15.3)$$

$$\theta = \frac{H}{k} \left(\frac{l_c}{4} \right)^{-2} + \sqrt{2} \frac{M}{k} \left(\frac{l_c}{4} \right)^{-3} \quad (15.4)$$

In the two equations above, the subgrade reaction analysis of the pile with bending rigidity EI embedded in soils with the subgrade reaction constant k yields a critical length of pile $l_c \simeq 4 [EI/k]^{1/4}$, beyond which the pile behaves as if infinitely long and then the length of the pile does not influence the deformation at the pile head [781, 782].

15.4.3 Natural Frequency of Non-uniform Beams

In engineering practice, non-uniform beams, such as monopile structures supporting offshore wind turbines shown in Fig. 15.9, are sometimes constructed in the form of a stepped beam, for which the mass (m_i) and stiffness ($E_i I_i$) within each constant cross-sectional segment can be assumed to be constant. A concentrated mass M is located at the tip of the beam.

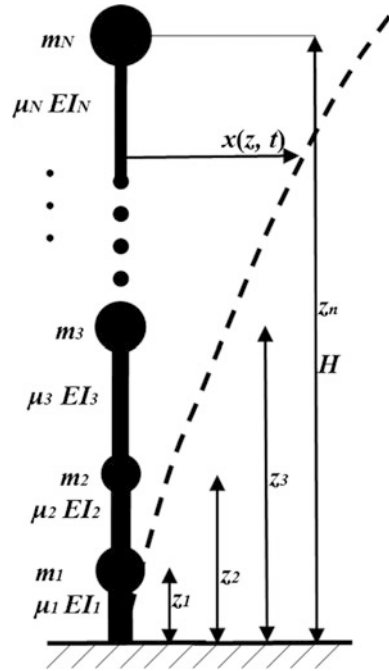
Consider the physical realization of a monopile structure with varied stiffness and mass as shown in Fig. 15.10. By assuming an approximate vibration mode shape $X(z)$, the deflection of the beam at position z and time t can be written as:

$$X(z) = \left(1 - \cos\left(\frac{\pi z}{2H}\right) \right) \quad (15.5)$$



Fig. 15.9 Monopile structures supporting offshore wind turbines

Fig. 15.10 Physical modeling of a cantilever stepped beam ($E_{(i)}I_i$, μ_i , m_i are the bending stiffness, weight per unit length and mass at z_i , respectively)



By using the Rayleigh energy method [123], the natural frequency of the stepped beam can be calculated as:

$$\omega_n^2 = \frac{\pi^4}{16H^4} \frac{\sum_{i=1}^N E_i I_i l_i \cos^2\left(\frac{\pi z_i}{2H}\right)}{\sum_{i=1}^N \left\{ m_i l_i \left[1 - \cos\left(\frac{\pi z_i}{2H}\right) \right]^2 \right\} + M} \quad (15.6)$$

where l_i is the length for segment i .

Furthermore, the monopile structure has foundation stiffness at its base, which can be modeled as rotational and translational coupled springs at mudline to represent pile head stiffness, as shown in Fig. 13.6. The natural frequency of the rigid beam with only foundation's rotation stiffness k_r and tip mass M presented is:

$$\omega_r^2 = \frac{k_r}{\left(\int_0^H \rho(z) A(z) z^2 dz + M \right)} \quad (15.7)$$

The natural frequency of the rigid beam (bending stiffness is infinitely high) with only foundation's lateral stiffness k_h and tip mass M presented is:

$$\omega_h^2 = \frac{k_l}{\left(\int_0^H \rho(z) A(z) dz + M \right)} \quad (15.8)$$

The stiffness of the system by including the flexibility of the beam and foundation can be taken as the individual beam stiffness (k_b), the foundation's lateral stiffness (k_h) and rotation stiffness (k_r) working in series. The natural frequency is [783]:

$$\begin{aligned} \omega_{\text{total}} &= \frac{\text{resultant stiffness of the entire system}}{\text{sum of the equivalent stiffness for springs in series}} \\ &= \frac{3 \sum_{i=1}^N E_i I_i l_i \cos^2\left(\frac{\pi z_i}{2H}\right) / H}{\left(\sum_{i=1}^N \left\{ m_i l_i \left[1 - \cos\left(\frac{\pi z_i}{2H}\right) \right]^2 \right\} + M \right) H^3 \cdot \left[\frac{H^3}{\pi^4 \sum_{i=1}^N E_i I_i l_i \cos^2\left(\frac{\pi z_i}{2H}\right) / H} + \frac{H^2}{k_r} + \frac{1}{k_h} \right]} \\ &= \frac{3(EI)_{\text{eq}}}{(M + m_{\text{eq}}H)H^3 \left[\frac{48}{\pi^4} + C_{\text{foundation}} \right]} \end{aligned} \quad (15.9)$$

where $(EI)_{\text{eq}} = \sum_{i=1}^N E_i I_i l_i \cos^2\left(\frac{\pi z_i}{2H}\right) / H$

$$m_{\text{eq}} = \sum_{i=1}^N \left\{ m_i l_i \left[1 - \cos\left(\frac{\pi z_i}{2H}\right) \right]^2 \right\} / H$$

$$C_{\text{foundation}} = \frac{3(EI)_{\text{eq}}}{K_{\text{eq}}H}$$

$$K_{\text{eq}} = \frac{k_r k_h H^2}{k_r + k_h H^2}$$

The term $C_{\text{foundation}}$ reflects the flexibility of the foundation, which varies between 0, for a very stiff foundation, and 0.5 for a reasonably flexible foundation.

In many cases, the simplified methods are not applicable because there is no information on lateral deflections [784]. Moreover, the simplified method cannot be used for analyzing pile groups. In these cases, numerical methods are preferred.

15.5 Increasing Existing Pile Foundation Capacity for Offshore Structures

There are several measures to increase the capacity for existing pile foundations, such as the installation of pile plugs to increase end-bearing capacity, infilling of scour pits to re-establish overburden pressure and to provide scour protection, inserting piles, “piggyback” piles, belled footings at pile tip, ballasting of piles to reduce critical tension loads and use of mudmats.

Jardine [750] and Price [785] discussed the drawbacks of those mitigation measures and pointed out that the mudmats may not be efficient to increase the pile foundation capacity due to creep and relative rates of mobilization of soil resistance between pile and mudmat, problems with scour, and uncertainties of connection to piles. Moreover, there is no agreement regarding whether pile plugs should be installed at the pile tip or at the top of the soil plug. Inserting piles and belled footings may only be effective on existing platforms with skirt piles unless work is done soon after pile installation before heavy topside modules are placed.

Chapter 16

Lateral Force–Displacement of Piles— p - y Curve

16.1 Introduction to p - y Curve

Many types of loading such as those induced from earthquakes, wind, ocean waves, traffic (bridges), thermal movement, water pressures (dams), and blast loads can generate lateral forces on vertical piles with a direction perpendicular to the axial direction of piles.

Piles resist lateral loads via shear, bending, and earth passive resistance. Thus, their resistance to lateral loads depends on pile stiffness and strength (pile configuration, in particular the pile length to diameter ratio, plays an important role in determining pile stiffness, hence its ability to resist shear and bending moments), soil type, soil stiffness, soil strength, and end conditions (e.g., fixed end versus free end) [31].

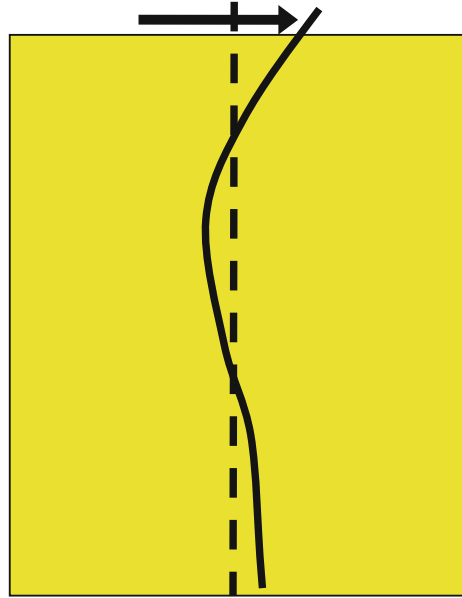
It is noted that, subject to lateral loading, the soil's lateral resistance and lateral pile stiffness are dominated by the characteristics of soils near the applied lateral loading, i.e., typically near the surface of soils. The soils below a certain depth do not significantly contribute to the lateral resistance and lateral pile stiffness, which is due to the pile's lateral deformation profile as shown in Fig. 16.1. This is different from the case when piles are subject to axial loading, in which soils along the entire effective length of piles contribute to axial resistance and axial pile stiffness as shown in Fig. 17.3.

Three methods are available to estimate the response of laterally loaded piles: elastic method, ultimate load method, and finite element method.

In the elastic method, the response of piles is calculated based on the assumption that the soil and the pile behave as elastic materials. Obviously, the ultimate pile resistance cannot be calculated based on the elastic method.

As a type of ultimate load method, by omitting the shear transfer between adjacent soil layers, the lateral resistance can be modeled with a series of uncoupled horizontal springs, known as Winkler springs, shown in Fig. 15.2. Each Winkler spring is represented with a lateral load–displacement curve to simulate the

Fig. 16.1 Deformation of a pile subject to lateral loading, soil resistance, and pile stiffness is mainly contributed by soils close to soil surface



mobilization of resistance from surrounding soils when the pile deflects, this load–displacement curve is normally referred to as p - y curve. The method of modeling the nonlinear soil springs using p - y curve is generally known as the p - y curve method, originally developed by Reese and his co-workers in 1970s [786, 787]. Semiempirical methods are normally used to estimate the p - y curves. The p - y curve can be used to solve problems including different soil types, layered soils, nonlinear soil behavior, different pile materials, cross sections, and different pile head connection conditions.

Subjected to horizontal loading, a pile embedded in soils can be modeled by the equilibrium equation:

$$EI \frac{d^4 y}{dz^4} - N \frac{d^2 y}{dz^2} + p + q = 0 \quad (16.1)$$

where y is the lateral deflection at a depth z along the pile; EI is the bending stiffness or flexural rigidity of the pile; N is the axial force in the pile; $p = -E_s y$ is the soil reaction per unit length; E_s is the secant modulus of soil reaction; q is the lateral distributed loads; the ratio p/y at any deflection represents the secant soil stiffness corresponding to that deflection.

To solve the equation above, boundary conditions for bending moments, shear forces, and rotations of the pile have to be defined:

$$M = -EI \frac{d^4 y}{dz^4} \quad (16.2)$$

$$Q = -\frac{dM}{dz} + N \frac{dy}{dz} \quad (16.3)$$

$$\theta = \frac{dy}{dz} \quad (16.4)$$

Figure 16.2 gives an example of deformation profiles, rotations, and the corresponding shear force and bending moment distribution along a pile's length. The pile has a diameter of 5 m and wall thicknesses varying from 0.12 m at top 10 m, 0.1 m from 10 to 20 m, and 0.08 m from 20 to 30 m. The pile is embedded in a sandy soil site. If one changes the pile diameter to 2.134 m and wall thickness into half of the original one, the deformation profiles, rotations, and corresponding shear force and bending moment distribution along the pile's length are illustrated in Fig. 16.3. It is observed that the pile's lateral/horizontal displacement increases significantly, while it reaches almost zero at a depth of 20 m below the soil surface. This is different from the original case (Fig. 16.2) with a pile diameter of 5 m, which shows that the lateral displacement at the pile tip (30 m below soil surface) is -0.01 m, indicating that the entire pile length is effective to contribute to the lateral resistance and stiffness. The maximum bending moment occurs at around 20 m depth for both cases, while for the case with smaller pile diameter, the value of the maximum bending moment is slightly lower due to the flexibility of the smaller diameter pile.

It is noticed that, for both clay and sand, the establishment of the p - y curves requires the determination of the ultimate lateral resistance p_u . The methods proposed by Matlock [788] for soft clays, by Reese et al. [789] for stiff clays, and by Reese et al. [786] and O'Neill and Murchison [789] for sands are often adopted to determine the p - y relationship.

The spacing between each two adjacent Winkler springs can be determined based on criteria that at least seven springs should be modeled in the natural deflection wavelength of a pile on elastic foundation. The wavelength can be simply calculated as:

$$l = 2\pi A \sqrt{\frac{4E_p I}{p_1 d}} \quad (16.5)$$

where E_p is the Young's modulus of a pile under study; I is the second moment of inertia of the pile's cross section; d is the pile diameter; and p_1 is the soil pressure per unit deflection per unit length of the pile.

For piles with diameters of up to 2.5 m, the lateral force–displacement relationship using p - y curves gives a good estimation of pile deflection. The soil is herein simulated by a number of uncoupled spring elements along the pile shaft. The corresponding p - y curves are usually taken from offshore guidelines by, for

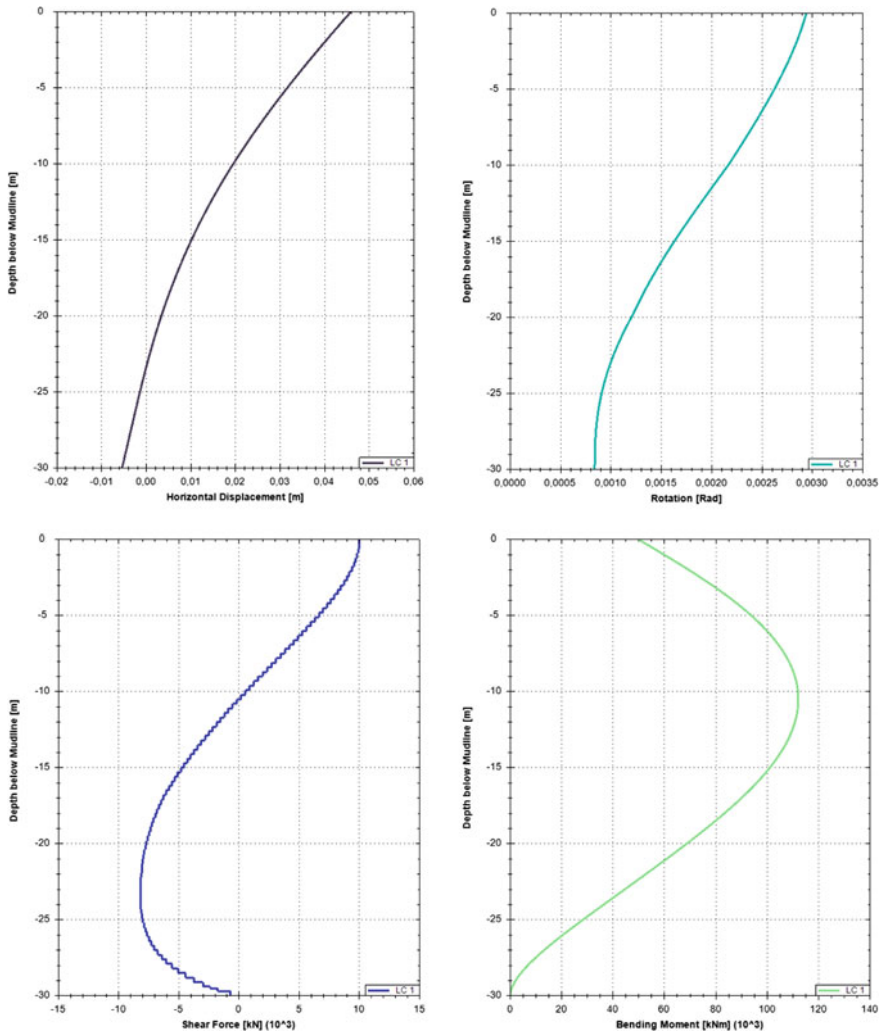


Fig. 16.2 Deformation profiles, rotations, and the corresponding shear force and bending moment distribution along the pile’s length, for a 5-m-diameter steel monopile, subject to a lateral/horizontal loading of 10,000 kN and a bending moment of 50,000 kNm at the pile head. The calculation is performed using IGtHPile (Institute of Geotechnical Engineering, Leibniz University Hannover)

example, the American Petroleum Institute [790–793] or Det Norske Veritas [794]. These guidelines recommend p - y approaches for different types of soils to reflect the respective load–displacement characteristic. Sand soils are often modeled by using the p - y approach originally developed by Murchison and O’Neill [795]. DNV describes the response of soft clays by the p - y relationship of Matlock [788]. In contrast, API uses approximated curves following the approach by Matlock [788].

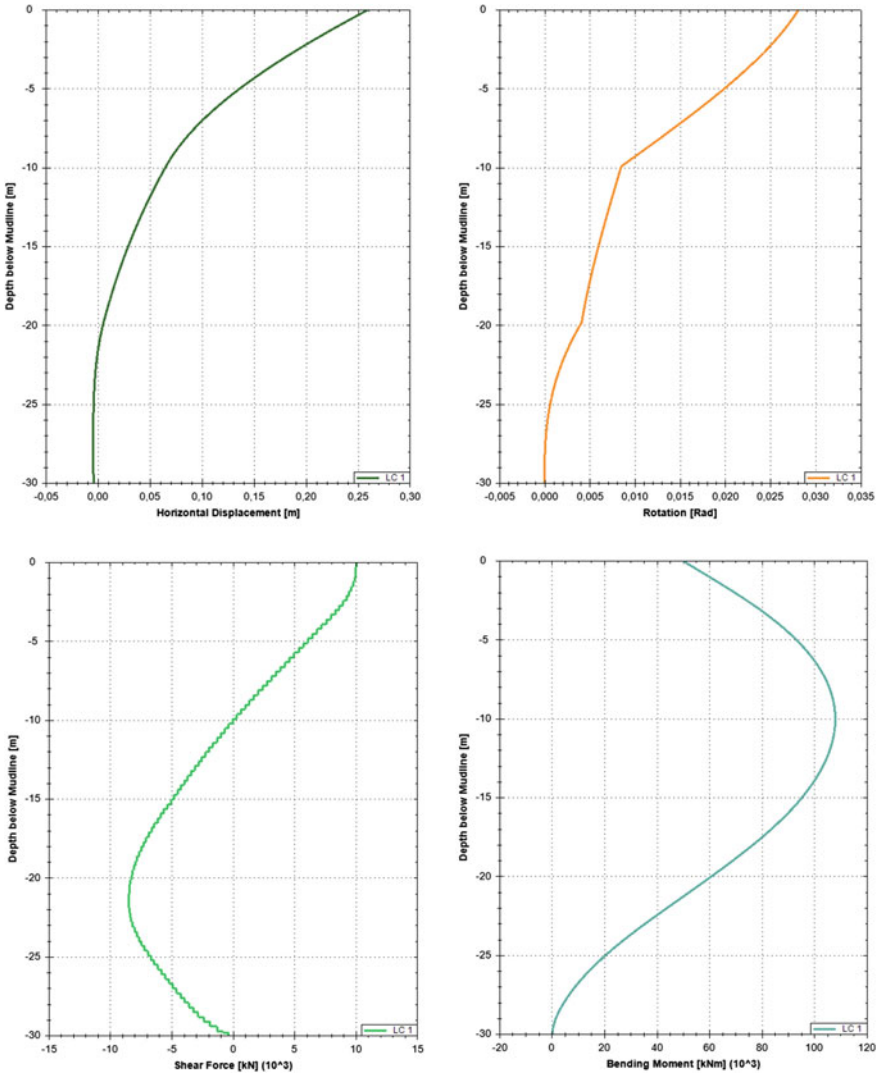


Fig. 16.3 Deformation profiles, rotations, and the corresponding shear force and bending moment distribution along the pile's length, for a 2.134-m-diameter steel pile, subject to a lateral/horizontal loading of 10,000 kN and a bending moment of 50,000 kNm at the pile head. The calculation is performed using IGtHPile (Institute of Geotechnical Engineering, Leibniz University Hannover)

The corresponding original approaches are based on field tests with diameters smaller than 0.61 m for sands and equivalent to 0.32 m for soft clay. The experiment-derived *p-y* curves were extrapolated to arbitrary pile dimensions and soil conditions by means of theoretical analysis. As *p-y* curves such as the ones recommended by API were originally developed for small diameter and flexible

piles, they generally yield a stiffness excessively high for large-diameter piles under significant lateral loading [796–798] and excessively low under small magnitude of loading, as will be discussed in Sect. 16.8.

Despite this limitation, p - y curves are still the predominant design and analysis method for calculating lateral responses of many pile foundations. For example, they are the method recommended by the offshore wind turbine design guideline DNV-OS-J101 [794]. This is because even if higher accuracy finite element models are available, they lead to a significant increase in modeling complexity. Also, experimental pile testings for large-diameter piles are rare because they are rather expensive to perform.

It should be noticed that, within a certain pile length determined by the pile cross-sectional dimension and soil condition, the embedded length has a dominating influence on controlling lateral displacements and rotations, as illustrated in Fig. 16.4, which shows that the calculated lateral pile head displacements and rotations of a large-diameter pile subject to a combined lateral force and bending moment at its head.

Even though in this book only p - y curves for clay and sand will be presented, readers need to bear in mind that the p - y curves for rock can also be established in a similar way, by using the basic rock and rock mass properties such as compressive strength of intact rock, rock quality designation, and initial modulus of rock. For details on this topic, Reese [800] is recommended.

Before leaving this section, it is worth mentioning that the calculation of ultimate lateral resistance of a pile almost always involves a consideration of plastic failure in both the pile and the soil, which is different from the determination of axial pile capacity, as will be discussed in Chap. 17. Sections 16.2 and 16.3 will present the method to calculate the ultimate resistance of clay and sand, respectively.

16.2 Calculation of p_u for Clays

Subject to pile loading, the ultimate resistance of clay p_u is generally related to the lowest value of two possible failure mechanisms: a wedge failure mechanism (Fig. 16.5) at shallow depths and a flow failure (Fig. 16.6) around the pile at greater depths. This dual approach is implemented in most of the proposed p - y curve expressions.

For the wedge failure mechanism at shallow depth, it is also accompanied by the failure of ground (Fig. 16.5) in front of the laterally loaded pile, which can extend for several pile diameters in front of the pile. In addition, the soil is pushed around the sides of the pile, leading to an active failure or a gap beside the pile.

For the flow failure at greater depth, the soil has to move around the pile but stays in the same horizontal plane through the motion because the overburden pressure is capable of restraining the ability of the soil to move vertically.

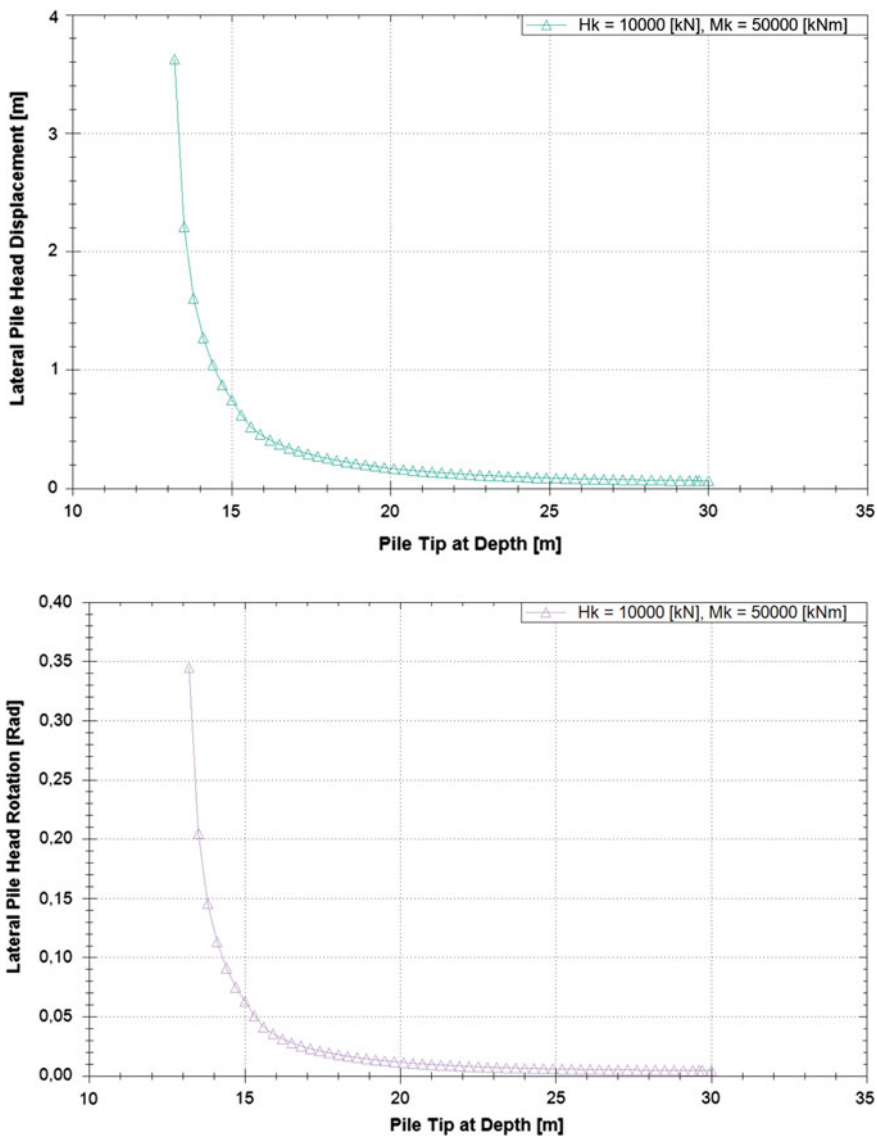


Fig. 16.4 Lateral displacement (upper) and rotations (lower) of a pile head varied with the embedded length. The pile head is subject to a lateral load of 10,000 kN and a bending moment of 50,000 kNm, the circular pile cross section has a diameter of 4 m and wall thickness varying from 0.08 to 0.12 m, and the pile is embedded in sand soils; the calculation is performed using IGtHPile (Institute of Geotechnical Engineering, Leibniz University Hannover) and the p - y curve formulated by Thieken et al. [799]

Fig. 16.5 Near ground surface, a pile will fail by shearing forward, i.e., pushing a passive wedge of soils up in front of it

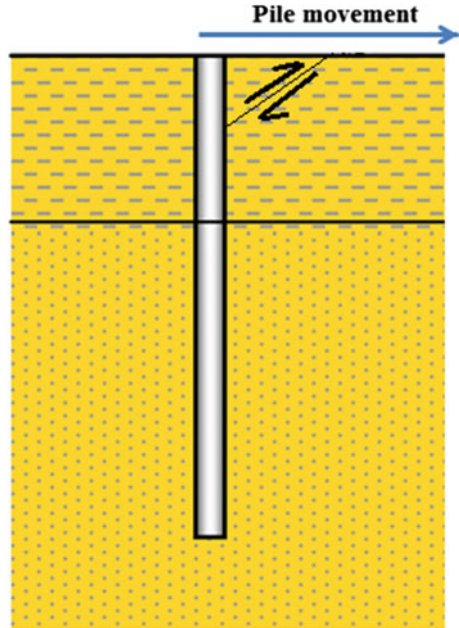
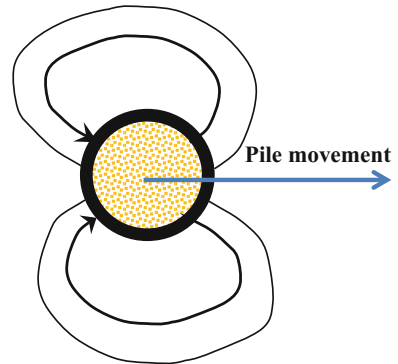


Fig. 16.6 At depth, plastic flow around a pile occurs only in horizontal planes



For clays, below a certain depth (typically 1.5 times the pile diameter), they are confined so that plastic flow around a pile occurs only in horizontal planes as shown in Fig. 16.6. The ultimate resistance per unit length of pile may be expressed as:

$$p_u = N_p s_u \quad (16.6)$$

where s_u is the undrained shear strength of clays; N_p is a non-dimensional ultimate resistance coefficient, which is increased to up to 9 [781] with depth. However, using $9s_u$ to calculate the ultimate resistance is a largely empirical method and has no solid theoretical justification.

Because, at locations close to soil surface, the pile will fail by shearing forward as shown in Fig. 16.5, the failure mode is a type of three-dimensional wedge failure. The corresponding N_p using the equation above can be taken in the range of 2–4, depending on whether the pile segment is considered as a plate with only frontal resistance or if it is a square cross section with soil shear acting along the sides, with its value being equal to 3 for cylindrical pile [788]. This value is based on limiting equilibrium solution for a smooth pile–soil interface.

The ultimate resistance of clay per unit length along the pile not only increases with the increase of depth z measured from soil surface downward, but also increases with the increase in overburden pressure σ_z , which can be expressed empirically by the following two equations [801]:

$$\begin{aligned} p_u &= 3s_u + \sigma_z + Js_u|z|/d \\ &= 3s_u + \gamma'|z| + Js_u|z|/d \end{aligned} \quad (16.7)$$

$$p_u \leq 9s_u \quad (16.8)$$

where J is a dimensionless empirical constant depending on the consistency of the clay and can be taken as 0.25 for stiff clay (e.g., often encountered in the North Sea) and 0.5 for soft clay (e.g., often encountered in the Gulf of Mexico and offshore areas in East Asia); γ' is the effective density of soils (see Sect. 1.4 for its definition); and d is the pile diameter.

In the first of the two equations above, readers may notice that the units between $Js_u|z|/d$ and $\gamma'|z|$ are not consistent. Therefore, the item $Js_u|z|/d$ may be replaced by $Js_u|z|/(d \cdot s^2)$ to make the units between the two items consistent, where s is second.

The first item in the right-hand side of the first of the two equations above indicates the lateral resistance at soil surface with a value of $3s_u$, the second term indicates the contribution from the overburden pressure, and the third item can be taken as a geometrically related restraint that even a weightless soil around a pile would provide against upward flow of the soil [788]. Moreover, due to rapid deterioration under cyclic loadings, the ultimate static resistance should also be reduced for cyclic design considerations [790].

It is noticed that in any case, p_u should be lower than $9s_u$; i.e., at certain depth X_R and below, the strength of soil is constant and does not increase with depth. This depth is called depth of transition, which can be determined as the point of first intersection of the two equations above:

$$X_R = \frac{6d}{\frac{\gamma'd}{s_u} + J} \quad (16.9)$$

Since s_u varies with depth, the solution of the equation above may be obtained numerically or graphically. X_R should normally not be less than 2.5 times the average diameter of the pile as recommended by API [790].

Again, in the equation above, the item $\frac{\gamma' d}{s_u}$ may be replaced by $\frac{\gamma' d}{s_u s^2}$ to make the unit between the item $\frac{\gamma' d}{s_u}$ and J consistent.

Note that the equations above only apply to soft clay. For stiff clay with $s_u > 96$ kPa (some studies define this limit as 100 kPa), the lateral resistance varies between $8s_u$ and $12s_u$.

It is worth mentioning that in a later study to analytically derive the ultimate lateral soil resistance, Randolph and Houlsby [802] presented that the ultimate lateral soil resistance is strongly dependent on the pile–soil interface, which develops in front of a laterally loaded rigid circular disk, the ultimate lateral soil resistance is $11.94s_u$ for a completely rough pile–soil interface, and this value changes to $9.14s_u$ for a smooth interface.

16.3 Calculation of p_u for Sands

Similar to clays, two major failure modes occur at depth and near the soil surface: Below a certain depth, they are confined so that plastic flow around a pile occurs only in horizontal planes; near the soil surface, the resisting force is assumed to be a three-dimensional wedge, but active soil pressures are also assumed to act with the pile displacement and so reduce the ultimate pressure [27]. The ultimate lateral soil strength/resistance of sand has been empirically found to vary with depth.

Based on a study by O'Neill and Murchison [789], at shallow soil depth, the soil's ultimate lateral strength per unit length can be calculated as:

$$p_{us} = (C_1|z| + C_2d)\gamma'|z| \quad (16.10)$$

At deeper depth, the lateral ultimate strength per unit length can be calculated as:

$$p_{ud} = C_3d\gamma'|z| \quad (16.11)$$

where C_1 , C_2 , C_3 are the lateral resistance coefficients dependent on the effective internal friction angle of sands, which are given in Table 16.1 according to API [790]; γ' is the effective density of soil; d is the pile diameter.

In practice, at a given depth, the smallest value calculated from the two equations above should be used as the ultimate bearing capacity [790]:

$$p_u = \min(p_{us}, p_{ud}) \quad (16.12)$$

Table 16.1 Values of C_1 , C_2 , C_3 as a function of angle of internal friction ϕ' [790]

Angle of internal friction ϕ' (°)	C_1	C_2	C_3
20	0.6	1.5	8.5
21	0.7	1.6	9.6
22	0.8	1.7	10.8
23	0.9	1.8	12.2
24	1.0	1.9	13.8
25	1.1	2.0	15.6
26	1.2	2.1	17.6
27	1.3	2.2	19.9
28	1.4	2.3	22.5
29	1.6	2.5	25.4
30	1.7	2.6	28.7
31	1.9	2.7	32.4
32	2.1	2.9	36.6
33	2.3	3.0	41.4
34	2.5	3.2	46.7
35	2.8	3.4	52.8
36	3.1	3.6	59.6
37	3.4	3.8	67.4
38	3.8	4.0	76.1
39	4.2	4.2	86.0
40	4.6	4.4	101.5

16.4 Constructing p - y Curves for Clays

The establishment of p - y curves is influenced by the type of soils, the type of loading, the remolding due to pile installation, the effect of scour, and the effect of mud slide forces.

The basic method to construct p - y was initially proposed for soft clays with a parabolic curve shape as shown in Fig. 16.7, based on the establishment of non-linear load–deflection curves from lateral resistance p_u , and a strain level ϵ_c , being the strain value that occurs at 50% of the maximum principal stress in laboratory undrained compression tests of undisturbed soil samples. If no values of ϵ_c are available, the ones proposed by Skempton (Table 16.2) [803] may be used.

In numerical analysis, p - y curves for clays are discretized and represented at a number of discrete points. For example, in the p - y curve for clay adopted by API [790], the first discrete point is at half of the ultimate lateral resistance p_u as shown in Tables 16.3 and 16.4. In these tables, p is the actual lateral resistance in kN/m; y is the actual lateral deflection.

Theoretically, the initial tangent modulus for a parabolic curve assumed for a clay p - y curve is infinite at zero deflection. Even though this is not realistic, since pile deflection at significant soil–structure interaction zone (e.g., at upper 8 pile

Fig. 16.7 Establishment of p - y curves for soft clays [788]

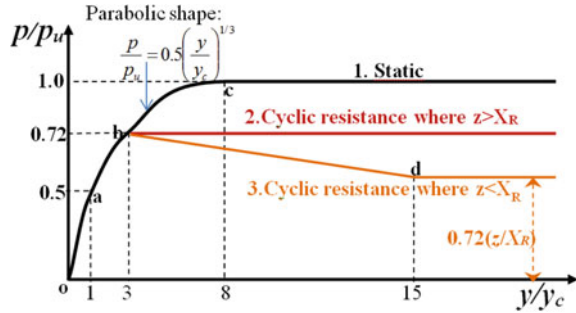


Table 16.2 Typical values of ϵ_c [803]

Consistency of clay	ϵ_c
Soft	0.02
Medium	0.01
Stiff	0.005

Table 16.3 p - y curve for soft clays under short-term static loading [790, 791]

p/p_u	y/y_c	Point marked in Fig. 16.7
0	0	o
0.50	1.0	a
0.72	3.0	b
1.00	8.0	c
1.00	∞	

Table 16.4 p - y curve for soft clays under cyclic loading [791]

$z > X_R$		$Z < X_R$		Point marked in Fig. 16.7
p/p_u	y/y_c	p/p_u	y/y_c	
0	0	0	0	o
0.5	1.0	0.5	1.0	a
0.72	3.0	0.72	3.0	b
0.72	∞	$0.72 \cdot z/X_R$	15.0	c/d
		$0.72 \cdot z/X_R$	∞	

diameter from the pile head downward) is well above the deflection range valid for using initial tangent modulus, the infinite value of initial tangent modulus rarely causes real problems when pile foundations are subjected to design ocean wave loading or earthquake loading.

To convert from strains measured in laboratory triaxial tests (Sect. 1.9.3) into pile deflections, the following relationship is used to calculate the reference displacement y_c , which is taken as the displacement of pile that occurs at 50% of the

ultimate soil resistance. When the ultimate soil resistance is reached, the clay is assumed to remain ideally plastic:

$$y_c = A \varepsilon_c d \quad (16.13)$$

A is a constant that varies from 0.35 to 3.0 and is often taken as 2.5 (the value adopted in API).

The part of the pre-plastic portion under static loading can be approximated with a parabola:

$$\frac{p}{p_u} = 0.5 \left(\frac{y}{y_c} \right)^{1/3} \quad \text{for } y \leq 8y_c \quad (16.14)$$

When the lateral displacement reaches y_c , no post-peak degradation is assumed:

$$\frac{p}{p_u} = 1.0 \quad \text{for } y > 8y_c \quad (16.15)$$

Based on full-scale lateral load tests on a 0.3-m-diameter instrumented steel pipe pile embedded in soft clay deposit at Lake Austin, Texas, Matlock [788] back-computed p - y curves from the test results. Table 16.3 shows the characteristic shape of the soft clay p - y curves under static loading case. For the case where equilibrium has been reached and piles are subjected to cyclic loading, the p - y curve can be established as shown in Table 16.4. The p - y curves for soft clays under both static and cyclic loadings are summarized and compared in Fig. 16.7, which comprise three segments.

In API 2007 [792], two additional points are added between point O and point A for soft clays under short-term static loading, with $p/p_u = 0.23$ when $y/y_c = 0.1$ and $p/p_u = 0.33$ when $y/y_c = 0.3$, regardless of whether $z > X_R$ or $z < X_R$. The two additional points are indicated by bold points in the left figure in Fig. 16.8, which give a smoother curve at the low level of lateral loading.

Even though in engineering practice, p - y curves characterized by the API recommendations essentially describe an approximation of the Matlock curve by four [790, 791] or six points [53] on the p - y curves that are connected linearly, compared to the original Matlock curve [788], the curves defined by API can be significantly different. This difference is illustrated in the right figure in Fig. 16.8, which shows that the initial stiffness between the Matlock curve and the curves defined by API is not close to each other. This can severely affect the foundation stiffness and dynamic characteristics of the superstructure, even though it is not fully recognized by many geotechnical engineers.

For stiff clays with $s_u > 96$ kPa (some literatures use 100 kPa), the stiffness and strength under cyclic loadings are greatly degraded, as shown in Fig. 16.9, which can be used for modeling piles under quasi-static loading. By comparing Figs. 16.7 and 16.9, it is noticed that, due to the more brittle behavior of stiff clay than that of the soft clay, particularly the post-peak portion of p - y curves has to be modified by

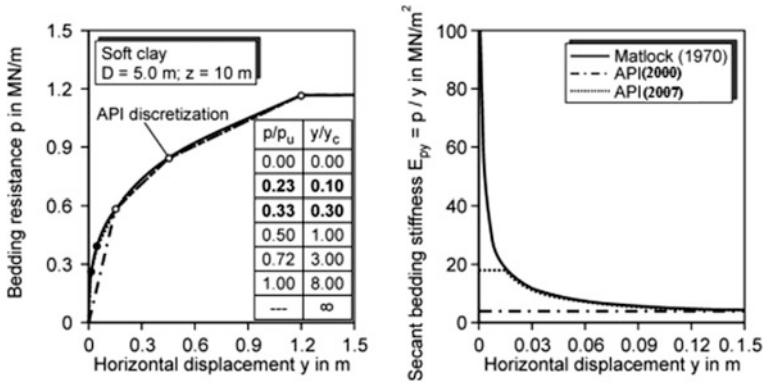
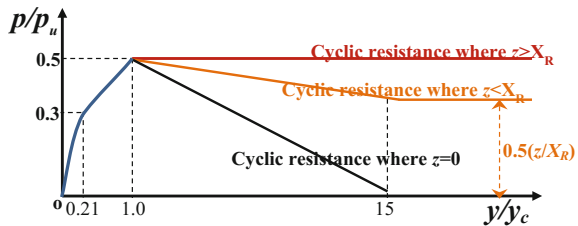


Fig. 16.8 Illustration of p - y curve according to Matlock [788] and approximation of the Matlock curve by API recommendations. The two additional points defined by API [792] compared to API [791] are emphasized by bold font in the left figure [849]

Fig. 16.9 Establishment of p - y curves for stiff clays (modified Matlock approach)



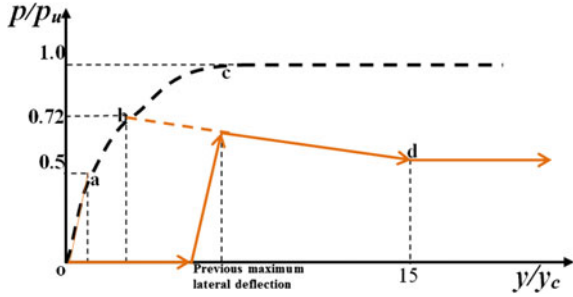
accounting for the stiffness degradation; i.e., stiff clay may experience more severe cyclic degradation. The degree of this degradation strongly depends on the specific stiff clay soil condition. For example, in fully saturated stiff clays at a deepwater site, a significant degradation in the post-peak portion may be considered [804].

Apart from a normal cyclic loading condition, after a significant cyclic loading process, gaps (cavities) may appear between the upper part of a pile and its surrounding soils, together with remolding, leading to a decrease in soil stiffness. Therefore, in case of reloading after the previous (more intensive) cyclic loading, a modification of the p - y curve by accounting for the previous loading is needed, which is shown in Fig. 16.10. At greater depths, overburden pressure will prevent gapping and may fill up the gaps, but remolding may still cause softening. However, the modification of the p - y curves may not be necessary because the lateral deflection at depth is small.

Practically, for offshore structures, a storm condition with 3–20-year return period of wave loading may be used to calculate the maximum lateral deflection, followed by the modeling of p - y curve as shown in Fig. 16.10.

Moreover, it is worth mentioning that, with time, gaps created due to intensive loading may be filled with soils. If the filling material is clay, the increase in the

Fig. 16.10 Modified p - y curve to account for the previous more intensive loading



lateral resistance is negligible, while if the filling material is sand (e.g., with a sand layer on top of a clay layer), there will normally be a significant improvement of lateral resistance.

Based on centrifuge tests [805] and finite element analyses [806], Jeanjean [805] proposed p - y curves as:

$$\frac{p}{p_u} = \tanh\left(\frac{G_{\max}}{100s_u} \left(\frac{y}{d}\right)^{1/2}\right) \text{ for } y \leq 8y_c \tag{16.16}$$

where G_{\max} and s_u are the initial shear modulus and undrained shear strength, respectively.

Note that in the equation above, G_{\max}/s_u is the only parameter that controls the shape of p - y curves, and the effects of stress-strain response beyond the initial shear modulus stage are not accounted for.

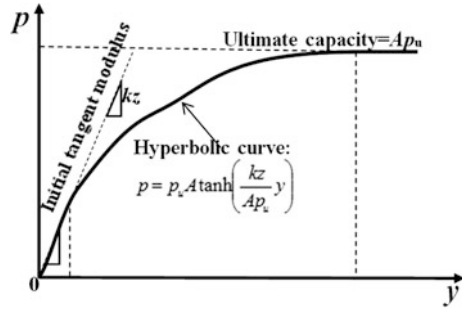
For a review of p - y curves for clays, O'Neill and Gazioglu [807] is recommended, which summarizes the Matlock soft clay p - y curve [788] along with other available stiff clay p - y curves and also reconciles the so-called pile diameter effects, and eventually recommends an alternative p - y curve for clays.

16.5 Constructing p - y Curves for Sands

Based on a study including both theoretical and field test of laterally loaded piles with a diameter of 610 mm in sands, Fig. 16.11 shows a schematic p - y curve for sands, which comprises an initial portion of a straight line with a constant slope representing the elastic behavior, followed by a hyperbolic (nonlinear) curve until it reaches the soil resistance p_u , after which the p - y curve becomes flat and extends to certain extent.

API RP2A [792] recommends that, in case no more information is available, the Reese's sand p - y curve [786] at depth z may be determined by (Fig. 16.11):

Fig. 16.11 Schematic representation of p - y curve for sands



$$p = p_u A \tanh\left(\frac{kz}{A p_u} y\right) \tag{16.17}$$

where p_u with the unit of kN/m is the ultimate resistance of the sand at depth z ; the factor A accounts for cyclic or static loading, which is determined by fitting the theoretical value of p_u (Sect. 16.3) to field test results: under static loading $A = (3.0 - 0.8z/d) \geq 0.9$ and under cyclic loading $A = 0.9$ at all depths, which is based on measurements; for static loading, the multiplier A is such that the lateral resistance at large displacement in sand can be as much as three times the representative resistance, but A reduces rapidly with z and is 0.9 for depths greater than $2.625d$; d is the diameter of piles; k is the initial modulus of subgrade reaction measured in force per volume unit (kN/m^3), and it increases linearly with depth and is determined as a function of the internal angle of friction ϕ' and the relative density as shown in Table 16.5, but is assumed to be independent of pile properties;

Table 16.5 Initial modulus of subgrade reaction k varied with the angle of internal friction ϕ' and the relative density for sands below water table [791]

Sand condition	ϕ' ($^\circ$)	Relative density (%)	Subgrade reaction k (kN/m^3)
Very loose	<29	20	265.7
Loose	29–30	25	426.3
		30	553.6
		35	744.6
		40	996.4
Medium dense	30–36	45	1356.3
		50	1716.1
		55	2026.1
		60	2491.1
Dense	36–40	65	2850.9
		70	3293.8
		75	3792.0
		80	4262.6

kz is called subgrade modulus (which is the initial slope of the p - y curve as shown in Fig. 16.11, also called initial bedding stiffness E_{py}); y is the lateral deflection.

From the equation above, it is noticed that p - y curves for sands are essentially controlled by the initial stiffness of the soil kz and the ultimate resistance p_u . Even if kz is assumed to be independent of pile diameter, the entire Reese's p - y curve is essentially pile diameter-dependent due to the influence of p_u (Sect. 16.3). Therefore, the equation to calculate p - y curve that is independent of pile diameter is only true for initial tangent modulus of the p - y curve. At any nonzero deflection values, the secant stiffness will be dependent on both the initial tangent modulus and p_u that is strongly dependent on pile diameter. Moreover, for piles with diameters larger than 2.5 m, k is also dependent on the pile diameter, as will be discussed in Sect. 16.8.2.

For soil below the water table, Augustesen et al. [808] proposed that k can be calculated as:

$$k[\text{MN/m}^3] = 0.008085\phi'^{2.45} - 26.09 \text{ for } 29 < \phi' < 45^\circ \quad (16.18)$$

As aforementioned, different from that of clays, the gaps created due to intensive loading in sands will normally be filled. Therefore, the effects of gaps for sands are normally neglected.

It should be noticed that the hyperbolic p - y curve described above is based on the testing of two identical, instrumented piles installed at Mustang Island [844]. The tests included a total of seven load cases, but were conducted for only one pile diameter, one type of sand, and circular pipe piles. A change in any of these factors might affect the behavior of a laterally loaded pile. For example, the slenderness ratio (the embedded length/pile diameter) of the Mustang Island test piles is 34.4, which is considered as flexible, while the slenderness ratios for many piles for offshore applications (such as monopiles used for offshore wind turbine foundations) are much less than 30. Therefore, validations of p - y curve used for stiff piles are needed.

Furthermore, modern offshore wind turbine foundations only allow small pile head rotations and have strict requirements on the foundation stiffness due to resonance sensitivity in the serviceability, while the initial bedding stiffness kz is independent of pile properties. Carter [859] and Ling [860] postulated that E_s (associated with the initial bedding stiffness) increases for larger-diameter piles (Sect. 16.8.3.5). By studying the results obtained from both testings and numerical analyses, Sørensen et al. [835] also concluded that initial bedding stiffness is highly affected by the pile diameter. On the other hand, Terzaghi [779], Ashford and Juirnarongrit [837], and Fan and Long [838] stated that effects of pile diameter on the initial bedding stiffness are insignificant.

Moreover, initial bedding stiffness kz is proportional to depth z . Researchers [835, 836] argued that this assumption is non-conservative at large depth, and a nonlinear stiffness should be used in such contexts instead.

16.6 Effects of Cyclic Loading on p - y Curves and Structural Dynamic Response

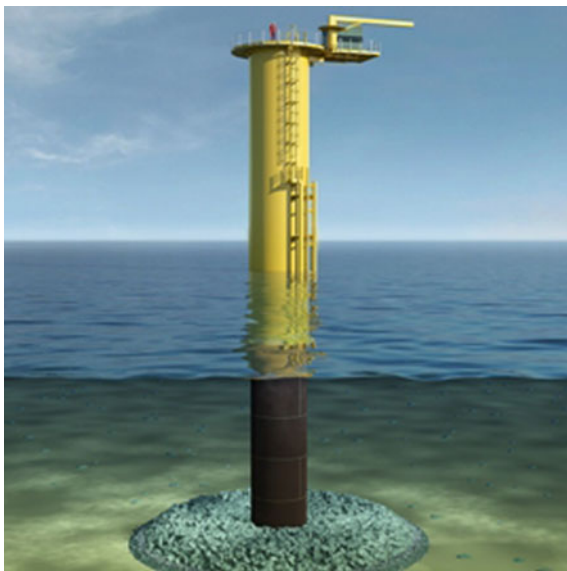
Compared to land-based structures, offshore environments pose additional challenges due to large numbers of ocean environmental load cycles. Cyclic loadings, either static or dynamic, acting on the foundations of offshore structures are likely to cause major changes to the bearing capacity of the foundations. Lateral cyclic loading of pile foundations can lead to deflections of the pile head which, if large enough, place considerable stress on the soil close to the pile head, with pile deflections being increased with an increase in number of load cycles. Furthermore, transient changes/accumulation of pore-water excess pressure around piles may reduce the soil resistance. Moreover, in cohesive soils underwater, permanent soil deformation may cause the formation of gaps between piles and soils, and a de-stabilization of the near-surface area, which reduce the bearing capacity of laterally loaded piles.

Cyclic loading effects are more significant for offshore wind turbine supporting structures as the static loads are relatively small compared to usual offshore oil and gas platforms, and the number of cyclic loadings is significantly higher than that of offshore platforms. For example, in the service life of an offshore structure, the number of cyclic loadings due to environmental loading is around a few million cycles (mainly due to waves) for an offshore platform, but this number is increased by more than 10 times (due to wave-, wind-, and turbine blade-induced loading) for an offshore wind turbine supporting structure. Therefore, cyclic loading due to wind and wave actions becomes more important. This can cause a change in the natural frequency of the offshore wind turbine–foundation system, posing additional challenges for the design of wind turbine foundations as they are sensitive to changes in natural frequency.

Therefore, even though these issues are still not fully understood, the effect of cyclic loading in both short term (a few cycles) and long term (around a million load cycles or more) should be fully recognized and accounted for in pile designs.

In saturated soils, extreme short-term cyclic loading often involves a pore-pressure buildup that can result in liquefaction and foundation failure. This is more apparent for large-diameter pile foundations, such as monopiles commonly used in offshore wind farms as shown in Fig. 16.12, which usually comprise a foundation pile with a diameter of a few meters. This is due to the progressive reduction of pore volume as the sand contracts under cyclic loading and the inability of soils to completely dissipate the overpressure between consecutive cycles. The advancing accumulation of excess of pore-water pressure has the consequence of a gradual decrease of effective stress in soils and the shift of the stress paths toward regions of lower confining pressures, which for the case of dense sands can lead to local phenomena such as cyclic mobility and considerable plastic deformations. Therefore, even if liquefaction does not take place, the foundation can still experience a softening and the appearance of residual

Fig. 16.12 A monopile used as offshore wind turbine foundation

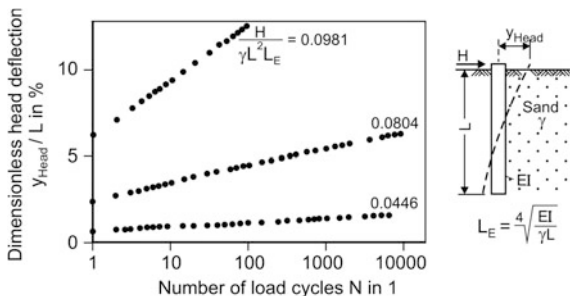


displacements. On the other hand, the effects of the long-term cyclic loading on the pile’s embedment and progressive inclination must also be fully recognized [809].

It is well known from various experimental investigations that the deflection of a horizontally loaded pile generally increases under cyclic loading. The deterioration in soil resistance due to cyclic loading is most significant at shallow depths with large lateral pile deflections. By applying cyclic loading on flexible piles in homogeneous sands, Hettler [810] showed how the horizontal displacement of pile head increases with the increase in the number of load cycles, as illustrated in Fig. 16.13.

The increase in lateral head deflection has been found to be influenced primarily by the number of load cycles and is normally assumed to be independent of the load amplitude. Furthermore, as long as the cyclic load amplitude is well below the ultimate pile capacity, sedimentation behavior can be expected, which means that the deflection rate decreases with increasing number of load cycles. Little and Briaud

Fig. 16.13 Horizontal pile head displacement (y_{Head}) increases with the increased number of applied load cycles [810, 811]



[812] proposed an equation to estimate the lateral displacement y_N of pile heads due to N load cycles, which fits the cyclic displacement curves of piles [813]:

$$y_N = y_1 \cdot N^m \quad (16.19)$$

where m is an empirical degradation parameter, which ranges from 0.10 to 0.25 for rigid piles [814], 0.04–0.09 for flexible piles [812], and 0.136 for driven piles in dense sand; y_1 are the horizontal pile head deflections after the first loading cycle.

Hettler [810] proposed a logarithmic type equation, which is regarded as a better formula to estimate cyclic displacement curves of flexible piles:

$$y_N = y_1 + (y_1 \times t \times \ln N) \quad (16.20)$$

where t is an empirical degradation parameter, which is besides others a function of soil properties and loading type (one-way or two-way loading). For one-way loading, t is around 0.20, which means that 1000 load cycles induce an increase in the pile head displacement of about 140%.

Note that the equation above can only calculate the displacement of cyclic loading with constant amplitude. A realistic loading history comprises load cycles with variable amplitudes. To solve this dilemma, Lin and Liao [815] extended this method by proposing a formulation to calculate equivalent number of loading cycles N^* :

$$N_k^* = e^{\left(\frac{y_{1,k}}{y_{1,1}}(1 + t \ln N_k) - 1\right)/t} \quad (16.21)$$

where $y_{1,1}$ is the static displacement under design load; $y_{1,k}$ is the static displacement under the load of different amplitude; and N_k is the number of load cycles.

By summing overall loads of different amplitudes, the resulting cyclic displacement can be calculated as:

$$y_{\text{Ges}} = k_{1,1} \left[1 + t \ln \left(N_1 + \sum_{k=2}^n N_k^* \right) \right] \quad (16.22)$$

Based on the two equations [815] above, Achmus et al. [816] performed a response calculation for a monopile with a diameter of 7.5 m and a penetration depth of 30 m embedded in dense sand soil, subject to wave loading associated with various sea states, and at a site with a water depth of around 30 m in the German part of the North Sea. During the service life of the target structure, it will be subjected to wave loading associated with more than 100 million waves from all directions, with a maximum wave height of 18.5 m. The calculated resulting cyclic displacement under the maximum design load is 43% higher than the static displacement due to only a single design wave load. The influence of sea states with mild wave condition on the cyclic loading effects is negligible.

Based on a combination of a pile–soil interaction analysis using finite element simulation and an evaluation of drained cyclic triaxial tests, Achmus [811, 854] also developed the Stiffness Degradation Method (SDM) to account for the cyclic loading effects.

As presented previously, essentially, cyclic load effects are included by softening p - y response near soil surface and by reducing peak lateral pressures as recommended by the API [791] or ISO 19902 [91] to modify the p - y curves for clays shown in Figs. 16.7, 16.9, and 16.10, and by using multiplier factor A for sand (Sect. 16.5). The cyclic behavior of soft clay is less significant than that for sand soil as the cyclic reduction for soft clay is limited for rather large deformations.

Deficiency in static curves not only affects the deformations and ultimate resistances considered for serviceability limit state (SLS) and ultimate limit state (ULS) design, but also influences the foundation stiffness for the dynamic analysis. For example, in API, subject to cyclic loading, the multiplier A to reduce the lateral resistance for sand, due to the cyclic effects, is set to 0.9. This treatment is normally regarded as conservative because the stiffness and ultimate resistance strength are degraded, thus decreasing the foundation stiffness by making the piles behave “softer.” In the meantime, this also leads to an increase in the natural period of the foundation–superstructure system. For fixed offshore structures subjected to wave loading, this normally results in a higher dynamic response as the structures’ natural period becomes closer to the wave period after accounting for the cyclic effects due to foundation stiffness degradation. Note that the cyclic degrading effects are calibrated for a large number of wind and wave loading cycles with long period in sensitive soils. For structures subject to dynamic seismic loading which is of transient type with short duration, this may lead to a non-conservative calculation of the structural responses. This is because an increase in natural period of structures generally reduces the calculated acceleration, as can easily be checked by reading the corresponding spectral acceleration level in an earthquake response spectrum [188]. Moreover, because earthquake loading has a large variation with regard to both frequency content and amplitude, procedures to modify the static loading p - y curves into a dynamic one, as proposed by Matlock [788], may be inaccurate to account for cyclic effects.

Furthermore, the A -factor approach used by API to account for cyclic loading effects is based on obtained data from in situ tests, in which different load levels were applied and these load cycles were not more than 100, mostly less than 50 [786, 817]. It was believed that with subsequent load cycles no significant further displacement accumulation occurs, even though several researchers [810, 817] disagreed with this assumption by arguing that although the accumulation rate decreases with an increase in the number of load cycles (shakedown behavior), it does not reach zero. They also proposed formulations to calculate the lateral pile head displacement mainly as a function of number of load cycles, as presented previously in this section.

In addition, the p - y curve expressions as discussed in the previous sections are mainly developed for static loading. Where cyclic effects are only accounted by reducing stiffness in a simplified manner, the resulting nonlinear p - y curves are in

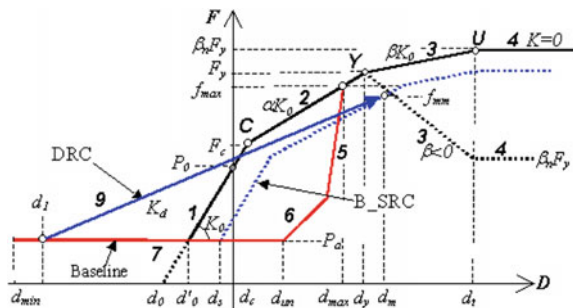
fact hypoelastic models as the unloading occurs along the loading path. However, to estimate the pile–soil interaction responses, it is sometimes necessary to ignore hysteretic behavior and possible residual displacements as observed for real soils. The hysteretic behavior is also vital to calculate a reasonable damping level for pile–soil interaction modeling. Even if an artificial damping modeling by introducing equivalent viscous dampers is efficient and in most cases leads to a reasonably accurate assessment of pile–soil interaction responses, it cannot calculate possible residual displacements. In order to overcome this problem, a time-domain analysis is recommended by adopting the p - y loops with an example shown in Fig. 16.14, which can adequately account for the hysteretic behavior of soils. By observing Fig. 16.14, it is also realized that the implementation of p - y loops requires many different parameter inputs. This essentially deters the engineering application of the p - y loops’ model.

For offshore wind turbine with monopile foundations, the serviceability of predominantly laterally loaded pile foundations can be assessed by applying the methods proposed by Grabe and Dührkop [819] and Achmus [820]. Additional information on calculations for assessing permanent deformation of piles subject to cyclic lateral loading is available in Hettler [810] and Long and Vanneste [814].

For closely spaced piles in a pile group, the dynamic p - y curve for pile group analysis can be established by a reduction of lateral pile resistance p_u with factors influenced by pile spacing, lateral pile displacement, the angle of loading, and the dominant frequency of excitation. See Sect. 21.5 for a discussion of this issue.

Recent studies show that the lateral stiffness of piles embedded in sand may even be increased due to cyclic pile loading. Baek et al. [821] performed a series of cyclic lateral model tests of piles in sands with relative density (D_r) of 40, 70, and 90%, respectively. Both monotonic and cyclic loading tests were performed. A comparison showed that the initial horizontal subgrade modulus increased for model piles installed in sandy soil with $D_r = 40\%$, while it decreased in relative densities of 70 and 90%. This finding can be explained by the fact that the cyclic lateral loads densified the surrounding soil in relatively loose sands ($D_r = 40\%$), while the surrounding soil was disturbed in relatively dense sands ($D_r = 70, 90\%$). Through small-scale experimental study, Bhattacharya et al. [822] presented that pile foundations embedded in both dry and saturated sands may exhibit near-field

Fig. 16.14 Modeling of p - y loops proposed by Allotey and El Naggar [274, 818]



soil stiffening. This phenomenon is also observed by Leblanc et al. [823], who reported that the stiffness of cyclically loaded stiff piles embedded in sands increased due to cyclic loadings.

16.7 Effects of Dynamic Loading on p - y Curves

Under dynamic loading, the pile–soil interaction along lateral directions is a function of loading frequency and rate dependence, as has been observed in fine-grained soils, implying a frequency dependence in dynamic stiffness. Compare to the stiffness degradation due to the cyclic loading, the response under dynamic loading generally exhibits a stiffer behavior than its static counterpart. The dynamic loading may induce a 5–20% increase in stiffness/strength for tenfold increase in strain rate (Sect. 2.5).

Different methods have been proposed to include this variation of dynamic loading rate effects with frequency. Most of them attempt to develop dynamic stiffness relations to be used for pseudo-static analysis. Based on tests of a pile with a diameter of 0.25 m subjected to dynamic excitations for a frequency range up to 10 Hz, El Naggar and Bentley [824] proposed a closed-form empirical formulation for dynamic single pile p - y curve, which uses a dynamic modifier as a function of a static single pile nonlinear p - y curve, soil type, and loading frequency. Essentially, this dynamic p - y curve contains a nonlinear spring coefficient and a nonlinear dashpot coefficient, as originally proposed by Naggar and Novak [825]:

$$f_a(a) = p_{\text{dyn}}/p_{\text{stat}} = \alpha + i[\beta a_0^2 + \lambda a_0(\omega y/d)^n] \quad (16.23)$$

where p_{dyn} is the dynamic value of p on the p - y curve at depth z ; p_{stat} is the static value of p on the p - y curve at depth z ; y is the lateral deflection of pile at depth z ; ω is the angular frequency of loading; d is the pile diameter; α , β , λ , and n are empirical constants related to soil type (from soft to stiff clay and loose to dense sand) as presented in Table 16.6; a_0 is the dimensionless frequency of loading, determined by:

$$a_0 = \omega d / (2v_s) \quad (16.24)$$

where v_s is the shear wave velocity of the corresponding soil.

El Naggar and Bentley [824] concluded that the resulted responses based on the proposed dynamic p - y curves are in good agreement with predictions based on a two-dimensional analysis. However, it was noted that the accuracy is low under very stiff soil conditions. The accuracy increases for frequencies greater than 4 Hz, since the plane-strain dynamic stiffness assumption tends to become less accurate when the condition approaches the static limit case.

As an indication of the effects of the dynamics varying with soil type and lateral displacement, at a frequency of 5 Hz, and lateral displacements ranging from 0.01

Table 16.6 Dynamic p - y curve parameters for different soil types [824, 826]

Soil type	Typical parameters	α^b	β		λ	n
			$a_0 < 0.025$	$a_0 > 0.025$		
Soft clay	$s_u < 50$ kPa, $v_s < 125$ m/s	1	-180	-200	80	0.18
Medium clay	50 kPa $< s_u < 100$ kPa, 125 m/s $< v_s < 175$ m/s		-120	-360	84	0.19
Stiff clay	$s_u > 100$ kPa, $v_s > 175$ m/s		-2900	-828	100	0.19
Medium dense sand (saturated) ^a	50% $< D_r < 85\%$, 125 m/s $< v_s < 175$ m/s		3320	1640	-100	0.1
Medium dense sand (unsaturated) ^a	50% $< D_r < 85\%$, 125 m/s $< v_s < 175$ m/s		1960	960	-20	0.1
Dense sand (saturated) ^a	$D_r > 85\%$, $v_s > 175$ m/s		6000	1876	-100	0.15

^a D_r is the relative density to water

^b $\alpha = 1.0$ to ensure that the dynamic stiffness is equal to static stiffness at zero frequency

to 0.1 m, the dynamic modifier function is approximately 2–8, 3–6, and 1–3 for soft clay, stiff clay, and dense sand, respectively [274].

By realizing that the seismic excitations are of transient types and cover a large range of frequencies, for a dynamic seismic analysis in time domain, the dynamic modifier function and p - y curve may be established by using only a predominant frequency. This predominant frequency can be taken as the predominant seismic wave frequency if the kinematic pile responses due to the forced seismic excitations are more important than the pile responses due to the inertia forces exerted from superstructures. However, the main disadvantage of using predominant frequency to determine dynamic modifier function lies in the fact that the frequency of seismic motions can vary at different depths and is different for different seismic motions. Therefore, in cases when the influence from the superstructure's inertia forces is dominant on piles' lateral response, the superstructure's natural frequency rather than the dominant frequency of seismic excitations should be used to calculate the dynamic modifier function.

The soil–pile–structure interaction accounting for cyclic and dynamic p - y curves has its research and applications in seismic and ocean wave dynamic analysis problems for both land-based and offshore structures [827–831], and the dynamic p - y curves have been implemented into a number of computational codes. Wang et al. [832] compared several implementations of the dynamic p - y curves and showed that calculations can be sensitive to the details of nonlinear springs and dashpots, but different codes did produce similar results when similar modeling details were used.

Similar to that of shallow foundations (Sect. 13.1), piles' foundation impedance can also be represented by the complex-valued impedance function, with a real part, representing the combined effect of stiffness and soil inertia, and an imaginary part,

representing the radiation and hysteretic damping. However, even for the idealized assumptions with linear-elastic or viscoelastic homogeneous soils and the piles being bonded to the soil, the interaction between the piles and surrounding soils is still complex to analyze. Therefore, approximations are often made for solving this problem. Readers may refer to source [774] for a discussion of this topic.

Different from that of shallow foundations, for soils around pile foundations, the influence of overburden pressure on the maximum dynamic shear stiffness G_{\max} is minor and can normally be neglected in engineering practice.

16.8 Effects of Pile Diameter on Lateral Load–Displacement Behavior

16.8.1 Introduction

Compared to a pile group with smaller pile diameters, a large-diameter monopile provides a significantly higher horizontal/lateral stiffness with a lower construction cost. Therefore, it is the preferred foundation form for offshore wind turbines at shallow water depth of less than 30 m, which are subject to both wind- and wave-induced loading simultaneously, and can be analyzed using the p - y curve to simulate the occurring lateral soil resistance as shown in Fig. 16.15.

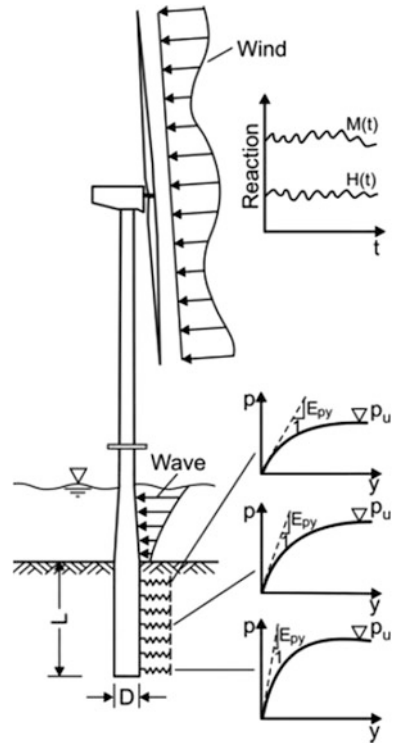
However, designs for large fixed offshore wind turbines installed in deeper waters require enormous monopile dimensions that are widely out of range with regard to common experience for pile foundations. Pile diameters up to 8 m are already installed, and even larger diameters are currently planned. Moreover, large-diameter piles have also been used to support bridges. For example, in the New East Span San Francisco-Oakland Bay Bridge shown in Fig. 14.7, piles of up to 2.5 m in diameter have been designed with penetration depths between 60 and 100 m, which are designed to resist tension loads of up to 90 MN and compression loads of up to 140 MN (due to design earthquakes) [833].

Terzaghi and Peck [68] suggested that the low-strain elastic soil stiffness against lateral movement of the pile should be independent of the pile diameter. They explained the influence of pile diameter on the coefficient of subgrade reaction by using the concept of a stress bulb to show that the larger pile diameter has a deeper stress influence than the smaller one [779]. Therefore, with an equivalent applied pressure, a pile with larger diameter encounters greater displacement with a simple proportion to the pile diameter, resulting in a lower coefficient of subgrade reaction:

$$k_n = p/y_n = p/ny_1 = k_1/\varphi \quad (16.25)$$

where k_n and k_1 are the coefficient of subgrade reaction for pile diameter d and d_1 , respectively; y is soil displacement at the specific point; p is the soil pressure (FL^2); $\varphi = d/d_1$; and $p/y_1 = k_1$.

Fig. 16.15 Schematic illustration for the modeling of monopile foundation subject to both wind and ocean wave loading [834] (courtesy of ISOPE)



From the equation above, it can be seen that the coefficient of subgrade reaction is linearly proportional to the inverse of pile diameter; i.e., the modulus of the subgrade reaction is independent of pile diameter. Ashford and Juirnarongrit [837] also supported this conclusion based on the full-scale pile load test results.

However, for piles with larger diameters, such as monopile foundations extensively used in recent offshore wind farm development, noticeable differences have been presented and must be addressed in the design, installation, and operation stages, especially for conditions in which those large-diameter piles are subjected to excessive cyclic loading. For example, the ratio of pile's end effects to side effects is different between large- and small-diameter piles, which affects the axial and lateral capacity and performance, and pile driveability. For the latter, a special follower may be required in order to use an available offshore hammer to drive large-diameter piles. The mass and stiffness characteristics of the follower can significantly affect the pile driveability.

Due to cost considerations, lateral force resistance in a large-diameter pile is complex and usually derived from three-dimensional FE analysis under monotonic or cyclic loading rather than testing, due to the high expenses of large-diameter pile testing (e.g., Chen and Kulhawy [839], Abdel-Rahman and Achmus [840], Leblanc et al. [823], Achmus et al. [841], and Bourgeois et al. [842]). These processes

include (1) passive lateral soil resistance along the leading face of piles; (2) shearing along the toe of the shaft and around the shaft perimeter. In addition, axial forces can affect the lateral behavior. A thorough analysis of such a force system requires sophisticated 3D numerical methods [843].

The application of nonlinear springs modeled by p - y curves, as recommended by API [792] and elaborated in previous sections, is used extensively in offshore pile foundation design, whereby the collected experiences only apply for piles with diameters of up to 2.5 m. This is because the method is based on semiempirical concepts developed for long slender piles and calibrated for piles with diameters ranging from 0.15 to 1.83 m [786–789, 844]. The validity of these semiempirical curves has been questioned for pile diameters outside the range of the original test piles.

Back calculations of instrumented monopile foundations for offshore wind turbines indicate that the foundation stiffness is underestimated when using the original p - y curves to represent the soil [845]. Achmus [846] presented that the horizontal deflections of large-diameter monopiles are underestimated under extreme lateral loads but are over-estimated for small operational loads. Achmus [811] also performed a numerical analysis of piles by establishing three-dimensional finite element modeling using ABAQUS, with a nonlinear soil stiffness modeled as stress dependent (Sect. 1.10) and a constant Poisson's ratio. An elasto-plastic material law with Mohr–Coulomb failure criterion was used. The interaction behavior between the monopile and the sand soil is simulated using contact elements, and the piles are subject to typical levels of design loads. The maximum shear stress in the contact area is determined by a friction coefficient. It was found that for a pile with a diameter of 4 m, the deviation between a p - y curve modeling and the 3D finite element modeling is 27% with respect to pile head deflection. For a pile with a diameter of 7.5 m, this deviation increases to 38%. Similarly, Kallehave et al. [845] stated that experience from operating offshore wind farms supported by monopiles indicated that the foundation stiffnesses for small operational loads are significantly underestimated.

In conclusion, for sand soil, subject to significant loading, the initial modulus of subgrade reaction for large-diameter piles calculated by API method (as presented in previous sections) is likely be over-estimated; i.e., under extreme loading, the deflections of large-diameter piles are underestimated by API method [840, 847]. Subject to small lateral loading, the initial modulus of subgrade reaction for large-diameter piles calculated by API method may be underestimated. An incorrect estimation of the foundation stiffness would result in an increase of uncertainties regarding the structural loading and response estimation [845], which can lead to either an over-estimation or an underestimation of the foundation stiffness.

For clay, limited research efforts have been devoted to investigating the effects of pile diameter on foundation stiffness. Based on numerical simulations, Haiderali and Madabhushi [848] showed that the stiffness of monopile foundations under extreme loads is underestimated by the Matlock approach [788] except at the monopile tip, where the base shear was not accounted for in the p - y curves, hence resulting in an over-estimation of the soil reaction. Consequently, the Matlock p - y

formulation significantly underestimates the monopile ultimate lateral capacity. On the other hand, based on the work by Achmus et al. [849], it is found that the most common p - y approach by Matlock [788] includes an infinite initial stiffness of the curves causing unreasonably large foundation stiffnesses for small loads. For larger loads, however, they showed that the Matlock approach either underestimates or over-estimates the foundation stiffness depending on the consistency of the clay.

16.8.2 Effects of Pile Diameter Under Sand Soil Conditions

16.8.2.1 Method Proposed by Wiemann et al.

For sands, Wiemann et al. [850] suggested a diameter-dependent correction factor to reduce the initial modulus of subgrade reaction k defined in Sect. 16.5:

$$k_{\text{Wiemann}} = k(d_{\text{ref}}/d)^{4(1-\alpha)/(4+\alpha)} \quad (16.26)$$

where $d_{\text{ref}} = 0.61$ m is the diameter of piles tested in Mustang Island (near to the Gulf of Mexico) in 1974 [786, 844]; d is the pile diameter; α is an exponent depending on the soil type, $\alpha = 0.5$ and 0.6 for very dense and medium dense sand, respectively.

From the equation above, it is obvious that the initial modulus of subgrade reaction decreases with an increase in pile diameter.

16.8.2.2 Sørensen Method

Sørensen [851] presented a formulation to degrade the p - y curve stiffness influenced by the pile diameter for extreme loading for sites in the North Sea, with the initial modulus of subgrade reaction (initial stiffness coefficient) $k_{\text{Sørensen}}$ being dependent on the depth z , the soil stiffness E_s , and the pile diameter d :

$$k_{\text{Sørensen}} = kz^{-1}a(z/z_{\text{ref}})^{\beta}(d/d_{\text{ref}})^{\gamma}(E_s/E_{s,\text{ref}})^{\lambda} \quad (16.27)$$

where $a = 1$ MPa is valid for a reference depth $z_{\text{ref}} = 1$ m, a reference pile diameter $d_{\text{ref}} = 1$ m, and a reference soil stiffness $E_{s,\text{ref}} = 1$ MPa; $\beta = 0.3$, $\gamma = 0.5$, and $\lambda = 0.8$ are dimensionless constants; the soil stiffness E_s can be calculated according to Sect. 1.10.

It is worth mentioning that the reduction in the initial subgrade modulus in Sørensen method is even more significant than that of the Wiemann method. Therefore, the Sørensen method leads to a significantly “softer” p - y curve than the one recommended by API.

16.8.2.3 Method Proposed by Kallehave et al.

To avoid an underestimation of the stiffness under small operational loads, Kallehave et al. [845] proposed a formulation to modify initial modulus of subgrade reaction, and this method should in general also be valid for primary initial loading [852]:

$$k_{\text{Kallehave}} = kz^{-1}z_{\text{ref}}(z/z_{\text{ref}})^m(d/d_{\text{ref}})^{0.5} \quad (16.28)$$

where $z_{\text{ref}} = 2.5$ m is a reference depth; m is a dimensionless parameter that rules the course with depth z , with a recommended value $m = 0.6$; $d_{\text{ref}} = 0.61$ m.

It is noticed that the formulation proposed by Kallehave et al. [845] in general gives much stiffer initial subgrade modulus k than the one proposed by API, especially at small depths. This may be due to the fact that, when subject to small lateral loading, in addition to the passive soil resistance on the leading edge of the pile, a significant surface shear stress must exist.

16.8.2.4 Method Proposed by Kirsch et al.

Kirsch et al. [853] presented a p - y approach to account for an underestimation of foundation stiffness under small operational loads and an underestimation of pile deflection under extreme loading. Different from the methods proposed by Sørensen [851] and Kallehave et al. [845], which do not account for the cyclic loading effects, the method proposed by Kirsch et al. [853] also accounts for an accumulation of pile deflection under cyclic loading. Kirsch's approach is based on a "cyclic" p - y curve (the factor $A = 0.9$ in Sect. 16.5), and the ultimate resistance p_u and initial subgrade modulus k are determined based on a reduced friction angle ϕ'_{red} :

$$\phi'_{\text{red}} = \phi' - 0.5(d - 2) \quad (16.29)$$

where ϕ' is the sand's internal angle of friction; d is the pile diameter in meter.

In this approach, to account for the dynamic loading on the soil stiffness, the initial modulus of subgrade reaction can be expressed as a function of dynamic to static soil stiffness moduli E_{sd}/E_s and the ratio of bedding resistance to ultimate resistance p/p_u :

$$k_{\text{Kirsch}} = k_{\text{red}}[1 + (1 - p/p_u)(E_{\text{sd}}/E_s - 1)] \quad (16.30)$$

where k_{red} is the initial bedding stiffness (Sect. 16.5) coefficient based on a reduced friction angle ϕ'_{red} presented above.

16.8.2.5 Evaluation of the Proposed Methods

Figure 16.16 shows a comparison of p - y curves for small- and large-diameter piles in a single depth. In this figure, the p - y approach by Reese et al. [786] divides the p - y curve into four sections. In the first section, the curve is identical to the API curve, as the identical initial bedding stiffness is assumed. In the second section, a parabolic curve is proposed crossing over to a linear course. The linear increase is limited by the ultimate bedding resistance, which is again almost identical to the API curve [834].

For an evaluation of all p - y approaches mentioned above, Achmus et al. [834] performed 3D FE analysis of a large-diameter monopile foundation in homogenous

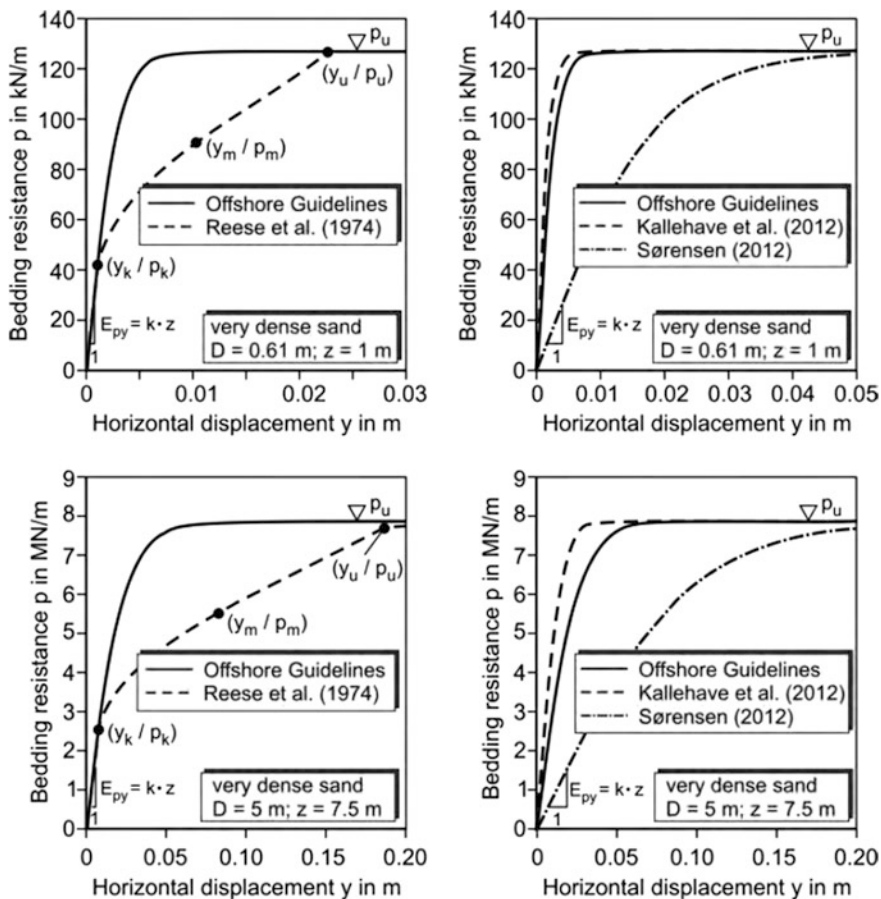


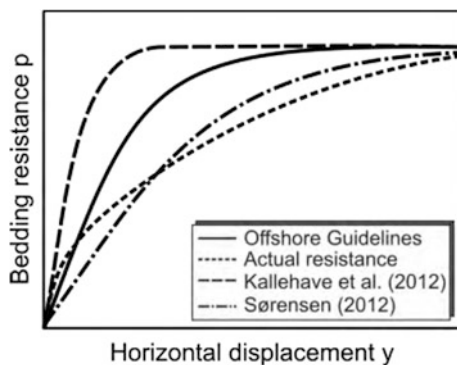
Fig. 16.16 Comparison of p - y curves for small- (upper: pile diameter $D = 0.61$ m) and large-diameter (lower: pile diameter $D = 5$ m) piles, in which “Offshore Guidelines” refers to API approach [834] (courtesy of ISOPE)

sands. The soil’s stiffness is modeled as strain-dependent, which enables a realistic determination of the pile–soil system stiffness under small loads. The numerical model is validated successfully by showing a good match with the results obtained from the Mustang Island field test [844]. Figure 16.17 shows a comparison of results of the FE analysis, API method, Kallehave et al. method, and Sørensen method. Based on the calculated results and their comparison, it is found that:

1. The foundation stiffness is strongly dependent on pile head displacements, reflecting the nonlinearity in the load-bearing behavior of the pile–soil system. This is particularly apparent for small loads.
2. For large pile head displacements, the foundation stiffness is smaller than that given by the API approach. For very large pile head displacements, the stiffness even falls below the results of the Sørensen method.
3. For small pile head displacements, the foundation stiffness is larger than that given by the API approach. For very small head displacements, the stiffness is close to the results of the method by Kallehave et al. [845], but the numerically determined stiffnesses do not reach these values for large pile diameters.

Based on the findings above, Achmus et al. [834] concluded that none of the proposed p - y approaches presented above is generally suitable for the design of large-diameter monopiles without additional calibrations regarding the considered pile–soil system and the load level. This is mainly because all p - y formulations introduced so far are based on the traditional p - y method, which has the limitations of uncoupled springs and failure to take the “pile tip effect” into consideration. The approach of uncoupled springs does not account for the soil as continuum; i.e., the bedding resistance on a pile segment is not influenced by the bedding resistance on adjacent pile segments. The omission of the pile tip effect means that the bedding resistances are considered to be independent of the distance to the pile tip, i.e., effects from the soil continuity beneath the pile are omitted.

Fig. 16.17 Schematic distribution of a realistic p - y curve, the actual resistance is obtained from the three-dimensional FE analysis [834] (courtesy of ISOPE)



16.8.2.6 Method Proposed by Thieken et al.

Through numerical simulations, Thieken et al. [799] discussed the consequences of these limitations for the bedding behavior of a large-diameter monopile. They further proposed a new method based on a two-step procedure, which is more complex than other methods presented so far:

1. The p - y relationship is determined for a pile of infinite length that exhibits a constant horizontal displacement along the pile shaft; this relationship will serve as the “basic p - y curve,” which excludes any effects of the pile deflection line or the pile tip.
2. The basic p - y curves are then modified in an iterative procedure to account for the interaction of deflection line and bedding resistance as well as for the pile tip effects.

It is worth mentioning that, by combining this method with the results of the Stiffness Degradation Method (SDM) [811, 854], which is often used for the design of monopile foundations for offshore wind turbines, this method can also be extended to capture the load-bearing behavior for piles subject to cyclic loading. Interested readers may read the relevant references cited above.

16.8.3 Effects of Pile Diameter Under Clay Soil Conditions

16.8.3.1 Method Proposed by Kim et al.

For piles embedded in clay, Kim et al. [855] described results of two field tests for piles with diameters of 1.02 and 2.4 m conducted for the construction of the Incheon Bridge in South Korea. By using theoretical analysis and field test data, they developed a new p - y curve approach for piles with arbitrary dimensions, with the initial stiffness described by a finite initial bedding stiffness coefficient k :

$$p = \frac{y}{\frac{1}{k} + \frac{y}{p_u}} \quad (16.31)$$

The initial bedding stiffness k is dependent on the undrained shear strength s_u , the stiffness factor k_c , the Poisson’s ratio ν , the reference diameter $d_{\text{ref}} = 1$ m, the pile diameter d , and the pile’s flexural rigidity $E_p I_p$:

$$k = \frac{17.4k_c s_u}{1 - \nu^2} \sqrt{\frac{d}{d_{\text{ref}}}} \left(\frac{k_c s_u d^4}{E_p I_p} \right)^{0.66} \quad (16.32)$$

where E_p and I_p are the elastic modulus and second moment of inertia of the cross section for the pile, respectively.

The stiffness factor k_c is described by a diagram taking into account the clay's plasticity index and OCR. For example, k_c is set to 450 representing a normally consolidated soft clay with OCR = 1 and a plasticity index of 40.

The ultimate bedding resistance p_u is defined as a function of the undrained shear strength s_u , the depth below soil surface/seabed z , and the reference depth $z_{\text{ref}} = 1$ m:

$$p_u = 3.25s_u d \left(\frac{z}{z_{\text{ref}}} \right)^{0.59} \quad (16.33)$$

16.8.3.2 Method Proposed by Kirsch et al.

Kirsch et al. [853] described a modification of the Matlock approach [788] by taking into account the utilization ratio of the bedding resistance and the ratio of the static soil stiffness modulus (Young's modulus) E_s to dynamic soil stiffness E_{sd} :

$$\varepsilon_{c,\text{Kirsch}} = \varepsilon_c \left[1 + \left(1 - \frac{p}{p_u} \right) \left(\frac{E_s}{E_{\text{sd}}} - 1 \right) \right] \quad (16.34)$$

It is noted that the method proposed by Kirsch et al. above generally results in a significant increase in the foundation stiffness for piles with all dimensions, especially at the initial part of the p - y curve.

16.8.3.3 Method Proposed by Stevens and Audibert

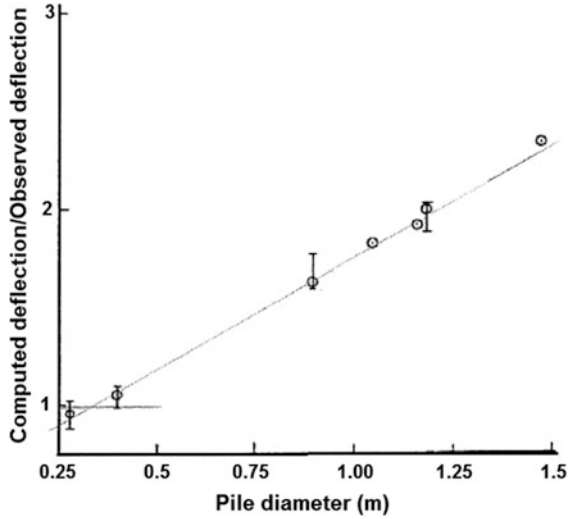
For pile diameters smaller than 1.5 m, Stevens and Audibert [857] presented that, as p - y curve is influenced by pile diameters, the Matlock soft clay p - y curve [788] needs to be modified to reflect diameter effects. By carrying out seven full-scale pile load tests in clays for piles with diameters ranging from 0.28 to 1.5 m, and compiling the test data, as shown in Fig. 16.18, they concluded that the pile diameter effects on p - y curves are apparent, and proposed several modifications to the Matlock p - y curve as follows:

1. Change the y_c value, to scale the deflection array in Matlock's p - y curves:

$$y_c = 2.5\varepsilon_c d_{\text{ref}} \left(\frac{d}{d_{\text{ref}}} \right)^{0.5} \quad (16.35)$$

where $d_{\text{ref}} = 0.32$ m is the reference diameter equivalent to field tests underlying the Matlock approach.

Fig. 16.18 Comparison between the computed pile deflections based on Matlock p - y criterion and the test data [857]



It is noticed that the modification above generally results in higher lateral foundation stiffness than the Matlock method [788] for piles with diameters larger than d_{ref} .

2. Modify the calibration factors in the p_u expression (compared with the p_u expression and the lateral resistance at the soil surface given in Sect. 16.2), which results in a higher bedding resistance and can be expressed as:

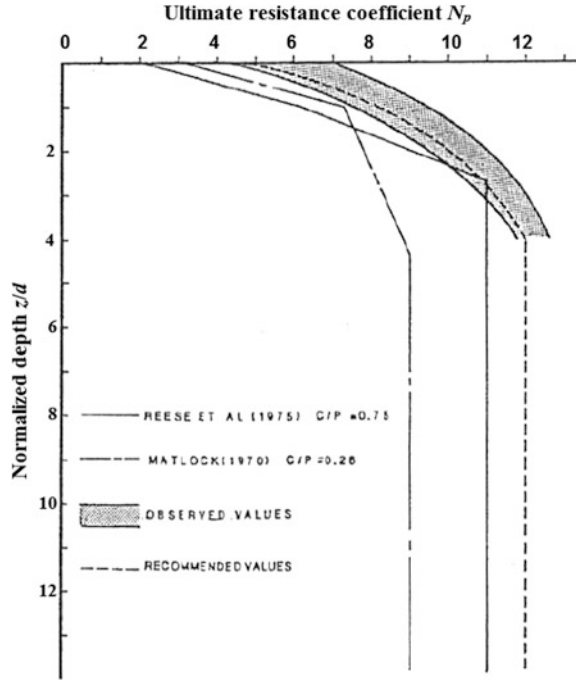
$$\begin{aligned}
 p_u &= 5s_u + \sigma_z + Js_u|z|/d \\
 &= 5s_u + \gamma'|z| + Js_u|z|/d
 \end{aligned}
 \tag{16.36}$$

$$p_u \leq 12s_u
 \tag{16.37}$$

As an alternative, by following the Stevens and Audibert method [857], the effects of pile diameter can also be accounted for by applying ultimate resistance coefficient N_p (Sect. 16.2) on the p - y curves from a depth-dependent function shown in Fig. 16.19. It is observed that N_p value varies from about 5 to about 12, in contrast to a value of 9 recommended by API. This difference is most significant (70%) for zones close to ground surface and less significant (30%) at depth. Therefore, the change in N_p value has far more significant effects on p - y curves than the change in y_c value [858].

It is noted that the y_c value used in the Matlock p - y curve [788] is determined based on the research by Skempton [803], which includes a comprehensive study combining elasticity theory, ultimate-strength methods, and laboratory soil property tests to estimate short-time load-settlement characteristics of buried strip footings in

Fig. 16.19 Values of ultimate resistance coefficient N_p as a function of normalized depth [857]



clay soils. On the other hand, the Stevens and Audibert method is purely based on pile loading test and therefore lacks a solid theoretical background; i.e., they did not explain the mechanistic reasons for the observed diameter effects, and their proposed equation is not dimensionally correct [858]. Moreover, the ultimate resistance coefficient N_p suggested by Stevens and Audibert is derived for a specific shear strength profile of clay.

16.8.3.4 Method Proposed by O’Neill and Gazioglu

To account for the pile diameter effects, O’Neill and Gazioglu [807] proposed the so-called Integrated Clay Criteria, described as below:

1. Change the y_c value (Sect. 16.4) to scale the deflection array in Matlock’s p - y curves:

$$y_c = A\epsilon_c d^{0.5} (E_p I_p / E_s) \tag{16.38}$$

where E_p and I_p are the elastic modulus and second moment of inertia of the cross section for the pile; d is the pile diameter; E_s is the Young’s modulus of the soil.

2. Calculate the ultimate resistance coefficient N_p from 3 at a zero depth to an ultimate value of 9 below the critical depth where the failure mechanism is changed to horizontal flow failure (Fig. 16.6) of soil around the pile. This is quite different from what is proposed by Stevens and Audibert [857], because when using the Stevens and Audibert method, an over-estimation of the N_p is likely to occur, as discussed by O' Neill and Gazioglu [807].

16.8.3.5 Method Proposed by Carter and Ling

By reviewing the pile load test data with different pile diameters ranging from 7.5 cm to 0.9 m, Carter [859] and Ling [860] found that E_s increases for larger-diameter piles:

$$E_{s2} = E_{s1}d_2/d_1 \quad (16.39)$$

where the values of E_{s1} and E_{s2} correspond to piles with diameters (or width) d_1 and d_2 , respectively.

From the equation above, it is noticed that the method proposed by Carter and Ling is theoretically applicable when the force–deflection relationship is modeled by linear Winkler spring. However, strictly speaking, this is not compatible for a nonlinear p - y curve adopted by API. Furthermore, the model above can be applied for both clay and sand soils.

16.8.3.6 Evaluations of Different Methods

Figure 16.20 illustrates a comparison of p - y curves for soft clay based on the methods proposed by Matlock [788], Stevens and Audibert [857], Kim et al. [855], and Kirsch et al. [853]. It is noticed that for both small- and large-diameter piles, the Matlock method generally gives a lower bedding resistance.

By carrying out a three-dimensional numerical analysis using PLAXIS3D [861], and validating the analysis based on four field tests with different pile dimensions and soil conditions, Achmus et al. [849] presented that the Matlock approach [788] either underestimates or over-estimates the foundation stiffness depending on the consistency of the clay for larger loads, and the discrepancy between the numerical results and the outcome of the p - y curves is nearly identical for all pile dimensions with diameters larger than 1.5 m. The approaches by Stevens and Audibert [857] and by Kirsch et al. [853] result in larger foundation stiffnesses in particular for small loads that additionally increase the over-estimation of foundation stiffness. The approach proposed by Kim et al. [855] yields foundation stiffnesses significantly larger than those obtained from the numerical simulations for all pile dimensions, clay consistencies, and horizontal head displacements.

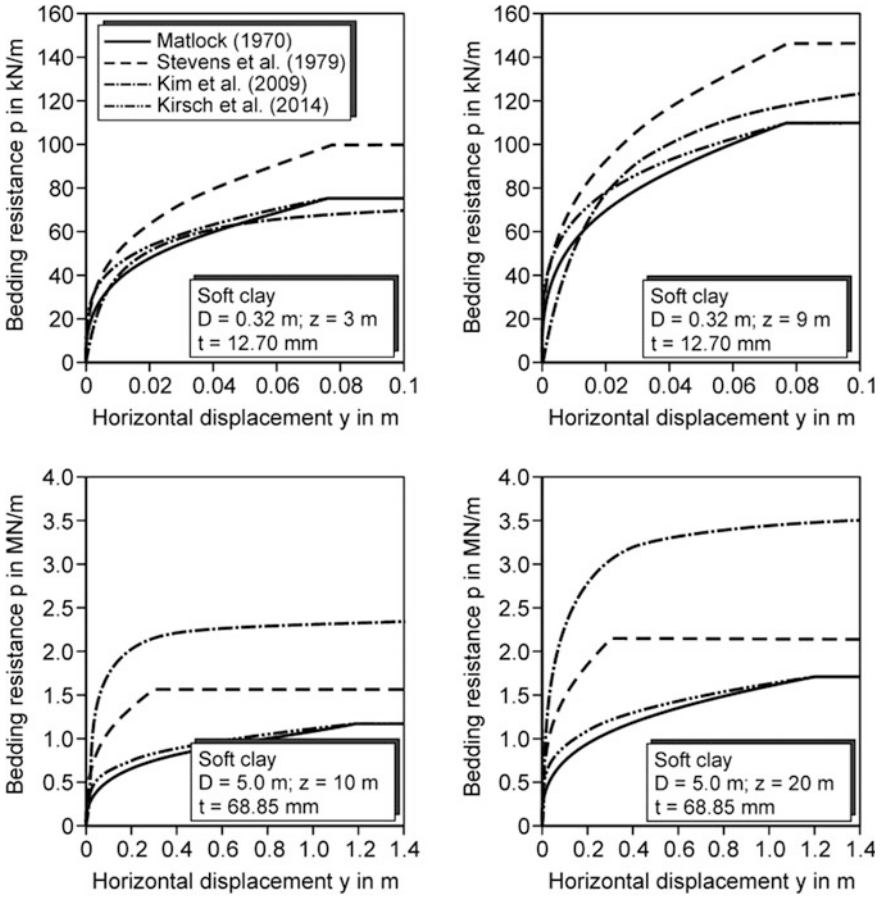


Fig. 16.20 Comparison of p - y curves among four different methods [849] (courtesy of ISOPE)

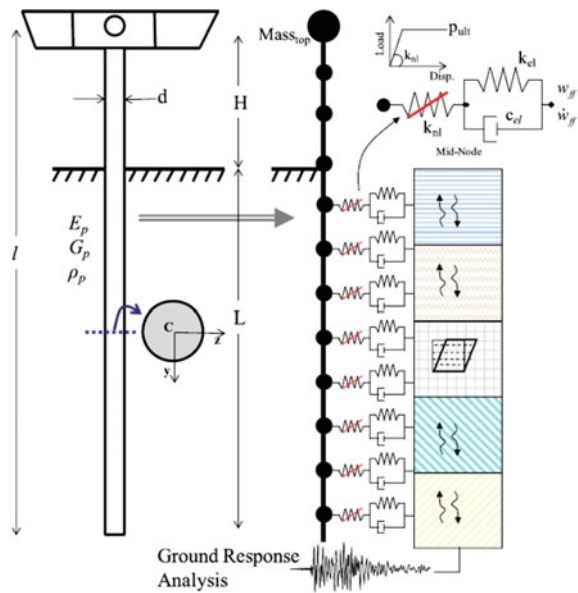
Therefore, among all five methods under investigation to generate p - y curves, the API/Matlock [788] method is found to be the closest one to that obtained from the numerical calculation, even though it results in foundation stiffnesses several times smaller for small loads and also affects the foundation behavior under large loads. As a general conclusion, Achmus et al. [849] found that none of the methods under investigation is able to represent the validated numerical simulation results in an adequate manner. The main reason for this is the application of a very large or even infinite initial stiffness and the poor agreement of the bedding stiffnesses along the pile shaft.

16.9 Hybrid Spring Model for Modeling Piles’ Lateral Force–Displacement Relationship

To account for soil nonlinearities in the near-field and viscoelastic characteristics in the far-field soil, a hybrid spring configuration consisting of a nonlinear (p - y) spring connected in series to an elastic spring-damper model can be adopted as shown in Fig. 16.21. The nonlinear spring captures the near-field plastification of the soil, while the spring-damper system (Kelvin–Voigt element) represents the far-field viscoelastic characteristics of the soil.

An even more complex but versatile means of approximating the lateral behavior of pile–soil interactions is illustrated in Fig. 16.22. This model is convenient for implementation in a displacement-based finite element program. The nonlinear p - y behavior is conceptualized as consisting of elastic (p - y_e), plastic (p - y_p), and gap

Fig. 16.21 Soil–pile–structure system with pile and soil modeled by nonlinear (p - y) springs connected in series to elastic spring-damper models [862]



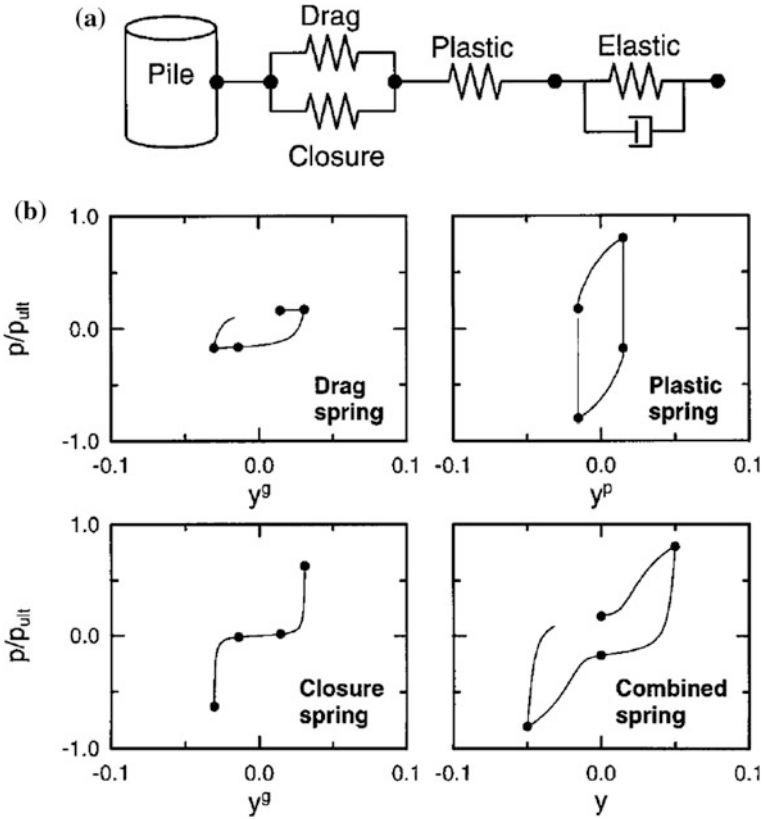


Fig. 16.22 Illustration of characteristics of a more complex lateral soil–pile interaction model: **a** physical modeling for each component; **b** constitutive relationship of each component in the physical modeling [831]

$(p-y_g)$ components in series. Radiation damping is modeled by a dashpot in parallel with the elastic component $(p-y_e)$. The gap component consists of a nonlinear closure spring (p_c-y_g) in parallel with a nonlinear drag spring (p_d-y_g) . For details of this modeling, readers may read Boulanger et al. [831].

Chapter 17

Axial Force–Displacement of Piles: t - z and Q - z Curve

The load transfer mechanics (side friction and tip resistance from soils) is determined by many factors such as the soil types, the installation method, the pile material and geometry. Moreover, if the pile is installed by driving, it will alter the characteristics of the soil and induce significant strains locally surrounding the piles [863].

In this chapter, two types of methods are introduced. The first type uses established empirical methods for computing the axial capacity of piles, which requires undrained shear strength in clay layers and internal friction angle in sand layers for calculating the side friction. Engineers need to gather all necessary soil parameters mainly based on the geotechnical investigation reports for the sites, in which the soil layers are identified based on the variation of soil properties with depth. More recently, as the CPT has been extensively adopted in subsurface explorations for sites both offshore and onshore, CPT-based methods have been recommended by the offshore industry for calculating the axial capacity of driven piles, which will be introduced in Sect. 17.13.

17.1 Pile–Soil Modeling Under Axial Pile Loading

Various analytical and numerical models have been proposed to calculate the pile response subjected to axial loading, which are solved by analytical procedure with closed forms of solutions, finite difference method or finite element method. The representation of pile–soil interaction and pile–soil modeling has been discussed in Sect. 15.2. For piles subject to axial loading, the relevant models are either a type of discrete element model or a type of continuum model [790], which represent the modeling from level 2 and above presented in Sect. 15.2.

In the discrete element models, soils around a pile are idealized as a series of uncoupled “springs” or elements attached between the pile and the far-field soils (usually assumed rigid or subject to seismic motions as shown in Fig. 15.2). The

material behavior of these elements may vary from linearly elastic to nonlinear, hysteretic, and rate dependent. The soil elements are commonly referred to as t - z (shaft resistance–displacement) and Q - z (tip resistance–displacement) elements, as will be presented in Sects. 17.7 and 17.10. Linear or nonlinear dashpots (velocity dependent resistances) can be modeled in parallel and series with the discrete elements to represent radiation damping and rate of loading effects. The pile can be modeled by a series of discrete elements, e.g., rigid masses interconnected by springs or modeled as a continuous rod, either linear or nonlinear. Material properties (soils and piles) in the discrete element models can vary along the pile length.

In the continuum models, soils around the pile are idealized as a continuum attached continuously to the pile. A linear or nonlinear stress–strain relationship of soil materials for each soil layer can be directly implemented. Depending on the degree of nonlinearity and heterogeneity, the continuum models can be quite complicated. Again, the pile is typically modeled as a continuous rod, with either linear or nonlinear properties. Material properties in the continuum models can vary in any direction.

17.2 Axial Compression Capacity

Similar to the lateral resistance model, along the pile’s axial direction, if the pile is under compression, the total bearing capacity (ultimate axial compression capacity) is the resultant of skin/side friction resistance and end-bearing (Fig. 17.1):

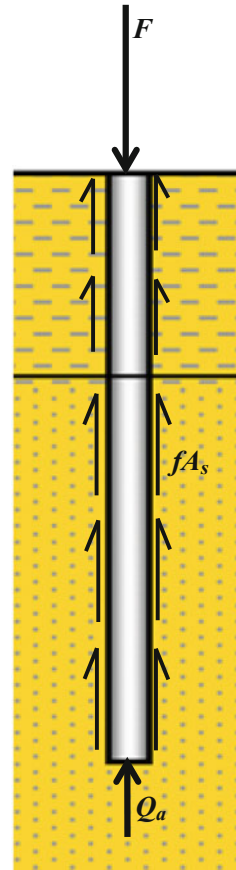
$$Q_{\text{ult}} = Q_f + Q_a = fA_s + q'_p A_a \quad (17.1)$$

where Q_f is the skin friction resistance in force units; Q_a is the total end-bearing capacity in force units; f is the unit skin friction capacity in stress units, it is generally higher in clays than in sands due to adhesion of clay comparing with that in sand soil; A_s is the embedded side surface area of the pile; q'_p is the unit end-bearing capacity in stress units, it is generally lower in clays than in sands; A_a is the gross cross-area of the pile tip.

Depending on whether or not a soil plug (Sect. 17.12) will form, Q_a is calculated based on either the complete enclosed area of the pile tip or the pile cross-sectional area.

Note that an open-ended pile is plugged if the resistance due to the internal wall friction is larger than the end-bearing resistance of the plug. The axial resistance corresponding to the critical failure mode is often taken as the smaller resistance value of the coring mode (the pile cuts through the soil, and the soil plug inside the pile stays where it is, see Sect. 17.12) Q_{in} and the plugged mode Q_{b} , i.e., the total resistance is the external friction plus the minimum of either: (1) pile’s annulus resistance and internal pile wall friction resistance or (2) pile’s annulus resistance and bearing/base resistance of the plug:

Fig. 17.1 Skin friction and end-bearing force subjected to an axial compression load F



$$Q_{ult} = Q_{out} + Q_a + \min(Q_{in}, Q_b) \quad (17.2)$$

where Q_{out} is the outer pile wall friction resistance; Q_a is the annulus resistance; Q_{in} is the inner pile wall friction resistance due to the presence of soil plug; and Q_b is bearing/base resistance of soil plug bottom or closed-end bottom. Figure 17.14 presents an illustration of these parameters.

In reality, the unit inner wall skin friction capacity can be greater than the unit outer wall skin friction capacity. This is mainly attributed to the higher contact stresses existing between the high compressed soil plug and the inner pile surface than those between the outer surface of the pile and the surrounding soil.

For piles in plugged condition, the bearing pressure acts over the entire enclosed area of the piles. For unplugged piles, the bearing pressure acts on the pile wall annulus only. Whether a pile is considered plugged or unplugged may be based on static calculations rather than driving condition. For example, a pile could be driven in an unplugged condition but behave plugged under static loading [791]. For

open-ended piles driving into soils at offshore sites, unplugged piles are very exceptional.

The first term in the right-hand side of the equation above, i.e., the soil–pile friction, is related to the undrained shear strength s_u for clays and the internal angle of friction and effective overburden pressure for sands. It is contributed by both external friction, and, if the pile fails in the coring mode, the internal friction between the soil plug and the pile’s inner wall surface. Note that most piles supporting offshore structures are purposely designed as open-ended for a better driving performance, and the inner wall friction often needs to be accounted for. For sands, this calculation may be conservative as the local compaction of sand may increase the resistance. On the other hand, the inner wall friction must be carefully addressed as the length of soil plug is likely to be less than the full penetration length of the pile (see Sect. 17.12 for a discussion). Furthermore, total end-bearing capacity Q_a should not exceed the internal plug capacity.

Figure 17.2 shows a calculation to estimate the tension and compression capacity of a 43-m long single pile under axial loading at pile head, with the

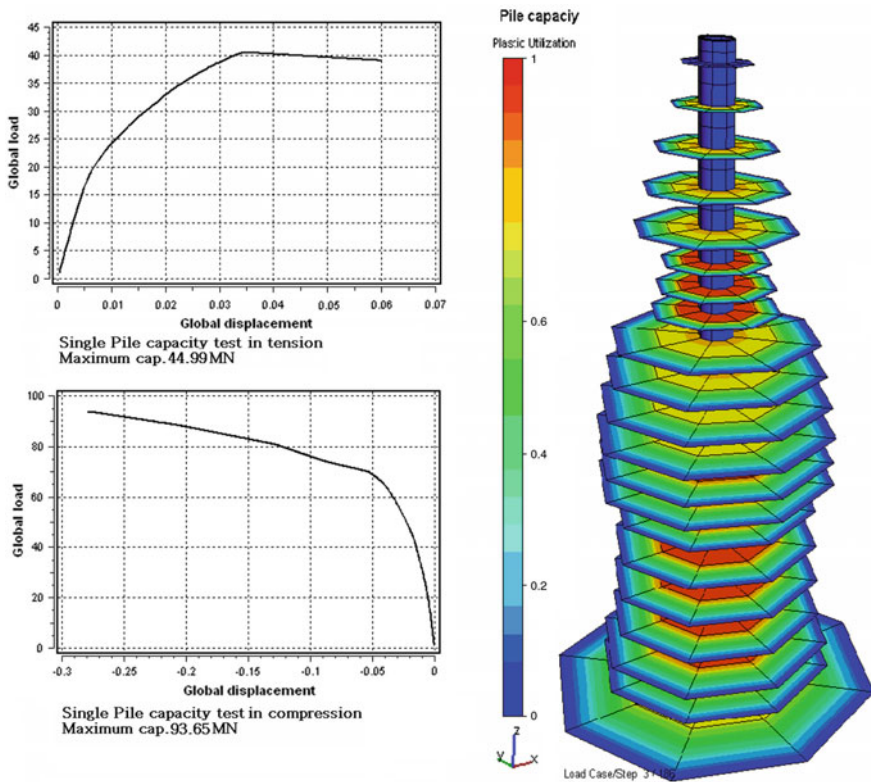


Fig. 17.2 Numerical analysis to calculate the tension (upper left) and compression (lower left) capacity of a single pile (right) under axial loading at pile head

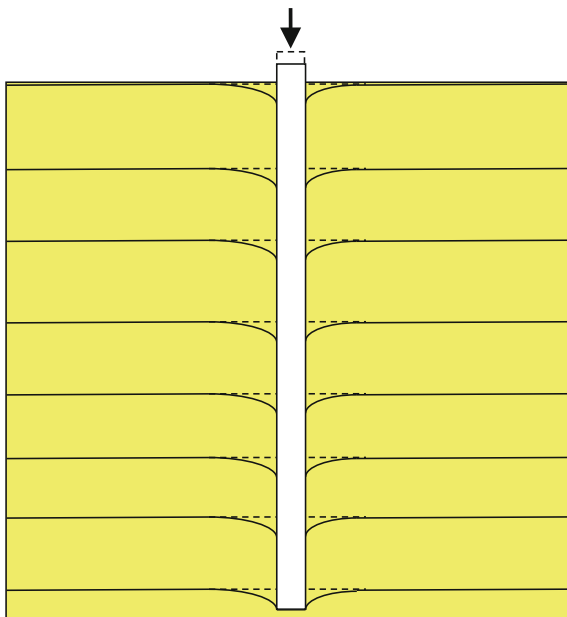
contribution from end-bearing. It is obvious that the axial compression capacity is much higher than the axial tension capacity.

In computing pile loading and capacity, the weight of the pile–soil plug system and hydrostatic uplift should be considered [792].

When the friction reaches its maximum resistance value, it will gradually drop if the pile is embedded in clays or maintained at the same resistance level if the pile is in the sand, as shown in Fig. 17.12. However, the pile tip resistance (end-bearing) normally does not reach its maximum value at this stage and continues to contribute to the increase of the pile's axial loading until the entire pile reaches the maximum value in axial resistance at a relatively large displacement. The above description is based on the assumption that the pile is rigid along its axial direction, which can normally be justified even if the axial deformation of the pile also slightly influences the pile's movement. As shown in Fig. 17.3, if the entire length of a pile is effective to carry the axial compression loading, when the pile reaches its axial capacity, the friction resistance of soils and interface strength along the entire length of the pile will be mobilized, followed by the tip resistance mobilized in a bulb beneath the bottom of the pile. Therefore, the vertical stiffness is influenced by the soil profiles corresponding to the entire length of the pile. This is different from the case with piles subject to lateral loading, in which the lateral resistance and stiffness are dominated by the soils near applied lateral loading, as shown in Fig. 16.1.

In reference to the discussion above, it is worth mentioning that the equation to assess the ultimate axial pile capacity presented in the beginning of Sect. 17.1 assumes that the maximum skin friction and the maximum end-bearing are

Fig. 17.3 Under extreme axial loading, soil friction resistance and interface strength will be mobilized along the full effective length of the pile, and the tip resistance will also be mobilized in the bulb beneath the base of the pile foundation



mobilized simultaneously. However, this may not be realistic as the ultimate skin friction can be reached at much smaller axial pile displacements (typically between 0.005 and 0.02 pile diameter) than the end-bearing capacity (0.05 and 0.01 pile diameter). After the friction resistance reaches its maximum value and with a further increase in axial loading, the skin friction will gradually decrease if the pile is embedded in the clay or maintained at the same resistance level if the pile is in sand, as mentioned before. Therefore, strictly speaking, the total capacity should not be estimated by simply adding the two terms together, even if this represents the practice in many preliminary pile designs, mainly because this effect is rather insignificant, especially for long piles where pile friction dominates the contribution to the axial capacity [27]. Figure 17.4 shows an example of the axial load–displacement relationship at the pile head for a 53-m long pile embedded in sand-dominated soils.

Figure 17.5 shows the axial and lateral capacity varied with pile length for piles embedded in clay with diameters of 2.134 and 1.0 m, respectively. It is noticed that for this particular case, with the soil layers dominated by clays, when the pile is short, the lateral capacity is comparable to that of the axial pile capacity, while it increases dramatically with the pile length. And for longer piles, which is more often the case for offshore applications, by assuming that the ultimate soil strength at each depth along the pile is reached simultaneously (this does not usually happen as, for loose soils or soils at high stress levels, the soil strength may not be fully mobilized at all depths simultaneously), the lateral capacity is higher than the axial capacity when the pile is above a length limit. From a comparison between the

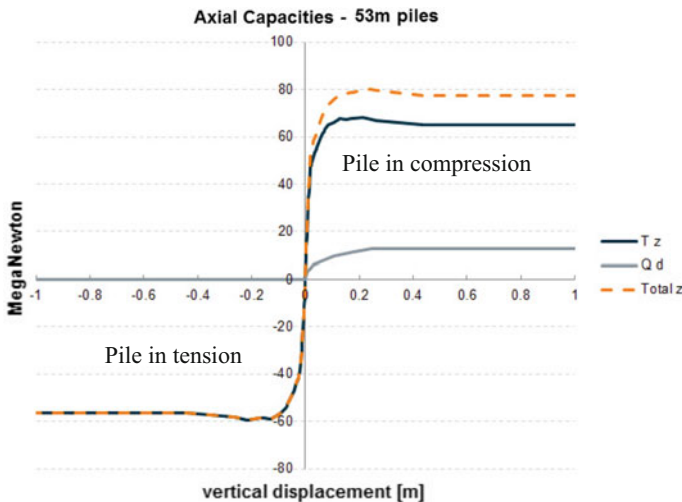


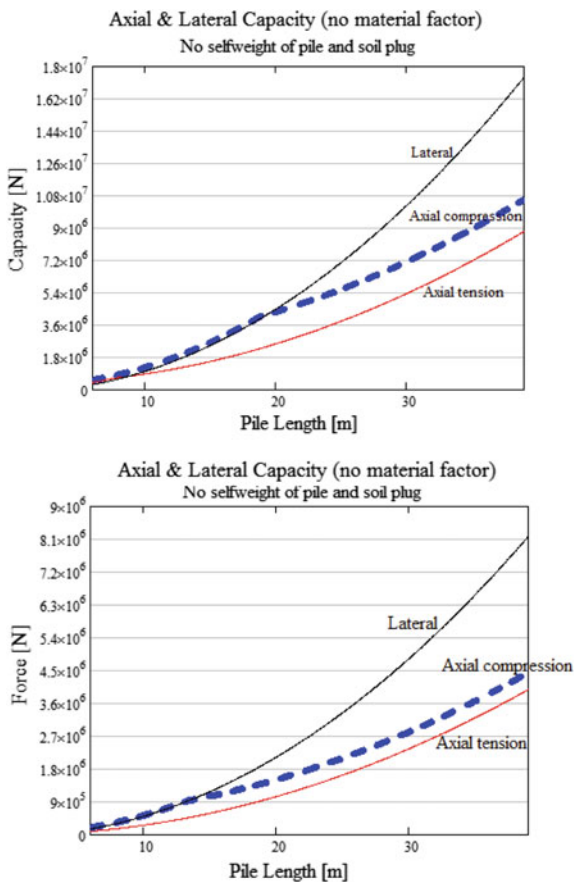
Fig. 17.4 Axial load–displacement relationship at the pile head for a 53-m long pile embedded in sand-dominated soils (the self-weight of the pile and the self-weight of soil plug are not accounted for)

upper and lower figures in Fig. 17.5, it can be seen that for piles with smaller diameter, this length limit is also smaller.

By observing Fig. 17.5, it is also noticed that the axial compression capacity is higher than the axial tension capacity due to the contribution from the end-bearing at the pile tip. However, the self-weight of the pile and the self-weight of the soil plug (if applicable) will increase the axial tension capacity and reduce the axial compression capacity by a difference of 2 times the self-weight for pile and soil plug. On the other hand, the skin friction for piles in tension is in reality lower than that in compression, as will be discussed in Sect. 17.5, but because it is suspected that many of the pile tests underestimate the residual stress caused by the pile driving, in the majority of engineering practice, the skin friction for piles in tension is assumed to be equal to that of piles in compression.

The stiffness contributed by the pile–soil friction along a pile’s axial direction is generally significantly higher than that along the lateral direction. However, the friction resistance increases dramatically and reaches its maximum value at a rather

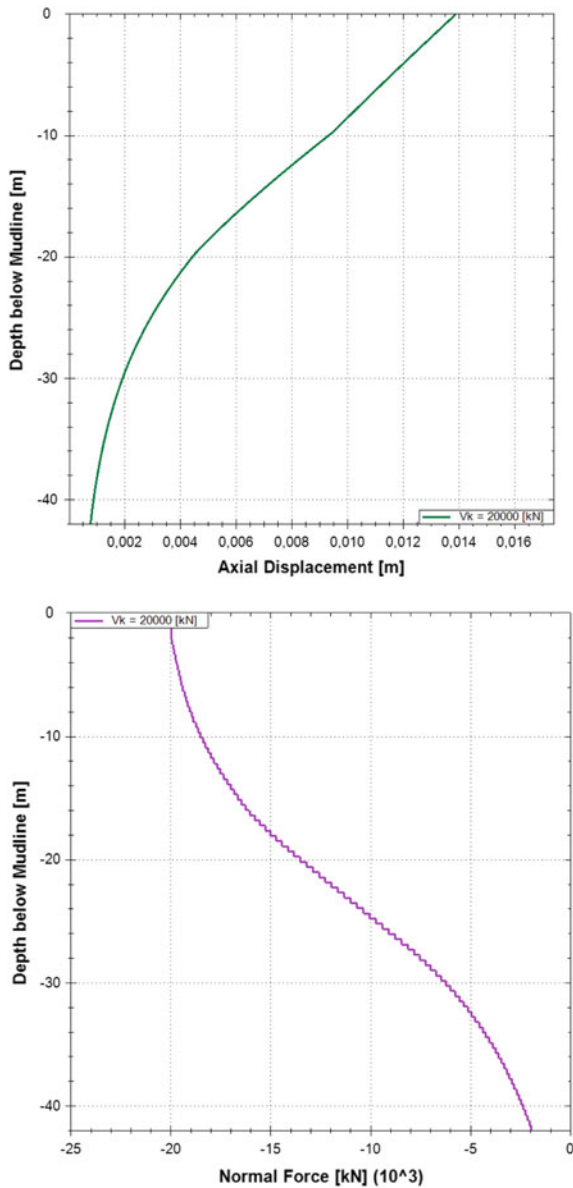
Fig. 17.5 Axial and lateral capacity varied with embedded pile length. The piles are embedded in clay layers with a diameter of 2.134 m (upper) and 1.0 m (lower), respectively; the selfweights of the pile and the soil plug are neglected



small displacement, which is often called the critical movement. This implies that the ductility along the axial direction of a pile is limited even if its stiffness can be rather high, as will be discussed in Chap. 23.

For a pile subject to axial compression load, the axial displacement and axial force of the pile increase with a decrease in depth, as illustrated in Fig. 17.6. Similarly, the axial force of a pile under tension load also increases with a decrease

Fig. 17.6 Axial displacement (upper) and axial/normal force (lower) of a pile subject to an axial compression load of 20 MN at its head. The pile has a diameter of 2.134 m embedded in soil layers dominated by sands, and the calculation is performed using IGtHPile (Institute of Geotechnical Engineering, Leibniz University Hannover)



in depth, as shown in Fig. 17.10. Therefore, it is a normal practice to perform an axial pile capacity control by comparing the calculated axial forces at the pile head (or close to the pile head) and the axial capacity (resistance) of the pile. However, generally, the axial displacement under the axial tension load does not vary significantly with depth as the friction resistance reached a limited displacement value compared with that of the end-bearing resistance.

Since the pile driving in normally to lightly over-consolidated clays disturbs the soil surrounding the pile, the stress state in the soil is altered, and the time required for driven piles to attain ultimate capacity in a cohesive soil can be up to 2–3 years.

As will be discussed in Sects. 17.5 and 17.9, both friction capacity and unit end-bearing capacity of a pile embedded in sands increase linearly with depth due to the linear increase in effective overburden pressure. However, tests on full-scale and model piles have indicated that these relationships are valid only at a critical depth of roughly 15 times the pile diameter or width [26]. Below the critical depth, both friction capacity and unit end capacity remain approximately constant at limiting values in uniform soil conditions. This is thought to be due to the arching of the soil around the lower part of the pile when the soil yields below the base. Another possible explanation is that the peak value of ϕ' decreases with increasing confining pressure until the limiting critical-state value is reached. Therefore, it is preferable to use SPT (Sect. 1.9.5) or CPT (Sect. 1.9.6) to estimate these two capacity parameters.

17.3 Axial Tension Capacity

For many structures with multiple piles, the overturning moments at the bottom of the substructure–pile interface may induce axial tension force in some piles and axial compression forces in some other piles, which is illustrated in Fig. 17.7. Figure 17.8 shows the layout of a jacket's pile foundation with 12 piles. Assuming that the center of the jacket's gravity in the horizontal plane is at the horizontal geometry center (point O in Fig. 17.8) of the 12 piles and by omitting the self-weight of the substructure (the jacket), if the jacket vibrates along the BD direction, overturning moment will induce tension and compression loads on piles in pile group B and D alternatively.

If a pile is under axial tension loading, the end-bearing load does not appear, as shown in Fig. 17.9, even though there may exist certain amount of momentary suction force on the pile tip if the tip is located in a clay layer or in an undrained sand layer. The ultimate axial tension pile capacity is the summation of the external shaft friction resistance plus the weight of the pile and the soil plug. An exception to this is when a pile is embedded with its head/top below the soil surface and subject to tension loads, the end/top bearing at the pile head should also be accounted for. This type of pile is sometimes installed as anchor piles embedded in soft clays, which can be used for anchoring mooring lines of floating offshore structures as shown in Fig. 25.2.

Fig. 17.7 Piles subjected to tensile and compressive axial loading due to the loading transferred from the substructure

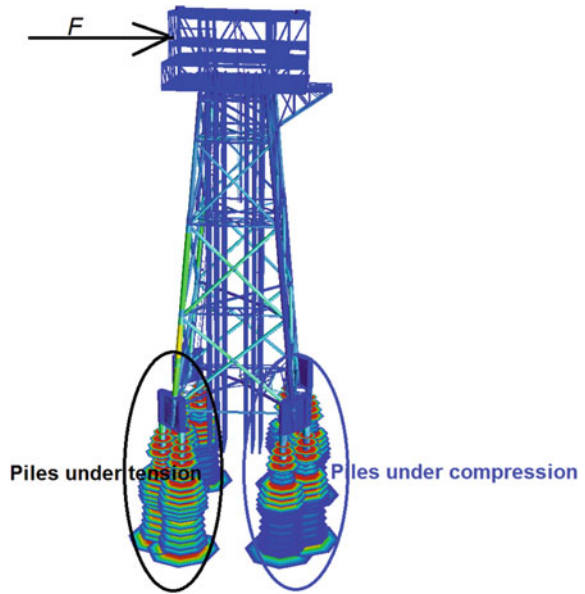
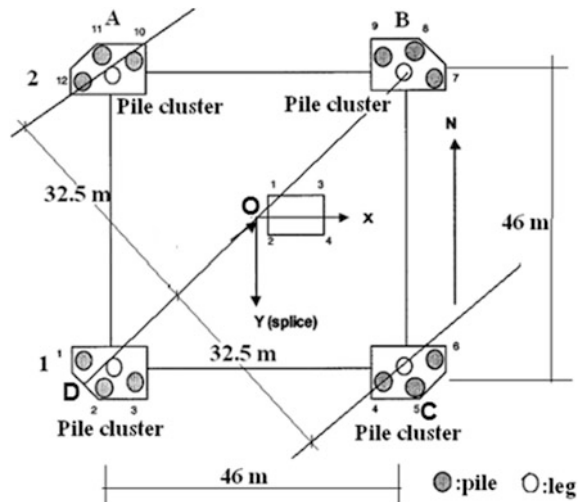
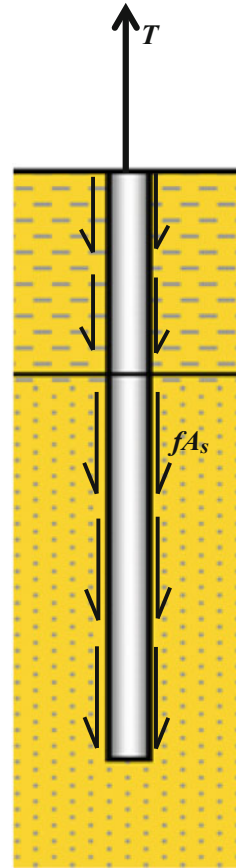


Fig. 17.8 Layout of a jacket’s pile foundations with 12 piles (numbered from 1–12). Each leg is supported by a pile group comprising three piles connected by a pile cluster



As previously discussed in Sect. 17.1, similar to the case for a pile subject to compression load, the axial tension force of a pile increases with a decrease in depth, as illustrated in Fig. 17.10.

Fig. 17.9 Skin friction subjected to an axial tension load of T



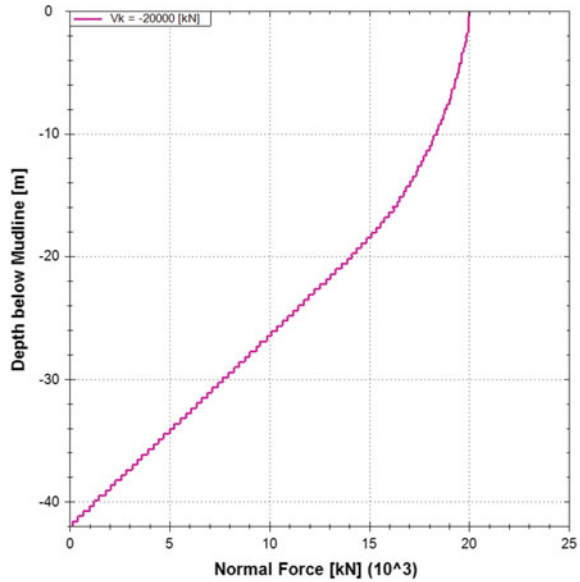
17.4 Determining Unit Friction Capacity for Cohesive Soils

The skin friction capacity for cohesive soil can be correlated empirically with the undrained shear strength s_u . In engineering practice, s_u can often be taken as half of the compression strength of soil samples obtained from unconsolidated, unconfined triaxial tests (Sect. 1.9.3).

17.4.1 Friction Capacity for Highly Plastic Clays by API

For highly plastic clays, the unit friction capacity is equal to s_u for under-consolidated (clays with excess pore pressures undergoing active consolidation) or normally consolidated clays.

Fig. 17.10 Axial force of a pile subject to an axial tension load of 20 MN at its head. The pile has a diameter of 2.134 m embedded in soil layers dominated by sand, and the calculation is performed using IGtHPile (Institute of Geotechnical Engineering, Leibniz University Hannover)



For over-consolidated clays, the unit friction capacity should not exceed 48 kPa for shallow penetrations or s_u equivalent to normally consolidated clay for deeper penetrations, whichever is greater [790].

17.4.2 Friction Capacity for Other Types of Clays by API

For other types of clays with low plasticity and high content of silty material, the friction capacity of pipe piles can be calculated as [791, 864]:

$$f = \alpha s_u \tag{17.3}$$

where α is empirical correlation factor (adhesion factor) between soil and pile, and it decreases with increasing s_u : $\alpha = 1.0$ when $s_u \leq 24$ kPa; $\alpha = 0.5$ when $s_u \geq 72$ kPa; α is linearly interpolated when $24 \text{ kPa} < s_u < 72 \text{ kPa}$.

There is a large database of in situ pile load tests including bored and driven piles dating back to the 1950s that supports this method. This method is often referred to as the α -method.

17.4.3 Friction Capacity by Revised API Method (α -Method)

API 2007 [792] has also proposed a revised equation for the coefficient of α :

$$f = \alpha s_u \quad (17.4)$$

where α is a coefficient depending on the type of clay, the method of installation and the pile material; $\alpha = 0.5\psi^{-0.5}$ if $\psi \leq 1.0$, and $\alpha = 0.5\psi^{-0.25}$ if $\psi > 1.0$, but in any case α should be smaller than 1.0; $\psi = s_u/\sigma_{vo}'$; σ_{vo}' is the effective overburden pressure (vertical stress) at the point in question.

For under-consolidated clays (clays with excess pore pressures undergoing active consolidation), α can usually be taken as 1.0.

However, the equation above should be used with caution for deep penetrating piles with high undrained shear strength s_u , where the computed shaft friction using the equation above is generally higher than what is previously specified in API [791]. Similar engineering judgment should be applied for $\psi > 3.0$, due to a lack of load tests in soils with high ψ values.

17.4.4 Friction Capacity for Long Piles in Clay

For very long piles, a deduction in friction capacity may be necessary, particularly where the shaft friction may degrade to some lesser residual value on continued displacement. This effect is discussed in more detail in the commentary of API [791].

Capacity degradation for long piles driven in clay soils can occur due to the following effects [791]:

1. Continued shearing of a particular soil horizon during pile installation.
2. Lateral movement of soils away from the pile due to “pile whip” during driving.
3. Progressive failure in soils due to strength reduction with continued displacement (softening).

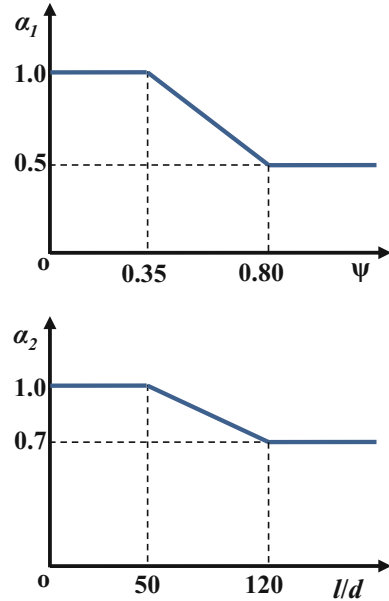
Various factors associated with both installation and soil behavior due to the effects above influence the capacity degradation. See sources [865–870] for alternative methods to assess the reduction in capacity of long piles.

Sample and Rigden [865] proposed a method to calculate the skin friction, which is especially applicable for very deep penetrating piles but installed without significant interruption:

$$f = \alpha s_u = \alpha_1 \alpha_2 s_u \quad (17.5)$$

where α_1 and α_2 are two parameters determined by ψ and ratios of pile penetration l to the pile diameter d , and they are given in Fig. 17.11.

Fig. 17.11 Values of α_1 and α_2 applicable for very long piles



17.4.5 β -Method

An alternative approach is to express skin friction in terms of effective stress (often referred to as β -method) originally proposed by Chandler [871] and Burland [872], by using a shaft/pile friction factor β -parameter (a dimensionless shaft friction factor, sometimes referred to as the Burland-Bjerrum coefficient):

$$f = c' + K_0 \sigma'_{vo} \tan(\phi') = \beta \sigma'_{vo} \tag{17.6}$$

where c' and ϕ' are the cohesion intercept (cohesion strength) and effective internal friction angle; K_0 is the mean lateral earth pressure coefficient (ratio of horizontal to vertical normal effective stress) in soils; σ'_{vo} is the effective vertical stress at a depth in question.

Failure is assumed to take place in the remolded soil close to the pile shaft. Therefore, the angle of friction between the pile and the soil is represented by the critical-state value of the angle of shearing resistance.

As the shear strength decreases significantly due to the remolding and softening effects during pile installation, the effective cohesion c' can be neglected along the pile shaft, particularly in coarse-grained soils and other soils with low percentage of fines such as silty sands and normally consolidated clays. Therefore, β in the equation above can be expressed as:

$$\beta = K_0 \tan(\delta') \quad (17.7)$$

where δ' is the effective friction angle at the soil–pile interface.

β typically ranges from 0.30 to 0.60 for fine and coarse-grained soils [871, 872], respectively. For normally consolidated clays, β is usually within 0.25–0.40, while for over-consolidated clays β values are significantly higher and vary in a relatively wide range [26].

Obviously, β -method can be taken as a firm criterion and more conveniently implemented than that of α -method, which is prone to error in the parameter determination and calculation. β -method is also used for estimating the negative drag load, as will be discussed in Sect. 24.1. Moreover, β -method is widely used for calculating skin friction capacity of piles embedded in sand, as will be discussed in Sect. 17.5.

17.4.6 λ -Method

To calculate the friction capacity of piles driven into fine-grained soils, λ -method [873] is proposed by combining the total (i.e., undrained) and effective (i.e., drained) stress approaches. The pile friction capacity per unit pile wall area can then be determined by:

$$f = \lambda(\sigma_{\text{vom}}' + 2s_{\text{um}})\pi d \quad (17.8)$$

where σ_{vom}' is the mean vertical effective stress between the ground and the pile tip; s_{um} is the mean undrained shear strength along the pile; d is the pile diameter; λ is the frictional capacity coefficient that is a function of pile penetration, it ranges from 0.12 to 0.5 for pile penetration of 0–70 m based on gathered 42 piles load tests [873].

Comparing to α -method and β -method, λ -method can reduce the sensitivity of shear strength parameters associated with the other two methods.

17.5 Determining Unit Friction Capacity for Cohesionless Soils

Based on experimental results for driven piles in sands, both skin friction and end-bearing show a considerable scatter, which is likely due to the influence of installation methods on soil properties and the stress state. This section and Sect. 17.9 present a description of how to determine the values of skin friction and end-bearing for piles in sands, which are consistent with the state of the practice.

However, these methods should be used with caution, and if possible, pile load tests are strongly recommended.

17.5.1 Unit Friction Capacity by API 1993 Method

In API 1993 [790], for piles in sands, the unit friction capacity can be derived from the normal effective stress acting on the pile shaft and the friction properties between the pile and soil interface, which is also termed the β -method:

$$f = K\sigma'_{vo} \tan(\delta) \leq f_1 \tag{17.9}$$

where K is the lateral earth pressure coefficient (ratio of horizontal to vertical normal effective stress) in the soil, API-RP-2A-WSD [790, 791] proposes that the skin friction under tension and compression is assumed to be the same, for a preliminary design, K may be taken as 0.8 for open-ended piles driven unplugged, and 1.0 for full-displacement piles (plugged or closed end), it can also be taken with values as follows: for coarse-grained soils, $K = 1 - [\sin\phi' \cdot (\text{OCR})^{\sin\phi'}]$, where ϕ' the angle of internal friction in effective stress measures, for fine-grained soils such as clays, $K = [0.44 + (0.42I_p(\%)/100)] \cdot \text{OCR}^{0.5}$; σ'_{vo} is the effective vertical stress at the depth in question, it is worth mentioning that K value recommended by API 1993[790] may be unconservative; δ is the angle of pile–soil interface friction, and it is a function of internal friction angle and interface materials, is typically a fraction of soil’s internal angle of friction, and may be taken according to Table 17.1 for different pile–soil interfaces and Table 17.2 for driven piles; f_1 is the limiting unit skin friction, see Table 17.2 for its value.

It is now widely recognized that the approach outlined above for calculating shaft and base resistances offers a poor representation of the real pile–soil system [790], and in many cases, it does not match measured pile capacities. It provides potentially non-conservative results for pile friction capacity in loose sands, and in loose to medium sands with high length-to-diameter ratios [750]. Moreover, the tension capacity due to pile–soil friction is lower than its compression counterpart. Therefore, in some other guidelines, this is taken into account by adopting a smaller value of lateral earthquake pressure coefficient K for piles in tension than that in compression. For example, in Germanischer Lloyd [875],

Table 17.1 Value of δ for different pile–soil interfaces [874]

Interface materials	Typical field analogy	δ/ϕ'
Sand-rough concrete	Cast-in-place	1.0
Sand-smooth concrete	Precast	0.8–1.0
Sand-rough steel	Corrugated	0.7–0.9
Sand-smooth steel	Coated	0.5–0.7
Sand-timber	Pressure treated	0.8–0.9

Table 17.2 Design parameters for axial resistance of driven piles in cohesionless silicious soils^a [877]

Density	Soil description	δ (°)	f_1 (kPa)	N_q^c	q_1 (MPa) ^c
Very loose Loose Medium	Silt Sand-silt ^b Silt	15	47.8	8	1.9
Loose Medium Dense	Sand Sand-silt ^b Silt	20	67.0	12	2.9
Medium Dense	Sand Sand-silt ^b	25	81.3	20	4.8
Dense Very dense	Sand Sand-silt ^b	30	95.7	40	9.6
Dense Very dense	Gravel Sand	35	114.8	50	12.0

^aThe parameters listed in this table are intended as guidelines only, where detailed information such as in situ cone penetrometer tests, strength tests on high-quality soil samples, model tests or pile driving performance is available, other values may be justified

^bSand-silt includes those soils with significant fractions of both sand and silt. Strength values generally increase with increasing sand fractions and decrease with increasing silt fractions

^c N_q is the bearing capacity factor; q_1 is the limiting unit end resistance

usually adopted for wind turbine supporting structures in the German part of the North Sea, the skin friction under tension load is assumed to be 2/3 of the compression. In some company specifications, such as the one by Fugro, based on a thorough review of pile load test data performed by Toolan and IMS [876], K is taken as 0.7 for piles under compression and 0.5 for piles under tension. In API 2007 [792], four new CPT-based methods (Sect. 17.13) are recommended to calculate pile friction capacity, and in those methods, the ultimate shaft friction mobilized in compression is also higher than that in tension.

While the angle of pile-soil interface friction δ can be measured with reasonable accuracy [878, 879], there is considerable uncertainty and debate over the appropriate choice of the horizontal stress coefficient K and the extent to which limiting values of shaft friction should be imposed. Different from the values recommended by API, Kraft [880] presented a calculation purely based on relative density of the soil (but independent of grain size) and effective area ratio of the pile (full or partial displacement). The obtained values of K lead to a lower pile friction compared with the API recommendation.

17.5.2 Unit Friction Capacity by API 2000 Method

In API 2000 [791], by incorporating K and δ together as dimensionless shaft/pile friction factor β parameter (dimensionless shaft friction factor), so that the

Table 17.3 Design parameters for axial resistance of open-ended pipe piles driven unplugged [792]

Density	Soil description	β	f_I (kPa)
Medium	Sand–silt	0.29	67
Medium Dense	Sand Sand–silt	0.37	81
Dense Very dense	Sand Sand–silt	0.46	96
Very dense	Sand	0.56	115

confusion with other nomenclature in the API-RP-2A code can be avoided, the equation used in API 1993 [790] above can then be expressed as (often called the β -method):

$$f = \beta \sigma'_{vo} \leq f_I \quad (17.10)$$

The value of β parameter for open-ended pipe piles driven unplugged is listed in Table 17.3; σ'_{vo} is the effective overburden pressure at the depth in question.

The β -method above implies that it is not appropriate to modify the empirical method with a measured interface friction angle δ .

For full-displacement piles such as open-ended pipe piles driven in fully plugged mode or for closed-ended pipe piles, API suggests that β should be increased by 25%.

The use of CPT results potentially allows a more precise reflection of soil density, compressibility, and stress level than the consideration of the subsoil only with regard to relative density in the β -method. The Errata and Supplement 3 in API-RP-2A [792] reflect, albeit in a simplified version, studies presented by several researchers [881–884]. However, offshore experience with the application of these CPT methods is still limited. Therefore, more experience is needed before they can be recommended for routine design, such as to replace the current API β -method [811], which is still a routine for offshore pile design today. Since from many numerical and experimental studies in recent years, it was fully realized that the API method underestimates the skin friction especially in dense sands, and the skin friction capacity for piles in compression should be higher than that for tensioned pile. These issues are also addressed by the recently developed CPT-based methods which are referred to as API 2007 [792]. Section 17.13 introduces the recently developed CPT methods.

17.6 Modeling of Pile–Soil Friction Behavior by FEM

As an alternative, the frictional behavior at soil–pile interface can be modeled by contact elements based on, for example, the slave–master concept, with friction angle and adhesion, or by interface elements with normal and tangential stiffness.

For sands, the ratio between the pile–soil friction angle and the internal friction angle ranges between 0 and 1 depending on surface roughness, mean particle size of sands, and method of installation. Its range varies between 0.5 and 0.7 for smooth steel pipe piles [885, 886]. Quite often, the characteristics of pile–soil friction can be represented by a friction factor. For more detailed modeling techniques of pile–soil friction, readers may read sources [31, 887]. Smaller size elements are normally used in the region surrounding the pile to increase calculation accuracy.

17.7 Modeling of t - z Curves

Similar to the p - y curve, the friction resistance can be modeled as a series of springs in the axial direction of a pile. Each of them is represented with a friction load–displacement curve, which is often called a t - z curve. As shown in Fig. 17.12, t - z curve can be modeled by Vijayvergiya’s method [888]:

$$\frac{t}{t_{\max}} = 2\sqrt{\frac{z}{z_c}} - \frac{z}{z_c} \text{ for } z \leq z_c \quad (17.11)$$

$$t = t_{\max} \text{ for } z \geq z_c \quad (17.12)$$

where t is the skin friction per unit length of a pile; t_{\max} is the maximum skin friction per unit length of the pile; z_c is the displacement at which the maximum skin friction is mobilized, for clays, it is sensitive to the change of pile diameter and length and is often taken as 9 mm, for sand, it is often taken as 7.5 mm; z is the axial displacement along the pile segment.

By observing Fig. 17.12, it is found that for clay, the t - z curve has a post-peak softening part with a residual t/t_{\max} value ranging between 0.7 and 0.9 [889]. This value may be determined as a function of stress–strain behavior, stress history, pile installation method, pile loading sequence, and other relevant factors. Experimentally, this value can be obtained from laboratory shear tests or from large-scale or model pile tests. By performing the dynamic axial loading test, King et al. [890] also presented that the ratio between the dynamic residual friction and the peak pile resistance ranges from 0.6 to 0.85, and the lowest ratio is associated with high loading rate.

Since the axial load deformation responses are not sensitive to the shape change of t - z curve, it can normally be modeled as a bilinear curve.

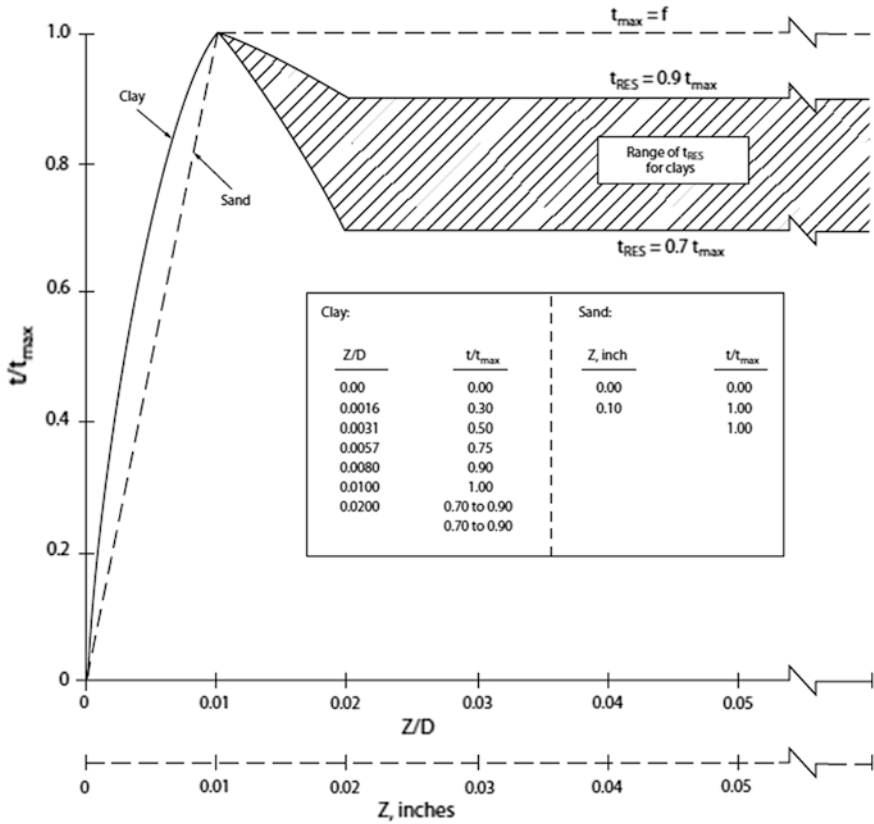


Fig. 17.12 Illustration of t - z curves [791]

17.8 Determining Unit End-Bearing Capacity for Cohesive Soils

Although sleeve friction measured during a CPT (Sect. 1.9.6) has been related to pile shaft friction [891], due to greater variability in sleeve friction measurements (among other issues), the unit end-bearing resistance of piles in clays can often be estimated by Skempton’s method [803]. For a convenient implementation in numerical codes, the unit end-bearing resistance can normally be taken as a limiting value of 9 times the undrained shear strength of the soil at the level of the pile tip [892], which is a type of α -method:

$$q_p' = 9s_u \tag{17.13}$$

It should be noted that the equation above is valid provided that the installation process has not reduced the shear strength, which can be a relevant engineering

problem. In addition, q_p' is measured as effective stress value rather than a total stress value.

For very stiff clay soils, as presented in the commentary part of API 1993 [790], the end-bearing resistance can be in the range of 9–12 times the undrained shear strength from large-diameter pile test data [889].

17.9 Determining Unit End-Bearing Capacity for Cohesionless Soils

The unit end resistance of piles in sands, typically measured based on a tip displacement of 10% of the pile diameter, can be calculated by Rankine's theory, which is a type of β -method:

$$q_p' = \sigma_{vo}' N_q \leq q_1 \quad (17.14)$$

where σ_{vo}' is the effective vertical stress at the pile tip; N_q is the bearing capacity factor/coefficient, if no results from CPTs are available, see Table 17.2 for its value; q_1 is the limiting unit end resistance, see Table 17.2 for its value.

For long piles, q_p' may not increase linearly with the overburden pressure. Therefore, the limiting unit end resistance q_1 above is introduced.

Depending on whether or not a soil plug will form, q_p' may act on either the complete enclosed area of the pile tip or the cross-sectional area.

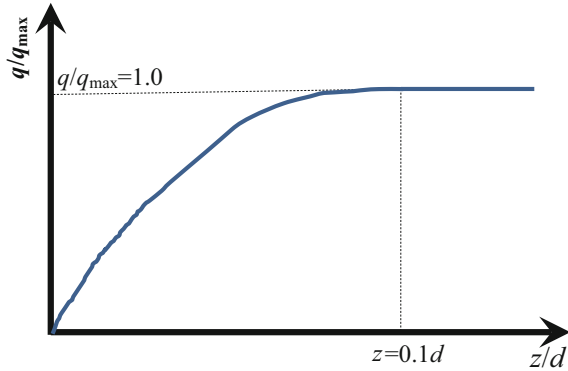
However, API-RP-2A states that many soils do not fit the description of those in Table 17.2, and the design parameters are not suitable for these soils. Examples are loose silts, soils containing large amounts of mica or volcanic grains, and calcareous sands. These latter soils are known to have substantially lower design parameters. Drilled and grouted piles may have higher capacities than driven piles in calcareous soils [863].

17.10 Modeling of Q - z Curves

The end-bearing force can be modeled with a nonlinear spring at the pile tip as shown in Fig. 15.2. The end-bearing resistance, i.e., the force–displacement relationship, can be represented by a Q - z curve shown in Fig. 17.13 [888] and expressed as:

$$\left(\frac{q}{q_{\max}} \right)^3 = \frac{z}{z_{\max}} \text{ for } Q \leq Q_{\max} \quad (17.15)$$

Fig. 17.13 Illustration of Q - z curve (d is the diameter of the pile)



where q is the unit end-bearing mobilized at displacement $z < z_{\max}$; q_{\max} is the maximum end-bearing mobilized at displacement $z > z_{\max}$, which is normally taken as the end resistance q_p' presented in the previous Sects. 17.8 and 17.9.

By observing Fig. 17.13, it is found that the unit end-bearing q is assumed to be fully mobilized at a pile tip displacement of $0.1d$. This is consistent with the manner in which pile load test data were interpreted.

It should be noticed that for very long piles with pile length to diameter larger than 25, the end-bearing force is insignificant compared with that of the skin friction force. In such a condition, the shape of Q - z curves has almost no influence on the axial load–deflection relationship at the pile head.

17.11 Effects of Soil Layer Boundaries on End-Bearing Capacity

For stratified soils that do not have a uniform soil condition along the depth, the end-bearing may be modified if a pile penetrates less than two pile diameters into a stronger soil or the pile tip is less than 2–3 pile diameters above a weaker soil [27]. Engineers normally simply use an averaging end-bearing over depth between two or three pile diameters from the boundary, or weighted averaging depending on the distance from the position of interest, or a graphical smoothing arranged to pass through the minimum capacity points [112].

In API 2000 [791], when calculating the end-bearing capacity, it is assumed that piles achieve penetration of two to three diameters or more into the layer in question and the tip is approximately three diameters above the bottom of the layer to preclude punch through. In the recently developed CPT-based methods recommended by API 2007 [792], the CPT cone tip resistance q_c data averaged between 1.5 pile diameter above and below the pile tip level is normally used, as will be discussed in Sect. 17.13.2.

17.12 Soil Plugging

When an open-ended pile is driven into the ground, soils normally enter the inside of the pile in the initial stage of pile driving at very shallow depths. As the pile is driven deeper into the soil, the soil friction on the inside of the pile wall increases until a soil plug is formed, which may prevent or partially restrict additional soil from entering the inside of the pile. In offshore applications, circular cross-sectional piles are often purposely designed to be open-ended to facilitate deeper penetration (lower blow-count for driving a pile into a certain depth). The soil plug will then be formed inside the piles.

Depending on the degree of soil plugging, an open-ended pile can produce a similar bearing capacity as a closed-ended pile. Figure 17.14 shows different modes of penetration of open- and closed-ended piles. If pile penetration depth is equal to the soil plug length, it is called fully coring or unplugged pile, as shown in Fig. 17.14a. Most piles in practice are driven under partially plugged mode [870, 893] as shown in Fig. 17.14b, and in many cases, the lengths of the pile plugs can be less than half of pile penetrations. A fully plugged open-ended pile (Fig. 17.14c) behaves similar to a closed-ended pile (Fig. 17.14d), and the soil plug settles with the pile as an intact body in a fully plugged pile during pile installation (or loading) [894].

If a pile is only driven into a shallow depth, an open-ended pile has lower load capacity than a closed-ended one. However, as penetration depth increases, the load capacity of the open-ended pile increases and may approach that of the equivalent closed-ended pile. This increase is significantly contributed by the soil plugging with larger penetration depth [895, 896]. On the other hand, a long soil plug may be developed in an unplugged (or fully coring) open-ended pile. Due to a lack of inner frictional resistance, it produces a smaller bearing capacity than its fully plugged or partially plugged counterparts.

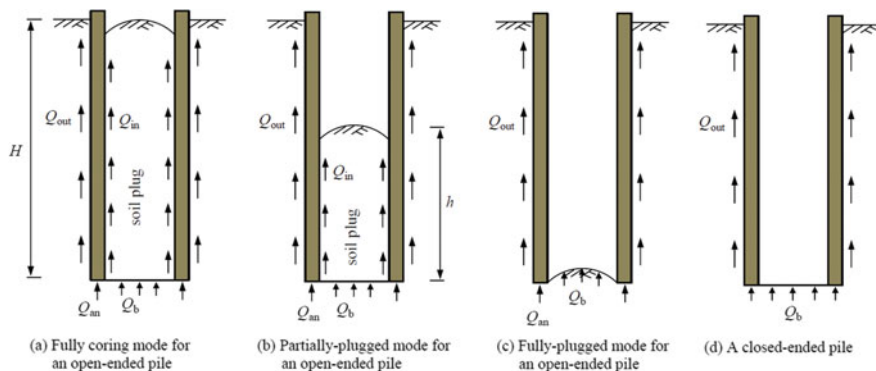


Fig. 17.14 Extensions of soil plug [894]

The installation methods, site conditions, and the geometry of piles influence the mechanism of the soil plug: Static methods generally encourage soil plugging better than do dynamic installation methods such as vibratory pile driving [897]; looser ground conditions generally lead to higher degree of plugging [898]; and smaller diameter piles produce a higher degree of soil plugging [899].

The extent of soil plug entering into the pile is characterized by a plugging ratio PLR, which is defined as the ratio between the length of soil plug l and the length of pile penetration h :

$$\text{PLR} = l/h \quad (17.16)$$

The plugging ratio is used to indicate influences of soil plug on the load-carrying capacity of piles. The plug status is strongly influenced by the driving resistance and the bearing capacity of open-ended piles [900]. Theoretical methods widely used to judge the plug effect are normally based on one-dimensional wave theory [901]. Obviously, if the plugging ratio is rather high (close to fully plugged condition), and if pile driving is adopted, a large energy hammer has to be selected or more blows are required for driving the pile to a desirable penetration, which will considerably increase the driving cost and risk of damage to the pile itself. Therefore, in practice, a fully plugged pile is often difficult to obtain during pile driving [898, 902].

By collecting PLR data from studies, Yu and Yang [903] suggested that PLR in sand is a function of internal pile diameter d_i :

$$\text{PLR} = \min(1, d_i^{0.15}) \quad (17.17)$$

It was demonstrated by experiments that the end-bearing capacity decreases with an increase in the plugging ratio. The closed-ended piles display a higher end-bearing capacity than open-ended piles as closed-ended piles prevent soil from entering the piles and introduce forces on the soil around the pile tip, leading to a higher confined stress state in this region. Through full-scale testing, Tan and Lin [904] presented that, although open-ended steel pipe piles experience a partially plugged condition during the process of penetrating through the upper thick clay silt deposits, a fully plugged condition can be considered in the design of their static compression capacities if they are end-bearing in dense cohesionless soils.

In addition to the PLR, incremental filling ratio (IFR) is also often used as an indicator of soil plugging. It is defined as the first derivative of PLR:

$$\text{IFR} = dl/dh \quad (17.18)$$

where dl is the increment of soil plug length corresponding to an increment of pile penetration depth dh . In the case of a fully coring mode, PLR and IFR are equal to 1.

As it is difficult to measure PLR for routine piling work, Lehane et al. [883] proposed a formula for estimating IFR, averaged over 20 pile diameters of penetration, as a function of the pile internal diameter d_i :

$$\text{IFR}_{\text{avg}} = \min \left[1, (d_i/1.5)^{0.2} \right] \quad (17.19)$$

While PLR is an adequate measure of degree of overall soil plugging, and researchers proposed to use PLR for estimating limit unit skin friction of open-ended pipe piles [898], a better measure of soil plugging on estimating end-bearing values may be IFR, as it can represent the condition of soil plugging at the final penetration depth from final pile driving [899].

When a pipe pile is driven into clay, the clay inside the pile forms a plug. The internal plugged clay may be highly disturbed by the pile driving, and therefore, a reduced strength (remolded shear strength) may be used to compute the skin friction along the inner surface of the pile wall.

For the design of pile driving, it is important to carefully review the pile toe area input and perform both optimistic (unplugged) and pessimistic (plugged) driveability analyses to establish lower and upper-bound driving resistance values. This will help to prepare for situations where piles reach refusal (refusal is normally specified in the contract and is regarded to occur if the blow-count reaches 200–300 blows/foot) prior to a required minimum pile tip penetration. Such preparations may include the requirement of a larger hammer or mobilization of installation aids such as jets or drilling equipment.

17.13 Recently Developed CPT-Based Methods to Assess the Axial Pile–Soil Interaction Capacity

The majority of the existing theoretical methods for predicting pile axial capacities in sands are influenced by a large number of variables [905]. Furthermore, note that soil density influences shaft friction and base capacity of open-ended piles, and interpretations of this influence are highly uncertain due to poor definitions of soil properties along the length of a pile [906]. Moreover, abundant comparisons of pile load test results and axial pile capacities predicted according to the recommendations of API 1993 [790] for piles in sand have proven that this method may be conservative for relatively short piles in very dense sand, while it may be unconservative for relatively long piles driven into loose sands [907]. The reasons above promote the use of the CPT for site characterization, which has been routinely performed as a part of offshore soil investigations for decades. This provides a large amount of repeatable information on the vertical variability of soil strength and compressibility and, therefore, gives an increased design reliability and accuracy in skin friction and end-bearing capacity assessment [908].

Based on extensive research over the past 30 years, particularly direct correlations of pile unit friction and end-bearing data with cone tip resistance (q_c) values obtained from CPTs, the commentary of API-RP-2A [792] recommends four recent CPT-based methods applied to calculate the axial pile capacity for sands, which all

reduce or eliminate the skewing associated with the API 1993 method [790] and cover a wider range of cohesionless soils:

- 1 ICP-05 [881], which was originally called Marine Technology Directorate (MTD) method [909]. More recently, this method was referred to as the Imperial College Pile (ICP) method because the Marine Technology Directorate in the UK no longer operates. The major feature of ICP method is that the ultimate unit friction and pile end-bearing are directly correlated with CPT resistance. Another noticeable feature of ICP method is that both unit friction and end-bearing are highly dependent on pile geometry.
- 2 Fugro-05 [882], which is a modified ICP-05 method, is based on a study of the axial pile capacity design method for offshore driven piles in sands. It provides data and information needed to improve pile design criteria and to propose an improved design method for axially loaded, open-ended, offshore driven pipe piles in sands.
- 3 NGI-05 [884] is established based on a database of well-documented results from tests of driven piles in sands by the Norwegian Geotechnical Institute (NGI).
- 4 UWA-05 [883, 910] is based on an extended database of static load tests and evaluations of the existing API recommendations [791] and three other CPT-based methods.

These CPT methods for offshore designs are intended to give a more realistic representation of the mechanisms that influence the axial capacity of piles embedded in sands and require a higher level of site investigation practice and geotechnical expertise than the traditional API method [790]. Therefore, they should be used only by qualified engineers who are experienced in interpreting CPT data and understand the limitations and reliability of these CPT-based methods.

17.13.1 Skin Friction Calculation for CPT-Based Method

Regarding the skin friction capacity, the CPT-based methods are distinguished from the traditional API 1993 method [790] mainly in two respects [906]:

1. The recognition that the local pile friction τ_f in a given soil layer reduces as a pile is driven deeper, which is associated with the phenomenon of “friction fatigue” [887, 911–913].
2. Open-ended piles tend to have lower τ_f values than closed-ended piles. These issues are important for long, large-diameter offshore piles, which are primarily driven open-ended in a coring manner (Sect. 17.12).

Even though refined upon different assumptions, the pile skin friction formulations proposed by ICP-05, Fugro-05, and UWA-05 methods are in general similar. The equation formats are based on studies with instrumented jacked

closed-ended Imperial College Model Pile [912, 914], indicating that radial stress after installation and equalization at a given depth is related to cone tip resistance and the distance above the pile tip normalized by the pile radius [906].

The unit skin friction f for open-ended steel pipe piles has a strong correlation with the CPT end resistance (q_c) and a few other factors:

$$f = uq_c(z) \left(\frac{\sigma'_{v0}(z)}{p_a} \right)^a A_r \left[\max \left(\frac{L-z}{d}, v \right) \right]^{-c} [\tan \delta_{cv}]^d \times \left[\min \left(\frac{L-z}{dv}, 1 \right) \right]^e \tag{17.20}$$

where $q_c(z)$ is the CPT cone tip resistance at depth z ; $p_a = 100$ kPa is the atmospheric pressure; $\sigma'_{v0}(z)$ is the soil's effective vertical stress at depth z ; $A_r = 1 - (d_i/d)^2$ is the pile displacement ratio; d_i and d are the inner and outer pile diameter, respectively; L is the embedded length of the pile below the soil surface; δ_{cv} is the pile-soil constant volume interface friction angle; $a, b, c, d, e, u,$ and v are unit skin friction parameters with recommended values given in Table 17.4.

Different from the methods proposed by ICP-05, Fugro-05, and UWA-05 methods, NGI-05 method [884] proposes that the ultimate unit skin friction for tension $f_t(z)$ and compression $f_c(z)$ for driven open-ended steel pipe piles can be expressed as:

$$f_t(z) = (z/L)p_a F_{sig} F_{D_r} > 0.1\sigma'_{v0} \tag{17.21}$$

$$f_c(z) = 1.3f_t(z) > 0.1\sigma'_{v0} \tag{17.22}$$

where $F_{sig} = (\sigma'_{v0}/p_a)^{0.25}$; $F_{D_r} = 2.1(D_r - 0.1)^{1.7}$; the relative density $D_r = 0.4 \ln \{q_c(z)/[22(\sigma'_{v0}p_a)^{0.5}]\} > 0.1$ is the sand's relative density, and if the calculated D_r is

Table 17.4 Unit skin friction parameters with recommended values for driven open-ended steel pipes [792]

Method	Parameter	a	b	c	d	e	u	v
Simplified ICP-05a	Compression	0.1	0.2	0.4	1	0	0.023	$4(A_r)^{0.5}$
	Tension	0.1	0.2	0.4	1	0	0.016	$4(A_r)^{0.5}$
UWA-05b	Compression	0	0.3	0.5	1	0	0.030	2
	Tension	0	0.3	0.5	1	0	0.022	2
Fugro-05c	Compression	0.05	0.45	0.90	0	1	0.043	$2(A_r)^{0.5}$
	Tension	0.15	0.42	0.85	0	0	0.025	$2(A_r)^{0.5}$

^aSimplified ICP-05 is a conservative approximation of the full ICP-05 method since dilatancy is ignored and some parameter values are conservatively rounded up/down. If the pile outer diameter is $d < 0.76$ m, the original "full" design equations [881] may be used, provided that larger safety factors are considered in the WSD (working stress design)

^bFor piles with $d < 0.76$ m, the "full" design equation by Lehane et al. [910] may be considered, provided larger safety factors can be considered in WSD

^cSimilar to the "full" ICP-05 and the "full" UWA-05 method, when using Fugro-05 method, it is recommended to consider larger factors of safety

larger than 1.0, it can still be accepted and adopted to calculate the ultimate skin friction.

Similar to the “full” ICP-05, the “full” UWA-05 method, and the Fugro-05 method, it is recommended to consider larger factors of safety when using the NGI-05 method.

It is noticed that all methods above assume that the ultimate shaft friction mobilized in tension is lower than that in compression. Among them, Fugro-05 method assumes different τ_f distributions under tension and compression loading, whereas the other three methods adopt a ratio of tension to compression capacity with a value between about 0.7 and 0.8.

Table 17.5 shows an example of comparison in skin friction capacity among different methods. Obviously, the ICP-05 method gives the highest skin friction capacity in both tension and compression, while the API method gives the lowest (most conservative) skin friction capacity. This is reasonable as it is widely recognized that API method underestimates the skin friction capacity, especially for dense sand, which is the case for this particular site shown in Fig. 1.23.

17.13.2 End-Bearing Capacity Calculation for CPT-Based Method

17.13.2.1 Cone Tip Resistance Calculation

Regarding the end-bearing capacity calculation for CPT method, API 2007 [792] recommends accounting for the influence of the soil layer boundary on the end-bearing capacity if the pile tip is within 2–3 pile diameters of a layer boundary, by using q_c data averaged between $1.5d$ above and $1.5d$ below the pile tip level:

$$q_{c,av} = \int_{L-1.5d}^{L+1.5d} q_c(z) dz / 3d \quad (17.23)$$

where L is the embedded length of the pile measured from the soil surface; d is the pile outer diameter; z is the depth below the soil surface.

Even though the averaging technique expressed in the equation above is applicable in many sites, this may not necessarily be the case when clay layers

Table 17.5 Characteristic skin friction capacity of a steel pipe pile (the penetration depth is 35 m and the pile diameter is 2.4 m) calculated from API, ICP-05, UWA-05, and NGI-05 methods for a site at borehole B5 in CPT shown in Fig. 1.23

	API	ICP-05	UWA-05	NGI-05
Tension [MN]	23	37	32	31
Compression [MN]	23	48	39	36

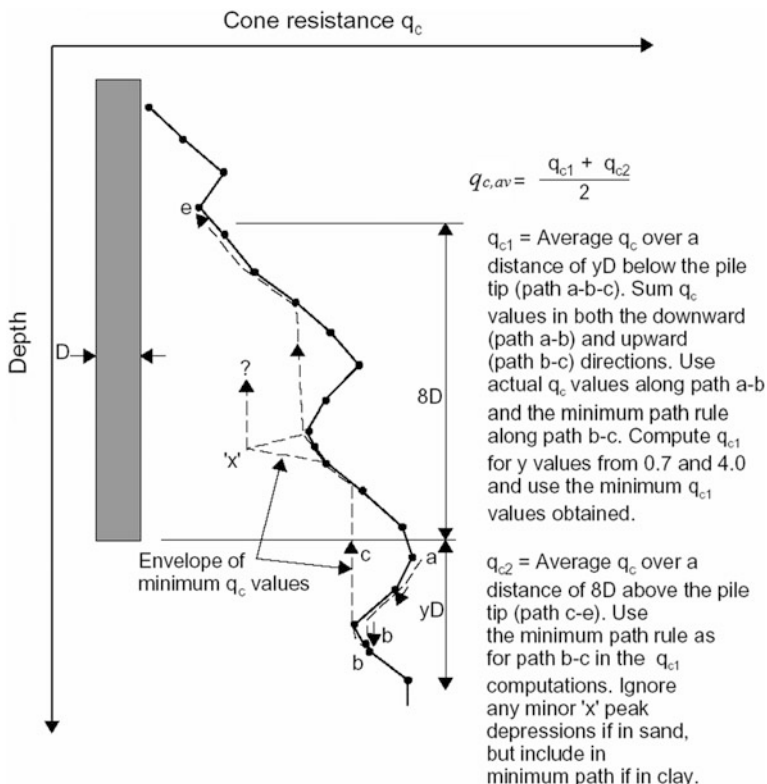


Fig. 17.15 Illustration of the Dutch averaging technique to obtain the $q_{c,av}$ [915] (courtesy of BM Lehane, The University of Western Australia)

occur: The q_c data used may have a substantial impact on q_p (fully plugged unit end-bearing). If significant q_c variations occur, the UWA-05 Dutch averaging technique (Fig. 17.15) [910] should be used to compute $q_{c,av}$ value, as it is slightly more conservative than the straight averaging technique above.

17.13.2.2 End-Bearing Capacity by ICP-05 Method

Based on the calculation of $q_{c,av}$, the ultimate unit end-bearing for plugged piles using the ICP-05 method can be calculated as:

$$q_p' = q_{c,av} [(0.5 - 0.25 \log_{10}(d/d_{CPT}))] \geq 0.15q_{c,av} \quad (17.24)$$

where d_{CPT} is the diameter of the CPT tool, which is typically taken as 36 mm for a standard 10 cm² base area cone.

For open-ended piles, the ultimate unit end-bearing q_p' can be assumed to act across the entire pile tip cross section only if the conditions according to the following two equations are fulfilled:

$$d_i < 0.02(D_r - 0.3) \quad (17.25)$$

$$d_i/d_{\text{CPT}} < 0.083q_c(z)/p_a \quad (17.26)$$

where d_i is the inner pile diameter in meters; D_r is the relative density of sand ranging from 0 to 1 with unit in [-] (not [%]).

If the two equations above cannot be fulfilled, the end-bearing capacity has to be calculated by assuming an unplugged condition, in which the piles are assumed to sustain end-bearing on the annular pile base area:

$$Q_a = \pi \cdot t_{\text{tip}}(d - t_{\text{tip}})q_c(z) \quad (17.27)$$

where t_{tip} is the pile wall thickness at pile tip (including driving shoe).

Furthermore, the calculated end-bearing capacity based on the plugged pile assumption should not be less than that based on an unplugged condition above.

17.13.2.3 End-Bearing Capacity by UWA-05 Method

By neglecting the favorable effect of partial plugging during pile driving, which is accounted for by an empirical term in the “full” design method, Lehane et al. [883, 910] suggest calculating the ultimate unit end-bearing acting across the entire tip cross section for plugged piles as:

$$q_p' = q_{c,\text{av}}(0.5 + 0.45A_r) \quad (17.28)$$

where $A_r = 1 - (d_i/d)^2$ is the pile displacement ratio; d_i and d are the inner and outer pile diameter, respectively.

However, when piles are embedded in sands and the sand profiles show significant variations in the vicinity of the pile tip, the use of $\pm 1.5d$ in the vicinity of the pile tip to calculate $q_{c,\text{av}}$ is not recommended. In this situation, Lehane et al. [910] recommended a method for estimating $q_{c,\text{av}}$ often referred to as the Dutch averaging technique, as illustrated in Fig. 17.15.

For offshore sites, continuous CPT soil profiles are often not available (e.g., when seabed CPT methods are not employed). Lehane et al. [915] proposed a conservative estimate of the Dutch q_c value:

$$q_{c,\text{av}} = (q_{c,a} + q_{c,b})/2 \quad (17.29)$$

where $q_{c,a}$ is the minimum value of q_c over the depth interval extending from the pile tip to a depth between $0.7d^*$ to $4d^*$ below the tip; $d^* = d \times A_r^{0.5}$ is the effective

diameter; $q_{c,b}$ is the average q_c value from the tip to a height of $8d^*$ above the pile tip.

17.13.2.4 End-Bearing Capacity by Fugro-05 Method

For plugged piles, the ultimate unit end-bearing by Fugro-05 method can be calculated as:

$$q_p' = 8.5p_a(q_{c,av}/p_a)^{0.5}A_r^{0.25} \quad (17.30)$$

Since the non-plugged condition for piles under static loading seldom occurs [916], neither the Fugro-05 method nor UWA-05 method presents a calculation for the unplugged pile condition. As a simple check, the assumption that an offshore pile is plugged is valid if either of the two conditions below is fulfilled:

7. The cumulative thickness of sand layers within a soil plug is in excess of $8d$.
8. The total end-bearing (Q_a) is limited as follows:

$$Q_a \leq Q_{f,I,clay} e^{Ls/d} \quad (17.31)$$

where $Q_{f,I,clay}$ is the cumulative frictional capacity of clay layers within the soil plug; Ls is the sand plug length.

It should be noticed that the criteria above apply only for fully drained behavior of sands within the pile plug. For undrained/partially drained sands, one may adopt the criteria presented by Randolph et al. [901].

For the exceptional case of unplugged end-bearing behavior in fully drained conditions, the end-bearing capacity may be assessed according to the methods presented by CUR [916] and Lehane and Randolph [917].

17.13.2.5 End-Bearing Capacity by NGI-05 Method

In the NGI-05 method, the ultimate unit end-bearing for plugged open-ended steel pipe piles is formulated through a specified correlation between nominal relative density and normalized cone tip resistance:

$$q_p' = 0.7q_{c,av}/(1 + 3D_r^2) \quad (17.32)$$

where the sand's relative density $D_r = 0.4 \ln\{q_{c,av}/[22(\sigma'_{v0}p_a)^{0.5}]\} > 0.1$, and in case the calculated D_r is larger than 1.0, it can still be accepted and adopted to calculate the ultimate unit end-bearing.

In addition, NGI-05 also proposes a calculation of resistance for non-plugged piles using an ultimate unit wall end-bearing value $q_w(z)$ given by:

$$q_w(z) = q_c(z) \quad (17.33)$$

An ultimate unit friction $f_p(z)$ between the soil plug and the pile's inner wall can be calculated as:

$$f_p(z) = 3f_c(z) \quad (17.34)$$

where $f_c(z)$ is the ultimate unit skin friction for piles in compression according to the NGI-05 method presented in Sect. 17.13.1.

Finally, the minimum value of q_p' , $q_w(z)$, and $f_p(z)$ expressed in the three equations above should be used in the design.

It is noticed that each method to calculate the end-bearing capacity is significantly different from others, with the ratio of q_p' (unit end-bearing resistance) to an average q_c (CPT tip resistance) value in the vicinity of the pile tip being assumed to vary with the pile diameter in ICP-05, with the effective area ratio in UWA-05, with cone tip resistance in Fugro-05, and with relative density in NGI-05. See Xu et al. [918] for a review and evaluation of formulations for each method.

Table 17.6 shows an example of comparison of end-bearing capacity among different methods. Obviously, the UWA-05 method gives the highest calculated end-bearing capacity, while the conventional API method also gives higher end-bearing capacity than the ICP-05 and NGI-05 methods. The NGI-05 method gives the most conservative end-bearing capacity. However, this trend may change when soil profiles change.

17.13.3 Comments on the CPT-Based Methods

Compared to the methods presented in API 1993 [790] and API 2000 [790, 791], the recently developed CPT-based methods cover a wider range of cohesionless soils and are considered fundamentally better: They have shown statistically closer predictions of pile load test results and, although not required, are in principle the preferred methods. These methods generally tend to provide a higher calculated axial pile capacity than that given by API 1993 [790] and API 2000 [791]. This is beneficial not only due to the increase in the pile capacity for in-place condition, but also due to the fact that it presents a more reliable assessment for pile driving (avoiding problems with refusal and pile buckling during driving) and removing piles from soils (better assessment for allocating suitable removal equipment).

Table 17.6 Characteristic end-bearing capacity ([MN]) of a steel pipe pile (penetration depth of 35 m and a pile diameter of 2.4 m) calculated from API, ICP-05, UWA-05, and NGI-05 methods for the soil profile at borehole B5 for CPT tests shown in Fig. 1.23

API	ICP-05	UWA-05	NGI-05
56	49	61	48

However, in cases where the new methods are adopted as the primary design tools, it is suggested that consideration be given to the more stringent WSD (working stress design) Factors of Safety and LRFD (load resistance factor design) Factors [881].

Lehane et al. [883] concluded that the UWA-05 method and the Imperial College ICP-05 (essentially the “MTD” approach by Jardine and Chow [909]) give the best reliability parameters, performing far more satisfactorily than the API 1993 [790] and better than the Fugro-05 and NGI-05 methods, even though UWA-05 and ICP-05 apply different weightings to factors for open-ended conditions and “friction fatigue,” and are therefore unlikely to give coincident results when applied to identical piles in the same soil profiles. By performing a database assessment of all CPT-based design methods, Schneider et al. [906] concluded that the more detailed method formulation of the UWA-05 method, which is based on recent research into the controlling mechanisms that influence pile capacity in sands, is the primary reason for its slightly better predictive performance against the database than that of ICP-05, NGI-05, and Fugro-05.

In spite of their merits, offshore experience with these CPT-based methods is either limited or nonexistent, and hence more experience is needed before they are recommended for routine design.

With regard to the adoption of material factor associated with the utilization of CPT-based methods, there are no particular explicit specifications. ISO [91] states that the designer should evaluate whether or not the commonly used material factor is sufficient, which is not practical because a re-calibration of the material factor would require probabilistic analyses of a large variety of structures and soil conditions, and in a typical pile design project carried out by a geotechnical engineer, it is not feasible to carry out such a large amount of work. Moreover, a material factor commonly used is not based on detailed calibrations using probabilistic analyses, but rather conformance to the existing LRFD design format. Therefore, it is not likely to cover uncertainties associated with the API method or the recently developed CPT-based methods. This may result in either a conservative or non-conservative design as the probability of failure may be increased or decreased by utilizing the CPT-based method. However, based on a large number of pile tests by various researchers [883, 906], it is concluded that the coefficient of variation of pile axial capacity is lower for the CPT-based methods than the API method, indicating that the uncertainties involved by using the CPT-based method are less than that of the API method. Note that in the large amount of tests in the references cited above, all have a significant contribution from skin friction. For artificially plugged piles having a significant amount of contribution from end-bearing capacity, the statistical data is not covered in the references above.

For a conservative pile–soil interaction capacity assessment, it is advisable to evaluate the capacity obtained from all CPT-based methods, with the one resulting in the lowest capacity being selected for a final pile design. On the other hand, if using one single particular method for calculating the axial pile capacity, the model uncertainty associated with each method is in the majority of cases the major contributor to the uncertainties related to the limit state of axial pile capacity failure

(compared to the uncertainties associated with geotechnical parameters, load prediction model, soil consolidations, cyclic degradation, etc.). It would then be advisable to determine the pile capacity as the average of the capacities predicted by all available CPT-based methods, which may produce negatively correlated capacity predictions to a certain extent. The model uncertainty based on the selected tests from the database decreases significantly, with a substantially lower resulting probability of failure.

17.14 Ultimate End-Bearing Capacity from Tests

Note that the limiting end-bearing capacity in either the conventional API method (Sects. 17.8 and 17.9) or CPT-based method capacity (Sect. 17.13.2) is determined by the stiffness properties of soils rather than the strength, in that the capacities derived from pile tests used to calibrate the limiting end-bearing values ended at a displacement equal to 10% of pile diameters as shown in Fig. 17.13. This means that the soil is still not plastified at the load level corresponding to the limiting end-bearing values, i.e., pile tests would in most cases give a higher capacity if larger deformations were allowed.

By carrying out tests with piles with an outer diameter of 0.762 m in dense sand (the typical soil condition in the North Sea) in the EURIPIDES project [919], it was found that the end-bearing resistance at 76 mm displacement (10% of the pile diameter) does not represent a realistic ultimate end-bearing capacity of the pile as shown in Fig. 17.16. Therefore, it is an advantage for assessing a more realistic end-bearing capacity if a deformation larger than 10% of the pile diameter is permitted.

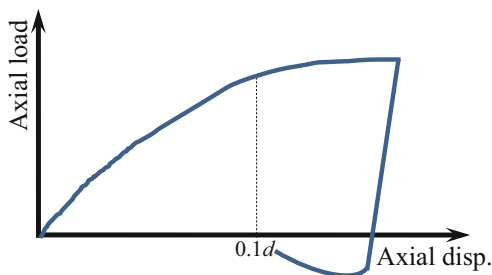
Moreover, it is also difficult or even impossible to re-establish the axial capacities determined from an empirical method in a finite element code using realistic soil properties. Therefore, the soil parameters such as friction angles have to be modified to match the empirical methods. Thereafter, the failure mechanism can be investigated through an observation of development of fully plastic zone in the calculated results from finite element analysis.

Ultimate end-bearing resistance under either static monotonic or cyclic loading is usually not reached because in most cases the pile movements required to mobilize the base capacity are well above the actual axial tip movement.

17.15 Effects of Cyclic Loading on Axial Capacity of Piles

Axial capacity of piles should be checked with regard to both static and cyclic axial response. Cyclic loadings, mainly caused by loadings associated with earthquakes, storm waves, and other sources of dynamic loadings, can have both positive and negative effects on the pile capacity and stiffness.

Fig. 17.16 Schematic illustration of a pile tip load–displacement relationship for a pile with an outer diameter (d) of 0.762 m embedded in dense sand with a penetration depth of 30.5 m



Compared with long-term static loading, the load-carrying resistance and/or stiffness of the pile can normally decrease under even rather slowly applied cyclic loadings. On the other hand, a rapid loading such as seismic loading can increase load-carrying resistance and stiffness of the pile. This is because the strain rate effects (Sect. 2.5) may compensate the strength and the stiffness degradation. Moreover, repetitive loadings can cause a temporary or permanent decrease in load-carrying resistance, and/or an accumulation of deformation. The resultant influence of cyclic loadings is then a function of the combined effects of magnitudes, cycles, and rates of applied pile loading, structural characteristics of the pile, soil characteristics, and factors of safety used in design of piles [790].

Figure 17.17 shows axial displacements of both tension and compression piles supporting an offshore jacket structure subjected to six continuous loading cycles of waves, with the maximum wave loading significant with a return period of 10,000 years. Even if unloading occurs after each wave loading peak, a gradual increase of the axial displacement for piles can be observed, indicating the effects of the plasticity occurrence and cyclic effects in soil–pile interaction. This is the main reason for the cause of excessive deformation at the structure’s topside as shown in Fig. 17.18.

Most of the previous research is focused on studying the effects of high level cyclic axial loading. However, its effects on lower levels of cyclic axial loading receive less attention even if it is relevant for many types of practical problems such as fatigue damage accumulation of substructures under cyclic wind and/or ocean wave loading.

Under cyclic loading, a compaction of soils beneath piles occurs due to cyclic shearing, leading to a reduction of the normal contact stresses acting between pile and soil and a decrease in shear strength. The shear strength degradation along the pile under different loading intensities will influence the axial pile resistance and displacement. Effects of cyclic loading on the axial pile resistance are more significant for clays than sands [792]. Repetitive loadings can cause a temporary or a permanent decrease in load-carrying resistance and/or an accumulation of deformation.

However, this type of soil compaction due to cyclic loading occurs mainly within a small shear band beneath the pile [920], and it occurs up to a distance at which a threshold value of cyclic shear stress in the soil is reached [921], i.e., no

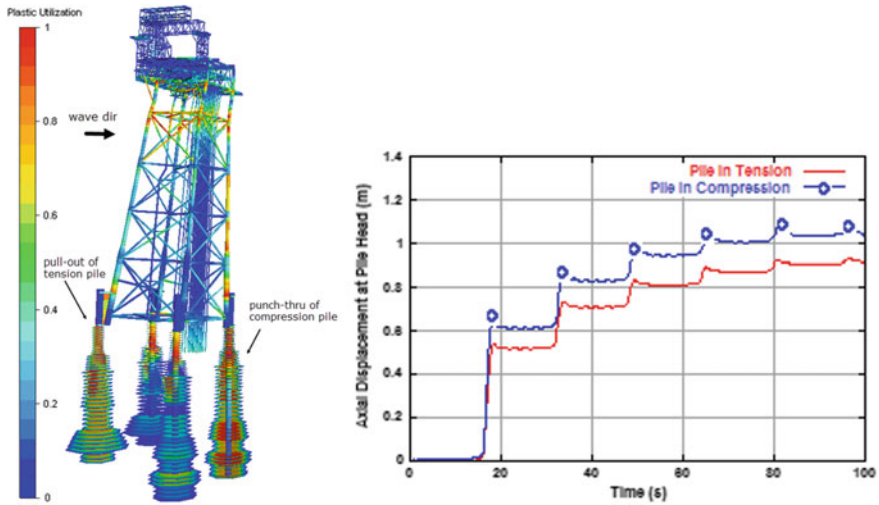


Fig. 17.17 Axial displacement (right) at pile head for both tension and compression piles supporting an offshore jacket structure (left) subjected to six continuous wave loading cycles (courtesy of Aker Solutions)

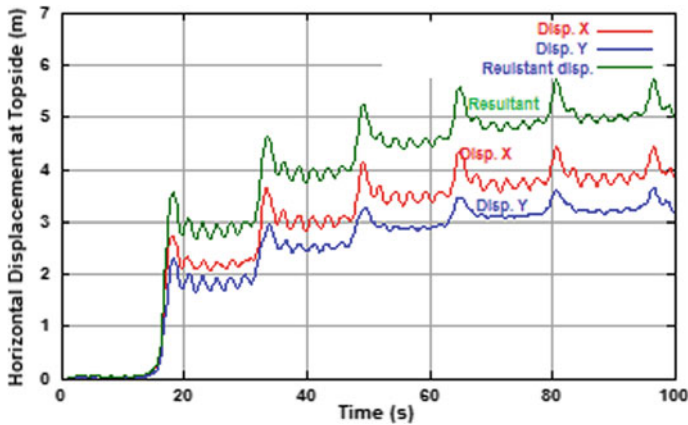


Fig. 17.18 Horizontal displacements at the topside of the jacket platform shown in Fig. 17.17 (courtesy of Aker Solutions)

axial pile capacity reduction needs to be considered if the ratio of cyclic axial load amplitude and static axial pile capacity is below this threshold value.

Based on the literature study, Schwarz [922] reported that no axial pile capacity reduction needs to be considered if the ratio between cyclic axial load amplitude ΔF_{cyc} and the static axial pile capacity R_s is below a threshold value, which is referred to as the critical level of repeated loading (CLRL):

$$\text{CLRL} = \Delta F_{\text{cyc}}/R_s \quad (17.35)$$

Values of CLRL under different types of soils are shown in Table 17.7. By observing this table, it is obvious that piles in non-cohesive soils are more sensitive to cyclic axial loading than piles in cohesive soils.

Cyclic pile capacity is defined as the sum of the average axial loading and cyclic load amplitude at the pile head that causes full mobilization of the soil resistance and consequently large displacement. Different load sequences and load levels should be analyzed in order to obtain a reliable assessment of the effects due to cyclic axial pile loading. It is especially advisable to analyze three different load scenarios as follows:

1. The static load is kept constant and the cyclic load amplitude is increased until failure is reached.
2. The cyclic load amplitude is kept constant and the static load is increased until failure is reached.
3. Both the static load and the cyclic load amplitude are increased by the same load factor until failure is reached.

In addition, engineers may specify other load scenarios (combinations of load factors on cyclic and average load components) to reach cyclic failure.

From the discussion above, it is obvious that the cyclic pile capacity does not have a unique definition and depends on the load path (e.g., combination of mean load and cyclic load amplitude) to failure. Most practices evaluate the cyclic capacity relative to the static capacity, and the static capacity itself could show significant variation depending on the method used.

Poulos [923] presented that long piles may exhibit a ductile type of cyclic response, while short piles may exhibit brittle cyclic response. Randolph [869] developed a way of estimating the boundary between the stable and metastable regions in the stability diagram, based on measures of the pile and soil compressibility and pile geometry.

For closely spaced piles in a pile group, the effects of cyclic axial loading can be more significant, leading to a more remarkable degradation of axial capacity under comparable cyclic loading levels [881]. Section 21.4 presents a brief discussion of this topic.

Table 17.7 Critical level of repeated loading (CLRL) for different types of soils [922]

Soil type	Critical level of repeated loading
Clay, normally consolidated	0.35–0.55
Clay, over-consolidated	0.85–1.0
Sand	0.1–0.4
Silt	0.4–0.6

Chapter 18

Torsional Moment–Rotation Relationship

18.1 General

Torsional moments can be introduced on piles due to lateral loadings on the supporting structures. Such lateral loadings can be induced by ship impacts, high-speed vehicle collision, and wind, wave, and current actions on superstructures. For example, for an anchor connected to mooring chain(s) or wire(s), due to subsea current forces applied on the mooring, the mooring chain may be dragged out of position and it may further apply significant torsional moments on the pile as shown in Fig. 18.1. Moreover, if a ship impacts on a bridge pier with an eccentricity from the centroid, an eccentric lateral load will be generated on supporting piles. In addition, when a single pile supports a structure that has a significant torsional flexibility, i.e., the center of torsion significantly deviates from the center of the gravity in the horizontal plane, under external excitations (e.g., seismic excitations) along horizontal directions, and significant inertia loading transferred from the superstructure may induce noticeable torsional movement of the single pile.

Even though the torsional moment may be marginal, inadequate design of the piles against torsional load may seriously affect the serviceability and safety of supported structures with catastrophic consequences [924, 925].

In API-RP-2A [792], it is required that rotations of individual piles and the total foundation system should be checked at all critical locations, which may include pile tops, points of contraflexure (zero bending location), mudline. The rotations should not exceed serviceability limits that would interfere with the structure carrying out its intended function.

Various pieces of research [926–930] are dedicated to the study of the torsional moment–rotation relationship due to pile–soil interaction. From those studies, it is concluded that the shear modulus of piles under torsional moments agree with that from axial load tests [927], and the torsional moment–rotation curves are similar to the T-z curve but interact with the axial loading of piles.

18.2 Behavior of Single Piles Under Torsion

In various numerical computation codes, the torsional behavior of a pile can be simply modeled with a “ τ - θ ” curve as shown in Fig. 18.2, with τ and θ representing the torsional shear stress due to the lateral pile–soil friction force at pile–soil interface (Fig. 15.1) and local twist angle (rotation) of the pile, respectively. It is also noticed that the curve indicates a “perfect plasticity,” i.e., the resistance to rotation remains constant at ultimate surface shear resisting rotation of the pile τ_u for additional rotation.

By assuming that soil is a radially linear-elastic and homogenous medium, and the pile is prismatic and linear-elastic and that the resistance of the soil at any point is a function of only the torsional displacement of the pile–soil interface at that point, the soil in any plane perpendicular to the axis of the pile is in a state of plane, pure shear. By using the theory of elasticity, the shear stress τ and the tangential displacement v at a radial distance r from the axis of the pile can be calculated as:

$$\tau = \tau_0 \left(\frac{R}{r} \right)^2 \tag{18.1}$$

$$v = \frac{\tau_0 R^2}{2G_s r^3} \tag{18.2}$$

where τ_0 is the shear stress at the pile–soil interface; R is the radius of the pile; $G_s = \tau_0/2\theta$ is shear modulus of the soil as shown in Fig. 18.2; θ is the pile’s torsional rotation in radians.

If there is no slippage between the pile and soil at the interface, the tangential displacement v on the pile–soil interface is:

Fig. 18.1 Current-induced torsion applied on an anchor pile

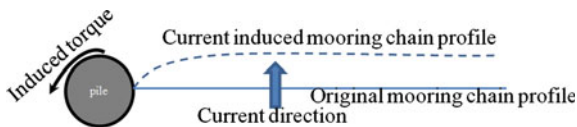
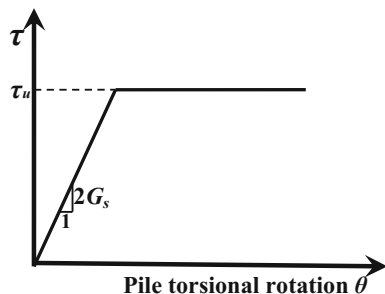


Fig. 18.2 Idealized pile’s torsional shear–rotation curve diagram



$$v = R\theta \quad (18.3)$$

The governing equation of the pile's torsion is:

$$dT/dz = \pi d^2 G_s / (G_p I_p) \int_{z=\infty}^{z=z^*} T dz \quad (18.4)$$

where T is the torsional moment at depth z below a point (often at the pile head) where the torsional moment is T_0 ; d is the pile's outer diameter; G_p and I_p are the shear modulus and the polar moment inertia of the pile.

The solution of the equation above is:

$$T = T_0 e^{-\alpha z} \quad (18.5)$$

where $\alpha = [\pi d^2 G_s / (G_p I_p)]^{0.5}$.

The torsional rotation of the pile at depth z can then be calculated as:

$$\theta = [T_0 / (\alpha G_p I_p)] \cdot e^{-\alpha z} \quad (18.6)$$

And the shear stress due to the torsion is:

$$\tau_0 = 2\theta G_s \quad (18.7)$$

For sands, the initial value of the soil modulus G_{s0} can be taken as:

$$G_{s0} = 0.5 E_{s0} / (1 + \nu) \quad (18.8)$$

where $E_{s0} = m \sigma_{\text{ref}} \cdot (\sigma'_{vo} / \sigma_{\text{ref}})^{0.5}$ is soils' initial modulus of elasticity; $\sigma_{\text{ref}} = p_a = 100 \text{ kN/m}^2$ is the reference (atmospheric) stress; σ'_{vo} is the vertical effective stress; ν is soils' Poisson's ratio; $m = 1000 \cdot \tan(\phi')$; ϕ' is the angle of internal friction of the sand.

For clays, based on the recommendation by NGI [67], the initial value of the soil modulus G_{s0} can be taken as:

$$G_{s0} = [300 - 85(\text{OCR} - 1.0)^{0.5}] \cdot s_u \quad (18.9)$$

where OCR is the over-consolidation ratio of the soil; s_u is the undrained shear strength of the soil; and G_{s0}/s_u ranges between 50 and 300.

Note that the calculation of G_{s0} for both sand and clay above is the initial value of the soil's shear modulus and is only valid when the shear strain of the relevant soil is low. Subjected to significant torsional loading, the realistic shear modulus is strain-dependent and can be much lower.

Example A 55-m-long pile is subjected to a torsional moment of 3.5 MNm at its head; the pile has an outer diameter of 2.134 m and a wall thickness $t = 0.05$ m; the pile's shear modulus is $G_p = 76$ GPa, and the soil's shear modulus G_s is approximately 7.8 MPa.

Calculate the pile's torsional moment T , rotation angle θ , and shear stress τ_0 along the pile depth z .

Solution: On the values given above, one obtains:

$$I_p = \pi(d - 0.5t)^3 \cdot t / 4 = 0.0726 \text{ m}^4$$

$$G_p I_p = 2.8 \cdot 10^{10} \text{ Nm}^2$$

$$\alpha = [\pi d^2 G_s / (G_p I_p)]^{0.5} = 0.06314.$$

Using formulas $T = T_0 e^{-\alpha z}$, $\theta = [T_0 / (\alpha G_p I_p)] \cdot e^{-\alpha z}$, and $\tau_0 = 2\theta G_s$, the results are listed in Table 18.1.

The linear relationship between surface shear and pile is assumed to terminate when the surface shear stress τ_0 reaches the ultimate surface shear τ_u that resists pile rotation.

For sand, τ_u can be determined as:

$$\tau_u = K \sigma'_{vo} \tan(\delta) \quad (18.10)$$

where $K = \sigma'_{ho} / \sigma'_{vo}$ is lateral (at rest) earth pressure coefficient, which has a significant uncertainty. Kraft [880] has presented an alternative approach for estimating K , based purely on relative density of soils (but independent of grain size)

Table 18.1 The pile's torsional moment T , rotation angle θ , and shear stress τ_0 varied with depth z

z	T (Nm)	θ (rad)	τ_0 (N/m ²)
0	3.500E+06	1.980E-03	3.089E+04
3	2.896E+06	1.638E-03	2.556E+04
6	2.396E+06	1.356E-03	2.115E+04
9	1.983E+06	1.122E-03	1.750E+04
12	1.641E+06	9.282E-04	1.448E+04
15	1.358E+06	7.681E-04	1.198E+04
20	9.901E+05	5.601E-04	8.739E+03
25	7.221E+05	4.085E-04	6.373E+03
30	5.266E+05	2.979E-04	4.648E+03
40	2.801E+05	1.585E-04	2.472E+03
50	1.490E+05	8.428E-05	1.315E+03
55	1.086E+05	6.146E-05	9.589E+02

and effective area ratio of the pile (full or partial displacement), for a preliminary design, its value may be taken as follows: for coarse-grained soils, $K = 1 - [\sin\phi' \cdot (\text{OCR})^{\sin\phi'}]$, where ϕ' is the angle of internal friction; for fine-grained soils, $K = [0.44 + (0.42I_p (\%)/100)] \cdot \text{OCR}^{0.5}$; σ'_{vo} is the vertical effective stress; and δ is the angle of pile–soil interface friction, which can be measured with reasonable accuracy [878, 879], and one may use the same values as that of the axial friction of piles; see Table 17.2.

For consolidated clay, τ_u can be calculated as:

$$\tau_u = \alpha s_u \quad (18.11)$$

where α is an adhesion factor similar to that used for determining the axial pile wall friction capacity, and s_u is the undrained shear strength.

Because the shear modulus surrounding each pile subjected to torsion agrees with that from axial load tests, if one ignores the interaction with T-z, the moment per unit pile area–rotation curve can simply be calculated by scaling the T-z curve so that the torsional moment is $td/2$ per unit area, and the rotation is $2z/d$ in radians, in which t is the skin friction per unit length of piles; d is the pile's outer diameter. Therefore, the torsional resistance may be described by a hyperbolic T_t – α (torque–torsional angle) relationship:

$$T_t = \alpha / (j + k\alpha) \quad (18.12)$$

where T_t is the mobilized torque; α is the torsional angle of the entire pile/shaft. j and k can be expressed as:

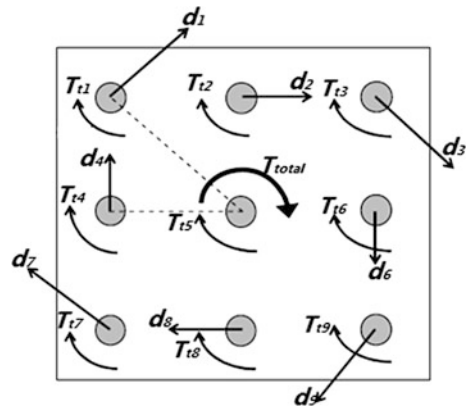
$$j = 1/4\pi R^2 G_s L \quad (18.13)$$

$$k = 1/T_u = 1/2\pi R^2 \tau_u L \quad (18.14)$$

where L is the length of the pile/shaft; T_u is the ultimate torque corresponding to the ultimate surface shear resisting rotation strength τ_u .

As the axial and torsional forces are coupled, the computation of the torsional and axial stiffness becomes more complex. In some pile analysis codes, this has been simplified by first calculating the axial and torsional stiffness separately, from which both the axial shear and torsional shear stress are calculated, and their resultant shear stress can be used to check if the resultant shear stress exceeds the maximum allowable shear stress at the pile–soil interface. However, the procedure above may lead to an over-estimation of the resulting shear stress of up to 41% if a pile is first loaded to failure in torsion and then the axial load is increased until failure occurs [931].

Fig. 18.3 Illustration of lateral translations (d_i) and rotations (T_{Ti}) of individual piles ($i = 1 \dots 9$) in a pile group subjected to applied torque T_{total}



18.3 Behavior of Pile Groups Under Torsion

When a pile group is subjected to torsion as shown in Fig. 18.3, the interaction between the torsion and lateral loading may govern the pile group responses. By performing a series of centrifuge model tests on torsionally loaded single piles and pile groups in sands, Kong [932] and Zhang and Kong [933–935] found that a pile group subjected to torsion simultaneously mobilizes lateral and torsional resistance on the individual piles, and the torsional contribution to the total applied torque is in a range of 20–50%. The tests also showed no evidence of significant interaction with respect to the effect of torsional movement on the torsional behavior of adjacent piles located at a distance of three pile diameters, thereby confirming the previous statement by Poulos [927].

Chapter 19

Modeling, Response Calculation, and Design of Piles Under Seismic Loading

19.1 Loading of Piles During Earthquakes

Soils, foundations, and structures are essentially a coupled system, and among them, foundations work as intermediate media transmitting loading between structures and soils. From the point of view of seismic wave transmission, the seismic wave generated due to the fault rupture is first transferred to far-field soils then to near-field soils surrounding the foundation. Moreover, when the body wave reaches the ground surface at far-field, surface wave will be generated and propagate to the near-field soil surface with a much lower rate of decrease due to the distance than that of the body wave. Both body wave and surface wave will be further applied on the foundation in the form of kinematic loading, causing the structure to vibrate. This induces excitations on the structure, which will then vibrate, generating inertia loading that is transmitted back to the foundation, causing deformations or vibrations of the foundation and generating dynamic loading applied on surrounding soil in the form of seismic wave (mainly shear wave). A large amount of energy contained in the shear wave will then be radiated through soil's radiation damping due to both the inertial interaction effects (referring to the response of the pile–structure system to excitations by d'Alembert forces or inertial force) and the kinematic interaction of the pile with the surrounding soil driven by the free-field response. In addition, the energy is also dissipated through the soil's hysteretic damping in both far-field and near-field. At the interface between the soil and the rock, the energy left will partially be reflected at the soil-rock boundary and partially be further transmitted downward to the rock. If the rock is of large thickness, the energy of the shear wave will be removed from the soil layers through radiation damping when the shear wave is transmitted through the rock. The wave propagation from source (fault rupture) to the foundation and the entire process of interaction of soil–foundation–structure system discussed above are illustrated in Fig. 19.1. More detailed discussions on the

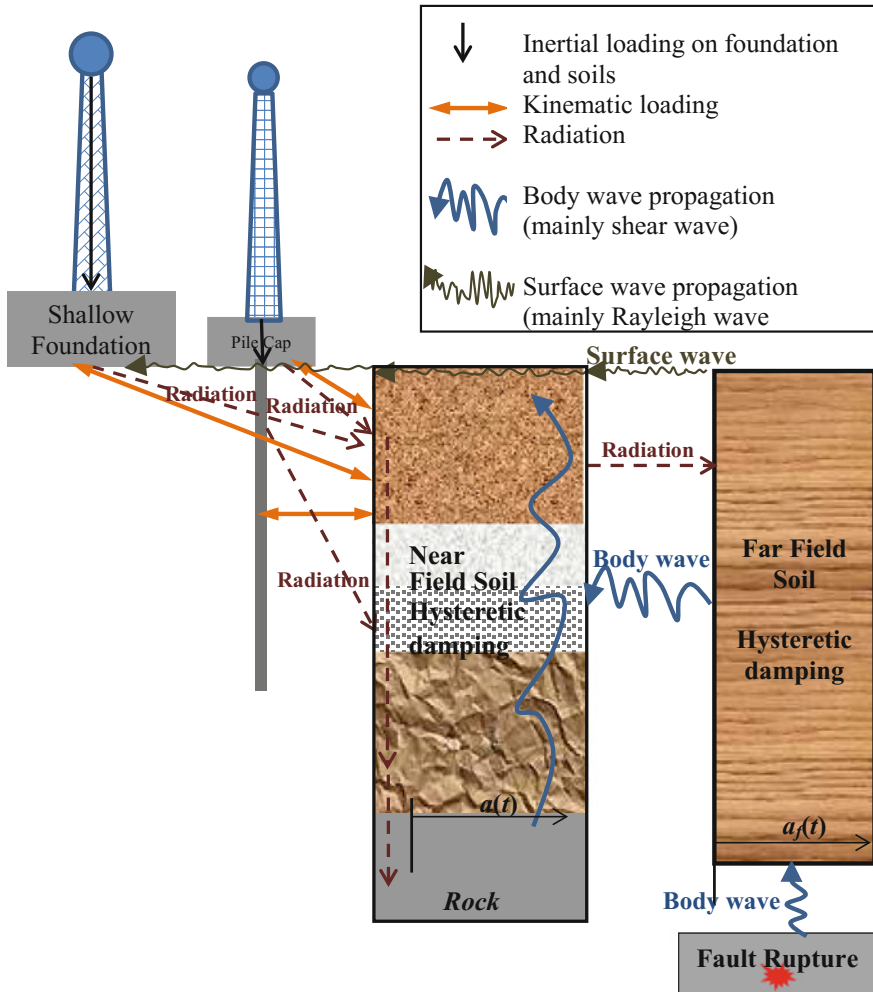


Fig. 19.1 Propagation of seismic waves from source (fault rupture) and interactions in the rock-soil-foundation-structure system

process of seismic wave propagation and the generated structural and foundation loading can be found in Jia [188].

Therefore, as illustrated in Fig. 19.2, under seismic excitations, piles are subjected to both (a) inertial forces transferred from superstructures and (b) kinematic forces arising from deformations of surrounding soils due to the passage of seismic waves, and loads can also be induced due to liquefaction (c) at the relevant soil layers. Therefore, pile failures due to seismic loading can be caused by excessive bending and shear forces generated from inertia loading, kinematic loading, a combination of the two, or large movements imposed to piles by soils which have

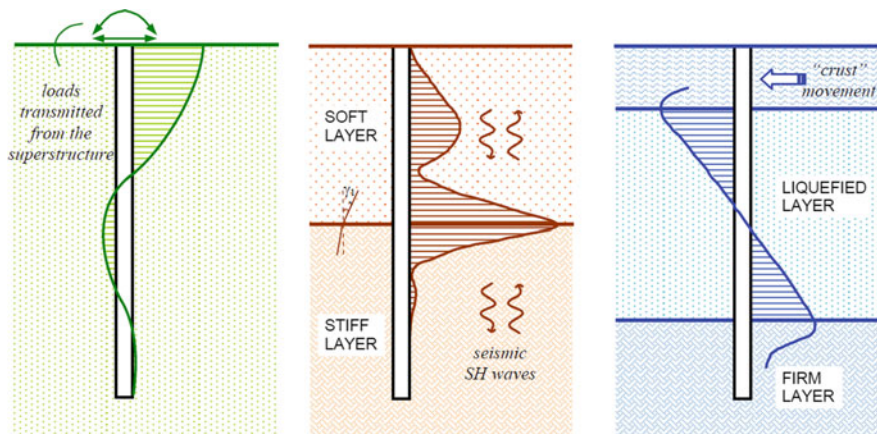


Fig. 19.2 Three fundamental types of causes to induce pile bending moments during earthquakes: **a** inertia loading; **b** kinematic loading; **c** liquefaction and subsequent lateral soil movement [953, 963] (courtesy of George Mylonakis, University of Bristol)

lost their shear stiffness (usually as a consequence of liquefaction or slope movement). Among the causes above, inertia and kinematic loadings are of inherently vibratory nature, while liquefaction is essentially unilateral and pseudo-static. Observed pile failures during past earthquakes also identify the causes above.

The inertial force increases the nonlinear behavior of the soil and reduces pile head stiffnesses. These effects increase the natural period of the structure–foundation system and change the seismic spectral response and hence the base shears and moments in the structure. The kinematic forces arose from the pressures generated against the pile to ensure that the seismic displacements of soil and the pile are compatible at points of contact along the pile. Therefore, they can exert significant forces on the pile if seismic soil response is significant.

As both inertia and kinematic forces can cause additional bending moments and shear forces on piles, past earthquakes have resulted in many cases of pile failures due to unacceptable bending moments or even shear force in the piles induced by combined kinematic and inertial action, resulting in unacceptable permanent deformations. Even though inertia and kinematic forces are coupled and should ideally be analyzed in a coupled system, their effects can normally be regarded/analyzed as uncoupled.

If a pile fails due to inertia loading, the location of failure is likely to be close to the pile head, as the inertia loadings due to seismic waves are normally limited to the top $10d$ (d is the diameter of the pile). On the other hand, kinematic loading can occur at any depth. If a pile fails at a greater depth, it is especially likely that the loading causing the damage on the pile is dominated by kinematic loading. Therefore, significant pile moment zones between the kinematic loading and inertia loading zone are naturally uncoupled. Moreover, if liquefaction occurs, since the time of peak moment due to liquefaction tends to occur toward the end of an

earthquake while the inertial loading occurs during the earthquake, the kinematic and inertia loadings are also almost uncoupled in time.

Therefore, the current engineering practice is usually to assess the pile stresses and pile–soil interactions induced only by the inertia effects due to oscillations of structures while neglecting the effects of kinematic interactions [936–938]. By following this design philosophy, the evaluation of the bending moments developed due to kinematic interaction is only required under extreme combinations of ground profile involving layered soils and at moderate or high-seismicity zones [198], though even in homogeneous soils kinematic moments may still be important [939]. Another method with more complete involvement of kinematic and inertia interactions is to follow a two-way approach that is based on the superposition of kinematic and inertial effects in order to obtain the governing maximum bending moments in piles. However, for many structures, the seismic response of piles is strongly coupled with superstructures, and therefore, a coupled analysis with both pile foundation and superstructure is desirable.

Various methods are available to obtain the pile loading and to calculate responses through either numerical or analytical approaches using finite element, finite difference, or boundary element techniques, etc. Winkler spring models introduced in previous chapters have been extensively used to calculate the pile response subject to seismic loading, even though the ability to accurately predict the pile behavior for sites with potentially liquefied soil is significantly reduced. The pseudo-static approach [940], as will be introduced in Sect. 19.2, is relatively simple to implement when compared to more complex dynamic analyses and hence is preferred by design engineers. This approach includes a two-step operation, of which a free-field site-response analysis is first performed to calculate the maximum ground displacement (or strain) and minimum effective vertical stress at various depths of soil deposits, and the maximum ground surface accelerations. This is followed by a static analysis by applying the maximum computed free-field ground displacement profile along the pile and the static loading at the pile head. The inertial loading at the pile head is normally accounted for by multiplying the maximum ground surface acceleration and the mass acting on the pile head/cap with a factor of safety.

19.2 Pseudo-static Approach

19.2.1 *Inertia Loading on Piles*

When seismic waves reach pile foundations, the pile(s) is excited and its motion is transferred to the main structure supported by the pile(s). Due to the acceleration of the main structure, its inertia load will act on the pile head and induce section shear forces and bending moments of the pile. The horizontal shear force of the pile head/cap can simply be estimated as:

$$V = \lambda \cdot M \cdot a \quad (19.1)$$

where λ is a load factor; M is the portion of the main structure's mass acting on the pile head/cap; a is the horizontal acceleration of the pile at its head, which can be approximated as horizontal PGA at ground surface.

With an increase in depth below the ground surface, the distribution of vertical inertia load for a fully embedded pile at depth z can be approximated as:

$$V(z) = \phi \cdot \beta(z) \cdot M \cdot a(z) \quad (19.2)$$

where ϕ is a load factor; $\beta(z)$ is defined as the fraction of vertical load (due to main structure's mass) that acts at different depths z along the pile length, which can be checked from references [941–943]; $a(z) = a[1 - (\chi z^2/l^2)]$ [944]; l is the embedded pile length; χ is a parameter varying between 0 and 1 and can normally be taken as 1.

19.2.2 Kinematic Loading and Pile Response

Kinematic interaction between soil and foundations arises from the incompatibility of the seismic free-field motion and the displacements of a more rigid embedded foundation. Obviously, subject to kinematic loading, pile responses tend to be amplified at interfaces of soil layers with high stiffness/moduli contrast. This is because, for layered soil with significant variation in soil stiffness along its depth, both soil–pile interactions and seismic excitations vary more significantly along the pile than is the case for soils with less variation of soil stiffness along the pile.

For very soft/slender piles, the deformation of a pile matches free-field kinematic deformation at soils surrounding the pile, and the pile's motion at ground surface is identical to the free-field motion without any rotation. However, if a pile is rigid, the deformation of the pile is different from that of the free-field kinematic deformation, and the pile can move rigidly and rotate. If the pile's motion at ground surface is not equal to the free-field motion, rotation and displacement of piles may occur. By performing model tests of micropiles (embedded in level, dry sand deposit, prepared in a laminar tank bolted to a shaking table) subject to low and high levels of seismic shaking, Yang et al. [945] found that at low level of tank-base shaking below 0.17 g at frequencies between 0.5 and 2.0 Hz, neglecting the soil–pile interaction and the pile inertia effects can give a reasonable approximation for estimating peak bending moment distributions of the micropiles because the piles exactly follow the soil motion. However, with a high level of base shaking, between 0.25 and 0.42 g at frequencies between 8.0 and 10.0 Hz, the interaction between the piles and surrounding soils is significant, and the application of a free-field response spectrum can lead to an underestimation of the pile bending moments.

For simplicity, it has been widely accepted to assume that the presence of piles embedded in soils has no effects on wave propagations and seismic excitations. However, in reality, the presence of piles and the ratio of the Young's modulus

between the pile and soil (E_p/E_s) do have influences on modifying seismic motions at periods shorter than the site period [946, 947]. At low period, even flexible piles (E_p/E_s is as low as 290) may not be able to follow the free-field movement and may thereby experience considerably reduced deformations. This filtering effect is substantial for stiffer piles ($E_p/E_s > 20,000$), to the point that after the second natural period of a soil column, the pile remains almost essentially still, while the free-field soil mass moves considerably. This is in agreement with observations of actual events [948, 949].

Eurocode 8 [426] suggests that kinematic effects should be taken into account when all the following conditions are met:

1. Seismicity of the area is moderate or high (specifying that moderate or high-seismicity areas are characterized by a peak ground acceleration $a_g S > 0.1$ g, where a_g is the design ground acceleration on type A subsoil and S is the soil factor).
2. Subsoil type is D or worse, characterized by sharply different shear moduli between consecutive layers.
3. The importance of the superstructure is of class III or IV (e.g., schools, hospitals, fire stations, power plants).

Compared to inertia loading, kinematic loading is more difficult to determine, as is pile response under kinematic loading.

19.2.2.1 Kinematic Loading and Pile Response for Homogeneous Soil Layers

For homogeneous soil layers, by assuming that a long pile follows free-field soil motions and the deflected shape of the pile can be approximated with a circular arc, Margason [955] and Margason and Holloway [956] developed a calculation of the maximum curvature $((1/R)_{\max})$ for end-bearing piles, caused by the kinematic seismic loading:

$$(1/R)_{\max} = n \cdot u_s / L^2 \quad (19.3)$$

$$(1/R)_{\max} \leq 0.02 \text{ m}^{-1} \quad (19.4)$$

where n is a parameter determined by the boundary conditions of piles, $n = 6$ for a pile with both ends fixed against rotation, and $n = 2$ for a pile with one end fixed; u_s is the maximum soil surface displacement; L is the embedded pile length.

By assuming that piles follow exactly the lateral free-field soil motions, NEHRP [957] recommends that:

$$(1/R) = a/v_s^2 \quad (19.5)$$

where a is the free-field soil acceleration; v_s is the shear wave velocity.

It is noticed that both methods above have significant drawbacks: (1) soil–pile interaction is not accounted for; (2) neither method is inapplicable to calculate pile responses at soil layer interface since soil curvature at those locations is infinite; (3) influences of shearing on pile responses are not considered.

By representing soil stiffness and damping (due to radiation damping and hysteretic energy dissipation) with continuously distributed Winkler springs and dashpots [951], seismic soil motions act as support excitations of the pile–soil system. The curvature of long fixed-head piles embedded in homogeneous soils can be calculated as:

$$(1/R) = \beta a/v_s^2 \quad (19.6)$$

where the dimensionless factor β is used to account for pile–soil interaction, which is not considered in the methods proposed by Margason [955] and NEHRP [957]. Under harmonic oscillations with a vibration frequency ω , β can be determined analytically [958]:

$$\beta = \left[1 + 4E_p I_p (\omega/v_s)^4 / k \right]^{-1} \quad (19.7)$$

where E_p and I_p are the pile's Young's modulus and second moment of inertia of the pile's cross section, respectively; k is the modulus of subgrade reaction.

It is noticed that β decreases monotonically with increasing frequency and never exceeds 1. As a preliminary approximation, β may be taken as a value ranging from 0.7 to 1 [958, 959].

For end-bearing piles, by assuming that: (1) the pile head follows free-field soil motions; (2) an identical pile whose head is unrestrained against displacement and rotation would experience a head rotation equal to average soil shear strain (u_s/L); (3) the pile can be modeled as beam on Winkler spring foundations, and to ensure that rotation atop a fixed-head is zero, Mineiro [960] presented that the curvature applied at the pile top is:

$$(1/R) = \lambda \cdot u_s/L \quad (19.8)$$

where $\lambda = [k/(4E_p I_p)]^{1/4}$ [1046]; u_s is the free-field soil displacement at the soil surface.

The equation above indirectly accounts for the soil–pile interaction. However, as the curvature decreases monotonically with increasing pile length, this equation will underestimate curvatures for piles with long embedded length. Moreover, the equation assumes that the maximum bending moment always occurs at the pile head, which may not be the case in reality.

After determining the maximum pile curvature ($1/R$) using one of the methods presented above, the bending moment at the corresponding position can be calculated as:

$$M = E_p I_p (1/R) \quad (19.9)$$

19.2.2.2 Kinematic Loading and Pile Response for Layered Soils

As aforementioned, pile responses are more pronounced at interfaces of soil layers with high stiffness/moduli contrast, which may be relevant to pile damages even at locations well below the ground surface. For layered soils, by assuming that two adjacent soil layers are thick enough that boundary effects outside the two layers (e.g., pile head and pile tip/bottom) do not influence the response at the layer's interface, and soils are subject to a uniform stress field within each layer, Dobry and O'Rourke [952] presented an explicit solution for the pile bending at the layer interface, expressed in terms of pile curvature:

$$(1/R) = \lambda_1 \gamma_{1-2} (c - 1)(c^2 - c + 1)/c^3 \quad (19.10)$$

$$c \geq \sqrt{2} \quad (19.11)$$

where $\lambda_1 = [k_1/(4E_p I_p)]^{1/4}$ [1046] for soil layer 1; k_1 is the modulus of subgrade reaction for layer 1. γ_{1-2} is the soil shear strain at the interface between two adjacent soil layers 1 and 2; $c = (G_2/G_1)^{1/4}$; G_2 and G_1 are shear modulus at soil layers 2 and 1, respectively.

From the equation above, it is noticed that if the two layers have the same stiffness ($G_2 = G_1$), $(1/R)$ is then zero, which is not realistic. Therefore, Dobry and O'Rourke [952] required that $c \geq \sqrt{2}$.

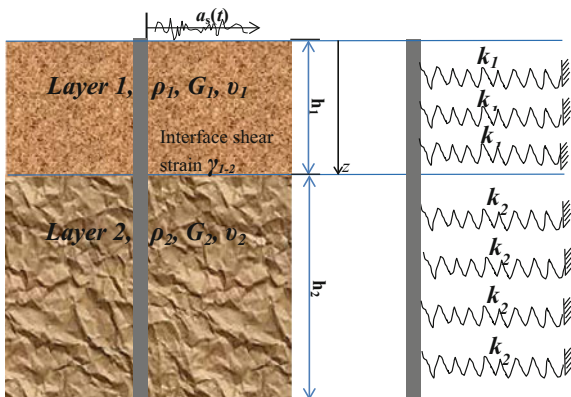
Even though the method above accounts for the soil-pile interaction, the dynamic nature of the excitation and the effect of the finite thickness of the soil layers are not incorporated [953].

To incorporate the geometric characteristics (thickness) of soil layers and the dynamic nature of excitations, by simplifying a pile in soil layers under horizontal seismic excitations as a beam supported by a series of springs with soil subgrade modulus k_i as shown in Fig. 19.3, a convenient hand calculation procedure proposed by Mylonakis [950] can be performed:

1. Calculate the effective soil peak (not average) strain γ_{1-2} at the interface between two adjacent soil layers 1 and 2 [950]:

$$\gamma_{1-2} = r_d \cdot \max(a_s(t)) \cdot \rho_1 \cdot h_1/G_1 \quad (19.12)$$

Fig. 19.3 A pile in soil layers under horizontal seismic excitations can be simplified as a beam supported by a series of springs with soil subgrade modulus k_i ; ρ_i , G_i , and ν_i are density, shear modulus and Poisson’s ratio for soil layer i , respectively; the horizontal acceleration at the soil surface is $a_s(t)$



where $r_d = 1 - 0.015z$ is the depth reduction factor that varies with depth z to the layer interface (in meters), and the seismic motion generally decreases with the increase in depth, as illustrated in Fig. 3.18; $a_s(t)$ is the acceleration at soil surface; ρ_1 and h_1 are the density and thickness for soil layer 1, respectively.

2. Calculate the soil subgrade modulus k_i (the unit is stiffness per unit length: force/length², such as N/m/m) for soil layer i [950]:

$$k_1 = E_1 \cdot \delta \tag{19.13}$$

$$k_2 = E_2 \cdot \delta \tag{19.14}$$

where E_i is the Young’s modulus of soil layer i , which can be calculated as $E_i = 2G_i(1 + \nu_i)$; ν_i is the Poisson’s ratio for layer i ; δ is a dimensionless parameter given by [951]:

$$\delta = \frac{3}{1 - \nu_1^2} \left[\left(\frac{E_p}{E_1} \right)^{-1/8} \cdot \left(\frac{L}{d} \right)^{1/8} \cdot \left(\frac{h_1}{h_2} \right)^{1/12} \cdot \left(\frac{G_2}{G_1} \right)^{-1/30} \right] \tag{19.15}$$

where E_p is the Young’s modulus of the pile; L and d are the length and diameter of the pile; h_1 and h_2 are the thickness of soil layers 1 and 2 shown in Fig. 19.3.

For relatively long piles ($L/d \approx 40$) and two soil layers of equal thickness ($h_1 = h_2$), based on the equation above, Kavvas and Gazetas [951] proposed a simpler form of δ :

$$\delta = 6(E_p/E_1)^{-1/8} \tag{19.16}$$

As an even simpler calculation, by knowing that the ratio k_i/G_i typically ranges from 2.5 to 4.0, k_i/G_i can be assumed to be 3.0 as recommended by Dobry and

O'Rourke [952]. Even though k_i/G_i value obtained from this approximation [952] can be half of that given by the equation [951] above, the differences in terms of maximum bending strain ε_p are usually much smaller since ε_p is proportional to the fourth root of k_i as can be observed in the equation given in step 3.

3. Calculate the maximum bending strain ε_p at the pile's outermost fiber. Note that the ratio of these parameters represents a sort of "strain transmissibility" function, which is strongly frequency-dependent. Therefore, one may neglect this frequency dependence. The strain transmissibility function only accounting for pile-soil interaction effects can then be calculated as [950]:

$$(\varepsilon_p)_{\omega=0} = \frac{(c^2 - c + 1) \left\{ \left[3 \left(\frac{k_1}{E_p} \right)^{\frac{1}{4}} \cdot \left(\frac{h_1}{d} \right) - 1 \right] c(c - 1) - 1 \right\}}{2c^4 \left(\frac{h_1}{d} \right)} \gamma_{1-2} \quad (19.17)$$

where $c = (G_2/G_1)^{1/4}$; d is the pile diameter.

From the equation above, it is noticed that the bending-induced strain of a pile is proportional to the $(k_1)^{1/4}$, as is the bending stress and moment.

With the equation above, the peak strain affected by frequency effects may be accounted for by multiplying the calculated $(\varepsilon_p)_{\omega=0}$ with a scaling factor Φ , which is a function of h_1/d , G_2/G_1 , and E_p/E_1 . Mylonakis [954] presented that Φ tends to increase with frequency and may exceed 2.0, especially for stiff piles and deep locations. However, Φ is normally less than 1.25 in the frequency range of interests. Therefore, as a rough estimation, Φ values between 1.0 and 1.2 are recommended.

Based on the equation above, Mylonakis [950, 953] performed a parametric study by varying the layer stiffness contrast (G_2/G_1), E_p/E_1 , and embedment ratio h_1/d within a reasonable range ($2 < G_2/G_1 < 100$, $100 < E_p/E_1 < 5000$). The results are illustrated in Fig. 19.4. By observing this graph, the strain transmissibility $\varepsilon_p/\gamma_{1-2}$ varies from about 0.05–0.4, i.e., up to 40% of the shear strain in the soil is transferred, as bending strain, to the pile. Obviously, strain transmission is higher for slender piles and higher layer stiffness contrasts. Even though $\varepsilon_p/\gamma_{1-2}$ generally increases with increasing h_1/d , the dependence appears to be weak compared to the strong dependence on G_2/G_1 and E_p/E_1 . For h_1/d larger than 20, $\varepsilon_p/\gamma_{1-2}$ is practically independent on pile diameter, which discredits the perception of the superior seismic performance of slender piles over large-diameter piles [955, 961].

4. Calculate the corresponding bending stress at the pile's outermost fiber and the bending moment:

$$\sigma_p = E_p \cdot \varepsilon_p \quad (19.18)$$

$$M = \sigma_p I_p / y \quad (19.19)$$

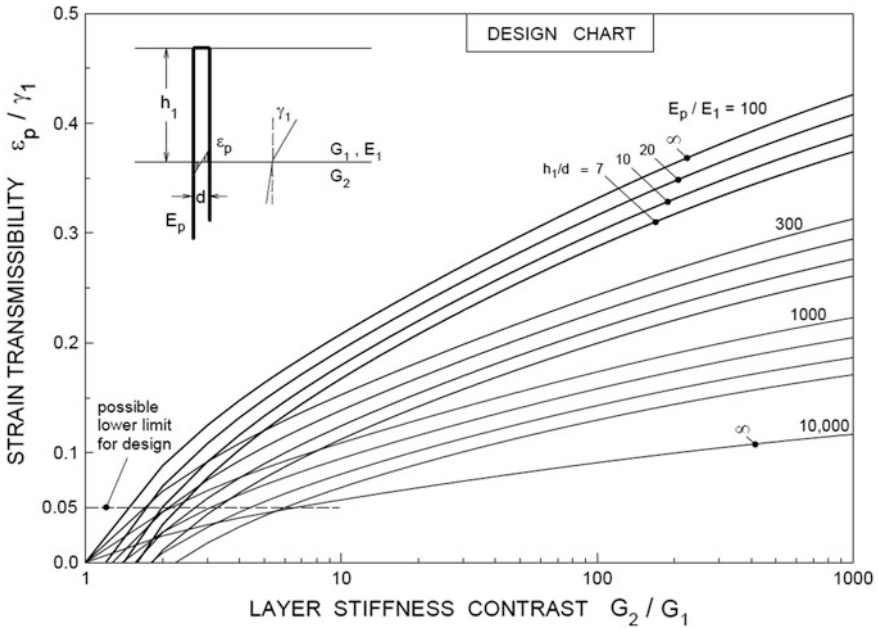


Fig. 19.4 Ratio of peak kinematic pile bending strain ϵ_p in a vertical solid cylindrical pile to the peak soil shear strain γ_1 , at the interface of two soil layers of different stiffnesses, at low excitation frequencies; curves were obtained for pile embedment ratios $h_1/d \rightarrow \infty, 20, 10,$ and 7 [963] (courtesy of George Mylonakis, University of Bristol)

where y is the distance between the neutral axis and the outermost fiber of the pile’s cross section, for a circular cross section with a diameter of d , it is taken as $d/2$.

In addition to the method/procedure presented above to assess the kinematic loading on piles, based on maximum shear stress τ_c induced at the layer interface by the free-field motion, Nikolaou et al. [962] proposed a fitted formula for harmonic excitations:

$$M = 0.042\tau_c d^3 \left[\left(\frac{E_p}{E_1} \right)^{0.65} \cdot \left(\frac{L}{d} \right)^{0.30} \cdot \left(\frac{v_{s1}}{v_{s2}} \right)^{0.50} \right] \tag{19.20}$$

where v_{s1} and v_{s2} are the shear wave velocities in the upper and lower soil layer, respectively; the maximum shear stress τ_c can be simplified as:

$$\tau_c = \rho_1 \cdot h_1 \cdot \max(a(t)) \tag{19.21}$$

where $a(t)$ is the acceleration at the layer interface.

To account for the transient nature of the seismic excitation, Nikolaou et al. [962] also introduced a reduction factor η depending on the duration of the accelerograms in terms of the effective number N_e of seismic loading cycles, the relative frequency characteristics between earthquake and soil deposits, and the effective damping of the soil–pile system:

$$\eta = \begin{cases} 0.04N_e + 0.23 & \text{for } T_1 \approx T_p \\ 0.015N_e + 0.17 & \text{for } T_1 \neq T_p \end{cases} \quad (19.22)$$

where T_p is the predominant period of ground motions and T_1 is the site period of the soil deposits.

By comparing the calculated seismic responses of piles between the two simplified methods presented above with a more dedicated Beam on Dynamic Winkler Foundation model shown in Fig. 15.2, Cairo et al. [964] found that the simplified methods tend to predict conservative moments at the subsoil interface, especially when the interface is deep.

19.3 The Location for Transferring the Earthquake Input Energy from Soils to Piles or Shallow Foundations

Sometimes, in order to calculate pile responses, it is much more convenient to apply seismic excitations on a single point or two points along the pile length than to apply the excitations to a large number of points along the length of the pile. Therefore, it is important to determine the locations of the resultant forces applied on the pile due to horizontal and vertical seismic excitations.

Bea [965] reported that the location on a foundation receiving the earthquake input energy differs according to foundation type (pile or mat supported) and the direction (lateral or vertical) of the excitation, as given in Table 19.1.

In addition to the foundation types and the direction of loading, this location also depends on soil conditions, diameter, and stiffness of piles or caissons, as well as

Table 19.1 Locations of the earthquake excitation energy transferred into foundations of offshore structures

Foundation type	Locations of the earthquake input energy to the foundation	
	Lateral pressure	Vertical pressure
Pile foundation	The maximum lateral earth pressures can be generated: generally, at 5 (for stiff soils) to 10 (for soft soils) pile diameters below the sea floor/soil surface	Along the pile where the soil–pile interface shear force is maximized: generally at 1/3 of the embedded pile length from the pile bottom
Mat-supported structure	The immediate vicinity of the sea floor	

characteristics of inertia loads transferred from superstructures. To be conservative, the location along the pile to transfer the seismic loading may be applied at a small distance below the location recommended in Table 19.1.

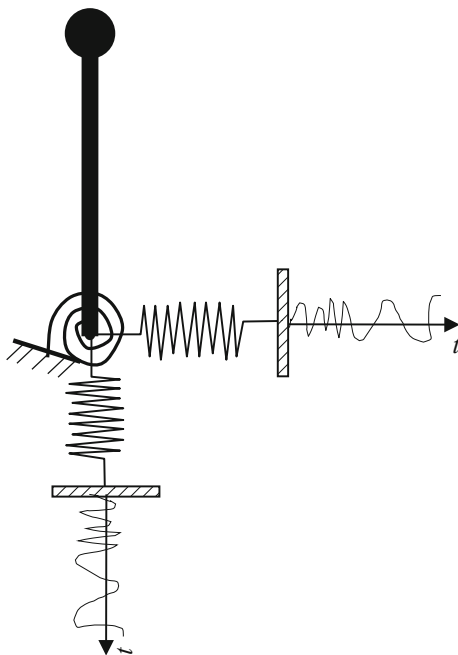
It should be noted that the method above to apply seismic excitations on piles should only be used for calculating responses of structures supported by piles, as pile responses induced by kinematic loading may not be accurately predicted using this simplified method.

19.4 Simple Modeling of Pile Impedance

If the response of a pile itself is not of interest, and the properties of soil layers gradually change with depth, the structure–foundation–soil system can be simplified as a structure supported by a foundation represented by a pile head impedance modeling (springs and damping), with the seismic motions/excitations applied on the pile head level, shown in Fig. 19.5. Sections 15.2 and 15.4 give an introduction to this method and a convenient estimation of pile head stiffness. Section 19.5 will discuss the method to determine the pile head impedance.

As an extension of the simplified modeling above, in many cases, the 3-step substructuring modeling can be adopted, as discussed in Sect. 5.2.2 and illustrated in Fig. 19.6, which includes the kinematic interaction, subgrade impedances, as

Fig. 19.5 The soil–foundation–structure system can be simplified as a structure supported by the foundation represented by a pile head impedance modeling at the bottom of the structure



well as the inertial interaction analysis. It makes use of the superposition of separate evaluation of the soil–pile system and structural system responses where inelasticity can be included in terms of effective (secant) properties. The approximation involved can be considered acceptable since the amount of inelasticity is normally limited. For applications in earthquake engineering, the first system is analyzed with the twofold objective of establishing the input motion to the structure (due to kinematic interaction) and of determining the dynamic impedance (subgrade impedances) to be applied at the structure’s base. Being a part of the structural engineering regime, the second system, consisting of the structure, impedance

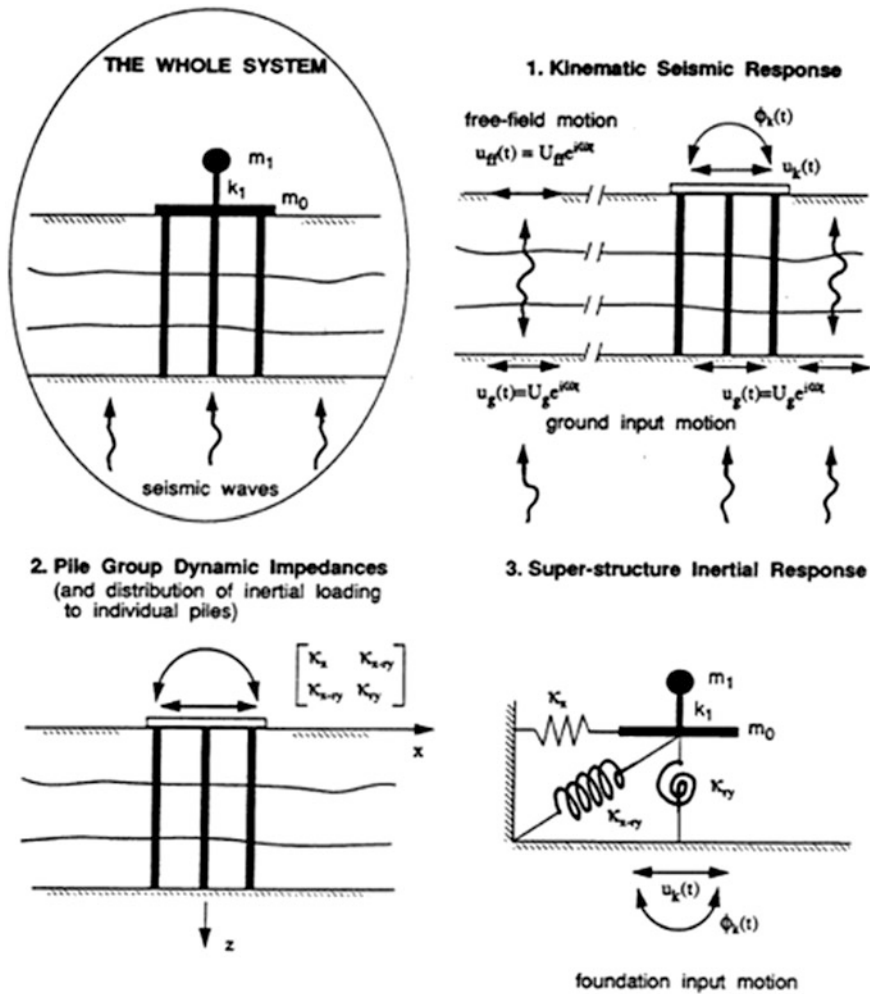


Fig. 19.6 Illustration of 3-step method in engineering practice to represent the actual soil–pile–structure interactions [966]

calculated from the first analysis, and connected to the support(s) of the structure, is then analyzed under the modified motions due to the presence of the first system.

For applications in earthquake engineering, it is noticed that neither simple method described in Sects. 19.3 and 19.4 can properly model the kinematic loading variation along the pile length, and these methods are normally used only for calculating the structural responses. An adequate representation of the kinematic loading variation has to be addressed with a more detailed modeling of pile–soil system, as will be discussed in Sect. 19.6, which is a type of direct analysis approach as presented in Sect. 5.2.1.

19.5 Determination of Pile Impedance

As a more dedicated method to model pile(s) and its surrounding soils than the simplified pile head stiffness modeling that has been presented in Sect. 15.4, dynamic pile impedance is often obtained by analytical method mainly for homogeneous half-space and layered soils, or by numerical analysis such as finite element method and boundary element method for more complicated soil layers, or by dynamic testing.

Similar to that of the shallow foundation impedance discussed in Sect. 13.1, pile head stiffness k and dashpot c can be applied to replace the modeling of the pile(s) and its surrounding soils at the forcing frequency ω :

$$k + ic\omega = \frac{F(t)}{x(t)} \quad (19.23)$$

where $F(t)$ and $x(t)$ are the amplitude of the forcing function and complex amplitude response in each degree of freedom, respectively.

For soil–structure interaction in lateral direction, the equation above can be expressed as:

$$k + ic(\omega)\omega = p_{\text{dyn}}/y \quad (19.24)$$

where p_{dyn} is the dynamic value of p on the p – y curve at depth z ; y is the lateral deflection of the pile at depth z .

$$k = p_{\text{stat}}/y \quad (19.25)$$

$$c(\omega) = p_{\text{stat}}[\beta a_0^2 + \lambda a_0(\omega y/d)^n]/\omega y \quad (19.26)$$

where p_{stat} is the static value of p on the p – y curve; ω is the angular frequency of loadings; d is the pile diameter; α , β , λ , and n are empirical constants related to soil type given in Table 16.6; a_0 is the dimensionless frequency of loading described in Sect. 16.7.

It should be noticed that $c(\omega)$ used above includes the contribution from both material hysteretic damping in the near-field and radiation damping in the far-field. This approach may lead to an excessively high damping value at the higher frequency range. An alternative way to model the damping is to determine the damping contributed from hysteretic material damping c_m and soil radiation damping c_r separately:

$$c = c_m + c_r \quad (19.27)$$

Hysteretic material damping accounts for the energy loss in soils due to viscosity and plastic deformations as the soils are loaded and unloaded. Hysteretic damping generally increases with the increase in the displacement and resulting shear strain. As described in Sect. 13.1, radiation damping occurs as energy is absorbed into soils when seismic waves radiate out from the point of loading and propagate through the soil medium, which is illustrated in Fig. 13.1.

The material damping can normally be determined based on the average shear strain amplitude γ_{avg} in the soil, which is related to local lateral pile displacement:

$$\gamma_{\text{avg}} = 0.4(1 + \nu/d)y(z) \quad (19.28)$$

where $y(z)$ is the pile's lateral displacement at depth z , often obtained from simplified dynamic analysis or by an iterative procedure; ν is the soil's Poisson's ratio.

Thereafter, the material damping corresponding to the average shear strain amplitude can be calculated as a hysteretic dashpot coefficient:

$$c_m = 2k_{\text{sec}}(y)\beta_s/\omega \quad (19.29)$$

where $k_{\text{sec}}(y)$ is the secant stiffness corresponding to the average shear strain amplitude γ_{avg} ; β_s is the hysteretic damping calculated from the hysteresis loop.

Several researchers [831, 832] recommended implementing the radiation soil damping effects by placing dashpots in parallel to or in series with the nonlinear springs (representing p - y curves). By using the analogy with one-dimensional wave radiation in a rod and accounting for radiation of energy in both the direction of energy transmission (along P or compression wave) and the transverse direction (S or shear wave), Berger et al. [967] proposed that the radiation damping can be determined by:

$$c_r = 2d\rho v_s [1 + (v_p/v_s)] \quad (19.30)$$

where d is the pile diameter; ρ is soil's unit density; v_p and v_s are the velocity of P-wave and S-wave during a seismic event; they are correlated through soil's Poisson's ratio ν :

$$\frac{v_p}{v_s} = \sqrt{\frac{2-2\nu}{1-2\nu}} \quad (19.31)$$

From the equation above, it is noticed that for perfect undrained soil condition that has a Poisson's ratio of 0.5, the velocity of P-wave is infinitely high, which is not realistic. Gazetas and Dobry [968] proposed a more realistic estimation of P-wave velocity:

$$v_p = \frac{3.4v_s}{\pi(1-\nu)} \approx v_s \quad (19.32)$$

Accordingly, the radiation damping can be simplified and approximated as:

$$c_r = 4d\rho v_s \quad (19.33)$$

Alternatively, by assuming radiating waves in four quarter-planes (shear waves for two quarter-planes and compression waves for two quarter-planes) and a horizontal plane-strain situation, the sum of the wave energy radiated away gives the dashpot value as follows:

$$c_r = 2d\rho v_s \left[1 + \left(\frac{3.4}{\pi(1-\nu)} \right)^{\frac{5}{4}} \right] \left(\frac{\pi}{4} \right)^{\frac{3}{4}} a_0^{-\frac{1}{4}} \quad (19.34)$$

where a_0 is the dimensionless frequency of loading described in Sect. 16.7.

By performing pile loading test, Zhu et al. [969] presented that, under dynamic loading, the horizontal force-deformation along piles can be represented by the static p - y curve combined with a damping proposed by Ghazzaly and Hwong [970]:

$$c_y \approx \frac{3.4d\sqrt{\rho G_s}}{\pi(1-\nu)} \quad (19.35)$$

By matching the dynamic pile head displacements between Winkler pile modeling and finite element analysis, Gazetas et al. [971] proposed the frequency-dependent pile impedance in the elastic regime as:

$$k_y \approx 1.2E_s \quad (19.36)$$

$$c_y \approx 2\beta_s \frac{k_y}{\omega} + \frac{6\rho v_s d}{\sqrt{4\omega d/v_s}} \quad (19.37)$$

$$k_z \approx 0.6E(1 + 0.5\sqrt{\omega d/v_s}) \quad (19.38)$$

$$c_z \approx 2\beta_s \frac{k_z}{\omega} + \frac{\rho v_s d}{\sqrt{4\omega d}/v_s} \quad (19.39)$$

where E_s is Young's modulus of soils; d is the pile diameter; v_s is the soil's shear wave velocity; β_s is the hysteretic damping; k_y and k_z are stiffness per unit length in horizontal and vertical direction, respectively; c_y and c_z are dashpot value in horizontal and vertical direction, respectively.

Similar to that of the shallow foundation as described in Sect. 13.1, in engineering practice, it is common to select impedance values corresponding to the main structural resonant period, or the site period of soil layers, or the predominant period of seismic motions. Among these, the first is more relevant if the pile's response is highly influenced by the inertia loading transferred from the superstructure; the second is preferred if the seismic motion has a large portion of frequency components close to the site period/frequency; and the last is more relevant if the kinematic seismic loading on piles is wide-banded (not concentrated at the site period) and more influential than the inertia loading. However, the drawback of using the predominant period of seismic motions lies in the fact that the seismic motions vary with depth (for pile foundations) and may also show significant differences for different bedrock/rock outcrop seismic time histories applied in site-response analyses.

If the dynamic effects of soils are not significant, by assuming that the pile head stiffness in each degree of freedom is independent from each other, the pile head stiffness is defined as the force (moment) to be applied on the pile head to produce a unit displacement (rotation) along the same direction (with the displacements/rotations along the other directions being zero) and is denoted by k_{HH} (horizontal stiffness), k_{MM} (flexural stiffness), and $k_{HM} = k_{MH}$ (cross-stiffness). Table 19.2 lists the static pile head stiffness of flexible piles embedded in three different soil models according to Eurocode 8 [426].

In Table 19.2, the soil's shear modulus G_s can either be determined from a site-response analysis or by hand calculation based on its relationship with ground accelerations (see Table 19.3 and Eurocode 8 [426]). For applications in geotechnical earthquake engineering, the ratio between the shear modulus and the initial shear modulus can even be less than 0.25. For machine vibration applications, this

Table 19.2 Constant static pile head stiffness of flexible piles embedded in three different soil models [426]

Soil model	$k_{HH}/(d \cdot E_s)$	$k_{MM}/(d^3 \cdot E_s)$	$k_{HM}/(d^2 \cdot E_s)$
$E(z) = E_s \cdot z/d$	$0.6(E_p/E_s)^{0.35}$	$0.14(E_p/E_s)^{0.80}$	$-0.17(E_p/E_s)^{0.6}$
$E(z) = E_s \sqrt{z/d}$	$0.79(E_p/E_s)^{0.28}$	$0.15(E_p/E_s)^{0.77}$	$-0.24(E_p/E_s)^{0.53}$
$E(z) = E_s$	$1.08(E_p/E_s)^{0.21}$	$0.16(E_p/E_s)^{0.75}$	$-0.22(E_p/E_s)^{0.5}$

$E(z)$ is Young's modulus of the soil at depth z , which equals to 3 times the soil's shear modulus G_s ; E_p is Young's modulus of the pile; E_s is Young's modulus of the soil at a depth equal to the pile diameter d

ratio typically ranges from 0.25 to 0.6. In the meantime, the damping of the soil can be twice the initial damping at zero strain. In an analytical and numerical analysis to obtain the pile foundation impedance, the region to apply this reduction of shear modulus and increased damping properties is referred to as the weak zone, which is normally assumed to be an envelope of one pile radius if the reduction ratio of shear modulus is less than 1.0 [329].

In many cases, the lateral stiffness is formulated based on the initial tangent p - y stiffness associated with low strain shear modulus at shallow depth. However, practically, it would be difficult to obtain reliable soil modulus data at such a shallow depth, especially if the soil properties are obtained from direct shear wave velocity measurements. Moreover, initial tangent stiffnesses observed from several soil-structure interaction experiments including full-scale and small model centrifuge pile load tests are usually much smaller than those implied from the theoretical elasticity solutions with soil modulus derived from low strain shear wave velocity data, with the discrepancies rising to as much as 10 times [972].

In case the soils' nonlinearity is significant, a reduction of seismic loads applied on the relevant structure may be considered by accounting for nonlinearity of the soil stiffness. This can be performed either by carrying out a nonlinear time-domain analysis or through an iterative quasi-linear approach using secant stiffness.

Mudmat(s) is sometimes installed together with piles to form an integrated pile group footing system. To calculate the impedance for such a footing system, the impedance of the piles and the mudmat(s) can first be calculated separately and transferred to a predefined global coordinate system for the footing. The total impedance matrix of the footing system can then be determined by summing up the impedance of the piles and the mudmat(s), both with coordinate system transferred to the global coordinate system.

Table 19.3 Average soil damping ratios and average reduction factors (\pm one standard deviation) for shear wave velocity v_s and shear modulus G within 20 m depth [426]

Design ground acceleration (g)	Damping ratio	$v_s/v_{s,\max}$	G/G_{\max}
0.10	0.03	0.90(\pm 0.07)	0.80(\pm 0.10)
0.20	0.06	0.70(\pm 0.15)	0.50(\pm 0.20)
0.30	0.10	0.60(\pm 0.15)	0.36(\pm 0.20)

$v_{s,\max}$ is the average shear wave velocity (the travel path distance of the waves divided by the sum of the travel times) of v_s not exceeding 360 m/s at small strain ($<10^{-5}$) condition; G_{\max} is the average shear modulus at small strain. With the \pm one standard deviation ranges, the designer can introduce different degrees of conservatism, depending on such factors as stiffness and layering of the soil profile; values of $v_s/v_{s,\max}$ and G/G_{\max} above the average could, for example, be used for stiffer profiles, and values of $v_s/v_{s,\max}$ and G/G_{\max} below the average could be used for softer profiles

19.6 Kinematic and Inertia Loading Modeling in the Direct Analysis Approach

To account for soil–pile interactions along the depth of the pile in a more refined manner, the soil–foundation–structure system is often modeled by representing the soil–pile interaction with a series of Winkler nonlinear springs as elaborated in Chaps. 15–17. Each of the springs has one end connected to the pile and the other end subject to kinematic seismic motions, as illustrated in Fig. 19.7. Figure 19.8 shows an example of jacket’s piles subjected to excitations along different depths of piles supporting a jacket structure, and the response of the topside structure. It is noticed that the excitations among different depths are almost identical. This is partially because the excitation time histories are plotted in displacement rather than in accelerations, and partially due to the fact that the soil profile has a rather high and similar shear stiffnesses along the depth. However, in case the graph is illustrated in accelerations or/and the soil profile shows significant stiffness variations along the depth, noticeable differences in horizontal seismic motions will be observed among different depths.

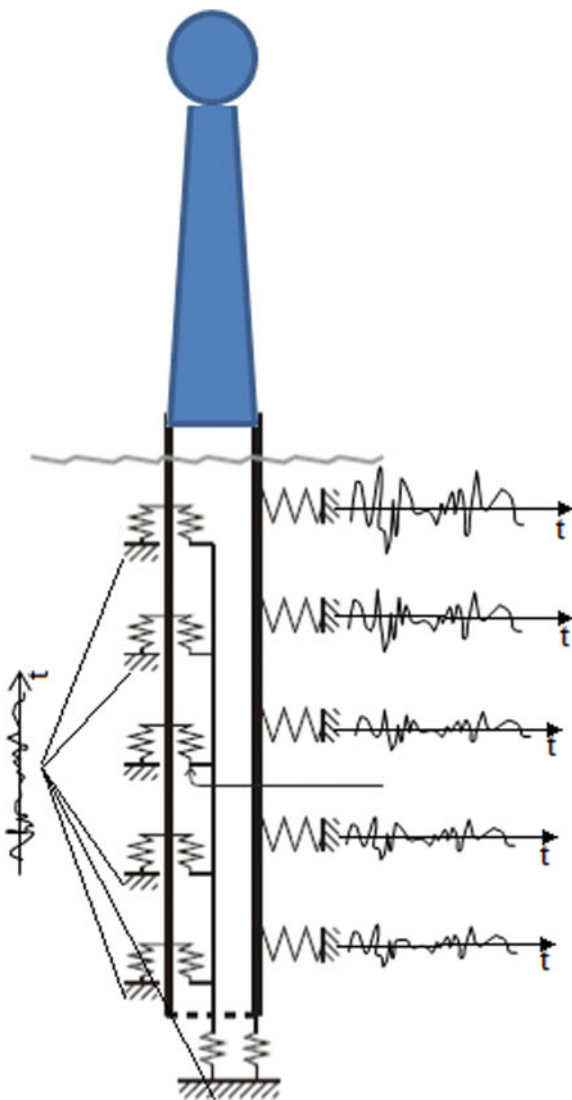
For vertical excitations, as P-wave (in most cases, the major contributor of vertical soil motions) velocities among different soil layers and underlying rock are usually very similar, the vertical ground motion time histories (and response spectra) are practically very similar/identical in all soil layers and may be simply assumed to be equal to that in the bedrock, even though a dedicated site-response analysis is still regarded as more reliable (see Sect. 3.10 for more details).

In the example shown in Fig. 19.8, the responses of all piles and soil–pile interactions are rather low. The horizontal motion at each depth of the soil is calculated by performing site-response analyses. It is particularly important to note that a nonlinear site-response analysis (Sect. 3.5.3) in time domain is preferred to the equivalent linear analysis (Sect. 3.5.2) in frequency domain, because the non-linearity of the springs and more importantly the phase of motions at different soil depths can be explicitly accounted for in a nonlinear site-response analysis in time domain.

By performing a dynamic time-domain seismic analysis for a jacket structure, Chen et al. [973] strongly recommended using depth-varying ground motions for seismic analyses. If uniform ground motions are used, the predicted pile bending moments should be increased nominally to account for the potential higher bending moment due to depth-varying ground motions and compared with the structural capacity of the piles to ensure that a double-hinge collapse mechanism of piles is not likely to form. This is because the double-hinge collapse mechanism may lead to excessive axial and lateral pile head displacements and potential collapse of the jacket structure. They further presented that a 50% to 100% increase in the pile bending moments is reasonable for the case they studied.

As discussed in Sect. 19.2.2, the presence of piles and the ratio of the Young’s modulus between a pile and soils (E_p/E_s) do have an influence that is able to modify the seismic motions. Therefore, if the coupling between the pile and surrounding

Fig. 19.7 Modeling of structure–foundation–soil system by representing the soil–pile interactions with a series of Winkler nonlinear springs, each of which is subjected to seismic motions at the corresponding soil depth



soil media is important to determine the responses among soils, pile, and even superstructure, the Winkler model to represent the soil–pile interaction has then to be replaced by modeling soil continuum using a decent type of finite elements and piles using beam or solid finite elements as shown in Fig. 19.9. Elastic or nonlinear soil behavior can be modeled by giving inputs of elastic constants (e.g., Young’s modulus and Poisson’s ratio) or by adopting adequate nonlinear constitutive relationships (Chap. 2) of soils.

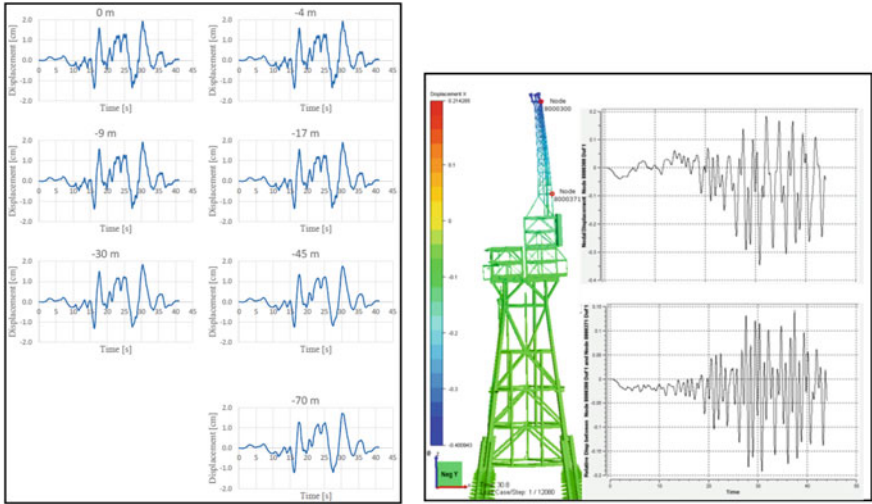


Fig. 19.8 Example of piles subjected to horizontal unidirectional excitations (left) along various depths of piles supporting a jacket structure (middle) and the horizontal response along global X-direction on two locations of the topside structure (right) (courtesy of Aker Solutions)

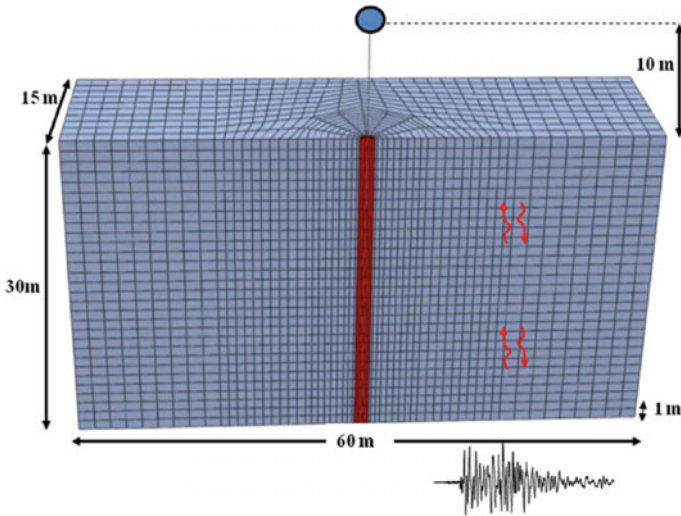


Fig. 19.9 Modeling of soils using solid elements and pile by beam elements. The acceleration time-histories at 30 m depth calculated from a site-response analysis with SHAKE91 [222] were used as the input excitation in the three-dimensional FE model [862]

If the soil media are modeled as elastic materials, an equivalent or Rayleigh damping [123] may be applied to each soil element to represent the hysteretic damping effect. This model has the advantages of being capable of performing soil–pile–superstructure analysis in a fully coupled manner, without resorting to independent calculations of sites or structural responses or applying pile group interaction factors. However, due to its complexity, this method is seldom used unless no other more convenient methods can fulfill the analysis objective. Care must be taken to simulate the boundary of the soil media. Artificial boundaries (Sect. 5.7) to absorb the seismic wave energy need to be introduced to account for the radiation of the energy into the far-field soil regions, thus reducing the infinite system to one with finite size. This may be performed through two types of boundaries:

1. On each node along the boundaries of the three-dimensional soil media model, 3 dashpots along three directions, with each perpendicular to others, are modeled at their one end. The free-field soil motions calculated from a site-response analysis can then be applied at each corresponding depth on the other end of these dashpots at the boundaries
2. Appropriate kinematic constraints are imposed to the four vertical sides of boundaries, allowing them to move like that of the free-field, and only seismic soil motions at the model bottom, which can be calculated from a site-response analysis, are applied at the bottom side (for example, at 30 m depth as shown in Fig. 19.9)

Chapter 20

Scour for Pile Foundations

20.1 Introduction to Scour

Due to the abrasion of the soil surface by the passing of current, wave, and flood, the shear stress generated from the flowing water may exceed the threshold value of the soil erosion resistance (sediment critical shear stress), removing sediment such as sands and rocks from around foundations (such as piles, bridge abutments, or piers). A hole is then formed at the upper soil surface, which is usually called scour, as shown in Fig. 20.1.

The process of scour development is relatively rapid within the first few years of pile installations. Table 20.1 shows the scour depth development of a 6-m-diameter monopile installed in an offshore area with a mean water depth of 7 m. The seabed consists of fine to medium dense sand. Scour protection was not applied. However, patches of gravel were detected in the area around the monopile. Less than two years after the pile's installation, the scour has developed to a maximum depth of 4.0 m and an extent of about 200 m [974].

The buildup of scour is mainly dependent on wave-induced flows at seabed/riverbed, currents at seabed/riverbed, structures/foundation size and shape, and sediment type (cohesion and grain size). When the flow is approaching pile foundations, its velocity increases, as does the bottom shear stress. The bottom shear stresses can increase by up to a factor of 4.

Figure 20.2 shows a conceptual model for scour development around marine foundations influenced by sediment type, which also indicates how scour is expected to develop under normal (i.e., non-extreme) prevailing conditions and extreme (i.e., annual storm) conditions. The conceptual model takes sand as the benchmark case for scour. In general, a decrease of scour depth can be expected for both coarser and finer soils as the susceptibility to erosion reduces, although muds and clays may be quite variable in their response depending on their formation history and degree of compaction [975]. Traditionally, clays with undrained shear strength of order 100 kPa are normally regarded as resistant to scouring in open sea

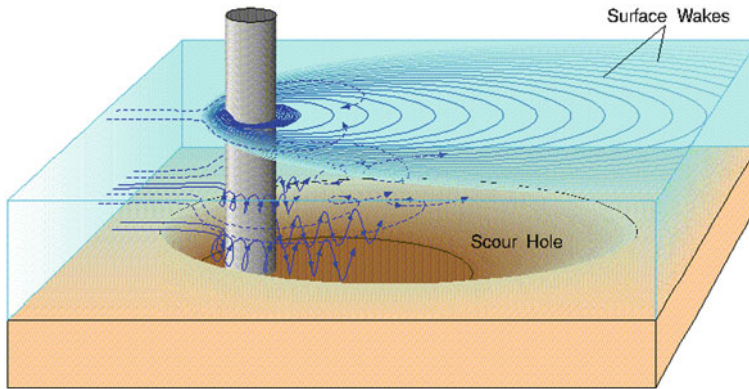


Fig. 20.1 The formation of a local scour hole around a pile (courtesy of USGS)

Table 20.1 Measured scour depth for a 6 m diameter monopile embedded in sands [974]

Time after installation (years)	Scour depth (m)	
	Mean scour depth	maximum scour depth
0	0.0	0.0
0.05	1.8	2.5
0.39	2.7	3.2
0.72	3.0	3.3
1.76	3.5	4.0
4.73	4.8	6.3

environments, as shown in Fig. 20.2. However, Jiang et al. [976] observed a scour depth of 5 m in firm clay adjacent to an oil-unloading terminal in a tidal river. Moreover, measurements for offshore wind turbine monopile foundations also show that the scour depth in stiff clay can be higher than what is indicated in Fig. 20.2 [977]. As shown in the lower figure of Fig. 20.2, for some types of sediments, the scour depth may increase with increased hydraulic forcing associated with storm waves, while for other sediments, ocean waves may actually help to decrease the scour depth. Moreover, marine soils are rarely found to be uniform around foundations and can be multi-modal in their grading as well as exhibiting a varying amount of cohesion. When this is coupled with the high rate of variability found in currents and waves, the assessment of the extent of scouring in these real soils become rather complex [978].

The scour can be characterized as one or a combination of local scour, global/dishpan/general scour, and overall seabed movement. Local scour (Fig. 20.3) is concentrated around individual piles, which causes a steep-sided scour pit with a roughly elliptical shape. Global scour is characterized by a general erosion and removal of soil over a large area, leading to a scoured basin with shallow and wide depression, possibly due to overall structure effects, multiple structure interaction,

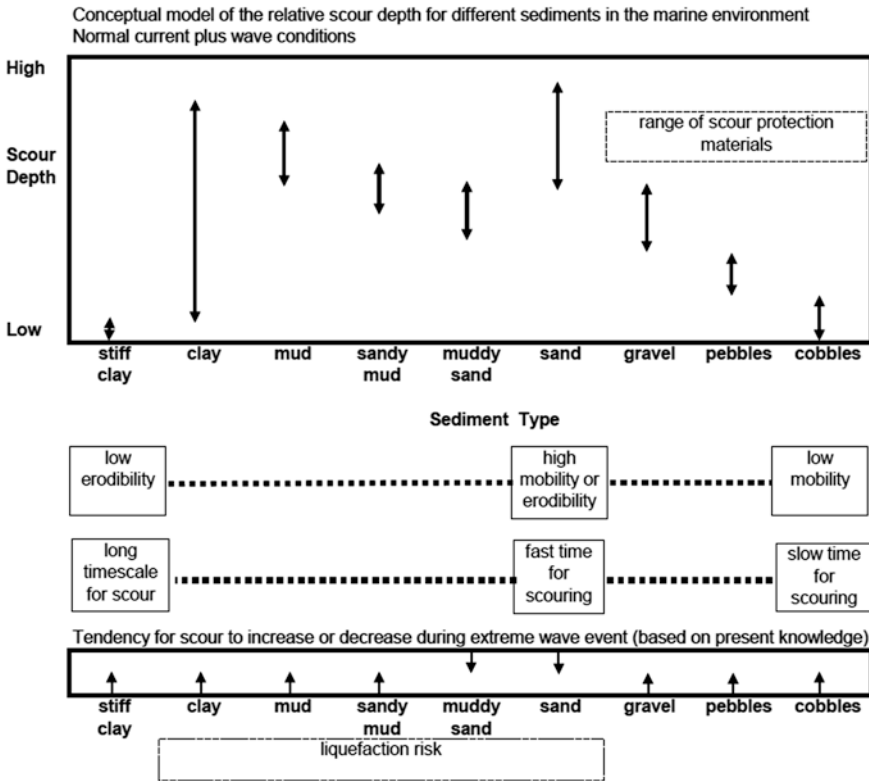


Fig. 20.2 A conceptual model for scour development around marine foundations proposed by Whitehouse [975] (courtesy of RJS Whitehouse, HR Wallingford)

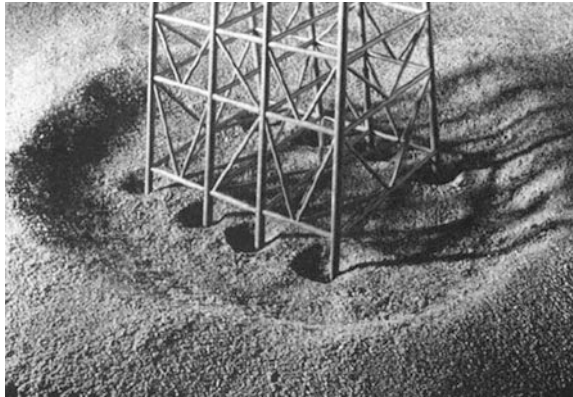
and/or wave–soil–structure interactions. Figure 20.4 shows typical appearances of both global and local scour around a jacket foundation at seabed (laboratory test). The overall seabed movement is the movement of sand waves, ridges, and shoals that would occur in the absence of a structure. The movement of the seabed is not affected by the presence of structures, but is a result of large-scale morphological effects. This can cause seabed lowering or accumulation. The movement of these sand waves is a slow process covering several years. This means that the general seabed level may have changed several meters a few years after the installation of a structure at that site. The flow pattern, the size of the seabed material, and flow depth play important roles in the formation of scours.

The target foundations/structures subject to the scour are pile foundations, gravity-based foundations, bridge abutments or piers, and pipelines of offshore structures. For example, many foundations supporting bridge structures are subject to scour, as shown in Figs. 20.5 and 20.6. Scour can result in a removal of vertical and lateral support for foundations, causing undesirable settlements of mat foundations and over-stressing of foundation elements.

Fig. 20.3 Steep-sided local scour pits around a monopile foundation



Fig. 20.4 Global and local scour at the bottom of a jacket structure (courtesy of RJS Whitehouse, HR Wallingford)



At sites, the development of scour can normally be monitored by either visual (using divers or ROVs) or through acoustic methods using such as multi-beam echo sounders or SONAR devices.

20.2 Influence of Scours

Scour leads to a reduction in capacity for both superstructures and foundations, reduces the stability of foundations and increases the maximum design moments in the pile, and decreases axial pile capacity, especially in sands. These effects require a larger pile penetration depth and pile cross-sectional area. By carrying out a series of sensitivity analyses of the lateral resistance of piles with small diameters under monotonic load using p - y curve method, Diamantidis and Arnesen [979] found that maximum pile bending stress increases almost linearly with scour depth. By studying the lateral capacity of piles in cohesive deepwater sediments influenced by the presence of scour, Li et al. [980] reported that the scour caused a significant reduction in lateral capacity for piles with slenderness ratios (length to diameter) >20 .

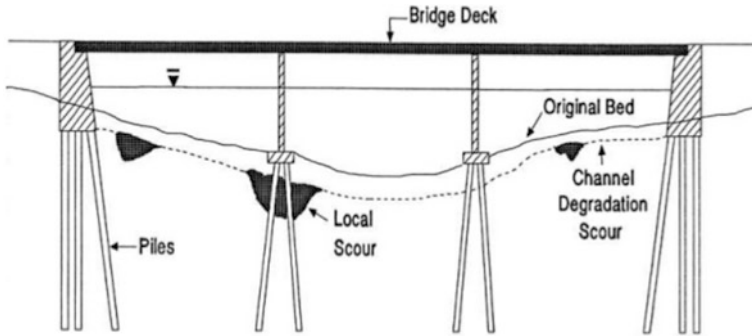


Fig. 20.5 Illustration of scour at the bottom of a bridge foundation

Fig. 20.6 Mississippi Highway 33 Bridge over the Homochitto River collapsed due to flood-induced erosion that caused scours



Due to degradation in foundation stiffness, the presence of scour hole also decreases natural frequency of superstructures. Zaaijer [981, 982] investigated effects of a scour hole on the natural frequency of support structures for a monopile system for offshore wind energy converters and reported a 5% reduction of the natural frequency compared with the case without a scour hole. Based on studies associated with FINO 3 research platform [983], it is reported that for a monopile structure under study, a 14% reduction of natural frequency due to scour is possible in case a scour depth of $2.5d$ is reached [984]. For pile groups with significant scour, the change of natural frequency is also significant, and this can dramatically alter (decrease or increase) the seismic spectral acceleration value corresponding to the natural period, thus significantly changing the seismic force and responses in foundations and superstructures. This variation in natural frequency can also significantly influence the

fatigue damage. This is because the fatigue damage of structures is proportional to the stress amplitude, with the power typically in the range from 3.0 to 5.0 (for steel and welded joints), and a slight variation of the stress amplitude in structures due to the variation in natural frequency may induce significant changes in the calculated fatigue damage. Note that scour depth varies with time, as illustrated in Table 20.1, indicating that the natural frequency of support structures will also vary during their lifetime. This requires a sensitivity analysis to confirm that the variation in the natural frequency over time should not cause resonance or significant response magnification of the support structures. In addition, geometrical variations of the mudline lead to more complicated design requirements for the pipeline and cables at seabed.

The negative influence due to scour is a concern for both bridges and offshore structures supported by pile foundations. For example, in the USA, 60% of all bridge failures result from scour and other hydraulic-related causes. In this regard, scour is the primary cause of bridge failure [987].

Therefore, where scour has the potential to occur in association with infrastructures, it should always be accounted for in design and/or its mitigation should also be considered.

To minimize the negative influence due to scour, a reliable estimation of scour and its implementation in pile design and scour protection are essential. The estimation of scour requires a reliable site investigation (wave data, current data, water levels, topographic and ground data, etc.) and a suitable engineering method such as hydrodynamic modeling. Typical scour protection includes placement of sand or gravel bags, stones and rocks, rock-filled filter bags, or geotextile/frond mattresses/mat or even tires around the protected foundations. However, the cost-effectiveness of such measures still needs to be further improved. For the development of offshore wind farms, long-term scour protection against erosion of seabed around typical monopile foundations can account for 6–10% of the total average project cost [988]. As an alternative, in case the seabed environment is not driven by strong unidirectional currents (e.g., a design current speed of less than 1.0 m/s in a sandy seabed), the presence of scour can be greatly minimized or even eliminated by using bucket foundations (Fig. 26.8) rather than traditional pile foundations to support offshore structures, provided that the environment is not driven by strong unidirectional currents. The beneficial effects of bucket foundations are mainly due to the fact that the soil trapped in bucket caissons cannot be flushed away, which is important because it ensures the stiffness and the mass preservation of the foundation [989]. This has been discussed by Stroescu et al. [991] based on observations of results from both experiments and field measurements.

20.3 Scour Modeling

For the calculation of pile responses, scour can be modeled by a reduced apparent fixity length in case the simplified calculation of pile head stiffness (Sect. 15.4) is adopted to model the pile, or setting the stiffness corresponding to p - y (Chap. 16)

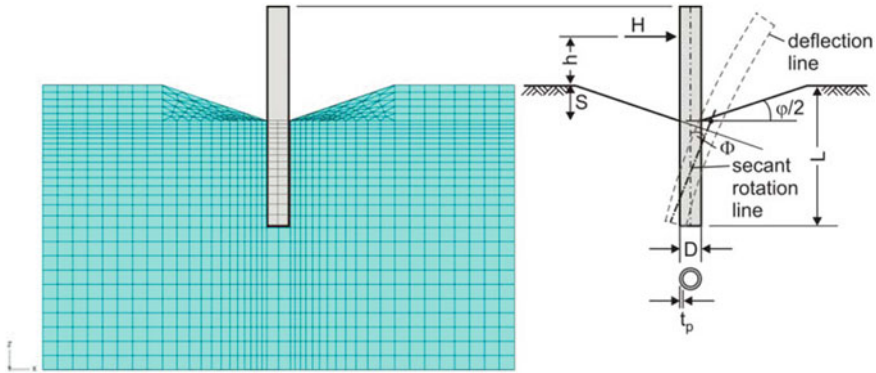


Fig. 20.7 Scour modeling in a finite element analysis and required parameters in the analysis [986]

and $t-z$ (Chap. 17) curve of Winkler models at zero at the corresponding depth of the scour, or modeling the geometry (Fig. 20.7) of the scour so that effects of both scours and surrounding soils can be more realistically accounted for.

20.4 Determination of Scour Depth for Single Piles and Bridge Piers

Although the prediction of scour depends on different factors, as previously mentioned in Sect. 20.1, and involves significant uncertainties, the size of the obstruction caused by structures or foundations is a key part of the scour process, and there exists a strong relationship between the scour depth and the obstruction size and flow condition. The scour analysis for single piles is focused on the development of the maximum scour depth with time.

To emphasize the mechanisms responsible for the scouring phenomenon, calculations of temporal variation of scour have been proposed by various researchers [990–993].

On the other hand, an equilibrium scour depth is normally achieved when the transport of bed material into the scour hole equals that removed from it. However, the exact definition of the equilibrium scour depth varies. Rouse [990] stated that scour is an ever-increasing phenomenon, and there is no real equilibrium scour depth, which is also confirmed by Breusers [995, 996] and Kohli and Hager [992]. However, more investigators believe that an equilibrium scour depth does exist [997, 998, 991] and have provided definitions of this. Franzetti et al. [999] defined equilibrium as the state of scour development where no further change occurs with time. Anderson [994] argues that “by virtue of the logarithmic character of the development of the scour region with time, a practical equilibrium is reached after a

relatively short time, after which the increase in the depth and extent of scour becomes virtually imperceptible.” Equilibrium can also be defined as the asymptotic state of scour reached as the scouring rate becomes small or insignificant [1000, 1001].

For non-cohesive soils, Shen et al. [1002] proposed a calculation of equilibrium scour depth that is dependent on the Reynolds number Re :

$$S_e = 0.000223 Re^{0.619} \quad (20.1)$$

where $Re = u_m d / \nu$; u_m is the mean flow velocity at the seabed/riverbed; d is the pile diameter; and ν is the kinematic viscosity of the fluid, which can be taken as $10^{-6} \text{ m}^2/\text{s}$ for water.

For cohesive soils, based on sample tests in an erosion function apparatus [1003] to obtain the rate of scour against the applied hydraulic shear stress and combining this information with the maximum shear stress prior to scour development, Briaud et al. [1004] proposed a simple relationship for the maximum scour depth S_{\max} :

$$S_{\max} = 0.00018 Re^{0.635} \quad (20.2)$$

By comparing the two equations above, it is clear that the equilibrium scour in cohesive and non-cohesive soils is similar. This is also confirmed by Ting et al. [1005], who reported that although the rates of scour in clays were much slower than in sands, the equilibrium scour depth between them was similar. They also noted that the shape of scour holes correlated with the pier’s Reynolds numbers, with the scour developing relatively uniformly around the pier at low Re . At higher Re , the scour holes developed mainly behind the piers with much less scour forming in front of the piers.

For cohesive soils, based on a limited number of tests using three different model cylinders with diameters of 50, 90, and 110 mm embedded in a silty clays, Rambabu et al. [1006] also proposed a general and more complicated relationship for scour, which is dependent on Froude number F_r , Reynolds number Re , and the undrained shear strength of soil s_u :

$$S_e = d F_r^{0.641} Re^{0.640} \left(\frac{s_u}{\gamma h} \right)^{-0.976} \quad (20.3)$$

where $F_r = u_m / (gh)^{0.5}$; u_m is the mean flow velocity at the seabed/riverbed; g is the acceleration of gravity; h is the flow depth; γ is the unit weight of the soil. Various empirical methods [1007, 1008] to predict scour evolution at mainly cylindrical structures have been proposed for the applications in offshore structures. Based on these methods, current design guidelines recommend scour depth calculations for mainly single pile foundations, ranging typically from 1.3 to 2.5 times the pile diameter. Table 20.2 shows the recommended local scour depth for offshore pile foundations extracted from several publications. For example, in the absence of specific data, API-RP-2A [792] recommends that for an isolated pile, the local

Table 20.2 Recommended local scour depth

Sources	Recommended scour depth ^a
DNV-OS-J101 [794]	$1.3d$
Sumer and Fredsøe [1008, 1009]	$1.3d$ with a standard deviation of 0.7
GL 2005 [875]	$2.5d$
Ansari and Qadar [1010]	$3.6d^{0.4}$
Dahlberg [1011]	3 m
Boon et al. 2004 [1012]	$1.75d$
Nielsen and Hansen 2007 [1013]	$1.30d$
Roulund et al. [1014]	$0.04d-1.18d$
Whitehouse et al. [1015]	$1.4d$

^a d pile diameter

scour depth can be approximately taken as 1.5 times the pile diameter and an overburden reduction depth equal to 6 times the pile diameter. However, for pile foundations with large diameters, this ratio is much lower, e.g., a pile with a diameter of 6 and 3.5 m will normally have a scour of less than 4 and 3.5 m, respectively. For a dynamic sensitive structure such as an offshore wind turbine supporting structure, the uncertainties in scour depth require more dedicated considerations, and several scour depths may then be assumed to assess their influence on the dynamic structural and foundation responses.

Regarding the lateral extent for local scour holes measured from pile surface, it is typically in the range between $1.5d$ and $2.0d$ for a single pile at offshore environments [794].

20.5 Scour Depth Influenced by Pile Groups

The most intensive part of studies related to scour depth is focused on the scenarios with single pile cases as presented in Sect. 20.4. However, scour depth influenced by pile group effects has not been researched sufficiently. Salim and Jones [1016] presented that different factors, such as spacings between piles, skew angles of flow, and pile cap locations in reference to undisturbed stream bed, can affect the scour depth. Based on experimental study, Sumer et al. [1017] presented an empirical formula to determine scour depth given in Table 20.3, which relates scour depth to the diameter of each pile and the pile group configurations (Fig. 20.8). It is clearly shown in Table 20.3 that the global and total scour depth increase with the increasing number of piles in a pile group, while the local scour has its maximum depth under single pile or circular group configuration.

Note that the scour develops over time, as is more obvious for bridge foundations affected by flood. Therefore, the combined effects due to earthquake and scour hazard also change with time [1018]. Recently, research [1019–1022] has been

Table 20.3 Recommended total, global, and local scour depth affected by the pile group effects (pile group configuration is illustrated in Fig. 20.8) [1017]^a

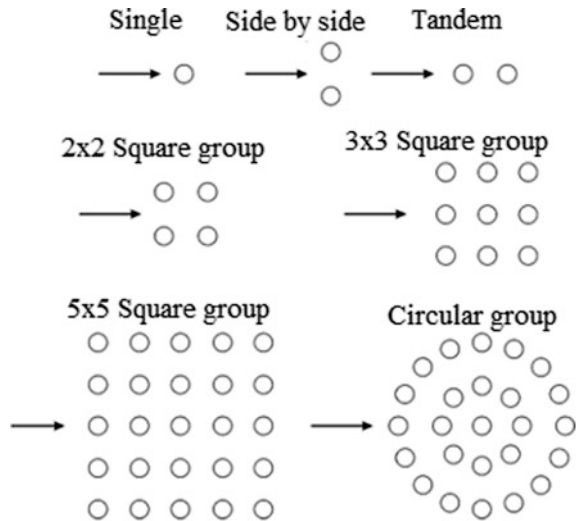
Pile group	Maximum total scour depth	Maximum global scour depth	Maximum local scour depth
Single pile	$1.1d$	—	$1.1d$
Side by side	$1.5d$	$0.78d$	$0.70d$
2×2 square group	$1.2d$	$0.37d$	$0.85d$
3×3 square group	$1.8d$	$0.92d$	$0.90d$
5×5 square group	$2.05d$	$1.2d$	$0.85d$
Circular group	$2.6d$	$1.5d$	$1.1d$

^a d pile diameter

carried out to identify the failure probability of bridge structures under seismic loading due to variations in scour depth, and those studies have concluded that the failure probability of structures is significantly affected by the scour depth and the type of the bridge foundations and superstructures.

For more detailed information on scour for offshore structures, readers may read sources [1008, 975, 974, 1023]. For an elaboration of scour and its effects on bridge structures, see sources [1024–1029].

Fig. 20.8 Pile group configuration to determine scour depth [1017]



20.6 Influence of Scour on Pile's Capacity

Scour will lead to a complete loss of lateral and axial resistance down to the depth of scour below the original seabed/riverbed. Both general and local scours shall be considered. However, as the development of scour depth for cohesive soil (such as clays and silts) is generally much slower than that of the cohesionless soil, it is often not a concern for piles embedded in cohesive soils, even though clays may be quite variable in their response depending on their formation history and degree of compaction, as previously mentioned in Sect. 20.1.

20.6.1 Influence of Scour on Axial Pile Capacity

Scour decreases axial pile capacity. In addition to a reduction of embedded pile length, both wall friction and end-bearing components of piles may also be affected. This is because scour reduces both q_c (CPT tip resistance) and σ'_v (vertical effective stress) [1030].

For excavations (i.e., general scour), API 2007 [792] recommends that q_c may be assumed to be simply proportional to σ'_v :

$$q_{c,f} = \chi q_{c,o} \quad (20.4)$$

where $q_{c,f}$ = final (i.e., after general scour) q_c value; $q_{c,o}$ = original (before the occurrence of general scour) q_c value; χ = dimensionless scour reduction factor = $\sigma'_{vf}/\sigma'_{vo}$; σ'_{vf} = final σ'_v (vertical effective stress) value; σ'_{vo} = original σ'_v value.

For large general scour depths, API 2007 [792] presents an alternative conservative approach recommended by Fugro [1031] for normally consolidated sands:

$$\chi = \left(\frac{1}{1 + 2K} \sqrt{\frac{z_s + 2K\sqrt{Sz_s + z_s^2}}{S + z_s}} \right) \quad (20.5)$$

where $K = \sigma'_{ho}/\sigma'_{vo}$ is the lateral earth pressure coefficient, which is the ratio between the effective horizontal (σ'_{ho}) and the vertical (σ'_{vo}) in situ soil stress; S is the general scour depth; $z_s = z - S$ is the depth below the final seabed level.

20.6.2 Influence of Scour on Lateral Pile Capacity

In cohesionless soils, scour leads to a reduction of lateral soil support. This is because scour causes a decreased vertical effective stress σ'_v leading to a lower

ultimate lateral pressure and a decreased initial modulus of subgrade reaction modulus E_s .

Even though there is no generally accepted method to evaluate the effects of general scour and local scour on the lateral pile capacity and p - y curve formulation, API 2007 [792] recommends a method for evaluating σ'_v and E_s as a function of scour depths, in which the general scour reduces the σ'_v profile uniformly with depth, whereas local scour reduces σ'_v linearly with depth to a certain depth below the base of the scour pit. E_s may be computed by adopting the general scour condition only. Other methods, based on local practice and/or experience, may be used instead.

20.6.3 The Consideration of Scour in Pile Designs by DNV-OS-J101

For design of pile foundations for offshore wind turbine structures, DNV-OS-J101 [794] requires that both p - y and t - z curves be constructed with due consideration of scour effects.

To consider effects of general scour, all p - y and t - z curves are to be generated on the basis of a modified seabed level that can be taken as the original seabed level lowered by a height equal to the depth of the general scour.

As presented in Sects. 20.6.1 and 20.6.2, general scour reduces the vertical effective stress. This has an impact on the lateral and axial pile resistances in cohesionless soils. This also has an impact on the depth of transition (Sect. 16.2) between shallow and deep ultimate lateral resistances for piles in cohesive soils.

In the case of local scour, the p - y and t - z curves should be generated with due account for the depth of the scour hole as well as for the lateral extent of the scour hole. The scour-hole slope and the lateral extent of the scour hole can be estimated based on the soil type and the soil strength. Over the depth of the scour hole below the original seabed level, no soil resistance and thus no p - y or t - z curves are to be applied.

DNV-OS-J101 [794] suggests that, unless data indicate otherwise, the depth of a current-induced scour depth around a pile in sands can be taken as 1.3 times the pile diameter (Table 20.2). For large-diameter piles such as monopiles, scour protection is needed unless the piles are designed with additional lengths to counteract any relevant negative scour effects.

Chapter 21

Effects of Pile Group, Adjacent Structures, and Construction Activities

21.1 Introduction to Pile Group

Pile groups or clusters are often used to carry significant loads transferred from superstructures, as shown in Fig. 21.1. They are widely used for offshore jacket structures, tripod structures (Fig. 21.2), bridges, and many other land-based structures. The majority of pile foundations contain group of piles. Pile groups are often more cost effective than single piles because a single large-diameter pile normally requires much heavier equipment for installation than that required for a number of smaller diameter piles. Unfortunately, this advantage is often accompanied by an increase in construction time, especially if there is a need to construct a pile cap over water.

For offshore jacket structures, the transfer of loads from upper structures to pile groups is often ensured by the installation of pile sleeves, as shown in Fig. 21.3. Moreover, additional piles, often called skirt piles, can be inserted through and connected to sleeves at sleeve-base and along the perimeter of structures.

Compared to a single pile, a pile group will affect the installation insofar as the driving of one pile will affect nearby soils into which the next pile is to be driven. Further, scours around a pile group can be different from that of a single pile: Local scours at adjacent piles can coalesce into a wider scour that will affect the effective stresses in the soil to a greater depth [112]. Moreover, a pile group will also influence the ultimate axial capacity of each individual pile, as will be discussed in Sects. 21.2 and 21.3.

Moment loading at mudline for a pile group is translated into axial pile loading as shown in Fig. 21.4, which provides more stability since the pile–soil interaction stiffness along the axial pile direction is normally at least a few times higher than that along the lateral pile direction. In addition, the lateral pile deflections are also restrained by superstructures' stiffness. Therefore, the behavior of the pile group is less sensitive to lateral than to axial capacity and stiffness, making a pile group more efficient than a single pile to resist overturning and torsional moment.

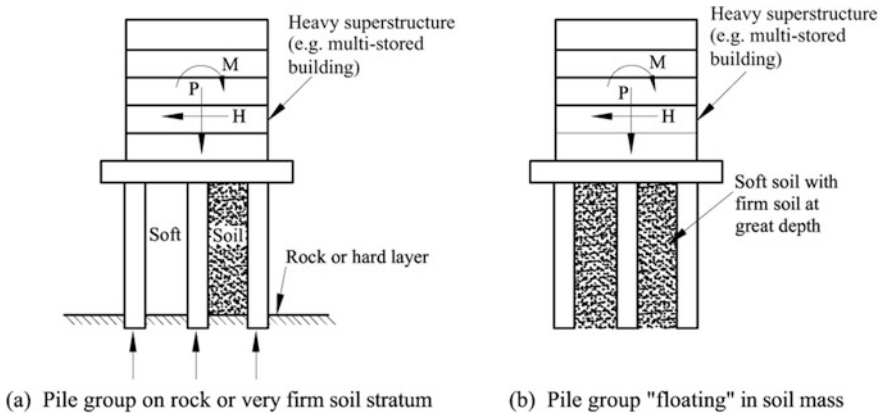
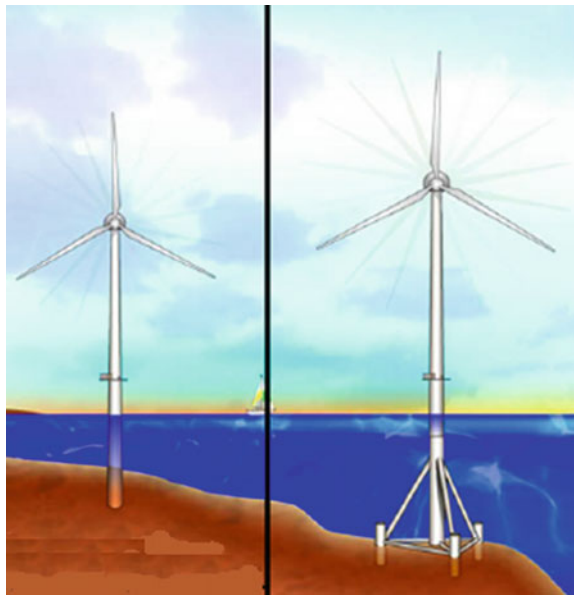


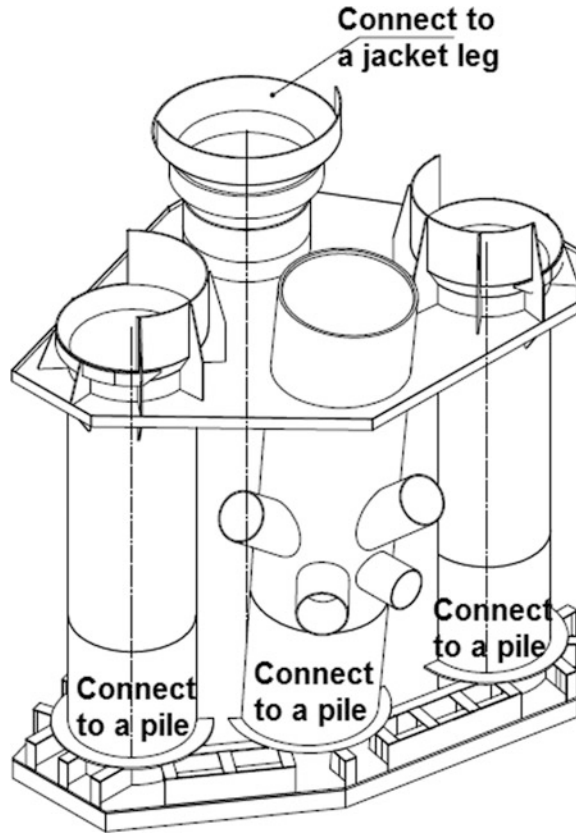
Fig. 21.1 Pile groups carrying heavy superstructures [777]

Fig. 21.2 Foundations with a single pile supporting a monotower (left) and a pile group supporting a tripod structure (right)



In geotechnical designs of pile groups, two major types of group effects are of great concern: (1) the ultimate capacity of the group, axially and laterally, may be different from (normally smaller than) the sum of the capacity of individual piles, as a result of close spacing between the piles; (2) the forces transmitted from one pile to soils cause the soil volume surrounding other piles to displace in the direction of applied loading, and as a result, the load–displacement behavior of the group becomes “softer” than the sum of the individual isolated piles [931].

Fig. 21.3 Pile sleeves connecting three piles to an offshore jacket leg



The first group effect must be investigated in advance. If the effect is found to be significant, it must be included as a reduction of the soil resistance in lateral and/or axial directions. The second group effect is actually a pile–soil–pile interaction problem. Field measurements of foundation response under both static and storm loading indicate that the standard practice by applying pile–soil interaction analyses using Winkler springs (used for single piles) for pile groups can overpredict displacements considerably [750]. This can be analyzed by assuming that each pile node interacts with other piles' node(s) and vice versa, and the interaction is simply the deformation of soil surrounding that pile node caused by the forces transmitted from other piles' node(s). This is often computed through iterations after which forces transmitted from all pile elements to soils are obtained, and the displacements of the soil volume surrounding all pile nodes can be computed by different methods such as Mindlin equation [1032]. Moreover, fully nonlinear analyses that recognize the departure from elasticity at even small strains are important to reproduce field behavior [1033, 1034].

The group effects under static pile loading have been investigated by several researchers based on continuum mechanics [1035, 1036, 761, 1037, 1038]. It is

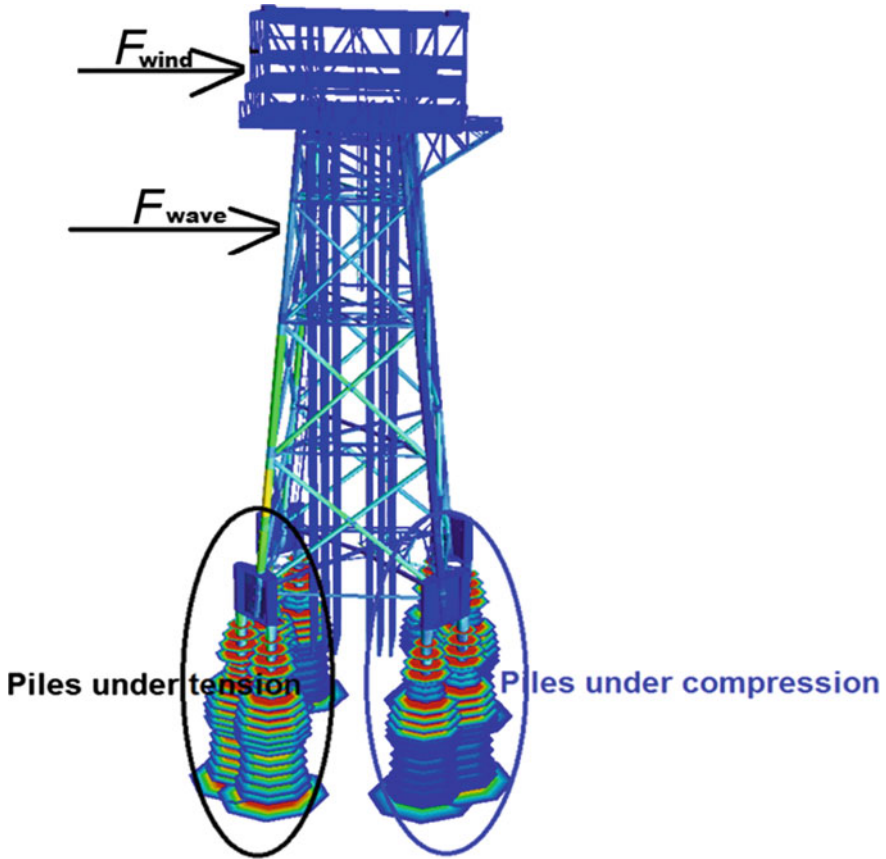


Fig. 21.4 Overturning moments at seabed induced by the applied wind (F_{wind}) and ocean wave (F_{wave}) loads are translated into axial pile loading for each pile in a pile group

well recognized that the following parameters affect the pile group efficiency, generally listed in order of importance:

1. Pile spacing,
2. Group arrangement,
3. Group size,
4. Pile head fixity,
5. Soil type and density,
6. Pile displacement,
7. The ratio of pile penetration to diameter.

Compared with a single pile capacity, a change in vertical (axial) load capacity for a pile group is mainly influenced by the pile spacing (in Sect. 21.2), while a reduction in lateral load capacity (Sect. 21.3) for closely spaced piles is mainly

influenced by the row location (i.e., leading or trailing rows). Pile group effects are usually more significant in offshore foundations, which frequently employ closer pile spacing ratios than their onshore counterparts.

Moreover, if a pile group is subjected to both moments and axial loading, the moment is balanced by piles' axial forces through moment equilibrium. The moment loading then is transferred to the subsoil by axial compressive and tensile pile loads, with the combined ultimate axial capacity normally less than the capacity due to only axial load [503].

21.2 Pile Group Effects Under Axial Loading

21.2.1 General

As briefly mentioned in Sect. 21.1, under axial loading, when the center to center distance between piles, namely pile spacing, is less than 8 times the pile diameter [792], the following two issues need to be addressed: (1) The behavior of one pile influences the behavior of another in a group of piles through the interaction of the zones of influence of each pile, i.e., the overlaps of stress fields from different piles in a pile group interfere with each other. Typical stresses/soil pressures produced from pile/shaft friction or end-bearing of a single pile and a group of piles are shown in Fig. 21.5. In case the overlap is large, the soil may fail in shear or settlement can be rather large. Even though the overlapping zone of stress decreases with increased pile spacing, pile groups with large pile spacing may not be practical since the pile cap size then becomes too large and hence expensive [777]; (2) the total capacity of a group of piles is not the same as the sum of capacities of each individual pile, which is partially caused by the effects of installation and partially due to different possible modes of failure, as failure of a group of piles may occur by failure of a single pile or failure of the block of soil encompassing the pile group [27], of which the failure of the block is mainly associated with the close spacing between piles. For clays, under cyclic loading, in case the pile spacing in a group is less than 2–2.5 times the pile diameter, the failure mode of the pile foundation may change from single pile failure to block shear mechanism. This is the major reason why center–center distance between two piles is seldom less than 1.8 times of piles' diameter. An optimum spacing is normally between $2.5d$ and $3.5d$ (d is the pile diameter) for circular cross-sectional piles, and $2H$ and $3H$ (H is the diagonal distance of the rectangular cross sections of piles) for rectangular cross-sectional piles. The required minimum spacing also depends on whether the piles in a pile group are of friction type or of end-bearing type. As a rule of thumb, for friction piles, the pile spacing should normally be more than $3d$; while for end-bearing piles passing through relatively compressible strata, the minimum pile spacing can be around $2.5d$. The bearing capacity of the block for a pile group may be calculated in a similar way as that of a single pile, by assuming that the pile group fails as a block (Fig. 21.6).

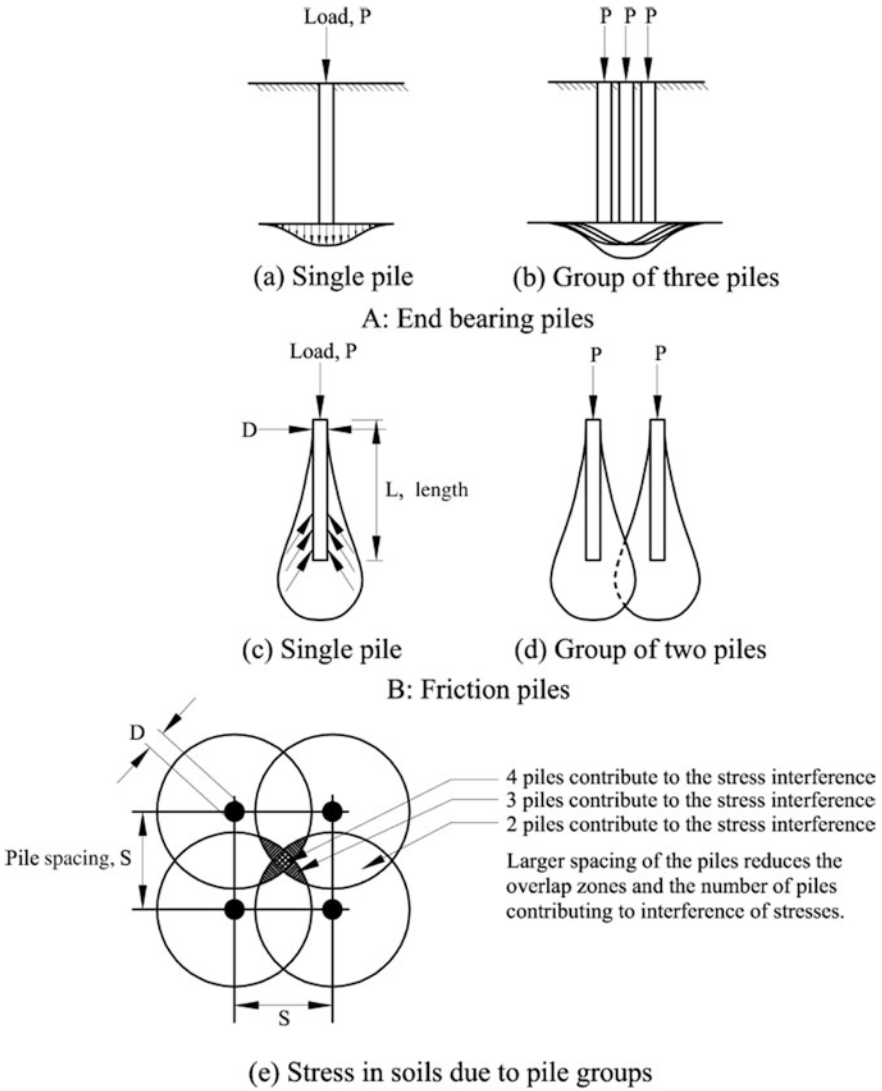


Fig. 21.5 Stress fields induced by different piles (under axial loading in a pile group) interfere with each other [777]

The change in pile group capacity can be accounted for by a group efficiency factor η , which is defined as the ratio between the ultimate load capacity of the pile group and the sum of the ultimate load capacity of each single pile without considering the pile group effects.

Compared to a single pile, a pile group's capacity can decrease or increase. η is below unity for pile groups driven into cohesive soils. However, η for a pile group

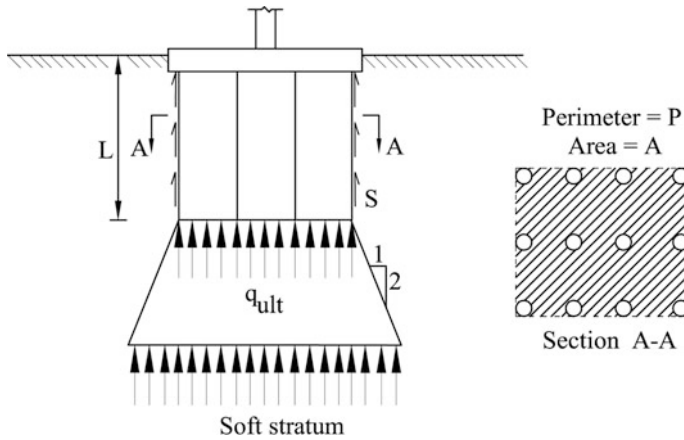


Fig. 21.6 Maximum capacity of a pile group [777]

driven into granular soils can increase to more than 1. In loose sands and gravel deposits, because the pile group due to the pile driving into sands can increase the effective stress acting on the piles within the group, the axial capacity of a pile group in sands may be higher than the sum of capacities of the individual piles without accounting for pile group effects. Hence, η can be as high as 3 for piles in sands [1039]. In a conservative manner, the load capacity of the pile group in sands is often taken as the sum of load capacity in each individual pile without considering group effects ($\eta = 1$). An exception would be a situation where a weak soil layer is beneath the sand layer so that the group action of piles could cause them to punch through the sand layer into the weaker layer or cause excessive settlement of the weak layer located below the pile tips [711].

Even though the axial capacity of a pile group may be calculated in a very similar way as that for a single pile, an additional check has to be carried out by assuming that the pile group fails as a block as aforementioned, which is illustrated in Fig. 21.6.

As previously mentioned, with regard to pile group efficiency for clays, the opposite trend to that for sands can be identified. The group efficiency decreases as piles in a pile group come closer together. Generally, if the spacing between piles in the group is greater than about 7 times pile diameter, there is no reduction in pile capacity. On the other hand, if the pile spacing in a pile group embedded in clays is less than 2–2.5 times the pile diameter, the failure mode of the pile foundation may change from single pile failure to block shear mechanism as mentioned before. In addition, the group action also exacerbates the effects of the cyclic loading [881], as will be discussed in Sect. 21.4.

The group efficiency in clays is in the range of 0.7–0.9 at a spacing/diameter ratio of 4 [1039]. As a rough estimation, for a rectangular group of $m \times n$ piles with diameter d and a center-to-center spacing of s , the group efficiency η can be approximated as [1040]:

$$\eta = 1 - \left(\frac{n-1}{m} + \frac{m-1}{n} \right) \frac{\tan^{-1}(d/s)}{90^\circ} \quad (21.1)$$

Even though the equation above is less frequently used nowadays, it gives an approximated estimation of pile group efficiency [1041].

21.2.2 Modifying Friction Resistance

In API [791, 792], the pile group effects on the pile–soil friction resistance in the vertical direction are calculated by a reduction in axial pile friction resistance t_{API} with factors $f_{sf}(s/d)$ $f_z(z/d)$ $f_\theta(\theta)$ associated with the pile spacing s , axial pile displacement z , and the angle of loading θ :

$$t = t_{API} \cdot f_{sf}(s/d) \cdot f_z(z/d) \cdot f_\theta(\theta) \quad (21.2)$$

$f_{sf}(s/d)$ can be calculated as:

$$f_{sf}^{\text{sand}}(s/d) = 0.0001(s/d)^5 - 0.0031(s/d)^4 + 0.0471(s/d)^3 - 0.3271(s/d)^2 + 0.9979(s/d) + 0.2926 \text{ for sand} \quad (21.3)$$

$$f_s^{\text{soft-clay}}(s/d) = 0.0016(s/d)^5 - 0.0418(s/d)^4 + 0.3955(s/d)^3 - 1.7767(s/d)^2 + 3.8976(s/d) + 2.6878 \text{ for soft clay} \quad (21.4)$$

$$f_s^{\text{stiff-clay}}(s/d) = 0.0032(s/d)^5 - 0.0762(s/d)^4 + 0.6746(s/d)^3 - 2.8090(s/d)^2 + 5.5896(s/d) - 3.4798 \text{ for stiff clay} \quad (21.5)$$

$f_z(z/d)$ can be calculated as:

$$f_z(z/d) = 1.0 - 0.155e^{(-16z/d)} \quad (21.6)$$

Since effects of loading angle on the axial pile resistance are rather insignificant, $f_\theta(\theta)$ can normally be taken as unity:

$$f_\theta(\theta) = 1.0 \quad (21.7)$$

For piles in sands or clays, the group settlement will normally increase compared to a single pile's axial displacement.

21.2.3 Modifying Tip Resistance

Regarding the pile tip resistance, it is calculated by a reduction in axial pile tip resistance q_{API} with factors $f_{se}(s/d)f_{ze}(z/d)f_{\theta}(\theta)$. The $f_{se}(s/d)$ can be determined as:

$$f_{se}(s/d) = [\pi\alpha + 2(s - 1)] / (2\pi\alpha) \quad (21.8)$$

where α is determined as:

$$\alpha = \begin{cases} 0.5 \text{ to } 1.0 & \text{for clays} \\ \frac{t_g(\phi' - 5^\circ)}{t_g \phi'} & \text{for sands} \end{cases} \quad (21.9)$$

where ϕ' is the internal angle of friction for sands; for North Sea sites, $\alpha \approx 0.5$ for over-consolidated clay; and $0.65 \leq \alpha \leq 0.85$ for sands, which gives a $f_{se}(s/d)$ above unity.

$f_{ze}(z/d)$ can be calculated as:

$$f_{ze}(z/d) = 1.0 - 0.35e^{(-16z/d)} \quad (21.10)$$

$f_{\theta}(\theta)$ can normally be taken as unity.

21.3 Pile Group Effects Under Lateral Loading

21.3.1 General

For closely spaced piles subjected to lateral loading, each pile pushes against soils in front of it, creating a shear zone in soils. As shown in Fig. 21.7, with an increase in lateral load, these shear zones begin to enlarge and overlap, forming soil wedges and soil gap, and more overlapping occurs if piles are spaced closer to each other. On the one hand, this causes a reduction in resistance for the trailing row: The passive soil wedge in the trailing row of piles overlaps into the leading row of piles, resulting in a reduction of passive resistance, which is often referred to as the shadowing process as shown in Fig. 21.7. This causes the edge effect, which is also called the effect of overlapping zones of influence between piles in the same row. On the other hand, the effects of overlapping zones of influence between piles in different rows are also effective, which are referred to as the shadowing [1042]. For offshore structures, it is typical for several piles in a pile group to be installed around the longitudinal axis of a superstructure leg; if those piles are closely spaced, the yielded zones of soils around individual piles overlap, forming larger yielded

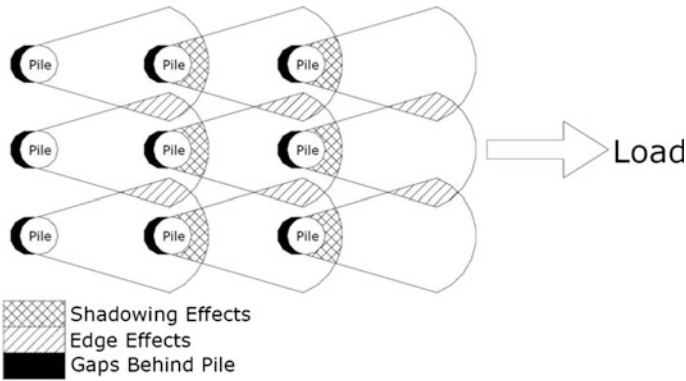


Fig. 21.7 Illustration of shadow and edge effects on a laterally loaded pile group [1044]

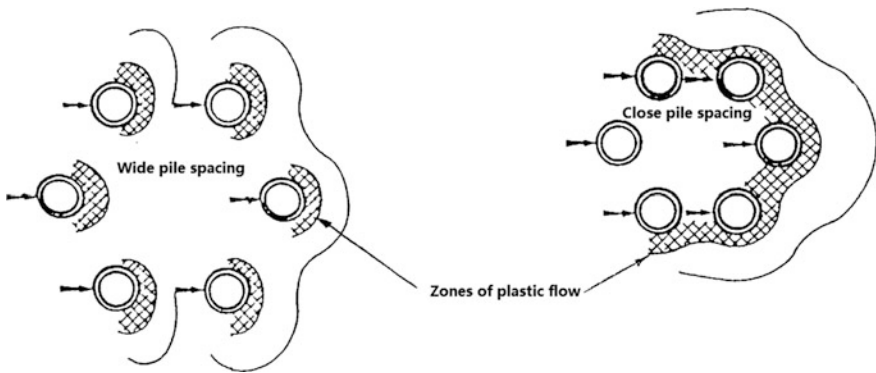


Fig. 21.8 Schematic illustration of pile group-soil interaction under lateral loading [1045]

zones in soils surrounding the pile group as shown in Fig. 21.8. This leads to a higher lateral deflection for the group before reaching a level of lateral resistance equivalent to that for a single pile [1043].

Therefore, for piles in either sands or clays, the pile group would normally experience greater lateral deflection than a single pile under the average pile load of the corresponding group. For example, under a significant wave loading with a return period of 100 years, by accounting for the pile group effects, the maximum calculated lateral tip displacement of the pile foundation supporting a North Sea drilling platform (Fig. 21.10) shown in Fig. 21.9 is 72 mm (due to waves from platform North), which is 34% higher than that if the pile group effects were not accounted for.

The major factors influencing the group deflections and load distribution among the piles are the pile spacing, the ratio of pile penetration to diameter, the pile flexibility relative to soils, the dimension of the group, and variations in shear

Fig. 21.9 Illustration of a pile foundation layout for a drilling platform as shown in Fig. 21.10 (disks attached to the pile foundations represent various soil layers)



strength and stiffness of soils with depth. Moreover, not all piles in a group have the same resistance and loading: Leading row piles normally take the greatest load, even though multiple loading cycles can diminish this row effect [792]. The effects of shadowing lead to the development of row reduction factors. Reductions up to 60% for ultimate capacity and 75% for lateral stiffness have been suggested by Poulos and Davis [1035]. Source [826] suggests even more significant reductions for subgrade modulus of piles positioned in groups, decreasing to approximately 30% for the second or the third trailing pile row.

Through modeling an elastic homogeneous semi-infinite soil medium around piles in a group based on Mindlin's principle, the pile-soil-pile lateral interaction was initially studied by Polous and Davis [1046]. To account for the soil's nonlinear and non-homogeneous behavior, Reese and Impe [1047], and Duncan and Evans [1048] have studied the pile-soil nonlinear pseudo-static response under lateral loading. For details, readers may read relevant sources cited above.

However, the pile group effects on lateral capacity have not received enough attention. This is because that the lateral capacity of soils can rarely be reached, as

Fig. 21.10 A drilling platform at North Sea



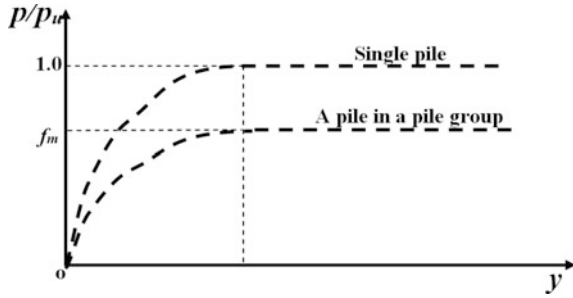
the piles are usually designed so that the allowable stresses in the piles are reached first and therefore govern design, ensuring that most of the soil remains in a pre-plastic state of strain [788]. On the other hand, the lateral stiffness (related to the modification of p - y curve as will be presented in Sect. 21.3.2) can be significantly influenced by the group effects, which was traditionally regarded as unimportant.

21.3.2 Modifying Soil Resistance

To account for interactions among piles in a pile group, the most widely adopted method using the Winkler approach is to modify p - y curves using so-called p -multipliers [1049], or, more precisely, to modify the p values by superimposing the interaction effects calculated according to the theory of elasticity and elastic half-space solutions [1050, 1035]. In this approach, to account for the loss of soil resistance, the soil resistance is reduced by multiplying a constant factor f_m (“ p -multiplier” or p -reduction factor) on the soil resistance p_u of a single isolated pile, as shown in Fig. 21.11 [711].

The value of p -multiplier in a pile group design is mainly determined by the row spacing in the loading direction. Obviously, the p -multiplier for a leading row is higher than that for a trailing row due to the shadowing effect. It is noticed that, under seismic and cyclic wave loading, the direction of loading changes repeatedly

Fig. 21.11 Comparison of p - y curves between single pile and pile group (f_m is a p -multiplier that is applied to all points of p - y curve on every single pile of a pile group to give a set of p - y curves for a group of piles)



and often unpredictably during the loading event and each load reversal converts a leading row, with a high p -multiplier, into a trailing row, with a low p -multiplier. Based on full-scale tests, Rollins et al. [1051] presented the values of p -multipliers for both clays and sands. They also suggested that the behavior of piles at row 3, row 4, and row 5 are rather similar. For a given load, compare to that of a single pile, group effects increase maximum bending moments on piles due to the reduced soil resistance. Moreover, in many engineering practices, rather than defining p -multipliers row by row, an average p -multiplier for all piles in the group is used that gives the same pile cap load–deflection curve [826]. This average p -multiplier is sometimes referred to as the group reduction factor for p - y curves.

Based on various experimental studies, different design guidelines such as AASHTO [1052] and FEMA P-751 [1053], and Reese and Impe [1047] have presented methods to calculate reduction factors due to the presence of pile group. Table 21.1 gives p -multipliers recommended by AASHTO [1052], which are significantly more conservative but simpler than what Rollins et al. [1051] presented. However, different from what Rollins and his co-workers proposed, AASHTO [1052] does not consider the effects of variation in soil conditions, and it only provides p -multipliers for pile groups with s/d between 3 and 5. It has no specific recommendations for $s/d > 5$. Moreover, ASHTO recommendations are based on data from free head pile group tests. All these tests were performed on 3×3 pile groups except for the test performed by Ruesta and Townsend [1054], which was a full-scale test on a 4×4 pile group. To calculate the group reduction factors using AASHTO recommendations, the average value of the related p -multipliers for different rows of each pile group should be used.

Other researchers [1049, 1055, 1056] also presented approximate values of p -multiplier for different soil conditions as shown in Table 21.2. By observing Table 21.2, it is found that, for sands, even though the leading row (row 1) may

Table 21.1 p -multipliers recommended by AASHTO [1052]

Pile spacing in the direction of loading	Row 1	Row 2	Row 3
$3d$	0.8	0.4	0.3
$5d$	1	0.85	0.7

Table 21.2 p -multipliers proposed by different researchers

Soil type	Row 1	Row 2	Row 3
Clean sand [1049]	0.8	0.4	0.3
Stiff clay [1055]	0.7	0.5	0.4
Soft silty clay [1056]	0.9	0.5	NA

have a very slight reduction in lateral capacity, the trailing pile rows (2 and 3) behind the leading row could have reduction factors of 0.3–0.4. For clays, typical values of row reduction factors are 0.7–0.9 for the leading row and 0.4–0.5 for the trailing rows.

To account for influences due to pile spacing, lateral pile displacement, and the angle of loading, the lateral load can be calculated by a reduction of lateral resistance p_u with factors $f_{sm}(s/d)$, $f_z(y/d)$, and $f_\theta(\theta)$ associated with the pile spacing s , lateral pile displacement y , and the angle of loading θ , respectively:

$$p = f_m(s/d) \cdot f_y(y/d) \cdot f_\theta(\theta) \cdot p_u \quad (21.11)$$

where $f_y(y/d)$ may be approximated as:

$$f_y(y/d) = 1.0 - 0.35e^{[-22.5y/d]} \quad (21.12)$$

$f_\theta(\theta)$ can normally be taken as unity.

The upper-bound values of f_m for both soft and stiff clays may be approximated as:

$$f_m^{\text{soft-clay}}(s/d) = 0.397 \cdot \ln(s/d) + 0.221 \quad (21.13)$$

$$f_m^{\text{stiff-clay}}(s/d) = 0.335 \cdot \ln(s/d) + 0.339 \quad (21.14)$$

The lower-bound values of f_m for both soft and stiff clays may be approximated as:

$$f_m^{\text{soft-clay}}(s/d) = 0.490 \cdot \ln(s/d) - 0.020 \quad (21.15)$$

$$f_m^{\text{stiff-clay}}(s/d) = 0.601 \cdot \ln(s/d) - 0.234 \quad (21.16)$$

The value of f_m for loose sands may be approximated as:

$$f_m^{\text{loose-sand}}(s/d) = 1.0 - e^{[-0.225(s/d) + 0.15]} \quad (21.17)$$

The value of f_m for dense sand may be approximated as:

$$f_m^{\text{dense-sand}}(s/d) = 1.0 - e^{[-0.425(s/d) + 0.25]} \quad (21.18)$$

Kuo et al. [503] stated that p -multipliers are in general dependent on the pile group system. They are usually derived for a plate located directly on the soil surface with either pinned or fixed connection of the pile heads to the plate. Other p -multipliers apply if piles stick out of the soil and the plate and the horizontal load acts on a level above the soil surface. Therefore, the p - y curve approach accompanied by p -multipliers is a very rough idealization, and it is preferred that the method be validated through a comparison with numerical analysis by a more dedicated modeling of pile group(s).

21.4 Effects of Cyclic Loading on Pile Group Behavior

For clays, pile group actions can exacerbate the effects of the cyclic loading, leading to a more marked degradation of axial capacity [881].

Pile–soil–pile interaction has been investigated by various researchers. Mostafa and Naggar [1057] studied the soil–structure interaction of offshore structures subject to ocean wave and current loading. By performing a series of tests on pile groups with 3×5 pile arrangement, Rollins et al. [1051] presented that even though repeated cyclic lateral loading only leads to a 15–20% reduction in capacity at the peak pile loading, it can lead to a much lower resistance for a pile group at loads less than the peak pile loads.

21.5 Effects of Dynamic Loading on Pile Group Behavior

21.5.1 General

Dynamic stiffness and damping of pile groups can vary significantly at different frequencies of loading. Compared with a single pile, depending on loading frequency, pile spacing, and other factors, stiffness and damping of a pile group can increase or decrease due to piles' interactions [923]. Under seismic loading or ocean wave loading, each pile in a pile group will emanate cylindrical SH-wave, SV-wave, and P-wave that will in turn affect the adjacent piles in the group.

21.5.2 Modifying Pile Resistance Due to Dynamic Loading

21.5.2.1 Dynamic t - z Curve

The dynamic t - z curve for pile group analysis can be established by a reduction of axial pile friction resistance t_{API} with factors $f_{sf}(s/d)$, $f_z(z/d)$, $f_\theta(\theta)$, and

$f_a(a)$ associated with the pile spacing s , axial pile displacement z , the angle of loading θ , and the dominant frequency of excitation a :

$$t = t_{API} \cdot f_{sf}(s/d) \cdot f_z(z/d) \cdot f_\theta(\theta) \cdot f_a(a) \quad (21.19)$$

The calculations of $f_{sf}(s/d)$, $f_z(z/d)$, and $f_\theta(\theta)$ are related to the group effects under static loading, which have been described in Sect. 21.2.

$f_a(a)$ is the non-dimensional frequency-dependent function, based on the results of rigorous linear dynamic analysis of disk-cone model for pile groups performed by Wolf [1058], $f_a(a)$ can be established as:

$$f_a(a) = 0.8714a^5 - 3.9172a^4 + 5.5381a^3 - 2.6026a^2 + 0.4351a + 0.9377 \quad (21.20)$$

where $a = \omega r/v_s$ is a dimensionless frequency; ω is the dominant angular frequency of excitation of seismic waves or ocean waves; r is the radius of piles in the group; v_s is the shear wave velocity.

21.5.2.2 Dynamic p - y Curve

Similar to the establishment of $f_a(a)$, the dynamic p - y curve for pile group analysis can be established by a reduction of lateral pile lateral resistance p_u with factors $f_m(s/d)$, $f_y(y/d)$, $f_\theta(\theta)$, $f_a(a)$ associated with the pile spacing s , lateral pile displacement y , the angle of loading θ , and the dominant frequency of excitation:

$$p = f_m(s/d) \cdot f_y(y/d) \cdot f_\theta(\theta) \cdot f_a(a) \cdot p_u \quad (21.21)$$

where $f_m(s/d)$ and $f_y(y/d)$ are presented in Sect. 21.3; $f_a(a)$ is a non-dimensional frequency-dependent function that is described in Sect. 16.7.

Naggar and Bentley [824] presented that the angle of loading with the pile's longitudinal axis did not have a strong effect on a pile group's dynamic lateral response. Therefore, in practice, $f_\theta(\theta)$ is normally taken as 1.0.

21.6 Modifying Pile Displacement to Account for Both Pile Group and Dynamic Loading Effects

It is noted that in the methods described in Sects. 21.2, 21.3, and 21.5, to account for the group or dynamic effects for a pile group, the pile resistance, i.e., t or p , are modified. As an alternative, the displacement (z or y) at a given depth along a single pile in a pile group can be modified to account for both the group and dynamic effects, as originally proposed by Wolf [1058] and later modified by Emami Azadi [889].

For t - z curves, since the axial displacement in a pile group might be increased compared to a single pile, the shear stress transferred at the pile-soil interface is redistributed and the axial displacement may be modified by a z -modifier:

$$z = z_{\text{API}} \left[1 + (N - 1) \sqrt{\frac{\bar{d}}{2\bar{s}}} e^{\left(\frac{-\xi\omega\bar{d}}{v_s}\right)} e^{\left(-\frac{\omega\bar{d}}{v_s}\right)} \right] \quad (21.22)$$

where z_{API} is the axial pseudo-static displacement of a single pile-soil system according to API-RP2A [792] without accounting for pile group and dynamic loading effects; N , \bar{d} , and \bar{s} are the number of piles in a pile group, the average diameter of piles and the average pile spacing in the pile group, respectively; ξ , ω , and v_s represent the hysteretic soil damping ratio, excitation frequency of the pile group, and the soil's shear wave velocity, respectively.

From the equation above, it is noticed that the pile group effects are accounted for by $(N - 1) \sqrt{\frac{\bar{d}}{2\bar{s}}}$, and the dynamic loading effects are considered by $e^{\left(\frac{-\xi\omega\bar{d}}{v_s}\right)} e^{\left(-\frac{\omega\bar{d}}{v_s}\right)}$. On the one hand, the dynamic effects under typical ocean wave loadings and low-frequency earthquake loadings can be neglected since $e^{\left(\frac{-\xi\omega\bar{d}}{v_s}\right)} e^{\left(-\frac{\omega\bar{d}}{v_s}\right)}$ is close to unity. On the other hand, the group effects can be significant.

Similarly, for p - y curves, one may modify the static p - y curves by modifying the lateral displacement y of a pile in a pile group using a dynamic interaction function, which is often referred to as the y -modification method (in contrast to the p -multiplier approach as discussed in Sect. 21.3):

$$y = y_{\text{API}} \left\{ 1 + \sqrt{\frac{\bar{d}}{2\bar{s}}} \sum_{j=1}^{N-1} \left[e^{\left(\frac{-\xi\omega\bar{d}}{v_p}\right)} e^{\left(-\frac{\omega\bar{d}}{v_p}\right)} \cos^2 \theta_j + e^{\left(\frac{-\xi\omega\bar{d}}{v_s}\right)} e^{\left(-\frac{\omega\bar{d}}{v_s}\right)} \sin^2 \theta_j \right] \right\} \quad (21.23)$$

where y_{API} is the lateral pseudo-static displacement of a single pile-soil system according to API-RP2A [792] without accounting for pile group and dynamic loading effects; θ_j is the angle between the longitudinal axis of a pile j in the pile group and the direction of dynamic loading; v_p is the P -wave velocity in soils; other notations have the same meaning as those in the z -modifier equation.

By studying the equation above, it is found that, similar to those of the z -modifiers, the dynamic effects under typical ocean wave loading and low-frequency earthquake loading on the p - y curve can normally be neglected.

Readers need to bear in mind that if piles are extremely close to each other, the additional pile interaction effects cannot be adequately included in the two equations above. In this case, a more rigorous pile-soil-pile interaction analysis must be performed.

21.7 Pile Cap

Because the upper part of a pile close to the pile head is more vulnerable to movement and stress than the bottom part of the pile is, it is often necessary to tie pile heads of several piles (in a pile group) together so that the load of a single pile can be shared almost equally on each pile over the pile group. Pile movement and settlement can then be dramatically reduced, thus significantly increasing the stability of the pile group. As a tool to meet this objective, a pile cap, as shown in Fig. 21.12, can typically be used to tie the pile heads together. It is normally a thick concrete mat resting on concrete or timber piles that have been installed to provide a suitable stable foundation. The pile cap mainly functions to transmit loads from the superstructure to the group of piles, which further transfers loads to soils.

Design of pile caps is very similar to that of the spread footing foundation. Pile caps must have sufficient punching shear capacity, and the bearing force between individual piles or shafts and caps must not exceed the capacity of either element. Moreover, both the backfill of the excavation (Fig. 21.13) and the compaction characteristics of backfill soils are important to provide substantial lateral resistance and stiffness.

High-rise pile cap foundation comprising a group of elevated piles, as shown in Fig. 23.1, is one of the most popular foundation types in the design of offshore wind turbine and bridge foundations.

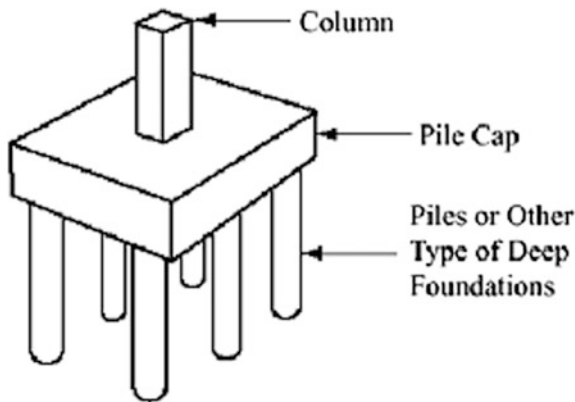


Fig. 21.12 A pile cap made of a concrete block cast on the head of a group of piles

Fig. 21.13 Backfill of the excavation is necessary to provide lateral resistance and stiffness



21.8 Influence of Adjacent Structures and Construction Activities on the Existing Piled Foundations

21.8.1 Problem Description

Extensive geotechnical engineering applications and research place a strong focus on existing foundations. However, many problems with existing pile foundations have challenged engineers. Among them, influences of adjacent structures and construction activities on the existing piled foundations have been recognized as an important engineering issue.

The engineering realizations of this issue include (but are not limited to) carrying out construction or placing structures adjacent to existing pile foundations, construction activities nearby existing piles (such as constructions of tunnels, pile driving, pile jacking), drilling holes near existing pile foundations, excavations of ground for pile cap constructions, deep excavations.

Effects of all the relevant engineering realizations above can be investigated through experiments or numerical analyses using, for example, finite element method or finite difference method.

Since soil is a continuous material, similar to the pile–soil–pile interaction problems for pile groups, force or deformation on one location of soil will induce additional soil deformation in other locations. This can be analyzed by various numerical methods using, for example, Mindlin’s equation [1032].

For pile foundations, displacements of the soil volume surrounding all pile nodes can be computed as the sum of forces times Mindlin interaction values for the node. This means that soil displacements at all pile nodes caused by forces applied to soil volume or soil surface are computed from elastic half-space theory, by using Mindlin’s formulae [1032]. Secant stiffnesses to be used between pile and soil are then computed from the expected relative displacement between pile and soil. The load–displacement of the piles under the influence of ground motion x_0 can be expressed as:

$$[K_p + C]x = [C]x_0 \quad (21.24)$$

where K_p , C , and x are the pile stiffness matrix, inverse of soil flexibility matrix, and pile displacement (along either vertical or lateral direction), respectively; the vector $[C]x_0$ represents the nodal forces acting on the piles induced by soil movements.

The equation above can be solved for the vertical and lateral soil movements induced by adjacent structures or construction activities, i.e., axial forces, shear forces, and bending moments can be obtained from the deflections and rotations.

21.8.2 Pile–Soil Interaction Influenced by the Presence of Spudcan

A particular offshore engineering issue is that when, for a jack-up unit (Fig. 21.14) installed in close proximity to a piled structure, soil displacements caused by spudcan (Fig. 21.15) penetration apply lateral loads to the nearby piles. The amount of soil displacement will mainly depend on the soil type, spudcan-pile spacing, spudcan size, and penetration [750]. Price and Jardine [785] stated that as axial loads can be significant if the jack-up is close to pile(s), a rule of thumb is that the distance between the edge of the pile group and the edge of the spudcan should be larger than the diameter of the spudcan. Furthermore, if the site is dominated by soft clays, the reverse problem due to the release of soil pressure caused by the removing of spudcan can also be significant.

Large soil displacements due to spudcan penetrations induce displacement controlled loading to adjacent piles. As Xie et al. [1060, 1061] explained in detail, the lateral pile response induced by spudcan penetration is much more severe than that of the axial pile response. Therefore, pile bending moment is one of the key parameters to evaluate pile behavior under the influence of spudcan penetrations. The pile response can be calculated by either coupled or uncoupled approach. In the coupled approach, pile and soil deformation are coupled in a linear or nonlinear

Fig. 21.14 Spudcans supporting three independent legs for a jack-up [1059]



finite element analysis. In the uncoupled approach, soil displacements are applied to the pile to determine the pile response, in which the soil displacements are calculated using finite element analysis at the pile location without modeling the pile. By studying pile responses using both coupled and uncoupled approaches, Arslan and Wong [1059] showed that, due to simplified assumptions in the uncoupled approach, pile bending moments predicted by it may be overly conservative, as indicated in Fig. 21.16.

Moreover, since the load–displacement due to pile–soil interaction is nonlinear, the stiffness of pile–soil interaction can change due to influences from spudcan. Subject to ocean wave or seismic loading, pile and soil response can alter due to changes in the stiffness.

As the spudcan penetration can induce extremely high soil strains, which can reach a level of 1000%, and also because the contact problem is involved between spudcan and surrounding soils, numerically, it is recommended to adopt the explicit method in the direct time integration [123]. This requires employing very small time increments and a large number of time steps. However, the method does not need the iteration and checking for solution convergence after every time step that is required by the implicit method.

Fig. 21.15 A spudcan in close proximity to a pile [1059]

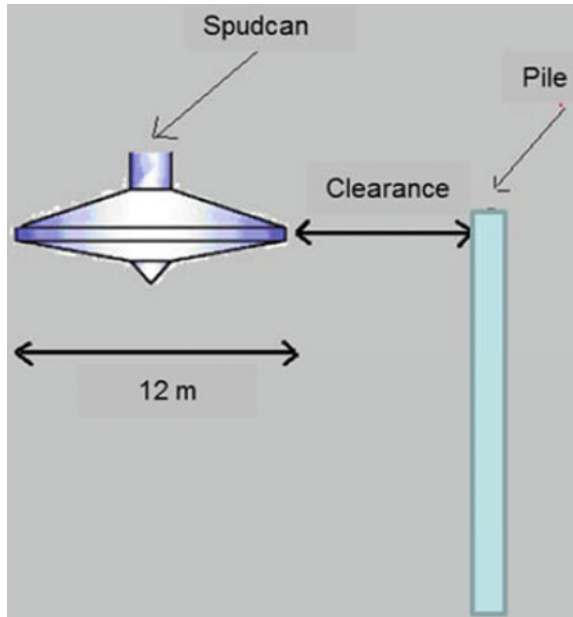
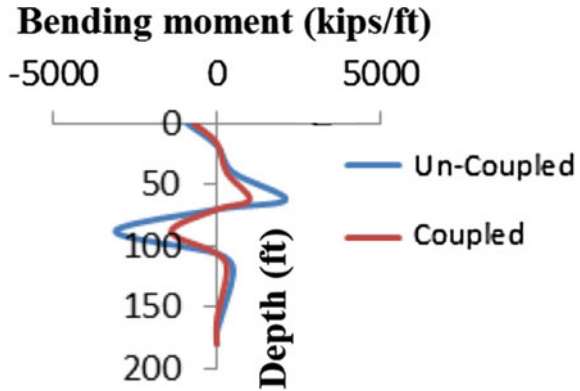


Fig. 21.16 A pile’s bending moment distribution along depth with a 1.5 m clearance (Fig. 21.15). The spudcan’s diameter and penetration are 12 and 18 m, respectively, and the pile has a diameter of 0.76 m [1059]



21.8.3 Influence of Pile–Soil Interaction Due to Construction Activities

It is important to characterize the influence of construction activities, including pile driving, pile installation by jacking drilling holes near existing piles, the excavation of the ground for pile cap construction, and deeper excavations near existing piles.

Poulos [1062] stated that parametric studies to identify the possible influence are normally time consuming and not ideally suitable. He further proposed an alternative approach including analysis in two distinct aspects: (1) an estimation of the

“free-field” soil movements that would occur if the pile(s) was not present; (2) calculations of the response of the pile(s) to these computed ground movements. Based on this alternative approach, he performed analyses for five cases of construction activities and concluded that construction activities caused ground movements that interact with existing pile foundations, thus inducing additional forces, moments, and deflections in these piles. Even though such effects may not be very significant in a “green-field” situation, where constructions are carried out in ground that is not stressed by existing loaded foundations, the effects can be notable where the existing piles carry significant amount of loads and, therefore, have stressed the ground in which the construction activities are carried out, such as the case when additional or remedial foundations are being installed adjacent to the existing pile foundation system. Among all the five cases studied, which all have potential to cause damage to the existing piles or to induce undesirable movements of the existing piles, pile driving or excavations have the most significant effects.

Tunnel excavation is associated inevitably with ground loss, which, in turn, results in associated ground movement. It is important to minimize ground loss when tunneling through urban areas. Loganathan [1063] presented a review of analysis methods to assess the tunneling-induced risks to adjacent structures. Xu and Poulos [1064] and Loganathan et al. [1065] employed a three-dimensional coupled boundary element approach to calculate responses of vertical piles subjected to ground movements induced by tunneling. Kitiyodom et al. [1066] proposed a simplified analytical method for the analysis of deformations and load distributions of pile foundations subjected to ground movements induced by tunneling. In their method, the flexible pile raft is modeled as thin plates, the pile is represented by elastic beams, and the soil is treated as interactive springs. The interaction between structural members, including pile–soil–pile interaction, pile–soil–raft interaction, and raft–soil–raft interaction, are calculated based on Mindlin’s solutions for both vertical and lateral forces.

Chapter 22

Grout Connections

22.1 Introduction

Foundations of offshore jacket structures, which are normally supported by piles, usually include pile clusters that are inserted through and connected to sleeves around the corner legs at the base of the structures, as shown Fig. 21.3. This ensures the transfer of loads from the upper structures to pile groups. In a pile sleeve, the pile grout connection (Fig. 22.1) connects the pile sleeve with each individual pile.

Moreover, Fig. 22.2 shows grout connection used to connect the substructure/tower to the monopile (single pile) foundation widely adopted for offshore wind turbine foundations. It is noted that during the grout casting process, no particular adhesion between the grout and steel surfaces can be achieved. The fixation of the pile and transition piece by means of grout is mainly obtained by the static friction due to the surface roughness of the contact areas [1067].

In recent years, failure accidents of pile grout connections for offshore jacket-, tripod-, and wind turbine supporting structures have been reported across the world. For example, in 2009, grouting failures were detected between the monopile and the transition piece on several monopile structures at Horns Rev I wind farm (constructed in 2002, including 80.2 MW wind turbines, considered the world's first commercial offshore wind farm) in the Danish waters of the North Sea. One reason for such failure was that the grouting connection was insufficiently engineered to enable the transfer of bending moment from the tower. This may partially be due to the fact that the grout connection of the monopile foundation is subject to a combined bending moment and shear forces, while the previous experience for the design of grout for offshore structures is mainly applied for the design of piles in a pile group, where the grout connection is mainly subject to axial loading.

As adequate structural health monitoring measures were not implemented for the majority of offshore structures, the grout failures were sometimes only detected (luckily) by observing excessive motions/vibrations at the associated topside structures than motions documented before the grout failure or than motions on

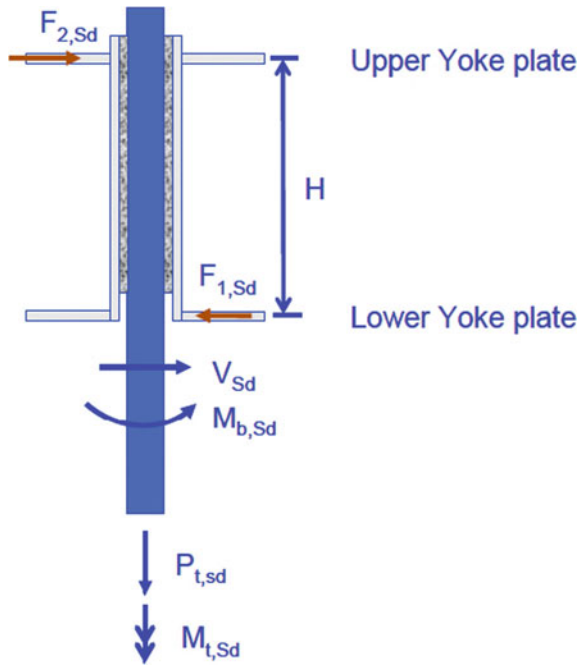


Fig. 22.1 Actions on a pile grout connecting a substructure with pile foundations (courtesy of Standard Norway)

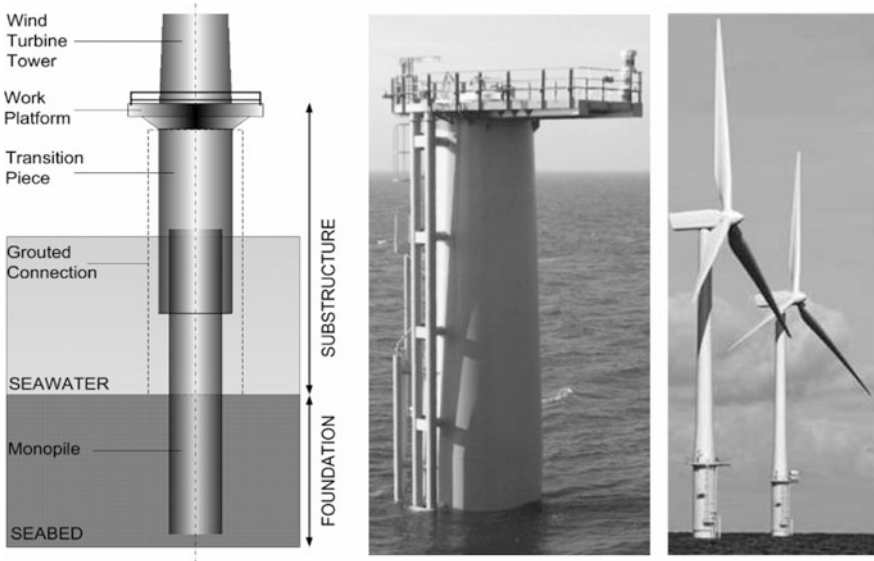


Fig. 22.2 Illustration of grout connection for connecting offshore wind turbine towers with monopile foundations (courtesy of Institute of Mechanical Engineering, Aalborg University)

similar offshore structures nearby in the same time period. This situation poses a significant threat to the safety offshore structures.

22.2 Grout Connection Capacity Control

The capacity control of grout connections is essential for ensuring structural integrity of offshore structures supported by pile foundations. This requires a thorough understanding of the load transfer and failure mechanisms of grout connections. Based on the recent knowledge regarding pile grout capacity, Norsok N-004 [1068] issued a pile grout connection capacity control (K.5) requirement that is generally more stringent than previous grout capacity control for offshore structures in the Norwegian continental shelf. It requires the check of grout capacity for 7 failure modes under the axial, shear, bending and torsional load actions, and it includes the control associated with ultimate limit states (ULS), accidental limit states (ALS), and fatigue limit states (FLS):

1. Mode 1: failure of the grout to pile connection due to interface shear from axial load (ULS, ALS).
2. Mode 2: failure of the grout to pile connection due to interface shear from torsional moment (ULS, ALS).
3. Mode 3: failure of the grout to pile connection due to combined axial and torsional shear (ULS, ALS).
4. Mode 4: check of compressive stresses at lower end of the grout due to bending moment and shear in the pile (ULS, ALS).
5. Mode 5: fatigue of the grouted connection for alternating interface shear stress due to axial load and bending moment in the pile (FLS).
6. Mode 6: fatigue of the grout due to compression and shear stresses at the lower end of the grout due to bending moment and shear force in the pile (FLS).
7. Mode 7: fatigue check due to torsion (FLS).

It is worth mentioning that, even though an offshore wind farm includes multiple or many structures with similar or almost identical structures, foundations and environmental loading, it is still possible to significantly reduce the project cost by dedicated individual designs for each foundation including the grout connections (expensive material cost).

22.3 Typical Mechanical Properties of Grout

The most widely used grout material in offshore wind turbine industry is DENSIT Ducorit[®] high performance concrete [1069], which currently has four different classes depending on the percentage of certain contents such as quartz sand or

	Ducorit® D4	Ducorit® S5	Ducorit® S2	Ducorit® S1
Mean compressive strength f_c [MPa/psi]	200 / 29,000	130 / 18,850	90 / 13,000	110 / 16,000
Static modulus of elasticity E_c [GPa/ksi]	70 / 10,000	55 / 8,000	40 / 5,800	35 / 5,000
Dynamic modulus of elasticity E_d [GPa/ksi]	88 / 12,800	60 / 8,700	50 / 7,250	37 / 5,400
Tension strength f_t [MPa/psi]	10 / 1,500	7 / 1,000	6 / 870	5 / 725
Flexural strength f_{bt}^* [MPa/psi]	23.5 / 3,400	18 / 2,600	-	13.5 / 2,000
Density ρ [kg/m ³]	2740	2440	2385	2250
Poisson's ratio ν	0.19	0.19	0.18	0.19
Fracture energy G_f^* [kN/m]	12	5.6	-	4.0
Consistence Class ¹⁾	-	F6 (>630mm)	-	-
Consistence Class ²⁾	a2	a1	a2	-
Compressive Strength class (EN 206-1)	>C100/115	C100/115	C70/85	-
Compressive Strength class (24h) ²⁾	Class A	Class A	Class B	Class A
Shrinkage ²⁾ $\epsilon_{s,m,91}$	SKVB I (0,413 ‰)	SKVB I (0,147 ‰)	SKVB I (0,576 ‰)	-
Shrinkage ²⁾ $\epsilon_{s,l,91}$	SKVB I (0,421 ‰)	SKVB I (0,165 ‰)	SKVB I (0,579 ‰)	-

Fig. 22.3 Mechanical properties of Ducorit® grout materials [1070]

bauxite: Ducorit® S1, Ducorit® S2, Ducorit® S5 and Ducorit® D4. Figure 22.3 presents mechanical properties (with minimum 28 days of curing at 20 °C) of Ducorit® grout materials. Their major mechanical properties are: mean compressive strength varying from 110 to 200 MPa; dynamic modulus of elasticity ranging from 37 to 88 GPa; static modulus of elasticity varying from 35 to 70 GPa; density varying from 2250 to 2740 kg/m³; and Poisson's ratio of 0.18 for Ducorit® S2 and 0.19 for the remaining three types.

The grout is pumpable up to several hundred meters through hoses. After 24 h of curing at 20 °C, the strength reaches approximately 25% of the long-term value. The development of modulus of elasticity (related to stiffness) is even more pronounced. The fatigue strength is also high and can be up to more than five times the strength of the normal concrete [1070].

Chapter 23

Vertical Piles Versus Inclined/Battered/Raked Piles

23.1 Introduction to Inclined/Battered Piles

Compared to vertical piles (Fig. 14.1), inclined/battered/raked piles (Fig. 14.7) generally have higher horizontal stiffness, mainly due to the fact that inclined piles provide partial horizontal resistance from their axial capacity, and the axial stiffness due to pile–soil interaction is normally higher than that along the lateral pile direction (perpendicular to the piles' axial direction).

Common batter (horizontal:vertical) of inclined piles varies from 1:12 to 5:12. When batter exceeds 3:12, special driving equipment may be required and hence may be very costly. A usual assumption in the design of battered piles is that they are capable of resisting the same axial load, as a vertical pile of the same type and size and driven into the same soil stratum [777].

23.2 Seismic Performance of Pile Groups with Battered Piles

Battered piles are mainly used when pile foundations are subjected to excessive horizontal loads. However, note that piles' ultimate capacity in pile's axial direction may in certain conditions be lower than that along the piles' lateral direction, as illustrated in Fig. 17.5, while the higher stiffness along the pile's axial direction can sometimes lead to a non-ductile foundation design. Battered piles should then be designed with caution especially regarding their seismic performance. The caution is even further emphasized due to the following facts:

1. As inclined piles tend to attract more horizontal seismic loading due to their higher horizontal stiffness than that of vertical piles, they can fail or reach their ultimate axial capacity before vertical piles (with similar dimensions as the inclined piles) are activated to take substantial lateral loads. Therefore, inclined

piles should not be used together with vertical piles unless the inclined piles alone have sufficient capacity [1071].

2. Inclined piles increase the horizontal stiffness of the structure compared to vertical piles, generally leading to a decreased natural period corresponding to the global bending vibrations of the structures, and the decrease in natural period is likely to increase the seismic response of the superstructure and the subsequent inertia forces and moments applied to the pile heads and cap from the superstructure.
3. Unless battered piles are designed for unreduced (elastic-level) seismic forces, or there is consideration of developing an inelastic mechanism, compression and/or shear failure is likely to occur, resulting from lateral movement, rotation and axial overload of the piles [1072].
4. There is a lack of understanding of coupled sliding–overturning system for inclined pile systems. This is because a foundation design usually considers sliding (lateral forces) and overturning (resulting in tension and compression on the piles) separately. However, sliding and overturning are coupled for the battered pile system.
5. There are concerns of vertical settlement and potential lateral spreading in soft or liquefiable soils (following an earthquake) and soil consolidation (before the earthquake) possibly increasing the lateral forces and moments on battered piles [1072].
6. Inclined piles can cause a possible reduction in bending moment capacity due to seismically induced tensile forces.
7. Undesirable permanent rotations of pile caps can occur when inclinations of the piles are not symmetric.

Due to the considerations above, and also due to the fact that beneficial or detrimental role of battered piles on seismic responses of structures and foundations is still not well understood, or at least well-engineered designs of raked piles are beyond the capability of the majority of structural and geotechnical engineers, several design codes discourage the use of inclined piles in areas with high seismicity, including the French Seismic Code (“Inclined piles should not be used to resist seismic loads”) [1073], Eurocode 8 (“It is recommended that no inclined piles be used for transmitting lateral loads to the soil. If, in any case, such piles are used, they must be designed to carry safely axial as well as bending loading”) [426] and NTC [1074]. Other codes such as IBC [1075] require that design forces of the inclined pile system be multiplied by an over-strength factor, because of the perceived and observed poor performance of the system.

Poor performance of inclined piles supporting wharfs and bridge abutments has also been reported [1076, 1077]. The investigations on actual causes of failure often revealed the inadequacy of the pile reinforcements, particularly at the head section, and the improperly designed connection of piles to the cap, as a consequence of early analysis methodologies, which treat piles as exclusively axial elements. Moreover, inclined piles may induce large forces on pile caps, and the high axial

force applied on piles may decrease the piles' capacity to resist bending moment [1078, 1079].

However, sound seismic performances of battered piles and benefits of using inclined piles have also been shown [1080, 1081, 1082, 1078, 1072, 1083, 1084, 1085, 1086]. Some of those studies argue that damages observed in past earthquakes may be attributed to design inadequacies rather than to intrinsic drawbacks of the inclined pile system.

Indeed, inclined pile systems have been re-established in their traditional role of withstanding large horizontal loads applied to deep foundations [1087]. A significant engineering example of its application is the design of piers for the new San Francisco Bay Bridge East Span (79 m wide bridge deck with 10 lanes) shown in Fig. 14.7, which lies on the San Andreas and Hayward faults at the interface between the North American and Pacific plates and is designed to resist an 8.5 moment magnitude of earthquake. For this, 160 battered piles were constructed with diameters and penetration depth up to 2.6–90 m, respectively.

By performing a series of analyses using code EMBankment Pile Group (EMPIG), Poulos [1088] studied the behavior of pile groups containing battered piles by adopting three load scenarios: (1) pile group subjected to vertical and lateral loadings, with no seismic ground motions; (2) pile group subjected to vertical and lateral loads, but with vertical ground motions also acting on the group; (3) pile group subjected to vertical and lateral loadings, but with horizontal ground motions of the group. Through investigating the calculated results, he concluded that, in general, if ground motions are not presented, it is beneficial to make the front piles in a group inclined, which can lead to a reduction in settlement, lateral deflection, cap rotation, vertical pile load, and pile head moment. However, in the presence of ground motions, the performance of a pile group with battered piles may be affected adversely compared to a group with only vertical piles. Especially, rotations and vertical movements of the group may change in sign and increase significantly in magnitude, and all the loads on the battered piles may increase.

Based on a substructuring model to obtain the impedance and kinematic interaction factors of the pile–superstructure system, Medina et al. [1086] investigated the influence of the rake/inclination angle of piles on the dynamic response of pile-supported structure, measured by the pile–structure system's vibration period and maximum based shear. They presented that an increase in the rake angle of battered piles generally leads to a reduction of the spectral acceleration (tested by 1940 El Centro earthquake acceleration records) of the supported structure. However, these reduction effects are less significant for slender superstructures. For short squat buildings, the pile–structure system's vibration period is reduced as the rake angle increases due to an increase in the horizontal stiffness. However, for slender tall structures, vibration periods generally increase with the increase in rake angle, due to a reduction of the rocking impedance, except for the case where the piles are closely spaced.

By considering 6 pile groups (2×1 group configuration) each with different pile batter angles ranging from 0° to 25° , and modeling each pile with a series of beam elements rigidly linked to the peripheral (soil) nodes using ABAQUS,

Giannakou et al. [1079] studied the seismic responses of the pile group by applying seismic acceleration time-histories on each pile. The responses measured by lateral pile head stiffness, the kinematic (due to exclusively horizontal shaking of soils, which is relative to inertia response; see Chaps 19 for descriptions of these) pile deformation and the inertial soil–pile–structure response were calculated. By investigating the results, they found that kinematic bending moments and axial forces increase with the increase in batter angles, which is also confirmed by a previous study by Poulos [1088]. However, when both kinematic and inertial loading are accounted for, the role of batter can be either quite beneficial or detrimental depending on the relation between shear force and overturning moment: (1) for tall slender structures, configurations with battered piles undergo smaller horizontal displacements than the group comprising vertical piles, but at the same time, they develop larger pile cap rotations, which are often out-of-phase with lateral displacements. The total bending moments on battered piles increase with the increase in batter angle. Therefore, proper reinforcements of the pile cap connection are required to resist this bending moment and securing adequate inelastic deformation in case of unpredictably large (exceeding the design) seismic motions. The lateral distortion (and drift) of a structure on batter piles is significantly smaller than that on vertical piles; (2) for a short squat structure, bending moments on battered piles are smaller than that of vertical piles, while the axial forces on the battered piles are higher; the horizontal drift of the superstructure is less sensitive to pile batter and batter angle.

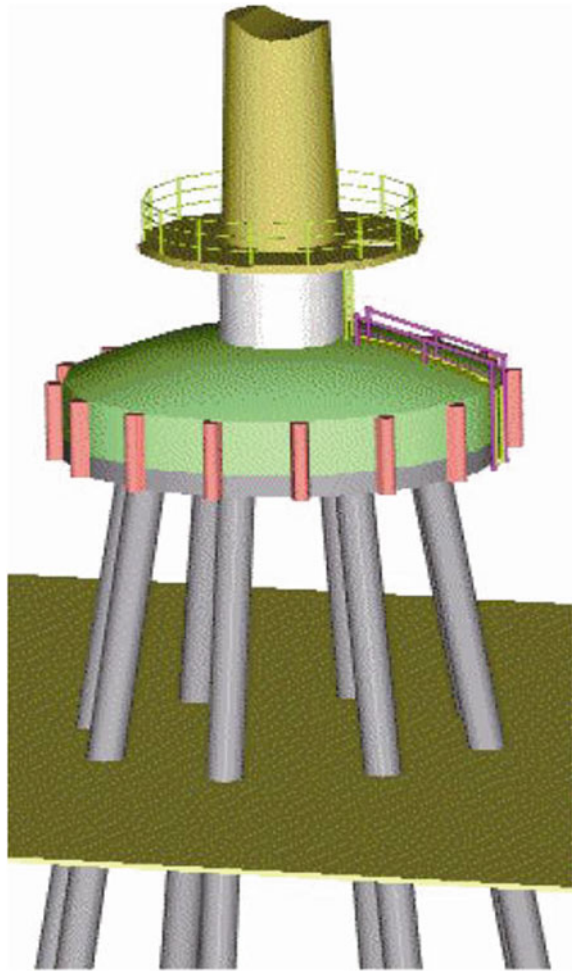
By studying a seismic design and a retrofitting design of a hospital and a library building, Moore [1072] presented that well-engineered battered piles provide a ductile system that is far superior to conventional shallow and deep foundation systems for resisting lateral and overturning forces and displacements. This is primarily due to the fact that they couple sliding and overturning forces, which, in turn, lead to a better lateral system behavior, and, if applied correctly, superior performance.

23.3 Wave- and Wind-Induced Response of Pile Group with Battered Piles

Pile group foundations with elevated piles are one of the most popular foundation types for bridges and large offshore wind turbines, in which piles in a group are often inclined as shown in Fig. 23.1. This type of pile system has a sound performance to resist both the horizontal ocean wave and current loading as well as to carry heavy vertical loads. In fact, piles supporting many offshore jacket structures are slightly inclined.

Figure 23.2 shows a pile group comprising eight inclined steel piles (pile diameter: 1.8 m, length: 61 m, pile wall thickness: 28 mm), and the applied loads (caused by wave and wind loading and the self-weight of structure and wind

Fig. 23.1 An illustration of high-rise pile cap foundation comprising a pile group with elevated battered piles [1089]



turbine) on the top of the pile group [1090]. They are built to support offshore wind turbine substructures for 3 MW wind turbines. The profile of soils below the mudline is first a 35 m of sand with $\phi' = 36^\circ$ (the majority pile length is within this soil layer), followed by a 6 m clay with $s_u = 15$ kPa, below the clay, there is a 30 m of sand layer with $\phi' = 33^\circ$. By varying the slope (horizontal: vertical) of the inclined piles from 1:5, 1:7 to 1:10, the calculated horizontal displacement at both the mudline and the top of the pile group influenced by the pile slope and diameter is shown in Fig. 23.3. It is clearly shown that with the increase in batter angle and diameter, the horizontal displacement decreases. By observing Fig. 23.4 that shows the maximum forces on piles influenced by the pile slope and diameter, it is noticed that while the increase in pile slope can significantly decrease the forces on piles, the increase in pile diameter has much less influence in reducing the axial pile

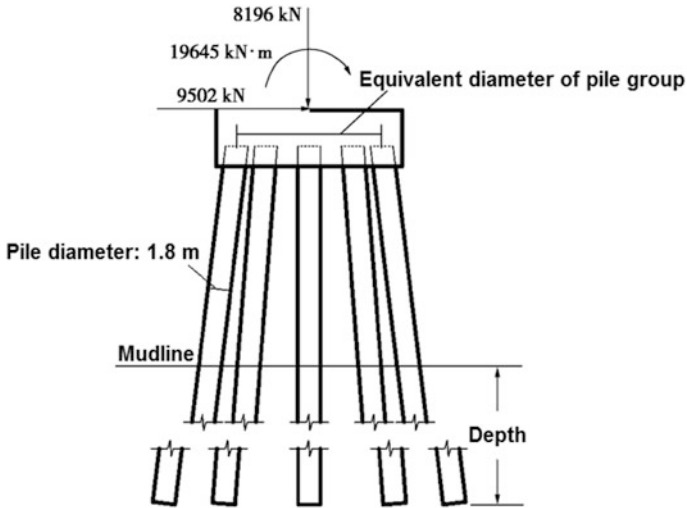


Fig. 23.2 An illustration of a pile group comprising eight inclined elevated steel piles and the applied loads on the top of the pile cap [1090]

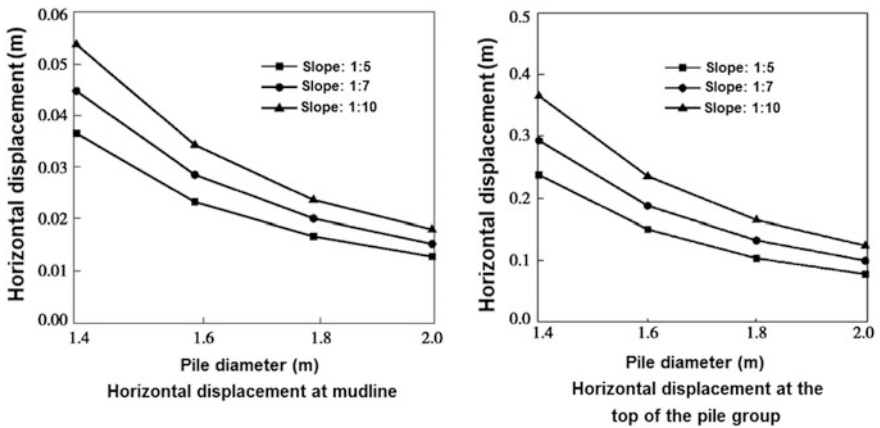


Fig. 23.3 Horizontal displacement at the mudline (left) and the top (right) of the pile group varying with both slope and the pile diameter [1090]

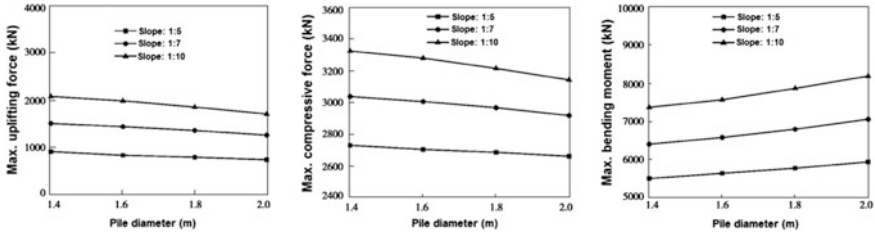


Fig. 23.4 Maximum uplifting force (left), compressive force (middle), and bending moment (right) among all eight inclined piles [1090]

forces in both compression and tension. Moreover, the bending moment even increases with the increase of pile diameter. Therefore, in order to reduce the pile forces, it is normally more efficient to increase the pile slope rather than to increase the pile cross-sectional area.

Chapter 24

Negative (Downward) Friction and Upward Movement

24.1 Negative Friction

If a clay layer(s) is located above or beneath sands, the consolidation process in the clay will introduce a downward drag force, which will apply on piles. Moreover, if the water table is lowered so that an increase of vertical effective stress occurs in soils, the consolidation in the clay will induce settlement, which will also introduce a downward drag force on a pile. In addition, placing fills on compressible soil can also cause soil layer(s) to consolidate. The causes above are illustrated in Figs. 24.1 and 24.2.

The net effect of the negative friction is to increase the axial loading on piles, and its severity depends on the interaction of skin friction in the settling soil, the type of soil layering, and the characteristics of the bearing strata [33].

It is recognized that a 15 cm downward movement is sufficient to mobilize the full negative skin friction. However, in general, rather than affecting the ultimate pile–soil interaction capacity, the negative friction can increase the stress on piles and pile cap. The deleterious effects also arise from an increased settlement and axial force in piles, which can influence structural integrity [1092]. Moreover, the effects of negative skin friction may even increase the pile capacity due to a change in location of the transition from negative to positive pile–soil friction force direction, where the pile and the soil move equally. This location is sometimes referred to as the neutral plane. A pile that experiences no negative skin friction has a neutral plane at the ground surface, i.e., the foundation settles with the settling ground surface, often resulting in undesirable situations for pile capacity control [1093].

On the other hand, in some cases, the downward friction force is sufficiently significant to cause the failure of the foundation. Figure 24.3 shows the mechanics of the negative friction on a pile. It is clearly observed that the axial load (Q_{\max}) on the pile at a certain depth range is even larger than the axial loading (Q_{Top}) applied on the pile head.

Fig. 24.1 Down-drag situation due to fill weight [1052, 1091]

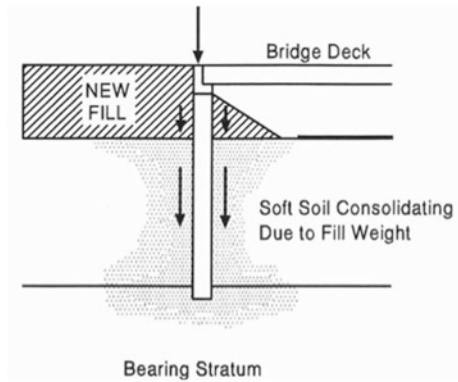


Fig. 24.2 Down-drag situation [1052]

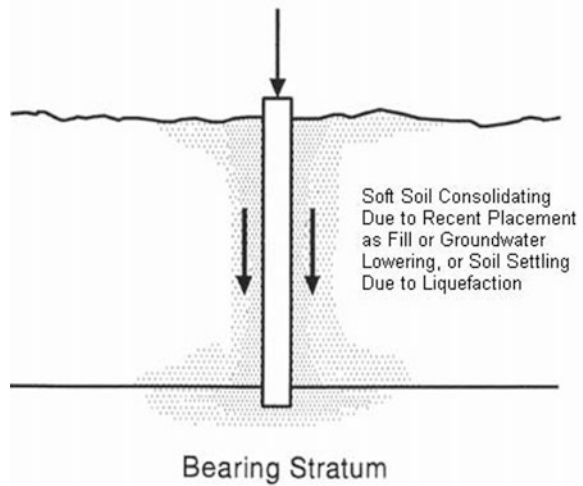
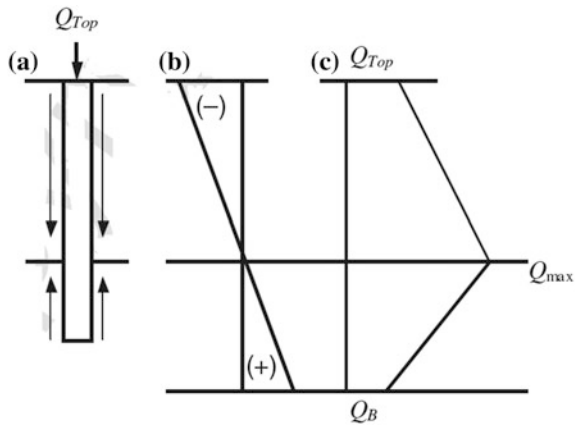


Fig. 24.3 Illustrations of negative friction: **a** example problem; **b** movement of the pile relative to soils; **c** distribution of the pile's axial load [33]



AASHTO [1052] states that possible development of down-drag on piles or shafts shall be evaluated where:

1. Sites are underlain by compressible material such as clays, silts, or organic soils.
2. Fill will be or has recently been placed adjacent to the piles or shafts, such as the case for bridge approach fills.
3. The groundwater is substantially lowered.
4. Liquefaction of loose sandy soil can occur.

The estimation of negative skin friction loads is different for a single pile and a pile group. For a single pile, the load is equal to unit friction resistance (downward) \times length of the pile above bottom of the compressible layer \times perimeter of the pile cross section. For pile group with closely spaced piles, in case no relative movement between individual piles and surrounding soils is assumed to occur, the downward force is equal to the weight of the soil block held between piles + weight of the piles and pile caps + downward drag along the pile group perimeter due to negative skin friction. For more details, readers may read AASHTO code [1052].

The negative friction F_n can be calculated using α -method based on the total stress approach, in which a reduction factor α is employed:

$$F_n = \alpha s_u \quad (24.1)$$

See Sect. 17.4 for a description of the parameters in the equation above. This method can be wisely used if the actual undrained shear strength of soils is known. However, it is understood that the undrained shear strength of soils changes in conjunction with the time and construction condition. Therefore, the concept of this method limits the ability to calculate the final or maximum drag load, unless the future undrained shear strength after consolidation has been predicted or investigated [1094].

The negative skin friction can also be calculated using β -method based on the effective stress analysis:

$$F_n = [\tan(\delta) / \tan(\phi')] K \sigma'_{vo} \tan(\phi') = \beta \sigma'_{vo} \quad (24.2)$$

where K is the lateral earth pressure coefficient (ratio of horizontal to vertical normal effective stress) in the soil. Descriptions of other parameters in the equation above can be found in Sect. 17.4.5.

Bjerrum et al. [1095] suggested that β -value ranges from 0.20 to 0.25 for soft silty clay. Bjerin [1096] recommended a β -value between 0.20 and 0.25 for clay with firm to medium consistency. Garlanger [1097] suggested $\beta = 0.20$ – 0.25 , while Burland [872] proposed to use 0.25. More recent centrifuge results performed by Leung et al. [1098] suggest a β -value of 0.25, which is also recommended by Craig [26] as a reasonable upper limit for normally consolidated clays.

A reduction in effective overburden pressure adjacent to the pile in the bearing stratum will occur due to the transfer of part of the overlying soil weight to the pile:

If the bearing stratum is dominated by sands, this will result in a reduction in bearing capacity above the critical depth.

Negative skin friction on a pile may be reduced by putting bitumen or asphalt on the pile surface. Usually, a proprietary system should be used. Extreme care should be taken to avoid damage to the coating. It may be necessary to demonstrate by site trials that the coating will not be damaged during the pile installation. Other details, such as the use of a double skin permanent liner infilled with inert flexible materials, may also be considered to reduce or eliminate negative skin friction [1099].

24.2 Upward Movement

Due to the variation of the moisture content of soils from dry to wet condition, expansive clays where rainfall varies significantly from one year to another may have a significant shrink-swell potential with plasticity index above 35%. This may cause an upward movement of piles due to the expansive uplift (see source [33] for details).

Chapter 25

Anchor Piles

25.1 Introduction

Anchor piles can transfer both compressive and tensile forces as well as bending moments to the ground, making them ideal as anchors for offshore moorings, basements, and tunnels, etc.

Moored floating offshore structures impose a variety of load conditions on the anchor system. These loads range from vertical uplift loads for a tension leg platform (TLP) to horizontal loads on a catenary mooring line such as the one used for a floating production system. Part of the load is sustained, such as a pretension in TLP tendons, while environmental components tend to be cyclic with a range of periods. In a catenary mooring system (left figure of Fig. 25.1), the anchor line is laid along the seabed, thus imposing large horizontal loads on the anchors, and the anchoring force provided to the floating structure includes the weight the mooring line, the friction of mooring line with seabed, the frictional resistance from the soil on the embedded part of the anchor line, as well as the pull-out resistance of the anchor itself. For a taut mooring system (right figure in Fig. 25.1), typically used for the mooring system for single point anchor reservoir (SPAR) platforms or vertical mooring system for TLPs, the anchor line rises from the seabed without passing along the seafloor, and the load inclination in the mooring system varies from horizontal to vertical. Therefore, the major difference between a catenary mooring and a taut mooring is that the catenary mooring arrives at the seabed almost horizontally, while the taut mooring arrives at the seabed at an angle. This means that in a taut leg mooring the anchor point needs to be capable of resisting both horizontal and vertical forces, while in a catenary mooring the anchor point is mainly subjected to horizontal forces. Moreover, in a catenary mooring, most of the restoring forces are generated by the weight of the mooring line, and while in a taut mooring, the restoring forces are generated by the elasticity of the mooring line.

Both catenary and taut mooring system generally consist of three parts: fore-runner (anchor line segment being embedded in the soil), middle line, and top line.

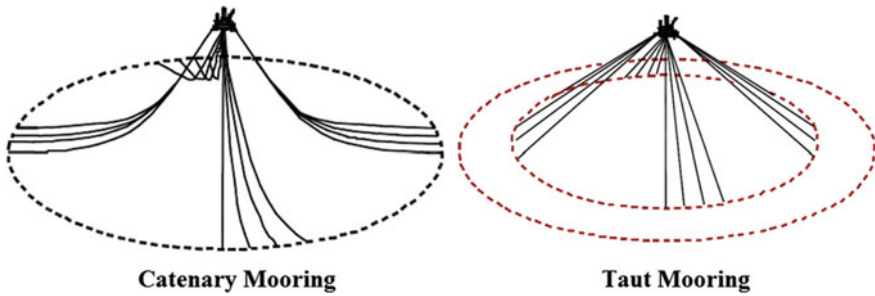


Fig. 25.1 Catenary and Taut mooring system [1100]

Depending on the mooring system requirements, the type of line for each part may be different [1100].

An anchor system is normally required to provide resistance with both cyclic and static loading components for mooring system of floating structures such as FPSOs, TLPs, or floating bridges. The system consists of an anchor line which is also named as forerunner and the anchor connection as shown in Fig. 25.2. Table 25.1 shows typical components for both catenary and taut mooring system. The forerunner is normally either a chain or a wire embedded into soils to connect the anchor connection as shown in Fig. 25.2. And an anchor with a wire forerunner usually penetrates deeper than the same anchor with a chain forerunner.

A number of anchor concepts are available, including conventional driven anchor piles (Fig. 25.2), the drag (embedment) anchor (Fig. 25.3), suction anchor piles (Fig. 26.2), as well as hybrids such as the suction embedded plate anchor (SEPLA).

A drag anchor, as shown in Fig. 25.3, penetrates into the seabed, as it is dragged horizontally with wire or chain to generate a required capacity. A drag anchor can develop typical holding capacity of 5–55 times its self-weight. The holding capacity

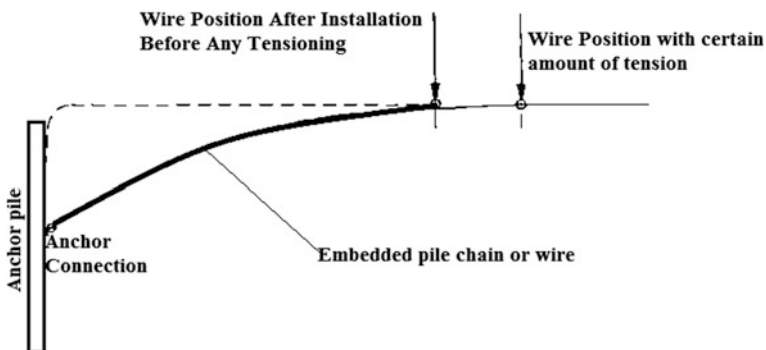


Fig. 25.2 Layout for a typical anchor pile

Table 25.1 Typical components of mooring system [1100]

	Mooring system	
	Catenary mooring system	Taut leg mooring system
Anchor type	Drag embedment anchor	Vertically loaded anchor
Forerunner	Chain	Wire
Middle part/line	Steel cable	Polyester cable
Top part/line	Chain	Chain



Fig. 25.3 Drag anchors

of a drag anchor is mobilized primarily by bearing resistance and side resistance on the anchor and friction along the embedded portion of the mooring line.

25.2 Behavior of Anchor Lines

25.2.1 Behavior of Anchor Lines on Seabed

For the anchor line laid on the seabed with cohesive soil, the resistance due to seabed friction can be calculated as:

$$\Delta R_{fric} = f \cdot L_s = \mu \cdot W'_1 \cdot L_s \tag{25.1}$$

where f is the unit friction that is of cohesive nature; L_s is the line length on seabed under the characteristic line tension; μ is the coefficient of seabed friction (see Table 25.2 for its values recommended by DnV-GL [1101]), which includes lower-bound, default, and upper-bound values for performing sensitivity analyses so that conservative results can be reached; W'_1 is the submerged weight of the anchor line per unit length.

Table 25.2 Coefficient of seabed friction [1101]

Wire	Lower bound	Default value	Upper bound
μ	0.1	0.2	0.3
Chain	Lower bound	Default value	Upper bound
μ	0.6	0.7	0.8

25.2.2 Behavior of Buried Anchor Lines

The soil resistance along the length of a buried anchor line can be a significant portion of the overall anchoring resistance. Through the soil, forces on the anchor line are reduced and the direction of forces is altered to certain extent. As the line is tensioned up, it cuts through the soil in a quasi-inverse catenary shape. The soil resists the line by bearing (normal load q) and shear (tangential load f) as shown in Fig. 25.4. The loss in line tension dT over one element length ds is calculated by [1102]:

$$\frac{dT}{ds} = -f \cdot AS - W'_i \sin \theta \tag{25.2}$$

where T is the anchor line tension load; θ is the anchor line angle relative to the horizontal direction; ds is the element length; AS is the effective surface of the anchor line per unit length, its value can be taken from Table 25.3; f is the unit friction along the anchor line, in cohesive soils, f can be calculated as:

$$f = \alpha \cdot s_u \tag{25.3}$$

where α is the adhesion factor of anchor lines, which can be checked from Table 25.4; s_u is the undrained shear strength (direct simple shear strength s_{uD} is recommended)

The angular advance from one anchor line element to the next is then conveniently solved by iterations from the following equation (only valid for small ds and θ):

$$\frac{d\theta}{ds} = \frac{q \cdot AB - W'_i \cos \theta}{T} \tag{25.4}$$

Fig. 25.4 Equilibrium of an anchor line segment embedded in soils [1102]

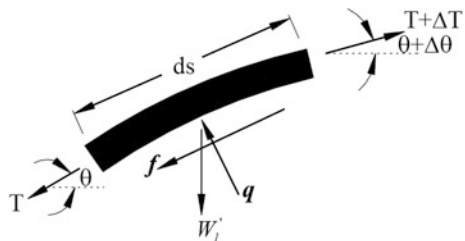


Table 25.3 Effective surface (AS) and bearing area (AB) [1101]

Type of forerunner	AS (m ² /m)	AB (m ² /m)
Chain	11.3·d	2.5d
Wire or rope	π·d	d

d is the nominal diameter of the chain and the actual diameter of the wire or rope

Table 25.4 Values of adhesion factor α [1101]

Wire	Lower bound	Default value	Upper bound
α	0.2	0.3	0.4
Chain	Lower bound	Default value	Upper bound
α	0.4	0.5	0.6

where AB is the effective bearing area per unit length of the anchor line, its value can be taken from Table 25.3; q is the normal stress; in cohesive soils, it can be calculated as:

$$q = N_c \cdot s_u \tag{25.5}$$

where N_c is a bearing capacity factor, which can be checked from Table 25.5.

For non-cohesive soils, readers may refer to DNV Classification Notes 30.4 [715] for general guidance on bearing capacity formulas.

By applying three wire loading conditions at the mudline (Fig. 25.2) to represent three critical mooring load cases of a semi-submersible floating structure, including intact condition (7410 kN with a wire angle of 0.9° above the horizontal direction), single line failure case (SLF, 9185 kN with a wire angle of 3.8° above the horizontal direction), and double line failure (DLF, 9720 kN with a wire angle of 3.3° above the horizontal direction), Figs. 25.5 and 25.6 show the variation trend of tension force and mooring line angle as a function of adhesion factor and bearing capacity factor N_c. The wire has a bearing diameter d = 0.173 m, by checking Table 25.3, AB = 0.173 m²/m, and AS = 0.544 m²/m, and the weight of the wire is 0.923 kN/m. The padeye is located at a depth 24 m below the mudline. It is observed from Figs. 25.5 and 25.6 that, when the adhesion factor and bearing capacity factor are within a reasonable range, the adhesion factor has more influence on the variation in tension load, while the bearing capacity factor is more influential on the variation of anchor line angle at padeye.

Since no restoring forces on the mooring line are assumed after a storm, the pretension loads at the anchor line embedded in soils can normally be assumed to be equal to a similar magnitude of tension load caused by a storm event with a return period between 10 and 1000 years.

Table 25.5 The bearing capacity factor N_c [1101]

Wire/Chain	Lower bound	Default value	Upper bound
N _c	9	11.5	14

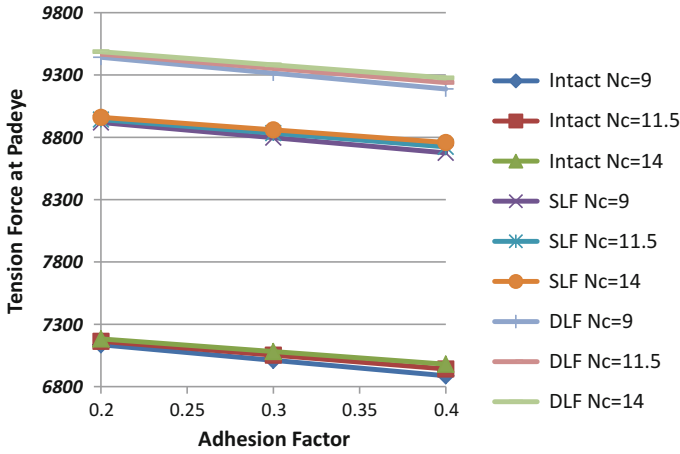


Fig. 25.5 Tension force varied with the variation in adhesion factor α and N_c

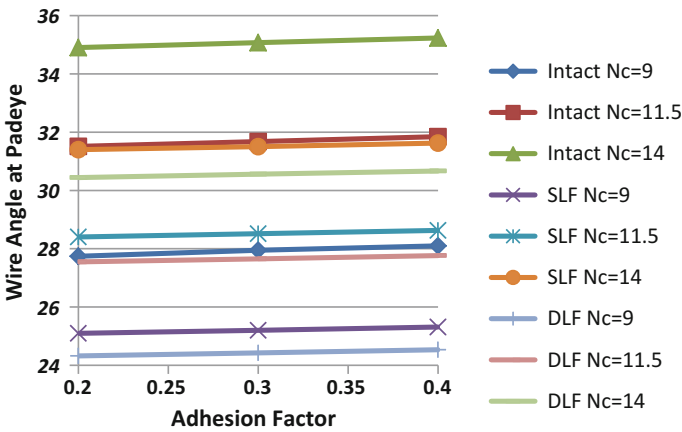


Fig. 25.6 Anchor line angle at padeye varied with the variation in adhesion factor α and bearing capacity factor N_c

25.3 Anchor Pile Padeye(s)

The connection between the anchor chain/wire and the anchor pile typically consists of padeye(s) as shown in Fig. 25.7. A pin with horseshoe locking device connects the link plate to the padeyes. To centralize the link plate between the two padeyes, typically a bulb at each side at the inner end is designed. The link plate is connected at the outer end to a socket that is the termination of the anchor segment of the anchor line.

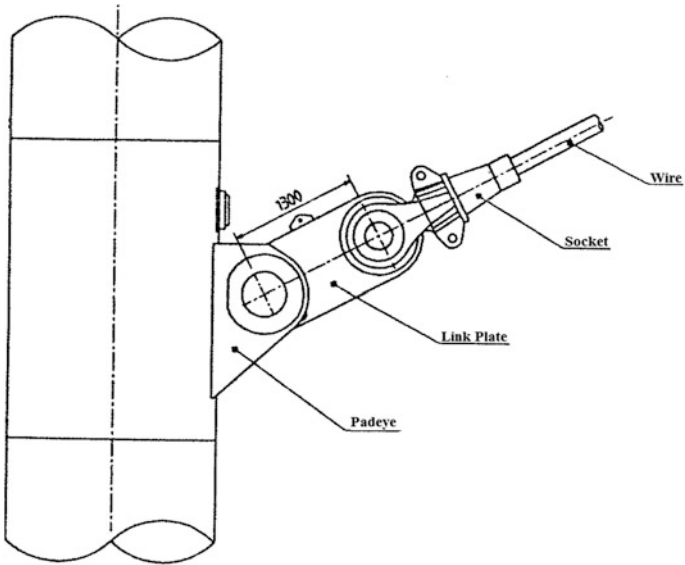


Fig. 25.7 Illustration of a typical anchor connection

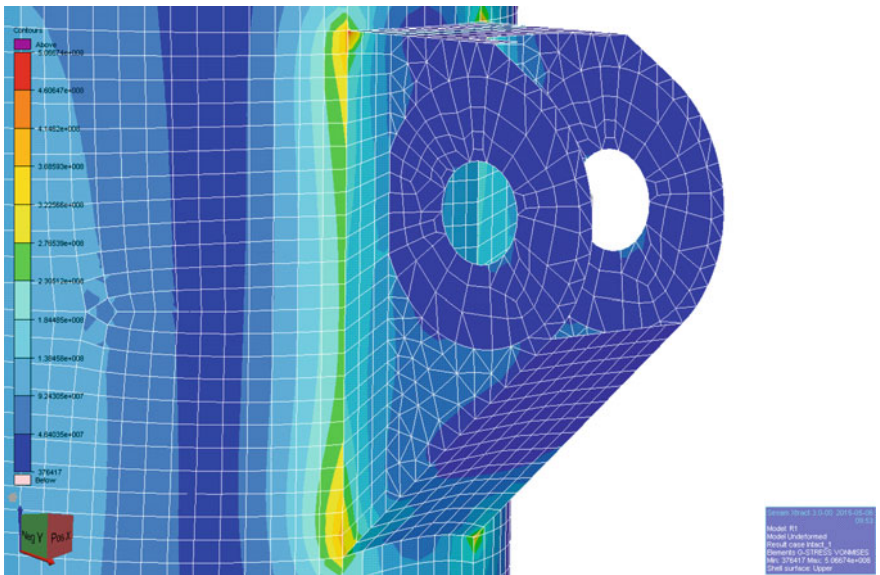


Fig. 25.8 von Mises stress (Pa) distribution for the local pile and padeye connection subjected to the intact mooring load at padeye (courtesy of Aker Solutions)

Figure 25.8 shows an example of stress distribution for a local pile and padeye connection due to the maximum mooring load under intact condition (Figs. 25.5 and 25.6) at the padeye.

Calculations for anchoring systems are described in API-RP-2SK [1103]. It is noticed that the design of the anchor pile can be similar to that of a single pile, based on the check of soil resistance (the pile's axial capacity and lateral soil pressure capacity) and the capacity of the pile itself, and the capacity check for the anchor connection.

25.4 Seismic Response of Anchor Pile

For the seismic design of an anchor pile, the kinematic interaction (Fig. 19.2) due to seismic motions at various depths is the only dominating action effect. This is because the probability for the simultaneous occurrence of both significant earthquake and other loading (e.g., ocean wave loading) is extremely low. Moreover, for areas with moderate seismicity, it is unlikely that earthquake action will be the governing load for anchor pile design.

25.5 Required Safety Factors for Offshore Anchor Pile Design

The minimum requirements for safety factors for anchor piles specified in ISO 19901-7 [1104] are shown in Table 25.6, which adopt a collective factor of safety to include both the material and load factor. These safety factors are equal to API-2SK [1103] requirements for suction, pile, and gravity anchors. It is noticed that the use of the collective factor of safety is similar to what has been adopted in an allowable stress design (ASD) method rather than in a load resistance factor design (LRFD) method (Sect. 1.13). This is mainly due to the fact that the separation of load categories associated with both mooring line and anchor line loads to which different partial safety factors could be applied is not straightforward. However, this could bring a conceptual challenge when the design is calibrated by the probability of failure, as uncertainties associated with load and resistance in this case are incorporated implicitly. See Sect. 1.13 for a discussion of this issue.

It is worth mentioning that other codes and standards, and some energy companies, specify different safety factors for anchor pile designs. See Chap. 27 for a brief presentation.

Table 25.6 ULS design safety factors for anchor piles of floating offshore structures

Analysis condition ^a	Permanent mooring		Mobile mooring	
	Axial	Lateral	Axial	Lateral
Intact	2.00	1.60	1.50	1.20
Redundancy	1.50	1.20	1.20	1.00

^aIntact condition means that none of the mooring lines fails; redundancy condition means that at least one mooring line fails

25.6 Fatigue Capacity Control of Anchor Line–Pile Connection

25.6.1 Method

Subjected to cyclic/repeated loading, a component can reach premature failure or damage well below the yielding stress of the component material, known as fatigue. This is because small crack-like defects exist and when they are subject to a sufficiently large cyclic tension stress, they will grow in size and eventually cause the member to reach fatigue failure. The cracks are developed in four stages:

1. Crack initiation (usually starts from the surface and can be detected by common technical means, e.g., 1 mm in length and 0.5 mm in depth).
2. Stable crack growth.
3. Unstable crack growth (rupture).
4. Ultimate ductile failure.

The connection (such as a padeye shown in Fig. 25.7) between the anchor line and anchor pile can sometimes be critical in terms of fatigue damage. Different methods can be used for performing fatigue assessment of those connections, such as the stress-based approach, fracture mechanics, or strain-based approach (for low cycle fatigue assessment associated with the development of plastic strain). Among these, the stress-based fatigue assessment approach is the most commonly used one due to its convenience and accuracy for assessing high cycle fatigue damage. The analysis can be carried out based on time domain, frequency domain (spectrum based) analysis, or a simplified fatigue assessment method (through a proper assumption of long-term probability distribution of stress responses). For details of those methods, see Jia [123].

The material performance is typically characterized by the S–N curve (Wöhler curve) or T–N curve, which defines the log-linear dependence between predicted number of cycles to failure N and a force range T or a stress range S as shown in Figs. 25.9 and 25.10.

It is quite often the case that, before a fatigue assessment of anchor piles, a fatigue analysis of the associated mooring line above the seabed is already performed. It would then be quite convenient to establish a relationship between

mooring line fatigue damage and fatigue damage for the anchor line–pile connection, which is based on the following information:

1. The properties of the T–N curves for mooring line versus S–N curve for anchor line–pile connection, with examples shown in Figs. 25.9 and 25.10.
2. Calculated hot-spot stresses, e.g., the hot-spot stresses of the welds on the anchor line–pile connection or welds between the connection and the pile.
3. Mooring line properties.

The relationship between the fatigue damage at hot-spot locations of welds on the anchor line–pile connection and at the mooring line can be approximated as:

$$f = [(\Delta\sigma_h|_{\Delta F_{wire}}/\Delta F_{wire}) (T_{wire|N=N'}/S_{|N=N'})]^m \tag{25.6}$$

$\Delta\sigma_h|_{\Delta F_{wire}}$ is the hot-spot stress range at the welds under study when the force range at the connection is ΔF_{wire} .

$T_{wire|N=N'}$ is the force at T–N curve when the number of force cycles $N = N'$; m is inverse slope of the S–N and T–N curve when the number of force cycles is N' .

For example, for stud-linked chain, from Table 25.7, one obtains fatigue parameters $M = 3$ and $K = 1000$. By inserting values of these two fatigue parameters into the equation for the T–N curve, one obtains:

$$NR^M = K \tag{25.7}$$

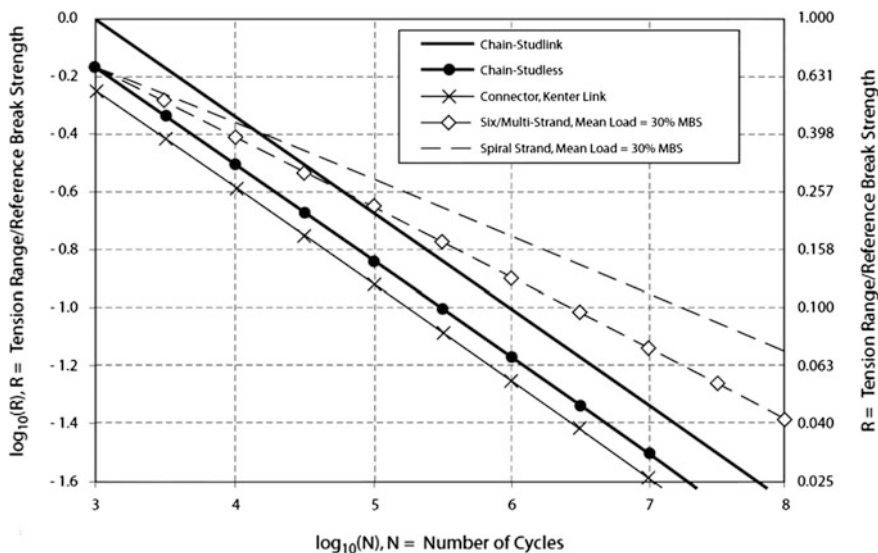


Fig. 25.9 Illustration of T–N curves for mooring fatigue design [1103]

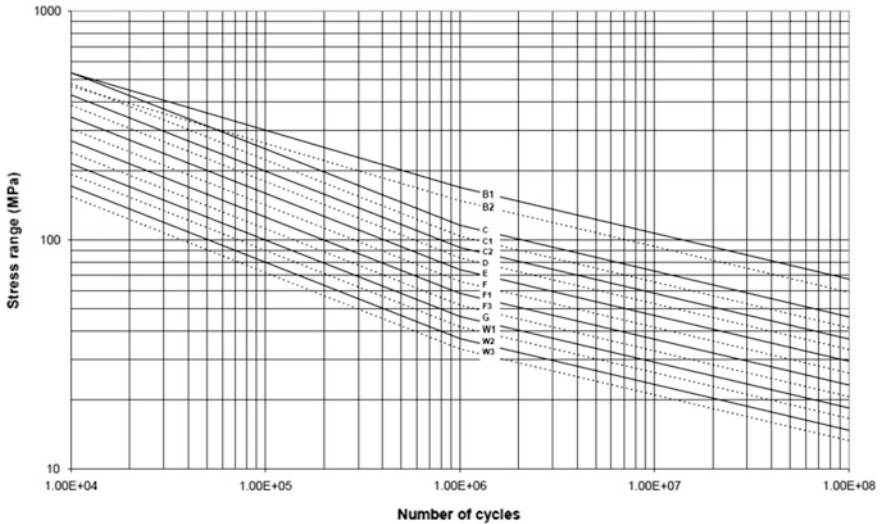


Fig. 25.10 Illustration of S–N curves for anchor line–pile connection design [1107]

Here, N is the number of cycles; R is the ratio of tension range to reference breaking strength; and M and K are the fatigue parameters listed in Table 25.7.

With, for example $N = 10^6$, the equation above gives $R = 0.1$.

$S_{|N=N'}$ is the stress at S–N curve for the number of stress cycles $N = N'$. For example, using the S–N D curve show in Fig. 25.10, the stress range corresponding to $N = 10^6$ is 83 MPa.

Once f is established, the fatigue damage can be estimated based on the fatigue damage already determined for mooring line analysis.

It is noted that the validity of this methodology depends on the following assumptions:

1. The fatigue damage is independent from the mean load of the bottom anchor line at seabed.
2. The force range applied on the padeye is equal to the force range on the bottom anchor line at the mudline.

Table 25.7 T–N curve data [1103]

Line component	M	K
Stud-linked chain	3.00	1000
Spiral strand wire	5.05	$10^{(3.25-3.43L_m)}$

25.6.2 Derivation of Hot-Spot Stress

Here, the hot-spot stress, also known as structural stress or geometric stress, is an engineering (rather than a physical) definition of stress measures shown in Fig. 25.11. It includes nominal stresses and stresses due to structural discontinuities and the presence of attachments, i.e., it contains the stress increase due to the structure geometry, but not the nonlinear stress peak due to the local weld geometry (which usually refers to the weld toe), which is implicitly accounted for in the hot-spot stress method by degrading the relevant S–N curve. This is because singularities at the weld toe are difficult to predict with a reasonable accuracy even by using FE modelling [1108, 1109]. The relationship between the hot-spot stress (σ_{ht}) and the nominal stress (σ_{nom}) is:

$$\sigma_{ht} = K_g \sigma_{nom} \quad (25.8)$$

where K_g is the structural/geometric stress concentration factor.

Therefore, unlike the nominal stress method [123], in the hot-spot stress method, a unique structural class for each joint type is not required, leading to a decrease in the number of joint classes and a reduced number of S–N curves needed. The relevant S–N curves that are linked to the hot-spot methods can be found from various design codes and recommendations such as DNVGL-RP-0005 [1107] for offshore structures, and IIW [1110] for air environments. In addition, misalignment of plates at welded connections and weld imperfections can also be roughly taken into account by suitable stress magnification factors from relevant design codes and recommended practices.

When deriving hot-spot stress using finite element analysis, it is strongly recommended to read the stress values at the element integration points rather than the element nodes, as the nodal stress is normally taken as the average of two elements located on both sides of the weld toe normal. If the element size is $t \times t$ (t is the thickness of the modeled plate close to welds), for shell or plate elements, the

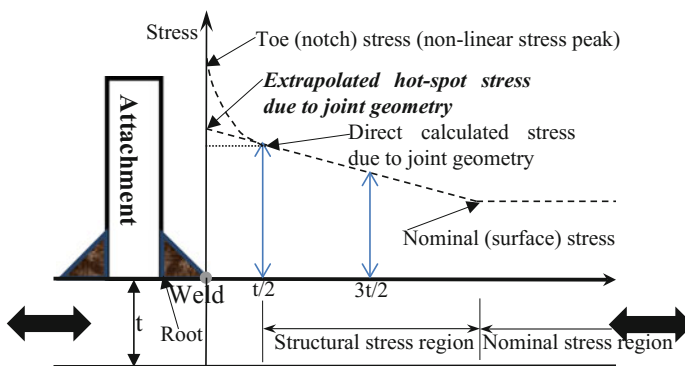


Fig. 25.11 Derivation of hot-spot stress and its relation with nominal and notch stress [123]

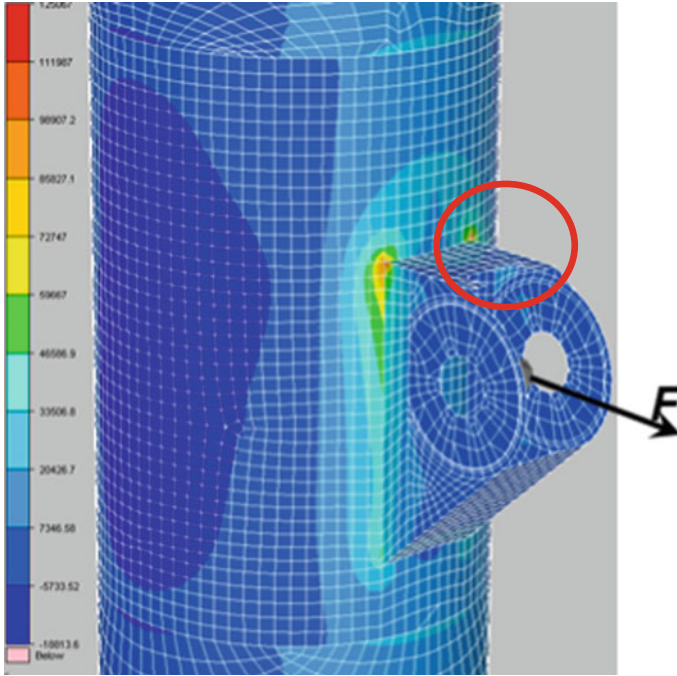


Fig. 25.12 A padeye connection subjected to a unit horizontal force (courtesy of Aker Solutions)

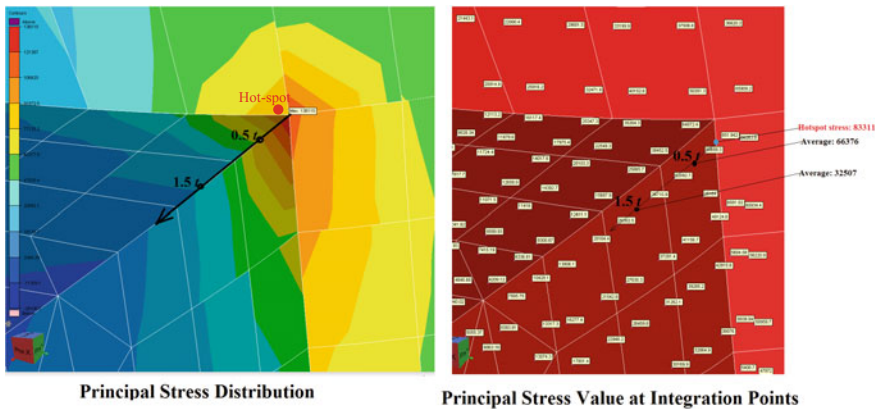


Fig. 25.13 An example illustrating the derivation of hot-spot stress by reading principle stress values at element integration points at a distance of $1.5t$ and $0.5t$ from the hot-spot location

surface stress may also be evaluated at the corresponding mid-side points; for solid elements, the stress may first be extrapolated from the integration points to the surface. These stresses can then be interpolated linearly to the surface center or be

extrapolated to the edge of the elements. Figure 25.13 gives an example of how to derive the hot-spot stress (using the method shown in Fig. 25.11) for a padeye connection subjected to a unit horizontal force shown in Fig. 25.12; the principal stress values read from shell element integration points at 1.5t (32,507 Pa) and 0.5t (66,376 Pa) from the hot-spot location, are extrapolated to the welds (hot-spot), resulting in a hot-spot stress of 83,311 Pa.

Chapter 26

Suction Piles/Caissons

26.1 Introduction

A suction pile is a foundation embedded into the sediment at seafloors through either pushing due to the weight of the pile and its associated mass, or creating a negative pressure inside the suction pile. Both of these techniques enable the pile to penetrate into the seabed and to finally reach a desirable penetration depth. Actually, “suction” is a reference to both the negative pressure created within the pile during the installation process, and the passive reduction of pressure mobilized during uplift [1111].

Suction piles can be categorized as a slender suction pile if the length to diameter ratio is large, which is mainly used for mooring applications, suction caisson (bucket foundation) if the ratio is close to or less than 1, or suction anchor if it is used as an anchor for structures. The size of suction piles can vary considerably. Small diameter suction piles are often used for anchorages, as they can withstand tension and be removed rapidly with a minimum cost. Large-diameter caissons have been manufactured using both concrete and steel. For example, the diameter of the concrete skirt for Gullfaks GBS is 28 m. The thickness to diameter ratio of steel suction piles can range from 0.3 to 0.5%. This ratio increases to 1–2% for concrete suction skirt.

It should be mentioned that the term “suction pile” is in a sense misleading since most of the suction piles have little similarity to a traditional pile. In many cases, the term is used for short “piles” with a large diameter that is not as slender as a traditional pile. The lengths of some suction piles can be equal to or even less than their diameters, as aforementioned.

A suction pile usually comprises a single or multiple cylinders of large diameter and relatively shallow penetration depths (a length to diameter ratio of 2:1 is common), where the volume of soil inside the pile typically acts as a permanent gravity base foundation, as shown in Fig. 26.1. Ring stiffeners and/or longitudinal



Fig. 26.1 Suction piles supporting tripod substructures [1112]

stiffeners are sometimes welded inside the pile wall. More complex design such as a change in diameter over suction piles' length can also be employed.

The first application of suction pile was reported by Mackereth [1113] in 1958, which was used to install an anchor pile using pumps to create a vacuum inside the pile for holding down a piston corer during lake-bed sampling operations. As will be presented in Sect. 26.5, extensive applications of suction piles in the offshore industry began in the middle of the 1970s. Original research work conducted on marine sit-on-bottom suction foundations was undertaken by Clausen et al. [1114]. Over the years hundreds of suction piles have been successfully installed in a variety of field conditions spanning worldwide applications in soft and strong soils, shallow and deep water, and for various purposes. For a review of the historic development of suction piles, readers may read source [1115].

26.2 Suction Pile Installations

Suction caissons are similar to gravity-based foundations in shape but differ in the method of installation and primary mode of stability. They can be installed by crane vessel or launched over the stern of an anchor handler tug.

During installation, a suction foundation, skirt, hollow cylindrical concrete, or steel walls are lifted to touch the seabed by an installation vessel. An ROV

(remotely operated vehicle) may be used to monitor the seabed processes, together with depth, tilt, and other instrumentation on and in the suction pile.

Due to the self-weight of the suction pile, it will first penetrate into soils to transmit loads to deeper and normally stronger soil strata, as shown in Fig. 26.2. With limited efforts, the suction piles are often submerged with trapped air. When it touches the seabed, the valve on top of the pile will be opened so that air and water trapped inside the pile are free to escape due to the relative negative pressure inside the suction pile. In addition, the water inside the suction pile is often pumped out to obtain a higher negative pressure (suction). This negative pressure generated during pumping (suction penetration) or escaping of air and water inside the pile is the total pressure difference between the inside and the outside of the pile and is limited by zero absolute pressure (or vacuum) on the inside. This negative pressure also sets up seepage flow that reduces tip resistance and internal friction during penetration. If a site comprises sand or gravel strata, large suction can degrade skirt tip resistance to approximately zero. The outside hydrostatic pressure related to water depth yields an ultimate limit for maximum under pressure available during suction penetration. During this process, it is important to apply sufficient suction to overcome the soil resistance, but the suction should not be so high as to make the soil plug inside the suction pile fluidize or fail, as this can significantly reduce the bearing capacity of the suction pile after installation. This is typically fulfilled by deducting the suction pressure with a factor between 1.3 and 1.7. For offshore applications, the water depth is normally not the limiting factor for the maximum suction penetration depth. Rather, the maximum penetration depth is determined by the aspect (length to diameter) ratio of the pile [1116]. Furthermore, by changing the hydrostatic pressure inside the pile in the horizontal plane, the inclination of the structure due to heterogeneous soil condition or slope at seabed can be controlled.

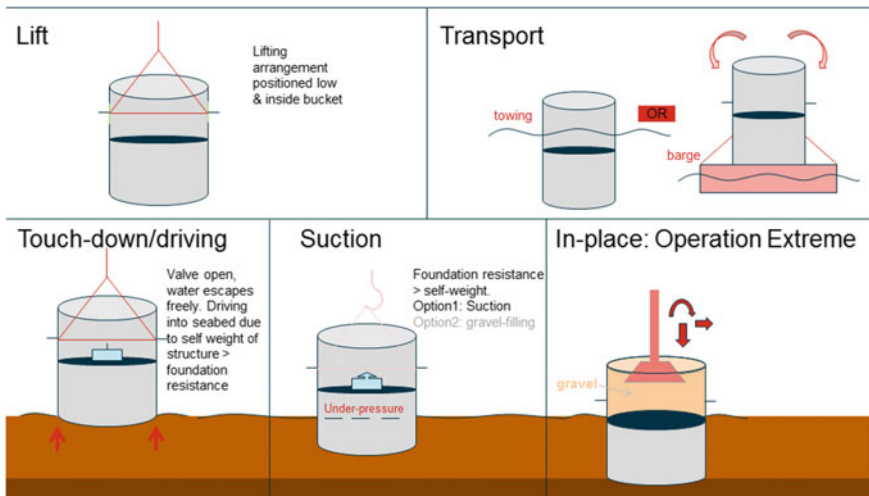


Fig. 26.2 Installation of suction piles (courtesy of Aker Solutions)

During the entire process, the penetration in each phase is determined by equating the driving force (pile's self-weight and suction force) with the resistance provided by pile wall friction (inner and outer side) and end-bearing.

If there are no stiffeners welded to the inside of the anchor pile or below the first ring stiffener (in case they are installed), the soil's shear strength inside the pile wall is calculated as the same as that of the shear strength outside the pile. However, the installation of ring stiffeners inside the pile wall not only adds weight to the driving force, but also, more importantly, gives additional resistance to penetration, thus potentially pushing the clay away from the wall above it. And once the clay has passed a sufficient distance, it will collapse back against the wall, trapping water, which can significantly soften the soil and reduce the pile resistance over time [112, 1117].

The suction pile foundation can also be rapidly removed/lifted by reversing the installation process, i.e., applying an overpressure inside the pile (normally by pumping water into it). This operation is also occasionally used for the leveling of the supported structures.

By adopting an axisymmetric finite difference numerical model to simulate the suction pile installation, and using both total stress and effective stress analyses, Fakharian and Irajil [1118] presented a numerical modeling of a suction pile installation in clay in the southern Caspian Sea area. They discovered that the calculation using effective stress analysis shows a substantial increase in effective stress for soils adjacent to inner wall due to pore-water pressure decrease during suction insertion, while a cylindrical core of about $2/3$ of the suction pile diameter within the pile experienced higher pore pressures and hence lower effective stresses. Maniar and Tassoulas [1119] developed a numerical model using finite element method for suction pile installation. The Mohr-Coulomb model was used for the pile-soil interface, and a new mesh was generated to represent a gradually increased penetration of the suction pile. Fakharian and Soltanmohammadlou [1120] also presented a finite element modeling for suction pile installation in a Caspian Sea clay site. Behavior of the Mohr-Coulomb type was assumed for both soil and soil-pile interface. A total stress condition was assigned to clay throughout the step-by-step installation process, and at each step, the required suction was estimated.

26.3 Modeling and In-place Capacity Control for Suction Piles

After installation, several issues are important to maintain an anchor pile's position. During normal operations, the weight of the pile and ballast, the weight of the soil plug inside the pile, and the skin friction between the pile and surrounding soils, all act to keep the pile in place. Under extreme environmental conditions, passive

suction is mobilized. The passive suction develops at the top of the pile and is translated down through the soil plug to the bottom of the unit. At the base of the pile, passive suction is manifested as reverse end-bearing capacity [1115].

For in-place capacity control, three types of analysis methods can be used to assess the holding capacity of suction piles: (1) simplified method, which often uses Winkler springs, as presented in Chaps. 16 and 17. It is especially suitable for piles with diameters less than 2.5 m; for piles with larger diameters, Winkler nonlinear springs can be modified to reflect the softening of the p - y curve stiffnesses, as discussed in Sect. 16.8; (2) limit-equilibrium or plastic limit analysis methods, which usually employ the concept of soil failure mechanisms; (3) finite element analysis.

Provided an appropriate constitutive model of soils and a reasonable meshing are employed, the finite element analysis aims to search for the critical failure mechanism without prior user assumptions. It is relatively rigorous and can handle complex geometries, spatially varying soil properties, non-linear constitutive behavior with failure criterion, and partial consolidation under long-term loading, etc. [1121]. Its applications on analyzing suction piles have been studied by various researchers [1116, 1122–1126]. Figure 26.3 shows a finite element modeling used in capacity assessment of a suction pile. By taking the advantage of symmetry, a half-circular soil domain with a diameter of 22 m and a depth of 20 m is modeled. The modeled soil domain is large enough compared with the size of the caisson. Therefore, significant boundary effects are not expected on calculated load, displacement and deformation mechanism. The vertical plane of symmetry is restrained from any displacement perpendicular to it, while other sides of the soil domain are restrained from any lateral displacement using roller supports at the nodes. The bottom boundary is restrained from any vertical displacement, while the top boundary is free to displace. The soil is modeled using the C3D8R solid homogeneous elements available in Abaqus element library [344], which is an eight-noded linear brick element with reduced integration and hourglass control. Sand soil is modeled by the Mohr-Coulomb model available in Abaqus. A suction caisson 6 m in length, 3 m in diameter, and with a wall thickness of 100 mm is modeled. The soil/caisson interaction is modeled using the Coulomb friction model, which defines the friction coefficient [1127].

Figure 26.4 shows a 30-m-diameter bucket foundation embedded into soils with a penetration depth of 33 m. Again, due to symmetry of the loads and the geometry, only half of the structure and soils was modeled. The dimensions of the FE soil model in the global X - and Y -directions are 400 and 120 m, respectively. The bottom boundary is set at 65 m depth. The soils consist of three clay layers from seabed to 65 m depth, where a sand layer begins, which is not modeled within the boundaries of the model.

By borrowing the idea of moment-force diagram to calculate the plastic capacity of a beam, Senders [1128] proposed a failure interaction diagram method to estimate the holding capacity of a suction anchor pile:

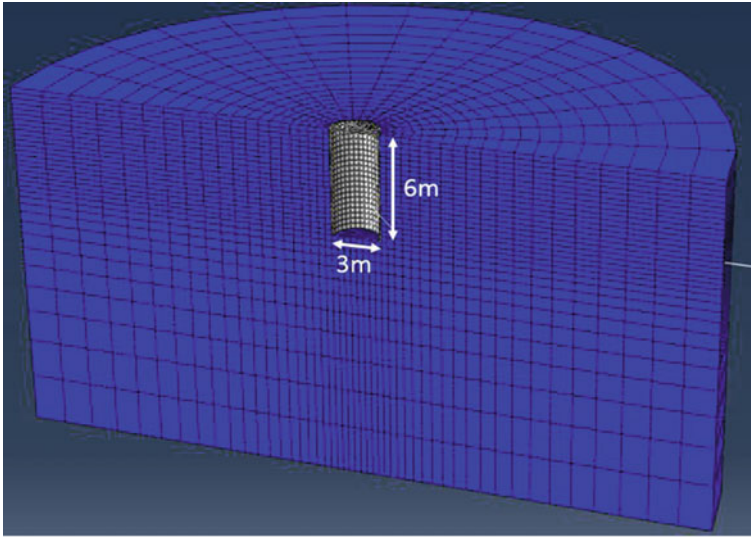


Fig. 26.3 Finite element mesh used in capacity assessment of a suction pile [1127]

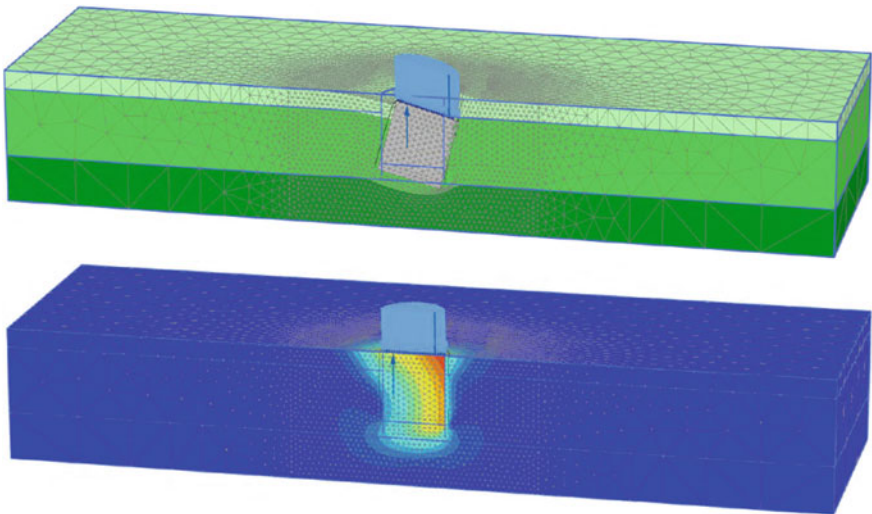


Fig. 26.4 Three-dimensional FE-model for soil-bucket foundation modeling comprising 159,000 elements, and the displacements under storm load condition (horizontal load = 11 MN, vertical load = 191 MN, bending moment = 904 MNm) (courtesy of Aker Solutions and NGI)

$$(V/V_{\max})^{\alpha} + (H/H_{\max})^{\beta} = 1 \quad (26.1)$$

where V and H are the forces applied on the suction pile in vertical and horizontal direction, respectively; V_{\max} and H_{\max} are the values of the maximum bearing force component when the other force components are zero; Exponents α and β are constants determined by curve fitting based on the data obtained from either experiments or finite element analyses, which can normally be assumed to be identical and close to a value of 2 [1129] or 3 [1130], respectively. They are influenced by the depth of the padeye for the suction anchor.

By assuming that the suction pile is rigid and subject to both vertical force V , horizontal force H , and bending moment M , the capacity may be estimated by a three-force resultant diagram:

$$(V/V_{\max} + \eta)^{\alpha} + (H/H_{\max})^{\beta} + (M/M_{\max})^{\gamma} = 1 \quad (26.2)$$

where V_{\max} , H_{\max} , and M_{\max} are the values of the maximum bearing force component when the other two force components are zero; η , α , β , and γ are constants determined by curve fitting based on the data obtained from either experiments or finite element analyses.

For more details about the capacity control and installation design of suction piles, readers may read API-RP-2SK [1103] and sources [1121, 1131–1133].

26.4 Modeling of Suction Piles Subjected to Seismic Loading

Research on the design, analysis, and performance of suction piles under earthquake loading is rare. Common design methods for evaluating the dynamic behavior of suction piles have been based on either using solutions for shallow foundations or flexible piles, or on three-dimensional numerical analyses [1140].

By evaluating soil–structure interactions using a direct, integrated soil–structure method and a simplified, practical multi-step method, Brandt [1141] performed a series of seismic analyses of a subsea structure supported by a suction pile foundation. The analysis was performed for two models with either lateral boundaries free in the horizontal direction without viscous dampers or standard fixity boundary conditions with viscous dampers. The former model was found to be the more adequate modeling, even though it does not account for the absorption of incoming stress waves generated by the vibrating suction foundation. From a nonlinear analysis using the direct method, Brandt [1141] also observed that gapping will occur between the top of the foundation and the soil under seismic excitations.

Parker and his co-workers [1142] studied the seismic performance of a suction pile foundation, which supports a 140-ton subsea manifold (Fig. 26.5) at a subsea site with very soft clay. Since the manifold structure itself has a sufficient resistance

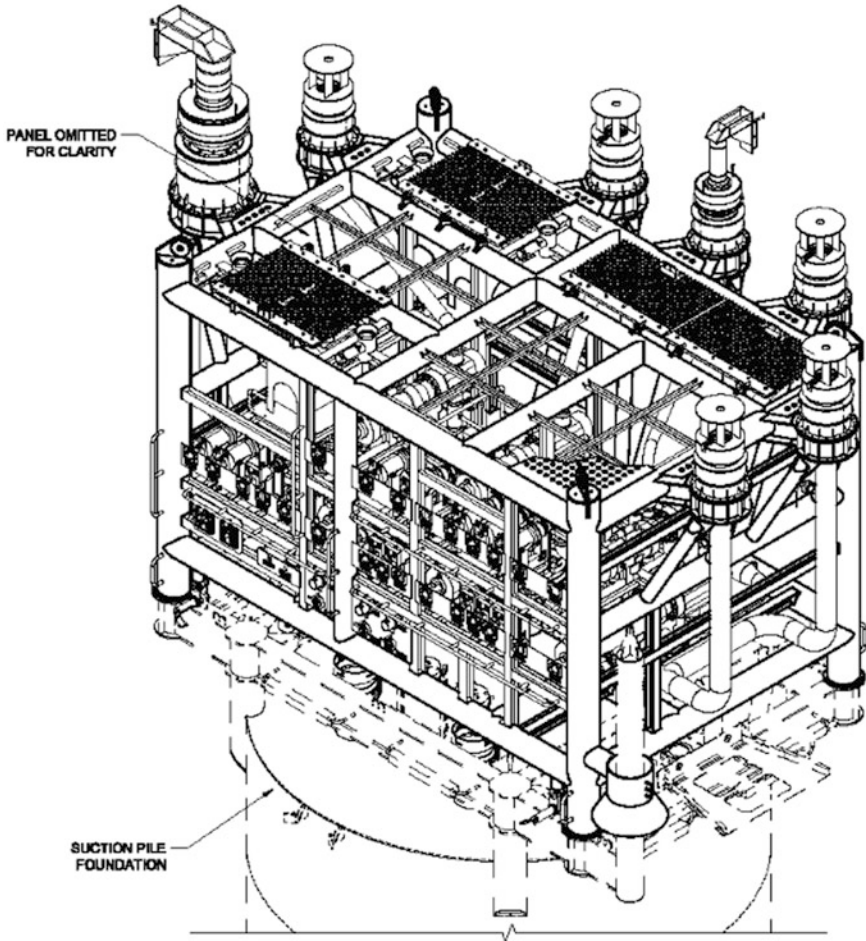


Fig. 26.5 A 140-ton subsea manifold supported by a suction caisson 8 m in diameter, 11 m in length, and with wall thickness of 20–30 mm (upper 2.5 m) [1142]

to seismic loading, they focused on checking the over-stressing of the jumpers with an acceptable stress or damage to connections at the structure–foundation/connections, both of which are caused by relative displacements of its terminations at the connection level. This objective was achieved by evaluating the possible rigid-body displacements of the structure–foundation system.

Figure 26.6 shows the three-dimensional finite element model for analyzing the manifold and the suction pile using FE code OpenSees [272]. The soil domain is modeled with eight-node solid elements and extended sufficiently. The symmetry about a vertical plane through the pile axis is considered for the soil model. Seismic motions along vertical and one horizontal direction are applied. The manifold structure was modeled as a lumped mass at the center of gravity (CoG), while the

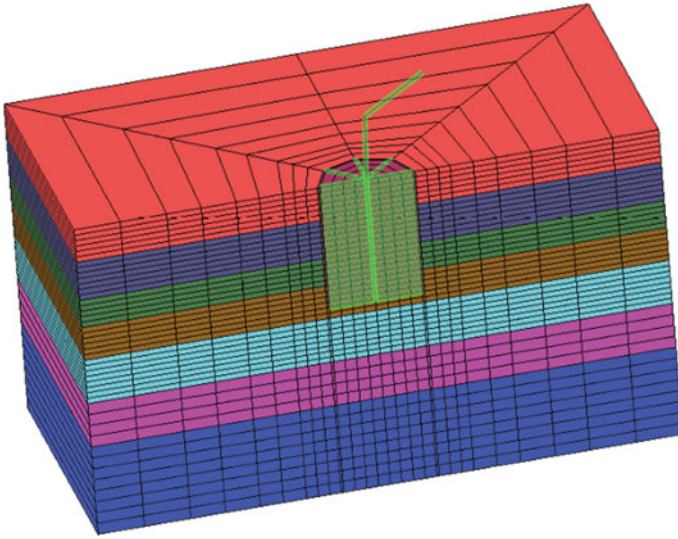


Fig. 26.6 FE modeling of a subsea manifold and suction pile [1142]

pile and soil plug are condensed and modeled by elastic beams. The lateral boundaries of the model are represented by a shear beam constraint. The vertical sides of the soil domain are constrained to deform similarly in the lateral direction by imposing equal horizontal and vertical degree-of-freedom constraints to pairs of lateral nodes at the same elevation. Nodes at the base of the soil domain are fixed. This modeled boundary has a strong impedance contrast at the base of the soil domain meeting the bedrock, which reflects waves returning from the mudline. This is normally regarded as conservative due to the underestimation of radiation damping.

Ground motions are input as a set of scaled time histories applied at the base of the model. Relative displacements between CoG of the manifold and the flange and a free-field point on the seabed were studied. From a series of analyses, it was concluded that for this modeled manifold supported by the suction pile, the pile tilt (modeled by applying an equivalent force to the pile–structure’s CoG to represent the overturning moment caused by the non-verticality) due to installation tolerances and the mild seabed slopes (modeled by rotating the mesh) at the site can significantly increase displacements. For example, a foundation tilt of 5° increases the maximum horizontal displacement by 46%, and the residual displacement increases from 3 to 8 cm. With combined pile tilt and seabed slope, the maximum horizontal displacement even doubles from 6 cm for a vertical pile at seabed level to 12 cm for the worst case. The vertical settlements are increased by 17%, and the residual displacements are also strongly influenced, even though they still remain less than 15 cm. Vertical displacements increase by 51% for the combined 5.0° tilt and 3.5° slope. However, predicted displacements at flange level were considered to be acceptable.

26.5 Advantages of Suction Piles/Caissons

The technology of suction piles is especially developed for projects where gravity loading is not sufficient for pressing piles into the ground, or in deep waters where pile driving is costly and complex, or for anchors subject to large tension forces. Suction piles normally perform well in soft clays or other low strength sediments. Even in very dense sand, the technology can still be utilized provided a dedicated design is performed [1134].

Compared to traditional offshore pile foundations, suction piles have the advantage of being convenient to install: pile driving is not needed during installation, as they rely on pumps rather than underwater pile drivers for installation. The installation time for a suction pile is also short, ranging from a few hours to one day, which reduces the relevant cost significantly. At sites with soft clay condition, the suction penetration rate can reach up to 20 m/h without any significant rate effects if the pumping capacity is sufficient. The maximum suction penetration depth is normally determined by the pile's length-to-diameter ratio. The final penetration depth is substantially shallower than conventional driving pile foundation, which also makes the installation easier and quicker [1111]. For example, in the development of Snorre A Tension Leg Platform (TLP) located in the North Sea and operated by Statoil, since it was difficult to use traditional long piles due to the presence of huge pebbles 60 m below the seabed, suction caissons were selected so that the platform could be safely secured by suction caissons of only 12 m long.

The penetration force can be predefined if the suction is controlled. This also ensures that no further penetration occurs if the additional vertical load added to the structure does not exceed the suction force used during installation. A side benefit of this is that, after installation, the settlement during service can be reduced to some extent.

The bearing capacity in vertical direction can normally be further increased by end-bearing.

The suction piles also have other functions such as compensating for seabed irregularities, reducing scours, etc. Therefore, no soil improvement and dredging are required in the case of soft soil deposits under seabed.

The noise and vibration due to the installation can also be reduced to a great extent, making the construction work more environmentally friendly.

With the increase of pile diameter, suction force increases faster than that of the penetration resistance, and deep penetration can then be reached without excessive increase in suction pressure. This is because the penetration resistance at a certain depth is linearly proportional to the pile diameter (the embedded area of pile skirt walls), and the suction force in addition to the pile weight is also proportional to the square of the pile diameter.

As previously mentioned in Sect. 20.2, the presence of scour can be greatly minimized or even eliminated by using bucket foundations rather than traditional pile foundations.

26.6 Engineering Applications

As previously mentioned, suction piles can have various usages in offshore engineering, leading to their applications in the form of suction skirt piles, suction caissons, suction anchors, and suction buckets.

It should be noted that a well-performed monitoring system is essential for the success of the installation. In addition, for suction piles that are not able to penetrate into soils by their own self-weight, an efficient pumping system to create a significant and reliable negative pressure inside the suction piles is also important.

It is worth mentioning that the Norwegian Geotechnical Institute (NGI) has significantly contributed to concept developments, designs, and installations of suction anchors for offshore applications.

26.6.1 *Application for Offshore Structures*

To assist penetrations of the skirts into foundation soils, skirt suction piles were first used as solutions for foundation design of large GBS installed in the North Sea, when offshore oil production started there at the beginning of the 1970s. Before this, huge concrete gravity structures were only used at dense sand or over-consolidated clay sites, and the long skirt concept was believed to be beyond the control of the available technology. Therefore, a more traditional solution such as building several steel jackets was normally selected. Meanwhile, the concrete platforms were gradually developed for more complex and often softer soils, and in the early 1980s, several platforms were constructed with long skirts up to 5 m [1136]. The first gravity oil platform utilizing a skirt suction foundation was at Ekofisk oil field. It had a foundation area as big as a football field, even though it was placed on a seabed comprising very dense sand. This platform was designed to sustain waves up to 24 m high [1137].

Today, around 30 gravity-based structures worldwide with water depths ranging from 50 to 300 m have skirt suction foundations, such as the highest fixed offshore structures Troll A as shown in Fig. 26.7. In 1989, the Gullfaks C platform with a topside weight of more than 70,000 tons was installed. It has a foundation comprising 16 large-diameter skirt suction caissons penetrating 22 m into the seabed.

The first major structure installed in dense sand using suction caissons was Statoil's Draupner E riser jacket (water depth: 70 m) in the North Sea, installed in 1994. The suction caisson has a diameter of 12 m and the skirt is 6 m long. The design for the installation was based on a combination of field testing, laboratory



Fig. 26.7 Troll A platform (481 m high) with a skirt suction foundation

testing, and finite element modeling [1131]. During a storm with a maximum wave height of 26 m impacting the Draupner E platform, both the suction caisson and the platform sustained significant wave loading. Later calculations showed that the suction caissons moved about 10 mm horizontally and 5 mm vertically, well within design limits. Moreover, the foundation could have sustained significantly higher wave forces without losing its stability [1135].

Skirt suction pile foundations have also been used to support subsea pipelines and bridge piers, and proposed for use for foundations of offshore wind turbine supporting structures (e.g., monopod, tripod, or jacket).

26.6.2 Application as Deep-Water Anchors

As water depth is always a barrier for the offshore industry to develop deep-water projects, suction piles are an ideal solution for riser and mooring anchors, since no water depth limitations are presented to prevent the technology from following deep-water developments. Furthermore, deep-water soil conditions often consist of homogenous soft clay, which facilitate the penetration flexibility of suction piles during their installations [1116].

Their applications are largely motivated by accumulated experiences gained from skirt suction caissons for gravity platforms (Sect. 26.6.1). They have been applied for offshore projects in water depths up to 2000 m and in soil conditions including soft clays, very stiff glacial till, dense homogenous sands, and mixed layers. Suction foundations were also used as skirted anchors for floating structures in deep waters that do not require drag-in operations or proof loading, as traditional mooring anchors do.

The first suction pile moorings for permanent use were installed in 1995 at 100–200 m water depth and with catenary anchor lines [1138]. Today, there are more than 300 suction piles operated as a part of permanent mooring systems around the world, at water depths above 100 m, with the deepest one installed at a water depth of 2500 m in the Mississippi Canyon.

Suction piles have also been installed at sites with great seabed topographical irregularities. For example, at the Haltenbanken area offshore mid-Norway, due to grounding icebergs during the last glaciation period, the seafloor is very irregular

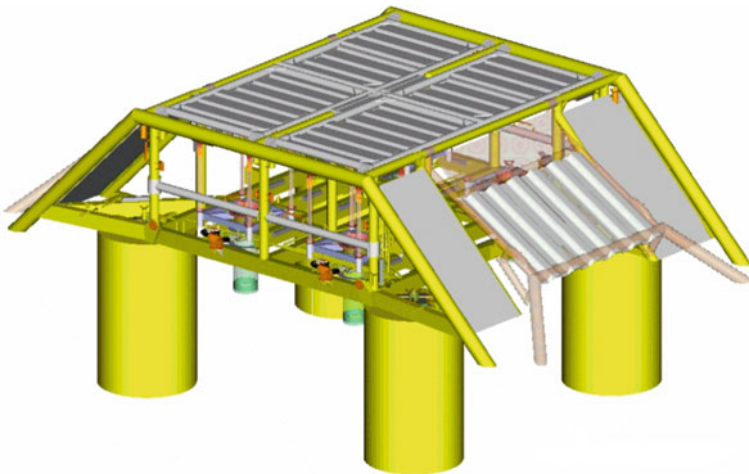


Fig. 26.8 A Foundation and Protection Structures (FPS) with four bucket foundations to support subsea production facilities at Snøhvit field, 140 km off the coast of Finnmark in the Barents Sea, with a water depth of 345 m (courtesy of Aker Marine Contractors AS and Aker Solutions)

and uneven. Despite these difficulties, suction anchor moorings for six floating production and/or storage units have been installed in this area [1136].

26.6.3 Application for Subsea Production Facility Foundations

Figure 26.8 shows a special type of skirt foundation, a design of four-bucket suction piles to support subsea production facilities at Snøhvit field in the Barents Sea, designed by Aker Marine Contractors. The structure is designed to be self-penetrated into the seabed with the hatches on top of the suction piles in the open position to allow for water evacuation. An ROV operated suction kit can be utilized if additional leveling or penetration is required [1139]. Figure 26.5 shows a design of a 140-ton subsea manifold supported by suction piles in the Saipem deep-water installation.

Chapter 27

General Design Issues for Offshore Foundations and Relevant International Codes and Guidelines

For different types of offshore foundations categorized as either shallow foundations or deep foundations, various design issues at different stages need to be carefully addressed. These are presented by Shin and his co-workers [1143] as given in Table 27.1.

Although offshore geotechnical principles are the same as those for land-based structures, for offshore geotechnical engineering applications, site investigations are more expensive, soil conditions are often more difficult, structural loads are usually more significant, and the focus of offshore geotechnical design is often placed on capacity, while the foundation stiffness is important for predicting the dynamic response of the soil–foundation–structure system [1145].

For foundation designs of offshore structures, the most widely accepted guideline is the API-RP-2A, which includes:

1. The WSD version of API-RP-2A, comprising the API-RP-2A [791] and its errata and supplement [792], which provides the commentary on CPT-based methods (Sect. 17.13) for pile capacity control (C6.4.3 c).
2. The LRFD version of API RP2A [790].

Section 1.13 presents the background knowledge on WSD and LRFD.

Readers need to bear in mind that the use of API-RP-2A in many countries other than the USA is supplemented by additional local regulatory requirements and performance criteria, but the design methodology and basic code check equations are unified worldwide. This is more apparent for the LRFD version of API-RP-2A, and the variance of criteria between US regional conditions and other nations is accounted for by different partial safety factors and can therefore be calibrated to provide more consistent safety levels.

A factor of safety of 1.5 for design environmental load and 2.0 for operating environmental load are normally required. Due to large uncertainties involved in the estimation of foundation load, an even higher factor of safety may be required by some company specified guidance.

Table 27.1 Design issues for shallow and deep foundations [1143]

Design topics	Typical tasks and deliverables
Design basis	Codes, standards, guidelines, soil parameters, geometry of supporting structures, design load cases, detailed bathymetry, scour protection, and grout
Soil parameters	Design soil parameters, material factors, etc.
Installation	Geotechnical issues related to the installation of the foundations, e.g., monopile (driveability), suction piles (suction pressure), GBS (grouting and scour protection, etc.), jacket foundations (pre-/post-installed pile, etc.) during the installation phase
Bearing capacity	Establish soil design strengths, required foundation dimensions
Settlements	Calculate settlements and other permanent displacements (e.g., tilt, horizontal displacements, etc.) of foundations during the design lifetime
Foundation stiffness	Establish vertical, horizontal, and moment load–displacement (or rotation) relationships or spring stiffness. Intended to be used for soil–structure interaction (SSI) analysis, soil response for dynamic amplification assessment, soil support for fatigue limit state check, etc.
Soil reactions	Establish the soil–foundation contact stress distribution for the relevant design load cases intended for use in structural designs of foundations
Removal	Geotechnical issues related to the removal of foundations, e.g., methods for removal, skirt uplift resistance, soil plugging, etc.
Seismic loading	Relevant geotechnical earthquake engineering issues such as seismic response spectra, foundation stiffness matrix, liquefaction potential

Some energy companies specify their own material factor (resistance factor or partial safety factor) for geotechnical design. For example, in the technical and professional requirement [1105] by Statoil, it is specified that a material factor of 1.5 shall be used on pile group capacity. If a lower material factor is used, a probabilistic analysis is needed to document compatibility with overall target reliability of 10^{-4} . In Norsok N-001 [1106] applied for offshore installations in the Norwegian part of the North Sea, a material factor of 1.3 is required for piles and anchors. In addition, if a pile group has sufficient capacity, a material factor lower than 1.3 is permitted for single/individual piles in that group.

Based on API standards [790–792], ISO 19902 (2007) [91], DNV Classification Notes 30.4 [715], and DNV-OS-J101 [794] describe similar design methods.

Beyond the international guidelines, specific national government requirements must first be complied with, such as, the rules of US Department of Energy (DoE), Norwegian Petroleum Directorate (NPD) for all offshore installations in USA and Norway, respectively. In the UK, the responsibility for regulatory control has been moved to the Health and Safety Executive (HSE), following the explosion and fire accident of the production platform Piper alpha in the North Sea [1144]. In addition, government authorities require that recognized bodies appraise the aspects of structural and foundation integrity and issue a certificate to that purpose. Those recommended bodies are normally referred to certification or classification

organizations, and the major certification or classification organizations worldwide are: Det Norske Veritas Germanischer Lloyd (DnV-GL), Lloyds Register of Shipping (LRS), American Bureau of Shipping (ABS), and Bureau Veritas (BV), China Classification Society (CCS), etc.

Appendix

Unit Conversions

Quantity	Unit	x	Unit	x	Unit
Length	in	25.4	mm	0.03937	In
	ft	0.3048	m	3.281	Ft
Area	in ²	645.16	mm ²	1550 × 10 ⁻³	in ²
	ft ²	0.0929	m ²	10.76	ft ²
	ft ²	2.3 × 10 ⁻⁵	Acre	43500	ft ²
Volume	cubic yard	21.7	Bushels	1.244	ft ³
	in ³	1.639 × 10 ⁻⁴	mm ³	6.102 × 10 ⁻⁵	in ³
Mass	slug	14.594	kg	2.205	lb _m
	slug	32.2	lb _m	0.454	Kg
Pressure	lb/in ²	6.895	kPa	0.1450	lb/in ²
	lb/ft ²	0.0479	kPa	20.89	lb/ft ²
	psi	6.895	kPa	0.1450	psi
	ksi	6.895	MPa	0.1450	ksi
	psi	6.895 × 10 ⁻⁶	GPa	1.450 × 10 ⁻⁵	psi
	ksi	6.895 × 10 ⁻³	GPa	145	ksi
	lb _m /ft ³	16.02	kg/m ³	0.0624	lb _m /ft ³
Force	lb _f	4.448	N	0.2248	lb _f
Moment	lb-in	0.1130	N·m	8.851	lb-in
	lb-ft	1.356	N·m	0.7376	lb-ft
Energy	in·lb	0.113	Joule	8.85	in·lb
	kw-h	2655.18	klbs-ft	3.766 × 10 ⁻⁴	kw-h
Velocity	m/s	2.237	mph	0.447	m/s
	mph	1.467	ft/s	0.682	mph
	mph	17.6	in/s	5.68 × 10 ⁻²	mph
	knot	0.514	m/s	1.944	knot
Power	watt	0.73755	ft-lb/s	1.356	watt
	watt	1.341 × 10 ⁻³	hp	745.7	watt

Acceleration of gravity (1g) = 9.81 m/s² = 32.2ft/s² (at latitude 45°)

References

1. Kramer SL (1996) Geotechnical earthquake engineering. Prentice Hall, Upper Saddle River, NJ
2. Terzaghi Karl, Peck RB, Mesri G (1996) Soil mechanics in engineering practice, 3rd edn. Wiley, New York
3. Whitehouse RJS, Soulsby RL, Roberts W, Mitchener HJ (2000) Dynamics of estuarine muds. ThomasTelford, London
4. Winterwerp JC, van Kesteren WGM (2004) Introduction to the physics of cohesive sediment in the marine environment. Elsevier, Amsterdam
5. ASTM (2009) American society for testing and materials, vol 04.08, soil and rock (I): D420–D5779, and Volume 04.09, soli and rock (II): D5780–latest. Geosynthetics
6. BS 5930 (1999) Code of practice for site investigations. British Standards Institution
7. MIL-HDBK-1007/3 (1983) Soil dynamics and special design aspects. Department of Defense
8. Georgiadis K (2003) Development, implementation and application of partially saturated soil models in finite element analysis. Imperial College of Science, Technology and Medicine, London
9. Alonso EE, Gens A, Josa A (1990) A constitutive model for partially saturated soils. *Géotechnique* 40:405–430
10. Gonzalez NA, Gens A (2008) Report: implementation of unsaturated soil model in Plaxis
11. Briaud JL (2013) Geotechnical engineering. Unsaturated and saturated soils. Wiley, Chichester
12. Galavi V (2010) Fully coupled flow deformation and undrained analyses in Plaxis 2D and 3D, Plaxis BV
13. Hsieh PG, Ou CY, Lim A (2010) Use of the total stress undrained model to the analysis of deep excavation. In: Proceedings of the 17th Southeast Asian Geotechnical Conference, Taipei, Taiwan
14. Lim A, Ou CY, Hsieh PG (2010) Evaluation of clay constitutive models for analysis of deep excavation under undrained conditions. *J Geoen* 5(1):9–20
15. Burland JB (1965) The yielding and dilation of clay. *Géotechnique* 15:211–214
16. Schanz T, Vermeer PA, Bonnier PG (1999) The hardening soil model: formulation and verification, beyond 2000 in computational geotechnics—10 years Plaxis. Balkema, Rotterdam
17. Benz T, Vermeer PA, Schwab R (2009) A small-strain overlay model. *Int J Numer Anal Methods Geomech* 33(25–44)
18. Vermeer PA, Meier CP (1998) Stability and deformations in deep excavations in cohesive soils. In: Proceedings international conference on soil-structure interaction in urban civil engineering, darmstadt geotechnics, vol 1, Issue 4

19. Terzaghi K, Die Berechnung der Durchlässigkeitsziffer des Tones aus dem Verlauf der hydrodynamischen Spannungserscheinungen (in German), Sitz. Akad. Wissen. Wien, Math-Naturw. Kl. Abt. IIa. 132:105–124
20. Bishop AW (1960) The principle of effective stress. Norwegian Geotechnical Institute, Oslo, Pub. 32, pp 1–5
21. Osipov VI (2015) Physicochemical theory of effective stress in soils. Springer, Heidelberg
22. Skempton AW (1960) Significance of Terzaghi's concept of effective stress. In: Bjerrum L, Casagrande A, Peck R, Skempton AW (eds) From theory to practice in soil mechanics. Wiley, New York
23. Mitchell JK, Soga K (2005) Fundamentals of soil behavior, 3rd edn. Wiley, New York
24. Michael Duncan J, Wright Stephen G (2005) Soil strength and slope stability. Wiley, Hoboken, New Jersey
25. Das BM, Sobhan K (2013) Principles of geotechnical engineering, 8rd edn. CL Engineering
26. Craig RF (2004) Craig's soil mechanics, 7th edn. Spon Press, London
27. Barltrop NDP, Adams AJ (1991) Dynamics of fixed marine structures, 3rd edn. Butterworth-Heinemann, Oxford
28. Day RW (2012) Geotechnical earthquake engineering handbook, 2nd edn. McGraw Hill, New York
29. Lambe TW, Whitman RV (1969) Soil mechanics. Wiley, New York
30. Sarma SK, Tsatsanifos CP (1984) Effective stress method for dynamic response analysis of horizontally layered soil. In: Proceedings of the 8th world conference on earthquake engineering, vol 1, San Francisco, CA, pp 1025–1032
31. Helwany S (2007) Applied soil mechanics. WileyInc, Hoboken
32. Reddy KR, Saxena SK, Budiman JS (1992) Development of a true triaxial testing apparatus. Geotech Test J (ASTM) 15(2):89–105
33. Reese LC, Isenhower WM, Wang ST (2006) Analysis and design of shallow and deep foundations. Wiley, USA
34. Bjerrum L (1973) Problems of soil mechanics and construction on soft clays. In: Proceedings of the 8th international conference of SMFE, Moscow, vol 3, pp 111–159
35. ISO 22476-3 (2005) Geotechnical investigation and testing—field testing—Part 3: standard penetration test
36. ASTM D1586-11 (2011) Standard test method for standard penetration test (SPT) and split-barrel sampling of soils, ASTM
37. Skepton AW (1986) Standard penetration test procedures and the effects in sands of overburden pressure. Relative Density Part Size Aging Overconsolidation Géotech 3 (3):425–447
38. Clayton CRI (1990) SPT energy transmission: theory. Meas Significance Ground Eng 23 (10):35–43
39. Youd TL, Idriss IM (1997) Proceedings of the NCEER workshop on evaluation of liquefaction resistance of soils, No. MCEER-97-0022
40. Liao SSC, Whitman RV (1986) Overburden correction factors for SPT in sand. J Geotech Eng ASCE 112(3):373–377
41. Washington State Department of Transportaion (2015) Geotechnical design manual, M 46-03.11, Tumwater, WA
42. Kuo CH, Wen KL, Hsieh HH, Chang TM, Lin CM, Chen CT (2011) Evaluating empirical regression equations for V_s and estimating V_{s30} in Northeastern Taiwan. Soil Dyn Earthquake Eng 31:431–439
43. Ohba S, Toriumi I (1970) Dynamic response characteristics of Osaka Plain. In: Proceedings of the annual meeting AIJ (in Japanese)
44. Marto A, Soon TC, Kasim F (2013) A correlation of shear wave velocity and standard penetration resistance. Electron J Geotech Eng 18

45. Thaker TP, Rao S (2011) Development of statistical correlations between shear wave velocity and penetration resistance using MASW technique. In: 14th Pan-American conference on soil mechanics and geotechnical engineering, Toronto
46. Anbazhagan P, Sheikh N, Tsang H (2010) Seismic site classification practice in Australia, China and India: suitability. In: Abraham R, Latheswary S, Unnikrishnan N (eds) International conference on materials mechanics and management (pp 189-197). Excel India Publishers, New Delhi
47. Anbazhagan P, Sitharam TG (2009) Estimation of ground response parameters and comparison with field measurements. *Indian Geotech J* 39(3):245–270
48. Lunne T (2012) The fourth James K. Mitchell lecture: the CPT in offshore soil investigations—a historic perspective. *Geomech Geoeng* 7(2)
49. Zuidberg HM, Richards AF, Geise JM (1986) Soil exploration offshore. In: Proceedings of the 4th international geotechnical seminar on field instrumentation and in situ measurements, Nanyang Technical Institute, Singapore, pp 3–11, 1986
50. Lunne T (2001) In situ testing in offshore geotechnical investigation. In: Proceedings international conference on in situ measurement of soil properties and case histories, Bali, Indonesia, pp 61–81
51. Power P, Geise J (1994) Offshore soil investigation techniques and equipment for the next century. *Proc Behav Offshore Struct Boston* 1:97–109
52. Zuidberg HM (1972) Seabed penetrometer tests, Fugro symposium on penetrometer testing, vol. 16. Fugro Ltd., Leidschendam, Holland
53. API (2007) Errata and supplement 3—API recommended practice 2A-WSD, recommended practice for planning, designing, constructing fixed offshore platforms—working stress design. American Petroleum Institute (API), Dallas
54. Harder LF, Seed HB (1986) Determination of penetration resistance for coarse-grained soils using the Becker Hammer Drill, Report No. UCB/EERC-86-06, NTIS PB87 124210, Earthquake Engineering Research Center, College of Engineering, University of California, Berkeley, California
55. Sy A, Campanella RG (1994) Becker and standard penetration tests (BPT-SPT) correlations with consideration of casing friction. *Can Geotech J* 31(3):343–356
56. Ghafghazi M, Thururajiah A, DeJong JT, Wilson DW, Armstrong R (2014) Instrumented Becker penetration test for improved characterization of gravelly deposits. In: Proceedings of Geocongress 2014, American Society of Civil Engineers Geotechnical Special Publication No. 234, Atlanta, Georgia, pp 37–46, 2014
57. Beresnev IA, Wen KL (1996) Nonlinear soil response—a reality? *Bull Seism Soc Am* 86(6):1964–1978
58. Burland JB (1989) Small is beautiful—the stiffness of soils at small strains, 9th Laurits Bjerrum memorial lecture. *Can Geotech J* 26:499–516
59. Lo Presti DCF, Jamiolkowski M, Pallara O, Cavallaro A (1996) Rate and creep effect on the stiffness of soils. In: Chsahan TC, Kaliakin VN (1996) Measuring and modeling time dependent soil behavior, No. 61, Geotechnical Special Publication, pp 166–180, ASCE
60. Achmus M, Abdel-Rahman K, Kuo YS (2008) Design of monopile foundations for offshore wind energy plants. In: 11th Baltic geotechnical conference—geotechnics in maritime engineering, vol 1, Gdansk, Poland, pp 463–470
61. Sun J, Gong M, Tao X (2013) Dynamic shear modulus of undisturbed soil G_{max} under different consolidation ratios and its effects on surface ground motion. *Earthquake Eng Vib* 12(4):561–568
62. Hardin BO, Black WL (1968) Vibration modulus of normally consolidated clay. *J Soil Mech Found Div ASCE* 94(2):353–369
63. Sun J, Yuan XM (2008) The effect of consolidation ratios on dynamic shear modulus of soil. In: The 14th world conference on earthquake engineering, Beijing
64. He CR (1997) Dynamic triaxial test on dynamic modulus and damping ratio. *Chin J Geotech Eng* 19(2):39–48

65. Eide O, Andersen KH, Lunne T (1979) Observed foundation behavior of concrete gravity platforms installed in the North Sea 1973–1978. In: Proceedings of the BOSS'79 International conference on the behavior of off-shore structures, vol 2, London, pp 435–456
66. Lunne T, Myrsvoll F, Kjekstad O (1981) Observed settlements of five North Sea gravity platforms. Proc Offshore Technol Conf 4:305–317 Houston
67. Eide O, Andersen KH (1984) Foundation engineering for gravity structures in the Northern North Sea. Norwegian Geotechnical Institute, Publication No. 154
68. Terzaghi K, Peck RB (1948) Soil mechanics in engineering practice. Wiley, New York
69. Fox EN (1948) The mean elastic settlement of a uniformly loaded area at a depth below the ground surface, 2nd ICSMFE. Rotterdam 1:129–132
70. Meyerhof GG (1976) Bearing capacity and settlement capacity of pile foundations, the 11th Terzaghi lecture, ASCE. J Geot Eng 102:195–228
71. Schmertmann JH (1970) Static cone to compute static settlement over sand. ASCE J Soil Mech Found Div 96:1011–1043
72. Poulos HG (1993) Settlement prediction for bored pile groups. In: Proceedings of the 2nd geotechnical seminar on deep foundations on Bored and Auger Piles, Ghent, pp 103–117
73. Fellenius BH (2009) Basics of foundation design. Revised Electronic Edition, www.Fellenius.net
74. Chow FC, Jardine RJ, Bruzy F, Nauroy JF (1998) Effects of time on capacity of pipe piles in dense marine sand, ASCE. J Geotech Geoenviron Eng 124(3):254–264
75. Karlsrud K, Haugen T (1985) Axial static capacity of steel model piles in over-consolidated clay. In: Proceedings of the 11th ICSMFE, San Francisco
76. Komurka VE, Wagner AB, Edil TB (2003) Estimating soil/pile set-up. Wisconsin Department of Transportation, Sept 2003
77. Karlsrud K, Kalsnes B, Nowacki F (1992) Response of piles in soft clay and silt deposits to static and cyclic axial loading based on recent instrumented pile load tests. Society of Underwater Testing, London
78. Karlsrud K, Clausen CJF, Aas PM (2005) Bearing capacity of driven piles in clay, the NGI approach. Frontiers in Offshore Geotechnics: ISFOG 2005, Perth, Australia, pp 775–782
79. Geotechnical re-analyses of pile capacities, Oseberg—Re-analysis, No. 20100370-00-4-R, Contracted report by NGI for Aker Solutions, 2010
80. Ishihara K (1996) Soil behaviour in earthquake geotechnics. Oxford Engineering Science Series 46
81. Lefebvre GS, Leboeuf D, Demers B (1989) Stability threshold for cyclic loading of saturated clay. Can Geotech J 26(1):122–131
82. Casagrande A, Wilson SD (1951) Effect of rate of loading on the strength of clays and shales at constant water content. Géotechnique 2(3):251–263
83. Graham J, Crooks JHA, Bell AL (1983) Time effects on the stress-strain behaviour of natural soft clays. Géotechnique 33(3):327–340
84. Martindale H, Basu D (2011) constitutive model for rate dependent behavior of clay, internal geotechnical report 2011-3. Department of Civil and Environmental Engineering, University of Connecticut
85. Kim DS, Stokoe KH, Hudson WR (1991) Deformational characteristics of soils at small to intermediate strains from cyclic tests, 1177-3. Center of Transportation Research, Bureau of Engineering Research, Austin Texas
86. Matesic L, Vucetic M (2003) Strain-rate effect on soil secant shear modulus at small cyclic strains. J Geotech Geoenviron Eng 129(6):536–539
87. Youssef Hashash MA, Phillips C, Groholski DR (2010) Recent advances in non-linear site response analysis. In: 5th international conference on recent advances in geotechnical earthquake engineering and soil dynamics, San Diego, California, USA

88. Park D, Hashash YMA (2008) Rate-dependent soil behavior in seismic site response analysis. *Can Geotech J* 45(4):454–469
89. Ding J, Sui T, Zhang C, Li Y (2017) Effects of initial consolidation on the 3D wave-induced seabed response around a pile. In: *Proceedings of the 36th international conference on Ocean, offshore and arctic engineering*, June 25–30, Trondheim, Norway
90. Norsok G-001 (2004) Marine soil investigations. Standard Norway, Lysaker
91. ISO 19902 (2007) Petroleum and natural gas industries—fixed steel offshore structures
92. ISO 19901-4 (2003) Petroleum and natural gas industries—specific requirements for offshore structures—Part 4: geotechnical and foundation design considerations
93. DNVGL-RP-C212, Offshore soil mechanics and geotechnical engineering, Høvik, 2017
94. Roeder CW (1990) Comparison of LRFD and allowable stress design methods for steel structures. *Fifth Seminario de Ingenieria Estructural*, San Jose, Costa Rica
95. Ulf Björkenstam (1998) Reliability based design, 1st edn. Chalmers University of Technology
96. Cornell C (1969) A probability-based structural code. *J Am Concr Inst* 66(12):974–985
97. Transportation Research Board of the National Academies (2010) National cooperative highway research program, LRFD design and construction of shallow foundations for highway bridge structures. NCHRP Report 651, Washington, DC
98. Phoon K, Kulhawy F, Grigoriu M (1995) Reliability-based design of foundations for transmission line structures, report TR-105000. Electrical Power Research Institute, Palo Alto
99. Thoft-Christensen P, Murotsu Y (1986) Application of structural systems reliability theory. Springer, Berlin
100. Ryden J (2011) Failure probabilities and safety index (lecture notes). Uppsala University, Spring
101. Hasofer AM, Lind NC (1974) Exact and invariant first order second-moment code format. *ASCE J Eng Mech Div* 100(EM1):111–121
102. Tvedt L (1989) Second order reliability by an exact integral. In: Thoft-Christensen P (ed) Reliability and optimization of structural systems. In: *Proceedings of the second IFIP WG7.5 conference* (1988). Springer, London
103. Björkenstam U (2002) Exercise in ship structures basic course. Department of Naval Architecture and Ocean Engineering, Chalmers University of Technology
104. Ditlevsen O, Madsen HO (2007) Structural reliability methods. Wiley, Chichester
105. Melchers RE (1999) Structural reliability analysis and prediction, 2nd edn. Wiley, New York
106. Coleman HW, Steele WG (1999) Experimentation and uncertainty analysis for engineers, 2nd edn. Wiley, New York
107. Jensen JJ (2001) Load and global response of ships. Elsevier Science Ltd, Oxford
108. DnV-RP-C207 (2012) Statistical representation of soil data. DET NORSKE VERITAS AS, Høvik, Norway
109. Eurocode 7 (2004) Geotechnical engineering, Part 1: general rules. EN-1997-1, European Committee for Standardization, Brussels, Belgium
110. Andersen LV, Sørensen JD, Kim SB, Yi JH, Yoon GL, Manuel L (2015) Influence of characteristic-soil-property-estimation approach on the response of monopiles for offshore wind turbine. *J Ocean Wind Energy* 2(3):160–167
111. ISO 2394 (2015) General principles on reliability for structures, 4th edn
112. Dean ETR (2010) Offshore geotechnical engineering—principles and practice. Thomas Telford, Reston, VA, USA
113. Luna R, Jadi H (2000) Determination of dynamic soil properties using geophysical methods. In: *Proceedings of the first international conference on the application of geophysical and NDT methodologies to transportation facilities and infrastructure*, St. Louis, MO
114. Chen CF (1985) Mechanics of geomaterials. In: Bazant Z (ed) Wiley, pp 65–86

115. Hardin BO, Drnevich VP (1972) Shear modulus and damping in soils: measurement and parameter effects. *J Soil Mech Found Div ASCE* 98(6):603–624
116. Idriss IM, Dobry R, Singh RD (1978) Nonlinear behaviour of soft clays during cyclic loading. *J Geotech Eng* 104(12):1427–1447
117. Likitlersuang S (2003) A hyperplasticity model for clay behavior: an application to Bangkok Clay. PhD thesis, University of Oxford, UK
118. Vucetic M (1992) Soil properties and seismic response. In: *Proceedings of the 10th world conference on earthquake engineering*, Rotterdam
119. Peck RB, Hanson WE, Thornburn TH (1974) *Foundation engineering*. Wiley, New Jersey
120. Hardin BO, Richart FE (1963) Elastic wave velocities in granular soils. *J Soil Mech Found Div ASCE* 89(SM1):33–65
121. Jardine RJ, Symes MJ, Burland JB (1984) The measurement of soil stiffness in the triaxial apparatus. *Géotechnique* 34(3):323–340
122. Hird CC, Yung PCY (1989) The use of proximity transducer for local strain measurements in triaxial tests. *ASTM Geotech Test J* 12(4):292–296
123. Jia J (2014) *Essentials of applied dynamic analysis*. Springer, Heidelberg, p 424
124. EPRI (Electric Power Research Institute) (1993) *Guidelines for determining design basis ground motions*, Final Rep. No. TR-102293, Palo Alto, California
125. II Stokoe KH, Hwang SK, Lee NJ, Andrus RD (1994) Effects of various parameters on the stiffness and damping of soils at small to medium strains. In: *Proceedings international symposium prefailure deformation characteristics of geomaterials*, vol 2, Sapporo, Japan, pp 785–816
126. Vucetic M (1994) Cyclic threshold shear strains in soils. *ASCE J Geotech Eng* 120:2208–2228
127. Santamarina JC (2001) *Soils and waves*. Wiley, New York
128. Jardine RJ (1992) Some observations on the kinematic nature of soil stiffness. *Soils Found* 32(2):111–124
129. Atkinson JH, Salfors G (1991) Experimental determination of soil proper-ties. In: *Proceedings of the 10th ECSMFE*, vol 3, Florence, pp 915–956
130. Matsui T, Ohara H, Ito T (1980) Cyclic stress-strain history and shear characteristics of clay. *ASCE J Geotech Eng* 106(10):1101–1120
131. Ansal AM, Erken A (1989) Undrained behaviour of clay under cyclic shear stresses. *J Geotech Eng* 115(7):968–983
132. Hsu C, Vucetic M (2004) Volumetric threshold shear strain for cyclic settlement. *J Geotech Geoenviron Eng* 130(1):58–70
133. Hsu C, Vucetic M (2006) Threshold shear strain for cyclic pore-water pressure in cohesive soils. *J Geotech Geoenviron Eng* 132(10):1325–1335
134. Díaz-Rodríguez JA (1989) Behavior of Mexico City clay subjected to undrained repeated loading. *Can Geotech J* 26(1):159–162
135. Diaz-Rodríguez JA, Santamarina C (2001) Mexico City soil behavior at different strains: observation and physical interpretation. *J Geotech Geoenviron Eng* 127(9):783–789
136. McCarron WO, Lawrence JC, Werner RJ, Germaine JT, Cauble DF (1995) Cyclic direct simple shear testing of a Beaufort Sea clay. *Can Geotech J* 32:584–600
137. Houston WN, Herrmann HG (1980) Undrained cyclic strength of marine soils. *ASCE J Geotech Eng Div* 106(6):691–712
138. Karlsrud K, Haugen T (1983) Cyclic loading of piles and anchors—field model test, final report, summary and evaluation of test results. *NGI Report No. 40010-28*
139. Diaz-Rodríguez JA, López-Molina JA (2008) Strain thresholds in soil dynamics. In: *The 14th world conference on earthquake engineering*, Beijing
140. Likitlersuang S, Teachavorasinskun S, Surarak C, Erwin O, Balasubramaniam A (2013) Small strain stiffness and stiffness degradation curve of Bangkok Clays. *Soils Found* 53(4):498–509

141. Hardin BO, Drnevich VP (1972) Shear modulus and damping in soils: design equations and curves. *J Soil Mech Found Div* 98(SM7):667–692
142. Pyke RM (1993) Modeling of dynamic soil properties, guidelines for determining design bases ground motions. Appendix 7.A, Electric Power Research Institute, 7.A-1–7.A-90
143. II Stokoe KH, Darendeli MB, Andrus RD, Brown LT (1999) Dynamic soil properties: laboratory, field and correlation studies. In: *Proceedings of the 2nd international conference on earthquake geotechnical engineering*, Lisbon, vol 3, pp 811–845
144. Darendeli MB (2001) Development of a new family of normalized modulus reduction and material damping curves. PhD Thesis, Department of Civil Engineering, University of Texas, Austin
145. Zhang J, Andrus RD, Juang CH (2005) Normalized shear modulus and material damping ratio relationships. *J Geotech Geoenviron Eng* 131(4):453–464 ASCE
146. Stewart JP, Kwok AOL, Hashash YMA, Matasovic N, Pyke R, Wang Z, Yang Z (2008) Benchmarking of nonlinear geotechnical ground response analysis procedures. PEER Report 2008/04, Pacific Earthquake Engineering Research Center, University of California, Berkeley
147. Hardin BO (1978) The nature of stress-strain behaviour of soils: measurement and parameter effects. In: *Proceedings of earthquake engineering and soil dynamics*, ASCE Pasadena, CA, vol 1, pp 3–89
148. Jamiolkowski M, Leroueil S, Lopresti DCF (1991) Theme lecture: design parameters from theory to practice. In: *Proceedings of geo-coast 91*, Yokohama, pp 1–4
149. Seed HB, Idriss IM (1970) Soil moduli and damping factors for dynamic response analyses. Report EERC 70-10, EERC, University of California, Berkeley
150. Rix GJ, Stokoe KH (1992) Correlation of initial tangent modulus and cone resistance. In: *Proceedings of the international symposium on calibration chamber testing*, Potsdam, New York, 1991, pp. 351–362, Elsevier, Amsterdam
151. Weiler WA (1988) Small strain shear modulus of clay. In: *Proceedings of ASCE conference on earthquake engineering and soil dynamics ii: recent advances in ground motion evaluation*, Geotechnical Special Publication 20, ASCE, New York, pp 331–335
152. Mayne PW, Rix GJ (1993) G_{\max} - q_c relationships for clays. *Geotech Test J* GTJODJ 16:54–60
153. Sugito M, Goda H, Masuda T (1994) Frequency dependent equi-linearized technique for seismic response analysis of multi-layered ground, *Doboku Gakkai Rombun-Hokokushu. Proc Jpn Soc Civ Eng* 493(3–2):49–58
154. Assimaki D, Kausel E, Whittle AJ (2000) Model for dynamic shear modulus and damping for granular soils. *J Geotech Geoenviron Eng* 126(10):859–869
155. Santos JA (2000) Behavior of piles under lateral static and dynamic loading. PhD Thesis, Technical University of Lisbon, Portugal
156. Santos JA, Gomes Correia A (2000) Shear modulus of soils under cyclic loading at small and medium strain level. In: *Proceedings of 12th world conference on earthquake engineering*, New Zealand
157. Borden RH, Shao L, Gupta A (1996) Dynamic properties of piedmont residual soils. *J Geotech Eng* 122(10):813–821
158. Ishibashi I, Zhang XJ (1993) Unified dynamic shear moduli and damping ratios of sand and clay. *Soils Found* 33(1):182–191
159. II Stokoe KH, Darendeli MB, Gilbert RB, Menq FY, Choi WK (2004) Development of a new family of normalized modulus reduction and material damping curves. In: *Proceedings NSF/PEER international workshop on uncertainties in nonlinear soil properties and their impact on modelling dynamic soil response*, University of California at Berkeley, Berkeley, California
160. Masing G (1926) Eigenspannungen und Verfertigung beim Messing. In: *Proceedings of 2nd international congress on applied mechanics*, Zurich

161. Vucetic M (1990) Normalized behavior of clay under irregular cyclic loading. *Can Geotech J* 27:29–46
162. Matasovic N (1993) Seismic response of composite horizontally-layered soil deposits. PhD Thesis, University of California
163. Wang ZL, Han QY, Zhou GS (1980) Wave propagation method of site seismic response by visco-elastoplastic model. *Proc Seventh World Conf Earthq Eng* 2:379–386
164. Pyke RM (2000) TESS: a computer program for nonlinear ground response analyses. TAGA Engineering Systems & Software, Lafayette, California
165. Hashash YMA, Park D (2001) Non-linear one-dimensional seismic ground motion propagation in the Mississippi embayment. *Eng Geol* 62:185–206
166. Vucetic M, Dobry R (1986) Pore pressure buildup and liquefaction at level sandy sites during earthquakes. Research report CE-86-3, Department Civil Engineering, Rensselaer Polytechnic Institute, New York
167. Lanzo G, Vucetic M (1999) Effect of soil plasticity on damping ratio at small cyclic strains. *Soils Found* 39(4):131–141
168. Phillips C, Hashash YM (2009) Damping formulation for nonlinear 1D site response analyses. *Soil Dyn Earthq Eng* 29(7):1143–1158
169. Clough RW, Penzien J (2003) Dynamics of structures, 3rd edn. Computers and Structures, Berkeley, CA
170. Kwok AOL, Stewart JP, Hashash YMA, Matasovic N, Pyke R, Wang Z, Yang Z (2007) Use of exact solutions of wave propagation problems to guide implementation of nonlinear, time-domain ground response analysis routines. *J Geotech Geoenviron Eng ASCE* 133(11):1385–1398
171. Park D, Hashash YMA (2004) Soil damping formulation in nonlinear time domain site response analysis. *J Earthq Eng* 8(2):249–274
172. Hudson M, Idriss I, Beirkae M (1994) QUAD4M user's manual
173. Bathe KJ (1982) Finite element procedures in engineering analysis. Prentice-Hall, Englewood Cliffs, NJ
174. Dafalias Y, Herrmann LR (1982) Bounding surface formulation of soil plasticity, soil mechanics cyclic and transient loads. In: Pande GN, Zienkiewicz OC (eds) Chapter 10. Wiley, New York, pp 253–282
175. Hashiguchi K (1985) Two- and three-surface models of plasticity. In: Proceedings 5th international conference numerical methods in geomechanics, Nagoya, pp 285–292
176. Whittle AJ (1993) Evaluation of a constitutive model for over consolidated clays. *Géotechnique* 43(2):289–313
177. Roscoe KH, Schofield AN, Thirairajah A (1963) Yielding of clays in states wetter than critical. *Géotechnique* 13(3):211–240
178. Ti KS, Huat BBK, Noorzaei J, Jaafar MS, Gue See Sew MS (2009) A review of basic soil constitutive models for geotechnical applications. *Electron J Geotech Eng* 14:1–18 (bund. J)
179. Drucker DC, Prager W (1952) Soil mechanics and plastic analysis or limit design. *Quart Appl Math* 10(2):157–165
180. Duncan JM, Chang CY (1970) Nonlinear analysis of stress and strain in soils. *ASCE J Soil Mech Found Div* 96:1629–1653
181. Schanz T, Vermeer PA, Bonnier PG (1999) The Hardening soil model: formulation and verification, beyond 2000 in computational geotechnics—10 years of PLAXIS, Rotterdam
182. Roscoe KH, Burland JB (1968) On the generalized stress-strain behaviour of wet clay. In: Heyman J, Leckie FA (eds) Engineering plasticity. Cambridge University Press, London, pp 535–609
183. Schofield A, Wroth P (1968) Critical state soil mechanics—lecture notes. Cambridge University
184. Gens A, Potts DM (1988) Critical state models in computational geomechanics. *Eng Comput* 5:178–197

185. Brinkgreve RBJ (2005) Selection of soil models and parameters for geotechnical engineering application. In: Yamamuro JA, Kaliakin VN (eds) *Geotechnical special publication ACSE*, vol 128, pp 69–98
186. Gudehus G (1985) Requirements for constitutive relations for soils. In: Baazant Z (ed) *Mechanics of geomaterials*. Wiley, pp 47–63
187. Manzari MT, Dafalias YF (1997) A critical state two-surface plasticity model for sands. *Géotechnique* 47(2):255–272
188. Jia J (2017) *Modern earthquake engineering*. Springer, Heidelberg, p 848
189. Dobry R, Martin GM, Parra E, Bhattacharyya A (1992) Development of site-dependent ratios of elastic response spectra (RRS) and site categories for building seismic codes. In: Martin GM (ed) *Proceedings of the 1992 NCEER/SEAOC/BSSC workshop on site response during earthquakes and seismic code provisions*. National Center for Earthquake Engineering Research Special Publication NCEER-94-SP01 (Buffalo, NY), University of Southern California, Los Angeles, 18–20 Nov 1992
190. Joyner WB, Warrick R, Fumal T (1981) The effect of quaternary alluvium on strong ground motion in the Coyote Lake, California earthquake of 1979. *Bull Seismol Soc Am* 71:1333–1349
191. Aki K (1988) Local site effects on strong ground motion. In: L Von Thun (ed) *Proceeding of the specialty conference on earthquake engineering and soil dynamics ii: recent advances in ground-motion evaluation*. ASCE Geotechnical Special Publication No. 20, pp 103–155, Park City, Utah, 27–30 June 1988
192. Boore DM, Joyner WB, Fumal TE (1997) Equations for estimating horizontal response spectra and peak acceleration from western North American earthquakes: a summary of recent work. *Seismol Res Lett* 68(1):128–153
193. Elnashai AS, Di Sarno L (2008) *Fundamentals of earthquake engineering*. Wiley, USA
194. Towhata I (2008) *Geotechnical earthquake engineering*. Springer, Heidelberg
195. Broderick BM, Elnashai AS, Ambraseys NN, Barr JM, Goodfellow RG, Higazy EM (1994) The Northridge (California) earthquake of 17 January 1994: observations, strong motion and correlative response analysis. In: *Engineering seismology and earthquake engineering*, Research Report No. ESEE 94/4, Imperial College, London, UK
196. Dobry R, Iai S (2000) Recent developments in the understanding of earthquake site response and associated seismic code implementation. *GeoEng2000*, Melbourne
197. Seed HB, Romo MP, Sun JI, Jaime A, Lysmer J (1988) The Mexico earthquake of Sept 19, 1985: relationships between soil conditions and earthquake ground motions. *Earthq Spectra* 4(4):687–729
198. Eurocode 8 (2004) *Design of structures for earthquake resistance—Part 1: general rules, seismic actions and rules for buildings*
199. China Net for Engineering Construction Standardization (2010) *Code for seismic design of buildings*, GB 50011-2010. China Building Industry Press, Beijing
200. Bozorgnia Y, Bertero VV (eds) (2004) *Earthquake engineering: from engineering seismology to performance-based engineering*. CRC Press, Boca Raton
201. Richter CF (1935) An instrumental earthquake scale. *Bull Seismol Soc Am* 25:1–32
202. Zhou XY, Hu YX (2001) An overview and preview of China-US joint research on earthquake engineering. In: Spencer BF Jr, Hu YX (eds) *Earthquake engineering frontiers in the new millennium*. Swets & Zeitinger BV, Lisse
203. Riks E (1972) The application of Newton’s method to the problem of elastic stability. *J Appl Mech* 39:1060–1065
204. Papadrakakis M, Lagaros ND, Fragiadakis M (2006) *Seismic design procedures in the framework of evolutionary based structural optimization, computational mechanics? Solids, structures and coupled problems*. Springer, Netherlands
205. Conte JP (1992) Effects of earthquake frequency nonstationary on inelastic structural response. In: *Proceedings of the 10th world conference on earthquake engineering*, Madrid, Spain, pp 3645–3651

206. Paradimitriou K, Beck JL (1992) Stochastic characterization of ground motion and applications to structural response. In: Proceedings of the 10th world conference on earthquake engineering, Madrid, Spain, pp 835–844
207. Wang J, Zhou J (1997) The influence of non-stationarity of seismic motions on the nonlinear response of structures. *Earthq Eng Eng Vibr* 17(2):16–20
208. Naga P (2011) Analyzing the effect of moving resonance on seismic response of structures using wavelet transforms. Virginia Polytechnic Institute and State University
209. Anderson JC, Bertero VV (1987) Uncertainties in establishing design earthquakes. *J Struct Eng ASCE* 113(8):1709–1724
210. PEER center (2000) ATC, Japan Ministry of education, science, sports and culture, US-NSF, effects of near-field earthquake shaking. In: Proceedings of the US–Japan Workshop, Mar 2000, San Francisco, pp 20–21
211. Duek CM, Luco JE, Carriveau AR, Hradilek PJ, Lastrico R, Ostrom D (1970) Strong earthquake motion and site conditions, Hollywook. *Bull Seismol Soc Am* 60(4):1271–1289
212. GovindaRaju L, Ramana GV, Hanumantha C, Sitharam TG (2004) Site-specific ground response analysis. *Current Sci* 87(10):1354–1362
213. Lysmer J, Seed HB, Schnabel PB (1971) Influence of base-rock characteristics on ground response. *Bull Seismol Soc Am* 61(5):1213–1232
214. Roesset JM, Whitman RV (1969) Theoretical background for amplification studies. No. R69-15, Soils Publication No. 231, MIT, Cambridge
215. Matthesen RB, Duke CM, Leeds DJ, Fraser JC (1964) Site characteristics of Southern California strong-motion earthquake stations. Part Two, No. 64-15, Department of Engineering, University of California, Los Angeles
216. Kanai K (1952) Relation between the nature of surface layer and the amplitude of earthquake motions. *Bull Tokyo Earthq Res Inst* 30:31–37
217. Idriss IM, Seed HB (1968) Seismic response of horizontal soil layers. *J Soil Mech Found Div ASCE* 94(SM4):1003–1031
218. Pacific Earthquake Engineering Research Center (PEER), Guidelines for Performance-Based Seismic Design of Tall Buildings, Version 1.0, California, November 2010
219. Roesset P (1970) Fundamentals of soil amplification. *Seismic Design for Nuclear Power Plants*, pp 183–244.
220. US Army Corps of Engineers (1999) Engineering and design–response spectra and seismic analysis for concrete hydraulic structures, EM 1110-2-6050
221. Seed HB, Idriss IM (1969) Influence of soil conditions on ground motions during earthquakes. *ASCE J Soil Mech Found Div* 95:99–137
222. Idriss IM, Sun JI (1992) SHAKE91: a computer program for conducting equivalent linear seismic response analyses of horizontally layered soil deposits. User’s Guide, University of California, Davis
223. Schnabel PB, Lysmer J, Seed HB (1972) SHAKE: a computer program for earthquake response analysis of horizontally layered sites. Report EERC 72-12, Earthquake Engineering Center, University of California, Berkeley
224. Idriss IM (1990) Response of soft soil sites during earthquakes. In: Proceedings of H. Bolton Seed memorial symposium. University of California, Berkeley
225. Chatterjee K, Choudhury D, Poulos HG (2015) Seismic analysis of laterally loaded pile under influence of vertical loading using finite element method. *Comput Geotech* 67: 172–186

226. Hudson M, Idriss IM, Beikae M (2003) QUAD4M: a computer program to evaluate the seismic response of soil structures using finite element procedures and incorporating a compliant base, rev. 2003. Center for Geotechnical Modeling Department of Civil and Environmental Engineering University of California Davis
227. Zeghal M, Elgamal AW (1994) Analysis of site liquefaction using earthquake records. *J Geotech Eng ASCE* 120(6):996–1017
228. Elgamal AW, Zeghal M, Parra E (1996) Liquefaction of reclaimed island in Kobe, Japan. *ASCE J Geotech Eng* 122(1):39–49
229. SHAKE 2000 (2008) A computer program for the 1-D analysis of geotechnical earthquake engineering problem. University of California, Berkeley
230. www.shake2000.com
231. Vucetic M, Dobry R (1991) Effect of soil plasticity on cyclic response. *J Geotech Eng ASCE* 117(1):89–107
232. Yoshida N, Iai S (1998) Nonlinear site response and its evaluation and prediction. In: Proceedings of the 2nd international symposium on the effect of surface geology on seismic motion, Yokosuka, Japan, pp 71–90
233. Martin PP, Seed HB (1978) MASH: a computer program for the non-linear analysis of vertically propagating shear waves in horizontally layered deposits. University of California at Berkeley, San Francisco
234. Streeter VL, Wylie EB, Richart FE (1974) Soil motion computation by characteristic method. *J Geotech Eng Div* 100:247–263
235. Ramberg W, Osgood WR (1943) Description of stress-strain curves by three parameters. Technical Note No. 902, National Advisory Committee For Aeronautics, Washington
236. Lee MK, Finn WDL (1978) DESRA-2, dynamic effective stress response analysis of soil deposits with energy transmitting boundary including assessment of liquefaction potential. Soil Mechanics Series, No. 36, Department of Civil Engineering, University of British Columbia, Vancouver, Canada
237. Gerolymos N, Gazetas G (2005) Constitutive model for 1-D cyclic soil behaviour applied to seismic analysis of layered deposits. *Soils and Foundation* 45(3):147–159
238. Bard PY (1994) Effects of surface geology on ground motion: recent results and remaining issues. In: Proceedings of 10th European conference earthquake engineering, vol 1, Vienna, Austria, pp 305–323
239. Faccioli E (1991) Seismic amplification in the presence of geological and topographic irregularities. In: Proceedings of the 2nd international conference on recent advances in geotechnical earthquake engineering and soil dynamics, vol 2, University of Missouri-Rolle, St. Louis, Missouri, pp 1779–1797
240. Chávez-García FJ, Sanchez LR, Hatzfeld D (1996) Topographic site effects and HVSR, a comparison between observations and theory. *Bull Seism Soc Am* 86:1559–1575
241. Ötilakis K, Raptakis D, Makara K, Ktenidou OH, Pandi K, Manakou M, Pitilakis D, Diagourtas D (2004) Effects of surface and subsurface topography on strong ground motion at the city of Aegion –Greece. In: 13th world conference on earthquake engineering, Vancouver
242. Angot A (1910) Le tremblement de terre du 11 juin 1909 dans le Sud-Est de la France, I, Enquête du Bureau Central Météorologique. *Ann. Géogr.* 103:8–15
243. Brambati A, Faccioli E, Carulli GB, Cucchi F, Onofri R, Stefanini S, Ulcigrai F (1980) Studio de microzonazione sismica dell'area di Tarcento (Friuli), Regione Autonomia Friuli-Venezia Giulia and Università degli Studi di Trieste con la collaborazione del Politecnico di Milano, Trieste
244. Siro L (1982) Southern Italy November 23 1980 earthquake. In: Proceedings of the 7th European conference on earthquake engineering, Athens, Greece, Sept 1982
245. Çelebi M, Hanks T (1986) Unique site response conditions of two major earthquakes of 1985: Chile and Mexico. In: Proceedings of the international symposium of engineering geology problems in Seismic Areas, vol 4, Bari, Italy, Apr 1986

246. Hartzell SH, Carver DL, King KW (1994) Initial investigation of site and topographic effects at Robinwood Ridge, California. *Bull Seismol Soc Am* 84:1336–1349
247. Huang BS (2000) Two-dimensional reconstruction of the surface ground motion of an earthquake: the Sept 21, 1999, Chi-Chi, Taiwan earthquake. *Geophys Res Lett* 27:3025–3028
248. Assimaki D, Gazetas G, Kausel E (2005) Effects of local soil conditions on the topographic aggravation of seismic motion: parametric investigation and recorded field evidence from the 1999 Athens earthquake. *Bull Seismol Soc Am* 95:1059–1089
249. Boore DM (1972) A note on the effect of simple topography on seismic SH waves. *Bull Seismol Soc Am* 62:275–284
250. Chavez-Garcia FJ, Rodriguez M, Field EH, Hatzfeld D (1997) Topographic site effects, a comparison of two non-reference methods. *Bull Seism Soc Am* 87:1667–1673
251. Nechtschein S, Bard PY, Gariel JC, Meneroud JP, Dervin P, Coushing M, Gaubert B, Vidal S, Duval AM (1995) A topographic effect study in the Nice region. In: Proceedings of the 5th International Conference on Seismic Zonation, October 17–19, Nice, France, Ouest Edition Nantes, II, pp 1067–1074
252. Aki K (1988) Local site effects on strong ground motion. In: VonThun JL (ed) *Earthquake engineering and soil dynamics ii—recent advances in ground motion evaluation*, June 27–30. Utah, Park City, pp 103–155
253. Castellani A, Peano A, Sardella L (1982) On analytical numerical techniques for seismic analysis of topographic irregularities. In: Proceedings of the 7th European conference on earthquake engineering, Athens, Greece
254. Bard PY (1982) Diffracted waves and displacement field over two-dimensional elevated topographies. *Geophys J R Astr Soc* 71:111–120
255. D.M. 14 GENNAIO (2008) Norme Tecniche per le Costruzioni, G.U. n. 29 del 4 febbraio
256. Vidale JE, Helmberger DV (1988) Elastic finite difference of the 1971 San Fernando earthquake. *Bull Seismol Soc Am* 78(1):122–141
257. Chávez-García FJ, Faccioli E (2000) Complex site effects and building codes: making the leap. *J Seismol* 4:23–40
258. Makra K, Raptakis D, Chávez-García FJ, Pitilakis K (2001) Site effects and design provisions: the case of EUROSEISTEST. *Pure Appl Geophys* 158(12):2349–2367
259. Frankel A, Vidale J (1992) A three-dimensional simulation of seismic waves in the Santa Clara Valley, California, from a Loma Prieta aftershock. *Bull Seismol Soc Am* 82:2045–2074
260. Olsen KB, Archuleta RJ, Matarese JR (1995) Three-dimensional simulation of a magnitude 7.75 earthquake on the San Andreas fault. *Science* 270:1628–1632
261. Raptakis D, Chávez-García FJ, Makra K, Pitilakis K (2000) Site effects at EUROSEISTEST—I, determination of the valley structure and confrontation of observations with 1D analysis. *Soil Dyn Earthq Eng* 19(1):1–22
262. Chávez-García FJ, Raptakis D, Makra K, Pitilakis K (2000) Site effects at EUROSEISTEST—II, results from 2D numerical modeling and comparison with observations. *Soil Dyn Earthq Eng* 19(1):23–39
263. Bard PY, Bouchon M (1985) The two-dimensional resonance of sediment-filled valleys. *Bull Seismol Soc Am* 75(2):519–541
264. Vessia G, Russo S, Presti DL (2011) A new proposal for the evaluation of the amplification coefficient due to valley effects in the simplified local seismic response analyses, vol 4, *Rivista Italiana Di Geotecnica*
265. Silva WJ, Turcotte T, Moriawaki Y (1988) Soil response to earthquake ground motion, EPRI report NP-5747. Electric Power Research Institute, Palo Alto, CA
266. Faccioli E (1996) On the use of engineering seismology tools in ground shaking scenarios. In: Proceedings of 11th world conference earthquake engineering, Acapulco, No. 2007
267. Aki K (1993) Local site effects on weak and strong ground motion. *Tectonophysics* 218:93–111

268. Bard PY, Bouchon M (1980) The seismic response of sediment-filled valleys. Part 1. The case of incident SH waves. *Bull Seism Soc Am* 70:1263–1286
269. Bard PY, Bouchon M (1980) The seismic response of sediment-filled valleys. Part 2. The case of incident P and SV waves. *Bull Seism Soc Am* 70:1921–1941
270. Bard PY, Bouchon M (1985) The two-dimensional resonance of sediment filled valleys. *Bull Seism Soc Am* 75:519–554
271. Bouaanani N, Renaud S (2014) Effects of fluid–structure interaction modeling assumptions on seismic floor acceleration demands within gravity dams. *Eng Struct* 67:1–18
272. McKenna F, Fenves GL, Scott MH, Jeremic B (2000) Open system for earthquake engineering simulation (OpenSees). Pacific Earthquake Engineering Research Center, University of California, Berkeley, California
273. Rahmani A, Taiebat M, Liam Finn WF (2014) Nonlinear dynamic analysis of Meloland Road Overpass using three-dimensional continuum modeling approach. *Soil Dyn Earthq Eng* 57:121–132
274. Besseling F (2012) Soil-structure interaction modeling in performance based seismic jetty design. Technical University of Delft
275. Mononobe HA et al (1936) Seismic stability of the earthquake dam. In: *Proceedings of the 2nd congress on large dams*, vol 4, Washington, DC
276. Gazetas G (1987) Seismic response of earth dams; some recent development. *Soil Dyn Earthq Eng* 6(1):2–47
277. Stara-Gazetas E (1986) A method for inelastic response analysis of earthquake dam. PhD dissertation, Rensselaer Polytechnic Institute, Troy, NY
278. Martin GR, Dobry R (1994) Earthquake site response and seismic code provisions. *National Center for Earthquake Engineering Research Bulletin*, vol 8, No. 4, Buffalo, New York
279. Crouse CB, McGuire JW (1997) Site response studies for purpose of revising NEHRP seismic provisions. Dames and Moore Consultants, Seattle, Washington
280. NGI, NORSAR, PRINCIPIA (188) Earthquake loading on the Norwegian Continental Shelf, Oslo
281. Bozorgnia Y, Campbell KW (2004) The vertical-to-horizontal response spectral ratio and tentative procedures for developing simplified V/H and vertical design spectra. *J Earthq Eng* 8:175–207
282. Bozorgnia Y, Campbell K (2016) NGA-West2 vertical-to-horizontal (V/H) ground motion model. *Earthq Spectra Prof J Earthq Eng Res Inst* 32(2):979–1004
283. Papazoglou AJ, Elnashai AS (1996) Analytical and field evidence of the damaging effect of vertical earthquake ground motion. *J Earthq Eng Struct Dyn* 25(10):1109–1137
284. Elgamal A, He LC (2004) Vertical earthquake motions records: an overview. *J Earthq Eng* 8(5):663–697
285. Richter CF (1958) *Elementary seismology*. W.H. Freeman and Company, San Francisco, CA
286. Mok CM, Chang CY, Legaspi DE (1998) Site response analyses of vertical excitation. In: *Geotechnical earthquake engineering and soil dynamics III*, Seattle, WA, pp 739–753
287. Elgamal A, Lai T, Yang Z, He L (2001) Dynamic soil properties, seismic downhole arrays and applications in practice. In: *4th international conference on recent advances in geotechnical earthquake engineering and soil dynamics*, San Diego, California, USA
288. ISO19901-2 (2017) *Petroleum and natural gas industries-specific requirements for offshore structures-Part 2: seismic design procedures and criteria*, 2nd ed.
289. ISO19901-2 (2004) *Petroleum and natural gas industries-specific requirements for offshore structures-Part 2: seismic design procedures and criteria*, 1st ed.
290. Building Seismic Safety Council (BSSC) (2009) NEHRP recommended seismic provisions for new buildings and other structures, Rep. FEMA P-750, FEMA, Washington, DC

291. JTG/T B02-01-2008 (2008) Guidelines for seismic design of high bridges. Ministry of Transport of the People's Republic of China
292. Smith CE (1997) Dynamic response of steel-jacket platform subject to measured seafloor earthquake ground motions. In: Proceedings 8th international conference on the behavior of offshore structures, vol 3, Pergamon, Elsevier Science Ltd., Oxford, England
293. Sleaf GE (1990) The long-term measurement of strong-motion earthquakes offshore South California. In: Proceedings of OTC 1990, society of petroleum engineers, Richardson, Texas
294. Crouse CB, Quilter J (1991) Seismic hazard analyses and development of design spectra for Maui A platform. In: Proceedings of the Pacific conference on earthquake engineering, Auckland, New Zealand
295. Dolan DKM, Crouse CB, Quilter JM (1992) Seismic reassessment of Maui A. In: Proceedings of the offshore technology conference, OTC 1992, Society of petroleum engineers, Richardson, Texas
296. Boore DM, Smith CE (1999) Analysis of earthquake recordings obtained from the seafloor earthquake measurement system (SEMS) instruments deployed off the coast of Southern California. *Bull Seismol Soc Am* 89(1):260–274
297. Brown LA (2003) Assessment of seismic risk for subsea production systems in the Gulf of Mexico. Thesis of Master of Science, Texas A&M University, USA, December 2003
298. Pacific Earthquake Engineering Research Center (PEER) (2010) Guidelines for performance-based seismic design of tall buildings, Version 1.0, California, November 2010
299. Baker JW, Shahi SK, Jayaram N (2011) New ground motion selection procedures and selected motions for the PEER transportation research program. Pacific Earthquake Engineering Research Center, University of California, Berkeley, CA, PEER Report 2011/03, 2011
300. Willford M, Whittaker A, Klemencic R (2008) Recommendations for the seismic design of high-rise buildings, council on tall buildings and Urban Habitat
301. ASCE 7-05 (2005) Minimum design loads for buildings and other structures. American Society of Civil Engineers
302. Chordati Amiri G, Ashtrai P, Rahami H (2006) New development of artificial record generation by wavelet theory. *Struct Eng Mech* 22:185–195
303. Chordati Amiri G, Asadi A (2008) New method for simulation of earthquake records by using adapted wavelet. In: The 14th world conference on earthquake engineering, Beijing
304. Abrahamson NA (1992) Non-stationary spectral matching. *Seismol Res Lett* 63(1):30
305. Hancock J, Watson-Lamprey J, Abrahamson NA, Bommer JJ, Markatis A, McCoy E, Mendis R (2006) An improved method of matching response spectra of recorded earthquake ground motion using wavelets. *J Earthq Eng* 10:67–89
306. Seifried AE (2013) Response compatibilization and impact on structural response assessment. PhD thesis, Stanford University
307. Shome N, Cornell CA, Bazzurro P, Carballo JE (1998) Earthquakes, records and nonlinear responses. *Earthq Spectra* 14(3):469–500
308. Hancock J, Bommer JJ, Stafford PJ (2008) Numbers of scaled and matched accelerograms required for inelastic dynamic analyses. *Earthq Eng Struct Dyn* 37(14):1585–1607
309. Shome N, Cornell CA, Bazzurro P, Carballo JE (1998) Earthquakes, records, and nonlinear responses. *Earthq Spectra* 14:469–500
310. Bazzurro P, Luco N (2006) Do scaled and spectrum-matched near-source records produce biased nonlinear structural responses? In: Conference, national engineering, earthquake engineering
311. Luco N, Bazzurro P (2007) Does amplitude scaling of ground motion records result in biased nonlinear structural drift responses? *Earthq Eng Struct Dyn* 36:1813–1835

312. Han SW, Wen YK (1994) Method of reliability-based calibration of seismic structural parameters. University of Illinois and Urbana-Champaign. UIUC-ENG-94 2016, Structural Research Series No. 595, Champaign, IL, p 170
313. Papadrakakis M, Lagaros ND, Fragiadakis M (2006) Seismic design procedures in the framework of evolutionary based structural optimization, computational mechanics: solids, structures and coupled problems, Springer, Netherlands
314. Carballo JE, Cornell CA (2000) Probabilistic seismic demand analysis: spectrum matching and design. Report No. RMS-41, Department of Civil and Environmental Engineering, Reliability of Marine Structures Program, Stanford University, Stanford, CA
315. Watson-Lamprey J, Abrahamson N (2006) Bias caused by use of spectrum compatible motions. In: 8th US national conference on earthquake engineering, San Francisco, CA
316. Iervolino I, De Luca F, Cosenza E (2010) Spectral shape-based assessment of SDOF nonlinear response to real, adjusted and artificial accelerograms. *Eng Struct* 32(9):2776–2792
317. Heo Y, Kunnath S, Abrahamson N (2011) Amplitude-scaled versus spectrum-matched ground motions for seismic performance assessment. *J Struct Eng* 137(3):278–288
318. Grant DN, Diaferia R (2013) Assessing adequacy of spectrum-matched ground motions for response history analysis. *Earthq Eng Struct Dyn* 42(9):1265–1280
319. Moehle JP (2008) Performance-based seismic design of tall buildings in the US. In: 14th world conference on earthquake engineering, Beijing
320. Bommer JJ, Acevedo AB (2004) The use of real earthquake accelerograms as input to dynamic analysis. *J Earthq Eng* 8:43–91
321. Srbulov Milutin (2008) Geotechnical earthquake engineering—simplified analyses with case studies and examples. Springer, Heidelberg
322. Douglas J (2003) What is a poor quality strong—motion record? *Bull Earthq Eng* 1(1):141–156
323. Lanzi A (2011) Approximate analysis of dynamic soil–structure interaction. University of California, San Diego
324. Kaynia A (2009) Seismic analyses of Staffjord B, Norwegian Geotechnical Institute, 16th of April
325. Idriss IM (1979) Chairman et al. Analyses for soil–structure interaction effects for nuclear power plants. Report Structural div. ASCE, New York
326. DNV (1994) Documentation of computer program package for structure/pile/soil interaction analysis, program SPLICE, 1 July, Høvik, Norway
327. Lysmer J, Tabatabaie-Raissi M, Tajirian F, Vahdani S, Ostadan F (1981) SASSI—a system for analysis of soil–structure interaction. Report UCB/GT 81-02, University of California, Berkeley, USA
328. <http://www.plaxis.nl>
329. Reese LC, Wang ST, Arrellaga JA, Vasquez L (2012) Computer program DYNAN version 3.0, April
330. Novak M (1991) Pile under dynamic loads: State of the Art. In: 2nd international conference on recent advances in geotechnical earthquake engineering and soil dynamics, vol 3, St. Louis, pp 2433–2456
331. Todorovska MI, Hayir A, Trifunac MD (2001) Flexible versus rigid foundation models of soil-structure interaction: incident SH waves. In: The 2nd UJNR workshop on soil-structure interaction, Tsukuba, Japan
332. Ghobarah A (2001) Performance-based design in earthquake engineering: state of development. *Eng Struct* 23(8):878–884
333. Gazetas G (2006) Seismic design of foundations and soil-structure interaction. In: 1st European conference on earthquake engineering and seismology, Geneva
334. Somerville PG (1998) The amplitude and duration effects of rupture directivity in near fault ground motions. In: Dakoulas P, Yegian MK, Holtz RD (eds) Geotechnical earthquake engineering and soil dynamics III, ASCE

335. Lysmer J, Waas G (1972) Shear waves in plane infinite structures. *Journal of Engineering Mechanics Division, ASCE* 98(1):85–105
336. Kausel E (1994) Thin-layer method: formulation in time domain. *Int J Numer Meth Eng* 37:927–941
337. Lysmer J, Kuhlemeyer RL (1969) Finite dynamic model for infinite media. *J Eng Mech Div ASCE* 95(4):859–877
338. Kontoe S, Zdravkovic L, Potts D, Salandy N (2007) The use of absorbing boundaries in dynamic analyses of soil–structure interaction problems. In: *Proceedings of 4th international conference on earthquake engineering, Thessaloniki, Greece*
339. Novak M, Mitwally H (1988) Transmitting boundary for axisymmetric dilation problems. *J Eng Mech Div ASCE* 104(4):953–956
340. Novak M, Nogami T, Aboul-Ella F (1978) Dynamic soil reactions for plane strain case. *J Eng Mech Div ASCE* 104(4):953–959
341. Wolf JP, Song C (1995) Doubly asymptotic multi-directional transmitting boundary for dynamic unbounded medium-structure interaction analysis. *Earthq Eng Struct Dyn* 24:175–188
342. Kellezi L (2000) Local transmitting boundaries for transient elastic analysis. *Soil Dyn Earthq Eng* 19:533–547
343. Gazetas G (1983) Analysis of machine foundation vibrations: state of the art. *Soil Dyn Earthq Eng* 2(1):2–42
344. Abaqus Inc., *Abaqus Analysis User's manual, Version 6.8-2, 2010*
345. Safak E (2006) Time domain representation of frequency-dependent foundation impedance functions. *Soil Dyn Earthq Eng* 26:65–70
346. Larsson R, Mulabdic M (1991) Shear moduli in Scandinavian clays, measurement of initial shear modulus with seismic cones. Report No. 40, Swedish Geotechnical Institute, Linköping
347. Stokoe KH, Lee SHH, Knowx DP, Shear Moduli measurements under the true triaxial stress. In: *Proceedings, advances in the art of testing soils under cyclic conditions, ASCE, New York*, pp 166–185
348. Yan L, Byrne PM (1991) Stress state and stress ratio effects in downhole and crosshole in shear wave velocities on sand. In: *Proceedings 2nd international conference on recent advances in geotechnical earthquake engineering and soil dynamics, vol 1, St. Louis, Missouri*, pp 299–306
349. Amorosia A, Boldinib D, Lernia A (2016) Seismic ground response at Lotung: hysteretic elasto-plastic-based 3D analyses. *Soil Dyn Earthq Eng* 85:44–61
350. Stokoe KH, Santamarina JC (2000) Invited paper: seismic-wave-based testing in geotechnical engineering. In: *International conference on geotechnical and geological engineering, GeoEng 2000, Melbourne, Australia*, pp 1490–1536
351. Gosar A (1998) Seismic reflection surveys of the Krško basin structure: implications for earthquake hazard at the Krško nuclear power plant. *Southeast Slovenia* 39(3):131–153
352. Corps of Engineers, Geophysical Exploration, *Engineering Manual 1110-1-1802, U.S. Department of Army, 1979*
353. Reapath BB (1973) Seismic refraction exploration for engineering site investigations. Technical Report E-73-4, U.S. Army Corps of Engineers Waterways Experiment Station, Explosive Excavation Research Laboratory, CA, p 55
354. Soske JL (1959) The blind zone problem in engineering geophysics. *Geophysics* 24:359–365
355. NRC (2000) *Seeing into the Earth, Committee for Noninvasive Characterization of the Shallow Subsurface for Environmental and Engineering Applications*, 129 p
356. Stokoe KH, Wright SG, Bay JA, Roesset JM (1994) Characterization of geotechnical sites by SASW method, geophysical characteristics of sites, ISSMFE, technical committee 10 for XIII ICSMFE. *International Science Publishers, New York*, pp 15–25

357. Stoll RD, Bryan GM, Bautista EO (1994) Measuring lateral variability of sediment geoaoustic properties. *J Acoustical Soc Am* 96(1):427–438
358. Tokimatsu K (1995) Geotechnical site characterization using surface waves. In: 1st international conference on earthquake geotechnical engineering, vol 3, Tokyo, pp 1333–1368
359. Luke BA, Stokoe KH (1998) Application of SASW method underwater. *J Geotech Geoenviron Eng* 124(6):523–531
360. Karray M, Lefebvre G (2009) Techniques for mode separation in Rayleigh wave testing. *Soil Dyn Earthq Eng* 29(4):607–619
361. Fuhrman MD (1993) Crosshole seismic tests at two Northern California sites affected by the 1989 Loma Prieta earthquake. University of Texas at Austin
362. Thompson EM (2007) Surface-source downhole seismic analysis. U.S. Geological Survey, Report 2007-1124
363. Liu HP, Warrick RE, Westerlund RE, Fletcher JB, Maxwell GL (1988) An air-powered impulsive shear-wave source with repeatable signals. *Bull Seismol Soc Am* 78(1):355–369
364. Daniels JJ, Keys WS (1990) Geophysical well logging for evaluating hazardous waste sites, investigations in geophysics no. 5. *Geotech Environ Geophys* 10:263–286
365. Howard WF (1992) Geophysical well logging methods for detection and characterization of fractures in hard rocks, investigations in geophysics no. 5. *Geotech Environ Geophys* 1:287–308
366. Labo J (1992) A practical introduction to borehole geophysics. *Soc Explor Geophys*
367. Nigbor RL, Imai T (1994) The suspension P - S velocity logging method, geophysical characteristics of sites, ISSMFE, technical committee 10 for XIII ICSMFE. International Science Publishers, New York, pp 57–63
368. Marchetti S (1980) In situ tests by flat dilatometer. *J Geotech Eng Div*
369. Mair RJ, Wood DM (1987) Pressuremeter testing: methods and interpretation. Butterworth, London, p 160
370. Hardin BO, Black WL (1968) Vibration modulus of normally consolidated clays. *J Soil Mech Found Div ASCE* 94(SM2, Proc Paper 5833):353–369
371. Drnevich VP (1978) Resonant column testing—problems and solutions. *Dyn Geotech Test ASTM* 654:394–398
372. Drnevich VP, Hall JR, Richart F (1967) Effects of amplitude vibration on the shear modulus of sand. In: Albuquerque NM (ed) Proceedings of the international symposium on wave propagation and dynamic properties of earth material, pp 189–199
373. Hou YJ, Xu ZP, Liang JH (2004) Centrifuge modeling of cutoff wall for CFRD built in deep overburden. In: Proceedings of international conference of hydropower, Yichang, China, pp 86–92
374. Woods RD (1991) Field and laboratory determination of soil properties at low and high strains. In: Proceedings of 2nd international conference on recent advances in geotechnical earthquake engineering and soil dynamics, vol 3, St. Louis, Missouri, pp 1727–1741
375. Prange B (1981) Stochastic excitation of rock masses. In: Proceedings of 10th international conference on soil mechanics and foundation engineering, vol 4, Stockholm, pp 879–880
376. Richter S, Huber G (2003) Resonant column tests with cohesive and non-cohesive granular materials. In: Fecker N, Pimentel (eds) Geotechnical measurement and modeling, pp 381–387
377. Menq FY (2003) Dynamic properties of sandy and gravelly soils. PhD thesis, University of Texas at Austin
378. Hardin BO, Kalinski ME (2005) Estimating the shear modulus of gravelly soils. *ASCE J Geotech Geoenviron Eng* 131(7):867–875
379. Goto S, Tatsuoka F, Shibuya S, Kim YS, Sato T (1991) A simple gauge for local small strain measurements in the laboratory. *Soil Found* 31(1):169–180

380. Lawrence FV (1963) Propagation velocity of ultrasonic waves through sand. MIT Research Report R63-8, Massachusetts Institute of Technology
381. Nacci VA, Taylor KJ (1967) Influence of clay structure on elastic wave velocities. In: Proceedings of international symposium on wave propagation and dynamic properties of earth materials, Albuquerque, New Mexico, pp 491–502
382. Dyvik R, Madshus C (1985) Laboratory measurements of G_{\max} using bender elements, advances in the art of testing soils under cyclic conditions. ASCE, New York, pp 186–196
383. Geotesting (2015) Resonant column and torsional shear test. Boston
384. Meymand PJ (1998) Shaking table scale model tests of nonlinear soil-pile-superstructure interaction in soft clay. PhD Dissertation, University of California, Berkeley
385. Xilin Lu, Chen Yueqing (2000) Shaking table test of the structure-foundation interaction. *Earthq Eng Eng Vibr* 20(4):20–29 (in Chinese)
386. Xiuli D, Li X, Chen G, Huang H (2012) Design and test verification of suspension multidirectional laminar shear model box. *Chin J Geotech Eng* 34(3):424–432
387. Scott R (1980) Analysis of centrifuge pile tests: simulation of pile driving. Research Rpt., API OSPAR Project 13, California Institute of Technology, Pasadena
388. Schofield AN (1980) Cambridge geotechnical centrifuge operations. *Geotechnique* 30(3):227–268
389. Kutter BL, James RG (1989) Dynamic centrifuge model tests on clay embankments. *Geotechnique* 39(1):91–106
390. Andersen KH (2015) Cyclic soil parameters for offshore foundation design. In: Meyer V (ed) The 3rd ISSMGE McClelland lecture, in frontiers in offshore geotechnics III, CRC Press, Boca Raton
391. Xu C, Jia J, Sun Y, Du X, Gao Y (2017) Cyclic strength of saturated sand under bi-directional cyclic loading. *Engineering Geology*, article in press
392. de Groot MB, Bolton MD, Foray P, Meijers P, Palmer AC, Sandven R, Sawicki A, Teh TC (2006) Physics of Liquefaction phenomena around marine structures. *J Waterway Port Coastal Ocean Eng* 132(4):227–243
393. Mutlu Sumer B (2014) Liquefaction around marine structures. World Scientific Press, London, p 472
394. Ishihara K, Yasuda S, Nagase H (1996) Soil characteristics and ground damage, special issue of soils and foundations on Kobe earthquake. Japanese Geotechnical Society, pp 109–118
395. Kuwabara F, Yoshimi Y (1973) Effect of subsurface liquefaction on strength of surface soil ASCE. *JGE* 13(2):67–82
396. NRC (1985) Liquefaction of soils during earthquakes. Report No. CETS-EE-001, National Academic Press, Washington DC
397. Hamada MKW, Yasuda S (1992) Liquefaction-induced ground deformation during the 1923 Kanto earthquake, case studies of liquefaction and lifeline performance during past earthquakes, Volume 1. Technical Rep.NCEER-92-001, National Center for Earthquake Engineering Research, Buffalo, NY
398. Wang Z (2008) May 12, 2008 Sichuan, China earthquake reconnaissance. University of Kentucky, Lexington, KY
399. https://en.wikipedia.org/wiki/2016_Christchurch_earthquake
400. Youd TL (1993) Liquefaction-induced lateral spread displacement, NCEL N-1862, Navel Civil Engineering Laboratory Port, Hueneme California
401. Jefferies M, Been K (2015) Liquefaction soil a critical state approach, 2nd edn. CRC Press, Boca Raton
402. Yoshida N, Tazoh T, Wakamatsu K, Yasuda S, Towhata I, Nakazawa H, Kiku H (2007) Causes of Showa Bridge collapse in the 1964 Niigata earthquake based on eyewitness testimony. *Soils Found* 47(6):1075–1087

403. Kazama M, Sento S, Uzuoka R, Ishimaru M (2008) Progressive damage simulation of foundation pile of the Showa Bridge caused by lateral spreading during the 1964 Niigata earthquake. In: Liu H, Deng A, Chu J (eds) *Geotechnical engineering for disaster mitigation and rehabilitation*. Science Press and Springer, Beijing, Berlin, pp 170–176
404. Bhattacharya S, Tokimatsu K, Goda K, Sarkar R, Shadlou M, Rouholamin M (2014) Collapse of Showa Bridge during 1964 Niigata earthquake: a quantitative reappraisal on the failure mechanisms. *Soil Dyn Earthq Eng* 65:55–71
405. Kudo K, Uetake T, Kanno T (2000) Re-evaluation of nonlinear site response during the 1964 Niigata earthquake using the strong motion records at Kawagishi-cho, Niigata City. In: *Proceedings of the 12th world conference on earthquake engineering*
406. <http://kyoshin.eri.u-tokyo.ac.jp/SMAD>
407. Byrne PM, Park SS, Beaty M, Sharp M, Gonzalez L, Abdoun T (2004) Numerical modeling of liquefaction and comparison with centrifuge tests. *J Can Geotech J* 41(2): 193–211
408. Seed HB (1987) Design problems in soil liquefaction. *J J Geotech Eng ASCE* 113(8):827–845
409. Seed HB, Harder LF (1990) SPT-based analysis of cyclic pore pressure generation and undrained residual strength. In: Duncan JM (ed) *Proceedings, H Bolton Seed memorial symposium, University of California, Berkeley, vol 2*, pp 351–376
410. Seed HB, Idriss IM (1971) Simplified procedures for evaluating soil liquefaction potential. *J Soil Mech Found Div* 97(9):1249–1273
411. Poulos SJ, Castro G, France W (1985) Liquefaction evaluation procedure. *J Geotech Eng Div ASCE* 111(6):772–792
412. Finn WD (2002) State of the art for the evaluation of seismic liquefaction potential. *J Comput Geotech* 29:329–341
413. Elgamal A, Yang ZH, Parra E (2002) Computational modeling of cyclic mobility and post-liquefaction site response. *J Soil Dyn Earthq Eng* 22:259–271
414. Elgamal A, Yang Z, Parra E, Ragheb A (2003) Modeling of cyclic mobility in saturated cohesionless soils. *J Int J Plasticity* 19(6):883–905
415. FEMA 356 (2000) *Prestandard and commentary for the seismic rehabilitation of buildings*
416. Youd TL, Idriss IM, Andrus RD, Arango I, Castro G, Christian JT, Dobry R, Finn WDL, Harder LF Jr, Hynes ME, Ishihara K, Koester JP, Liao SSC, Marcuson WF III, Martin GR, Mitchell JK, Moriwaki Y, Power MS, Robertson PK, Seed RB, Stokoe KH II (2001) Liquefaction resistance of soils, summary report from the 1996 NCEER and 1998 NCEER/NSF workshops on evaluation of liquefaction resistance of soils. *J Geotech Geoenviron Eng ASCE* 127(10):817–833
417. Seed HB, Idriss IM (1971) Simplified procedure for evaluating soil liquefaction potential. *J Soil Mech Found Div ASCE* 107(SM9):1249–1274
418. Liao SSC, Whitman RV (1986) Overburden correction factor for SPT in sand. *J Geotech Eng ASCE* 112(3):373–377
419. Idriss IM (1999) An update to the Seed-Idriss simplified procedure for evaluating liquefaction potential. In: *Proceedings of the TRB workshop on new approaches to liquefaction*, Publication No. FHWA-RD-99-165, Federal Highway Administration, January 1999
420. Kayen RE, Mitchell JK, Seed RB, Lodge A, Nishio S, Coutinho R (1992) Evaluation of SPT-, CPT-, and shear wave-based methods for liquefaction potential assessment using Loma Prieta data. In: *Proceedings of 4th Japan-U.S. workshop on earthquake-resistant design of lifeline facilities and countermeasures for soil liquefaction, vol 1*, pp 177–204
421. Moss RES (2003) *R CPT-based probabilistic assessment of seismic soil liquefaction initiation*. PhD Thesis, Department of Civil and Environmental Engineering, University of California, Berkeley

422. Seed HB, Mori K, Chan CK (1975) Influence of seismic history on the liquefaction characteristics of sands. Report EERC 75-25, Earthquake Engineering Research Center, University of California, Berkeley
423. Idriss IM, Boulanger RW (2008) Soil Liquefaction during earthquakes. Monograph MNO-12, Earthquake Engineering Research Institute, Oakland, California
424. Dobry R, Abdoun T (2011) An investigation into why liquefaction charts work: a necessary step toward integrating the states of art and practice. In: Proceedings of the 5th international conference on earthquake geotechnical engineering, pp 13–45, Santiago, Chile
425. Seed HB, Idriss IM (1982) Ground motions and soil liquefaction during earthquakes. Earthquake Engineering Institute Monograph
426. Eurocode 8 (2004) Design of structures for earthquake resistance – part 5: foundations, retaining structures and geotechnical aspects
427. Idriss IM (1999) An update to the Seed-Idriss simplified procedure for evaluating liquefaction potential. In Proceedings, TRB workshop on new approaches to liquefaction, Publication No. FHWA-RD-99-165, Federal Highway Administration, January, 1999
428. Idriss IM, Boulanger RW (2004) Semi-empirical procedures for evaluating liquefaction potential during earthquakes. In: Proceedings of the 11th international conference on soil dynamics and earthquake engineering, and 3rd international conference on earthquake geotechnical engineering, vol 1, Stallion Press, pp 32–56
429. Andrus R, Stokoe KH (1997) Liquefaction resistance based on shear wave velocity. In: Proceedings of NCEER workshop on evaluation of liquefaction resistance of soils
430. Youd TL, Noble SK (1997) Liquefaction criteria based on statistical and probabilistic analyses. In: Proceedings of the NCEER workshop on evaluation of liquefaction resistance of soils, NCEER Technical Rep. No: NCEER-97-0022, pp 201–205
431. Hynes ME, Olsen RS (1999) Influence of confining stress on liquefaction resistance. In: Proceedings of the international workshop on physics and mechanism of soil liquefaction, Balkema, Rotterdam, Netherlands, pp 145–152
432. Seed HB (1983) Earthquake resistance design of earth dams, symposium on seismic design of earth dams and caverns. ASCE, New York, pp 41–64
433. Youd TL, Idriss IM, Andrus RD, Arango I, Castro G, Christian JT, Dobry R, Liam Finn WDL, Harder LF, Hynes ME, Ishihara K, Koester JP, Liao SSC, Marcuson WF, III, Martin GR, Mitchell JK, Moriwaki Y, Power MS, Robertson PK, Seed RB, Stokoe II KH (1997) Summary report, proceedings of the NCEER workshop on evaluation of liquefaction resistance of soils, national center for earthquake engineering research technical report NCEER-97-0022, pp 1–40
434. Idriss IM, Boulanger RW (2003) Estimating K_s for use in evaluating cyclic resistance of sloping ground. In: Hamada M, O'Rourke TD, Bardet JP (eds) Proceedings of the 8th US Japan workshop on earthquake resistant design of lifeline facilities and countermeasures against liquefaction. Report MCEER-03-0003, MCEER, SUNY Buffalo, NY, pp 449–468
435. Sachan A (2013) Liquefaction, IIT Gandhinagar
436. Moss RES, Seed RB, Kayen RE, Stewart JP, Der Kiureghian A, Cetin KO (2006) CPT-based probabilistic and deterministic assessment of in situ seismic soil liquefaction potential. *J Geotech Geoenviron Eng* 132(8):1032–1051
437. Dobry R, Stokoe II KH, Ladd RS, Youd TL (1981) Liquefaction susceptibility from *S*-wave velocity. In: Proceedings of ASCE national convention, in situ tests to evaluate liquefaction susceptibility, ASCE, New York
438. Dobry R, Ladd RS, Yokel FY, Chung RM, Powell D (1982) Prediction of pore water pressure buildup and liquefaction of sands during earthquakes by the cyclic strain method, NBS Build. Sci. Ser. 138, National Bureau of Standards, Gaithersburg, Maryland
439. Bierschwale JG, Stokoe II KH (1984) Analytical evaluation of liquefaction potential of sands subjected to the 1981 Westmorland earthquake, geotechnical engineering Report GR-84-15, Civil Engineering Department, University of Texas at Austin

440. Andrus RD, Stokoe KH (2000) Liquefaction resistance of soils from shear wave velocity. *J Geotech Geoenviron Eng* 126(11):1015–1025
441. Yi F (2010) Case study of CPT application to evaluate seismic settlement in dry sand. In: *The 2nd international symposium on cone penetration testing*, Huntington Beach, California, USA
442. Juang CH, Jiang T, Andrus RD (2002) Assessing probability-based methods for liquefaction potential evaluation. *J Geotechn Geoenviron Eng ASCE* 128(7):580–589
443. Dorby R, Ladd RS (1980) Discussion to “soil liquefaction and cyclic mobility evaluation for level ground during earthquakes”, by H.B. Seed and “liquefaction potential: science versus practice” by RB Peck. *J Geotech Eng Div ASCE* 106(GT6):720–724
444. Dorbry R, Ladd RS, Yokel FY, Chung RM, Powell D (1982) Prediction of pore water pressure buildup and liquefaction of sands during earthquakes by the cyclic strain method. *NBS Building Science Series 138*, National Bureau of Standards, Gaithersburg, Maryland
445. Seed HB, Booker JR (1977) Stabilization of potentially liquefiable sand deposits using gravel drains. *J Geotechn Eng Div ASCE* 103(GT7):757–768
446. Onoue A (1988) Diagrams considering well resistance for designing spacing ratio of gravel drains. *Soils Found Jpn Soc Soil Mech Found Eng* 28(3):160–168
447. Rollins KM, Anderson JKS, McCain AK, Goughnour RR (2003) Vertical composite drains for mitigating liquefaction hazard. In: *Proceedings of the 13th international offshore and polar engineering conference*, Honolulu, Hawaii
448. Boulanger DP, Hashish Y, Schmidt B (1997) Drainage capacity of stone columns or gravel drains for mitigating liquefaction. In: *2nd geotechnical earthquake engineering and soil dynamics conference*, Seattle, vol 1, pp 678–690, 1997
449. Federal Highway Administration (1995) Dynamic compaction, FHWA-SA-95-037. US Department of Transportation, Washington
450. Jibson RW, Harp EL, Michael JA (1998) A method for producing digital probabilistic seismic landslide hazard maps: an example from the Los Angeles, California, Area, Open-File Report: 98-113, Geologic Hazard, USGS
451. Stewart JP, Blake TF, Hollingsworth RA (2003) A screening analysis procedure for seismic slope stability. *Earthq Spectra* 19:697–712
452. Jibson RW (2011) Methods for assessing the stability of slopes during earthquakes—a retrospective. *Eng Geol* 122:43–50
453. Seed HB (1979) Considerations in the earthquake-resistant design of earth and rock fill dams. *Géotechnique* 29(3):215–263
454. Bray JD, Rathje EM (1998) Earthquake-induced displacements of solid-waste landfills. *J Geotech Geoenviron Eng* 124:242–253
455. Bray JD, Travasarou T (2009) Pseudostatic coefficient for use in simplified seismic slope stability evaluation. *J Geotech Geoenviron Eng* 135:1336–1340
456. Melo C, Sharma S (2004) Seismic coefficients for pseudostatic slope analysis. In: *13th world conference on earthquake engineering*, Vancouver, B.C., Canada
457. Terzaghi K (1950) *Mechanics of landslides, engineering geology* (Berkeley) volume. Geological Society of America, Boulder, CO, pp 83–123
458. Pham Ha TV, Fredlund DG (2003) The application of dynamic programming to slope. *Can Geotech J* 40:830–847
459. Saeed MS, Maarefvand P, Yaaghubi E (2015) Two and three-dimensional slope stability analyses of final wall for Miduk mine. *Int J Geoen* 6(9)
460. Duncan JM (1996) State of the art: limit-equilibrium and finite element analysis of slopes. *J Geotech Eng* 122(7):577–596
461. Clough RW, Chopra AK (1966) Earthquake stress analysis in earth dams. *ASCE J Eng Mech Div* 92:197–211
462. Kondner RL (1963) Hyperbolic stress-strain response: cohesive soils. *J Soil Mech Found Div ASCE* 89(SM1):115–144

463. Duncan JM, Byrne PM, Wong KS, Mabry P (1980) Strength, stress-strain, and bulk modulus parameters for finite element analysis of stresses and movements in soil mass. Report UCB/GT/80-01, University of California at Berkeley
464. Prevost JH (1981) JDYNAFLOW: A nonlinear transient finite element analysis program. Department of Civil Engineering, Princeton University, Princeton, NJ
465. Griffiths DV, Prevost JH (1988) Two- and three-dimensional finite element analyses of the Long Valley Dam. Technical Report NCEER-88-0015, National Center for Earthquake Engineering Research, Buffalo, NY
466. Elgamal AM, Scott RF, Succarieh MF, Yan LP (1990) La Villita dam response during five earthquakes including permanent deformation. *J Geotech Eng* 116:1443–1462
467. Li AJ, Merifield RS, Lyamin AV (2009) Limit analysis solutions for three dimensional undrained slopes. *Comput Geotech* 36:1330–1351
468. Li AJ, Merifield RS, Lyamin AV (2010) Three-dimensional stability charts for slopes based on limit analysis methods. *Can Geotech J* 47:1316–1334
469. Michalowski RL (2010) Limit analysis and stability charts for 3D slope failures. *J Geotech Geoenviron Eng* 136(4):583–593
470. Leong EC, Rahardjo H (2012) Two and three-dimensional slope stability reanalyses of Bukit Batok slope. *Comput Geotech* 42:81–88
471. Newmark NM (1965) Effects of earthquakes on dams and embankments. *Géotechnique* 15 (2):139–160
472. Goodman RE, Seed HB (1966) Earthquake-induced displacements in sand embankments. *J Soil Mech Found Div* 92:125–146
473. Wartman J, Bray JD, Seed RB (2003) Inclined plane studies of the Newmark sliding block procedure. *J Geotech Geoenviron Eng* 129:673–684
474. Wartman J, Seed RB, Bray JD (2005) Shaking table modeling of seismically induced deformations in slopes. *J Geotech Geoenviron Eng* 131:610–622
475. Wilson RC, Keefer DK (1983) Dynamic analysis of a slope failure from the 6 Aug 1979 Coyote Lake, California, earthquake. *Bull Seismol Soc Am* 73:863–877
476. Makdisi FI, Seed HB (1978) Simplified procedure for estimating dam and embankment earthquake-induced deformations. *ASCE J Geotech Eng Div* 104:849–867
477. Pradel D, Smith PM, Stewart JP, Raad G (2005) Case history of landslide movement during the Northridge earthquake. *J Geotech Geoenviron Eng* 131:1360–1369
478. Lin JS, Whitman RV (1983) Earthquake induced displacements of sliding blocks. *J Geotech Eng* 112:44–59
479. Bray JD, Travararou T (2007) Simplified procedure for estimating earthquake-induced deviatoric slope displacements. *J Geotech Geoenviron Eng* 133:381–392
480. Rathje EM, Abrahamson NA, Bray JD (1998) Simplified frequency content estimates of earthquake ground motions. *J Geotech Eng* 124:150–159
481. Rathje EM, Faraj F, Russell S, Bray JD (2004) Empirical relationships for frequency content parameters of earthquake ground motions. *Earthq Spectra* 20:119–144
482. Marcuson WF, Hynes ME, Franklin AG (1990) Evaluation and use of residual strength in seismic safety analysis of embankments. *Earthq Spectra* 6(3):529–572
483. Jibson RW, Keefer DK (1993) Analysis of the seismic origin of landslides: Examples from the New Madrid seismic zone. *Geol Soc Am Bull* 105:521–536
484. Blake TF, Hollingsworth RA, Stewart JP (2002) Recommended procedures for implementation of DMG Special Publication 117—Guidelines for Analyzing and Mitigating Landslide Hazards in California. Southern California Earthquake Center, Los Angeles, CA, 127
485. Jibson RW, Harp EL, Michael JA (1998) A method for producing digital probabilistic seismic landslide hazard maps—an example from the Los Angeles, California, area. U.S. Geological Survey Open-File Report 98-113, p 17
486. Jibson RW, Harp EL, Michael JA (2000) A method for producing digital probabilistic seismic landslide hazard maps. *Eng Geol* 58:271–289

487. Guo M (2011) Slope stability analysis under seismic load by vector sum analysis method. *J Rock Mech Geotech Eng* 3(3):282–288
488. Turner AK, Shuster RL (1996) Landslides: investigation and mitigation. Transport Research Board, Rep No. 247
489. <http://blog.sina.com.cn/u/1222264142>
490. Keefer DK (1984) Landslides caused by earthquakes. *Geol Soc Am Bull* 95:406–421
491. Wilson RC, Keefer DK (1985) Predicting aerial limits of earthquake-induced landsliding. In: Ziony JI (ed) *Evaluating earthquake hazards in the Los Angeles region: an earth-science perspective*, USGS Professional paper 1360, pp 16–345
492. Harp EL, Wilson RC (1995) Shaking intensity thresholds for rock falls and slides: Evidence from the 1987 Whittier Narrows and Superstition Hills earthquake strong motion records. *Bull Seismol Soc Am* 85(6):1739–1757
493. van Westen J, Terlien MTJ (2007) Seismic landslide hazard zonation, <http://www.itc.nl/ilwis/applications/application07.asp>
494. Chakrabarti Subrata (ed) (2005) *Handbook of offshore structures*. Elsevier Publication, Oxford, UK
495. Gerwick BCJ (1986) *Construction of offshore structures*. Wiley, New York, NY
496. Reddy DV, Arockiasamy M (1991) *Offshore structures*. Krieger Publishing Company, Malabar, Florida
497. Clauss G et al (1992) *Offshore structures Vol. 1. In: Conceptual design and hydromechanics* (trans: Shields MJ). Springer, Berlin
498. Jia Junbo, *Dynamics Soil, Modeling Foundation* (2016) *Offshore and earthquake engineering*. Springer, Heidelberg
499. Chakrabarti S (2008) Challenges for a total system analysis on deepwater floating systems. *Open Mechan J* 2:28–46
500. Chandrasekaran S (2015) *Advanced marine structures*. CRC Press, Boca Raton, FL
501. Pike J (2011) Compliant tower, <http://www.globalsecurity.org/military/systems/ship/platform-compliant-tower.htm>
502. van Wijngaarden M (2013) Concept design of steel bottom founded support structures for offshore wind turbines. Delft University of Technology
503. Kuo YS, Abdel-Rahman K, Wu KT, Huang TY, Achmus M (2014) Suitability of a Pile Group Foundation for an offshore wind turbine. In: *Proceedings of the 24th international ocean and polar engineering conference*, Busan
504. Naess A, Moan T (2012) *Stochastic dynamics of marine structures*. Cambridge University Press, Cambridge
505. Jia J (2016) The effect of gravity on the dynamic characteristics and fatigue life assessment of offshore structures. *J Construct Steel Res* 118(1):1–21
506. Sharpe RL, Newmark NM (1977) Extending seismic design provisions for buildings to the design of offshore structures, offshore technology conference, Houston, Texas
507. Diamantidis D, Arnesen K (1986) Scour effects in piled structures: a sensitivity analysis. *Ocean Eng* 13:497–502
508. Smith CE (1997) Dynamic response of steel-jacket platform subject to measured seafloor earthquake ground motions. In: *Proceedings 8th international conference on the behaviour of offshore structures*, BOSS'97, Delft: vol 3, Pergamon, Elsevier Science Ltd., Oxford, England
509. Sleaf GE (1990) The long-term measurement of strong-motion earthquakes offshore South California. In: *Proceedings of OTC 1990*, society of petroleum engineers, Richardson, Texas
510. Morison JR, O'Brian MP, Johnson JW, Schaaf SA (1950) The force exerted by surface waves on piles. *J Pet Technol* 2(5):149–154
511. Borgman LE (1967) Spectrum analysis of ocean wave forces on piling. *J Waterways Harbours ASCE* 93(2):129–156

512. Borgman LE (1969) Ocean wave simulations for engineering design. *J Waterways Harbours ASCE* 557–583
513. Det Norske Veritas, DNV-RP-C205 (2014) Environmental conditions and environmental loads, Høvik
514. Faltinsen OM (1990) Sea loads on ships and offshore structures. Cambridge University Press, Cambridge
515. Chakrabarti SK (1993) Hydrodynamics of offshore structures, 2nd edn. Computational Mechanics Publications, Southampton
516. Chakrabarti SK (1987) Hydrodynamics of offshore structures. Springer, Heidelberg
517. Venkataramana K, Kawano K (1995) Nonlinear dynamics of offshore structures under sea wave and earthquake forces. *Adv Nonlinear Struct Dyn* 20(2):501–512
518. Gurpinar A, Gryspeert BJ, Cole-Baker JR (1980) Dynamic analysis of offshore platforms under seismic excitation. In: Proceedings of the seventh world conference of earthquake engineering, Istanbul, vol 8
519. Jin DY, Matsui T (1997) Stochastic response analysis of jacket-type ocean platforms under simultaneously acting waves and earthquakes. *Am Soc Mech Eng Safety Reliab* 2:297–302
520. Etemad AK, Gharabaghi ARM, Chenaghloou MR (2004) Nonlinear dynamic behavior of fixed jacket-type offshore platforms subjected to simultaneously acting wave and earthquake loads. In: Proceedings of the 23rd international conference on offshore mechanics and arctic engineering, Vancouver
521. Bargi Khosro, Hosseini S Reza, Tadayon Mohammad H, Sharifian H (2011) Seismic response of a typical fixed jacket-type offshore platform (SPD1) under sea waves. *Open J Marine Sci* 1:36–42
522. Blevins RD (1979) Formulas for natural frequency and mode shape. Robert E. Krieger Publishing, Malabar, USA
523. Jusoh I, Wolfram J (1996) Effects of Marine growth and hydrodynamic loading on offshore structures. *Jurnal Mekanikal Jilid* 1:77–98
524. Schnabel PB, Lysmer J, Seed HB (1972) SHAKE, A computer program for earthquake response analysis of horizontally layered sites. No. EERC 72-12, Earthquake Engineering Research Center, College of Engineering, University of California, Berkeley
525. Schuëller GI (1991) Structural dynamics, recent advances. Springer, Berlin
526. Wilson ED (2015) Termination of the response spectrum method (RSM), 13 July 2015
527. Gupta VK (2009) Wavelet-based random vibrations in earthquake engineering (lecture), IIT Kanpur, India
528. Yue QJ, Qu Y, Bi XJ, Kärnä T (2007) Ice force spectrum on narrow conical structures. *Cold Reg Sci Technol* 49(2):161–169
529. Schuster A (1898) On the investigation of hidden periodicities with application to a supposed 26 day period of meteorological phenomena. *Terrestr Magnet* 3:13–41
530. Schuster A (1900) The periodogram of magnetic declination as obtained from the records of greenwich observatory during the years 1871–1895. *Trans Camb Phil Soc* 18:107–135
531. Schuster A (1906) The periodogram and its optical analogy. *Proc Roy Soc Lond Ser A* 77: 136–140
532. Wilson JF (2003) Dynamics of Offshore Structures, John Wiley and Sons, New Jersey, 2003
533. Weisstein EW (2011) Maximum entropy method, MathWorld—a wolfram web resource
534. Kanai K (1967) Semi-empirical formula for the seismic characteristics of the ground. *Bull Earthq Res Inst Univ Tokyo* 35:309–25
535. Tajimi H (1960) A statistical method of determining the maximum response of a building structure during an earth-quake. *Proc Second World Conf Earthq Eng* 2:781–798

536. Kubo T, Penzien J (1979) Simulation of three-dimensional strong ground motions along principal axes. San Fernando earthquake, *Earthquake Engineering and Structural Dynamics* 7:265–278
537. Moustafa Abbas (2010) Identification of resonant earth-quake ground motion. *Sādhanā, Indian Academy of Science* 5(3):355–371
538. Kanaji H, Hamada N, Naganuma T (2005) Seismic retrofit of a cantilever truss bridge in the Hanshin expressway. In: *Proceedings of the international symposium on earthquake engineering*
539. Chen G, Wu J (2001) Optimal placement of multiple tuned mass dampers for seismic structures. *J Struct Eng ASCE* 127(9):1054–1062
540. Li C, Liu Y (2004) Ground motion dominant frequency effect on the design of multiple tuned mass dampers. *J Earthq Eng* 8(1):89–105
541. Clough RW, Penzien J (1993) *Dynamics of structures*, 2nd edn. McGraw-Hill, New York
542. Der Kiureghian A, Neuenhofer A (1992) Response spectrum method for multi-support seismic excitations. *Earthq Eng Struct Dyn* 21:713–740
543. Bessason B (1992) Assessment of earthquake loading and response of seismically Isolated Bridges. PhD thesis, MTA-rapport 1991: 88, Norges Tekniske Høgskole, Trondheim
544. Hanks TC, McGuire RK (1986) The character of high frequency strong ground motion in space and time. *Eng Mech* 112:154–174
545. Boore DM (1983) Stochastic simulation of high frequency ground motions based on seismological models of the radiated spectra. *Bull Seismol Soc of Am* 73(6):1865–1894
546. Herman RB (1985) Letter to the editor? An extension of random vibration theory estimates of strong ground motion to large distances. *Bull Seismol Soc Am* 75(5):1447–1453
547. Biot MA (1932) Transient oscillations in elastic systems. PhD thesis No. 259, Aeronautics Department, California Institute of Technology, Pasadena, USA
548. Biot MA (1943) Analytical and experimental methods in engineering seismology. *Trans ASCE* 108
549. Suyehiro K (1926) A seismic vibration analyzer and the records obtained therewith. *Bull Earthq Res Inst Tokyo* 1
550. Housner GW (1941) An investigation of the effects of earthquakes on buildings. PhD thesis, California Institute of Technology
551. Housner GW, Martel RR, Alford JL (1953) Spectrum analysis of strong motion earthquake. *Bull Seismol Soc Am* 43(2):97–119
552. Clough RW, Benuska KL, Wilson EI (1965) Inelastic earthquake response of tall buildings. In: *3rd world conference on earthquake engineering, New Zealand*
553. Chopra AK (2000) *Dynamics of structures: theory and application to earthquake engineering*, 2nd ed. Prentice-Hall, NJ
554. Baker JW, Cornell CA (2005) A vector-valued ground motion intensity measure consisting of spectral acceleration and epsilon. *Earthq Eng Struct Dyn* 34(10):1193–1217
555. Baker JW, Cornell CA (2006) Spectral shape, epsilon and record selection. *Earthq Eng Struct Dyn* 35(9):1077–1095
556. Izuru T (2007) *Critical excitation methods in earthquake engineering*, 1st edn. Elsevier Science, Oxford
557. Brune JN (1970) Tectonic stress and the spectra of seismic shear waves from earthquakes. *J Geophys Res* 75:4997–5009
558. Brune JN (1971) Correction. *J Geophys Res* 76:5002
559. Hanks TC (1982) f_{max} . *Bull Seismol Soc Am* 72:1867–1879
560. Papageorgiou AS, Aki K (1983) A specific barrier for the quantitative description of inhomogeneous faulting and the prediction of strong ground motion. II. Applications of the model. *Bull Seismol Soc Am* 73:953–978
561. Spudich P, Chiou BSJ (2008) Directivity in NGA earthquake ground motions: analysis using isochrone theory. *Earthq Spectra* 24:279–298

562. Lin YK, Zhang R, Yong Y (1990) Multiply supported pipeline under seismic wave excitations. *J Eng Mech ASCE* 116:1094–1108
563. Boore DM, Bommer JJ (2005) Processing of strong motion accelerograms: needs, options and consequences. *Soil Dyn Earthq Eng* 25:93–115
564. Akkar Sinan, Boore DM (2009) On baseline corrections and uncertainty in response spectra for baseline variations commonly encountered in digital accelerograph records. *Bull Seismol Soc Am* 99(3):1671–1690
565. Boore DM (2001) Effect of baseline corrections on displacements and response spectra for several recordings of the 1999 Chi-Chi, Taiwan, earthquake. *Bull Seismol Soc Am* 91:1199–211
566. www.seisimosoft.com
567. Iwan WD, Moser MA, Peng CY (1985) Some observations on strongmotion earthquake measurement using a digital accelerograph. *Bull Seismol Soc Am* 75:1225–1246
568. Yang J, Li JB, Lin G (2006) A simple approach to integration of acceleration data for dynamic soil–structure interaction analysis. *Soil Dyn Earthq Eng* 26:725–734
569. Zhou Y, Zhang W, Yu H (1997) Analysis of long-period error for accelerograms recorded by digital seismographs. *Earthq Eng Eng Vibr* 17(2): 1–9 (in Chinese)
570. Lin T, Haselton CB, Baker JW (2013) Conditional spectrum-based ground motion selection, Part I: hazard consistency for risk-based assessments. *Earthq Eng Struct Dyn* 42 (12):1847–1865
571. www.pge.com/diabloseismic
572. US Nuclear Regulatory Commission (2012) Confirmatory analysis of seismic hazard at the diablo canyon power plant from the shoreline fault zone, Sept 2012
573. Baker DR (2015) PG&E: Diablo Canyon nuclear plant can withstand 10,000-year quake, SFGATE, 12 Mar 2015
574. American Society of Civil Engineers (ASCE) (2010) ASCE standard ASCE/SEI 7-10: minimum design loads for buildings and other structures
575. Panza GF, Peresan A, La Mura C (2013) Seismic hazard and strong ground motion: an operational neo-deterministic approach from national to local scale. In: UNESCO-EOLSS Joint Committee (ed) *Encyclopedia of life support systems (EOLSS), geophysics and geochemistry*. Developed under the Auspices of the UNESCO, Eolss Publishers, Oxford, UK, pp 1–49
576. Abrahamson NA (2006) Seismic hazard assessment: problems with current practice and future developments, keynote paper. In: 1st European conference on earthquake engineering and seismology, Geneva, Switzerland
577. Abrahamson NA (2006) Probabilistic seismic hazard analysis—an overview. Rose School, Pavia, Italy
578. Baker JW (2008) An introduction to probabilistic seismic hazard analysis (PSHA), US Nuclear Regulatory Commission
579. Cornell CA (1968) Engineering seismic risk analysis. *Bull Seismol Soc Am* 58(5):1583–1606
580. Gutenberg B, Richter CF (1954) *Seismicity of the earth and associated phenomena*. Princeton University Press, Princeton, NJ
581. Marrow PC (1992) Seismic monitoring of the North Sea—prepared by global seismology for the health and safety executive. *Health Saf Executive OTH* 90:323
582. Schwartz DP, Coppersmith KJ (1984) Fault behavior and characteristic earthquakes: examples from the Wasatch and San Andreas fault zones. *J Geophys Res* 89(B7):5681–5698
583. Youngs RR, Coppersmith KJ (1985) Implications of fault slip rates and earthquake recurrence models to probabilistic seismic hazard analysis. *Bull Seismol Soc Am* 75 (4):939–964

584. Kossobokov VG, Mazhkenov SA (1994) On similarity in the spatial distribution of seismicity. In: Computational seismology and geodynamics, vol 1, Washington, DC, pp 6–15
585. Kossobokov VG, Nekrasova A (2007) Unified scaling law for earthquakes: implications for seismic hazard and risk assessment. In: IUGG2007, Perugia, Italy
586. Panza Giuliano, Kossobokov Vladimir G, Peresan Antonella, Nekrasova Anastasia (2014) Why are the standard probabilistic methods of estimating seismic hazard and risks too often wrong. In: Wyss Max, Shroder John (eds) Earthquake hazard, risk, and disasters. Elsevier, Amsterdam
587. Der Kiureghian A, Ang AHS (1977) A fault rupture model for seismic risk analysis. Bull Seismol Soc Am 67(4):1173–1194
588. Bungum H, Selnes PB (1988) Earthquake loading on the Norwegian Continental Shelf—Summary Report, NORSAR, NGI and Principia Mechanica Ltd, Oslo
589. Wang Z (2006) Understanding seismic hazard and risk assessments: an example in the New Madrid Seismic Zone of the central United States. In: Proceedings of the 8th national conference on earthquake engineering, San Francisco, Paper 416
590. Wang Z (2007) Seismic hazard and risk assessment in the intraplate environment: the New Madrid Seismic Zone of the central United States. In: Stein S, Mazzotti S (eds) Continental intraplate earthquakes: science, hazard, and policy issues, Geological Society of America Special Paper 425, pp 363–373
591. Baker JW (2011) Conditional mean spectrum: tool for ground motion selection. J Struct Eng 137(3):322–331
592. Srbulov M (2008) Geotechnical earthquake engineering—simplified analyses with case studies and examples. Springer, Heidelberg
593. Ritsema AR (1981) On the assessment of seismic risk in the North Sea area. Koninklijk Nederlands Meteorologisch Instituut Report, 1981
594. Gumbel EJ (1958) Statistics of extremes. Columbia University Press, New York
595. Marrow PC (1992) Seismic monitoring of the North Sea—prepared by global seismology for the health and safety executive. Health Saf Executive
596. Ellsworth WL (1999) A physically-based earthquake recurrence model for estimation of long-term earthquake probabilities, workshop on earthquake recurrence: state of the art and directions for the future. Institute Nazionale de Geofisica, Rome, Italy
597. Nishenko SP, Buland R (1987) A generic recurrence interval distribution for earthquake forecasting. Bull Seismol Soc Am 77:1382–1399
598. Kameda H, Takagi H (1981) Seismic hazard estimation based on non-poisson earthquake occurrences. Memory Faculty of Engineering, Kyoto University, v. XLIII, Pt. 3, July, Kyoto
599. Anagnos T, Kiremidjian AS (1984) Temporal dependence in earthquake occurrence. In: Proceedings of the 8th world conference on earthquake engineering, vol 1, Earthquake Engineering Research Institute, Oakland, CA, pp 255–262
600. Chen WF, Lui EM (2006) Earthquake engineering for structural design, 1st edn. CRC Press, Boca Raton
601. Bungum H (2012) Recent advances in earthquake hazard assessment. NORSRA, Oslo
602. Pinto AV (2003) Earthquake performance of structures—behavioural, safety and economical aspects. Special Publication No. I.98.111, EC Joint Research Center, ISPRA, October 2003
603. McGuire RK (1995) Probabilistic seismic hazard analysis and design earthquakes: closing the loop. Bull Seismol Soc Am 85(5):1275–1284
604. National Research Council (1988) Probabilistic seismic hazard analysis, report of the panel on seismic hazard analysis. National Academy Press, Washington
605. McGuire RK (1978) FRISK: computer program for seismic risk analysis using faults as earthquake sources. In: US geological survey, reports, United States Geological Survey Open-file 78–1007, p 71

606. Yule DE, Kala R, Matheu EE (2005) DEQAS-R: standard response spectra and effective peak ground accelerations for seismic design and evaluation (computer program) Version 1.0. US Army Engineer Research and Development Center, Vicksburg, MS
607. Molina S, Lang DH, Meslem A, Lindholm CD (2015) User manual for the earthquake loss estimation tool, SELENA v6.5, User and Technical Manual v6.5, June 2015
608. Sahin C (2014) Seismic retrofitting of existing structures. Portland State University
609. Bazzurro P, Cornell CA (1999) Disaggregation of seismic hazard. *Bull Seismol Soc Am* 89(2):501–520
610. McGuire RK (2004) Seismic hazard and risk analysis. Report MNO-10, Earthquake Engineering Research Institute Publication, 221, Oakland, CA
611. Kulkarni RB, Youngs RR, Coppersmith KJ (1984) Assessment of confidence intervals for results of seismic hazard analysis. In: *Proceedings of the 8th world conference on earthquake engineering*, Prentice-Hall, Englewood Cliffs, NJ, 1, pp 263–270
612. Coppersmith KJ, Youngs RR (1986) Capturing uncertainty in probabilistic seismic hazard assessments with intraplate tectonic environments. In: *Proceedings of the 3rd US national conference on earthquake engineering*, vol 1, Charleston, South Carolina, pp 301–312
613. Frankel A, Mueller C, Barnhard T, Perkins D, Leyendecker E, Dickman N, Hanson S, Hopper M (1996) National seismic hazard maps—Documentation June 1996. US Geological Survey Open-File Report 96–532, 110
614. Kafka AL (2002) Statistical analysis of the hypothesis that seismicity delineates areas where future large earthquakes are likely to occur in the Central and Eastern United States. *Seismol Res Lett* 73(6):992–1003
615. US Geological Survey (2008) Documentation for the 2008 update of the United States National Seismic Hazard Maps, Open-File Report 2008–1128
616. Anderson JG, Trifunac MD (1977) Uniform risk absolute acceleration spectra, advances in civil engineering through engineering mechanics. In: *Proceedings of the 2nd annual engineering mechanics division specialty conference*, American Society of Civil Engineers, New York, pp 332–335
617. McGuire RK (1999) Deterministic versus probabilistic earthquake hazards and risks. *Soil Dyn Earthq Eng* 21:377–384
618. Mutlu Sumer B (2014) Liquefaction around marine structures. World Scientific Press, London
619. Matheu EE, Yule DE, Kala RV (2005) Determination of standard response spectra and effective peak ground accelerations for seismic design and evaluation. US Army Engineer Research and Development Center Vicksburg, MS
620. Frankel AD, Mueller C, Barnhard T, Perkins D, Leyendecker EV, Hanson S, Hopper M (1996) National seismic hazard maps, June 1996 documentation, open-file report 96-532. US Geological Survey, Golden, CO
621. Frankel AD, Petersen MD, Mueller CS, Haller KM, Wheeler RL, Leyendecker EV, Wesson RL, Harmsen SC, Cramer CH, Perkins D, Rukstales S (2002) Documentation for the 2002 update of the national seismic hazard maps, open-file report 02-420. US Geological Survey, Golden, CO
622. Mutlu Sumer B, Ansal A, Onder Cetin K, Damgaard J, Riza Gunbak A, Ottesen Hansen NE, Sawicki A, Synolakis CE, Cevdet Yalciner A, Yuksel Y, Zen K (2007) Earthquake-induced liquefaction around marine structures. *J Waterway Port Coast Ocean Eng ASCE* 133(1):55–82
623. Cornell CA (1996) Reliability-based earthquake-resistant design: the future. In: *Proceedings of the 11th world conference on earthquake engineering*, Acapulco, Mexico, Paper No. 2166
624. Popov EP, Yang TS, Grigorion CE (1994) New directions in structural seismic designs. *Earthq Spectra* 9(4):845–875
625. US DOE (Department of Energy) (1994) Natural phenomena hazards design and evaluation criteria for DOE facilities, DOE-STD-1020-94, Washington, DC

626. Cornell CA (1996) Calculating building seismic performance reliability: a basis for multi-level design norms. In: Proceedings of 11th world conference on earthquake engineering, Acapulco, Mexico
627. NORSOK Standard N-003 (2004) Actions and action effects, Rev. 2, Oct 2004
628. International Association of Oil and Gas Producers (2014) Reliability of offshore structures: current design and potential inconsistencies, OGP Report No. 486, March 2014
629. NORSAR (1998) Seismic zonation for Norway, prepared for Norwegian Council for Building Standardization by NORSAR and Norwegian Geotechnical Institute
630. NORSAR and Risk Engineering, Inc. (1991) Ground motions from earthquake on Norwegian continental shelf. Summary Report. Report for Operatørkomite Nord (OKN), Stavanger, Norway
631. Gazetas G (2006) Seismic design of foundations and soil–structure interaction. In: First European conference on earthquake engineering and seismology, Geneva
632. Mylonakis G, Gazetas G, Nikolaou A, Michaelides O (2000) The role of soil on the collapse of 18 piers of the elevated Hanshin Expressway in the Kobe earthquake. In: Proceedings of the 12th world conference on earthquake engineering, New Zealand
633. Iervolino I, Cornell CA (2005) Record selection for nonlinear seismic analysis of structures. *Earthq Spectra* 3:685–713
634. Newmark NM, Blume JA, Kapur KK (1973) Seismic design spectra for nuclear power plants. *J Power Div ASCE*, pp 287–303
635. NORSOK Standard N-003 (2004) Actions and action effects, Rev. 2, October 2004
636. ICC, Standards Australia (2007) Structural design actions—earthquake actions in Australia. AS 1170.4-2007, Sydney, Australia
637. International Code Council (ICC) (2006) International building code, 5th ed. Falls Church, VA
638. Building Seismic Safety Council (BSSC) (2009) NEHRP recommended seismic provisions for new buildings and other structures, Rep. FEMA P-750, FEMA, Washington, DC
639. Rodriguez-Marek AR, Bray JD, Abrahamson NA (2001) An empirical geotechnical seismic site response procedure. *Earthq Spectra* 17(1):65–87
640. Anbazhagan P, Parihar A, Rashmi HN (2011) Amplification based on shear wave velocity for seismic zonation: comparison of empirical relations and site response results for shallow engineering bedrock sites. *Geomech Eng* 3(3):189–206
641. Anbazhagan P, Sheikh N, Parihar A (2013) Influence of rock depth on seismic site classification for shallow bedrock regions. *Natural Haz Rev ASCE* 14(2)
642. Lee VW, Trifunac MD, Todorovska M, Novikova EI (1995) Empirical equations describing attenuation of peaks of strong ground motion, in terms of magnitude, distance, path effects and site conditions. Rep. No. CE 95-02, Department of Civil Engineering, University of Southern California, Los Angeles
643. Kokusho T, Sato K (2008) Surface-to-base amplification evaluated from KiK-net vertical array strong motion records. *Soil Dyn Earthq Eng* 28(9):707–716
644. Anbazhagan P, Sheikh MN, Tsang HH (2010) Seismic site classification practice in Australia, China and India, suitability. In: Abraham R, Latheswary S, Unnikrishnan N (eds) International conference on materials mechanics and management, New Delhi, pp 189–197
645. Boore DM (2004) Estimating V_s (30) (or NEHRP site classes) from shallow velocity models. *Bull Seismol Soc Am* 94(2):591–597
646. Atkinson GM, Boore DM (2003) Empirical ground-motion relations for subduction-zone earthquakes and their application to Cascadia and other regions. *Bull Seismol Soc Am* 93:1703–1729
647. Boore DM, Joyner WB, Fumal TE (1997) Equations for estimating horizontal response spectra and peak acceleration from western North American earthquakes: a summary of recent work. *Seismol Res Lett* 68(1):128–153

648. Dobry R, Iai S (2000) Recent developments in the understanding of earthquake site response and associated seismic code implementation. In: Proceedings of GeoEng2000, international conference on geotechnical & geological engineering, Melbourne, Australia, pp 186–129
649. Dobry R, Ramos R, Power MS (1997) Site factors and site categories in seismic codes: a perspective. In: Power MS, Mayes RL (eds) Proceedings of the NCEER workshop on the national representation of seismic ground motion for new and existing highway facilities, Report NCEER-97-0010, May 29–30, San Francisco, pp 137–170
650. Papageorgiou AS, Kim J (1991) Study of the propagation and amplification of seismic waves in Caracas Valley with reference to the 29 July 1967 earthquake: SH waves. *Bull Seismol Soc Am* 81(6):2214–2233
651. Chang SW, Bray JD (1995) Seismic response of deep, stiff soil deposits in the Oakland, California area during the Loma Prieta earthquake. Report. No. UCB/GT/95-06, Geotechnical Engineering, Department of Civil and Environmental Engineering, University of California, Berkeley, California
652. Motosaka M, Nagano M (1997) Analysis of amplification characteristics of ground motions in the heavily damaged belt zone during the 1995 Hyogo-ken Nanbu earthquake. *Earthq Eng Struct Dyn* 26(3):377–393
653. Beltsos AS, Newmark NM (1960) Effect of inelastic behaviour on the response of simple systems to earthquake motions. In: Proceedings of the 2nd world conference on earthquake engineering, pp 895–912, Tokyo
654. Penzien J (1960) Elasto-plastic response of idealized multi-story structures subjected to a strong motion earthquake. In: Proceedings of the 2nd world conference on earthquake engineering
655. Berg GV, Thomaides SS (1960) Energy consumption by structures in strong motion earthquakes. In: Proceedings of the 2nd world conference on earthquake engineering
656. Naeim F (2001) *The seismic design handbook*, 2nd edn. Kluwer Academic Publisher, USA
657. Wakabayashi M (1980) *Design of earthquake resistant buildings*. McGraw-Hill, New York
658. Blume JA, Newmark NM, Corning L (1961) *Design of multistory reinforced concrete buildings for earthquake motions*, Portland Cement Association, Chicago, Illinois
659. ASCE 7-05 (2006) *Minimum design loads for buildings and others structures*. American Society of Civil Engineers, Reston, VA
660. Kumar M, Stafford PJ, Elghazouli AY (2013) Influence of ground motion characteristics on drift demands in steel moment frames designed to Eurocode 8. *Eng Struct* 52:502–517
661. Kumar M, Stafford PJ, Elghazouli AY (2013) Seismic shear demands in multi-storey steel frames designed to Eurocode 8. *Eng Struct* 52:69–87
662. Brunesi E, Nascimbene R, Casagrande L (2016) Seismic analysis of high-rise mega-braced frame-core buildings. *Eng Struct* 115:1–17
663. Clough RW, Benuska KL, Wilson EI (1965) Inelastic earthquake response of tall buildings. In: 3rd world conference on earthquake engineering, New Zealand
664. Chen WF, Lui EM (2006) *Earthquake engineering for structural design*, 1st edn. CRC Press, London
665. Clough RW (1955) On the importance of higher modes of vibration in the earthquake response of a tall building. *Bull Seismol Soc Am* 45(4)
666. Wang Gang (2011) A ground motion selection and modification method capturing response spectrum characteristics and variability of scenario earthquakes. *Soil Dyn Earthq Eng* 31:611–625
667. Baker JW, Cornell CA (2006) Spectral shape, epsilon and record selection. *Earthq Eng Struct Dyn* 35(9):1077–1095
668. Baker JW, Cornell CA (2006) Correlation of response spectral values for multi-component ground motions. *Bull Seismol Soc Am* 96(1):215–227

669. Baker JW, Jayaram N (2008) Correlation of spectral acceleration values from NGA ground motion models. *Earthq Spectra* 24(1):299–317
670. Baker JW (2007) Evaluation of ground motion selection and scaling techniques for long period structures. USGS Award No. 07HQAG0129
671. Somerville PG, Thio HK (2011) Development of ground motion time histories for seismic design. In: Proceedings of the Ninth Pacific conference on earthquake engineering: building an earthquake-resilient society, Auckland, New Zealand
672. Mousavi M, Ghafory-Ashtiany M, Azarbakht A (2011) A new indicator of elastic spectral shape for the reliable selection of ground motion records. *Earthq Eng Struct Dyn* 40(12):1403–1416
673. Mousavi Mehdi, Shahri Mohamadreza, Azarbakht Alireza (2012) E-CMS: a new design spectrum for nuclear structures in high levels of seismic hazard. *Nucl Eng Des* 252:27–33
674. Boore DM, Atkinson GM (2008) Ground-motion prediction equations for the average horizontal component of PGA, PGV, and 5%-damped PSA at spectral periods between 0.01 and 10.0 s. *Earthq Spectra* 24(1):99–138
675. Aki K, Richards PG (2002) *Quantitative Seismology*. University Science Books, Sausalito, CA
676. Bilham R (2009) The seismic future of cities. *Bull Earthq Eng* 7(4):839–887
677. Wang Z, Cobb C (2012) A critique of probabilistic versus deterministic seismic hazard analysis with special reference to the new Madrid seismic zone. *Recent Advances in North American Paleoseismology and Neotectonics East of Rockies*
678. Geller RJ, Mulargia F, Stark PB (2016) Why we need a new paradigm of earthquake occurrence. In: Morra G, Yuen DA, SD King, SM Lee, S Stein (eds) *Subduction dynamics: from mantle flow to mega disasters*, geophysical monograph, Wiley, New York, pp 210
679. Mulargia F, Stark PB, Geller RJ (2017) Why is probabilistic seismic hazard analysis (PSHA) still used? *Phys Earth Planet Inter* 264(March):63–75
680. Parvez IA, Magrin A, Vaccari F, Ramees A, Mir R, Peresan A, Panza GF (2017) A neo-deterministic seismic hazard scenarios for India—a preventive tool for disaster mitigation. *J Seismol* 17(3):1–17
681. Panza GF, Peresan A, La Mura C (2013) Seismic hazard and strong ground motion: an operational neo-deterministic approach from national to local scale. In: UNESCO-EOLSS Joint Committee (ed) *Encyclopedia of life support systems (EOLSS), geophysics and geochemistry*. Developed under the Auspices of the UNESCO, Eolss Publishers, Oxford, pp 1–49
682. Fasan M, Magrin A, Amadio C, Romanelli F, Vaccari F, Panza GF (2016) A seismological and engineering perspective on the 2016 Central Italy earthquakes. *Int J Earthq Impact Eng* 1(4):395–420
683. Peresan A, Magrin A, Nekrasova A, Kossobokov VG, Panza GF (2013) Earthquake recurrence and seismic hazard assessment: a comparative analysis over the Italian territory. *WIT Trans Built Environ* 132:23–34
684. Zuccolo E, Vaccari F, Peresan A, Panza GF (2011) Neo-deterministic and probabilistic seismic hazard assessments: a comparison over the Italian territory. *Pure Appl Geophys* 168(1):69–83
685. Castañón H, Lomnitz C (2002) PSHA: is it science? *Eng Geol* 66:315–317
686. Panza GF, Irikura K, Kouteva M, Peresan A, Wang Z, Saragoni R (eds) (2011) *Advanced seismic hazard assessment*. *Pure Appl Geophys* 168(1):1–9
687. Wang Z (2011) *Seismic hazard assessment: issues and alternatives*. *Pure Appl Geophys* 168
688. Bak P (1996) *How nature works: the science of self-organized criticality*. Copernicus Press, New York, NY
689. Sornette D, Ouillon G (2012) Dragon-kings: mechanisms, statistical methods and empirical evidence. *Eur Phys J Spec Top* 205(1):1–26

690. Sornette D, Woodard R, Zhou WX (2009) The 2006–2008 oil bubble: evidence of speculation, and prediction. *Phys A* 388:1571–1576
691. Rundle JB, Holliday JR, Graves W, Turcotte DL, Tiampo KF, Klein W (2012) Probabilities for large events in driven threshold systems. *Phys Rev E* 86
692. Braja M (2016) Das, principles of foundation engineering, 8th edn. Cengage Learning, Boston
693. Chappell S (1998) The alternative building sourcebook: for traditional, natural, and sustainable building products and services. Brownfield, Me.: Fox Maple Press
694. Chen Wai-Fah, Duan Lian (2000) The bridge engineering handbook. CRC Press, Boca Raton
695. Ismael NF, Vesic AS (1981) Compressibility and bearing capacity. *ASCE J Geotech Found Eng Div* 107(GT12):1677–1691
696. Vesic AS (1963) Bearing capacity of deep foundations in sand. *National Acad Sci National Res Council Highway Res Rec* 39:112–153
697. Vesic AS (1973) Analysis of ultimate loads of shallow foundations. *ASCE J Soil Mech Found Eng Div* 99:45–73
698. De Beer EE (1967) Proefondervindelijke bijdrage tot de studie van het gransdraagvermogen van zand onder funderingen p staal, Bepaling von der vormfactor sb. *Ann Trav Publics Belg*
699. Lambe TW, Whitman RV (1969) Soil mechanics. Wiley, New York
700. Vesic AS (1975) Bearing capacity of shallow foundations, Chapter 3. In: Winterkorn HF, Fang HY (eds) *Foundation engineering handbook*, Van Nostrand Reinhold, New York
701. Sabatini PJ, Bachus RC, Mayne PW, Schneider JA, Zettler TE (2002) Geotechnical engineering circular 5 (GEC5)—evaluation of soil and rock properties
702. Prandtl L (1921) Über die Eindringungsfestigkeit (Härte) plastischer Baustoffe und die Festigkeit von Schneiden, (On the penetrating strengths (hardness) of plastic construction materials and the strength of cutting edges) *Zeitschrift für angewandte Mathematik und vol 1, No 1*
703. Terzaghi K (1943) *Theoretical soil mechanics*. Wiley, New York
704. Chai J (2000) Shallow foundations. In: Chen WF, Duan L (eds) *Bridge engineering handbook*. CRC Press, Boca Raton
705. Naval Facilities Engineering Command (1982) *Foundations and earthquake structures, design manual 7.02 (revalidated by change 1 Sept 1986)*
706. Peck RB (1974) *Foundation engineering*, John Wiley & Sons, 2nd edn. Hoboken, New Jersey
707. Castelli F, Motta E (2010) Bearing capacity of strip footings near slopes. *Geotech Geol Eng J* 28(2):187–198
708. Castelli F, Motta E (2012) Seismic bearing capacity of shallow foundations. In: Moustafa A (ed) *Earthquake-resistant structures—design, assessment and rehabilitation*, Intech, Rijeka, Croatia
709. Paolucci R, Pecker A (1997) Seismic bearing capacity of shallow strip foundations on dry soils. *Soils Found* 37(3):95–105
710. Cascone E, Carfi G, Maugeri M, Motta E (2004) Effetto dell'inerzia del terreno sul fattore di capacità portante N_{γ} . In: *Proceedings IARG 2004, Trento (Italy), 7–9 Jul 2004*
711. Day RW (2010) *Foundation engineering handbook*, 2nd ed. McGraw-Hill Professional, New York
712. Clausen CJF, Dimaggio E, Duncan JM, Andersen KH (1975) Observed behavior of ekofisk oil storage tank foundation. In: Paper OTC 2373, offshore technology conference
713. Bonin JP, Deleuil G, Zaleski-Zamenhof LC (1976) Foundation analysis of marine gravity structures submitted to cyclic loading. In: Paper OTC 2475, offshore technology conference
714. Foss I, Dahlberg R, Kvalstad T (1978) Foundation design for structures with respect to failure in cyclic loading. In: OTC 3114, offshore technology conference

715. DNV Classification Notes No. 30.4 Foundations, det norske veritas, February 1992
716. Gazetas G (1975) Foundation engineering handbook. In: Winterkorn HF, Fang HY (eds) Van Nostrand Reinhold, New York
717. Luco JE, Westmann RA (1971) Dynamic response of circular footings. *J Eng Mech* 97(5):1381–1395
718. Veletsos AS, Wei YT (1971) Lateral and rocking vibrations of footings. *J Soil Mech Found Div* 97(9):1227–1248
719. NEHRP Consultants Joint Venture and National Institute of Standards and Technology (2012) Soil-Structure Interactions for building structures. Gaithersburg, MD, USA
720. Richart FE, Whitman RV (1967) Comparison of footing vibration tests with theory. *J Soil Mech Found Eng Div*
721. Richart FE, Woods RD, Hall JR (1970) Vibrations of soils and foundations. Prentice-Hall
722. Whitman RV (1976) Soil-platform Interaction. In: Proceedings of the conference on behavior of offshore structure, vol 1, NGI, Oslo, paper No. 817, Oslo
723. Gazetas G (1991) Formulas and charts for impedances of surface and embedded foundations. *J Geotech Eng ASCE* 117(9)
724. Gazetas G, II Stokoe KH (1991) Vibration of embedded foundations theory versus experiment. *J Geotech Eng ASCE* 117(9):1382–1401
725. Stewart JP, Kim S, Bielak J, Dobry R, Power M (2003) Revisions to soil structure interaction procedures in NEHRP design provisions. *Earthq Spectra* 19(3):677–696
726. Gazetas G, Roesset JM (1979) Vertical vibration of machine foundations. *J Geotech Eng Div ASCE*
727. Hadjian AH, Luco JE, Tsai NC (1974) Soil-structure interaction: continuum or finite element? *Nuclear Eng Des* 31
728. Jakub M, Roseest JM (1977) Dynamic stiffness of foundations: 2-D versus 3-D solutions. Research Report R77-36, MIT
729. Waas G (1972) Analysis method for footing vibrations through layered media. PhD thesis, University of California, Berkeley
730. Kausel E, Roesset José M (1975) Dynamic stiffness of circular foundations. *J Eng Mech Div ASCE* 101:771–785
731. Tassoulas JL (1981) Elements for numerical analysis of wave motion in layered media. Research report R81.12, Department of Civil Engineering, MIT
732. Norwegian Geotechnical Institute (1987) SHAKE(N)—computer program for analysis of earthquake response in horizontally layered sites. NGI report No. 51508-23, Aug 1987
733. Caughey TK (1960) Classical normal modes in damped linear dynamic systems. *J Appl Mech* 27:269–271
734. Roesset JM, Whitman RV, Dobry R (1973) Modal analysis for structures with foundation interaction. *J Struct Div Proc Am Soc Civ Eng*
735. Lacasse S, Robbetstad L, Boisard P, Ohm K (1991) The foundation of the Frigg CDP-1 platform: a case study. In: OTC paper No. 6512, offshore technology conference
736. Bos KJ, Verheij HJ, Kant G, Kruisbrink ACH (2002) Scour protection around gravity based structures using small size rock. In: The 1st international conference on scour of foundations, Texas
737. Malhotra S (2011) Selection, design and construction of offshore wind turbine foundations, wind turbines. In: Al-Bahadly I (ed) *In Tech*, Rijeka
738. White DJ, Finlay TCR, Bolton MD, Bearss G (2002) Press-in piling: ground vibration and noise during pile installation. International Deep Foundations Congress, Orlando, USA, ASCE, Special publication 116, pp 363–371
739. Deeks AJ, White DJ, Bolton MD (2005) A comparison of jacked, driven and bored piles in sand. In: 16th international conference on soil mechanics and geotechnical engineering, vol 3, Osaka, Japan, Millpress, Japan, pp 2103–2106
740. Yetginer AG, White DJ, Bolton MD (2006) Field measurements of the stiffness of jacked piles and pile groups. *Géotechnique* 56(5):349–354

741. NCHRP (2006) Rock-socketed shafts for highway structure foundations
742. Boyd P, Ozsoy B (2013) High capacity rock socketed piles in Scotland, UK. In: International conference on case histories in geotechnical engineering
743. Tomlinson MJ (1970) The adhesion of piles in stiff clay. Construction Industry Research and Information Association Research Report No. 26. CIRIA, London
744. Vijayvergiya VN, Focht JA (1972) A new way to predict the capacity of piles in clay. In: Proceedings of 4th offshore technology conference, vol 2, Houston, pp 865–874
745. Det Norske Veritas, DNV-RP-B401 (2010) Cathodic protection design. DNV, Høvik, Norway, Oct 2010
746. NACE International, NACE SP0176-2007 (2007) Corrosion control of submerged areas of permanently installed steel offshore structures associated with petroleum production, No. 21018, Houston
747. Standard Norway, Norsok M-503 (2007) Cathodic protection, 3rd ed. May 2007
748. Baker CN (1969) How to determine pile depth of embedment, pile foundations: know-how. American Wood Preservers Institute
749. Overy R (2007) The use of ICP design methods for the foundations of nine platforms installed in the UK North Sea. In: Proceedings of the 6th international conference on offshore site investigations, SUT, London, pp 359–366
750. Jardine RJ (2009) Review of technical issues relating to foundations and geotechnics for offshore installations in the UKCS. Research Report 676, Health and Safety Executive
751. Randolph MR, Cassidy M, Gourvenec S, Erbrich C (2005) Challenges of offshore geotechnical engineering, Keynote lecture. In: Proceedings of 16th ICSMGE, vol 1, Osaka, Millpress, Rotterdam, pp 123–176
752. Alm T, Snell RO, Hampson KM, Olaussen A (2004) Design and installation of the Valhall piggyback structures. In: Proceedings of 36th offshore technology conference. Houston, Paper OTC 16294
753. Clarke J (ed) (1993) Large scale pile tests in clay. Thomas Telford, London
754. Williams RE, Chow FC, Jardine RJ (1997) Unexpected behaviour of large diameter tubular steel piles. In: International conference on foundation failures, Singapore Institution of Engineers, pp 363-378
755. Kolk HJ, Baaijens AE, Vergobbi P (2005) Results from axial load tests on pile piles in very dense sands: the EURIPIDES JIP. In: International symposium on frontiers in offshore geotechnics, Perth, Ed Gourvenec and Cassidy, Taylor and Francis, London, pp 661–675
756. Rahmani A, Taiebat M, Finn WDL, Ventura CE (2012) Determination of dynamic p - y curves for pile foundations under seismic loading. In: 15th world conference on earthquake engineering, Lisboa
757. Zaijier MB (2000) Sensitivity analysis for foundations of offshore wind turbines. Section Wind Energy, WE 02181, Delft
758. Binkgreve RBJ (2007) PLAXIS 3D foundation, version 2. PLAXIS, Netherlands
759. Fan C, Huang YHS, Alba J (2014) Three dimensional FEA for subsea pile drivability and fatigue analysis. In: Proceedings of the twenty-fourth (2014) international ocean and polar engineering conference, Busan, Korea, 15–20 June, pp 697–702
760. Poulos HG (1971) Behavior of laterally loaded piles: I—single piles. *J Soil Mech Found Div* 97(SM5):711–731
761. Poulos HG (1971) Behavior of laterally loaded piles: II – pile groups. *J Soil Mech Found Div* 97(SM5):733–751
762. Poulos HG (1972) Behavior of laterally loaded piles: III—socketed piles. *J Soil Mech Found Div* 98(SM4):341–360
763. Finn WDL, Fujita N (2002) Pile in liquefiable soils: seismic analysis and design issues. *Soil Dyn Earthq Eng* 22:731–742
764. Cheng Z, Jeremic B (2009) Numerical modeling and simulation of pile in liquefiable soil. *Soil Dyn Earthq Eng* 29:1404–1416

765. Rahmani A, Pak A (2012) Dynamic behavior of pile foundations under cyclic loading in liquefiable soils. *J Comput Geotech* 40:114–126
766. Badoni D, Makris N (1996) Nonlinear response of single piles under lateral inertial and seismic loads. *Soil Dyn Earthq Eng* 15:29–43
767. Novak M (1991) Piles under dynamic loads. In: *Proceedings of 2nd international conference on recent advances in geotech. Earthquake engineering and soil dynamics*, St. Louis, Missouri, pp 2433–2457
768. Hadjian AH, Fallgren RB, Tufenkjian MR (1992) Dynamic soil–pile–structure interaction the state-of-practice. In: *Parkash S (ed) Piles under dyanmics loads*, vol 34. *Geotechnical Special Publication*, pp 1–25
769. Matsui T, Oda K (1996) Foundation damage of structures. *Special issue of Soils and Foundations*, pp 189–200
770. Tokimatsu K, Mizuno H, Kakurai M (1996) Building damage associated with geotechnical problems. *Special issue of Soils Found*, pp 219–234
771. Finn WDL, Byrne PM, Evans S, Law T (1996) Some geotechnical aspects of the Hyogo-ken Nanbu (Kobe) earthquake of January 17, 1995. *Can J Civ Eng* 23:778–796
772. Chau KT, Yang X (2000) Nonlinear soil–pile–structure interaction for structures resting on a 2×2 pile group under earthquake excitations. In: *Proceedings of the China-U.S. millennium symposium of earthquake engineering: earthquake engineering frontiers in the new millennium*, Beijing, 8–11 Nov 2000
773. Eid HT, Bani-Hani K (2012) Settlement of axially loaded piles entirely embedded in rock-analytical and experimental study. *Geomech Geoeng* 7(2):139–148
774. Han Yingcai (1995) *Dynamic behavior of pile foundations with soil-pile Interactions*. Memorial University of Newfoundland, St. John’s Newfoundland, Canada
775. Randolph MF (1994) Design methods for pile groups and pile rafts. In: *Proceedings of 13th international conference on soil mechanics and foundation engineering*, vol 5, New Delhi, pp 61–82
776. Mandolini A, Viggiani C (1997) Settlement of piled foudnations. *Géotechnique* 47 (4):791–816
777. NSV Kameswara Rao (2011) *Foundation design: theory and practice, theory and practice*. Wiley, Hoboken
778. Kocsis Peter (1976) The equivalent length of a pile or caisson in soil. *Civ Eng* 46(12):63
779. Terzaghi K (1955) Evaluation of coefficients of subgrade reactions. *Géotechnique* 5 (4):297–326
780. Hetenyi M (1946) *Beams on elastic foundations*. University of Michigan Press, Michigan
781. Broms BB (1964) Lateral resistance of piles in cohesive soils. *Proc ASCE J Soil Mech Found Eng* 90(SM3):27–63
782. Randolph MF (1981) The response of flexible piles to lateral loading. *Géotechnique* 31 (2):247–259
783. Zaaizer Michiel, *Notes Lecture (2007) Dynamics and structural design, offshore windfarm design (OE 5662)*. Delft University of Technology, Delft
784. Hansen JB (1961) The ultimate resistance of rigid piles against transversal forces. *Geoteknisk Institut, Bull.*, No. 12, Copenhagen
785. Price J, Jardine RJ (2007) *Notes from interview with Mr John price–independent consultant, conducted on 27th March 2007 to assess current practice and thinking relating to piled foundation design in UK Sector, North Sea, 2007*
786. Reese LC, Cox WR, Koop FD (1974) Analysis of laterally loaded piles in sand. In: *Proceedings of 6th offshore technology conference*, Houston, Texas, OTC 2080, pp 473–483
787. Reese LC, Cox WR, Koop FD (1975) Field testing and analysis of laterally loaded piles in stiff clay. In: *Proceedings of 7th offshore technology conference*, Houston, Texas, OTC 2312, pp 671–690

788. Matlock H (1970) Correlations for design of laterally loaded piles in soft clay, offshore technology conference, Dallas, Texas
789. O'Neill MW, Murchison JM (1983) An evaluation of p - y relationships in sands. A Report to American Petroleum Institute, (PRAC 82-41-1), University of Houston University Park, Department of Civil Engineering, Research Report No. GT-DF02-83
790. American Petroleum Institute (1993) API recommended practice for planning, designing and constructing fixed offshore platform-load and resistance factor design, Washington, 1st ed.
791. American Petroleum Institute (2000) API recommended practice for planning, designing and constructing fixed offshore platforms-RP-2A-WSD, Version Dec 2000
792. American Petroleum Institute (2007) API Recommended practice for planning, designing and constructing fixed offshore platforms-RP-2A-WSD, Version December 2000 and errata and supplement 2007
793. American Petroleum Institute (2014) Recommended practice 2GEO, geotechnical and foundation design considerations, 1th edn. April 2011 and Addendum 1, 2014
794. Det Norske Veritas (2014) Offshore standard DNV-OS-J101, design of offshore wind turbine structures
795. Murchison JM, O'Neill MW (1984) Evaluation of p - y -relationship in cohesionless soils, analysis and design of pile foundations. In: Meyer JR (ed) ASCE, New York, pp 174-191
796. Hamre L, Feizi Khankandi S, Strøm PJ, Athanasiu C (2011) Lateral behavior of large diameter monopiles at Sheringham Shoal Wind Farm. In: Frontiers in offshore geotechnics II, pp 575-580
797. Krolis VD, van der Tempel J, de Vries W (2008) Evaluation of foundation design for monopile support structures for offshore wind turbines
798. Lesny K, Paikowsky S, Gurbuz A (2007) Scale effects in lateral load response of large diameter monopiles. In: Proceedings of sessions of geo-denver 2007: contemporary issues in deep foundations 2007, Denver, CO
799. Thieken K, Achmus M, Lemke K (2015) A new static p - y approach for piles with arbitrary dimensions in sand, Geotechnik
800. Reese LC (1997) Analysis of laterally loaded piles in weak rock. J Geotech Geoenviron Eng 123(11):1010-1017
801. Reese LC (1975) Laterally loaded piles. In: Proceedings of ASCE, Geotech, Group and Continuing Education Committee, San Francisco section, University of California at Berkeley
802. Randolph MF, Houlsby GT (1984) The limiting pressure on circular pile loaded laterally on cohesive soil. Géotechnique 34(4):613-623
803. Skempton AW (1951) The bearing capacity of clay. In: Proceedings of the building research congress, Division 1, London
804. Hamilton JM, Dunnivant TW (1992) Analysis of behavior of the Tilbrook Grange lateral test pile. In: Clarke J (ed) Large-scale pile tests in clay. London, Thomas Telford, pp 448-461
805. Jeanjean P (2009) Re-assessment of p - y curves for soft clays from centrifuge testing and finite element modeling. In: Offshore technology conference, Houston, Texas, OTC 20158
806. Templeton JS (2009) Finite element analysis of conductor/seafloor interaction. In: Offshore technology conference, Huston, Texas, OTC 20197
807. O'Neill MW, Gazioglu SM (1984) An evaluation of p - y relationships in clays. A Report to the API (Prac 82-41-2), Univeristy of Houston, Department of Civil Engineering, Research Report No. UHCE-84-3
808. Augustensen AH, Brødbæk KT, Møller M, Sørensen SPH, Ibsen LB (2009) Thomas Schmidt Pedersen, Lars Vabbersgaard Andersen, Numerical modeling of large diameter steel piles at horns rev. In: Proceedings of 12th International conference civil structure environment engineering computer, Stirlingshire, UK, Paper 239

809. von Pablo Cuéllar (2011) Pile foundations for offshore wind turbines numerical and experimental investigations on the behaviour under short-term and long-term cyclic loading. Technical University of Berlin, Berlin
810. Hettler A (1981) Verschiebungen starrer und elastischer Gründungskörper in Sand bei monotoner und zyklischer Belastung. PhD Thesis, Department of Civil Engineering, Geo- and Environmental Sciences, Institute of Soil Mechanics and Rock Mechanics, University of Karlsruhe, Germany
811. Achmus M (2010) Design of axially and laterally loaded piles for the support of offshore wind energy converters, Indian geotechnical conference—2010. GEOTrendz, IGS Mumbai Chapter & IIT Bombay, 16–18 Dec 2010
812. Little RL, Briaud JL (1988) Full scale cyclic lateral load tests on six single piles in sand. Miscellaneous paper GL-88-27, Texas: Geotechnical Division, Texas A&M University
813. Achmus M, Müller M (2010) Evaluation of pile capacity approaches with respect to piles for wind energy foundations in the North Sea. In: 2nd International symposium on frontiers in offshore geotechnics ISFOG, Perth
814. Long JH, Vanneste G (1995) Effect of cyclic lateral loads on piles in sand. *J Geotech Eng Div (ASCE)* 120(1):33–42
815. Lin SS, Liao JC (1999) Permanent strains of piles in sand due to cyclic lateral loads. *ASCE J Geotech Geoenviron Eng*
816. Achmus M, Abdel-Rahman K, Peralta P (2005) On the design of monopile foundations with respect to static and quasi-static cyclic loading. Copenhagen Offshore Wind, Copenhagen
817. Long JH, Vanneste G (1994) Effects of cyclic lateral loads on piles in sand. *ASCE J Geotech Eng* 120(1):225–244
818. Allotey NK, El Naggar MH (2005) Cyclic normal force displacement model for nonlinear soil structure interaction analysis: seismostruct implementation. Report No. GEOT 02-05, Geotechnical Research Centre, Department of Civil and Environmental Engineering, University of Western Ontario, Ontario
819. Grabe J, Dührkop J (2008) Zum Tragverhalten von überwiegend horizontal belasteten Pfählen. Tagungsband zur 30. Baugrundtagung 2008 der DGGT in Dortmund, pp 143–150
820. Achmus M, Kuo YS, Abdel-Rahman K (2008) Zur Bemessung von Monopiles für zyklische Lasten. *Bauingenieur*, 83, Heft 7–8, pp 303–311
821. Baek SH, Kim JY, Lee SH, Chung CK (2014) Effect of relative density on P – Y backbone curves for cyclic lateral load on pile foundations in sandy soil. In: Proceedings of the 33rd international conference on ocean, offshore and arctic engineering, OMAE 2014, San Francisco, California
822. Bhattacharya S, Cox JA, Lombardi D, Wood DM (2013) Dynamics of offshore wind turbines supported on two foundations. *Geotech Eng* 166(GE2)
823. Leblanc C, Houlshby GT, Byrne BW (2010) Response of stiff piles to long-term cyclic lateral load. *Géotechnique* 60(2):79–90
824. El Naggar MH, Bentley KJ (2000) Dynamic analysis for laterally loaded piles and dynamic p – y curves. *Can Geotech J* 37:1166–1183
825. El Naggar MH, Novak M (1994) Non-linear model for dynamic axial pile response. *J Geotech Eng* 120(2):308–328
826. Transportation Research Board (2001) NRC NCHRP Report 461, Static and Dynamic Lateral Loading of Pile Groups
827. Matlock H, Foo SH, Bryant LL (1978) Simulation of lateral pile behavior. In: Proceedings of the earthquake engineering and soil dynamics, ASCE, New York, pp 600–619
828. Kagawa T, Kraft LM (1980) Soil-pile-structure interaction of offshore structures during an earthquake. In: 12th Annual offshore technology Conference, vol 3, pp 235–245

829. Novak M, Sheta M (1980) Approximate approach to contact problems of piles. In: Proceedings ASCE national convention, dynamics response of pile found: analytical aspects, ASCE, New York, pp 55–79
830. Nogami T, Otani J, Konagai K, Chen HL (1992) Nonlinear soil–pile interaction model for dynamic lateral motion. *J Geotech Eng ASCE* 118(1):89–106
831. Boulanger RW, Curras CJ, Kutter BL, Wilson DW, Abghari A (1999) Seismic soil pile structure interaction experiments and analysis. *J Geotech Geoenviron Eng ASCE* 125(9):750–759
832. Wang S, Kutter BL, Chacko JM, Wilson DW, Boulanger RW, Abghari A (1998) Nonlinear seismic soil–pile–structure interaction. *Earthq Spectra* 14(2):377–396
833. Mohan S, Khotan VK, Stevens RF, Chacko MJ, Kapuskar M (2004) Design and construction of large diameter impact driven pipe pile foundations New East Span San Francisco-Oakland Bay Bridge. In: International conference on case histories in geotechnical engineering, Paper No. 43
834. Achmus M, Thieken K, Lemke K (2014) Evaluation of p – y approaches for large diameter monopiles in sand. In: Proceedings of the 24th international ocean and polar engineering conference, Busan, Korea
835. Sørensen SPH, Brødbæk KT, Møller M (2009) Evaluation of load-displacement relationships for large-diameter piles. Candidate Report, Aalborg University
836. Lesny K, Wiemann J (2006) Finite-element-modeling of large diameter monopiles for offshore wind energy converters. *Geo Congress 2006*, Atlanta, GA
837. Ashford S, Juirnarongrit T (2003) Evaluation of pile diameter effect on initial modulus of subgrade reaction. *J Geotech Geoenviron Eng ASCE* 129(3):234–242
838. Fang CC, Long JH (2005) Assessment of existing methods for predicting soil response of laterally loaded piles in sand. *Comput Geotech* 32:274–289
839. Chen Y, Kulhawy F (1994) Case history evaluation of the behavior of drilled shafts under axial and lateral loading. EPRI TR-104601s, Cornell University, Ithaca
840. Abdel-Rahman K, Achmus M (2005) Finite element modeling of horizontally loaded monopile foundations for offshore wind energy converters in Germany. In: International Symposium on frontiers in offshore geotechnics, ISFOG, Perth, Australia, pp 391–396
841. Achmus M, Kuo YS, Abdel-Rahman K (2009) Behavior of monopile foundations under cyclic lateral load. *Comput Geotech* 36:725–735
842. Bourgeois E, Rakotonindriana MHJ, Le Kouby A, Mestat P, Serratrice JF (2010) Three-dimensional numerical modeling of the behaviour of a pile subjected to cyclic lateral loading. *Comput Geotech* 37:999–1007
843. Kim Y, Jeong S (2011) Analysis of soil resistance on laterally loaded piles based on 3D soil–pile interaction. *Comput Geotech* 38:248–257
844. Cox W, Reese L, Grubbs B (1974) Field testing of laterally loaded piles in sand, offshore technology conference, Houston, pp 459–472
845. Kallehave D, LeBlanc C, Liingaard MA (2012) Modification of the API p – y formulation of initial stiffness of sand, offshore site investigation and geotechnics. *Integrated Technologies—Present and Future*, Society for Underwater Technology, London, UK, pp 465–472
846. Achmus M (2011) Bemessung von monopiles für die Gründung von offshore-windenergieanlagen. *Bautechnik* 88(9):602–616
847. Achmus M, Abdel-Rahman K, Kuo YS (2007) Numerical modeling of large diameter steel piles under monotonic and cyclic horizontal loading. In: 10th international symposium on numerical models in geomechanics, Rhodes/Greece, pp 453–459
848. Haiderali A, Madabhushi G (2013) Evaluation of the p – y method in the design of monopiles for offshore wind turbines, offshore technology conference OTC, pp 1824–1844

849. Achmus M, Terceros M, Thieken K (2016) Evaluation of p - y approaches for large diameter monopiles in soft clay. In: Proceedings of the 25th international offshore and polar engineering conference, Rhodes
850. Wiemann J, Lesny K, Richwien W (2004) Evaluation of the pile diameter effects on soil-pile stiffness. In: Proceedings of the 7th German wind energy conference (DEWEK), Wilhelmshaven
851. Sørensen SPH (2012) Soil-structure interaction for non-slender, large-diameter offshore monopiles. PhD Thesis, Aalborg University, Denmark
852. Thieken K, Achmus M (2013) Small strain effects on the stiffness of monopile foundations in sand. In: International symposium on computational geomechanics (ComGeoIII), Poland
853. Kirsch F, Richter T, Coronel M (2014) Geotechnische Aspekte bei der Gründungsdimensionierung von Offshore-Windenergieanlagen auf Monopfählen mit sehr großen Durchmessern, Stahlbau Spezial 2014: Erneuerbare Energien, vol 83, pp 61–67
854. Achmus M, Kuo YS, Abdel-Rahman K (2008) On the design of monopiles with respect to cyclic loads. Bauingenieur 83:303–311
855. Kim Y, Jeong S, Won J (2009) Effect of lateral rigidity of offshore piles using proposed p - y curves in marine clay, marine georesources and geotechnology, pp 53–77
856. Kirsch F, Richter T, Coronel M (2014) Geotechnische Aspekte bei der Gründungsdimensionierung von Offshore-Windenergieanlagen auf Monopfählen mit sehr großen Durchmessern, Stahlbau Spezial - Erneuerbare Energien, pp 61–67 (in German)
857. Stevens JB, Audibert JME (1979) Re-examination of p - y curve formulations. In: Proceedings of 11th annual offshore technology conference, Houston, Texas, vol I, Paper No. 3402, pp 397–403
858. Po Lam I (2009) Diameter effects on p - y curves, in deep marine foundations: a perspective on the design and construction of deep marine foundations. In: Bittner RB, Jr Ellman RA (eds) Deep Foundations Institute
859. Carter DP (1984) A nonlinear soil model for predicting lateral pile response. Report No. 359, Civil Engineering, University of Auckland
860. Ling LF (1988) Back analysis of lateral load test on piles. ME Thesis, Civil Engineering Department, University of Auckland
861. Brinkgreve RBJ, Engin E, Swolfs WM (2013) PLAXIS 3D 2013 manual
862. Kampitsis AE, Sapountzakis EJ, Giannakos SK, Gerolymos NA (2013) Seismic soil–pile–structure kinematic and inertia interaction—a new beam approach. Soil Dyn Earthq Eng 55:211–224
863. Reese LC, Wang ST, Arrellaga JA, Vasquez LG (2014) APILE v2014-technical manual. Ensoft, Inc, Austin
864. API-RP 24 (1982) Recommended practice for planning, designing, and constructing fixed offshore platforms
865. Semple RM, Rigden WJ (1984) Shaft capacity of driven pipe piles in clay. In: Proceedings of the symposium on analysis and design of pile foundations, San Francisco, American Society of Civil Engineers
866. Randolph MF, Murphy BS (1985) Shaft capacity of driven piles in clay. In: Proceedings 17th annual offshore technology conference, OTC 4883, Houston
867. Kolk HJ, Van Der Velde E (1996) A reliable method to determine friction capacity of piles driven into clays. In: 28th annual offshore technology conference, OTC 7993, Houston, Texas: OTC
868. Murff JD (1980) Pile capacity in a softening soil. Int J Numer Anal Methods Geomech 4 (2):185–189
869. Randolph MF (1983) Design considerations for offshore piles. In: Proceedings of the conference on geotechnical practice in offshore engineering, Austin, Texas, New York, American Society of Civil Engineers, pp 422–439
870. Tomlinson MJ (2004) Pile design and construction practice. E. and F.N. Spon, London

871. Chandler RJ (1968) The shaft friction of piles in cohesive soils in terms of effective stress. *Civ Eng Pub Works Rev* 63:48–51
872. Burland JB (1973) Shaft friction of piles in clay. *Ground Eng* 6(3):30–42
873. Vijayvergiya VN, Focht JA (1972) A new way to predict capacity of piles in clay. In: *Proceedings of Offshore technology Conference*, pp 865–871
874. Stas CV, Kulhawy FH (1948) Critical evaluation of design methods for foundations under axial uplift and compression loading. Report EI-3771, Electric Power Research Institute, Palo CA
875. Lloyd G (200) Germanischer Lloyd rules and guidelines, IV industrial services, guideline for the certification of offshore wind turbines, Germanischer Lloyd wind energie GmbH, Hamburg, Germany
876. Toolan FE, Ims BW (1988) Impact of recent changes in the API recommended practice for offshore piles in sand and clays. In: *Oceanology international conference*
877. American Petroleum Institute (1987) Recommended practice for planning, designing and constructing fixed offshore platforms, API-RP 2A, 17th ed.
878. Kishida H, Uesugi M (1987) Tests of the interface between sand and steel in the simple shear apparatus. *Géotechnique* 37(1):45–52
879. Jardine RJ, Everton SJ, Lehane BM (1992) Friction coefficients for piles in cohesionless materials. In: *Offshore site investigations and foundation behaviour*. Dordrecht: Kluwer, pp 661–680
880. Kraft LM (1990) Computing axial pile capacity in sands for offshore conditions. *Marine Geotechnol* 9:61–92
881. Jardine RJ, Chow FC, Overy RF, Standing JR (2005) ICP design methods for driven piles in sands and clays. Telford, London
882. Kolk HJ, Baaijens AE, Senders M (2005) Design criteria for pipe piles in silica sands. In: *International symposium on frontiers in offshore geomechanics*, ISFOG, Taylor & Francis, London, pp 711–716
883. Lehane BM, Schneider JA, Xu X (2005) The UWA-05 method for prediction of axial capacity of driven piles in sand. In: *Proceedings of the international symposium on frontiers in offshore geotechnics (ISFOG)*, Perth, Australia, pp 683–689
884. Clausen CJF, Aas PM, Karlsrud K (2005) Bearing capacity of driven piles in sand, the NGL approach. In: *International symposium on frontiers in offshore geomechanics*, ISFOG, Taylor & Francis, London, pp 677–681
885. Tiwari B, Al-Adhath AR (2014) Influence of relative density on static soil-structure frictional resistance of dry and saturated sand. *Geotech Geol Eng* 32(2):411–427
886. Coduto DP, Kitch WA, Yeung MR (2015) *Foundation design: principles and practices*, 3rd ed. Prentice-Hall, Upper Saddle River, NJ, USA
887. Randolph MF, Dolwin J, Beck R (1994) Design of driven piles in sands. *Géotechnique* 44(3):427–448
888. Vijayvergiya VN (1977) Load movement characteristics of piles, *Ports 77 conference*, Long Beach, California
889. Emami Azadi MR (1998) Static and dynamic analysis of pile-soil-jacket-behavior. PhD thesis, Norwegian University of Science and Technology, Trondheim, Norway
890. King GJW, Dickin EA, Lyndon A, Wei MJ (2000) The influence of rate of loading on the behavior of continuous-flight-auger bored piles in soft clay. *Geotech Geol Eng J* 18:139–153
891. Ph Begemann HKS (1965) The maximum pulling force of a single tension pile calculated on the basis of results of the adhesion jacket cone. In: *Proceedings 6th international conference on soil mechanics and foundation engineering*, vol 2, Balkema, Rotterdam, pp 229–233
892. Skempton AW (1959) Cast insitu bored piles in London Clay. *Géotechnique* 9(4): 153–173

893. Kikuchi Y (2010) Mechanism of inner friction of an open-ended pile. In: Proceedings of the 3rd IPA international workshop (Press-in Engineering 2011), Shanghai, pp 65–83
894. Kumara JJ, Kikuchi Y, Kurashina T (2016) Effects of the lateral stress on the inner frictional resistance of pipe piles driven into sand. In: *Int J Geo-eng* 7(1)
895. Klos J, Tejchman A (1981) Bearing capacity calculation for pipe piles. In: Proceedings of 10th international conference on soil mechanics and foundation engineering, vol 2, Stockholm, pp 751–754
896. Paikowsky SG, Whitman RV (1990) The effect of plugging on pile performance and design. *Can Geotech J Ottawa Canada* 27:429–440
897. Henke S, Grabe J (2013) Field measurements regarding the influence of the installation method on soil plugging in tubular piles. *Acta Geotech* 8(3):335–352
898. Paik K, Salgado R (2003) Determination of bearing capacity of open-ended piles in sand. *J Geotech Geoenviron Eng ASCE* 129(1):46–57
899. Gudavalli SR, Safaqaq O, Seo H (2013) Effect of soil plugging on axial capacity of open-ended pipe piles in sands. In: Proceedings of the 18th international conference on soil mechanics and geotechnical engineering, Paris, pp 1487–1490
900. Paikowsky SG, Whitman RV (1990) The effects of plugging on pile performance and design. *Canada Geotech J* 27:429–440
901. Randolph MF, Leong EC, Houlsby GT (1991) One-dimensional analysis of soil plugs in pipe piles. *Géotechnique* 41(4):587–598
902. Paikowsky SG, Whitman RV, Baligh MM (1989) A new look at the phenomenon of offshore pile plugging. *Mar Geotechnol* 8:213–230
903. Yu F, Yang M (2012) Base capacity of open-ended steel pipe piles in sand. *Geotech Geoenviron Eng* 138(9):1116–1128
904. Tan Y, Lin G (2013) Full-scale testing of open-ended steel pipe piles in thick varved clayed silt deposits along the Delaware River in New Jersey. *J Geotech Geoenviron Eng* 139(3)
905. Randolph MF (2003) Science and empiricism in pile foundation design. *Géotechnique* 53(10):847–875
906. Schneider JA, Xiangtao Xu, Lehane BM (2007) Database assessment of CPT-based design methods for axial capacity of driven piles in siliceous sands. *J Geotech Geoenviron Eng* 134(9):1227–1244
907. Reese LC, Wang ST, Arrellaga JA, Vasquez LG (2014) *APILE 2014—user’s manual: a program for the study of driven piles under axial loads*, Austin
908. Briaud JL, Tucker LM (1988) Measured and predicted axial response of 98 pies. *J Geotech Eng* 114(9):984–1001
909. Jardine R, Chow F (1996) *New design methods for offshore piles*. Marine Technology Directorate, London
910. Lehane BM, Schneider JA, Xu X (2005) A review of design methods for offshore driven piles in siliceous sand. University of Western Australia Geomechanics Group, Report No. GEO: 05358, Sept 2005
911. Toolan FE, Lings ML, Mirza UA (1990) An appraisal of API RP2A recommendations for determining skin friction of piles in sand. In: 22nd offshore technology conference, OTC, Houston, OTC 6422, pp 33–42
912. Lehane BM, Jardine RJ, Bond AJ, Frank R (1993) Mechanisms of shaft friction in sand from instrumented pile tests. *J Geotech Eng* 119(1):19–35
913. White DJ, Lehane BM (2004) Friction fatigue on displacement piles in sand. *Géotechnique* 54(10):645–658
914. Chow FC (1997) *Investigations into the behaviour of displacement piles for offshore foundations*. PhD thesis, Imperial College, London
915. Lehane BM, Schneider JA, Xu X (2005) CPT based design of driven piles in sand for offshore structures, geo: 05354. The University of Western Australia

916. CUR Centre for Civil Engineering Research and Codes (2001) Bearing capacity of steel pipe piles, CUR, Gouda, CUR-Report, 2001-8
917. Lehane BM, Randolph MF (2002) Evaluation of a minimum base resistance for driven pipe piles in siliceous sand. *ASCE Journal Geotechnical and Geoenvironmental Engineering* 128(3):198–205
918. Xu X, Schneider JA, Lehane BM (2008) Cone penetration test (CPT) methods for end-bearing assessment of open- and closed-ended driven piles in siliceous sand. *Can Geotech J* 45(8):1130–1141
919. Fugro Engineers B.V. (2004) Axial pile capacity design method for offshore driven piles in sand. Fugro report P1003, No. 3. Aug 2004
920. Randolph M (2009) Mechanical behavior of soils under environmentally induced cyclic loads. Lecture at the International Centre for Mechanical Sciences (CISM), Udine, 8–12 Jun 2009
921. Richter T, Kirsch F (2010) Ein analytisch-empirischer Ansatz zur Bestimmung der Tragfähigkeit und der Verformungen von axial zyklisch belasteten Pfählen. Workshop Offshore-Gründungen von Windkraft-anlagen, Karlsruhe, 2010
922. Schwarz P (2002) Beitrag zum Tragverhalten von Verpresspfählen mit kleinem Durchmesser unter axialer uyklicher Belastung. Lehrstuhl und Prüfamt für Bodenmechanik und Felsmechanik der Technischen Universität München, Schriftenreihe Heft 33
923. Poulos HG (1988) *Marine geotechnics*. Unwin Hyman, London
924. Vickery BJ (1979) Wind effects on building and structures—critical unsolved problems. In: Symposium, Karlsruhe, Germany, pp 823–828
925. Barker RM, Puckett JA (1997) Design of highway bridges-based on AASHTO LRFD Bridge design specification. Wiley, New York, pp 1169
926. MW O'Neill (1964) Determination of the pile-head torque-twist relationship for a circular pile embedded in a clay soil. Master Thesis, University of Texas, Austin
927. Poulos HG (1975) Torsional response of piles. *J Geotech Eng ASCE*, GT10
928. Scott RF (1981) *Foundation analysis*. Prentice-Hall, Englewood Cliffs
929. Stoll UW (1972) Torque shear test of cylindrical friction piles. *Civ Eng Am Soc Civ Eng* 42:63–65
930. Chow YK (1985) Torsional response of piles in non-homogeneous soil. *J Geotech Eng Div ASCE* 111(7):942–947
931. NGI (1996) Documentation of computer program package for structure-pile-soil interaction analysis. Høvik, Norway
932. Kong LG (2006) Behavior of pile groups subjected to torsion. PhD Thesis, The Hong Kong University of Science and Technology, Hong Kong
933. Zhang LM, Kong LG (2006) Centrifuge modeling of torsional response of piles in sand. *Can Geotech J* 43(5):500–515
934. Kong LG, Zhang LM (2007) Centrifuge modelling of torsionally loaded pile groups. *J Geotech Geoenviron Eng ASCE* 133(11):1374–1384
935. Kong LG, Zhang LM (2008) Experimental study of interaction and coupling effects in pile groups subjected to torsion. *Can Geotech J* 45:1006–1017
936. Maiorano RMS, deSanctis L, Aversa S, Mandolini A (2009) Kinematic response analysis of piled foundations under seismic excitation. *Can Geotech J* 46:571–584
937. Castelli F, Maugeri M (2009) Simplified approach for the seismic response of a pile foundation. *J Geotech Geoenviron Eng* 135:1440–1451
938. Dezi F, Carbonari S, Leoni G (2010) Kinematic bending moments in pile foundations. *Soil Dyn Earthq Eng* 30:119–132
939. Laora RD, Mandolini A, Mylonakis G (2012) Insight on kinematic bending of flexible piles in layered soil. *Soil Dyn Earthq Eng* 43:309–322
940. Liyanapathirana DS, Poulos HG (2005) Pseudo-static approach for seismic analysis of piles in liquefying soil. *J Geotech Geoenviron Eng ASCE* 131:1480–1487

941. Japanese Road Association (1996) Part V specification for highway bridges: seismic design. Japanese Road Association
942. Japanese Road Association (2002) Part V. Design specifications for highway bridges: seismic design
943. Kawashima K, Unjoh S (2004) Seismic design of highway bridges. *J Jpn Assoc Earthq Eng* 4(3):174–83
944. Reddy AS, Valsangkar AJ (1970) Buckling of fully and partially embedded piles. *J Soil Mech Found Div ASCE* 96(SM6):1951–1965
945. Yang JX, Mcmanus KJ, Berrill JB (2000) Kinematic Soil-micropile Interaction. In: 12th world conference on earthquake engineering, Auckland, New Zealand
946. Gazetas G (1984) Seismic response of end-bearing single piles. *Soil Dyn Earthq Eng* 3 (2):82–93
947. Wu L, Jiang X (2011) Regulation analysis of pile-soil seismic response based on structure-pile-soil shaking table test. *Eng Mech* 28(Sup.1):201–210
948. Tajimi H (1977) Seismic effects on piles. State-of-the-Art Report No. 2. international conference of soil mechanics foundation engineering, Precision Specialty Session 10, pp 15–26
949. Ohta T, Uchiyama S, Niwa M, Ueno K (1980) Earthquake response characteristics of structure with pile foundation on soft subsoil layer and its simulation analysis. In: Proceedings of 7th world conference on earthquake engineering, Istanbul, pp 467–470
950. Mylonakis G (2001) Simplified model for seismic pile bending at soil layer interfaces. *Soils Found Jpn Geotech Soc* 41(4):47–58
951. Kavvadas M, Gazetas G (1993) Kinematic seismic response and bending of free-head piles in layered soil. *Géotechnique* 43(2):207–222
952. Dobry R, O'Rourke MJ (1983) Discussion—seismic response of end bearing piles. *J Geotech Eng* 109(5):778–781
953. Mylonakis G, Nikolaou S (2002) Design method for earthquake-induced pile bending. In: DFI conference
954. Mylonakis G (1999) Seismic pile bending at deep interfaces. Report GEL-99-01, Geotechnical Laboratory, City College of New York, 1999
955. Margason E (1975) Pile bending during earthquakes. Lecture, ASCE/UC-Berkeley seminar on design construction & performance of deep foundations, 6 Mar 1975
956. Margason E, Holloway DM (1977) Pile bending during earthquakes. In: Proceedings of 6th world conference on earthquake engineering, Sarita Prakashan, India, II, pp 1690–1696
957. NEHRP (1997) Recommended provisions for seismic regulations for new buildings and other structures. Building Seismic Safety Council, Washington
958. Nikolaou A, Mylonakis G, Gazetas G (1995) Kinematic bending moments in seismically stressed piles, NCEER-95-0022. National Center for Earthquake Engineering Research, Buffalo, NY
959. Makris N, Gazetas G (1992) Dynamic pile-soil-pile interaction, part II: lateral and seismic response. *Earthq Eng Struct Dyn* 21(2):145–162
960. Mineiro AJC (1990) Simplified procedure for evaluating earthquake loading on piles, Lisbon
961. Sheppard DA (1983) Seismic design of concrete piling. PCI J
962. Nikolaou S, Mylonakis G, Gazetas G, Tazoh T (2001) Kinematic pile bending during earthquakes: analysis and field measurements. *Géotechnique* 51(5):425–440
963. Mylonakis G (2001) Simplified model for seismic pile bending at soil layer interfaces. *Soils and Found* 41(4):47–58
964. Cairo R, Conte E, Dente G, Sica S (2009) Armando Lucio Simonelli, Soil-pile kinematic interaction: new perspectives for EC8 improvement. In: Cosenza E (ed) Eurocode 8 perspectives from the Italian standpoint workshop. Italy, Napoli

965. Bea R (1998) Continued development of earthquake load and resistance. Report 2, Seismic Hazard Characterizations, University of California at Berkeley, May 1998
966. Gazetas G, Fan K, Tazoh T, Shimizu K (1993) Seismic response of the pile foundation of Ohba-Ohashi Bridge. In: Proceedings 3rd international conference on case histories in geotechnical engineering, vol 3, St. Louis, pp 1803–1809
967. Berger E, Mahin SA, Pyke R (1977) Simplified method for evaluating soil–pile–structure interaction effects. In: Proceedings of the 9th offshore technology conference, offshore technology conference, paper 2954, Houston, pp 589–598
968. Gazetas G, Dobry R (1984) Simple radiation damping model for piles and footings. *J Eng Mech ASCE* 110:937–956
969. Zhu B, Zhu R, Luo J, Chen R, Kong L (2010) Model tests on characteristics of ocean and offshore elevated piles with large lateral deflection. *Chin J Geotech Eng* 32(4):521–530
970. Ghazzaly OI, Hwong ST (1976) Approximate analysis of a pile under dynamic lateral loading. *Comput Struct* 6:363–368
971. Gazetas G, Fan K, Kaynia A (1993) Dynamic response of pile groups with different configurations. *Soil Dyn Earthq Eng* 12(4):239–257
972. Po Lam I (2013) Diameter effects on p - y curves in deep marine foundations—a perspective on the design and construction of deep marine foundations. In: Bittner RB, Jr Ellman RA (eds) *Deep Foundation Institute*, Hawthorne, NJ
973. Chen JY, Litton R, Albert K, Fraser R, Jeanjean P (2016) Seismic soil-structure interaction design considerations for offshore platforms. OMAE, Busan
974. Rudolph D, Bos KJ, Luijendijk AP, Rietema K (2004) JMM out, scour around offshore structures, analysis of field measurements. In: 2nd international conference on scour erosion, vol 1, Meritus Mandarin, Singapore, pp 400–407
975. RJS Whitehouse (2006) Scour at coastal structures (invited lecture). In: Proceedings of 3rd international conference on scour and erosion, Gouda, Netherlands, pp 52–59
976. Jiang J, Ganju NK, Mehta AJ (2004) Estimation of contraction scour in riverbed using SERF. *J Waterway Port Coastal Ocean Eng* 130:215–218
977. Harris JM, RJS Whitehouse (2015) Scour prediction in non-uniform soils: undrained shear strength and erodibility. In: Cheng, Draper, An (eds) *Scour and erosion*. Taylor & Francis Group, London
978. Nortek RA, RJS Whitehouse (2012) The power of scour. *Oilfield Technology*, Aug 2012
979. Diamantidis D, Arnesen K (1986) Scour effects in piled structures—a sensitivity analysis. *Ocean Eng* 13:497–502
980. Li Y, Chen X, Fan S, Briaud JL, Chen HC (2009) Is scour important for pile foundation design in deepwater? In: Offshore technology conference (OTC), Houston, Texas, USA, 4–7 May 2009
981. Zaaijer MB (2002) Design methods for offshore wind turbines at exposed sites—sensitivity analysis for foundations of offshore wind turbines. Delft University of Technology
982. Zaaijer MB (2002) Foundation models for the dynamic response of offshore wind turbines. In: Proceedings of MAREC, Newcastle
983. <http://www.fino-offshore.de>
984. Forschungs- und Entwicklungszentrum, Fachhochschule Kiel GmbH, Scour, 2014
985. Melville BW, Coleman SE (2000) *Bridge scour*. Water Resources Publications, Highlands Ranch
986. Achmus M, Kuo YS, Abdel-Rahman K (2010) Numerical investigation of scour effect on lateral resistance of windfarm monopiles. In: Proceedings of the twentieth international offshore and polar engineering conference, Beijing, pp 619–623
987. Lagasse PF, Richardson EV, Schall JD, Price GR (1997) Instrumentation for measuring scour at bridge piers and abutments. NCHRP Report 396, Transportation Research Board
988. DHI (2012) Predicting scour in offshore wind turbine—now a breeze. DHI Water and Environment

989. Stroescu IE, Frigaard P, Fejerskov M (2016) Scour development around bucket foundation. *Int J Offshore Polar Eng* 26(1):57–64
990. Rouse H (1965) *Engineering hydraulics: sediment transportation*. Wiley, New York
991. Gill MA (1972) Erosion of sand beds around spur-dikes. *J Hydraul Div Am Soc Civ Eng* 98:1587–1602
992. Kohli A, Hager WH (2001) Building scour in floodplains. *Water Maritime Eng Inst Civ Eng London* 148:61–80
993. Coleman SE, Lauchlan CS, Melville BW (2003) Clear-water scour development at bridge abutments. *J Hydraul Res* 41(5):521–531
994. Anderson AG (1963) Sediment transportation mechanics: erosion of sediment. *J Hydraul Div Am Soc Civ Eng* 89:237–248
995. Breusers HNC (1963) Discussion of ‘sediment transportation mechanics: erosion of sediment’, by task force on preparation of sedimentation manual. *J Hydraul Div Am Soc Civ Eng* 89:277–281
996. HNC Breusers (1967) Time scale of two-dimensional local scour. In: 12th Congress IAHR, vol 3, pp 275–282
997. Laursen EM (1952) Observation on the nature of scour. In: Proceedings 5th hydraulics conference, pp 179–197
998. Carstens MR (1966) Similarity laws for localized scour. *J Hydraul Div Am Soc Civ Eng* 92:13–36
999. Franzetti S, Larcán E, Mignosa P (1982) Influence of the test duration on the evaluation of ultimate scour around circular piers. In: International conference hydraulics and modeling of civil structures, Coventry, England, pp 381–396
1000. Patrick A (2006) Time development of local scour at a bridge pier fitted with a collar. University of Saskatchewan
1001. Zhai Y (2010) Time-dependent scour depth under bridge-submerged flow. University of Nebraska—Lincoln
1002. Shen HW, Schneider VR, Karaki SS (1969) Local scour around bridge piers. *J Hydraulics Div ASCE* 96 (HY6):1919–1940
1003. Briaud JL, Ting F, Chen HC, Cao Y, Han SW, Kwak KW (2001) Erosion function apparatus for scour rate predictions. *J Geotech Geoenviron Eng ASCE* 127(2):105–113
1004. Briaud JL, Ting CK, Chen HC, Gudavalli R, Perugu S, Wei G (1999) SRICOS: prediction of scour rate in cohesive soils at bridge piers. *J Geotech Geoenviron Eng ASCE* 125 (4):237–246
1005. Ting FCK, Briaud JL, Chen HC, Gudavalli R, Perugu S (2001) Flume tests for scour in clay at circular piers. *J Hydraul Eng* 127(11):969–978
1006. Rambabu M, Narasimha RS, Sundar V (2003) Current-induced scour around a vertical pile in cohesive soil. *Ocean Eng* 30:893–920
1007. Nakagawa H, Suzuki K (1976) Local scour around bridge pier in tidal currents. *Coastal Eng Jpn* 19:89–100
1008. Sumer BM, Fredsøe J (2002) *The mechanics of scour in the marine environment*. World Scientific Publishing Co. Pte. Ltd., Singapore. ISBN 981-02-4930-6
1009. Sumer BM, Fredsøe J (2001) Scour around pile in combined waves and current. *J Hydraul Eng* 127(5):403–411
1010. Ansari SA, Qadar A (1994) Ultimate depth of scour around bridge piers. In: Proceedings of the ASCE national conference on hydraulic engineering, vol 1, Buffalo, USA, pp 51–55
1011. Dahlberg P (1983) Observations of scour around offshore structures. *Can Geotech J* 20:619–628
1012. Boon JH, Sutherland J, Whitehouse R, Soulsby R, Stam CJM, Verhoeven K, Hogedal M, Hald T (2004) Scour behavior and scour protection for monopile foundations of offshore wind turbines. In: European wind energy conference and exhibition, London

1013. Nielsen AW, Hansen EA(2007) Time-varying wave and current-induced scour around offshore wind turbines. In: Proceedings of the 26th international conference on offshore mechanics and arctic engineering, vol 5, pp 399–408
1014. Roulund A, Sumer BM, Fredsøe J, Michelsen J (2005) Numerical and experimental investigation of flow and scour around a circular pile. *J Fluid Mech* 534:351–401
1015. Whitehouse RJS, Sutherland J, O'Brien D (2006) Seabed scour assessment for offshore wind farm. In: Proceeding of 3rd international conference on scour and erosion, Amsterdam, pp 245–246
1016. Salim M, Sterling Jones J (1996) Scour around exposed pile foundation. American Society of Civil Engineers, North American Water and Environment Congress, June
1017. Mutlu Sumer B, Bundgaard K, Fredsøe J (2005) Global and local scour at pile groups. *Int J Offshore Polar Eng* 15(3):204–209
1018. Dong Y, Frangopol DM, Saydam D (2013) Time-variant sustainability assessment of seismically vulnerable bridges subjected to multiple hazards. *Earthq Eng Struct Dyn* 42(10):1451–1467
1019. Alipour A, Shafei B, Shinozuka M (2013) Reliability-based calibration of load and resistance factors for design of rc bridges under multiple extreme events: scour and earthquake. *ASCE J Bridge Eng* 18(5):362–371
1020. Wang Z, Padgett JE, Dueñas-Osorio L (2014) Influence of scour effects on the seismic response of reinforced concrete bridges. *Eng Struct* 76:202–214
1021. Wang Z, Padgett JE, Dueñas-Osorio L (2014) Risk-consistent calibration of load factors for the design of reinforced concrete bridges under the combined effects of earthquake and scour hazards. *Eng Struct* 79:86–95
1022. Guo X (2014) Seismic vulnerability analysis of scoured bridge systems. PhD dissertation of University of Missouri-Kansas City
1023. Whitehouse RJS (1998) Scour at marine structures: a manual for practical applications. Thomas Telford Publishing, London
1024. Ettema R, Melville B, Barkdoll B (2001) Scale effect in pier-scour experiments. *J Hydraul Eng* 124(6):639–642
1025. Lim SY, Cheng NS (1998) Prediction of live-bed scour at bridge abutments. *J Hydraul Eng* 124:635–642
1026. Melville B, Sutherland AJ (1988) Design method for local scour at bridge piers. *J Hydraul Eng* 114(10):1210–1226
1027. Melville B (1997) Pier and abutment scour: integrated approach. *J Hydraul Eng* 123:125–136
1028. Mia F, Nago H (2003) Design method of time dependent local scour at circular bridge pier. *J Hydraul Eng* 129(6):420–427
1029. Parola AC, Mahavadi SK, Brown BM, Elkhoury A (1996) Effect of rectangular foundation geometry on local pier scour. *J Hydraul Eng* 122:35–40
1030. API (2000) Errata and Supplement 3, API Recommended Practice 2A-WSD. Recommended practice for planning, designing and constructing fixed offshore platforms—working stress design, 21st edn.
1031. Fugro, Final Report (1995) Foundation design—bridge piles. Jamuna Bridge, Bangladesh, Fugro Engineers BV Confidential Report No. K-2380/120 to HDEC
1032. Mindlin RD (1936) Force at a point in the interior of a semi-infinite solid. *J Appl Phys* 7(5):195–202
1033. Jardine RJ, Potts DM (1988) Hutton tension leg platform foundations, an approach to the prediction of pile behaviour. *Géotechnique* 38(2):231–252
1034. Jardine RJ, Potts DM (1993) Magnus foundations: soil properties and predictions of field behaviour. In: Conference on large scale pile tests in clay, Thomas Telford, London, pp 69–83
1035. Poulos HG, Davis EH (1980) Pile foundations analysis and design, vol 1080. Wiley, 397 pp

1036. Poulos HG (1968) Analysis of settlement of pile groups. *Géotechnique* 18:449–471
1037. Poulos HG (1979) Group factors for pile-deflection estimation. *J Geotech Eng Div ASCE* No. GT12:1489–1509
1038. Banerjee PK (1978) Analysis of axially and laterally loaded pile groups, *Developments. In: Mechanics Soil* (ed) CR Scott. Appl. Sci. Pub, London, pp 317–346
1039. Vesic AS (1969) Experiments with instrumented pile groups in sand. *ASTM Special Technical Publication, No. 444, Performance of Deep Foundations*, pp 172–222
1040. Moorhouse DC, Sheehan JV (1968) Predicting safe capacity of pile groups. *ASCE Civ Eng* 38(10):44–48
1041. Bowles JE (1996) *Foundation analysis and design*. McGraw-Hill, New York, NY
1042. Larkela A (2008) *Modeling of a pile group under static lateral loading*. Helsinki University of Technology
1043. Chaudhry AR (1994) *Static pile-soil-pile interaction in offshore pile groups*. PhD thesis, University of Oxford, Oxford
1044. Walsh JM (2005) *Full-scale lateral load tests of a 3×5 pile group in sand*. Master's thesis, Brigham Young University
1045. Bogard D, Matlock H (1983) *Procedures for analysis of laterally loaded pile groups*. In: *Proceedings of ASCE conference on geotechnical practice in offshore engineering*, Austin, Texas, pp 499–535
1046. Polous H, Davis E (1980) *Pile foundation analysis and design*. Wiley, NY
1047. Reese LC, van Impe WF (2010) *Single piles and pile groups under lateral loading*. 2nd edn. CRC Press
1048. Duncan J, Evans L (1994) Lateral load analysis of single piles and drilled shafts. *J Geotech Eng ASCE* 120(6):1018–1033
1049. Brown DA, Morrison C, Reese LC (1988) Lateral load behavior of pile group in sand. *J Geotech Eng ASCE* 114(11):1261–1276
1050. Focht JA, Koch JJ (1973) Rational analysis of lateral performance of offshore pile groups. In: *Proceedings of the offshore technology conference*, vol 2. Paper No. 1896, Houston
1051. Rollins KM, Olsen RJ, Egbert JJ, Olsen KG, Jensen DH, Garrett BH (2003) *Response analysis and design of pile groups subjected to static and dynamic lateral loads*. Report No. UT03.03, Utah, USA
1052. American Association of State Highway and Transportation Officials (2012) *AASHTO LRFD bridge. Design Specifications*
1053. FEMA P-751 (2012) *Foundation analysis and design, in NEHRP recommended provisions: design examples*. National Institute of Building Sciences, Building Seismic Safety Council, Washington, D.C., chapter 5
1054. Ruesta P, Townsend F (1997) Evaluation of laterally loaded pile group at Roosevelt bridge. *J Geotech Geoenviron Eng* 123(12):1153–1161
1055. Brown DA, Reese LC, O'Neill MW (1987) Cyclic lateral loading of a large-scale pile group. *J Geotech Eng ASCE* 113(11):1326–1343
1056. Meimon Y, Baguelin F, Jezequel JF (1986) Pile group behaviour under long time lateral monotonic and cyclic loading. In: *Proceedings of the 3rd international conference on numerical methods in offshore piling*, Inst. Francais du Petrole, Nantes, France, pp 285–302
1057. Mostafa YE, Naggat MHEI (2004) Response of fixed offshore platforms to wave and current loading including soil–structure interaction. *J Dyn Earthq Eng* 24(4):357–368
1058. Wolf JP, Meek JW (1994) Cone models for an embedded foundation. *J Geotech Eng ASCE* 120: 60–80
1059. Arslan HA, Wong PC (2014) Advanced continuum modeling of pile response to jack-up spudcan penetration. In: *Proceedings of the 24th International Ocean and polar engineering conference*, Busan, pp 506–513

1060. Xie Y, Leung CF, Chow YK (2006) Effects of spudcan penetration on adjacent pile. In: Proceedings of the 6th international conference on physical modeling in geotechnics, Hong Kong, pp 701–706
1061. Xie Y, Leung CF, Chow YK (2011) Soil movements and pile responses during spudcan penetration. In: Proceedings of 13th international conference jack-up platform design, construction and operation, London, UK, 2011
1062. Poulos HG (2005) The influence of construction “side effects” on existing pile foundations. In: Proceedings of the institution of civil engineers. Geotechnical engineering, vol 36, pp 51–67
1063. Loganathan N (2009) An innovative method for assessing tunneling-induced risks to adjacent structures. William Barclay Parsons Fellowship Monograph 25, Parsons Brinckerhoff Inc., New York
1064. Xu KJ, Poulos HG (2001) 3-D elastic analysis of vertical pile subjected to “passive” loadings. *Comput Geotech* 28:349–375
1065. Loganathan N, Poulos HG, Xu KJ (2001) Ground and pile-group responses due to tunneling. *Soils Found* 41(1):57–67
1066. Kitiyodom P, Matsumoto T, Kawaguchi K (2006) Analyses of pile foundations subjected to ground movements induced by tunneling. In: Proceedings of 5th international symposium geotechnical aspects of underground construction in soft ground, Amsterdam, Taylor & Francis, London, UK
1067. Sørensen EV (2009) Personal interview with the Associate Professor M.Sc. Ph.D. Eigil V. Sørensen from Department of Civil Engineering, Aalborg University, DK, 10th of February, 2009
1068. Norsok N-004 (2013) Design of steel structures
1069. Schaumann P, Wilke F (2007) Design of large diameter hybrid connections grouted with high performance concrete. In: ISOPE 2007—proceedings of the 17th international offshore and polar engineering conference, Lisboa
1070. Ducorit (2015) Data sheet, Ducorit D—ultra high performance grout
1071. Chen WF, Duan L (2003) Deep bridge engineering, volume 2: substructure design. CRC Press, Boca Raton
1072. Moore MA (2005) Raked piles, battered and misunderstood, structure magazine, December, pp 49–53
1073. Association Française de Génie Parasismique (AFPS) (1990) Recommandations AFPS 90. Presses des Ponts et Chaussées, Paris
1074. NTC2008 (2008) Technical rules for constructions
1075. International Code Council (2015) International building code. Washington
1076. Mitchell D, Tinawi R, Sexsmith RG (1991) Performance of bridges in the 1989 Loma Prieta earthquake—lessons for Canadian designers. *Can J Civ Eng* 18(4):711–734
1077. Priestley N, Singh J, Youd T, Rollins K (1991) Costa Rica earthquake of April 22, 1991: reconnaissance report. *Earthq Eng Res Inst Publ* 91–02:59–91
1078. Gerolymos N, Giannakou A, Anastasopoulos I, Gazetas G (2008) Evidence of beneficial role of inclined piles: observations and summary of numerical analyses. *Bull Earthq Eng* 6(4):705–722
1079. Giannakou A, Gerolymos N, Gazetas G, Tazoh T, Anastasopoulos I (2010) Seismic behavior of batter piles: elastic response. *J Geotech Geoenviron Eng* 136:1187–1199
1080. Gazetas G, Mylonakis G (1998) Seismic soil–structure interaction: new evidence and emerging issues. *Soil Dyn III Am Soc Civ Eng (ASCE) Specialty Geotech Conf Seattle* 2:1119–1174
1081. Lam I, Martin GR (1986) Seismic design of highway bridge foundations, vol. II: design procedures and guidelines. No. FHWA/RD-86/102, Federal highway Administration, Virginia
1082. Berrill JB, Christensen RJ, Keenan RJ, Okada W, Pettinga JR (2001) Case study of lateral spreading forces on a piled foundation. *Géotechnique* 51(6):501–517

1083. Guin J (1997) Advances in soil–pile–structure interaction and non-linear pile behaviour. PhD thesis, State University of New York at Buffalo
1084. Sadek M, Shahrour I (2004) Three-dimensional finite element analysis of the seismic behavior of inclined micropiles. *Soil Dyn Earthq Eng* 4(6):473–85
1085. Medina C, Padrón LA, Aznárez JJ, Santana A, Maeso O (2014) Kinematic interaction factors of deep foundations with inclined piles. *Earthq Eng Struct Dyn* 43(13):2035–2050
1086. Medina C, Padrón LA, Aznárez JJ, Maeso O (2015) Influence of pile inclination angle on the dynamic properties and seismic response of piled structures. *Soil Soil Dyn Earthq Eng* 69:196–206
1087. Kavazanjian E (2006) A driven-pile advantage: batter piles. *Piledriver* 4:21–25
1088. Poulos HG (2006) Raked piles—virtues and drawbacks. *J Geotech Geoenviron Eng ASCE* 132(6):795–803
1089. Lu Z (2010) Study on key technologies employed in planning and construction of shanghai donghai bridge offshore wind farm. *Eng Sci* 12(11):19–24 (in Chinese)
1090. Zhu B, Jiang Y, Chen R, Chen Y (2011) Investigation on pile group foundations for offshore wind turbines. *Chin J Geotech Eng* 33(Supp. 01):91–91 (in Chinese)
1091. Hannigan PJ, Goble GG, Thendean G, Likins GE, Rausche F (2005) Design and construction of driven pile foundations, Vol. I and II. Federal Highway Administration Report No. FHWA-HI-05. Federal Highway Administration, Washington, DC
1092. Poulos HG (1997) Piles subjected to negative friction. *A Procedure Des* 28(1):23–44
1093. Fellenius BH (1997) Discussion: piles subjected to negative friction. *A Procedure Des* 28(2):277–281
1094. Haryono IS (2013) Pile foundation and soil response to deep excavation. Technische Universiteit Delft, Delft
1095. Bjerrum L, Johannessen JJ, Eide O (1969) Reduction of skin friction on steel piles to rock. *Proc 7th Int Conf Mech Found Eng* 2:27–34
1096. Bjerin L (1977) Dragloads on long concrete piles. Swedish Geotechnical Institute Report, No.2, pp 62
1097. Garlanger JE (1974) Measurement of pile downdrag Beneath a bridge abutment. *Highway Res Board Trans Res Rec* 517:61–69
1098. Leung CF, Liao BK, Chow YK, Shen RF, Kog YC (2004) Behaviour of pile subject to negative skin friction and axial load. *Soils Found* 44(6):17–26
1099. Buildings Department (2004) The Government of Hong Kong Special Administrative Region, Code of Practice for Foundations
1100. Kim BM (2005) Upper bound analysis for drag anchors in soft clay. PhD thesis, Texas A&M University, Dec 2005
1101. DNV-GL, DNV-RP-E301 (2012) Design and Installation of Fluke Anchors, Høvik
1102. Vivatrat V, Valent PJ, Ponterio AA (1982) The influence of chain friction on anchor pile design, OTC 4178. In: Proceedings of the 14th annual offshore technology conference, Houston, pp 153–156
1103. American Petroleum Institute (API) (2008) API recommended practice 2SK, design and analysis of stationkeeping systems for floating structures
1104. ISO 19901-7 (2013) Stationkeeping systems for floating offshore structures and mobile offshore units
1105. Statoil (2012) Technical and professional requirement, TR3050, platform technology, technical requirements and standards
1106. NORSOK N-001 (2012) Integrity of offshore structures, ed. 8, Lysaker, Norway
1107. DNV, DNVGL-RP-0005 (2014) Fatigue design of offshore steel structures
1108. Doerk O, Fricke W, Weissenborn C (2003) Comparison of different calculation methods for structural stresses at welded joints. *Int J Fatigue* 25(5):359–369
1109. Fricke W, Kahl A (2005) Comparison of different structural stress approaches for fatigue assessment of welded ship structures. *Marine Struct* 18:473–488

1110. Hobbacher A (2008) Recommendations for fatigue design of welded joints and components, IIW document IIW-1823-07 ex XIII-2151r4-07/XV-1254r4-07. International Institute of Welding
1111. Morrison MJ, Clukey EC, Garnier J (1994) Behavior of suction caissons under static uplift loading. Proc Int Conf Centrifuge 94:823–828 Singapore
1112. Kwag D, Ryu M, Kwon O, Bang S (2014) Design and installation of meteorological towers with tripod suction piles for offshore wind farms. In: Proceedings of the 24th international ocean and polar engineering conference, Busan, pp 484–491
1113. Mackereth FJH (1958) A portable core sampler for lake deposits. *Limnol Oceanogr* 3:181–191
1114. Clausen CJF, DiBiagio E, Duncan JM, Andersen KH (1975) Observed behavior of the Ekofisk oil storage tank foundation. In: Proceedings of the 7th annual offshore technology conference, Houston
1115. Bang S (1998) Use of suction piles for mooring of mobile offshore bases. South Dakota School of Mines and Technology, Rapid City, SD
1116. Sparrevik P (2002) Suction pile technology and installation in deep waters, OTC 14241. In: Offshore technology conference, Houston
1117. Dendani H (2003) Suction anchors: some critical aspects for their design and installation in clayey soils. In: Paper No. 15376, offshore technology conference
1118. Fakharian K, Iraj A (2010) Numerical modeling of suction pile installation in Caspian Sea clay with effective and total stress analyses. *Int J Offshore Polar Eng* 20(4):1–8
1119. Maniar DR, Tassoulas L (2003) Simulation of suction caisson behavior during and after installation in normally consolidated soil. In: Proceedings of the 16th ASCE engineering mechanics conference, University of Washington, Seattle
1120. Fakharian K, Soltanmohammadlou A (2005) Some design guidelines for suction pile installation under self-weight and suction in Caspian Sea. In: Proceedings of the 15th international offshore and polar engineering conference, Seoul, ISOPE, vol 2, pp 366–370
1121. Murff JD, Aubeny C, Randolph MF, Supachawarote C, Sharma P, Jostad HP, Clukey EC, Andersen KH, Erbrich CT, Hansen B (2005) Suction anchors for deepwater applications. In: Proceedings of the international symposium on frontiers in offshore geotechnics (IS-FOG 2005), Perth, Australia, Taylor & Francis, London
1122. Al-Khafaji ZA, Audibert JME, Hossain MK, Templeton JC, Clukey EC, de Jong PR (2003) Suction Caisson foundation design for vortex-induced vibration loading. In: Paper No. 15239, offshore technology conference
1123. Aubeny CP, Murff JD (2003) Simplified limit solutions for undrained capacity of suction anchors. In: International symposium. Deepwater Mooring Systems, ASCE
1124. Maniar DR, Vasquez LFG, Tassoulas JL (2005) Suction Caisson: finite element modeling. In: Proceedings of 5th GRACM international congress on computational mechanics, Limassol
1125. Cao J, Audibert JME, Tjok KM, Hossain MK (2005) Validation of the use of finite element method for suction Caisson design. In: Proceedings of international conference on frontiers in offshore geotechnics, Taylor and Francis, pp 333–339
1126. Zdravkovic L, Potts DM (2005) Parametric finite element analyses of suction anchors. In: International conference on frontiers in offshore geotechnics, Taylor and Francis, pp 297–302
1127. Sharif Ahmed S, Chandra Hawlader B (2014) Finite element modeling of inclined load capacity of suction Caisson in sand with abaqus/explicit. Proceedings of the 24th international ocean and polar engineering conference, Busan
1128. Senders M (2001) Contribution to workshop: design methodologies and criteria for suction Caissons for deepwater mooring applications. Houston
1129. Zdravkovic L, Potts DM, Jardine RJ (2001) A parametric study of pull-out capacity of bucket foundations in soft clay. *Géotechnique* 51(1):55–67

1130. Hesar M, Geotechnical design of the barracude and caratinga suction anchors. In: Paper No. 15137, offshore technology conference
1131. Houlsby GT, Byrne BW (2005) Design procedures for suction caissons in clay and other materials. *Geotech Eng* 158(2):75–82
1132. Cotter O (2010) Installation of suction caisson foundations for offshore renewable energy structures. PhD thesis, Oxford University
1133. El-Gharbawy SL (1998) The pullout capacity of suction caisson foundations for tension leg platforms. PhD thesis, University of Texas, Austin
1134. Johansson P, Aas PM, Hansen SB (2003) Field model tests for a novel suction anchor application. In: Myrvoll F (ed) *Field measurements in geomechanics, proceedings of the 6th international symposium*, Taylor & Francis, Oslo, Norway, 23–26 Sept 2003, pp 145–153
1135. Røsjo B, Hauge K (2011) Proof: monster waves are real. *Sci Nordic*
1136. Inge Tjelta T (2001) Suction piles: their position and application today. In: *Proceedings of the 11th international offshore and polar engineering conference*, Stavanger
1137. Suction caisson (2014) Wikipedia
1138. Sparrevik P (1996) Suction anchor piles—state of the art. In: *Proceedings, mooring and anchoring conference*, Aberdeen
1139. Tveitnes I, Johan Lindaas O, Gramnaes J (2003) Subsea structure installation on Snøhvit field using a new construction vessel. In: *Deep offshore technology conference*, Marseilles, France
1140. Varun AD, Gazetas G (2009) A simplified model for lateral response of large diameter caisson foundations—I linear elastic formulation. *Soil Dyn Earthq Eng* 1(29):268–291
1141. Brandt M (2014) Earthquake analysis of Subsea structure on caisson foundation using 3D finite element solutions. Mater thesis, Norwegian University of Science and Technology
1142. Parker EJ, Ardoino F, Bughi S (2012) Seismic performance of suction pile foundations—practical solutions. In: *Proceedings of the 22nd international offshore and polar engineering conference*, Rhodes, Greece
1143. Shin Y, Langford T, Cho K, Park J (2014) Design of composite pile foundations for offshore wind turbines. In: *Proceedings of the 24th international ocean and polar engineering conference*, Busan, pp 211–217
1144. BBC (2008) Steven duff remembering disaster piper alpha. BBC News. In: 6th of June 2008
1145. Sørli E (2013) Bearing capacity failure envelope of suction caissons subjected to combined loading. Department of Civil and Transport Engineering, Norwegian University of Science and Technology, June 2013

Index

A

Accidental limit state, 56
Active source, 192–194
Active zone, 417
Activity rate parameter, 370
Actuator, 24
Added mass coefficient, 303
Added soil mass, 439, 440
Adhesion factor, 532, 563, 644–646
Adjacent structures, 55, 78, 619, 620, 623
Ageing, 52
Aggravation factor, 148
Aleatory uncertainties, 368
Aliasing, 322
Alignment, 455
Allowable stress design, 395, 648
Alluvium, 34, 149, 344, 346
A-method, 461, 532, 535, 540, 639
Anchor handler tug, 656
Anchor pile, 560, 642, 646–649, 656, 658
Angle of loading, 502, 608, 614, 616
Angle of shear resistance, 430 *See also*
 effective friction angle, angle of internal
 friction
Angle of shear resistance, 18
Angles of incidence, 188, 198
Anisotropic consolidation condition, 228
Anisotropic stress condition, 193
Annual frequency of exceedance, *see* Average
 recurrence rate
Annual probability of exceedance, 375–378,
 381, 396, 397, 405
Annual probability of occurrence, 57, 372
Annual rate of exceedance, *see* Average
 recurrence rate
API method, 507, 511, 538, 546, 548, 552–554
Apparent fixity length, 476, 477, 595
Area source, 370, 373
Arias intensity, 264, 265

Artificial accelerogram, 168, 357
Artificial boundary restrains, 188, 219
Artificial island, 269, 270
Atmosphere pressure, 83, 95
Atmospheric pressure, 33, 85, 96, 241, 244,
 248, 547
Attenuation relationship, 110, 175, 365, 374,
 375, 392, 408
Atterberg limit, 23, 421, 463, 464
Average rate of annual occurrence, *see*
 Average recurrence rate
Average recurrence rate, 378
a/v ratio, 123
Axial capacity, 72, 465, 521, 525, 526, 529,
 546, 553, 555, 558, 601, 605, 607, 615,
 629, 647

B

Backbone curve, 45, 79, 80, 95, 98–100, 143
Ballast, 215, 281, 658
Ballasting of piles, 480
Barcelona Basic Model, 6
Baseline-corrected time series, 360, 361
Baseline-correction, 358–361
Baseline-offset, 359
Base shear, 335, 353, 354, 474, 475, 507
Basins, 114, 121, 146, 149, 154–156, 162
Batter, 629, 631–633
Battered piles, *see* Inclined piles
Bearing area, 461, 645
Bearing capacity factor, 422, 426, 427, 537,
 645, 646
Bearing capacity factor, 422, 537, 541, 645,
 646
Becker penetration test, 42
Bedrock, 5, 102, 110–113, 115–117, 119, 121,
 126–132, 134–144, 149, 151, 157,
 159–163, 167–169, 174, 179, 180, 237,
 350, 365, 384, 393, 470, 582, 584, 663

- Bedrock motion, 113, 174
 Belled footing, 480
 Bending moment, 283, 477, 483–487, 569, 571, 572, 574, 584, 620, 622, 630–632, 635, 660, 661
 Bending rigidity, 477
 Bending stiffness, 475, 478, 479, 482
 Best estimate, 58, 72, 131, 168, 174
 B-method, 461, 534–536, 538, 541, 639
 Blind zones, 200
 Body wave, 125, 154, 565
 Borgman's linearization, 304
 Boundary conditions, 213, 221, 255, 482, 570, 661
 B-parameter, 534
 Bridge abutments, 302, 589, 591, 630
 Buckling, 56, 234, 465, 466, 553
 Buried anchor line, 644
 Burland-Bjerrum coefficient, *see* β -parameter
- C**
- Caissons, 182, 455, 576, 594, 655, 656, 664–667
 Cam-Clay, 104
 Cam-Clay model, 104
 Cantilever footing, 414
 Capillary effect, 8
 Capillary rise, 8
 Catenary mooring system, 641, 643
 Caughey damping, 102, 103
 Cavities, 494
 Central safety factor, 70
 Central unbiased estimates, 72
 Centrifuge test, 223, 225
 Chain, 559, 642–646, 650, 651
 Characteristic value, 57, 70–72
 Chlorite, 4
 Clay, 3–5, 8, 10–12, 17–20, 22–24, 31, 34, 43–48, 51–53, 57, 74–76, 81, 82, 84, 90, 105–107, 132, 141, 142, 209, 224, 230, 236, 251, 420, 426, 429, 431, 483, 485, 486, 489–495, 501, 503, 504, 507, 508, 512, 513, 515, 516, 521, 522, 526, 527, 529, 532, 533, 539, 541, 544, 545, 549, 551, 557, 561, 563, 590, 609, 614, 633, 637, 639, 658, 659, 662, 664, 665, 667
 Closed-ended pile, 543
 Close-form solution, 332
 Coherent deep-seated slumps, 264
 Cohesion intercept, 18, 20, 534
 Cohesionless soil, 17, 21, 34, 105, 421, 598
 Cohesive force, 3
 Cohesive resistance, 11, 17, 18
 Cohesive shear strength, 422
 Cohesive soil, 3, 4, 11, 18, 21, 29, 31, 34, 230, 529, 531, 598, 643
 Combined footing, 413–415
 Common depth point, 196
 Common depth point pattern, 195
 Common offset, 195, 196
 Complementary solution, 289, 290
 Completely dry soils, 6
 Compliant piled tower, 269, 270
 CONDEEP, 272
 Conditionally stable, 145
 Conditional mean spectrum, 173, 384, 400
 Conditioning stage, 26
 Cone boundary, 188
 Cone penetration test, 17, 24, 36, 84, 207
 Cone resistance, 17, 36, 37, 84, 85
 Cone tip resistance, 542, 546–548, 552
 Confidence level, 69, 72
 Confining pressure, 17, 19, 26, 27, 32, 44, 91–96, 215, 224, 228, 529
 Consistent boundaries., 188
 Consolidated–Drained (CD) test, 28, 304, 348
 Consolidated state condition, 104
 Consolidated–Undrained (CU) test, 28, 29
 Consolidation, 9, 27–29, 46–53, 72, 74, 83, 227, 229, 233, 421, 531, 533, 630, 637, 639, 659
 Consolidation ratio, 48, 228
 Contact element, 470, 507, 538
 Container wall, 221, 223
 Continuum mechanics, 77, 435, 443, 603
 Convolution integral, 332, 334
 Convolution procedure, 406
 Corner frequency, 320
 Corrected blowcount, 33
 Corrected BPT blowcount, 42
 Correction coefficient, 349
 Correction factor, 30, 33, 148, 192, 248, 348, 382, 397, 426, 508
 Correction for the area of contact, 12
 Correlation coefficient, 63, 371, 400, 401
 Corrosion, 461, 463
 Corrosion allowance, 466
 Coulomb friction, 659
 Coulomb model, 7
 Coupled analysis, 260, 261, 568
 Coupled finite element analysis, 157
 Crack initiation, 649
 Crane vessel, 656
 Critical angle of incidence, 198
 Critical damping, 162, 288, 289, 331, 340, 348
 Critical excitation analysis, 185
 Critical flow regime, 305

- Critical length of pile, 477
 Critical level of repeated loading, 557
 Critical-state strength, 107
 Cross-hole test, 81, 193, 194, 203–206
 Crystalline rock, 346
 Cumulative distribution function, 371
 Cumulative frictional capacity, 551
 Cutoff frequency, 319, 320, 324
 Cyclic degradation, 99, 115, 494, 554
 Cyclic direct shear test, 217
 Cyclic loading, 13, 49, 53, 73, 75, 76, 78–81, 86, 90, 91, 93, 97–100, 108, 138, 139, 143, 191, 227–229, 250, 252, 253, 259, 431, 432, 462, 466, 474, 492–494, 496, 498–503, 506, 509, 512, 554–556, 558, 605, 607, 615
 Cyclic pore pressure component, 227
 Cyclic resistance ratio, 237, 240, 241
 Cyclic strain approach, 237, 248
 Cyclic stress approach, 237, 240, 248
 Cyclic stress ratio, 237, 238, 240
 Cyclic torque, 211
 Cyclic torsional shear test, 217
 Cyclic triaxial test, 217
 Cylindrical friction sleeve, 36
- D**
 DAF-to-FRF ratio, 355
 Damping, 75, 76, 78, 80, 81, 86–89, 91–93, 95–97, 99–103, 107, 113, 114, 129, 130, 133, 134, 136, 138, 139, 144, 145, 162, 163, 165, 171, 172, 178, 180, 183, 186, 189, 191, 204, 214–218, 283, 284, 286, 288, 290, 291, 294, 301, 304, 306, 327, 329, 336–344, 346, 348–351, 356, 432, 437–441, 443–451, 472, 502, 571, 576, 577, 580, 581, 583, 615
 Damping correction factor, 339, 348
 Damping ratio, 77, 90, 91, 93, 94, 96, 97, 101, 130, 141, 142, 162, 177, 211, 218, 289, 292, 327, 329, 331, 339, 348, 349, 583, 617
 Dams, 42, 158, 190, 215, 251, 252, 254–256, 379, 455, 481
 Dashpot, 144, 436–438, 446, 447, 503, 519, 579–582
 Deaggregation, 163, 167, 378, 385–389, 400, 403, 405
 Deconvolution, 129
 Decoupled analysis, 259, 261
 Deep soil mixing, 249
 Defocusing, 146
 Degradation strain threshold, 91
 Degree of water-saturation, 10
 Depth of transition, 489, 600
 Design ground acceleration, 406, 407, 570, 583
 Design response spectrum, 159, 168, 169, 174, 175, 339, 342, 392
 Design spectrum, *see* Design response spectrum
 Deterministic analysis, 363, 368
 Deterministic Seismic Hazard Analysis, 364, 367
 Diffraction forces, 306
 Dilatancy, 76, 105, 143, 547
 Dilatancy angle, 26, 104
 Dilatometer test, 210
 Dimensionless frequency, 503, 579, 581, 616
 Dimensionless soil parameter, 52
 Dirac delta function, 332
 Direct analysis approach, 113, 178, 579
 Direct Scaling, 169, 173
 Direct shear test, 24, 25
 Disaggregation, *see* Deaggregation
 Dishpan scour, *see* global scour
 Disjoining effect, 12
 Dispersed seismic activity, 370
 Disrupted soil slides, *see* Rock falls
 Dominant frequency of excitation, 502, 616
 Donut hammer, 34
 Double resonances, 116
 Doubly asymptotic multi-directional boundary, 188
 Down-hole test, 81, 193, 204–207, 237
 Downward drag, 637, 639
 Downward friction, 637
 Drag anchor, 642, 643
 Drag coefficient, 303, 305, 311
 Drag embedment anchor, 643
 Dragon-king, 410
 Drainage, 6–8, 11, 25–28, 49, 81, 227, 249, 250, 413, 416
 Drainage system, 49, 50
 Drained behavior, 6, 551
 Drift correction, 361
 Drift Phenomenon, 357
 Drilled pile, 457
 Drilled shaft, 413, 455, 459
 Drilling, 31, 37, 38, 41, 53, 55, 126, 192, 202, 204, 207–210, 269–272, 276, 280, 413, 457, 459, 460, 462, 464, 545, 610–612, 619, 622
 Driven anchor piles, 642
 Drucker-Prager, 76, 77, 104, 105
 Ductile system, 632
 Ductility-modified spectrum, 329, 354, 355

- Duhamel's integral, 335
 Dutch qc value, 550
 Dynamic compaction, 249
 Dynamic modulus of elasticity, 628
- E**
- Earthquake input energy, 576
 Earthquake scenarios, 363, 365, 367, 403, 406
 Edge effect, 609
 Effective cohesion, 257, 421, 430, 534
 Effective diameter, 551
 Effective duration, 315
 Effective normal stress, 19, 83, 85, 245, 430
 Effective octahedral stress, 83
 Effective shear strain, 133
 Effective stress, 4, 7–12, 17, 18, 20–22, 26, 46, 51–53, 75, 76, 81, 84, 100, 105, 107, 138, 139, 143, 211, 227–229, 240, 249, 250, 254, 257, 429, 430, 461, 534–536, 541, 561, 563, 599–601, 607, 637, 639, 658
 Effective surface, 644, 645
 Elastic half-space, 131, 435, 441, 612, 620
 Elastic method, 481
 Elastic response spectrum, 329, 355
 Elastic zone, *see* Active zone
 Elasto-plastic, 44, 77, 105
 Elasto-plastic material law, 45, 507
 Elementary boundaries, 188
 Element integration points, 652–654
 Embankment, 421, 460, 631
 Embedded side surface area, 522
 End bearing capacity, 232, 234, 552, 554, 659
 End-bearing piles, 465, 570, 571, 605
 End-bearing resistance, 460, 522, 529, 540, 541, 552, 554
 Endurance time analysis, 185, 467
 Energy-absorbing boundary, *see* local absorbing boundary
 Energy radiation, 435, 436
 Energy-transmitting boundary, *see* local absorbing boundary
 Environmental and operational load, 299
 Environmental load, 498, 669
 Epistemic uncertainties, 368
 Equal-probability-of-exceedance design spectra, *see* Uniform Hazard Spectrum
 Equilibrium approach, 427
 Equilibrium of momentum, 332
 Equilibrium scour depth, 595, 596
 Equivalent foundation radius, 443, 445
 Equivalent length (height) of pile-structure system, 476, 477
- Equivalent linear material parameters, 89
 Equivalent linear soil model, 132, 134, 136, 138, 143
 Equivalent viscous damping, 86, 438
 Erosion, 3, 20, 47, 302, 589, 590, 593, 594, 596
 Expansive clay, 640
 Exploratory Drilling Structure, 269
 Explosive compaction, 249
- F**
- Factored load, 58, 59
 Factored resistance, 58, 59
 Factor of safety, 56, 71, 245, 246, 254–259, 568, 648, 669
 Failure criterion, 105, 467, 659
 Failure surface, 30, 60, 63, 64, 66, 67, 252, 254, 259, 426
 Far-field, 181, 188, 518, 521, 565, 580, 587
 Fast Fourier Transformation, 325
 Fatigue, 57, 58, 72, 284, 297, 298, 466, 467, 469, 649–651
 Fatigue damage, 283, 285, 466, 467, 555, 594, 649–651
 Fatigue limit state, 56, 670
 Fault geometry, 363, 370
 Fault mechanism, 342, 370
 Fault rupture, 109–111, 118, 187, 263, 265, 328, 370–372, 375, 392, 565, 566
 Field testing, 421, 463, 464, 665
 Fines, 5, 242, 247, 248, 250, 534
 Finite difference method, 251, 255, 256, 521, 619
 Finite element analysis, 50, 114, 147, 152, 157, 162, 167, 178, 179, 256, 259, 415, 472, 554, 581, 595, 621, 652, 659
 Finite element free-field site response, 157
 Finite element method, 6, 113, 137, 157, 219, 251, 255, 443, 471, 481, 521, 579, 619, 658
 First blade excitation period, 282
 First-order-reliability index, 65, 66
 First-order reliability method, 62, 65
 Flexural rigidity, *see* Bending stiffness
 Floating production system, 641
 Flooded member, 309
 Flow, 6, 107, 134, 246, 250, 263, 264, 270, 303–305, 308, 331, 432, 486, 488–490, 516, 589, 591, 595, 596
 Flow rule, 76, 97, 104
 Focusing, 146, 148
 Forerunner, 641–643, 645
 Foundation's lateral stiffness, 479

- Foundation impedance, 177, 178, 181, 182, 184, 301, 437, 439, 440, 444, 446, 504, 579, 583
- Fourier amplitude, 126, 181, 260, 284, 286, 318–322, 324, 325
- Fourier analysis, 318
- Fourier series, 317, 318, 321, 322
- Fourier series expansion, 133
- Fourier spectrum, 315, 318, 319, 321, 322, 337, 361
- FPSO, 269, 270, 275
- Fracture mechanics, 58, 649
- Free-field, 157, 178, 180, 182, 183, 219–221, 444, 446, 470, 565, 568–571, 587, 623, 663
- Free-field motion, 180, 569, 575
- Frequency dependence, 96, 136, 181, 439, 503, 574
- Frequency dependent stiffness function, 437, 446
- Frequency domain, 82, 96, 113, 115, 129, 137, 139, 157, 178, 189, 190, 202, 315–317, 319, 337, 361, 446, 584, 649
- Frequency-independent amplification, 148
- Frictional capacity coefficient, 535
- Friction fatigue, 546, 553
- Friction ratio, 36
- Froude-Kriloff force, *see* Froude Krylov force
- Froude Krylov excitation force, 303
- Froude number, 596
- Fugro-05, 37, 546–548, 551–553
- Full-probabilistic method, 69
- Fully coring, 543, 544
- Fully elastic, 104
- Fully plastic, 104, 105, 554
- Fully saturated, 6, 7, 10, 28, 494
- G**
- Gaussian random number generator, 68
- GBS, 44, 45, 49, 108, 182, 183, 190, 230, 270, 272–275, 284, 285, 309, 414–416, 432, 439, 440, 444, 445, 447, 449, 462, 655, 665, 670
- General scour, *see* global scour
- General shear, 416–421, 426
- Geologic evidence, 363
- Geometric spreading, 109
- Geophone, 192, 195, 207
- Geophysical test, *see* low-strain field test
- Geotechnical earthquake engineering, 31, 35, 186, 189, 468, 582, 670
- Global approach, 467, 469
- Global scour, 590, 598
- Grains, 3, 8, 10, 541
- Grain size, 75, 215, 421, 463, 464, 537, 562, 589
- Granular soil, 3, 4, 12, 237
- Gravel, 3–6, 18, 26, 31, 34, 35, 39, 42, 43, 82, 215, 249, 250, 537, 589, 594, 607, 657
- Gravel drains, *see* Stone columns
- Gravity based foundation, 275
- Ground loss, 623
- Ground motion prediction equation, 163
- Ground response analysis, 113, 179, 180
- Groundwater, 6, 421, 464, 639
- Group efficiency factor, 606
- Grout connection, 625, 627
- Gutenberg-Richter recurrence law, *see* Gutenberg-Richter relationship
- Gutenberg-Richter relationship, 370–372, 374, 381, 390
- Guyed tower, 273
- H**
- Half-power/bandwidth method, 214
- Half-space, 183, 184, 440, 442, 443, 579
- Hammer efficiency, 33
- Hardening, 7, 91, 97, 103–105
- Hardening plasticity, 105
- Hardening soil model, 7, 105
- Hard growth, 311
- Harmonic complex force, 436
- Hashiguchi model, 104
- Hasofer-Lind safety index, 66, 67
- Heaving, 47
- Hidden mass effects, 439
- Highly-plastic clays, 531
- High-rise pile-cap foundation, 618, 633
- Historical seismicity, 363, 390
- Homogenous zone model, 370
- Horizontal amplification factor, 159
- Horizontal equivalent acceleration, 259
- Hot-spot stress, 650, 652–654
- Hybrid method, 185
- Hydrate films, 12
- Hydraulic suction pump, 459
- Hydrodynamic damping, 299, 301, 304, 308
- Hydrodynamic interaction, 303
- Hypocentral distance, 370, 375
- Hysteresis loop, 78, 79, 88, 580
- Hysteretic damping, 86, 87, 97, 437, 505, 565, 580, 582, 587
- Hysteretic material damping, 580
- I**
- IBPT method, 42
- ICP-05, 37, 546–549, 552, 553
- Illite, 4, 22

- Impedance contrast, 132, 134, 663
 Impulse source, 196, 207
 Impulsive response, 333
 Incident wave
 Inclined piles, 629–631, 633, 635
 Incremental dynamic analysis, 185, 467
 Incremental filling ratio, 544
 Individual beam stiffness, 479
 Inertia coefficient, 304–306, 309
 Inertia interaction, 177, 179, 184
 Inertia force, 283, 294, 301, 303–305, 309, 352–354
 Inertial force, 565, 567
 Inertia loading, 107, 108, 428, 450, 559, 565–567, 570, 582
 Inertia mass, 439, 447
 Infinite boundary, *see* local absorbing boundary
 Inherent variability, 73
 Initial bedding stiffness, 497, 509, 510, 512
 Initial bedding stiffness coefficient, 512
 Initial loading curve, *see* Backbone curve
 Initial modulus of subgrade reaction, 496, 507–509, 600
 Initial shear modulus, 44, 76, 98, 107, 495, 582
 Initial stiffness, 437, 493, 497, 508, 512, 517
 Initial stress condition, 26, 27
 Initial stress conditions, 81, 103, 191
 Initial yield, 104
 Inner pile wall friction resistance, 523
 In-place performance, 73, 465
 Instrumental seismicity records, 363
 Inter-particle contact, 9
 Inverse of soil flexibility matrix, 620
 Irregular ground surface, 114, 146, 155
 Iterative algorithm, 469
- J**
- Jacket, 269–273, 275, 277, 278, 280, 281, 284, 286, 288, 289, 294–296, 300, 303, 306, 308, 309, 312, 313, 466, 473–475, 529, 530, 555, 556, 584, 586, 591, 592, 601, 603, 632, 665, 666, 670
 Jacket platform, 313, 556
 Jackups, 269, 300
 Joint distribution, 382, 400, 401
 Joyner-Boore distance, 372
- K**
- Kanai-Tajimi model, 326, 328
 Kanai-Tajimi power spectral density function, *see* Kanai-Tajimi model
 Keulegan-Carpenter (KC) number, 305
 Kaolinite, 4, 22
- Kelvin element, 188
 Kelvin-Voigt solid, 114, 128, 129, 144
 Kelvin-Voigt solid model, 144
 Kinematic force, 462, 566, 567
 Kinematic hardening, 103, 104
 Kinematic interaction, 113, 141, 177, 179–181, 184, 189, 565, 568, 569, 577, 578, 631, 647
 Kinematic interaction factor, 179, 189
 Kinematic loading, 82, 565–567, 569, 570, 572, 575, 577, 579
- L**
- Laboratory element test, 211
 Laminar container, 222, 223
 Λ -method, 461, 535
 Land-based structure, 300
 Landslides, 251, 256, 260, 262–265
 Large strain regime, 89
 Lateral earth pressure coefficient, 534, 536, 599, 639
 Lateral load, 459, 477, 481, 487, 493, 559, 604, 609, 614
 Lateral pile displacement, 502, 580, 614, 616
 Lateral resistance capacity, 465
 Lateral spread, *see* lateral spreading
 Lateral spreading, 231–234, 630
 Layered inelastic shear beam method, 157
 Leading row piles, 611
 Length-to-diameter ratio, 25, 481, 536, 607, 655, 664
 Lift force, 303, 307
 Limit equilibrium, 29, 251, 252, 254, 256, 257
 Limiting unit end resistance, 537, 541
 Limit state, 56, 115, 554
 Linear (areal) source, 370
 Linear correlation coefficient, 401
 Linear differential equation, 287, 436
 Linearized point, 66
 Linear threshold shear strain, 89, 90
 Liner correction factor, 33
 Link plate, 646
 Liquefaction, 5, 9, 13, 31, 33, 49, 75, 100, 125, 139, 227–234, 236, 237, 239–250, 256, 259, 262, 264, 421, 427, 428, 462–464, 498, 566, 567, 639
 Liquefaction potential, 22, 42, 77, 217, 231, 236, 237, 245, 465, 670
 Liquid index, 23
 Liquid limit, 23
 Liquid state, 23, 227
 Load cell, 24
 Load-deflection curve, 613

- Loading frequency, 94, 201, 212, 215, 294, 297, 309, 503, 615
 Load resistance factor design, 56, 553, 648
 Load scaling factor, 415
 Local absorbing boundary, 188
 Local scour, 590–592, 597, 598, 600
 Local Shear, 416–419
 Logic tree method, 391
 Log-linear dependence, 649
 Lognormal distribution, 62, 400
 Long and flapping weed, 311
 Longitudinal stiffener, 656
 Long-term probability distribution, 649
 Loss factor, 214
 Low cycle fatigue, 649
 Lower bound, 57
 Lower-tail quantile, 72
 Low-permeable fine-grained soils, 11
 LRFD, 56–59, 62, 69–71, 425, 475, 553, 648, 669
 Lumped mass, 127, 151, 178, 438, 439, 441, 442, 445, 446, 448, 449, 663
- M**
- Macroseismic intensity, 407
 Magnitude scaling factor, 243
 Margin of safety, *see* Safety margin
 Marine growth, 301, 306–309, 311–313
 Masing behavior, 99
 Masing rule, 97, 99
 Mass matrix, 144, 145, 438
 Material damping, 90, 92–94, 96, 110, 580
 Material strength, 57, 71, 357, 466
 Maximum Considered Earthquake, 365, 367
 Maximum credible earthquake, 366, 408
 Maximum horizontal equivalent acceleration, 259
 Maximum scour depth, 590, 595, 596
 Maximum shear modulus, 80, 82–84, 98, 100
 Maximum shear stiffness, 182
 Maximum shear strain response, 133, 134
 Maximum skin friction, 525, 539
 Mean compressive strength, 628
 Mean flow velocity, 596
 Mean principal effective stress, 83
 Mean value, 58, 60, 62, 63, 69, 70, 72, 159, 175, 321, 367, 376, 400, 401
 Measurement error, 73
 Medium strain regime, 89
 Memoryless model, 378
 Micro-seismicity, 193
 Middle line, 641
 Mindlin equation, 603
 Mineral particles, 3
- Mine tailings, 29
 Mini-tension leg platform, 270
 Mobile mooring, 649
 Modal damping, 101, 102, 437, 446, 447, 449–451
 Modal mass participation, 294, 300
 Modal matrix, 450
 Model test, 220, 224
 Modified Cam-Clay, 7, 104, 105
 Modified Duncan-Chang, 104, 105
 Modulus reduction curve, 79, 80, 91, 93, 94, 99, 141, 211
 Mohr's circle, 14–17
 Mohr's envelope, 421, 430
 Mohr–Coulomb, 20, 104, 105, 658, 659
 Mohr–Coulomb failure, 24
 Mohr–Coulomb failure criterion, 18, 19, 45, 507
 Moment magnitude, 238, 239, 242, 243, 260, 265, 631
 Monopile, 278, 280, 281, 477–479, 484, 499, 500, 502, 505–508, 510, 512, 589, 590, 592–594, 670
 Mono-pile system, 275, 280, 511, 583, 593, 617, 623, 631, 632, 641, 642, 662, 667
 Monotonic loading, 103, 191, 227
 Monotower, 602
 Monte Carlo simulation, 68
 Montmorillonite, 4, 22
 Moored tension leg, 270
 Morison's equation, 303, 306
 Most probable value, 72
 Moving resonance, 125, 126, 293
 Mud, 5, 208, 233, 480
 Mud slide force, 491
 Multi-degrees-of-freedom, 144, 145
 Multiple points of excitations, 219
 Multi-surface concept, 76
 Mustang Island field test, 511
- N**
- Natural frequency, 44, 102, 125, 213, 214, 274, 279, 286, 290, 291, 293, 294, 302, 313, 327, 328, 336, 447, 450, 479, 498, 504, 593, 594
 Natural-Time-Weibull (NTW) model, 410
 Near-field, 181, 502, 518, 565, 580
 Negative friction, *see* Downward friction
 Negative skin friction, 637, 639, 640
 Neo-deterministic seismic hazard assessment, 365, 406
 Net bearing capacity, 425
 Newmark displacement, 262
 Newmark sliding block approach, 256

- Newtonian fluid, 229
 NGI-05, 37, 546–548, 551–553
 Nodal relative acceleration, 145
 Nodal relative displacement, 145
 Nodal relative velocity, 145
 Nodal stress, 652
 Nominal diameter, 645
 Nominal factor of safety, 70
 Nominal relative density, 551
 Nominal stress, 652
 Non-associated flow rule, 104
 Non-associative flow rule, 76
 Non-destructive test, 192
 Non-flooded members, 310
 Non-Gaussian, 69, 184
 Non-homogeneous equation, 289
 Non-linear dynamic time domain analysis, 22, 185, 316
 Nonlinear Safety Margin Function, 65
 Non-linear static pushover analysis, 185
 Nonlinear Winkler Foundation, 469
 Non-liquefiable sand layer, 430
 Non-oscillatory motion, 288
 Non-reversible displacement
 Non-verticality, 663
 Normalized cone tip resistance, 551
 Normalized residual, 337
 Normalized shear modulus, 79–81, 93
 Normally consolidated, 20, 47, 74, 83, 104, 105, 513, 531, 532, 534, 535, 557, 599, 639
 Normal moveout, 195, 196
 Notch stress, 652
 Nullah, 421
 Nyquist frequency, 322, 323
- O**
- Obstruction, 311, 595
 Oedometer test, 421
 Offshore environment, 303
 Offshore structures, 55, 74, 75, 91, 185, 269–271, 275–278, 291, 299–304, 306–309, 393, 396, 431, 438, 456, 460, 462, 463, 466, 494, 498, 501, 504, 524, 529, 576, 591, 594, 596, 598, 609, 615, 641, 649, 652, 665, 669
 Offshore wind energy, 282, 593
 Offshore wind turbine, 280, 282, 430, 486, 497–499, 502, 590, 597, 600, 618, 633, 666
 One-dimensional site response analysis, 114, 127, 128, 132, 134, 141, 142, 146, 149, 152, 154, 156, 179
 Open-ended pile, 460, 522, 543
- Organic muck, 29
 Overall seabed movement, 590, 591
 Overburden correction factor, 33, 244
 Overburden pressure, 8, 9, 33, 37, 47, 126, 182, 210, 224, 228, 237, 241, 244, 249, 420, 422, 425, 444, 445, 480, 486, 489, 494, 505, 524, 529, 533, 538, 541, 639
 Over-consolidated, 20, 21, 23, 26, 47, 49, 105, 259, 529, 532, 535, 557, 609, 665
 Over-consolidation ratio, 46, 47, 75, 76, 80–82, 94, 95, 220, 561
 Over-consolidation ratio exponent, 83, 84
 Overlapping zone, 605
- P**
- Padeye, 645–649, 651, 653, 654, 661
 Parseval's theorem, 321
 Partially-plugged, 543, 544
 Partially plugged mode, 522
 Partially saturated soils, 6
 Partial safety factor, 57, 70–72, 670
 Particular solution, 289, 290, 436
 Passive zone, 417
 Path effect, 109
 Peak ground acceleration, 117, 121, 134, 135, 161, 344, 346, 348, 356, 376, 377, 380, 383, 570
 Peak ground displacement, 122, 344, 346, 358
 Peak ground velocity, 122, 344, 346, 348
 PEER, 168, 175, 394
 Penetration, 31, 32, 35–39, 42, 81, 84, 207, 210, 241, 242, 246, 421, 460, 462, 465, 466, 505, 524, 542–545, 620–622, 655, 657, 658, 664, 667, 668
 Penetration depth, 281, 500, 543, 545, 548, 552, 555, 631, 655, 657, 659, 664
 Perfect plasticity, 259, 560
 Perfectly elastic, 76
 Performance based design, 115, 185
 Permanent-displacement analysis method, *see* Newmark sliding block approach
 Permanent mooring, 649, 667
 Permanent pore pressure component, 227
 Phase difference, 202
 Physicochemical forces, 12
 Pier, 233, 455, 559, 596
 'Piggy-back' pile, 480
 Pile, 36, 37, 42, 46, 50–53, 55, 71–74, 82, 157, 181–183, 232–234, 271, 275, 278, 280, 286, 302, 309, 345, 414, 445, 450, 455–477, 479–519, 521–530, 532–587, 589–592, 594–623, 629–635, 637–640, 647, 648, 650, 651, 655–659, 662–665, 669, 670

- Pile cap, 473, 634
 - Pile cap connection, 632
 - Pile cap location, 597
 - Pile clusters, 625
 - Pile diameter to wall thickness ratio, 466
 - Pile displacement ratio, 547, 550
 - Pile driving, 51, 52, 58, 193, 455–457, 459, 460, 462, 465, 467, 475, 527, 529, 537, 543–545, 550, 553, 607, 619, 622, 623, 664
 - Pile group, 310, 462, 466, 471, 473, 502, 505, 529, 530, 558, 564, 583, 587, 597–599, 601, 602, 604–613, 615–618, 620, 631–634, 639, 670
 - Pile hammer, 455, 459
 - Pile impedance, 579, 581
 - Pile installation, 456, 461, 466, 480, 491, 533, 534, 539, 543, 622, 640
 - Pile jacking, 456–458, 619
 - Pile loading test, 515, 581
 - Pile penetration, 302, 533, 535, 543, 544, 592, 604, 610
 - Pile plug, 551
 - Pile reinforcement, 460, 630, 632
 - Pile sleeve, 465, 601, 603, 625
 - Pile spacing, 466, 502, 604, 605, 607, 608, 610, 613–617, 620
 - Pile stiffness matrix, 620
 - Pile-structure connections, 465
 - Pile-tip effect, 511, 512
 - Pile wall-soil friction, 460
 - Pile wall thickness, 466, 550, 632
 - Piping actions, 415, 432
 - Plastic equilibrium, 417
 - Plasticity index, 17, 23, 30, 34, 52, 76, 80, 81, 83, 89, 90, 94–96, 141, 142, 230, 236, 513, 640
 - Plastic limit, 23, 659
 - Plastic soil behavior, 76
 - Plastic state, 23, 422
 - Plastic strain, 97, 104, 105, 649
 - PLAXIS soft soil, 104, 105
 - Plugged condition, 523, 544, 551
 - Plugging ratio, 544
 - P-multiplier, 612, 613, 617
 - Poisson's ratio, 44, 45, 75, 104, 127, 128, 183, 191, 201, 432, 435, 441, 445, 471, 507, 512, 561, 573, 580, 581, 585
 - Poisson model, 378
 - Poisson process, 378, 379
 - Poisson's ratio, 42, 44, 75, 104, 127, 128, 183, 191, 201, 432, 441, 445, 471, 507, 512, 561, 573, 580, 581, 585
 - Polyester cable, 643
 - Pore water, 432
 - Porosity, 11
 - Positively buoyant, 270
 - Post-earthquake slope instability, 262
 - Power spectral density, 44, 45, 324, 325, 327, 328
 - Power spectrum, 44, 122, 315, 316, 325–329, 337, 361
 - Power spectrum density, 321
 - P-reduction factor, *see* p-multiplier
 - Pre-plastic state of strain, 612
 - Prescriptive design codes, 115
 - Pressuremeter test, 210, 463
 - Pretension load, 645
 - Primary consolidation, 46, 217
 - Principal stress, 15, 19, 26–28, 44, 46, 77, 104, 228, 420, 491, 654
 - Principal stress axes, 103
 - Probabilistic analysis, 73, 363, 368, 670
 - Probabilistic seismic hazard analysis, 367, 340
 - Probability-based seismic design, 185
 - Probability density function, 59, 60, 63, 64, 66, 67, 70, 72, 371, 372, 375
 - Probability of failure, 56, 59, 60, 62, 67, 69–71, 262, 396, 397, 467, 553, 554, 648
 - Production structures, 269
 - Pseudo-acceleration spectrum, 335
 - Pseudo-relative-velocity spectrum, 335
 - Pseudo-static analysis approach, 251–253, 259, 261
 - Pseudo-static displacement, 617
 - Pseudo-velocity spectrum, *see* Pseudo-relative-velocity spectrum
 - P-SV wave, 148
 - Pumping capacity, 664
 - Punching shear analysis, 465
 - Punching shear failure, 416, 419, 420, 425, 426
 - P-wave, 121, 124, 152–154, 161–163, 192, 193, 195, 196, 201, 203–205, 208, 209, 580, 581, 584, 615, 617
 - p-y, 46, 472, 475, 482–487, 491–497, 501–505, 507–518, 539, 579–581, 583, 592, 595, 600, 612, 613, 615–617, 659
- Q**
- Q-z, 472, 475, 522, 541, 542
- R**
- Radial shear zone, *see* Transition zone
 - Radiation damping, 110, 130, 188, 206, 436–439, 443, 446, 447, 449, 519, 522, 565, 571, 580, 581, 663

- Raft stress, 50
 - Raked piles, *see* Inclined piles
 - Random vibration analysis, 185
 - Rankine zone, 422
 - Rayleigh damping, 97, 101, 102, 450, 587
 - Rayleigh energy method, 479
 - Rayleigh wave, 192, 200–202
 - Receiver, 194, 195, 199–202, 204–206
 - Rectangular footing, 414, 415, 418, 442
 - Recurrence interval, *see* Return period
 - Reduced friction angle, 509
 - Reduction factor, 100, 133, 239, 354, 355, 425, 444–446, 573, 576, 599, 613, 639
 - Reduction phase, 469
 - Reference breaking strength, 651
 - Reference depth, 180, 508, 509, 513
 - Reference stress, 33, 46, 248
 - Reference time, 52
 - Reflection, 80, 126, 153, 154, 194–197, 200, 221, 538
 - Refracted waves, 197, 198
 - Refraction, 80, 126, 151–154, 198, 200
 - Region constant, 370
 - Relative density, 31, 36, 84, 244, 426, 496, 502, 504, 537, 538, 548, 550, 552, 562
 - Reliability index, 60, 64–67
 - Reloading, 78, 97–100, 494
 - Remotely operated underwater vehicle, 459
 - Remotely operated vehicle, 657
 - Remote subsea well, 270
 - Remoulding, 494, 534
 - Resonant column test, 81, 211–216
 - Resonant frequency, 212, 474
 - Response spectrum, 115, 117, 126, 134, 142, 143, 159, 169–171, 173, 175, 181, 185, 315, 316, 328–331, 336–339, 341–343, 351, 355, 357, 361, 367, 386, 392, 393, 399, 400, 404, 438, 450, 501, 569
 - Response spectrum analysis, 117, 132
 - Restoring term, 306
 - Re-tracking phase, 469
 - Return period, 57, 159, 163, 175, 185, 298, 329, 365, 366, 377–381, 384, 386, 392, 393, 396–400, 406–408, 415, 494, 555, 610, 645
 - Reversal loading, 98, 103
 - Reversal strain, 98
 - Reynolds (Re) number, 305, 307, 309, 596
 - Reynolds number, 305
 - Rigid-block method, *see* Newmark sliding block approach
 - Rigid perfectly plastic, 76
 - Ring stiffener, 658
 - Rock falls, 264
 - Rock outcrop, 110–113, 116, 126, 128–132, 134, 141–144, 159–161, 168, 169, 174, 179, 180, 384, 582
 - Rod length correction factor, 33
 - Roesset's site response amplification, 130, 131
 - Rotation stiffness, 479
 - Row reduction factor, 611, 614
 - Rupture mechanism, 109, 110, 375
- S**
- Safety hammers, 33
 - Safety margin, 56, 59, 60, 62, 63, 65–67, 71
 - Sample disturbance, 22
 - Sand, 3–6, 8–11, 13, 17–19, 23, 26, 34, 35, 43–46, 48, 49, 51, 57, 74, 76, 81, 82, 84, 105, 106, 137–141, 227–230, 232, 233, 242, 246, 247, 250, 302, 418, 420, 424, 426, 430, 483, 484, 486, 487, 490, 495–498, 500–504, 507–509, 516, 521, 522, 524–526, 529, 532, 535–539, 544, 545, 548, 550–552, 554, 555, 557, 561, 562, 569, 589, 591, 594, 607, 614, 633, 657, 659, 664, 665
 - SASW, 193, 201–203
 - Saturated soil, 5, 6, 8–10, 193, 230
 - Saturation, 7, 75, 80, 92–94
 - Scale invariance, 371
 - Scaling factor, 169, 173, 327, 349, 574
 - Scenario-based methodology, 407
 - Scour, 281, 302, 415, 421, 433, 463, 464, 480, 491, 589–601, 665, 670
 - Scour depth, 302, 589, 590, 592, 594, 595, 597–600
 - Seabed, 11, 37, 40, 53, 73, 110, 111, 117, 126, 134, 142, 143, 159–161, 164, 165, 174, 175, 177, 179, 180, 274, 277, 278, 280, 281, 302, 432, 456, 459, 462, 513, 550, 589, 591, 594, 596, 598–600, 604, 641–643, 649, 651, 655–657, 659, 663–665, 667, 668
 - Seabed friction, 643, 644
 - Seabed irregularities, 664
 - Seabed protection, 433
 - Seabed slope, 663
 - Secant shear modulus, 78–80, 88, 89
 - Secant stiffness, 78, 497, 580, 583
 - Secondary consolidation, 47
 - Second blade excitation period, 282
 - Second-order-reliability index, 65, 67
 - Sediment source, 47
 - Seepage flow, 657
 - Seismic cone penetrometer test, 193
 - Seismic Hazard Analysis, 111, 113, 343, 363, 364, 373, 374, 384, 406

- Seismic hazard curve, 375, 376, 382, 383, 392, 395–397, 399
- Seismic hazard map, 175, 392, 393, 399
- Seismic reserve capacity factor, 398
- Seismic source, 109, 365, 366, 370, 386
- Self-organized criticality, 374, 410
- Self-similarity, 371
- Semi-probabilistic method, 69
- Semisolid state, 23
- Semi-submersible, 276, 280, 645
- Sensitivity analysis, 58, 72, 77, 131, 174, 594
- Sensor, 81, 359
- Serviceability limit state, 56, 501
- Settlement, 46, 48–50, 55, 229, 234, 250, 418–421, 460, 463, 464, 467, 514, 605, 607, 608, 618, 630, 631, 637, 664
- Shadowing, 609, 611, 612
- Shaking table test, 218, 219, 221, 262
- Shale, 43, 82
- Shallow explosive, 192, 193
- Shear bands, 26
- Shear beam approach, 157, 158
- Shear box, 24
- Shear failure, 13, 17–20, 417–421, 426, 630
- Shear force, 24, 483–485, 567, 568, 576, 632
- Shearing stage, 27, 29
- Shear modulus, 8, 43, 44, 47, 48, 75–79, 81, 83, 90–94, 97, 100, 107, 108, 118, 127–129, 133, 134, 136, 138, 139, 141, 180, 182, 183, 191–193, 212–217, 228, 229, 248, 432, 435, 440, 441, 444–446, 559–563, 572, 573, 582, 583
- Shear strain, 43, 44, 76–82, 88–90, 92–95, 98, 100, 107, 108, 129, 133, 134, 137–139, 141, 143, 192, 193, 211, 214, 215, 217, 218, 223, 228, 242, 248, 249, 561, 571, 572, 574, 575, 580
- Shear strain amplitude, 76, 79, 81, 580
- Shear strength, 4, 8, 11, 12, 17–22, 24, 26, 28–30, 44, 47, 51, 52, 72, 74, 97, 98, 100, 106, 107, 217, 227–229, 251, 252, 254, 255, 262, 419, 421, 422, 426, 428–431, 461, 463–465, 488, 495, 512, 513, 515, 521, 524, 531, 533–535, 540, 541, 545, 555, 561, 563, 589, 596, 611, 639, 644, 658
- Shear stress, 13–15, 17–21, 24–26, 43, 77, 78, 88, 92, 94, 100, 128, 134, 143, 227–230, 237–240, 244, 245, 252, 254, 302, 429, 430, 507, 509, 556, 560–563, 575, 589, 596, 617
- Shear wave velocity, 35, 75, 80, 82, 83, 92, 116–120, 126, 130, 132, 134, 140, 145, 162, 183, 194, 201, 202, 204, 211, 213, 237, 246–248, 349, 350, 439, 442–446, 503, 571, 582, 583, 616, 617
- Shear zone, 609
- Shrinkage limit, 23
- Shrink-swell potential, 23, 640
- SH wave, 114, 128, 148, 152–154, 179, 180, 183, 184, 192, 203, 207, 615
- Signal processing, 123, 194, 195, 202
- Silent boundary, *see* local absorbing boundary
- Silt, 3–5, 18, 31, 43, 45, 48, 51, 82, 230, 236, 250, 537, 538, 544, 557
- Similitude, 218, 224
- Simplified fatigue assessment method, 649
- Simplified static coefficient method, 185
- Single-degree-of-freedom, 145
- Single degree-of-freedom oscillator, 329
- Single pile failure, 467, 605, 607
- Single Point Anchor Reservoir, 641
- Single point anchor reservoir platform, 270
- Site conditions, 5, 123, 124, 136, 137, 154, 160, 161, 164, 200, 244, 294, 297, 299, 364, 428, 544
- Site effect, 34, 109, 112, 151, 157, 168, 320, 364, 365, 405, 406
- Site investigation, 71, 546, 594
- Site period, 102, 110, 116–120, 131, 134, 136–138, 140, 230, 260, 293, 350, 450, 570, 576, 582
- Site response amplification, 131
- Site-specific response analysis, 167
- Site specific response analysis, 113, 350, 357, 363
- Skeleton, 4, 8, 12, 90, 193
- Skeleton curve, *see* Backbone curve
- Skempton's method, 540
- Skew angles of flow, 597
- Skin friction resistance, 461, 522
- Skirt pile, 480, 601, 665
- Skirt suction pile, 666
- Sleeve friction, 36, 540
- Sleeve resistance, 36
- Slenderness ratio, 497
- Slender tubular member, 303
- Sliding-overturning system, 630
- Sliding region, 26
- Slip plane, 18, 420, 430
- Slope instability, 76, 251, 252, 256, 259, 261
- Sloping, 114, 146, 155, 244
- Sloping layer boundaries, 114, 146, 155
- Slotted drain pipe, 250
- Small strain regime, 89, 90, 191
- S–N curves, 58, 72, 649–652
- Soft growth, 311
- Soft-soft design, 282, 283

- Soft-stiff design, 282
- Soil amplification, 254, 350, 365
- Soil-bedrock velocity contrast, 149
- Soil condition, 49, 134, 271, 477, 486, 494, 542, 554, 581, 657
- Soil consistency, 22
- Soil densification, 249, 250
- Soil factor, 348, 570
- Soil gap, 609
- Soil layer, 8, 35, 114, 118–120, 126, 128–130, 133, 136–138, 141, 143, 145, 148, 154, 162, 180, 182, 195, 198–200, 203, 234, 237, 239, 246, 327, 426, 429, 430, 444–446, 465, 476, 522, 546, 548, 571–573, 575, 607, 633, 637
- Soil plasticity, 80, 81, 465, 467, 474
- Soil profile, 3, 4, 12, 34, 102, 113, 116, 131–134, 141, 146, 174, 194, 238, 443, 552, 583, 584
- Soil stiffness, 35, 43–46, 76, 80, 89, 90, 92, 93, 103, 108, 120, 160, 191, 195, 237, 432, 443, 447, 476, 481, 482, 494, 505, 507–509, 513, 569, 571, 583
- Solid state, 23
- Solution phase, 469
- Source distance, 162, 260, 372
- Source effect, 109
- Source-to-site distance, 109, 110, 124, 125, 152, 167, 170, 175, 337, 363–368, 370, 372, 374, 375, 399, 400
- Spectral acceleration, 157, 164, 170, 253, 260, 302, 309, 337, 342, 375–377, 384, 386, 388, 389, 393, 394, 396, 398–403, 501, 594, 631
- Spectral amplification factor, 346
- Spectral analysis of surface waves, 193, 201
- Spectral bounds, 346
- Spectrum/spectral matching, 44, 161, 164, 168–171, 173, 181, 186, 187, 235, 315–322, 324, 325, 327, 331, 336, 337, 339, 341–344, 346–348, 351–357, 361, 376, 377, 383, 384, 392, 403–405, 649
- Spread footing, 413–415, 429, 618
- Spring-to-ground element, 447
- SPT-N value, *see* N-values, SPT blow-counts
- Spudcan, 620–622
- Squat structure
- SSI, *see* Soil-structure interaction
- Stability diagram, 558
- Stable crack-growth, 649
- Standard deviation, 60, 68, 342, 364, 367, 375, 400, 402, 404, 583, 597
- Standard normal cumulative distribution function, 375
- Standard normal distribution function, 60, 61
- Standard penetration test, 17, 24, 31
- State boundary surface, 104
- Static modulus of elasticity, 628
- Static shear stress correction factor, 244
- Static stiffness, 437–440, 442, 446, 504
- Stationary Gaussian type motion, 325
- Stationary process, 315, 316
- Statistical regression, 110
- Steady-state response, 436
- Steel cable, 643
- Stepped beam, 477–479
- Stiffness matrix, 101, 145, 181, 469, 670
- Stiff-stiff design, 282
- Stochastic dynamics, 316
- Stone columns, 249, 250
- Storage structure, 269
- Strain-based approach, 649
- Strain-compatible shear moduli, 182
- Strain-controlled, 28, 90
- Strain-dependent, 511, 561
- Strain rate, 22, 75, 76, 81, 82, 97, 106–108, 115, 224, 251, 262, 431, 503, 555
- Strain transmissibility function, 574
- Strength parameters of soils, 19
- Stress-based approach, 649
- Stress-deformation analysis approach, 251, 261
- Stress-dependent, 45, 105
- Stress path, 76, 227, 431
- Stress reduction factor, 238, 239
- Strip footing, 413, 414, 422, 424, 427
- Structural/geometric stress concentration factor, 652
- Structural health monitoring, 302
- Structural integrity, 637
- Subgrade impedance, 113, 184
- Subgrade reaction, 469, 477, 496, 505, 506, 571, 572
- Subgrade reaction constant, 476, 477
- Submerged member, 311
- Subsea pipeline, 666
- Subsea structure, 661
- Sub-structure, 281
- Substructure approach, 113, 178, 179, 183, 189, 467
- Subsurface irregularities, 146, 149, 150
- Subsurface profile, 421, 463, 464
- Suction anchor pile, 659
- Suction caisson
- Suction embedded plate anchor, 642
- Suction pile, 157, 462, 655–664, 667
- Sudden subsidence, 299, 302
- Surcharge pressure, 422
- Surface irregularities, 146

- Surface reflection test, 193–195, 197, 200
 Surface refraction test, 193, 196, 197, 199, 200, 206
 Surface roughness, 305, 306, 311, 325, 539
 Surface topographic effects, 148
 Surface wave, 114, 123, 125, 152, 154, 200, 202, 203, 243, 293, 341, 565
 Suspension logging test, 193, 208–210
 SV-wave, 152–154, 203–205, 615
 S-wave, 124, 192, 193, 196, 203, 205, 206, 208, 209, 580
 Swelling, 47
 System damping, 349, 437
- T**
- Tangential displacement, 560
 Tangent shear modulus, 78, 79
 Target probability of failure, 399
 Target spectrum, 169, 170, 357, 404
 Taut mooring system, 641, 642
 Taylor series, 65
 Tectonic evidence, 363
 Tectonic movement, 315
 Tension buoyant tower, 275
 Tension leg platform, 641, 664
 Terzaghi–Peack equivalent depth approach, 51
 Thermal excitation, 47
 3-step method, 179, 180, 189, 262, 578
 Time-dependent model, 380
 Time domain, 82, 178, 189, 190, 316, 317, 321, 472, 504, 584, 649
 Time history method, 316, 356, 357
 Tip resistance, 36, 37, 72, 84, 237, 280, 521, 522, 525, 552, 599, 609, 657
 T–N curve, 649–651
 Top line, 641
 Topple, 263
 Torsional moment, 559, 561–563, 601
 Torsional resistance capacity, 465
 Total scour depth, 597, 598
 Total stress, 7–9, 11, 20–22, 26, 139, 143, 228, 239, 254, 430, 541, 639, 658
 Total stress method, *see* α -method
 Total unit weight, 10, 22, 426
 Trailing pile row, 611
 Transfer function, 129–131, 137, 183, 184
 Transformation uncertainty, 73
 Transitional zone, 104
 Transition piece, 280
 Transition zone, 417
 Transparent boundary, *see* local absorbing boundary
 Trapezoidal footing, 414
 Triaxial compressional test, 24
 Tripod, 278, 280, 281, 601, 602, 656, 666
 Tuned mass damper, 298
 Tunnel excavation, 623
 Turbidite sequence, 74
 Two-surface model, 104
 T–z, 472, 475, 522, 539, 540, 559, 563, 595, 600, 615, 617
- U**
- Ultimate distributed pressure, 417
 Ultimate ductile failure, 649
 Ultimate effective pressure, 421, 425
 Ultimate limit state, 56, 73, 396, 501
 Ultimate load method, 481
 Ultimate resistance, 486, 488, 489, 496, 497, 501, 509
 Ultimate resistance coefficient, 488, 514–516
 Ultimate torque, 563
 Unconditionally stable, 145
 Unconsolidated–undrained (UU) test, 20, 28
 Under-consolidated, 47, 531, 533
 Undrained condition, 6, 7, 44, 90, 91
 Undrained soft clay model, 7
 Unified Scaling Law, 374
 Uniform cyclic strain, 248, 249
 Uniform Hazard Spectrum, 168, 377, 382, 393, 399
 Uniform stress cycles, 239, 242, 243
 Unit impulse response procedure, 332
 Unit skin friction, 522, 536, 545, 547, 552
 Unloading, 21, 78, 80, 90, 97–100, 103, 105, 502, 555, 590
 Unplugged condition, 523, 550
 Unplugged pile, *see* fully coring
 Unplugged piles, 523, 524
 Unstable crack-growth, 649
 Upper bound, 356, 367
 Upward movement, 640
 UWA-05, 37, 546–553
- V**
- Vane shear test, 17, 22, 24, 29, 210, 463, 464
 Vertical gravel drains, 250
 Vertical impact, 192, 193, 204
 Vertically loaded anchor, 643
 Vertically-sensitive geophone, 195, 197
 Very small strain regime, 89
V/H spectra, 162–164
 Vibratory hammer, 455
 Vibro-compaction, 249
 Viscous damper, 87, 435
 Viscous damping matrix, 103, 145
 Void ratio, 10, 45, 76, 80–85, 92, 93, 95, 105, 107, 211

- Voids, [3–6](#), [8](#), [10](#), [11](#), [46](#)
- Volume preserving deformation, [26](#)
- Volumetric component, [5](#)
- Volumetric cyclic threshold shear strain, [89](#), [90](#)
- Volumetric sources, [370](#)
- Von-Mises, [76](#), [77](#)
- Von Mises stress, [648](#)

- W**
- Wöhler curve, *see* S-N curve
- Water column, [12](#), [162](#), [165](#), [302](#)
- Water content, [22](#), [23](#), [34](#)
- Water particle acceleration, [303](#)
- Water particle velocity, [303](#)
- Water Table , [236](#)
- Water table, [8](#), [10](#), [22](#), [46](#), [47](#), [75](#), [82](#), [207](#), [236](#), [241](#), [422](#), [496](#), [497](#), [637](#)
- Wavelet analysis., [185](#)
- Wave load, [286](#), [500](#)
- Wave scattering, [109](#), [121](#), [123](#), [162](#)
- Wedge failure, [486](#), [489](#)
- Welded connections, [652](#)
- Weld imperfection, [652](#)
- Wharf, [630](#)
- Windowed filter process, [361](#)
- Winkler non-linear springs, [584](#), [585](#), [659](#)
- Winkler spring, [481](#), [516](#), [568](#), [571](#)
- Wire, [210](#), [559](#), [642–646](#), [651](#)
- Wöhler curve, *see* S-N curve
- Working stress design, *see* Allowable stress design

- Y**
- Yielded zone, [609](#)
- Yield surface, [97](#), [103](#), [104](#)
- Y-modification method, [617](#)
- Young's modulus, [42](#), [43](#), [104](#), [471](#), [476](#), [483](#), [513](#), [515](#), [570](#), [571](#), [573](#), [582](#), [584](#), [585](#)

- Z**
- Zero displacement boundary conditions, [188](#)
- Z-modifier, [617](#)